

Advanced Combustion Systems and Fuels

2017 Annual Progress Report

Vehicle Technologies Office

(This page intentionally left blank)

Disclaimer

This report was prepared as an account of work sponsored by an agency of the United States government. Neither the United States government nor any agency thereof, nor any of their employees, makes any warranty, expressed or implied or assumes any legal liability or responsibility for the accuracy, completeness, or usefulness of any information, apparatus, product, or process disclosed or represents that its use would not infringe privately owned rights. Reference herein to any specific commercial product, process, or service by trade name, trademark, manufacturer, or otherwise does not necessarily constitute or imply its endorsement, recommendation, or favoring by the United States government or any agency thereof. The views and opinions of authors expressed herein do not necessarily state or reflect those of the United States government or any agency thereof.

Acknowledgements

We would like to express our sincere appreciation to Alliance Technical Services, Inc., and Oak Ridge National Laboratory for their technical and artistic contributions in preparing and publishing this report.

In addition, we would like to thank all the participants for their contributions to the programs and all the authors who prepared the project abstracts that comprise this report.

Acronyms

List of Abbreviations, Definitions, and Nomenclature

0D	zero-dimensional
124 TMB	1,2,4-trimethylbenzene
1D	one-dimensional
2D	two-dimensional
2MB25	25% by mass 2-methyl-1-butanol, 75% by mass EEE
2WD	two-wheel drive
3D	three-dimensional
<i>A</i>	normalization constant in the phi-sensitivity metric
ACEC	Advanced Combustion and Emission Control
ACI	advanced compression ignition
ACS	Advanced Combustion Systems
ADC	advanced distillation curve
ADC	analog to digital converter
AEC	Advanced Engine Combustion
AFIDA	Advanced Fuel Ignition Delay Analyzer
AFR	air–fuel ratio
AHRR	apparent heat release rate
AISI	American Iron and Steel Institute
AKI	anti-knock index
ALCC	ASCR Leadership Computing Challenge
ALE	arbitrary Lagrangian–Eulerian
AMECS	Accelerated Multi-Zone for Engine Cycle Simulation
AMT	automated manual transmission
ANL	Argonne National Laboratory
ANN	artificial neural network
ANR	ammonia-to-NO _x ratio
Ar	argon
ARB	Air Resources Board
ASCR	Advanced Scientific Computing Research

ASI	advanced spark ignition
ASME	American Society of Mechanical Engineers
aSOI	after the start of injection
ASOI	after the start of injection
ASOI _m	after the start of main injection
atdc	after top dead center
aTDC	after top dead center
ATDC	after top dead center
aTDC _f	after top dead center firing
atm	atmospheres
a.u.	arbitrary units
A.U.	arbitrary units
AVFL	Advanced Vehicles/Fuels/Lubricants
AW	antiwear
BATO	Bridgestone Americas Tire Operations
BDC	bottom dead center
BMEP	brake mean effective pressure
Bo	Bond number
BOB	blendstock for oxygenate blending
B.o.D	ball-on-disc
BP	boiling point
BRS	bio-reformate surrogate
BS BR	butadiene rubber
FC	brake specific fuel consumption
bTDC	before top dead center
BTE	brake thermal efficiency
BTU	British thermal unit
BU	Boston University
B-W	BorgWarner
C12	<i>n</i> -dodecanethiol
Ca	calcium

Ca	capillary number
CA	crank angle
CA10	crank angle at 10% mass fraction burned
CA50	crank angle at 50% mass fraction burned
CAC	charge air cooler
CAD	crank angle degree
CAN	Controller Area Network
CAS	combustion analysis system
CB	carbon black
CCC	$\text{CuO-CO}_3\text{O}_4\text{-CeO}_2$
CCD	charged-coupled device
CCE	closed cycle efficiency
CD	combustion duration
CDC	conventional diesel combustion
CD_{wa}	wind-averaged drag coefficient
Ce	cerium
CEI	controlled electronic ignition
CFD	computational fluid dynamics
CFP	capillary flow porometry
CFPH	central fuel property hypothesis
CFR	Cooperative Fuel Research
CFR	constant pressure flow rig
CH_4	methane
CHA	chabazite
CI	cast iron
CI	compression ignition
CI	confidence interval
CI	conversion inflection
CJ-4	API commercial engine service category
CLEERS	Cross-Cut Lean Exhaust Emissions Reduction Simulations
cm	centimeter

CMC	conditional moment closure
CMOS	complementary metal oxide semiconductor
CN:L	low cetane number fuels
CN:M/H	medium/high cetane number fuels
CO	carbon monoxide
CO ₂	carbon dioxide
COF	coefficient of friction
CoV	coefficient of variation
COV _{IMEP}	coefficient of variation in indicated mean effective pressure
COV IMEP	coefficient of variation in indicated mean effective pressure
CP25	25% by mass cyclopentanone, 75% by mass EEE
CPD	cells per diameter
CPFR	constant pressure flow rig
cpsi	cell per square inch
CPU	central processing unit
CP _{wa}	wind-averaged pressure coefficient
CR	common rail
CR	compression ratio
CRADA	cooperative research and development agreement
CT	computed tomography
Cu	copper
CVCC	constant volume combustion chamber
CW	continuous wave
d	day
D	diameter
dB	decibel
DBE	double bond equivalent
DBI	diffused background illumination
DBIEI	diffused back-illumination extinction imaging
dbTDC	degrees before top dead center
DC	duty cycle

DCN	derived cetane number
dCVC	degree of constant volume combustion
DDI-PFS	double direct injection partial fuel stratification
deg	degrees
DeG	degreened
DEGR	dedicated exhaust gas recirculation
DFI	ducted fuel injection
DGE	diesel gallon equivalent
DI	direct injection
DISI	direct injection spark ignition
DLC	diamond-like carbon
DMF20	20% dimethyl furan, 80% gasoline blend
DNS	direct numerical simulation
DOC	diesel oxidation catalyst
DOE	U.S. Department of Energy
DPF	diesel particulate filter
DRIFTS	diffuse reflectance infrared spectroscopy
DSE	duration of solenoid energizing
DSF	Dynamic Skip Fire
DTNA	Daimler Trucks North America
E10	10% ethanol, 90% gasoline blend
E20	20% ethanol, 80% gasoline blend
E30	30% ethanol, 70% gasoline blend
E85	85% ethanol, 15% gasoline blend
EATS	exhaust aftertreatment system
EAVS	electrically assisted variable speed supercharger
EB25	25% by mass ethylbenzene, 75% by mass EEE
ECN	Engine Combustion Network
EC	elemental carbon
ECU	engine control unit
ED	energy deposition

EDAX	X-ray energy dispersive spectroscopy
e-DEAC	electrically actuated cylinder deactivation
EEE	certification gasoline
EFA	Exhaust Filtration Analysis
e.g.	<i>exempli gratia</i> , “for example”
EGR	exhaust gas recirculation
EGR	exhaust gas residual
HER	exhaust heat recovery
EIHC	emissions index of hydrocarbons
EIVC	early intake valve closing
EO	engine-out
EOI	end of injection
EOPMB	end of pre-mixed burn
EP	extreme pressure
EPA	Environmental Protection Agency
EQR	equivalence ratio
ERC	Engine Research Center at University of Wisconsin–Madison
eSC	electric supercharger
ESS	energy storage system
EtOH	ethanol
eVOF	evaporation submodel
eWHR	electrified waste heat recovery
FACE	Fuels for Advanced Combustion Engines
FAged	field-aged
FBP	final boiling point
FDA	flame development angle
Fe	iron
FE	fuel efficiency
FEI	fuel economy improvement
FEM	finite element method
f-GnP _s	functionalized graphene nanoplatelets

FIB	focused ion beam
FID	flame ionization detector
FM	friction modifier
FMEP	friction mean effective pressure
FoV	field of view
FPF	front propagation formulation
FPS	functional precipitated silica
FREI	Flames with Repetitive Extinction and Ignition
FSN	Filter Smoke Number
ft	foot
FTE	freight ton efficiency
FTP75	Federal Test Procedure
ft/s	feet per second
$f_{\nu}L$	soot volume-fraction-path-length product
FWG	Fuels Working Group
FY	Fiscal Year
g	gravity
G	gap or standoff distance from injector orifice exit to duct inlet plane
GC	gas chromatograph
GCI	gasoline compression ignition
GDI	gasoline direct injection
GDCI	gasoline direct injection compression ignition
GHG	greenhouse gas
GHSV	gas hourly space velocity
GIE	gross indicated efficiency
GM	General Motors
GnPs	graphene nanoplatelets
GPF	gasoline particulate filter
GPU	graphics processing unit
GS	gasoline surrogate
GTL	gas-to-liquids derived fuels

H ₂	diatomic hydrogen
H ₂ O	water
H ₂ O ₂	hydrogen peroxide
H _{avg}	liftoff length averaged over injection duration
HC	hydrocarbon
HCCI	homogeneous charge compression ignition
HCT	hydrocarbon trap
HD	heavy-duty
HDD	deavy-duty diesel
HDS	highly dispersible silica
HECC	high efficiency clean combustion
HECO-SING	High-Efficiency Cost-Optimized, Spark-Ignited Natural Gas
H _{exh}	cycle exhaust enthalpy losses
HFIR	High Flux Isotope Reactor
HO ₂	hydroperoxyl radical
HoV	heat of vaporization
hp	horsepower
HPC	high performance computing
HPF	high performance fuel
HRM	homogeneous relaxation model
HR-MZ	momogeneous reactor–multi-zone model
HRR	heat release rate
HT	high temperature
HTA	hydrothermal aging
HTAged	hydrothermally aged
HTHR	high-temperature heat release
HTHS	high temperature high shear
HVAC	heating, ventilation, and air conditioning
HWY	highway
HWFET	Highway Fuel Economy Test
IAT	intake air temperature

IB20	20% iso-butanol, 80% gasoline blend
IBP	initial boiling point
ICCD	intensified charge-couple device
ICE	internal combustion engine
ID	ignition delay
IDT	ignition delay time
i.e.	<i>id est</i> , “that is”
IL	ionic liquid
IMEP	indicated mean effective pressure
IMEPg	gross indicated mean effective pressure
IMEPn	net indicated mean effective pressure
IQR	interquartile range
IQT	ignition quality tester
IR	infrared
ISCO	indicated specific carbon monoxide
ISFC	indicated specific fuel combustion
ISHC	indicated specific hydrocarbons
ISNO _x	indicated specific NO _x
ISPM	indicated specific particulate matter
J	joule
K	kelvin
KAUST	King Abdullah University of Science and Technology
kg	kilogram
KH-ACT	Kelvin-Helmholtz Aerodynamic Cavitation Turbulence
KH-RT	Kelvin-Helmholtz–Rayleigh-Taylor
kHz	kilohertz
KL	soot optical density on natural-logarithmic scale
KL	soot optical thickness
KL-CA50	knock-limited combustion phasing
KV	kinematic viscosity
KV100	kinematic viscosity at 100°C

KV40	kinematic viscosity at 40°C
kWh	kilowatt-hour
L	duct length
L	liter
LB	lattice Boltzmann
LBL	line-by-line
lbs	pounds
LCHP	low compression height piston
LD	light-duty
LDV	laser Doppler vibrometry
LE	Lagrangian–Eulerian
LED	light-emitting diode
LES	large eddy simulation
LFE	laminar flow element
LFS	laminar flame speed
LHT	low heat transfer
LHV	lower heating value
Li	lithium
LIVC	late intake valve closing
LLNL	Lawrence Livermore National Laboratory
LM	lean Miller cycle
LNF	lean NO _x filter
LNT	lean NO _x trap
LOO	leave-one-out
LS	least squares
LSPI	low speed pre-ignition
LST	stoichiometric air–fuel ratio
LSU	Louisiana State University
LT	low temperature
LTAT	Low Temperature Aftertreatment
LTC	low temperature combustion

LTGC	low-temperature gasoline combustion
LTHR	low temperature heat release
LTP	low-temperature plasma
LWP	long wave pass
MAT	mixture air temperature
MB	methyl butyrate
MBMS	molecular beam mass spectrometer
MBT	maximum brake torque
MD	medium-duty
MD	molecular dynamics
MFB50	50% fuel mass burned
Mg	magnesium
M/G	motor/generator
MH	maximum torque
mil	one thousandth of an inch
MIP	mercury intrusion porosimetry
ML	minimum torque
mm	millimeter
MoDTC	molybdenum dithiocarbamate
MON	Motor Octane Number
MPa	megapascal
mpg	miles per gallon
mph	miles per hour
MPI	Message Passing Interface
ms	millisecond
m/s	meters per second
MS	mass spectrometer
MSD	mean square displacement
MSF	modified surrogate fuel
MSS	microsoot sensor
MTU	Michigan Technological University

MUA	mercaptoundecanoic acid
MY	model year
N	newton
NA	naturally aspirated
NA	no additive
NEDC	New European Driving Cycle
NFPS	non-functional precipitated silica
NGA	turbulent combustion code initially developed at Stanford
NGC	next generation Cascadia
NH ₃	ammonia
NIOSH	National Institute of Occupational Safety and Health
NL	natural luminosity
NMR	nuclear magnetic resonance spectroscopy
NO	nitric oxide
NO _x	oxides of nitrogen
NP	nanoparticle
NPD	nanosecond pulsed discharge
NR	natural rubber
NREL	National Renewable Energy Laboratory
ns	nanosecond
NSFC	net specific fuel consumption
NTC	negative temperature coefficient
NUIG	National University of Ireland, Galway
NVO	negative valve overlap
O	atomic oxygen
O ₂	diatomic oxygen
O ₃	ozone
OASC	optically accessible spark calorimeter
OBD	on-board diagnostics
OBS	on-board sensor
OC	organic carbon

OC	oxidation catalyst
OCP	olefin copolymer
OEM	original equipment manufacturer
OES	optical emission spectroscopy
OFM	organic friction modifier
OH	hydroxyl radical
OI	octane index
OLCF	Oak Ridge Leadership Computing Facility
ORC	organic Rankine cycle
ORNL	Oak Ridge National Laboratory
OS	octane sensitivity
OSC	oxygen storage capacity
OSP	oil soluble polyalkylene glycol
P	phosphorus
PAG	polyalkylene glycol
PAH	polycyclic aromatic hydrocarbons
PAMA	polyalkylmethacrylate
PAO	poly(alphaolefin)
PAO4	poly(alphaolefin) 4 cSt
PB	particulate blackening
PC-11	Proposed Category 11 for heavy-duty engine oil
PCA	principle component analysis
PCN	piston cooling nozzle
Pd	palladium
PF	particulate filter
PFI	port fuel injection
PGM	platinum group metal
phr	part per hundred rubber
PIB	polyisobutylene
P_{in}	intake pressure
PIV	particle image velocimetry

PLIF	planar laser-induced fluorescence
PM	particulate matter
PMC	photon Monte Carlo
PMEP	pumping mean effective pressure
PMI	Particulate Matter Index
PNA	passive NO _x adsorber
PNNL	Pacific Northwest National Laboratory
PoE	polyol ester
ppm	parts per million
PPRR	peak pressure rise rate
PRF	Primary Reference Fuel
PRISME	Pluridisciplinaire de Recherche Ingénierie des Systèmes, Mécanique Énergétique
PSCCI	partially stratified charge compression ignition
psf	pounds per square foot
PSO	passive soot oxidation
P _{ST}	cylinder pressure at spark timing
PT	pressure–temperature
PTWA	plasma transfer wire arc
PXRD	power X-ray diffraction
Q _{HT}	cycle heat transfer losses
RA	road-aged
RANS	Reynolds-averaged Navier–Stokes
RCCI	reactivity controlled compression ignition
RCM	rapid compression machine
Re	Reynolds number
Rel int.	relative intensity
RF	radio frequency
RI	Ringing Intensity
RIM	refractive index matching
ROC	rate of consumption
RON	Research Octane Number

RPA	rubber process analyzer
rpm	revolutions per minute
RRC	rolling resistance coefficient
RSD	rainbow schlieren deflectometry
r.t.	room temperature
S	sensitivity
S	sulfur
S_ϕ	natural logarithm of the ignition delay ratio
SA	spark-assist
SA	spray angle
SAMR	scattering-absorption measurement ratio
SBR	styrene–butadiene–rubber
scm	standard cubic centimeters per minute
SCE	single-cylinder engine
SCO	selective catalytic oxidation
SCR	selective catalytic reduction
SCRf	integrated selective catalytic reduction and diesel particulate filter
SEC	size exclusion chromatography
SEM	scanning electron microscopy
SEN	octane sensitivity
sfRK	signal flow Runge–Kutta
SHC	synthetic hydrocarbon
SI	spark ignition
SiC	silicon carbide
SIDI	spark ignition direct injection
SM	stoichiometric Miller cycle
SMD	Sauter mean diameter
SnFs	silica nanofibers
SNL	Sandia National Laboratories
SOC	state of charge
SOI	start of injection

SpaciMS	spatially resolved capillary inlet mass spectrometry
SPH	smoothed particle hydrodynamics
Sr	strontium
SS	start–stop
SS	steady-state
SSE	start of solenoid energizing
ST	shock tube
ST1	SuperTruck 1
ST2	SuperTruck 2
SUNDIALS	SUite of Nonlinear and DIfferential/ALgebraic Equation Solvers
T	temperature
T	turbocharged
T10	temperature at which 10% of the fuel volume was recovered during a distillation
T_{50}	temperature at which a catalyst achieves 50% conversion of a particular species
T50	time to 50% maximum torque
T50	temperature at 50% fuel boiled
T50	temperature at which 50% of the fuel volume was recovered during a distillation
T_{90}	temperature at which a catalyst achieves 90% conversion of a particular species
T90	time to 90% maximum torque
T90	temperature at 90% fuel boiled
T90	temperature at which 90% of the fuel volume was recovered during a distillation
TAMU	Texas A&M University
TBD	to be determined
TBR	truck and bus radial tires
TCD	thermal conductivity detector
TCR	thermochemical recuperation
TDC	top dead center
TEM	transmission electron microscopy
TES 295®	Allison transmission fluid
tf	transfer function exponent
TFM	tabulated flamelet model

TFP	thin filament pyrometry
TG	test gasoline
TGA	thermogravimetric analysis
THC	total hydrocarbons
T_{in}	intake temperature
TMC	Test Monitor Center
TOST	Thermal Oxidative Stability Testing
TPRF	toluene + primary reference fuel
TR	time-resolved
TRF	toluene reference fuel
TSF	toluene standardization fuel
TWC	three-way catalyst
UA	University of Alabama
U/C	speed ratio
UCM	University of California, Merced
UConn	University of Connecticut
UDDS	Urban Dynamometer Driving Schedule
UDF	user defined function
$U_{fuel,exh}$	exhausted cycle fuel energy
ULSD	ultra-low sulfur diesel
U-M	University of Michigan
UPS	United Parcel Service
UQ	uncertainty quantification
US06	Supplemental Federal Test Procedure
USAXS	ultra-small angle X-ray scattering
V	volt
VCR	variable compression ratio
VGT	variable geometry turbocharger
VI	viscosity index
VII	viscosity index improver
VM	viscosity modifier

VN	vanadium nitride
VOF	volume of fluid
VP	vapor pressure
VSI	Vehicle Systems Integration Laboratory at Oak Ridge National Laboratory
VVL	variable valve lift
W	cycle work
WBG	wood-based biogasoline
WHR	waste heat recovery
WIES	wall-impinged expanding spray
WLTC	Worldwide harmonized Light vehicles Test Cycle
w/o	without
wt%	percentage by weight
ZDDP	zinc dialkyldithiophosphate
Zero-RK	Zero Order Reaction Kinetics software package
Zr	zirconium

List of Symbols

Å	angstrom
α	duct configuration with non-rounded inlet and non-tapered outlet
β	duct configuration with rounded inlet and non-tapered outlet
η	natural log of pressure
°	degrees
°aTDC	degrees after top dead center
°C	degrees Celsius
°CA	degrees crank angle
ΔP	peak pressure of LSPI event minus peak pressure of mean of non-LSPI
ΔP	total CVCV pressure rise during combustion
ΔT_{carb}	temperature drop across carburetor
γ	ration of specific heats
γ	duct configuration with non-rounded inlet and tapered outlet
>	greater than
λ	equivalence ratio (ratio of actual air-to-fuel ratio to stoichiometric air-to-fuel ratio)

<	less than
μg	microgram
μ_g	viscosity of the gas phase
μ_l	viscosity of the liquid phase
μL	microliter
$\mu\text{L}/\text{min}$	microliters per minute
μm	micrometer
μs	microsecond
%	percent
ϕ	equivalence ratio
ϕ_{crit}	critical equivalence ratio below which the mixture is too lean to burn
Φ	phi-sensitivity metric
ρ_{amb}	ambient density
ρ_g	density of the gas phase
ρ_l	density of the liquid phase
σ	surface tension
τ_1	ignition delay time for the leaner condition ($\phi = 0.25$)
τ_{max}	maximum ignition delay time (1 ms)
τ_{min}	minimum ignition delay time (1 ms)
τ_r	ignition delay time for the richer condition ($\phi = 0.5$)
ξ	1,000 K divided by temperature

Executive Summary

On behalf of the Vehicle Technologies Office (VTO) of the U.S. Department of Energy (DOE), we are pleased to introduce the Fiscal Year (FY) 2017 Annual Progress Report for the Advanced Combustion Systems and Fuels Program. The program supports VTO's goal for future U.S. economic growth by focusing early-stage research and development on improving the understanding of the combustion processes, fuel properties, and emission control technologies. The program generates knowledge and insight necessary for industry to develop the next generation of engines for the efficient, cost-effective, and secure transportation of people and goods across America.

Introduction of the next generation higher-efficiency, very-low-emission combustion engines for passenger and commercial vehicles is one of the most promising and cost-effective approaches to improving the fuel economy of the U.S. vehicle fleet. Advanced fuel formulations that can incorporate non-petroleum-based blending agents could further enhance engine efficiency and provide fuel diversification. The expected national economic, environmental, and energy security benefits from these next generation engines and fuels would be significant since the vast majority of vehicles sold during the next several decades will still include an engine.

The Advanced Combustion Systems and Fuels Program supports VTO's goal and focuses early-stage research and development (R&D) to improve understanding of the combustion processes, fuel properties, and emission control technologies while generating knowledge and insight necessary for industry to develop the next generation of engines. Innovations in combustion, fuels, emission control, air control, turbomachinery, and energy recovery could potentially increase fuel efficiency considerably compared to today's vehicles. The program has set the following goals for passenger and commercial vehicle fuel economy improvements.

- By 2030, improve light-duty engine efficiency to demonstrate 35% improvement in passenger vehicle fuel economy (25% improvement from engine efficiency and 10% from fuel optimization), relative to a 2015 baseline vehicle.
- By 2030, improve heavy-duty engine efficiency by 35% relative to a 2009 baseline vehicle and identify cost-effective high-performance fuels that can further increase efficiency up to an additional 4%.

This report highlights progress achieved by the Advanced Combustion Systems and Fuels Program during FY 2017. The nature, current focus, and recent progress of the program are described. Included are abstracts of national laboratory, industry, and university projects that highlight the exciting work being conducted to address critical technical barriers and challenges to commercializing the next generation of higher-efficiency engine, emission control, and fuel technologies for passenger and commercial vehicles.

Gurpreet Singh, Program Manager
Advanced Combustion Systems and Fuels Program
Vehicle Technologies Office

Kenneth C. Howden
Vehicle Technologies Office

Kevin Stork
Vehicle Technologies Office

Roland M. Gravel
Vehicle Technologies Office

Michael Weismiller
Vehicle Technologies Office

Table of Contents

Acknowledgements	ii
Acronyms	iii
List of Abbreviations, Definitions, and Nomenclature	iii
List of Symbols	xx
Executive Summary	xxii
Vehicle Technologies Office Overview	1
Vehicle Technologies Office Organization Chart.....	1
Advanced Combustion Systems and Fuels Program Overview	2
Introduction	2
Goals	2
State of the Art	2
Current Technical Focus Areas and Objectives	4
Technical Highlights	6
Invention and Patent Disclosures	28
I. Combustion Research	29
I.1 Light-Duty Diesel Combustion.....	29
I.2 Heavy-Duty Low-Temperature and Diesel Combustion and Heavy-Duty Combustion Modeling.....	36
I.3 Spray Combustion Cross-Cut Engine Research	43
I.4 Low-Temperature Gasoline Combustion (LTGC) Engine Research	50
I.5 Gasoline Combustion Fundamentals	58
I.6 Advancements in Fuel Spray and Combustion Modeling with High Performance Computing Resources	65
I.7 Fuel Injection and Spray Research Using X-Ray Diagnostics	72
I.8 RCM Studies to Enable Gasoline-Relevant Low Temperature Combustion.....	77
I.9 Advances in High Efficiency Gasoline Compression Ignition	82
I.10 Advanced Ignition Systems for Gasoline Direct Injection (GDI) Engines.....	86
I.11 High Efficiency Clean Combustion in Light-Duty Multi-Cylinder Engines	93
I.12 Stretch Efficiency for Combustion Engines: Exploiting New Combustion Regimes.....	98
I.13 Neutron Imaging of Advanced Transportation Technologies	104
I.14 Chemical Kinetic Models for Advanced Engine Combustion.....	111
I.15 Model Development and Analysis of Clean and Efficient Engine Combustion.....	117
I.16 Improved Solvers for Advanced Combustion Engine Simulation.....	122
I.17 2017 KIVA-hpFE Development: A Robust and Accurate Engine Modeling Software	128
I.18 Accelerating Predictive Simulation of Internal Combustion Engines with High Performance Computing.....	136
I.19 Large Eddy Simulation Applied to Advanced Engine Combustion Research.....	141

I.20	Development and Validation of Predictive Models for In-Cylinder Radiation and Wall Heat Transfer	145
I.21	Model Development for Multi-Component Fuel Vaporization and Flash Boiling	151
I.22	Spray-Wall Interaction at High-Pressure and High-Temperature Conditions.....	157
I.23	Development and Validation of a Lagrangian Soot Model Considering Detailed Gas Phase Kinetics and Surface Chemistry.....	166
I.24	Development and Validation of Physics-Based Sub-Models of High Pressure Supercritical Fuel Injection at Diesel Conditions.....	172
I.25	Development of a Physics-Based Combustion Model for Engine Knock Prediction	179
I.26	Development and Multiscale Validation of Euler–Lagrange-Based Computational Methods for Modeling Cavitation within Fuel Injectors	186
I.27	Turbulent Spray Atomization Model for Diesel Engine Simulations.....	193
II.	Co-Optimization of Fuels and Engines.....	198
II.1	Alternative Fuels DISI Engine Research: Autoignition Metrics.....	198
II.2	Studies of Research Octane Number (RON) and Heat of Vaporization (HoV).....	205
II.3	Improving Vehicle Fuel Economy Through Increasing Fuel Octane Ratings	210
II.4	Advanced Light-Duty SI Engine Fuels Research: Multiple Optical Diagnostics of Well-Mixed and Stratified Operation.....	215
II.5	Fuel Effects on EGR and Lean Dilution Limits on SI Combustion.....	222
II.6	Fuel Pressure Sensitivity and High-Load EGR Dilution Effects in SI Combustion.....	227
II.7	Fuel Effects on Emissions and Aftertreatment.....	233
II.8	Fuel Impacts on Emissions Control Performance and Durability	241
II.9	Fuel Impact on GDI PM Formation and Gaseous Emissions During Cold-Start	247
II.10	Fuel Contribution to PM from Kinetically-Controlled Combustion.....	252
II.11	Ignition Kinetic Experiments and Simulations to Support Advanced Engine Combustion Development.....	255
II.12	Fuel Effects on Low Speed Pre-Ignition.....	261
II.13	Fuel Effects on Combustion Stability and Noise for GCI	267
II.14	Autoignition Fundamentals of Fuels for Multi-Mode Boosted SI and LTGC Engines	272
II.15	Accelerate Development of ACI/LTC.....	279
II.16	Co-Optima Project E2.2.2: Accelerate Development of ACI/LTC, Fuel Effects on RCCI Combustion	284
II.17	Improved Mixing-Controlled Combustion Technologies and Fuels for High- Efficiency Compression Ignition Engines.....	290
II.18	Characterization of Biomass-Based Fuels and Fuel Blends for Low-Emissions, Advanced Compression Ignition Engines.....	296
II.19	Fuel Property Database	302
II.20	Fuel Property Blending Model.....	308
II.21	Kinetic Mechanism Development.....	312
II.22	Kinetic Mechanism Development and Validation	318
II.23	Small Volume Fuel Autoignition Reactor	322
II.24	Virtual Fuel Blend Optimization for Advanced Compression Ignition Engines	327

II.25	Dynamic Species Reduction for Multi-Cycle CFD Simulations	333
II.26	Micro-liter Fuel Characterization and Property Prediction	336
II.27	The Development of Yield-Based Sooting Tendency Measurements and Modeling to Enable Advanced Combustion Fuels	340
III.	Alternative Fueled Engines.....	346
III.1	Unconventional and Renewable Hydrocarbon Fuels.....	346
III.2	Single-Fuel Reactivity Controlled Compression Ignition Combustion Enabled by Onboard Fuel Reformulation	348
III.3	High-Efficiency Cost-Optimized Spark-Ignited Natural Gas (HECO-SING) Engines – 2017.....	354
III.4	Innovative Dual-Fuel Aftermarket Emissions Solution.....	361
III.5	Utilizing Alternative Fuel Ignition Properties to Improve SI and CI Engine Efficiency.....	365
IV.	Emission Control R&D.....	370
IV.1	Joint Development and Coordination of Emission Control Data and Models: Cross-Cut Lean Exhaust Emissions Reduction Simulations (CLEERS) Analysis and Coordination	370
IV.2	CLEERS Aftertreatment Modeling and Analysis	377
IV.3	Low-Temperature Emission Control to Enable Fuel-Efficient Engine Commercialization	384
IV.4	Emissions Control for Lean-Gasoline Engines.....	390
IV.5	Cummins-ORNL SmartCatalyst CRADA: NO _x Control and Measurement Technology for Heavy-Duty Diesel Engines.....	395
IV.6	Ash-Durable Catalyzed Filters for Gasoline Direct Injection (GDI) Engines.....	401
IV.7	Fuel-Neutral Studies of PM Transportation Emissions	407
IV.8	Next Generation Ammonia Dosing System.....	413
IV.9	Advanced Emission Control for High-Efficiency Engines.....	417
IV.10	Development and Optimization of a Multi-Functional SCR–DPF Aftertreatment System for Heavy-Duty NO _x and Soot Emission Reduction	422
IV.11	Metal Oxide-Based Nano-Array Catalysts for Low Temperature Diesel Oxidation.....	428
V.	High Efficiency Engine Technologies	436
V.1	Volvo SuperTruck 2: Pathway to Cost-Effective Commercialized Freight Efficiency.....	436
V.2	Cummins/Peterbilt SuperTruck II.....	442
V.3	SuperTruck 2 Advanced Combustion Development at Navistar	447
V.4	Improving Transportation Efficiency Through Integrated Vehicle, Engine, and Powertrain Research – SuperTruck 2	453
V.5	Ultra-Efficient Light-Duty Powertrain with Gasoline Low Temperature Combustion	458
V.6	High Efficiency Variable Compression Ratio Engine with Variable Valve Actuation and New Supercharging Technology: VCR Technology for the 2020 to 2025 Market Space.....	464
V.7	Lean Miller Cycle System Development for Light-Duty Vehicles.....	468
V.8	Improved Fuel Efficiency Through Adaptive Radio Frequency Controls and Diagnostics for Advanced Catalyst Systems.....	473
V.9	Integrated Boosting and Hybridization for Extreme Fuel Economy and Downsizing	481
V.10	Cummins 55% BTE Project.....	488

V.11	Solenoid Actuated Cylinder Deactivation Valvetrain for Dynamic Skip Fire	492
VI.	Lubricant Technologies.....	498
VI.1	Surface and Lubricant Interactions	498
VI.2	Compatibility of Lubricant Additives with Non-Ferrous Bearing Materials and Wear Mechanism in Sooted Engine Oils.....	505
VI.3	Technology Innovation: Base Fluids, Additives, and Coatings	513
VI.4	High Efficiency Lubricant Oils, Additives, and Coatings.....	518
VI.5	Lubricant Effects on PM Formation, Emissions Control, and Vehicle Fuel Economy	525
VI.6	Development of PAG (Polyalkylene Glycol)-Based Lubricant for Light- and Medium-Duty Axle Applications.....	530
VI.7	Power Cylinder Friction Reduction Through Coatings, Surface Finish, and Design	536
VI.8	Hybrid Ionic-Nano-Additives for Engine Lubrication to Improve Fuel Efficiency	541
VI.9	Integrated Friction Reduction Technology to Improve Fuel Economy Without Sacrificing Durability	547
VI.10	A Novel Lubricant Formulation Scheme for 2% Fuel Efficiency Improvement.....	554
VI.11	Improved Fuel Economy through Formulation Design and Modeling.....	562
VII.	System-Level Efficiency Improvement	567
VII.1	DOE's Effort to Improve Heavy Vehicle Fuel Efficiency Through Improved Aerodynamics	567
VII.2	Advanced Bus and Truck Radial Materials for Fuel Efficiency	575
VII.3	Improved Tire Efficiency Through Elastomeric Polymers Enhanced with Carbon-Based Nanostructured Materials.....	581
VII.4	Advanced Non-Tread Materials for Fuel-Efficient Tires	586
VII.5	Heavy-Duty Powertrain Optimization	591
VIII.	Index of Principal Investigators	597
IX.	Project Listings by Organizations	601

List of Figures

Figure 1 - Research areas within advanced combustion systems and fuels.....	5
Figure 2 - Example diffused back-illumination extinction imaging images using the original setup (top) and optimized setup (bottom). The light and dark regions in the top image are caused by beam steering and introduce significant error when attempting to quantify soot or liquid penetration in high-pressure sprays (Pickett, report I.3).....	7
Figure 3 - Vapor mass fraction contours through a cut-plane passing through a single orifice of Spray G showing the propensity of ethanol blends to flash boil significantly more than the pure components. The simulations were performed under the standard Spray G conditions from Engine Combustion Network. (Som, report I.6)	8
Figure 4 - Improved model of the spark channel elongation and energy deposition at non-quiescent flow conditions (Scarcelli, report I.10)	8
Figure 5 - Enthalpy fraction of H ₂ , CO, and CH ₄ at the catalyst outlet relative to the initial fuel with 700°C initial temperature for iso-octane (Szybist, report I.12)	9
Figure 6 - New constant pressure flow rig with air exhaust, injector cooling, and instrumentation installed (Agrawal, report I.24)	11
Figure 7 - Premixed flame propagation and end-gas ignition in a constant volume configuration. A base conditional moment closure front propagation formulation solver has been coupled with a large eddy simulation solver. Total enthalpy and density fields at the initial time (top) and when the ignition kernels have formed (bottom) are shown. (Kim, report I.25)	11
Figure 8 - Laser-based measurements allow the detection of fuel wall films for various combinations of fuels and operating conditions that are prone to pool fires (Sjöberg, report II.4).....	13
Figure 9 - Full factorial experimental design fuel matrix. Tested fuels are indicated by red dots; aromatic hydrocarbon vapor pressures are at 443 K. (Ratcliff, report II.7).....	13
Figure 10 - Schematic diagram of the heavy-duty, single-cylinder optical diesel engine and optical setup with infrared emission and visible natural combustion luminosity cameras (Musculus, report II.16).....	15
Figure 11 - Two-color soot pyrometry image processing. (Left) double image of burner showing tip in focus, no filters. (Middle) double image of flames at two wavelengths. (Right) Pixel-by-pixel intensity ratio on the left and calculated temperature on the right. (Agrawal, report II.18).....	16
Figure 12 - Example calculation of the constant volume ignition delay times (IDT) used to construct the phi-sensitivity metric for iso-octane (McNenly, report II.24).....	17
Figure 13 - CONVERGE computation fluid dynamics model of the diesel Ricardo Hydra engine (Lawler, report III.2).....	18
Figure 14 - Catalyst locations within small cross-sections of a commercial selective catalytic reduction filter (catalyst shown in red false color; note that inlet channels are larger and outlet channels are smaller in this asymmetric honeycomb filter design) (Wang, report IV.2).....	20

Figure 15 - Three-dimensional reconstruction of a small section of the C2 material from X-ray computed tomography data and an associated flow field (color key indicates local gas velocities in cm/s) (Stewart, report IV.7)..... 21

Figure 16 - Gen3 GDCI powertrain (Confer, report V.5)..... 23

Figure 17 - Critical hardware components (Battiston, report V.7)..... 23

Figure 18 - Electrically assisted variable speed electric waste heat recovery unit (Source: Eaton) (Patil, report V.9) 24

Figure 19 - Plasma transfer wire arc coated cylinder bores in a linerless engine block (Source: Ford Motor Company) (Gangopadhyay, report VI.7) 26

Figure 20 - Splitter plate dimensions and three-vehicle platoon in the Army 7 ft × 10 ft wind tunnel located at National Aeronautics and Space Administration Ames (Salari, report VII.1)..... 27

Figure 21 - ISX450 engine with UltraShift Plus automated manual transmission under test in the powertrain test cell at Oak Ridge National Laboratory’s Vehicle Systems Integration Laboratory (Deter, report VII.5) 28

Figure I.1.1 - In a diesel engine, increasing the work extracted by the piston is significantly more effective at improving thermal efficiency than reducing the amount of energy lost through the combustion chamber walls 31

Figure I.1.2 - Thermal efficiency (the fraction of fuel energy extracted as work) is higher with the stepped-lip piston for some injection timings. The efficiency differences correlate with differences in the degree of constant volume combustion. Wall heat loss does not change with piston bowl geometry in a significant way. 31

Figure I.1.3 - As the main injection timing is delayed, the combustion takes place later in the expansion stroke. Piston bowl geometry does not affect the first half of the combustion event (until CA50), but the second half of combustion is faster with the stepped-lip piston. 32

Figure I.1.4 - Comparison between fuel vapor concentrations measured experimentally by planar, laser-induced fluorescence of a fuel tracer (left), and fuel vapor concentration predicted by the CFD simulation (right). Results are shown in false-color for three horizontal cutting planes for the conventional bowl geometry (depicted at the bottom). The latest simulation results reliably predict vapor penetration above and into the piston bowl, as well as jet deflection by the swirling in-cylinder flow. 33

Figure I.1.5 - Simulated vertical-plane projection of flow fields (shown with colored vectors) and the fuel concentrations (false-colored field data) for the conventional (left) and stepped-lip (right) pistons. Yellow arrows have been added to indicate the motion of the fuel jets. Crank angles are shown in $CAD ASOI_m$ 34

Figure I.2.1 - Optical engine schematic showing LED beam path (propagating from top to bottom) and two-camera setup for simultaneous DBI and NL imaging 37

Figure I.2.2 - Mean PB for using various single- and post-injection schedules. 18% intake O_2 , 15.8 kg/m³ and 910 K TDC motored..... 38

Figure I.2.3 - KL evolution within the DBI FoV from ensemble-averaged images with post-injections of various DSE added to a main injection of 2,350 μs DSE, as indicated in the legend. 18% intake O_2 , 15.8 kg/m³ and 910 K TDC motored 38

- Figure I.2.4 - Correlation between the late-cycle FoV-averaged KL and engine-out PB data in Figure I.2.2 that have three replicates. Dotted lines show the 95% confidence interval. 39
- Figure I.2.5 - Composite graphic showing injector solenoid energizing schedule (top left), in-cylinder geometry (bottom left), soot KL measured by ensemble-averaged DBI (top row of images) and ensemble-averaged soot NL (bottom row of images). Each KL and NL row shows images with the single injection only (left), a load-equivalent schedule with a post-injection (middle) and a false-colored image of the difference in between the post- and single-injection images. The red dots and lines identify regions that are discussed in the text. 40
- Figure I.2.6 - Top row: measured 2D NL image (left), predicted 2D NL image (right), predicted three-dimensional (3D) soot distribution (right). Bottom row: transfer function map overlaid on measured NL (left), estimated experimental $f_v L$ (middle) and predicted 3D f_v distribution. 40
- Figure I.3.1 - Example DBIEI images using the original setup (top) and optimized setup (bottom). The light and dark regions in the top image are caused by beam steering and introduce significant error when attempting to quantify soot or liquid penetration in high-pressure sprays..... 45
- Figure I.3.2 - A collage of images demonstrating three high-speed, quantitative diagnostics. The liquid length and soot images were obtained using a Sandia-developed LED driver that generates unprecedented light intensity at high repetition rates, while the mixture fraction field used a newly developed 100-kHz pulse-burst laser. The mixture fraction and soot images correspond to the same time after start of injection (1.8 ms after start of injection) for 1,500 bar n-dodecane sprays injected into a 900 K, 60 bar ambient. All images are to scale. 45
- Figure I.3.3 - Instantaneous ensemble-averaged (top) and single-injection (bottom) liquid phase images, 2.5 ms after start of injection of Spray D (magenta) and Spray C (green) at standard non-reacting conditions. Measurements have been superimposed and distinguished using false color. The white region depicts where Spray D and Spray C overlap. 46
- Figure I.3.4 - Ensemble averaged reacting and non-reacting vapor penetration rate for Sprays D and C with error bars indicated. The nominal ambient conditions are stated in the figure. 46
- Figure I.3.5 - Scatter plots of the quasi-steady lift-off length (left) and ignition delay time (right) as a function of ambient temperature (top) and ambient density (bottom). The grey markers represent the Spray C data and the black markers represent the Spray D data. Because the SE cannot be resolved in the full axis, inset axes are provided in the top and middle panels with the mean values and the SE for select cases. The width of the boxed region indicates the error in the X-variable while the height indicates the error in the Y-variable. 47
- Figure I.4.1 - CA50 control using DDI-PFS to vary charge reactivity for a wide range of intake pressures for (a) CR = 16:1 and (b) CR = 14:1. The curves have been offset to align the CA50s for a second DI timing of 280°C. 0°C = TDC intake. $\phi_m = 0.36$, except for $P_{in} = 2.0$ bar with CR = 16:1 where $\phi_m = 0.4$. 1,200 rpm. All Pins are absolute. 52
- Figure I.4.2 - NO_x and PM measurements for the CA50 control sweeps in Figure I.4.1a. PM data are those provided by AVL smoke meter measurements..... 53
- Figure I.4.3 - (a) Spark timings required for SA to compensate for a reduction in T_{in} for $P_{in} = 1.0$ –1.3 bar, or to compensate for a reduction in intake O₂ for $P_{in} = 1.6$ bar. (b) Maximum T_{in} reductions below the CI-only point (DT) for which combustion phasing (and RI) can be maintained using SA. CR = 14:1; $\phi_m = 0.42$; 1,200 rpm. 0°C = TDC intake. 54

Figure I.4.4 - CA50 control authority with spark timing for $\phi = 0.38, 0.42, \text{ and } 0.45$ at $P_{in} = 1.0$ bar 55

Figure I.4.5 - Uncertainties in the cylinder pressure measurement through a typical engine cycle, (a) in kPa and (b) as a fraction of the total pressure 56

Figure I.5.1 - Fuel energy utilization breakdown for two low-load (1.4 and 3.0 bar indicated mean effective pressure [IMEP]) ACI operating points with a fixed 265 J fuel injection during the NVO period and the balance fuel energy injected early during the main period 59

Figure I.5.2 - Map of CA50 for a range of intake temperatures and O_3 concentrations with a fixed -230 °CA start of injection (SOI) and 1,000 rpm engine speed. Charge ϕ was maintained at 0.3, which produced an approximate 2.8 bar IMEP load. 60

Figure I.5.3 - Quantitative in-cylinder O_3 measurements compared to chemistry modeling results of O_3 and O 61

Figure I.5.4 - Measured apparent heat release rate and O_3 profiles compared to simulation O_3 results and important radicals (top). Model-predicted fuel ROC by O, OH, and HO_2 (bottom). Intake temperature was adjusted to get CA50 close to 4 °CA. 61

Figure I.5.5 - Pressure rise calorimetry for 20 kV LTP discharges at a 2.8 bar initial pressure and varying H_2O/CO_2 concentrations 62

Figure I.5.6 - Qualitative images of excited state O for two initial pressures along with a schlieren image of temperature gradients for a 20 kV LTP discharge (top) compared to VizGlow predictions of LTP discharge O and temperature distributions (bottom)..... 63

Figure I.6.1 - Gas phase axial velocity vs. time is plotted for simulations performed using both LES and RANS turbulence models compared against experimental PIV data obtained from Sandia National Laboratories in a constant volume vessel 67

Figure I.6.2 - Vapor mass fraction contours through a cut-plane passing through a single orifice of Spray G show the propensity of ethanol blends to flash boil significantly more than the pure components. The simulations were performed under the standard Spray G conditions from ECN. 67

Figure I.6.3 - Ignition delay vs. ambient temperature predicted using TFM and HR-MZ models and compared against experimental data from Sandia National Laboratories 68

Figure I.6.4 - Flame structure in terms of CH_2O , OH, and temperature predicted using TFM approach for both 750 K and 900 K cases. The stoichiometric mixture fraction line is also shown. 68

Figure I.6.5 - Ignition delay and flame lift-off lengths for a new four-component diesel surrogate mechanism developed and validated against experimental data from Army Research Laboratory 69

Figure I.7.1 - Simulations of flow through two diesel nozzles and the emerging liquid jets, courtesy of M. Battistoni at the University of Perugia. The results at left show the flow simulated using the nominal nozzle geometry. The results at right show the flow disturbances generated by the irregularities when using the realistic measured geometry. 73

Figure I.7.2 - A cutaway though a GDI injector measured using a combination of X-ray and neutron tomography. Five of the eight spray holes are visible at the center of the image..... 74

Figure I.7.3 - A cross section of the fuel density as the liquid jet emerges from a single-hole diesel injector 74

Figure I.8.1 - Experimentally measured (symbols) and modeled (lines) ignition delay times as a function of inverse temperature for FACE-F and various surrogate blends.....	79
Figure I.8.2 - Representative pressure–time histories for syngas/O ₂ /diluent mixture illustrating the influence of hot-spot ignited flames. Inset time-shifts pressure traces corresponding to τ_{ign} , highlighting slow pressure rise due to flame propagation.	80
Figure I.9.1 - Influence of turbocharger duty cycle (DC) upon engine efficiency.....	84
Figure I.9.2 - Influence of injection pressure upon smoke (FSN) and combustion noise.....	84
Figure I.10.1 - Improved model of the spark channel elongation and energy deposition at non-quiescent flow conditions.....	88
Figure I.10.2 - Impact of in-cylinder turbulence on the performance of laser ignition and conventional spark.....	88
Figure I.10.3 - Improved dilution tolerance with non-equilibrium plasma systems versus conventional spark (top) and occurrence of arc events during the non-equilibrium discharge (bottom).....	89
Figure I.10.4 - Effect of ambient conditions on the characteristics of the streamers (top) and transition from LTP to arc regime (bottom)	90
Figure I.10.5 - Qualitative comparison between modeling and experiments in terms of chemical (left) and thermal (right) LTP properties.....	91
Figure I.11.1 - Advanced combustion strategies shown as a continuum based on the level of fuel stratification at start of combustion.....	94
Figure I.11.2 - Concept of fuel reactivity stratification with single-fuel (GCI) to dual-fuel	95
Figure I.11.3 - CFD modeling of RCCI across a span of delta in fuel reactivities	95
Figure I.11.4 - Control authority of RCCI allows for rapid and stable mode switches	96
Figure I.12.1 - Schematic of the in-cylinder reforming process in which one cylinder has an isolated intake and exhaust, feeds the reforming catalyst, and is incorporated into the intake for the other three cylinders.....	99
Figure I.12.2 - Enthalpy fraction of H ₂ , CO, and CH ₄ at the catalyst outlet relative to the initial fuel with 700°C initial temperature for iso-octane.....	100
Figure I.12.3 - Transient response of the exit concentration of catalytic (Cat) reforming products and monolith temperature profile at an O ₂ catalyst flow rate of 12 g/min and $F_{catalyst} = 7$	101
Figure I.12.4 - PMEP as a function of intake manifold pressure for conventional EGR and catalytic reforming.....	101
Figure I.12.5 - Brake thermal efficiency as a function of intake manifold pressure for conventional EGR and the catalytic reforming strategy.....	102
Figure I.12.6 - In-cylinder temperature of (a) conventional SI combustion and (b) the dilute combustion strategy supported by reforming. The high dilution reduces in-cylinder temperature by more than 550 K.....	102

Figure I.13.1 - (a) Mass-attenuation coefficients versus atomic number, and (b) schematic of neutron imaging apparatus (Source: (a) Banhart [1], (b) Nanda et al. [2]).	104
Figure I.13.2 - System used to study intra-nozzle dynamics of fuel injection including (a) high-pressure fuel delivery system and (b) the aluminum spray chamber with optical viewport. The spray chamber is designed with (c) directed fans to minimize fuel buildup on the chamber walls and the fuel injector.	105
Figure I.13.3 - Detection and scaling of neutron attenuation by fluid to obtain cumulative injector spray mass.	106
Figure I.13.4 - (a) Sagittal slice of neutron CT data, with X-ray CT domain marked, and (b) internal fluid velocities from a computational fluid dynamics simulation (Courtesy of Argonne National Laboratory)	107
Figure I.13.5 - Results from successive GPF regeneration study to date for (a) E0 and (b) E30, including the recently imaged 60% regeneration state, with (c) comparison of activation energies for diesel- and gasoline-generated soot.	108
Figure I.13.6 - Neutron attenuation at various axial locations for a single channel both with the original field-loaded DPF (ash+soot) and after regeneration (ash only). Inset images show attenuation intensity in the channel at each axial location (brighter means more neutron attenuation).	108
Figure I.14.1 - Experimentally measured (symbols) and simulated (curves) IDTs of n-decane in shock tubes (Pfahl, Fieweger, and Adomeit 1996; Tekawade, Xie, and Oehlschlaeger 2017; Zhukov, Sechenov, and Starikovskii 2008). (Source: LLNL)	112
Figure I.14.2 - Experimentally measured (symbols) and simulated (curves) IDTs of decalin in a shock tube and RCM (Zhu, Davidson, and Hanson 2014; Oehlschlaeger et al. 2009; Wang et al. 2017). (Source: LLNL)	112
Figure I.14.3 - Measured (symbols) and simulated (lines) IDTs of a 1-methylnaphthalene (AMN)/n-dodecane stoichiometric blend for a pressure of 15 bar (Kukkadapu and Sung 2018) (Source: LLNL)	113
Figure I.14.4 - Simulated (lines) and experimentally measured (symbols) of IDTs for iso-octane. The dash lines are from the previous LLNL iso-octane detailed chemical kinetic model and the solid lines from the improved one. The symbols are measurements from the ANL RCM. P1, P2, P3 are different unspecified pressures. $P3 > P2 > P1$. (Source: LLNL)	114
Figure I.14.5 - Simulated (curves) and experimentally measured (symbols) IDTs for gasoline primary reference fuel PRF90. The symbols are experimental measurements from the ANL RCM. The dashed curves are from the previous chemical kinetic model and the solid curves are from the improved model. (Source: LLNL)	114
Figure I.14.6 - Simulated (lines) and experimentally measured (symbols) IDTs for TPRF for stoichiometric fuel/air mixtures at 20 bar. The dash lines are from the LLNL detailed chemical kinetic model for n-heptane, iso-octane, and toluene. The symbols are experimental measurements from a RCM (Javed et al. 2016). (Source: LLNL)	115
Figure I.15.1 - Improvement in emissions prediction as a function of simulation complexity. (a) Results for baseline simulations, (b) baseline simulations with more chemical detail, (c) baseline simulations with more chemical detail and higher mesh resolution (d) baseline simulations with more chemical detail, higher mesh resolution, and improved spray modeling	118

Figure I.15.2 - (a) Baseline and (b) revised estimates of in-cylinder pressure uncertainty in LTGC engine experiments	119
Figure I.16.1 - Parallel scaling efficiency of the adaptive preconditioner method applied to a fully-coupled, multi-species transport solver used to model the unsteady flame dynamics in a millimeter-scale flow reactor	124
Figure I.16.2 - Fraction of species in a detailed gasoline surrogate chemistry model that have a mass fractions below a specified extinction level over the course of a constant volume ignition delay calculation	125
Figure I.16.3 - The dormant order classification of the system states representing the species mass fraction composition and temperature evolution of iso-octane in a constant volume ignition delay calculation	125
Figure I.17.1 - Computational grid using GridPro and overset valve and piston surfaces. In close-up, the valves and the injector module are easily married to the cylinder domain.	130
Figure I.17.2 - Two-Port engine. (a) No valves showing the magnitude of velocity and the streamline of the fluid entering the intake port at 33° after top dead center and (b) two valves in ports, showing magnitude of velocity and vectors at 70° after top dead center.	131
Figure I.17.3 - Multiphase flow simulation with VOF method, gasoline injected into quiescent air at 3 bar. (a) Gasoline jet primary break-up into ligaments and (b) primary break-up and w-component of velocity of air showing recirculation.	131
Figure I.17.4 - The Spray G ECN case with the grid in cut-away showing the nozzles.....	132
Figure I.17.5 - The ECN Spray A case: injection of diesel in quiescent air at 1.97 MPa	132
Figure I.17.6 - KIVA-hpFE's ever increasing advantage in computational speed over KIVA-4mpi; at 0.38 s of simulation time, KIVA-hpFE is 1.44× faster (for the problem being solved by both systems with exactly the same settings)	133
Figure I.18.1 - Comparison of experimentally measured emissions index for NO _x and HC with simulation predictions using different levels of modeling detail. (Figure Credit/Source: K. Dean Edwards, ORNL)	138
Figure I.19.1 - Instantaneous cross-section of the scalar dissipation field showing modeled instantaneous fluctuations of the equivalence ratio versus time at two locations in the flow	143
Figure I.19.2 - Transient ignition sequence predicted by LES at conditions identical to the experiment	143
Figure I.20.1 - (a) Axial velocity and (b) temperature contours on horizontal slices at $z = -3.75$ mm and $z = -0.9375$ mm (distances below the head) at 346° after top dead center. (This is Figure 4 of Schmitt et al. 2016.)	147
Figure I.20.2 - Left: Schematic of the experimental setup for the Hencken burner spectral radiation measurements at the University of Michigan. Right: Measured infrared spectra for a one atmosphere stoichiometric methane–air Hencken burner flame with and without quartz.	147
Figure I.20.3 - Schematic of the metal engine configuration at ORNL.....	148
Figure I.20.4 - Schematic of a simplified spectral box model for high-pressure combustion systems. ...	148

Figure I.21.1 - Temporal history of multi-component droplet vaporization for ethanol–isooctane binary system under atmospheric pressure at 200°C (E0 = pure ethanol; E85 = 85% ethanol, 15% iso-octane by volume)	153
Figure I.21.2 - The density contours (a) iso-octane, (b) ethanol, (c) E30, (d) E85 across a horizontal plane placed 10 mm downstream of the injector tip when subjected to Spray G2 condition	153
Figure I.21.3 - Tower chamber and heating system (Source: University of Illinois at Urbana-Champaign).....	154
Figure I.21.4 - Spray evolution for flash and non-flash boiling at 400 K and varying injection (P_{inj}) and environment (P_{env}) pressures: (a) $P_{inj} = 2$ bar, $P_{env} = 0.5$ bar; (b) $P_{inj} = 5$ bar, $P_{env} = 0.5$ bar; (c) $P_{inj} = 8$ bar, $P_{env} = 6$ bar; and (d) $P_{inj} = 10$ bar, $P_{env} = 6$ bar	155
Figure I.21.5 - The droplet and film chamber components and system (Source: University of Illinois at Urbana-Champaign).....	155
Figure I.21.6 - Droplet diameter evolution during vaporization for various ethanol–iso-octane blends (E0: 0% ethanol, 100% iso-octane by volume; E100: 100% ethanol, 0% iso-octane by volume).....	156
Figure I.22.1 - The impinged spray radius (left) and the impinged spray height (right) versus ASOI with various ambient densities (14.8 kg/m ³ , 22.8 kg/m ³ , and 30 kg/m ³) (top) and various injection pressures (1,200 bar, 1,500 bar, and 1,800 bar) (bottom)	159
Figure I.22.2 - Effects of ambient density at injection pressure of 1,500 bar (left) and injection pressure at ambient density of 22.8 kg/m ³ (right) on film thickness	160
Figure I.22.3 - Effects of ambient density at injection pressure of 1,500 bar on heat flux at three locations	160
Figure I.22.4 - Comparison of axial (top) and radial (bottom) impinged spray quantities against experiments, O'Rourke and Amsden's model (OA), and new implementation (YW) based on Yarin and Weiss' theory	161
Figure I.22.5 - DNS results of the surface impingement of a train of 109-micron ethanol drops at non-splashing (top row) and splashing (bottom row) regimes at grid resolution of (a, c) 2.5 microns and (b, d) 1.25 microns. Simulation results agree well with the experiments of Yarin and Weiss.	162
Figure I.22.6 - Splashed mass ratio versus time in surface impingement of a train of diesel droplets of 5.96 micron diameter impacting at 77 m/s from two DNS studies at 40 CPD and 80 CPD resolutions. The dimensionless velocity, based on deposition frequency, is $u = 24$	162
Figure I.23.1 - Validation of LES model through comparisons with (a) non-reacting fuel distributions, (b) bulk combustion characteristics (cylinder pressure and heat release rate [HRR]), and (c) locations of key intermediates during the combustion process	167
Figure I.23.2 - Overview of detailed soot model and Lagrangian soot parcels	168
Figure I.23.3 - (Top) soot parcels with velocity vectors showing implementation of soot model. (Bottom) output of soot parcel model late in the cycle for HCCI and conventional diesel combustion.....	169
Figure I.23.4 - Comparison of measured and predicted particle size distributions. The predictions use the soot model developed in the current program in the one-way coupled approach.	170

Figure I.23.5 - (a) Comparison of a baseline mode, our current model, and measured particle size distribution at several times. (b) Resulting particle size distributions with several levels of stratification (denoted as the standard deviation in equivalence ratio (σ_ϕ)).....	170
Figure I.24.1 - New CPFR with air exhaust, injector cooling, and instrumentation installed (Figure source: University of Alabama)	174
Figure I.24.2 - First reacting sprays captured in new CPFR, one (left) with longer exposure time and another (right) with less exposure time (Figure source: University of Alabama).....	174
Figure I.24.3 - Image processing steps for RSD images at 0.625 ms aSOI for <i>n</i> -heptane injected at 1,000 bar for 4 ms into ambient air at 30 bar and 825 K. A total of 50 injections were captured in this case.....	175
Figure I.24.4 - RSD images during combustion at 1.3 ms aSOI for <i>n</i> -heptane injected at 1,000 bar for 4 ms into ambient air at 30 bar and 825 K. A total of 50 injections were captured in this case.	176
Figure I.24.5 - (a) Fuel mass fraction and (b) temperature.....	177
Figure I.24.6 - (a) Molecular viscosity and (b) thermal conductivity.....	177
Figure I.24.7 - (a) Specific heat and (b) fuel mass fraction along jet center.....	177
Figure I.24.8 - Two-dimensional distributions of pressure, density, and velocity at 0.18 ms aSOI	178
Figure I.25.1 - Premixed flame propagation and end-gas ignition in a constant volume configuration. A CMC–PPF solver has been coupled with an LES solver. Total enthalpy and density fields at the initial time (top) and when the ignition kernels have formed (bottom) are shown. The red color represents the maximum value, while the blue color represents the minimum value.	181
Figure I.25.2 - DNS datasets. (a) and (b) 2D reduced chemistry DNS of end-gas ignition. Temperature fields at (a) $t = 2.5$ ms and (b) 2.84 ms for a representative case with the temperature inhomogeneity level of 20 K are shown. Scalar dissipation of the sensible enthalpy in 3D two-step chemistry DNS of end-gas ignition. (d) DNS of a premixed flame. The progress variable field (blue: unburned, red: burned) for DNS with the Taylor-scale Reynolds number of 169 is shown.	181
Figure I.25.3 - Assessment of CMC reaction rate closure models using 2D reduced chemistry DNS of end-gas ignition. Sensible-enthalpy-based CMC performs very well for the entire duration of the ignition process (bottom), while total- enthalpy-based CMC leads to substantial errors except for a very early stage of ignition processes (top). (left column: $t = 2.5$ ms, center column: $t = 2.72$ ms, right column: $t = 2.84$ ms). The blue filled squares represent the conditional mean heat release rates from the DNS data. The black hollow circles denote the heat release rates at the DNS grid points.	182
Figure I.25.4 - Experimental data of knock limited combustion phasing with 15% EGR (red) and without EGR (black) at two different air flow rates (i.e., loads). Data highlights that as airflow and thus load is increased EGR effectiveness at mitigating knock can be reduced or eliminated.	184
Figure I.25.5 - Evolution of flame fronts in LES of an SI engine. The model parameters in a turbulent subfilter flame speed model (Pitsch 2005) are (top) $b_1 = 10$ and $b_2 = 2$; and (bottom) $b_1 = 10$ and $b_3 = 2$	184
Figure I.26.1 - (a) High pressure fuel delivery system and (b) spray chamber installed at HFIR. (c) Computer-aided drawing of injector holder and the necessary sweep gases to minimize fuel build-up on the chamber walls and injector.....	187

Figure I.26.2 - Left: Bubble shapes in time results from Verma et al. (top) and current BU OpenFOAM simulations (bottom) for TC2. Non-dimensional times displayed are (a) $t = 0$, (b) $t = 1.5$ and (c) $t = 3.0$. Right: Rise velocity (top) and center of mass (bottom) in time from Klostermann and Verma et al. compared to BU OpenFOAM and SPH simulations. Error bars showing a deviation of 2% have been introduced for the center of mass curves and 5% for the rise velocity curves..... 189

Figure I.26.3 - Left: LDV signal of fuel injector tip excitation from pintle opening and closing. Right: Max amplitude of LDV at the tip and 10, 15, 20, 25, and 30 mm away from the free end..... 190

Figure I.26.4 - Contrast-enhanced radiograph showing fluid in the sac and the area of interest in the sac–nozzle interface (left). Radiograph with traverse used in calibrating neutron attenuation intensity over known distances and fluid masses (right). 191

Figure I.26.5 - Attenuation within the area of interest, with a guideline defining the threshold of liquid detection, and conversion to the deviation from this threshold representing detected mass (left). Cumulative mass detected at the sac–nozzle interface (right). The detected fluid flow time is ~ 1 ms, compared with a commanded injection duration of 0.367 ms. 191

Figure I.27.1 - USAXS measurements of spray centerline SMD within the first 20 mm of Spray D over a wide range of ambient backpressures and injection pressures..... 195

Figure I.27.2 - SAMR measurements of spatially resolved SMD in Spray D at $r_{amb} = 2.4 \text{ kg/m}^3$, $P_{inj} = 50 \text{ MPa}$ 195

Figure I.27.3 - Validation of SMD predictions by new KH-Faeth primary atomization model against USAXS measurements. Also shown are predictions by two benchmark models in current use within engine CFD codes: KH-RT model and KH-ACT model. Validation conditions are for ECN Spray A ($d_{nozz} = 90 \text{ }\mu\text{m}$). 196

Figure II.1.1 - Illustration of repeating Fire20-Skip80 sequence used to mimic the thermal state that an engine may experience during vehicle acceleration. Figure by Magnus Sjöberg..... 199

Figure II.1.2 - Knock-limited combustion phasing as a function of intake pressure for both steady-state and transient operation with 30°C intake temperature. Transient operation is shown in dashed lines. Figure by David Vuilleumier, SNL. 200

Figure II.1.3 - Indicated thermal efficiency as a function of intake pressure for all nine fuels for both steady-state and transient operation. Transient operation is shown in dashed lines. Figure by David Vuilleumier, SNL. 201

Figure II.1.4 - Best-fit linear regression between octane index and knock-limited combustion phasing for an intake pressure of 146 kPa under transient operation. Figure by David Vuilleumier, SNL..... 202

Figure II.1.5 - Distribution of R^2 values at the 146 kPa intake pressure, 30°C intake temperature, transient operating mode condition. Figure by David Vuilleumier, SNL..... 202

Figure II.1.6 - K-values as a function of intake pressure and operation type accompanied by the 10th and 90th percentiles of the K distribution, as well as the mode of the distribution. Figure by David Vuilleumier, SNL. 203

Figure II.2.1 - The effect of ethanol blending on the base fuel RON requirement for PRFs to get a blended RON 98 206

Figure II.2.2 - Temperature drop across the carburetor with increasing level of ethanol, causing super-saturation.....	207
Figure II.2.3 - Minimum temperature (°C) for full vaporization with increasing level of ethanol and calculated uncertainty	207
Figure II.2.4 - Change in Δ RON for PRF–ethanol blends between standard RON operating conditions (Case 1), compensated mixture temperature (Case 2), and pressure at spark timing (P_{ST}) (Case 3).....	208
Figure II.2.5 - Change in Δ RON for PRF–ethanol blends between standard RON operating conditions (Case 1) and each, compensated mixture temperature (Case 2), pressure at spark timing for that PRF–ethanol blend (Case 3), pressure at spark timing of PRF 98 (Case 4), and IMEP compensated for PRF 98 (Case 5).....	209
Figure II.3.1 - Crank angle at 50% fuel burned (CA50) phasing versus brake mean effective pressure at 2,000 rpm for the 97 RON fuels using CR11.4 pistons	212
Figure II.3.2 - Volumetric heating value for the 97 RON expanded matrix fuels	212
Figure II.3.3 - Modeled volumetric fuel economy for a typical mid-size sedan using CR11.4 and the 97 RON fuels	213
Figure II.4.1 - For boosted, stratified charge, direct injection SI operation at 2,000 rpm, engine-out soot increases monotonically with the fuels' PMI, as the soot formation is primarily occurring in the bulk gases. But for naturally aspirated operation at 1,000 rpm, soot emissions for E30 are higher than predicted from PMI due to the formation of pool fires. PMI values were provided by Fioroni et al. [3]. Figure by Magnus Sjöberg and Carl-Philipp Ding, SNL.	217
Figure II.4.2 - A change of NO_x –PM trade-off indicates a change of the dominating soot production pathway with fuel type and operating conditions. Figure by Magnus Sjöberg.....	217
Figure II.4.3 - Laser-based measurements allow the detection of fuel wall films for various combinations of fuels and operating conditions that are prone to pool fires. Figure by Carl-Philipp Ding, Xu He, and Magnus Sjöberg, SNL.....	218
Figure II.4.4 - Conceptual comparison of fuel injection and spark timing strategies for operation with partial fuel stratification and full stratification. Figure by Magnus Sjöberg and Zongjie Hu, SNL.	219
Figure II.4.5 - IR fuel–vapor imaging reveals extent of fuel stratification relative to the flame spread for operation with a late injection of 3.6 mg gasoline at the time of spark. Figure by Magnus Sjöberg, SNL.....	219
Figure II.4.6 - Injection of 1.6 mg of fuel at the time of spark stabilizes combustion, enabling studying autoignition of lean end-gas with $\phi = 0.50$, 1,400 rpm, $P_{in} = 100$ kPa. Figure by Magnus Sjöberg, SNL.....	220
Figure II.5.1 - Effect of adding high LFS ethanol component on combustion stability with EGR dilution	224
Figure II.5.2 - Variation of EGR tolerance with various fuel mixtures plotted against their LFS at 5.6 bar IMEPn.....	224
Figure II.5.3 - Variation of EGR tolerance with various fuel mixtures plotted against their LFS at 3.2 bar IMEPn.....	224

Figure II.5.4 - Comparison of timing of key combustion events for various fuel blends at constant 25% EGR	225
Figure II.5.5 - Comparison of timing of key combustion events with E30 fuel mixture at 5.6 bar and 3.2 bar load at 23% EGR	225
Figure II.6.1 - Knock-limited combustion phasing as a function of octane index for a single engine operating condition	228
Figure II.6.2 - Cylinder pressure and heat release rate for engine operating Conditions 1 and 6 for select fuels.....	229
Figure II.6.3 - Notional PT trajectories for changing intake manifold pressure. Solid lines 9.2:1 compression ratio, dashed lines represent continuation of trajectory for compression ratio of 14:1.	230
Figure II.6.4 - Ignition delay contour in the PT space for the aromatic fuel without EGR highlighting the different ignition zones	231
Figure II.6.5 - PT path of the unburned fuel–air mixture during compression for different intake manifold pressure (P_{in}). Also shown are lines of constant ignition delay (8 ms) for 0%, 10%, and 20% EGR.....	231
Figure II.7.1 - Full factorial experimental design fuel matrix. Tested fuels are indicated by red dots; aromatic hydrocarbon vapor pressures are at 443 K.....	234
Figure II.7.2 - PM results from cumene at 20 vol%; error bars are 95% confidence intervals	236
Figure II.7.3 - PM results from 4-t-butyltoluene at 10 vol%; error bars are 95% confidence intervals ...	236
Figure II.7.4 - PM results from 4-t-butyltoluene at 20 vol%; error bars are 95% confidence intervals ...	237
Figure II.7.5 - ADC results for p-cymene fuel blends with and without ethanol, showing ethanol suppression of p-cymene evaporation while ethanol remains in the liquid phase.....	238
Figure II.7.6 - Modeled vapor phase concentrations of ethanol, paraffins, and aromatics from the surface of a droplet evaporating near the end of compression	238
Figure II.8.1 - Total hydrocarbon conversion as a function of temperature for an E10 surrogate fuel over a hydrothermally aged commercial TWC at lambdas ranging from 0.995 to 0.999	243
Figure II.8.2 - Comparison of total hydrocarbon conversion light-off curves over a hydrothermally aged commercial TWC for selected fuel components representative of alcohols (ethanol), linear ketones (2-butanone), esters (ethyl acetate), aromatic ethers (FuranMix: 2-methylfuran, 2,5-dimethylfuran), alkanes (n-octane, iso-octane, methylcyclohexane), aromatic hydrocarbons (toluene), and alkenes (1-octene, diisobutylene).....	244
Figure II.8.3 - Comparison of T_{50} and T_{90} total hydrocarbon light-off temperatures over the hydrothermally aged commercial TWC for all of the fuel components investigated. Error bars represent 95% confidence intervals calculated from three replicate runs.	245
Figure II.8.4 - Comparison of T_{50} and T_{90} CO light-off temperatures over the hydrothermally aged commercial TWC for all of the fuel components investigated. Error bars represent 95% confidence intervals calculated from three replicate runs.	245

Figure II.9.1 - Six fuels, including the BOB and five bio-fuel blends, were tested for PM mass emissions on a GDI engine during a 90-s cold-start transient. The average mass measurements can be viewed in terms of mass per 90-s cold-start transient (left axis) or in terms of a cold-start FTP equivalent mass per mile (right axis). The gravimetric (Teflo; dot pattern) and thermal-optical (EC/OC; vertical line pattern) mass measurements have min/max error bars and the photoacoustic (MSS; solid pattern) has standard deviation error bars. The box around the fuel names (see Table II.9.I) indicates the 30 vol% oxygenated fuel blends.	249
Figure II.9.2 - Six fuels, including the BOB and five bio-fuel blends, were tested for PM mass emissions on a GDI engine. All five fuels were at or above the California Air Resources Board's 1 mg/mi gravimetric mass target (blue dashed line) for the FTP combined cold- and hot-start cycle during the 90-s cold-start transient. The difference in the graph's two-plot series, Total PM and Dry-Soot, indicates the amount of semi-volatile PM mass that was counted in a gravimetric mass measurement (Total PM, squares), but not measured by an online Micro Soot Sensor (circles). The six fuels are BOB (purple), E10 (blue), E30 (green), ester (yellow), ketone (orange), and ether (red).	250
Figure II.10.1 - Three-dimensional chromatogram of ionic species extracted from soot. Each color band represents a compound and the amount of the compound is represented by the color with red being the highest concentration. The circled compounds are identified in Table II.10.1.	253
Figure II.11.1 – Three-dimensional surface maps of ID for two gasoline surrogate blends, a 25% ethanol blend into TRF88 on the left and neat TRF88 on the right [11]	257
Figure II.11.2 - Constant mass injection temperature sweeps at 1.0 MPa are shown with data plotted every 25 K. A 10% ethanol blend increases ID compared to iso-octane, but it maintains negative temperature coefficient region behavior. A 20% blend exhibits much higher ID, more than a 50% blend or even neat ethanol. [11]	258
Figure II.11.3 - Constant mass injection temperature sweeps at 1.0 MPa are shown with data plotted every 25 K. Ethanol blending effects into PRF95 are much more linear than with neat iso-octane (illustrated in Figure II.11.2).	258
Figure II.12.1 - LSPI count for the four tested fuel combinations. (solid) LSPI event count, (crosshatch) LSPI cluster count (Figure Credit: Derek Splitter).	263
Figure II.12.2 - The effect of different fuels on LSPI event start location (Figure Credit: Derek Splitter)	266
Figure II.12.3 - Impact of various fuels on LSPI dwell (Figure Credit: Derek Splitter)	264
Figure II.12.4 - Example of LSPI dwell times for EB25 exhibiting short and long dwell effects knocking behavior (Figure Credit: Derek Splitter).....	265
Figure II.12.5 - LSPI intensity observed with various fuels (Figure Credit: Derek Splitter)	265
Figure II.13.1 - Fueling rate and CMT as a function of EGR for each fuel	269
Figure II.13.2 - Tradeoff between intake air temperature and intake boost for constant combustion phasing (CA50)	270
Figure II.13.3 - Engine out smoke (Filter Smoke Number) as a function of EGR for the three 98 RON fuels.....	270
Figure II.13.4 - Soot luminosity for three 98 RON fuels as a function of engine crank angle.....	271

Figure II.13.5 - Heat release profiles for each 98 RON fuel.....	271
Figure II.14.1 - Combustion phasing (CA50) as a function of intake temperature (T_{in}) for various fuels for fully premixed LTGC operation at $P_{in} = 1.0$ bar, $\phi = 0.4$, 1,200 rpm.....	274
Figure II.14.2 - CA50 for $T_{in} = 154^{\circ}\text{C}$ as a function of $\text{OI} = \text{RON} - \text{K} \cdot \text{S}$. Based on the $T_{in} = 154^{\circ}\text{C}$ data in Figure II.14.1.	274
Figure II.14.3 - CA50 as a function of T_{in} for early DI fueling compared to premixed prevaporized fueling for the Co-Optima E30 and high-aromatic fuels. The larger HOV of E30 is evident in the greater difference in T_{in} between premixed and early DI fueling compared to the high-aromatic fuel. $P_{in} = 1.0$ bar, $\phi = 0.4$, 1,200 rpm.....	275
Figure II.14.4 - T_{BDC} required for a CA10 of 368.7°CA (solid lines) or 371.5°CA (dashed lines) as a function of P_{in} for the Co-Optima E30 and high-aromatic fuels and regular E10. The E30 and high-aromatic fuels are shown for both premixed prevaporized and early DI fueling. $\phi_m = 0.38$, 1,200 rpm.	276
Figure II.15.1 - Diagram of the multi-cylinder 1.9-L ACI engine	280
Figure II.15.2 - Collaboration between metal engine and optical engine experiments	281
Figure II.15.3 - RCCI injection strategy used in the present study: single PFI during early intake stroke and single DI with timing swept from bottom dead center to near-top dead center of compression stroke.....	281
Figure II.15.4 - Mode transitions into RCCI with various combinations of PRF blends as a function of SOI timing	282
Figure II.16.1 - Schematic diagram of the heavy-duty, single-cylinder optical diesel engine and optical setup with IR emission and visible natural combustion luminosity cameras	285
Figure II.16.2 - Combustion phasing for both the single-cylinder optical engine (with standard deviation over 36 fired cycles), and the multi-cylinder metal engine (with standard deviation over four cylinders during steady-state).....	286
Figure II.16.3 - Simultaneous IR and visible NL images during HTHR period for 300 CAD CR SSE near the early injection control authority limit. Each pair of images corresponds to different combustion cycles, not successive images in time. The imaging crank angle is indicated in the top-left of each image.....	287
Figure II.16.4 - Simultaneous IR and visible NL images, during HTHR period for 310 CAD CR SSE, slightly retarded from the early injection control authority limit. Each pair of images corresponds to different combustion cycles, not successive images in time. The imaging crank angle is indicated in the top-left of each image.	287
Figure II.16.5 - Simultaneous IR and visible NL images during HTHR period for 320 CAD CR SSE slightly advanced from the late injection control authority limit. Each pair of images corresponds to different combustion cycles, not successive images in time. The imaging crank angle is indicated in the top-left of each image.	288
Figure II.16.6 - Simultaneous IR and visible NL images during HTHR period for 330 CAD CR SSE near the late injection control authority limit. Each pair of images corresponds to different combustion cycles, not successive images in time. The imaging crank angle is indicated in the top-left of each image.....	288

Figure II.17.1 - Quantitative images of soot optical thickness (KL) from diffused back illumination movies of free-spray combustion (left column) vs. DFI combustion (right column). False color is used to indicate higher KL values and thus higher soot concentrations. Each row of images corresponds to a different nominal ambient temperature in the combustion vessel. The actual ambient temperature and density values are indicated in the lower right region of each image frame. Each displayed image was acquired at 3.000 ms after the start of fuel injection. The duct configuration is D2L16G1.4 δ , as described in the text. The white rectangle on each DFI image indicates the location of the inner diameter of the duct.....	291
Figure II.17.2 - Comparison of duct inlet and outlet shape effects on DFI performance. The duct shape that corresponds to each Greek letter is shown for reference. All data are for D2L8G3.79 ducts at a nominal ambient density of 22.8 kg/m ³	292
Figure II.17.3 - (a) Shortening duct length from 16 mm to 8 mm does not have a detrimental effect on soot mass for a duct with 2-mm diameter and δ configuration. (b) Decreasing the standoff distance from 5.9 mm to 1.4 mm lowers the soot mass.	293
Figure II.17.4 - Lines show predicted HC emissions indices from overlean fuel during the mixing-controlled burn, for 21% oxygen and ϕ_{ent} values of 0.35 and 0.5 for the 180-MPa and 80-MPa injection pressures, respectively. Experimental data points are plotted for comparison.	294
Figure II.18.1 - Two-color soot pyrometer schematic (left) and optical hardware (right) (Source: University of Alabama).....	298
Figure II.18.2 - Two-color soot pyrometry image processing. (Left) double image of burner showing tip in focus, no filters. (Middle) double image of flames at two wavelengths. (Right) Pixel-by-pixel intensity ratio on the left and calculated temperature on the right.	298
Figure II.18.3 - New CFR with air exhaust, injector cooling, and instrumentation installed (Source: University of Alabama).....	299
Figure II.18.4 - First reacting sprays captured in new CFR, one (left) with longer exposure time and another (right) with less exposure time (Source: University of Alabama)	299
Figure II.18.5 - Image processing steps for RSD images at 0.625 ms after start of injection (aSOI) for <i>n</i> -heptane injected at 1,000 bar for 4 ms into ambient air at 30 bar and 825 K. A total of 50 injections were captured in this case.	300
Figure II.18.6 - RSD images during combustion at 1.3 ms aSOI for <i>n</i> -heptane injected at 1,000 bar for 4 ms into ambient air at 30 bar and 825 K. A total of 50 injections were captured in this case.	301
Figure II.19.1 - Representative models for DCN and T10. Observed values are compared to predicted using the full data set (Full Set, red circles), and leave-one-out predictions (LOO, blue asterisks), where one data point is removed from the model and the predictions re-run without that point. Close agreement between these values suggests that the models are not overly dependent upon any one data point. (a) Model for DCN data from ASTM D6890, where the model contains seven terms, including the intercept, five predictors, and one two-factor interaction, yielding an $R^2 = 0.9625$, $adj-R^2 = 0.9512$. (b) Model for simulated distillation T10 data from ASTM D2887, where the model contains seven terms, and uses only four regions as predictors, $R^2 = 0.9642$, $adj-R^2 = 0.9544$	304

Figure II.19.2 - Blending model development. The charts above show the pairwise interactions between two sets of functional groups on the value of DCN. In both charts, the population of Functional Group A is increased from left-to-right along the X-axis. A second functional group (Functional Group B for Chart a and Functional Group C for Chart b) is held at the lowest measured value (blue line) or the highest measured value (red line). For Chart a when Functional Group B is held at the lowest measured value (blue line), the effect of increasing Functional Group A on the DCN value is nearly negligible. However, when Functional Group B is held at the highest measured value (red line), DCN increases with increasing Functional Group A, suggesting that Functional Groups A and B interact synergistically in the prediction of DCN. For Chart b when Functional Group C is held at the lowest measured value (blue line), DCN values increase with the amount of Functional Group A present in the sample. Similarly, when Functional Group C is held at the highest measured value (red line), DCN values also increase with the amount of Functional Group A. In Chart b the red and blue lines are similarly curved, but offset, suggesting that both functional groups influence predicted DCN values; however, the curvature of the red line is slightly less than that of the blue line indicating that when Functional Group C is at a maximum value, the influence of Functional Group A on predicting DCN is diminished, suggesting a slightly antagonistic interaction in the prediction of DCN with this pair of functional groups. Thus from Chart a, a blending model would benefit from using Functional Groups A and B together to predict DCN, and not benefit from comparing the Functional Groups A and C. In this figure, the functional groups are more explicitly described by the following: Functional Group A represents “C in open chains. CH₂ benzylic and CH₂ not adjacent to CH in an alkyl group;” Functional Group B represents “CH in allylic and benzylic groups and in joining tetralin ring;” and Functional Group C represents “CH, CH₂ beta from a secondary carbon and in cyclopentyl and cyclohexyl rings.” 304

Figure II.19.3 - Comparison of the solid–liquid equilibria for four diesel fuel surrogates, V0a, V0b, V1, and V2, and GTL-Diesel. Data points for each material are shown in various colors. Compositions for each surrogate were previously reported [1,2]. Trendlines and the second order polynomial fits are presented in boxes outlined in colors corresponding to each surrogate. Each material can be expected to remain a liquid at temperatures above its respective trendline at a given pressure. Below its respective trendline, a pure material will solidify, and a multicomponent material will have at least one component freeze out..... 305

Figure II.19.4 - Comparison of the solid–liquid equilibria for diesel fuel surrogate V0b with eight cold flow improvers. The larger graph documents cold flow improver performance across a broad range of pressures, while the inset graph focuses on the area around 205 MPa, where most testing occurred. Shown here are the results derived from treat rates of 5,000 ppm for each cold flow improver in surrogate V0b..... 306

Figure II.20.1 - The predictions of octane blending of Co-Optima Tier 3 HPFs in a four-component base gasoline using the Co-Optima chemical kinetic model (curves) compared experimentally measured RON and OS (symbols) for the same four-component base gasoline (HPFs). The measurements are from McCormick et al. [1]. (Source: LLNL)..... 309

Figure II.20.2 - RON is correlated to the IDT (Tau) computed by the kinetic model for stoichiometric fuel/air mixtures at 775 K and 25 atm (lower left plot). Octane sensitivity (SEN) is correlated to the computed minimum slope in the NTC region (lower right plot). The minimum slope in the NTC is defined as shown in the upper plot. (Source: LLNL)..... 310

Figure II.20.3 - Laminar flame speeds (LFS) computed by the LLNL chemical kinetic model for gasoline for a high-octane and moderate-octane sensitivity over a wide pressure and temperature range relevant to ASI engines (Source: LLNL)..... 310

Figure II.21.1 - Experimentally measured (symbols) and simulated (lines) ignition delay times of methyl acetate in a shock tube at NUIG (LLNL).....	314
Figure II.21.2 - Simulated (curves) and experimentally measured (symbols) IDTs of n-heptane in a shock tube over a range of pressures and fuel/air equivalence ratios (Φ). The predictions by the improved LLNL model are represented by the solid curves and those by the previous model are the dashed curves. Experimental data sets are from Ciezki et al. [1]. (LLNL).....	315
Figure II.21.3 - Simulated and measured IDTs for a toluene/n-heptane 50:50 molar blend at a fuel/air equivalence ratio (Φ) of 0.5. The IDTs were measured in a shock tube and an RCM at NUIG. (LLNL).....	315
Figure II.21.4 - Simulated (curves) and experimentally measured (symbols) laminar flame speeds for n-heptane and iso-octane. The measurements are from Ji et al. [4,5]. (LLNL).....	315
Figure II.22.1 - Experimentally measured pressure–time histories for Co-Optima core fuels indicating reactivity trends for the fuels in different combustion regimes, (a) high pressure, lower temperature, and (b) moderate pressure, intermediate temperature.....	319
Figure II.22.2 - Computationally derived isopleths of ignition delay times (τ) and normalized heat release rates (ϵ) for PRF70 – PRF100 covering a wide range of thermodynamic conditions relevant to boosted SI and ACI combustion schemes.....	320
Figure II.23.1 - PCA model validation via leave-one out cross validation for prediction of RON and S.....	323
Figure II.23.2 - Gaussian process regression model validation via leave-one out cross validation for prediction of RON and S.....	324
Figure II.23.3 - RON and S classification results for linear model and Gaussian process.....	324
Figure II.23.4 - Comparison of isooctane in NREL flow reactor to LLNL 1D plug flow model.....	325
Figure II.23.5 - Comparison of reactor results and simulations for (a) anisole conversion, (b) phenol formation, (c) benzaldehyde formation, and d) benzene formation. A skeletal reaction mechanism from Boot et al. [5] is also shown.....	325
Figure II.24.1 - Mathematical definition of the phi-sensitivity metric “big-phi,” which is developed to estimate the ability of a fuel blend to improve the controllability of a PSCCI engine.....	329
Figure II.24.2 - Example calculation of the constant volume ignition delay times used to construct the phi-sensitivity metric for iso-octane.....	329
Figure II.24.3 - Trade-off between high octane sensitivity and phi-sensitivity for three four-component gasoline blends with a model-based RON estimate greater than 95. The blends containing 1-pentanol perform the best with some combination reaching nearly 90% of the target performance, specifically, an octane sensitivity better than ethanol and a phi-sensitivity better than iso-octane.....	330
Figure II.25.1 - Predicted second cycle cylinder pressure showing good agreement between the baseline simulations and those conducted with species reduced to ~40 during gas exchange; but less agreement with further reduction to 10 species. (Proof of concept results with KIVA.).....	335

Figure II.25.2 - Reduction in computational flow (a) and kinetics costs (b) using dynamic species reduction during an exploratory homogeneous charge compression ignition simulation. (Proof of concept results with KIVA.)	335
Figure II.26.1 - Micro-combustion at elevated pressure: unsteady FREI and stable flames at 4.46 bar (I. Schoegl/LSU)	338
Figure II.26.2 - Preliminary results for four-wavelength TFP: 5.6 mil (142 μm) SiC filament yields calibration-free temperature measurements within 20 K of reference measurements, while 3 mil (76 μm) filament requires calibration (I. Schoegl/LSU)	338
Figure II.26.3 - Flame speeds of TPRF95.6–air mixture (T. Lu/UConn)	339
Figure II.27.1 - YSI measured for several oxygenated hydrocarbons formed by adding oxygen atoms to toluene	341
Figure II.27.2 - YSIs measured for the five Co-Optima test gasolines (TGs)	342
Figure II.27.3 - Comparisons between YSI results for surrogate fuel components obtained using three different methodologies: physical measurement (Yale), empirical estimate (NREL), and kinetic simulation (Penn State)	343
Figure II.27.4 - Comparisons between YSI results for surrogate fuels obtained using three different methodologies: physical measurement (Yale), empirical estimate (NREL), and kinetic simulation (Penn State)	344
Figure II.27.5 - Predicted YSIs for a range of chemical compounds at 1 atm and 2 atm	344
Figure III.2.1 - PRF mapping that allows the determination of an effective PRF number of any liquid or gaseous fuel within this range of compression ratio (CR) and intake temperature	350
Figure III.2.2 - Determination of the effective PRF number for each of the reformat fuel mixtures	351
Figure III.2.3 - GT-POWER model of the diesel Ricardo Hydra engine used for dual-fuel RCCI and single-fuel RCCI	352
Figure III.2.4 - CONVERGE CFD model of the diesel Ricardo Hydra engine	352
Figure III.2.5 - CFD results of pressure and heat release rates of single-fuel RCCI using diesel as the parent fuel	352
Figure III.3.1 - Passive SCR concept. Ammonia generation mode is created by running stoichiometric or nominally 5–6% rich, generating ammonia across the TWC, which is stored in the SCR. In high efficiency mode, lean operation is performed and the NO_x created in this mode is broken down by the stored ammonia.	355
Figure III.3.2 - High dilution concepts results	356
Figure III.3.3 - Camera arrangement for optical in-cylinder measurement. Two optical probes were positioned toward the spark plug for viewing of ignition point and flame propagation. Cylinder #6 (rear cylinder) was used for instrumentation access. Top view. (Figure source: Bosch)	356

Figure III.3.4 - Two optical probes are positioned toward spark plug for viewing of ignition point and flame propagation. The cylinder #6 (rear cylinder) is used for instrumentation access. Combustion pressure probe is positioned between the two optical probes. Combustion chamber view. (Figure source: Bosch) 356

Figure III.3.5 - Clearancing of piston crown is required for optical probe protrusion into the combustion chamber and for obtaining field of view for ignition and combustion. Concerns were that modification may have affected the instrumented cylinder’s effective compression ratio. As a means to quantify any impact, the combustion properties before and after the modification were compared. Results of the comparison are shown in Figure III.3.6. (Figure source: Bosch) 357

Figure III.3.6 - Verification of combustion. Comparison of combustion parameters prior to and after combustion chamber modifications indicates post modification performance equivalent to normal cycle-to-cycle variation of the pre-modification results. 357

Figure III.3.7 - Image processing progression: → Raw → Background Subtracted → Median Filtered → Binarized → Threshold 357

Figure III.3.8 - CoV images for five crank angles for two operating conditions. Left: 1,000 rpm, 6.8 bar IMEP, $\lambda = 1.0$, minimum (3%) EGR, $CoV_{IMEP} = 0.32\%$. Right: 1,000 rpm, 6.8 bar IMEP, $\lambda = 1.6$, 10% EGR, $CoV_{IMEP} = 1.60\%$ 358

Figure III.3.9 - Process used to assess each system’s projected results over various drive cycles. Assessment of each system will be performed by a combination of simulation and actual test results. Engine map test data will be uploaded into a Bosch developed CV drive cycle program (PoET) to determine fuel efficiency and emissions projections. A scatter plot of drive data points over an engine map provides an indication of magnitude of time the vehicle operates in the improved region of the engine map on the selected drive cycle. Various drive cycles will be assessed to find applications where the HECO-SING might provide the best business case. 359

Figure III.3.10 - Current (rescoped) milestone 359

Figure III.5.1 - Sensitivity of BTE to multiple fuel injection events for different ethanol and gasoline (E0) blends 367

Figure III.5.2 - Summary of the benefits of ethanol blends on direct injection engine performance 367

Figure III.5.3 - Indicated thermal efficiency for air and EGR dilution versus syngas supplementation .. 368

Figure III.5.4 - Particle size distributions and total number emission for gasoline, and 20% blends of ethanol, iso-butanol and dimethyl furan 368

Figure IV.1.1 - Average priority scores for CLEERS organizational activities from the 2017 CLEERS Industry Priorities Survey. Responses were scored as 10 for high priority, 5 for medium priority, and 0 for low priority. The lengths of the colored segments are proportional to the fraction of respondents giving a particular priority rating. 372

Figure IV.1.2 - Average priority scores across technologies (vertical axis) and market sectors (horizontal axis) from the 2017 CLEERS Industry Priorities Survey. Responses were scored as 10 for high priority, 5 for medium priority, and 0 for low priority. The circle diameter is proportional to the average priority score for a given technology and market sector. 373

Figure IV.1.3 - Average priority scores across research areas (vertical axis) and market sectors (horizontal axis) from the 2017 CLEERS Industry Priorities Survey. Responses were scored as 10 for high priority, 5 for medium priority, and 0 for low priority. The circle diameter is proportional to the average priority score for a given research area and market sector.....	374
Figure IV.1.4 - NO storage capacity as a function of inlet NO concentration (X-axis) and temperature (data series) for a commercially relevant passive NO _x adsorber material	374
Figure IV.1.5 - NO temperature programmed desorption profiles obtained with a commercially relevant passive NO _x adsorber material after exposure to 1,000 ppm NO in the presence of (a) 0% H ₂ O, 0% O ₂ ; (b) 0% H ₂ O, 10% O ₂ ; (c) 5% H ₂ O, 0% O ₂ ; and (d) 5% H ₂ O, 10% O ₂	375
Figure IV.2.1 - Complete redox cycling of low-temperature NH ₃ -SCR that involves two Cu(I) centers in the oxidation half-cycle. Key intermediates are highlighted.	378
Figure IV.2.2 - Estimation of Cu ²⁺ , Cu(OH) ⁺ , and CuO _x in fresh and hydrothermally aged (HTA) samples. SCR catalyst with Si/Al = 12 and Cu loading of 2.1 wt% was used. HTA-T represents sample aged at temperature T (in °C) for 16 h in flowing air containing 10% water vapor.	379
Figure IV.2.3 - Low-temperature aftertreatment test protocol structure	380
Figure IV.2.4 - NO _x adsorption at 100°C for 10 min followed with temperature programmed desorption (10°C/min up to 500°C). The feed gas mixture contains 200 ppm of NO _x (185 ppm of NO and 15 ppm of NO ₂), 14% O ₂ , ~2.5% H ₂ O and 200 ppm of CO balanced with N ₂ at a flow rate of 300 sccm.	380
Figure IV.2.5 - Scanning transmission microscopy images of the freshly calcined (left), reduced (by 1% H ₂ /He at 400°C for 30 min, middle), and reoxidized (by 10% O ₂ /He at 500°C for 1 h, right) Pd/zeolite samples, where the upper, middle, and lower rows are images for Pd/Beta_0.92%, Pd/ZSM-5_0.62%, and Pd/SSZ-13_0.88%, respectively	381
Figure IV.2.6 - Catalyst locations within small cross-sections of a commercial SCR filter (catalyst shown in red false color – note that inlet channels are larger and outlet channels are smaller in this asymmetric honeycomb filter design).....	382
Figure IV.3.1 - (a) DRIFTS spectra of CO-binding over Pt/Al ₂ O ₃ (sulfated) and CCC+Pt/Al ₂ O ₃ physical mixture (sulfated) and CCC (degreened) catalysts. (b) Time-on-stream CO oxidation conversion during 5 ppm SO ₂ poisoning in low temperature combustion diesel stream conditions for various catalysts. (c) DRIFTS spectra of CO-binding over degreened (dashed) and sulfated (solid) CCC catalyst.	386
Figure IV.3.2 - (a) Overview of storage and release efficiencies for Ag and Pd-based zeolites under draft ACEC Tech Team trapping protocol. (b) THC storage and release profile (red) for Pd/ZSM-5 as determined by flame ionization detector (FID). (c) NO _x storage and release profile (red) for Pd/ZSM-5. Black lines indicate bypass baseline measurement.....	387
Figure IV.3.3 - Light-off comparisons of DOC (dashed) and dual-bed trap–DOC system (solid) after (a) 800°C, 4 h aging and (b) 800°C, 50 h ageing with repeated sulfations/desulfations. (c) Schematic of dual-bed trap–DOC system.....	388
Figure IV.4.1 - Pseudo-transient drive cycle used for engine-based studies of the passive SCR system	392
Figure IV.4.2 - NO _x and NH ₃ concentration data over the passive SCR lean-rich cycle for (a) a TWC with O ₂ and NO _x storage components and (b) a TWC without O ₂ and NO _x storage components.....	392

Figure IV.4.3 - Concentration of NO_x entering the TWC (“ NO_x in”) and NH_3 downstream of the TWC (“ NH_3 out”) as a function of the equivalence ratio during rich operation of a lean-rich cycle for average exhaust temperatures of (a) 395°C and (b) 492°C. Results are shown for the Pd-based TWC with a NO_x storage component.	393
Figure IV.5.1 - Spatiotemporal comparison of model results with measurements at 3/8L, 1/2L and 3/4L, where L is the overall catalyst length. Comparison is over the four-step protocol which includes step transients and SS sections. The grey sections are for analytical purposes and to be ignored. Top panels compare predicted and measured transient NO and NH_3 concentration distributions, and the lower panels highlight differences in the predicted and measured results.	396
Figure IV.5.2 - Spatiotemporal comparison of model results with measurements at 1/16L, 1/8L, 3/16L and 1/4L, where L is the overall catalyst length. Comparison is over the four-step protocol which includes step transients and SS sections. The grey sections are for analytical purposes and to be ignored. Top panels compare predicted and measured transient NO and NH_3 concentration distributions, and the lower panels highlight differences in the predicted and measured results.	397
Figure IV.5.3 - (Left) Spatiotemporally resolved SCR-onset transients throughout a field-aged commercial honeycomb-monolith-supported Cu/CHA catalyst, where L is the overall catalyst length. Field-aged commercial Cu/CHA, 400 cpsi, 40,000 hr^{-1} space velocity, 200 ppm NO + 200 ppm NH_3 + 10% O_2 + 5% H_2O + Ar balance, 400°C, 400 cpsi, 40,000 hr^{-1} space velocity (Partridge et al. 2015). (Right) N_2 transients associated with SCR-onset for various ANR (1, 1.5, 2.4) and NO_x concentrations (200 ppm, 300 ppm, 430 ppm, and ANR~1), at 400°C and 500°C, and under Standard SCR and Fast SCR conditions. Field-aged commercial Cu/CHA, 400 cpsi, 40,000 hr^{-1} space velocity, 10% O_2 + 5% H_2O + Ar balance, 1/8 length from catalyst inlet.	398
Figure IV.5.4 - Ammonia conversion distributions for a commercial Cu/CHA SCR catalyst in degreened (DeG), hydrothermally aged (HTAged), and field-aged (FAged) states. Conversion inflections occur in the front catalyst regions above a common NH_3 threshold for all aged states, extending deeper into the catalyst with increasing temperature. The threshold varies with operating temperature. In general, anything that causes high NH_3 and NO_x concentrations to exist deeper into the catalyst will correspondingly expand the CI zone [5].	399
Figure IV.6.1 - Gaseous emissions conversions of fresh and aged TWC–GPFs with temperatures at the space velocity of 40,000 h^{-1} from the lab-flow system	402
Figure IV.6.2 - Scanning transmission electron microscopy–electron dispersive X-ray spectroscopy measurements of (a) and (b) fresh TWC–GPF, and (c) and (d) field-aged TWC–GPF.	403
Figure IV.6.3 - PXRD patterns of TWC–GPF samples: “lab-aged” was aged with conventional engine oil, while “ZDDP” was aged with zinc dialkyldithiophosphate (ZDDP)-strengthened engine oil.	403
Figure IV.6.4 - Ce^{3+} percentages in a combined Ce^{3+} and Ce^{4+} for TWC–GPF samples using Ce L_3 -edge X-ray absorption near-edge structure measurements: “ZDDP” was aged with ZDDP-strengthened engine oil, while “oil” was aged with conventional engine oil.	404
Figure IV.6.5 - H_2 -temperature programmed reduction results of lab- and field-aged TWC–GPFs.	405
Figure IV.7.1 - Properties of filter substrates studied (measured permeabilities in m^2 shown in parentheses).....	408
Figure IV.7.2 - Summary of initial filtration data for ultrafine particles across seven different filter substrates.....	409

Figure IV.7.3 - Distributions of controlling pore throat diameters obtained by capillary flow porometry	409
Figure IV.7.4 - Distributions of pore body sizes in pore network models generated for the seven filter substrates examined	410
Figure IV.7.5 - Three-dimensional reconstruction of a small section of the C2 material from X-ray CT data and an associated flow field (color key indicates local gas velocities in cm/s).....	410
Figure IV.7.6 - Distributions of streamline tortuosities in flow fields through the various filter media studied.....	411
Figure IV.8.1 - (a) Powder X-ray diffraction plots of double salts synthesized by varying molar compositions of lithium chloride and magnesium chloride and (b) ammonia release profiles of corresponding samples obtained using a TGA instrument.....	414
Figure IV.8.2 - TGA profile for ammonia release from $MgCl_2 \cdot 6NH_3$ and corresponding material containing 10% $CoCl_2$ and $NiCl_2$, respectively.....	415
Figure IV.9.1 - NO_x adsorption and release on various zeolite supported Pd materials	418
Figure IV.9.2 - Methane oxidation on supported Pd catalysts	419
Figure IV.9.3 - PM number and concentration in the exhaust from diesel particulate filter.....	420
Figure IV.10.1 - Impact of different SCO phases on the NO_2 out of the SCR reaction.....	424
Figure IV.10.2 - Effect of SCO phase on standard (NO only) and fast (equimolar NO , NO_2) SCR performance	425
Figure IV.10.3 - Effect of catalyst washcoat symmetry on SCR NO_x reduction performance	426
Figure IV.10.4 - Effect of passive soot oxidation on fast SCR reaction behavior	426
Figure IV.11.1 - (a) Top view and (b) cross-section view SEM images of low-temperature processed TiO_2 nano-array. (c) Photograph of field-size Pt/ TiO_2 nano-array samples (5.66-in diameter \times 3 in) for engine dynamometer testing. (Source: Gao [9], Lu et al. [10]).....	429
Figure IV.11.2 - (a) DOC activity in LTC-D simulated exhaust, (b) X-ray diffraction patterns, and (c) transmission electron microscope and energy-dispersive X-ray spectroscopy scanning transmission electron microscope elemental mapping of Pt/ TiO_2 nano-array before and after hydrothermal aging (HTA) at 700°C for 100 h. (Source: Gao [9], Lu et al. [10])	430
Figure IV.11.3 - Aberration-corrected high-angle annular dark-field scanning transmission electron microscopy images of Pt/rutile TiO_2 nano-arrays: (a) fresh and (b) after hydrothermal aging at 700°C for 100 h, confirming single atom dispersion of Pt (bright spots). c) Transient responses and the corresponding cumulative emission of THC and CO, respectively, of the fresh and aged Pt/ TiO_2 samples. (Source: Gao [9])	431
Figure IV.11.4 - DOC activity of ultra-low Pt loading on rutile TiO_2 nano-array in the CDC simulated exhaust. The addition of H_2 in the exhaust as an upstream promoter can significantly reduce the light-off temperature. (Source: Hoang et al. [11]).....	432
Figure IV.11.5 - Sulfur poisoning effects on CO and THC oxidation activity of Pt-Pd/ TiO_2 nano-array (900 cpsi substrate, 70 g PGM/ft ³ , weight ratio of Pt/Pd = 3/5). (Source: Gao [9])	432

Figure V.1.1 - Project schedule and phasing (Volvo).....	436
Figure V.1.2 - SuperTruck evolves into SuperTruck 2 (Volvo)	437
Figure V.1.3 - System simulation plan for SuperTruck 2 concept selection (Volvo).....	438
Figure V.2.1 - Powertrain layout, highlighting the location and arrangement for the M/G system coupled to the rear facing power take off.....	444
Figure V.2.2 - Heat release rate in response to increased injection rate. The lowest rate is the baseline. Increased peak rate corresponds to increased injection rate.	445
Figure V.2.3 - Powertrain mule milestones.....	446
Figure V.3.1 - Results of LCHP kit evaluation. (a) BSFC comparison of baseline and LCHP engines at rated. (b) Friction power comparison of each component.	448
Figure V.3.2 - Comparison of DEGR and HP EGR.....	449
Figure V.3.3 - Advanced fuel injection strategy simulation with CONVERGE 2.2.....	450
Figure V.3.4 - ORC configurations for 55% BTE: (a) HT loop ORC, (b) LT loop ORC, (c) BTE gain projection	450
Figure V.3.5 - Effects of oil and coolant temperatures on BSFC and exhaust energy distribution	451
Figure V.3.6 - Efficiency breakdown and loss comparison between two gasoline fuels	451
Figure V.4.1 - ST2 program phases.....	453
Figure V.4.2 - ST2 proposed freight efficiency test cycle.....	454
Figure V.4.3 - Detroit simulation and design process	455
Figure V.4.4 - Detroit roadmap to reach the 55% BTE target.....	456
Figure V.4.5 - DTNA roadmap to reach the 115% freight efficiency target.....	456
Figure V.5.1 - Gen 3 GDCI powertrain.....	460
Figure V.5.2 - BSFC as a function of BMEP for Gen 1, Gen 2, and Gen 3 GDCI engines.....	461
Figure V.5.3 - Gen 3 gasoline direct injection injector spray and computational fluid dynamics simulation showing wetless injection process	461
Figure V.5.4 - HC, CO emissions and combustion efficiency for GDCI early and late injection timings.....	462
Figure V.5.5 - Smoke emissions as a function of injection dwell for Gen 3 gasoline direct-ignition injectors.....	462
Figure V.6.1 - The Envera VCR engine	465
Figure V.6.2 - Fuel consumption for an F-150 pickup truck on the EPA city (FTP75) and highway test cycle	466
Figure V.7.1 - Sensitivity of two different spray designs to injection timing	470

Figure V.7.2 - Sensitivity of flame turbulence and fuel/air ratio to dwell variation in a two-pulse injection strategy.....	470
Figure V.7.3 - CFD mapping of EQR and burn rate comparing 2 ms and 0.5 ms dwell times	471
Figure V.7.4 - Cycle fuel economy predictions based on weighted test points	471
Figure V.7.5 - Critical hardware components	472
Figure V.8.1 - Production-intent RF sensor including control unit and antennas (Source CTS).....	475
Figure V.8.2 - RF catalyst cavity simulation results and comparison with experimental measurements.....	476
Figure V.8.3 - Cavity resonance response of SCR samples in the presence and absence of stored ammonia.....	476
Figure V.8.4 - Cavity resonance response of TWC samples in the presence and absence of stored oxygen.....	477
Figure V.8.5 - Calibrated RF sensor output and correlation to estimated SCR ammonia storage levels (a) and RF antennas installed on full-size SCR for vehicle testing (b) (Source Filter Sensing Technologies).....	478
Figure V.8.6 - Analysis of RF signal response to individual exhaust gas species	479
Figure V.9.1 - Isuzu engine unmounted from the vehicle, mounted on the dynamometer (Source: Eaton).....	482
Figure V.9.2 - Engine dynamometer test setup schematic	483
Figure V.9.3 - EAVS unit (Source: Eaton).....	484
Figure V.9.4 - eWHR unit (Source: Eaton).....	484
Figure V.9.5 - System control coordinated between Eaton and Isuzu ECUs.....	485
Figure V.9.6 - Control hardware (Source: Eaton)	485
Figure V.9.7 - Dynamometer setup with EAVS and EGR valve installation (Source: Eaton).....	486
Figure V.9.8 - Engine torque, fuel, and NO _x versus boost pressure at an engine speed of 2,000 rpm.....	486
Figure V.10.1 - Effect of turning PCN flow on/off	489
Figure V.10.2 - Fuel injection rate shape comparison.....	490
Figure V.10.3 - Apparent heat release rate (AHRR) comparison.....	490
Figure V.10.4 - Closed cycle efficiency comparison	490
Figure V.11.1 - VW EA888 four-cylinder GT-POWER engine model.....	494
Figure V.11.2 - VW Jetta GT-SUITE vehicle model.....	494
Figure V.11.3 - Full valvetrain in-cylinder head packaging.....	495
Figure V.11.4 - Probe test solenoid force vs. stroke comparison.....	496

Figure V.11.5 - e-DEAC system mechanization	496
Figure VI.1.1 - Micrographs of gray cast iron liner surfaces subjected to a scuffing load test at flow rates of (a) 0.1 $\mu\text{L}/\text{min}$, (b) 0.2 $\mu\text{L}/\text{min}$, and (c) 0.5 $\mu\text{L}/\text{min}$	500
Figure VI.1.2 - Micrographs of surface of field-operated engine liner: (a) optical, (b) SEM, and (c) EDAX of tribofilm	501
Figure VI.1.3 - TEM micrograph of tribofilm: (a) overview and (b) substrate-film interface.....	501
Figure VI.1.4 - Tribofilm micrographs: (a) scanning transmission electron microscopy and (b) EDAX elemental mapping	502
Figure VI.1.5 - SEM micrograph of (a) polishing and fatigue wear and (b) sub-surface structure.....	503
Figure VI.1.6 - SEM micrograph of (a) local tribofilm removal, (b) plastic strain pattern on the surface, (c) sub-surface plastic deformation below scuffed surface, and (d) sub-surface structure with severe scuffing damage	503
Figure VI.2.1 - Effect of MoDTC and OFM on friction for a steel–bronze and steel–Teflon contacts and impact of AWs on OFM for the steel–bronze contact.....	507
Figure VI.2.2 - Friction and wear results of a steel–bronze contact lubricated by base oils containing a ZDDP, an IL, or a ZDDP+IL combination.....	508
Figure VI.2.3 - While CB alone significantly increased the wear of both contact surfaces with little change in the wear ratio between the 52100 steel ball and M2 tool steel flat, CB+ZDDP together surprisingly flipped over the ball:flat wear ratio from 5:1 to 1:4.....	509
Figure VI.2.4 - The wear scars on the M2 (top) and A2 (bottom) flats lubricated by the PAO+CB+ZDDP (right) appeared much smoother compared with those lubricated by PAO+CB (left).....	510
Figure VI.3.1 - Average wear volume for each sample where the error bars represent the standard deviation. Three runs were averaged (UCM).....	516
Figure VI.4.1 - Kinematic viscosity for binary ester–SHC composite fluids	520
Figure VI.4.2 - Friction and wear measurement under unidirectional and reciprocating sliding	521
Figure VI.4.3 - Wear measurement under four-ball testing for binary ester–PAO4 composite fluids.....	521
Figure VI.4.4 - Transmission electron micrographs from: (a) and (b) typical colloidal additives, and (c) typical fully formulated oil	522
Figure VI.4.5 - (a) Transmission electron and (b) optical micrographs of ZnFe_2O_4 colloidal additives. (c) Profilometry of wear track of flat specimen tested with ZnFe_2O_4 colloidal additives.	522
Figure VI.4.6. (Left) Coefficient of friction (COF) and (right) wear of a VN–Cu coated steel pin against steel flat during tests in a used oil (taken after 10,000 miles). Uncoated steel has slightly higher friction, and the red friction trace is from the first generation coating. The cyan colored trace is from latest/ optimized coating. Three-dimensional and line scan images confirm no wear on this coated surface despite heavily contaminated/used oil.	523
Figure VI.5.1 - Relationship between PM organic and elemental carbon (OC, EC) for the three lubricants evaluated. Points are averages of three filter samples and error bars span the max and min values for each lubricant.	527

Figure VI.5.2 - Chromatogram of the thermal desorption step for PM collected under cold-start conditions from a GDI engine with three different viscosity lubricants. The mass spectroscopy signal has been normalized to the mass of the PM per cold-start. The lightest weight oil, 0W-20, has the highest quantity of compounds and the heaviest oil, 20W-50, has the least amount removed by the thermal desorption step.	527
Figure VI.5.3 - Formation of CO ₂ in WGS reaction between 200°C and 550°C for TWCs aged with different lubricant additives	528
Figure VI.5.4 - Fuel economy improvement by test cycle for four vehicles with 5W-30 test lube compared to ASTM base lube.....	528
Figure VI.6.1 - Pinion drive spin loss data for AW0704-A and 75W-140. Depicted is power loss (hp) at various vehicle speeds (mph) at multiple temperatures. Graph (a) presents data at 185°F, (b) at 165°F, and (c) at 145°F. The data points represent the average of three runs and the error bars represent the standard deviation.....	532
Figure VI.6.2 - Graphical display of XPS analytical data for post L-42 test gear tooth sections that completed testing in AW0704-R and AU6615-E fluids. Each bar represents three measurements and the error bars represent the standard deviation. Chart (a) depicts the unworn area and (b) depicts worn area of the gear teeth.	532
Figure VI.6.3 - High speed load carrying capacity and shock load testing post-test hardware ratings per ASTM D7452. Inspection results for AW0704-A, AW0704-R, and AU6615-E. Passing requirements are indicated by the dashed lines.	534
Figure VI.7.1 - High porosity PTWA coating shows friction benefit under mixed lubrication regime....	538
Figure VI.7.2 - DLC-coated rings show additional friction benefit with high porosity PTWA coatings under boundary and mixed lubrication regimes.....	538
Figure VI.7.3 - Nano-composite VN-Cu coated rings show additional friction benefit with high porosity PTWA coatings under boundary and mixed lubrication regimes.....	538
Figure VI.7.4 - PTWA coated cylinder bores in a linerless engine block (Source Ford Motor Company).....	539
Figure VI.7.5 - Polyalkylene glycol (PAG) engine oil showed significant friction benefits over GF-5 5W-20 oil	539
Figure VI.7.6 - Linerless engine block with PTWA coating shows friction benefits compared to cast iron liner engine block.....	540
Figure VI.8.1 - Optical photos of (A) a 1.0 wt% freshly prepared dispersion and three 1.0 wt% dispersions of PC13-NP-9.7k in PAO after storage for 60 d at -15°C, room temperature (r.t.), and 100°C. (B) 1.0 wt% dispersion of PC6-NP-7.0k in PAO at 80°C and sitting at r.t. for 2 h, 24 h, and 7 d after removal from a 80°C oil bath. (C) 1.0 wt% dispersion of PC8-NP-7.8k in PAO at 80°C and sitting at r.t. for 5 min, 1 d, and 7 d after removal from a 80°C oil bath.	543
Figure VI.8.2 - Friction curves for PAO SpectraSyn™ 4 (i), PAO additized with 1.0 wt% PC18-NP-13.9k (ii), PC16-NP-8.3k (iii), PC13-NP-9.7k (iv), PC12-NP-9.5k (v), ZDDP (vi), and PC13-20.8k free polymer (vii). The tribological tests were performed using a Plint TE-77 tribo-tester at 100°C under a point contact load of 100 N for a sliding distance of 1,000 m.	544

Figure VI.8.3 - (A) Friction coefficient traces of the neat PAO base oil and PAO + 0.50 wt% oleyamine-Ag NP-MUA. (Inset) Wear rates corresponding to the tribotests. (B) Friction coefficient traces showed that organic-modified Ag and Pd NPs effectively reduced friction but the organic ligand alone had little impact.....	544
Figure VI.8.4 - Finite element model of a rough surface sliding with a nanoparticle-additized lubricant. (a) Representative model geometry and (b) close up view of the deformation of interacting asperities and a nanoparticle.....	545
Figure VI.9.1 - Comparison of friction modifiers using the Mini-Traction Machine at 50% slide-to-roll ratio	549
Figure VI.9.2 - Schematic diagram of the direct soft mask fabrication process with only one ultraviolet irradiation.....	551
Figure VI.9.3 - Conformal contact press jig for putting on soft mask on highly concave bearing surface (Source George Washington University)	552
Figure VI.10.1 - MD simulation results: interaction energy (a) and surface coverage (b) of alkyl-cyclen (dark solid-dot curves) and alkylamine (light open-dot curves) FM molecules at different temperatures.....	556
Figure VI.10.2 - MSD of the alkyl-cyclen (solid-dot curves) and alkylamine (open-dot curves) FM molecules recorded during the MD simulation at 120°C.....	557
Figure VI.10.3 - (a) Variation of friction coefficients versus S/R ratio in the presence of different diblock VMs at 125°C under 1 GPa contact pressure. (b) Variation of friction coefficients versus S/R ratio in the presence of different lubricants at 125°C under 800 MPa contact pressure.	558
Figure VI.10.4 - (a) Variation of viscosity ratio $[\eta_{(\text{mixture})}/\eta_{(\text{PAO4})}]$ versus VM concentration at 100°C. (b) Dynamic light scattering measurements of hydrodynamic diameters for different dilute VM-PAO4 oil solutions.	559
Figure VI.10.5 - Film thickness measurements at 125°C at 0% (a) and 10% (b) S/R ratio.....	560
Figure VI.11.1 - Statistical analysis of FE improvement on engine oils	565
Figure VII.1.1 - Splitter plate dimensions and three-vehicle platoon in the Army 7 ft × 10 ft wind tunnel located at National Aeronautics and Space Administration Ames.....	568
Figure VII.1.2 - Model instrumentation for body-axis force measurements and engine cooling air supply.....	569
Figure VII.1.3 - Particle image velocimetry setup in the wind tunnel test section and a sample trailer wake flow field	570
Figure VII.1.4 - Thermal images (top view) of a two-vehicle platoon with an 81-ft full-scale spacing at 0° and 9° yaw	570
Figure VII.1.5 - Wind-averaged drag and pressure coefficient vs. vehicle spacing for a two-vehicle platoon with and without trailer boattails	571
Figure VII.1.6 - (a) Percent benefit in CD_{wa} for the entire two-vehicle platoon. (b) CP_{wa} as a function of spacing for a two-vehicle platoon with and without trailer boattails.....	572

Figure VII.1.7 - (a) CD_{wa} for a 40-ft separation distance between the first and the second vehicle as a function of vehicle spacing for a three-vehicle platoon. (b) CD_{wa} for the entire three-vehicle platoon as a function of vehicle spacing. 572

Figure VII.1.8 - (a) CP_{wa} for a 40-ft separation distance between the first and the second vehicle as a function of vehicle spacing for a three-vehicle platoon. (b) CP_{wa} for the third vehicle with multiple separation distances between the first and second vehicles. 573

Figure VII.1.9 - CD_{wa} for a two-vehicle platoon (30-ft and 50-ft spacing) as a function of lateral misalignment..... 573

Figure VII.2.1 - Response effects obtained on design of experiment study 577

Figure VII.3.1 - Schematic images of organically modified GnPs 583

Figure VII.3.2 - Experimental setup for the synthesis of SnFs..... 583

Figure VII.3.3 - SEM images of synthesized silica fibers using the experimental setup in Figure VII.3.2. The diameter of the fibers is smaller than 100 nm..... 584

Figure VII.3.4 - (a) Modulus values of the synthesized composites at a broad temperature range. (b) T_{and} values of the synthesized composites at a broad temperature range. The respective values of a commercial elastomer that was provided by our industrial partner are also included..... 584

Figure VII.3.5 - Transmission electron microscopy images of the (a) unfilled SBR, (b) SBR filled with GnPs, and (c) SBR filled with functionalized GnPs 585

Figure VII.3.6 - SEM images of the (a) unfilled SBR, (b) SBR filled with GnPs, and (c) SBR filled with functionalized GnPs and SnFs 585

Figure VII.4.1 - Filler vs. $\tan \delta$ at 60°C, normalized to N330 588

Figure VII.4.2 - Flex fatigue of different fillers 588

Figure VII.4.3 - Ozone resistance by bent loop and crack growth 588

Figure VII.4.4 - Discoloration test..... 589

Figure VII.4.5 - 6-PPD concentration profile after cure and aging..... 589

Figure VII.5.1 - ISX450 engine with UltraShift Plus AMT under test in the powertrain test cell at ORNL's VSI Laboratory 593

Figure VII.5.2 - Distribution of Class 8 Trucks by On-Road Vehicle Weight (Source: National Academy of Sciences 2008) 593

Figure VII.5.3 - Engine operating area for the three high speed tests considered in this study: 65 mph cruise, 55 mph cruise, and HTDC..... 594

Figure VII.5.4 - Fuel consumption for different cycles and vehicle weight..... 595

Figure VII.5.5 - ORNL is beginning to work on modelling the new single supervisory controller using the offline validated model 596

List of Tables

Table 1 - Storage Efficiencies of Pd/ZSM-5 Trapping Material Before and After Severe Aging (Toops, report IV.3).....	20
Table 2 - Drive Cycle Fuel Consumption Improvement (Fernandez, report V.11).....	24
Table 3 - Fuel Efficiency Improvement of Each Valvoline Candidate (Wu, report VI.11).....	27
Table I.9.1 - Influence of Split Ratio upon Combustion Noise and Smoke (FSN).....	83
Table I.26.1 - Transport Properties and Bubble Characteristics for Considered Test Cases	188
Table II.1.1 - Fuel Properties and Composition for the Nine Fuels Used in This Study	200
Table II.2.1 - Fuel Properties with RON 98 and Operating Conditions	207
Table II.3.1 - FWG Expanded Matrix Fuel Formulations	211
Table II.5.1 - Fuel Mixture Matrix.....	223
Table II.6.1 - K value and R ² between knock-limited CA50 phasing and each of the three different anti-knock metrics: OI, RON, and AKI. Shading represents conditional formatting where green represents a high R ² value and red represents a low R ² value.	229
Table II.7.1 - Properties of Aromatics Blended into FACE B.....	234
Table II.7.2 - Engine Operating Conditions for PM Measurements; Intake Air Temperature Fixed at 35°C	235
Table II.7.3 - Results of Linear Regression Analysis for Condition A using mole% Concentrations of Ethanol and Aromatics in the Blends	237
Table II.8.1 - Gas Composition for Hydrothermal Aging and De-Greening the Catalyst	243
Table II.8.2 - Synthetic Engine Exhaust Gas Composition	243
Table II.9.1 - Fuel Blend Naming and Splash-Blending Volumetric Composition	248
Table II.10.1 - Polar Species Identified in Collected Soot	254
Table II.12.1 - Tested Fuels.....	263
Table II.13.1 - Fuel Properties	269
Table II.14.1 - ϕ -Sensitivities As Indicated by the Δ CA50 Between Premixed and PFS Fueling.....	276
Table II.21.1 - Fuel Palette for the GS with HPF Chemical Kinetic Model.....	313
Table II.24.1 - Comparison of the Model-Based Estimates for Octane Numbers and Phi-Sensitivity of Several Blendstocks in the Gasoline Chemistry Model.....	330
Table III.2.1 - Effective PRF Number for the Three Parent Fuels and Their Reformate Mixtures	351
Table III.3.1 - Drive Cycle Simulation Results.....	358

Table III.5.1 - Conditions Tested to Explore the Effects of Multiple Fuel Injection Events and Fuel Blends on Engine Performance..... 366

Table IV.3.1 - Storage Efficiencies of Pd/ZSM-5 Trapping Material Before and After Severe Aging..... 388

Table IV.9.1 - NO_x/Pd Ratio during NO_x Trapping at 100°C for 10 min..... 419

Table IV.10.1 - Passive Soot Oxidation (PSO) Light-Off Metrics and Comparison to the Presence and Absence of SCO Phase 425

Table V.6.1 - Fuel Economy Projections for a Ford F-150 Full-Size Pickup Truck..... 466

Table V.7.1 - Prime Path SCE Hardware Matrix 471

Table V.9.1 - Engine Dynamometer Test Plan, Including Baseline and EAVS/eWHR Technologies..... 483

Table V.11.1 - Drive Cycle Fuel Consumption Improvement..... 494

Table VI.2.1 - Compositions of Ball and Flat Steels 510

Table VI.2.2 - Summary of Wear Results Tested in PAO+CB and PAO+CB+ZDDP511

Table VI.3.1 - Kinematic Viscosities and VI Values for All Polymer Analogs and Benchmarks Studied 515

Table VI.3.2 - Shear Stability Data using the CEC L45 Test Method (20 h at 100°C) 515

Table VI.3.3 - Kinematic Viscosities and VI Values for the IL Polymers 517

Table VI.6.1 - Bench Test Results for Wear, Extreme Pressure, Thermal Oxidative Stability, Rust Prevention and Copper Corrosion for 75W-140, AW0704-A, AW0704-R, and AW0704-BN Formulations 533

Table VI.6.2 - Results for ASTM D5704 thermal oxidation testing. Results displayed for 75W-140, OSP options AW0704-A, AW0704-BN, and top-treat formula AU6615-E. 533

Table VI.6.3 - Ring and pinion gear inspection rating results after completion of ASTM D6121, load carrying capacity at low speed and high torques test. Results are shown for OSP AW0704-A and top-treat AU6615-E. 534

Table VI.8.1 - Characterization Data for Poly(alkyl methacrylate) Brush-Grafted, 23 nm Silica NPs and the Corresponding Free Polymers 542

Table VI.8.2 - Wear Volumes for Flats and Balls after Tribological Tests with PAO Additized with Organic-Modified Ag and Pd NPs 545

Table VI.9.1 - Sequence IV Engine Dynamometer Test Results 549

Table VI.11.1 - Valvoline Candidate Oils and Baselines for J1321 Test 563

Table VI.11.2 - J1321 Test Segment Design 564

Table VI.11.3 - J1321 Test Results..... 564

Table VI.11.4 - FE Improvement of Each Valvoline Candidate 564

Table VI.11.5 - Estimated Percent Improvements for Various Oil Combinations 565

Table VII.2.1 - Lab and Tire Data from First Tire Build	578
Table VII.2.2 - Lab Compound Data of Improved Prototype.....	579
Table VII.5.1 - Vehicle Parameters	593
Table VII.5.2 - Error Between Experimental and Simulation.....	595

(This page intentionally left blank)

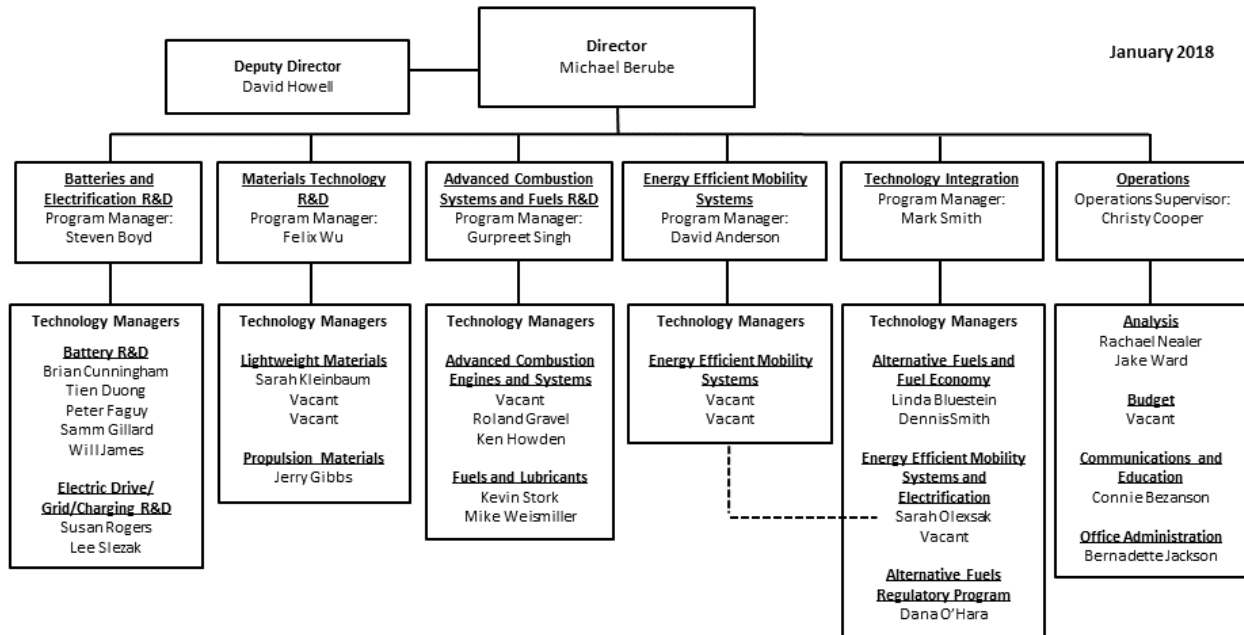
Vehicle Technologies Office Overview

Vehicles move our nation. Vehicles transport more than \$36 billion worth of goods each day¹ and move people more than 3 trillion vehicle-miles each year². Growing our national economy requires transportation and transportation requires energy. The average U.S. household spends nearly one-fifth of its total family expenditures on transportation³, making transportation the most expensive spending category after housing. The transportation sector accounts for 70% of U.S. petroleum use. The United States imports 25% of the petroleum consumed, sending more than \$10 billion per month⁴ overseas for crude oil.

To strengthen national security, enable future economic growth, and increase transportation energy efficiency, the Vehicle Technologies Office (VTO) funds early-stage, high-risk research on innovative vehicle and transportation technologies. VTO leverages the unique capabilities and world-class expertise of the national laboratory system to develop innovations in electrification, advanced combustion engines and fuels, advanced materials, and energy efficient mobility systems.

VTO is uniquely positioned to address early-stage challenges due to strategic public-private research partnerships with industry (e.g., U.S. DRIVE, 21st Century Truck Partnership). These partnerships leverage relevant expertise to prevent duplication of effort, focus DOE research on critical R&D barriers, and accelerate progress. VTO focuses on research that industry does not have the technical capability to undertake on its own, usually due to a high degree of scientific or technical uncertainty, or it is too far from market realization to merit industry resources. VTO’s research generates knowledge that industry can advance to deploy innovative energy technologies to support affordable, secure, and efficient transportation systems across America.

Vehicle Technologies Office Organization Chart



¹ <https://ops.fhwa.dot.gov/publications/fhwahop16083/ch1.htm#t1>

² <https://www.fhwa.dot.gov/policyinformation/statistics/2015/vm1.cfm>

³ <https://www.bls.gov/cex/2015/standard/multiyr.pdf>

⁴ Transportation Energy Data Book Edition 34, ORNL, Table 1.7 and Table 10.3; Overseas includes countries and territories outside the 50 States and the District of Columbia.

Advanced Combustion Systems and Fuels Program Overview

Introduction

The Advanced Combustion Systems and Fuels Program supports VTO's goal and focuses early-stage research and development (R&D) to improve understanding of the combustion processes, fuel properties, and emission control technologies while generating knowledge and insight necessary for industry to develop the next generation of engines.

Cutting-edge research using unique capabilities and expertise at the national laboratories, done in close collaboration with academia and industry, will strengthen the knowledge base of the next generation higher-efficiency, very-low-emissions combustion engines for passenger and commercial vehicles that meet future federal emissions regulations. In addition, science-based understanding of how engine efficiency and emissions are impacted by fuel properties and conversely how engines can be modified to take advantage of desirable fuel properties could enable further efficiency improvements. Approached as a system, engines, fuels, and emission control (exhaust aftertreatment) can be optimized together using the fundamental knowledge and new understanding developed by this program. Introduction of co-optimized high performance fuels and advanced engines that meet prevailing emissions regulations could expeditiously reduce petroleum use in U.S. highway transportation over the next several decades, during which time the vast majority of vehicles will still include an engine¹.

Goals

The Advanced Combustion Systems and Fuels R&D Program has set the following goals for passenger and commercial vehicle fuel economy improvements:

- By 2030, improve light-duty engine efficiency to demonstrate 35% improvement in passenger vehicle fuel economy (25% improvement from engine efficiency and 10% from fuel optimization), relative to a 2015 baseline vehicle.
- By 2030, improve heavy-duty engine efficiency by 35% relative to a 2009 baseline vehicle and identify cost-effective high-performance fuels that can further increase efficiency up to an additional 4%.

The program goals have to be achieved while meeting future U.S. Environmental Protection Agency (EPA) regulations on pollutant emissions that impact air quality. The U.S. EPA Tier 3 Bin 30 emission standard for passenger vehicles represents a greater than 80% reduction in combined emissions of nitrogen oxides (NO_x) and non-methane organic gases, and a 70% reduction in particulate matter (PM) emissions (to less than 3 mg/mi) compared to the previous Tier 2 Bin 5 standard. In order to achieve these extremely low criteria emission levels along with increasing fuel economy requirements, future catalyst and emission control systems must be developed to operate efficiently in lower exhaust temperatures (achieve greater than 90% conversion of criteria pollutants at 150°C).

State of the Art

Significant advances in engine combustion, emission controls, and advanced engine technologies continue to increase the thermal efficiency of internal combustion engines with simultaneous reduction in emissions. With these advances, gasoline and diesel engines continue to be attractive engine options for transportation vehicles. In addition, these engines can be readily adapted to use natural gas and biofuels, such as ethanol and biodiesel, and can be integrated with hybrid and plug-in hybrid electric vehicle powertrains.

Low temperature combustion (LTC) strategies such as homogeneous charge compression ignition, pre-mixed charge compression ignition, and reactivity controlled compression ignition, exhibit high efficiency with

¹Energy Information Administration, Annual Energy Outlook 2017. Reference case scenario forecasts that even in 2040, over 96% of all highway transportation vehicles sold will still have internal combustion engines.

significant reductions in engine-out emissions of NO_x and PM to levels that reduce the requirements for exhaust aftertreatment. Progress in LTC strategies continued to expand the operational range, covering speed and load combinations consistent with light-duty and heavy-duty drive cycles. Significant R&D effort has focused on fuel–air mixing, air handling, impact of fuel properties, and engine controls. These address major challenges of fuel mixing, conditioning of intake air, combustion timing control, transient response, and expansion of the operational range.

Spark ignition (SI) gasoline engines power the majority of the U.S. light-duty vehicle fleet and generally operate with stoichiometric combustion to allow use of highly cost-effective three-way catalysts for emission control. Engine technology advances in recent years contributing to substantial improvements in gasoline engine efficiency include direct fuel injection, flexible valve timing and lift systems, improved combustion chamber design, and reduced mechanical friction. Lean-burn gasoline engines have been introduced in countries with less stringent emission regulations. These engines have higher efficiencies at part load but require more costly lean- NO_x emission controls to meet the more stringent U.S. emissions regulations.

Advances in lean-burn gasoline emission controls are critical for introducing this higher-efficiency technology in the U.S. market. The challenge for high-efficiency potential of lean-burn gasoline technology is in creating combustible mixtures near the spark plug and away from cylinder walls in an overall lean environment. A comprehensive understanding of the dynamics of fuel–air mixture preparation is required, i.e., intake air flows and fuel sprays, as well as their interactions with the combustion chamber surfaces over a wide operating range and generating appropriate turbulence to enhance flame speed. Improved simulation tools are being developed for optimizing the lean-burn systems over the wide range of potential intake systems, piston geometries, and injector designs. Another challenge is the reliable ignition and combustion of lean (dilute) fuel–air mixtures. Robust, high-energy ignition systems and mixture control methods are also being developed to reduce combustion variability at lean and highly boosted conditions. Several new ignition systems have been proposed (e.g., high-energy plugs, plasma, corona, laser, etc.) and are being investigated.

Downsized, gasoline SI engines have been a major trend during the last decade to improve light-duty vehicle fuel economy. Higher power density downsized engines were enabled by boosted air handling systems and gasoline direct injection fueling systems. Efficiency improvement through higher compression ratios, however, has been constrained by current fuel properties. Fuel autoignition, which causes engine knock, has limited the compression ratio of SI engines.

Diesel engines are also well-suited for light-duty vehicle applications, delivering fuel economies that are considerably higher than comparable SI engines. Key developments in combustion and emission controls combined with the availability of low-sulfur diesel fuel have enabled manufacturers to achieve the mandated emission levels and introduce additional diesel-powered models to the U.S. market. DOE research has contributed to all of these areas. However, diesels in passenger cars have limited market penetration in the United States primarily due to the cost of the added components required to reduce emissions; hence, research was focused on increasing engine efficiency and reducing the cost of emissions compliance.

The heavy-duty diesel is the most common engine for commercial vehicles because of its high efficiency and outstanding durability. Efficiency gains were modest over the last decade when R&D efforts focused on meeting increasingly stringent heavy-duty engine emission standards. Efforts turned to improving the engine efficiency after EPA 2010 emission standards for NO_x and PM were met. Continued aggressive R&D to improve boosting, thermal management, and the reduction and/or recovery of rejected thermal energy has resulted in current heavy-duty diesel engine efficiencies in the 43–45% range. Advanced combustion regimes and demonstrated waste heat recovery technologies can potentially improve overall engine efficiency to 57%.

The Co-Optimization of Fuels and Engines (Co-Optima) initiative, which kicked-off in 2016, is a collaboration between the Advanced Engine and Fuels Technology program and the Bioenergy Technologies Office. The project formed a national laboratory consortium to investigate the co-development of advanced fuels and engines which offers a great opportunity to improve engine efficiency and diversify the fuel supply. Market introduction of advanced fuel and engine technologies can be accelerated by addressing the fuel property limitations and barriers described above to more efficient light-duty and heavy-duty engines. Research focused

on identifying fuel properties that enable optimized engine performance, and a fuel property-based approach could provide the technical information required to define future fuel requirements that are not based on composition, allowing the market to define the best means to blend and provide these fuels.

Although NO_x and PM engine-out emissions are significantly lower for advanced LTC strategies and lean-burn technologies such as conventional and advanced diesel combustion strategies for light- and heavy-duty engines as well as lean-burn gasoline engines, further reductions are needed to meet future more stringent regulations. Also, higher hydrocarbon and carbon monoxide (CO) emissions require additional controls which are often a challenge with the low exhaust temperatures (about 150°C).

Urea selective catalytic reduction (urea-SCR) technology has been used for NO_x control in Tier 3 light-duty vehicles, heavy-duty engines, and other diesel engine applications in the United States. Using urea-SCR, light-duty manufacturers have been able to meet the Tier 3 emissions standard. All heavy-duty diesel vehicle manufacturers have adopted urea-SCR since it has a broader temperature range of effectiveness than competing means of NO_x reduction and allows the engine/emission control system to achieve higher fuel efficiency. Although urea-SCR is a relatively mature catalyst technology, more support research to aid formulation optimization and minimize degradation effects such as hydrocarbon fouling was conducted.

The direct injection technology utilized for most advanced gasoline engines produces PM emissions that, although smaller in mass than diesel particulates, may still represent significant emissions in terms of particulate number counts. PM emissions from dilute combustion gasoline engines are not fully understood; their morphology and chemical composition are also affected by combustion. Research was conducted to develop filtration systems for smaller diameter PM that are durable and with low fuel economy penalty. Fuel economy penalties are caused by increased backpressure and the need to regenerate the filter.

Complex and precise engine and emission controls require sophisticated feedback systems employing new types of sensors. NO_x and PM sensors are under development and require additional advances to be cost-effective, accurate, and reliable. Upcoming regulations with increased requirements for onboard diagnostics will also challenge manufacturers trying to bring advanced fuel-efficient solutions to market. The role of sensors and catalyst diagnostic approaches is a key element of emission control research.

Cost is a primary limitation to further adoption of current light-duty diesels. Complex engine and exhaust gas recirculation systems, and the catalyst expense and volume associated with urea-SCR systems and diesel particulate filters, result in higher overall costs in comparison to conventional gasoline vehicle systems. Aggressive research has substantially decreased the combined fuel penalty for both devices to less than 4% of total fuel flow; further reductions are possible. Another improvement being pursued is to pair NO_x traps (LNT) technology with SCR catalysts. The advantage is that the SCR catalyst uses the NH_3 produced by the LNT, so no urea is needed. Formulation and system geometries have been researched to reduce the overall precious metal content of LNT+SCR systems to reduce cost and make the systems more feasible for light-duty vehicles.

Current Technical Focus Areas and Objectives

The Advanced Combustion Systems and Fuels Program supports early-stage R&D to improve the understanding of, and ability to manipulate, combustion processes, generating knowledge and insight necessary for industry to develop the next generation of engines and fuels. Unique facilities and capabilities at the national laboratories are used in cutting edge research, in close collaboration with academia and industry, to strengthen the knowledge base of high-efficiency, advanced combustion engines and fuels.

The program objectives are as follows:

- Further the fundamental understanding of advanced combustion strategies that simultaneously show higher efficiencies and very low emissions, elucidating on the effects of critical factors such as fuel spray characteristics, in-cylinder air motion, heat transfer, and others

- Develop science-based understanding of how engine efficiency and emissions are impacted by fuel properties and, conversely, how engines can be modified to take advantage of desirable fuel properties and control of emissions from co-optimized fuels/engines to meet future emission regulations
- Improve the effectiveness and durability of emission control (exhaust aftertreatment) devices to complement advanced combustion strategies and high performance fuels, as well as reduce their use of precious metals to reduce cost, which is another barrier to penetration of advanced combustion engines in the passenger and commercial vehicle markets
- Develop precise and flexible engine controls, and sensors for control systems and engine diagnostics, to facilitate adjustments of parameters that allow advanced combustion engines to operate over a wider range of engine speed and load conditions
- Further advance engine technologies such as turbo-machinery, flexible valve systems, advanced combustion systems, and fuel system components to reduce parasitic losses and other losses to the environment, and incorporate technologies such as bottoming cycles to recover energy from the engine exhaust.

The program maintains close collaboration with industry through a number of working groups and teams and utilizes these networks for setting goals, adjusting priorities of research, and tracking progress. These collaborative groups include the Advanced Combustion and Emission Control Technical Team and Fuels Working Group of the U.S. DRIVE Partnership and the Engine Powertrain Team of the 21st Century Truck Partnership. Focused efforts are carried out under the Advanced Engine Combustion Memorandum of Understanding and the Cross-Cut Lean Exhaust Emission Reduction Simulation activity (which include auto manufacturers, engine companies, fuel suppliers, national laboratories, and universities), and the Advanced Engine Cross-Cut Team consisting of light- and heavy-duty manufactures. In the fuels and engines co-optimization effort, the program works closely with a broad range of stakeholders representing vehicle and engine manufacturers, energy companies, biofuel producers, manufacturers of catalysts and emission control systems, fuel distributors, and retailers to identify and address critical issues.

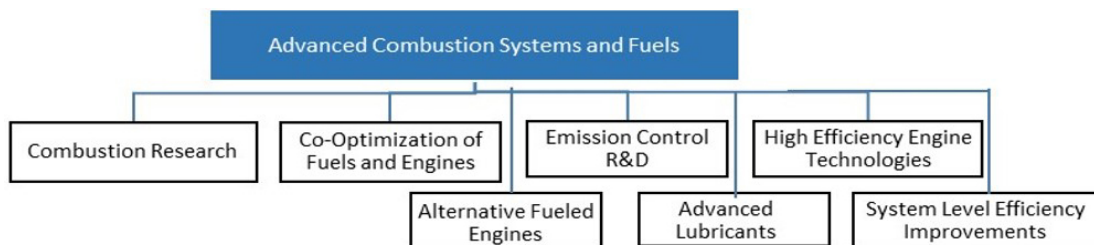


Figure 1 - Research areas within advanced combustion systems and fuels

The Advanced Combustion Systems and Fuels Program focuses on numerous research areas, including combustion fundamentals, co-optimization of fuels and engines, alternative fuel engines, emission control R&D, high-efficiency engine technologies, lubricant technologies, and system-level efficiency improvement. Projects competitively selected and awarded through Funding Opportunity Announcements are fully funded through the duration of the project in the year the funding is awarded. Directly funded work at the national laboratories is subject to change based on annual appropriations.

Combustion Research

Focus of research on combustion fundamentals is on the use of unique diagnostic tools, including advanced lasers, high-intensity X-rays, and neutron sources, to characterize fuel injection, air mixing, combustion, and pollutant formation within the engine. Experimental data are used to develop quantitative relationships between in-cylinder processes and efficiency improvement potential for both current and next-generation engines. In addition, this research area is focused on developing predictive high fidelity models to simulate the fundamental physics of in-cylinder processes using high performance computing resources at the national laboratories. Important aspects of this work include the development of detailed and accurate chemical kinetics

models of different fuels. Numerical routines are developed for models that can reduce the computational time to enable high fidelity engine models as viable engine design tools for industry.

Knowledge from experiments, in combination with predictive engine simulation, will enable companies to develop a new generation of low-temperature combustion engines.

Co-Optimization of Fuels and Engines

Early-stage research on fuel property impacts on combustion and determine fuel characteristics that enable higher efficiency in advanced combustion strategies. The research focus is on performance of tailored blend stocks including bio-derived, synthetic, and petroleum-based blend stocks that will increase vehicle efficiency, specifically on advanced fuels that enable maximum performance of advanced conventional and kinetically controlled engine technologies.

Alternative Fueled Engines

The focus of this activity is on overcoming technical barriers to the implementation of petroleum-displacing fuels. Alternative fuels, such as natural gas, and renewable fuels, such as drop-in biofuels, frequently have technical barriers that impede their implementation in traditional petroleum fuels equipment and infrastructure. Work to overcome these barriers will include support for new, alternative fuel engine offerings, testing and evaluation of refueling infrastructure, and evaluation of the emissions impact of novel alternative fuels.

Emission Control R&D

Meeting anticipated future emission standards will be challenging for LTC, high-efficiency diesel, and lean-burn gasoline engines. The lower exhaust temperatures of these engines make conventional aftertreatment systems unsuitable. Exhaust aftertreatment systems for advanced combustion engines will need catalyst technologies that are active at the lower exhaust temperatures, namely those that provide greater than 90% conversion efficiency at about 150°C. Early-stage fundamental research at the national laboratories, in close collaboration with industry and academia, will address barriers to achieving key performance metrics such as catalyst activity, selectivity, durability, and cost-effectiveness.

High Efficiency Engine Technologies

Projects of this activity research and develop technologies for more efficient, clean advanced engine/powertrain systems to improve passenger and commercial vehicle fuel economy.

Lubricant Technologies

Projects of this activity focus on research and development of technologies that can reduce friction losses in new and legacy vehicles to improve fuel economy.

System-Level Efficiency Improvement

Research and development projects focus on system level improvements to achieve vehicle performance targets, such as improvements in drivetrain efficiency, aerodynamic drag, and tire rolling resistance.

Technical Highlights

Combustion Research

- Sandia National Laboratories is providing the physical understanding of the in-cylinder combustion processes needed to minimize the fuel consumption and the carbon footprint of automotive diesel engines while maintaining compliance with emission standards and meeting customer expectations. In FY 2017 they (1) identified the degree of constant volume combustion as a key to improving thermal efficiency, (2) demonstrated that engine efficiency improves with a stepped-lip piston compared to a conventional piston because the second half of combustion occurs faster and the degrees of constant volume combustion is therefore higher, and (3) analyzed numerical simulation results to reveal the mechanism by which the stepped-lip piston changes turbulent flow structure and enhances mixing. (Busch, report I.1)

- Sandia National Laboratories is developing a fundamental understanding of how in-cylinder controls can improve efficiency and reduce pollutant emissions of advanced low-temperature combustion technologies. In FY 2017 (1) a new combined diffused background illumination and natural luminosity imaging technique showed clear evidence of post-injection soot reduction by increased local temperatures, strengthening suggestions from 2014 soot planar laser-induced incandescence and OH planar laser-induced fluorescence imaging data; (2) quantitative soot diffused background illumination imaging showed late cycle reduction of soot in post-jet, consistent with increased mixing from a second entrainment wave, a new fluid mechanic effect that was described in 2008; and (3) they developed a soot volume fraction to natural luminosity transfer function to aid in the interpretation of natural luminosity images. (Musculus, report I.2)
- Sandia National Laboratories is facilitating the improvement of engine spray combustion modeling and accelerating the development of cleaner, more fuel efficient engines. In FY 2017 they (1) developed optical theory leading to optimization of a diffused back-illumination extinction imaging diagnostic used to quantify liquid penetration and soot formation/oxidation processes in sprays and published theory and standardized procedures for dimensioning and implementing the diagnostic; (2) applied a high-speed (100 kHz) Sandia-developed pulsed burst laser to measure temporally resolved mixture fraction of diesel sprays using Rayleigh scattering; and (3) quantified spray spreading angle, liquid penetration, ignition, and combustion behavior of diesel Spray C (cavitation) and Spray D injectors. (Pickett, report I.3)



Figure 2 - Example diffused back-illumination extinction imaging images using the original setup (top) and optimized setup (bottom). The light and dark regions in the top image are caused by beam steering and introduce significant error when attempting to quantify soot or liquid penetration in high-pressure sprays (Pickett, report I.3)

- Sandia National Laboratories is providing the fundamental understanding (science base) required to overcome the technical barriers to the development of practical low temperature gasoline combustion (LTGC) engines for light-duty and medium- and heavy-duty applications. In FY 2017 they (1) showed double direct injection partial fuel stratification is a very effective technique for controlling combustion in as LTGC engine through changes in the autoignition reactivity of the charge; (2) determined spark assist limits for ϕ , P_{in} , and T_{in} for well-premixed LTGC; (3) conducted studies in collaboration with other national laboratories; (4) collaborated with Lawrence Livermore National Laboratory on an uncertainty quantification analysis of cylinder pressure data in the Sandia LTGC engine; and (5) supported Lawrence Livermore National Laboratory in the development of a kinetic model that worked well for RD5-87, the regular E10 gasoline used for the experiments. (Dec, report I.4)
- Sandia National Laboratories is determining fuel energy utilization pathways for gasoline advanced compression ignition strategies that involve retrained residuals and elucidating mechanisms responsible for enhanced auto-ignition with intake ozone addition. In FY 2017 they (1) evaluated the impact of in-cylinder negative valve overlap reformat on full-scale advanced compression ignition engine performance using a single-cylinder research engine with a 11.3:1 compression ratio and 1,200 rpm engine speed, (2) investigated intake ozone addition as an alternate method to improve charge reactivity for low-load advanced compression ignition that could potentially eliminate the larger parasitic heat losses that result from negative valve overlap recompression period, and (3) quantitatively measured in-cylinder ozone concentration using an ultraviolet light absorption diagnostic, with the results used to evaluate complementary chemistry modeling. (Ekoto, report I.5)

- Argonne National Laboratory is developing physics-based nozzle flow and spray models, and the capability to perform coupled nozzle flow and spray simulations. In FY 2017 they (1) predicted the onset of flash boiling for different fuels and fuel blends of interest ranging from gasoline to pure ethanol, (2) demonstrated that the one-way coupling approach along with high-fidelity turbulence model large eddy simulation can predict the on-set of plume merger and collapse for gasoline direct injection sprays, and (3) ran full chemistry mechanism (>2,500 species) in engine simulations with large eddy simulation. (Som, report I.6)

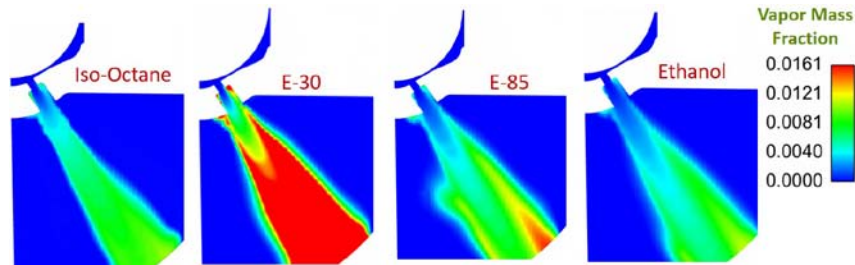


Figure 3 - Vapor mass fraction contours through a cut-plane passing through a single orifice of Spray G showing the propensity of ethanol blends to flash boil significantly more than the pure components. The simulations were performed under the standard Spray G conditions from Engine Combustion Network. (Som, report I.6)

- Argonne National Laboratory is demonstrating the ability to build a full three-dimensional model of a gasoline direct injection fuel injector using combined X-ray and neutron tomography in collaboration with Oak Ridge National Laboratory. In FY 2017 they completed high resolution measurements of the flow passages inside the Engine Combustion Network Spray C and Spray D injectors. (Powell, report I.7)
- Argonne National Laboratory is acquiring autoignition data using Argonne’s rapid compression machine at conditions representative of today’s and future internal combustion engines, including high pressure ($P = 15\text{--}80$ bar), low-to-intermediate temperatures ($T = 650\text{--}1,100$ K), and a range of fuel loadings. In FY 2017 they (1) acquired autoignition data over a range of conditions for bi- to multi-component surrogates of a research-grade, full boiling-range gasoline; (2) computationally investigated mild ignition phenomena using one-dimensional flame dynamics code; and (3) acquired autoignition data over a range of conditions for RD5-87, a research-grade full boiling-range gasoline representative of U.S. market E10 regular gasoline. (Goldsborough, report I.8)
- Argonne National Laboratory is optimizing the operating conditions to use low cetane fuel to achieve clean, high-efficiency engine operation and demonstrating the use of low temperature combustion as an enabling technology for high-efficiency vehicles. In FY 2017 they operated the engine at various engine speeds and medium-high engine loads with injection timing and exhaust gas recirculation sweeps. This approach provided significant information regarding the tradeoffs between the variables. (Ciatti, report I.9)
- Argonne National Laboratory is addressing the technological barrier of limited attainable gasoline direct injection engine efficiency due to the lack of robust spark ignition dilute combustion technology and controls. In FY 2017 they (1) developed a spark ignition model to include the effects of turbulence on the ignition source, (2) characterized laser ignition performance in gasoline direct injection engines by means of simulation and experiments, (3) characterized nonequilibrium plasma behavior using optical and engine diagnostics, and (4) initiated and validated nonequilibrium plasma modeling against experiments. (Scarcelli, report I.10)

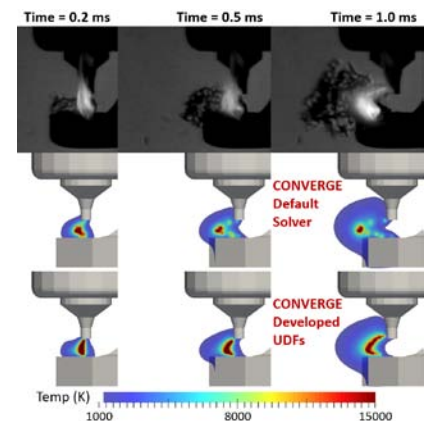


Figure 4 - Improved model of the spark channel elongation and energy deposition at non-quietest flow conditions (Scarcelli, report I.10)

- Oak Ridge National Laboratory is developing and assessing the potential of single- and dual-fuel high efficiency clean combustion concepts on multi-cylinder engines for improved efficiency and emissions. In FY 2017 they (1) showed lower delta reactivity dual-fuel low temperature combustion was able to match efficiency at lower loads, (2) developed a one-dimensional model to inform decision on a next generation air handling system, and (3) employed thermodynamic analysis to quantify the effect of combustion phasing and duration on thermal efficiency. (Curran, report I.11)

- Oak Ridge National Laboratory is quantifying the efficiency gain with the catalytic reforming strategy at an operating condition of 2,000 rpm, 4 bar brake mean effective pressure and determining the most thermodynamically favorable boundary conditions for the reforming catalyst at the engine operating condition studied. In FY 2017 they (1) achieved up to 10% reduction in fuel consumption with exhaust gas recirculation on multi-cylinder engine, (2) developed a catalyst operating strategy to continuously produce >15% H₂ without coking, and (3) employed thermodynamic modeling of catalyst and computational fluid dynamic modeling of combustion to provide insight and paths forward on favorable operating conditions. (Szybist, report I.12)

- Oak Ridge National Laboratory is implementing high-fidelity neutron imaging capabilities using the High Flux Isotope Reactor for advanced transportation research. In FY 2017 they demonstrated neutron imaging of fuel injection in a dynamic capacity at the High Flux Isotope Reactor and has shown the ability to visualize the rate of evaporation in the internal injector sac as a function of injector and chamber conditions. (Toops, report I.13)

- Lawrence Livermore National Laboratory is developing detailed chemical kinetic models for fuel components used in surrogate fuels for compression ignition, homogeneous charge compression ignition, and reactivity controlled compression ignition engines. In FY 2017 they (1) developed a chemical kinetic model for a nine-component diesel surrogate palette that represents a diesel certification fuel and (2) improved gasoline and diesel surrogate component models, and multi-component models to increase their accuracy when used in simulating gasoline and diesel engine experiments. (Pitz, report I.14)

- Lawrence Livermore National Laboratory is advancing the state of the art in engine simulation through the development of fast and accurate models. In FY 2017 they (1) deployed fast-chemistry solver on multiple Advanced Computing Research Leadership Computing Challenge award projects in collaboration with General Motors and Oak Ridge National Laboratory; (2) enabled improved predictions of hydrocarbon, nitrogen oxide, and soot in conventional diesel virtual calibration project; (3) reduced estimated uncertainty bounds of engine pressure measurements in collaboration with Sandia National Laboratories; and (4) identified key contributors to uncertainty if in-cylinder temperature estimates which are vital to engine models. (Whitesides, report I.15)

- Lawrence Livermore National Laboratory is accelerating development and deployment of high-efficiency clean combustion engine concepts through deeper understanding of complex fluid and chemistry interactions. In FY 2017 they (1) extended and parallelized the adaptive preconditioner method used in Zero-RK to solve fully coupled, chemically reacting flows with thousands of transported species, (2) quantified the potential computational speed-up offered by new multi-rate integration methods under development by the SUNDIALS team at Lawrence Livermore National Laboratory, and (3) deployed cloud-based tools to

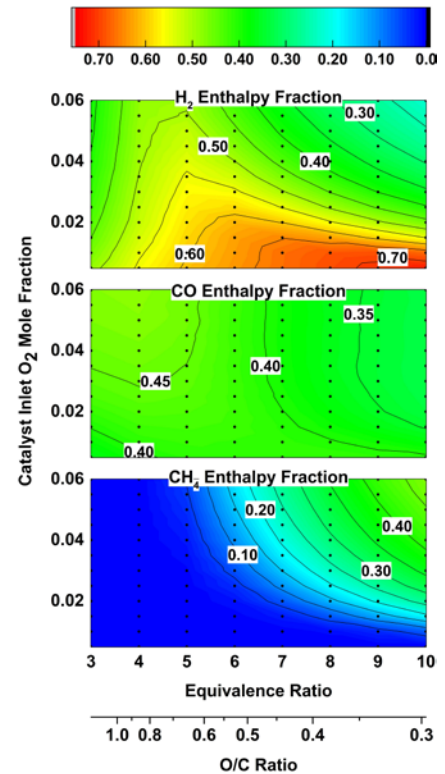


Figure 5 - Enthalpy fraction of H₂, CO, and CH₄ at the catalyst outlet relative to the initial fuel with 700°C initial temperature for iso-octane (Szybist, report I.12)

allow fuel and engine researchers around the world to analyze chemical kinetic mechanisms for non-physical behavior and repair the thermochemistry files for improved performance. (McNenly, report I.16)

- Los Alamos National Laboratory is developing mathematical and computer algorithms and software for the advancement of speed, accuracy, robustness, and range of applicability of KIVA, an internal combustion engine modeling software, to be a more predictive computer code. In FY 2017 they (1) invented the local-arbitrary Lagrangian–Eulerian method for moving bodies, (2) developed immersed boundary methods for moving bodies using the invented marker system, and (3) invented and developed volume of fluid methods in finite element method for true multi-phase flow. (Carrington, report I.17)
- Oak Ridge National Laboratory is using massively parallel high-performance computing resources and graphics processing unit-enabled numerical solvers to enable use of computational fluid dynamic engine models with significantly increased levels of detail and predictive submodels including detailed chemical kinetics. In FY 2017 they focused on using Lawrence Livermore National Laboratory’s Zero-RK graphics processing unit-enabled chemistry solvers on Titan to allow the use of detailed chemical kinetics in the computational fluid dynamic models with acceptable run times and evaluate the resulting impact on emissions predictions for skeletal, reduced, and detailed mechanisms with single- and multi-component fuel surrogates. (Edwards, report I.18)
- Sandia National Laboratories is combining a state of the art simulation capability based on the large eddy simulation technique with Advanced Engine Systems R&D activities. In FY 2017 they developed an Arrhenius-based chemical model to address the issue of variability in chemic kinetics mechanisms using Bayesian inference to predict autoignition over the ranges of conditions (pressure, temperature, equivalence ratio) relevant to the Spray A case. (Oefelein, report I.19)
- The Pennsylvania State University is quantifying the relative importance of turbulent boundary layer wall heat transfer, radiative heat transfer, and boundary layer/radiation couplings in engines. In FY 2017 they (1) identified two key datasets for validation of wall boundary layer wall heat transfer models, one from direct numerical simulation and one from experimental measurements; (2) performed the first spatially resolved measurements of infrared radiative intensity in an optical engine and initiated quantitative comparisons between computes and measured spectral radiative intensities; (3) exercised a photon Monte Carlo line-by-line radiation model to guide the design of the engine experiments to be performed at Oak Ridge National Laboratory, which focused on the potential influence of radiative heat transfer on knock; and (4) proposed a simplified computational fluid dynamics model for radiative heat transfer in high-pressure combustion systems that, for the range of conditions tested, predicts radiative emission, reabsorption, and wall heat loss within approximately 10% of those predicted using photon Monte Carlo line-by-line. (Haworth, report I.20)
- The University of Illinois at Urbana-Champaign is designing and developing a multi-component fuel droplet and wall film vaporization model using two approaches: discrete and continuous thermodynamics methods. In FY 2017 they (1) assembled and tested a droplet and film chamber for high pressure and high temperature conditions and (2) developed a new solver using discrete multi-component method and validated it for droplet vaporization in quiescent ambient conditions by comparing simulations results with measurements obtained in the experimental portion of the work. (Lee, report I.21)
- Michigan Technological University is quantifying spray rebound properties, film thickness, and heat flux on the heated surface for a single-hole nozzle impingement. In FY 2017 they (1) designed and fabricated a mounting fixture for the new Bosch injector, (2) finished the temperature calibration test with a closed-loop temperature control system and a data acquisition system, (3) completed the rate of injection test of the new single-hole injector and spray–wall impingement test with diesel and n-heptane on a new quartz window, (4) finished film thickness measurement calibration using refractive index matching method, (5) completed the critical heat flux measurements at three different locations in the impinging plates under various conditions including injection pressure, surface temperature, and ambient density, (6) completed Lagrangian–Eulerian computation fluid dynamic simulation validation with single-hole nozzle experiments, and (7) investigated the effect of injected parcels on the statistical significance of extracted data in Lagrangian–Eulerian simulations. (Lee, report I.22)

- The University of Wisconsin is improving soot modeling capabilities in government sponsored and commercial computation fluid dynamic codes to enable the engine industry to design high efficiency, clean engines for transportation applications. In FY 2017 they (1) coupled a detailed solution to Smoluchowski's population balance equation with engineering level computation fluid dynamic codes for use in engine computation fluid dynamic simulations to improve the prediction of particle size distributions under conventional and advanced combustion engines, (2) completed metal engine experiments to measure particle size distributions under a range of operating conditions and used the data to validate the newly developed soot model, and (3) evaluated the spray and mixing models through comparisons with optical engine data from the literature in both Reynolds-averaged Navier–Stokes and large eddy simulation framework. (Kokjohn, report I.23)
- The University of Alabama is producing a validated real-fluid property code which can be integrated with computation fluid dynamic solvers to improve their accuracy in simulating high-pressure diesel sprays. In FY 2017 they (1) integrated the new constant pressure flow rig with support equipment and verified its operation and attainment of design operating conditions, (2) conducted experiments new Engine Combustion Network spray conditions and acquired quantitative measurements of fuel–air mixing in the near field and in ignition and combustion zones, (3) developed a new approach that allows rainbow schlieren deflectometry technique to also measure the liquid jet boundary, (4) integrated a real-gas property model into an open source code and debugged the code, (5) implemented the developed real-fluid property module in CONVERGE, and (6) tested the numerical fidelity of the integrated code for a baseline test case involving supercritical fuel–air mixing. (Agrawal, report I.24)
- The Ohio State University is developing a combustion model that improves the predictive capability for engine knock by capturing turbulence–chemistry interactions in a physics-based way and incorporating high-fidelity chemistry into large eddy simulation of in-cylinder turbulent reacting flows. In FY 2017 they (1) developed a base conditional moment closure front propagation formulation solver coupled with an large eddy simulation code, (2) generated direct numerical simulation database for end-gas ignition and premixed flame propagation, (3) assessed the performance of the combustion model for the end-gas ignition using the direct numerical simulation database, (4) acquired in-cylinder pressure data from single-cylinder engine experiments over a range of knocking and knock-free conditions, and (5) implemented the premixed combustion model, FPF, into CONVERGE and performed a test large eddy simulation run. (Kim, report I.25)
- Boston University is developing and validating physics-based mathematical submodels for use in standard multiphase computation fluid dynamics software to enable better prediction of cavitation within fuel injectors. In FY 2017 they (1) validated the OpenFOAM computation fluid dynamics model and smoothed particle hydrodynamics

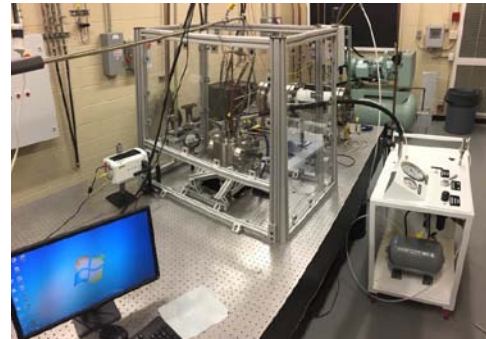


Figure 6 - New constant pressure flow rig with air exhaust, injector cooling, and instrumentation installed (Agrawal, report I.24)

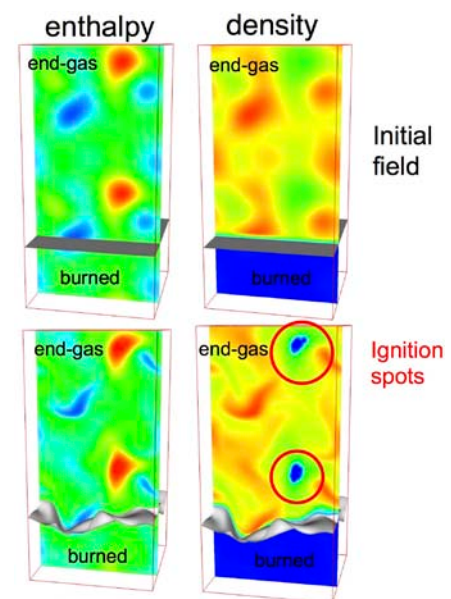


Figure 7 - Premixed flame propagation and end-gas ignition in a constant volume configuration. A base conditional moment closure front propagation formulation solver has been coupled with an large eddy simulation solver. Total enthalpy and density fields at the initial time (top) and when the ignition kernels have formed (bottom) are shown. (Kim, report I.25)

model of bubble dynamics in a hydrostatic tank under multiple conditions, (2) developed a quantitative analysis method for measuring void fraction in a fuel injector, and (3) analyzed data from first Oak Ridge National Laboratory High Flux Isotope Reactor campaign, which shows a significant difference in neutron attenuation between flashing and non-flashing conditions. (Ryan, report I.26)

- Georgia Institute of Technology is demonstrating a new spray atomization submodel for engine computation fluid dynamics codes with improved prediction accuracy for local spray morphology and global spray characteristics over a wide range of engine operating conditions, including conditions relevant for advanced combustion engines. In FY 2017 they (1) measured the near-nozzle centerline Sauter mean diameter (SMD) distribution of Engine Combustion Network Spray D for the first time using a new X-ray scattering diagnostic developed at Argonne National Laboratory, (2) implemented the scattering-absorption measurement ratio diagnostic developed in this project to measure the spatially resolved two-dimensional SMD distribution of Engine Combustion Network Spray D for the first time, and (3) demonstrated improvement of engine computational fluid dynamics spray SMD predictions with a newly developed KH-Faeth breakup model, reducing error in predicted centerline SMD by up to 80% for Engine Combustion Network Spray A (Genzale, report I.27)

Co-Optimization of Fuels and Engines

- Sandia National Laboratories is providing the science-base needed by industry to understand how emerging alternative fuels impact autoignition in highly efficient direct injection spark ignition light-duty engines being developed by industry. In FY 2017 they (1) developed methodology to measure knock limits under conditions that mimic vehicle accelerations, (2) measured stoichiometric knock limits for nine fuels, both steady-state and transient, (3) tested applicability of Octane Index framework for fuels of alternate composition and discovered that two fuels blended with butanol isomers performed better than expected based on Research Octane Number and Motor Octane Number, and (4) developed and used a Monte-Carlo-based uncertainty assessment of the Octane Index framework, results indicate a high likelihood that fuels' deviations from Octane Index predictions are real and not caused by experimental uncertainty. (Sjöberg, report II.1)
- Argonne National Laboratory is formulating primary reference fuel–ethanol blends with constant Research Octane Number (RON) 98 from 0 vol% to 50 vol% ethanol to study the effects of ethanol and heat of vaporization on the RON test at constant compression ratio. In FY 2017 they (1) extended the applicable fuel matrix with RON 98 in steps of 5 vol% of ethanol, (2) calculated vapor fraction at the intake port including anticipated uncertainty, (3) investigated the minimum required temperature for full vaporization of primary reference fuel–ethanol fuel blends, (4) developed a compressed air intake manifold configuration for the standard Cooperative Fuel Research RON test setup, and (5) evaluated the change in RON under increased intake air temperature and pressure compensated conditions. (Kolodziej, report II.2)
- Oak Ridge National Laboratory is quantifying combustion phasing and engine efficiency differences for ethanol and non-ethanol biofuels at a compression ratio of 11.4. This objective supports both the U.S. DRIVE Fuels Working Group and Co-optimization of Fuels and Engines Program. In FY 2017 they (1) completed engine studies at a compression ratio of 11.4 and vehicle modeling for the Fuels Working Group expanded fuel matrix and (2) studied ethanol and non-ethanol biofuel blends at well-matched Research Octane Number and sensitivity. (Sluder, report II.3)
- Sandia National Laboratories is providing the science base needed by industry to understand how emerging alternative fuels impact highly efficient direct injection spark ignition light-duty engines being developed by industry. In FY 2017 they (1) demonstrated when Particulate Matter Index (predicts smoke emissions for direct injection spark ignition operation and when it does not, (2) identified how soot production pathways change with fuel type and operating conditions for stratified charge spark ignition operation, (3) developed semi-quantitative wall-wetting diagnostics based on refractive index matching, (4) examined how the high heat of vaporization of E30 (30% ethanol, 70% gasoline) leads to increased

wall wetting and pool fires, and (5) established stratification technique to stabilize ultra-lean spark ignition combustion for effective parametric fuel studies of lean autoignition. (Sjöberg, report II.4)

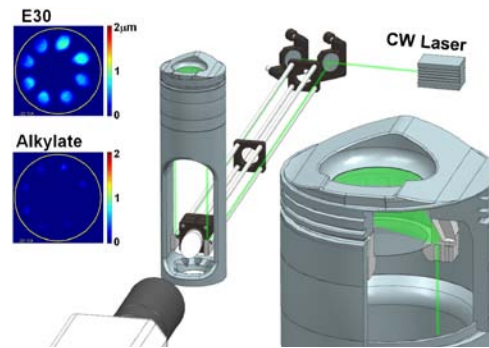


Figure 8 - Laser-based measurements allow the detection of fuel wall films for various combinations of fuels and operating conditions that are prone to pool fires (Sjöberg, report II.4)

- Argonne National Laboratory is measuring the effects of fuel blend laminar flame speed on engine exhaust gas recirculation dilution tolerance among eight fuel components blended at a constant 30 vol%. In FY 2017 they (1) blended a four-component blendstock of oxygenate blending surrogate to meet the 91 Research Octane Number and 83 Motor Octane Number characteristics of the E10 baseline fuel and (2) compared the exhaust gas recirculation dilution tolerance of the blendstock of oxygenate blending surrogate and the blendstock of oxygenate blending surrogate with 10 vol% ethanol to 30 vol% blend levels of eight fuel components. (Kolodziej, report II.5)
- Oak Ridge National Laboratory is testing the central fuel properties hypothesis with regards to highly boosted spark ignition combustion, including exhaust gas recirculation dilute combustion, and using these findings for the Co-Optima go/no-go milestone. In FY 2017 they (1) collected experimental data that supports the use of the central fuel properties hypothesis and (2) showed octane index correlates well with knock propensity. (Szybist, report II.6)
- National Renewable Energy Laboratory is quantifying the particulate matter emissions from a full-factorial designed experiment fuel matrix having the variables of aromatic vapor pressure, aromatic, and ethanol concentrations. In FY 2017 they (1) conceived a full-factorial designed experiment fuel matrix to test the hypothesis that increasing fuel heat of vaporization (via increasing ethanol content) while maintaining constant aromatic content can cause particulate matter emissions to increase, (2) computed particulate matter index and heat of vaporization values for fuels based on their detailed hydrocarbon analysis, and (3) measured particulate matter emissions from National Renewable Energy Laboratory's single-cylinder gasoline direct injection engine. (Ratcliff, report II.7)

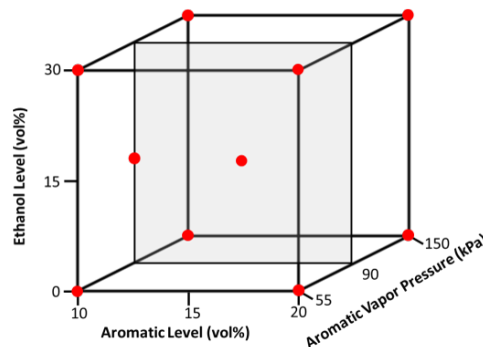


Figure 9 - Full factorial experimental design fuel matrix. Tested fuels are indicated by red dots; aromatic hydrocarbon vapor pressures are at 443 K. (Ratcliff, report II.7)

- Oak Ridge National Laboratory is developing mathematical terms that capture the impacts of changes in fuel composition on emissions control system performance and durability based on measurable fuel properties for inclusion in the Co-Optima merit functions. In FY 2017 they (1) developed an emissions control merit function term to quantify potential impacts of fuel composition changes on cold-start emissions of regulated pollutants (NO_x , non-methane organic gases, and CO) from light-duty spark ignition engines, (2) measured catalytic light-off temperatures of Co-Optima blendstock candidates and conventional petroleum-derived fuel components (30 organic compounds in total) over a hydrothermally-aged commercial three-way catalyst to enable evaluation of the emissions control term in the light-duty merit function, and (3) identified trends in catalytic reactivity based on organic compound chemical structure, including effects on conversion of NO_x and CO. (Toops, report II.8)
- Oak Ridge National Laboratory is demonstrating effectiveness of the particulate matter index to predict trends in particulate matter production for oxygenated fuel blends during cold-start. In FY 2017 they (1) demonstrated ~50% drop in particulate matter mass during cold-start by blending 30 vol% of non-aromatic, oxygenated bio-fuels regardless of oxygen fuel functional group, (2) demonstrated that the fuel particulate matter index predicted trends for particulate matter mass production during gasoline direct injection cold-start for oxygenated fuel blends, and (3) established that the linearity and magnitude of the particulate matter index predicted trend was dependent on how the particulate matter mass was measured with a reduced linear correlation by methods which could account for all of the semi-volatile hydrocarbons adsorbed on the soot particles. (Moses-DeBusk, report II.9)
- Oak Ridge National Laboratory is investigating the effects of fuel chemistry on emissions and the functionality of the emissions control systems to identify potential challenges as well as opportunities created by new fuel compositions. In FY 2017 they (1) collected particulate matter from a cooler used in an exhaust gas recirculation system and (2) mapped the oxygenated species from the soot. (Storey, report II.10)
- National Renewable Energy Laboratory is developing experimental and simulation tools to characterize fuel ignition behavior in support of advanced combustion engine development for both spark ignition and compression ignition. In FY 2017 they (1) extensively characterized and developed experimental methodology with the advanced fuel ignition delay analyzer to demonstrate significant expanded capability beyond ignition quality tester-based studies for high-quality ignition kinetics experiments simulations and (2) continued numerical simulation development with unique ignition quality tester and advanced fuel ignition delay analyzer data enable these experiments to be part of the feedback development loop for development of accurate, reduced kinetic mechanisms. (Zigler, report II.11)
- Oak Ridge National Laboratory is quantifying the relationship between fuel properties and low-speed pre-ignition (LSPI) frequency with respect to fuel distillation and molecular properties. In FY 2017 they (1) confirmed that LSPI number count is highly correlated with fuel increased distillation, (2) illustrated that increased fuel distillation is insufficient to describe LSPI phenomena and magnitude, even with near identical fuel distillation and octane number, and (3) revealed that additional fuel properties are required for LSPI propensity quantification and data supports hypothesis of increased fuel flame speed also could promote increased LSPI propensity. (Splitter, report II.12)
- Argonne National Laboratory is quantifying the differences in combustion characteristics for the three 98 Research Octane Number fuels by testing them in a gasoline compression ignition engine, varying boost, exhaust gas recirculation, and intake temperature. In FY 2017 they (1) used start of injection of the second injection to control combustion phasing at a given exhaust gas recirculation level, (2) examined the tradeoff between intake temperature and intake boost pressure to achieve identical ignition timing, and (3) identified the difference between forming a significant amount of soot in-cylinder and having a significant amount of soot leave the exhaust port. (Ciatti, report II.13)
- Sandia National Laboratories is providing fundamental understanding of the autoignition behavior of fuels at conditions relevant to low-temperature gasoline combustion operation and to other methods of advanced compression ignition, to support the co-development of LTGC engines and fuels that optimize

their performance. In FY 2017 they (1) showed that the Co-Optima E30 was the most easily autoignited fuel tested for naturally aspirated LTGC while the Co-Optima high-aromatic fuel was the most difficult fuel to autoignite, (2) showed that the octane index gives only a poor correlation for LTGC autoignition at naturally aspirated conditions, (3) compared LTGC autoignition for early direct injection fueling and premixed prevaporized fueling to show that the difference in heat of vaporization between the E30 and high-aromatic fuels accounts for only part of the difference in their autoignition reactivities, and (4) showed that E30 remains more reactive than the high-aromatic fuel from 1.0–2.0 bar absolute. (Dec, report II.14)

- Oak Ridge National Laboratory is quantifying the potential of the co-evolution of fuels and a subset of the advanced compression ignition (ACI) combustion strategies for both single- and dual-fuel ACI. In FY 2017 they (1) identified dual-fuel ACI transition points as a function of direct injection timing helping to better understand ACI behavior, (2) established a methodology for isolating chemical and physical properties to help identify the relative importance of chemical and physical properties for each fuel, and (3) established a methodology for linking optical and metal engine experiments to better understand fuel effects on ACI combustion performance. (Curran, report II.15)
- Sandia National Laboratories is measuring in-cylinder mixing and kinetics to optimize dual-fuel heat release for noise, efficiency, and load range. In FY 2017 they developed a method to match operating conditions of the Sandia heavy-duty, single-cylinder optical engine with those of the Oak Ridge National Laboratory light-duty, multi-cylinder all-metal engine. (Musculus, report II.16)

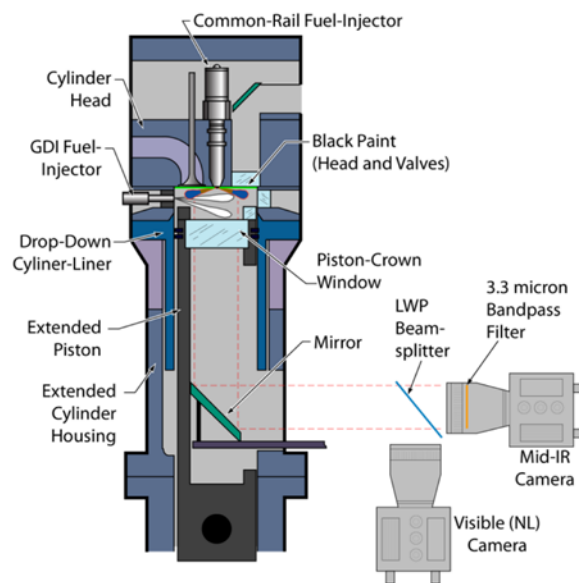


Figure 10 - Schematic diagram of the heavy-duty, single-cylinder optical diesel engine and optical setup with infrared emission and visible natural combustion luminosity cameras (Musculus, report II.16)

- Sandia National Laboratories is determining the extent to which ducted fuel injection (DFI) lowers soot mass in a diesel spray flame and the quantifying the effects on DFI performance of rounding the duct inlet and tapering its outlet. In FY 2017 they (1) showed that DFI can attenuate soot levels in mixing-controlled compression ignition spray flames by 50% to 100%, (2) demonstrated that rounding the duct inlet and tapering its outlet can lead to improved DFI performance, (3) found that they duct assembly can be shortened by more than half without loss of soot attenuation efficacy, (4) discovered that the primary mixing-controlled compression ignition combustion source of hydrocarbon emissions is likely fuel in overlean regions at the radial periphery of the fuel spray during the quasi-steady mixing-controlled burn, and (5) proved that the methodology previously developed with support from this project produces diesel surrogate fuels that closely approximate the sooting tendency of the target fuel in fundamental burner experiments. (Mueller, report II.17)

- The University of Alabama is experimentally investigating fuel–air mixing and subsequent ignition and combustion processes and properties in different fuel injection regimes, with particular focus on supercritical fuel injection when the surface tension is no longer present, and the mixing of the dense supercritical fluid with the ambient air depends mainly upon the influence of turbulence and real-gas effects on thermodynamics and transport properties. In FY 2017 they (1) designed, developed, and independently tested a two-color pyrometry system, (2) independently tested the OH* chemiluminescence system, (3) integrated the rainbow schlieren deflectometry system with the constant pressure flow rig, (4) developed plans to integrate OH* chemiluminescence and two-color pyrometry systems with constant pressure flow rig, (5) performed baseline experiments to demonstrate successful operation of the constant pressure flow rig at diesel condition demonstrating fuel–air mixing, ignition, and combustion, and (6) obtained quantitative rainbow schlieren deflectometry data for a baseline experiment using *n*-heptane fuel. (Agrawal, report II.18)

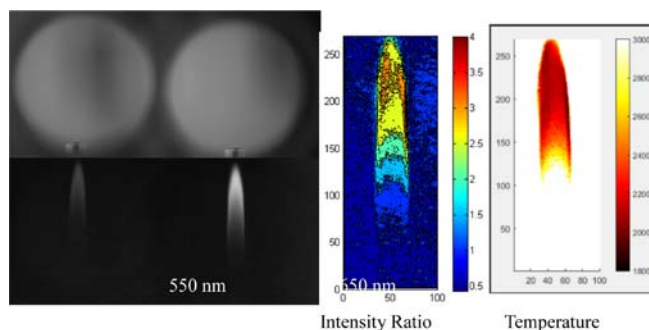


Figure 11 - Two-color soot pyrometry image processing. (Left) double image of burner showing tip in focus, no filters. (Middle) double image of flames at two wavelengths. (Right) Pixel-by-pixel intensity ratio on the left and calculated temperature on the right. (Agrawal, report II.18)

- Pacific Northwest National Laboratory is facilitating the successful co-optimization of fuels and advanced combustion engines, enabling the introduction of future fuel feedstocks and reducing the United States' dependence on foreign oil. In FY 2017 they (1) developed predictive models for derived cetane number, T10, T50, and T90, and started an Reid vapor pressure model by quantitatively assessing the pairwise interrelationships among 27 functional groups for each of the predicted properties; (2) developed an initial chemical structure-based fuel blending model based upon the predictive fuel property models for derived cetane number, T10, T50, and T90; (3) measured the liquid–solid equilibrium pressures and temperatures for four diesel fuel surrogates developed in conjunction with the Coordinating Research Council from atmospheric pressure to 350 MPa; and (4) assessed the influence of eight cold flow improvers at concentrations from 500 ppm to 10,000 ppm on the liquid–solid equilibrium values for one of the diesel surrogate fuels. (Bays, report II.19)
- Lawrence Livermore National Laboratory is developing chemical models and associated correlations to predict the blending behavior of high-performance fuels when mixed with conventional fuels like gasoline and diesel fuels. In FY 2017 they (1) predicted octane blending behavior for Co-Optima high-performance fuels in gasoline within ± 3 octane units and (2) developed new correlations to predict octane ratings using a new chemical kinetic model for gasoline with Co-Optima high-performance fuels. (Pitz, report II.20)
- Lawrence Livermore National Laboratory is developing chemical kinetic models for high-performance fuels (HPFs) and base fuels (e.g., gasoline and diesel) to predict their behavior at advanced spark ignition and advanced compression ignition engine conditions for Co-Optima. In FY 2017 they (1) developed and validated a chemical kinetic model for gasoline surrogate fuels with Co-Optima HPFs, (2) developed new kinetic models for the Co-Optima HPFs methyl-acetate and ethyl-acetate, (3) improved chemical kinetic models for methyl butanoate, di-iso-butylene, and anisole, (4) validated the chemical kinetic models for 18 other Co-Optima HPFs in the combined mechanism to ensure they performed as well as reported in their respective literature publication, and (5) improved and validated gasoline surrogate component models upon which the HPFs and gasoline surrogate mechanisms rely (1-hexene, toluene, xylenes, trimethylbenzenes, phenol, and benzene). (Pitz, report II.21)

- Argonne National Laboratory is acquiring autoignition data for a variety of conventional and future fuels using Argonne's rapid compression machine facilities at conditions relevant to boosted spark ignition, mixed-mode, and advanced compression ignition engines necessary for the development and validation of chemical kinetic models, and the prediction of fuel-engine interactions. In FY 2017 they (1) acquired autoignition data over a range of thermodynamic conditions for five, compositionally diverse, high Research Octane Number Co-Optima core fuels and (2) computationally investigated investigating chemical kinetics associated with engine knock for a range of primary reference fuels from PRF70 to PRF100. (Goldsborough, report II.22)
- National Renewable Energy Laboratory is validating an experimental and data analysis method for predicting Research Octane Number and sensitivity for unknown fuel blendstocks. In FY 2017 they (1) conducted oxidation experiments with iso-octane, a compound with well-known autoignition kinetics, and (2) conducted experiments examining the autoignition of the model biofuel anisole. (Fioroni, report II.23)
- Lawrence Livermore National Laboratory is developing a phi-sensitivity metric that can be computed from a detailed fuel chemistry model that quantifies desirable ignition behavior for partially stratified charge compression ignition engines. In FY 2017 they (1) developed a phi-sensitivity metric to estimate the suitability of fuel for partially stratified charge compression ignition engines that can be computed from the latest detailed fuel chemistry model for gasoline surrogate, (2) created an optimization framework that allows the performance of a large number of fuel blends to be evaluated on DOE computing resources to explore the tradeoff between phi-sensitivity and octane sensitivity, (3) searched over 150,000 fuel blends using nine hydrocarbon and 10 bio-derived blendstocks for combinations that delivered high phi-sensitivity and octane sensitivity while maintaining a Research Octane Number greater than 95, and (4) found that blends involving 1-pentanol were able to push the traditional tradeoff between the desirable partially stratified charge compression ignition properties to achieve nearly 90% the levels identified for the blendstock exemplars with good octane sensitivity (ethanol) and phi-sensitivity (iso-octane). (McNenly, report II.24)

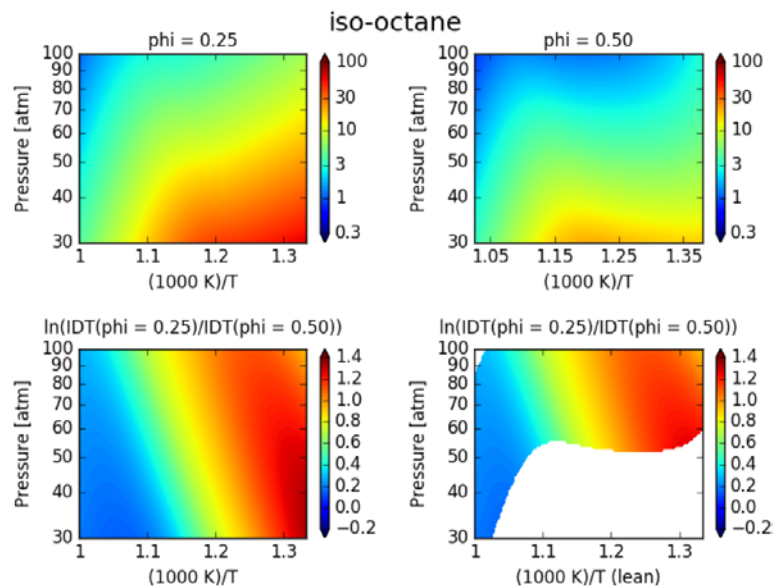


Figure 12 - Example calculation of the constant volume ignition delay times (IDT) used to construct the phi-sensitivity metric for iso-octane (McNenly, report II.24)

- The University of Michigan is developing a computationally efficient model for composition during the open portion of the engine cycle to dynamically reduce the number of species fluxed and reduce computational expense by 90% during gas exchange relative to a multi-zone simulation while maintaining accuracy. In FY 2017 they (1) have been provided with a chemical kinetic mechanism for primary reference fuel blends currently in use at Argonne National Laboratory for virtual Cooperative Fuels

Research simulations and (2) have been provided with a CONVERGE mesh of the Argonne National Laboratory virtual Cooperative Fuels Research engine. (Lavoie, report II.25)

- Louisiana State University is quantifying combustion metrics of transportation fuels (e.g., octane number, flame speed) and constructing an experimental prototype that can operate at elevated pressures. In FY 2017 they (1) identified points of contact and potential collaborators at DOE laboratories, (2) redesigned the microtube experiment for pressurized experiments (prior to the project, micro-combustion experiments were conducted at atmospheric pressure) and (3) developed a basis for improved temperature measurements via multi-wavelength thin filament pyrometry. (Schoegl, report II.26)
- Yale University is developing a database of quantitative sooting tendencies that includes all of the categories of hydrocarbons important to petroleum-derived and biomass-derived fuels. In FY 2017 they (1) combined the existing incompatible databases of yield sooting index (YSI) measurements together to produce a unified database, (2) measured YSIs for oxygenated aromatics, (3) measured sooting tendencies for the five Co-Optima test gasolines, (4) measured YSIs for surrogates to three of the test gasolines, and (5) validated YSI simulation framework over a range of species. (Pfefferle, report II.27)

Alternative Fueled Engines

- Pacific Northwest National Laboratory is facilitating the successful introduction of future fuel feedstocks compatible with advanced combustion engines to help reduce the United States' dependence on foreign oil. In FY 2017, no funds were spent from this project. Residual funds will be applied to meeting Co-Optima goals and documenting results. (Bays, report III.1)
- Stony Brook University is reforming gasoline, diesel, and natural gas to varying levels and characterize the constituent species of their reformat mixtures as well as the autoignition tendency of the reformat mixtures in the form of an effective primary reference fuel number. In FY 2017, (1) the autoignition tendency of reformat mixtures from gasoline, diesel, and natural gas were characterized using a Cooperative Fuels Research engine operating in homogeneous charge compression ignition as a diagnostic to determine an effective primary reference fuel number for each gaseous reformat fuel mixture; (2) the results showed that the primary reference fuel number separation between the parent fuel and the reformat mixture was around 16 points for gasoline, 25 points for natural gas, and 113 points for diesel; (3) an existing single-cylinder, diesel, research engine was modified to be able to test both conventional dual-fuel reactivity controlled compression ignition combustion, as well as reactivity controlled compression ignition using a parent fuel and its reformat; (4) system level models in GT-POWER were constructed and validated against experimental data for both the Cooperative Fuels Research engine as well as the Ricardo Hydra engine that will be used for the single-fuel reactivity controlled compression ignition combustion; and (5) a detailed computation fluid dynamics model was constructed in CONVERGE computation fluid dynamics and validated against experimental data from the Ricardo Hydra engine for both conventional diesel combustion and conventional, dual-fuel reactivity controlled compression ignition combustion. (Lawler, report III.2)

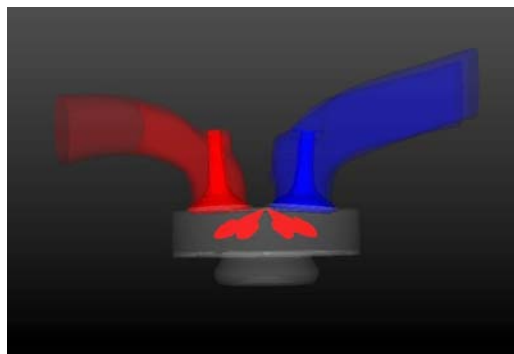


Figure 13 - CONVERGE computation fluid dynamics model of the diesel Ricardo Hydra engine (Lawler, report III.2)

- Robert Bosch LLC is developing and demonstrating a High-Efficiency Cost-Optimized, Spark-Ignited Natural Gas heavy-duty engine capable of approaching current near-diesel efficiency while achieving current Environmental Protection Agency emission regulations. In FY 2017 they (1) developed the optical measurement capability for in-cylinder measurements to provide quantification of differences between the advanced ignition systems and (2) quantified the performance benefits by running the steady-state engine map data points through a Bosch developed medium-duty/heavy-duty drive cycle simulation process. (White, report III.3)
- CALSTART is testing a stock United Parcel Service truck's original equipment manufacturer exhaust aftertreatment system consisting of chassis dynamometer and vehicle test track testing and operating multiple vehicles with the TechFlo exhaust combined with the BoostBox hydrogen catalyst. In FY 2017 they (1) participated in stock emissions and fuel testing at Pennsylvania State University's Larson Transportation Institute, (2) participated in vehicle test track and chassis dynamometer testing, (3) completed an SAE J1264 fuel test, and (4) performed three-dimensional computer-aided modeling, completing the final design intent along with constructing the diesel fuel injection and delivery system. (Ippoliti, report III.4)
- The University of Michigan is demonstrating the combination of fuel selection, fuel injection strategy, and mixture preparation that enables meeting the DOE targets for brake thermal efficiency of greater than 40% for spark ignition engines and greater than 50% for compression ignition engines. In FY 2017 they (1) completed the multi-cylinder gasoline turbocharged direct injection engine studies and the single-cylinder Hydra engine studies, (2) evaluated a large matrix of experimental conditions, (3) expanded the Hydra engine studies to consider various alternative fuels to complete the ongoing studies with ethanol, (4) expanded the Hydra engine studies to consider particle size distribution and number emissions when using various alternative fuels, and (5) conducted constant volume ignition delay and variable pressure reactor simulations to estimate knock limited load for the same conditions previously reported using an additional kinetic mechanism for gasoline. (Wooldridge, report III.5)

Emissions Control R&D

- Oak Ridge National Laboratory is coordinating the Cross-Cut Lean Exhaust Emissions Reduction Simulations (CLEERS) activity for the DOE Advanced Engine Cross-Cut Team and supporting precompetitive collaborative interactions and provide a consistent framework for sharing information among the emissions control research and development community. In FY 2017 they (1) organized the 2017 DOE Crosscut Workshop on Lean Emissions Reduction Simulation (CLEERS Workshop) in Ann Arbor, Michigan on October 3–5, 2017, (2) conducted the 2017 CLEERS Industry Priorities Survey, (3) developed and launched a completely new CLEERS website (www.cleers.org), (4) facilitated CLEERS Focus Group teleconferences, which continue to have strong domestic and international participation (typically over 40 participants, a majority of which are from industry), (5) provided regular update reports to DOE Advanced Combustion Engine Cross-Cut Team, (6) supported the Advanced Combustion and Emissions Control Low Temperature Aftertreatment Team in developing evaluation protocols for low temperature catalysts, and (7) measured the the equilibrium NO storage capacity and release temperature of a commercially relevant passive NO_x adsorber material as a function of temperature, NO concentration, and water concentration, and began developing strategies for modeling the NO adsorption/desorption process on passive NO_x adsorbers. (Pihl, report IV.1)
- Pacific Northwest National Laboratory is promoting the development of improved computational tools for simulating realistic full system performance of lean-burn engines and the associated emissions control systems. In FY 2017 they (1) identified that the low temperature activity of Cu/SSZ-13 catalyst is limited by the oxidation of Cu (I) which involves the two isolated Cu (I) ions to form a transient intermediate, (2) quantified Cu species in Cu/SSZ-13 as a function of hydrothermal aging temperature using electron paramagnetic resonance, (3) finalized the low temperature storage catalyst test protocol, and nearly complete the three-way catalyst test protocol, (4) confirmed NO_x storage and release properties of Pd-loaded zeolites (chabazite, ZSM-5, Beta), and identified that the NO_x uptake involves surface reaction between Pd species and NO, and (5) characterized catalyst location in three distinct coating regimes along

the axial length of a commercial selective catalytic reduction filter using X-ray computed tomography, which is essential to understand the properties such as permeability, filtration behavior, and chemical activity of the selective catalytic reduction filters. (Wang, report IV.2)

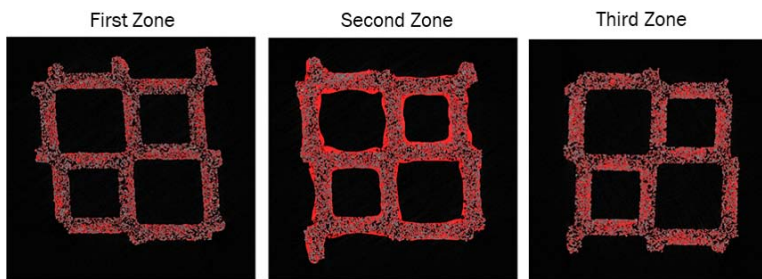


Figure 14 - Catalyst locations within small cross-sections of a commercial selective catalytic reduction filter (catalyst shown in red false color; note that inlet channels are larger and outlet channels are smaller in this asymmetric honeycomb filter design) (Wang, report IV.2)

- Oak Ridge National Laboratory is developing emission control technologies that achieve >90% reduction of pollutants at low temperatures (<150°C) to enable fuel-efficient engines with low exhaust temperatures to meet new U.S. Environmental Protection Agency Tier 3 emission regulations that require ~80% less NO_x and hydrocarbon emissions than current standards. In FY 2017 they (1) analyzed potential sulfur mitigation seen in CuO–Co₃O₄–CeO₂+Pt/Al₂O₃ mixture, (2) evaluated hydrocarbon and NO trapping materials under rigorous protocol conditions showing high potential for trapping long-chain and aromatic hydrocarbons in simulated exhaust conditions, and (3) demonstrated the effectiveness of integrating trapping materials with diesel oxidation catalysts. (Toops, report IV.3)

Table 1 - Storage Efficiencies of Pd/ZSM-5 Trapping Material Before and After Severe Aging (Toops, report IV.3)

	800 °C, 4 h	800 °C, 50 h + sulfation/desulfation
NO _x	10.1%	0%
THC (C ₁)	28.2%	24.8%
C ₂ H ₄	9%	0%
C ₃ H ₆	11%	2%
C ₁₀ H ₂₂	35%	34%

- Oak Ridge National Laboratory is assessing and characterizing catalytic emission control technologies for lean-gasoline engines. In FY 2017 they (1) conducted research on an emission control concept known as “passive SCR,” where SCR stands for selective catalytic reduction, (2) demonstrated NO_x emission reduction efficiencies over 99.8% on a four-cylinder lean gasoline engine, and (3) conducted experiments to identify catalyst material compositions that minimize fuel penalties associated with the technique and accelerated aging studies have been conducted to understand the durability of the passive SCR approach. (Parks, report IV.4)
- Oak Ridge National Laboratory is understanding the fundamental chemistry of automotive catalysts, identifying strategies for enabling self-diagnosing catalyst systems, and addressing critical barriers to market penetration. In FY 2017 they (1) assessed spatiotemporal performance of the selective catalytic reduction model and (2) characterized transient selective catalytic reduction onset conversion inflection. (Partridge, report IV.5)
- Argonne National Laboratory is understanding the performance of three-way catalyst-coated gasoline particulate filters (TWC-GPFs) with variation of filter and coating design parameters and determining whether TWC-GPFs are deactivated by engine oil-derived ash chemicals and find potential deactivation mechanisms. In FY 2017 they (1) demonstrated deactivation mechanisms of TWCs coated in GPFs under

engine oil-derived aging conditions based on extensive characterization results, distinct from surface-coated conventional TWCs on monoliths, (2) built a lab-flow system and evaluated TWC performances of lab- and field-aged TWC-GPFs under identical operating conditions, and (3) obtained newly formulated TWC-GPFs from a participant and completed evaluation of their initial TWC performances using the lab-flow system. (Seong, report IV.6)

- Pacific Northwest National Laboratory is shortening the time required for development of filtration technologies for future engines and developing modeling approaches relevant to the likely key challenge for gasoline particulate filtration: high number efficiency at high exhaust temperatures and low particulate loading. In FY 2017 they characterized a number of the porous ceramic materials used in the filtration tests through a variety of techniques, which included mercury intrusion porosimetry, capillary flow porometry, and micro X-ray computed tomography, in order to understand performance differences between the various products. (Stewart, report IV.7)

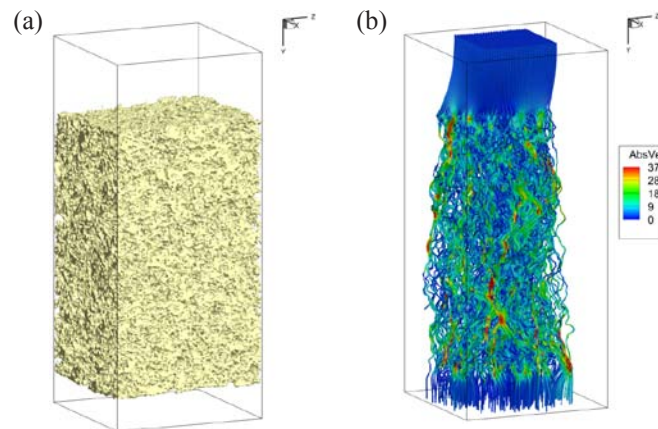


Figure 15 - Three-dimensional reconstruction of a small section of the C2 material from X-ray computed tomography data and an associated flow field (color key indicates local gas velocities in cm/s) (Stewart, report IV.7)

- Pacific Northwest National Laboratory is synthesizing novel composite materials to tune thermodynamics, quantifying the gravimetric ammonia capacity of the composites, and optimizing the molar composition of the double salts and eutectics. In FY 2017 they (1) synthesized double salts containing $\text{SrCl}_2/\text{MgCl}_2$, $\text{LiCl}/\text{MgCl}_2$, and $\text{CoCl}_2/\text{MgCl}_2$ to stabilize novel phases, (2) quantified the gravimetric capacity of the double salts and obtained comparable or higher ammonia storage capacity than the parent materials, (3) demonstrated the ability to tune the temperature of NH_3 release from the double salts, and (4) completed recycle studies on compacted pellets. (Karkamkar, report IV.8)
- Pacific Northwest National Laboratory is developing next generation materials to address the cold operation of passive NO_x absorbers, as driven by improved engine efficiency. In FY 2017 they (1) finished synthesis, characterization, and evaluation of the first series catalysts (Pd/ZSM-5, Pd/Beta, Pd/SSZ-13) synthesized via ion exchange, (2) finished preparation of the second series catalysts via incipient wetness impregnation, (3) evaluated a large group of Pd, Pt and PdAu catalysts supported on various supports including Al_2O_3 , CeO_2 , $\text{CeO}_2\text{-ZrO}_2$, ZSM-5, Beta, and SSZ-13, (4) characterized chemical and physical properties of individual exhaust particles emitted during more than 80 operating conditions, including different running cycles, two aftertreatment systems, sampling at different points of the aftertreatment systems, and (5) completed data processing and identified particles with various sizes, shapes, morphologies, and compositions. (Wang, report IV.9)
- Pacific Northwest National Laboratory is demonstrating successful integration of a diesel particulate filter with a binary catalyst system consisting of a selective catalytic reduction phase and a selective catalytic oxidation phase to enable sufficient passive soot oxidation capacity within the device. In FY 2017 they (1) assessed ZSM-5-based model system for the comparative impact of the variation of various chemical and physical properties of the integrated selective catalytic reduction–diesel particulate filter system and selective catalytic oxidation–selective catalytic reduction catalyst chemistry and (2) combined five

different ZrO₂-based selective catalytic oxidation phases with Cu/ZSM-5 and measured for performance. (Rappé, report IV.10)

- The University of Connecticut is synthesizing various metal oxide nano-arrays and porous materials (e.g., transition metal oxides, perovskites) onto monolithic cordierite substrates with high surface area, well-defined structure, and composition. In FY 2017 they (1) demonstrated scale-up synthesis of Pt/TiO₂ nano-array for diesel oxidation catalyst activity evaluation and sulfur resistance in the simulated exhausts (conventional diesel combustion and low temperature combustion) and engine dynamometers tests, (2) demonstrated high diesel oxidation catalyst performance in the conventional diesel combustion simulated exhaust on ultra-low Pt loading (1.1 g/ft³) catalysts using rutile TiO₂ nano-array catalysts and added H₂ as an upstream promoter, and (3) demonstrated TiO₂/Pt-Pd nano-array catalysts with superb low temperature diesel oxidation catalyst activity and sulfur tolerance in U.S. DRIVE protocolled low temperature combustion simulated exhaust gas conditions. (Gao, report IV.11)

High Efficiency Engine Technologies

- Volvo Group North America is demonstrating >100% improvement in vehicle ton-miles per gallon compared with a best in class 2009 truck, with a stretch goal of 120%. In FY 2017 they (1) finalized the complete vehicle configuration in preparation for the project concept freeze, (2) defined a base aerodynamic model which includes body-in-white architecture and key dimensions, (3) specified detailed weight targets for each subsystem in the complete vehicle, (4) defined a concept development plan which includes trailer aerodynamics and lightweight component development activities, and (5) prepared a test plan to evaluate the impact of the vehicle concept on tire design at Michelin's proving grounds during next fiscal year. (Amar, report V.1)
- Cummins Inc., is demonstrating a minimum of 55% brake thermal efficiency using 65 mph cruise conditions on an engine dynamometer test. In FY 2017 (1) nearly 275,000 miles of data logging and reduction to understand Walmart routes from three distribution centers was conducted, (2) new tread designs and compound mixing to significantly reduce the rolling resistance of the tires while maintaining tread life were developed, (3) a study to understand the benefit of using a 48 V mild hybrid system versus that of a high voltage/high power electric energy recovery system was conducted, (4) the layout and data communication plan for the combined energy recovery transmission coupled system was defined, (5) engine testing to confirm compression ratio, charge flow, and injection rates required to meet the closed cycle efficiency target for the demonstration conditions was conducted, and (6) the vehicle powertrain layout and build-up plan for a powertrain mule that will be the basis for system testing was developed, which will be utilized over the remainder of the program. (Ruth, report V.2)
- Navistar, Inc., is researching, developing, and demonstrating a heavy-duty engine that can meet 2010 federal emission standards and can achieve 55% brake thermal efficiency demonstrated in an operational engine at a 65 mph cruise point on a dynamometer. In FY 2017 (1) a modeling approach was applied to several subsystems to identify opportunities for brake thermal efficiency improvement, (2) engine thermal investigation was carried out in an engine test cell at Navistar, and (3) gasoline compression ignition testing was successfully kicked off at Argonne National Laboratory. (Zukouski, report V.3)
- Daimler Trucks North America is developing and demonstrating a greater than 100% improvement in overall freight efficiency on a heavy-duty Class 8 tractor-trailer measured in ton-miles per gallon. In FY 2017 they (1) completed simulation for goal setting for both the engine and the vehicle program, (2) created working teams for each workstream and aligned with high level schedules, and (3) identified design resources and are being put in place to support Phase 2 design work. (Yee, report V.4)
- Delphi is addressing a number of technical risks and issues that must be overcome for gasoline direct injection compression ignition (GDCI) to become a production-viable technology. In FY 2017 (1) the Gen 2 GDCI vehicle calibration was completed, (2) the Gen 2 GDCI vehicle testing yielded 35% improvement in combined fuel economy measured relative to the baseline vehicle, but Tier 3 emissions target was not met, (3) Gen 3 GDCI engine, thermal management, and aftertreatment were built for the vehicle, (4) Gen 3 gasoline direct injection injectors were characterized for low smoke using both early

and late injection strategies, (5) the Gen 3 GDCI engine was tested on a dynamometer, (6) GDCI late injection benefits in reducing hydrocarbon and CO were demonstrated, and (7) the Gen 3 GDCI vehicle build was started, the engine was installed, and Gen 3 controllers integrated. (Confer, report V.5)



Figure 16 - Gen3 GDCI powertrain (Confer, report V.5)

- ENVERA LLC is developing a high-efficiency variable compression ratio (VCR) engine having variable valve lift technology and an advanced high-efficiency supercharger to obtain up to a 40% improvement in fuel economy when replacing current production V8 engines with the new small displacement VCR engine. In FY 2017 they (1) tested the VCR engine on a dynamometer up to approximately 300 hp, (2) achieved 230.4 g/kWh at 2,000 rpm and 5.36 bar brake mean effective pressure, (3) achieved high efficiency values using stoichiometric combustion for attaining low tail pipe emission values using proven three-way catalytic converter technology, and (4) projected 35–43% fuel economy improvement for an F-150 full-size pickup truck equipped with the VCR engine. (Mendler, report V.6)
- General Motors LLC is demonstrating a new combustion concept combining lean stratified operation with Miller cycle in a gasoline engine. In FY 2017 they (1) optimized piston, port, valvetrain strategy, and preliminary multipulse injection strategy across engine load range, (2) defined combustion system design for multi-cylinder engine, (3) demonstrated capability to achieve vehicle efficiency cycle targets, (4) defined boost and aftertreatment systems using one-dimensional models to address the challenges of low-temperature lean exhaust, and define single-cylinder engine boundary conditions, and (5) finalized design and initiated procurement of the first mule multi-cylinder engine for dynamometer testing, including advanced thermal management. (Battiston, report V.7)

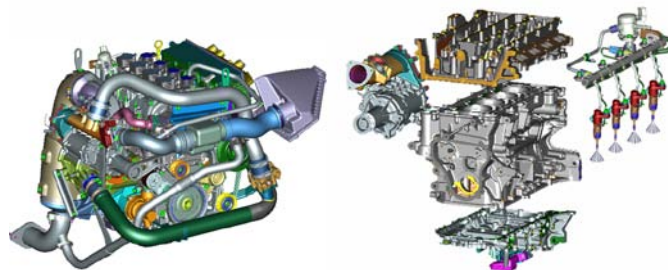


Figure 17 - Critical hardware components (Battiston, report V.7)

- Filter Sensing Technologies, Inc., is developing radio frequency (RF) sensors and evaluating RF sensing feasibility for selective catalytic reduction, three-way catalysts, and hydrocarbon trap applications. In FY 2017 they (1) developed production-intent RF sensor hardware and software, and supplied to project partners for engine and vehicle validation on various light-duty and heavy-duty applications, (2) applied RF cavity resonance models to quantify the spatial resolution of the cavity resonance measurements and validated simulation results relative to experimental measurements, (3) confirmed RF sensing feasibility for direct measurement of adsorbed gas species on diesel and gasoline aftertreatment system catalysts and developed calibration functions for selective catalytic reduction and three-way catalyst, (4) quantified the sensitivity of the RF measurements to the presence of other exhaust gas species and environmental noise

factors through carefully controlled bench reactor testing, and (5) demonstrated RF sensor robustness through fleet vehicle evaluations with full-size selective catalytic reduction systems on both medium- and heavy-duty vehicles operated in New York City (urban) drive cycles. (Sappok, report V.8)

- Eaton Corporation is developing, demonstrating, and evaluating commercialization of electrification of the air delivery and waste heat recovery (WHR) systems, to achieve a 20% fuel economy improvement at a commercially viable cost. In FY 2017 they (1) completed baseline engine testing for benchmarked comparison of fuel economy, emissions, and performance with electrically assisted variable speed electrified technology; (2) designed, procured, assembled, and functionally tested the electrically assisted variable speed electric waste heat recovery system; and (3) installed the electrically assisted variable speed electric waste heat recovery system on the baseline engine following removal of the variable geometry turbocharger and the system calibration to identify the optimal boost pressures to achieve best fuel economy. (Patil, report V.9)



Figure 18 - Electrically assisted variable speed electric waste heat recovery unit (Source: Eaton) (Patil, report V.9)

- Cummins Inc., is using a diesel system to demonstrate in a test cell peak engine system efficiency of 55% brake thermal efficiency. In FY 2017 they (1) demonstrated 50% brake thermal efficiency in a heavy-duty truck engine without waste heat recovery, (2) demonstrated emission compliance over Ramped Model Cycle Supplemental Emissions Test and hot Federal Test Procedure cycles, and (3) demonstrated +4.2% delta brake thermal efficiency from the waste heat recovery system. (Kocher, report V.10)
- Delphi Automotive Systems, LLC is improving engine fuel efficiency by developing a production-feasible electrically actuated cylinder deactivation valvetrain which will enable internal combustion engines to operate more efficiently. In FY 2017 (1) engine and vehicle simulations to characterize cylinder deactivation and to project fuel economy were completed, (2) the side pin concept was selected as the valve deactivation mechanism, (3) a suitable unidirectional electromagnetic solenoid actuator was selected during an actuator concept selection process, (4) a three-dimensional computer-aided drawing model confirmed that the side pin mechanism and its actuators fit within the available cylinder head volume, (5) a detail design and print package was completed for the probe hardware, (6) the probe hardware was ordered and received, and the build completed, and (7) force vs. displacement of the actuators was measured. (Fernandez, report V.11)

Table 2 - Drive Cycle Fuel Consumption Improvement (Fernandez, report V.11)

Cycle	Conservative	Aggressive
Metro-Highway ¹	7.3%	9.0%
FTP75	8.9%	10.5%
HWFET	4.4%	6.3%
NEDC	6.3%	7.3%
WLTC	5.2%	6.5%
JC08	7.0%	8.4%
Average	6.5%	7.8%

¹Computed from FTP75 and HWFET

Lubricant Technologies

- Argonne National Laboratory is developing test methodologies to enable rapid evaluation of new lubricant technologies and characterizing the structure and composition of surface tribochemical films. In FY 2017 they (1) investigated test protocols based on difference contact configurations to measure friction and wear of various engine oils and (2) examined the effects of starved lubrication on ring-on-liner tribological performance. (Ajayi, report VI.1)
- Oak Ridge National Laboratory is investigating the wear protection functionality of conventional and new antiwear additives (zinc dialkyldithiophosphate and ionic liquids) and friction reducing effectiveness of organic- and Mo-based friction modifiers in lubricating non-ferrous bearing materials. In FY 2017 (1) both molybdenum dithiocarbamate and organic friction modifier worked well for the steel-bronze contact with up to 65% and 40% friction reduction in the mixed lubrication regime, respectively; (2) zinc dialkyldithiophosphate was found to substantially reduce the effectiveness of organic friction modifier on friction reducing in lubricating the steel-bronze contact; (3) in boundary lubrication of a steel-bronze contact, zinc dialkyldithiophosphate could not protect the bronze surface but made the wear performance worse; and (4) blending 1% carbon black into a poly- α -olefin base oil significantly increased the wear volumes of both the ball and flat for an American Iron and Steel Institute 52100 bearing steel ball sliding against an M2 tool steel flat. (Qu, report VI.2)
- Pacific Northwest National Laboratory is supporting DOE's mission in increasing fuel economy by increasing fuel efficiency of gasoline internal combustion engines and developing ionic liquid-containing polymers with a linear architecture as viscosity index improvers. In FY 2017 they (1) prepared a series of low molecular weight polymers and evaluated their tribological properties, (2) demonstrated their superior shear stability compared to conventional viscosity index improvers, (3) achieved a multifunctional viscosity index improver that displayed 2.5 \times lower wear versus standard viscosity index improvers while maintaining a high viscosity index, (4) developed methodology to synthesize ionic liquid polymers, and (5) demonstrated the efficient synthesis of high viscosity index of ionic liquid-containing polymers via free radical polymerization. (Cosimbescu, report VI.3)
- Argonne National Laboratory is developing hybrid low-viscosity base fluids as lubricants to reduce viscous shear losses, developing and testing colloidal-based lubricant additives that reduce friction while ensuring reliability, and identifying and developing non-ferrous coatings that incorporate catalytically active ingredients that form lubricious carbon-based boundary films from long-chain hydrocarbon molecules of lubricating oils. In FY 2017 they (1) evaluated tribological performance which showed that mixed fluids exhibited noticeable friction reduction but very dramatic wear reduction compared to single-constituent fluids, (2) designed and developed nano-composite coatings with optimal thickness, hardness, surface roughness, and tribological properties, and (3) demonstrated their durability under severe boundary-lubricated sliding conditions. (Fenske, report VI.4)
- Oak Ridge National Laboratory is identifying and validating lubricant technologies that further a 4% fuel economy goal by reducing parasitic asperity and hydrodynamic friction losses by 25%. In FY 2017 they (1) demonstrated lubricant contribution to particulate matter during cold-start was greatest for low viscosity lubricants which enable higher fuel economy, (2) identified 40% reduction in key catalyst sensitivity due to accelerated aging, and (3) demonstrated up to 5% fuel economy improvement for low viscosity lubricants. (Storey, report VI.5)
- Ford Motor Company is formulating new polyalkylene glycol-based gear oils that will improve the fuel efficiency of light- and medium-duty applications by 2% over SAE 75W-140 grade axle oils without adverse impacts on vehicle performance or durability. In FY 2017 (1) AE0704-BN successfully exhibited improved or comparable performance to 75W-140 in bench screening testing and corrected the foaming issues of its predecessors; (2) the unviability of AW704-BN, the best attempt at a fully standalone polyalkylene glycol lubricant option, lead to the direction of oil soluble polyalkylene glycol top-treat options being the next pathway to success; and (3) the oil soluble polyalkylene glycol top-treat option AU6615-E/F successfully passed industry standard system level testing, meeting performance criteria and

showing improvement to previously tested oil soluble polyalkylene glycol formulations. (Gangopadhyay, report VI.6)

- Ford Motor Company is demonstrating deposition of plasma transfer wire arc coatings at various porosity levels on liners and engine blocks with improved surface finish. In FY 2017 (1) laboratory bench tests demonstrated high porosity plasma transfer wire arc coatings offer friction benefits over cast liner material in the mixed lubrication regime, (2) motored tests demonstrated a high porosity plasma transfer wire arc coating offers 5–24% friction benefit over a cast iron liner engine block at higher oil temperatures, and (3) polyalkylene glycol engine oil offered 6–25% friction benefit over GF-5 SAE 5W-20 oil. (Gangopadhyay, report VI.7)



Figure 19 - Plasma transfer wire arc coated cylinder bores in a linerless engine block (Source: Ford Motor Company) (Gangopadhyay, report VI.7)

- The University of Tennessee, Knoxville is synthesizing poly(alkyl methacrylate) brush-grafted silica nanoparticles (NPs) with various alkyl groups and determine the effects of alkyl pendant length on dispersibility and lubrication performance of hairy NPs in poly(alphaolefin) (PAO). In FY 2017 they (1) synthesized a series of poly(alkyl methacrylate) brush-grafted silica NPs and revealed the effects of alkyl pendant length on NPs' dispersibility and tribological properties, (2) attained significant reductions in friction (up to 38%) and wear volume (up to 90%) using 1 wt% clear, homogeneous dispersions of hairy NPs in PAO relative to neat PAO, (3) synthesized oil soluble ionic liquid-functionalized silver NPs and achieved >20% friction reduction and >90% wear reduction compared with PAO, (4) determined the role of the organic layer on Ag and Pd NPs in friction and wear reduction, and (5) elucidated the interrelated effects of initial surface roughness and NP size on friction and wear behavior using a finite element modeling approach. (Zhao, report VI.8)
- George Washington University is developing 0W-20 and 0W-16 low viscosity lubricants that will improve fuel economy by 2%. In FY 2017 (1) the 0W-20 low viscosity lubricant developed based on new chemistry successfully demonstrated 2.4% fuel economy improvement over current commercial lubricants in an industrial standard engine tests (ASTM engine dynamometer Sequence VIE test); (2) the new ultra-low viscosity lubricant developed, 0W-16, successfully passed the standard engine test, Sequence VIE with a 2.1% fuel economy improvement; and (3) a new 2018 platform engine was selected for engine durability test development. (Wu, report VI.9)
- Northwestern University is developing novel lubricant formulations for improving vehicle fuel efficiency by at least 2% without adversely impacting vehicle performance or durability. In FY 2017 they (1) developed alkyl-cyclen derivatives to be the most superior heterocyclic friction modifiers for boundary lubrication applications in terms of efficient friction reduction and great stability enhancement, (2) designed and synthesized novel diblock copolymer viscosity modifiers for hydrodynamic lubrication, (3) evaluated thermos-thickening and shear-thinning of the diblock copolymer viscosity modifiers, (4) established understanding of the viscosity modification process, and (5) compared miscibility and diffusivity for different viscosity modifier molecules. (Wang, report VI.10)
- Valvoline LLC is developing novel lubricant formulations that are expected to improve the fuel efficiency of medium-duty, commercial, and military vehicles by at least 2% (improvement based on comparative

results from engine dynamometer testing, chassis dynamometer testing or test track, e.g., SAE J1321) without adverse impacts on the vehicle performance or durability. In FY 2017 they conducted the SAE J1321 test for five Valvoline candidate lubricants. (Wu, report VI.11)

Table 3 - Fuel Efficiency Improvement of Each Valvoline Candidate (Wu, report VI.11)

Valvoline Candidate	Code	FE Improvement (%)
Engine Oil	EO 1	1.57%
Engine Oil	EO 2	1.86%
Axle Oil	GO 1	0.44%
Axle Oil	GO 2	0.72%
Transmission Fluid	TO 1	0.20%

System-Level Efficiency Improvement

- Lawrence Livermore National Laboratory is providing guidance to industry to improve the fuel economy of a Class 8 tractor-trailer through the use of aerodynamics. In FY 2017 they investigated the aerodynamic benefits of heavy vehicle platoons by means of a 1/50th scale wind tunnel test. (Salari, report VII.1)

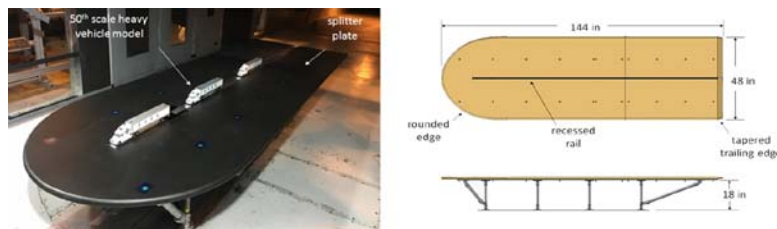


Figure 20 - Splitter plate dimensions and three-vehicle platoon in the Army 7 ft × 10 ft wind tunnel located at National Aeronautics and Space Administration Ames (Salari, report VII.1)

- PPG Industries, Inc., is developing a novel surface-modified silica technology and demonstrate 4–6% improved fuel efficiency of truck and bus radial tires built from the technology. In FY 2017 they (1) performed a systematic and thorough investigation of the properties that enable uniform dispersion of silica in both natural rubber and synthetic rubber, (2) scaled-up selected silicas from the first stage of the project, (3) performed rubber optimization work, (4) evaluated test results and performed further optimization based on actual tire data to optimize the silica-rubber combination, and (5) performed a final tire build. (Dos Santos Freire, report VII.2)
- Oak Ridge National Laboratory is reducing the hysteretic losses of elastomers that are used for manufacturing vehicle tires. In FY 2017 (1) graphene nanoplatelets were successfully functionalized and showed good dispersion in the polymer elastomer when mixed in solution, (2) electrospun silica nanofibers were synthesized with diameter smaller than 100 nm, (3) the combination of silica nanofibers and functionalized graphene nanoplatelets fillers synergistically improved the mechanical performance of the elastomer, (4) the weight content of the filler material was optimized, (5) elastomers filled with graphene nanoplatelets and silica nanofibers were synthesized, (6) spacer material was introduced between the graphene nanoplatelets to increase the surface area of the functionalized graphene powder, and (7) safety data sheets were generated for all synthesized material. (Polyzos, report VII.3)
- PPG Industries, Inc., is developing a new silica filler that can increase tire fuel efficiency by 2% while maximizing key performance properties in non-tread tire components compared to current carbon black-filled sidewall compounds. In FY 2017 they (1) systematically selected representative commercial silica and carbon blacks to provide a significant range in filler morphology and surface chemistries, (2) evaluated their performance in a model sidewall formulation, and (3) performed systematic studies varying silica morphology and surface chemistry. (Dos Santos Freire, report VII.4)

- Oak Ridge National Laboratory is investigating optimization opportunities throughout the entire powertrain across multiple vehicle architectures in the heavy-duty vehicle sector. In FY 2017 they (1) chose a Cummins 15-L 450 hp model year 2012 ISX15 engine and Eaton UltraShift Plus 10-speed automated manual transmission as the baseline for unintegrated powertrains, (2) installed the powertrain in the Oak Ridge Vehicle Systems Integration Laboratory to be tested in a hardware-in-the-loop set-up, (3) selected a Kenworth T700 as the emulated vehicle, (4) implemented three test drive cycles described by the Environmental Protection Agency plus the one from the Heavy Truck Duty Cycle database, (5) performed all four test cycles and weight combinations on the Vehicle Systems Integration Laboratory, and (6) modeled a Class 8 truck in Autonomie. (Deter, VII.5)



Figure 21 - ISX450 engine with UltraShift Plus automated manual transmission under test in the powertrain test cell at Oak Ridge National Laboratory's Vehicle Systems Integration Laboratory (Deter, report VII.5)

Invention and Patent Disclosures

1. International patent filed: Dec, J.E., and R. Renzi, September 2016. (Dec, report I.4)
2. International patent filed: Dec, J.E., and R. Renzi, November 2016. (Dec, report II.14)
3. Mueller, C.J. "Ducted Fuel Injection." U.S. Patent Application #15,363,966; filed November 29, 2016. (Mueller, report II.17)
4. Mueller, C.J. "Ducted Fuel Injection with Ignition Assist." U.S. Patent Application #15,364,002; filed November 29, 2016. (Mueller, report II.17)
5. Mueller, C.J. "Ducted Fuel Injection." U.S. Patent Application #15,666,321; filed August 1, 2017. (Mueller, report II.17)
6. Gao, P.X., and W. Tang. "Mn-Co Spinel Oxide Nano-array Based Monolith." U.S. provisional patent filed, University of Connecticut, 2017. (Gao, report IV.11)
7. Gao, P.X., and S. Hoang. "Low-temperature Diesel Oxidation Catalysts using TiO₂ Nano-Arrays Integrated Monolithic Substrates." U.S. provisional patent filed, University of Connecticut, 2017. (Gao, report IV.11)
8. Gao, P.X., X. Lu, and S. Hoang. "Microwave-assisted and low-temperature fabrication of TiO₂ nanostructured films on scalable 2D and 3D substrates." U.S. provisional patent filed, University of Connecticut, 2017. (Gao, report IV.11)
9. Gao, P.X., and W. Tang. "Cordierite nano-array integrated cordierite honeycomb monolith." U.S. provisional patent filed, University of Connecticut, 2017. (Gao, report IV.11)
10. Gao, P.X., and S. Wang. "Perovskite-Pt Nanotube Array Based Monoliths." U.S. provisional patent filed, University of Connecticut, 2017. (Gao, report IV.11)
11. One patent application and two defense disclosures. (Battiston, report V.7)
12. One patent application is being prepared. (Polyzos, report VII.3)

I. Combustion Research

I.1 Light-Duty Diesel Combustion

Stephen Busch, Principal Investigator

Sandia National Laboratories
PO Box 969, MS 9053
Livermore, CA 94551-0969
E-mail: sbusch@sandia.gov

Michael Weismiller, DOE Technology Manager

U.S. Department of Energy
E-mail: Michael.Weismiller@ee.doe.gov

Start Date: October 1, 2016	End Date: September 30, 2017	
Total Project Cost: \$885,000	DOE share: \$885,000	Non-DOE share: \$0

Project Introduction

Despite compliance issues in previous years, automakers have demonstrated that the newest generation of diesel powertrains are capable of meeting all federal and state regulations [1]. Diesels continue to be a cost-effective, efficient, powerful propulsion source for many light- and medium-duty vehicle applications [2]. Even modest reductions in the fuel consumption of light- and medium-duty diesel vehicles in the United States will eliminate millions of tons of CO₂ emissions per year. Continued improvement of diesel combustion systems will play an important role in reducing fleet fuel consumption, but these improvements will require an unprecedented scientific understanding of how changes in engine design and calibration affect the mixture preparation, combustion, and pollutant formation processes that take place inside the cylinder.

The focus of this year's research is to provide insight into the physical mechanisms responsible for improved thermal efficiency observed with a stepped-lip piston. Understanding how piston design can influence efficiency will help engineers develop and optimize new diesel combustion systems.

Objectives

- Provide the physical understanding of the in-cylinder combustion processes needed to minimize the fuel consumption and the carbon footprint of automotive diesel engines while maintaining compliance with emissions standards and meeting customer expectations
- Develop efficient, accurate computational models that enable numerical optimization and design of fuel-efficient, clean engines
- Provide accurate data obtained under well-controlled and characterized conditions to validate new models and to guide optimization efforts

Approach

The overall research approach involves carefully coordinated experimental, modeling, and simulation efforts. Detailed optical measurements of flow, mixture preparation, and combustion processes are made in an optical research engine facility based on a General Motors 1.9-L automotive diesel engine. Careful attention is also paid to obtaining accurate boundary conditions to facilitate comparisons with simulations, including intake flow rate and thermodynamic properties, and wall temperatures. The engine geometry and experimental data are made publically available [3]. These data support commercial code vendors' efforts to develop and evaluate numerical simulation tools that will be used to design and optimize the next generation of clean, efficient diesel combustion systems.

Close collaboration with numerical simulation experts at the University of Wisconsin (UW)–Madison (subcontractors) provides a much needed compliment to the optical engine experiments. The experimental results guide the development of advanced numerical models and enable the evaluation of computational simulations. In turn, analysis of the simulation results generates a deeper understanding of in-cylinder flow and combustion physics. The results of this combined approach are not possible to obtain with experimental data alone, and the analyses provide a fundamental, science-based understanding of mechanisms that increase thermal efficiency or influence tradeoffs between efficiency, emissions, and combustion noise. Publication of this knowledge helps guide the development and calibration of advanced diesel engines.

Results

Key accomplishments:

- Identified improvement of the degree of constant volume combustion as a key to improving thermal efficiency
- Demonstrated that engine efficiency improves with a stepped-lip piston compared to with a conventional piston, because the second half of combustion occurs faster and the degrees of constant volume combustion are therefore higher
- Analyzed numerical simulation results to reveal the mechanism by which the stepped-lip piston changes turbulent flow structure and enhances mixing.

Last year's experimental results demonstrated that a stepped-lip piston bowl can improve thermal efficiency by several percent and reduce smoke emissions by half, compared to a conventional, re-entrant piston bowl. These improvements depend on injection timing, but are generally in agreement with other results found in the literature. This year, research efforts have been devoted to understanding the physical mechanism responsible for the improvement in thermal efficiency. Two prevalent theories for the efficiency improvement are found in the literature. The first is that heat loss through the combustion chamber walls may be reduced with the stepped-lip piston, so that more energy is available to do mechanical work. The second theory is that the stepped-lip piston enhances mixing-controlled combustion rates, so that more work can be extracted from the combustion products during the expansion stroke. The extent to which either of these factors contributes to the improvement in thermal efficiency has not yet been demonstrated.

A simple thermodynamic model has been constructed to test both of these theories. Artificially generated heat release profiles are model inputs, and the model computes the cylinder pressure and the net amount of work extracted for the given amount of heat input. Variations in the heat-release phasing and duration change the degree of constant volume combustion. The degree of constant volume combustion (dCVC) is a measure of how closely the heat release profile mimics an idealized, constant-volume heat release at top dead center (TDC). A late, slow combustion event will result in a low value of dCVC, whereas rapid combustion near TDC will result in a value of dCVC closer to one. Wall heat loss is simulated using a commonly used algebraic model, and the ratio of the total amount of heat loss throughout the cycle to the total heat input is computed as a metric for comparison.

Figure I.1.1 compares the efficiency improvement resulting from a small increase in dCVC with the efficiency improvement resulting from a comparatively small decrease in wall heat loss. Increasing the degree of constant volume combustion is more effective at increasing thermal efficiency than decreasing the amount of wall heat loss. This is true for a wide range of main injection timings.

Experimental data are processed to estimate thermal efficiency, the degree of constant volume combustion, and wall heat loss for both the conventional and the stepped-lip piston geometries. These results are shown in Figure I.1.2 for a range of main injection timings. The efficiency improvements are most significant for main injections starting between 3 crank angle degrees after TDC (CAD ATDC) and 13 CAD ATDC. The residual plots shown in Figure I.1.2 demonstrate that total estimated wall heat-loss is not strongly affected by this change in piston bowl geometry. Furthermore, the efficiency improvements are strongly correlated with the change in dCVC, but not with the change in wall heat loss. This result, together with the theoretical

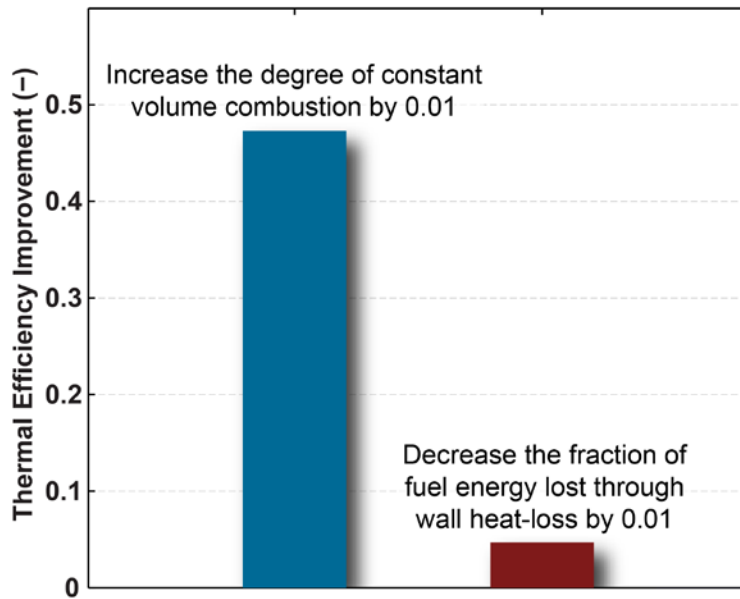


Figure I.1.1 - In a diesel engine, increasing the work extracted by the piston is significantly more effective at improving thermal efficiency than reducing the amount of energy lost through the combustion chamber walls

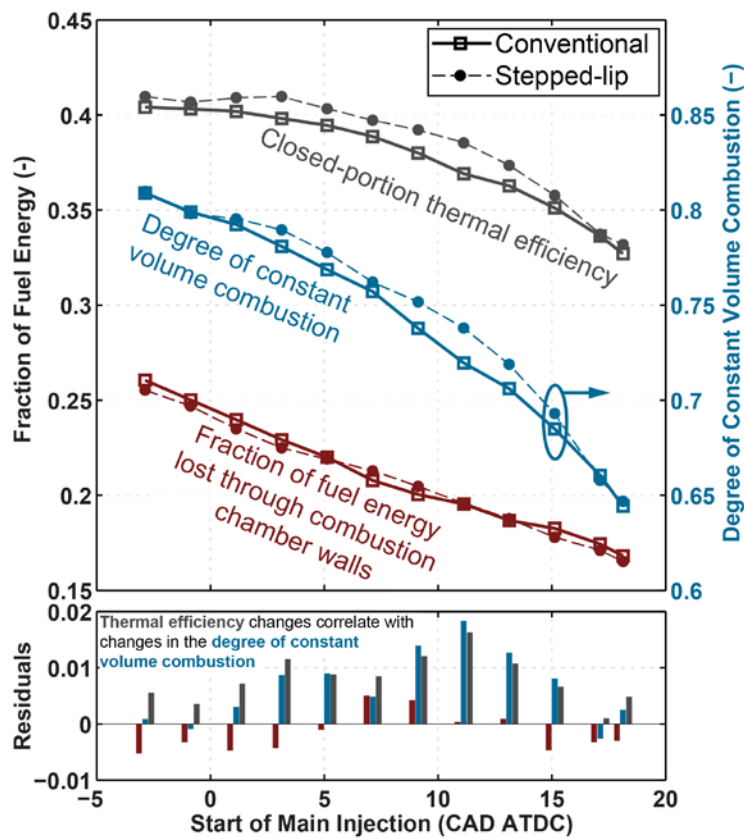


Figure I.1.2 - Thermal efficiency (the fraction of fuel energy extracted as work) is higher with the stepped-lip piston for some injection timings. The efficiency differences correlate with differences in the degree of constant volume combustion. Wall heat loss does not change with piston bowl geometry in a significant way.

consideration shown in Figure I.1.1, suggests that increasing the degree of constant volume combustion is an effective way to improve the thermal efficiency of direct injection diesel engines.

Data found in the literature suggest that stepped-lip pistons enhance rates of combustion during the second half of the combustion event, and analysis of the experimental data in the project confirms this finding. The crank angles at which 10%, 50%, and 90% of the fuel energy has been released (CA10, CA50, and CA90, respectively) are shown for a range of injection timings for both piston geometries in Figure I.1.3. CA10 and CA50 are affected by injection timing, but only to a very small extent by piston geometry. The effect of piston geometry is most evident after CA50; the duration between CA50 and CA90 is shorter by as much as 10 CAD with the stepped-lip piston. At an engine speed of 1,500 rpm, CA90 is achieved approximately 1 ms faster than with the conventional piston. This results in a higher degree of constant volume combustion and therefore in higher thermal efficiency with the stepped-lip piston. Because turbulent mixing processes in the cylinder control this second half of the main heat release event, changes to turbulent flow and mixing are fundamental to the mechanism of increasing efficiency with the stepped-lip piston.

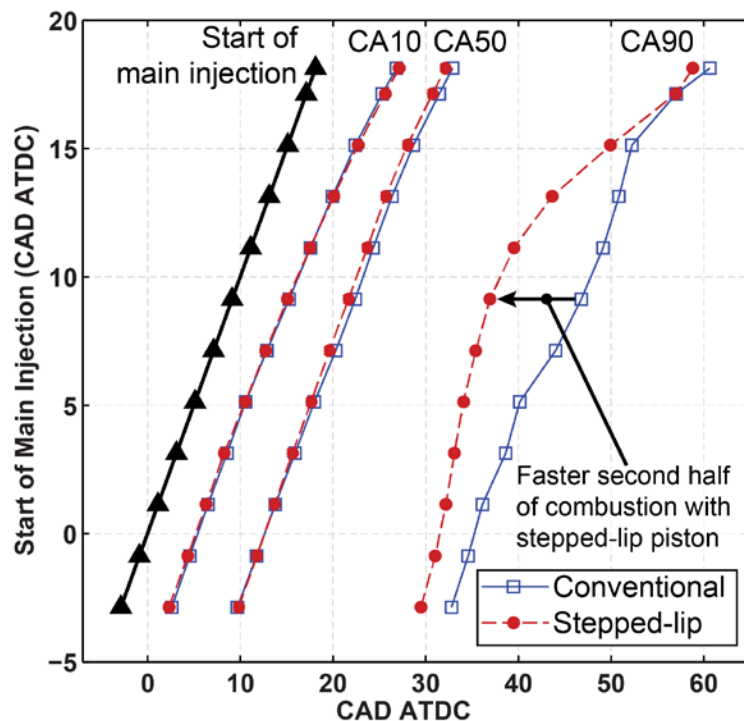


Figure I.1.3 - As the main injection timing is delayed, the combustion takes place later in the expansion stroke. Piston bowl geometry does not affect the first half of the combustion event (until CA50), but the second half of combustion is faster with the stepped-lip piston.

While ongoing experimental efforts to characterize the turbulent flow structure in the engine may provide further insight into the role of piston geometry in increasing efficiency, computational fluid dynamics (CFD) simulations are necessary to provide a more complete picture of this complex, dynamic, three-dimensional phenomenon. CFD capabilities at UW–Madison have been developed to simulate flow, fuel injection, mixing, and combustion on a model of the whole engine, including the intake system, the cylinder, and the exhaust system. Past work has been devoted to evaluating the code's ability to predict the flow in the cylinder, and the results have shown differences in the flow fields simulated with the conventional and the stepped-lip piston geometries [4]. This year, predictions of the liquid and vapor fuel spray behavior have been compared with experimental data. A comparison of fuel vapor concentrations is shown in Figure I.1.4 for the conventional piston bowl geometry. The data have been measured and/or computed in three horizontal planes, which are depicted at the bottom of Figure I.1.4.

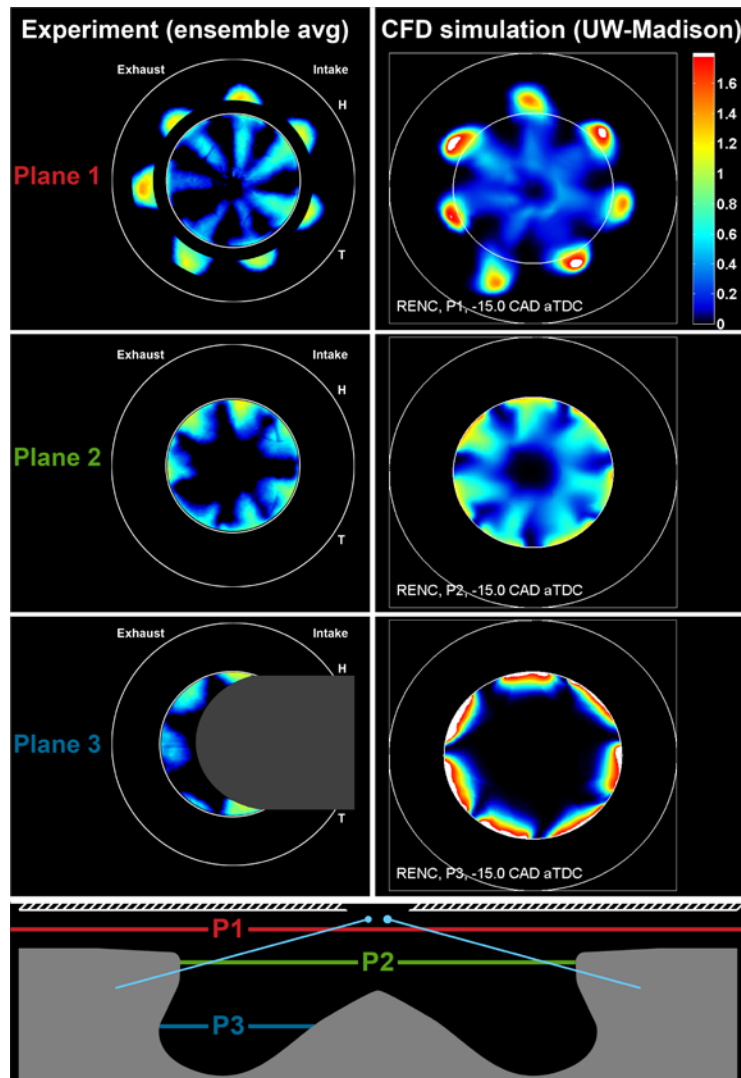


Figure I.1.4 - Comparison between fuel vapor concentrations measured experimentally by planar, laser-induced fluorescence of a fuel tracer (left), and fuel vapor concentration predicted by the CFD simulation (right). Results are shown in false-color for three horizontal cutting planes for the conventional bowl geometry (depicted at the bottom). The latest simulation results reliably predict vapor penetration above and into the piston bowl, as well as jet deflection by the swirling in-cylinder flow.

The comparisons indicate reliable prediction of fuel jet behavior with the full engine computational domain and the state-of-the-art spray models employed at UW–Madison. The results shown in Figure I.1.4 are a dramatic improvement compared to previous approaches, in which only a sector of the cylinder was simulated. The penetration rate of the jets, the gradients in fuel concentration, and the degree of penetration down into the bowl match more closely with experimental data than ever before. The deflections of the jets as they exchange momentum with the swirling in-cylinder flow are also well predicted. Simulation results compare favorably with experimental results for both piston geometries. The goal at this stage of the project is not 100% quantitative agreement between simulation and experiment, but reliable qualitative prediction of the phenomena associated with fuel injection, spray, and mixing processes.

The comparisons between experimental data and simulation results did not reveal any significant deficiencies in the modeling and simulation approaches, so the simulation results are used to provide insight into how piston bowl geometry interacts with the fuel injection to influence turbulent flow structure during and after the main injection. Figure I.1.5 shows a comparison between vertical-plane flow structures at two crank angles for the conventional piston (left) and the stepped-lip piston (right). This simulation is performed for a main

injection starting at 9.1 CAD ATDC, so differences in turbulent flow structure may be expected to appear after the experimentally determined value of CA50 of approximately 22 CAD ATDC (see Figure I.1.3), or at 12.9 CAD after the start of the main injection ($ASOI_m$). The top row of images shows what is happening shortly before CA50, and the bottom row of images depicts the evolution of the flow and mixing.

With the conventional bowl, a significant portion of the jet impacts on or below the vertical bowl rim, and is redirected down into the bowl. This reinforces the prevailing flow in the cylinder and results in the formation of a vertical-plane vortex structure, called a toroidal vortex (see second row, first column of Figure I.1.5). The toroidal vortex is energetic and long-lived; it contains the majority of the fuel and is the predominant flow feature for the conventional bowl. The uppermost portion of the fuel jet does not interact with the bowl, but instead continues to propagate outward into the so-called squish region. The outwardly propagating jet impinges on the cylinder wall, and much of this fuel remains in the outer portion of the squish region.

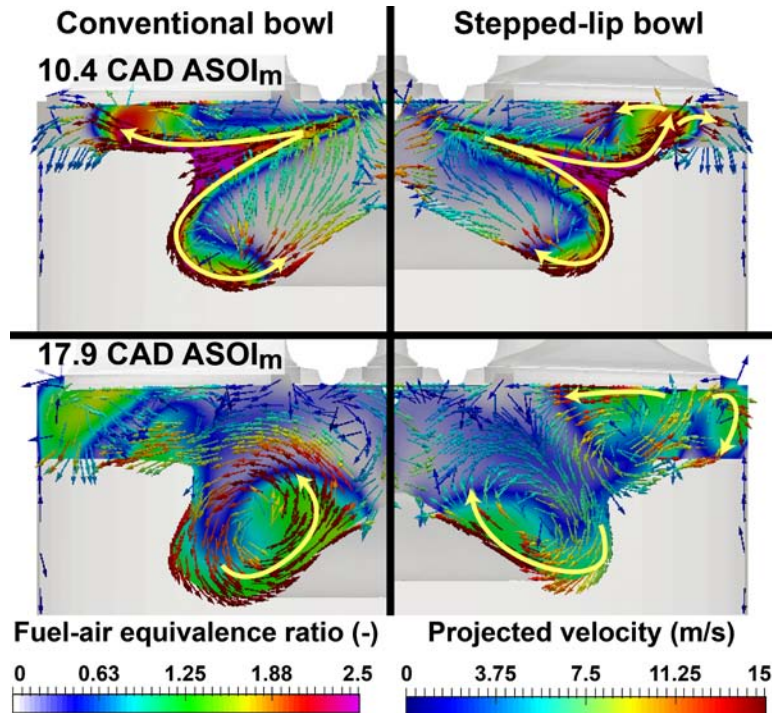


Figure I.1.5 - Simulated vertical-plane projection of flow fields (shown with colored vectors) and the fuel concentrations (false-colored field data) for the conventional (left) and stepped-lip (right) pistons. Yellow arrows have been added to indicate the motion of the fuel jets. Crank angles are shown in CAD $ASOI_m$.

As expected, the interaction between the fuel jets and the stepped-lip piston geometry produces a different flow structure than with the conventional piston. A toroidal vortex forms in the lower portion of the stepped-lip bowl, but it is smaller and less pronounced than with the conventional bowl. Differences in the flow structure above the piston begin to appear even before CA50, as seen in the first row of Figure I.1.5. The portion of the jet that impinges on the sloped step surface is deflected outward along the step and upward at the outer bowl rim. It forms a secondary jet that propagates upward and impinges on the cylinder head. This second impingement results in spreading of fuel–air mixture and turbulence, and in the formation of two additional recirculation zones (see the second row, right column of Figure I.1.5). One recirculation zone forms in the outermost portion of the cylinder, while the other forms above the step. Both act to transport fuel–air mixture and turbulence to regions with excess oxygen, which is believed to be the reason for enhanced combustion rates and improved thermal efficiency with the stepped-lip piston.

Sandia National Laboratories is a multimission laboratory managed and operated by National Technology and Engineering Solutions of Sandia, LLC., a wholly owned subsidiary of Honeywell International, Inc., for the U.S. Department of Energy’s National Nuclear Security Administration under contract DE-NA-0003525.

Conclusions

Investigations with a conventional, re-entrant piston bowl and a stepped-lip piston bowl demonstrate that the stepped-lip piston can improve thermal efficiency by several percent, and the focus of this year's research was to generate a deeper understanding of the mechanism responsible for the efficiency improvement. Thermodynamic analyses, validation of CFD simulations with data from optical experiments, and analysis of the CFD results reveals the following.

- Increasing the degree of constant volume combustion is more effective than reducing wall heat loss to improve thermal efficiency.
- Changing from the conventional piston to the stepped-lip piston results in a small change in estimated wall heat loss, and the changes in wall heat loss have an insignificant impact on thermal efficiency.
- The degree of constant volume combustion is higher for injection timings with improved efficiency with the stepped-lip piston; dCVC correlates strongly with thermal efficiency.
- Higher degrees of constant volume combustion with the stepped-lip piston are the result of enhanced heat release rates during the second half of combustion.
- Interactions between the fuel sprays and the stepped-lip piston bowl result in the spreading of mixture and turbulence, which likely increases the rate of combustion and thereby the thermal efficiency.

References

1. US EPA. "Proposed Determination on the Appropriateness of the Model Year 2022-2025 Light-Duty Vehicle Greenhouse Gas Emissions Standards under the Midterm Evaluation: Technical Support Document." Document EPA-420-R-16-021, November 2016.
2. The Martec Group. "Diesel engine technology and the midterm evaluation: An analysis of compliance costs and benefits." Accessed online July 10, 2017: <http://www.martecgroup.com/wp-content/uploads/2016/05/The-Martec-Group-White-Paper-Diesel-Engine-Technology-and-the-Midterm-Evaluation-Summer-2016.pdf>
3. Busch, S. "Small-Bore Diesel Engine." Accessed 11/8/2017. <https://ecn.sandia.gov/engines/engine-facilities/small-bore-diesel-engine/>.
4. Perini, F., Zha, K., Busch, S., Kurtz, E., Peterson, R., Warey, A., Reitz, R. "Piston geometry effects in a light-duty, swirl-supported diesel engine: flow structure characterization." *International Journal of Engine Research*. Accepted for publication October 2, 2017.

Key Fiscal Year 2017 Publications

1. Park, C. and S. Busch. "The influence of pilot injection on high-temperature ignition processes and early flame structure in a high-speed direct injection diesel engine." *International Journal of Engine Research*. DOI: 10.1177/1468087417728630

I.2 Heavy-Duty Low-Temperature and Diesel Combustion and Heavy-Duty Combustion Modeling

Mark PB Musculus, Principal Investigator

Sandia National Laboratories
PO Box 969, MS 9053
Livermore, CA 94551-0969
E-mail: mpmuscu@sandia.gov

Michael Weismiller, DOE Technology Manager

U.S. Department of Energy
E-mail: Michael.Weismiller@ee.doe.gov

Start Date: October 1, 2016	End Date: September 30, 2017	
Total Project Cost: \$580,000	DOE share: \$580,000	Non-DOE share: \$0

Project Introduction

Regulatory drivers and market demands for lower pollutant emissions, lower carbon dioxide emissions, and lower fuel consumption motivate the development of clean and fuel-efficient engine operating strategies. Most current production engines use a combination of both in-cylinder and exhaust emission control strategies to achieve these goals. The emissions and efficiency performance of in-cylinder strategies depend strongly on flow and mixing processes associated with fuel injection.

Various diesel engine manufacturers have adopted close-coupled post-injection combustion strategies to both reduce pollutant emissions and to increase engine efficiency for heavy-duty applications, as well as for light- and medium-duty applications. Close-coupled post-injections are typically short injections that follow a larger main injection in the same cycle after a short dwell, such that the energy conversion efficiency of the post-injection is typical of diesel combustion. Of the various post-injection schedules that have been reported in the literature, effects on exhaust soot vary by roughly an order of magnitude in either direction of increasing or decreasing emissions relative to single injections [1]. While several hypotheses have been offered in the literature to help explain these observations, no clear consensus has been established. For new engines to take full advantage of the benefits that post-injections can offer, the in-cylinder mechanisms that affect emissions and efficiency must be identified and described to provide guidance for engine design.

Objectives

This project includes diesel combustion research at Sandia National Laboratories and combustion modeling at the University of Wisconsin. The overall objectives are:

- Develop a fundamental understanding of how in-cylinder controls can improve efficiency and reduce pollutant emissions of advanced low-temperature combustion technologies
- Quantify the effects of fuel injection, mixing, and combustion processes on thermodynamic losses and pollutant emission formation
- Improve computer modeling capabilities to accurately simulate these processes.

Fiscal Year 2017 Objectives

- Measure how in-cylinder soot and/or soot precursor formation are affected by in-cylinder conditions and processes
- Use computer model simulations to complement experimental soot and spray data to provide a deeper mechanistic understanding of in-cylinder processes

Approach

This project uses an optically accessible, heavy-duty, direct-injection diesel engine (Figure I.2.1). A large window in the piston crown provides primary imaging access to the piston bowl, and other windows at the cylinder wall provide cross-optical access for laser diagnostics or imaging.

The optical setup in Figure I.2.1 uses two cameras to record simultaneous images of soot natural luminosity (NL) and diffused back-illumination (DBI) soot extinction. DBI measures the soot optical density through light transmission measurements, and mitigates beam-steering effects by using a diffused light source. The light source is a 632-nm pulsed light-emitting diode (LED) in the top right corner of Figure I.2.1. The LED emission is collimated using two lenses and a pinhole, after which the beam is directed down onto an engineered diffuser, through a cylinder-head window, the combustion chamber with soot, and piston crown window. Thereafter, a beamsplitter directs most of the beam to a high-speed complementary metal-oxide semiconductor (CMOS) camera, while a second high-speed CMOS camera captures NL simultaneously.

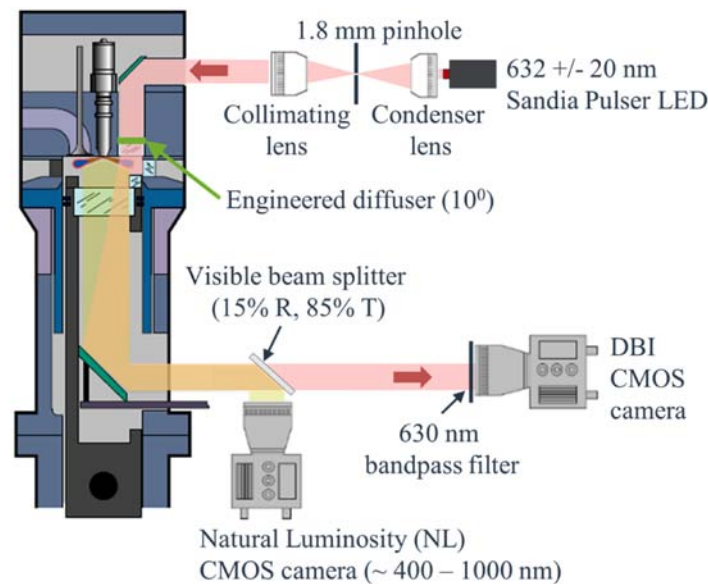


Figure I.2.1 - Optical engine schematic showing LED beam path (propagating from top to bottom) and two-camera setup for simultaneous DBI and NL imaging

Results

Figure I.2.2 shows the dependence of the paper-blackening (PB) measurement of engine-out smoke emission on the gross indicated mean effective pressure (IMEP_g) for various single-injection and post-injection schedules, all with the same 347 crank angle degree (CAD, where 360 is at end of compression) start of solenoid energizing (SSE) of the main injection, but different main injection duration of solenoid energizing (DSE) and/or different post-injection SSE and DSE. Operating conditions use nitrogen dilution to 18% intake O₂ and the estimated thermodynamic conditions at top dead center (TDC) for a motored charge are 15.8 kg/m³ and 910 K. The blue trendline for single-injection operating conditions shows monotonically increasing PB with increasing main injection DSE. The addition of post-injections of up to 550 μs DSE to the main injection (with a constant 2,350 μs DSE) does not increase the measured PB. A post-injection of 600 μs DSE increases the PB relative to the main injection alone, but the PB remains lower than the single-injection PB trend at the same load and SSE. As the post-injection DSE is increased to 800 μs, the PB exceeds the single-injection PB trend at the same load.

Insight into the in-cylinder mechanisms responsible for the engine-out emissions behavior in Figure I.2.2 may be gained through analysis of the in-cylinder imaging data. Figure I.2.3 shows crank-angle-resolved soot optical density on a natural-logarithmic scale (KL), averaged over the DBI field of view (FoV) for a reference

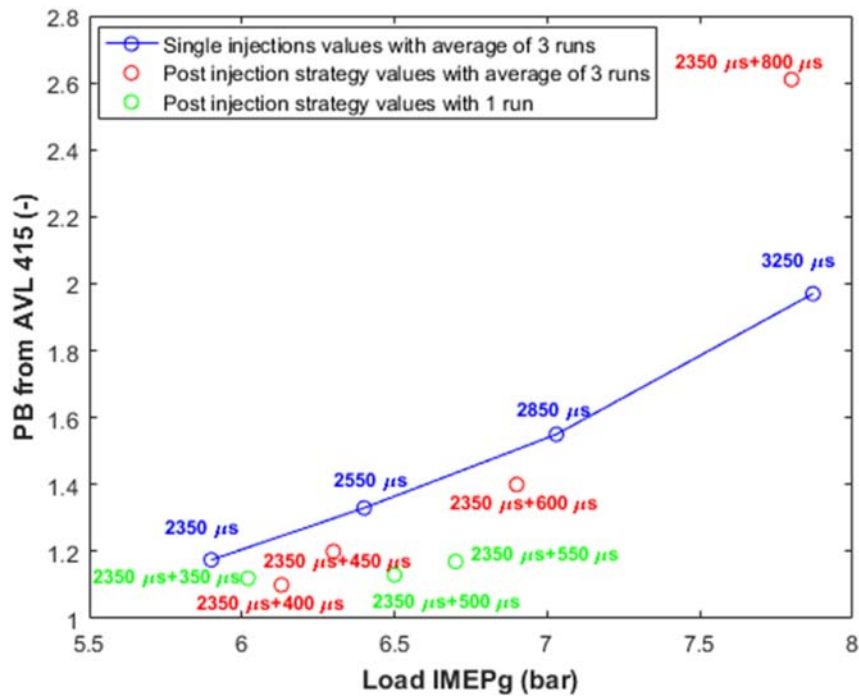


Figure I.2.2 - Mean PB for using various single- and post-injection schedules. 18% intake O_2 , 15.8 kg/m³ and 910 K TDC motored

single-injection and selected post-injection operating conditions in Figure I.2.2. The KL data in Figure I.2.3 shows two peaks. The left-hand peak is from the main injection, while the right-hand peak is due to the post-injection, the height of which depends on the DSE of the post injection. The 400- μ s DSE post injection (green line) has a minimal effect relative to the single-injection data, but larger post-injection DSEs show increasing departures from the single-injection data. The 800- μ s DSE post injection (magenta line) has the highest peak KL, even higher than the main injection peak. The late-cycle KL (far right in Figure I.2.3, when

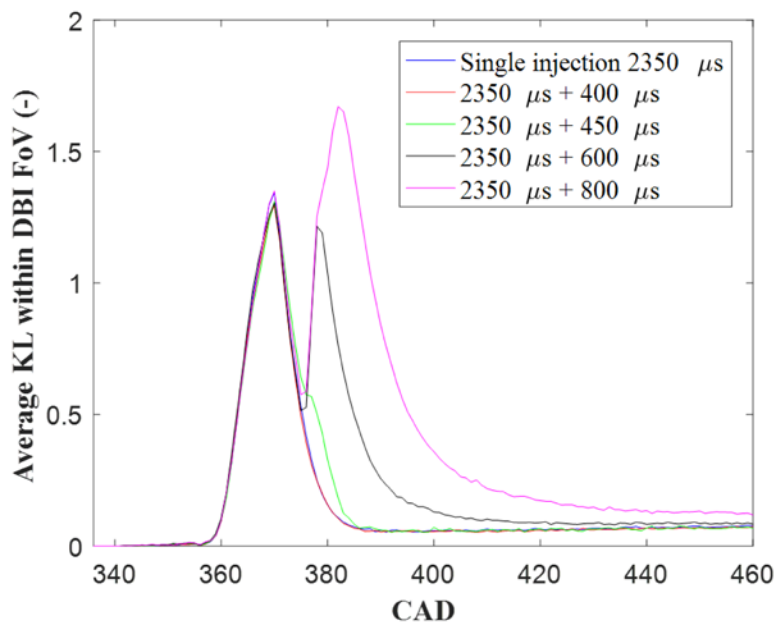


Figure I.2.3 - KL evolution within the DBI FoV from ensemble-averaged images with post-injections of various DSE added to a main injection of 2,350 μ s DSE, as indicated in the legend. 18% intake O_2 , 15.8 kg/m³ and 910 K TDC motored

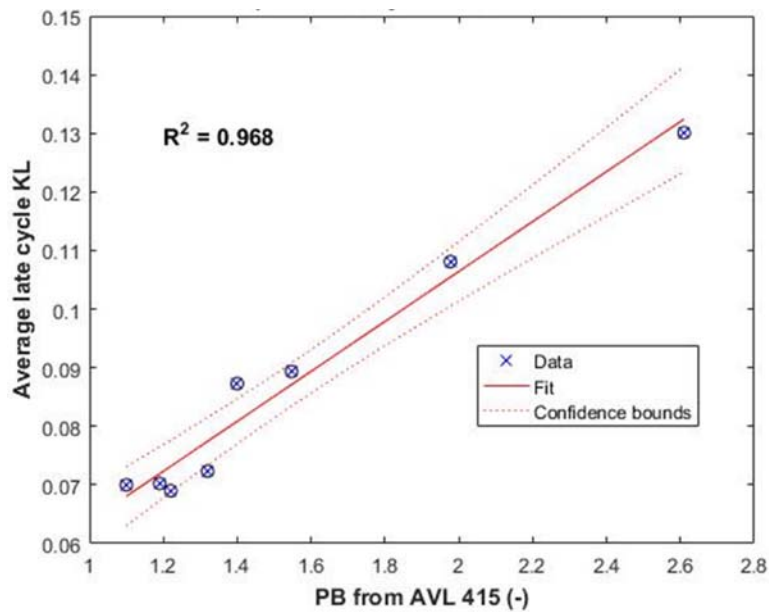


Figure I.2.4 - Correlation between the late-cycle FoV-averaged KL and engine-out PB data in Figure I.2.2 that have three replicates. Dotted lines show the 95% confidence interval.

cylinder contents are well mixed) also follows the exhaust emissions trends in Figure I.2.2, with the longer post-injections having higher late-cycle KL (Figure I.2.3) and engine-out PB (Figure I.2.2) than shorter post-injections. Indeed, Figure I.2.4 shows that the correlations between late-cycle KL and engine-out PB for the data in Figure I.2.2 is quite good (R-squared of 0.968).

Further insight into the in-cylinder processes by which post injections affect in-cylinder and engine-out soot may be gained by comparing the KL and NL images. Figure I.2.5 is a composite graphic comparing ensemble-averaged KL and NL data at one point in the cycle for two different conditions, one with a single-injection and one with a load-equivalent post-injection (see injector solenoid energizing schedule in top left of Figure I.2.5). The piston and spray geometry at the selected image timing of 379 CAD (with TDC of compression at 360 CAD) is shown in the bottom left of Figure I.2.5. The top row of images are false colored according to the DBI-measured soot KL for the single (left) and main+post (middle) injection schedules, and the difference between the two (right). Similarly, the bottom row shows corresponding NL images. The NL images show a partial view of the piston bowl, with the injector at the bottom right, and the piston bowl forming the outer circle. The curved white line shows the FoV of the DBI images. The KL difference image at the top right shows that the amount of soot (KL) is increased in some locations (green) and is decreased in others, while the NL difference image in the bottom right shows a different pattern. Of particular interest are the two regions identified by the red dots with connecting lines showing opposite trends in the KL and NL data. Both the KL and the NL increase near the upper-right dot pair in each image, while the KL decreases and the NL increases for the lower-left dot pair. The NL signal increases with both temperature and the amount of soot, and the KL data shows that the amount of soot decreases in the vicinity of the lower-left dot, which implies that the temperature must increase when the post-injection is added for the NL signal to increase. This provides in-cylinder evidence for a mechanism of soot reduction by increasing local temperatures, which should enhance local soot oxidation. This same mechanism was suggested by previous soot planar laser-induced incandescence and OH planar laser-induced fluorescence imaging data from this project [2], and the current temperature data further strengthen these indications of previous work regarding the in-cylinder mechanisms by which post-injections affect in-cylinder soot. Later in the cycle (not shown here), the KL difference data show lower KL after the post injection, which is consistent with the action of a second entrainment wave for the post injection that increases entrainment to aid soot oxidation, as shown in previous work on this project [3].

Finally, computer modeling simulations provide additional insight into these NL/KL comparisons. Figure I.2.6 illustrates how the two-dimensional (2D) NL images measured in the experiments can be predicted from the 3D in-cylinder soot distributions from the simulations. The top row shows a comparison of a measured 2D

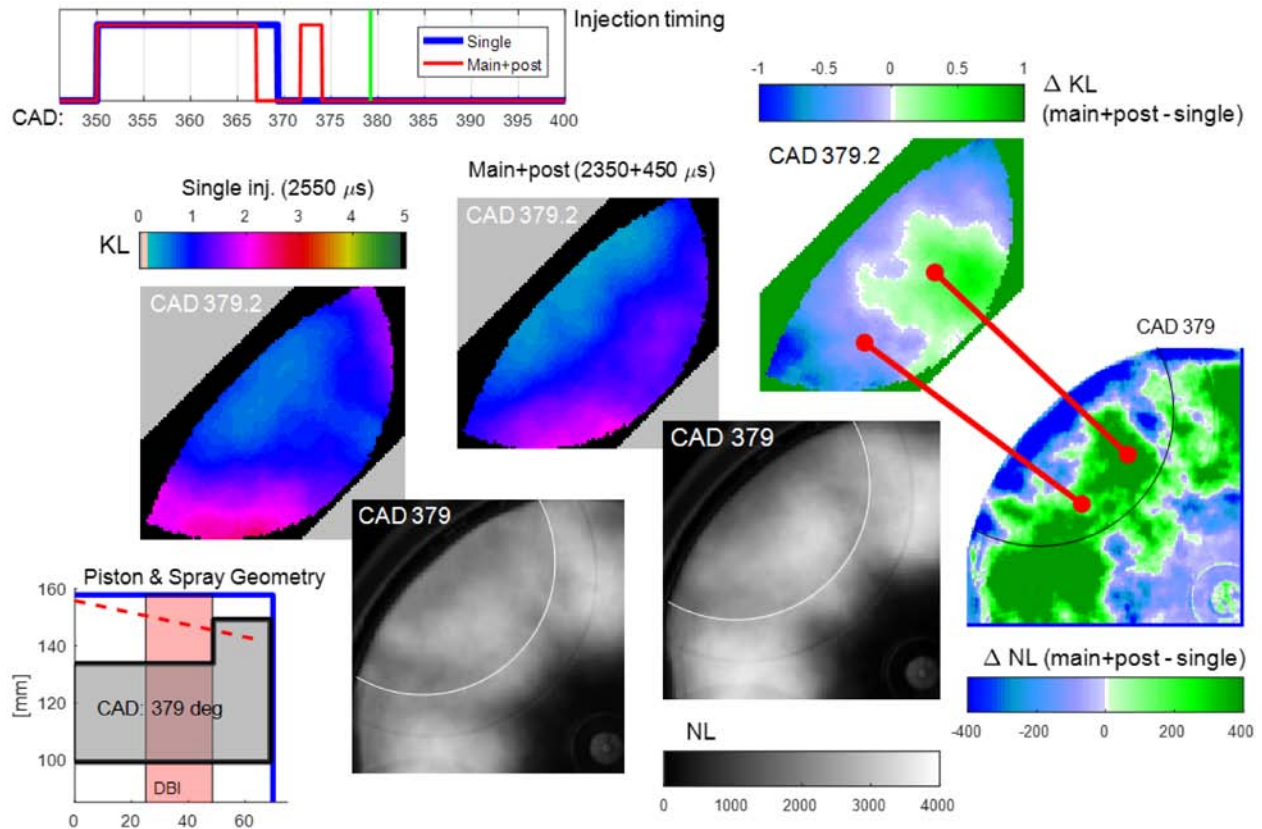


Figure I.2.5 - Composite graphic showing injector solenoid energizing schedule (top left), in-cylinder geometry (bottom left), soot KL measured by ensemble-averaged DBI (top row of images) and ensemble-averaged soot NL (bottom row of images). Each KL and NL row shows images with the single injection only (left), a load-equivalent schedule with a post-injection (middle) and a false-colored image of the difference in between the post- and single-injection images. The red dots and lines identify regions that are discussed in the text.

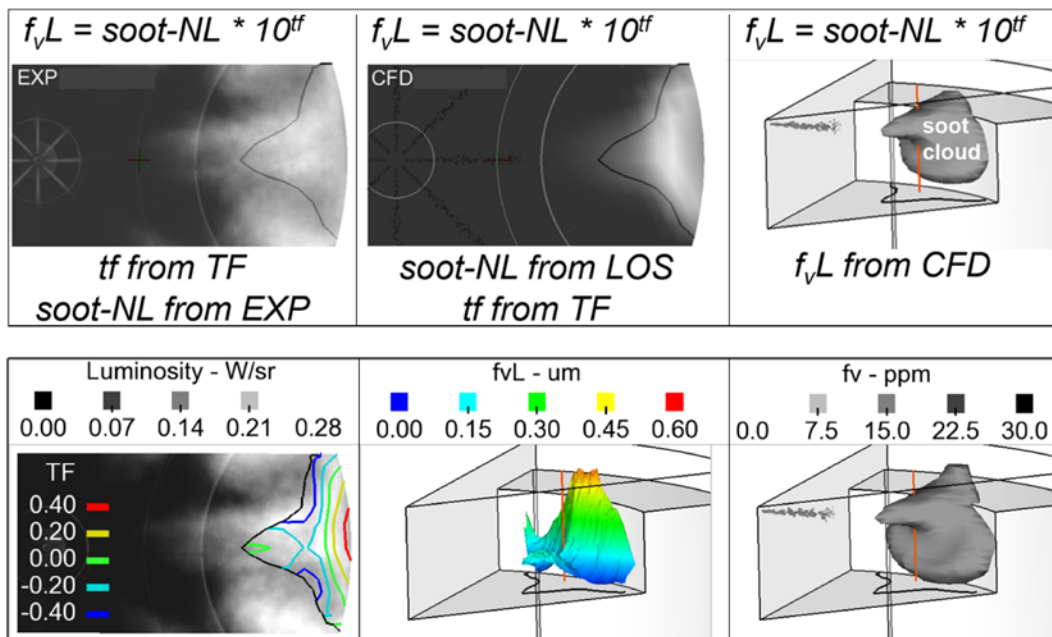


Figure I.2.6 - Top row: measured 2D NL image (left), predicted 2D NL image (right), predicted three-dimensional (3D) soot distribution (right). Bottom row: transfer function map overlaid on measured NL (left), estimated experimental f_vL (middle) and predicted 3D f_v distribution.

NL image (left) with a predicted 2D NL image (middle), which is based on the predicted 3D soot distribution (right). The equation at the top of Figure I.2.6 shows how the soot volume-fraction-path-length product ($f_v L$), which is related to KL , can be converted to NL using a base-ten transfer function with a variable exponent (tf). The bottom row shows that a static transfer function map overlaid on the experimental image (left) can be applied to estimate the $f_v L$ (middle), which agrees well with the simulation predictions (right).

Conclusions

- New combined DBI and NL imaging technique shows first clear evidence of post-injection soot reduction by increased local temperatures, strengthening suggestions from 2014 soot planar laser-induced incandescence and OH planar laser-induced fluorescence imaging data [3].
- Quantitative soot DBI imaging shows late-cycle reduction of soot in post-jet, consistent with increased mixing from a second entrainment wave, a new fluid-mechanic effect that was described in 2008 [2].
- Soot volume fraction ($f_v L$) to NL transfer function was developed to aid interpretation of NL images.

References

1. O'Connor J, MPB Musculus. "Post injections for soot reduction in diesel engines: a review of current understanding." *SAE Int. J. Engines* 6(1):400-421 (2013).
2. Musculus, MPB. "Heavy-duty low-temperature and diesel combustion & heavy-duty combustion modeling." FY 2014 DOE Hydrogen & Fuel Cells Program and Vehicle Technologies Program Annual Merit Review and Peer Evaluation Meeting, Advanced Combustion Engine R&D/Combustion Research, 2014.
3. Musculus, MPB. "Heavy-duty low-temperature and diesel combustion & heavy-duty combustion modeling." FY 2008 DOE Hydrogen & Fuel Cells Program and Vehicle Technologies Program Annual Merit Review and Peer Evaluation Meeting, Advanced Combustion Engine R&D/Combustion Research, 2008.

Key Fiscal Year 2017 Publications

1. Malbec, L.-M., W.E. Eagle, M.P.B. Musculus, and P. Schihl. "Influence of injection duration and ambient temperature on the ignition delay in a 2.34L optical diesel engine." *SAE Int. J. Engines* 9:47–70, April 2016.
2. Eagle, W.E., L-M. Malbec, and M.P.B. Musculus. "Measurements of liquid length, vapor penetration, ignition delay, and flame lift-off length for the Engine Combustion Network 'Spray~B' in a 2.34L Optical Heavy-Duty Diesel Engine." *SAE Int. J. Engines* 9:910–931, June 2016.
3. Eagle, W.E., M.P.B. Musculus, L.-M.C. Malbec, and G. Bruneaux. "An improved entrainment rate measurement method for transient jets from 10kHz particle image velocimetry." Accepted to *Atomization and Sprays*, July 2016.
4. O'Connor, J., M. Musculus, and L. Pickett. "Effect of post injections on mixture preparation and unburned hydrocarbon emissions in a heavy-duty diesel engine." *Combustion and Flame* 170:111–123, August 2016.
5. Eagle, W.E., M.P.B. Musculus. "Optical imaging to understand fuel reactivity effects on RCCI combustion." AEC Meeting, Detroit, MI, August 2016.
6. Roberts, G., M.P.B. Musculus. "On using diffuse back-illuminated imaging for soot extinction measurements within an optically accessible heavy-duty diesel engine." AEC Meeting, Detroit, MI, August 2016.
7. "Recent research toward the co-optimization of fuels and engines." FISITA 2016 World Automotive Congress, Busan, South Korea, September 2016.

8. "Infrared emission detection as a fuel-vapor penetration diagnostic." Thiesel Conference poster, Valencia, Spain, September 2016.
9. Musculus, M.P.B. "The co-optimization of fuels and engines: chemical kinetics and optical research." Lund University, Sweden, October 2016.
10. Roberts, G., M.P.B. Musculus. "Quantitative assessment of in-cylinder soot reduction mechanisms of post injections." AEC Meeting, USCAR, Southfield, MI, January 2017.
11. Musculus, M.P.B. "The in-cylinder intersection of thermofluids and chemistry as revealed by optical diagnostics." Thermal and Fluid Sciences Functional Excellence (TSFE) Conference, Cummins Tech Center, Columbus, IN, April 4, 2017.
12. Hessel, R.P, Z. Yue, R.D. Reitz, M.P.B. Musculus, J.A. O'Connor. "Guidelines for interpreting soot luminosity imaging." *SAE Int. J. Engines* 10(3), 2017.
13. Eagle, W.E., G. Roberts, M.P.B. Musculus, L.-M. Malbec, L. Sequino, and E. Mancaruso. "Comparing infrared emission from hydrocarbon C-H stretch during direct injection with and without reaction in an optical heavy duty engine." 10th U. S. National Combustion Meeting, College Park, MD, April 23–26, 2017.

I.3 Spray Combustion Cross-Cut Engine Research

Lyle M. Pickett, Principal Investigator

Sandia National Laboratories
 PO Box 969, MS 9053
 Livermore, CA 94551-9053
 E-mail: Impicke@sandia.gov

Michael Weismiller, DOE Technology Manager

U.S. Department of Energy
 E-mail: Michael.Weismiller@ee.doe.gov

Start Date: October 1, 2016	End Date: September 30, 2017	
Total Project Cost: \$950,000	DOE share: \$950,000	Non-DOE share: \$0

Acknowledgments

Co-Author

Scott A. Skeen, Sandia National Laboratories

Project Introduction

All future high-efficiency engines will have fuel directly sprayed into the engine cylinder. Engine developers agree that a major barrier to the rapid development and design of these high-efficiency, clean engines is the lack of accurate fuel spray computational fluid dynamic (CFD) models. The spray injection process largely determines the fuel–air mixture processes in the engine, which subsequently drives combustion and emissions in both direct injection gasoline and diesel systems. More predictive spray combustion models will enable rapid design and optimization of future high-efficiency engines, providing more affordable vehicles and also saving fuel.

Objectives

- Facilitate improvement of engine spray combustion modeling, accelerating the development of cleaner, more efficient engines
- Lead a multi-institution, international, research effort on engine spray combustion called the Engine Combustion Network (ECN), with focus on diesel and gasoline sprays and conduct ECN5
- Establish and optimize a rigorous standardized method for application of high-speed diffused back-illumination extinction imaging (DBIEI) diagnostic used to characterize liquid penetration and soot formation/oxidation in sprays
- Characterize and compare spray penetration, spray width, ignition delay, and lift-off length in sprays from heavy-duty cavitating and non-cavitating injectors
- Develop high-speed (100 kHz) Rayleigh scattering diagnostic to quantify mixture fraction in diesel sprays

Approach

To accelerate the progression of predictive CFD modeling capabilities and leverage the expertise of the global spray research community, a multi-institution collaboration called the Engine Combustion Network has been established. By providing highly vetted, quantitative datasets available online [1], CFD models may be evaluated more critically and in a manner that has not happened to date. Productive CFD evaluation requires new experimental data for the spray and the relevant boundary conditions, but it also includes a working methodology to evaluate the capabilities of current modeling practices. Activities include the gathering of experimental and modeling results at target conditions to allow a side-by-side comparison and expert review

of the current state of the art for diagnostics and engine modeling. Significant progress has been made for both diesel and gasoline injection systems.

Results

For brevity, only a few of the key advancements from our experimental spray combustion facility are highlighted. A more complete summary of this year's work is found in the ECN proceedings [1] and recent publications on these topics [2,3,4]. A major component of the annual effort includes organizing monthly web meetings for the ECN, developing plans for upcoming workshops, and leading/guiding the exchange between experimentalists and modelers to identify the state of art in spray combustion modeling and remedy known weaknesses for both gasoline and diesel targets. Efforts in Fiscal Year 2017 also included enhancements to the ECN website and data archive and organizing and conducting ECN5 at Wayne State University in Detroit, Michigan. Other key accomplishments are listed and described in more detail below.

- Developed optical theory leading to optimization of a DBIEI diagnostic used to quantify liquid penetration and soot formation/oxidation processes in sprays; published theory and standardized procedure for dimensioning and implementing the diagnostic
- Applied high-speed (100 kHz) Sandia-developed pulsed burst laser to measure temporally resolved mixture fraction of diesel sprays using Rayleigh scattering
- Quantified spray spreading angle, liquid penetration, ignition, and combustion behavior of diesel Spray C (cavitation) and Spray D injectors

The properties of a fuel spray (e.g., liquid phase penetration, atomization, air entrainment, and mixture formation) govern the combustion process (ignition, lift-off, pollutant formation) as they occur on a longer time scale than the chemical reactions taking place. In direct injection diesel engines these properties influence the engine performance and emission profiles. Furthering the understanding of nozzle design parameter effects on spray characteristics is essential in the development of predictive mathematical models used in the design and optimization of high-efficiency, low emission engines. Collaborative efforts within the ECN to better understand and improve CFD models are accelerated by standardized diagnostics that can be applied by the many participating institutions with relative ease. A popular diagnostic used among ECN participants to measure liquid penetration and soot formation/oxidation involves high-speed imaging of light attenuation by either the liquid spray or the soot particles formed during combustion. Perceived attenuation due to beam steering induces significant error in such measurements and is exacerbated at engine-relevant pressures. Artifacts due to beam steering can be eliminated by using a specialized illumination source and specifically designed collection optics. Prior to this year, an optimized standard method for this diagnostic had not been established and results varied considerably across institutions within the ECN.

Using commercial ray-tracing software combined with optical measurements, an optimized DBIEI diagnostic was developed. The optical theory describing its effectiveness at eliminating errors due to beam steering in high-pressure systems were published along with details for selecting optical components for its general application. Optimal illumination was achieved with a light-emitting diode (LED) driven by a Sandia-developed R&D 100 award winning LED pulser along with a large-area Fresnel lens and a custom large-area engineered diffuser. The drastic improvement to the performance of the diagnostic is illustrated in Figure I.3.1, which shows images from the original implementation of DBIEI (top panel) and the optimized setup (bottom panel). In these images, the injector is located on the left side of the image and the spray is penetrating left to right. The darkest regions on the right side of the image represent light attenuation or "extinction" by soot particles. The multitude of light and dark features throughout the left image are caused by refractive index gradients within the combusting spray. To accurately measure the quantity of soot in the spray flame as it relates to the attenuated light, these artifacts must be minimized. As can be seen, the bottom panel of Figure I.3.1 is characterized by a uniform intensity distribution outside of the region where soot particles exist and therefore provides a more accurate measurement of the instantaneous quantity of soot present in the spray flame.

Optimized fuel–air mixing is key to the development of cleaner and more efficient diesel combustion. Quantitative, temporally resolved measurements of the diesel fuel mixture field are needed to fully understand

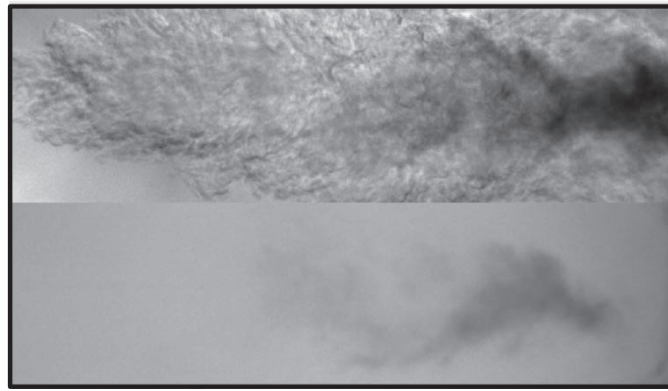


Figure I.3.1 - Example DBIEI images using the original setup (top) and optimized setup (bottom). The light and dark regions in the top image are caused by beam steering and introduce significant error when attempting to quantify soot or liquid penetration in high-pressure sprays.

the dynamics of spray vaporization and mixing, while quantitative measurements of the soot field evolution provide insight into the coupling between mixing and pollutant formation. A new light source developed at Sandia National Laboratories has enabled unprecedented measurements that allow accurate determination of time-resolved vapor-phase mixing.

A one-of-a-kind, high-power 100 kHz pulse-burst laser provides the higher photon energies necessary to quantify the fuel–air equivalence ratio field based on inducing Rayleigh scattering from the fuel molecules. Time-resolved images of the mixture field allow extraction of turbulent spatiotemporal correlations (structure functions), which are critical for constructing improved models applicable to the highly transient environment created by modern multiple injection schedules. Together with the detailed measurements of liquid characteristics and soot (see Figure I.3.2), the link between sprays, vapor mixing, and soot processes are illuminated and critical features that combustion models must capture are identified.

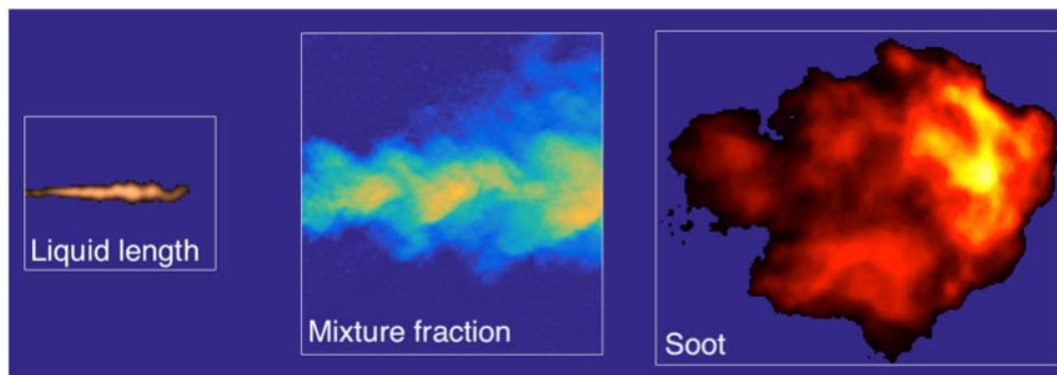


Figure I.3.2 - A collage of images demonstrating three high-speed, quantitative diagnostics. The liquid length and soot images were obtained using a Sandia-developed LED driver that generates unprecedented light intensity at high repetition rates, while the mixture fraction field used a newly developed 100-kHz pulse-burst laser. The mixture fraction and soot images correspond to the same time after start of injection (1.8 ms after start of injection) for 1,500 bar n-dodecane sprays injected into a 900 K, 60 bar ambient. All images are to scale.

While much of the past research of the ECN has dealt with small orifice, light-duty fuel injectors, there is a strong push to investigate the characteristics of heavy-duty injectors. The ECN prepared a set of heavy-duty injectors with different orifice profiles in which one is designed to induce cavitation (straight hole, Spray C) and the other is designed to resist cavitation (converging hole, Spray D). A series of diagnostics were applied to quantify the fuel spray penetration, evaporation, ignition, combustion, and lift-off length stabilization.

Ensemble-averaged and instantaneous, single-injection, liquid-phase measurements of Spray D (non-cavitating) and Spray C (cavitating) are shown in Figure I.3.3. The images are superimposed with false color

in order to enhance the differences in spray structure between the cavitating and non-cavitating nozzle. The overlaid images show that Spray C (green) has a shorter penetration length, appears wider, and that the liquid boundary displays larger radial fluctuations in the near-nozzle region compared to Spray D (magenta). High-speed movies of these injection events are also available on the ECN website [1].

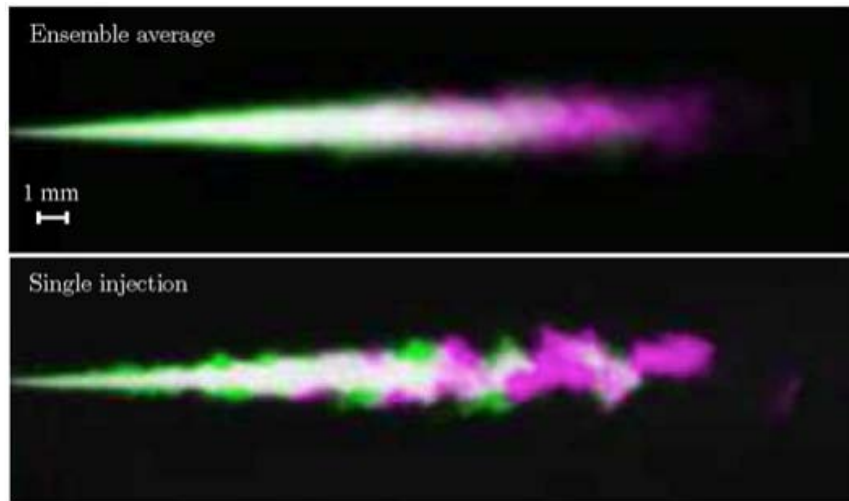


Figure I.3.3 - Instantaneous ensemble-averaged (top) and single-injection (bottom) liquid phase images, 2.5 ms after start of injection of Spray D (magenta) and Spray C (green) at standard non-reacting conditions. Measurements have been superimposed and distinguished using false color. The white region depicts where Spray D and Spray C overlap.

Further analysis confirmed that the shorter liquid length associated with Spray C is attributable to its larger near-nozzle spreading angle, even after considering differences in nozzle flow coefficients. While longer liquid penetration is expected for Spray D, a spray that emerges with a small spreading angle that gradually increases with axial position is needed to correctly mimic the axial and radial development and magnitude of the liquid penetration when applying a simple jet model [5] compared to the experiment. These findings suggest that the changes in near-field spreading angle are a critical element, more significant than the nozzle flow coefficient differences, affecting the mixing and liquid evaporation within the sprays. A key observation is that although Spray C begins with a wider spreading angle, after a characteristic distance of 3–4 mm (referred to as the similarity offset [SO]) the far-field spreading angles of Sprays C and D showed strong similarities. Vapor penetration rates in Figure I.3.4 show that Spray D penetrates slightly faster than Spray C, which is attributed to the higher momentum of Spray D and smaller near-field spreading angle. Though not shown, a faster

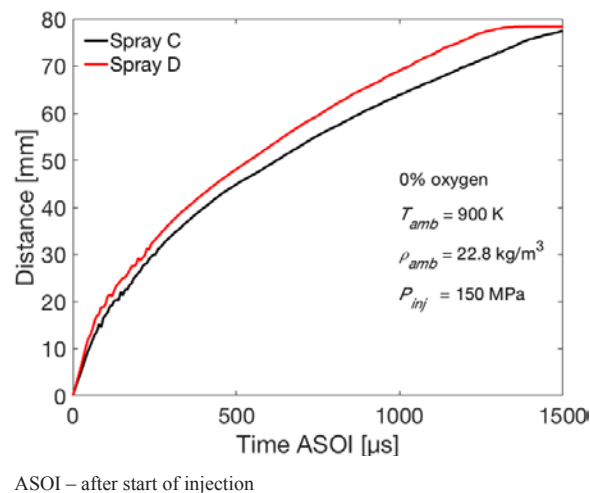


Figure I.3.4 - Ensemble averaged reacting and non-reacting vapor penetration rate for Sprays D and C with error bars indicated. The nominal ambient conditions are stated in the figure.

penetration is maintained when comparing reacting Spray D to Spray C, with each reacting jet penetrating slightly faster after ignition than its non-reacting counterpart due to effects of thermal expansion.

It is revealing to examine ignition timings and flame stabilization locations in light of the different spray penetration characteristics for the two injectors. Scatter plots of the mean lift-off length during the quasi-steady period of injection for flames with Sprays C and D are presented in the left panel of Figure I.3.5 with inset axes in the top and middle panels providing the mean and standard error (SE) of the mean for select cases. In the top panel inset axes, for ambient temperatures of 850 K and above, the mean experimental temperature of Sprays C and D runs is within about 10 K and the lift-off length for Spray C flames is consistently between 2–4 mm shorter than that of Spray D. A similar result is observed as a function of ambient density with the exception of the 7.6 kg/m³ ambient density case. At this low density, ignition and flame stabilization occur at the vessel wall potentially masking nozzle-shape effects. It is also interesting to note that the lift-off length scales quadratically with increasing injection pressure for both nozzles, which is consistent with the linear velocity scaling observed by Siebers and Higgins [6]. Over the various parametric variations, the 2–4 mm difference in lift-off length is very close to the difference in SO position identified for non-reacting conditions (~3 mm). Indeed, the difference in quasi-steady lift-off lengths between Spray C and Spray D appears invariant to ambient temperature, ambient density, and injection pressure. Thus, there appears to be a fundamental change in the mixing field and lift-off stabilization between the two nozzles at a given operating condition. Were the injector nozzles identical in design with the exception of orifice diameter, one would expect the liquid length to scale linearly with the orifice diameter and the lift-off length to scale linearly with the injection velocity, which scales inversely with the square of orifice diameter.

Scatter plots of ignition delay as a function of ambient temperature and ambient density are presented in the right panel of Figure I.3.5 with inset axes providing the mean and SE of the mean for select cases. As expected, ignition delay decreases with increasing ambient temperature, density, and injection pressure. In general, the

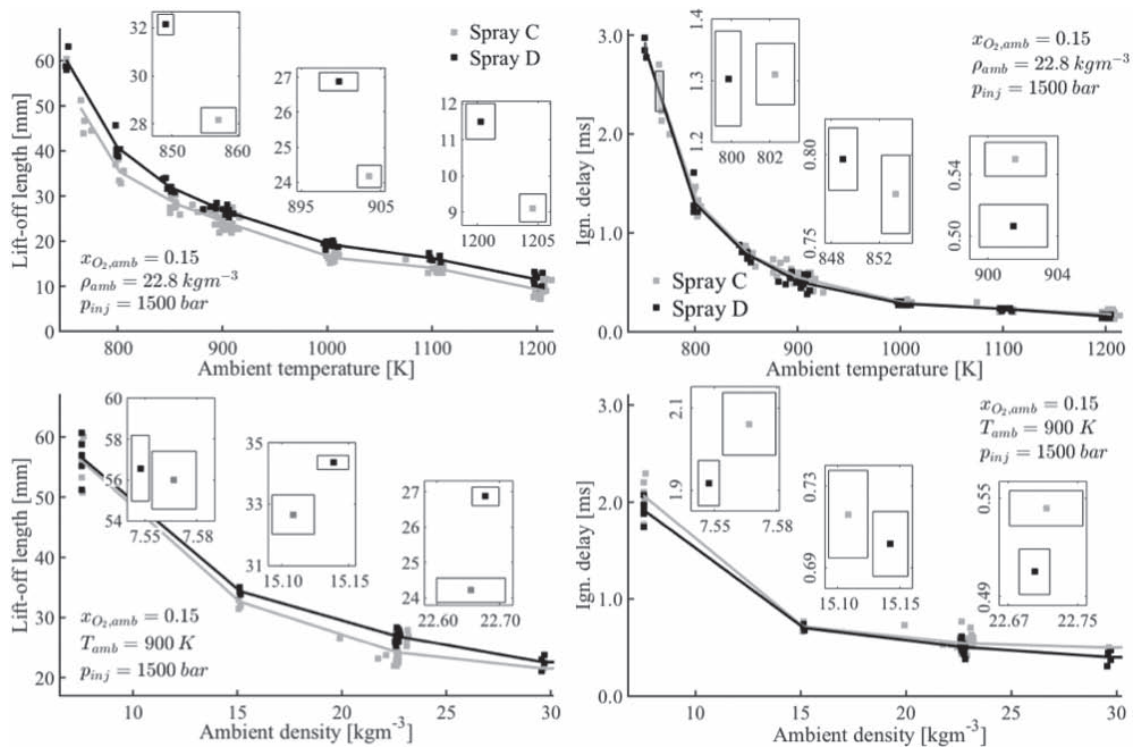


Figure I.3.5 - Scatter plots of the quasi-steady lift-off length (left) and ignition delay time (right) as a function of ambient temperature (top) and ambient density (bottom). The grey markers represent the Spray C data and the black markers represent the Spray D data. Because the SE cannot be resolved in the full axis, inset axes are provided in the top and middle panels with the mean values and the SE for select cases. The width of the boxed region indicates the error in the X-variable while the height indicates the error in the Y-variable.

ignition delays for the two different injectors are within 30 μs of each other with some evidence of a trend toward shorter ignition delays for the non-cavitating (Spray D) nozzle.

Conclusions

Using an optimized illumination setup with a custom large-area engineered diffuser and appropriately dimensioned collection optics, error in imaging extinction measurements due to beam steering induced perceived attenuation can be eliminated. Guidance to the broader spray research community was provided in a publication, which describes the theory and practical information necessary to implement the diagnostic as a standard tool for ECN research. A Sandia-developed high-speed pulse/burst laser was applied to acquire first-of-a-kind time-resolved mixture fraction measurements using Rayleigh scattering. Time-resolved images of the mixture field yield turbulent spatiotemporal correlations (structure functions), which are critical for constructing improved models applicable to the highly transient environment created by modern multiple-injection schedules used in modern direct injection engines. Liquid and vapor penetration measurements for two heavy-duty, single-hole injectors with different cavitation behavior demonstrated similarity in vapor width downstream of a characteristic offset distance. The characteristic offset distance appeared again when comparing the quasi-steady lift-off lengths of the two sprays. These findings suggest that the changes in near-field spreading angle are a critical element, more significant than the nozzle flow coefficient differences, affecting the mixing and liquid evaporation within the sprays.

References

1. Pickett, L.M. "Engine Combustion Network." 2017. <https://ecn.sandia.gov>
2. Westlye, F.R., S.A. Skeen, et al. "Penetration and combustion characterization of cavitating and non-cavitating fuel injectors." SAE Technical Paper 2016-01-0860, 2016. DOI: 10.4271/2016-01-0860.
3. Manin, J., L.M. Pickett, S.A. Skeen, and J.H. Frank. "Time-resolved measurements of mixing quantities in diesel jets." COMODIA 2017.
4. Westlye, F.R., K. Penney, S.A. Skeen, et al. "Diffused back-illumination setup for high temporally resolved extinction imaging." *Applied Optics* 56(17):5028–5038. 2017.
5. Musculus, M.P.B., K. and Kattke. "Entrainment waves in diesel jets." *SAE Int.J.Engines* 2, no. 1:1170–1193. 2009.
6. Siebers, D.L., and B. Higgins. "Flame Lift-off on Direct-Injection Diesel Sprays Under Quiescent Conditions." SAE Technical paper 2001-01-0530. 2001.

Key Fiscal Year 2017 Publications

1. Skeen, S.A., and K. Yasutomi. "Measuring the soot onset temperature in high-pressure n-dodecane spray pyrolysis." *Combustion and Flame* 188:483–487. 2017.
2. Mueller, C., C.W. Nilsen, D.J. Ruth, R.K. Gehmlich, L.M. Pickett, and S.A. Skeen. "Ducted fuel injection: A new approach for lowering soot emissions from direct-injection engines." *Applied Energy* 204:206–220. 2017.
3. Duke, D.J., A.L. Kastengren, S.A. Skeen, et al. "Internal near nozzle measurements of Engine Combustion Network 'Spray G' gasoline direct injectors." *Experimental Thermal and Fluid Science* 88:608–621. 2017.
4. Sphicas, P., L.M. Pickett, S.A. Skeen, and J.H. Frank. "Inter-plume aerodynamics for gasoline spray collapse." *International Journal of Engine Research*, 2017. (in print)
5. Manin, J., L.M. Pickett, S.A. Skeen, and J.H. Frank. "Time-resolved measurements of mixing quantities in diesel jets." COMODIA 2017.

6. Westlye, F.R., K. Penney, S.A. Skeen, et al. “Diffused back-illumination setup for high temporally resolved extinction imaging.” *Applied Optics* 56(17):5028–5038. 2017.
7. Sphicas, P., L.M. Pickett, S.A. Skeen, J. Frank, et al. “A comparison of experimental and modeled velocity in gasoline direct-injection sprays with plume interaction and collapse.” *SAE Int. J. Fuels Lubr.* 10(1):184–201. 2017. DOI: 10.4271/2017-01-0837

I.4 Low-Temperature Gasoline Combustion (LTGC) Engine Research

John E. Dec, Principal Investigator

Sandia National Laboratories
MS 9053, P.O. Box 969
Livermore, CA 94550
E-mail: jedec@sandia.gov

Michael Weismiller, DOE Technology Manager

U.S. Department of Energy
E-mail: Michael.Weismiller@ee.doe.gov

Start Date: October 1, 2016	End Date: September 30, 2017	
Total Project Cost: \$665,000	DOE share: \$665,000	Non-DOE share: \$0

Project Introduction

Improving the efficiency of internal combustion engines is critical for meeting global needs to reduce petroleum consumption and CO₂ emissions. Low temperature gasoline combustion (LTGC) engines (including homogeneous charge compression ignition [HCCI]) have a strong potential for contributing to these goals since their thermal efficiencies meet or exceed those of diesel engines. They also have very low NO_x and particulate emissions. LTGC can be applied either as a full-time operating strategy or for light-duty (LD) engines, as part of a multi-mode combustion strategy where the engine operates in LTGC mode at low and intermediate loads and switches to conventional spark ignition (SI) at high loads. This multi-mode approach provides high efficiencies at low and intermediate loads where LD engines operate most of the time and maintains high power density by switching to SI for high loads. Full-time LTGC provides high efficiencies at all loads as required for medium- and heavy-duty (MD/HD) applications, and recent research has shown that LTGC can reach similar high loads to turbocharged diesel engines with similar intake-boost levels [1]. LTGC engines are potentially lower cost than diesels and by providing MD/HD engines that use gasoline with high efficiency, LTGC could help balance the demand for gasoline and diesel fuel, a problem that is expected to worsen if only conventional technologies are used. In all applications, LTGC allows gasoline to be used with high efficiency for more effective use of crude oil supplies and lower overall CO₂ production.

Substantial progress has been made in understanding LTGC and extending its operating range; however, rapid control of combustion phasing remains a key technical barrier to the commercialization of LTGC engines. To address this challenge, investigations of two control techniques initiated last year have been substantially expanded. The first method is based on using changes in fuel injection timing to vary the fuel distribution within the charge and thereby adjust the reactivity of the charge mixture to control combustion phasing. More specifically, a double direct injection is used in which the second injection timing and fuel fraction are adjusted to vary the amount of partial fuel stratification (DDI-PFS) to change the charge reactivity. The second method, spark-assist (SA), uses a spark plug to create a weak flame (weak due to high charge dilution) that burns a small fraction of the total charge, but drives the main charge into autoignition at the desired time. Results of other, smaller-scale studies are also presented, including determining brake thermal efficiencies, an uncertainty quantification analysis, and chemical-kinetic model validation and improvement.

Objectives

Overall Objective

Sandia National Laboratories is providing the fundamental understanding (science-base) required to overcome the technical barriers to the development of practical LTGC engines for LD and MD/HD applications.

Fiscal Year (FY) 2017 Objectives

- Quantify the crank-angle range over which the 50% burn point (CA50) can be controlled for LTGC engines using double-pulse fuel injection strategies (DDI-PFS) for intake pressures from 1.0–2.0 bar and compression ratios (CRs) of 14:1 and 16:1
- Determine the range of intake pressures, temperatures, and equivalence ratios (ϕ) for which SA can provide CA50 control for well-premixed LTGC
- Quantify the range of CA50 control possible with SA at the various conditions studied
- Compute brake thermal efficiencies for a range of LTGC engine speeds and loads, and work with Argonne National Laboratory to determine potential vehicle fuel economy improvement for a particular operating mode of interest, as requested by DOE Vehicle Technologies Office
- Conduct an uncertainty quantification (UQ) analysis in collaboration with Lawrence Livermore National Laboratory (LLNL)
- Support chemical–kinetics model development at LLNL

Approach

Experimental studies were conducted in the Sandia LTGC Engine Laboratory using the all-metal single-cylinder LTGC research engine (displacement = 0.98 L). This facility allows operation over a wide range of conditions and it has been designed to provide precise control of virtually all operating parameters, allowing well-characterized experiments. This LTGC research engine was derived from a Cummins B-series diesel. The cylinder head has been modified to accommodate a spark plug (with assistance from Cummins) and the diesel piston was replaced with one of two LTGC pistons that have open combustion chambers with broad, shallow bowls to give CRs of 16:1 and 14:1. The engine was equipped with a centrally located gasoline-type direct injector capable of 300 bar injection pressures and a high-energy SI system, both supplied by General Motors. A representative regular grade E10 gasoline was used for all studies.

For CA50 control with DDI-PFS, the amount of fuel stratification was varied systematically by changing the second DI timing for intake pressures (P_{in}) from 1.0 to ≥ 2.0 bar absolute for CRs of both 14:1 and 16:1. In addition to determining the changes in CA50, the ringing intensity and combustion noise levels [2,3] were monitored. For studies of SA, P_{in} , T_{in} , and ϕ were systematically varied for premixed operation to map out the flame combustion limits and the potential for SA to control CA50 and to compensate for changes in initial charge temperature or exhaust gas recirculation (EGR) levels, data that is currently missing from the literature [4].

Brake thermal efficiencies were computed from net indicated thermal efficiencies using models supplied by General Motors to account for friction and turbocharger losses. Through a collaboration with Argonne National Laboratory, these data were used to determine the potential of LTGC for a vehicle application requested by DOE Vehicle Technologies Office. Collaborations with LLNL were established to conduct a UQ analysis of in-cylinder pressure data [5], and to develop and validate an improved chemical–kinetic mechanism for the regular E10 gasoline used for the experimental studies.

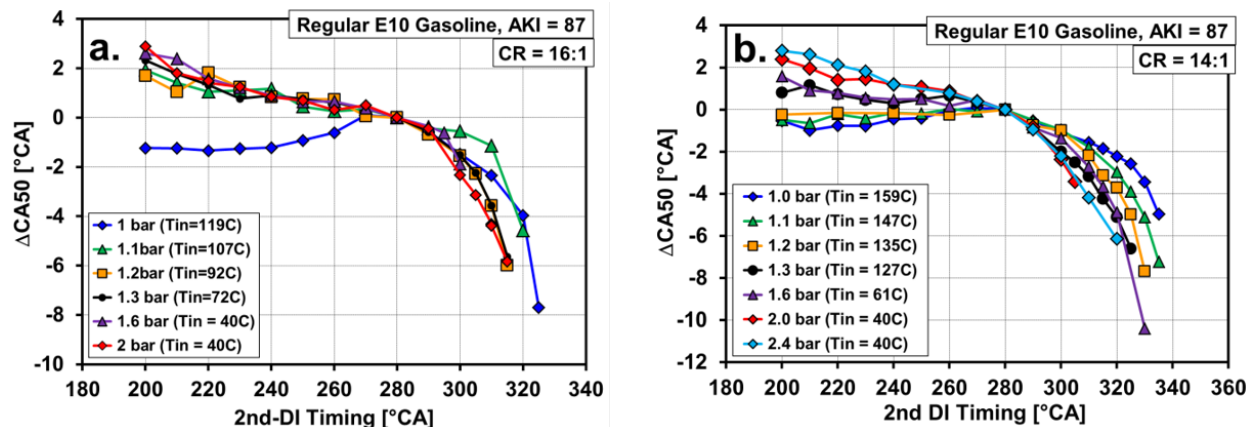
Results

Previous studies have shown that the autoignition reactivity of gasoline can be sensitive to the local equivalence ratio (ϕ -sensitive) under some conditions, particularly those using intake boost. For fuels exhibiting this behavior, richer regions autoignite faster than leaner regions, so partially stratifying the fuel distribution with a late fuel injection that does not mix completely can advance the combustion phasing, as measured by CA50. At the same time, it is critical to maintain sufficient homogeneity to avoid regions with $\phi > \sim 0.7$ that can make NO_x [6] or significantly over-rich regions that produce soot. To achieve CA50 control without high NO_x emissions, a technique called partial fuel stratification (PFS) was used, in which the majority of the fuel is supplied by an early direct injection (60° crank angle [CA] into the intake stroke) so that it is

fairly well mixed, and the remainder of the fuel is injected at various times during the compression stroke to provide a variable amount of stratification to control CA50.

A preliminary test of this DDI-PFS technique conducted last year showed that DDI-PFS worked well at a relatively high-boost condition ($P_{in} = 2.0$ bar absolute) with a CR = 16:1, for which the fuel is quite ϕ -sensitive. For practical applications, DDI-PFS must provide CA50 control at lower boost pressures, preferably down to naturally aspirated intake conditions ($P_{in} = 1.0$ bar). Accordingly, a series of studies were conducted during Fiscal Year 2017 to determine the ability of DDI-PFS to control CA50 at lower intake pressures and to determine the effect of reducing the CR from 16:1 to 14:1 because this lower CR has advantages for LTGC operation in some applications.

Figure I.4.1a shows the ability of DDI-PFS to control CA50 for a range of intake pressures from 1.0–2.0 bar absolute for CR = 16:1. For these data, 80% of the fuel was injected early in the intake stroke, and 20% was injected at various times during the compression stroke to vary the amount of PFS. Note that for all crank angles given in this report, $0^\circ\text{CA} = \text{top dead center (TDC) intake}$. For each P_{in} , the second DI timing sweep begins early in the compression stroke at 200°CA , which produces minimal stratification. At this timing, T_{in} or the amount of EGR was adjusted to retard CA50 as much as possible while maintaining acceptable stability (defined as the coefficient of variation in indicated mean effective pressure $\leq 3\%$). The second DI timing was then progressively retarded to increase the amount of stratification, which increases the ϕ of the richest regions making the charge autoignite faster, advancing CA50. The curves in Figure I.4.1a are quite similar for $P_{in} = 1.2$ –2.0 bar. Stratification initially increases slowly, with CA50 advancing only about 2°CA as the second DI timing is swept from 200°CA to 280°CA . Then, as the second DI timing is retarded beyond 280°CA , stratification increases more rapidly with CA50 advancing approximately another 6°CA as the second DI timing is retarded to 315°CA . For $P_{in} = 1.1$ bar, the CA50 control curve is also similar, except that the second DI timing must be more retarded to about 310°CA before CA50 begins to advance rapidly, presumably because the ϕ -sensitivity is less at this lower P_{in} , so more stratification is required. At $P_{in} = 1.0$ bar, the changes in stratification have little effect until the second DI timing is retarded to 270°CA , but for timings from 270 – 325°CA , CA50 advances about 8°CA , providing essentially the same amount of CA50 control authority as for the higher P_{in} s.



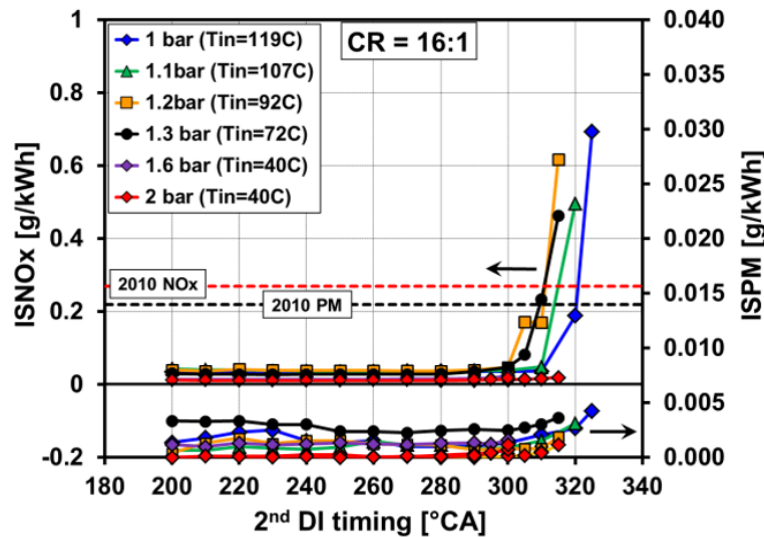
AKI – anti-knock index

Figure I.4.1 - CA50 control using DDI-PFS to vary charge reactivity for a wide range of intake pressures for (a) CR = 16:1 and (b) CR = 14:1. The curves have been offset to align the CA50s for a second DI timing of 280°CA . $0^\circ\text{CA} = \text{TDC intake}$. $\phi_m = 0.36$, except for $P_{in} = 2.0$ bar with CR = 16:1 where $\phi_m = 0.4$. 1,200 rpm. All P_{in} s are absolute.

DDI-PFS was also found to work well for CR = 14:1, as shown in Figure I.4.1b. Compared to CR = 16:1, the main difference is that greater stratification (later second DI timing) is required to produce the more rapid advancement in CA50 for second DI timings $>280^\circ\text{CA}$. This difference is in agreement with the expected reduction in the fuel's ϕ -sensitivity due to the lower in-cylinder pressures with CR = 14:1 and the higher T_{in} s required to achieve autoignition with these lower pressures (see T_{in} values in the figure legends). Overall, the

results in Figure I.4.1 show that DDI-PFS provides about 8°CA of CA50 control authority for almost all P_{in} s tested for both CR = 14:1 and 16:1.

Soot and NO_x emissions corresponding to the CA50 control sweeps for CR = 16:1 in Figure I.4.1a are presented in Figure I.4.2. Soot (particulate matter [PM]) emissions remain extremely low for P_{in} s at all second DI timings and NO_x emission are also very low except for the latest DI timings at the lower P_{in} s ($P_{in} \leq 1.3$ bar). As shown in the figure legend, higher T_{in} s are required to achieve autoignition at these lower P_{in} s, and greater stratification is required for the lowest two P_{in} s. Both the higher T_{in} and increased stratification act to increase peak combustion temperatures, increasing NO_x . NO_x emissions are a little higher for CR=14:1 (not shown) because of the higher T_{in} s and increased stratification, as discussed above, so some NO_x aftertreatment may be required. However, it should be noted that the fuel distribution produced by the stratification in this proof-of-concept study has not been optimized, and it is very likely that with such optimization, NO_x could be reduced significantly, while still maintaining good CA50 control authority.



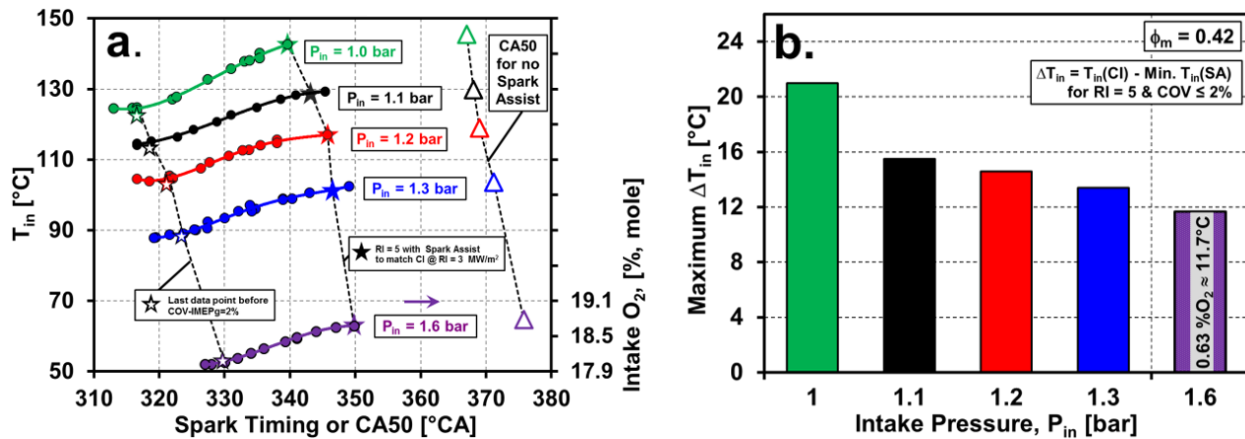
ISNO_x – indicated specific NO_x; ISPM – indicated specific PM

Figure I.4.2 - NO_x and PM measurements for the CA50 control sweeps in Figure I.4.1a. PM data are those provided by AVL smoke meter measurements.

SA is another potential technique for controlling LTGC combustion phasing, and several studies have been reported in the literature for various fuel blends, CRs, amounts of EGR/residuals, and amounts of charge stratification [4]. Lacking, however, are studies to determine the fundamental limits of SA, including the effects of ϕ , P_{in} , T_{in} , and EGR under well-characterized, dilute LTGC conditions. Because this information is central to all studies of SA-LTGC, a series of investigations has been conducted to determine these limits.

Figure I.4.3a shows the effect of increased boost pressure on the ability of SA to compensate for reductions in charge reactivity for a well-premixed charge with $\phi = 0.42$. For each P_{in} , stable LTGC engine operation was established with compression ignition (CI) only and a Ringing Intensity (RI) = 5 MW/m² [2] for high efficiency without knock, as shown by open-symbol points at the far right. As P_{in} increases from 1.0 bar to 1.6 bar, the fuel becomes more reactive and T_{in} must be reduced as shown. Also, the combustion phasing for CI-only has to be more retarded to maintain RI = 5 MW/m² due to the faster pressure rise rates with the increased charge density at higher P_{in} s. For $P_{in} = 1.6$ bar, the reactivity increases so much that in addition to reducing T_{in} to 60°C, the lowest value used for premixed fueling, EGR must be added as shown by the O₂ concentration on the right-hand axis. To evaluate the potential of SA, the charge reactivity for each P_{in} was reduced below that of the CI-only point by reducing T_{in} for $P_{in} = 1.0$ –1.3 bar or by adding more EGR (lower intake O₂) for $P_{in} = 1.6$ bar, and SA was applied to compensate for this reduced reactivity to maintain RI = 5 MW/m², i.e., to maintain a constant CA50. As shown, for each P_{in} , the spark timing had to be progressively advanced as the charge reactivity was reduced. This allows more time for flame propagation to compress the remaining charge into autoignition. As the spark timing is advanced further into the compression stroke, the charge temperature

is lower, making it more difficult to initiate a flame and reducing the flame speed once the flame is established. Eventually, these effects limit the ability of SA to compensate for the reduced reactivity and misfire cycles occur causing the coefficient of variation of the gross indicated mean effective pressure to suddenly increase well above 2%.



COV – coefficient of variation; IMEP – indicated mean effective pressure

Figure I.4.3 - (a) Spark timings required for SA to compensate for a reduction in T_{in} for $P_{in} = 1.0$ – 1.3 bar, or to compensate for a reduction in intake O_2 for $P_{in} = 1.6$ bar. (b) Maximum T_{in} reductions below the CI-only point (ΔT) for which combustion phasing (and RI) can be maintained using SA. CR = 14:1; $\phi_m = 0.42$; 1,200 rpm. 0°CA = TDC intake.

As can be seen, the curves in Figure I.4.3a have a similar appearance for all P_{in} s but a more careful examination shows that the ability of SA to compensate for T_{in} reductions (or equivalent O_2 reductions at $P_{in} = 1.6$ bar) diminishes with increased P_{in} . This is more obvious in Figure I.4.3b which shows the maximum reduction in T_{in} below the T_{in} for CI-only (ΔT) for which SA can maintain CA50 and RI. For $P_{in} = 1.6$ bar, the ΔO_2 has been scaled to an equivalent ΔT based on a separate series of measurements (not shown). As Figure I.4.3b shows, SA can compensate for the largest ΔT of 21°C at $P_{in} = 1.0$ bar (naturally aspirated). Increasing P_{in} from 1.0 bar to 1.1 bar causes the maximum ΔT for SA to drop from 21°C to 15.5°C, but further increases in P_{in} produce much smaller reductions in ΔT . These results show that SA has good potential for improving the robustness of LTGC by compensating for variations in T_{in} or EGR for P_{in} s from 1.0 bar to 1.6 bar.

The potential of SA to control CA50 was also examined for several combinations of P_{in} , ϕ , and T_{in} . Figure I.4.4 shows an example of the results at $P_{in} = 1.0$ bar for $\phi = 0.38, 0.42$, and 0.45 . For each ϕ , T_{in} was set so CI-only combustion was retarded to near the stability limit, then SA was applied to advance CA50 by an amount that varied with spark timing. As shown, varying the spark timing can sweep CA50 from retarded values that give low RIs = 1.0–1.5 MW/m² to advanced timings that give RIs >5 MW/m² (beyond the knock limit) for $\phi = 0.42$ and 0.45 . For $\phi = 0.38$, adjusting the spark timing could not advance CA50 earlier than 366°CA, which only increased the RI to 4 MW/m². This is thought to be a result of the very low flame speeds at this lower ϕ . Further advancing the spark beyond the timing that gives CA50 = 366°CA reduces the SA effect, causing CA50 to become more retarded again, as shown in the figure. Analysis shows that SA is most effective at $\phi = 0.42$, where it provides 6.9°CA of CA50 control authority compared to 5.4°CA for $\phi = 0.38$ and 5.9°CA for $\phi = 0.45$ if the $\phi = 0.45$ data are extrapolated out to the same RI limits as for the $\phi = 0.42$ data. The reduced effectiveness of SA at $\phi = 0.38$ is due primarily to the mixture being so dilute that it limits the ability of flame propagation to advance CA50 enough to obtain RIs >4 MW/m². Further reducing ϕ to 0.36 showed that SA had almost no effect on CA50, indicating that this is the lean limit for SA with a well-mixed charge. Thus, these data indicate that SA can control CA50 from strong knock (RI = 7 MW/m²) to near the stability limit for higher ϕ s (like 0.42 and 0.45), but its effectiveness diminishes as ϕ is reduced to 0.38 and essentially disappears when ϕ is reduced to 0.36.

Cylinder pressure measurements are used to determine many key parameters for evaluating the engine performance, e.g., indicated mean effective pressure, CA50, RI, and heat release rate. Because of the importance of these pressure measurements, a study was undertaken in collaboration with LLNL to evaluate their accuracy.

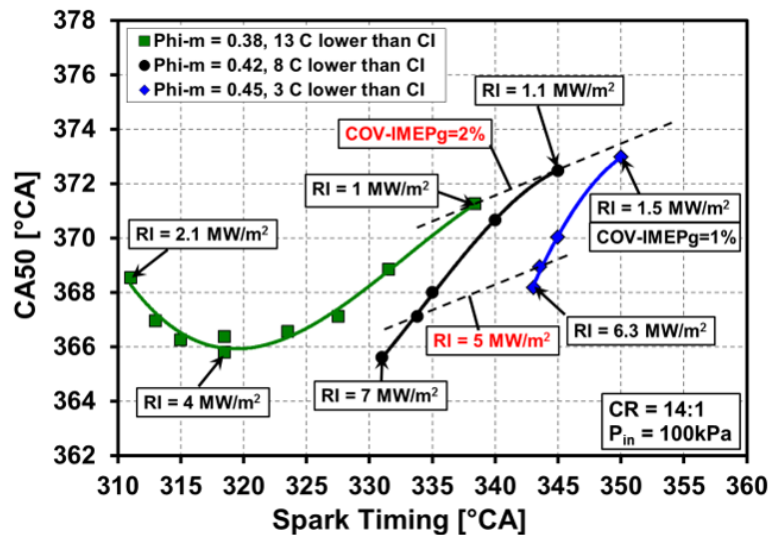


Figure I.4.4 - CA50 control authority with spark timing for $\phi = 0.38, 0.42,$ and 0.45 at $P_{in} = 1.0$ bar

These measurements involve the use of two pressure transducers: (1) a fast in-cylinder transducer that only gives relative pressures variations and (2) an intake pressure transducer that provides absolute pressure and is used to peg (i.e., to set) the in-cylinder transducer to an absolute value at a time in the cycle when the intake valve is open and the two pressures are in equilibrium. Several factors affect the uncertainty of the measurements for both transducers, such as their linearity, hysteresis, long-term stability, etc. The overall uncertainty of the pressure measurement is determined by combining the individual uncertainties due to these various factors for both transducers using an appropriate mathematical methodology. In the LTGC engine laboratory, good practices have been established to determine and minimize these uncertainties. For example, transducers are calibrated regularly using a National Institute of Standards and Technology-traceable dead weight tester eliminating uncertainties due to long-term drift, and providing linearity, hysteresis, and repeatability data for the actual transducers used. Figure I.4.5 shows the uncertainty of the measured cylinder pressure through an engine cycle for a typical operating condition, along with the contributions of the individual factors. As can be seen, the maximum systematic uncertainty is 0.6% during the middle of the compression and expansion strokes, but it is only 0.2% near TDC when combustion occurs and critical combustion parameters such as CA50 and heat release rate are computed. The narrow spike near TDC is not an uncertainty in the pressure measurement, but rather the effect of cycle-to-cycle variation in the combustion event, i.e., the uncertainty of the 100-cycle average representing the pressure of an individual cycle.

Conclusions

DDI-PFS is a very effective technique for controlling combustion phasing in an LTGC engine through changes in the autoignition reactivity of the charge.

- Demonstrated about 8°CA of combustion timing control authority for P_{in} s from 1.0 bar to ≥ 2.0 bar for CRs of 14:1 and 16:1 using regular gasoline
- Showed that DDI-PFS gave near-zero soot emissions for all P_{in} s and injection timings tested, and very low NO_x emissions except for the latest DI timings at the lower P_{in} s where some aftertreatment may be required
- Showed combustion noise levels were below the 89 dBA value suggested as a limit by Ford for the large majority of the CA50 timing sweeps

Determined SA limits for ϕ , P_{in} , and T_{in} for well-premixed LTGC

- Showed that SA can provide CA50 control and compensate for T_{in} variations, increasing robustness for $\phi \geq \sim 0.38$ for P_{in} s from 1.0–1.6 bar absolute

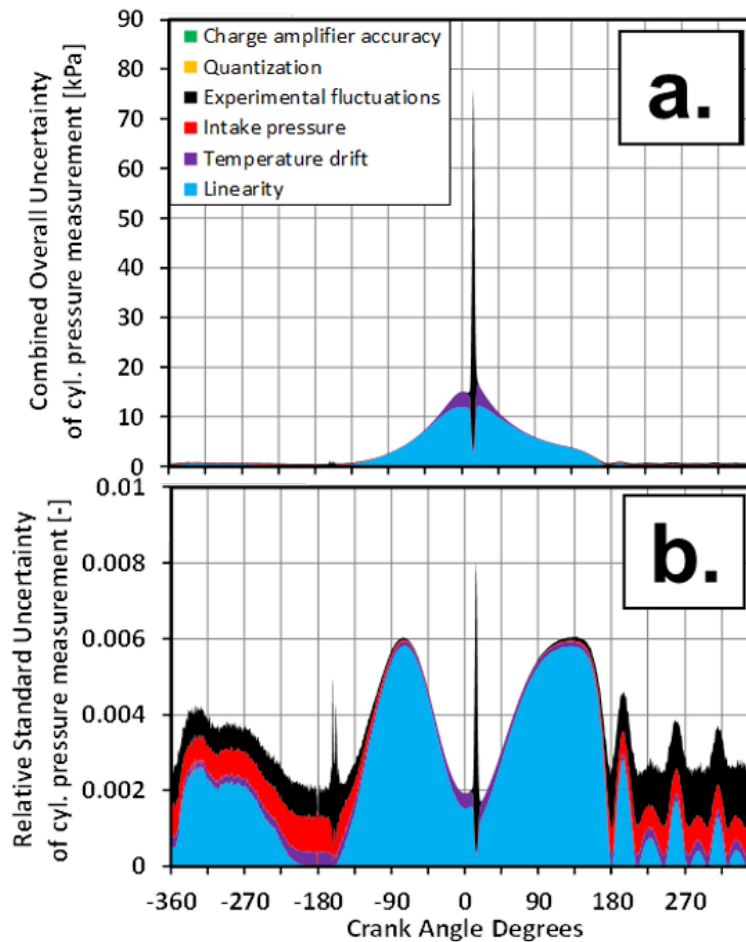


Figure I.4.5 - Uncertainties in the cylinder pressure measurement through a typical engine cycle, (a) in kPa and (b) as a fraction of the total pressure

- Demonstrated up to 7°CA of CA50 control authority at $\phi = 0.42$ and $P_{in} = 1.0$ bar
- Compensated for up to 21°C of T_{in} reduction, $\phi = 0.42$ and $P_{in} = 1.0$ bar
- Found that SA was not effective for CA50 control or T_{in} compensation for $\phi < 0.36$ at any P_{in} for a well premixed charged; fuel stratification will be required for effective SA at lower fueling rates

Conducted studies in collaboration with other national laboratories

- Determined a peak brake thermal efficiency of 44% for LTGC by correcting indicated thermal efficiencies using General Motors-supplied friction and turbocharger models; worked with Argonne National Laboratory to show that LTGC could give the best vehicle fuel economy for hybrid electric vehicle configurations of interest to DOE
- Collaborated with LLNL on a UQ analysis of cylinder pressure data in the Sandia LTGC engine; found a maximum uncertainty of 0.6% and an uncertainty of 0.2% during the combustion event
- Supported LLNL in the development of a kinetic model that worked well for RD5-87, the regular E10 gasoline used for the experiments

References

1. Dec, J.E., J. Dernotte, and C. Ji. "Increasing the Load Range, Load-to-Boost Ratio, and Efficiency of Low-Temperature Gasoline Combustion Engines (LTGC)." *SAE Int. J. Engines* 10, no. 3 (2017), doi:10.4271/2017-01-0731.
2. Eng, J.A. "Characterization of Pressure Waves in HCCI Combustion." SAE Technical Paper 2002-01-2859 (2002), doi:10.4271/2002-01-2859.
3. Dernotte, J., J. Dec, and C. Ji. "Investigation of the Sources of Combustion Noise in HCCI Engines." *SAE Int. J. Engines* 7, no.2 (2014), doi:10.4271/2014-01-1272.
4. Gentz, G., J. Dernotte, C. Ji, and J.E. Dec. "Spark Assist for CA50 Control & Improved Robustness in a Premixed LTGC Engine – Effects of Equivalence Ratio and Intake Boost." SAE Technical Paper 2018-01-1252, 2018.
5. Petitpas, G., R. Whitesides, J.E. Dec, and J. Dernotte. "Refining Measurement Uncertainties in HCCI/LTGC Engine Experiments." SAE Technical Paper 2018-01-1248, 2018.
6. Hwang, W., J.E. Dec, and M. Sjöberg. "Fuel Stratification for Low-Load Combustion: Performance & Fuel-PLIF Measurements." *SAE Transactions*, 116(3):1437-1460 (2007) and SAE Technical Paper 2007-01-4130, doi:10.4271/2007-01-4130.

Key Fiscal Year 2017 Publications

1. Gentz, G., J. Dernotte, C. Ji, and J.E. Dec. "Studies of Spark Assisted LTGC for CA50 Control and Improved Robustness." DOE Advanced Engine Combustion Working Group Meeting, August 2017.
2. Dec, J.E. "Low-Temperature Gasoline Combustion (LTGC) Engine Research." DOE Annual Merit Review, Office of Vehicle Technologies, June 2017.
3. Dernotte, J., J.E. Dec, and C. Ji. "Efficiency Improvement of Boosted Low-Temperature Gasoline Combustion Engines (LTGC) using a Double Direct-Injection Strategy." SAE Technical Paper 2017-01-0728, 2017 doi:10.4271/2017-01-0728.
4. Dec, J.E., J. Dernotte, and C. Ji. "Increasing the Load Range, Load-to-Boost Ratio, and Efficiency of Low-Temperature Gasoline Combustion Engines (LTGC)." *SAE Int. J. Engines* 10, no. 3 (2017), doi:10.4271/2017-01-0731, 2017.
5. Dec, J.E. "Low-Temperature Gasoline Combustion (LTGC) Engine Project." ACEC Tech Team Meeting, USCAR, Detroit, MI, November 2016.
6. Ji, C., J.E. Dec, J. Dernotte, and W.J. Cannella. "Boosted Premixed-LTGC / HCCI Combustion of EHN-doped Gasoline for Engine Speeds Up to 2400 rpm." *SAE Int. J. Engines* 9(4): 2016, doi:10.4271/2016-01-2295.
7. Dec, J.E., C. Ji, and J. Dernotte. "Controlling LTGC Combustion Timing for Intake Pressures from 1.0 – 2.0 bar." Invited presentation at Delphi Automotive, Detroit, MI, August 2016.
8. International Patent Filed: Dec, J.E, and R. Renzi, November 2016.

I.5 Gasoline Combustion Fundamentals

Isaac W. Ekoto, Principal Investigator

Sandia National Laboratories
7011 East Ave.
Livermore, CA 94551
E-mail: iekoto@sandia.gov

Michael Weismiller, DOE Technology Manager

U.S. Department of Energy
E-mail: Michael.Weismiller@ee.doe.gov

Start Date: October 1, 2016	End Date: September 30, 2017	
Total Project Cost: \$700,000	DOE share: \$700,000	Non-DOE share: \$0

Project Introduction

Advanced automotive gasoline engines that leverage a combination of reduced heat transfer, throttling, and mechanical losses; shorter combustion durations; and higher compression and mixture specific heat ratios are needed to meet aggressive DOE Vehicle Technologies Office fuel economy and pollutant emission targets. Central challenges include poor combustion stability at low-power conditions when large amounts of charge dilution are introduced and high sensitivity of conventional inductive coil ignition systems to elevated charge motion and density for boosted high-load operation. For conventional spark-ignited operation, novel low-temperature plasma (LTP) or pre-chamber-based ignition systems can improve dilution tolerances while maintaining good performance characteristics at elevated charge densities. Moreover, these igniters can improve the control of advanced compression ignition (ACI) strategies for gasoline at low to moderate loads.

The overarching research objective of the Gasoline Combustion Fundamentals project is to investigate phenomenological aspects related to enhanced ignition. The objective is accomplished through targeted experiments performed in a single-cylinder optically accessible research engine or an in-house developed optically accessible spark calorimeter (OASC). In situ optical diagnostics and ex situ gas sampling measurements are performed to elucidate important details of ignition and combustion processes. Measurements are further used to develop and validate complementary high-fidelity ignition simulations. The primary project audience is automotive manufacturers, Tier 1 suppliers, and technology startups—close cooperation has resulted in the development and execution of project objectives that address crucial mid- to long-range research challenges.

Objectives

- Determine fuel energy utilization pathways for gasoline ACI strategies that involve retained residuals
- Elucidate mechanisms responsible for enhanced autoignition with intake ozone (O₃) addition
- Develop methods to measure important LTP-generated radicals at engine-relevant conditions
- Identify the influence of pulse strategy and exhaust gas constituents on LTP physics

Approach

Performed research leverages experimental and numerical capabilities from multiple partners to characterize different aspects of advanced gasoline engine combustion. An industry call for low-cost, efficient, and onboard means of tailoring ACI fuel properties has motivated two independent research projects. The first project, performed in conjunction with Professor Will Northrop at the University of Minnesota, examined the use of negative valve overlap (NVO) strategies to facilitate autoignition control by retaining and compressing exhaust gases along with a pilot fuel injection. Detailed characterization of the recompression

stroke end-gas composition was performed, with results used to inform the development and validation of a fuel energy utilization analysis that clarifies the sources of inefficiency for relevant ACI operating points. The second project, performed in collaboration with Professor Fabrice Foucher of the PRISME Laboratory at the University of Orléans, France, explored the mechanisms responsible for enhanced fuel reactivity with intake-added O_3 through a combination of in situ optical measurements and complementary chemical kinetic modeling. Both projects were performed in direct injected, single-cylinder, optically accessible research engines with valve timings and injection strategies optimized for the respective strategy.

A parallel investigation explored the suitability of advanced ignition systems to expand the operation envelope for high-efficiency dilute spark ignition combustion. Experiments were performed in the OASC—a spark discharge research platform that replicates in-cylinder mixture composition and density at the time of spark. The OASC was used to measure LTP discharge thermal energy deposition, with integrated optical access used to measure important LTP-generated radicals via optical emission spectroscopy (OES) and laser-induced fluorescence. Impactful results were shared with Dr. Riccardo Scarcelli of Argonne National Laboratory, who modeled the LTP discharge using the high-fidelity non-equilibrium plasma code, VizGlow.

Results

The impact of in-cylinder-generated NVO reformat on full-cycle ACI engine performance was evaluated using a single-cylinder research engine with an 11.3:1 compression ratio and 1,200 rpm engine speed. Low-lift valves were used with the timing set to create a 150 degrees crank angle ($^{\circ}CA$) recompression period centered at top dead center (TDC) of the exhaust stroke. A custom sampling valve was used to collect recompression cycle end-gases with the total fuel energy content and overall reformat composition measured by gas chromatography or photo-ionization mass spectrometry [1]. A one-dimensional engine model was developed to determine bulk thermodynamic quantities at each portion of the cycle. Model outputs were used to analyze the sources of work (W), heat transfer loss (Q_{HT}), exhaust loss (H_{exh}), and cycle combustion efficiency ($U_{fuel,exh}$); results for two low-load conditions are illustrated in Figure I.5.1.

Major results are as follows:

- Combustion phasing advanced by more than 10 $^{\circ}CA$ with the use of in-cylinder-generated reformat due to the production of reactive species: namely acetylene, acetaldehyde, propene, and allene.

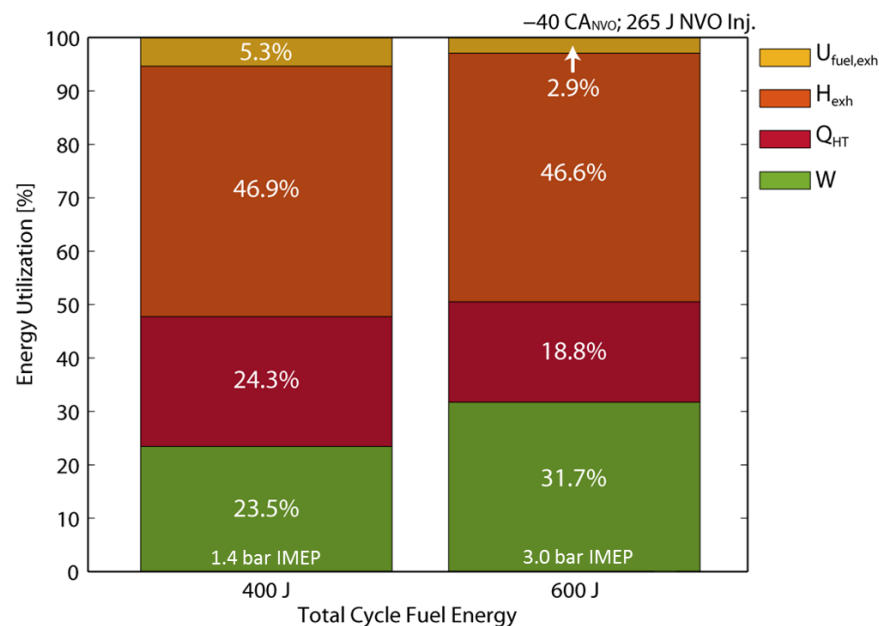


Figure I.5.1 - Fuel energy utilization breakdown for two low-load (1.4 and 3.0 bar indicated mean effective pressure [IMEP]) ACI operating points with a fixed 265 J fuel injection during the NVO period and the balance fuel energy injected early during the main period

- Reformate composition only influenced autoignition delay times, with no impact on subsequent heat release rates.
- Recompression period heat transfer losses amounted to roughly 30% of all cycle heat transfer losses or between 6% and 8% of the total injected fuel energy, a significant source of cycle inefficiency.

Intake O_3 addition was investigated as an alternate method to improve charge reactivity for low-load ACI [2] that could potentially eliminate the large parasitic heat losses that result from the NVO recompression period. Experiments were performed in an optically accessible single-cylinder engine with a 13:1 compression ratio. For all experiments, the engine speed (1,000 rpm), intake pressure (1 bar), and charge equivalence ratio (0.3) were fixed, while the intake temperature was varied between 50°C and 200°C. Ozone concentrations of up to 35 ppm were seeded into the air-only intake charge. The 50% burn angle (CA50) for a representative low-load ACI operating point (2.8 bar IMEP) is mapped in Figure I.5.2 as a function of intake O_3 and temperature. Results highlight the non-linear intake temperature reduction possible with O_3 addition, with the largest temperature reductions occurring for the smallest O_3 concentrations.

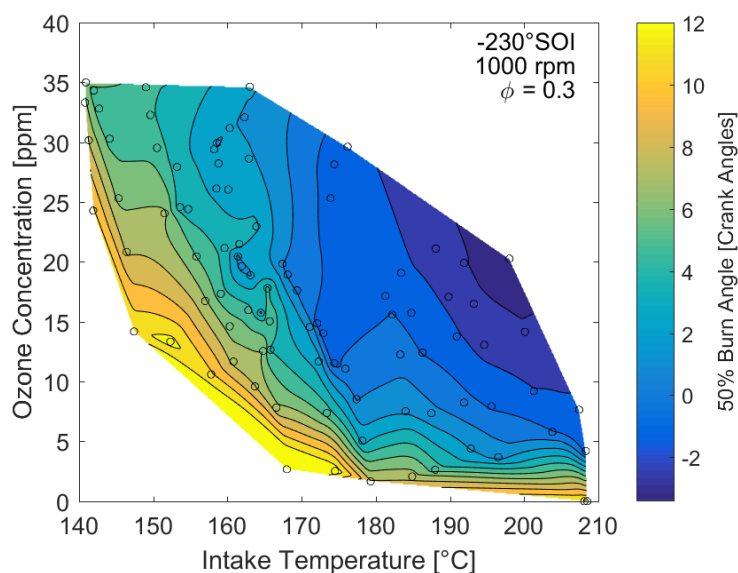


Figure I.5.2 - Map of CA50 for a range of intake temperatures and O_3 concentrations with a fixed -230 °CA start of injection (SOI) and 1,000 rpm engine speed. Charge ϕ was maintained at 0.3, which produced an approximate 2.8 bar IMEP load.

In-cylinder O_3 concentrations were also quantitatively measured using an ultraviolet light absorption diagnostic, with the results used to evaluate complementary chemistry modeling. Crank angle resolved O_3 concentration profiles for a motored engine, plotted in Figure I.5.3, illustrate the rapid thermally induced O_3 decomposition that occurs near TDC, behavior that is well captured by the chemistry modeling. The modeling further indicates the O_3 decomposition leads to a burst of reactive atomic oxygen (O).

An apparent heat release rate profile from the engine fueled by a five-component gasoline surrogate (isooctane, n-heptane, ethanol, 1-hexene, toluene) [3] and with O_3 addition is plotted in Figure I.5.4 along with the corresponding O_3 measurement. Measurements are compared to complementary chemical modeling results of O_3 , parent fuel, and important radical species along with parent fuel rates of consumption (ROC) by some of these radicals. A heat release bump that appeared about 20 °CA before low-temperature heat release correlates with an unexpected increase in ultraviolet light absorption. The light attenuation is attributed to the significant hydroperoxyl (HO_2) and hydrogen peroxide (H_2O_2) concentrations predicted by the model that strongly absorb ultraviolet light.

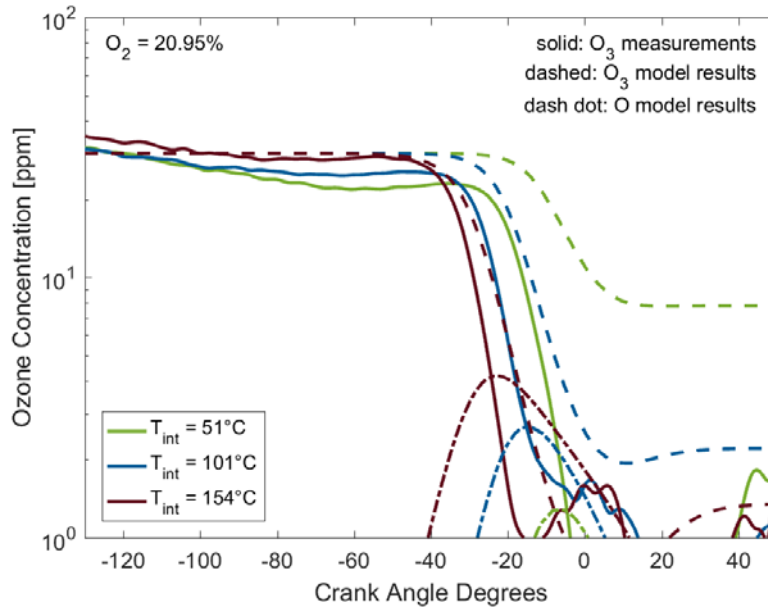


Figure I.5.3 - Quantitative in-cylinder O_3 measurements compared to chemistry modeling results of O_3 and O

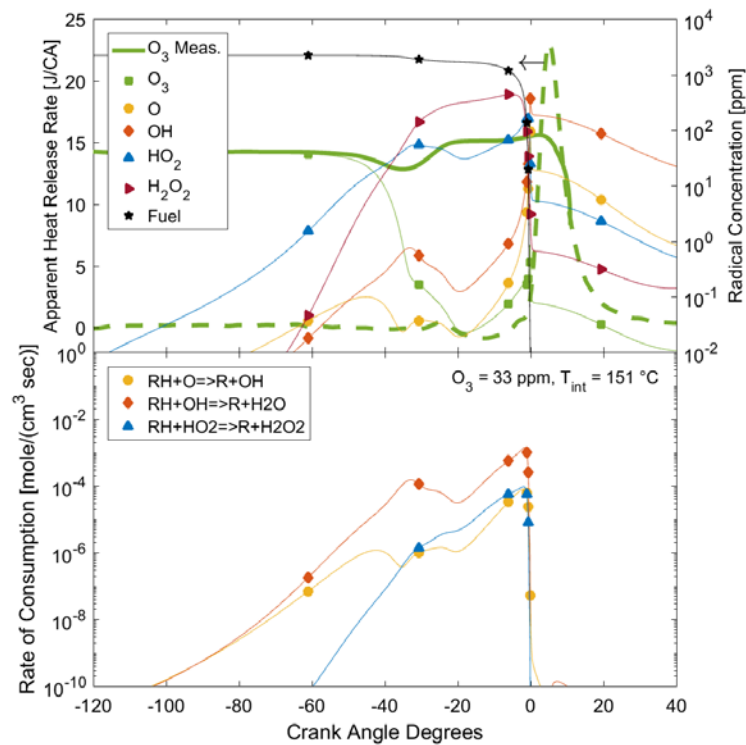


Figure I.5.4 - Measured apparent heat release rate and O_3 profiles compared to simulation O_3 results and important radicals (top). Model-predicted fuel ROC by O , OH , and HO_2 (bottom). Intake temperature was adjusted to get CA50 close to 4 °CA.

Major results are as follows:

- Cycle indicated thermal efficiencies in excess of 38% were measured; i.e., ACI cycle heat losses associated with NVO use were effectively recovered with O_3 addition.
- For fixed combustion phasing, 25 ppm of added O_3 reduced the required intake temperature by 65°C.

- For fixed intake temperature, O_3 variations between 0 and 35 ppm enabled CA50 control of $\pm 5^\circ\text{CA}$.
- Chemistry modeling of O_3 addition with fuel indicates O rapidly abstracts fuel hydrogen to form OH, which then alters and accelerates subsequent low-temperature ignition pathways.

A joint Sandia (experiments) and Argonne (modeling) National Laboratories research effort examined LTP discharge physics at relevant in-cylinder conditions. For the Sandia experiments, LTP was produced in the OASC cell via high voltage (up to 26 kV) electrical pulse discharges (12 ns) between pin-to-pin electrodes. Measurements included gas thermal energy deposition from calorimetry and qualitative O distributions obtained from OES. Methods to quantitatively measure ground state O population at pressure were also developed. The impact of initial pressure and mixture composition on discharge dynamics was evaluated. Complementary simulations at Argonne were performed using the VizGlow high-fidelity non-equilibrium plasma solver to elucidate processes that cannot be directly measured.

Pressure rise calorimetry profiles for 20 kV LTP discharges at a fixed 2.8 bar initial pressure with varying H_2O and CO_2 content are plotted in Figure I.5.5. The results highlight the rapid thermal energy deposition that results with even small amounts of added H_2O or CO_2 . Complementary LTP schlieren images (not shown) illustrate the thinner streamers and increased branching that occur with added H_2O or CO_2 . These features are thought to cause more rapid convective cooling and thus explain the faster pressure rise rates in the calorimeter volume.

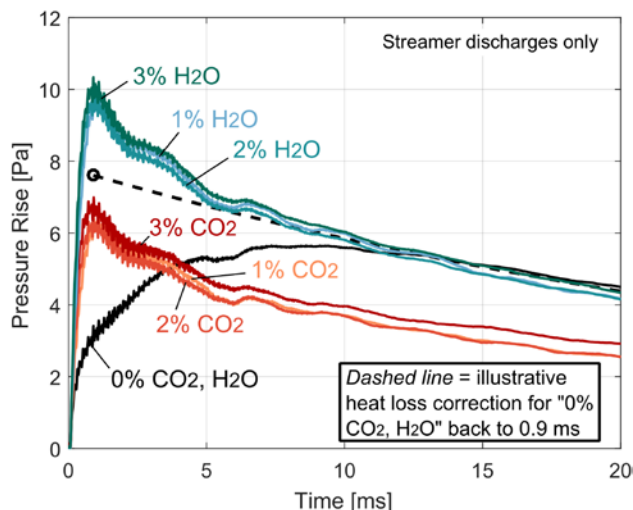


Figure I.5.5 - Pressure rise calorimetry for 20 kV LTP discharges at a 2.8 bar initial pressure and varying H_2O/CO_2 concentrations

Qualitative images of excited state O along with an image of thermal gradients via schlieren imaging from the Sandia experiments are compared in Figure I.5.6 to predictions of ground state O and temperature distributions from the Argonne simulations. The spatial distribution of observed emission correlates well with the simulation results. Moreover, the trend of decreased signal with increased pressure is likewise well matched.

Major results are as follows:

- A model was developed to correct for pressure effects associated with two-photon laser-induced fluorescence measurements of ground state O. Validation of the model is ongoing.
- Initial pressure boundaries where LTP transition to arc occurred along with LTP streamer branching ratios and diameters were well predicted by the Argonne simulations.
- Simulation results indicate the LTP discharge heating was due to electronic fast-gas heating from excited state species within the streamers.

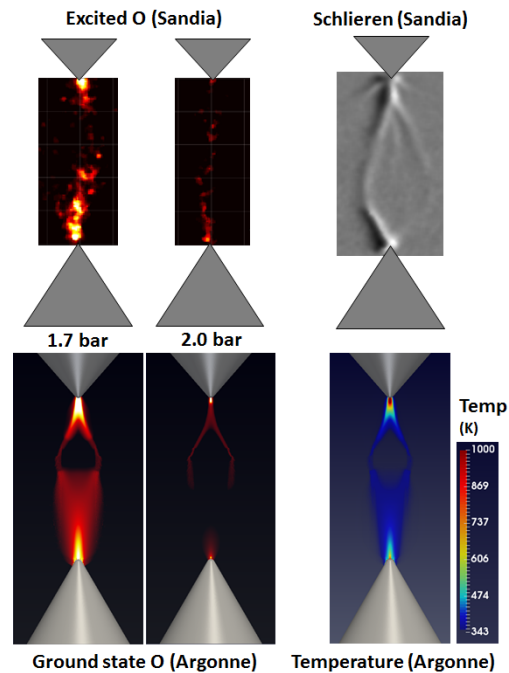


Figure I.5.6 - Qualitative images of excited state O for two initial pressures along with a schlieren image of temperature gradients for a 20 kV LTP discharge (top) compared to VizGlow predictions of LTP discharge O and temperature distributions (bottom)

Conclusions

- Improved ACI combustion phasing control is possible with the use of an NVO period that retains hot exhaust residuals and improved charge reactivity through in-cylinder fuel reforming. However, an energy analysis indicates NVO period heat losses account for up to 8% of the injected fuel energy.
- Ozone addition enables similar ACI combustion phasing control benefits achieved with NVO operation, but without the heat loss penalty. The increased reactivity is attributed to thermal decomposition of O_3 that leads to a burst of O near TDC. Exothermic reactions of O and subsequently formed OH with fuel alter and accelerate low-temperature reaction pathways responsible for ignition.
- The Argonne numerical simulations of LTP discharges validated against Sandia experimental data provide the automotive research community with a new tool that can be leveraged to quickly and accurately aid in the design of production-ready LTP igniters.

References

1. Wolk, B., I. Ekoto, W.F. Northrop, K. Moshhammer, and N. Hansen. "Detailed speciation and reactivity characterization of fuel-specific in-cylinder reforming products and the associated impact on engine performance." *Fuel*, 185:348–61, 2016.
2. Masurier, J.B., F. Foucher, G. Dayma, and P. Dagaut. "Homogeneous Charge Compression Ignition Combustion of Primary Reference Fuels Influenced by Ozone Addition." *Energ Fuel*, 27 (9):5495–505, 2013.
3. Mehl, M., J.Y. Chen, W.J. Pitz, S.M. Sarathy, and C.K. Westbrook. "An Approach for Formulating Surrogates for Gasoline with Application toward a Reduced Surrogate Mechanism for CFD Engine Modeling." *Energ Fuel*, 25 (11):5215–23, 2011.

Key Fiscal Year 2017 Publications

1. Ekoto, I., “Quantitative Measurement of Important Low-Temperature Plasma-Generated Radicals at Engine-Relevant Conditions.” Gordon Research Conference on Laser Diagnostics in Combustion, Mount Snow, VT, August 6–11, 2017.
2. Ekoto, I.W., B.M. Wolk, W.F. Northrop, N. Hansen, and K. Moshhammer, “Tailoring Charge Reactivity Using In-Cylinder Generated Reformate for Gasoline Compression Ignition Strategies.” *Journal of Engineering for Gas Turbines and Power*, 139 (12):122801–10, 2017.
3. Ekoto, I., B. Wolk, and W. Northrop. “Energy Analysis of Low-Load Low-Temperature Gasoline Combustion with Auxiliary-Fueled Negative Valve Overlap.” *SAE Int J Engines*, 10 (3):1238–55, 2017.
4. Wolk, B.M. and I.W. Ekoto, “Calorimetry and Imaging of Plasma Produced by a Pulsed Nanosecond Discharge Igniter in EGR Gases at Engine-Relevant Densities.” *SAE Int. J. Engines*, 10 (3) 2017.
5. Kane, S., X. Li, B. Wolk, I. Ekoto, and W.F. Northrop. “Investigation of Species from Negative Valve Overlap Reforming Using a Stochastic Reactor Model.” SAE WCX, Detroit, MI, 2017-01-0529, 2017.

I.6 Advancements in Fuel Spray and Combustion Modeling with High Performance Computing Resources

Sibendu Som, Principal Investigator

Argonne National Laboratory
9700 S. Cass Avenue
Argonne, IL, 60439
E-mail: ssom@anl.gov

Michael Weismiller, DOE Technology Manager

U.S. Department of Energy
E-mail: Michael.Weismiller@ee.doe.gov

Start Date: October 1, 2016	End Date: September 30, 2017	
Total Project Cost: \$390,000	DOE share: \$390,000	Non-DOE share: \$0

Acknowledgments

Co-Authors

Kaushik Saha, Prithwish Kundu, Muhsin Ameen; Argonne National Laboratory

Project Introduction

Internal combustion engine (ICE) processes are multi-scale and highly coupled in nature and are characterized by turbulence, two-phase flows, and complicated spray physics. Furthermore, the complex combustion chemistry of fuel oxidation and emission formation makes engine simulations a computationally daunting task. Given the cost for performing detailed experiments spanning a wide range of operating conditions and fuels, computational fluid dynamics (CFD) modeling aided by high performance computing (HPC) has the potential to result in considerable cost savings. Development of physics-based CFD models for nozzle flow, spray, turbulence, and combustion are necessary for predictive simulations of the ICE. HPC can play an important role in ICE development by reducing the cost for design and optimization studies. This is largely accomplished by being able to conduct detailed simulations of complex geometries and moving boundaries with high-fidelity models describing the relevant physical and chemical interactions, and by resolving the relevant temporal and spatial scales. These simulations provide unprecedented insights into the complex processes taking place in these engines, thus aiding designers in making judicious choices. The major focus of our research in Fiscal Year 2017 has been towards the validation of nozzle flow and spray models for gasoline direct injection (GDI) applications and development and validation of turbulent combustion models for ICE applications, aided by HPC tools.

Objectives

- Development of physics-based nozzle flow and spray models; develop capability to perform coupled nozzle flow and spray simulations
- Development and validation of reduced chemical–kinetic models for realistic fuel surrogates; develop robust turbulence chemistry interaction models for engine simulations
- Development of HPC tool for codes used by the industry for ICE applications

Approach

The approach to improved modeling capability is highlighted here.

- In-nozzle flow simulation capability was extended to capture both gasoline and diesel fuel injection using a robust homogeneous relaxation-based two-phase flow model (HRM) within a volume of fluid approach [1] framework. The boundary conditions for the simulations are obtained from X-ray phase-contrast

imaging at Argonne, which includes the needle lift and wobble profiles for both diesel and gasoline injectors.

- A one-way coupling approach was developed in collaboration with Convergent Science, Inc., that couples the flow from the injector to the ensuing spray. This is performed by transitioning at the orifice exit from an Eulerian to a Lagrangian framework. Best practices for performing these one-way coupled simulations for both diesel and gasoline injectors using high-fidelity turbulence models have also been developed. The approach can account for injection transients such as those detailed in our recent publications.
- The approach to robust and accurate turbulent combustion modeling includes development of a tabulated flamelet model (TFM) that accounts for turbulence chemistry interaction for compression ignition engines [2]. The approach now allows for integration of full detailed chemistry into engine simulations, rather than using reduced mechanisms. The TFM approach can be coupled to any academic or commercial code of interest. Artificial neural network (ANN) techniques are then being used to tabulate the full chemistry so that the table sizes for CFD are reasonable.
- Argonne is ensuring that the engine modeling codes evolve with the architecture by continuing to scale CONVERGE code on Mira and Theta (next-generation supercomputer) which enable the possibility to run both capacity and capability computations. Under capacity computing, a large number of engine simulations (>1,000) are bundled together and run as an ensemble job using >10,000 processors. Under capability computing, fewer but high-fidelity simulations are performed, still using >10,000 processors. This two-pronged approach for capacity and capability computing allows the use of CFD for both design optimization as well as providing unprecedented insights into the combustion process [3].

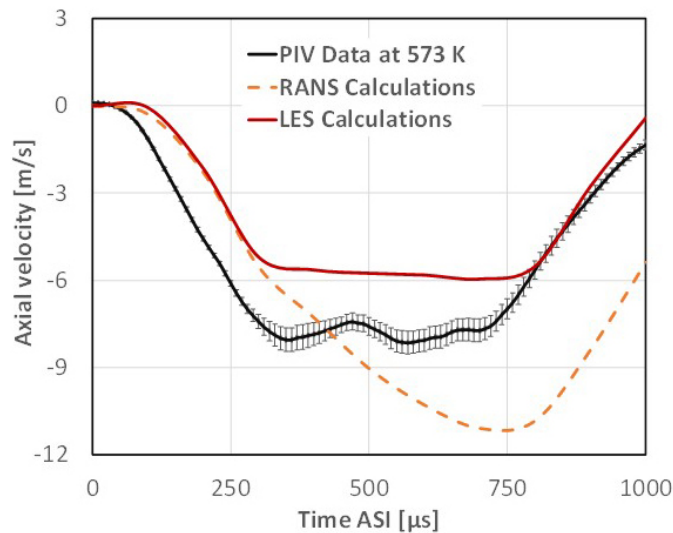
Results

Key accomplishments for Fiscal Year 2017 are as follows.

- The onset of flash boiling was predicted for different fuels and fuel blends of interest ranging from gasoline to pure ethanol. This was possible due to the development of a multi-component flash boiling approach.
- The one-way coupling approach, along with high-fidelity turbulence model large eddy simulation (LES), can predict the onset of plume merger and collapse for GDI sprays. Reynolds-averaged Navier–Stokes (RANS) turbulence models cannot capture the qualitative trends correctly.
- For the first time ever, the full chemistry mechanism (>2,500 species) was run in engine simulations with LES. In the past, engine simulations have been typically performed with less than 250 species.

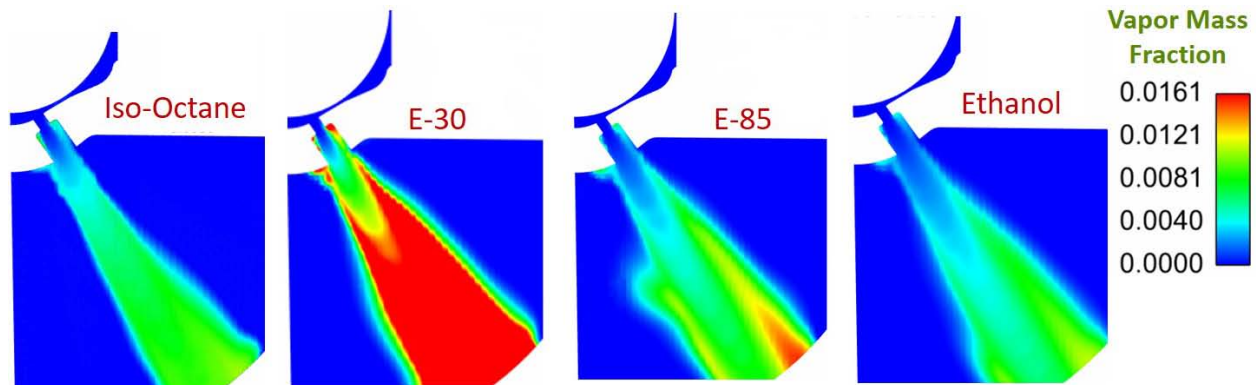
The gas phase axial velocity vs. time is plotted (Figure I.6.1) from experiments at Sandia National Laboratory and simulations using two different turbulence models. The conditions for experiments and simulations are representative of standard GDI operation. The injector is Spray G of the Engine Combustion Network (ECN) consisting of eight orifices. The experimental particle image velocimetry (PIV) data shows that initially the plumes merge creating a suction between the plumes, which results in negative gas phase axial velocity. Eventually, these plumes collapse, resulting in pressure recovery and increase in gas phase axial velocity. The lower fidelity RANS cannot capture this trend accurately, while the higher fidelity LES can capture the timing of the plume merger and collapse phenomenon fairly well, along with the magnitude of the gas phase velocity. Although not shown here, the simulation results were compared with calculations performed by other researchers from Europe, and it was observed that the Argonne simulations were much more accurate than other predictions.

Single component HRM for flash boiling shown by Argonne in previous Annual Merit Reviews was modified to account for multi-component effects. Multi-component HRM will allow for accurate capture of the effect of fuel properties on spray evolution. In-nozzle flow simulations under flash-boiling conditions were then performed for pure components (iso-octane as well as ethanol) and blends of iso-octane and ethanol. Figure I.6.2 shows that the extent of vapor formation is similar for the pure components (iso-octane and ethanol) while the blends are more volatile than the individual components owing to their higher saturation



ASI - after start of injection

Figure I.6.1 - Gas phase axial velocity vs. time is plotted for simulations performed using both LES and RANS turbulence models compared against experimental PIV data obtained from Sandia National Laboratories in a constant volume vessel



E-30 – 30% ethanol, 70% gasoline; E-85 – 85% ethanol, 15% gasoline

Figure I.6.2 - Vapor mass fraction contours through a cut-plane passing through a single orifice of Spray G show the propensity of ethanol blends to flash boil significantly more than the pure components. The simulations were performed under the standard Spray G conditions from ECN.

pressures. Multi-component HRM allows accurate capture of the effect of fuel properties on spray evolution. The simulations were performed under standard Spray G condition, of ECN.

Extensive validation of the TFM approach that was developed by Argonne and presented at the 2016 Annual Merit Review has been performed against experimental spray flame data from ECN (for n-dodecane fuel) and optical engine data (for methyl decanoate fuel) from C.J. Mueller at Sandia National Laboratories. It should be noted that the flamelet tables are generated with detailed chemistry mechanisms for both these fuels without any mechanism reduction. Figure I.6.3 shows that for spray flame simulations, the TFM is demonstrated to be more accurate than state-of-the-art models in commercial code (shown as HR-MZ). The computational cost for TFM is 50–75% lower, depending on the ambient conditions. Best practices for mesh size, TFM table granularity, etc., have been published.

Figure I.6.4 shows the contour plots for flame structure in terms of CH_2O , OH, and temperature predicted using TFM approach for both 750 K and 900 K cases. The stoichiometric mixture fraction line is also shown. These plots are made from a cut-plane passing through the center of the spray flame. The simulation consists of more than 20 million cells using an LES turbulence model. Ignition was not observed with the HR-MZ model at 750 K and overestimated at 900 K, while TFM can accurately capture both ignition delay and flame

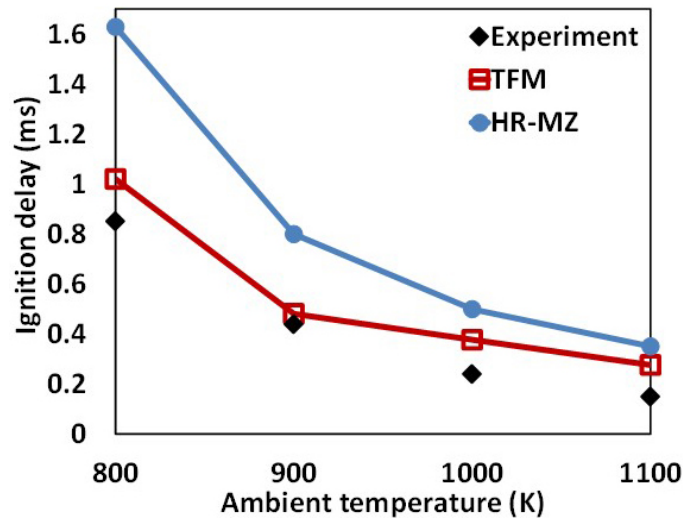


Figure I.6.3 - Ignition delay vs. ambient temperature predicted using TFM and HR-MZ models and compared against experimental data from Sandia National Laboratories

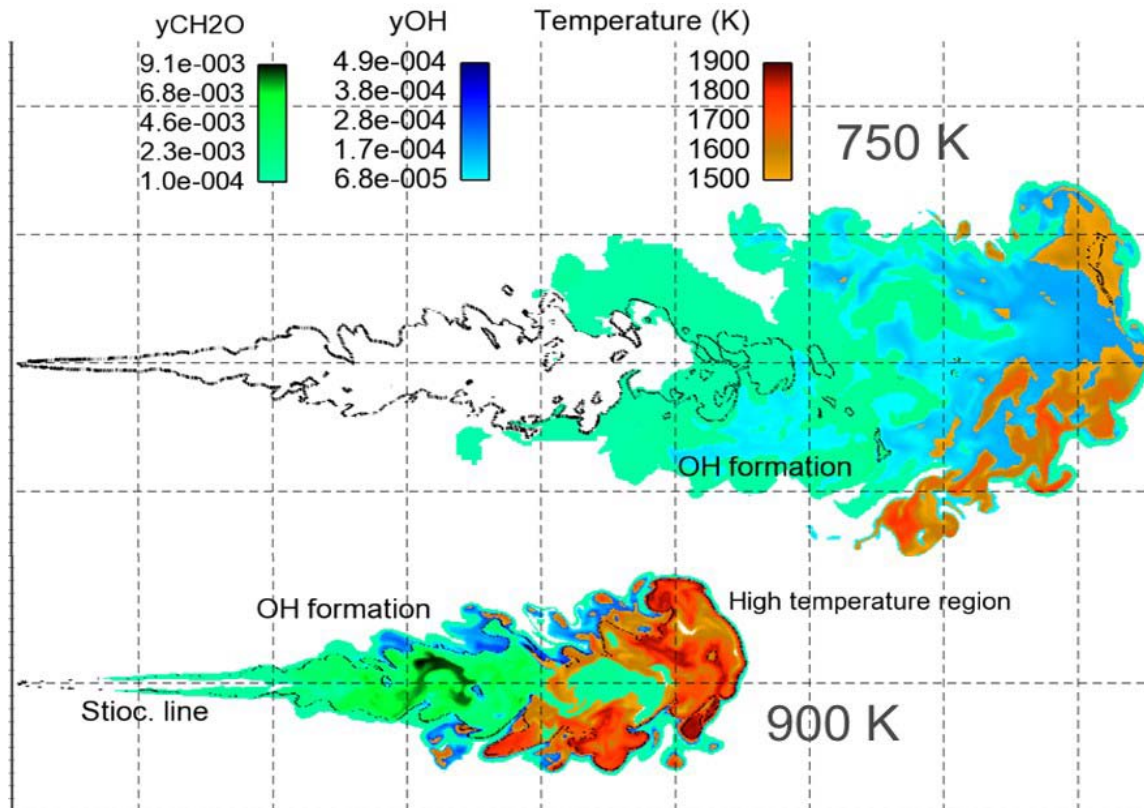


Figure I.6.4 - Flame structure in terms of CH_2O , OH , and temperature predicted using TFM approach for both 750 K and 900 K cases. The stoichiometric mixture fraction line is also shown.

lift-off lengths. Turbulence chemistry interaction (TCI) is observed to play a key role in species diffusion from the first stage ignition, thereby enhancing the main ignition, especially under the low-temperature condition of 750 K. TFM can capture this effect while the HR-MZ model cannot. Significantly lower temperatures and species concentration are observed at 750 K compared to 900 K condition. At 750 K, CH_2O formation starts at significantly lean regions due to longer ignition delays leading to more mixing compared to 900 K. Similar conclusions are drawn for OH as well. In order to understand the role of TCI at lower temperatures, unsteady

flamelets are simulated with Argonne's flamelet code with different scalar dissipation rates (χ_{st}), i.e., with $\chi_{st} = 0$ (homogeneous reactor) vs. $\chi_{st} = 2 \text{ s}^{-1}$. Two main observations can be made: (1) lean regions ($\phi < 1$) do not ignite with homogeneous reactor assumption (HR-MZ model) and (2) scalar dissipation leads to diffusion of radical species enhancing ignition in the lean regions. The published research from Argonne clearly demonstrates the need for turbulent combustion models accounting for TCI effects, such as the TFM approach.

A new four-component surrogate mechanism was developed at Lawrence Livermore National Laboratory and was reduced in collaboration with University of Connecticut. The reduced mechanism consisted of about 1,000 species and is significantly larger than typical mechanisms used for CFD. The mechanism was run in conjunction with high-fidelity LES consisting of best practices developed in our group in the past few years. The constant volume vessel simulations consist of about 22 million cells and multiple realization averaging was performed to calculate the ignition delays and flame lift-off lengths. Experimental data is obtained from Army Research Laboratory. Overall the simulations (Figure I.6.5) can capture the right trends with increase in ambient oxygen concentration. However, there is still room for improvement in the simulations and the reaction mechanism is being further updated by the Livermore group. Overall, TFM enables running extremely large chemistry mechanisms with high-fidelity CFD calculations without compromising on the chemical kinetics. Since the table sizes can get large with detailed chemistry mechanisms, ANN can be used to tabulate the chemistry and reduce the table size for CFD calculations.

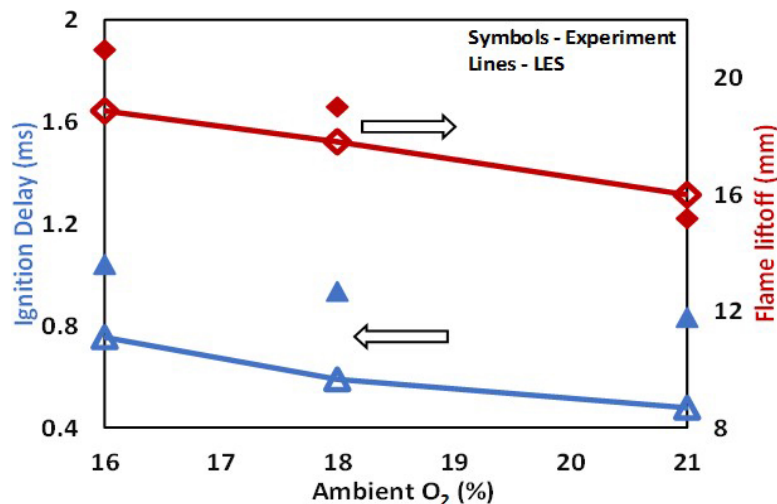


Figure I.6.5 - Ignition delay and flame lift-off lengths for a new four-component diesel surrogate mechanism developed and validated against experimental data from Army Research Laboratory

While the use of detailed chemistry-based mechanisms, high fidelity turbulence models, accurate in-nozzle flow calculations result in increased computational time, the use of high performance computing systems from Argonne enables running these simulations with a reasonable turn-around time. All the above results have been published in peer-reviewed conference or journal publications.

Conclusions

- The robust approach for predicting in-nozzle flow features for both diesel and gasoline injector applications can capture flash boiling for GDI injectors. The simulations captured experimentally observed trends and is expected to predict the extent of flash boiling under different ambient and injection conditions for not only single but also multi-component fuel blends.
- The one-way coupling approach together with high-fidelity LES turbulence model can capture the influence of in-nozzle flow and spray dynamics. The complex phenomenon of GDI injection, plume merger, and collapse can be accurately predicted by the simulations.
- TFM is shown to be more predictive than a standard HR-MZ model that does not account for TCI effects and is also a factor of two faster. TFM can now account for full detailed chemistry and does not require

any mechanism reduction. Since the mechanisms can be large, ANN can be used to reduce the table sizes for chemistry tabulation in CFD.

- TFM together with LES are validated against both spray flame and engine data available in literature. While the industry standard is to use RANS and reduced kinetic mechanisms, the approach developed at Argonne truly pushes the state of the art as it allows for the use for full mechanisms without reduction.

References

1. Xue, Q., M. Battistoni, S. Som, S. Quan, P.K. Senecal, E. Pomraning, and D. Schmidt. "Eulerian CFD modeling of coupled nozzle flow and spray with validation against x-ray radiography data." *SAE International Journal of Fuels and Lubricants*, 7(2):2014.
2. Kundu, P., T. Echehki, Y. Pei, and S. Som. "An equivalent dissipation rate model for capturing history effects in non-premixed flames." *Combustion and Flame*, 2016.
3. Kodavasal, J., K. Harms, P. Srivastava, S. Som, S. Quan, K.J. Richards, and M. Garcia. "Development of stiffness-based chemistry load balancing scheme, and optimization of I/O and communication, to enable massively parallel high-fidelity internal combustion engine simulations." *Proceedings of the ASME 2015 Internal Combustion Engine Division Fall Technical Conference*, ICEF2015-1035, Houston, TX, November 2015.

Key Fiscal Year 2017 Publications

1. Zhao, L., A. A. Moiz, S. Som, N. Fogla, M. Bybee, S. Wahiduzzman, M. Mirzaeian, F. Mollo, J. Kodavasal. "Multi-cycle large eddy simulation to capture cycle-to-cycle variation (CCV) in spark ignition (SI) engines." *International Journal for Engine Research*, 1-19, (2017) DOI: 10.1177/1468087417732447.
2. He, Z., L. Zhang, S. Som, Q. Wang, K. Saha. "Investigations of Effect of Phase Change Mass Transfer Rate on Cavitation Process with Homogeneous Relaxation Model." *International Communications in Heat and Mass Transfer* 89, 98–107, 2017.
3. Kundu, P., M. Ameen, S. Som. "Importance of Turbulence Chemistry Interaction at Low Temperature Engine Conditions." *Combustion and Flame* 183, 283–298, 2017 <https://doi.org/10.1016/j.combustflame.2017.05.025>.
4. Torelli, R., S. Som, Y. Pei, Y. Zhang, A. Voice, M. Traver, D. Cleary. "Influence of Fuel properties on internal nozzle flow development in a multi-hole diesel injector." *Fuel* 204, 171–184, 2017 <https://doi.org/10.1016/j.fuel.2017.04.123>.
5. Pei, Y., Y. Zhang, P. Kumar, M. Traver, D. Cleary, M. Ameen, S. Som, D. Probst, T. Burton, E. Pomraning, P.K. Senecal. "Combustion System Optimization of Gasoline-like Fuel in a Heavy-Duty Engine Using Design of Experiments." SAE Paper No. 2017-01-0550, *SAE International Journal of Commercial Vehicles* 10 (2): 2017, doi:10.4271/2017-01-0550.
6. Wang, Z., M. Ameen, S. Som, J. Abraham. "Assessment of Large-Eddy Simulations of Turbulent Round Jets using Low-Order Numerical Schemes." SAE Paper No. 2017-01-0575, *SAE International Journal of Commercial Vehicles* 10 (2): 2017, doi:10.4271/2017-01-0575.
7. Pal, P., D. Probst, Y. Pei, Y. Zhang, M. Traver, D. Cleary, S. Som. "Numerical Investigation of Gasoline-like Fuel in a Heavy-Duty Compression Ignition Engine Using Global Sensitivity Analysis." SAE Paper No. 2017-01-0578, *SAE International Journal of Fuels and Lubricants* 10 (1): 2017, doi:10.4271/2017-01-0578.
8. Zhao, L., R. Torelli, X. Zhu, R. Scarcelli, S. Som, H. Schmidt, J. Naber, S.Y. Lee. "An Experimental and Modeling Study of Diesel Spray Impingement on Flat Plate." SAE Paper No. 2017-01-0854, *SAE International Journal of Fuels and Lubricants* 10 (1): 2017, doi:10.4271/2017-01-0854.

9. Sphicas, P., L. Pickett, S. Skeen, K. Saha, S. Som, T. Lucchini, D. Sinoir, G. D'Errico. "A Comparison of Experimental and Modeled Velocity in Gasoline Direct-Injection Sprays with Plume Interaction and Collapse." SAE Paper No. 2017-01-0837, *SAE International Journal of Fuels and Lubricants* 10 (1): 2017, doi:10.4271/2017-01-0837.
10. Saha, K., S. Som, M. Battistoni. "Investigation of homogeneous relaxation model parameters and their implications on GDI spray formation." *Atomization and Sprays*, 2017, 10.1615/AtomizSpr.2017016338.
11. Yao, T., Y. Pei, B.J. Zhong, S. Som, T. Lu, K.H. Luo. "A compact skeletal mechanism for n-dodecane with optimized semi-global low-temperature chemistry for diesel engine simulations." *Fuel* 191, 339–349 2017 <http://dx.doi.org/10.1016/j.fuel.2016.11.083>.
12. Kundu, P., M. Ameen, U. Unnikrishnan, S. Som. "Implementation of a Tabulated Flamelet Model for Investigation of Methyl Decanoate Combustion in an Optical Direct Injection Engine." SAE Paper No. 2017-01-0564, *SAE 2017 World Congress*, Detroit, MI, April 2017.
13. Saha, K., S. Quan, M. Battistoni, S. Som, P.K. Senecal, E. Pomraning. "Coupled Eulerian Internal Nozzle Flow and Lagrangian Spray Simulations for GDI Systems." SAE Paper No. 2017-01-0834, *SAE 2017 World Congress*, Detroit, MI, April 2017.
14. Torelli, R., S. Som, Y. Pei, Y. Zhang, A. Voice, M. Traver, D. Cleary. "Comparison of In-Nozzle Flow Characteristics of Naptha and N-dodecane Fuels." SAE Paper No. 2017-01-0853, *SAE 2017 World Congress*, Detroit, MI, April 2017.

I.7 Fuel Injection and Spray Research Using X-Ray Diagnostics

Christopher F. Powell, Principal Investigator

Argonne National Laboratory
9700 S. Cass Ave.
Lemont, IL 60439
E-mail: powell@anl.gov

Michael Weismiller, DOE Technology Manager

U.S. Department of Energy
E-mail: Michael.Weismiller@ee.doe.gov

Start Date: October 1, 2016	End Date: September 30, 2017	
Total Project Cost: \$505,000	DOE share: \$505,000	Non-DOE share: \$0

Acknowledgments

Co-Authors

Daniel Duke, Alan Kastengren, Katarzyna Matusik, Brandon Sforzo; Argonne National Laboratory

Project Introduction

Fuel injection systems are one of the most important components in the design of combustion engines with high efficiency and low emissions. A detailed understanding of the fuel injection process and the mechanisms of spray atomization is needed to implement advanced combustion strategies with improved engine performance. The limitations of visible light diagnostics have spurred the development of X-ray diagnostics for the study of fuel sprays. X-rays are highly penetrative and can generate quantitative, unambiguous measurements of useful spray properties, even in the optically opaque region very near the nozzle.

Objectives

- Demonstrate the ability to build a full three-dimensional (3D) model of a gasoline direct injection (GDI) fuel injector using combined X-ray and neutron tomography in collaboration with Oak Ridge National Laboratory
- Deliver a high resolution 3D model of a diesel injector nozzle to be used for simulations of internal flow
- Measure the 3D density distribution of the fuel in a diesel jet as it first emerges from the nozzle with excellent spatial and temporal resolution

Approach

The aim of this project is to develop and perform high precision measurements of fuel injection and sprays to further the development of accurate computational spray models. These measurements are performed at the Advanced Photon Source at Argonne National Laboratory. This source provides a very high flux beam of X-rays, enabling quantitative, time resolved measurements of sprays with very high spatial resolution. The X-rays are used for four different measurement techniques, radiography to measure spray density, phase contrast imaging to acquire high speed images, fluorescence to track atomic elements, and small-angle scattering to measure droplet size [1]. Each of these techniques complements other diagnostics by providing unique and useful information that cannot be obtained in other ways.

In the process of making these measurements, Argonne collaborates with industrial partners including engine and fuel injection system manufacturers. Industry access to these diagnostics increases the understanding of the fundamental science behind their products. The group also collaborates with spray modelers to incorporate this previously unknown information about the spray formation region into new models. This leads to an improved understanding of the mechanisms of spray atomization and facilitates the development of fuel injection systems designed to improve efficiency and reduce pollutants.

In addition to measurements of injectors and sprays, the group explores other applications of X-ray diagnostics for combustion research. Measurements of cavitating flows provide unique data to improve the fundamental understanding of internal fuel flow and its role in spray atomization, as well as the relationship between injector geometry, cavitation, and nozzle damage. Recent measurements have also evaluated the use of X-rays as a diagnostic for shock tubes, natural gas injectors, and spark ignition. These new applications broaden the impact of the work and help to improve the fundamental understanding in other areas important to advanced combustion, including fundamental chemistry, gas jets, and ignition.

Results

A significant amount of effort over the last several years has been spent performing experiments in collaboration with the Engine Combustion Network (ECN) [2]. This collaboration is led by Sandia National Laboratories, who defined a specific set of operating conditions and procured a set of shared identical hardware. Argonne uses its full suite of unique injector and spray diagnostics to contribute to the ECN community. This partnership puts Argonne's data in the hands of simulation groups worldwide, and maximizes the impact of the work on improving computational simulations of sprays, combustion, and engines. In Fiscal Year 2017, high resolution measurements of the flow passages inside the ECN "Spray C" and "Spray D" diesel injectors were completed. These measurements have been shared with spray simulation groups worldwide, and are now being incorporated into high fidelity computational fluid dynamics (CFD) simulations. A noteworthy example of this collaboration is shown in Figure I.7.1. Here, we see the results of CFD simulations done at the University of Perugia using Argonne's data. The image at left shows the liquid (green) emerging from the nozzle (red) when simulated using the ideal, nominal nozzle geometry. At right, the nozzle geometry measured using Argonne's X-ray tomography was used. While the simulations using the ideal geometry show a smooth liquid jet emerging from the nozzle, the real geometry generates a liquid jet that is more complex, with an asymmetric distribution and corrugated features that generate faster spray breakup and mixing. Comparing the two simulations reveals the significant impact that the geometric imperfections can have on the fuel as it emerges from the nozzle. Incorporating the real geometry in the simulations allows the CFD to better predict the fuel distribution, and ultimately to better predict engine performance and emissions.

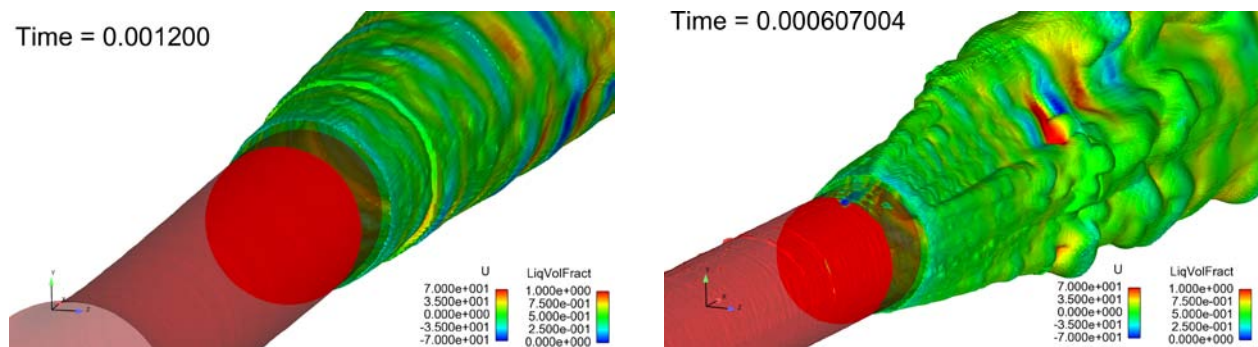


Figure I.7.1 - Simulations of flow through two diesel nozzles and the emerging liquid jets, courtesy of M. Battistoni at the University of Perugia. The results at left show the flow simulated using the nominal nozzle geometry. The results at right show the flow disturbances generated by the irregularities when using the realistic measured geometry.

Figure I.7.2 shows a 3D cutaway view through a GDI injector. This 3D geometry measurement is the result of collaboration between Argonne and Oak Ridge National Laboratories. The blue portions of the figure were measured at Oak Ridge using neutron tomography, while the grey portion containing the spray holes was measured using X-ray tomography at Argonne. This collaboration utilizes the strengths of the two techniques, neutron tomography's ability to penetrate through the thickest parts of the injector, and X-ray tomography's high spatial resolution at the spray holes where it is needed most. The full 3D geometry of the injector was used for CFD simulations of flow through the entire injector [3]. These simulations demonstrated the capability for 3D simulations of flow through an entire GDI injector, and captured pressure waves inside the body of the injector that could have an impact on fuel flow.

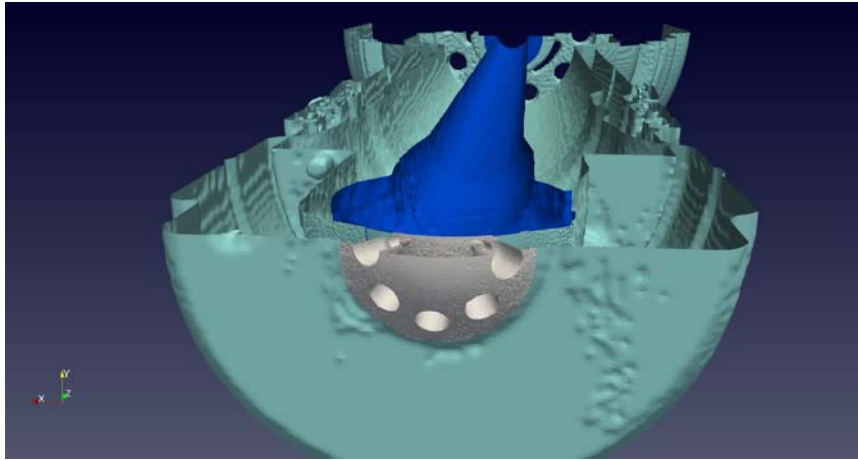


Figure I.7.2 - A cutaway through a GDI injector measured using a combination of X-ray and neutron tomography. Five of the eight spray holes are visible at the center of the image.

In Figure I.7.3, the cross-sectional density distribution of a diesel jet is shown as it first emerges from an injector. These data were acquired 100 mm downstream of the tip of the ECN Spray D injector at an injection pressure of 1,500 bar and ambient density of 22.8 kg/m^3 . Note that even though the spray hole for this injector has been shown to be nearly circular, the fuel distribution just 100 mm downstream deviates significantly from a circular shape. The distribution suggests that the fuel flow may separate from the injector wall in some locations, which is unexpected for this injector. Another interesting result of the measurement is that the maximum density of the fuel is approximately 750 mg/mm^3 , which is about 10% lower than the density of the bulk liquid fuel at room temperature. The reasons for this discrepancy are unknown and are under investigation.

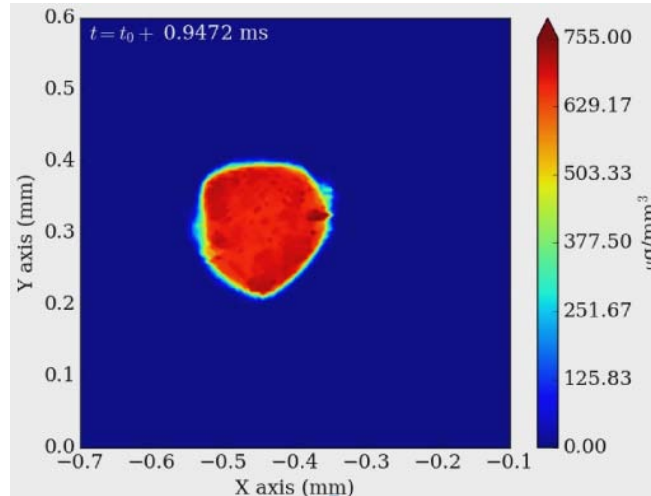


Figure I.7.3 - A cross section of the fuel density as the liquid jet emerges from a single-hole diesel injector

Conclusions

X-ray diagnostics can reveal the flows inside fuel injectors as well as the mixing of fuel and air in the engine. Such measurements are not possible using other imaging techniques and represent a powerful data set for validating computational models of fuel flow. This data is crucial for the development of accurate spray models and for the detailed understanding of spray behavior. Improvements to these models will speed the development of cleaner, more efficient engines.

References

1. Kastengren, A.L., and C.F. Powell. "Synchrotron X-Ray Techniques for Fluid Dynamics." *Experiments in Fluids* 55:1686, February 2014.
2. Kastengren, A.L., F.Z. Tilocco, C.F. Powell, J. Manin, L.M. Pickett, R. Payri, and T. Bazyn. "Engine Combustion Network (ECN): Measurements of Nozzle Geometry and Hydraulic Behavior." *Atomization & Sprays* 22 (12), pp 1011–1052 (2012).
3. Duke, Daniel J., Charles E.A. Finney, Alan L. Kastengren, Katarzyna E. Matusik, Nicholas Sovis, Christopher F. Powell, and Todd J. Toops. "High-resolution x-ray and neutron computed tomography of an Engine Combustion Network Spray G gasoline injector." *SAE Int. J. Fuels Lubr.* 10(2):328–343, 2017, <https://doi.org/10.4271/2017-01-0824>.

Key Fiscal Year 2017 Publications

1. Matusik, Katarzyna E., Daniel J. Duke, Alan L. Kastengren, and Christopher F. Powell. "X-Ray radiography measurements of the thermal energy in spark ignition plasma at variable ambient conditions." *SAE Int. J. Engines* 10(5):2017, <https://doi.org/10.4271/2017-24-0178>.
2. Duke, Daniel J., Alan L. Kastengren, Katarzyna E. Matusik, Andrew B. Swantek, Christopher F. Powell, Raul Payri, Daniel Vaquerizo, Lama Itani, Gilles Bruneaux, Ronald Grover, Scott Parrish, Lee Markle, David Schmidt, Julien Manin, Scott A. Skeen, and Lyle M. Pickett. "Internal and Near Nozzle Measurements of Engine Combustion Network "Spray G" Gasoline Direct Injectors." *Experimental Thermal and Fluid Science*, <https://doi.org/10.1016/j.expthermflusci.2017.07.015>.
3. Nguyen, D., D. Duke, A. Kastengren, K.E. Matusik, A.B. Swantek, C.F. Powell and D. Honnery. "Spray flow structure from twin-hole diesel injector nozzles." *Experimental Thermal and Fluid Science* 86, pp 235–247, <https://doi.org/10.1016/j.expthermflusci.2017.04.020>, September 2017.
4. Kastengren, A.L., J. Ilavsky, J. Viera, R. Payri, D. Duke, A. Swantek, F.Z. Tilocco, N. Sovis, C.F. Powell. "Measurements of Droplet Size in Shear-Driven Atomization Using Ultra-Small Angle X-Ray Scattering." *International Journal of Multiphase Flow* 92, pp 131–139, <http://dx.doi.org/10.1016/j.ijmultiphaseflow.2017.03.005>, June 2017.
5. Swantek, A.B., D.J. Duke, A.L. Kastengren, N. Sovis, C.F. Powell, L Bartolucci, R., Scarcelli, and T. Wallner. "An Experimental Investigation of Gas Fuel Injection with X-ray Radiography." *Experimental Thermal and Fluid Science* 87 pp. 15–29. <https://doi.org/10.1016/j.expthermflusci.2017.04.016>, April 2017.
6. Duke, Daniel J., Charles E.A. Finney, Alan L. Kastengren, Katarzyna E. Matusik, Nicholas Sovis, Christopher F. Powell, and Todd J. Toops. "High-resolution x-ray and neutron computed tomography of an Engine Combustion Network Spray G gasoline injector." *SAE Int. J. Fuels Lubr.* 10(2):328–343, 2017, <https://doi.org/10.4271/2017-01-0824>.
7. Pandal, A., J.M. Pastor, R. Payri, A. Kastengren, D. Duke, K. Matusik, J. S. Giraldo, C.F. Powell and D.P. Schmidt. "Computational and Experimental Investigation of Interfacial Area in Near-Field Diesel Spray Simulations." *SAE Int. J. Fuels Lubr.* 10(2):2017, <https://doi.org/10.4271/2017-01-0859>
8. Duke, Daniel J., Katarzyna E Matusik, Alan L Kastengren, Andrew B Swantek, Nicholas Sovis, Raul Payri, Juan P Viera, and Christopher F Powell. "X-ray radiography of cavitation in a beryllium alloy nozzle." *International Journal of Engine Research*, January 2017. <https://doi.org/10.1177/1468087416685965>.
9. Duke, D.J., A.L. Kastengren, A.B. Swantek, K.E. Matusik, C.F. Powell. "X-Ray Fluorescence Measurements of Dissolved Gas and Cavitation." *Experiments in Fluids* 57:162. <https://doi.org/10.1007/s00348-016-2250-5>, September 2016.

10. Baldwin , E.T., D.P. Schmidt, R.O. Grover, Jr., S.E. Parrish, D.J. Duke, K.E. Matusik, C.F. Powell, and A.L. Kastengren. "String Flash-Boiling in Gasoline Direct Injection Simulations with Transient Needle Motion." *International Journal of Multiphase Flow* (2016), pp. 90-101, September 2016.

I.8 RCM Studies to Enable Gasoline-Relevant Low Temperature Combustion

S. Scott Goldsborough, Principal Investigator

Argonne National Laboratory
9700 S. Cass Avenue
Argonne, IL 60439
E-mail: scott.goldsborough@anl.gov

Michael Weismiller, DOE Technology Manager

U.S. Department of Energy
E-mail: Michael.Weismiller@ee.doe.gov

Start Date: October 1, 2016 End Date: September 30, 2017
Total Project Cost: \$410,000 DOE share: \$410,000 Non-DOE share: \$0

Acknowledgments

Co-Authors

Jeffrey Santner, Dongil Kang; Argonne National Laboratory

Project Introduction

Accurate, predictive combustion models are necessary towards the reliable design and control of next-generation engines that are able to meet mandated fuel economy and emissions standards, with associated reductions in development times and costs for new configurations [1]. The imprecision of available models prevents adoption of detailed simulation techniques within current design processes. Existing engineering-scale models can achieve satisfactory performance at some operating points, however they are not sufficiently robust to cover complete ranges of conventional engine operation, or when novel/advanced combustion concepts are utilized. Towards this, there is a critical need to improve the understanding of the multiple physical and chemical processes that occur within combustion engines, including chemical ignition, fluid–chemistry interactions, and pollutant formation and decomposition. To advance these understandings, fundamental data are necessary which can be acquired at conditions that are representative of engine combustion chambers and can be acquired with sufficiently low experimental uncertainties. In particular, there is a lack of sufficient data which can be used to quantify the autoignition behavior of full boiling range fuels, formulate robust multi-component surrogate blends to replicate these fuels, and to develop and validate chemical kinetic models for individual constituents and blends. Moreover, the capability to accurately quantify and thereby reduce uncertainties in kinetic models for transportation fuels is not satisfactorily advanced.

Objectives

- Acquire autoignition data using Argonne National Laboratory’s (ANL’s) rapid compression machine (RCM) at conditions representative of today’s and future internal combustion engines, including high pressure ($P = 15\text{--}80$ bar), low-to-intermediate temperatures ($T = 650\text{--}1,100$ K), and a range of fuel loadings
- Collaborate with combustion researchers within DOE’s Vehicle Technologies Office and Basic Energy Science programs to accurately quantify uncertainties in chemical kinetic models in order to improve their predictability for a range of fuels

Approach

RCMs are sophisticated experimental tools that can be employed to acquire fundamental insight into fuel ignition and pollutant formation chemistry, as well as fluid–chemistry interactions, especially at conditions that are relevant to advanced, low-temperature combustion concepts, as well as boosted spark-ignition strategies [2]. They are capable of creating and maintaining well-controlled, elevated temperature and pressure environments (e.g., $T = 650\text{--}1,100$ K, $P = 5\text{--}80$ bar) where the chemically active period preceding autoignition

can be monitored and probed via advanced in situ and ex situ diagnostics. The ability to utilize wide ranges of fuel and oxygen concentrations within RCMs, from ultra-lean to over-rich (e.g., $\phi = 0.2\text{--}2.0+$), and spanning dilute to oxy-rich regimes (e.g., $O_2 = 5$ to $>21\%$), offers specific advantages relative to other laboratory apparatuses such as shock tubes and flow reactors, where complications can arise under such conditions. The understanding of interdependent, chemico-physical phenomena such as non-uniform ignition that can occur at some conditions within RCMs is a topic of ongoing investigation within the combustion community, while interpretation of facility influences on datasets is also being addressed [3]. Approaches to implement novel diagnostics which can provide more rigorous constraints for model validation compared to integrated metrics such as ignition delay times, e.g., quantification of important radical and stable intermediates such as H_2O_2 and C_2H_4 [4,5], are under development by many combustion researchers.

Argonne's twin-piston RCM is utilized in this project to acquire data necessary for a broad range of fuels, while improvements to the facility's hardware and data analysis protocol are performed to extend its capabilities and fidelity. Multi-disciplinary collaborations are undertaken at ANL and other U.S. laboratories, as well as with researchers at national and international institutions, including complementary RCM facilities.

Results

Key accomplishments for Fiscal Year 2017 include:

- Acquiring autoignition data over a range of conditions for bi- to multi-component surrogates of a research-grade, full boiling-range gasoline. Two surrogate blends were mixed with ethanol at varying fractions with responses to doping quantified; comparisons were made with ethanol-gasoline blends under identical conditions. Deficiencies in surrogate formulation methodologies were identified; deficiencies in gasoline chemical kinetic model were identified.
- Computationally investigating mild ignition phenomena using one-dimensional flame dynamics code. Identified physical and chemical parameters governing the process; formulated new scaling analyses to facilitate modifications to experimental design to avoid mild ignition.
- Acquiring autoignition data over a range of conditions for RD5-87, a research-grade full boiling range gasoline representative of U.S. market E10 (10% ethanol, 90% gasoline blend) regular gasoline (Research Octane Number = 92, Motor Octane Number = 84.5).

Experiments were conducted to evaluate the capabilities of state-of-the-art surrogate formulation methodologies towards replicating the autoignition behavior of a research-grade, full boiling range fuel and its blends with ethanol. FACE-F, one of the gasolines formulated by the Coordinating Research Council [6], was selected due to its mid-octane rating (Research Octane Number = 94.4, Motor Octane Number = 88.8) and fair compositional simplicity. Four surrogate blends covering bi- to multi-component formulations were tested [7]. These included PRF91.5 (n-heptane/iso-octane), TPRF-F (n-heptane/iso-octane/toluene), FGF-LLNL (n-heptane/iso-octane/toluene/1-hexene/cyclopentane), and FGF-KAUST (n-butane/2-methylbutane/2-methylhexane/iso-octane/1,2,4-trimethylbenzene/1-hexene/cyclopentane). These surrogates were originally created to facilitate chemical kinetic modeling of FACE-F, but to this point, no experimental measurements have been available for comparison against the full boiling range fuel, especially at low to intermediate temperatures and high pressure. In addition to testing the neat surrogates, their responses to ethanol blending were also investigated with comparisons made to the response of FACE-F to ethanol blending. The capability of a surrogate to properly replicate the blending effects of ethanol, or any other blending agent, is critical towards developing robust empirical correlations, as well as accurately simulating fuel effects in advanced combustion engines. Ethanol blend ratios of 10% v/v, 20% v/v and 30% v/v were explored.

Figure I.8.1 presents representative results for the neat fuels, i.e., E0 (0% ethanol), including the full boiling range gasoline and four surrogates. First stage and main ignition delay times are plotted as a function of inverse temperature ($T_c = 700\text{--}1,000$ K) and at two compressed pressures ($P_c = 21$ bar, 40 bar). Figure I.8.1a shows the PRF91.5 and TPRF-F results, where it can be seen that significant discrepancies exist in first-stage ignition trends (the two surrogates are significantly more reactive), as well as trends with temperature and pressure. Figure I.8.1b shows the FGF-LLNL and FGF-KAUST results with these demonstrating much closer

agreement with FACE-F. While FGF-KAUST is slightly less reactive than FACE-F, the overall trends with temperature and pressure are fairly close to the full boiling range fuel. Model results are also included in Figure I.8.1 using the most recent version of the Lawrence Livermore National Laboratory (LLNL) gasoline surrogate model. It is apparent that, in general, the experimental trends are replicated by the simulations, however there are discrepancies in the calculated ignition times. Collaborations with LLNL are underway to design additional experimental tests using the ANL RCM to improve the performance of the model.

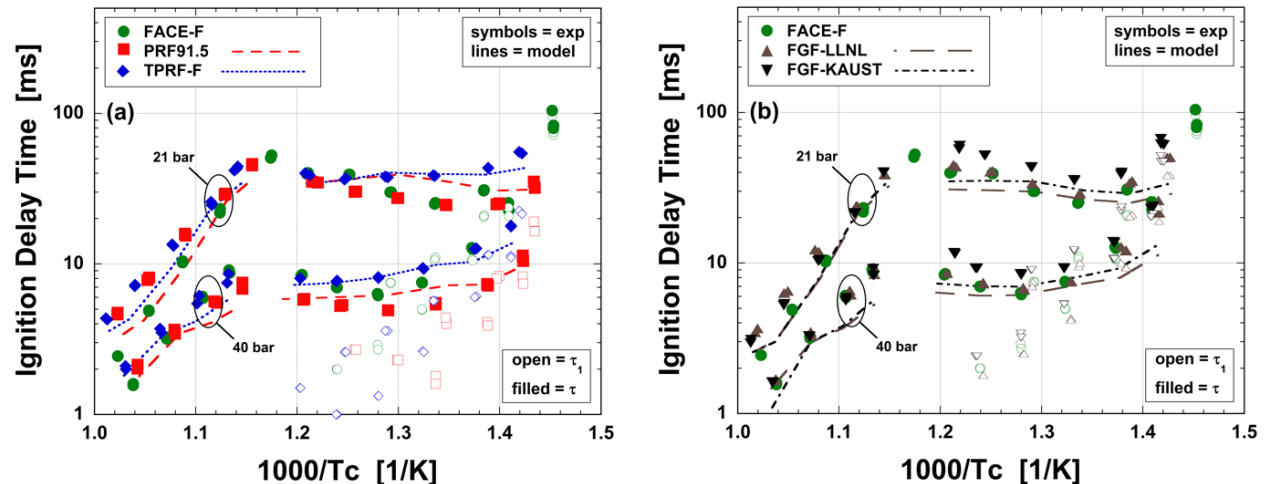


Figure I.8.1 - Experimentally measured (symbols) and modeled (lines) ignition delay times as a function of inverse temperature for FACE-F and various surrogate blends

Another topic investigated in Fiscal Year 2017 was the challenge of non-uniform ignition, sometimes termed mild ignition, which is a non-ideal process observed in some situations in RCMs, as well as shock tube and flow reactor experiments, where flames and/or reaction fronts initiate due to non-uniformities within the test mixture [8]. Experiments exhibiting mild ignition behavior cannot be used facily with comparisons against chemical kinetic models. This was encountered in previous work at ANL with cyclopentane [9]. In mild ignition tests, the propagating flames/fronts can consume the entire mixture or compression-heat the unburned gas forcing bulk autoignition at times advanced of homogeneous conditions similar to the evolution of engine knock. Optical techniques have been used previously to document the formation and growth of flames/fronts [10,11], and can be particularly beneficial when configured with large-access windows. However, optical setups are costly and can limit the achievable compressed conditions, as well as fuel loading due to structural constraints.

In an attempt to better understand mild ignition phenomenology and formulate approaches to identify suspect tests and/or mitigate it, numerical simulations of hot-spot initiated mild ignition were undertaken. Characteristic features in the simulations were found to be similar to those observed in previous RCM experiments. The computational fluid dynamics setup utilized a spherically symmetric configuration with a centrally located, Gaussian-distributed temperature non-uniformity. Reflective boundary conditions were applied at the far-field (2 cm). Dynamic meshing (3.9–500 μm) enabled the flames to be fully resolved with detailed chemistry employed. Only subsonic regimes were considered with syngas blends ($\text{CO}/\text{H}_2 = 80/20$) used as the fuel mixed with air at $\phi = 0.2$ and 0.5 . A wide range of temperature and pressure were spanned ($T = 900\text{--}1,120$ K, $P = 1.5\text{--}15$ bar), while the singular hot-spots covered sizes of 0–2 mm at temperatures of 1–90% greater than the surroundings, i.e., $T' = 1.01\text{--}1.90$.

Representative results are presented in Figure I.8.2 where pressure–time histories for six tests are shown with hot-spot sizes ranging from 0–1.0 mm, at a hot-spot temperature of $T' = 1.15$. Here, it can be seen that as the hot-spot size is increased the ignition time is advanced. This trend is caused by a reduction in initial thermal decay of the hot-spot owing greater heat retention caused by surface area: volume effects. This facilitates earlier hot-spot ignition and flame formation. The inset in Figure I.8.2 time-shifts the results to the point of bulk autoignition. With this it is clear that there is an extended period of slowly rising pressure, and associated

compression heating of the end gas before the autoignition event. This is due to the increasing time available for flame propagation, and thus fuel consumption, before the end gas is forced to ignite. Such features have been noted in numerous experimental studies of mild ignition [2].

Based on a wide range of parametric simulation results, new scaling analyses have been formulated that will enable modifications to experimental design to be conducted to avoid mild ignition.

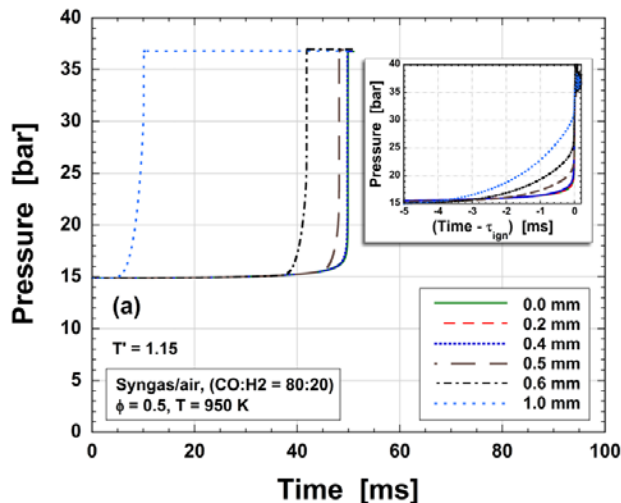


Figure I.8.2 - Representative pressure–time histories for syngas/ O_2 /diluent mixture illustrating the influence of hot-spot ignited flames. Inset time-shifts pressure traces corresponding to τ_{ign} , highlighting slow pressure rise due to flame propagation.

Finally, a sweep of experiments was conducted with RD5-87, a research-grade, U.S. market representative E10 gasoline covering a range of temperatures, pressures, and fuel loadings. Initial comparisons with chemical kinetic model predictions using the LLNL gasoline surrogate model are encouraging. Extended testing is planned in Fiscal Year 2018 with comparisons made not only against model predictions, but against experimental measurements using RD5-87 in Sandia’s Low-Temperature Gasoline Combustion engine.

Conclusions

- ANL’s RCM has been used to acquire autoignition data for bi- to multi-component surrogates of a full boiling range gasoline and blends of these with ethanol at various blending ratios.
- ANL’s RCM has been used to acquire autoignition data for a research grade, U.S. market-representative E10 gasoline over a range of conditions.
- Measured ignition delay times are combined with quantifications of pre-ignition heat release, i.e., low- and intermediate-temperature heat release, for chemical kinetic model validation and to identify deficiencies in state-of-the-art surrogate formulation methodologies.
- Detailed flame simulations are conducted to formulate a new approach to identify experimental conditions within ANL’s RCM that are susceptible to non-uniform ignition phenomena and create ways to avoid these.

References

1. McIlroy, A. “Basic Research Needs for Clean and Efficient Combustion of 21st Century Transportation Fuels.” DOE Office of Science. 2006. http://science.energy.gov/~media/bes/pdf/reports/files/ctf_rpt.pdf
2. Goldsborough, S.S., Hochgreb, S., Vanhove, G., Wooldridge, M.S., Curran, H.J., Sung, C.-J. *Prog. Energy Combust. Sci.* 63, 1–78, 2017.

3. Goldsborough, S.S., D. Longman, M.S. Wooldridge, R.S. Tranter and S. Pratt. "1st International RCM Workshop Meeting Report." August 28–29, 2012.
4. Bahrini, C., O. Herbinet, P.-A. Glaude, C. Schoemaeker, C. Fittschen, and F. Battin-Leclerc, *J. Am. Chem. Soc.* (139) 11944–11947, 2012.
5. Stranic, I., S.H. Pyun, D.F. Davidson, and R.K. Hanson. *Combust. Flame* (159) 3242–3250, 2012.
6. Coordinating Research Council. Report No. AVFL-24, 2014.
7. Sarathy, S.M., G. Kukkadapu, M. Mehl, T. Javed, A. Ahmed, N. Naser, A. Tekawade, G. Kosiba, M. Al Abbad, E. Singh, S. Park, M. Al Rashidi, S.H. Chung, W.L. Roberts, M.A. Oehlschlaeger, C.-J. Sung, and A. Farooq. *Combust. Flame* 169, 171–193, 2016.
8. Grogan, K.P., S.S. Goldsborough, and M. Ihme. *Combust. Flame* 162, 3071–3080, 2015.
9. Fridlyand, A., Goldsborough, S.S., Al Rashidi, M., Sarathy, S.M., Mehl, M., Pitz, W.J., *Combust. Flame*, 2018.
10. Walton, S.M, X. He, B.T. Zigler, and M.S. Wooldridge. *Proc. Combust. Inst* 31, 3147–3154, 2007.
11. Mansfield, A.B., and M.S. Wooldridge. *Combust. Flame*, 161, 2242–2251, 2014.

Key Fiscal Year 2017 Publications

1. Goldsborough, S.S., G. Vanhove, M.S. Wooldridge, H.J. Curran, C.J. Sung, S. Hochgreb. "Rapid compression machines: reducing the uncertainties in the low temperature combustion regime." *Progress in Energy and Combustion Science*, 63 (2017) 1–78.
2. Fridlyand, A., S.S. Goldsborough, M. Al Rachidi, M. Sarathy, M. Mehl, W.J. Pitz. "Experimental and modeling investigation of autoignition characteristics of substituted cyclopentanes at engine-relevant conditions." *Combustion Flame*, 2017.
3. Bourgeois, N., S.S. Goldsborough, M. Duponcheel, H. Jeanmart, F. Contino. "CFD simulations of rapid compression machines using detailed chemistry: evaluation of the 'crevice containment' concept." *Combustion Flame*, 2017.
4. Goldsborough, S.S., A. Fridlyand, R.H. West, M.J. McNenly, M. Mehl, W.J. Pitz. "Quantifying uncertainty in predictions of kinetically modulated combustion: application to HCCI using a detailed transportation fuel model." SAE World Congress (18PFL-0661), 2017.
5. Santner, J., and S.S. Goldsborough. "Quenching, ignition, flame propagation, and extinction in hot-spots at elevated temperature and pressure." 10th US National Combustion Meeting, College Park, MD, 2017.
6. Kang, D., A. Fridlyand, S.S. Goldsborough, M. Mehl, S. Wagnon, W.J. Pitz, and M.J. McNenly. "Chemical kinetic interactions of ethanol with a full boiling range gasoline and its surrogates at engine conditions." 10th International Conference on Chemical Kinetics, Chicago, IL, 2017.
7. Santer, J. and S.S. Goldsborough. "Hot-spot dynamics: quenching, ignition, flame propagation and extinction." 26th International Colloquium on the Dynamics of Explosive and Reactive Systems, Boston, MA, 2017.
8. "Progress towards robust surrogate formulation of ethanol-blended gasolines: insights from recent RCM measurements." AEC Summer Review Meeting, Detroit, MI, 2017.

I.9 Advances in High Efficiency Gasoline Compression Ignition

Stephen Ciatti, Principal Investigator

Argonne National Laboratory
9700 S. Cass Ave.
Bldg. 362
Argonne, IL 60439
E-mail: sciatti@anl.gov

Michael Weismiller, DOE Technology Manager

U.S. Department of Energy
E-mail: Michael.Weismiller@ee.doe.gov

Start Date: October 1, 2016	End Date: September 30, 2017	
Total Project Cost: \$420,000	DOE share: \$420,000	Non-DOE share: \$0

Project Introduction

Current diesel engines already take advantage of the most important factors for efficiency: no throttling, high compression ratio, and low heat rejection. However, diesel combustion creates a significant emissions problem. Mixing or diffusion combustion creates very steep gradients in the combustion chamber because the ignition delay of diesel fuel is extremely short. Particulate matter and NO_x are the result of this type of combustion, requiring expensive aftertreatment solutions to meet Environmental Protection Agency emissions regulations.

The current work seeks to overcome the mixing controlled combustion dilemma by taking advantage of the long ignition delay of gasoline to provide much more premixing of fuel and air before ignition occurs. This premixing allows for the gradients of fuel and air to be much less steep, drastically reducing the particulate matter– NO_x tradeoff relationship of mixing controlled combustion. In addition, this process leads to rapid combustion events, promoting higher efficiency.

Objectives

- Optimize the operating conditions to use low cetane fuel to achieve clean, high-efficiency engine operation
- Demonstrate the use of low temperature combustion as an enabling technology for high efficiency vehicles
- Develop injection approach for low combustion noise, Filter Smoke Number (FSN), and emission
- Investigate the effects of turbocharge boosting and low pressure exhaust gas recirculation (EGR) upon gas/thermal efficiency for different loads and speeds
- Identify a pathway to improve efficiency and meet all constraints for the entire engine map

Approach

As has been demonstrated in previous work, the single injection approach is not suitable or robust enough for gasoline compression ignition (GCI) operation over a wide range of loads due to the emissions trade-off and the difficulty in controlling combustion timing with early injection. More importantly, a single injection approach restricts the fuel stratification level opportunity. Indeed, using late single injection at high loads, very high injection pressure is necessary for rapid mixing to keep FSN low.

However, using a multiple injection strategy, a more desirable distribution of fuel stratification level can be delivered to meet all the requirements of emissions and combustion noise. The start of injection (SOI) of each injection of the multiple injection scheme can be determined based upon previous SOI sweep studies. For example, the first injection (pilot) should be, for this engine, near -70° after top dead center (aTDC) or earlier to provide quasi-homogeneous premixing of fuel and air. The second injection (main) should be between -40° and -50° aTDC where the transition from quasi-homogeneous charge compression ignition to stratified

combustion is expected. Finally, the last injection (post) should be reasonably close to top dead center, with the capability to influence ignition timing/combustion phasing.

In addition, the post injection should be no earlier than -30° aTDC, as this SOI band creates very high levels of reactivity of the charge that leads to early combustion and high combustion noise. With late post injection, modest levels of EGR (20–25%) coupled with increased injection pressure are effective in controlling NO_x emissions without undue penalties in FSN or combustion noise.

To achieve the objectives in Fiscal Year 2017, the engine was operated in GCI mode using previous work as a guide to determine the optimal parameters to pursue for increased efficiency while still meeting target goals for combustion noise, smoke, and gaseous emissions. To that end, the engine was operated at various engine speeds and medium-high engine loads with injection timing and EGR sweeps. This approach provided significant information regarding the tradeoffs between the variables.

Results

The engine was operated by utilizing several different injection approaches to determine the most likely conditions to lead to high efficiency while meeting emissions and noise targets. Triple injections were found to create the best opportunity to achieve the required level of fuel stratification for these goals. The timing of the injections was guided by past experience in how reactive the fuel–air charge becomes under these injection parameters. Fuel distribution between injections was also examined, as shown in Table I.9.1.

Table I.9.1 - Influence of Split Ratio upon Combustion Noise and Smoke (FSN)

Split Ratio	Pilot (%)	Main (%)	Post (%)	Noise (dB)	FSN
More in last injection	22	32	46	86.7	1.079
	25	35	40	91.5	0.211
More in premixes	26.5	37	36.5	94.7	0.122

The engine was then operated utilizing low pressure EGR to determine the influence of EGR upon efficiency and emissions. It was found that while EGR has a significant influence upon NO_x emissions, the efficiency penalty in this engine was substantial due to pumping losses needed to move the exhaust gas into the inlet of the turbocharger. In addition, the turbocharger duty cycle was found to have a major influence upon the gas-exchange or pumping efficiency of the engine. Previous work has shown that the reactivity of gasoline-type fuels is sensitive to boost pressure. However, the turbocharger on this engine provides relatively poor efficiency when the duty cycle (position of the variable vanes) is high; in effect, it becomes an exhaust throttle and degrades the gas-exchange efficiency significantly, as seen in Figure I.9.1. Even at higher loads (10–14 bar brake mean effective pressure [BMEP]), this effect was significant. This effect is reduced at higher engine speeds because there is more exhaust enthalpy available, even at modest loads.

However, other efficiencies, such as combustion efficiency, thermodynamic efficiency, and mechanical efficiency, were unchanged. Gas exchange efficiency was the most influential parameter influencing the overall brake thermal efficiency of the engine operating in GCI mode.

- An injection approach was developed to obtain desirable noise, soot, and emissions: triple injection (moderate to heavy stratification level) with high injection pressure (800 bar), see Figure I.9.2.
- Results from the speed/load sweep showed low combustion noise (~ 90 dB in most cases), however increase in FSN (>1.0) at high load (>14 bar BMEP). High combustion efficiency ($>99\%$) was achieved for all points.
- Higher EGR can reduce NO_x , but EGR availability was limited due to difficulty in operating the turbocharger for sufficient boost (gasoline reactivity is quite boost sensitive).
- Reduced turbocharger performance indicated a potential pathway to improve air handling (gas-exchange efficiency) and overall brake specific fuel consumption (20% relative change, based upon turbocharger duty cycle).

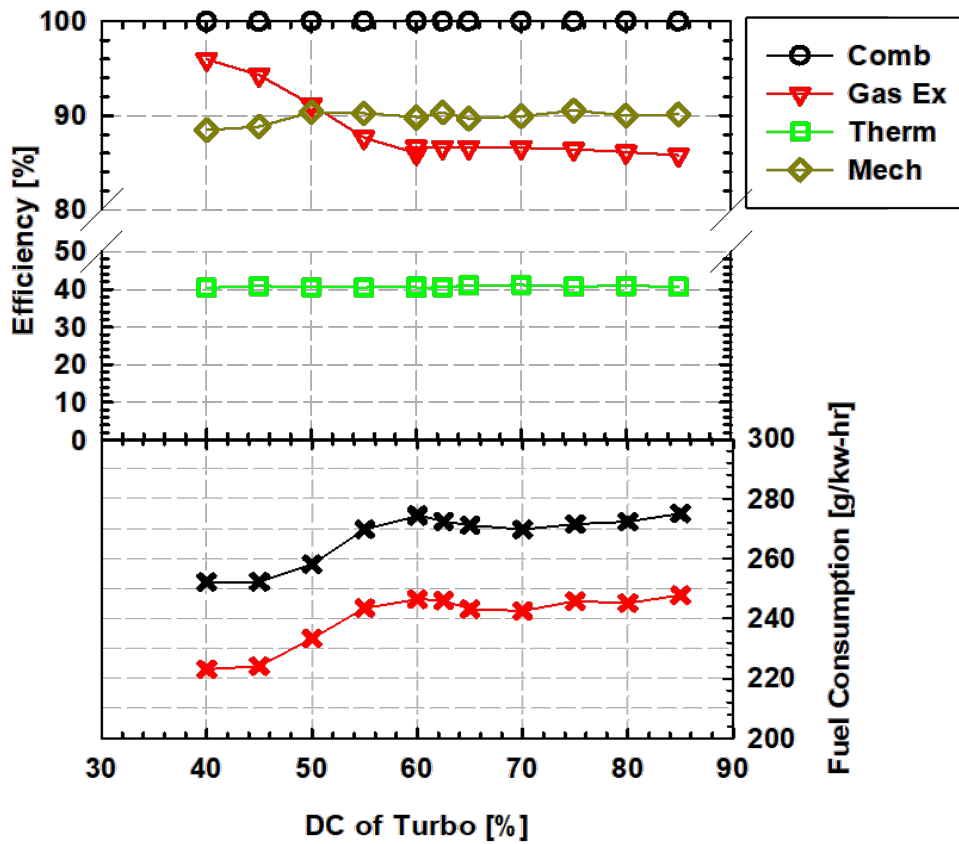


Figure I.9.1 - Influence of turbocharger duty cycle (DC) upon engine efficiency

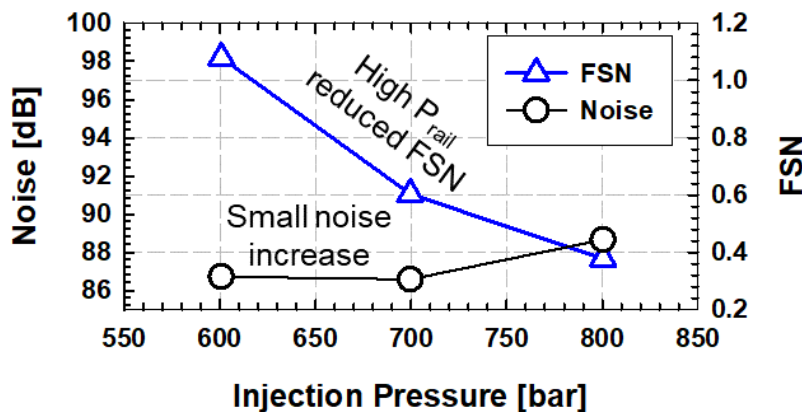


Figure I.9.2 - Influence of injection pressure upon smoke (FSN) and combustion noise

Conclusions

A study of injection strategy was carried out to improve combustion noise and FSN at high loads (8–14 bar BMEP) under GCI operating condition. Parameters including SOI of each injection (pilot, main, and post), EGR, split ratio, and injection pressure were varied. An optimized injection strategy was applied for each engine speed/load sweep. The current findings of this study are summarized below.

- SOI of pilot with a wide range of operation has very little effect on the combustion process. SOI of -70° aTDC was selected as the best option to avoid a high level of premixed combustion (from early injections) that would result in high combustion noise as engine load increases. There was a narrow range to operate the SOI of the main injection (-58° to -48° aTDC) with -50° aTDC being selected as optimal timing. Post

injection had a strong linear relationship with combustion phasing. Later injection gave lower combustion noise, but higher FSN.

- No EGR was used in engine load sweep, as higher EGR (up to 25%) led to high smoke and high heat release rate peak, thus high combustion noise.
- Change in the split ratio (distribution of fuel between injections) with more fuel in post injection was useful in reducing combustion noise. Combining with higher injection pressure of 800 bar, FSN was kept below 0.4 at 8 bar BMEP.
- High engine loads up to 14 bar BMEP were achieved with good control of combustion noise and low emissions of NO_x , hydrocarbons, and CO. However, FSN increased above 1.0 with an engine load of 13–14 bar BMEP.
- Further investigation to optimize turbocharger performance for improving gas exchange efficiency showed that a low DC of the turbocharger provided up to ~95% gas-exchange efficiency, thus higher brake thermal efficiency. However, poor air handling at this low DC decreases intake pressure (lower oxygen), resulting in higher FSN.
- Engine speed increasing from 1,000 rpm to 3,000 rpm delayed the combustion phasing, which reduced combustion noise. Similar emission performance and engine efficiency were maintained during engine speed sweep. Best engine speed for engine load sweep was suggested to around 2,000–2,500 rpm.

Key Fiscal Year 2017 Publications

1. Kodavasal, J., C.P. Kolodziej, S.A. Ciatti, and S. Som. “Effects of injection parameters, boost, and swirl ratio on gasoline compression ignition operation at idle and low-load conditions.” *International Journal of Engine Research*. November 2016.
2. Cung, K., M.T. Rockstroh, and S.A. Ciatti. “Parametric Study of Ignition and Combustion Characteristics from a Gasoline Compression Ignition Engine Using Two Different Reactivity Fuels.” ASME Technical Paper ICEF 2016-9395, ASME ICED Fall Technical Conference, Greenville, SC, October 2016.
3. Kodavasal, J., S.A. Ciatti, and S. Som, S. “Analysis of the Impact of Uncertainties in Inputs on CFD Predictions of Gasoline Compression Ignition.” ASME ICEF2016-9328, ASME ICED Fall Technical Conference, Greenville, SC, October 2016.

I.10 Advanced Ignition Systems for Gasoline Direct Injection (GDI) Engines

Riccardo Scarcelli, Principal Investigator

Argonne National Laboratory
9700 S. Cass Avenue
Lemont, IL 60439
Email: rscarcelli@anl.gov

Michael Weismiller, DOE Technology Manager

U.S. Department of Energy
E-mail: Michael.Weismiller@ee.doe.gov

Start Date: October 1, 2016	End Date: September 30, 2017	
Total Project Cost: \$410,000	DOE share: \$410,000	Non-DOE share: \$0

Project Introduction

Due to the United States' heavy reliance on gasoline engines for automotive transportation, efficiency improvements of advanced GDI combustion concepts have the potential to dramatically reduce foreign oil consumption. However, combustion strategies such as stratified, dilute, and boosted operation present challenging conditions for conventional ignition systems thereby limiting the attainable benefits of these advanced combustion concepts.

Advanced ignition systems for GDI engines enable the continued use of conventional combustion systems (reducing cost/risk) while providing potentially substantial benefits to fuel economy. In-depth understanding of the ignition physics and advanced ignition models will aid the development of dilution-tolerant, high-efficiency and low-emissions GDI combustion systems.

Objectives

This research program addresses the technological barrier of limited attainable GDI engine efficiency, due to the lack of robust spark ignition dilute combustion technology and controls which is essentially caused by:

- Limited GDI engine dilute operation.
- Limited assessment of advanced ignition systems enabling dilute combustion in GDI engines.
- Limited availability of modeling tools to evaluate and improve advanced ignition systems.

While the ultimate benefit is the improvement of GDI engine efficiency, the goal of this project is to expand the tools (knowledge and models) to enable significant improvement of the current ignition technology.

Approach

Modeling and experiments are both crucial components that allow an objective assessment of the potential of innovative ignition systems to be successfully implemented in production GDI engines. Advanced diagnostics from Argonne and project partners Sandia National Laboratories (SNL) and Michigan Technological University, are leveraged with the intent to enhance the fundamental understanding of ignition processes of nonconventional technologies and provide a valuable dataset for model validation. Improved understanding is leveraged to develop comprehensive models that can accurately describe nonconventional ignition processes. Simulations are performed with the engine code CONVERGE (Convergent Science) and the non-equilibrium plasma code VIZGLOW (Esgee Technologies). Novel simulation capabilities are intended to serve as a tool to evaluate the performance of advanced ignition systems and understand trade-offs with engine parameters by looking at fundamental interactions between the specific ignition source and the engine flow and thermal properties. The main tasks planned at Argonne are to:

- Conduct experiments that expand the basic knowledge of nonconventional ignition technologies and how those technologies perform at typical engine operation.
- Develop comprehensive and predictive ignition models for nonconventional ignition systems that can be used to accurately simulate the early combustion stages in a spark ignition engine.
- Use developed models to guide the research and development of advanced ignition systems to achieve highly dilute and highly efficient combustion in GDI engines.

Results

Major accomplishments in Fiscal Year (FY) 2017 can be listed as follows.

- Spark ignition model developed to include the effects of turbulence on the ignition source
- Laser ignition performance in GDI engines characterized by means of simulation and experiments
- Non-equilibrium plasma behavior characterized using optical and engine diagnostics
- Non-equilibrium plasma modeling initiated and validated against experiments

Spark Ignition Model Developed to Include the Effects of Turbulence on the Ignition Source

In FY 2016 the expanded energy deposition (ED) approach in CONVERGE that models spark ignition through deposition of thermal energy and provides realistic inputs to the ignition model was proposed and validated against experimental data from Michigan Technological University at quiescent conditions. Features like energy amount, release profile, shape of the energy source, and conjugate heat transfer calculations were shown to have a significant impact on the numerical results and be decisive to properly capture the experimental trend (ignition success or misfire) at challenging operation.

In FY 2017 the expanded ED model was evaluated at non-quiescent conditions, leading to the conclusion that the basic implementation in CONVERGE needs to be improved to properly manage the interaction of the ignition source (spark channel) with the in-cylinder flow. A dedicated user defined functions (UDFs) package was built into the CONVERGE framework to properly simulate the elongation of the spark channel as an effect of the flow as well as the thermal energy deposition along the spark channel. Results shown in Figure I.10.1 indicate that the developed ED approach is capable of capturing the effect of the turbulent flow on the spark channel elongation and delivering the spark energy consistently along the channel.

Laser Ignition Performance in GDI Engines Characterized by Means of Simulation and Experiments

In FY 2016 simulations using a simplified ED approach suggested that laser ignition could potentially match the performance of conventional spark systems at GDI dilute operation by leveraging the flexibility of laser systems, i.e., placing the ignition source more central into the combustion chamber and far from the walls. Simulations results showed improved combustion metrics and indicated efficiency by progressively protruding the ignition point up to 4 mm with respect to the original location (equivalent to the spark plug center gap).

Experimental validation was carried out in FY 2017 to investigate and characterize the interaction between the ignition source from laser systems and the in-cylinder turbulent flow. Improvements in terms of indicated efficiency, combustion duration (CD), and flame development angle (FDA) were observed experimentally by using laser as compared to conventional spark, in particular when running the engine in its original low-tumble configuration (i.e., without tumble plates in the intake ports). However, high-tumble operation was beneficial to conventional spark and detrimental to laser ignition (see Figure I.10.2, COV_{IMEP} plot). More detailed analysis of the engine data revealed that misfires were likely to occur at low-dilution operation for laser ignition, in particular in a highly-turbulent environment (high-tumble configuration and protruded ignition location). This had a negative effect on FDA and combustion stability. This joint numerical and experimental analysis has concluded that laser ignition still holds a potential for improved performance with respect to conventional spark, nevertheless a major effort has to be put in stabilizing the early flame kernel growth. In addition, laser ignition models (still based on the ED approach) need to be refined to capture misfires.

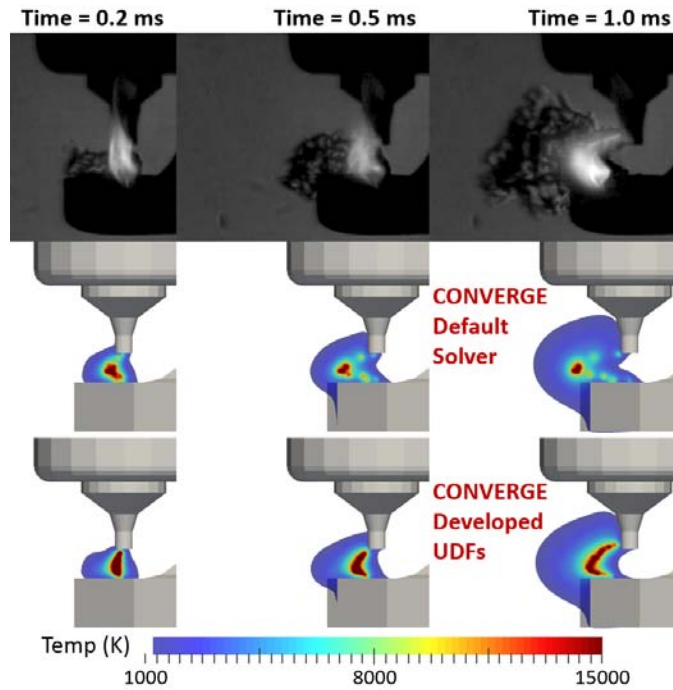
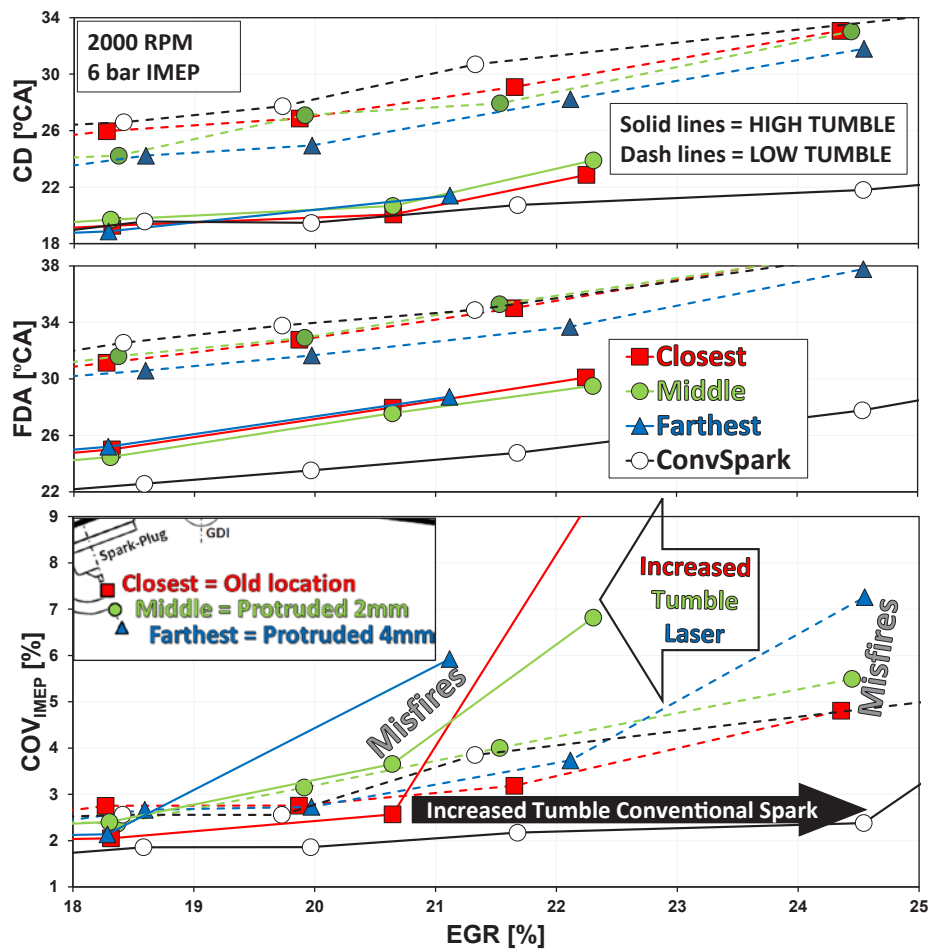


Figure I.10.1 - Improved model of the spark channel elongation and energy deposition at non-quietest flow conditions



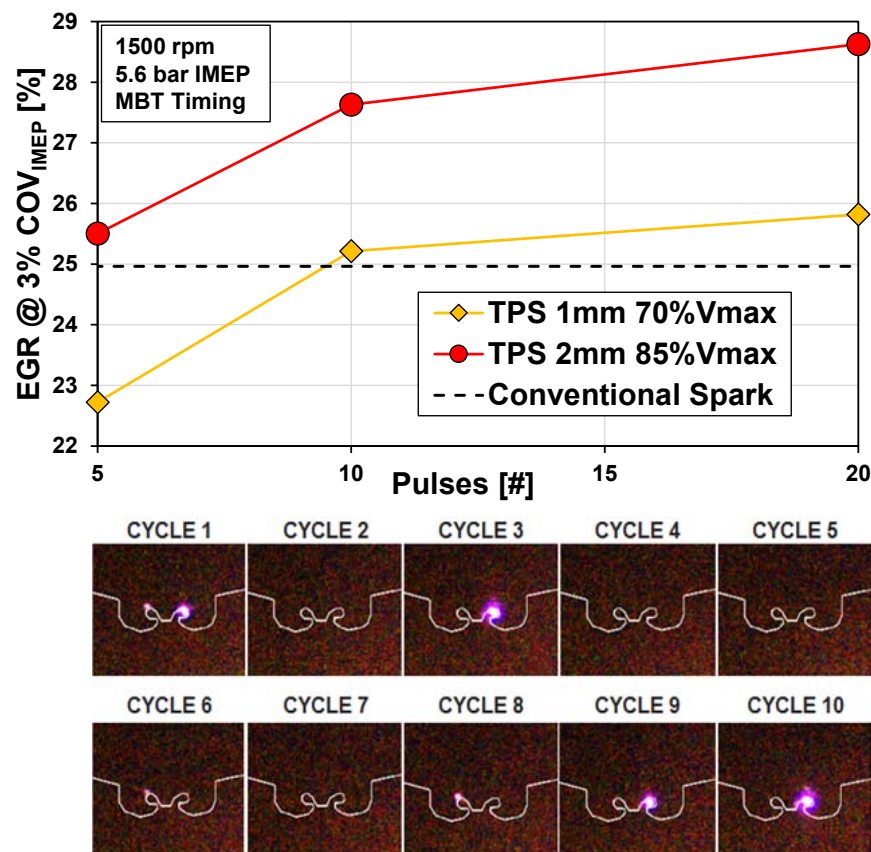
COV_{IMEP} – coefficient of variation in indicated mean effective pressures; °CA – degrees crank angle

Figure I.10.2 - Impact of in-cylinder turbulence on the performance of laser ignition and conventional spark

Non-Equilibrium Plasma Behavior Characterized using Optical and Engine Diagnostics

In FY 2017 a joint effort was carried out between Argonne and SNL to investigate the impact of operating conditions on the characteristics of non-equilibrium plasma generated by a nanosecond pulsed discharge (NPD). Both X-ray radiography at Argonne and optical diagnostics from calorimetry experiments at SNL indicated that the low-temperature plasma (LTP) regime can turn into an undesired arc event depending on ambient density, voltage applied to the electrodes, and size of the gap between the electrodes. SNL experiments also identified thermal pre-conditioning of the mixture in the gap as the major reason for the transition LTP-to-arc during a sequence of consecutive pulses in a multi-pulse mode.

Metal engine testing carried out at Argonne showed that an NPD ignition system can surpass the performance of conventional spark systems, in particular when multiple pulses, high voltage, and large gap sizes are used (see Figure I.10.3, top). This also implicates that further improvement in terms of engine dilution tolerance can be achieved by acting on these parameters. However, endoscopic access on the metal engine indicated that at high voltage the occurrence of undesired arc events might increase. Arcing can occur only in some of the engine cycles and can change location from cycle to cycle (see Figure I.10.3, bottom). It was also observed that LTP-to-arc transition can likely occur in a multi-pulse delivery. In that case, after the first arc event occurs, any subsequent pulse will generate an arc at the same identical location, consistently with the observation at Sandia and the assumption of pre-conditioning of the mixture in the gap.



EGR – exhaust gas recirculation; MBT – maximum brake torque

Figure I.10.3 - Improved dilution tolerance with non-equilibrium plasma systems versus conventional spark (top) and occurrence of arc events during the non-equilibrium discharge (bottom)

Non-Equilibrium Plasma Modeling Initiated and Validated Against Experiments

Following the experimental observations, the non-equilibrium plasma multi-dimensional modeling effort was initiated in FY 2017 to comprehensively characterize the LTP regime and the transition to arc. The VIZGLOW solver was used to mimic the experiments carried out at SNL and simulate the non-equilibrium plasma generated from a pin-to-pin electrode configuration with a single-pulse NPD at different ambient pressure

values. Simulations first evaluated the effect of ambient conditions (pressure) on the characteristics and dynamics of the generated streamers. Simulations matched the experimental observations consisting of slower, thinner, and increasingly branching streamers at increasing pressure values and correctly captured the transition from LTP regime to undesired arc at lower pressure values (see Figure I.10.4, top).

From a quantitative validation standpoint, simulations closely agreed with the experiments in terms of LTP-to-arc transition pressure threshold. Simulations predicted the transition to happen at 1.6 bar versus 2.2 bar from experiments. Several potential causes for the offset between experiments and simulations include the experimental uncertainty shown in Figure I.10.4 (bottom), where different gas bottles used in the experiments generated an offset in the transition pressure that is of the same order of the discrepancy between experiments and simulations. Other potential causes include the geometry of the electrodes (some irregularities not considered in simulations could enhance the local electric field and lead to faster streamer propagation and easier chance of arc events) and the relaxation of excited states (not included in the simulations) which could heat the gas and lead to easier breakdown. Not reported here, simulations also closely matched the time of occurrence of the arc event from experiments.

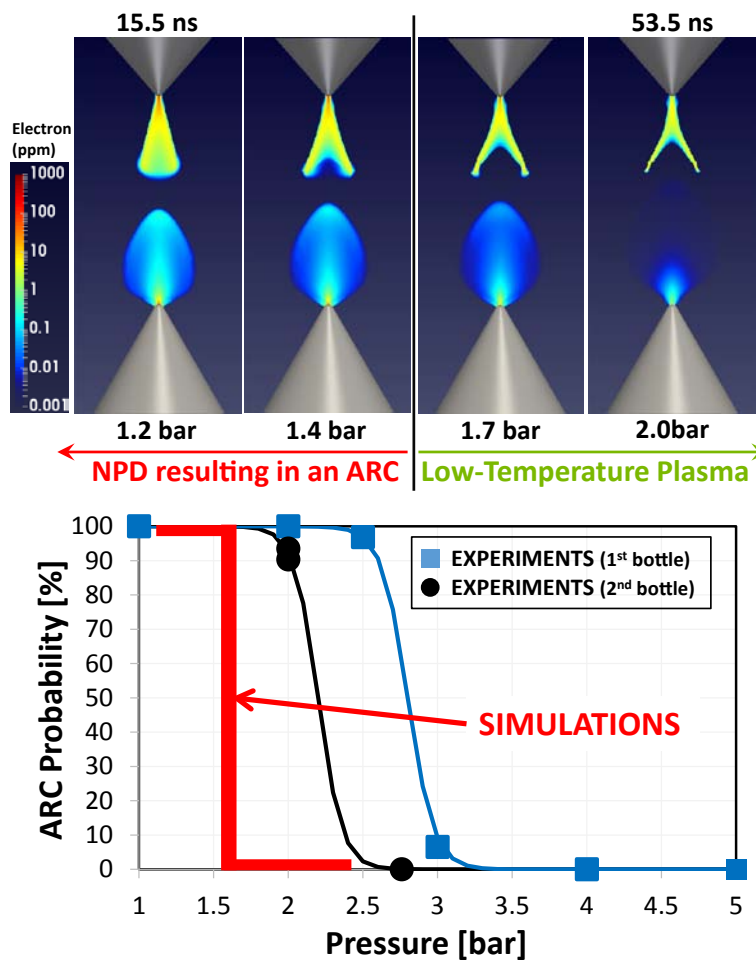


Figure I.10.4 - Effect of ambient conditions on the characteristics of the streamers (top) and transition from LTP to arc regime (bottom)

From a qualitative standpoint, simulations captured the chemical and thermal properties of LTP. While a side-by-side comparison of the same quantities between modeling and experiments was not possible, the effect of the ambient pressure on the distribution of active radicals within the streamers and on the streamer thickness was predicted by simulations (see Figure I.10.5, left). Simulations also confirmed that a non-negligible increase of temperature is to be expected even in the LTP regime, especially in the proximity of the electrodes

(Figure I.10.5, right). This confirms the assumption of thermal pre-conditioning of the mixture in the gap that can lead to an unexpected arc event between subsequent pulses in a multi-pulse discharge.

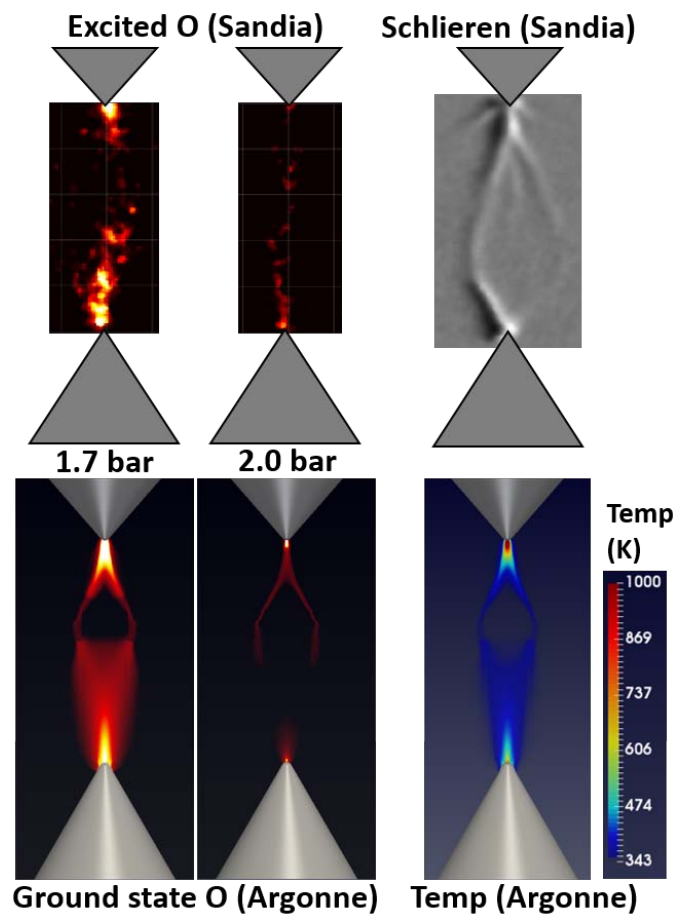


Figure I.10.5 - Qualitative comparison between modeling and experiments in terms of chemical (left) and thermal (right) LTP properties

Conclusions

This research project has continued to expand the knowledge and tools to properly characterize advanced ignition strategies for GDI engines. The main conclusions are listed below.

- The spark ignition modeling approach developed at Argonne was further improved to take the effect of turbulence on the ignition source (spark channel) into account. This is relevant to the DOE mission as GDI engines move towards operations (boosted and dilute) that are characterized by increasing turbulence levels.
- Laser ignition performance in modern GDI engines was characterized comprehensively through combined simulations and experiments. It was shown that laser still holds a potential for improvement versus conventional spark, nevertheless, strong turbulence has a negative effect on the early growth of the flame kernel generated with laser. Future research on laser ignition for GDI applications will have to focus on preventing misfires.
- Conventional and advanced diagnostics have clarified that the LTP ignition technology can surpass the performance of conventional spark systems but need to be properly understood in order to be successfully improved and optimized.

- Multi-dimensional modeling of non-equilibrium plasma was initiated and successfully validated against experiments. This is a novel research effort that can provide the proper knowledge and tools to guide the development of the LTP technology to improve the efficiency of GDI engines.

Future research work will invest on developing comprehensive ignition models that can cover the entire spectrum of advanced ignition technologies that enable high-efficiency GDI engines.

Key Fiscal Year 2017 Publications

1. Scarcelli, R. “Advanced Ignition Systems for GDI Engines.” 2017 DOE Annual Merit Review, Washington, D.C., June 2017 (oral presentation).
2. Scarcelli, R. “Advances in Modeling Ignition Processes to Enable High-Efficiency SI Combustion.” 2017 Fall AEC Program Review Meeting, Southfield, MI, August 2017 (oral presentation).
3. Scarcelli, R. “Development of a Predictive Spark Ignition Model for Dilute/Lean Engine Combustion Simulations.” 2017 CONVERGE User Conference, Detroit, MI, September 2017 (oral presentation).
4. Scarcelli, R. “GDI Combustion Work at Argonne: The Impact of Ignition Characteristics on Combustion Stability at Lean and EGR Dilute Operation.” 2017 VERIFI Workshop, Argonne National Laboratory, IL, November 2017 (oral presentation).
5. Scarcelli, R., Zhang, A., Wallner, T., et al. “Multi-dimensional modeling of non-equilibrium plasma for automotive applications.” SAE paper proposal 18PFL-0513, submitted to 2018 SAE WCX, currently under review.

I.11 High Efficiency Clean Combustion in Light-Duty Multi-Cylinder Engines

Scott J. Curran, Principal Investigator

Oak Ridge National Laboratory
2360 Cherahala Blvd.
Knoxville, TN 37830
E-mail: curransj@ornl.gov

Michael Weismiller, DOE Technology Manager

U.S. Department of Energy
E-mail: Michael.Weismiller@ee.doe.gov

Start Date: October 1, 2016	End Date: September 30, 2017	
Total Project Cost: \$310,000	DOE share: \$310,000	Non-DOE share: \$0

Acknowledgments

Co-Authors

Robert M. Wagner, Vitaly Prikhodko, Martin L. Wissink; Oak Ridge National Laboratory

Project Introduction

The goal of this project is to develop and assess the potential of reactivity stratified advanced combustion concepts on multi-cylinder engines for improved fuel efficiency and reduced emissions and, thereby, reduced petroleum use. The scope of the project focuses on the technical challenges of implementing advanced combustion concepts on production-viable multi-cylinder engines and includes addressing emissions with advanced emission control technologies (aftertreatment). More specifically, this effort includes investigating high-efficiency concepts developed on single-cylinder engines and addressing challenges related to dilution levels, heat rejection, boosting, thermal management, adaptive controls, and aftertreatment requirements. Work focuses on understanding the synergies between aftertreatment and combustion modes with the expectation that engines may operate in both conventional and advanced combustion modes (“multi-mode”).

Objectives

- Develop and assess the potential of single- and dual-fuel high efficiency clean combustion (HECC) concepts on multi-cylinder engines for improved efficiency and emissions
- Address barriers to meeting DOE Vehicle Technology Office goals of reducing petroleum energy use (engine system) including potential market penetration with efficient, cost-effective aftertreatments
- Expand the HECC operational range for conditions consistent with real-world drive cycles in a variety of driveline configurations including down-sized and hybrid electric
- Characterize low temperature combustion implementation losses on thermodynamic basis including hardware effects to better identify the associated opportunities, barriers, and tradeoffs
- Characterize the controls challenges including transient operation and fundamental instability mechanisms which may limit the operational range of potential of HECC
- Understand the interdependent emissions and efficiency challenges including integration of exhaust aftertreatments for HECC and multi-mode operation

Approach

The approach taken for this project is a combination of engine experiments along with computational fluid dynamics (CFD) and one-dimensional modeling for further insight and guidance for achieving higher efficiency with advanced combustion concepts. These advanced low temperature combustion (LTC) concepts

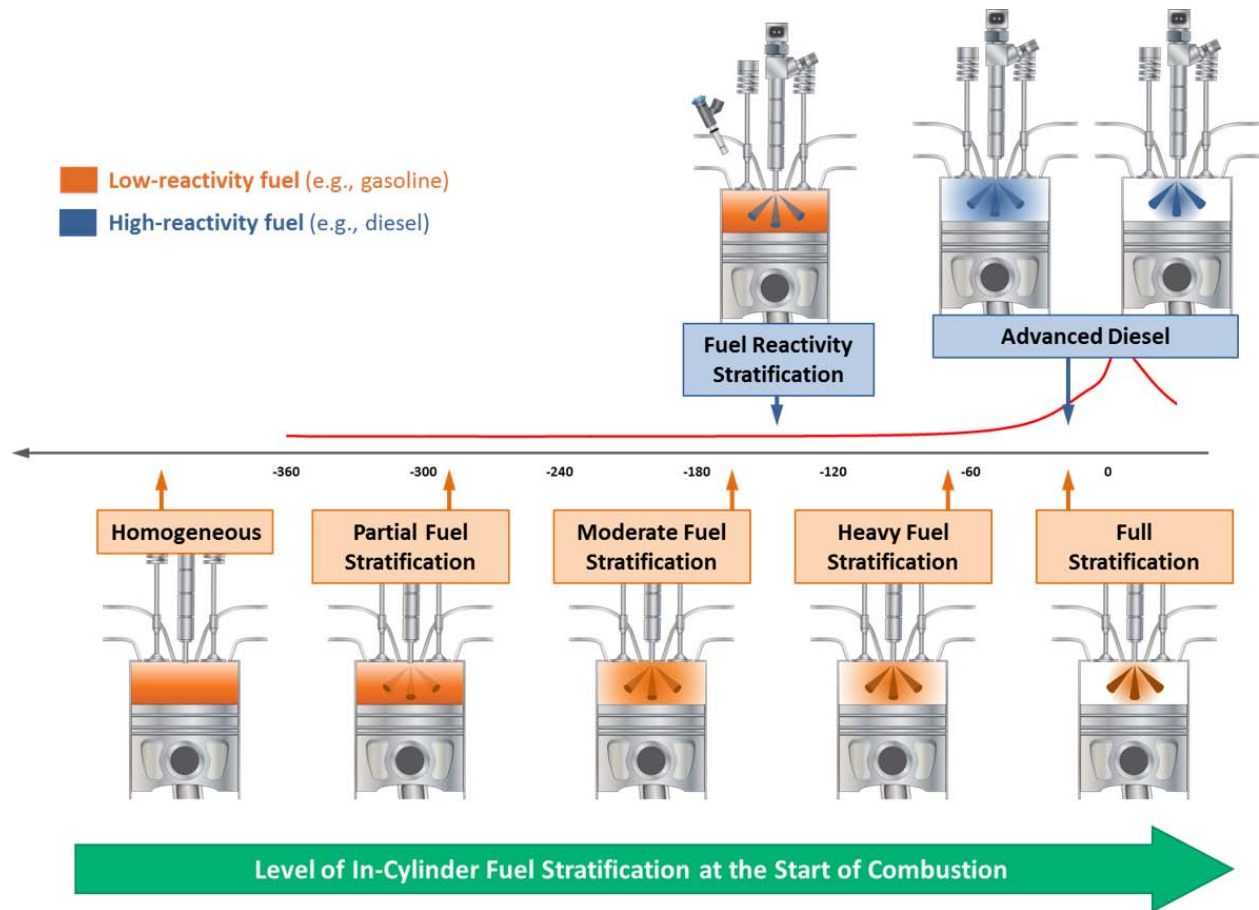


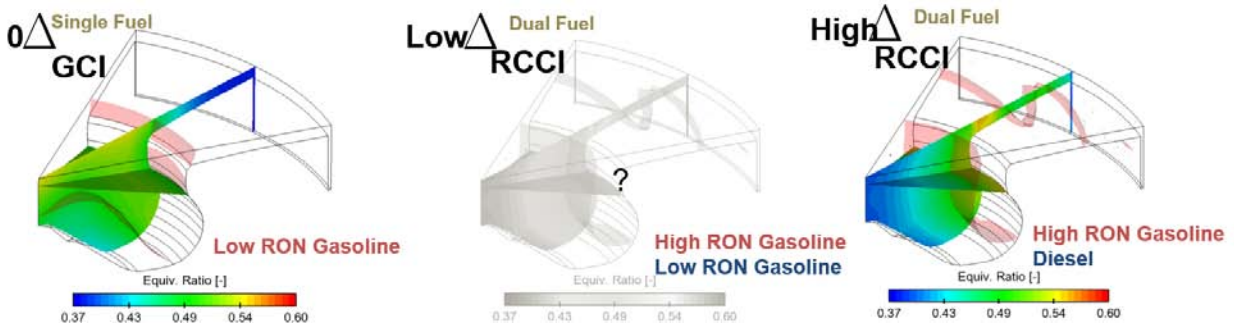
Figure I.11.1 - Advanced combustion strategies shown as a continuum based on the level of fuel stratification at start of combustion

can be either single-fuel or dual-fuel and can span a wide spectrum of stratification of reactivity at start of combustion as shown in Figure I.11.1.

A light-duty engine laboratory capable of both steady-state and transient engine experiments is in operation based on a modern 1.9-L common rail turbocharged diesel platform with moderate swirl. This research platform has advanced and flexible control systems that enable non-standard fuel delivery approaches, permit the override of all engine control parameters, and enable new control schemes to be evaluated on-engine. Single- and dual-fuel LTC are investigated on their own and as part of a multi-mode strategy. For advanced combustion modes that are not able to achieve the engine speed and load coverage (power density) needed to operate over the light-duty drive cycles, it is expected that future engines may operate in both conventional and advanced combustion modes. Technical challenges associated with transient operation of advanced combustion, as well as transient emissions, can also be addressed using this facility. For both full-time and multi-mode operation, it is important to understand the energy use implications of meeting current and future emissions control requirements. Integration of the engine and emissions control activities at Oak Ridge National Laboratory provide an avenue for detailed study of the aftertreatment integration issues for advanced combustion approaches. The use of CFD modeling and cycle simulations are integrated to accelerate the development of advanced combustion modes and enhance analytical capabilities on understanding the opportunities and challenges of achieving high engine efficiency and minimizing engine out emissions. In addition, thermodynamic analysis is used to perform a comparative analysis between measured and modelled efficiency to illustrate fundamental sources of efficiency reductions or opportunities inherent to various advanced combustion modes. The combination of these research capabilities and analytical tools permits a thorough and detailed study of the critical technical issues associated with the implementation of advanced combustion approaches. Collaborations with industry, university, and national laboratory partners leverage expertise at Oak Ridge National Laboratory to meet the project objectives.

Results

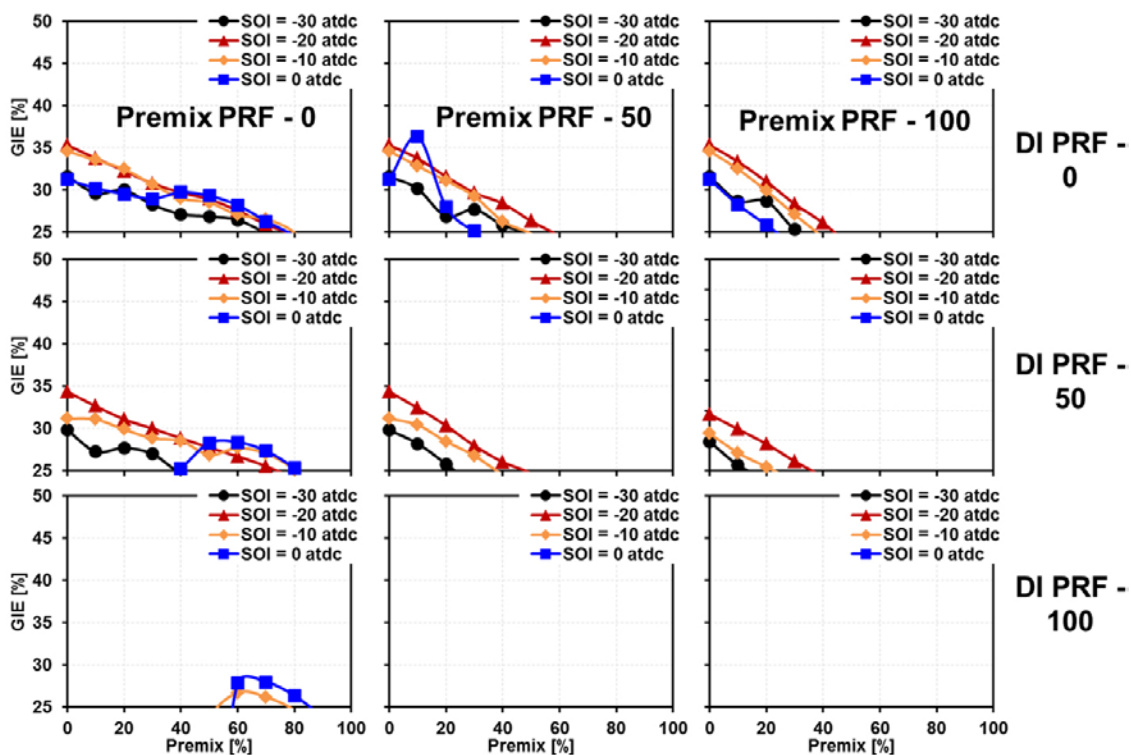
LTC concepts can use stratification of fuel reactivity to gain control over combustion phasing, duration and to control pressure rise rate and combustion noise. Single-fuel LTC approaches can achieve reactivity stratification through equivalence ratio and temperature stratification and dual-fuel approaches have the additional ability to set up fuel composition stratification. In previous years, this project had focused on dual-fuel approaches that used a large delta in fuel reactivity through fuel combinations such as port injection of high octane gasoline and direct-injection of ultra-low sulfur diesel fuel, and single-fuel modes using a selected reactivity (Figure I.11.2).



GCI – gasoline compression ignition; RON – Research Octane Number; RCCI - reactivity controlled compression ignition

Figure I.11.2 - Concept of fuel reactivity stratification with single-fuel (GCI) to dual-fuel

To further understand the continuum of LTC concepts, this project investigated the narrowing of the delta in fuel reactivity to bridge the high delta dual-fuel approaches and single-fuel approaches. Dual-fuel engine experiments were performed a 2,000 rpm, 3.0 bar brake mean effective pressure with a port injection of a 70 RON gasoline and direct-injection (DI) of ultra-low sulfur diesel (Figure I.11.3). The start of injection (SOI) of the DI event was swept for different premixed ratios. While the results showed that the control authority over combustion phasing as a function of DI SOI was dimensioned with the low delta approach, it was

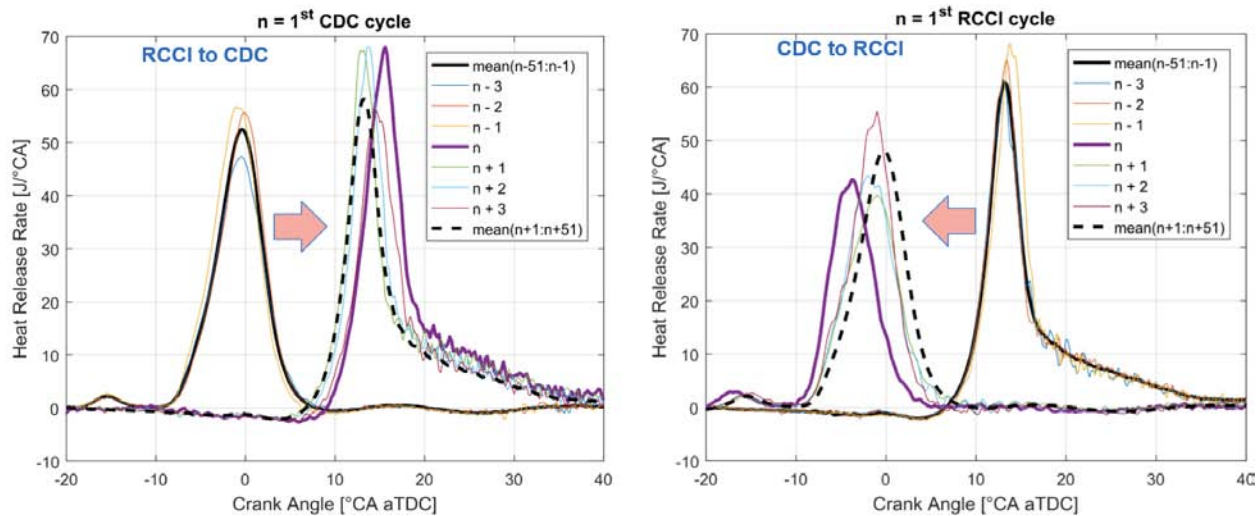


PRF – primary reference fuel; atdc – after top dead center; GIE – gross indicated efficiency

Figure I.11.3 - CFD modeling of RCCI across a span of delta in fuel reactivities

possible to match peak brake thermal efficiency at a similar combustion phasing with both approaches. Further experimental investigation is needed to see how more of the engine operating map would be affected. To help accelerate this, a collaboration with the University of Wisconsin to use CFD was employed to investigate the effect of narrowing the delta in fuel reactivity to a single-fuel over a wide speed and load range.

In addition to efficiency implications, it is also important to understand how changing the operational range of an LTC mode might affect multi-mode implementation including emissions controls challenges and opportunities. For both low and high delta dual-fuel LTC, the engine system can revert to conventional diesel combustion (CDC) in high load or very low load operation outside the LTC operating range. To better understand the combustion behavior during mode switching, as shown in Figure I.11.4, carefully controlled experiments were completed switching from LTC to CDC under different scenarios including zero exhaust gas recirculation (EGR) with matched boost, zero EGR with differing boost, matched combustion noise, and dual-fuel LTC to + dual-fuel CDC. High speed combustion analysis was performed on all four cylinders to investigate the cycle resolved combustion behavior. Compared to previous diesel only single-fuel LTC which required high amounts of cooled EGR to maintain low NO_x and soot, the high degree of control authority of with dual-fuel LTC allowed for rapid and stable mode switches between LTC and CDC modes. To better understand the emissions controls implications for mode switching, transient engine dynamometer experiments were performed for both repeated same engine speed and load mode switches and emulated drive cycles. A fast hydrocarbon measurement instrument was used to capture the behavior during these transients and the results of small spikes of hydrocarbon emissions correlated to unintended combustion phasing excursions.



aTDC – after top dead center; °CA – degrees crank angle

Figure I.11.4 - Control authority of RCCI allows for rapid and stable mode switches

Further analysis into loss mechanisms of LTC were completed in Fiscal Year 2017. The thermodynamic analysis approach first used in Fiscal Year 2016 was completed to perform a comparative analysis between measured and modelled efficiency to illustrate fundamental sources of efficiency reductions or opportunities inherent to various advanced combustion modes. The findings highlighted the importance of examining the measured efficiency in context of what is thermodynamically possible with the working fluid and boundary conditions prescribed by a strategy. Analysis of the implications of air handling with multi-cylinder implementations of advanced combustion concepts was completed for heavy fuel stratification GCI which requires high amounts of EGR and higher boost pressure than required for more premixed LTC modes. This analysis used a combination of experimental engine experiments and one-dimensional cycle simulation modeling to better understand the challenges with supplying the air handling requirements for LTC modes.

Conclusions

- Lower delta reactivity dual-fuel LTC shown to be able to match efficiency at lower loads, reduced control authority over combustion phasing
- One-dimensional model developed to inform decision on next generation air handling system
- Control authority of RCCI allows for rapid and stable mode switches between RCCI and mixing controlled combustion modes
- Thermodynamic analysis employed to quantify the effect of combustion phasing and duration on thermal efficiency

Key Fiscal Year 2017 Publications

1. Curran, S. and R. Wagner. "Range extenders as an enabling technology for future engines." 2016 SAE Rex Symposium, Knoxville, TN, November 2016.
2. Wissink, M., D. Splitter, A. Dempsey, S. Curran, B. Kaul, and J. Szybist. "An Assessment of Thermodynamic Merits for Current and Potential Future Engine Operating Strategies." *Int. J. Engine Res*, Vol 18, Issue 1–2, pp. 155–169, 2017. DOI: 10.1177/1468087416686698.
3. Curran, S. and R. Wagner. "Addressing Barriers to LTC From an International Perspective." IEA Technology Collaboration Programmes (TCP) for Clean and Efficient Combustion, 39th Task Leaders Meeting in Baiona, Spain, June 18–22, 2017.
4. Curran, S. and J. Storey. "Evolution and current understanding of physicochemical characterization of particulate matter from RCCI." 39th Task Leaders Meeting in Baiona, Spain, 2017.
5. Curran, S., and P. Chambon. "Transient Multi-Mode RCCI-CDC Experimental Results." AEC program review, Livermore, CA, February 2017.
6. Curran, S., and R. Wagner. "Low temperature combustion enabled by multi-mode including vehicle electrification." SAE International High Efficiency Engine Symposium, Detroit, MI, April 2017.
7. Hanson, R., S. Curran, et al. "Fuel economy and emissions testing of an RCCI series hybrid vehicle." *Int. J. Powertrains*, Vol. 6, No. 3, 2017.
8. Gowda Kodebyle Raju, N., A. Dempsey, and S. Curran. "Analysis of Engine Air Handling Systems for Light-Duty Compression Ignition Engines Using 1-D Cycle Simulation: Achieving High Dilution Levels for Advanced Combustion." ICEF2016-9459, 2016.

I.12 Stretch Efficiency for Combustion Engines: Exploiting New Combustion Regimes

James P. Szybist, Principal Investigator

Oak Ridge National Laboratory
2360 Cherahala Blvd.
Knoxville, TN 37932
E-mail: szybistjp@ornl.gov

Michael Weismiller, DOE Technology Manager

U.S. Department of Energy
E-mail: Michael.Weismiller@ee.doe.gov

Start Date: October 1, 2016	End Date: September 30, 2019	
Total Project Cost: \$880,000	DOE share: \$880,000	Non-DOE share: \$0

Acknowledgments

Co-Authors

Josh A. Pihl, Daniel W. Brookshear, Yan Chang; Oak Ridge National Laboratory

Project Introduction

The overarching goal of this project is to use a thermodynamics-based approach to identify and pursue opportunities for improved efficiency in internal combustion engines. The project is guided by combined input from industry, academia, and national labs, such as that summarized in the report from the Colloquium on Transportation Engine Efficiency [1]. The resultant strategy identified as the most promising approach to improving light-duty engine efficiency is high dilution from exhaust gas recirculation (EGR) for spark-ignited (SI) combustion enabled by fuel reforming through thermochemical recuperation (TCR).

The overall efficiency advantages for high EGR conditions are summarized in a thermodynamic modeling study by Caton [2] and include decreased pumping work, decreased heat transfer, and increased ratio of specific heat (γ). The amount of EGR that can be used is limited due to combustion instabilities, but the dilution limit can be extended for additional efficiency improvements with the use of high flame speed components, namely H_2 . This project is pursuing fuel reforming to generate H_2 in an effort to extend the EGR dilution limits for SI combustion in the most thermodynamically favorable way possible. Ideally, this involves using exhaust heat to drive endothermic reforming reactions to increase the chemical fuel energy to achieve TCR, a form of waste heat recovery.

Objectives

- Quantify the efficiency gain with the catalytic reforming strategy at an operating condition of 2,000 rpm, 4 bar brake mean effective pressure
- Determine the most thermodynamically favorable boundary conditions for the reforming catalyst at the engine operating condition studied
- Assess the fundamental reasons for the efficiency benefits observed

Approach

This project combines multiple experimental and simulation approaches to investigate thermodynamically favorable catalytic fuel reforming. Ideally, the reforming process is able to utilize waste heat in the exhaust to drive endothermic reactions to achieve TCR. The first experimental effort consists of synthetic exhaust gas flow reactor investigations to identify boundary conditions that produce thermodynamically favorable reforming. The results from the flow reactor experiments are used to guide multi-cylinder engine experiments. The engine experiments use an alternative engine configuration to supply the desired boundary conditions and

maximum EGR dilution while maintaining a stoichiometric air-to-fuel ratio in the engine exhaust, making it compatible with conventional three-way catalyst emissions control. The results presented in this annual report focus on the multi-cylinder engine investigations.

Two modeling efforts were also included in this study. The first utilized equilibrium calculations through the minimization of the Gibbs free energy to develop expectations of the fuel reforming thermodynamics using ANSYS Chemkin. The second modeling effort used computational fluid dynamics (CFD) to develop an understanding of the basis for the efficiency improvements. More specifically, the simulations were used to provide insight on in-cylinder temperature, heat loss, and γ of the in-cylinder contents with and without the reformed fuel.

Results

A schematic of the engine configuration used for the EGR loop reforming strategy being developed in this project is shown in Figure I.12.1. In this strategy, one of the cylinders has an isolated intake and exhaust manifold. The entirety of the exhaust from this cylinder is fed directly to the reforming catalyst, which then feeds into the intake for the remaining cylinders. In prior synthetic exhaust gas flow reactor experiments at Oak Ridge National Laboratory, it was found that significant reformate production requires a small amount of oxygen in the reformer feed. In the engine experiment, this is accomplished by operating the main combustion event in Cylinder 4 fuel-lean, but then using a post-injection when the exhaust valve opens to feed the catalyst the appropriate fuel-rich mixture.

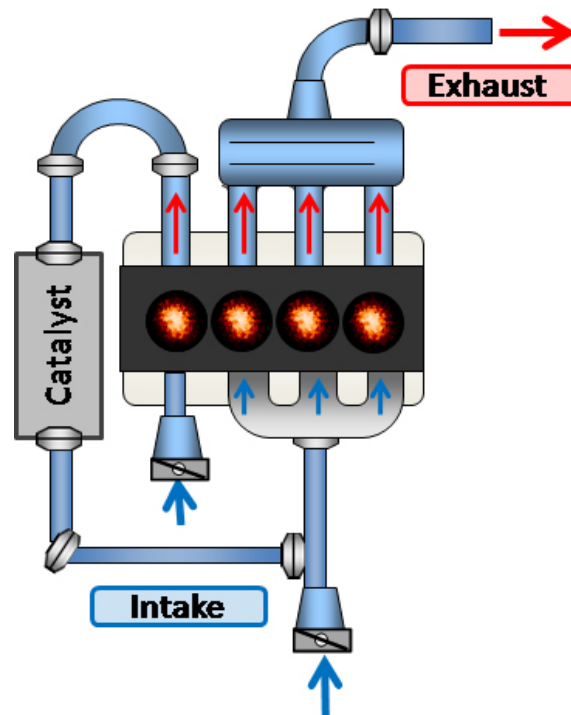


Figure I.12.1 - Schematic of the in-cylinder reforming process in which one cylinder has an isolated intake and exhaust, feeds the reforming catalyst, and is incorporated into the intake for the other three cylinders

In order to identify the expected reforming products across the feasible engine operating conditions, equilibrium calculations were performed. The results are shown in Figure I.12.2 as the enthalpy fraction of each reforming product (H_2 , CO , and CH_4) as functions of the initial O_2 mole fraction (which scales with total flow through the catalyst at a fixed equivalence ratio $[\Phi]$) and Φ . There is evidence of competing reactions above an initial O_2 mole fraction of 0.02, where $4 < \Phi < 6$ favors H_2 , but higher Φ favors CH_4 . The formation of CH_4 is not thermodynamically favorable in that it does not result in TCR, and it forms only when there is insufficient enthalpy in the mixture to convert the reactants to the final reforming products of H_2 and CO . Thus,

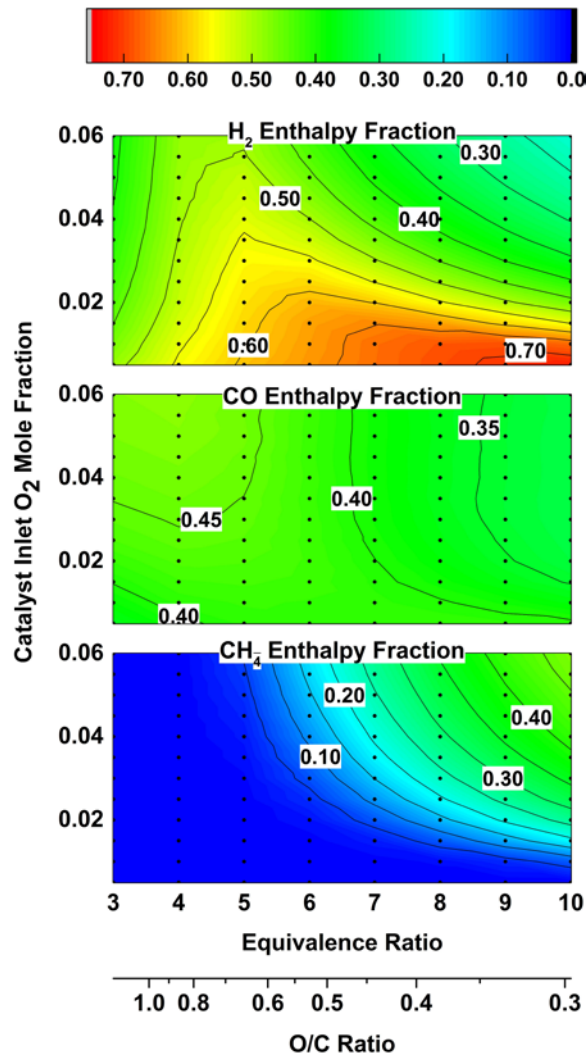


Figure I.12.2 - Enthalpy fraction of H₂, CO, and CH₄ at the catalyst outlet relative to the initial fuel with 700°C initial temperature for iso-octane

the thermodynamic modeling indicated that high initial O₂ mole fraction combined with high Φ were operating conditions to be avoided.

In applying the reforming strategy in the engine, the catalyst had a transient response when fuel injection was initiated to start the reforming event. The transient response, shown in Figure I.12.3, illustrates that while the catalyst inlet temperature remains nearly constant, there is a substantial decrease in the catalyst mid-bed and catalyst outlet temperatures, indicating endothermic reactions which are necessary to achieve TCR. The concentration of water in the exhaust further supports this, with a decrease in concentration from 10% to 5%. This shows that water is being consumed by steam reforming reactions that can yield TCR, and while doing so, produce a steady-state concentration of H₂ of 10–15%.

While a thermodynamically favorable reforming process is critical for an efficiency benefit, the manner in which the reformat is used in the other cylinders is also important. The components in reformat, principally H₂, have a high flame speed and are capable of reducing the cycle-to-cycle variability that occurs when dilution is added in SI engines, thereby allowing higher levels of EGR dilution while maintaining stable combustion. As a result, the engine is capable of operating with 45–55% EGR dilution on a volumetric basis compared to the stability limit of <25% with conventional EGR, which greatly reduces the pumping work of the engine. Figure I.12.4 illustrates the pumping work, quantified as the pumping mean effective pressure (PMEP) as a function of intake manifold pressure, for both conventional operation and with the reforming strategy. Pumping work in SI engines is one of the main efficiency penalties under part-load operating conditions.

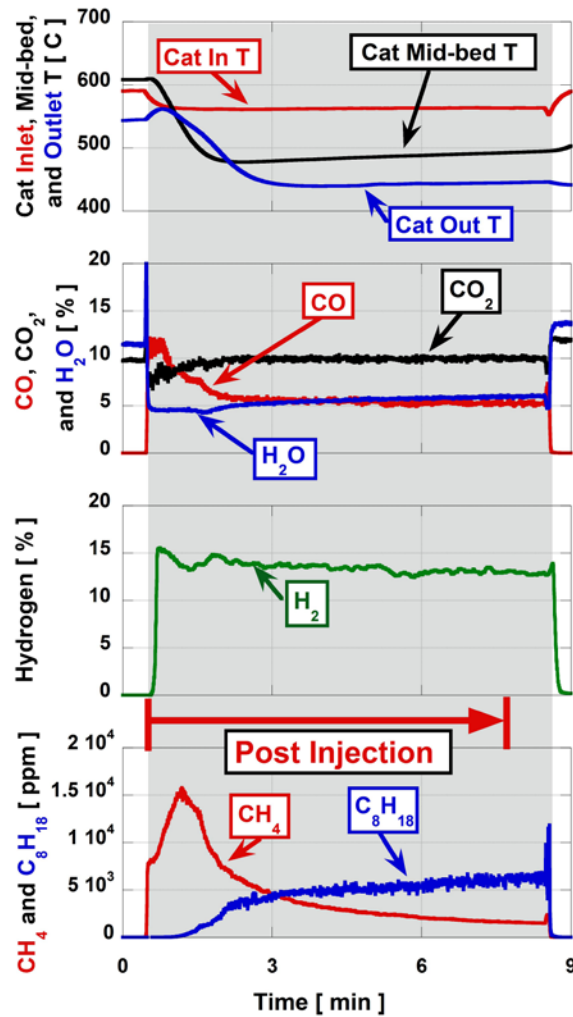


Figure I.12.3 - Transient response of the exit concentration of catalytic (Cat) reforming products and monolith temperature profile at an O₂ catalyst flow rate of 12 g/min and $F_{catalyst} = 7$

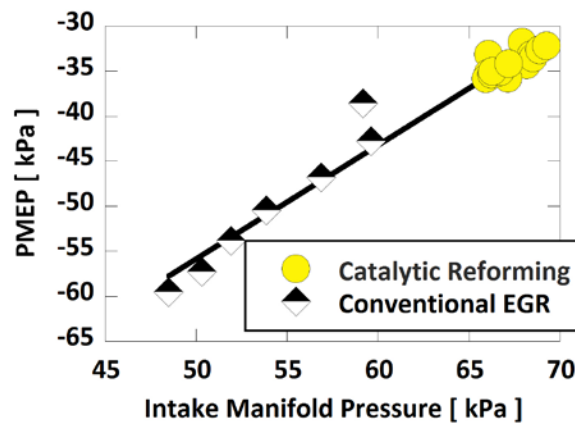


Figure I.12.4 - PMEP as a function of intake manifold pressure for conventional EGR and catalytic reforming

The resultant efficiency at an engine operating condition of 2,000 rpm and 4 bar brake mean effective pressure is shown in Figure I.12.5. The reforming strategy enables efficiency to be increased up to 32%, which is an increase of 2.5 efficiency points compared to conventional operation without EGR. This increase in efficiency represents a nearly 10% decrease in fuel consumption at this operating condition, which is significant.

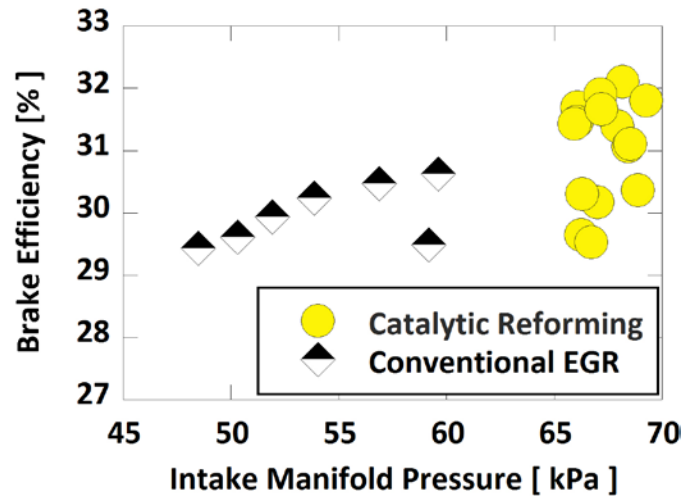


Figure I.12.5 - Brake thermal efficiency as a function of intake manifold pressure for conventional EGR and the catalytic reforming strategy

CFD modeling was used to help identify the mechanisms by which this efficiency gains in the engine experiments occurred. Figure I.12.6 shows a comparison of the in-cylinder temperature for conventional operation vs. the reforming strategy investigated in this work. There is a decrease in the temperature of the combustion gases of more than 550 K. The temperature decrease resulted in a reduction in heat transfer of 25% and an increase in γ . Together, these can account for an increase of 2 efficiency points, before taking into account the pumping benefits.

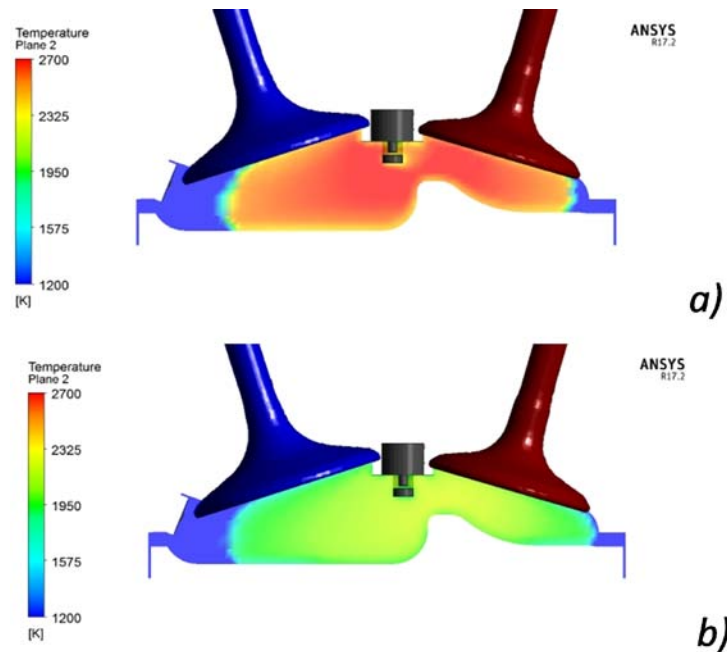


Figure I.12.6 - In-cylinder temperature of (a) conventional SI combustion and (b) the dilute combustion strategy supported by reforming. The high dilution reduces in-cylinder temperature by more than 550 K.

In addition to these efficiency benefits, there are additional benefits that could be obtained by further changing the engine configuration. Specifically, there is a strong possibility that efficiency could be increased with higher compression ratio without encountering knock, due to the cooler temperature associated with the dilution and the fuel properties of the reformed fuel.

Conclusions

- Achieved up to 10% reduction in fuel consumption with EGR loop reforming on a multi-cylinder engine
- Developed catalyst operating strategy to continuously produce >15% H₂ without coking
- Employed thermodynamic modeling of catalyst and CFD modeling of combustion to provide insight and paths forward on favorable operating conditions

References

1. Daw, C.S., R.L. Graves, R.M. Wagner, and J.A. Caton. "Report on the Transportation Combustion Engine Efficiency Colloquium Held at USCAR, March 3-4, 2010." ORNL/TM-2010/265, October 2010.
2. Caton, J. "A Comparison of Lean Operation and Exhaust Gas Recirculation: Thermodynamic Reasons for the Increases of Efficiency." SAE Technical Paper 2013-01-0266, 2013, doi:10.4271/2013-01-0266.

Key Fiscal Year 2017 Publications

1. Chang, Y., Szybist, J., Pihl, J., Brookshear, D. "Catalytic EGR-Loop Reforming for High Efficiency through TCR and Dilution Limit Extension. 1. Catalyst Performance and Fuel Effects." Submitted to *Energy & Fuels* for publication consideration, August 2017.
2. Chang, Y., Szybist, J., Pihl, J., Brookshear, D. "Catalytic EGR-Loop Reforming for High Efficiency through TCR and Dilution Limit Extension. 1. Engine Performance." Submitted to *Energy & Fuels* for publication consideration, August 2017.
3. Brookshear, D., Pihl, J., Szybist, J. "Catalytic Steam and Partial Oxidation Reforming of Liquid Fuels for Application in Improving the Efficiency of Internal Combustion Engines." Submitted to *Energy & Fuels* for publication consideration, August 2017.

I.13 Neutron Imaging of Advanced Transportation Technologies

Todd J. Toops, Principal Investigator

Oak Ridge National Laboratory
 1 Bethel Valley Road
 Oak Ridge, TN 37763
 E-mail: toopstj@ornl.gov

Michael Weismiller, DOE Technology Manager

U.S. Department of Energy
 E-mail: Michael.Weismiller@ee.doe.gov

Start Date: October 1, 2016 End Date: September 30, 2018
 Total Project Cost: \$800,000 DOE share: \$800,000 Non-DOE share: \$0

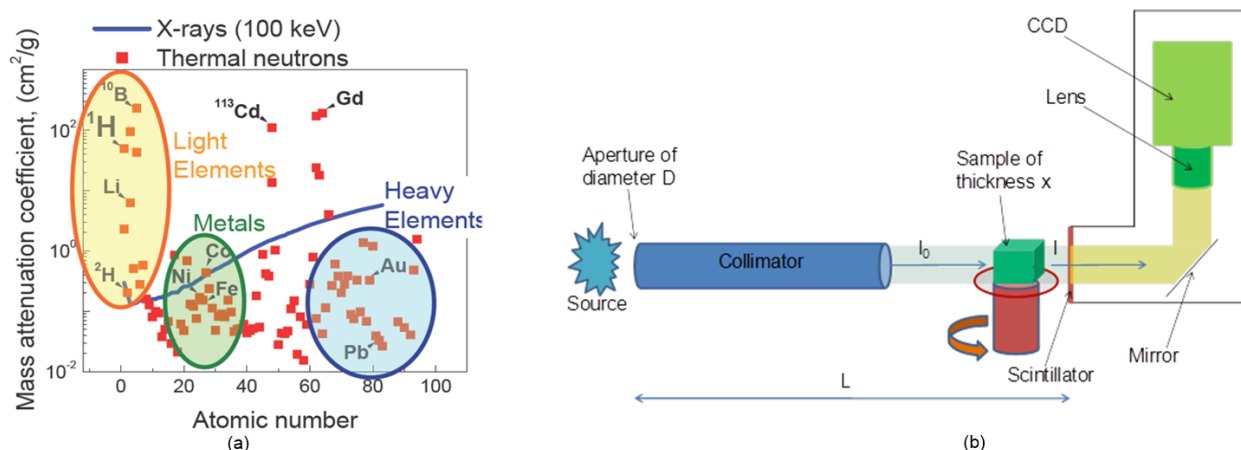
Acknowledgments

Co-Authors

Charles E.A. Finney, Eric J. Nafziger, Derek Splitter, Hassina Bilheux; Oak Ridge National Laboratory

Project Introduction

Unlike X-rays, neutrons are very sensitive to light elements such as hydrogen (H) atoms and can penetrate through thick layers of metals (Figure I.13.1a). These two properties suggest neutrons are well suited to probe engine parts such as diesel particulate filters, exhaust gas recirculation coolers, fuel injectors, oil in engines, oil residues in filters, batteries, advanced materials, etc. Neutron imaging is based on the interactions of a sample with a neutron beam. The interactions are dependent on sample thickness/density and elemental make-up and result in absorption and scattering of neutrons within the sample. A two-dimensional position-sensitive detector placed behind the sample can measure the transmitted neutron flux (Figure I.13.1b). When combined with a high-precision (~1/100 of a degree) rotational stage, it is possible to perform computed tomography (CT) scans and thus generate three-dimensional images of working fluids inside real devices. Samples can be analyzed at one position or a complete reconstruction can provide a cross-section of the entire sample at a resolution of the detector; the detector resolution is currently at ~50–80 microns (at the detector).



CCD – charged-coupled device

Figure I.13.1 - (a) Mass-attenuation coefficients versus atomic number, and (b) schematic of neutron imaging apparatus (Source: (a) Banhart [1], (b) Nanda et al. [2]).

Objectives

- Implement high-fidelity neutron imaging capabilities using the High Flux Isotope Reactor (HFIR) for advanced transportation research
 - Once fully developed, this advanced capability will allow the imaging of a range of processes that occur in advanced vehicle systems.
- Employ technique to aid improved design and control of complex advanced combustion systems and help to guide model validation and input
- Report findings to the research community and work with industrial partners to ensure research is focused on the most critical topics

Approach

This project is focused on using this unique neutron imaging capability to advance the understanding of two components being employed in modern vehicles: the in-cylinder fuel injector and the particulate filter. Recent efforts are aimed at investigating intra-nozzle fuel injector fluid dynamics while spraying. A specialized fuel delivery system and spray chamber are employed in this study that mesh well with the neutron beamline and gasoline direct injection-based injectors (Figure I.13.2). These efforts are designed to improve understanding of how injector design, external conditions, and fuel properties influence internal dynamics, especially as it relates to advanced combustion regimes and injector durability. Particulate filters are a key component of the emissions control system for modern diesel engines and possibly gasoline engines in the future, yet there remain significant questions about the basic behavior of the filters. In particular, understanding how ash, or non-regenerable metal oxide-based particulate, fills the particulate filter and interacts with the wall is a focus of this effort. The results of these measurements will provide important data to the aftertreatment modeling community on the soot and ash profiles, which change over the course of the vehicle's lifetime. In carrying out

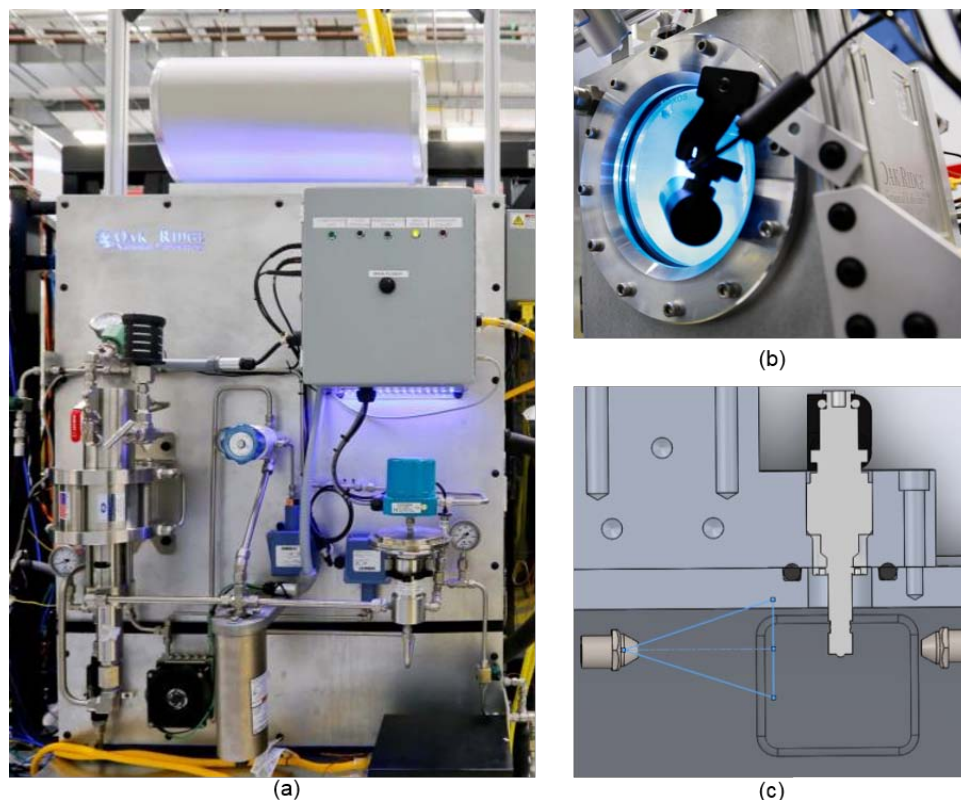


Figure I.13.2 - System used to study intra-nozzle dynamics of fuel injection including (a) high-pressure fuel delivery system and (b) the aluminum spray chamber with optical viewport. The spray chamber is designed with (c) directed fans to minimize fuel buildup on the chamber walls and the fuel injector.

these studies, we work closely with industrial partners to obtain relevant systems and devices. The proximity of our research facility to the neutron beam allows for iterative studies when appropriate.

Results

In the previous year, the dynamic imaging effort was refocused to facilitate coordination with the Engine Combustion Network (ECN). This global community has set guidelines as to which baseline experimental conditions should be employed and even goes as far as supplying injectors and other hardware. The experimental results can then be shared with the modeling community to help accelerate findings. This project is targeting two specific conditions prescribed for the Spray G injector. We can approximate the early injection conditions G2 and G3 in our current chamber and we can verify the amount of fuel that is being injected. Although we were not able to procure the specific eight-hole injector from the ECN, General Motors provided a single-hole injector that has the same internal geometries and injector hole sizes and angles.

Using the ECN-preferred fuel, iso-octane, a neutron imaging campaign was performed for the G2 and G3 condition at the end of Fiscal Year 2016. Analysis in Fiscal Year 2017 of these data focused on sac emptying rates for non-flash and flash spray conditions and on quantifying the spray mass based on estimated neutron-attenuation. This analysis seeks to quantify the fluid in the sac by estimating how much of the fuel entering the sac is in the liquid phase versus the vaporization in the sac. The low density of the vapor fuel essentially renders it invisible to neutrons, especially when compared with the liquid phase.

Figure I.13.3 depicts the process used to quantify liquid in the sac. An observation area of several pixels spanning the sac–nozzle interface is selected and a calibration plane in the injector barrel is chosen to relate intensity attenuation to a liquid mass based on the liquid density and a known neutron pass length through the injector based on prior CT scans. From the observed time record of the injection event, the mean attenuation profile in the observation area is calculated and then inverted to represent attenuation due to fluid. Using the calibration scaling, this detected fluid deviation is related to mass and a cumulative spray mass profile.

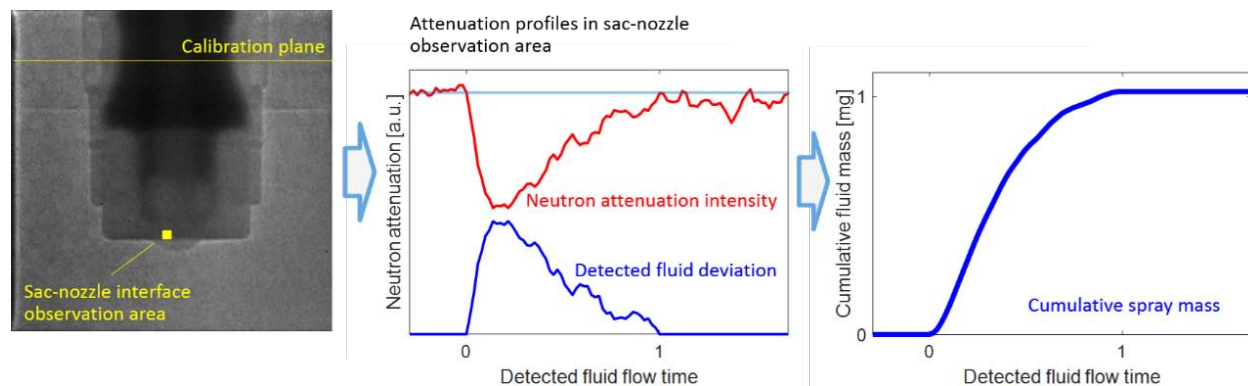


Figure I.13.3 - Detection and scaling of neutron attenuation by fluid to obtain cumulative injector spray mass

In the example depicted, the cumulative liquid mass was estimated to be ~ 1 mg (for a target of 1.125 mg). While this agrees well with the target, significant challenges remain to evaluate and account for various sources of noise and measurement uncertainty. Work in the coming year will focus on mitigating noise and quantifying the uncertainty of the mass calculations before specific conclusions can be drawn regarding liquid versus vapor mass fractions in the sac.

Additional ECN-relevant effort this year was in the publication of work to construct the full internal flow geometry using CT scans of the Spray G gasoline direct injection injector. In collaboration with Argonne National Laboratory (ANL), a two-part CT scan had been completed in Fiscal Year 2016 employing X-rays for the very tip of the eight-hole injector and neutrons in the thick metal section that is difficult to fully penetrate with X-rays. Figure I.13.4a shows a sagittal slice of the neutron CT of the injector, obtained at the HFIR at Oak Ridge National Laboratory, with an area surrounding the nozzle which was the focus of the high-resolution X-ray CT, obtained at the Advanced Photon Source at ANL.

Measured internal surfaces from both the neutron and X-ray CTs were merged using sophisticated co-registration software at ANL. The resulting surface model allowed for high-fidelity computational fluid dynamics simulations of the internal fluid dynamics (Figure I.13.4b). The construction of the internal surface model was significant in that it provided modelers with real-world production geometry, which often differs markedly from design specifications. These results were promulgated in the open automotive engineering literature this fiscal year.

Another area of focus continues to be particulate layers that are observed in gasoline particulate filter (GPF) studies. GPFs that were filled with particulate from a gasoline direct injection-based engine using either E0 or E30 (30% ethanol, 70% gasoline blend) were imaged at HFIR using CT techniques. The GPFs were originally filled to 4 g/L and then sequentially regenerated followed by imaging. This fiscal year saw two imaging campaigns for 60% and 80% regeneration levels. In contrast to diesel particulate filter (DPF)-based particulate layers, there is minimal decrease in thickness until 40% of the particulate is regenerated, as seen in Figure I.13.5a for E0 and Figure I.13.5b for E30. These differences in regeneration rates may be reflective of observed differences in activation energies, as seen in Figure I.13.5c, in soot produced from conventional diesel versus GPF engines. Work will continue in Fiscal Year 2018 to complete the study to 100% regeneration and to publish the results.

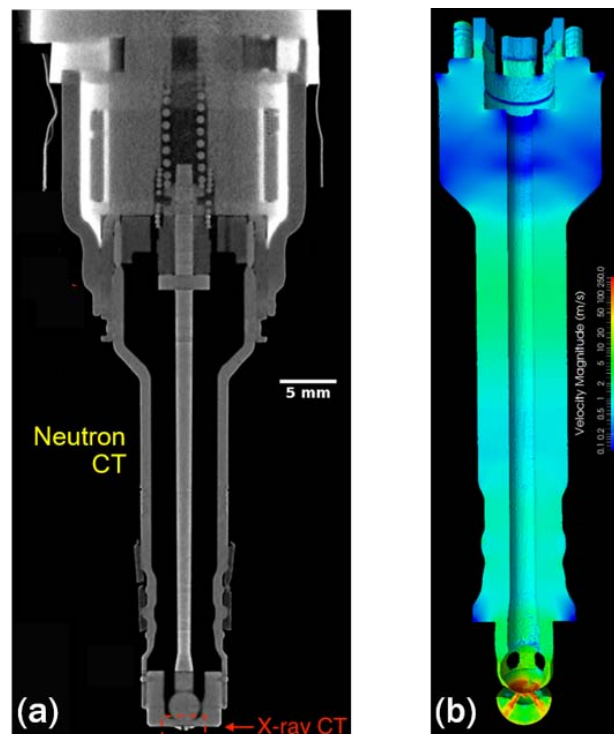
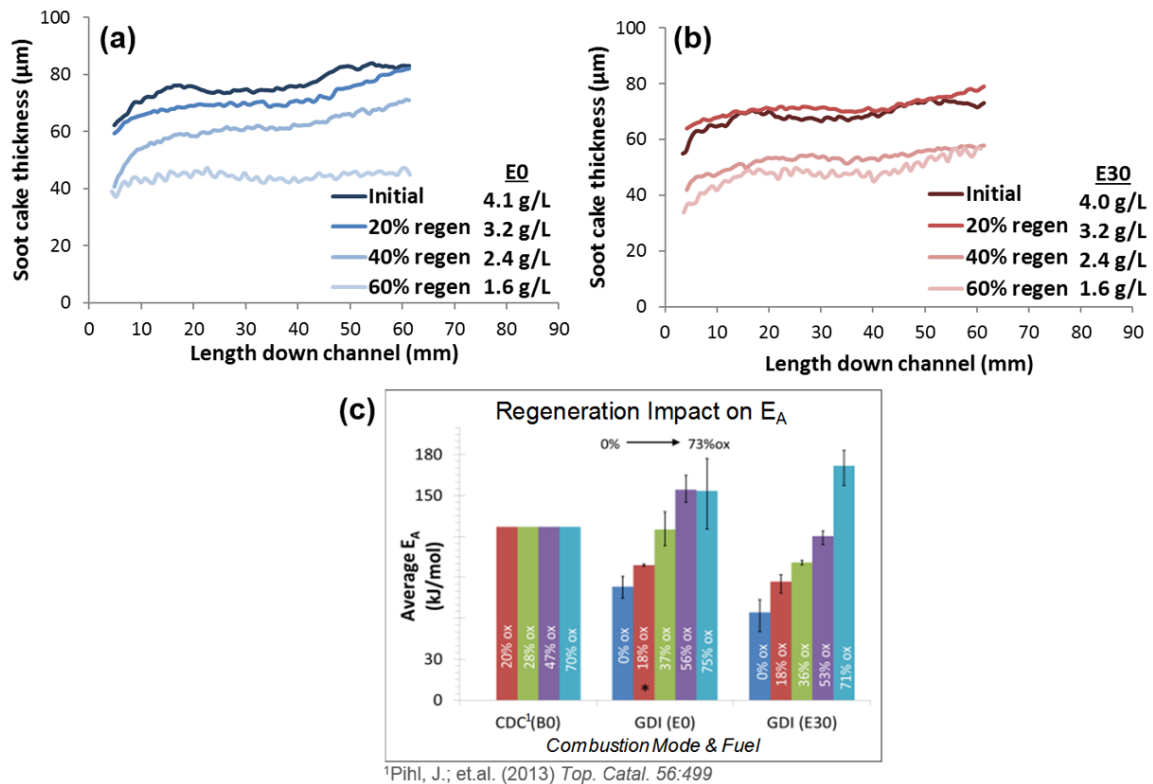


Figure I.13.4 - (a) Sagittal slice of neutron CT data, with X-ray CT domain marked, and (b) internal fluid velocities from a computational fluid dynamics simulation (Courtesy of Argonne National Laboratory)

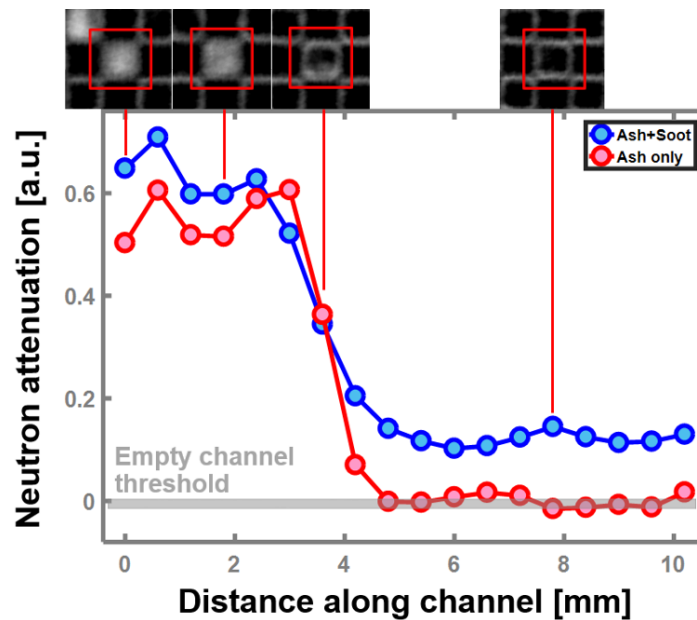
Work also continued regarding nondestructive techniques to map soot and ash distributions in DPFs. In this fiscal year, a comparative study was continued on two field-loaded DPFs using physical and X-ray measurements provided by a researcher at Massachusetts Institute of Technology, and neutron measurements provided by Oak Ridge National Laboratory using the HFIR imaging beamline. One strength of the neutron imaging is the ability to detect soot in addition to ash in the particulate filter channels. Two selected DPF cores were imaged as received, with soot and ash, and after regeneration, with ash only. The first stage in the analysis was to detect the presence and later deposition layer thickness profiles of soot. An example is seen in Figure I.13.6, which depicts neutron attenuation for a selected channel in one of the studied DPFs, both before and after regeneration. In the attenuation profiles, the presence of soot is apparent. Full quantification will continue

in Fiscal Year 2018 in collaboration with the University of Tennessee for advanced image reconstruction and processing techniques.



CDC – conventional diesel combustion; GDI – gasoline direct injection

Figure I.13.5 - Results from successive GPF regeneration study to date for (a) E0 and (b) E30, including the recently imaged 60% regeneration state, with (c) comparison of activation energies for diesel- and gasoline-generated soot



a.u. – arbitrary units

Figure I.13.6 - Neutron attenuation at various axial locations for a single channel both with the original field-loaded DPF (ash+soot) and after regeneration (ash only). Inset images show attenuation intensity in the channel at each axial location (brighter means more neutron attenuation).

Conclusions

- Neutron imaging of fuel injection in a dynamic capacity has been demonstrated at the HFIR CG-1D imaging beamline and has shown the ability to visualize the rate of evaporation in the internal injector sac as a function of injector and chamber conditions. Dynamic neutron imaging allows insight into intra-nozzle fluid dynamics in fuel injectors and is being used to estimate liquid versus vapor phases in the sac during injection.
 - Quantification is limited by data signal quality.
 - Estimation and reduction of uncertainties and noise is essential for accurate analysis of fluid–vapor dynamics.
- Joint HFIR (neutron) and Advanced Photon Source (X-ray) studies can provide the research community with data otherwise unattainable. An example of this is seen in the production of an internal surface model of a manufactured Spray G injector, which provides modelers and analysts with valuable data to support further studies of injector dynamics.
- Gasoline particulate differs in behavior from diesel particulate. The successive regeneration and imaging strategy employed in this project is yielding unique insights not otherwise attainable with other methodologies.
- Field loading of DPFs is a complex process and nondestructive techniques to map soot and ash interactions with filter walls is helping to define deposition patterns of both ash and soot, which can aid modelers and designers in refining operating strategies.

Future directions could include the following.

- Translation of dynamic fuel injection data to modeling
 - Improve data collection, image processing and analysis to derive more quantitative data sets for modeling; operate at more conditions including multiple injection sequences
 - Continue collaborations with ANL, Boston University, and the University of Tennessee
- Expand collaboration with ANL to leverage the strengths and unique capabilities of ANL’s Advanced Photon Source for X-ray imaging and diagnostics and Oak Ridge National Laboratory’s HFIR and Spallation Neutron Source for neutron imaging and diagnostics
 - Continue to focus on high-impact advanced transportation technologies
- Unknown behavior of gasoline particulate and how it differs from diesel particulate
 - Complete study for full regeneration of the GPFs to provide visualization of oxidation characteristics
 - Continue collaboration with the University of Tennessee
- Soot and ash interactions in DPFs
 - Continue collaboration with Massachusetts Institute of Technology and the University of Tennessee

References

1. Banhart, J. 2008 *Advanced Tomographic Methods in Materials Research and Engineering* (Oxford: Oxford University Press).
2. Nanda J., Bilheux H.Z., Voisin S., Veith G.M., Archibald R., Walker L., Allu S., Dudney N., Pannala S., “Anomalous discharge product distribution in lithium-air cathodes.” *Journal of Physical Chemistry C*, 116, 15, 8401-8408 (2012).

Key Fiscal Year 2017 Publications

1. Duke, D.J., C.E.A. Finney, A.L. Kastengren, K.E. Matusik, N.M. Sovis, L.J. Santodonato, H.Z. Bilheux, D.P. Schmidt, C.F. Powell, and T.J. Toops. “High-Resolution X-Ray and Neutron Computed Tomography of an Engine Combustion Network Spray G Gasoline Injector.” *SAE International Journal of Fuels and Lubricants* 10(2): 328–343, 2017. doi: 10.4271/2017-01-0824.
2. Finney, C.E.A., C.J. Kamp, and T.J. Toops. “Ash-filter interactions in diesel particulate filters.” SAE World Congress and Expo (WCX17), Detroit, MI, April 5, 2017.
3. Toops, T.J., C.E.A. Finney, E.J. Nafziger, D.A. Splitter, M.M. DeBusk, and A.E. Pawlowski. “Neutron Imaging of Advanced Transportation Technologies.” 2017 U.S. DOE Vehicle Technologies Office Annual Merit Review, Presentation ACS052.

I.14 Chemical Kinetic Models for Advanced Engine Combustion

William J. Pitz, Principal Investigator

Lawrence Livermore National Laboratory
7000 East Avenue
Livermore, CA 94551
E-mail: pitz1@llnl.gov

Michael Weismiller, DOE Technology Manager

U.S. Department of Energy
E-mail: Michael.Weismiller@ee.doe.gov

Start Date: October 1, 2017	End Date: September 30, 2019	
Total Project Cost: \$1,596,000	DOE share: \$1,596,000	Non-DOE share: \$0

Acknowledgments

Co-Authors

Goutham Kukkadapu, Kuiwen Zhang, Marco Mehl, Scott W. Wagnon, Charles K. Westbrook;
Lawrence Livermore National Laboratory

This work was performed under the auspices of the U.S. Department of Energy by Lawrence Livermore National Laboratory under Contract DE-AC52-07NA27344.

Project Introduction

Predictive engine simulation models are needed to make rapid progress towards DOE's goals of increasing combustion engine efficiency and reducing pollutant emissions. To assess the effect of fuel composition on engine performance and emissions, these engine simulations need to couple fluid dynamic and fuel chemistry submodels. Reliable chemical kinetic submodels representative of conventional and next-generation transportation fuels need to be developed to fulfill these requirements.

Objectives

- Develop detailed chemical kinetic models for fuel components used in surrogate fuels for compression ignition, homogeneous charge compression ignition, and reactivity controlled compression ignition engines
- Combine component models into surrogate fuel models to represent real transportation fuels; use them to model low-temperature combustion strategies in homogeneous charge compression ignition, reactivity controlled compression ignition, and compression ignition engines that lead to low emissions and high efficiency

Approach

Gasoline and diesel fuels consist of complex mixtures of hundreds of different components. These components can be grouped into chemical classes including n-alkanes, iso-alkanes, cyclo-alkanes, alkenes, oxygenates, and aromatics. Since it is not feasible to develop chemical kinetic models for hundreds of components, specific components need to be identified to represent each of these chemical classes. Then detailed chemical kinetic models can be developed for these selected components. These component models are subsequently merged together to produce a surrogate fuel model for gasoline, diesel, and next-generation transportation fuels. This approach creates realistic surrogates for gasoline or diesel fuels that can reproduce experimental behavior of the practical real fuels that they represent. Detailed kinetic models for surrogate fuels can then be simplified as needed for inclusion in multidimensional computational fluid dynamic simulations of engine combustion.

Results

Key accomplishments for Fiscal Year 2017:

- Developed chemical kinetic model for a nine-component diesel surrogate palette that represents a diesel certification fuel
- Improved gasoline and diesel surrogate component models and multi-component models to increase their accuracy when used in simulating gasoline and diesel engine experiments

Mueller et al. [1] proposed a nine-component surrogate palette to represent the ignition behavior of a representative diesel fuel in terms of distillation characteristics, density, and chemical composition. In Fiscal Year 2017 for the first time, a chemical model for all nine-components in this surrogate palette has been assembled and tested using experimental data for the surrogate components (e.g., Figures I.14.1 and I.14.2) and their binary mixtures (e.g., Figure I.14.3). In Figure I.14.1, the kinetic model for n-decane, a representative n-alkane, is shown to well simulate its ignition behavior over a wide pressure range in a shock tube. In Figure I.14.2, ignition delay times (IDTs) from the chemical kinetic model for surrogate-component decalin,

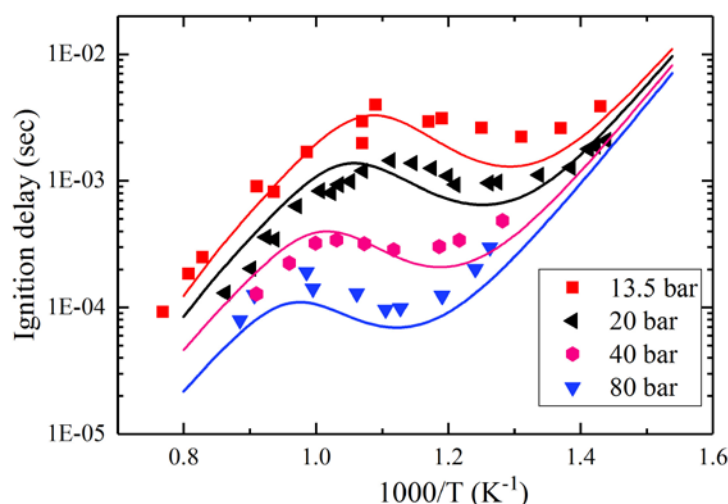
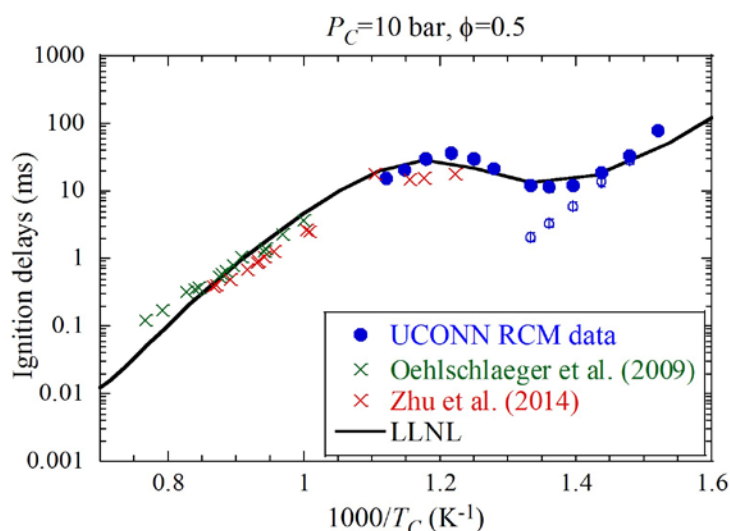


Figure I.14.1 - Experimentally measured (symbols) and simulated (curves) IDTs of n-decane in shock tubes [2,3,4]. (Source: Lawrence Livermore National Laboratory [LLNL])



UCONN – University of Connecticut; ST – shock tube

Figure I.14.2 - Experimentally measured (symbols) and simulated (curves) IDTs of decalin in a shock tube and RCM [5,6,7]. (Source: LLNL)

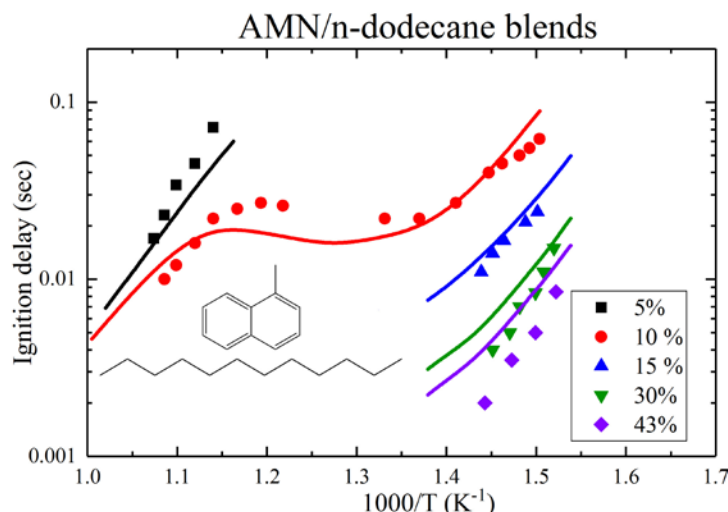


Figure I.14.3 - Measured (symbols) and simulated (lines) IDTs of a 1-methylnaphthalene (AMN)/n-dodecane stoichiometric blend for a pressure of 15 bar [8] (Source: LLNL)

which represents cycloalkanes in diesel fuel, are compared with IDTs from a shock tube and rapid compression machine (RCM). The agreement between the simulated and measured IDTs is reasonable. Finally, blending behavior of the diesel surrogate model was tested by comparing experimental and simulated results IDTs of five different blend fractions of α -methylnaphthalene and n-dodecane which are representative of aromatic and alkane components (Figure I.14.3). Reasonable agreement was again obtained. Overall, the comparison between simulated IDTs of the surrogate components and their mixtures shows good to reasonable agreement giving confidence in the use of this diesel surrogate model.

This is the first time that a detailed chemical kinetic mechanism has been developed for a surrogate mixture that represents so many key properties of diesel fuel. Developing a detailed model of diesel components is challenging because of the large size of the fuel components that necessitates the inclusion of many species and reactions each which require thermodynamic property and reaction rate estimates, respectively.

In Fiscal Year 2017, the LLNL gasoline surrogate component and component blend models have been improved to increase their accuracy and enable reliable predictions under internal combustion engine conditions. For single-component gasoline surrogate compounds, the chemical kinetic model for iso-octane was enhanced using new RCM data from Argonne National Laboratory (ANL) (Figure I.14.4). The predictability of the chemical kinetic model at temperatures in the negative temperature coefficient region and the low temperature region is considerably better (solid curves) than the previous version of the model (dashed curves). It is important to simulate ignition behavior accurately in these temperature regions to predict autoignition at temperatures and pressures relevant for automotive engine knock. For binary blends, the chemical kinetic model of n-heptane and iso-octane (primary reference fuels [PRFs]) was improved to make it more predictive. It is critical to simulate ignition behavior of fuel component blends so that their interactions which are present in practical fuels can be reproduced. PRF fuel blends are important because they are used to represent gasoline for standard fuel property tests such as Motor Octane Number and Research Octane Number. Figure I.14.5 shows the comparison of model predictions with experimental measurements of the ignition of PRF90 from the ANL RCM for a range of different pressures. The chemical kinetic model for PRFs represents the experimental behavior very well. For three-component blends, the kinetic model for toluene, n-heptane, and iso-octane blends (toluene primary reference fuel [TPRF]) was also validated by comparison to experimental data from a shock tube and RCM. TPRFs are a common surrogate for gasoline fuel that have the ability to reproduce gasoline autoignition behavior in an engine. Figure I.14.6 demonstrates that the chemical kinetic model for this tri-component blend simulates well the experimental RCM data of Javed et al. [9].

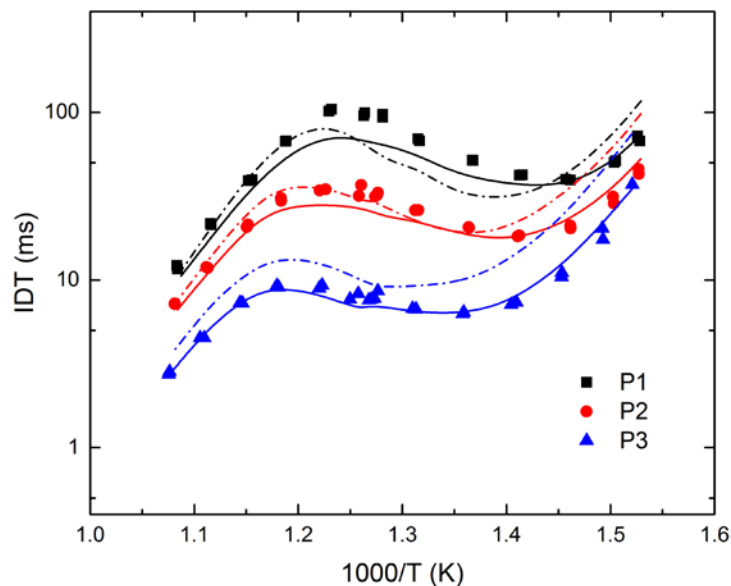


Figure I.14.4 - Simulated (lines) and experimentally measured (symbols) of IDTs for iso-octane. The dash lines are from the previous LLNL iso-octane detailed chemical kinetic model and the solid lines from the improved one. The symbols are measurements from the ANL RCM. P1, P2, P3 are different unspecified pressures. $P3 > P2 > P1$.
(Source: LLNL)

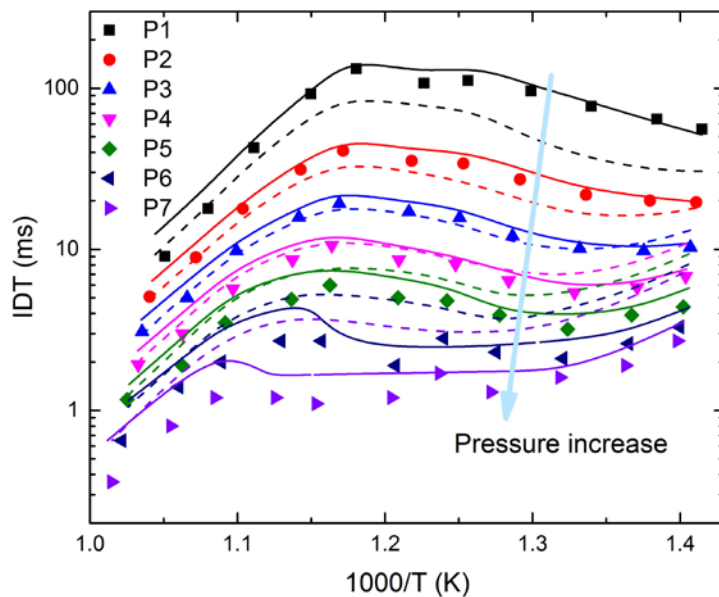


Figure I.14.5 - Simulated (curves) and experimentally measured (symbols) IDTs for gasoline primary reference fuel PRF90. The symbols are experimental measurements from the ANL RCM. The dashed curves are from the previous chemical kinetic model and the solid curves are from the improved model. (Source: LLNL)

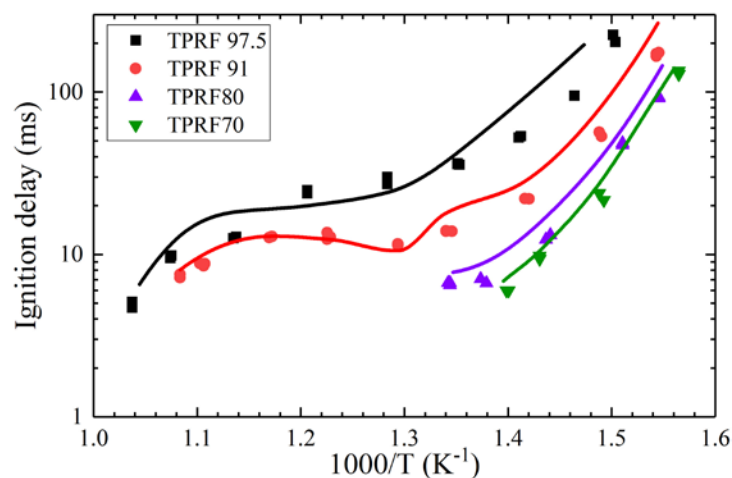


Figure I.14.6 - Simulated (lines) and experimentally measured (symbols) IDTs for TPRF for stoichiometric fuel/air mixtures at 20 bar. The dash lines are from the LLNL detailed chemical kinetic model for n-heptane, iso-octane, and toluene. The symbols are experimental measurements from a RCM [9]. (Source: LLNL)

Conclusions

- For the first time, a detailed chemical-like mechanism for a realistic diesel surrogate has been developed.
- The detailed chemical models for diesel components and binary blends were improved using experimental data from the RCM at UCONN and from the literature.
- Using the new experimental data from the RCM at ANL, the detailed chemical kinetic models for gasoline components and blends (iso-octane and PRF) were improved using experimental data over a wide pressure range relevant to internal combustion engines.

References

1. Mueller, Charles J., William J. Cannella, Thomas J. Bruno, Bruce Bunting, Heather D. Dettman, James A. Franz, Marcia L. Huber, Mani Natarajan, William J. Pitz, Matthew A. Ratcliff, and Ken Wright. "Methodology for Formulating Diesel Surrogate Fuels with Accurate Compositional, Ignition-Quality, and Volatility Characteristics." *Energy & Fuels* 26 (6):3284–3303. 2012. doi: 10.1021/ef300303e.
2. Pfahl, U., K. Fieweger, and G. Adomeit. "Self-Ignition of Diesel-Relevant Hydrocarbon-Air Mixtures under Engine Conditions." *Proc. Combust. Inst.* 26:781–789. 1996. doi: [http://dx.doi.org/10.1016/S0082-0784\(96\)80287-6](http://dx.doi.org/10.1016/S0082-0784(96)80287-6).
3. Tekawade, Aniket, Tianbo Xie, and Matthew A. Oehlschlaeger. "Comparative Study of the Ignition of 1-Decene, trans-5-Decene, and n-Decane: Constant-Volume Spray and Shock-Tube Experiments." *Energy & Fuels* 31 (6):6493–6500. 2017. doi: 10.1021/acs.energyfuels.7b00430.
4. Zhukov, Victor P., Vladislav A. Sechenov, and Andrey Yu. Starikovskii. "Autoignition of n-decane at high pressure." *Combustion and Flame* 153 (1-2):130–136. 2008.
5. Zhu, Y., D.F. Davidson, and R.K. Hanson. "Pyrolysis and oxidation of decalin at elevated pressures: A shock-tube study." *Combustion and Flame* 161 (2):371–383. 2014. doi: <http://dx.doi.org/10.1016/j.combustflame.2013.09.005>.
6. Oehlschlaeger, Matthew A., Hsi-Ping S. Shen, Alessio Frassoldati, Sauro Pierucci, and Eliseo Ranzi. "Experimental and Kinetic Modeling Study of the Pyrolysis and Oxidation of Decalin." *Energy & Fuels* 23 (3):1464–1472. 2009. doi: doi:10.1021/ef800892y.

7. Wang, Mengyuan, Goutham Kukkadapu, Kuiwen Zhang, William J. Pitz, and Chih-Jen Sung. "Autoignition of trans-Decalin, a Diesel Surrogate Compound: Rapid Compression Machine Experiments and Chemical Kinetic Modeling." In *U.S. National Combustion Meeting*. College Park, MD: U.S. National Combustion Meeting, 2017.
8. Kukkadapu, Goutham, and Chih-Jen Sung. "Autoignition study of binary blends of n-dodecane/1-methylnaphthalene and iso-cetane/1-methylnaphthalene." *Combustion and Flame* 189 (Supplement C):367–377. 2018. doi: <https://doi.org/10.1016/j.combustflame.2017.07.025>.
9. Javed, T., C. Lee, M. AlAbbad, K. Djebbi, M. Beshir, J. Badra, H. Curran, and A. Farooq. "Ignition studies of n-heptane/iso-octane/toluene blends." *Combustion and Flame* 171:223–233. 2016. doi: [10.1016/j.combustflame.2016.06.008](https://doi.org/10.1016/j.combustflame.2016.06.008).

Key Fiscal Year 2017 Publications

1. Atef, Nour, Goutham Kukkadapu, Samah Y. Mohamed, Mariam Al Rashidi, Colin Banyon, Marco Mehl, Karl Alexander Heufer, Ehsan F. Nasir, A. Alfazazi, Apurba K. Das, Charles K. Westbrook, William J. Pitz, Tianfeng Lu, Aamir Farooq, Chih-Jen Sung, Henry J. Curran, and S. Mani Sarathy. "A comprehensive iso-octane combustion model with improved thermochemistry and chemical kinetics." *Combustion and Flame* 178:111–134. 2017. doi: <http://dx.doi.org/10.1016/j.combustflame.2016.12.029>.
2. Rashidi, Al, Mariam J., Marco Mehl, William J. Pitz, Samah Mohamed, and S. Mani Sarathy. "Cyclopentane combustion chemistry. Part I: Mechanism development and computational kinetics." *Combustion and Flame* 183:358–371. 2017. doi: <http://dx.doi.org/10.1016/j.combustflame.2017.05.018>.
3. Rashidi, Al, Mariam J., Juan C. Mármol, Colin Banyon, Muhammad B. Sajid, Marco Mehl, William J. Pitz, Samah Mohamed, Adamu Alfazazi, Tianfeng Lu, Henry J. Curran, Aamir Farooq, and S. Mani Sarathy. "Cyclopentane combustion. Part II. Ignition delay measurements and mechanism validation." *Combustion and Flame* 183:372–385. 2017. doi: <http://dx.doi.org/10.1016/j.combustflame.2017.05.017>.
4. Fridlyand, Aleksandr, Matthew S. Johnson, S. Scott Goldsborough, Richard H. West, Matthew J. McNenly, Marco Mehl, and William J. Pitz. "The role of correlations in uncertainty quantification of transportation relevant fuel models." *Combustion and Flame* 180:239–249. 2017. doi: <https://doi.org/10.1016/j.combustflame.2016.10.014>.

I.15 Model Development and Analysis of Clean and Efficient Engine Combustion

Russell Whitesides, Principal Investigator

Lawrence Livermore National Laboratory
L-792, 7000 East Ave.
Livermore, CA 94550
E-mail: whitesides1@llnl.gov

Michael Weismiller, DOE Technology Manager

U.S. Department of Energy
E-mail: Michael.Weismiller@ee.doe.gov

Start Date: October 1, 2016	End Date: September 30, 2017	
Total Project Cost: \$441,000	DOE share: \$441,000	Non-DOE share: \$0

Acknowledgments

Co-Authors

Nicholas Killingsworth, Guillaume Petitpas, Matthew McNenly; Lawrence Livermore National Laboratory

This work was performed under the auspices of the U.S. Department of Energy by Lawrence Livermore National Laboratory under Contract DE-AC52-07NA27344.

LLNL Document Number: LLNL-AR-742221

Project Introduction

Internal combustion engine design is increasingly driven by computational models which are used to predict performance metrics which previously would have been made by limited design intuition or expensive and time-consuming physical testing. Improved model capabilities shorten design cycles and enable the production of cleaner and more efficient engines. This project focuses on advancing the state of the art in internal combustion engine simulations. The overarching goal is enable predictive models and reduced time to solution for simulations that impact combustion engine design.

Objectives

- Advance state of the art in engine simulation through the development of fast and accurate models
- Continue to work with industry partners to prove capability and impact of combustion chemistry software
- Extend and refine estimates of uncertainty in advanced combustion engine experiments

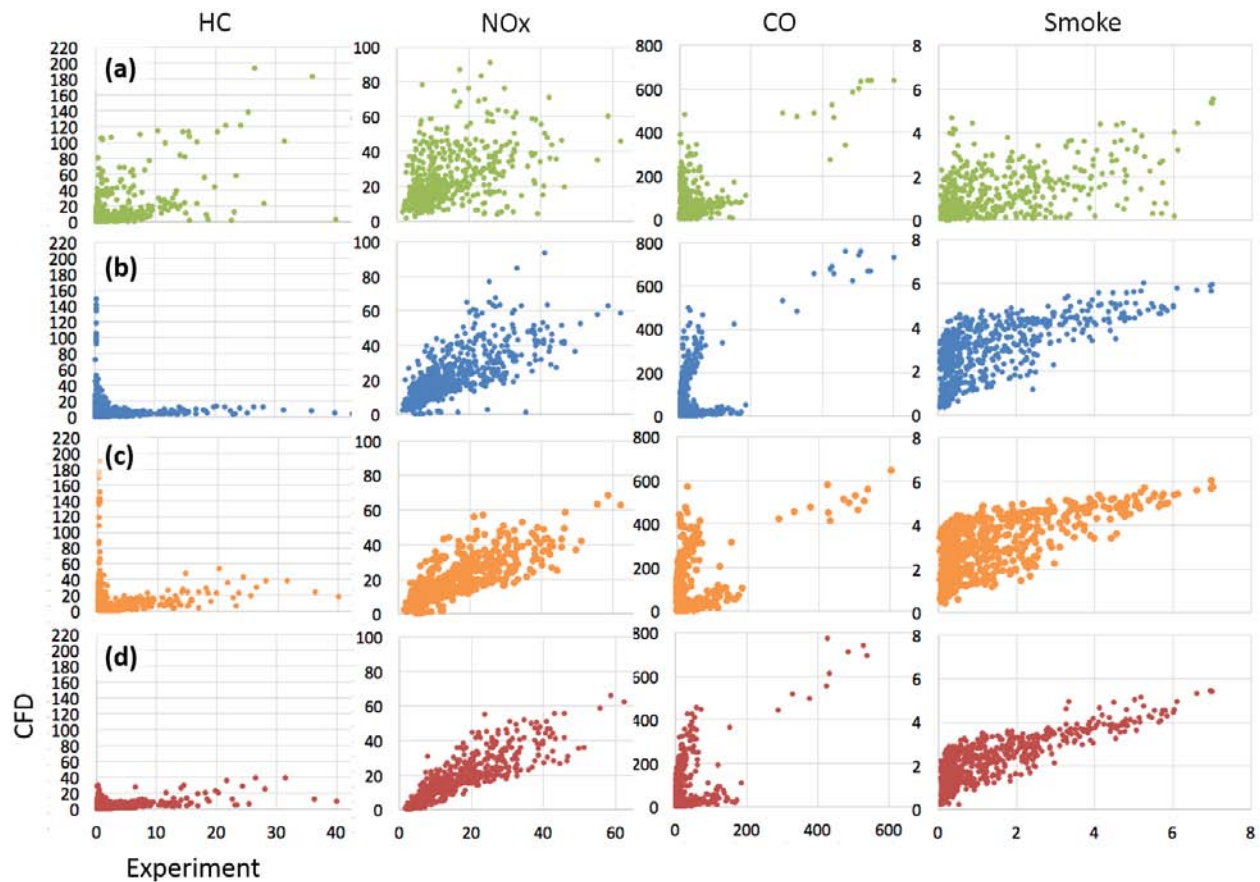
Approach

This project is an ongoing research effort under the Advanced Combustion Systems subprogram with annual feedback and direction from program managers and memorandum of understanding partners. During the current performance period, this project has focused on two areas: (1) development and deployment of fast chemistry solvers in engine simulations, and (2) refinement of uncertainty quantification for low-temperature combustion engine experiments. The first focus area was performed in close collaboration with General Motors and Oak Ridge National Laboratory (ORNL) [1] as part of an Advance Scientific Computing Initiative Leadership Computing Challenge grant. The second task included collaborative support from Sandia National Laboratories [2]. This project is also closely linked with related Lawrence Livermore National Laboratory projects [3,4].

Results

Fast Chemistry Solver Deployed on Supercomputer

This year saw the full deployment of the Zero-RK chemical kinetics software on the TITAN supercomputer at ORNL. Zero-RK is a collection of software tools which have been developed in this project along with the project led by McNenly to significantly accelerate simulations including detailed chemical reaction models. Working with ORNL and General Motors as part of multiple Advanced Scientific Computing Research Leadership Computing Challenge grants, the graphical processing unit enabled fast-chemistry solver was used to run massively parallel simulations of conventional diesel and partially premixed compression ignition engines. Altogether, over 1,600 engine simulations with detailed chemistry have been performed as part of this collaboration. The inclusion of detailed chemistry is vital to accurate predictions of ignition timing and emissions. The goal of the diesel simulations was to move towards virtual engine calibration. Over 400 individual diesel engine operating points were considered, with predictions compared at different levels of simulation complexity. Significant improvements in hydrocarbon, nitrogen oxides, and soot predictions were achieved by including more detailed chemical models as well as improvements in mesh resolution and spray modeling (see Figure I.15.1). The capability to perform large studies of many operating points is only currently possible with the combination of leadership class computing hardware at ORNL and the chemical software tools developed in this project.

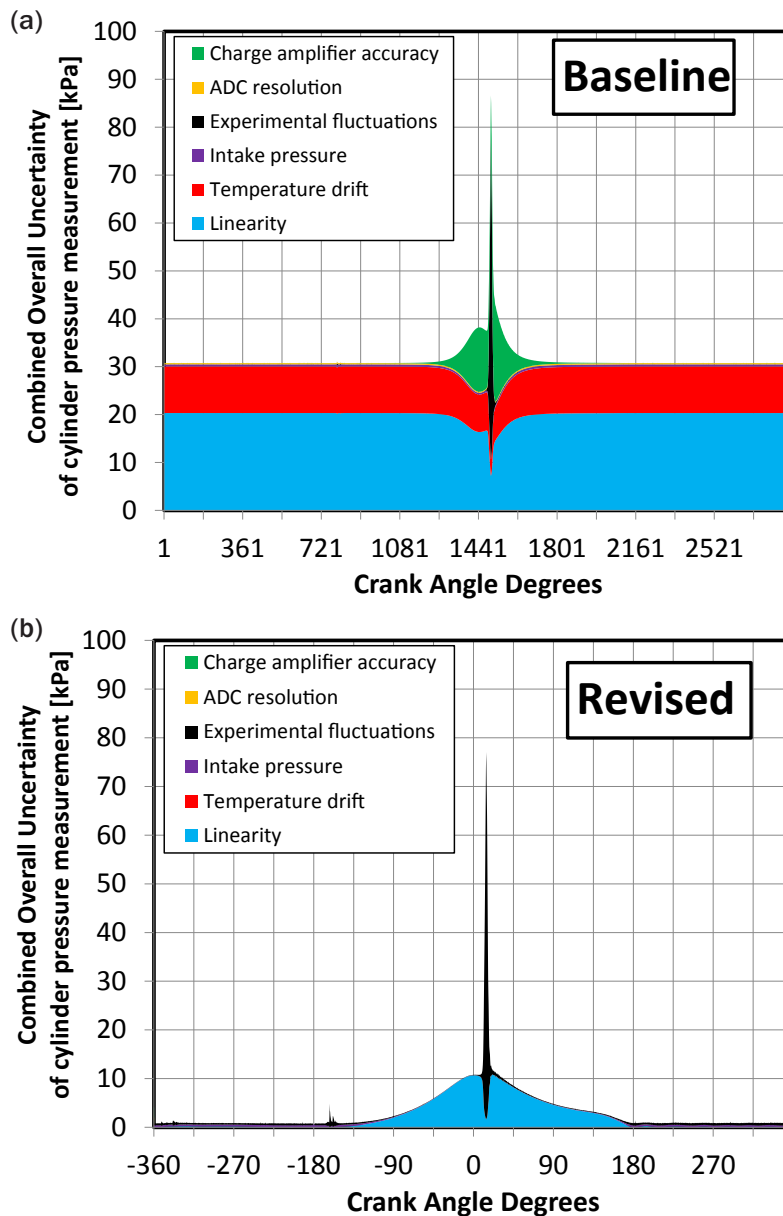


CFD – computational fluid dynamics; HC – hydrocarbons

Figure I.15.1 - Improvement in emissions prediction as a function of simulation complexity. (a) Results for baseline simulations, (b) baseline simulations with more chemical detail, (c) baseline simulations with more chemical detail and higher mesh resolution (d) baseline simulations with more chemical detail, higher mesh resolution, and improved spray modeling.

Rigorous Confidence Intervals on Low-temperature Combustion Engine Measurements

This task built on the previous years’ effort in the same area. Previously, a framework for identifying sources of uncertainty in low-temperature gasoline combustion engines and the effect of those uncertainties on measured quantities of interest was developed. During the current fiscal year, the framework was published as a reference work in the SAE World Congress and as a set of software available online for use and adaptation by engine researchers. The framework has also been further developed in the current performance period in collaboration with John Dec at Sandia National Laboratories. The improvements to the analysis are the result of better information on sensor calibration and experimental practice by the experimenters. During the original development of the uncertainty framework, manufacturers’ specifications for sensor uncertainty were used along with assumptions about sensor ages and calibration. The additional information about calibration frequency, operating conditions, and other laboratory specific practices in the low-temperature gasoline combustion (LTGC) experiments has significantly reduced the expected uncertainty in the pressure measurements with respect to the original analysis. Figure I.15.2 shows the combined overall uncertainty in cylinder pressure measurement using the original framework and that with the updated analysis. In addition



ADC – analog to digital converter

Figure I.15.2 - (a) Baseline and (b) revised estimates of in-cylinder pressure uncertainty in LTGC engine experiments

to the improved pressure sensor analysis, the uncertainty analysis was extended by including the effect of mechanical deformation of the engine during operation and investigation of sensitivity of estimated in-cylinder temperatures to accuracy of pressure, engine speed, and mixture composition. Mechanical deformation was found to have a small but noticeable effect on apparent heat release and engine work. Temperature estimates were found to be most sensitive to uncertainty in the amount of exhaust gas recirculation and engine speed.

Key accomplishments for Fiscal Year 2017:

- Deployed fast-chemistry solver on multiple Advanced Scientific Computing Research Leadership Computing Challenge award projects in collaboration with General Motors and ORNL
- Enabled improved predictions of hydrocarbon, nitrogen oxide, and soot in conventional diesel virtual calibration project
- Reduced estimated uncertainty bounds of engine pressure measurements in collaboration with Sandia National Laboratories
- Identified key contributors to uncertainty of in-cylinder temperature estimates which are vital to engine models

Conclusions

- Continued collaboration with ORNL and General Motors using fast-chemistry solvers on world-class computing platforms has enabled increasingly accurate simulations, in particular with respect to predictions of emissions.
- Uncertainty quantification remains an incompletely developed practice within the combustion community. This project is aimed at allowing for closer comparison between experiments and models and developments in this year have tightened the uncertainty estimates and continued to evangelize for the use of uncertainty metrics in engine research.

References

1. Edwards, K.D. “Accelerating Predictive Simulation of IC Engines with High Performance Computing.” In *Advanced Combustion Engine Research and Development 2017 Annual Progress Report*, U.S. Department of Energy, 2017.
2. Dec, J.E. “Low-Temperature Gasoline Combustion (LTGC) Engine Research.” In *Advanced Combustion Engine Research and Development 2017 Annual Progress Report*, U.S. Department of Energy, 2017.
3. McNenly, M.J. “Improved solvers for advanced engine combustion simulation.” In *Advanced Combustion Engine Research and Development 2017 Annual Progress Report*, U.S. Department of Energy, 2017.
4. Pitz, W.J. “Chemical Kinetics Models for Advanced Engine Combustion.” In *Advanced Combustion Engine Research and Development 2017 Annual Progress Report*, U.S. Department of Energy, 2017.

Key Fiscal Year 2017 Publications

1. Petitpas, Guillaume, Matthew J. McNenly, and Russell A. Whitesides. “A Framework for Quantifying Measurement Uncertainties and Uncertainty Propagation in HCCI/LTGC Engine Experiments.” *SAE International Journal of Engines* 10, no. 3 (March 28, 2017). <https://doi.org/10.4271/2017-01-0736>.
2. “LLNL/UQ_combustion.” Accessed November 20, 2017. https://github.com/LLNL/UQ_combustion.
3. Gao, J., R.O. Grover, V. Gopalakrishnan, W. Elwasif, K.D. Edwards, C.A. Finney, and R.A. Whitesides. “Steady-state Calibration of a Diesel Engine in CFD using a GPU-based Chemistry Solver.” ASME Internal Combustion Engine Fall Technical Conference, Seattle, WA, November 4–7, 2017.

4. Whitesides, R.A., W.R. Elwasif, W.R., R.O. Grover, J. Gao, S. Keum, V. Gopalakrishnan, R. Diwaker, K.D. Edwards, C.A. Finney. "Application and Performance of Chemistry Solvers on the Titan Supercomputer." Converge User Conference North America, Dearborn, MI, September 26–27, 2017.
5. Petitpas, G., R.A. Whitesides, J.E. Dec, J. Dernote. "Refining Measurement Uncertainties in HCCI/LTGC Engine Experiments," *SAE International Journal of Engines*, in press.

I.16 Improved Solvers for Advanced Combustion Engine Simulation

Matthew McNenly, Principal Investigator

Lawrence Livermore National Laboratory
7000 East Avenue
Livermore, CA 94550
E-mail: mcnenly1@llnl.gov

Michael Weismiller, DOE Technology Manager

U.S. Department of Energy
E-mail: Michael.Weismiller@ee.doe.gov

Start Date: October 1, 2016	End Date: September 30, 2017	
Total Project Cost: \$460,000	DOE share: \$460,000	Non-DOE share: \$0

Acknowledgments

Co-Authors

Simon Lapointe, Nick Killingsworth, John Consolati, Anthony Epshteyn, and Russell Whitesides;
Lawrence Livermore National Laboratory

Project Introduction

This project fills the present knowledge gap through substantial improvements in the performance and accuracy of combustion models and software. The project focuses on the applied mathematics underpinning efficient algorithms and the development of combustion software on new computing architectures. It is a natural complement to the other Lawrence Livermore National Laboratory (LLNL) projects in the quest to gain fundamental understanding of the new engine modes investigated under the Advanced Combustion Systems (ACS) program. Other LLNL projects include the multidimensional engine simulation project led by Whitesides (see I.15) and the high-fidelity chemistry mechanisms developed for real transportation fuels by Pitz (see I.14). The long-term goal of this project is to develop predictive combustion software that is computationally fast enough to impact the design cycle and reduce the deployment time for new high-efficiency, low-emissions engine concepts. Toward this goal, the project developed a new thermochemistry library and chemistry solver [1] that achieves multiple orders of magnitude speed-up over the traditional approaches found in computational fluid dynamics (e.g., OpenFOAM) without any loss of accuracy. Further, the LLNL library and solver are 5–15 times faster than sophisticated commercial solvers like Chemkin-Pro. This performance has led to the LLNL library, named Zero-RK, to win a 2015 R&D 100 award in the Software and Services category. As a consequence of this project, it is now possible to model high fidelity fuel mechanisms (on the order of a thousand species) in multidimensional engine simulations that run in a day on industry-scale computational resources.

Objectives

- Accelerate development and deployment of high-efficiency clean combustion (HECC) engine concepts through deeper understanding of complex fluid and chemistry interactions
- Develop truly predictive combustion models and software that are fast enough to impact the engine design cycle
- Improve the mechanism development tools to better identify potential errors and provide automatic correction whenever possible
- Extend LLNL's accelerated combustion solvers to include more reaction classes that are needed for accurate multi-component fuel surrogates and soot formation

- Verify and validate the generalized framework for LLNL's adaptive preconditioner approach for fully coupled fluid dynamics and chemistry models using canonical steady and unsteady flame experiments

Approach

The project is focused on creating combustion software capable of producing accurate solutions in a short time relative to the engineering design cycle on commodity computing architectures. The approach advances engine simulations along several fronts simultaneously. Major bottlenecks in the software are found through detailed code profiling, while bottlenecks in the general computational-aided analysis are identified through engagements with the original equipment manufacturers, universities, and national laboratories. New algorithms are created for the slowest code sections and existing algorithms are adapted to new applications that can accelerate the overall analysis workflow for HECC design. The algorithms seek performance gains by implementing new theories from applied mathematics and exploiting the new low-cost, massively parallel computing architectures like the general purpose graphics processing units.

Results

There are three key accomplishments from Fiscal Year 2017.

- Extended and parallelized the adaptive preconditioner method used in Zero-RK to solve fully coupled, chemically reacting flows with thousands of transported species
- Quantified the potential computational speed-up offered by new multirate integration methods under development by the SUNDIALS team at LLNL
- Deployed cloud-based tools to allow fuel and engine researchers around the world to analyze chemical kinetic mechanisms for non-physical behavior and repair the thermochemistry files for improved performance

The software framework for the LLNL adaptive preconditioner method in Zero-RK was updated in Fiscal Year 2017 to accelerate fully coupled fluid chemistry models with thousands of transporting species. This is crucial for the simulation capabilities of the ACS program and its industry partners, and was previously identified as a major code bottleneck limiting the use of realistic transportation fuel models in engine design. The adaptive preconditioner method in McNenly, Whitesides, and Flowers [1] was extended to take advantage of parallel computing architectures when solving the chemical system at each spatial location. This approach has the ability to achieve significant speed-up over the range applications and simulations used in the ACS program and the larger HECC research community. These applications include fully coupled computational fluid dynamics, canonical one-dimensional flame analyses (e.g., laminar flame speed, and opposed flame diffusion and extinction), and reduced order engine model like the AMECS multizone [2].

The parallel scaling results are shown in Figure I.16.1 for two small chemical mechanisms: hydrogen with nine species and n-heptane with 187 species. Even with small mechanisms, the scaling efficiency is roughly 90% of the theoretical linear speed-up possible for 128 processors when solving an unsteady, one-dimensional flame. For the n-heptane results in Figure I.16.1, the near-linear speed-up is achieved with as few as eight spatial locations per processor. With larger, more realistic transportation fuel models, such as the 2,800 species gasoline surrogate developed at LLNL [3], the parallel efficiency is even greater. The unsteady flame simulation was verified against calculations using the FlameMaster code [4] and the NGA turbulent chemistry code initially developed at Stanford University [5]. The verification study found the parallel, adaptive preconditioner approach gave the same results to within the expected numerical accuracy of all the test codes. Further, the new solver was validated against experimental measurements made in a millimeter-scale flow reactor with flames with repetitive extinction and ignition as part of a separate project [6].

This project, starting in Fiscal Year 2017, collaborated with members of the SUNDIALS team in LLNL's Computation Directorate (SUNDIALS 2017) to create engine-relevant combustion problems in the test suite for new multirate integrator research. Multirate integrators evolve a time dependent system of equations using the most efficient time step size for each dynamic subsystem. For engine combustion applications, the governing equations can be split in to these dynamic subsystems a number of ways: separating highly reactive

chemical spray species, separating the chemical processes from the multi-species transport, and separating the fuel droplet dynamics from the bulk flow processes. Unlike the physics splitting methods commonly found in current engine simulation tools in industry, the multirate integrator achieve computational speed-up without loss of accuracy. By creating test problems that capture one of the major bottlenecks in predictive engine simulation (i.e., multi-species transport with realistic transportation fuel models), the ACS program and its industry partners are able to apply any future algorithm advances without considerable additional investment. This is especially important to unlock the massively parallel architectures planned for exascale, where multirate integrators are seen as a key enabler for real-world applications to be solved efficiently.

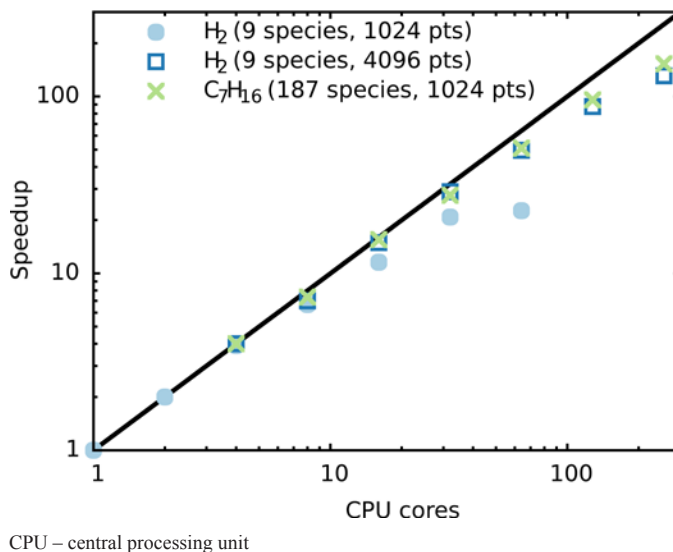


Figure I.16.1 - Parallel scaling efficiency of the adaptive preconditioner method applied to a fully-coupled, multi-species transport solver used to model the unsteady flame dynamics in a millimeter-scale flow reactor

As part of the development of an engine combustion test problem for multirate integrators, the constant volume ignition delay calculation was analyzed in the context of the signal flow Runge–Kutta (sfRK) method [7]. The sfRK method introduces the concept of semi-dormant and dormant states (also referred to as semi-latent and latent states) to integrate the physical system efficiently. A semi-dormant state is one that did not change over the last time step by an amount greater the integrator tolerances. A dormant state is one that is semi-dormant over the last time step along with all the states on which it depends. A dormant state of order n , is one that is dormant for the last n time steps. If the order of the dormant state is greater than or equal to the order of accuracy of the time discretization, the state can be ignored when integrating the system of equation without a loss of accuracy in the final solution, which leads to an overall computational speed-up.

It is expected that the separation of chemical timescales in detailed fuel models would be able to take advantage of multirate integrators. However, initial test of the sfRK approach for a detailed gasoline surrogate [3] showed that only 5% of the species were classified as dormant order 5 or more, which means that the multirate integrator was unlikely to provide any computational savings. This unexpected result was traced back to the strict dependency definition used to classify dormant states. The initial implementation did not take in to account that many of the reactions responsible for dependency between states were effectively inactive. This inactivity is caused by one or more reactants being extinct; that is, the mass fraction of the species was so small that it was unlikely to even have a single molecule present in the combustion chamber of an engine. The fractions of species below a specified extinction level is shown in Figure I.16.2. Note that more than 50% of the species on average have a mass fraction below the integrator absolute tolerance of 10^{-20} , which means that it is indistinguishable from zero in the solver.

The sfRK dormant state definition is modified to ignore any state dependency arising from inactive reactions. With this change, the sfRK method identifies over 50% of the states as being dormant order 5 or more, which indicates that there is a potential for a factor of two speed-up using multirate integrators (see Figure I.16.3). As a result of this project, a necessary feature is identified for future algorithm development in order for engine

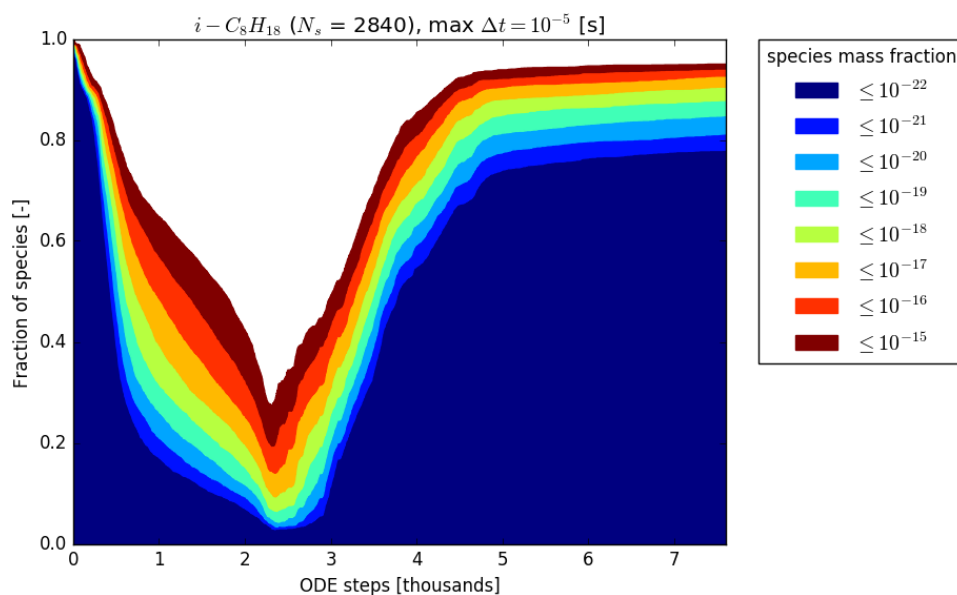


Figure I.16.2 - Fraction of species in a detailed gasoline surrogate chemistry model that have a mass fractions below a specified extinction level over the course of a constant volume ignition delay calculation

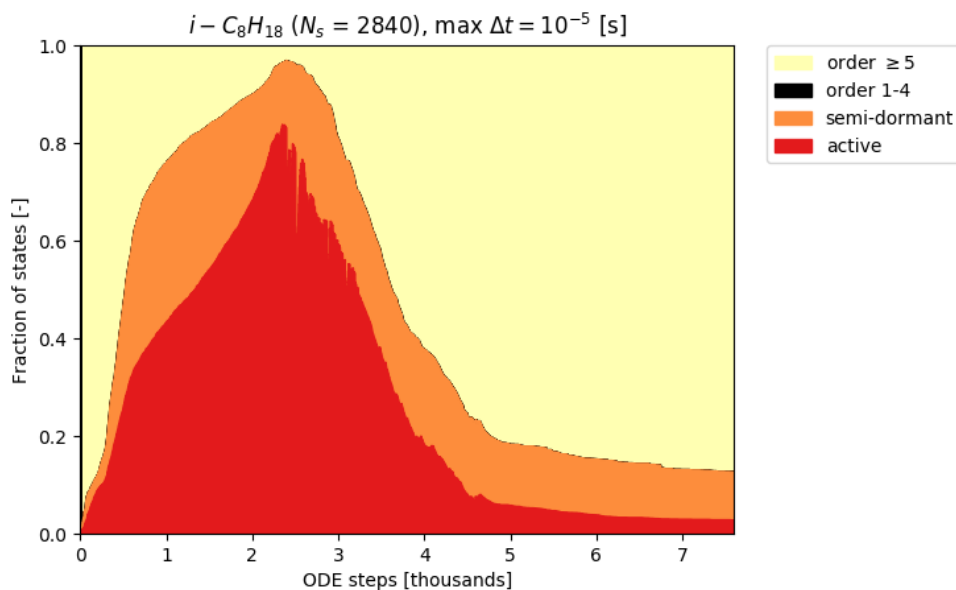


Figure I.16.3 - The dormant order classification of the system states representing the species mass fraction composition and temperature evolution of iso-octane in a constant volume ignition delay calculation

combustion simulations to take full advantage of multirate integrators. While a factor of two speed-up is beneficial, the potential gains in computational efficiency are expected to be even greater when the multirate integrators are applied to fully-coupled fluid chemistry simulations.

In previous years, work under this task resulted in the development of software tools to identify errors in large chemical kinetic mechanisms and their associated thermochemistry files. These tools were only available on the LLNL network and required training to use. To allow outside user access and improve utilization of these tools, LLNL researchers collaborated with information technology professionals at LLNL to develop a web application that provides a user-friendly interface and cloud-based environment to run them. This implementation gives users around the world access to the tool without the need to install any software or

perform updates. The web application is available at <https://combustiontools.llnl.gov> [8]. Here tools for analysis or chemical mechanism files can be found to identify non-physical behavior, which is then flagged such that researchers can investigate and make the appropriate fixes. There is also a thermochemistry repair tool that determines if the file contains any discontinuous functions and automatically repairs these files. The presence of discontinuous thermodynamic functions in the fuel chemistry model can cause simulations to take unphysically small-time steps, which leads to unnecessary increases in the computational cost. Improved access to these tools will help improve the accuracy and performance of detailed chemical mechanisms and improve the work flow of fuel and engine researchers throughout the ACS program and its industry partners.

Conclusions

This project developed two approaches for accelerating multi-species transport in engine simulations, which addresses one of the key analysis bottlenecks identified for the ACS research community and industry partners. The simulation and analysis tools that aid in the development of realistic transportation fuel models were published online for all fuel and engine researchers to use. In summary, there are three key accomplishments from Fiscal Year 2017.

- Extended and parallelized the adaptive preconditioner method used in Zero-RK to solve fully-coupled, chemically reacting flows with thousands of transported species
- Quantified the potential computational speed-up offered by new multirate integration methods under development by the SUNDIALS team at LLNL
- Deployed cloud-based tools to allow fuel and engine researchers around the world to analyze chemical kinetic mechanisms for non-physical behavior and repair the thermochemistry files for improved performance

References

1. McNenly, Matthew, Russell Whitesides, and Daniel Flowers. "Faster Solvers for Large Kinetic Mechanisms Using Adaptive Preconditioners." *Proceeding of the Combustion Institute* 35: 581–587. 2015. <https://doi.org/10.1016/j.proci.2014.05.113>.
2. Kodavasal, Janardhan, Matthew McNenly, Aristotelis Babajimopoulos, Salvador Aceves, Dennis Assanis, Mark Havstad, and Daniel Flowers. "An Accelerated Multi-Zone for Engine Cycle Simulation (AMECS) of HCCI Combustion." *International Journal of Engine Research*, 14: 416–433. 2013. <https://doi.org/10.1177/1468087413482480>.
3. Mehl, M., S.W. Wagnon, K. Zhang, G. Kukkadapu, W.J. Pitz, C.K. Westbrook, Y. Zhang, H.J. Curran, N. Atef, M.J. Al Rashidi, M.S. Sarathy, A. Ahmed. "A comprehensive detailed kinetic mechanism for the simulation of transportation fuels," 10th US National Combustion Meeting (2017), paper 1A17.
4. Pitsch, Heinz. "FlameMaster: A C++ Computer Program for 0D Combustion and 1D Laminar Flame Calculations." 2017. <http://www.itv.rwth-aachen.de/downloads/flamemaster/>.
5. Desjardins, Olivier, Guillaume Blanquart, Guillaume Balarac, and Heinz Pitsch. "High Order Conservative Finite Difference Scheme for Variable Density Low Mach Number Turbulent Flows." *Journal of Computational Physics*, 227: 7125–7159. 2008.
6. Lapointe, Simon, Ingmar Schoegl, Clara Druzgalski, and Matthew McNenly. "Simulations of a Micro-Liter Fuel Ignition Tester." 10th US National Combustion Meeting, paper 2G06, College Park, MD, April 23–26, 2017.
7. Klus, Stefan. "Signal-Flow Based Runge-Kutta Methods for the Simulation of Complex Networks." 2015. Accessed July 20, 2017. <https://arxiv.org/abs/1504.06413>.
8. Killingsworth, Nick, Matthew McNenly, Russell Whitesides, Anthony Epshteyn, and John Consolati. "Mech Checker." 2017. Accessed December 1, 2017. <https://combustiontools.llnl.gov/>.

Key Fiscal Year 2017 Publications

1. Lapointe, Simon, Ingmar Schoegl, Clara Druzgalski, and Matthew McNenly. "Simulations of a Micro-Liter Fuel Ignition Tester." 10th US National Combustion Meeting, paper 2G06, College Park, MD, April 23–26, 2017.
2. Killingsworth, Nick, Matthew McNenly, Russell Whitesides, Anthony Epshteyn, and John Consolati. "Mech Checker." 2017. Accessed December 1, 2017. <https://combustiontools.llnl.gov/>.
3. Whitesides, Russell, and Matthew McNenly. "Meta-models for Ignition Delay Times with Applications to Surrogate Fuel Mixture Generation." 10th US National Combustion Meeting, paper 2A18, College Park, MD, April 23–26, 2017.

I.17 2017 KIVA-hpFE Development: A Robust and Accurate Engine Modeling Software

David B. Carrington, Principal Investigator

Los Alamos National Laboratory

P.O. Box 1663

Los Alamos, NM 87545

E-mail: dcarrington@lanl.gov

Michael Weismiller, DOE Technology Manager

U.S. Department of Energy

E-mail: Michael.Weismiller@ee.doe.gov

Start Date: October 1, 2015

End Date: September 30, 2018

Total Project Cost: \$1,670,000

DOE share: \$1,670,000

Non-DOE share: \$0

Acknowledgments

Co-Authors

Jiajia Waters, Brad Philipbar; Los Alamos National Laboratory

Project Introduction

Research and development of KIVA-hpFE for turbulent reactive and multiphase flow, particularly as related to engine modeling, is relevant to the DOE Vehicle Technologies Office efforts at addressing national energy security. Less dependence on petroleum products leads to greater energy security. By Environmental Protection Agency standards, some vehicles are now reaching the 42–50 mpg mark. These are conventional gasoline engines. With continued investment and research into new technical innovations, the potential exists to save more than 4 million barrels of oil per day or approximately \$200 to \$400 million per day. This would be a significant decrease in emissions and use of petroleum and a very large stimulus to the U.S. economy.

Better understanding of fuel injection and fuel–air mixing, thermodynamic combustion losses, and combustion/emission formation processes enhances our ability to minimize fuel use and unwanted emissions. Helping to accomplish this understanding, the KIVA development program is providing a state-of-the-art capability for accurately simulating combustion processes: to have a predictive methodology in a software helping industry and researchers not only meet national goals on fuel usage and emissions, but global goals. In addition, a predictive, robust, and accurate capability for simulating the engine combustion process helps to minimize time and labor for development of new engine technology.

Objectives

A main goal of the KIVA development project is to help provide better understanding of engine combustion processes in order to enhance the ability to minimize fuel use and unwanted emissions. The KIVA development program is providing a state-of-the-art capability for accurately simulating combustion processes and is providing a more predictive methodology than currently available in a software to supply industry and researchers a tool to help meet national goals on emissions and engine efficiencies. In addition, a predictive, robust, and accurate capability for simulating engine combustion processes helps to minimize time and labor for development of new engine technology. To meet these goals our program objectives are to:

- Develop mathematical and computer algorithms and software for the advancement of speed, accuracy, robustness, and range of applicability of KIVA, an internal engine combustion modeling software, to be a more predictive computer code. This is to be accomplished by employing higher-order, spatially accurate methods for reactive turbulent flow and more predictive spray injection, combined with a robust and accurate actuated parts simulation along with more appropriate turbulence modeling. The code combines state-of-the-art chemical reaction simulators, such as Chemkin-Pro.

- Provide engine modeling software that is easier to maintain and is easier to add models to than the current KIVA and reduce code development costs into the future via more modern code architecture.
- Provide a software capable of producing fast turn-around times needed by industry. The code not only functions well on small computer platforms but addresses high performance computing aspects required for high-fidelity and more predictive solutions.

Approach

Our approach is founded in designing, inventing, and developing new modeling methods and code. The new design is a change of discretization to finite element method (FEM) from which essentially every other beneficial and salient attribute of the software stems. We invented and developed the following systems to date (details are provided in the publications as referenced).

- Developed the FEM-predictor–corrector scheme projection method for high accuracy and all the benefits the FEM system brings to computational fluid dynamics (CFD) modeling of engines [1,2]
- Developed the *hp*-adaptive system for higher order accuracy [3]
- Invented the local-arbitrary Lagrangian–Eulerian (ALE) method for moving bodies [4]
 - Invented a moving marker system to track any chosen interfaces
 - Invented reconstruction of elements to match the interface
- Developed immersed boundary methods for moving bodies using the invented marker system [5]
- Developed new dynamic large eddy simulation (LES), specifically designed for wall bounded flows [6]
 - Self-damping turbulence at the walls negates the need for a law-of-the-wall system that, in general, is flawed for unsteady flow in complex domains
- Invented and developed volume of fluid (VOF) methods in FEM for true multi-phase flow
 - To fully represent the spray break-up process, to have predictive spray modeling [7].
- Developed fast linear solver system
- Developed parallel solution method that is super-linear [8]
 - Delivers 30× speed-up over serial code given the same problem and settings
 - Delivers superlinear scalability
- Developed implicit solutions methods for 10× speed-up over serial parallel for an overall 300× speed-up for the same test problems [8]
- Invented a method for implementing Message Passing Interface (MPI) for today’s and future platforms [8]

We are building models and code so that they meet all the objectives in a clean, easy to maintain software that easily handles addition of others’ submodels. Careful verification and validation of the methods and code is required. The development of this technology utilizes many areas of expertise in multi-species turbulent reactive flow modeling with liquid sprays, modeling of immersed moving bodies, and the extensive numerical methods for the solution of the model and governing equations developed in the software.

Results

Our efforts this year continue to push toward a comprehensive tool for the future with the accomplishment of grid generation, immersed moving part, KH-RT spray model, multiphase compressible turbulent flow with LES and VOF for predictive sprays, and computational speed.

Grid Generation

- In conjunction with Program Development Company who developed GridPro, we are working on providing high quality grids for the engine system with an eye toward ease of use. The overset parts system used in the moving parts algorithm allows of easy grid generation of the cylinders and ports, with the spark and injector modules easily inserted. The piston and valves surfaces simply are also inserted by overlaying their surface representations after a quality grid is automatically generated.
- The overset gridding greatly simplifies the gridding process, removing the need to work around immersed bodies employed in traditional gridding methods.
- The injector and spark systems are built separately with the idea of making various types of injectors and spark plug modules that are simply connected to the engine cylinder grid. The final gridded engine system is shown in Figure I.17.1 with four million cells.
- It cannot be overstated: **a quality grid is needed to produced reliable simulations**. Gridding is a major component of CFD, where we seek to provide that quality with a minimum of labor.

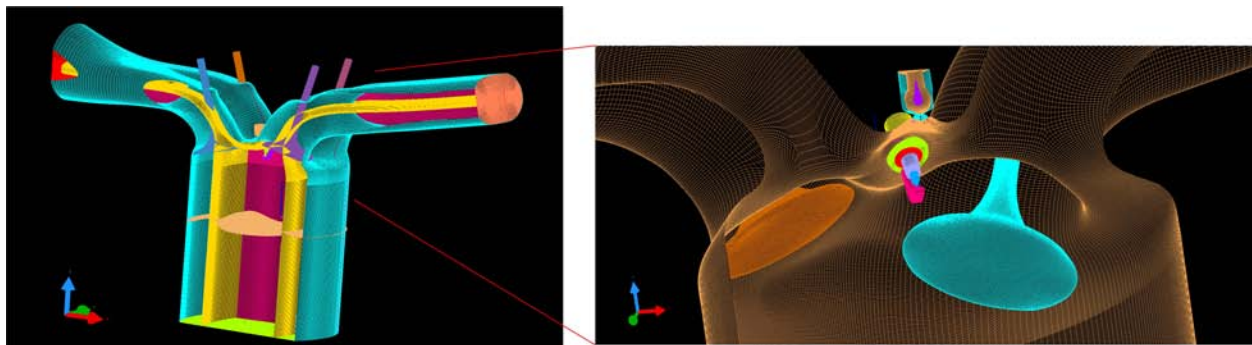


Figure I.17.1 - Computational grid using GridPro and overset valve and piston surfaces. In close-up, the valves and the injector module are easily married to the cylinder domain.

Immersed Moving Parts

- Developed immersed boundary methods for moving bodies using the invented marker system
 - Partially based on methods used in our local- ALE system for moving bodies
 - The moving marker system utilizes track moving boundary interfaces [4].
 - Employing the FEM shape functions for interpolation and a projection system to place a point along the normal to the surface from which the nearest node is projected, the fluid's motion and thermodynamic state is calculated [5].
 - A two-valve engine test case is functioning as shown in Figure I.17.2 using the immersed boundary methods, showing flow (a) into the combustion chamber when the intake valve is at 80° after top dead center and (b) flow out of the chamber when the exhaust valve is at 640° after top dead center.

Spray Modeling

- Invented and developed VOF in FEM for true multi-phase flow for the following improvements in predictive modeling

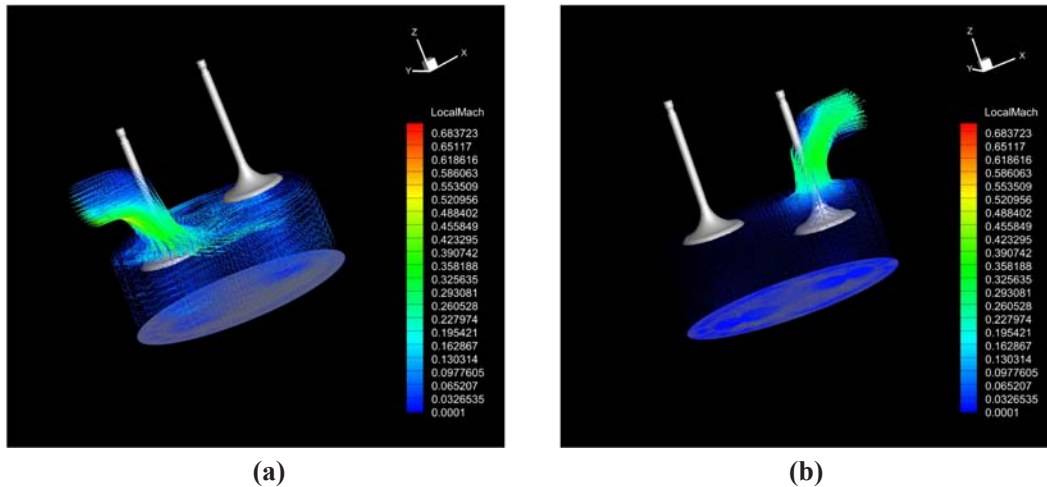


Figure I.17.2 - Two-Port engine. (a) Intake valve operating showing the magnitude of velocity of the fluid entering at 80° after top dead center and (b) exhaust valve operating showing magnitude of velocity and vectors at 640° after top dead center.

- To fully represent the spray break-up process; to produce predictive spray modeling. The results being produced on the highly resolved system will allow us to develop a model to transition from a true spray break-up to the Lagrangian particle and Rayleigh–Taylor secondary break-up systems, thereby producing solid engineering modeling for the injection system. Figure I.17.3 shows liquid being injected into air at 3 bar through an orifice of 0.01-mm diameter early in time. The liquid inlet is slug flow and laminar, no turbulence is applied to the fluid entering the domain. The break-up length where the wave instabilities are large enough to cause ligamentation is five orifice diameters downstream of inlet, which is near the results obtained by direct numerical simulation as reported in Waters et al. [3].

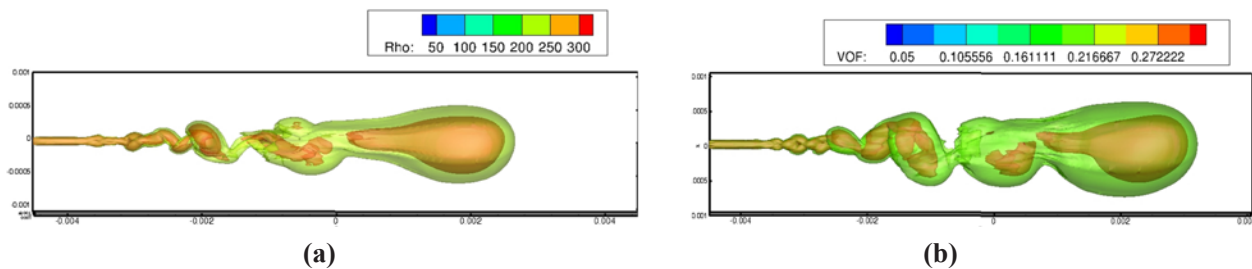


Figure I.17.3 - Multiphase flow simulation with VOF method, gasoline injected into quiescent air at 3 bar. (a) Gasoline jet primary break-up into ligaments and (b) primary break-up and w-component of velocity of air showing recirculation.

- In collaboration with Sandia National Laboratories, a highly resolved solution to engine injection using the KIVA-hpFE VOF system along with Chemkin-Pro for reactive chemistry will be used to develop a flamelet model useful for all flow regimes, low-speed to highly turbulent. In Figure I.17.4 the grid for the injector of the Engine Combustion Network (ECN) Spray G case is shown with a cut-away revealing the interior. The needle valve is a surface that overlays the grid, just as the valves over the cylinder grid. Spray solutions are currently be developed.
- Adding the KH-RT spray model [9] and validating on ECN Spray A case. The Spray A case with injection of diesel into quiescent nitrogen at 2.2 MPa is shown in Figure I.17.5. Validation continues in collaboration with Oakland University and Texas Technology University.

Computational Efficiency

- Continued work on parallel solution method
- Delivers superliner scalability [8]

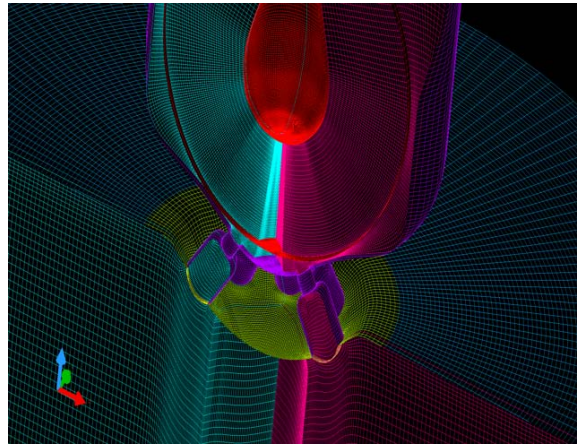


Figure I.17.4 - The Spray G ECN case with the grid in cut-away showing the nozzles

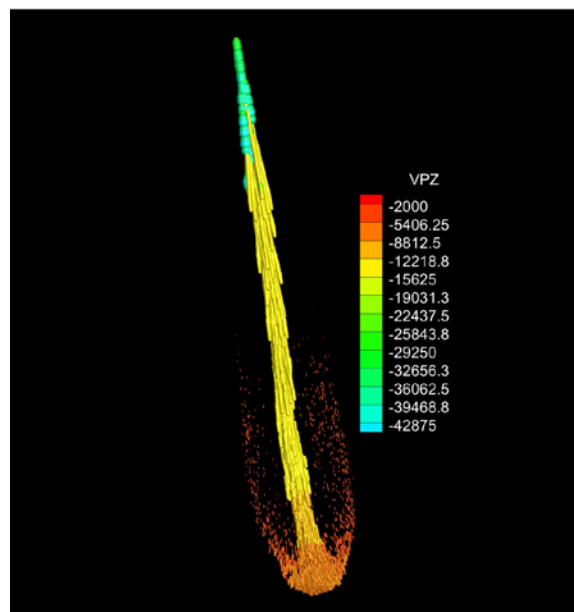


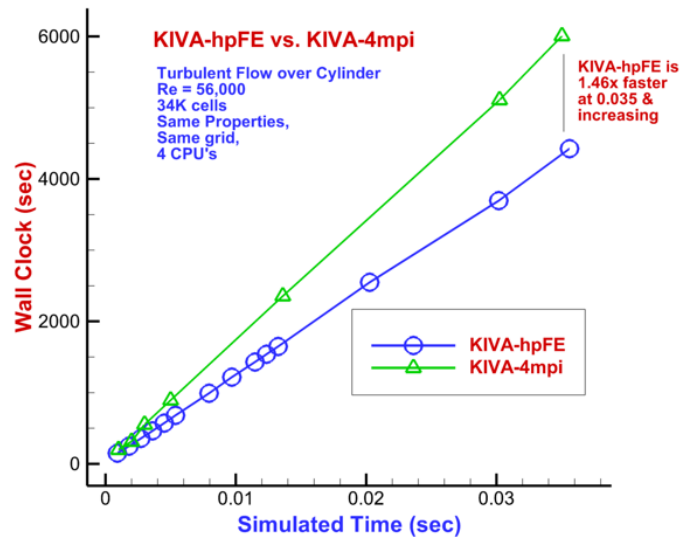
Figure I.17.5 - The ECN Spray A case: injection of diesel in quiescent nitrogen at 2.2 MPa, KH-RT spray model

- A code $12\times$ faster than KIVA-4mpi (Los Alamos National Laboratory's previous unstructured grid code for engines) per engine cycle on the same problems with exact same settings and grid size while being much more accurate. In addition, KIVA-hpFE produces better accuracy than previous codes on coarser grids. Hence, the new code is not only capable of being faster on the same resolution as old codes, but is more accurate even on less resolved problems, providing additional advantages. Figure I.17.6 demonstrates the ever increasing computational speed versus KIVA-4mpi; at 0.38 s of simulation time, KIVA-hpFE is $1.44\times$ faster. The improvement in speed translates to $12\times$ faster than the previous version of parallel KIVA over an engine cycle running at 1,000 rpm.

Conclusions

The KIVA development program at Los Alamos National Laboratory is nearing the objective of having a robust state-of-the-art CFD software for turbulent reactive flow, particularly well-suited for combustion modeling in engines or machines where immersed moving boundaries are involved, all with an eye toward solutions produced on quality grids created with a minimal amount of labor.

- Predictive spray modeling with the addition of VOF method



CPU – central processing unit

Figure I.17.6 - KIVA-hpFE's ever increasing advantage in computational speed over KIVA-4mpi; at 0.38 s of simulation time, KIVA-hpFE is 1.44x faster (for the problem being solved by both systems with exactly the same settings)

- Collaborating with Sandia National Laboratories on modeling spray combustion
- Developing transition to Lagrangian particle transport from predictive spray break-up for engineering type simulations
- KH-RT spray model added to the code with validation ongoing via the ECN test cases
- ECN Spray G and Spray A simulations in progress
 - Spray G case with VOF method for predictive liquid core break-up
 - Spray A case with KH-RT for validation
- Exascale possibilities because most operations are local to elements (vectorizable and Cuda friendly)
 - Graphics processing unit friendly CFD
- Robust moving immersed boundary method has been developed
- Fast grid generation: computer-aided drawing to CFD grid in nearly a single step
- Chemkin-Pro added for faster, larger, and more robust chemistry
- Improving memory handling for hp-adaptive FEM and exponentially grid convergent system
- A software for industry and researchers via commercialization and collaboration

References

1. Carrington, D.B. "A characteristic-based split hp-adaptive finite element method for combustion modeling in KIVA-hpFE." LANL Scientific Report no. LA-UR-09-06527, 2009.
2. Carrington, D.B., X. Wang, and D.W. Pepper. "A predictor-corrector split projection method for turbulent reactive flow." *Journal of Computational Thermal Sciences*, Begell House Inc., vol. 5, no. 4, pp.333–352, 2014.

3. Carrington D.B., X. Wang, and D.W. Pepper. "An *hp*-adaptive Predictor-Corrector Split Projection Method for Turbulent Compressible Flow." Proceedings of the 15th International Heat Transfer Conference, IHTC-15, Kyoto, Japan, August 10–15, 2014.
4. Carrington, D.B., M. Mazumder, and J.C. Heinrich. "Three-Dimensional Local ALE-FEM Method for Fluid Flow in Domains Containing Moving Boundaries/Objects Interfaces." *Progress in Computational Fluid Dynamics*, to appear.
5. Carrington, D.B., J. Waters, and B. Philipbar. "KIVA-hpFE: 2017 Updates of the 3M's: methods, models & meshes KIVA Update." Los Alamos Scientific Report no. LA-UR-17-27375. AEC/HCCI Working Group Meeting at USCAR, Detroit, MI, August 22, 2017.
6. Waters J., D.B. Carrington, and D.W. Pepper. "An Adaptive Finite Element Method with Dynamic LES for Incompressible and Compressible Flows." *Journal of Computational Thermal Sciences*, Begell House Inc., Vol.8(1), pp.57–71, 2016.
7. Waters, J., D.B. Carrington, and M.M. Francois. "Modeling Multi-phase Flow: Spray Break-up Using Volume of Fluids in a Dynamic LES FEM method." *Numerical Heat Transfer, Part B*, vol. 72, no. 4, pp. 285–299, 2017.
8. Waters, J., and D.B. Carrington. "A parallel Large Eddy Simulation in a finite element projection method for all flow regimes." *Numerical Heat Transfer, Part A*, vol, 70, n0. 2, pp. 117–131, 2016.
9. Reitz, R.D. "Modeling Atomization Processes in High-Pressure Vaporizing Sprays." *Atomization and Sprays Technology*, vol 3, pp. 309–337, 1987.

Key Fiscal Year 2017 Publications

1. Waters, J., D.B. Carrington, and M.M. Francois. "Modeling Multi-phase Flow: Spray Break-up Using Volume of Fluids in a Dynamic LES FEM method" *Numerical Heat Transfer, Part B*, vol. 72, no. 4, pp. 285–299, 2017.
2. Waters, J., and D.B. Carrington. "A Dynamic Large Eddy Model for Simulating Turbulent Reactive, Flow in Engines: A Parallel adaptive Finite Element Method." Proceedings of WCX™17: SAE International World Congress Experience, Detroit, MI, April 2–4, 2017.
3. Waters, J., D.B. Carrington, X. Wang, and D.W. Pepper. "A Dynamic Large Eddy Model for Simulating Turbulent Reactive Flow with an Adaptive Finite Element Method," Proceeding of the 2nd Thermal and Fluid Engineering Conference, TFEC2017, ASTFE, Las Vegas, NV, April 2–5, 2017.
4. Waters, J, and D.B. Carrington. "Modeling Turbulent Reactive Flow in Internal Combustion Engines with an LES in a semi-implicit/explicit Finite Element Projection Method." Proceedings of the ASME 2016 Internal Combustion Fall Technical Conference, ICEF2016, Greenville, SC, October 9–12, 2016.
5. Waters J., and D.B. Carrington. "Parallel Large Eddy Simulation for Modeling 3D Turbulent Flow in Engines." Proceedings of the ASME 2016 Fluids Engineering Division Summer Meeting, Washington, DC, July 10–14, 2016.
6. Waters, J., and D.B. Carrington. "A parallel Large Eddy Simulation in a finite element projection method for all flow regimes." *Numerical Heat Transfer, Part A*, vol, 70, n0. 2, pp. 117–131, 2016.
7. Waters J., D.B. Carrington, and D.W. Pepper. "An Adaptive Finite Element Method with Dynamic LES for Incompressible and Compressible Flows." *Journal of Computational Thermal Sciences*, Begell House Inc., Vol.8(1), pp.57–71, 2016.

8. Carrington, D.B., J. Waters, and B. Philipbar. "KIVA-hpFE: 2017 Updates of the 3M's: methods, models & meshes KIVA Update." Los Alamos Scientific Report no. LA-UR-17-27375. AEC/HCCI Working Group Meeting at USCAR, Detroit, MI, August 22, 2017.
9. Waters, J., and D.B. Carrington. "Parallel local ALE, hp-adaptive FEM for Modeling Engines with Injection and LES." Los Alamos Scientific Report no. LA-UR-17-20578. AEC/HCCI Program Review Meeting, Livermore, CA, January 31, 2017.

I.18 Accelerating Predictive Simulation of Internal Combustion Engines with High Performance Computing

K. Dean Edwards, Principal Investigator

Oak Ridge National Laboratory
National Transportation Research Center
2360 Cherahala Blvd.
Knoxville, TN 37932
E-mail: edwardskd@ornl.gov

Michael Weismiller, DOE Technology Manager

U.S. Department of Energy
E-mail: Michael.Weismiller@ee.doe.gov

Start Date: October 1, 2016	End Date: September 30, 2017	
Total Project Cost: \$340,000	DOE share: \$340,000	Non-DOE share: \$0

Acknowledgments

Co-Authors

Charles E.A. Finney, Wael R. Elwasif, Oak Ridge National Laboratory

Project Introduction

This project supports rapid advancements in engine design, optimization, and control through the development and application of advanced simulation tools and novel techniques to best utilize high performance computing (HPC) resources and detailed predictive models. This project couples Oak Ridge National Laboratory's (ORNL's) experimental and modeling expertise for engine and emissions-control technologies with DOE's Advanced Scientific Computing Research (ASCR) leadership HPC resources and fundamental research tools. Access to these resources is allocated primarily via a competitive process for the DOE ASCR Leadership Computing Challenge (ALCC) program. Specific focus areas evolve according to the needs of industry and DOE with the project typically supporting one or more tasks in collaboration with industry partners.

During Fiscal Year 2017, this project primarily supported a multi-year collaborative effort between General Motors, ORNL, Lawrence Livermore National Laboratory (LLNL), and Convergent Science which is using HPC resources and graphics processing unit (GPU)-enabled numerical solvers to evaluate the impact of increased simulation detail on the predictive accuracy and computational needs of computational fluid dynamics (CFD) diesel engine simulations. Current commercially available computing resources provide capability for reasonably detailed engine simulations when the field of study is relatively narrow and fast turn-around time is not crucial. However, for applications such as virtual engine design and calibration where hundreds or thousands of individual simulations are needed with rapid throughput, CFD engine simulations must be overly simplified resulting in a trade-off between accuracy and speed. The use of massively parallel HPC resources and faster, GPU-enabled numerical solvers provide a more favorable trade-off enabling highly detailed (and hopefully more accurate) simulations with more acceptable computational times. Under this project, the team is using ORNL's Titan and LLNL's Zero-RK chemistry solvers to systematically increase the level of simulation detail and add more first principle, predictive submodels. The resulting impact on simulation accuracy and computational time is then evaluated. Efforts during Fiscal Year 2017 focused on enabling highly detailed chemical kinetics in the CONVERGE CFD engine model to improve the accuracy of combustion and emissions predictions. These efforts were supported by a 2016 ALCC award of 16 Mhrs and a 2017 ALCC award of 5.2 Mhrs on Titan.

Objectives

- Use massively parallel HPC resources and GPU-enabled numerical solvers to enable use of CFD engine models with significantly increased levels of detail and predictive submodels including detailed chemical kinetics
- Evaluate the impact of model refinements on predictive accuracy, computational speed, and extent of operational space covered without further tuning and calibration.

Approach

As part of a multi-year collaborative effort between General Motors, ORNL, LLNL, and Convergent Science, the project team is using HPC and GPU-enabled numerical solvers to enable increased levels of simulation detail in CFD diesel engine models. Our approach involves systematically adding increased detail and first principles-based submodels to improve the predictive accuracy of combustion performance and emissions over more of the engine operating range while reducing the need for tuning and calibration. The baseline model for this effort is a closed-valve sector-mesh diesel engine model in CONVERGE. Efforts during Fiscal Year 2017 focused on using LLNL's Zero-RK GPU-enabled chemistry solvers on Titan to allow the use of detailed chemical kinetics in the CFD models with acceptable run times and to evaluate the resulting impact on emissions predictions for skeletal, reduced, and detailed mechanisms with single- and multi-component fuel surrogates. The impact of mesh refinement and every-cell versus multi-zone chemistry solutions in conjunction with the more detailed combustion modeling were also evaluated. Finally, efforts were begun to transition to a full-cylinder, open-cycle model with gas exchange and conjugate heat transfer to provide more accurate boundary conditions for the refined chemistry models. These efforts will continue into Fiscal Year 2018 under the current ALCC project which began in July 2017.

Results

By systematically applying additional refinements to the baseline model, it was possible to evaluate the impact of each approach and determine which refinements proved most beneficial. The baseline model consists of a closed-valve, sector-mesh model of a production 1.6-L General Motors diesel engine using a coarse mesh with a maximum cell count of approximately 170,000 cells. For the baseline, a skeletal n-heptane mechanism with 47 species and 74 reactions and the Hiroyasu soot model with a particulate size mimic approach was used. Simulations were performed for 602 cases in a design-of-experiments grid of ten engine control parameters representing the full calibration space of the engine including many extreme operating points which stretch the capabilities of a single model. This baseline model is representative of the typical level of detail possible in CFD engine simulations when a large number of simulations must be performed with rapid throughput on conventional, commercially available computing resources (workstations and small clusters). With these limitations, the baseline model fails to accurately capture the combustion performance and emissions observed experimentally for many of the 602 cases examined.

Figure I.18.1 compares an experimentally measured emissions index for nitrogen oxides (NO_x) and hydrocarbons (HC) with simulation predictions using different levels of modeling detail made possible by running the GPU-enabled Zero-RK chemistry solvers on Titan. For the baseline model (top plots) the worst agreement occurs for cases with late injection, high exhaust gas recirculation rates, and rich operation. In many of these cases, the model underpredicts combustion rate, resulting in incomplete combustion and high HC levels. Moving to a reduced n-heptane mechanism with 144 species and 900 reactions provided significant improvement in NO_x and HC emissions accuracy for many points (second plots from the top), although burn rate is still underpredicted for some high exhaust gas recirculation and rich cases. A refined mesh with maximum cell count of approximately 615,000 cells provides an expected improvement in NO_x prediction with refined resolution of in-cylinder temperature gradients. However, HC predictions showed little improvement overall and became worse for some cases due to over-refinement near the walls. By further adjusting the grid near the walls and recalibrating the spray model, the best overall prediction accuracy for NO_x and HC was achieved for this part of the study (bottom plots). However, predictions of carbon monoxide (CO) and soot (not shown) still need considerable improvement at most of the simulated conditions.

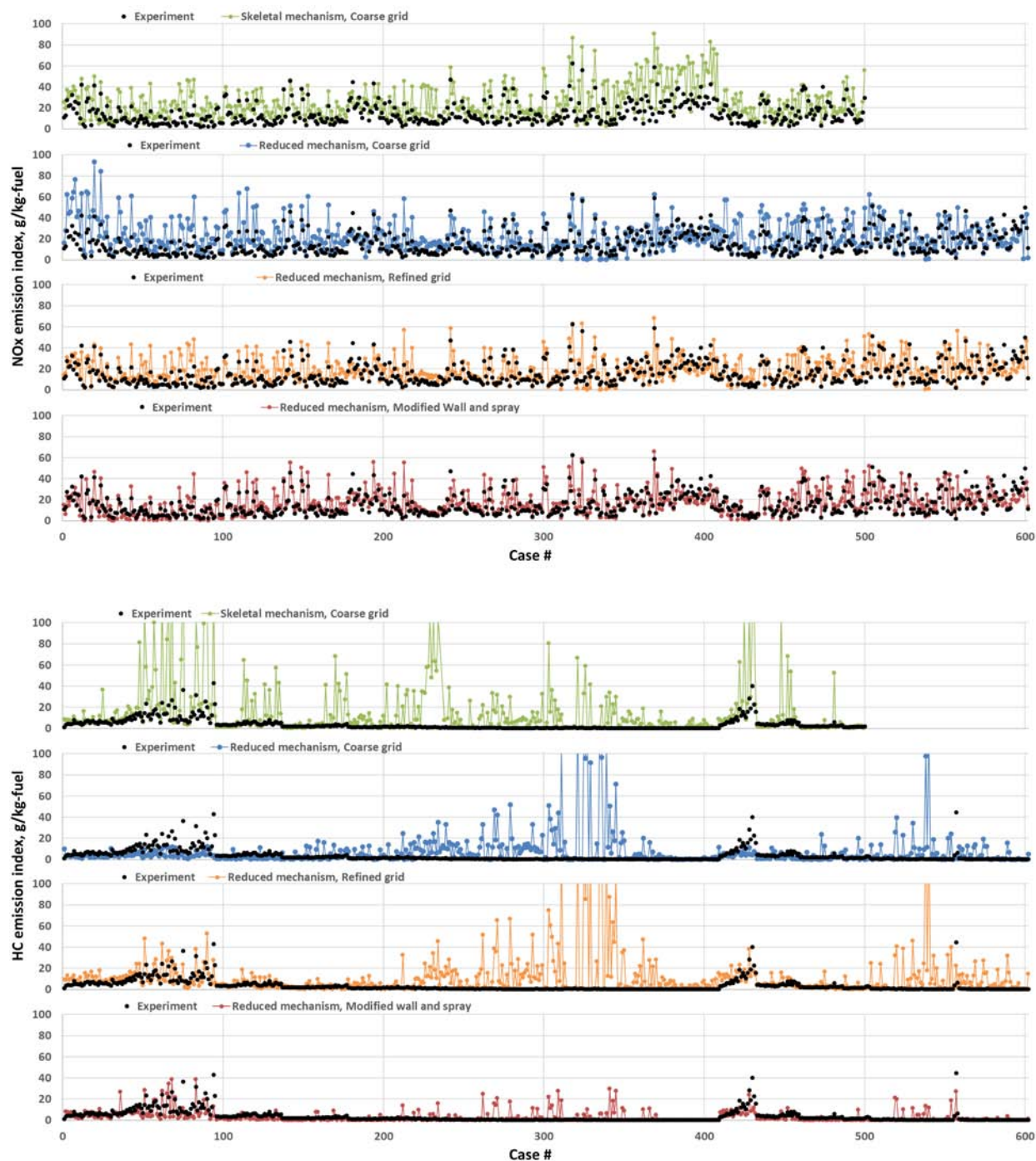


Figure I.18.1 - Comparison of experimentally measured emissions index for NO_x and HC with simulation predictions using different levels of modeling detail. (Figure Credit/Source: K. Dean Edwards, ORNL)

In addition to improved accuracy, the use of the GPU-enabled chemistry solvers on Titan provided significant reductions in computational time. With the reduced, 144-species mechanism, a 33% speed-up of the chemistry solution and 10–20% overall reduction in simulation time was observed using Zero-RK and Titan's GPUs compared to a conventional cluster without GPUs. Simulations with a four-component fuel surrogate and detailed mechanism (766 species, ~6,800 reactions) could not be completed with the conventional cluster but were completed in approximately five days using Titan's GPUs. Similarly, with proper binning strategies, a multi-zone chemistry approach can provide significant speed-up over an every-cell approach without compromising accuracy. For simulations using the reduced n-heptane mechanism (144 species), solving

chemistry in every cell required 10–13 days of computation time whereas a multi-zone approach with proper binning for accuracy only took two days (roughly 6× speed-up). However, the achievable speed-up decreases as the level of chemistry detail increases. Using a four-component fuel surrogate and detailed mechanism (766 species), the multi-zone bin tolerances had to be tightened to accurately match every-cell results which reduced the computational speed-up to approximately 2×.

Despite the significant improvements achieved to date, further refinements are needed to fully capture engine performance over the full calibration space. In particular, CO and soot predictions still need to be substantially improved. Efforts have begun under the current, 2017 ALCC project to improve the boundary and initial conditions for the model. The current closed-valve, sector mesh model with initial in-cylinder conditions at intake valve closing provided by a separate GT-POWER model is being replaced with a full-cylinder, open-cycle model with gas exchange to better capture mixing and breathing. A conjugate heat transfer model for the engine is being developed in CONVERGE to provide better thermal boundary conditions inside the cylinder. Efforts with these model refinements will continue in Fiscal Year 2018.

Conclusions

- Using GPU-enabled solvers on HPC resources such as Titan allows the introduction of greater detail into CFD engine models resulting in wider coverage of the engine calibration and design space without additional tuning or calibration.
- Solving chemistry in every cell significantly increases computational time without providing an accuracy improvement over a multi-zone chemistry approach with proper binning tolerances.
- Mesh refinement increases computational requirements but can significantly improve resolution of temperature gradients and thus the accuracy of NO_x predictions. However, over-refinement of the grid near the wall had an adverse effect on HC and CO predictions.
- Increasing detail in the chemical kinetic mechanism can significantly expand the extent of the operating space that the model can accurately cover.
- Further refinements are needed to accurately predict CO and soot emissions over the full calibration space.

Key Fiscal Year 2017 Publications

1. Pasunurthi, S.S., R.S. Jupudi, S.D. Wijeyakulasuriya, S.R. Gubba, H. Im, M.J. Ali, R.J. Primus, A.E. Klingbeil, and C.E.A. Finney. “Cycle-to-cycle variation study in a dual-fuel operated engine.” SAE 2017-01-0772, 2017.
2. Gao, J., R.O. Grover Jr., V. Gopalakrishnan, R. Diwakar, W.R. Elwasif, K.D. Edwards, C.E.A. Finney, and R.A. Whitesides. “Steady-state calibration of a diesel engine in CFD using a GPU-based chemistry solver.” ASME ICEF2017-3631, 2017.
3. Gubba, S.R., R.S. Jupudi, S.S. Pasunurthi, S.D. Wijeyakulasuriya, R.J. Primus, A.E. Klingbeil, and C.E.A. Finney. “Capturing pressure oscillations in numerical simulations of internal combustion engines.” ASME ICEF2017-3527, 2017.
4. Edwards, K.D., C.E.A. Finney, W.R. Elwasif, and R.A. Whitesides. “Enabling increased simulation detail with HPC and GPU-enabled solvers to improve predictive accuracy.” AEC Program Review Meeting, Southfield, MI, August 2017.
5. Wagner, R.W. “HPC driving advances in multi-physics simulations.” Invited keynote address, 2017 CONVERGE User Conference, Dearborn, MI, September 2017.
6. Whitesides, R.A., W.R. Elwasif, R.O. Grover Jr., J. Gao, V. Gopalakrishnan, R. Diwakar, K.D. Edwards, and C.E.A. Finney. “Application and performance of chemistry solvers on the Titan supercomputer.” 2017 CONVERGE User Conference, Dearborn, MI, September 2017.

7. Keum, S., R.O. Grover Jr., W.R. Elwasif, K.D. Edwards, C.E.A. Finney, and R.A. Whitesides. "Modeling Partial Fuel Stratification in a Homogeneous Charge Compression Ignition Engine using General Purpose Graphical Processing Unit (GPGPU) enabled CFD Tools." 2017 OLCF Users Meeting, Oak Ridge, TN, May 23–25, 2017.
8. Gao, J., R.O. Grover Jr., V. Gopalakrishnan, R. Diwakar, W.R. Elwasif, K.D. Edwards, C.E.A. Finney, and R.A. Whitesides. "Steady State Calibration for Diesel Engines using General Purpose GPU enabled CFD Tools." 2017 OLCF Users Meeting, Oak Ridge, TN, May 23–25, 2017.

I.19 Large Eddy Simulation Applied to Advanced Engine Combustion Research

Joseph C. Oefelein, Principal Investigator

Sandia National Laboratories
7011 East Avenue, MS 9051
Livermore, CA 94551-0969
E-mail: oefelei@sandia.gov

Michael Weismiller, DOE Technology Manager

U.S. Department of Energy
E-mail: Michael.Weismiller@ee.doe.gov

Start Date: October 1, 2015	End Date: September 30, 2018	
Total Project Cost: \$1,100,000	DOE share: \$1,100,000	Non-DOE share: \$0

Acknowledgments

Co-Author

Guilhem Lacaze, Sandia National Laboratories

Project Introduction

Developing an improved understanding of transient injection, mixing, and combustion processes inherent in diesel injection continues to be an important element in the design of advanced engines. To provide a more detailed understanding, a series of calculations were performed using large eddy simulation (LES) with the goal of quantifying the transient turbulent mixing and combustion phenomena that dominate at typical engine operating conditions. Conditions were selected that match those of the Sandia Spray A experiment (see www.sandia.gov/ecn). Liquid n-dodecane at 363 K was injected through a 0.09-mm diameter injector nozzle into a gaseous ambient mixture at 900 K and 60 bar. The peak injection velocity was 620 m/s, which was selected to provide the same injected mass flow rate as the experiment. Three-dimensional renderings of the instantaneous fields highlight the many intricate features of the flow that are not captured by current models. For example, the structure of turbulence, temperature, scalar dissipation, and ignition.

Initial studies served to validate the models used to represent turbulent scalar mixing processes, which is an important first step toward detailed studies of autoignition. Relevant data was extracted and utilized to develop an optimized chemical scheme that was capable of reproducing key quantities such as the autoignition delay time over the full range of conditions encountered in the domain with quantified uncertainties. Design of the optimized chemical mechanism was achieved using Bayesian inference, which quantifies the optimal values of the model parameters together with the associated uncertainties. It was demonstrated that the optimized mechanism provided predictions within the same variability as leading detailed mechanisms. The benchmark configuration was then used to study the effects of broadband transient dynamics by extracting data not available from the experiments. First, results were compared with available experimental data (e.g., penetration data, spreading angles, and shadowgraphs) to establish a validated correspondence with the experimental cases. The studies were then extended by coupling the system of submodels to a first principles combustion closure with emphasis on capturing the inherent autoignition processes observed in the experiment.

Objectives

- Combine a state-of-the-art simulation capability based on the LES technique with Advanced Engine Systems R&D activities
- Perform companion simulations that directly complement optical engine and supporting experiments being conducted at the Combustion Research Facility and elsewhere
- Maximize benefits of high-performance massively parallel computing for advanced engine combustion research using DOE leadership class computer platforms

- Test and demonstrate use of a coupled model framework for LES that simultaneously treats high-pressure thermodynamics, transport, and turbulence–chemistry interactions
- Quantify the combined effects of broadband (small-scale) turbulence and transient mixing dynamics on the development of ignition kernels and combustion

Approach

LES calculations are performed using a single unified code framework called RAPTOR. Unlike conventional LES codes, RAPTOR is a direct numerical simulation solver that has been optimized to meet the strict algorithmic requirements imposed by the LES formalism. The theoretical framework solves the fully coupled conservation equations of mass, momentum, total energy, and species for a chemically reacting flow. It is designed to handle high Reynolds number, high-pressure, real-gas and/or liquid conditions over a wide Mach operating range. It also accounts for detailed thermodynamics and transport processes at the molecular level. A noteworthy aspect of RAPTOR is it was designed specifically for LES using non-dissipative, discretely conservative, staggered, finite volume differencing. This eliminates numerical contamination of the subfilter models due to artificial dissipation and provides discrete conservation of mass, momentum, energy, and species, which is an imperative requirement for high quality LES.

Results

A major goal in the development of closure strategies for turbulent combustion is to use first principles models designed specifically for LES (i.e., using all the information available from the LES formalism in contrast to current closures derived from Reynolds-averaged Navier–Stokes that make use of relatively limited information). Recently, for example, a class of reconstruction models has been proposed that combines the purely mathematical approximate deconvolution procedure with physical information from an assumed scalar spectrum to match specific scalar moments. Using this method, a surrogate to the exact scalar field can be estimated such that filtered moments match to a specified order. In principle, the surrogate field can be used to calculate the subfilter contribution of any related nonlinear function. In practice, however, the extent of the nonlinearity limits the accuracy of reconstruction methods and it has been shown that they cannot be used reliably to close the filtered chemical source terms directly. They can be used, however, to obtain highly accurate representations of polynomial nonlinearities such as the subfilter variances and covariances in the filtered equations for LES if appropriate levels of resolution are applied. These are precisely the input required to generate subfilter fluctuations stochastically. Given these findings, an extension to the reconstruction approach has been derived by coupling it to a stochastic technique. The matrix of subfilter variances and covariances are obtained via reconstruction, then used as input to a Cholesky decomposition to obtain a correlated approximation of the subfilter velocity and scalar fluctuations in time. The modeled instantaneous fields (i.e., Favre averaged resolved-scale contribution plus the correlated subfilter fluctuations) are used to evaluate the filtered chemical source terms directly. The filtered source terms are closed using the optimized chemical mechanism described in previous work. The corresponding model coefficients are evaluated locally in a manner consistent with the dynamic modeling procedure. Thus, the only adjustable parameters are the filter size, time step, and boundary conditions. In the limit as the filter size and time step approach the smallest relevant scales, subfilter contributions approach zero and the solution converges to a direct numerical simulation. A novel feature of this approach is that it naturally accounts for multiscalar mixing at subfilter timescales, which is an important requirement, both in general, and for modeling ignition transients.

To address issue of variability in chemical kinetics mechanisms, an Arrhenius-based chemical model was developed using Bayesian inference to predict autoignition over the ranges of conditions (pressure, temperature, equivalence ratio) relevant to the Spray A case (see Hakim et al. 2017 for details). The chemical model was coupled to the combustion closure outlined above along with models to treat real-fluid (gas–liquid) thermodynamics and transport. The coupled system of models was then used to performed detailed LES of injection, mixing and the resultant autoignition processes in the Spray A case. The structure of the scalar dissipation field and representative time traces of the modeled instantaneous subfilter fluctuations of equivalence ratio are shown in Figure I.19.1. Sensitizing the simulations to subfilter scales in time facilitates formation of ignition kernels in a manner consistent with the chemical timescales.

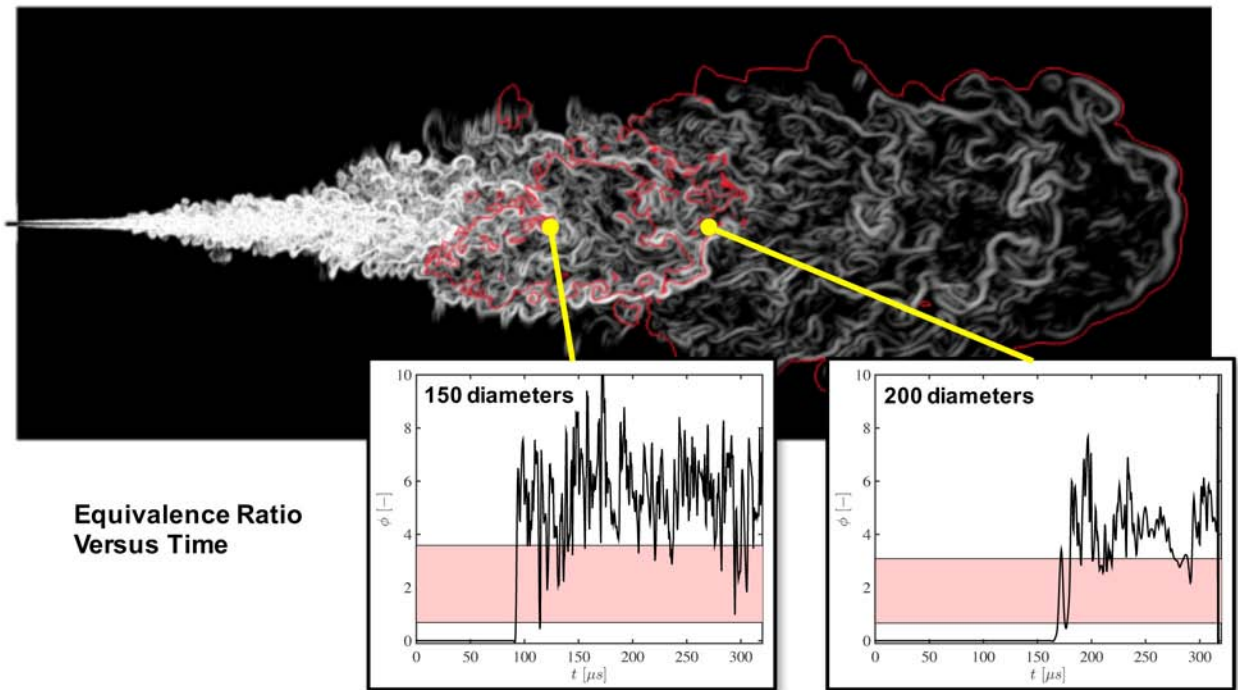
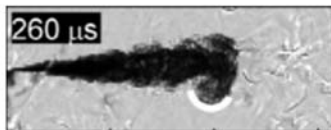


Figure I.19.1 - Instantaneous cross-section of the scalar dissipation field showing modeled instantaneous fluctuations of the equivalence ratio versus time at two locations in the flow

The transient ignition sequence predicted by LES at conditions identical to the experiment are shown in Figure I.19.2. On the left are a set of shadowgraph images that highlight the structure of the autoigniting jet in the experiment. On the right is a three-dimensional rendering of the instantaneous liquid n-dodecane fuel jet

First kernel, diameter = 500 μm
(too small to be optically detected)
Location: tip of the jet, off-axis

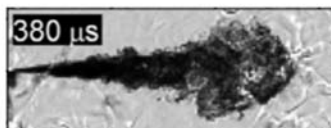
Independent kernels appear,
diameter = 500 μm to 2mm (still
very small for optical detection)
Location: tip of the jet, off-axis



Many small kernels present in the "jet edge" region, what is the impact on Schlieren?

Single flame structure with upstream independent kernels, flame expands through dilatation and autoignition

Main flame region at the jet extremity, autoignition locations observed ahead of main front



Schlieren images by Skeen *et al.*, PCI, 2015

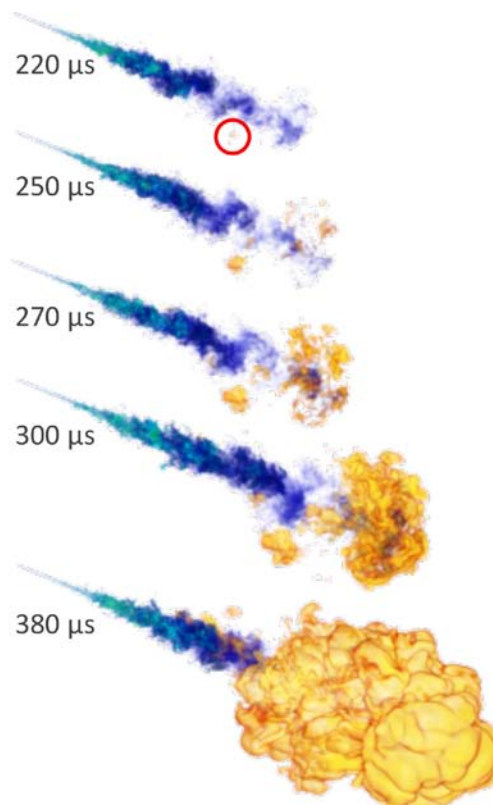


Figure I.19.2 - Transient ignition sequence predicted by LES at conditions identical to the experiment

injected at a temperature of 363 K into the high pressure chamber at 60 bar, 900 K, with 15% oxygen. Scalar mixing is represented by a blue volume rendering based on the fuel mixture fraction. The development of ignition kernels and resultant flame structure are tracked by a yellow volume rendering based on temperature. The locations of the first flame kernels are in good agreement with the shadowgraphs. The first kernels appear initially in the downstream region of the jet where large vortical structures carry fuel away from the high-speed jet. In those regions, turbulence and hot ambient conditions enhance the mixing of the fuel with the ambient. Subsequently, other locations reach a burning state by either autoignition or propagation mechanisms. The spatial and temporal fidelity provides access to the detailed broadband three-dimensional characteristics of injection, ignition, and combustion at conditions that (1) match the experiment, and (2) are directly relevant to practical systems. Further details are given in the Fiscal Year 2017 publications.

Conclusions

The current high-resolution benchmark cases have revealed the instantaneous three-dimensional structure of injected fuel jets with a degree of fidelity that is not accessible by current experimental diagnostics or engineering computational fluid dynamics codes. Corresponding mixture fraction, temperature, density, Mach number, and speed of sound distributions (for example) were analyzed. Large density gradients associated with the compressed liquid core triggers a cascade of processes characteristic of supercritical flows, where high-pressure nonlinear mixing and diffusion profoundly modify turbulent mixing. These mixing processes happen concurrently to chemical runaway that is captured in the present work with the optimized chemical mechanism and companion turbulent combustion closure. Using this combined system of subfilter models, accurate prediction of the autoignition sequence has been obtained. The current work aims to find an optimal balance in requirements between the coupled system of turbulence and chemical models. Since the present approach is based on an Arrhenius formulation, its implementation in most research and design codes is greatly facilitated as well as its interface with any turbulent combustion closure. In future work, the uncertainties on the input parameters will be propagated through the LES to gain insights into the uncertainty on the simulation results.

Key Fiscal Year 2017 Publications

1. Hakim, L., G. Lacaze, M. Khalil, K. Sargsyan, H. Najm, and J. Oefelein. "Probabilistic Parameter Estimation of a 2-Step Chemical Kinetics Model for n-dodecane Jet Autoignition." *Combustion Theory and Modelling* (2017). Accepted.
2. Oefelein, J.C. "Dynamics of Gas-Liquid Interfaces in High-Pressure Systems." Invited topical lecture and paper at the 24th International Congress of Theoretical and Applied Mechanics, August 21–26, 2016.
3. Dahms, R.N. and J.C. Oefelein. "The Significance of Drop Non-Sphericity in Sprays." *International Journal of Multiphase Flow* (2016). 86:67–85.
4. Hakim, L., G. Lacaze, M. Khalil, H.N. Najm, and J.C. Oefelein. "Modeling Auto-Ignition Transients in Reacting Diesel Jets." *Journal of Engineering for Gas Turbines and Power* (2016). 138:112806 1–8.
5. Ruiz, A.M., G. Lacaze, J.C. Oefelein, R. Mari, B. Cuenot, L. Selle, and T. Poinso. "A Numerical Benchmark for High-Reynolds Number Supercritical Flows with Large Density Gradients." *AIAA Journal* (2016). 54(5):1445–1460.
6. Arienti, M., F. Doisneau, and J.C. Oefelein. "Computation of the Break-up of a Drop under Sudden Acceleration." Proceedings of the 28th Annual Conference on Liquid Atomization and Spray Systems, May 15–18, 2016.
7. Hakim, L., G. Lacaze, and J.C. Oefelein. "Large Eddy Simulation of Autoignition Transients in a Model Diesel Injector Configuration." SAE World Congress, Paper 2016-01-0872, Detroit, MI, April 12–14, 2016.
8. Gottiparthi, K.C., R. Sankaran, A.M. Ruiz, G. Lacaze, and J.C. Oefelein. "Large Eddy Simulation of a Supercritical Fuel Jet-in-Cross-Flow using GPU Acceleration." 54th AIAA Aerospace Sciences Meeting and Exhibit, Paper 2016-1939, San Diego, CA, January 4–8, 2016.

I.20 Development and Validation of Predictive Models for In-Cylinder Radiation and Wall Heat Transfer

Daniel C. Haworth, Principal Investigator

The Pennsylvania State University
140 Research East Building
University Park, PA 16802
E-mail: dch12@psu.edu

Michael Weismiller, DOE Technology Manager

U.S. Department of Energy
E-mail: Michael.Weismiller@ee.doe.gov

Start Date: January 1, 2016	End Date: December 31, 2018	
Total Project Cost: \$716,660	DOE share: \$639,236	Non-DOE share: \$77,424

Acknowledgments

Co-Authors

Volker Sick, University of Michigan
Joseph C. Oefelein, Sandia National Laboratories
James P. Szybist, Oak Ridge National Laboratory

This material is based upon work supported by the Department of Energy, Office of Energy Efficiency and Renewable Energy (EERE) and the Department of Defense, Tank and Automotive Research, Development, and Engineering Center (TARDEC), under Award Number DE-EE0007278.

Project Introduction

The lack of accurate submodels for in-cylinder radiation and heat transfer has been identified as a key shortcoming in developing truly predictive, physics-based computational fluid dynamics (CFD) models that can be used to develop and design combustion systems for advanced high-efficiency, low-emissions engines. Recent measurements of wall layers in engines show discrepancies of up to 100% with respect to standard CFD boundary layer models. And recent analysis of in-cylinder radiation based on the most recent spectral property databases and high-fidelity radiative transfer equation solvers has shown that at operating pressures and exhaust gas recirculation (EGR) levels typical of modern compression ignition truck engines, radiative emission can be as high as 40% of the wall heat losses, that molecular gas radiation (mainly carbon dioxide and water vapor) can be more important than soot particle radiation, and that a significant fraction of the emitted radiation (50% or more) can be reabsorbed before reaching the walls.

A hierarchical modeling approach is adopted that ranges from high-resolution “scientific” large eddy simulation (LES) to medium-resolution “engineering” LES to low-resolution time-dependent Reynolds-averaged Navier–Stokes (RANS). The submodels are being implemented in a code-neutral manner to facilitate implementation into CFD codes other than the ones that are used to carry out the research. Experimental data for model validation are being generated in single-cylinder research engines, and additional data for model development and validation are being derived using high-resolution LES. The overarching goal of this project is to develop, implement, and provide to the community open submodels for radiation and boundary-layer wall heat transfer in medium-resolution LES and unsteady RANS that (when coupled with models of equal fidelity for other key physical processes, such as liquid fuel sprays) provide truly predictive capability for CFD of in-cylinder processes in engines, including couplings between different modes of heat transfer.

Objectives

- Quantify the relative importance of turbulent boundary layer wall heat transfer, radiative heat transfer, and boundary layer/radiation couplings in engines

- Provide new experimental datasets that can be used to provide physical insight into heat transfer processes in engines, and to validate models
- Augment the experimental measurements with data from high-resolution numerical simulations
- Develop, implement, and validate a hierarchy of CFD-based models that can be used as part of predictive engine simulations to develop new high-efficiency, low-emissions engines

Approach

Four different engine configurations are being explored experimentally and/or computationally: (1) a canonical engine configuration that is an idealized version of a two-valve, single-cylinder optical research engine; (2) the two-valve, single-cylinder optical research engine itself; (3) a four-valve, single-cylinder optical research engine; and (4) a four-valve metal engine. The program builds on the efforts of projects that have been funded through the National Science Foundation/DOE Advanced Engine Combustion Program, and on other ongoing projects and collaborations among the investigators.

The research program has three novel elements that together, will enable significant advances in predictive CFD submodels for in-cylinder heat transfer: (1) explicit accounting for couplings between radiation and wall heat transfer modeling; (2) tight collaboration between modeling and experiment, including new experimental measurements and high-resolution LES data for model validation; and (3) a hierarchical modeling approach that includes high-fidelity modeling for physics discovery (high-resolution LES) to augment the experimental measurements, and predictive models that can be used for medium-resolution LES and unsteady RANS for engine combustion system development and design.

Results

Two high-quality datasets for wall heat transfer model validation in engines have been identified. The first is a direct numerical simulation (DNS) dataset for an idealized motored engine configuration [1]. There the data are limited to the compression stroke (no combustion). However, this high-resolution DNS dataset (Figure I.20.1) has the advantage of allowing the fundamental physical underpinnings of the various wall models to be assessed directly. For example, the assumptions that have been made in wall-function-based models can be assessed directly. The second dataset is high-speed Micro-PIV data from an optical engine [2]. There experimental data are available for both motoring and firing conditions, at a single spatial location on the head.

At the University of Michigan, initial spectrally resolved infrared (IR) radiation measurements were made in an optical engine. A complication is the quartz cylinder liner that is used in the experiment, which has complex spectral absorption and reflection characteristics at the IR wavelengths of interest. To better understand the optical qualities of the quartz, measurements were made in a simpler flame configuration: a Hencken burner. There, spectral radiation measurements were made with and without the quartz. This provided insight into the spectral radiation characteristics of the quartz, and guidance on what adjustments will be needed on the experimental and simulation sides to allow accurate quantitative comparisons of spectral infrared radiation to be made. Simulations of the Hencken burner have been performed, and computed radiation spectra have been extracted to compare with the experimental measurements.

The experimental configuration and examples of measured spectral IR radiative intensities for the Hencken burner flame are shown in Figure I.20.2. The strong attenuation of the radiation by the quartz in wavenumber bands corresponding to strong emission by carbon dioxide and water vapor can be seen.

A high-fidelity photon Monte Carlo (PMC) radiation model with line-by-line (LBL) spectral resolution was exercised to guide the design of engine experiments to be performed at Oak Ridge National Laboratory (ORNL). The purpose is to explore the potential influence of radiative heat transfer on knock in a spark-ignition engine. To this end, the concentrations of the two primary radiatively participating molecular gases (carbon dioxide and water vapor) and of soot particles were varied, allowing for different amounts in the unburned gases ahead of the flame and in the burned gases behind the flame. The spatial and temporal dependence of the local time-rate-of-increase of temperature due to radiative reabsorption in the end gas ahead

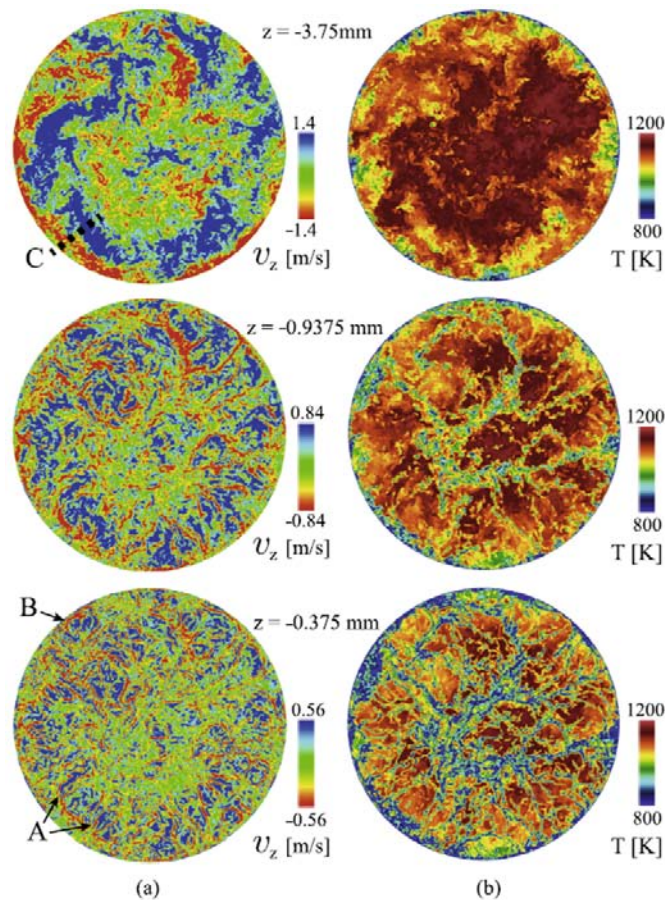


Figure I.20.1 - (a) Axial velocity and (b) temperature contours on horizontal slices at $z = -3.75$ mm and $z = -0.9375$ mm (distances below the head) at 346° after top dead center. (This is Figure 4 of Schmitt et al. [1].)

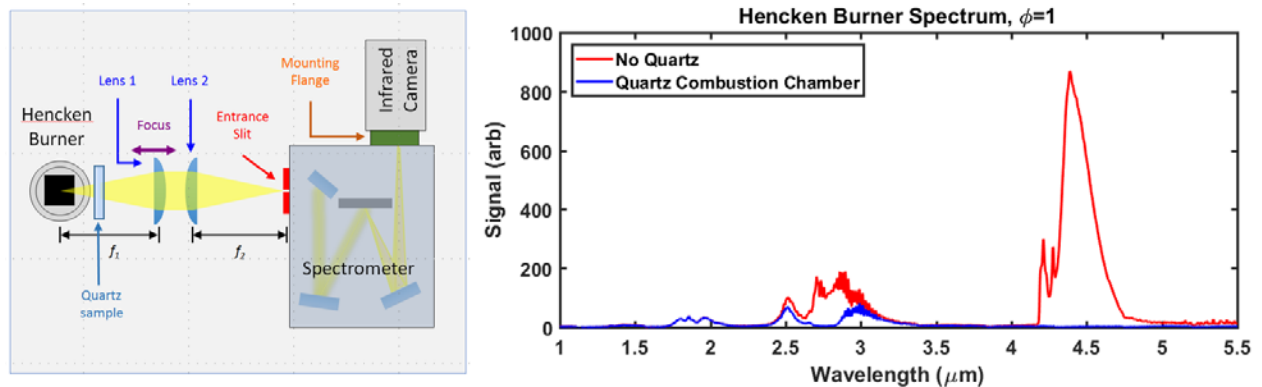


Figure I.20.2 - Left: Schematic of the experimental setup for the Hencken burner spectral radiation measurements at the University of Michigan. Right: Measured infrared spectra for a one atmosphere stoichiometric methane-air Hencken burner flame with and without quartz.

of the propagating flame was computed. Temperature increases due to radiation of 10 K to 20 K were found, depending of the concentrations of the participating gases and their temperature. The results have been found to be especially sensitive to the assumed degree of wall reflectivity of the incident radiation. The reflectivity of most metals increases with increasing wavelength, and can exceed 95% at the IR wavelengths that are of interest for in-cylinder heat transfer. With consideration of wall reflection, the radiation that reflects from the walls passes back through the end gas, resulting in an increase in radiative reabsorption.

Based on the findings from the modeling study, the engine experiments at ORNL were redesigned. The original design (Figure I.20.3) was to use exhaust gas from a diesel engine to provide the desired amounts of carbon dioxide, water vapor, and soot particles. This was based on the initial thinking that soot particles should play an important role in radiative heat transfer to the end gas. The modeling revealed that this is not the case, and that participating molecular gas radiation is more important. The revised plan calls for varying the amounts of carbon monoxide and water vapor to be fed into the intake of the engine, taking care to do this in a manner that does not alter the nonradiative aspects of the in-cylinder thermal environment (e.g., the ratio of specific heats).

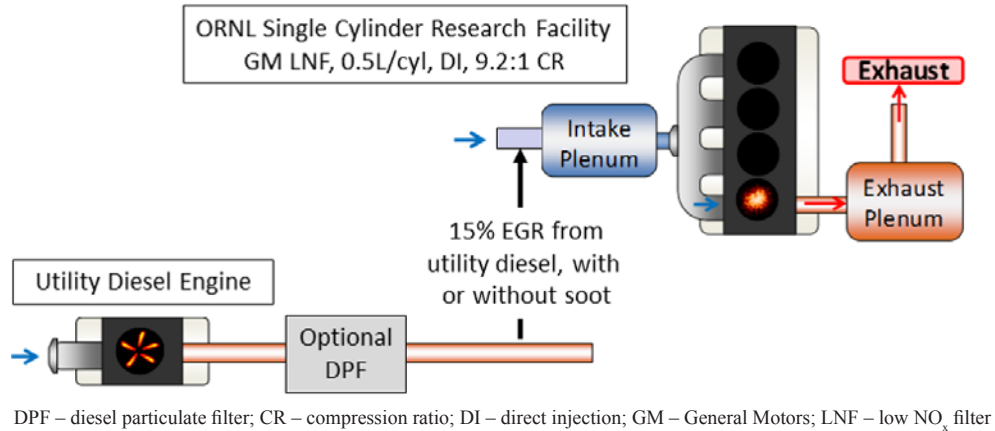


Figure I.20.3 - Schematic of the metal engine configuration at ORNL.

Finally, a highly simplified model for radiative heat transfer in engines and other high-pressure turbulent combustion systems was proposed. The model is based on observations from PMC-LBL computed spectral radiation characteristics in high-pressure turbulent spray flames and in engines. There it has been found that, to a good approximation, (1) the system is optically thin with respect to broadband soot radiation; (2) the system is optically thick at the primary carbon dioxide band (~4.2 μm), and little carbon dioxide radiation reaches the walls; and (3) the system is of intermediate optical thickness at the primary carbon dioxide–water vapor overlap band (~2.8 μm), and most of the radiation that reaches the walls is from water vapor. A simple box model for spectral radiation properties has been constructed that captures these key features (Figure I.20.4), and this is combined with a simple radiative transfer equation solver: a first-order spherical harmonics method, which requires the solution of a single elliptic partial differential equation for each band. Results from the simplified model have been compared with those from PMC-LBL. For the conditions tested, results from the simplified model are quite close to those from PMC-LBL, at a small fraction of the computational cost of PMC-LBL.

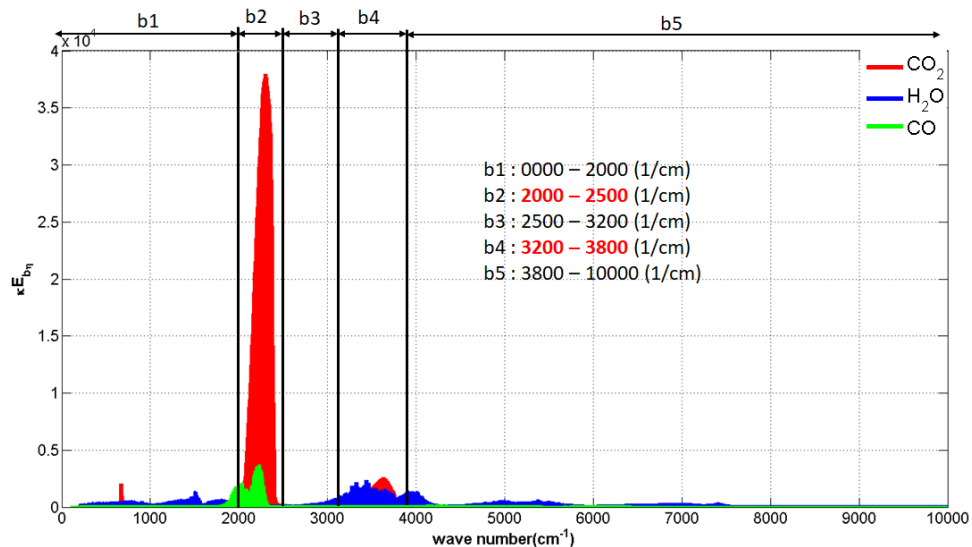


Figure I.20.4 - Schematic of a simplified spectral box model for high-pressure combustion systems.

A summary of key accomplishments for Fiscal Year 2017 is as follows.

- Identified two key datasets for validation of wall boundary layer wall heat transfer models, one from DNS and one from experimental measurements
- Performed the first spectrally resolved measurements of IR radiative intensity in an optical engine, and initiated quantitative comparisons between computed and measured spectral radiative intensities
- Exercised PMC–LBL radiation model to guide the design of the engine experiments to be performed at ORNL, which focus on the potential influence of radiative heat transfer on knock
- Proposed a simplified CFD model for radiative heat transfer in high-pressure combustion systems that, for the range of conditions tested, predicts radiative emission, reabsorption, and wall heat loss within approximately 10% of those predicted using PMC–LBL at less than 10% of the computational cost of PMC–LBL

Conclusions

In this second year of the project, the focus has been on (1) exercising high-fidelity CFD-based PMC–LBL models for in-cylinder radiative heat transfer to guide the design of the engine experiments, and to provide physical insight from which simplified models that are more suitable for engineering development and design can be proposed and validated and (2) making the first quantitative measurements of spectrally resolved measurements of IR radiative intensity in an optical engine, and comparing those with computed spectral IR radiative intensities.

- Initial comparisons between computed and measured spectral IR radiative intensities in an optical engine revealed the importance of accounting for the IR spectral absorption characteristics of the transparent (in visible wavelengths) engine liner.
- A plan for experimental measurements in a metal engine has been established, to explore the potential influence of radiation on knock.
- A simplified model for in-cylinder radiative heat transfer has been proposed that appears promising in initial comparisons with a high-fidelity PMC–LBL model.

References

1. Schmitt, M., C.E. Frouzakis, Y.M. Wright, A. Tomboulides, and K. Boulouchos. “Direct numerical simulation of the compression stroke under engine relevant conditions: Local wall heat flux distribution.” *International Journal of Heat and Mass Transfer*, 92:718–731 (2016).
2. Ma, P.C., T. Ewan, C. Jainski, L. Lu, A. Dreizler, V. Sick, and M. Ihme. “Development and analysis of wall models for internal combustion engine simulations using high-speed Micro-PIV measurements.” *Flow, Turbulence and Combustion*, 98:283–309 (2016).

Key Fiscal Year 2017 Publications

1. Haworth, D.C., S. Ferreyro-Fernandez, C. Paul, A. Sircar, A. Imren, S.P. Roy, W. Ge, M.F. Modest. “Soot and spectral radiation modeling in ECN Spray A and in engines.” International Multidimensional Engine Modeling User’s Group Meeting at the SAE Congress, Detroit, MI, (April 3, 2017).
2. Sircar, A., C. Paul, S. Ferreyro-Fernandez, A. Imren, D.C. Haworth, S.P. Roy, W. Ge, M.F. Modest. “Turbulence-radiation coupling in boundary layers of heavy-duty diesel engines.” 16th International Conference on Numerical Combustion, Orlando, FL (April 3–5, 2017).
3. Paul, C., A. Sircar, S. Ferreyro-Fernandez, A. Imren, D.C. Haworth, S.P. Roy, W. Ge, M.F. Modest. “Modeling radiative heat transfer and turbulence-radiation interactions in engines.” 10th U.S. National Combustion Meeting, College Park, MD (April 23–26, 2017).

4. Haworth, D.C. “Applications of turbulent combustion modeling.” von Karman Institute for Fluid Dynamics Lecture Series on Turbulent Combustion, Rhode-Saint-Genèse, Belgium (April 24–28, 2017).
5. Sick, V. “Optical diagnostics for engines going fast, small, and long.” Gordon Research Conference on Laser Diagnostics in Combustion, Mount Snow, VT (August 6–8, 2017).
6. Ferreyro-Fernandez, S., C. Paul, A. Sircar, A. Imren, D.C. Haworth, S. Roy, M.F. Modest. “Soot and spectral radiation modeling for high-pressure turbulent spray flames.” *Combustion and Flame*. Accepted for publication.

I.21 Model Development for Multi-Component Fuel Vaporization and Flash Boiling

Chia-Fon Lee, Principal Investigator

University of Illinois at Urbana-Champaign
1206 W. Green St.
Urbana, IL 61801
E-mail: cflee@illinois.edu

Michael Weismiller, DOE Technology Manager

U.S. Department of Energy
E-mail: Michael.Weismiller@ee.doe.gov

Start Date: January 1, 2016	End Date: December 31, 2018	
Total Project Cost: \$761,000	DOE share: \$685,000	Non-DOE share: \$76,000

Acknowledgments

Co-Author

Sibendu Som, Argonne National Laboratory

Project Introduction

Modern internal combustion engines are designed to maximize efficiency and minimize pollutant emissions. One factor that can greatly deteriorate engine performance is poor fuel atomization, which is characterized by incomplete fuel vaporization and spray impingement on cylinder walls. Residual fuel in the cylinder causes high levels of unburned hydrocarbons and carbon monoxide emissions while altering engine fuel dilution. Thus, enhancing fuel vaporization is crucial for engine improvement. The design procedure is done through numerical model simulations that search for optimal parameters. However, the performance of available submodels for fuel vaporization is limited by the complexity of fuel representation that is both computationally efficient and quantitatively accurate. The lack of experimental data to support and validate the numerical models is another key factor impeding model development. The current project aims to overcome the barriers of inadequate predictive tools and data for (1) fuel property effects on combustion and engine efficiency optimization and (2) fuel effects on emissions and emission control system impacts.

The key innovation of this work is to apply novel approaches to represent the complexity of fuel composition in models and to validate these approaches through experimental observation. Under engine environments, flash boiling may also take place during the vaporization process of multi-component fuels. Promoting the occurrence of flash boiling can dramatically improve the spray atomization process, which is closely tied to the parameters that govern vaporization. Hence, a unified model to predict the occurrence of flash boiling is developed in this work. These phenomena are important for improving engine design through fuel vaporization enhancement. The appropriate methodology for evaluating mixing rules and saturation properties of the multi-component fuel are examined and validated through experiments. The outcome of this project will advance current design process with greater efficiency and accuracy for internal combustion engines and related applications.

Objectives

- Design and develop a multi-component fuel droplet and wall film vaporization model using two approaches: discrete and continuous thermodynamics methods
- Design and develop an analytical model for multi-component flash boiling
- Integrate the multi-component droplet and film model into multi-dimensional engine calculations to predict the fuel vaporization process under engine operation condition

- Conduct multi-component droplet and fuel film vaporization experiments in a non-combusting chamber to verify the proposed vaporization models
- Characterize flash-boiling phenomena of multi-component fuel sprays by optical and laser diagnostic techniques

Approach

To develop a state-of-the-art numerical model for predicting the multi-component fuel vaporization process, two numerical approaches are implemented and tested: discrete and continuous method. The discrete method keeps track of key surrogate species, while the continuous method uses a probability distribution function to represent thermodynamic properties of multi-component fuel. Fuel droplet, spray, and film vaporizations are the model applications examined in this work. A comprehensive numerical model to predict the occurrence of flash boiling for multi-component fuel is constructed in collaboration with Dr. Sibendu Som's group at Argonne National Laboratory. Due to the high computational cost from the complexity of multi-component fuel simulations, the world-leading computing resource center at Argonne National Laboratory is invaluable in the success of this work. Extensive parametric study of flash boiling phenomenon are executed through both experimental and numerical endeavors.

Parallel to the model development endeavor, experiments are performed to verify the proposed models, where an extensive dataset is created to bridge the gap between single-component and multi-component combustion. More specifically, measurements of multi-component fuel spray characteristics under flash boiling and non-flash boiling conditions are made along with observations of droplet and film vaporization trends. New spray, droplet and film chambers are designed and assembled to obtain datasets of multi-component fuel vaporization characteristics, including temperature and concentration histories, temporal droplet size evolution and fuel film thickness evolution. These experiments employ optical and laser diagnostic techniques. These validated submodels are implemented into engine simulation models for final testing and validation. Comprehensive multi-component fuel datasets will provide invaluable information for model development and engine design.

Results

During Fiscal Year 2017, a new solver using discrete multi-component method is developed, and it is validated for droplet vaporization in quiescent ambient conditions by comparing simulation results with measurements obtained in the experimental portion of this work. The model is tested for both single- and multi-component fuel droplets. Measurements are done using the banded single-filament droplet suspension technique developed in the principal investigator's lab. The droplet vaporization evolution and the droplet interior temperature acquisition are carried out separately due to the significant heat conduction through the thermocouple to the droplet, especially at the low ambient temperature conditions. Results shown in Figure I.21.1 are the variation of the normalized time history of diameter squared of droplet consisting of ethanol and iso-octane. The evolution of droplet size predicted by the model agrees well with the experiment for all four test conditions. Increasing ethanol content increases droplet lifetime considerably. The larger heat of vaporization of ethanol (921 kJ/kg) is responsible for the lengthened lifetime. For pure iso-octane droplet (E0 case), the estimated droplet vaporization rate is similar to the measurement. In the simulations, a two-stage vaporization trend can be observed for predicted E30 (30% ethanol), E50 (50% ethanol), and E85 (85% ethanol) cases. Iso-octane molecular weight is heavier (114 g/mol) compared to ethanol (46.1 g/mol), but it has a smaller heat of vaporization (272 kJ/kg). As a result, there is a competing force between the thermal-controlled and the diffusion-controlled vaporization. However, such preferential vaporization behavior is not obvious in the experimental tests.

An Eulerian-Lagrangian-Spray-Atomization model is designed and implemented by the Argonne National Laboratory collaborator to examine flash boiling characteristics. The injection system of interest is the Spray G moving needle, which has been studied extensively previously for non-flash boiling conditions. The proposed approach extends from single-component fuel to blended fuel vaporization and flashing in the Lagrangian framework. Blends of iso-octane and ethanol were considered. Both non-flashing (Spray G case) and moderate flashing (Spray G2 case) conditions are tested under conditions that are similar to those stated on Spray G Engine Combustion Network webpage. The specific details of these tests are: Spray G:

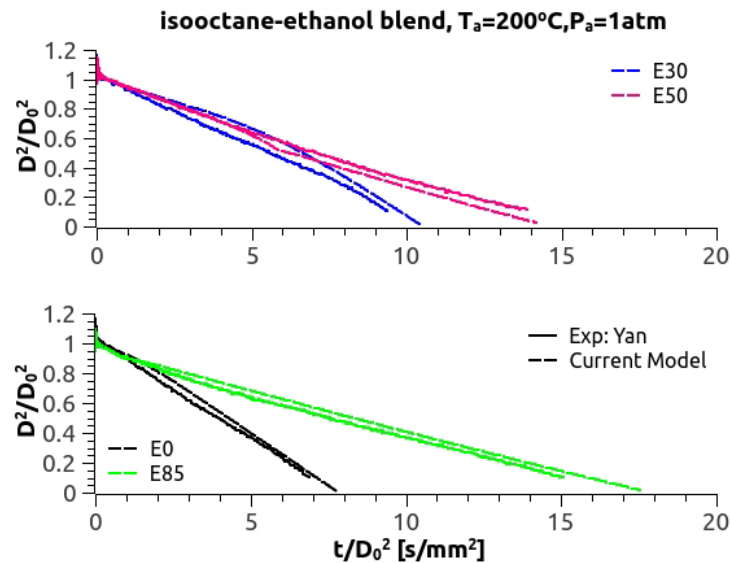


Figure I.21.1 - Temporal history of multi-component droplet vaporization for ethanol–isooctane binary system under atmospheric pressure at 200°C (E0 = pure ethanol; E85 = 85% ethanol, 15% iso-octane by volume)

$P_{\text{chamber}} = 600 \text{ kPa}$, $T_{\text{chamber}} = 573 \text{ K}$, $T_{\text{fuel}} = 363 \text{ K}$, Spray G2: $P_{\text{chamber}} = 53 \text{ kPa}$, $T_{\text{chamber}} = 293 \text{ K}$, and $T_{\text{fuel}} = 363 \text{ K}$. In the case of Spray G, the fuel does not superheat, so the result is a non-flashing spray. For the Spray G2 case, moderate flashing can be expected. The peak injection pressure is around 20 MPa, with an injection duration of 0.78 ms. The rate of injection based blob injection methodology is used. For blended fuels the mass fractions of the constituent species in the injected parcels are specified in the simulation setup along with the physical thermodynamic and transport properties of ethanol and iso-octane. The density contours at 10 mm downstream of the injector tip are shown in Figure I.21.2. The effect of fuel physical properties is considerable. Nonetheless, it is vital to carry out further study and compare with experimental data when available.

Two experimental vaporization apparatuses have been designed and constructed during Fiscal Year 2017. The first is a spray tower used for spray experiments with window design that allows both pressurization

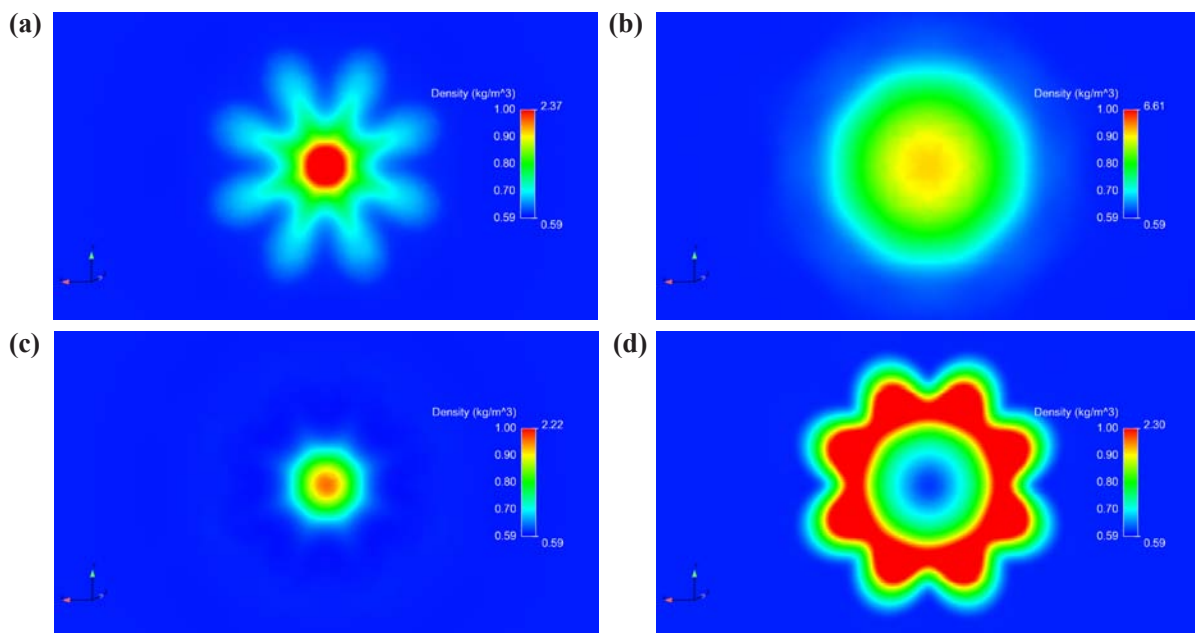


Figure I.21.2 - The density contours (a) iso-octane, (b) ethanol, (c) E30, (d) E85 across a horizontal plane placed 10 mm downstream of the injector tip when subjected to Spray G2 condition

and vacuum within the chamber. The chamber environment is modified and heated by a nitrogen delivery system composed of a liquid nitrogen dewar and a heater that heats the gas to 400 K. The chamber can be pressurized to 10 bar, or be vacuumed down to 0.75 bar below atmospheric pressure with pure nitrogen. Using a combination of heated nitrogen in the chamber and heating tape around the chamber, the chamber can be heated to 500 K. An insulation blanket surrounds the chamber. The chamber and heating system are shown in Figure I.21.3.

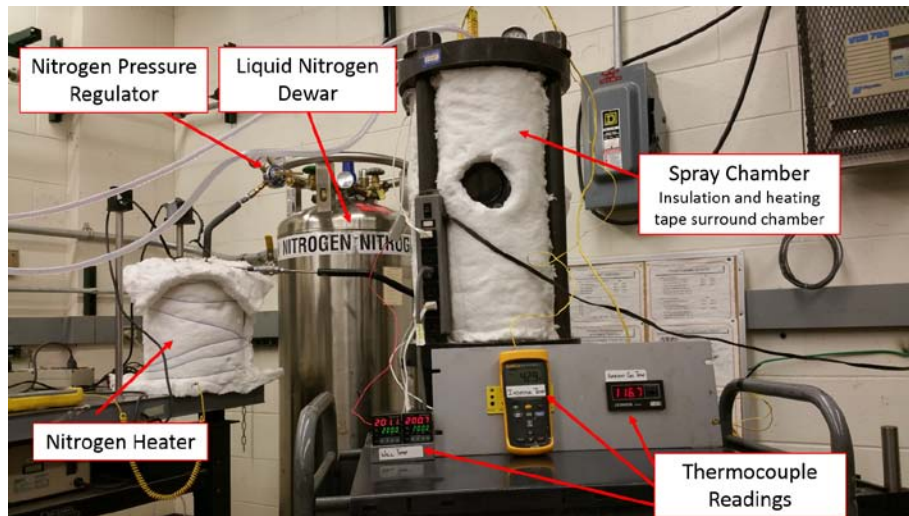
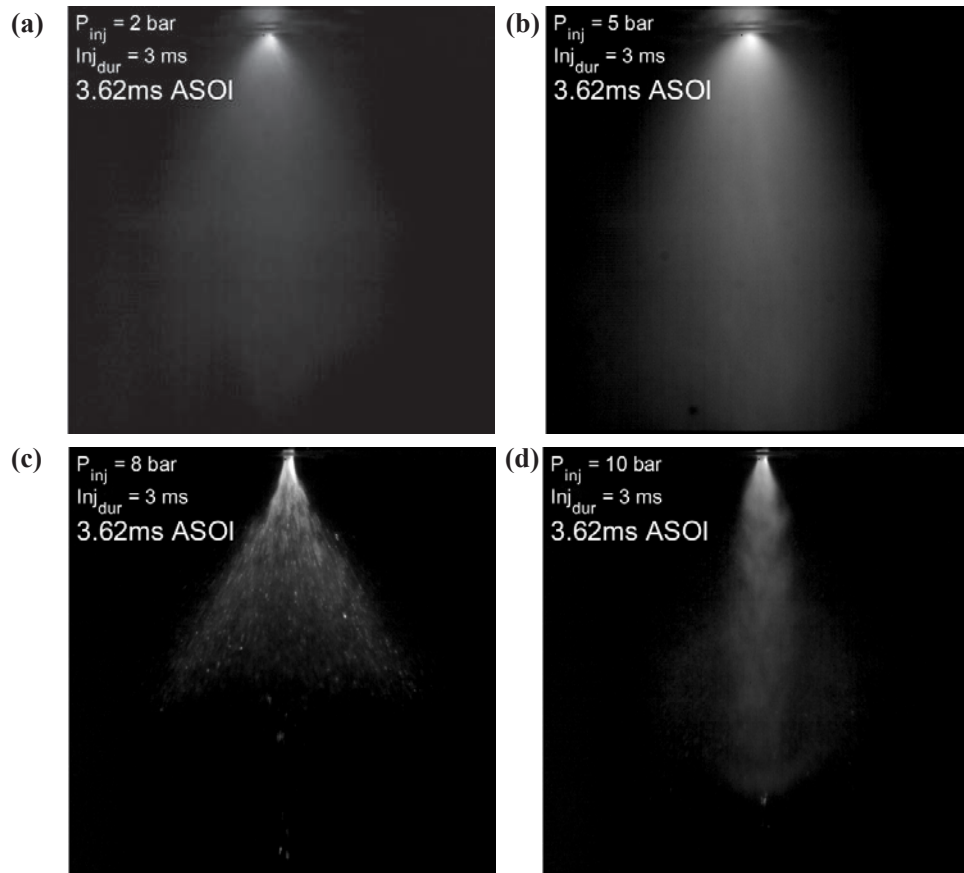


Figure I.21.3 - Tower chamber and heating system (Source: University of Illinois at Urbana-Champaign)

Flash and non-flash boiling cases using the hollow cone injector are imaged in the spray tower as preliminary tests. For the non-flash boiling case, the chamber environment is pressurized to 6 bar and heated to 410 K. The injection pressures are set at 8 bar and 10 bar. For the flash boiling cases, 0.5 bar below atmospheric pressure is set in the chamber, and the nitrogen environment is heated to 410 K. The fuel itself is heated to 100°C, and the injection pressures are at 2 bar and 5 bar. The results for all cases are shown in Figure I.21.4. The flashing trends can be clearly observed through the lack of defined spray droplets and shapes.

The second new experimental system designed, assembled and tested during Fiscal Year 2017 is the droplet and film chamber. The purpose of this chamber is to provide a nitrogen environment at elevated temperatures and pressures. Six 1,000-W heaters are embedded in the chamber wall to provide rapid and uniform heating. All the heaters can be controlled individually. Two quartz windows are installed on the front and the backside of the chamber to provide optical access. The droplet generator has been completed and tested in the chamber, and the surface temperature of the droplet is measured using an FLIR E40 thermal imaging camera in conjunction with a chamber window that transmits infrared light. Pure nitrogen is introduced from a liquid nitrogen tank. Figure I.21.5 shows the detailed schematic of the system. Results of bi-component (ethanol and iso-octane) droplet vaporization experiments are shown in Figure I.21.6. As mentioned previously, the large heat of vaporization of ethanol is responsible for the lengthened lifetime, hence the decrease in vaporization rates with increasing ethanol content.



ASOI – after start of injection

Figure I.21.4 - Spray evolution for flash and non-flash boiling at 400 K and varying injection (P_{inj}) and environment (P_{env}) pressures: (a) $P_{inj} = 2$ bar, $P_{env} = 0.5$ bar; (b) $P_{inj} = 5$ bar, $P_{env} = 0.5$ bar; (c) $P_{inj} = 8$ bar, $P_{env} = 6$ bar; and (d) $P_{inj} = 10$ bar, $P_{env} = 6$ bar

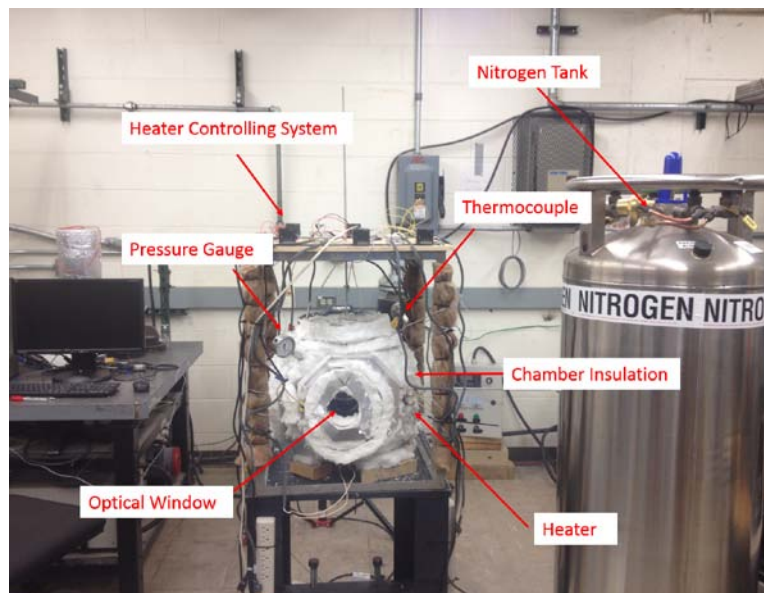


Figure I.21.5 - The droplet and film chamber components and system (Source: University of Illinois at Urbana-Champaign)

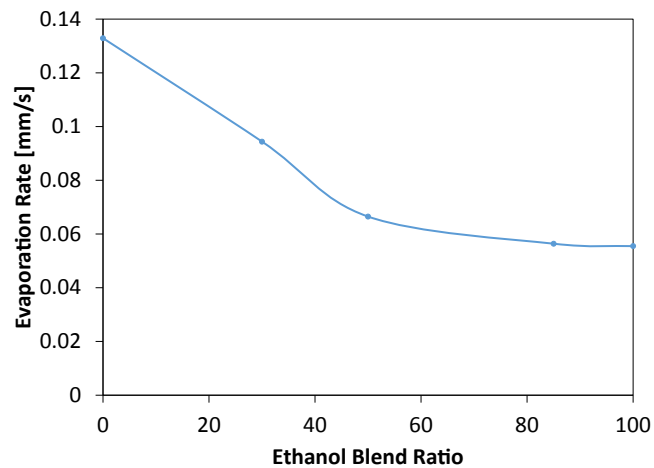


Figure I.21.6 - Droplet diameter evolution during vaporization for various ethanol–iso-octane blends (E0: 0% ethanol, 100% iso-octane by volume; E100: 100% ethanol, 0% iso-octane by volume)

Conclusions

- Droplet evaporation model using the discrete methodology shows good agreement with experimental results for both single- and multi-component fuels.
- Multi-component droplet vaporization trends are influenced by competing forces between thermal properties and the diffusion properties of the individual components.
- Flash boiling model results show considerable fuel physical properties influence on multi-component fuel flashing behaviors.
- Droplet and film chamber is assembled and tested for high pressure and high temperature conditions.

Key Fiscal Year 2017 Publications

1. “Coupled Eulerian Internal Nozzle Flow and Lagrangian Spray Simulations for GDI Systems.” SAE World Congress, 2017.
2. “A Comparison of Experimental and Modeled Velocity in Gasoline Direct-Injection Sprays with Plume Interaction and Collapse.” SAE World Congress, 2017.

I.22 Spray-Wall Interaction at High-Pressure and High-Temperature Conditions

Seong-Young Lee, Principal Investigator

Michigan Technological University
815 R.L. Smith Bldg. 1400 Townsend Drive
Houghton, MI 49931
E-mail: sylee@mtu.edu

Michael Weismiller, DOE Technology Manager

U.S. Department of Energy
E-mail: Michael.Weismiller@ee.doe.gov

Start Date: January 1, 2016	End Date: December 31, 2018	
Total Project Cost: \$835,000	DOE share: \$750,000	Non-DOE share: \$85,000

Acknowledgements

Co-Authors

Jeffrey Naber, Michigan Technological University
Riccardo Scarcelli, Sibendu Som; Argonne National Laboratory
Mehdi Raessi, University of Massachusetts Dartmouth

Project Introduction

The goals of this research project are to develop, implement, and validate a volume of fluid (VOF) approach for modeling evaporation, which is integrated into computational fluid dynamics (CFD) codes to provide accurate and predictive simulation of spray-wall interactions without extensive need of parameter tunings. This is accomplished by development and inclusion of an evaporation submodel in existing VOF modeling framework. This submodel will be validated through extensive experimentation of the spray-wall interaction and film formation, spreading, and vaporization dynamics.

Objectives

- Quantify spray rebound properties, film thickness, and heat flux on the heated surface for a single-hole nozzle impingement
- Optimize the high-fidelity Lagrangian-Eulerian (LE) spray model and code usability
- Validate LE spray model with experiments and generate boundary conditions for subsequent direct numerical simulation (DNS) framework studies
- Demonstrate the non-vaporizing droplet DNS impingement criteria for splashing and non-splashing cases and formulate the evaporation DNS submodel

Approach

First, targeted experimentation of the spray-wall interactions and liquid wall film under conditions matching the thermodynamic charge state and surface temperatures to those of engines is performed. Second, the experimental data is used to support development and validation of an advanced spray-wall interaction and associated film formation and vaporization modeling approach via application of a VOF method with an integrated evaporation submodel (eVOF). With the inclusion of a vaporization submodel for the film and the results of the DNS analysis of spray-wall impingement, accurate predictive simulations of spray impingement can be eventually performed without the need of parameter tuning.

Results

Fiscal Year 2017 Accomplishments

- Designed and fabricated mounting fixture for new Bosch injector
- Finished temperature calibration test with closed-loop temperature control system and data acquisition system
- Completed rate of injection test for the new single-hole injector and spray–wall impingement test with diesel and n-heptane on a new quartz window (front, side, and bottom views)
- Finished film thickness measurement calibration using refractive index matching (RIM) method
- Completed the critical heat flux measurements at three different locations in the impinging plate under various conditions including injection pressure, surface temperature, and ambient density
- Completed LE CFD simulations validation with Michigan Technological University (MTU) single-hole nozzle experiments
- Investigated the effect of injected parcels on the statistical significance of extracted data in LE simulations
- Extended Yarin and Weiss’s theory to LE sprays for the prediction of droplet splash and formalized a rigorous mathematical formulation of the droplet impingement frequency for such applications
- Implemented and preliminarily tested the modified spray–wall interaction model into CONVERGE code
- Performed DNS runs of surface impingement of single and multi-train of droplets and validated the results with experiments of Yarin and Weiss
- Validated numerical contact angle model with MTU single-droplet impingement experimental results in DNS framework
- Continued working on developing the DNS framework of spray–wall interaction and evaporation model
- Developed a benchmark test for evaluating the accuracy of evaporation modeling in finite domains and transient regimes

Single-Hole Nozzle Spray–Wall Test

A single-hole diesel injector (with off-axis injector nozzle) was mounted in the middle of the injector window, which resulted in the vertical distance of 40 mm between the injector tip and impinging window surface. Front, side, and bottom views were obtained by using a simultaneous Mie scattering and schlieren optical setup. The nozzle was characterized by a 200- μm diameter, K-factor of zero, enclosed angle of 120° , and impinging angle of 60° . The test conditions involved injection pressures of 1,200 bar, 1,500 bar, and 1,800 bar; ambient densities of 14.8 kg/m^3 , 22.8 kg/m^3 , and 30.0 kg/m^3 ; and ambient and fuel temperatures of 423 K and 363 K, respectively. Free spray and impinged spray quantities were measured. Figure I.22.1 (top left) shows the effect of the ambient density on the front radius of the wall-impinged expanding spray (WIES) for both axial and radial directions after the first impingement. Both directional radii started increasing after the first impingement, with the 14.8 kg/m^3 case impinging on the surface earlier than the other two cases. Both radii increased until the end of injection at ~ 2.45 ms after start of injection (ASOI). Figure I.22.1 (top right) reports the measurements of the axial impinged height at ambient densities. It was observed that the impinged spray height decreased as the ambient density was increased. Figure I.22.1 (bottom row) provides the effect of injection pressure (1,200 bar, 1,500 bar, and 1,800 bar) on WIES radius (left) and WIES height (right) at the ambient density of 22.8 kg/m^3 . Both axial and radial radii started increasing after the first impingement, with the 1,800 bar case impinging on the surface earlier than the other two cases. The radii continued increasing until the end of the injection. The directional radii and the WIES height tended to increase with the injection pressure at any given time. Because high injection pressure accelerated the free spray, an increase in the impinged spray axial/radial expansion rates and the WIES height was observed.

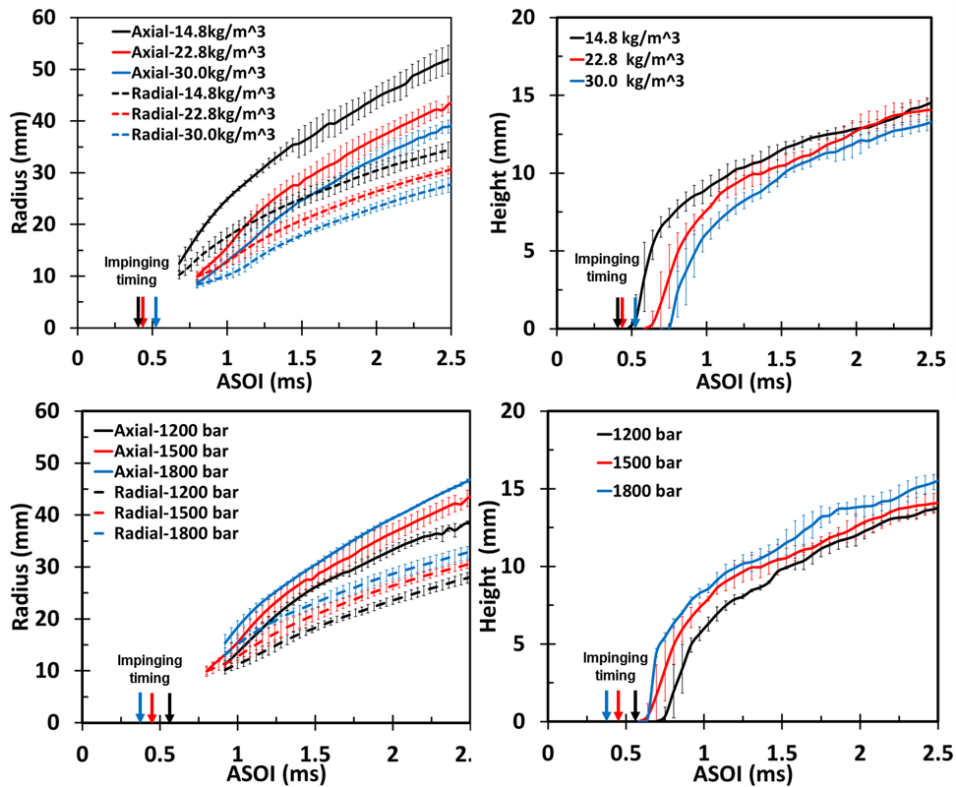


Figure I.22.1 - The impinged spray radius (left) and the impinged spray height (right) versus ASOI with various ambient densities (14.8 kg/m³, 22.8 kg/m³, and 30 kg/m³) (top) and various injection pressures (1,200 bar, 1,500 bar, and 1,800 bar) (bottom)

Film Thickness Measurement Using RIM Technique

RIM technique is an optical method to measure the spatial and temporal distribution of liquid film thickness, which is used to depict the fuel impingement on the wall. The relation between the fuel film thickness and the variation of intensity in the scattered light was extracted after applying the RIM technique [1]. The film characteristics such as local film thickness, averaged film thickness, film mass, and film occupied area can be extracted via the calibrated result. The film thickness of n-heptane was estimated based on the above calibration results and a small area (2×2 mm²) near the impinging point was selected for averaged film thickness estimation. The film thickness at each condition was averaged from five repeats. The effects of ambient density and injection pressure on film thickness are shown in Figure I.22.2. Overall, from Figure I.22.2, it can be seen that the film thickness decreased with ambient density and injection pressure and the thickness range was between 0.5 and 1.2 μm.

Heat Flux Measurement

The employed heat flux probe was a three-wire unit that consisted of a 0.060-in probe and two welded junctions. The three-wire probe provided the ability to measure surface, embedded, and differential temperatures. The probe was essentially made of two “J” type thermocouples, one installed at the surface of the plate and the other one at 2 mm, directly under the surface thermocouple. Figure I.22.3 shows the effect of the ambient density on the heat flux at three different locations using diesel fuel. The surface temperature is maintained at about 250°C with injection pressure of 1,500 bar, ambient density of 22.8 kg/m³, and ambient temperature of 150°C. Before the injection, there exists already heat flux due to the ΔT between the ambient gas and plate. After the impingement, there’s fuel film deposited on the plate which evaporates after the end of injection. The surface temperature recovers toward the initial temperature. With the density is increased, the peak heat flux becomes lower. This phenomenon is due to the fact that the high ambient density will slow the spray velocity and further lead to low heat transfer coefficient. As can be seen in the figure, the heat flux peak at low-density case happens earlier than that at the high-density case.

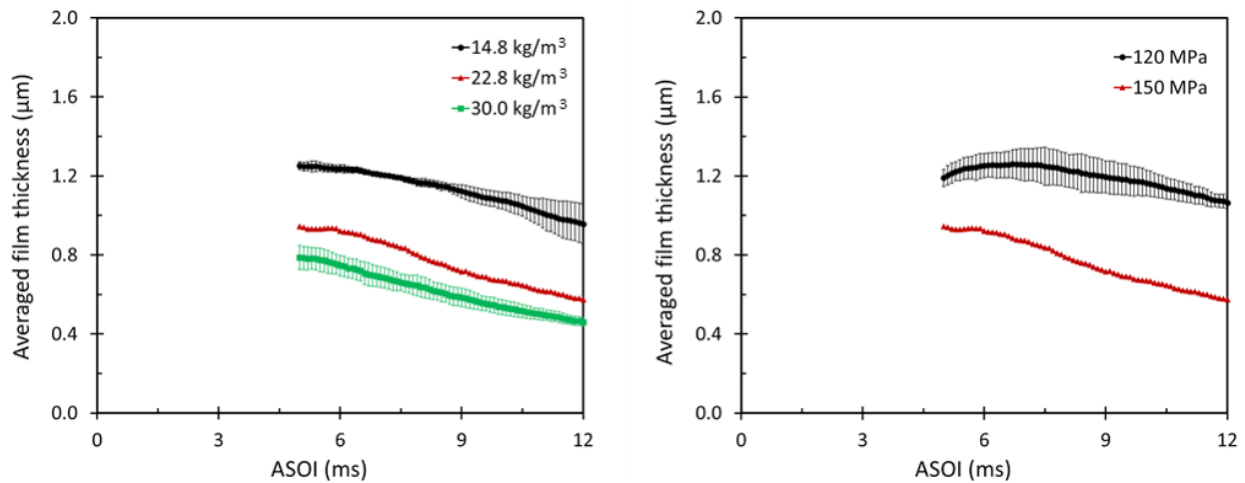


Figure 1.22.2 - Effects of ambient density at injection pressure of 1,500 bar (left) and injection pressure at ambient density of 22.8 kg/m³ (right) on film thickness

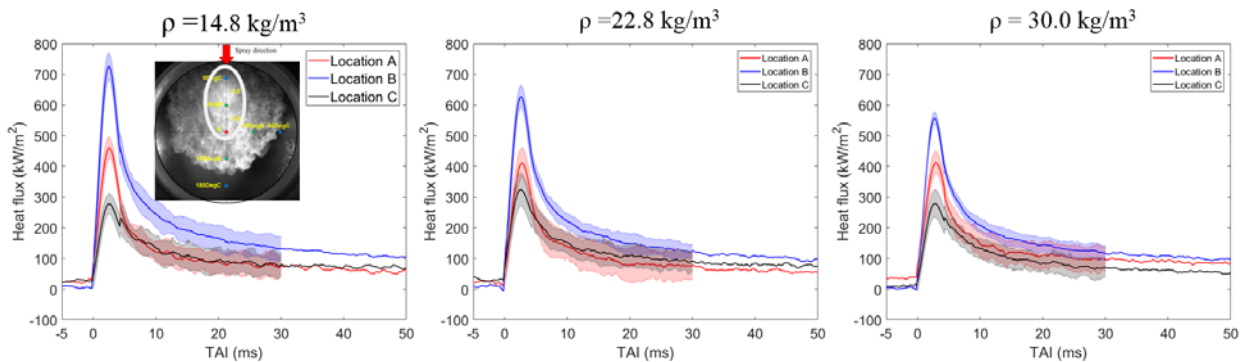


Figure 1.22.3 - Effects of ambient density at injection pressure of 1,500 bar on heat flux at three locations

LE Simulations

LE spray simulations were performed for the MTU seven-hole and single-hole injectors. The setup was shown to be robust to the change in operating conditions, injector specifications, and fuel. Very good agreement between calculated and measured free-spray liquid penetration was obtained. The effect of spray-wall interaction was taken into account by employing the available O'Rourke and Amsden model [2], which is based on empirical correlations obtained with single droplet impacts. For both MTU injectors, good agreement was found with respect to the axial and radial spreading of the spray, while the spray height resulted to be considerably underestimated. This finding confirmed the necessity for improvement of the current state-of-the-art models used in LE simulations.

Automated in-house post-processing tools were further optimized and employed to extract meaningful information about the local spray morphology in the vicinity of the spray impingement location. The liquid spray was characterized in terms of average droplet size and Weber and Reynolds numbers in small cubic subsets (0.25 mm³) around the impingement point. An analysis on varying the number of injected parcels was performed in order to assess the effect of the parcel count on the subset sample size and consequently on its statistical validity. This study revealed that convergence of global quantities such as liquid penetration and Sauter mean diameter with respect to the injected number of parcels does not imply convergence of spray morphology quantities on a local scale. In order to characterize the Lagrangian spray in such small volumes, a sixteen-fold parcel count increase (from 150,000 to 2,400,000) was required for the correct local characterization of the spray.

The extracted set of information was fed to the DNS calculations performed at University of Massachusetts Dartmouth in order to run high-fidelity, high-resolution simulations of the impingement of both single droplets

and train of droplets on the wall. The outcome of the DNS highlighted the necessity to involve the droplet frequency of impingement in the LE calculations, due to the dynamic nature of the splashing phenomena.

In literature, the effect of the droplet impingement frequency is accounted for in the theory of Yarin and Weiss [3]. Stanton and Rutland [4] proposed a spray-wall interaction model in which a frequency-based splashing criterion that accounted for Yarin and Weiss's theory was used. In their implementation, the frequency was estimated on the basis of the droplet size and impact velocity, therefore not accounting for the actual frequency of multiple droplets impinging on a wall. On the basis of the physics observed with DNS, a novel approach for calculating the droplet impingement frequency of Lagrangian particles was formalized. By assuming a uniform spherical distribution of the droplets around the location of the Lagrangian parcel that represents them, the droplet impingement frequency could be estimated with an algebraic formula. A modified Stanton and Rutland model was implemented in CONVERGE using the new definition of the impingement frequency. Furthermore, an improved correlation for the prediction of the rebound and splash velocity was also proposed.

The preliminary simulation tests performed with MTU's single-hole injector showed an improvement of the results (Figure I.22.4). The spray radii and rebound on wall, as well as the spray height, improved along both radial and axial directions. DNS calculations also provided an explanation for the underestimation of the spray height. The splashing thresholds commonly found in the literature are generally valid for water and droplet sizes up to two orders of magnitude larger than those typically found in sprays for internal combustion engine applications. The analysis of DNS results suggested that the splashing thresholds need to be updated to take into account the different conditions in which internal combustion engine sprays evolve and operate.

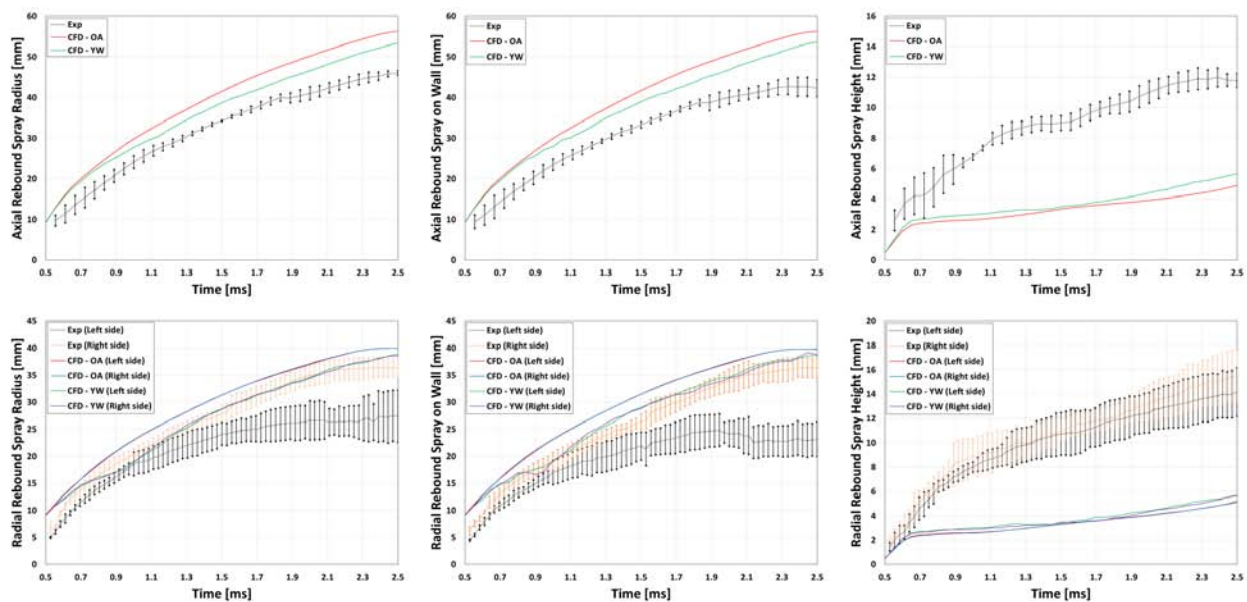


Figure I.22.4 - Comparison of axial (top) and radial (bottom) impinged spray quantities against experiments, O'Rourke and Amsden's model (OA), and new implementation (YW) based on Yarin and Weiss' theory

DNS Simulations

DNS studies, started in January 2017, have been focused on two main areas: (1) impact of spray droplets on solid walls under non-evaporating conditions and (2) development of an accurate VOF-based evaporation modeling approach. Using the University of Massachusetts Dartmouth multiphase flow solver [5], the surface impingement of a train of ethanol drops was simulated by following the experiments of Yarin and Weiss [3]. The simulation results, a sample of which are shown in Figure I.22.5, agree very well with Yarin and Weiss experiments in the film formation, drop spreading, and splashing dynamics. They also capture very well the splashing threshold observed experimentally. Furthermore, quantitative comparisons of splashing mass ratio between the simulations and experiments showed very good agreements. Having established confidence in the multiphase flow solver's capability in capturing details of drop splashing dynamics, we turned to diesel spray

droplets to investigate if the splashing threshold observed by Yarin and Weiss [3] is applicable to single-micron diesel droplets. The simulation data of ANL Group was used to determine a representative diesel droplet size ($5.97 \mu\text{m}$) and impact velocity (77 m/s). The preliminary simulations of surface impingement of a train of diesel droplets suggest that the splashing threshold of micron-sized diesel droplets may be different than that of Yarin and Weiss. Further simulations are in progress, which will resolve the splashing threshold. The splashed mass ratio, representing the ratio of splashed mass to the total injected mass, was calculated for the surface impingement of a train of the representative diesel droplets at a dimensionless velocity, $u = 24$. The results are presented in Figure I.22.6 for two grid resolutions of 40 cells per diameter (CPD) and 80 CPD. The splashed mass ratios are 47% and 55% at 40 and 80 CPD, respectively. The difference in airborne mass is believed to be

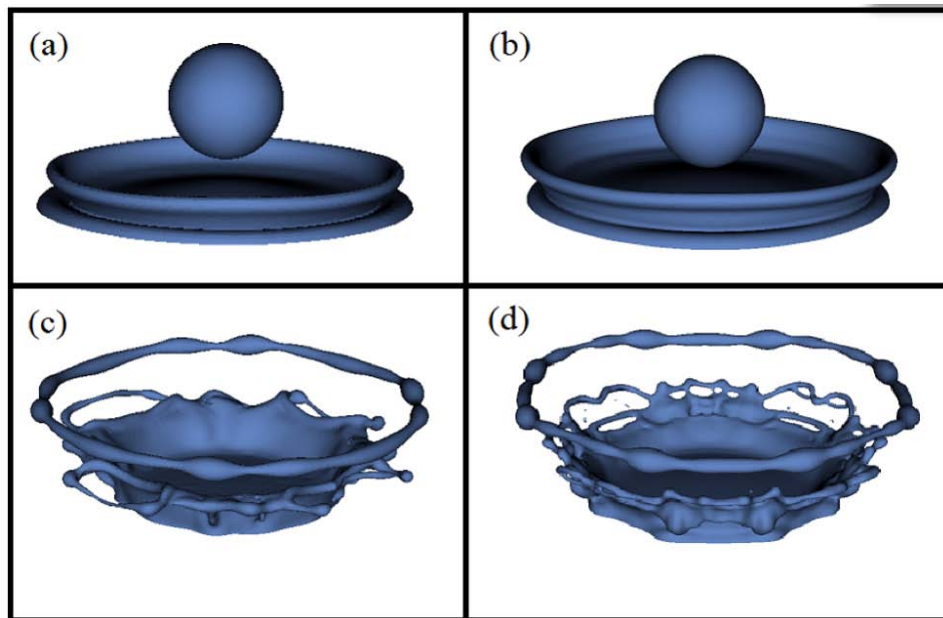


Figure I.22.5 - DNS results of the surface impingement of a train of 109-micron ethanol drops at non-splashing (top row) and splashing (bottom row) regimes at grid resolution of (a, c) 2.5 microns and (b, d) 1.25 microns. Simulation results agree well with the experiments of Yarin and Weiss.

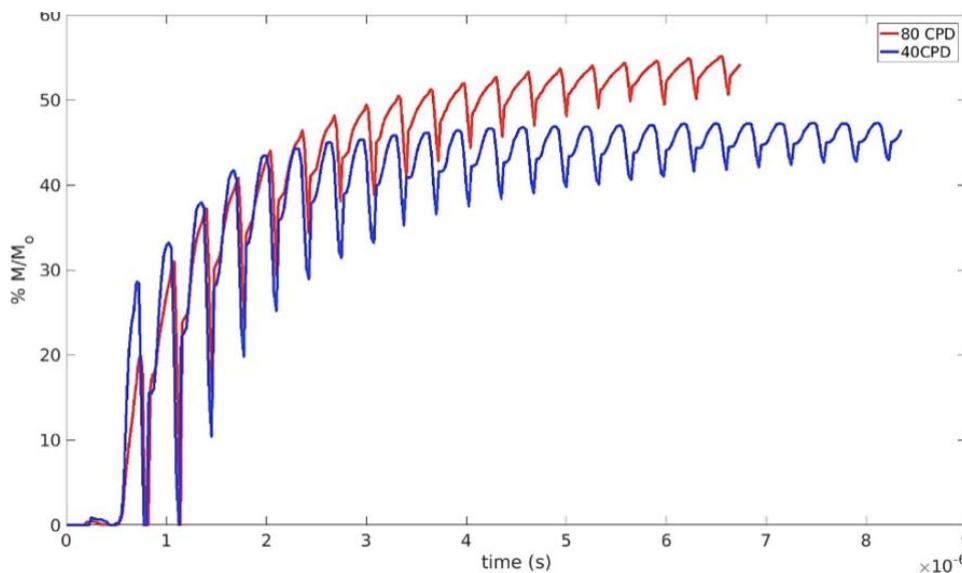


Figure I.22.6 - Splashed mass ratio versus time in surface impingement of a train of diesel droplets of 5.96 micron diameter impacting at 77 m/s from two DNS studies at 40 CPD and 80 CPD resolutions. The dimensionless velocity, based on deposition frequency, is $u = 24$.

due to the numerical fracturing of the lamellae at 40 CPD. At 80 CPD the lamellae were better resolved both in visualization and numerically. To ensure we have converging airborne mass results, a simulation will be run at 160 CPD and will be compared to the previous results. It should be noted that the model of O'Rourke and Amsden [2] predicts the splashed mass ratio of the above diesel case to be 75%, which is clearly an over prediction by 20%, calling for revised models.

To gain further insight into the droplet impingement process that occurs upon injection of the diesel fuel, a fuel spray reconstruction method was developed. Each parcel in the CFD simulations performed by the ANL team represents a certain number of identical droplets. To recreate the spray, each parcel was translated into a 'parcel sphere,' which was uniformly and randomly populated with the number of droplets it represented. The size of this sphere was determined by a 5% volume fraction of fuel, following the dilute spray assumption. To determine the parcel sphere volume, the volume of the fuel droplets was determined based on the size and number of droplets the parcel represented. Based on the dilute spray assumption, this volume was then divided by 0.05 to yield the volume of the parcel sphere in which the droplets were distributed. The sphere was centered at the parcel location and created a statistically accurate representation of each parcel. This led to a recreation of the spray with individual droplets versus parcels representing droplets. This method was applied to the parent parcels contained in a 1.00 mm, 0.50 mm, and 0.25 mm cube centered at the impingement point. The focus of this recreation was on parent parcels, which have not been broken into multiple child parcels by any interaction such as impingement. Including the child parcels would mean that the parcels could have already impacted the surface/film and represented post-impingement droplets. Two simulations with 1,200,000 and 2,400,000 parcels were post-processed. The 1,200,000-parcel results show that the average droplet spacing is 1.35D, 1.31D, and 1.28D in the 0.25 mm, 0.5 mm, and 1 mm cubes, respectively, where D is the droplet diameter. At 2,400,000 parcels, the average droplet spacing is 1.29D, 1.27D, and 1.26D in the 0.25 mm, 0.5 mm, and 1 mm cubes, respectively. The condensed variation in droplet spacing seen in the 2,400,000-parcel simulation provided confidence in the droplet spacing results. Droplet spacing varies in the range of 1.2–1.5D. It should be noted that all cubes have droplet spacing that falls well within the interaction distance of 3.3D. This means that all of the impinging droplets interact with their neighboring droplets, calling the need for studying surface impingement of multi-trains of drops, which is currently in progress.

The efforts on development of an accurate VOF-based evaporation modeling approach included development of a one-dimensional radial evaporation model, which provides a benchmark solution to the three-dimensional (3D) Cartesian DNS solver. This is an improvement over the d^2 law (analytical expression) currently used as a benchmark, which is based on the steady-state and infinite domain assumption. Given the transient nature of micron-sized fuel droplet evaporation and computational restriction in accommodating infinite domain by DNS solvers, the significance of the proposed one-dimensional model is readily evident. Our 3D Cartesian DNS solver for evaporation modeling, which is currently under development, is based on the following assumptions. The flow in each phase, liquid and gas, is assumed to be incompressible. Local thermodynamic equilibrium is considered at the droplet–film surface, which allows the use of thermodynamic relations such as Clausius–Clapeyron and ideal gas laws to determine the vapor mass fraction at the droplet–film surface. Saturation temperature and enthalpy of evaporation at the surface are computed at the prescribed ambient pressure and assuming pressure continuity across the gas–liquid interface. Here the pressure jump due to capillary forces and pressure change due to dynamic effects are assumed to be negligible. The isobaric assumption also allows the use of temperature formulation of the energy equation presented in the next section. Thermo-physical properties are assumed to be constant to facilitate the comparison with benchmark results. In a numerical framework, however, the properties can be made temperature-dependent in a straightforward manner. The evaporation modeling algorithm has six main steps, briefly described below. We have completed four steps and are on track to finish the remaining two steps in the next few weeks. Here is a brief description of the algorithm. Initially available fields are (U_ℓ^0, T_ℓ^0) in the liquid domain, (U_g^0, T_g^0, Y^0) in the gaseous domain, and VOF field f^0 . A pseudo time-step projection is performed to yield a divergence-free initial velocity field. Afterwards, the following time cycle is performed:

do $n = 1$, *max step*

1. Convect (U_ℓ^n, T_ℓ^n) as well as (U_g^n, T_g^n, Y^n) along with the interface f^n , i.e., $f^n \Rightarrow f^{n+1/2}$

2. Compute T_r and Y_r as well as \dot{m}
3. Using m^n , retract the interface ($f^{n+1/2} \Rightarrow f^{n+1}$)
4. Update \mathbf{U}_t^n and \mathbf{U}_g^n due to viscous and body forces to yield \mathbf{U}_t^* , \mathbf{U}_g^*
5. Solve the diffusion equation for T and Y to yield (T^{n+1} , Y^{n+1}) in both liquid and gas phases
6. Solve the sharp interface balanced force pressure Poisson equation to yield divergence-free \mathbf{U}^{n+1}

end do

Conclusions

- In experiment: (1) Completed impinging spray test with n-heptane on new quartz window (front, side, and bottom views) and surface temperature effect exploration of n-heptane impinging spray on heated metal window. (2) Finished film thickness measurement calibration and data acquisition using the RIM method. The film thickness showed a trend of decreasing with increasing ambient density and injection pressure. (3) Heat flux at several locations during the spray-wall interaction was measured. High surface temperature led to high heat transfer rate. The overall heat flux at all locations are decreased with increasing ambient density due to the reduction in the impinging spray speed.
- In LE simulation: (1) Validated LE setup for different injectors, operating conditions, and fuels. Further developed automated tools for spray morphology characterization and investigated the effect of injected parcel number on the correct local characterization of the impinging spray. (2) Evaluated available state-of-the-art models for spray-wall interaction and identified issues with prediction of rebounded spray height. (3) Formulated, implemented, and preliminarily tested novel approach for the calculation of droplet impingement frequency in Lagrangian sprays.
- In DNS simulation: (1) The diesel droplet train impingement simulation ($u = 24$) showed signs of cusp formation and secondary droplet ejection, inferring splashing threshold in terms of Yarin and Weiss' dimensionless velocity (u) may be below $u = 24$. (2) The splashed mass model of O'Rourke and Amsden over-predicts the splashed mass by approximately 20%, showing the model needs revision to accurately predict splashed mass during micron-sized droplet impingement. (3) The analytical expression known as the d^2 law, widely used as the benchmark, is not suited for evaporation of micron-sized droplets in finite domains because the d^2 law is based on the steady-state and infinite domain assumption, while the micron-sized droplets spend a majority of their lifetime in transient. A one-dimensional radial evaporation model was developed to provide an accurate benchmark solution to the 3D Cartesian DNS solver.

References

1. Yang, B. and J. Ghandhi. "Measurement of Diesel Spray Impingement and Fuel Film Characteristics Using Refractive Index Matching Method." SAE Technical Paper 2007-01-0485, 2007, doi:10.4271/2007-01-0485.
2. O'Rourke, P. and A. Amsden "A Spray/Wall Interaction Submodel for the KIVA-3 Wall Film Model." SAE Technical Paper 2000-01-0271, 2000.
3. Yarin, A.L., and D.A. Weiss. "Impact of drops on solid surfaces: self-similar capillary waves, and splashing as a new type of kinematic discontinuity." *Journal of Fluid Mechanics* 283:141–173, 1995.
4. Stanton, D. and C. Rutland. "Modeling Fuel Film Formation and Wall Interaction in Diesel Engines." SAE Technical Paper 960628, 1996.
5. Pathak, A. and M. Raessi. "A 3D, fully Eulerian, VOF-based solver to study the interaction between two fluids and moving rigid bodies using the fictitious domain method." *Journal of Computational Physics*, 311, pp. 87–113 (2016).

Key Fiscal Year 2017 Publications

1. Zhao L., Torelli R., Zhu X., Scarcelli R., Som S., Schmidt H., Naber J., and Lee S.-Y. “An Experimental and Numerical Study of Diesel Spray Impingement on a Flat Plate.” *SAE International Journal of Fuels and Lubricants* 10, no. 2017-01-0854 (2017).
2. Zhu X., Zhao L., Zhao Z., Ahuja N., Naber J., and Lee S.-Y. “An Experimental Study of Diesel Spray Impingement on a Flat Plate: Effects of Injection Conditions.” ILASS–Europe 2017, 28th Conference on Liquid Atomization and Spray Systems, 2017.
3. Zhao L., Torelli R., Zhu X., Scarcelli R., Som S., Naber J., and Lee S.-Y., “A Lagrangian Spray-wall Interaction Model Applied to High-pressure Diesel Sprays.” CONVERGE User Group Meeting, Detroit, MI, September 26, 2017.
4. Zhao L., Torelli R., Zhu X., Scarcelli R., Som S., Naber J., Raessi M., and Lee S.-Y. “Evaluation of Diesel Spray-wall Interaction and Morphology around Impingement Location.” Under review, SAE Paper, 2018.
5. Zhao L., Ahuja N., Zhu X., Zhao Z., and Lee S.-Y. “Splashing Criterion and Topological Features of a Single Droplet Impinging on the Flat Plate.” Under review, SAE Paper, 2018.
6. Zhao L., Zhao Z., Zhu X., Ahuja Z., Naber J., and Lee S.-Y. “High Pressure Impinging Spray Film Formation Characteristics.” Under review, SAE Paper, 2018.
7. Markt D., Roberto Torelli, Pathak A., Som S., Scarcelli R., Naber J., Lee S.-Y., and Raessi M. “Using a DNS Framework to Test a Splashed Mass Sub-Model for Lagrangian Spray Simulations.” Under review, SAE Paper, 2018.

I.23 Development and Validation of a Lagrangian Soot Model Considering Detailed Gas Phase Kinetics and Surface Chemistry

Sage Kokjohn, Principal Investigator

University of Wisconsin System
21 N Park St., Suite 6401
Madison, WI 53715
E-mail: kokjohn@wisc.edu

Michael Weismiller, DOE Technology Manager

U.S. Department of Energy
E-mail: Michael.Weismiller@ee.doe.gov

Start Date: January 1, 2016	End Date: December 31, 2018	
Total Project Cost: \$501,919	DOE share: \$441,727	Non-DOE share: \$60,192

Acknowledgments

Co-Authors

Mark Musculus, Sandia National Laboratories
Kelly Senecal, Convergent Science, Inc.

Project Introduction

Computational fluid dynamics (CFD) modeling is used to develop current and future production engines. A key shortcoming of CFD driven engine design is the ability to predict soot emissions. The objective of this project is to improve soot modeling capabilities to enable the engine industry to design advanced combustion engines. A focus of the project is developing and validating a detailed reaction mechanism including polycyclic aromatic hydrocarbon (PAH) chemistry up to benzo[a]pyrene. The advanced soot model will consider surface chemistry, collision, condensation, and wall interactions. The model will be rigorously validated through comparisons with existing constant volume vessel experiments and engine experiments.

The model will be developed in a Lagrangian framework that will use a statistical representation of the soot aggregates to allow detailed tracking of soot makeup without the need to assume a fractal dimension. Optical and metal engine experiments necessary to validate PAH growth and soot formation and soot number density will be conducted. Additionally, the overall CFD codes ability to predict spray, mixing, and combustion processes to ensure the inputs to the soot model are as accurate as possible will be validated. The final outcome of the project will be a new soot model that is validated under conditions ranging from conventional diesel to advanced, low temperature combustion.

Objectives

- Improve soot modeling capabilities in government sponsored and commercial CFD codes to enable the engine industry to design high efficiency, clean engines for transportation applications
- Identify, develop, and validate a semi-detailed reaction mechanism capable of predicting PAH chemistry up to at least benzo[a]pyrene
- Perform high fidelity optical and metal engine experiments to measure in-cylinder PAH formation and engine-out soot mass and particle size distribution to improve the combustion community's fundamental understanding of soot formation

Approach

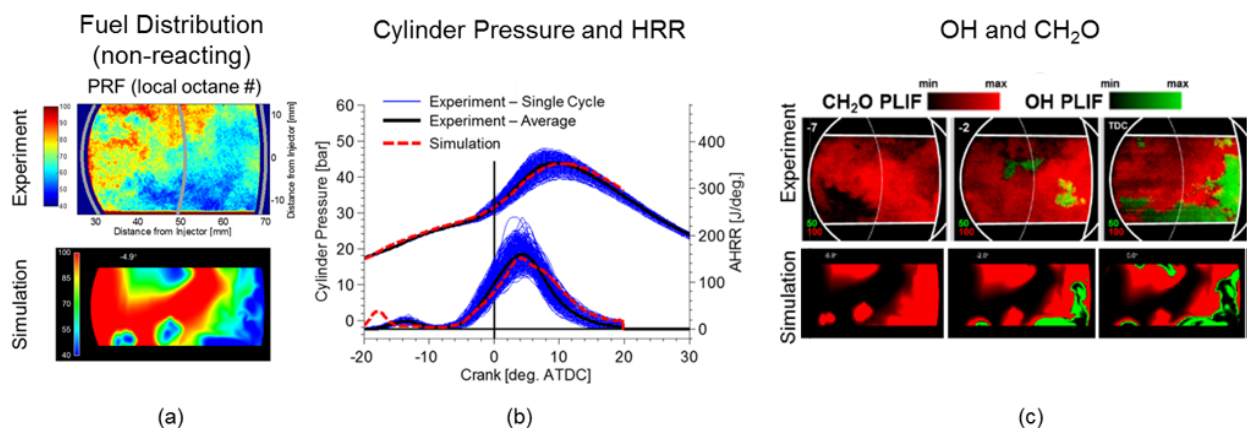
An advanced soot modeling framework is being developed in the government sponsored CFD code (KIVA) and commercial CFD code (CONVERGE) and a targeted validation effort is being undertaken to ensure the

computational tools are able to adequately capture all of the upstream processes influencing soot formation (spray, mixing, ignition, combustion). Simultaneously, optical and metal engine experiments are being performed to enable detailed characterization of PAH formation and soot production. The final effort will combine the validation experiments and simulation framework development to test the soot model and make comparisons to existing models.

Results

Model Validation Effort

Soot is sensitive to all upstream processes. This includes, spray, mixing, ignition, and combustion; accordingly, a targeted validation effort was performed to ensure models are capable of reproducing the measured results. The experiments of Kokjohn et al. [1] and Kokjohn [2] were used. In this data set, several diagnostics were applied. Quantitative fuel-vapor concentrations were measured using toluene fuel tracer fluorescence under non-reacting conditions. Under combustive conditions, planar laser-induced fluorescence (PLIF) imaging was used to track formaldehyde and OH throughout the combustion process. Simulations were performed using the validated reaction mechanism developed during Year 1 of the project and the CONVERGE CFD code [3]. A large eddy simulation approach was used for turbulence with the dynamic structure turbulence model [4]. Adaptive mesh refinement and local embedding was used during spray and combustion resulting in a minimum cell size of 250 μm with a cell count near 3 million during much of the spray and combustion event. The simulations took approximately 24 hours on 160 cores. Figure I.23.1a shows a comparison of the measured and predicted local octane number (Primary Reference Fuel [PRF]) at a crank angle corresponding to the time slightly before the transition from first stage to second stage ignition. It can be seen that not only are the bulk spray and mixing characteristics captured well, but the local features and structure of the spray appears to be adequately captured. Comparisons were also made between measured and predicted fuel distributions using both KIVA and CONVERGE with the Re-Normalisation Group (RNG) $k-\epsilon$ turbulence model [5] and CONVERGE with large eddy simulation (LES). Both the KIVA and CONVERGE Reynolds-averaged Navier-Stokes approaches show very good agreement with the measured fuel distribution; however, the results are not included for brevity. Simulations of combustive experiments were then performed. Figure I.23.1b shows the comparison of the measured and predicted cylinder pressure and heat release rate for combustive cases with the same operating conditions used for the non-reacting experiments and simulations. The simulations show slightly earlier low temperature heat release (LTHR). This is thought to be due to the poor resolution of the combustion process away from the imaging location. The high temperature heat release is captured accurately, showing that the simulations are able to reproduce the bulk combustion characteristics. In addition to bulk combustion characteristics, it is important that the modeling approaches capture the local reaction evolution. Figure I.23.1c shows comparisons of the measured and predicted CH_2O and OH distributions in the imaging location. The simulations accurately capture the location and buildup of CH_2O during the LTHR in the imaging



ATDC – after top dead center; AHRR – apparent heat release rate

Figure I.23.1 - Validation of LES model through comparisons with (a) non-reacting fuel distributions, (b) bulk combustion characteristics (cylinder pressure and heat release rate [HRR]), and (c) locations of key intermediates during the combustion process

location, providing evidence that the under resolved regions may be the source of the advanced LTHR shown in the comparisons with the bulk combustion characteristics. The transition to second stage ignition is shown to be in the near liner region in both the experiments and simulations. The LES captures not only the bulk locations of the second stage ignition kernels, but also qualitatively reproduces the temporal evolution of the size and structure of the reaction zones.

Completion of Detailed Soot Model

The detailed soot model was completed to enable coupling of a stochastic solution to the population balance equations with engineering level CFD calculations. Figure I.23.2 shows an overview of the model. Details of the soot population evolve using a Monte Carlo particle technique that provides a balance of accuracy and computational cost between moment methods and direct integration. The solution converges to the direct integration solution as the number of stochastic particles is increased. To contain the information from the soot population, Lagrangian soot parcels are used. This enables prediction of soot makeup, particle count, and morphology. Particle inception is modeled as two body collisions using the transition kernel taken as harmonic mean of free molecular regime and slip flow regime. Surface reactions use an Arrhenius type equation considering effects of particle volume, mass, collision diameter, surface area, and active surface area. Condensation is considered through collisions between polycyclic aromatic hydrocarbons and soot particles.

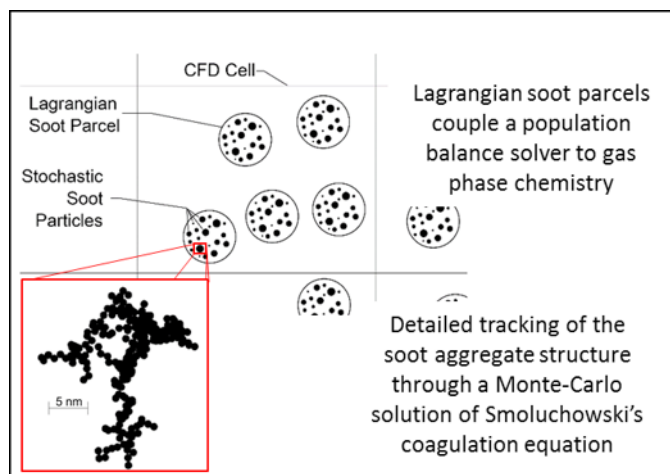


Figure I.23.2 - Overview of detailed soot model and Lagrangian soot parcels

The soot model is complete and has been demonstrated in a two-way coupled and one-way coupled approach. In the two-way coupled approach, the soot model directly interacts with the gas phase chemistry and provides feedback to the evolution of the gas phase chemical kinetics. In the one-way coupled approach, the soot model acts without feedback to the gas phase chemistry. The results between the two approaches have been shown to be similar, but the one-way coupled approach reduces computational cost by orders of magnitude. Accordingly, the one-way coupled approach is discussed here. In the one-way coupled approach, the soot parcel model is used to store the information needed for the stochastic population balance solver. This information is then passed to the population balance solver in parallel to or after the CFD solution is completed. The population balance solver is the most computationally intensive step in the solution. The process is often limited by a few parcels with large population sizes. By using a one-way coupling between the CFD and soot model (i.e., population balance solver), the computational time can be reduced by orders of magnitude because the CFD solution is no longer rate limited by the soot model. The CFD solution proceeds as normal, with a small amount of additional overhead due to transport of soot parcels, and the population balance equations are solved independently. Currently, each soot parcel is sent to its own central processing unit. The solution of each parcel takes between 10 min and 1 d for a typical engine application. The soot solution is solved on University of Wisconsin-Madison's high throughput computing resources. Using 30,000 cores through the Center for High Throughput Computing (<http://chtc.cs.wisc.edu/>), the additional run time for the soot model is approximately 1 d. To illustrate the model functionality, Figure I.23.3 shows the predicted soot particle size distribution under

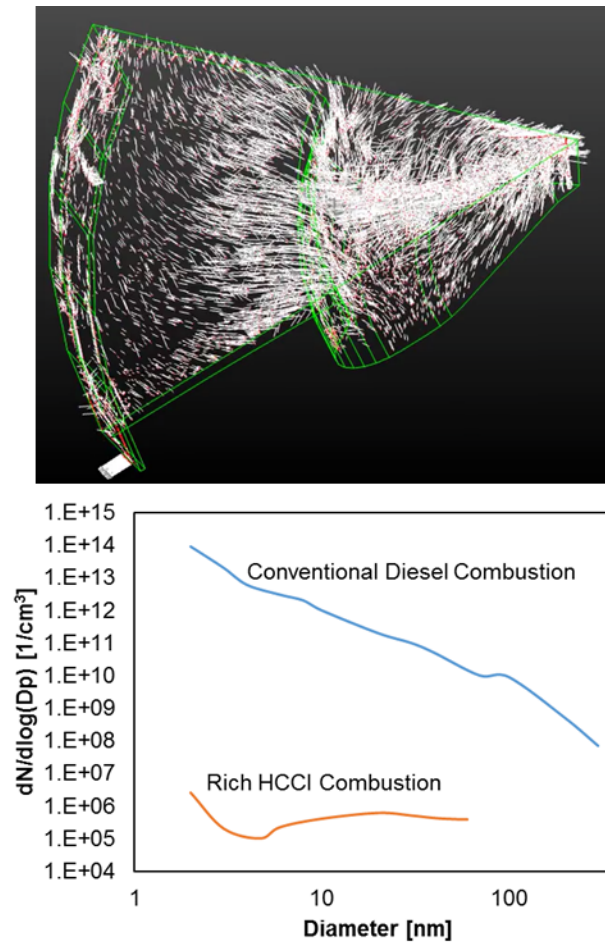


Figure I.23.3 - (Top) soot parcels with velocity vectors showing implementation of soot model. (Bottom) output of soot parcel model late in the cycle for HCCI and conventional diesel combustion.

homogeneous charge compression ignition (HCCI) conditions (i.e., low temperature combustion) and under conventional diesel conditions.

Application of Detailed Soot Model

To provide model validation data, particle size distribution measurement were performed. The engine exhaust was sampled downstream of the exhaust surge tank in fully developed flow. The sample was diluted by a two-stage micro-diluter (Dekati FPS-4000 equipped with a Dekati thermodenuder) after which a scanning mobility particle sizer (TSI 3080 + TSA 3025A) measured the particle size distributions at a dilution ratio of 97 +/- 9. Figure I.23.4 compares the measured and predicted particle size distribution. Note that no model constants were adjusted to achieve the agreement shown in Figure I.23.4. The results are very promising and show the suitability of the one-way coupled approach.

Further evaluation was performed by using the new soot model in a post processing step where the fuel distribution was imposed. Figure I.23.5a shows the results when the new soot model is coupled to a multi-zone model and fuel distribution is imposed with a standard deviation of equivalence ratio (σ_ϕ) equal to 0.2. The results show rather good agreement with the measured data over the range of crank angles considered. This approach was further used to investigate the sensitivity of the particle size distribution to the equivalence ratio distribution. Figure I.23.5b shows the impact of the equivalence ratio distribution on the resulting particle size distribution. The number of inception mode particles are relatively insensitive to the imposed equivalence ratio distribution suggesting that the count of inception mode particles is dominated by the PAH chemistry; however, the large particles are very sensitive to the imposed distribution. When the imposed fuel distribution is narrowed from σ_ϕ to σ_ϕ , the size of the largest particle decreases proportionally to σ_ϕ .

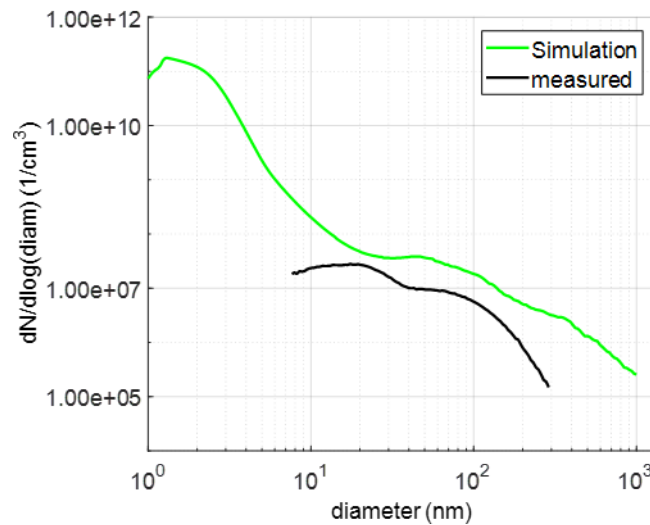


Figure I.23.4 - Comparison of measured and predicted particle size distributions. The predictions use the soot model developed in the current program in the one-way coupled approach.

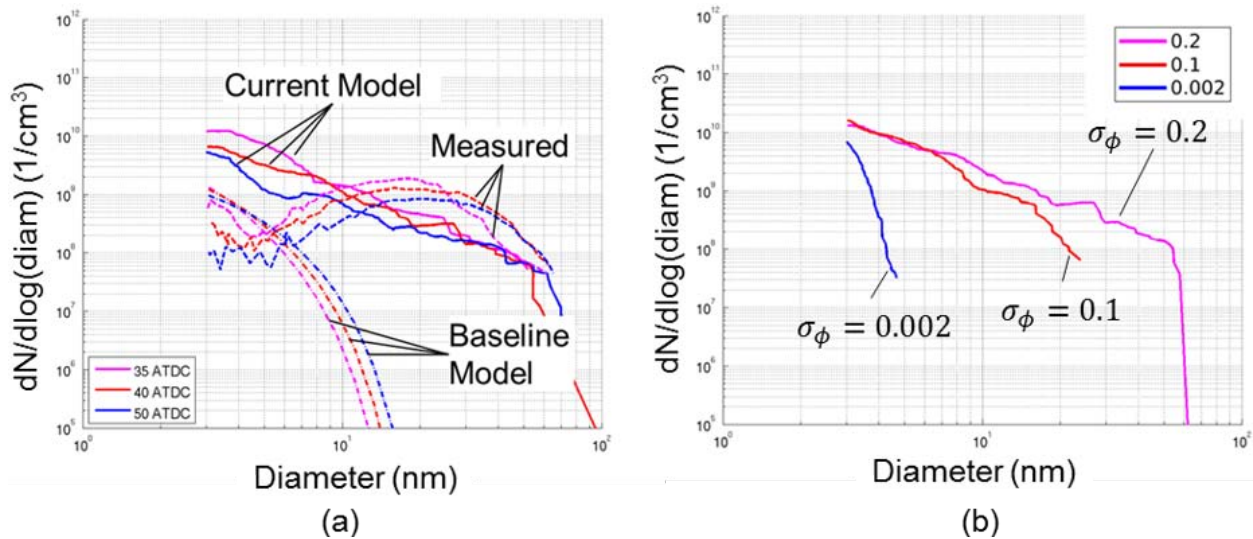


Figure I.23.5 - (a) Comparison of a baseline mode, our current model, and measured particle size distribution at several times. (b) Resulting particle size distributions with several levels of stratification (denoted as the standard deviation in equivalence ratio (σ_ϕ)).

Conclusions

- We coupled a detailed solution to Smoluchowski's population balance equation with engineering level CFD codes for use in engine CFD simulations to improve the prediction of particle size distributions under conventional and advanced combustion engines.
- Metal engine experiments were completed to measure particle size distributions under a range of operating conditions and the data was used to validate the newly developed soot model.
- The spray and mixing models were evaluated through comparisons with optical engine data from the literature in both a Reynolds-averaged Navier–Stokes and large eddy simulation framework.
- The detailed soot model was shown to reproduce the measured particle size distribution without adjustment of model constants. Further work is needed to identify robustness to operating conditions.

- We exercised detailed soot model to identify the impact of mixture non-uniformity and fuel properties on particle size distributions.

References

1. Kokjohn, S.L., M.P.B. Musculus, and R.D. Reitz. "Evaluating Temperature and Fuel Stratification for Heat-Release Rate Control in a Reactivity-Controlled Compression-Ignition Engine using Optical Diagnostics and Chemical Kinetics Modeling." *Combustion and Flame*, Vol. 162, No. 6, 2015.
2. Kokjohn, S.L., "Reactivity Controlled Compression Ignition (RCCI) Combustion." PhD Thesis in Mechanical Engineering, University of Wisconsin-Madison, 2012.
3. Richards, K.J., P.K. Senecal, and E. Pomraning. "CONVERGE (v2.3)." Convergent Science, Madison, WI (2016).
4. Pomraning, E. and C.J. Rutland. "Dynamic One-Equation Nonviscosity Large-Eddy Simulation Model", *AIAA Journal*, Vol. 40, No. 4, pp. 689–701 (2002).
5. Han, Z. and R. Reitz. "Turbulence Modeling of Internal Combustion Engines Using RNG k-e Models." *Combustion Science and Technology*, 106:267-295, 1995.

Key Fiscal Year 2017 Publications

1. Paz, J., D. Staaden, T. Strickland, and S.L. Kokjohn. "The Impact of Post Injections on Conventional Diesel Combustion and Gasoline Compression Ignition at High and Low Load." Submitted, SAE World Congress 2017.
2. Strickland, T. and S.L. Kokjohn. "Impact of mixture distribution and fuel properties on particle size distributions." In Preparation, U.S. Comb. Meeting.
3. Kokjohn, S.L. "Advanced Combustion: Challenges and Opportunities." Syracuse College of Engineering Symposium, October 2017.

I.24 Development and Validation of Physics-Based Sub-Models of High Pressure Supercritical Fuel Injection at Diesel Conditions

Ajay Agrawal, Principal Investigator

University of Alabama
359 H.M. Corner Hall
Tuscaloosa, AL 35487
E-mail: aagraval@eng.us.edu

Michael Weismiller, DOE Technology Manager

U.S. Department of Energy
E-mail: Michael.Weismiller@ee.doe.gov

Start Date: January 1, 2016	End Date: December 31, 2018	
Total Project Cost: \$542,487	DOE share: \$467,012	Non-DOE share: \$66,475

Acknowledgments

Co-Authors

Joshua Bittle, Chih-Hsiung Cheng; University of Alabama
Sibendu Som, Argonne National Laboratory

Project Introduction

In this research we seek to develop and validate accurate, physics-based, numerical submodels and framework, which can be implemented in computational fluid dynamics (CFD) software codes to enable accurate predictions of high-pressure diesel spray. This capability is required to support the development of high-efficiency diesel engines that operate at higher chamber pressures and temperatures than current systems. The combined experimental–computational effort has four major objectives: (1) acquire spatially and temporally resolved scalar measurements of fuel–oxidizer mixing in the near field of the jet for a range of supercritical or nearly supercritical test conditions relevant to diesel engines; (2) develop real-fluid model and code to calculate thermo-physical properties of diesel surrogates and their mixtures with the oxidizer of interest at a wide range of operating conditions, especially at pressures near and above the critical conditions; (3) integrate the real-fluid model into a commercial and an open-source CFD codes to demonstrate the use of the model to accurately simulate high-pressure diesel spray; and (4) assess the robustness, accuracy, and uncertainty of the integrated CFD solvers in computing injection spray.

Objectives

- Produce a validated real-fluid property code which can be integrated with CFD solvers to improve their accuracy in simulating high-pressure diesel sprays
- Provide documentation containing information associated with CFD code modifications needed for supercritical fluid spray simulations using the Eulerian–Eulerian approach
- Establish the accuracy assessment of the Eulerian–Eulerian approach to simulate fuel spray at high-pressure diesel engine operating conditions
- Produce an extensive experimental data set to validate CFD models simulating high-pressure diesel fuel spray

Approach

Experiments were conducted in a constant pressure flow rig (CPFR) whereby a low-speed flow of heated, pressurized air is supplied to the test chamber, and the fuel is injected against this flow. High-speed rainbow schlieren deflectometry (RSD), a novel optical diagnostics technique pioneered in our laboratory to acquire

quantitative scalar measurements in jets and flames, and supersonic flows is utilized to resolve the highly dynamic features of the mixing process. Experiments are conducted initially at conditions approximating the Engine Combustion Network Spray A, and then at different chamber and fuel injection conditions and fuel types, i.e., pure or mixtures of surrogate species and eventually with the real diesel fuel.

A real-fluid model, which accounts for the compressibility effects in diesel fuels, has been developed and validated using the available National Institute of Standards and Technology database. The property models are integrated with CFD codes (open-source developed by co-principal investigator and ANSYS Fluent), which is being validated using experimental data. The models are also being integrated into a commercial CFD code in collaboration with our partner team at Argonne National Laboratory.

Results

- Met key milestones and the project budget is on track
- Integrated the new CPFR with support equipment and verified its operation and attainment of design operating conditions
- Conducted experiments near Engine Combustion Network spray conditions and acquired quantitative measurements of fuel–air mixing in the near field and in ignition and combustion zones
- Developed a new approach that allows RSD technique to also measure the liquid jet boundary, thereby, making RSD an all-encompassing diagnostics technique eliminating the need for Mie-scattering to identify the liquid phase
- Integrated real-gas property model into an open-source code and debugged the code
 - Integrated real-gas property model with ANSYS Fluent code and the numerical performance of the integrated code has been tested for two-dimensional axisymmetric simulations of supercritical fuel–air mixing
- Implemented the developed real-fluid property module in CONVERGE code
- Tested the numerical fidelity of the integrated code for baseline test case involving supercritical fuel–air mixing
- Conducted experiments to demonstrate technical go/no-go milestone for “RSD accuracy sufficient to serve as quantitative validation for model development”

Specifically, we have obtained equivalence ratio and mixture temperature profiles in the jet at different times after start of injection. Measurements are consistent with observed trends of ignition and combustion, thereby, allowing us to quantify the fuel–air mixing process in the near field.

Experimental Research

The new CPFR shown in Figure I.24.1 has been installed and integrated with the air supply and exhaust systems. The system has been tested with air flow at the maximum pressure attainable with the air compressor (34 bar) and with a heater set point of 1,100 K. To demonstrate the successful chamber operation, we include the images in Figure I.24.2 showing a single frame from high-speed videos acquired by simple visual imaging. The ambient air is at 33 bar and 825 K. The fuel is *n*-heptane injected for 2 ms at 1,000 bar injection pressure. The injector is located towards the top of the image, and the thermocouple used to characterize the near injector temperature is visible protruding from the left side below the injector on the left image. The image on the left was recorded at 10 kHz with an exposure time of 99 μ s, while the image on the right was recorded at 20 kHz with an exposure time of 49 μ s. These two images represent two separate injections illustrating fuel–air mixing in the near field and combustion downstream resulting from autoignition. The fuel is no longer being injected at the time of these images.

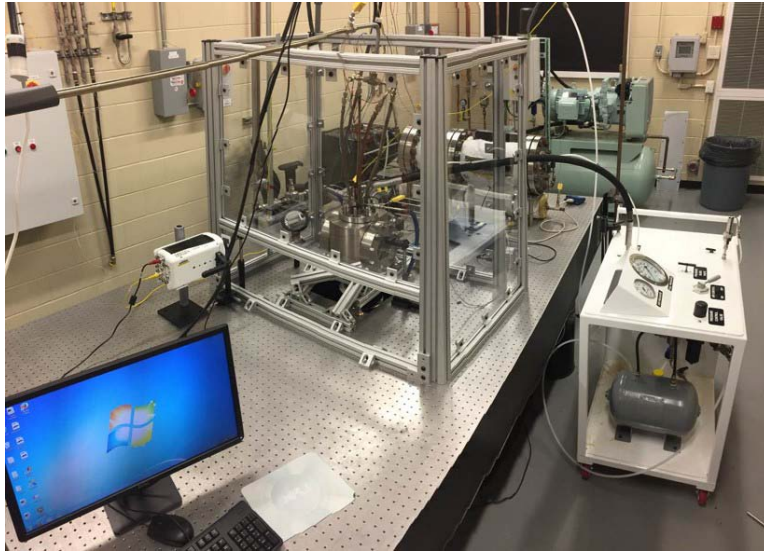


Figure I.24.1 - New CPFR with air exhaust, injector cooling, and instrumentation installed
(Figure source: University of Alabama)

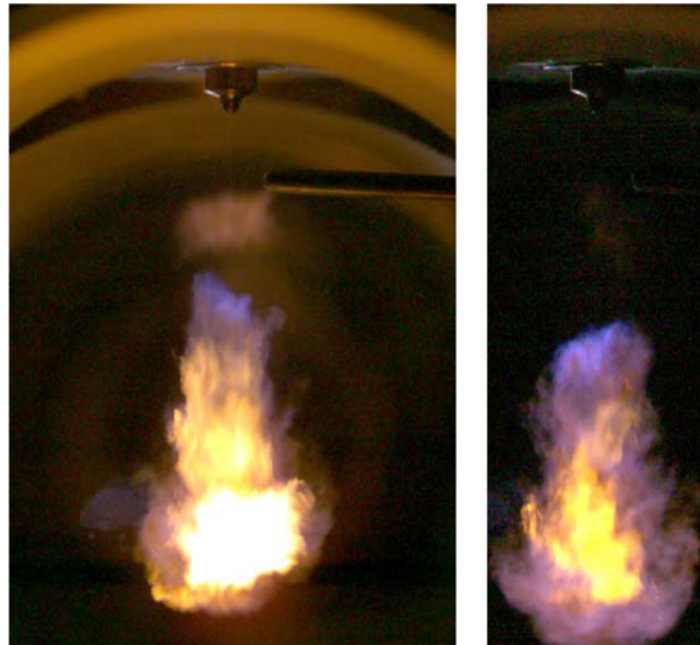


Figure I.24.2 - First reacting sprays captured in new CPFR, one (left) with longer exposure time and another (right) with less exposure time (Figure source: University of Alabama)

Figure I.24.3 illustrates the RSD analysis steps. (1) The raw schlieren images are converted from red, green, and blue format as saved by the camera to hue, saturation, and value format. (2) The hue at each pixel is converted to ray deflection angle at the pixel location based on a calibration of the rainbow filter. (3) A single image provides the instantaneous ray deflection angle value at each pixel location. We perform a number of injection experiments, and ensemble average of 50 images is taken at each injection time. Thus, average deflection angle is obtained at each time step after start of injection (aSOI) by ensemble averaging instantaneous deflection angle at each pixel in the frame over all injections (50 in this case). (4) The average deflection angle is used to estimate the center plane fuel volume fraction in the spray through the Abel inversion process, which converts deflection angle to local fuel mass fraction. This process requires assumptions of axisymmetry and binary mixing between the fuel and air. Thus, quantitative results are valid only in the vapor region upstream of the combustion zone.

We have also computed another feature the deflection angle, its fluctuations are quantified by root mean square (RMS) deflection angle, which is a useful way to visualize the highly turbulent regions of the jet. Specifically, notice the edges of the spray near the injector representing a shear layer between the fuel jet and the ambient air. Downstream as the fuel and air become well mixed the entire spray becomes highly variable.

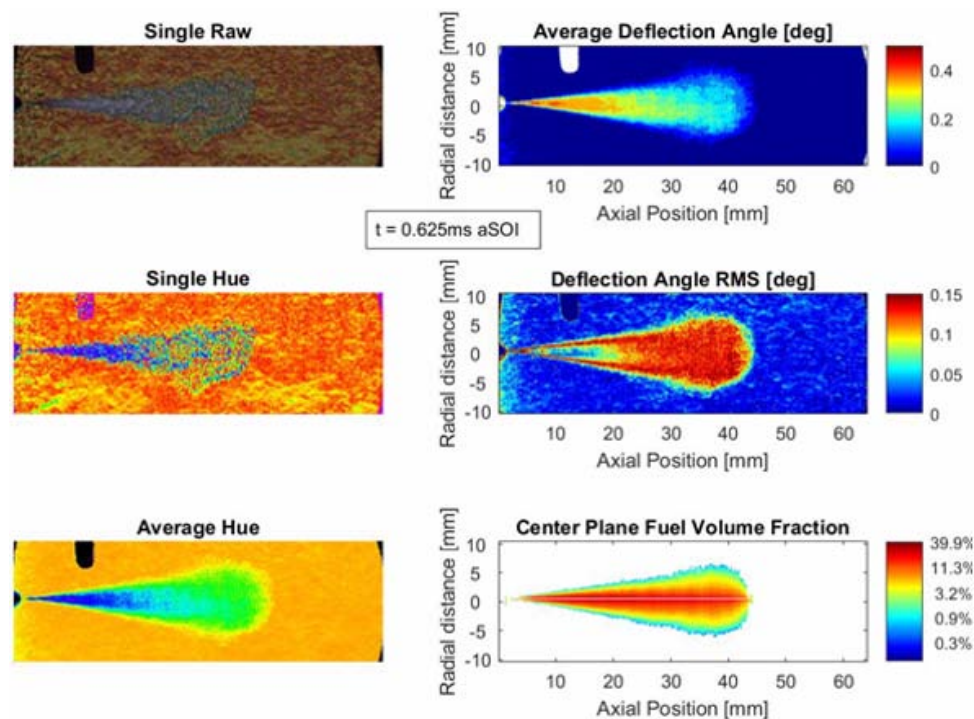


Figure I.24.3 - Image processing steps for RSD images at 0.625 ms aSOI for *n*-heptane injected at 1,000 bar for 4 ms into ambient air at 30 bar and 825 K. A total of 50 injections were captured in this case.

Figure I.24.4 shows the results at 1.3 ms aSOI at which time the reaction is underway downstream. The first thing to note is the high deflections in the reaction zone resulting from temperature induced density gradients. This is as opposed to the mixing induced density gradients near the injector. Another interesting feature is the reduction in deflection angle between the near injector spray and the downstream reaction zone. We believe this is caused by initial reactions causing slight temperature rise (reducing density to near that of the ambient in this case) prior to subsequent primary ignition. In other words there is a transition region between the dense spray near the injector and the low density reaction zone downstream in which the density gradient is approximately zero through the spray. In the future data processing codes we will have to ensure the reacting regions of the spray are not included in the fuel volume fraction calculations.

We have determined that the RSD technique can replace the Mie-scattering technique to identify the liquid boundary. We have recently published a journal paper in the journal *Applied Optics* describing this approach [1]. Thus, in the future, we will replace the Mie-scattering technique to visualize droplets with the newly developed RSD technique. Future experiments will zoom into the near field fuel–air mixing region.

Computational Research

The computational research had two major objectives: (1) integrate real-gas property models with CFD codes and (2) perform computations for baseline test cases. Integration involved two different CFD codes to demonstrate the versatility of the real-gas models. Originally, we focused on an open-source code available to the research team, but debugging issues with code integration prompted us to consider ANSYS Fluent code. ANSYS Fluent offers access to the code through user defined functions (UDF) to implement real-gas models developed for this research, while other features and capabilities of the code remain intact. Concurrently, our Argonne National Laboratory collaborators have integrated the real-gas models with the CONVERGE code, widely used by the internal combustion engine community. CONVERGE integration is also made possible by UDF capability offered by the vendor.

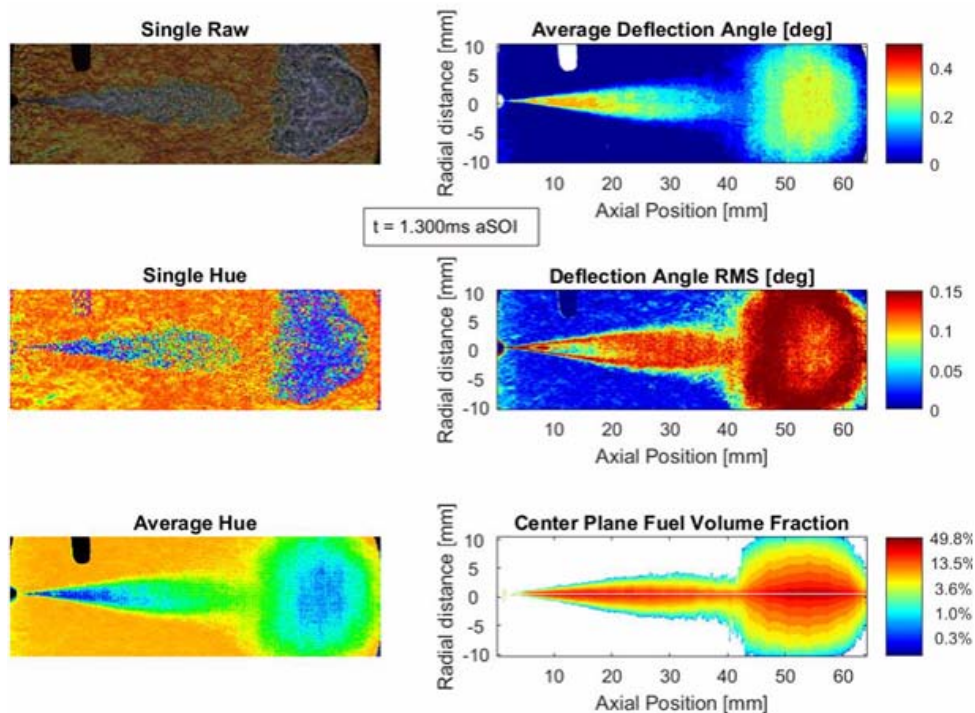


Figure I.24.4 - RSD images during combustion at 1.3 ms aSOI for *n*-heptane injected at 1,000 bar for 4 ms into ambient air at 30 bar and 825 K. A total of 50 injections were captured in this case.

Three made up test cases were created to test the integrated codes. Fuel injection conditions for these test cases are (1) supercritical injection, (2) trans-critical injection, and (3) sub-critical injection. Integrated codes have been tested for fuel–air mixing at supercritical injections, and we expect to complete the remaining two test cases during the fourth quarter of this budget period.

ANSYS Fluent Integration

Sample results from Fluent integration are based on the solution of coupled compressible Reynolds-averaged Navier–Stokes equations together with the energy and species equation. The temperature at the inlet and inside the chamber was specified at 800 K. The fuel (*n*-dodecane) inlet velocity was set to 100 m/s. The chamber pressure was set to 3.0 MPa. A structured grid was chosen to discretize the domain. A slight taper from the exit nozzle was necessary to avoid high skewness towards the exit of the chamber where a pressure outlet was imposed. The diffusion coefficient was assumed constant.

Figures I.24.5a and I.24.5b show, respectively, the fuel mass fraction and temperature contours, affected by compressibility at supercritical conditions. Transport properties (molecular diffusivity and thermal conductivity) are shown in Figures I.24.6a and I.24.6b. Specific heat and mass fraction of the fuel at the center line from the tube exit are shown in Figures I.24.7a and I.24.7b. Typical exponential decay is predicted. These results demonstrate that fuel–air mixing process at supercritical conditions can be simulated without numerical issues or related difficulties using the Fluent software integrated with real-gas models. Presently, we are working to simulate trans-critical and sub-critical test cases.

CONVERGE Integration

A CONVERGE UDF has been developed, which provides an interface between the CONVERGE solver and the University of Alabama real-fluid property model. Instead of using an equation of state or assuming ideal gas law, the fluid solver is now able to acquire thermodynamic properties from the real-fluid property model with given temperature and pressure, or given enthalpy and pressure. Current implementation uses a look-up table for testing purpose to provide internal energy, enthalpy, C_v , C_p , viscosity, conductivity, and compressibility factor, as functions of temperature and pressure. The tabulation range are from 100–2,000 K and 2–60 bar.

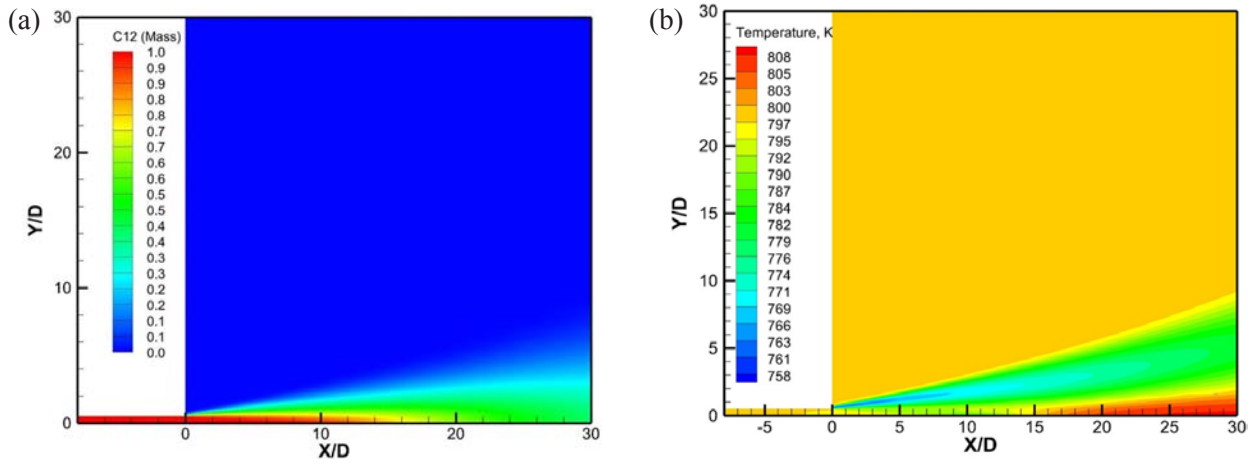


Figure I.24.5 - (a) Fuel mass fraction and (b) temperature

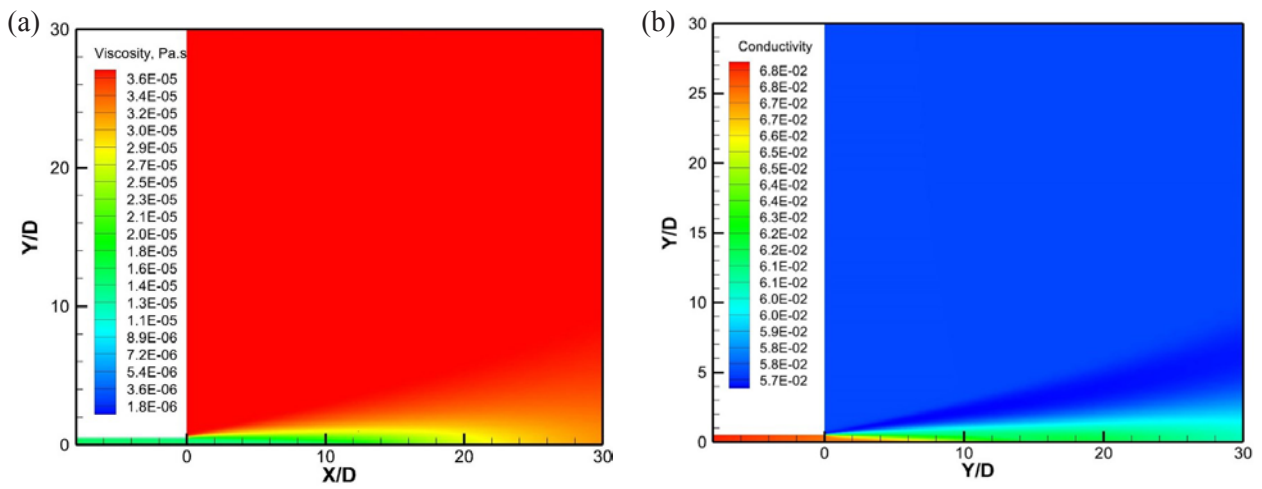


Figure I.24.6 - (a) Molecular viscosity and (b) thermal conductivity

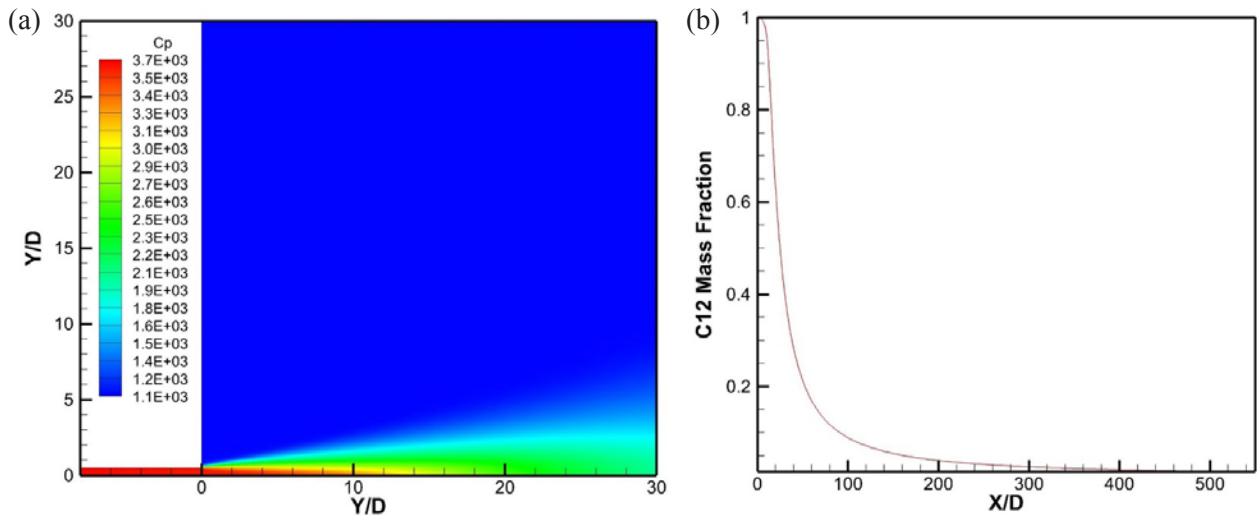


Figure I.24.7 - (a) Specific heat and (b) fuel mass fraction along jet center

The integrated code was tested in an *n*-dodecane-N₂ fuel injection problem. *n*-dodecane is injected at 900 K, 30 bar, into a chamber filled with N₂ at 900 K, 25 bar. This test condition was chosen such that pressure and density gradients are relatively small to avoid numerical issues, which will be address subsequently. For this test case, both in-nozzle and chamber are at supercritical conditions for *n*-dodecane. Computational mesh embedding and adaptive mesh refinement with minimum cell size of 20 μm are applied to resolve the nozzle flow and spray structure. Figure I.24.8 shows contours of pressure field, density, and velocity distributions at 0.18 ms aSOI. It is seen that pressure decreases along the nozzle as velocity increases and peaks at the location of nozzle exit. Fluid density decreases as *n*-dodecane mixes with the ambient.

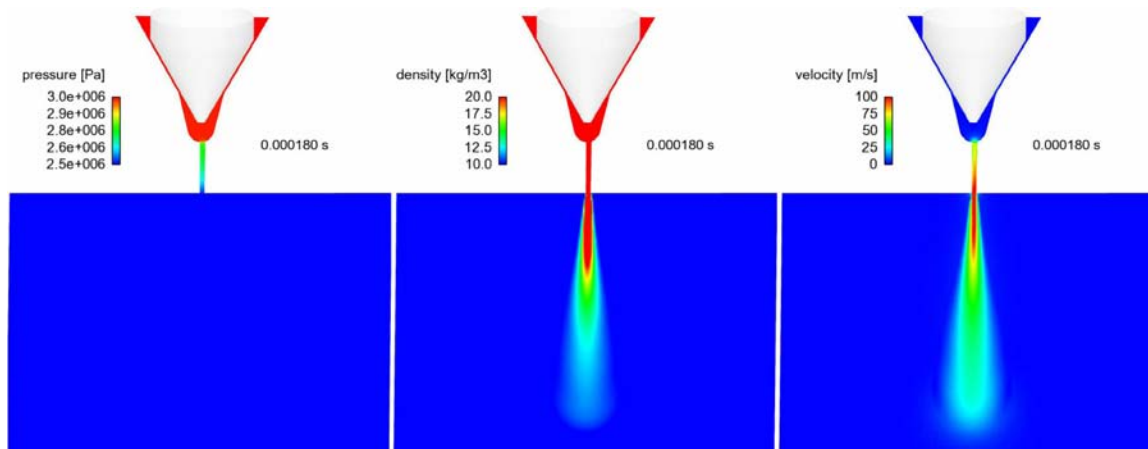


Figure I.24.8 - Two-dimensional distributions of pressure, density, and velocity at 0.18 ms aSOI

Conclusions

- The CPFR has been operated successfully for a range of chamber pressures and temperatures.
- RSD techniques have been applied to acquire quantitative fuel–air mixing data throughout the field of view at high spatial and temporal resolutions.
- Real-gas models developed during the previous year have been integrated with two CFD codes.
- Integrated CFD codes have been used to compute fuel–air mixing at supercritical conditions.

References

1. Wanstall, Christopher, Ajay K. Agrawal, and Joshua Bittle. “Quantifying liquid core of a fuel spray by rainbow schlieren deflectometry.” *Applied Optics* 56, No. 30 (2017). 8385–8393.

Key Fiscal Year 2017 Publications

1. Wanstall, Christopher, Ajay K. Agrawal, and Joshua Bittle. “Quantifying liquid core of a fuel spray by rainbow schlieren deflectometry.” *Applied Optics* 56, No. 30 (2017) 8385–8393.
2. Agrawal, A.K., Bittle, J., Cheng, C-H., and Som, Sibendu. “High pressure supercritical fuel injection at diesel conditions.” Presentation at the 2017 DOE Annual Merit Review, Washington, DC, April 17, 2017.
3. Agrawal, A.K., Bittle, J., Cheng, C-H. “Development and validation of physics-based submodels of high pressure fuel injection at supercritical conditions at diesel conditions.” AEC update, Sandia National Laboratories, Livermore, CA, January 2017.

I.25 Development of a Physics-Based Combustion Model for Engine Knock Prediction

Seung Hyun Kim, Principal Investigator

The Ohio State University
201 W. 19th Ave.
Columbus, OH 43210
E-mail: kim.5061@osu.edu

Michael Weismiller, DOE Technology Manager

U.S. Department of Energy
E-mail: Michael.Weismiller@ee.doe.gov

Start Date: February 1, 2016	End Date: January 31, 2019	
Total Project Cost: \$715,933	DOE share: \$643,839	Non-DOE share: \$72,094

Acknowledgments

Co-Authors

Derek Splitter, K. Dean Edwards; Oak Ridge National Laboratory

This material is based upon work supported by the Department of Energy, Office of Energy Efficiency and Renewable Energy (EERE) and the Department of Defense, Tank and Automotive Research, Development, and Engineering Center (TARDEC), under Award Number DE-EE0007334. The computational resources for DNS are provided by the Oak Ridge Leadership Computing Facility and the Ohio Supercomputer Center. The principal investigator also thanks Convergent Science for their help in using CONVERGE CFD.

Project Introduction

Engine knock is a primary factor that limits the fuel efficiency of the passenger cars. It is caused by undesired ignition of fuel–air mixture before spark-ignited (SI) premixed flame fronts consume the fresh gas and is accompanied by rapid rise and oscillation of in-cylinder pressure and potential engine damage. An approach to increase the fuel efficiency of SI engines, such as increasing the compression ratio and downsizing, often generates thermodynamic conditions that are prone to autoignition and thus engine knock.

The ultimate goal of this project is to improve the predictive capability for computational fluid dynamics (CFD) simulation of engine knock phenomena. Toward this goal, this project will develop a physics-based combustion model for large eddy simulation (LES) of engine knock processes. The model is developed in the context of LES to reproduce the stochastic nature of knocking phenomena. To advance the predictive capability of knock models, the emphasis of the model development is placed on turbulence–chemistry interactions during end-gas ignition and high-fidelity chemistry description. In typical engine conditions, in-cylinder flows are highly turbulent. Complex turbulent motions substantially affect heat release rates and end-gas ignition. The physics-based and accurate modeling of such turbulence–chemistry interactions is necessary, in particular to predict processes in high scalar dissipation layers. Accurate description of end-gas ignition requires the use of a high-fidelity chemical mechanism. This project aims to enable engine knock LES where ignition chemistry is described by a reduced mechanism that contains about 100 species, while employing a physics-based model for turbulence–chemistry interactions.

Objectives

- Develop a combustion model that improves the predictive capability for engine knock by capturing turbulence–chemistry interactions in a physics-based way and incorporating high-fidelity chemistry into LES of in-cylinder turbulent reacting flows
- Advance a fundamental understanding of turbulence–chemistry interactions during end-gas ignition through engine LES, high-fidelity direct numerical simulation (DNS), and engine experiments

Approach

The overall approach includes joint computational and experimental efforts focusing on the model development and validation with high-fidelity numerical and experimental data. The physics-based and mathematically consistent modeling framework consists of separate models for SI premixed flame propagation and end-gas ignition processes to consider fundamentally different turbulence–chemistry interactions during the two processes. Conditional moment closure (CMC) [1] is used to model end-gas ignition, while the front propagation formulation (FPF) [2] is used to model SI premixed flame propagation. The model is developed in the context of LES to reproduce the stochastic nature of the knocking phenomena. For thorough validation, DNS and engine experiments are performed to provide high-fidelity datasets. DNS data will guide the model development by providing detailed statistical information.

Results

The key accomplishments for Fiscal Year (FY) 2017 are the following:

- Developed a base CMC–FPF solver coupled with an LES code
- Generated DNS database for end-gas ignition and premixed flame propagation
- Assessed the performance of the combustion model for end-gas ignition using the DNS database
- Acquired in-cylinder pressure data from single-cylinder engine experiments over a range of knocking and knock-free conditions
- Implemented the premixed combustion model, FPF, into CONVERGE CFD and performed a test LES run

CMC–FPF Base Code Development

The base CMC solver developed in FY 2016 has been coupled with the premixed combustion model, FPF, and interfaced with an LES code, NGA [3]. The CMC–FPF solver is tested for end-gas ignition in a constant volume configuration. The premixed flame is initially located near the bottom of the computational domain. The upper part of the premixed flame is the end-gas region. Initial pressure is 20 bar. The initial mean temperature is set to be 950 K and the initial root mean square fluctuation of temperature is 50 K. With this temperature field, end-gas ignition occurs in a very early stage of the simulation, which helps the numerical test procedure. The fuel is iso-octane. A reduced mechanism for a primary reference fuel (PRF), which consists of 116 species [4], is used. The test results are shown in Figure I.25.1.

DNS and Model Validation

Three sets of DNSs have been performed to provide detailed statistical data for validating various submodels in the modeling framework. The first set is a two-dimensional (2D) reduced chemistry DNS of end-gas ignition. In FY 2017, DNSs with refined resolution for thin ignition fronts in near-stoichiometry PRF–air mixtures have been performed. Other numerical details remain the same as those for the DNS performed in FY 2016. A second order finite difference solver for low Mach number reacting flows is used [3]. A reduced chemical mechanism of Luong et al. [4] is used. The emphasis is placed on the effects of temperature inhomogeneity on ignition processes. The level of temperature fluctuations in the five DNS cases considered ranges from 10 K to 40 K. The reference value of root mean square fluctuations of temperature is taken as 20 K, which is similar to the experimentally measured root mean square fluctuations of temperature at the top dead center in an optical homogeneous charge compression ignition engine [5]. The domain size is 5 mm² for four of the five cases, which is discretized into 3,072² grid points. The initial pressure is 30 atm. The initial mean temperature is 850 K or 900 K. Figures I.25.2a and I.25.2b show temperature fields at two time instances, $t = 2.5$ ms and 2.83 ms, which correspond to the first occurrence of an ignition spot and the occurrence of the maximum heat release rates, respectively. The second set is three-dimensional (3D) DNS of iso-octane–air ignition using a two-step chemical mechanism [6]. 3D DNS is necessary to obtain the scalar dissipation statistics and to validate the conditional scalar dissipation model used in CMC in a meaningful way. In the 3D DNS case, ignition of the stoichiometric iso-octane–air mixture under the constant pressure condition is simulated. The scalar dissipation rate of the sensible enthalpy in the 3D DNS of end-gas ignition is shown in Figure I.25.2c.

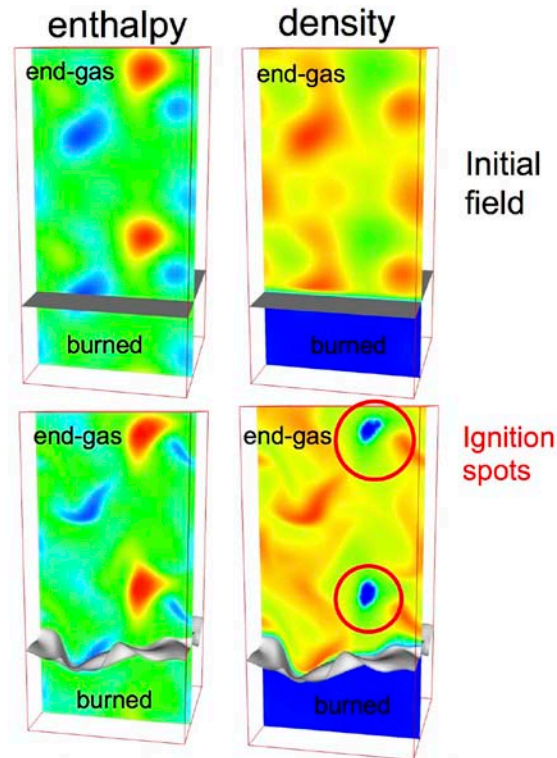


Figure I.25.1 - Premixed flame propagation and end-gas ignition in a constant volume configuration. A CMC-PPF solver has been coupled with an LES solver. Total enthalpy and density fields at the initial time (top) and when the ignition kernels have formed (bottom) are shown. The red color represents the maximum value, while the blue color represents the minimum value.

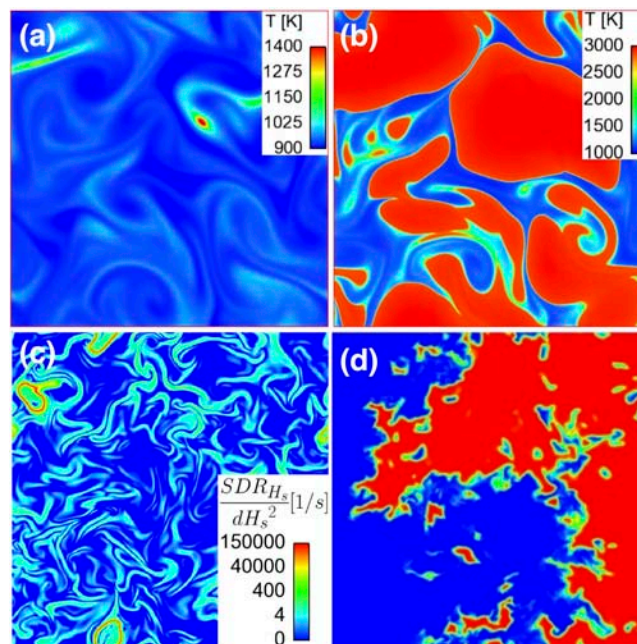


Figure I.25.2 - DNS datasets. (a) and (b) 2D reduced chemistry DNS of end-gas ignition. Temperature fields at (a) $t = 2.5$ ms and (b) 2.84 ms for a representative case with the temperature inhomogeneity level of 20 K are shown. Scalar dissipation of the sensible enthalpy in 3D two-step chemistry DNS of end-gas ignition. (c) DNS of a premixed flame. The progress variable field (blue: unburned, red: burned) for DNS with the Taylor-scale Reynolds number of 169 is shown.

The third set is DNS of premixed flames with various Reynolds numbers. The datasets include four DNSs with the Taylor-scale Reynolds numbers of 52, 68, 105, and 169 in the thin reaction zone regimes, which will be used to develop FPF for SI premixed flame propagation and investigate the influence of the Reynolds number on the subfilter flame speed. The instantaneous flame structures for the DNS case with the largest Reynolds number of 169 are shown in Figure I.25.2d. The number of grid points used is $4,000 \times 1,024 \times 1,024$. The scale separation between the laminar flame thickness and the turbulence integral length scale is large enough to investigate the effects of filter sizes on the subfilter flame speed and other quantities used in premixed combustion modeling. Previous large-scale DNS has been focusing on detailed chemistry aspect or distributed reaction zones regime, and had limited scale separation. The scale ratios in the present DNS data will offer an unprecedented opportunity to explore the physics of flame wrinkling with a sufficiently broad spectrum of length scales, thereby improving our understanding of burning rate enhancement in SI engines.

Here, the validation results for end-gas ignition CMC are presented. The focus of the validation is placed on the choice of a conditioning variable in CMC. The key assumption of CMC is the existence of a scalar that shows strong correlations with other reacting scalars. Taking this scalar as a conditioning variable allows for accurate estimation of filtered reaction rates. For end-gas ignition, the total enthalpy or the sensible enthalpy is a good candidate for the conditioning variable. This is because autoignition delay of the end-gas is substantially influenced by temperature inhomogeneity initially imposed through the mixture preparation or through wall heat transfer for given mixture composition and the temperature fluctuations are related to the enthalpy fluctuations. For ignition and combustion of hydrocarbon fuels, chemical reaction rates show the strong nonlinear dependence on temperature, leading to the sensitivity of the reaction rates to temperature. For the samples having a particular value of the enthalpy, temperature fluctuations can be small when there is a strong correlation between the chosen enthalpy and the reacting scalars. As a result, the estimation of the reaction rates can be made accurate. In Figure I.25.3, heat release rates predicted by the total-enthalpy-based CMC and by the sensible-enthalpy-based CMC are compared with the DNS data at three different time instances

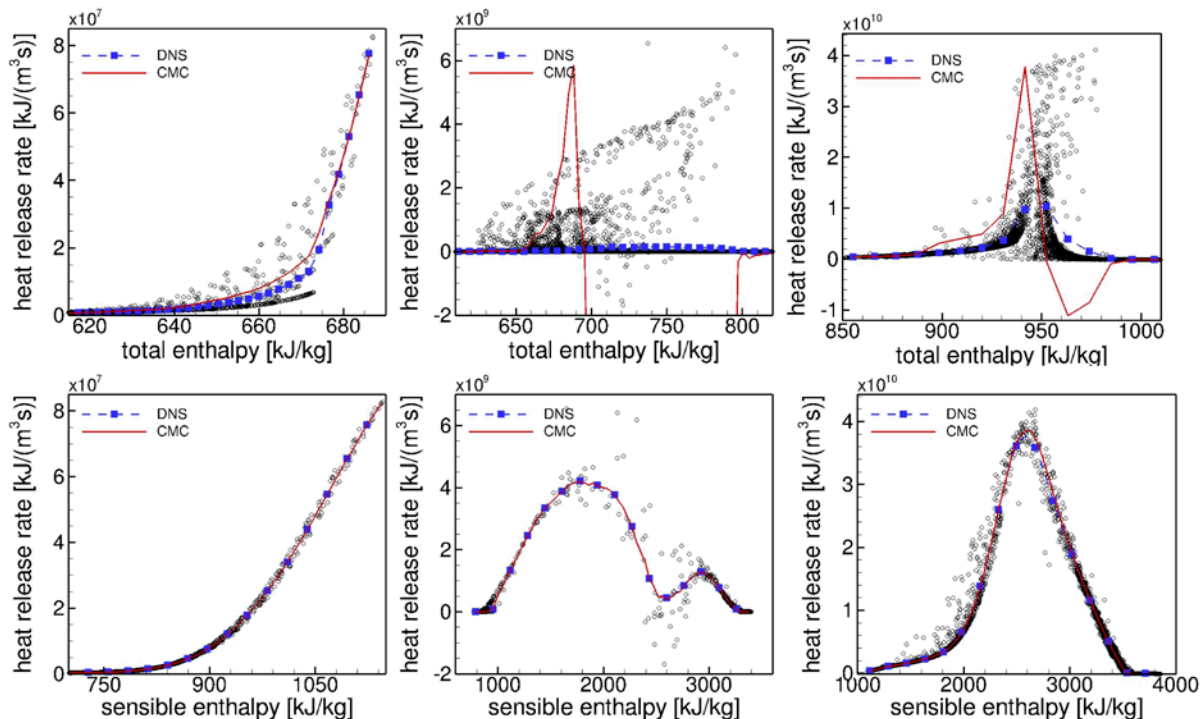


Figure I.25.3 - Assessment of CMC reaction rate closure models using 2D reduced chemistry DNS of end-gas ignition. Sensible-enthalpy-based CMC performs very well for the entire duration of the ignition process (bottom), while total-enthalpy-based CMC leads to substantial errors except for a very early stage of ignition processes (top). (left column: $t = 2.5$ ms, center column: $t = 2.72$ ms, right column: $t = 2.84$ ms). The blue filled squares represent the conditional mean heat release rates from the DNS data. The black hollow circles denote the heat release rates at the DNS grid points.

from the very early stage of ignition processes to the time when the heat release rate reaches its maximum value, for a representative case with temperature root mean square fluctuations of 20 K (the case for which the temperature fields are shown in Figure I.25.2). Both total-enthalpy-based CMC and sensible-enthalpy-based CMC perform well at the very early ignition stage, $t = 2.5$ ms. It is also seen that the heat release rates at DNS grid points (black circles) are more scattered when plotted in the total enthalpy space (Figure I.25.3 top row) than in the sensible enthalpy space (Figure I.25.3 bottom row), suggesting that reacting scalars are better correlated with the sensible enthalpy and thus that the sensible enthalpy is a better conditioning variable. As ignition progresses, total-enthalpy-based CMC begins to overpredict heat release rates. At $t = 2.64$ ms, when the total heat release rate becomes close to 10% of the maximum heat release rate, total-enthalpy-based CMC leads to substantial errors. At $t = 2.84$ ms, when the total heat release rate is very close to its maximum, the error in total-enthalpy-based CMC is reduced as compared with that at $t = 2.64$ ms, but still substantial. The error in total-enthalpy-based CMC is due to large fluctuations of temperature and species mass fractions, which originate from the coexistence of unburned, burned, and ignition fronts within the samples having similar total enthalpy values. Note that sensible-enthalpy-based CMC performs well during the entire ignition process. The good performance of sensible-enthalpy-based CMC indicates that the sensible enthalpy is a good conditioning variable in the end-gas ignition problem. The good performance comes from the strong correlation of the sensible enthalpy with other reacting scalars, especially temperature, as can be seen in the scatter plot of the DNS reaction rates (black circles).

Experimental Campaign

This portion of the work occurs at Oak Ridge National Laboratory and utilizes a single-cylinder version of the General Motors LNF 2.0 L four-cylinder design turbocharged gasoline direct injection engine from the 2007 Pontiac Solstice. The experimental results consist of two campaigns to isolate conditions of knock. PRF grade iso-octane was used in these campaigns with various levels of boost. Engine operation consisted of several operating conditions while sweeping intake manifold temperature at 2,000 rpm. In this test, four different air flow rates, 581 g/min, 684 g/min, 804 g/min, and 946 g/min, were used. At each condition both 0% and 15% external cooled exhaust gas recirculation (EGR) were used, with stoichiometric fueling used throughout. At each operating temperature and intake air flowrate a spark timing sweep was conducted, where the engine was operated from the knock limit and spark was retarded at even intervals to produce combustion phasing sweep of 50% of the mass fraction burned (CA50) from the knock limit to CA50 of 50° crank angle (°CA) after top dead center firing (aTDC). Figure I.25.4 illustrates the CA50 phasing of the knock limit for 0% and 15% EGR engine operation at 804 airflow (dashed) and 946 airflow (solid). The results show that at the increased airflow conditions EGR had no effect at knock mitigation. However, at reduced airflow rates, EGR seemed to improve knock resistance at all but the highest intake temperatures.

Base Engine Simulation

The objective of this task is to set up the baseline simulation capability and conditions for LES of engine experiments. The engine simulation is to be performed using the CONVERGE CFD code. In this task, as the first part of the engine simulations, knock-free cases are considered. The simulation of engine experiments conducted at Oak Ridge National Laboratory has been initiated. As a first step toward LES, the set up and boundary conditions are being tested in the Reynolds-averaged Navier–Stokes simulations. Here, the implementation of the premixed combustion model into CONVERGE CFD and initial LES results for an example SI engine geometry are reported.

In FY 2017, the premixed combustion model, FPF, including a spark ignition model, has been implemented into CONVERGE CFD through a user defined function. FPF is a newly developed subfilter premixed combustion model for LES. In LES where the grid scale is taken as the filter scale, filtered flame fronts can be substantially under-resolved when the filter scale is larger than or comparable to the laminar flame thickness. With the under-resolved flame fronts, the predicted propagation speed in LES can be erroneous regardless of the accuracy of the physical model used. FPF resolves this problem by adopting a specially designed reaction rate formulation that preserves the integrated reaction rates. It is similar to the widely-used G-equation approach, but solves the filtered progress variable equation directly and is not subject to the flamelet assumption. To capture the initial flame kernel that is typically not resolved in LES, a spark ignition model is developed by extending the model of Colin and Truffin [7]. In the spark ignition model, a flame kernel

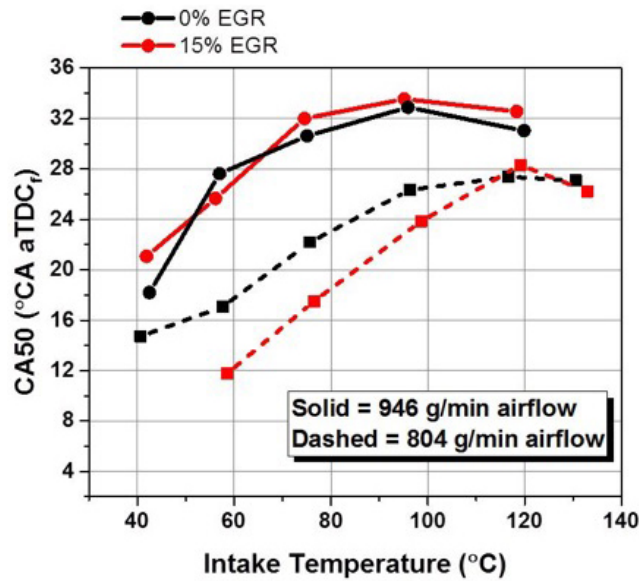


Figure I.25.4 - Experimental data of knock limited combustion phasing with 15% EGR (red) and without EGR (black) at two different air flow rates (i.e., loads). Data highlights that as airflow and thus load is increased EGR effectiveness at mitigating knock can be reduced or eliminated.

is generated by depositing the burned gas at the location of the spark plug. The subfilter kernel growth model is used until the developed progress variable field is resolvable on an LES grid. Once the flame kernel grows sufficiently large to be resolved on an LES grid, the flame propagation is described by FPF. LES of an SI engine has been performed using CONVERGE CFD with FPF being implemented as the user defined function. The SI8 engine case in an example directory in the CONVERGE distribution is simulated. The iso-octane is used as the fuel. The subfilter turbulent flame speed model used in FPF is the extension of the Peters flame speed model to LES [8]. The evolution of the filtered flame fronts in the test runs is shown in Figure I.25.5.

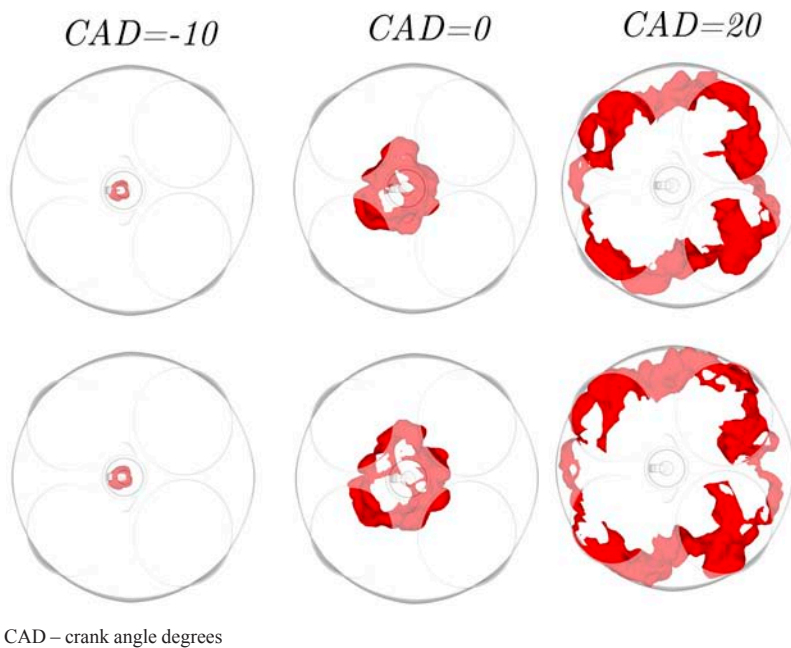


Figure I.25.5 - Evolution of flame fronts in LES of an SI engine. The model parameters in a turbulent subfilter flame speed model [8] are (top) $b_1 = 10$ and $b_2 = 2$; and (bottom) $b_1 = 10$ and $b_3 = 2$.

Conclusions

The summary of the progress and the key findings for FY 2017 is the following.

- A base CMC–FPF solver has been coupled with an LES code.
- DNS databases for end-gas ignition and premixed flame propagation have been generated.
- The combustion model for end-gas ignition has been validated using the end-gas ignition DNS database. The results show that the sensible-enthalpy-based CMC performs very well for the entire duration of ignition processes, while the total-enthalpy-based CMC leads to substantial errors except for a very early stage of ignition processes. This suggests that the sensible enthalpy is a good conditioning variable in the end-gas ignition problem.
- In-cylinder pressure data for stoichiometric and dilute SI operation over a wide range of load, speed, and intake temperature conditions have been acquired experimentally to isolate the conditions of knock.
- The implementation of the developed premixed combustion model, FPF, and the spark ignition model into CONVERGE CFD has been completed. LES has been performed using an example SI engine geometry.

References

1. Klimenko, A.Y. and R.W. Bilger, *Prog. Energy Combust. Sci.*, 25: 595–687 (1999).
2. Kim, S.H. *J. Comput. Phys.* 285: 193–207 (2015).
3. Desjardins, O., G. Balnquart, G. Balarac, and H. Pitsch, *J. Comput. Phys.* 227:7125–7159 (2008).
4. Luong, M.B., Z. Luo, T.F. Lu, S.H. Chung, C.S. Yoo, *Combust. Flame* 160:2038–2047 (2013).
5. Dronniou, N. and J. Dec, *SAE Int. J. Engines*: 2012-01-1111 (2012).
6. Misdariis, A., O. Vermorel, and T. Poinsot, *Proc. Combust. Inst.* 35: 3001–3008 (2015).
7. Colin, O. and K. Truffin, *Proc. Combust. Inst.* 33: 3097–3104 (2011).
8. Pitsch, H., *Combust. Flame* 143:587–598 (2005).

Key Fiscal Year 2017 Publications

1. Su, Y. and S.H. Kim. “An improved consistent, conservative, non-oscillatory and high order finite difference scheme for low Mach number turbulent flow simulation.” *J. Comput. Phys.* submitted.

I.26 Development and Multiscale Validation of Euler–Lagrange-Based Computational Methods for Modeling Cavitation within Fuel Injectors

Emily Ryan, Principal Investigator

Boston University
110 Cummington Mall
Boston, MA 02215
E-mail: ryanem@bu.edu

Michael Weismiller, DOE Technology Manager

U.S. Department of Energy
E-mail: Michael.Weismiller@ee.doe.gov

Start Date: February 1, 2016	End Date: January 30, 2019	
Total Project Cost: \$826,395	DOE share: \$743,074	Non-DOE share: \$83,321

Acknowledgments

Co-Authors

Sheryl Grace, Glynn Holt, Jacy Bird; Boston University

Subcontractors

Todd Toops, Eric Nafziger, Derick Splitter, Charles Finney; Oak Ridge National Laboratory

The material presented in this report is based upon work supported by the Department of Energy, Office of Energy Efficiency and Renewable Energy and the Department of Defense, Tank and Automotive Research, Development, and Engineering Center, under Award Number DE-EE0007332.

Project Introduction

The main objective of this research project is to develop and validate more accurate, physics-based, mathematical submodels for use in computational fluid dynamics (CFD) software to enable better prediction of cavitation within fuel injectors. The outcome of the research will be two new submodels for cavitation that can be used in conjunction with CFD: one for preliminary design and the second for final design analysis.

Controlled cavitation in fuel injectors can improve the atomization of the spray, which improves combustion and reduces emissions. However, excess cavitation can be detrimental to efficiency and can damage the injector. Therefore, the global motivation for research into cavitation in fuel injectors stems from the fact that improvements in fuel injection systems will increase fuel efficiency, reduce the emission of harmful pollutants, and improve the lifetime and reliability of nozzles.

Objectives

- Develop and validate physics-based, mathematical submodels for use in standard multiphase CFD software to enable better prediction of cavitation within fuel injectors
- Develop a small-scale experimental setup to investigate cavitation in a canonical nozzle over a range of flow and geometry conditions
- Image cavitation in a fuel injector using the High Flux Isotope Reactor (HFIR) at Oak Ridge National Laboratory (ORNL)

Approach

This project is developing methods for simulating cavitation dynamics in a fuel injector that can be used in preliminary design and for final design analysis, and performing experiments for validation of the models.

Research focuses on three specific thrusts: computational model development, small-scale cavitation experiments, and HFIR imaging of a real fuel injector.

Computational Model Development

The computational submodels that are being developed rely on cavitation analysis performed with a high-resolution model of bubble dynamics and use both a Lagrangian frame solver in the form of the smoothed particle hydrodynamics (SPH) method and the Eulerian CFD solver OpenFOAM. One submodel will create constitutive relations for inclusion in a CFD solver using an upscaling process based on the results from detailed computational studies of canonical injectors. Detailed simulations of cavitation in nozzles using SPH and OpenFOAM will form a database from which an upscaling method will be used to define a new submodel that can be integrated into a Reynolds-averaged Navier–Stokes (RANS)-based multiphase CFD code (much like turbulence models are used in CFD). The second submodel will consist of the SPH model itself by defining the two-way coupling interface equations for use with unsteady RANS CFD. Using a two-way coupled SPH and CFD approach will create a more detailed and accurate model but will be much more computationally expensive than upscaling and as such is proposed for final design analysis. Development and validation of the SPH tool and the subsequent full simulation capabilities based on the new submodels rely on outcomes from experimental studies of detailed flow characteristics for canonical and real geometry injectors performed at Boston University (BU) and ORNL.

Small-Scale Cavitation Experiments

Small-scale cavitation experiments are being conducted at BU using a canonical nozzle setup with both optical and passive acoustical measurements. Untreated tap water is forced through the nozzle at various flow rates to investigate cavitation onset. Initial experiments were run continuously, with no valving between the pump and test section, and the pump was run continuously at a range of target voltages. Newer experiments are also using a real fuel injector (provided by ORNL) with an actuator to simulate fuel injection events.

HFIR Imaging

In performing dynamic studies of fuel injector operation, a heated and pressure-controlled spray chamber is employed. A closed-loop fuel injection system (Figure I.26.1a) with heated spray chamber (Figure I.26.1b) is installed at the neutron imaging beamline at ORNL's HFIR. The sophisticated system is designed to operate with commercial and prototype injectors and deliver fuel to the injectors at rail pressures up to 150 bar. The spray chamber can be operated at absolute pressures as low as 0.2 bar and currently has a maximum pressure

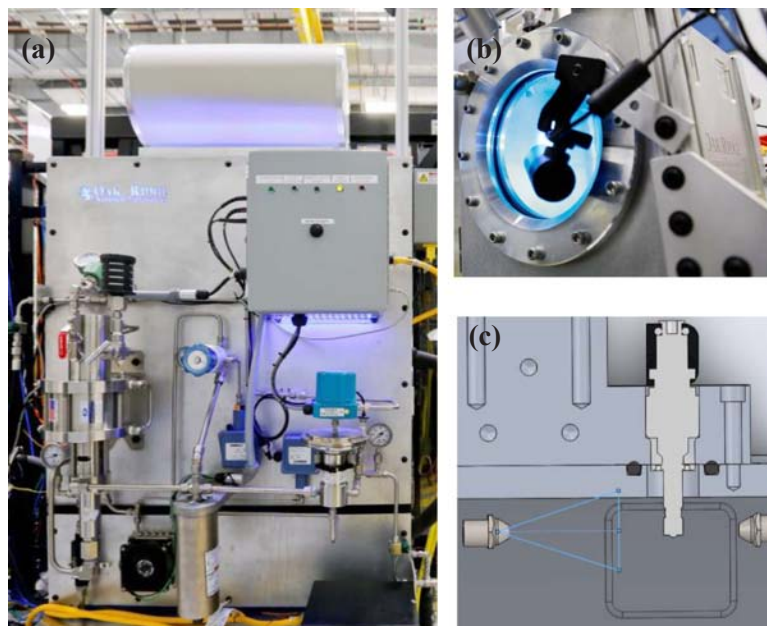


Figure I.26.1 - (a) High pressure fuel delivery system and (b) spray chamber installed at HFIR. (c) Computer-aided drawing of injector holder and the necessary sweep gases to minimize fuel build-up on the chamber walls and injector.

of approximately 4 bar and can be heated to over 100°C while also flowing 10–40 L/min of directed sweep gas to further eliminate condensation build-up (Figure I.26.1c). These conditions are necessary to avoid condensation of the fuel in the chamber, which will block neutron flux.

Results

Key accomplishments for Fiscal Year 2017 include:

- Validated the OpenFOAM CFD model and SPH model of bubble dynamics in a hydrostatic tank under multiple conditions
- Developed a quantitative analysis method for measuring void fraction in a fuel injector
- Analyzed data from first ORNL HFIR campaign, which shows a significant difference in neutron attenuation between flashing and non-flashing conditions

During Fiscal Year 2017, research for this project focused on the three complimentary tasks discussed in the Approach section. A brief description of the results for each of these areas is given below.

Computational Model Development

Computational model development has focused on small-scale models of bubble dynamics using SPH and RANS CFD models of bubbles using OpenFOAM. SPH model development has focused on the selection of discretizations and formulations for the physics including surface tension, density and pressure calculations and equations of state, and the setup of a canonical nozzle simulation for comparison to the BU small-scale cavitation experiments. We have applied these efforts to numerical benchmark cases for the deformation of bubbles rising through quiescent fluid and compared the SPH results to literature results and the OpenFOAM modeling efforts.

One benchmark case being considered is the problem of a bubble rising in a column of water due to buoyancy. Two tests cases (TC1 and TC2) are considered with major differences between the two being density (ρ_l/ρ_g) and viscosity (μ_l/μ_g) ratios. The transport properties and bubble characteristics for the test cases being considered are shown in Table I.26.1.

Table I.26.1 - Transport Properties and Bubble Characteristics for Considered Test Cases

Case	ρ_l	ρ_g	μ_l	μ_g	g	σ	Re	Bo	Ca	ρ_l/ρ_g	μ_l/μ_g
TC1	1000	100	10	1	0.98	24.5	35	10	0.286	10	10
TC2	1000	1	10	0.1	0.98	1.96	35	125	3.571	1000	1000

The results from OpenFOAM (setup at BU) and the BU SPH model are compared to those from Verma et al. [1] and Klostermann [2]. Figure I.26.2 shows the results of the bubble shapes and bubble position/velocity for TC2. As can be seen from the figures, the OpenFOAM and SPH simulations at BU match well with work published by Verma and Klostermann, and all the qualitative and quantitative features of the bubble are realized. For TC2, the low value of surface tension causes the bubble to deform and become skirted toward the end of the simulation. For TC1, the higher surface tension holds the bubble together. Results for TC1 are not shown but show similarly good comparison between the BU simulations and the literature data for both qualitative and quantitative metrics.

In addition to simulations considering the bubble dynamics, models are also being developed to consider cavitation packages in OpenFOAM, bubble expansion and collapse, and to model the canonical experimental BU nozzle in OpenFOAM and SPH.

Small-Scale, Detailed Cavitation Experiments

To compare with and augment our data from canonical acrylic nozzle experiments at BU, we have set up a flow experiment using a commercial fuel injector, ACDelco Model ACD# 217-3086. In addition to replicating our passive cavitation detection experiments, we wanted to prepare for experiments at ORNL using the fuel

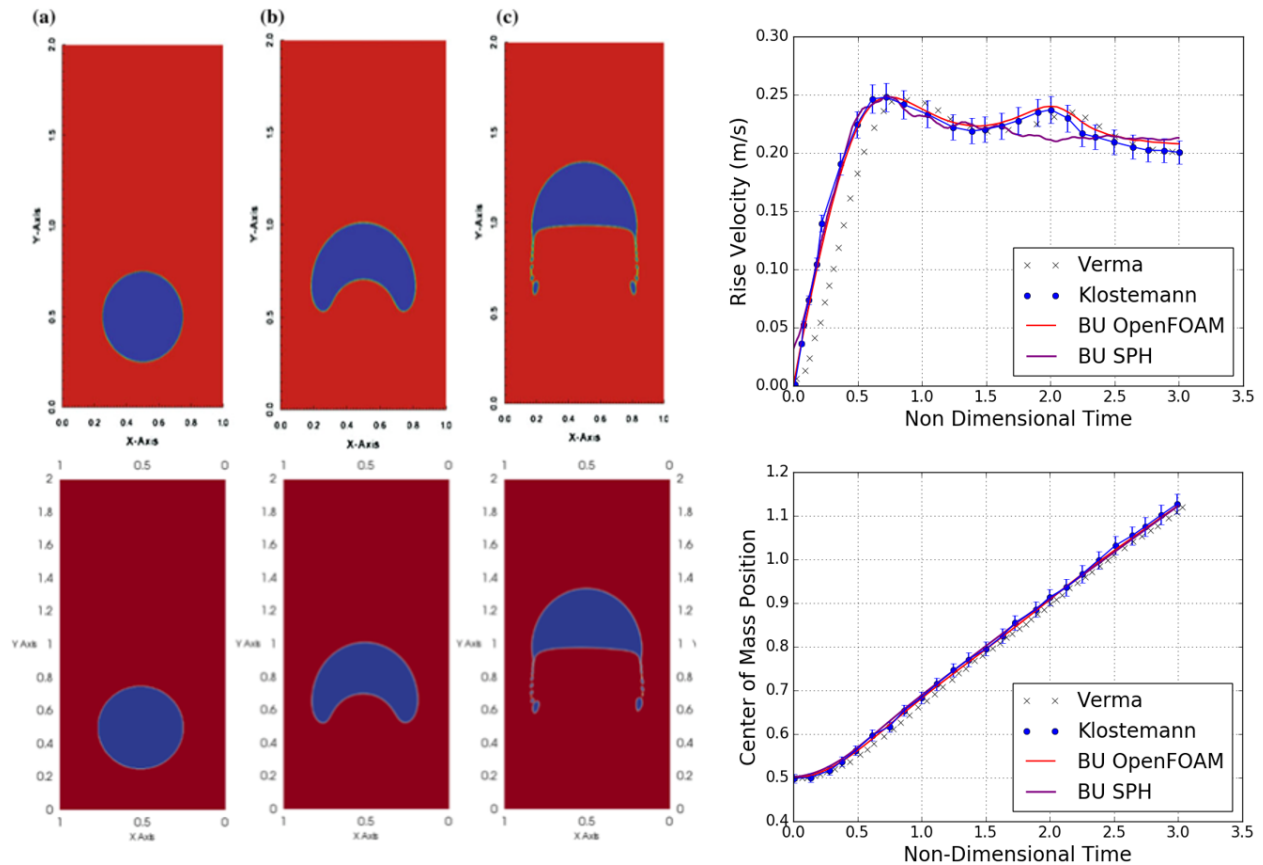


Figure I.26.2 - Left: Bubble shapes in time results from Verma et al. (top) and current BU OpenFOAM simulations (bottom) for TC2. Non-dimensional times displayed are (a) $t = 0$, (b) $t = 1.5$ and (c) $t = 3.0$. Right: Rise velocity (top) and center of mass (bottom) in time from Klostermann and Verma et al. compared to BU OpenFOAM and SPH simulations. Error bars showing a deviation of 2% have been introduced for the center of mass curves and 5% for the rise velocity curves.

injector experimental setup developed by ORNL for pressure and temperature control. At BU and also at ORNL, we employed a laser Doppler vibrometer (LDV), Polytec OFV-3001 controller with OFV-303 sensor head, operating in velocity mode, to collect data at a point nearest the end of the injector tip. This was done because the only available window for the LDV diagnostic beam was through an existing plug port on the ORNL apparatus, which exposed only the last few millimeters of the injector tip. A dominant feature of the LDV signal from a pintle-lift excitation (flow and no-flow) was the fundamental cantilever beam mode.

Seeing this signature gave us the idea that, in addition to broadband signals to detect cavitation, we could exploit the cantilever beam vibration to infer the fuel vapor mass fraction (the “void fraction”). The stiffness, mass, mode (fundamental, $n = 1$), and moment of inertia of an empty fuel injector can be determined. Thus, the $n = 1$ frequency of an empty fuel injector can be calculated analytically (with thin beam theory), computationally (with finite element solvers and a computer-aided design file) and benchmarked with an empty beam measurement. Then, the $n = 1$ frequency of a full fuel injector can be determined; it will represent a mass-loaded cantilever beam. During operation, if cavitation develops, there will be an instantaneous reduction of this added mass proportional to the void fraction. By employing a mixture law to account for the total mass (steel, liquid fuel, vapor fuel), we will be able to infer the void fraction of the fuel by monitoring the temperature-corrected measured frequency of the fuel injector $n = 1$ mode.

To measure the dominant vibrational mode of the structure (injector) at BU, we performed experiments of an impulse excited empty fuel injector with fixed and free end conditions. The response was obtained using LDV in velocity mode. Controlled pintle actuation provided impulse excitation. The left plot in Figure I.26.3 is the response of the structure for a pintle opening of 5 ms; the measurement was made at the tip (free end).

Qualitatively, the response is similar to observations made on an ORNL campaign in May 2017 with initial vibration due to pintle opening and a secondary vibration response due to pintle closing. Additionally, the ring downs show low quality factors, an indicator of high damping. The right plot in Figure I.26.3 shows the results when the max amplitude is evaluated for distances away from the free end. As shown, the dominant mode indeed does appear to be the fundamental mode for a cantilever beam.

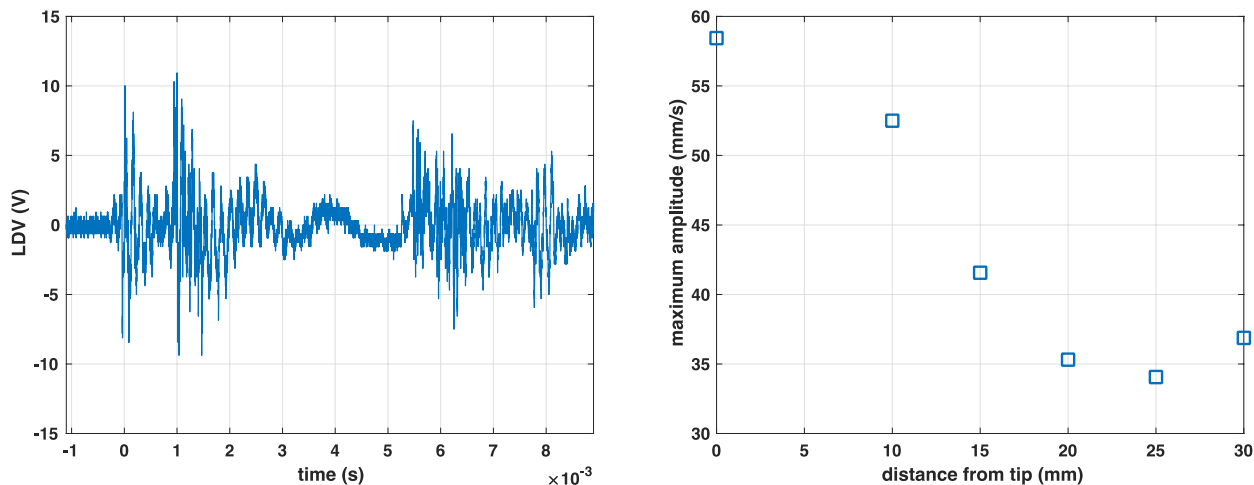


Figure I.26.3 - Left: LDV signal of fuel injector tip excitation from pintle opening and closing. Right: Max amplitude of LDV at the tip and 10, 15, 20, 25, and 30 mm away from the free end.

HFIR Imaging Campaign

In September 2016, a joint ORNL–BU team conducted a neutron imaging campaign at the CG-1D Imaging Beamline at the HFIR at ORNL. Stroboscopic imaging using a gasoline direct injector and a novel, previously developed technique was employed to record a fuel injection event at 25 Hz with 20 μ s temporal resolution. This technique required observing $\sim 10^6$ periodic injection events and integrating sparse neutron counts in each snapshot to produce a high-contrast injection moving-image record. Two conditions were imaged, both with 0.367 ms injection duration of pressurized cyclopentane: (1) a higher temperature, lower ambient pressure condition to induce flashing (70°C and 30 kPa), and (2) a lower temperature, higher ambient pressure condition to inhibit flashing (40°C and 110 kPa).

Analysis of the data during Fiscal Year 2017 focused on estimating the detectable fluid mass flow rates exiting through the nozzle using calibrated attenuation profiles. The procedure involved calibrating the attenuation levels based on neutron paths through known distances of liquid phase cyclopentane and using this calibration to estimate the mass passing through the sac–nozzle interface. Figure I.26.4 shows the areas of interest in the estimation area. In the figure, the left radiograph is contrast-enhanced to show fluid cyclopentane during injection, and the approximate sac–nozzle interface area of interest is denoted; the right radiograph shows the same frame unenhanced and with the traverse used in calibrating observed neutron attenuation over known path lengths.

The calibrated attenuation rate was used to transform the observed attenuation profile in the area of interest to a mass rate of cyclopentane entering the nozzle. Figure I.26.5 shows the observed attenuation and the cumulative injected mass for Condition 1 from the September 2016 HFIR experiment. In the figure, the left panel displays the mean intensity in the averaging area consisting of six pixels at the sac–nozzle interface, with a guideline defining the approximate threshold for fluid detection and the conversion to deviation from that threshold. The right panel shows the cumulative mass estimated using this methodology. Approximately 1 mg of cyclopentane was measured, compared with a targeted injection of 1.25 mg.

Conclusions

- Validated SPH and OpenFOAM RANS CFD models' ability to simulate bubble dynamics over a range of material properties and flow conditions

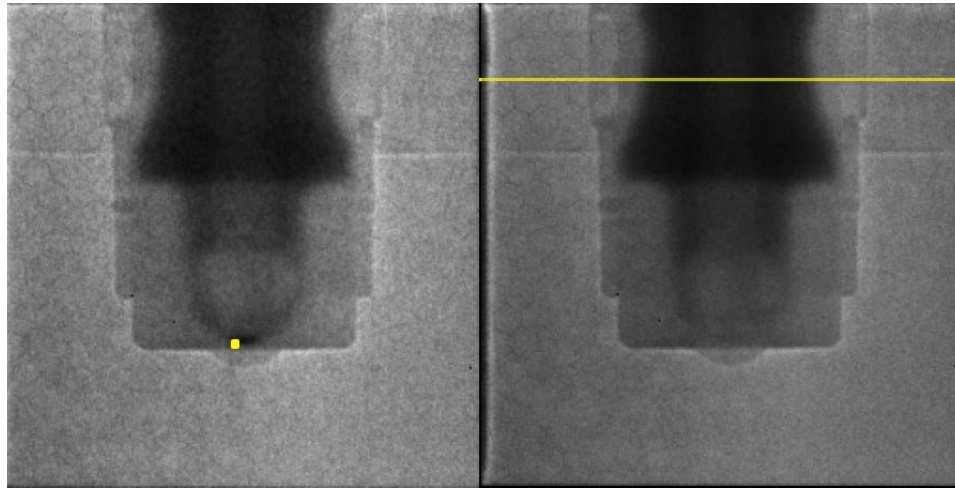


Figure I.26.4 - Contrast-enhanced radiograph showing fluid in the sac and the area of interest in the sac–nozzle interface (left). Radiograph with traverse used in calibrating neutron attenuation intensity over known distances and fluid masses (right).

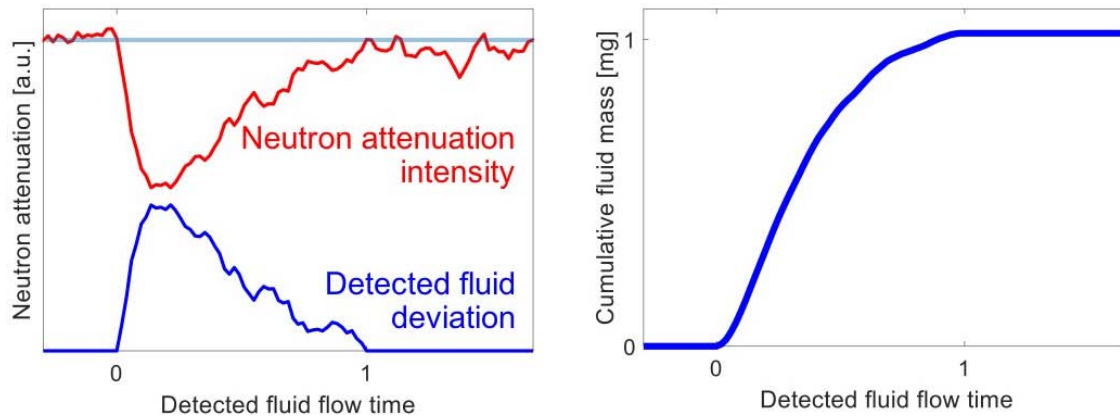


Figure I.26.5 - Attenuation within the area of interest, with a guideline defining the threshold of liquid detection, and conversion to the deviation from this threshold representing detected mass (left). Cumulative mass detected at the sac–nozzle interface (right). The detected fluid flow time is ~1 ms, compared with a commanded injection duration of 0.367 ms.

- Developed an experimental method for quantitatively measuring void fraction in a nozzle
- Analyzed HFIR data to extract fluid mass accumulation in real fuel injector nozzle during injection event

References

1. Verma, A., R. Babu, and M.K. Das. “Modelling of a Single Bubble Rising in a Liquid Column.” *Fluid Mechanics and Fluid Power - Contemporary Research*, edited by Saha A., Das D., Srivastava R., Panigrahi P., Muralidhar K. Springer, New Dehli, 2017.
2. Klostermann, J., K. Schaake, and R. Schwarze. “Numerical simulation of a single rising bubble by VOF with surface compression.” *International Journal for Numerical Methods in Fluids* 71: 960–982, 2013.

Key Fiscal Year 2017 Publications

1. Ryan, et al. “Modeling and Experimental Studies of Cavitation in Fuel Injectors.” Advanced Engine Combustion Meeting, Sandia, February 2017.

2. Ryan, Arai, Grace. "Predicting cavitation in fuel injectors using smoothed particle hydrodynamics." SIAM – Computational Science and Engineering Conference, Atlanta, GA, March 2017.
3. Do, Dele-Oni, Tang, Poe, Bird, Grace, Ryan, Holt. "Cavitation detection in a nozzle flow." *Acoust. Soc. Am.* 141, 3738 (2017).
4. Toops, Finney, Nafziger, Splitter, DeBusk, Pawlowski. "Neutron Imaging of Advanced Transportation Technologies." 2017 U.S. DOE Vehicle Technologies Office Annual Merit Review, ACS052, June 7, 2017.
5. Ryan, et al. "Cavitation Within Fuel Injectors: Development and Multiscale Validation of Euler-Lagrange based Computational Methods for Modeling Cavitation within Fuel Injectors." DOE Vehicle Technologies Office Annual Merit Review, ACS104, Washington, DC, June 7, 2017.

I.27 Turbulent Spray Atomization Model for Diesel Engine Simulations

Caroline L. Genzale, Principal Investigator

Georgia Institute of Technology
 GW Woodruff School of Mechanical Engineering
 771 Ferst Drive
 Atlanta, GA 30332
 E-mail: caroline.genzale@me.gatech.edu

Michael Weismiller, DOE Technology Manager

U.S. Department of Energy
 E-mail: Michael.Weismiller@ee.doe.gov

Start Date: January 18, 2016	End Date: January 17, 2019	
Total Project Cost: \$576,597	DOE share: \$492,807	Non-DOE share: \$83,790

Acknowledgments

Co-Author

Christopher Powell, Argonne National Laboratory

Project Introduction

This project aims to improve the predictive capabilities of spray submodels used in engine computational fluid dynamics (CFD) codes. The objective is to develop a new spray submodel that appropriately captures the role of injected liquid turbulence on diesel jet breakup, addressing shortcomings in the widespread adoption of submodels that treat atomization as a process primarily governed by aerodynamic inertial forces at the injected fluid interface. Our objective is motivated by (1) a significant body of literature that demonstrates the importance of internal injector flows on atomization, (2) experimental data indicating that liquid turbulence plays a fundamental role in spray atomization when gas inertial forces are low, and (3) a systematic lack of predictive capabilities for current aerodynamic-governed spray submodels. Even when global spray characteristics are well predicted, current spray submodels can vary widely in predictions of local spray morphology (e.g., local drop sizes). These inaccuracies suggest a fundamental mismatch of the modeled atomization physics and the actual physics governing the atomization process.

Modeling inaccuracies can largely be attributed to a lack of quantitative measurements to guide fundamental understanding and submodel development. Measurements of local spray morphology are needed within practical diesel sprays and especially under engine-relevant operating conditions. This project aims to fill this measurement gap. An innovative experimental approach is under development, which leverages the joint capabilities of Georgia Tech's high-pressure continuous-flow spray chamber and Argonne National Laboratory's near-nozzle X-ray diagnostics at the Advanced Photon Source. Joint measurements at the two institutions yield two-dimensional (2D) liquid volume fraction and drop size distribution within practical diesel sprays.

Objectives

- Demonstrate a new spray atomization submodel for engine CFD codes with improved prediction accuracy for local spray morphology and global spray characteristics over a wide range of engine operating conditions, including conditions relevant for advanced combustion engines
- Develop an improved understanding of the fundamental physics governing atomization in diesel fuel sprays, especially for advanced combustion regimes
- Develop and demonstrate a new 2D diagnostic for spatially resolved measurement of diesel spray morphology, including spatially resolved distributions of Sauter mean diameter (SMD) and liquid volume fraction, over a wide range of engine-relevant operating conditions

Approach

Two new droplet measurement diagnostics were developed to address the existing spray measurement gaps in real-world fuel injection sprays at engine-relevant operating conditions. These new measurements then provide the necessary physical insight to formulate and validate a new, more predictive, spray atomization submodel for engine CFD codes. First, a new X-ray scattering diagnostic under recent development at Argonne National Laboratory (ultra-small angle X-ray scattering [USAXS]), is applied to diesel sprays to quantify droplet sizes within optically thick regions near the injector nozzle and along the spray centerline. Second, a new 2D measurement technique was developed to quantify the spatially resolved atomization of diesel sprays. The new diagnostic, termed the scattering-absorption measurement ratio (SAMR), results from coupling two measurements performed at two institutions: (1) 2D measurements of optical thickness via liquid-scattering extinction performed at Georgia Tech, and (2) 2D measurements of liquid volume fraction via X-ray radiography performed at Argonne National Laboratory. A ratio of the two measurements yields the spatially resolved SMD. Diesel spray experiments were replicated at the two institutions using shared Engine Combustion Network (ECN) Spray D and Spray A injectors. Several existing spray atomization submodels were then benchmarked against this data to identify model formulation inaccuracies, leading to the formulation of a new modeling approach that incorporates fundamental understanding gleaned from the USAXS and SAMR measurement campaigns. The measurement campaign and new spray atomization modeling approach were formulated based on the hypothesis that liquid turbulence plays an important contributing role in spray breakup, especially under low ambient density conditions of relevance for advanced combustion engines.

Results

Key Accomplishments for Fiscal Year 2017

- Measured the near-nozzle centerline SMD distribution of ECN Spray D for the first time using a new X-ray scattering diagnostic (USAXS) developed at Argonne National Laboratory
- Implemented the SAMR diagnostic developed in this project to measure the spatially resolved 2D SMD distribution of ECN Spray D for the first time
- Demonstrated improvement of engine CFD spray SMD predictions with newly developed KH-Faeth breakup model, reducing error in predicted centerline SMD by up to 80% for ECN Spray A

Spatially Resolved Diesel Spray Morphology Measurements

Centerline measurements of SMD were accomplished for ECN Spray D ($d_{\text{nozz}} = 180 \mu\text{m}$) using the recently developed USAXS diagnostic at Argonne National Laboratory's Advanced Photon Source. These measurements represent the first droplet size measurements accomplished for ECN Spray D and the first accomplishment of such measurements in the near-nozzle and centerline regions of a diesel spray. In the measurements shown in Figure I.27.1, dodecane sprays ($\rho_{\text{liq}} = 750 \text{ kg/m}^3$) were injected at two different injection pressures ($P_{\text{inj}} = 50 \text{ MPa}$ and 150 MPa) into near-quiescent gas environments under non-vaporizing ambient temperature (300 K) environments with a range of ambient densities ($\rho_{\text{amb}} = 1.2\text{--}22.8 \text{ kg/m}^3$). The targeted ambient density range includes liquid-to-gas density ratios greater than 500, where aerodynamic forces are low and breakup is expected to be dominated by injected liquid turbulence characteristics [1]. The measurements demonstrate a diminishing effect of ambient density on the measured centerline SMD as ambient densities become low. By contrast, changes in injection pressure result in significant variation of the centerline SMD at low ambient densities. Combined, these results suggest that aerodynamic forces do not play a central role on spray breakup at low ambient densities, consistent with previous conclusions by Faeth and coworkers [2]. Rather a different instability mechanism that scales with injection pressure must be responsible for breakup, such as turbulent eddies within the injected liquid jet.

A further spatially resolved measurement of SMD was accomplished for ECN Spray D using the SAMR diagnostic newly developed in this project. An example of the first SAMR measurements accomplished in this project are shown in Figure I.27.2. At the condition shown in Figure I.27.2, dodecane sprays were injected from a single-orifice axially drilled nozzle, located at [0,0], into a near-quiescent environment at an ambient density of 2.4 kg/m^3 at an injection pressure of 50 MPa . This condition is representative of a

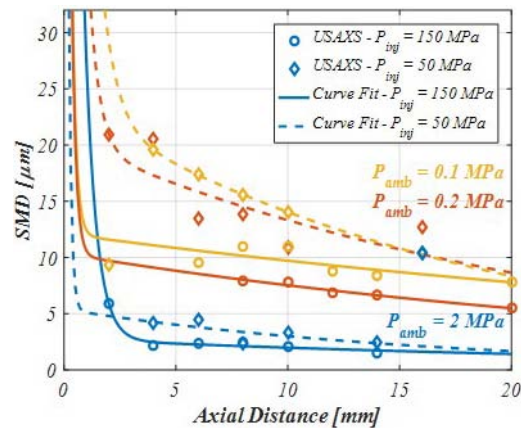


Figure I.27.1 - USAXS measurements of spray centerline SMD within the first 20 mm of Spray D over a wide range of ambient backpressures and injection pressures

very early injection that might be used for a homogeneous charge compression ignition engine or for post-injection diesel particulate filter regeneration. The SAMR technique is based on the joint analysis of light scattering measurements of optical thickness and X-ray absorption measurements of liquid volume fraction, and is limited to regions of the spray where both measurements are quantitatively viable. Light scattering measurements with visible wavelength illumination suffer from multiple scattering errors in regions of high optical thickness and are not quantitatively viable in the near-nozzle region or along the centerline of a diesel spray. Thus, as shown in Figure I.27.2, SAMR measurements are confined to the downstream peripheral regions of the spray. Nonetheless, the SAMR measurements demonstrate spatial resolution of the SMD field throughout significant portions of the spray, enabling improved visualization and understanding of the atomization process and useful data for model validation. The SAMR measurements also correlate well with the USAXS centerline SMD measurements, providing an initial cross-validation of the measurement techniques. The SAMR measurements indicate SMDs of 10–12 μm nearing the spray centerline position, while the USAXS measurements show SMDs around 12 μm along the spray centerline, starting from about 6 mm downstream of the injector nozzle. In future work, we plan to acquire USAXS measurements radially across the spray for direct cross-validation of SAMR results.

Spray Atomization Model Development

A new hybrid-physics spray breakup model, termed the KH-Faeth model, was formulated, implemented, and validated against USAXS measurements of centerline SMD for Spray A ($d_{\text{nozz}} = 90 \mu\text{m}$). Validation of the new modeling approach, shown in Figure I.27.3, demonstrates SMD prediction errors of less than 1 μm along most

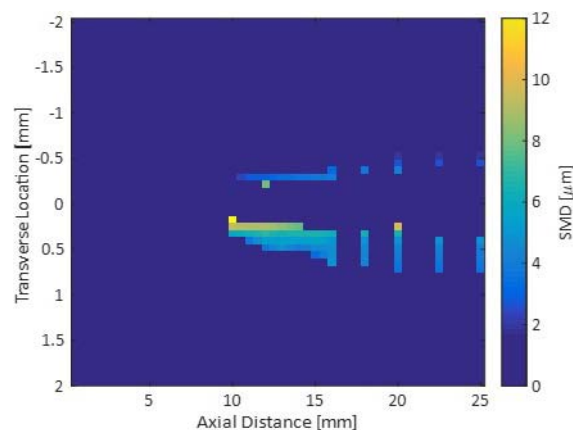


Figure I.27.2 - SAMR measurements of spatially resolved SMD in Spray D at $r_{\text{amb}} = 2.4 \text{ kg/m}^3$, $P_{\text{inj}} = 50 \text{ MPa}$

of the spray centerline (some USAXS measurement points that strongly fluctuate in downstream regions of the spray are believed to be non-physical measurement outliers). Figure I.27.3 also shows predictions from two other breakup models that are widely available and employed in today's engine CFD codes, including the Kelvin–Helmholtz Rayleigh–Taylor (KH-RT) model and the Kelvin–Helmholtz Aerodynamic Cavitation Turbulent (KH-ACT) model. All three models were verified to accurately predict global measurements of liquid penetration rate at these conditions. However, prediction errors of up to 4 μm and 5 μm in the centerline SMD are seen for the KH-ACT and KH-RT models, respectively, most prominently in the early upstream atomization process. Thus, the newly developed KH-Faeth model improves prediction accuracy of the local droplet field by up to 80% over current approaches at the conditions tested. The KH-Faeth model incorporates liquid turbulence as a competing mechanism of jet instability and breakup to the commonly employed Kelvin–Helmholtz aerodynamic instability. The new model adopts primary droplet sizing equations developed by Faeth and co-workers from holographic imaging experiments of turbulent primary breakup in round liquid jets [1]. Further validation of the KH-Faeth model is ongoing against the growing database of spatially resolved SMD measurements accomplished to date in this project.

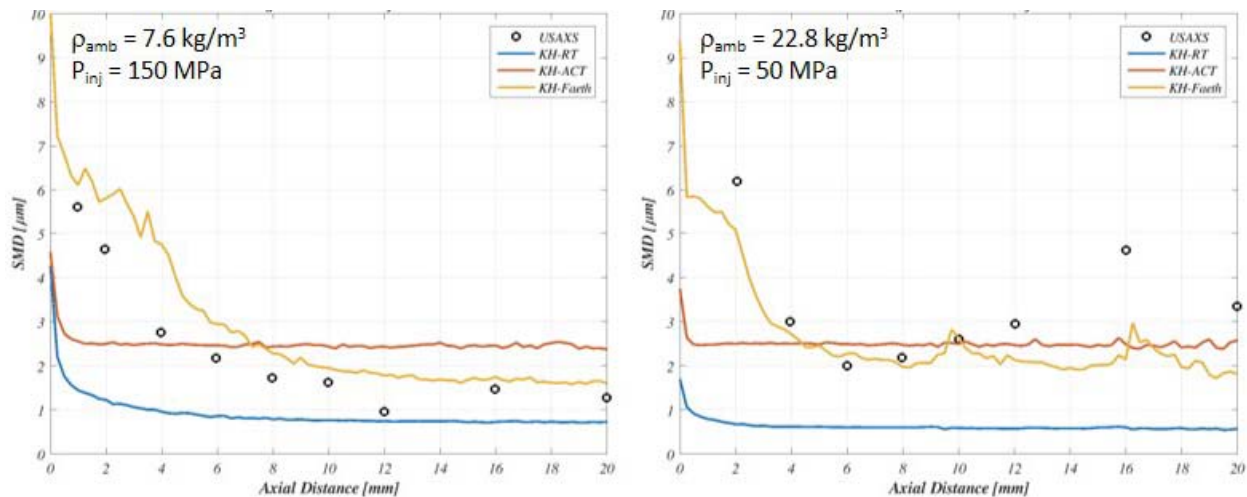


Figure I.27.3 - Validation of SMD predictions by new KH-Faeth primary atomization model against USAXS measurements. Also shown are predictions by two benchmark models in current use within engine CFD codes: KH-RT model and KH-ACT model. Validation conditions are for ECN Spray A ($d_{\text{nozz}} = 90 \mu\text{m}$).

Conclusions

- USAXS measurements of centerline SMD for ECN Spray D under low ambient density conditions correlate with literature investigations of turbulent round jets, demonstrating that atomization and breakup are influenced by the injected liquid velocity despite a lack of significant aerodynamic forces acting on the injected liquid interface. This implies that other physical mechanisms, such as turbulent eddies formed in the upstream injector flow, contribute to jet instability and breakup.
- Spatially resolved measurements of SMD were demonstrated in diesel sprays using the newly developed SAMR diagnostic. These 2D measurements provide significant opportunities for detailed validation of spray atomization submodels and enable improved visualization and understanding of the atomization development process in diesel sprays. SAMR measurements further demonstrated consistency with USAXS measurements, providing an initial cross-validation of the measurement technique.
- The newly developed KH-Faeth primary breakup model significantly improved prediction accuracy of centerline SMD for Spray A compared to current modeling approaches. Prediction errors were reduced by up to 80% over the widely adopted KH-RT model.

References

1. Wu, P.-K. and G.M. Faeth. "Aerodynamic Effects on Primary Breakup of Turbulent Liquids." *Atomization and Sprays* 3:265–289. 1993.

2. Wu, P.-K., L.-K. Tseng, and G.M. Faeth. "Primary Breakup in Gas/Liquid Mixing Layers for Turbulent Liquids." *Atomization and Sprays* 2:295–317. 1992.

Key Fiscal Year 2017 Publications

1. Magnotti, G.M. and C.L. Genzale. "Exploration of turbulent atomization mechanisms for diesel spray simulations." SAE Technical Paper 2017-01-0829, 2017.
2. Magnotti, G.M., K.E. Matusik, D.J. Duke, B.W. Knox, G.L. Martinez, C.F. Powell, A.L. Kastengren, and C.L. Genzale. "Modeling the influence of nozzle-generated turbulence on diesel sprays." 29th Annual Conference of the Institute for Liquid Atomization and Spraying Systems (ILASS)-Americas Conference, Atlanta, GA, May 2017.
3. Martinez, G.L., G.M. Magnotti, B.W. Knox, K.E. Matusik, D.J. Duke, A.L. Kastengren, C.F. Powell, and C.L. Genzale. "Quantification of sauter mean diameter in diesel sprays using scattering-absorption extinction measurements." 29th Annual Conference of the Institute for Liquid Atomization and Spraying Systems (ILASS)-Americas Conference, Atlanta, GA, May 2017.

II. Co-Optimization of Fuels and Engines

II.1 Alternative Fuels DISI Engine Research: Autoignition Metrics

Magnus Sjöberg, Principal Investigator

Sandia National Laboratories
MS9053, PO Box 969
Livermore, CA 94551-0969
E-mail: mgsjobe@sandia.gov

Kevin Stork, DOE Technology Manager

U.S. Department of Energy
E-mail: Kevin.Stork@ee.doe.gov

Start Date: October 1, 2016	End Date: September 30, 2017	
Total Project Cost: \$300,000	DOE share: \$300,000	Non-DOE share: \$0

Acknowledgments

Co-Author

David Vuilleumier, Sandia National Laboratories

The work was performed at the Combustion Research Facility, Sandia National Laboratories, Livermore, CA. Sandia National Laboratories is a multi-mission laboratory managed and operated by National Technology and Engineering Solutions of Sandia, LLC., a wholly owned subsidiary of Honeywell International, Inc., for the U.S. Department of Energy's National Nuclear Security Administration under contract DE-NA0003525.

Project Introduction

Improved engine efficiency is required to comply with future fuel economy standards. Alternative fuels have the potential to enable more efficient engines while addressing concerns about energy security. This project contributes to the science base needed by industry to develop highly efficient direct injection spark ignition (DISI) engines that also beneficially exploit the different properties of alternative fuels. Here, the emphasis is on quantifying autoignition behavior for a range of spark-ignited engine conditions, including directly injected boosted conditions. The efficiency of stoichiometrically operated spark ignition engines is often limited by fuel-oxidizer end-gas autoignition, which can result in engine knock. A fuel's knock resistance is assessed empirically by the Research Octane Number (RON) and Motor Octane Number (MON) tests. By clarifying how these two tests relate to the autoignition behavior of conventional and alternative fuel formulations, fuel design guidelines for enhanced engine efficiency can be developed.

Objectives

- Provide the science base needed by industry to understand how emerging alternative fuels impact autoignition in highly efficient DISI light-duty engines being developed by industry
- Develop and apply knock testing methodologies that are relevant for both transient and steady-state engine operation
- Measure knock limits for a range of fuels with varying octane rating and compositions
- Assess the applicability of the Octane Index framework to rank order fuels, including an assessment of measurement uncertainty

Approach

The Alternative Fuels DISI Engine Lab at Sandia houses an engine that is capable of both performance testing and in-cylinder optical diagnostics. Here, research is focused on performance testing with an all-metal fully lubricated engine configuration. The lab features in-house developed control and data acquisition hardware and software that are capable of complex engine operation, including load transients.

Results

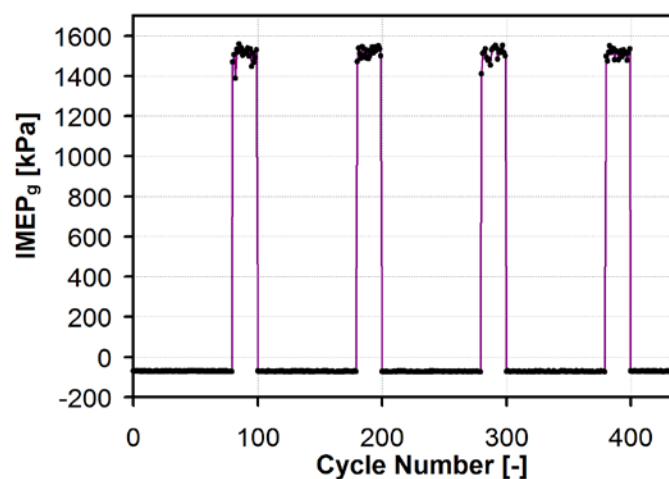
Key Accomplishments for Fiscal Year 2017

- Developed methodology to measure knock limits under conditions that mimic vehicle accelerations
- Measured stoichiometric knock limits for nine fuels, both steady-state and transient
- Tested applicability of Octane Index framework for fuels of alternate composition and discovered that two fuels blended with butanol isomers performed better than expected based on RON and MON
- Developed and used a Monte-Carlo-based uncertainty assessment of the Octane Index framework; results indicate a high likelihood that fuels' deviations from Octane Index predictions are real and not caused by experimental uncertainty

In the following sections, detailed examples of Fiscal Year 2017 accomplishments are presented.

Knock-Limited Stoichiometric Operation

The knock limits of stoichiometric charge DISI engines have a significant effect on engine efficiency. Fuels exhibit varying degrees of knock resistance depending on their composition and this is quantified by RON and MON ratings. However, while knock-limited testing is nearly exclusively performed under steady-state conditions, real engines experience transient conditions, especially those found in light-duty vehicles. This mismatch could affect the real-world performance of fuels due to the difference in conditions between transient high-load operation and steady-state high load operation, with the key difference being the higher thermal state of the engine under steady-state conditions. To investigate the differences between transient and steady-state operation, a transient test regime was developed and experiments were performed over a range of steady-state and transient conditions. The particular transient test regime implemented here was chosen to magnify differences between steady-state and transient operation by producing a marked shift in engine thermal state. This is accomplished by firing 20 cycles under knock-limited conditions, followed by 80 cycles of motoring, in which no fuel is injected and no combustion occurs, as illustrated in Figure II.1.1. This 20% duty cycle of the engine results in lower in-cylinder wall temperatures and higher volumetric efficiency, which reflect the lower



IMEP_g – gross indicated mean effective pressure

Figure II.1.1 - Illustration of repeating Fire20-Skip80 sequence used to mimic the thermal state that an engine may experience during vehicle acceleration. Figure by Magnus Sjöberg.

thermal state of the engine [1]. A secondary benefit of this transient test regime is the ability to test higher load conditions than are possible to test under steady-state conditions, due to the reduced knocking tendency at lower thermal conditions.

Measured knock-limited combustion phasing (KL-CA50) from both steady-state and transient testing at a fixed engine speed (1,400 rpm) and intake temperature (30°C) are presented in Figure II.1.2. KL-CA50 indicates the combustion phasing which causes a predetermined knocking threshold to be met; lower KL-CA50 values indicate that a fuel is less knock limited. Figure II.1.2 presents data taken with nine fuels, which have their properties listed in Table II.1.1. Of the fuels, eight fuels share a RON rating of 98 and seven of these fuels share octane sensitivity (S) ratings, the difference of RON and MON ratings, of approximately 10. The ninth fuel included in this test matrix is an E10 (10% ethanol, 90% gasoline) blend mimicking regular grade pump gasoline.

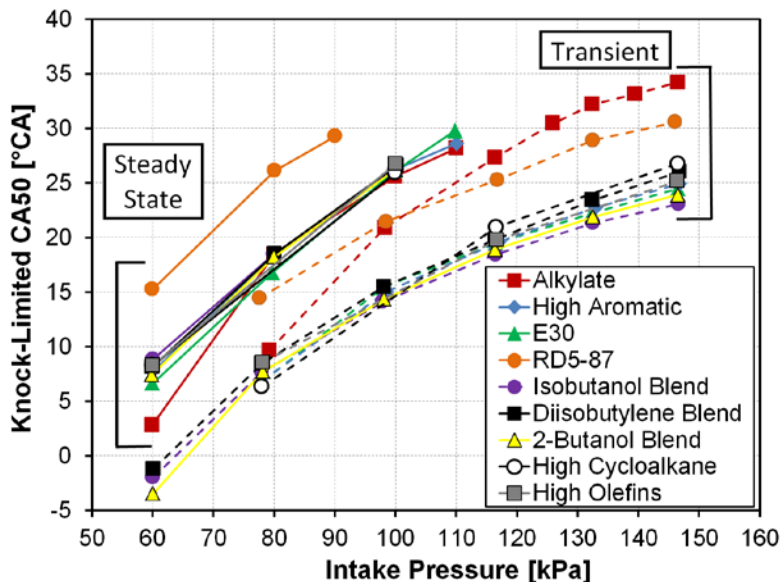


Figure II.1.2 - Knock-limited combustion phasing as a function of intake pressure for both steady-state and transient operation with 30°C intake temperature. Transient operation is shown in dashed lines. Figure by David Vuilleumier, Sandia National Laboratories (SNL).

Table II.1.1 - Fuel Properties and Composition for the Nine Fuels Used in This Study

	Iso-butanol blend	2-butanol blend	Diisobutylene blend	Alkylate	E30	High Aromatic	High Olefins	High Cycloalkanes	RD5-87
RON	98.1	98.2	98.3	98.0	97.9	98.1	98.3	97.8	92.1
MON	88.0	89.1	88.5	96.7	87.1	87.6	87.9	86.9	84.8
AKI (R+M)/2	93.1	93.7	93.4	97.3	92.5	92.8	93.1	92.3	88.5
Octane Sensitivity	10.1	9.1	9.8	1.3	10.8	10.5	10.4	11.0	7.3
Aromatics (Vol. %)	19.0	17.9	20.1	0.7	13.8	39.8	13.4	33.2	21.5
Olefins (Vol. %)	3.8	3.6	23.6	0.1	5.6	4.5	26.5	1.6	5.7
Alkanes (Vol. %)	53.1	50.1	56.3	98.8	40.5	46.2	56.4	40.6	49.0
Cycloalkanes (Vol. %)	0	0	0	0	7.0	8.0	2.9	24.2	11.4
Oxygenates (Vol. %)	24.1	28.4	0	0	30.4	0	0	0	10.2
Heat of Vaporization (kJ/kg)	412*	415*	337*	308*	532*	361*	333*	373*	-

*Heat of vaporization data provided by Fioroni et al. [2]

Figure II.1.2 shows that under steady-state, naturally aspirated conditions, the RON = 98 fuels perform nearly identically to one another. However, as conditions shift to throttled operation, or to transient conditions,

divergence in fuel performance is observed. Of particular interest is the spread in behavior of the RON = 98, S = 10 fuels at the highest tested intake pressure, which raises questions about the use of RON and MON to describe fuel knock resistance. Of further interest is the crossover in relative knock performance between the alkylate fuel (RON = 98, S = 1) and the RD5-87 (RON = 92, S = 7), which indicates that knock resistance must be described in relation to the conditions encountered by the fuel.

While Figure II.1.2 shows the knock limits of the nine fuels, Figure II.1.3 plots the corresponding indicated efficiencies. The measured efficiencies are a function of many factors, including throttling losses, thermodynamics, average charge temperature, and combustion efficiency. However, under knock-limited conditions, which can force the use of non-optimal combustion phasing, the knock resistance of a fuel has an outsize effect on its efficiency. This is reflected in Figure II.1.3, which shows that under steady-state conditions, where the RON = 98 fuels behaved similarly to one another, similar efficiencies are observed. Conversely, with transient operation, where differences in knock-resistance were noted, indicated efficiency also varies among the fuels with the most knock resistant fuels having relative efficiency gains of approximately 10% over the regular grade gasoline.

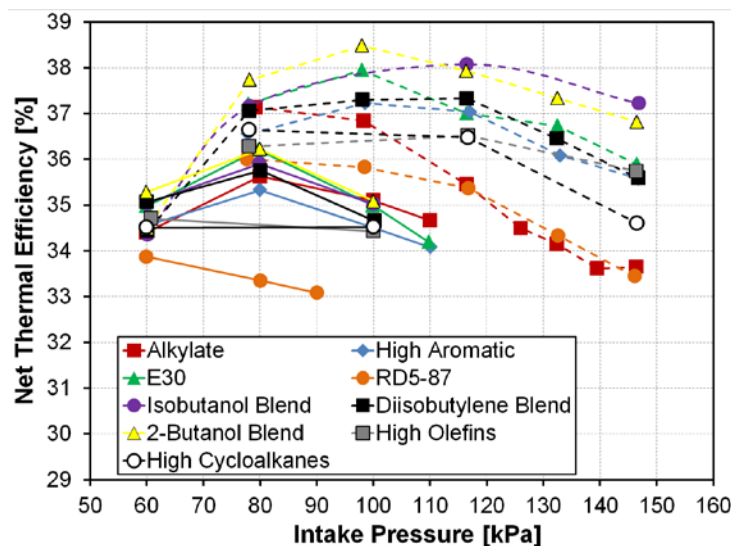


Figure II.1.3 - Indicated thermal efficiency as a function of intake pressure for all nine fuels for both steady-state and transient operation. Transient operation is shown in dashed lines. Figure by David Vuilleumier, SNL.

Octane Index Applicability

As previously noted, the crossover in performance of the alkylate and RD5-87 as intake pressure changes, shown in Figure II.1.2, indicates that a single rating of a fuel is insufficient to describe its behavior. The leading methodology for describing fuel anti-knock quality with regards to conditions is the Octane Index [3], which is presented in Equation 1. This approach considers both the RON and MON rating of a fuel, as well as a weighting factor, K , which is dependent on the conditions the fuel is subject to. It may be observed that when $K = 1$, the Octane Index value is the same as the MON rating, while if $K = 0$, the Octane Index value is equal to the RON rating.

$$OI = (1 - K) \cdot RON + K \cdot MON = RON - K \cdot S \quad (1)$$

The K term in the Octane Index equation is an empirical term, although it is generally related to the conditions experienced by the end gas with higher temperatures and lower pressures raising the K value and vice versa. Nonetheless, K must be calculated by a regression (typically linear) between a parameter which indicates the knock resistance of a fuel (such as the knock-limited combustion phasing, knock-limited spark advance, knock-limited vehicle acceleration, etc.) and the Octane Index value of a fuel. However, each of the parameters which feed into the regression has some uncertainty associated with it, such as a fuel's RON and MON ratings, or the knock metric. This uncertainty results in two questions: (1) how certain is the K value which is determined

and (2) when discrepancies between the Octane Index and observed performance occur, is this a failing of the Octane Index methodology or is it caused by experimental uncertainty?

To answer these questions, the experimental data presented in the previous section were combined with Monte Carlo simulations to quantify the uncertainty associated with the Octane Index. The experimental results were used to perform a linear regression at each operating condition to determine the most appropriate K value. The Monte Carlo simulations piggybacked on the linear regression methodology by rerunning the linear regression at each operating condition for 100,000 permutations of the RON, MON, and KL-CA50 inputs, which are reflective of the uncertainty in each of these terms.

An example of the linear regression between Octane Index and KL-CA50 is shown in Figure II.1.4. This figure uses experimental data from the highest tested intake pressure of 146 kPa and plots the best-fit relationship between Octane Index and KL-CA50, which stems from $K = -2.1$, and results in an R^2 value of 0.84. This figure illustrates that while the Octane Index generally describes experimental results, some discrepancies exist and these may be due to the effects of fuel composition. Figure II.1.5 presents the distribution of R^2 values from the Monte Carlo simulations which are associated with the results shown in Figure II.1.4. Figure II.1.5 indicates that when the uncertainty of the measured parameters are considered, the linear regressions between KL-CA50 and Octane Index produce a range of R^2 values from approximately 0.7 to 0.9. Figure II.1.5 also

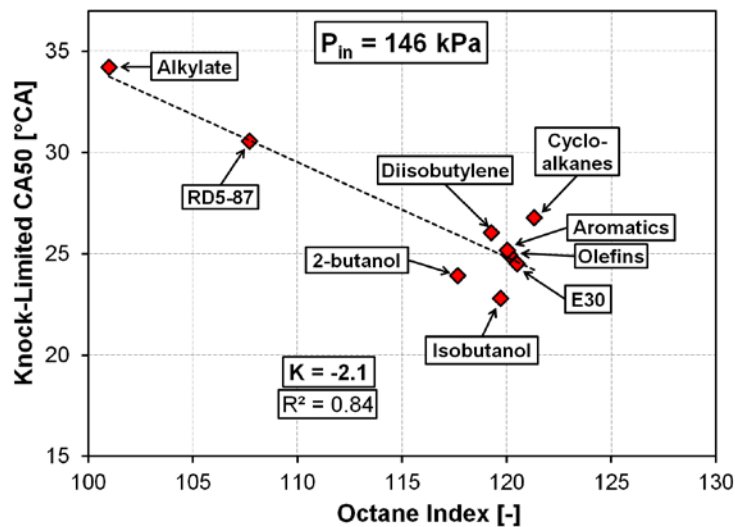


Figure II.1.4 - Best-fit linear regression between octane index and knock-limited combustion phasing for an intake pressure of 146 kPa under transient operation. Figure by David Vuilleumier, SNL.

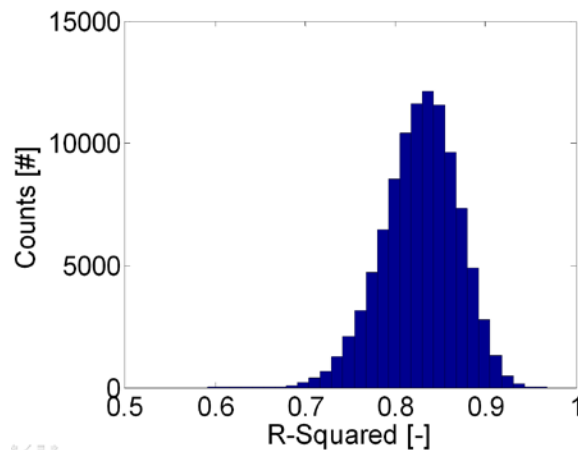


Figure II.1.5 - Distribution of R^2 values at the 146 kPa intake pressure, 30°C intake temperature, transient operating mode condition. Figure by David Vuilleumier, SNL.

indicates that it is extremely unlikely that the Octane Index would provide a perfect fit for the measured knock behavior, even when uncertainty is considered.

Figure II.1.6 summarizes the K-value uncertainty quantification results from the range of tested operating conditions. It may be seen from this figure how different experimental conditions influence K. Broadly, higher intake pressure conditions reduce K as expected. Further, lower initial temperatures, such as those encountered in the transient operation, further reduce K. Figure II.1.6 shows that K becomes significantly negative for transient, boosted operating conditions. This has a major implication for fuel formulation. As turbocharged engines gain market share, they become knock-limited at conditions which are represented by negative values of K. At these conditions, fuels with a large difference between RON and MON ratings perform better than fuels which have a higher MON rating. This is not reflected in the way fuels are sold in the United States, as fuels are marketed by the average of RON and MON, which penalizes fuels with lower MON ratings for a given RON rating.

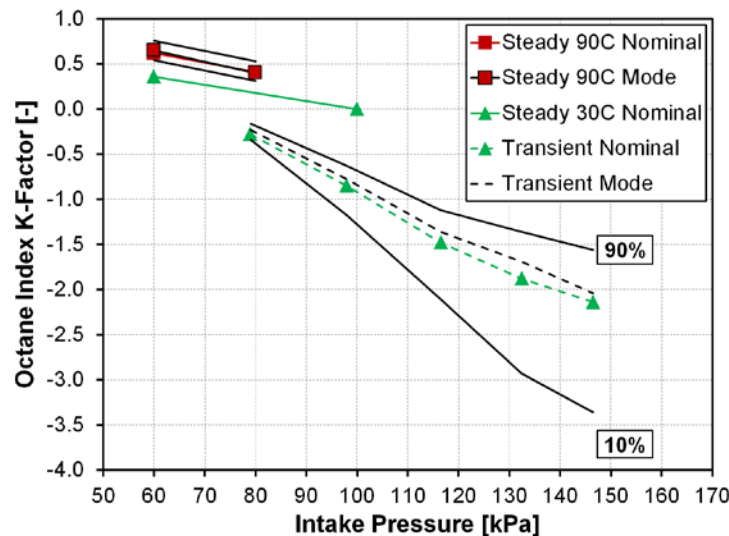


Figure II.1.6 - K-values as a function of intake pressure and operation type accompanied by the 10th and 90th percentiles of the K distribution, as well as the mode of the distribution. Figure by David Vuilleumier, SNL.

Finally, Figure II.1.6 also presents the 80% certainty range in the K-value. It can be seen that when the K-value ranges between 0 and 1, the uncertainty range spans approximately 0.2 units of K. However, as the K-value becomes negative and therefore relies on the extrapolation of RON and MON results, the uncertainty in K increases dramatically, such that at the most extreme condition tested, the 80% certainty range spans over two units of K. This presents a problem when determining the relative merits of two fuels for a downsized-boosted engine; depending on the magnitude of K, a higher-RON lower-S fuel may perform better, or a lower-RON higher-S fuel may perform better.

Conclusions

This project used both existing and newly developed methodologies to assess the knock resistance of nine fuels over a wide range of engine operating conditions. Beyond the experimental data provided here, uncertainty quantification was carried out to assess the performance of a leading fuel classification scheme, the Octane Index, in describing the observed behavior. The following findings are noted:

- A transient test methodology was developed for autoignition studies which simulates a brief but sometimes aggressive load transient.
- Transient operation allows the investigation of high-load, boosted, beyond RON conditions while using a relatively high compression ratio of 12.
- Differences in fuel knock resistance are observed under high-load conditions which uncertainty analysis confirmed are not explained by the RON and MON ratings of the fuels.

- In the Octane Index framework, extrapolation of RON and MON results leads to high uncertainty in computed K values, undermining the ability of the Octane Index to rank order fuel performance at these extreme conditions.
- The two fuels blended with iso-butanol and 2-butanol overperform their RON and MON ratings at boosted engine-operating conditions.

References

1. Vuilleumier, D. and M. Sjöberg. “The Use of Transient Operation to Evaluate Fuel Effects on Knock Limits Well Beyond RON Conditions in Spark-Ignition Engines.” SAE paper 2017-01-2234.
2. Kalghatgi, G. “Fuel Anti-Knock Quality - Part I. Engine Studies.” SAE Technical Paper 2001-01-3584, 2001, doi: 10.4271/2001-01-3584.
3. Fioroni, G., L. Fouts, E. Christensen, R. McCormick, NREL, Private Communication, February 16, 2017.

Key Fiscal Year 2017 Publications

1. Vuilleumier, D. and M. Sjöberg. “Significance of RON, MON, and LTHR for Knock Limits of Compositionally Dissimilar Gasoline Fuels in a DISI Engine.” *SAE Int. J. Engines* 10(3), 2017.
2. Vuilleumier, D. and M. Sjöberg. “The Use of Transient Operation to Evaluate Fuel Effects on Knock Limits Well Beyond RON Conditions in Spark-Ignition Engines.” SAE paper 2017-01-2234.
3. Sjöberg, M., and Xu He. “Combined Effects of Intake Flow and Spark-Plug Location on Flame Development, Combustion Stability and End-gas Autoignition for Lean SI Engine Operation using E30 Fuel.” ENCOM 2017.

II.2 Studies of Research Octane Number (RON) and Heat of Vaporization (HoV)

Christopher P. Kolodziej, Principal Investigator

Argonne National Laboratory
9700 S Cass Avenue
Argonne, IL 0439
E-mail: ckolodziej@anl.gov

Kevin Stork, DOE Technology Manager

U.S. Department of Energy
E-mail: Kevin.Stork@ee.doe.gov

Start Date: October 1, 2016	End Date: September 30, 2017	
Total Project Cost: \$300,000	DOE share: \$300,000	Non-DOE share: \$0

Acknowledgments

Co-Authors

Alexander Hoth, Toby Rockstroh, Thomas Wallner; Argonne National Laboratory

Project Introduction

Research Octane Number (RON) is the most common and recognized measurement of gasoline knock propensity worldwide. Increased fuel RON allows spark ignition gasoline engines to operate at higher indicated thermal efficiency by increased compression ratio and reduced combustion phasing retard due to knock, thus reducing petroleum consumption. Ethanol is one of the high RON fuel components blended into gasoline, but it has a heat of vaporization (HoV) (charge cooling potential) nearly three times that of other gasoline components. This project focuses on the effects of blending high HoV fuel components on the Cooperative Fuel Research (CFR) engine operation during RON measurement.

In 2016, this project evaluated the effects of ethanol intake charge cooling by heating the intake air temperature (IAT) upstream of the CFR carburetor until the temperature downstream of the carburetor matched that of the standard primary reference fuel (PRF) used for rating the octane number, consequently negating the HoV cooling effect. This was similar to the method performed by Foong et al. [1] except the base PRF blends were reformulated for each ethanol level tested in order to maintain a constant RON 98 rating. After compensating for the HoV cooling effect, the equivalent reduction in RON rating for each ethanol blend was assessed. Although the IAT downstream of the carburetor was compensated to be that of PRF 98, it was observed that additional artifacts were introduced from the increased temperature upstream of the carburetor by reduced air and fuel mass flow to the engine and the cylinder pressure.

In 2017, the CFR engine's intake and carburation system was modified to operate on a compressed air supply instead of naturally aspirated. This allowed for controlling the air and fuel mass flows and cylinder pressure losses when heating the intake air upstream of the carburetor to compensate for the effects of increased fuel HoV. As a result, the effects of HoV charge cooling on the RON measurement method could be tested.

Objectives

- Formulate PRF–ethanol blends with constant RON 98 from 0 vol% to 50 vol% ethanol to study the effects of ethanol and HoV on the RON test at constant compression ratio
- Measure the effects of ethanol blending on standard RON engine operating conditions and combustion characteristics
- Estimate the vapor fraction of each PRF–ethanol blend in the intake port for a range of IATs upstream of the carburetor to improve cylinder temperature calculations

- Determine the HoV contribution to the RON rating of PRF–ethanol blends from 0 vol% to 50 vol% ethanol by both temperature and cylinder pressure compensation

Approach

A standard CFR F1/F2 octane rating engine was outfitted with modern engine combustion research instrumentation: thermocouple temperature measurements, high speed pressure transducers, humidity probe in the intake system, digitized knockmeter measurement, wide-range lambda sensor, Coriolis meter fuel rate, emissions, etc. To compensate for reduced cylinder pressure when heating the intake air, a compressed air system was installed and baselined on the engine.

In order to test the effect of HoV on the RON test, PRF–ethanol blends were formulated from 0 vol% to 50 vol% so that they maintained RON 98, which was chosen to be representative of the octane level of premium gasoline. As the HoV of the fuel increased with ethanol content, the mixture air temperature (downstream of the carburetor) was maintained constant to that of PRF 98 by increasing the temperature of the standard RON intake air heater (upstream of the carburetor). This gave a temperature compensated RON reduction for each PRF–ethanol blend. However, it was observed that several key engine operating conditions were affected by the higher IAT, such as reduced fuel and air mass flows, indicated mean effective pressure (IMEP), and cylinder pressure at spark timing. To compensate for these effects, the intake air pressure was increased in small increments and the temperature and pressure compensated RON reduction for each PRF–ethanol blend was quantified.

Results

Within the Fiscal Year 2017 the following major accomplishments were achieved.

- Extension of applicable fuel matrix with RON 98 in steps of 5 vol% of ethanol (Figure II.2.1)
- Calculation of vapor fraction at the intake port, including anticipated uncertainty
- Investigation of the minimum required temperature for full vaporization of PRF–ethanol fuel blends (Figure II.2.2)
- Development of a compressed air intake manifold configuration for the standard CFR RON test setup
- Evaluation of the change in RON (Δ RON) under increased IAT and pressure compensated conditions (Figures II.2.4 and II.2.5)

Compared to studies by Foong et al. [1], who used splash blends of ethanol in the same PRF, obtaining differing RON, this investigation formulated constant RON 98 fuel blends using match blends of varied PRF base fuels and ethanol. In order to achieve more detailed results over the previous year, the non-linear blending

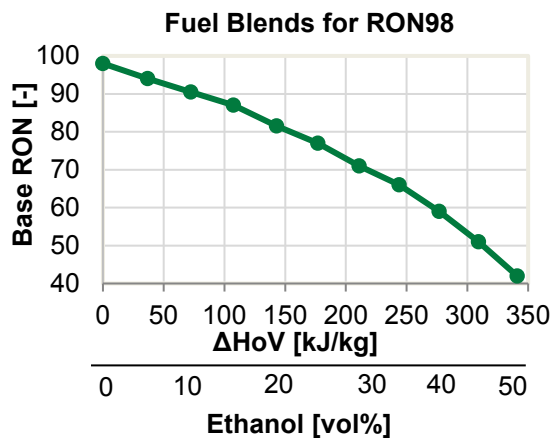


Figure II.2.1 - The effect of ethanol blending on the base fuel RON requirement for PRFs to get a blended RON 98

relationship of ethanol into PRF was measured in steps of 5 vol% up to 50 vol% ethanol (Figure II.2.1). By keeping the standard IAT heater, a level beyond 50 vol% of ethanol was not accessible when compensating for mixture temperature. Previous data showed an increase in HoV (using a linear blending rule) with ethanol causing a decrease in mixture temperature [2]. In addition, fuel properties like lower heat value, stoichiometric air fuel ratio, and peak knock lambda were also affected by increased ethanol, and therefore operating conditions including air-, fuel- and energy-flows were affected (Table II.2.1). In Table II.2.1, fuel power to the engine was calculated using measurements of fuel mass flow at standard conditions and with increased IAT to match the mixture air temperature (MAT) to that of PRF 98 at standard conditions.

Table II.2.1 - Fuel Properties with RON 98 and Operating Conditions

Fuel blend	HoV [kJ/kg]	LST [-]	LHV [MJ/kg]	Peak Knock Lambda [-]	Fuel Power (Standard) [kW]	Fuel Power (MAT-match) [kW]
PRF98	308	15.1	44.32	0.88	119.7	-
PRF90.5-E10	381	14.4	42.59	0.90	120.2	117.2
PRF81.5-E20	451	13.8	40.91	0.92	117.1	114.1
PRF71-E30	519	13.1	39.28	0.92	117.4	112.8
PRF59-E40	585	12.5	37.68	0.94	115.6	111.5
PRF42-E50	649	11.9	36.12	0.95	114.6	109.2

LHV – lower heating value; LST – stoichiometric air–fuel ratio

Under standard RON conditions, based on ASTM 2699 (ASTM International 2015), high HoV fuels result in a considerable reduction in mixture temperatures downstream of the carburetor, effecting the quality of vaporization. The impact of droplets entering the intake port is yet not completely understood but knowledge about the vapor fractions entering the cylinder are desired for estimating cylinder temperature using a one-dimensional GT-POWER three-point analysis model [2]. Under standard RON conditions with a constant IAT and increasing fuel HoV, the temperature drop across the carburetor (ΔT_{carb}) shows a concave response (Figure II.2.2). In contrast, when increasing IAT to match MAT the temperature drop remains linear and the difference between the two lines is mainly affected by fuel saturation. The effects of varying heat transfer to the surfaces of the intake system due to higher temperatures were found to have a minor impact.

The next steps in calculating the vapor fraction included a calculation of the ratio of change of enthalpy across carburetor (based on thermocouples and mass flows) and the change of the HoV of the fuel blends with variations in IAT. Fully vaporized fuel mixtures gave a linear response in the enthalpy ratio with decreasing IAT for a given fuel blend until saturation occurred. The vapor fraction was estimated by dividing the actual enthalpy ratio by the enthalpy ratio expected if the fuel had continued to follow the linear response observed at higher intake temperatures when the fuel was fully evaporated. Consequentially, the minimum required

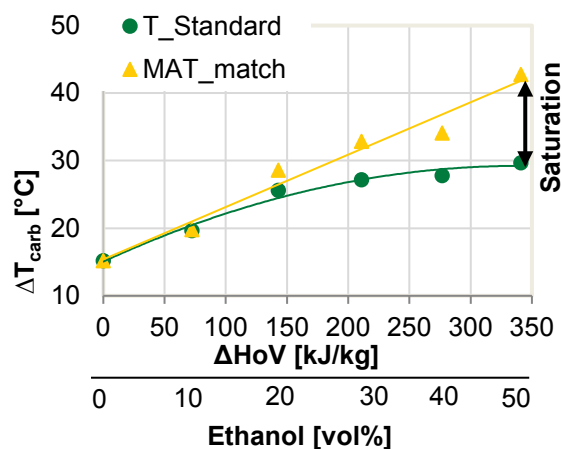


Figure II.2.2 - Temperature drop across the carburetor with increasing level of ethanol, causing super-saturation

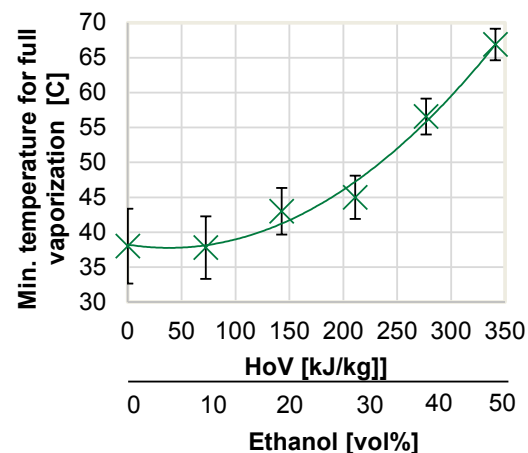


Figure II.2.3 - Minimum temperature (°C) for full vaporization with increasing level of ethanol and calculated uncertainty

temperature for full fuel vaporization was found to be increasing with higher levels of HoV (Figure II.2.3). In addition, uncertainties of temperatures for full vaporization were calculated based on the data available.

Previous studies have shown a reduced RON rating when the cooling effect of increased HoV fuel components was compensated by increasing IAT to match MAT [2]. Due to changes in air density, fuel mass flow, air mass flow, cylinder pressure, and engine IMEP were reduced from standard RON conditions of a given increased HoV fuel. Using a compressed intake air supply, cylinder pressure could be recovered and the HoV contribution to the RON rating of a given PRF–ethanol blend could be evaluated in three steps.

- Standard RON conditions at constant naturally aspirated pressure level [3]
- Matched MAT at constant naturally aspirated pressure
- Matched MAT and increased intake manifold pressure to recover cylinder pressure at spark timing (P_{ST})

Figure II.2.4 displays the ΔRON between standard RON and the equivalent RON when compensating for just temperature (Case 2) or temperature and pressure (Case 3). From the standard conditions (Case 1) to matching MAT (Case 2), ΔRON increased, but P_{ST} decreased. Under Case 3, ΔRON showed a further increase when P_{ST} was recovered for a given PRF–ethanol blend back to its value under standard RON conditions (Case 1). Generally, the higher the HoV of the PRF–ethanol blend, the higher the ΔRON and necessary temperature and pressure recovery.

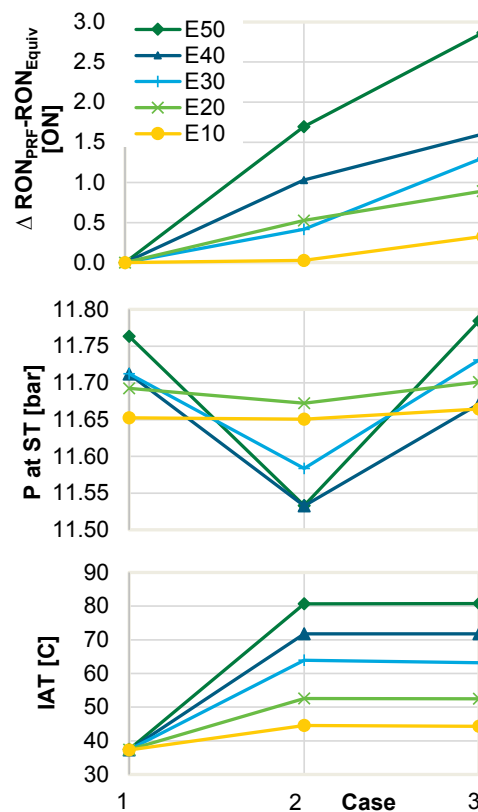


Figure II.2.4 - Change in ΔRON for PRF–ethanol blends between standard RON operating conditions (Case 1), compensated mixture temperature (Case 2), and pressure at spark timing (P_{ST}) (Case 3)

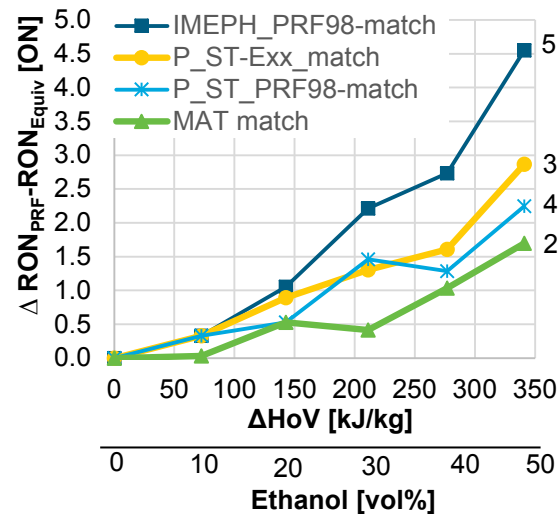


Figure II.2.5 - Change in Δ RON for PRF-ethanol blends between standard RON operating conditions (Case 1) and each, compensated mixture temperature (Case 2), pressure at spark timing for that PRF-ethanol blend (Case 3), pressure at spark timing of PRF 98 (Case 4), and IMEP compensated for PRF 98 (Case 5)

It was noticed that there were different potential boost levels in order to match IMEP, pressure at spark timing, or air flow of either PRF 98 or the respective PRF-ethanol fuel blend under standard conditions (Figure II.2.5). In order to recover similar cylinder conditions, pressure at spark timing was chosen to be the most suitable.

Conclusions

1. Constant RON 98 blending found the expected non-linear relationship between base RON and ethanol level.
2. The temperature drop across the carburetor helped identify the vapor fraction during standard RON testing.
3. Calculations of vapor fraction found the minimum temperature required for full vaporization.
4. In temperature and pressure compensated conditions, Δ RON can increase by as much as 2 RON when testing PRF-ethanol blends up to 50 vol% ethanol.

References

1. Foong, T.M., K.J. Morganti, M.J. Brear, G. da Silva, et al. "The Octane Number of Ethanol Blended with Gasoline and its Surrogates." *Fuel* 115:727-739, 2010.
2. Kolodziej, C.P., T. Wallner, A. Ickes, et al. "Studies of Research Octane Number (RON) and Heat of Vaporization (HoV)." FY 2016 Annual Progress Report / Fuel & Lubricant Technologies, 2016.
3. ASTM International. "Standard Test Method for Research Octane Number of Spark-Ignition Engine Fuel." ASTM D2699-15a, 2015.

Key Fiscal Year 2017 Publications

1. Kolodziej, C., and T. Wallner. "Combustion characteristics of various fuels during research octane number testing on an instrumented CFR F1/F2 engine." *Combustion Engines*. 2017, 171(4), 164-169. DOI: 10.19206/CE-2017-427.

II.3 Improving Vehicle Fuel Economy Through Increasing Fuel Octane Ratings

Scott Sluder, Principal Investigator

Oak Ridge National Laboratory
2360 Cherahala Boulevard
Knoxville, TN 37932
E-mail: sluders@ornl.gov

Kevin Stork, DOE Technology Manager

U.S. Department of Energy
E-mail: Kevin.Stork@ee.doe.gov

Start Date: October 1, 2016

End Date: September 30, 2019

Total Project Cost: \$1,450,000

DOE share: \$1,450,000

Non-DOE share: \$0

Project Introduction

Engine downsizing is an important facet of increasing vehicle fuel efficiency while maintaining performance at a level that customers demand. As the original equipment manufacturers have begun to increase the power density of smaller displacement engines, the onset of knock has emerged as an important challenge that currently limits the degree to which engine displacement (and fuel consumption) can be reduced in a practical automobile. A recent study by researchers from AVL, BP, John Deere, Ford Motor Company, and ICM has shown that increasing the fuel octane rating can allow substantial engine efficiency improvements at the knock limit [1]. Improvements were shown to be enabled through both a chemical octane effect as well as a charge-cooling effect derived from the heat of vaporization of the fuel. The charge cooling effect was shown to be approximately the same order of magnitude improvement as the octane increase effect. Other studies have begun to show similar results.

The U.S. certification driving cycles on which fuel economy ratings are based typically result in engines operating well away from their peak efficiency values. Engine downsizing results in engines operating at higher loads more often during normal driving, thus reducing throttling and other losses and moving towards higher efficiency areas of their operating maps. However, in order to satisfy consumer demands, these engines must be able to deliver performance similar to non-downsized engines. These performance demands can cause downsized engines to operate in knock-limited regimes more frequently. In the past, some vehicles have utilized “premium” fuel for its potential to improve performance, but these engines were not typically downsized to use the added anti-knock capability of the premium-grade fuel to increase efficiency.

When engines reach the knock limit, one common technique that is used to protect the engine from damage is to retard the ignition timing. Retarding the timing has the effect of moving the onset of combustion to a cooler, lower pressure point, thus removing the knocking condition. However, this technique also results in a loss in fuel efficiency. Thus, when an engine reaches the knock limit, fuel efficiency is reduced in favor of engine durability. Increasing the knock limit through changes in fuel formulation, such as increasing the octane rating, offers the potential to improve fuel efficiency under these conditions and enable further engine downsizing. This project will study how differing high-octane fuel formulations can be used to enable increased engine efficiency and to estimate the magnitude of the effect that increased engine efficiency has on vehicle fuel economy.

Objectives

- Quantify combustion phasing and engine efficiency differences for ethanol and non-ethanol biofuels at a compression ratio of 11.4 (CR11.4). This objective supports both the U.S. DRIVE Fuels Working Group (FWG) and Co-optimization of Fuels and Engines Program.
- Support U.S. DRIVE FWG studies by estimating vehicle energy use and volumetric fuel economy results for the fuels in the FWG expanded fuels matrix and compare with the AVFL-20 baseline case.

Approach

Oak Ridge National Laboratory (ORNL) will investigate the potential fuel economy impacts of the use of higher octane gasoline blends. ORNL is partnering with Ford Motor Company to make use of its EcoBoost 1.6 L engine to examine the potential fuel efficiency benefits of octane improvement in a downsized engine application. Ford has provided ORNL with the engine and engineering support for the 1.6 L engine. Vehicle modeling using Autonomie will be used to estimate vehicle-level impacts from data gathered during engine-based studies. Hybridization presents opportunities to improve market penetration of engines designed to use high-octane fuels. These opportunities are possible through the use of hybridization strategies that can mitigate the performance penalties that occur when an engine designed for use with high-octane fuels is operated using a fuel with lower octane rating. These strategies will be investigated alongside conventional vehicles using vehicle models to estimate the potential fuel economy benefits that are possible. In the studies for the project, data will be collected using fuel formulations that explore the co-optimization program central fuel hypothesis, that fuel performance and engine efficiency derive from the measured combustion properties of the fuel. The project will also study fuels blended using the Tier 3 blendstock candidates identified by the program and provide data in support of the Tier 3 evaluations by other teams.

Results

In Fiscal Year 2017, engine experiments and vehicle modeling efforts supporting the U.S. DRIVE FWG lifecycle analysis study were completed. This study focused on a matrix of study fuels that expanded on those published through the Coordinating Research Council's AVFL-20 study [2]. The AVFL-20 study focused on ethanol-blended fuels with an ethanol content of 10 volume percent (E10) and 30 volume percent (E30). The FWG fuel matrix expanded on AVFL-20 by studying a 20 volume percent ethanol blend (E20) and additional non-ethanol biofuel formulations including wood-based biogasoline (WBG) and bioreformate surrogate (BRS) blends. Table II.3.1 shows the fuel formulations for the expanded fuel matrix.

Table II.3.1 - FWG Expanded Matrix Fuel Formulations

Expanded Matrix	RON	MON	Sensitivity	Nominal Biologically Derived Compound Content (volume %)
#18	101.0	89.0	12.0	20% (ethanol)
#20	97.3	86.6	10.7	20% (ethanol)
BRS1	97.6	87.2	10.4	9% (bioreformate surrogate)
BRS2	97.3	87.0	10.3	27% (bioreformate surrogate)
BRS3	101.1	90.0	11.1	9% (bioreformate surrogate)
BRS4	101.0	90.3	10.7	27% (bioreformate surrogate)
WBG2	97.7	87.5	10.2	9% (wood-based biogasoline)
WBG4	97.3	87.1	10.2	27% (wood-based biogasoline)

RON – Research Octane Number; MON – Motor Octane Number

The fuels that had RON values of nominally 97 were studied using pistons that produced CR11.4. Combustion phasing was held constant at approximately 6 crank angle degrees (CAD) after top dead center (ATDC) in the maximum brake torque region where knock does not occur. This region occurs at low brake mean effective pressure levels up to about 800 kPa. As the brake mean effective pressure increased beyond the maximum brake torque region, the combustion phasing was retarded relative to top dead center to avoid knock. Since the 97 RON fuels had well-matched RON and octane sensitivity, the combustion phasing profiles for all of these fuels were similar (see Figure II.3.1). This finding supports the central fuel hypothesis within the Co-Optima program, in that fuels with matched properties (in this case RON and sensitivity) have similar combustion performance regardless of their formulation.

The similarity in combustion phasing also meant that the engine thermal efficiency at a given condition was similar for these fuels. Thus, the principle difference in these fuels that impacts volumetric fuel economy is their energy content. Since ethanol has a lower energy content than non-oxygenated hydrocarbons, the E20 fuel

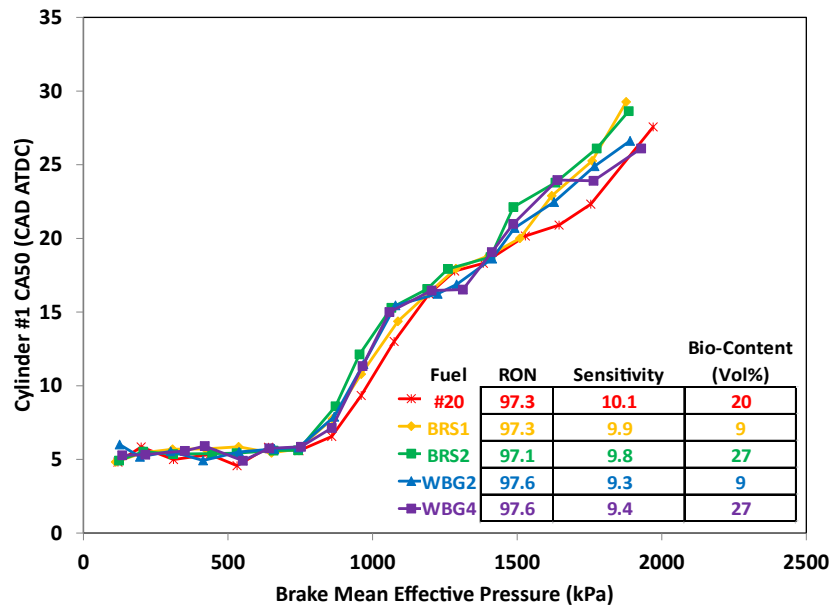


Figure II.3.1 - Crank angle at 50% fuel burned (CA50) phasing versus brake mean effective pressure at 2,000 rpm for the 97 RON fuels using CR11.4 pistons

blend has a lower energy content than the other 97 RON fuels (Figure II.3.2). Studies were anticipated for the 101 RON fuels using pistons that produced a compression ratio of 13.2. However, results indicated that these pistons were not producing as much efficiency increase as expected. Computational fluid dynamics simulations showed that these pistons were causing overly delayed and lengthened combustion, leading to lower efficiency. As a result of this difficulty, engine studies with the 101 RON fuels were put on hold.

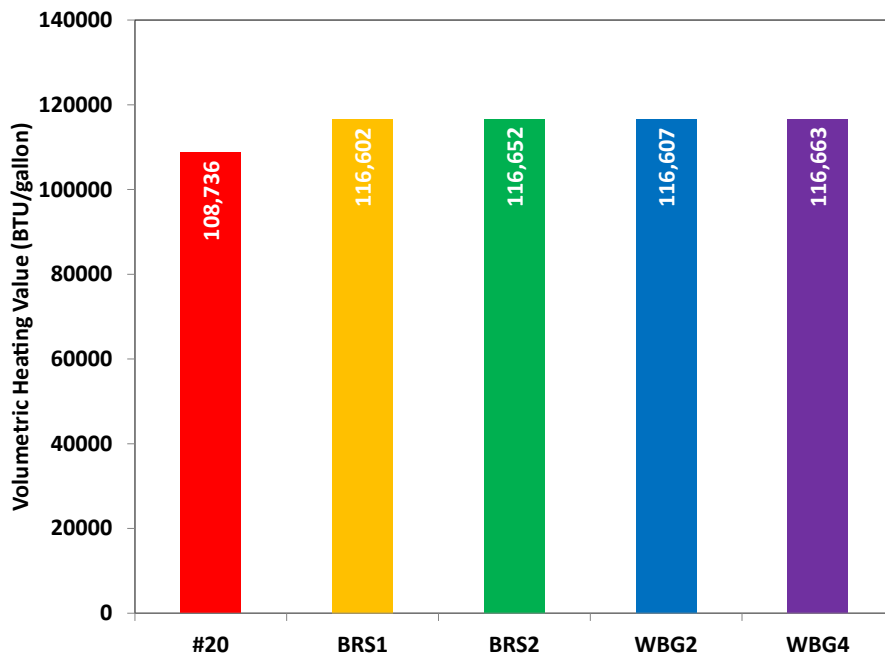


Figure II.3.2 - Volumetric heating value for the 97 RON expanded matrix fuels

Vehicle modeling was conducting using Autonomie to model an industry-average, mid-size sedan. The engine data gathered previously were used in Autonomie to estimate fuel consumption for the modeled vehicle at each point in a drive cycle. Three typical certification cycles were studied, the Urban Dynamometer Driving Schedule (UDDS), the Highway Fuel Economy Test (HWFET), and the US06 cycle. Figure II.3.3 shows the

estimated volumetric fuel economy for these cycles for each of the 97 RON fuels. The US06 cycle results are broken into the city and highway portions of the cycle. The volumetric fuel economy results for the non-ethanol blends were similar to one another and were higher than the E20 blend. These results are consistent with very similar engine efficiency values for all of the fuels and the observed differences in energy content. When these vehicle model results are compared against the baseline condition defined in the AVFL-20 project for 91 RON E10 fuels and the production compression ratio of 10.1, they indicate results ranging from a detriment of 0.9% to an improvement of 4.3% in vehicle energy consumption depending upon the cycle and fuel. Volumetric fuel economy varied from a detriment of 2.3% to an improvement of 7.9% depending upon the cycle and fuel. Though the E20 fuel blend demonstrated improvements in energy consumption, they were only sufficient to overcome the lower energy content of the E20 fuel on the US06 cycle.

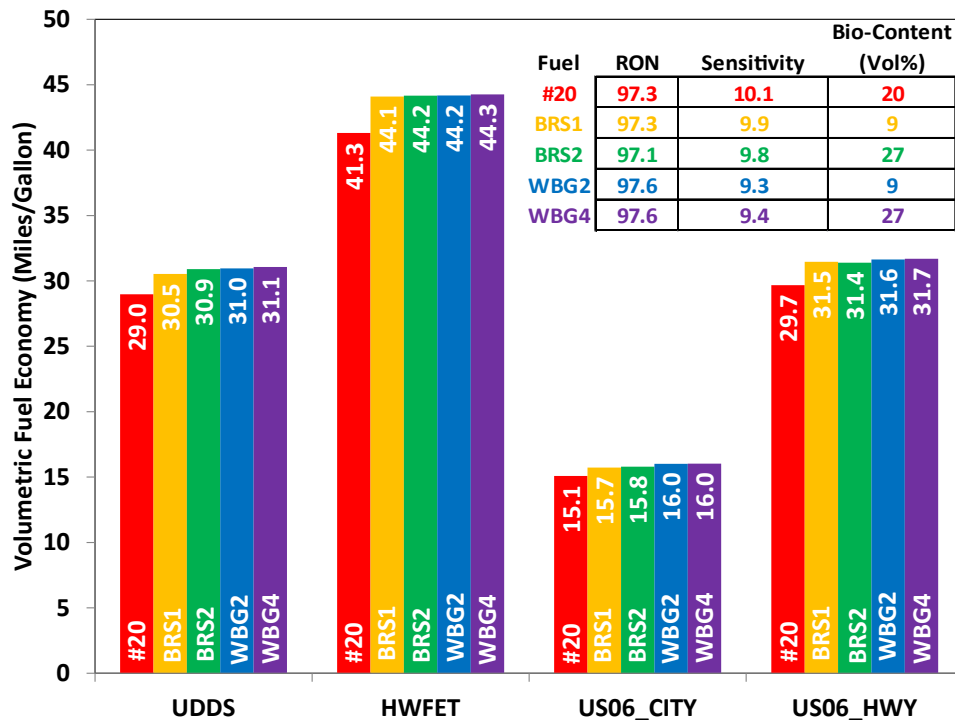


Figure II.3.3 - Modeled volumetric fuel economy for a typical mid-size sedan using CR11.4 and the 97 RON fuels

Conclusions

- Engine studies at CR11.4 and vehicle modeling for the FWG expanded fuel matrix were completed.
- Ethanol and non-ethanol biofuel blends studied at well-matched RON and sensitivity demonstrated similar combustion phasing and engine efficiency results, supporting the Co-Optimization of Fuels and Engines Program central fuel hypothesis.
- Volumetric fuel economy results for the 97 RON fuels were consistent with their energy content values.
- Vehicle energy consumption estimates ranged from a detriment of 0.9% to an improvement of 4.3% compared to the baseline case depending upon the drive cycle and fuel for a typical mid-size sedan.
- Vehicle fuel economy estimates range from a detriment of 2.3% to an improvement of 7.9% compared to the baseline case depending upon the drive cycle and fuel for a typical mid-size sedan.

References

1. Stein, Robert A., Dusan Polovina, Kevin Roth, Michael Fost, Michael Lynskey, Todd Whiting, James E. Anderson, Michael H. Shelby, Thomas G. Leone, and Steve Vandergrind. "Effect of Heat of Vaporization, Chemical Octane, and Sensitivity on Knock Limit for Ethanol – Gasoline Blends." *SAE Int. J. Fuels Lubr.* 5(2):2012, doi: 10.4271/2012-01-1277.

2. Sluder, C. Scott, David E. Smith, Martin Wissink, James E. Anderson, Thomas G. Leone, and Michael H. Shelby, "Effects of Octane Number, Sensitivity, Ethanol Content, and Engine Compression Ratio on GTDI Engine Efficiency, Fuel Economy, and CO₂ Emissions." Coordinating Research Council Report# AVFL-20, 2017.

Key Fiscal Year 2017 Publications

1. Sluder, C. Scott. "Performance of Biofuel Blends at Increased Compression Ratio." Presented at the Co-Optimization of Fuels and Engines Program 2016 All-Hands Meeting, Livermore, CA, 2016.
2. Sluder, C. Scott and Kristi Moriarty. "The Challenge of Backwards Compatibility." Presented at the Co-Optimization of Fuels and Engines Program Stakeholders Meeting, November 2016.

II.4 Advanced Light-Duty SI Engine Fuels Research: Multiple Optical Diagnostics of Well-Mixed and Stratified Operation

Magnus Sjöberg, Principal Investigator

Sandia National Laboratories
MS9053, PO Box 969
Livermore, CA 94551-0969
E-mail: mgsjobe@sandia.gov

Kevin Stork, DOE Technology Manager

U.S. Department of Energy
E-mail: Kevin.Stork@ee.doe.gov

Start Date: October 1, 2016	End Date: September 30, 2017	
Total Project Cost: \$652,000	DOE share: \$652,000	Non-DOE share: \$0

Acknowledgments

Co-Author

David Vuilleumier, Sandia National Laboratories

The work was performed at the Combustion Research Facility, Sandia National Laboratories, Livermore, CA. Sandia National Laboratories is a multi-mission laboratory managed and operated by National Technology and Engineering Solutions of Sandia, LLC., a wholly owned subsidiary of Honeywell International, Inc., for the U.S. Department of Energy's National Nuclear Security Administration under contract DE-NA0003525.

Project Introduction

Ever tighter fuel economy standards and concerns about energy security motivate efforts to improve engine efficiency and to develop alternative fuels. This project contributes to the science base needed by industry to develop highly efficient direct injection spark ignition (DISI) engines that also beneficially exploit the different properties of alternative fuels. Here, the emphasis is on lean operation, which can provide higher efficiencies than traditional non-dilute stoichiometric operation. Since lean operation can lead to issues with ignition stability, slow flame propagation and low combustion efficiency, the focus is on techniques that can overcome these challenges. Specifically, fuel stratification is used to ensure ignition and completeness of combustion but this technique has soot and NO_x emissions challenges. For ultra-lean well-mixed operation, turbulent deflagration can be combined with controlled end-gas autoignition to render mixed-mode combustion for sufficiently fast heat release. However, such mixed-mode combustion requires very stable inflammation, motivating studies on the effects of near-spark flow and turbulence, and the use of small amounts of fuel stratification near the spark plug.

Objectives

- Provide the science base needed by industry to understand how emerging alternative fuels impact highly efficient DISI light-duty engines being developed by industry
- Elucidate how engine design and operation can be optimized for most efficient use of future fuels
- Develop and apply advanced optical diagnostics for probing in-cylinder processes

Approach

The Alternative Fuels DISI Engine Lab at Sandia houses an engine that is capable of both performance testing and in-cylinder optical diagnostics. First, performance testing with an all-metal engine configuration is conducted over wide ranges of operating conditions and alternative fuel blends. This allows quantifying fuel efficiency and exhaust emissions behavior. Second, in-cylinder processes are examined with high-speed

optical diagnostics, including advanced laser-based techniques. This reveals the mechanisms that govern the combustion process. Computer modeling provides additional insight of the governing combustion fundamentals. The combination of performance testing, exhaust emissions measurements, optical diagnostics, and modeling allows building a comprehensive science base.

Results

Key accomplishments for Fiscal Year 2017:

- Demonstrated when Particulate Matter Index (PMI) predicts smoke emissions for DISI operation, and when it does not
- Identified how soot production pathways change with fuel type and operating conditions for stratified charge spark ignition (SI) operation
- Developed semi-quantitative wall-wetting diagnostics based on refractive index matching (RIM)
- Examined how the high heat of vaporization of E30 (30% ethanol, 70% gasoline) leads to increased wall wetting and pool fires
- Established stratification technique to stabilize ultra-lean SI combustion for effective parametric fuel studies of lean autoignition

In the following sections, selected detailed examples of Fiscal Year 2017 accomplishments are presented.

Fully Stratified Operation

Spray-guided stratified charge SI operation is one promising approach to lean operation that can provide high thermal efficiency, but fuel stratification can cause high engine-out smoke levels. The Co-Optima effort requires an understanding of soot formation pathways and how they are affected by fuel composition and fuel specifications. In this research task, the applicability of PMI is assessed for both stratified lean and well-mixed stoichiometric operation. However, only results for stratified operation are presented in this report. PMI is a fuel property metric that is intended to be predictive of particulate emissions from SI engines [1]. For stratified operation with moderate boost at 2,000 rpm, the plotted brown circles in Figure II.4.1 show that the engine-out soot increases monotonically with increased PMI, consistent with literature results. However, for naturally aspirated operation at 1,000 rpm, the light blue squares show that the measured engine-out soot is highest for the E30 fuel. Hence, PMI is not predictive of engine out-soot for these naturally aspirated conditions. In-cylinder optical diagnostics have revealed that under these conditions, the enhanced vaporization cooling associated with the ethanol fraction in E30 causes wall wetting and pool fires, as illustrated in the top right portion of Figure II.4.1. These findings highlight the need to further develop fuel property metrics that can predict the effect of fuel on engine particulate matter (PM) emissions, and also to closely monitor the formation of fuel wall films for advanced combustion systems that utilize direct fuel injection.

To minimize the exhaust aftertreatment burden, low engine-out NO_x is required for lean stratified charge SI operation, which in turn mandates the use of exhaust gas recirculation (EGR) to limit peak combustion temperatures. However, Figure II.4.2 shows that the response of engine-out soot to EGR varies greatly with fuel and operating conditions. For moderately boosted operation at 2,000 rpm using the High-Aromatic Co-Optima Core fuel, the application of EGR increases engine-out soot while NO_x is suppressed. Simplistically, engine-out soot = (soot formed) - (soot oxidized). Soot oxidation is impeded by EGR, explaining this NO_x -PM trade-off, which is analogous to that of diesel combustion. For this type of stratified charge SI engine operation at 2,000 rpm, previous work has indicated that soot formation is a bulk-gas phenomenon [2]. For such conditions with bulk-gas soot as the dominating path to exhaust soot, Figure II.4.1 shows that PMI is predictive. In stark contrast, for non-boosted operation at 1,000 rpm using E30 fuel, Figure II.4.2 shows that engine-out soot goes down with NO_x as EGR is applied, suggesting a different soot production pathway. Since soot oxidation is hampered by EGR, the reduction of engine-out soot with increasing EGR must be caused by a strong reduction of the soot formation. The fouling of the piston bowl window can be used as an indicator of the amount of soot formed in pool fires. The upper part of Figure II.4.2 shows that the soot deposit rate is

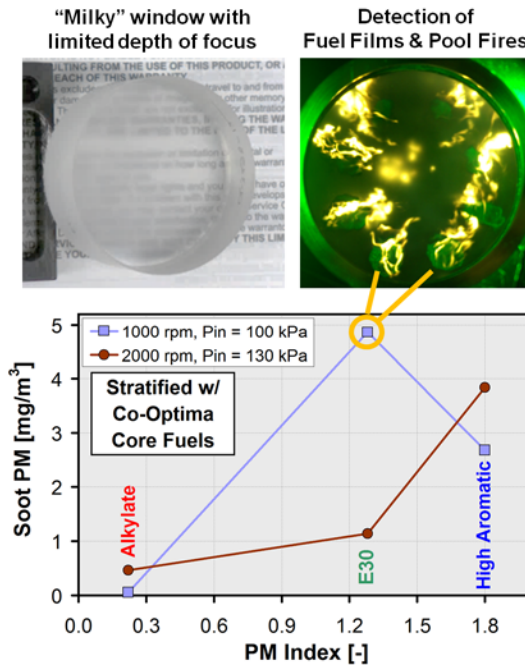
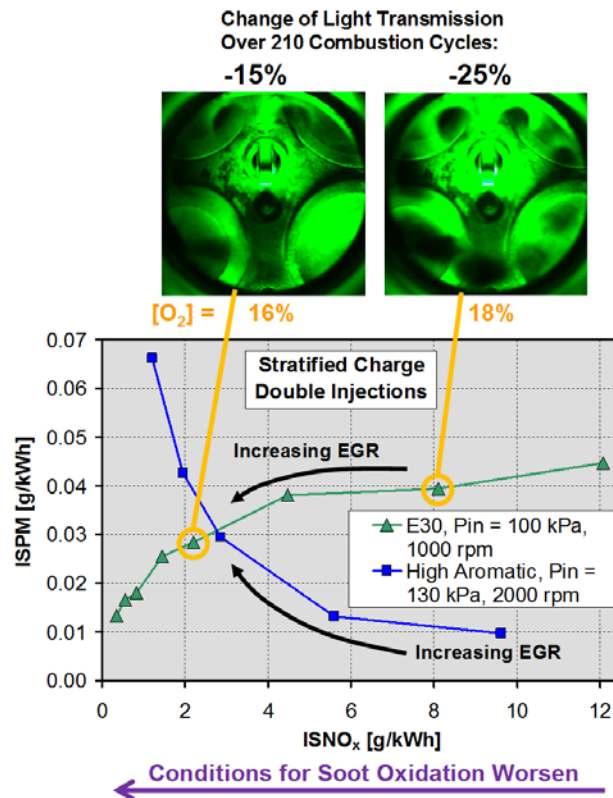


Figure II.4.1 - For boosted, stratified charge, direct injection SI operation at 2,000 rpm, engine-out soot increases monotonically with the fuels' PMI, as the soot formation is primarily occurring in the bulk gases. But for naturally aspirated operation at 1,000 rpm, soot emissions for E30 are higher than predicted from PMI due to the formation of pool fires. PMI values were provided by Fioroni et al. [3]. Figure by Magnus Sjöberg and Carl-Philipp Ding, Sandia National Laboratories (SNL).



ISNO_x – indicated specific NO_x; ISPM – indicated specific PM

Figure II.4.2 - A change of NO_x-PM trade-off indicates a change of the dominating soot production pathway with fuel type and operating conditions. Figure by Magnus Sjöberg.

much greater for the case with 18% O₂ in the intake, indicating more sooting near-wall flames. Hence, it can be surmised that the soot formation is controlled by the intensity of pool fires. For these conditions, Figure II.4.1 shows that PMI is not predictive of engine-out soot.

Optical Diagnostics Development

The interaction of fuel sprays and piston surfaces can be problematic for specific combinations of fuels and operating points, causing soot formation. To identify sources of exhaust smoke, efforts were devoted to the development of optical diagnostic techniques to quantify both wall wetting and pool fires in a direct injection SI engine. The technique that was selected to measure wall wetting is RIM, as first published by Drake et al. [4]. Several aspects of the RIM application were not clear from published papers, prompting further development work at Sandia. During Fiscal Year 2017, the quest for quantitative fuel film measurements involved the use of various light sources and light application approaches. In addition, substantial effort was spent on calibration methodologies and quantifying the influence of the surface roughness of the RIM windows being used. Figure II.4.3 highlights one successful implementation. Here, a continuous-wave (CW) laser beam is split into two beams, which are used to illuminate the upper rough surface of the piston-bowl window from two directions. As demonstrated in Figure II.4.3, the contrast between the wall films seen for the E30 and the alkylate fuels provides a good example of the strong effect of fuel properties on the tendency to form fuel films.

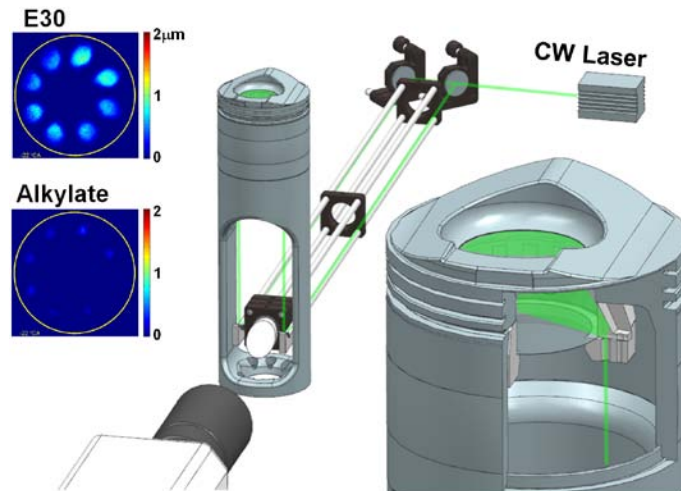


Figure II.4.3 - Laser-based measurements allow the detection of fuel wall films for various combinations of fuels and operating conditions that are prone to pool fires. Figure by Carl-Philipp Ding, Xu He, and Magnus Sjöberg, SNL

In addition to the measurement of fuel film thickness, the use of a piston bowl window with a rough surface and a “milky” appearance allows separation of flames from pool fires from sooting flames in the bulk gases. Effectively, the surface roughness limits the depth of focus as demonstrated in the upper left portion of Figure II.4.1. Therefore, flames that originate in pool fires appear sharp because they are located very close to the piston surface.

Lean Autoignition Studies

Lean or dilute well-mixed SI engine operation can improve thermal efficiency, but one key challenge is to maintain stable combustion without misfires. Another challenge is to maintain a 10–90% burn duration below 30° crank angle (°CA). The latter can be achieved via the use of mixed-mode combustion, which features a combination of turbulent deflagration and end-gas autoignition [5]. Although dubbed mixed-mode combustion here, it is conceptually the same as spark-assisted compression ignition combustion studied by others [6]. The main differences are that a larger fraction of the combustion is flame-based and that the level of internal residuals (or external EGR) is much lower. For both spark-assisted compression ignition and the current mixed-mode approach, practical implementation requires that suitable fuels are available in the marketplace, and that appropriate autoignition metrics are available to specify the fuels being used. Consequently, the applicability

of Research Octane Number and Motor Octane Number for autoignition under lean conditions is currently being assessed for a range of fuels. To enable effective parametric studies of lean autoignition, it is important to overcome challenges associated with unstable flame development. To this effect, recent work has been devoted to establishing an operating methodology that is applicable over wide ranges of fuels and operating conditions.

The stratified charge capable DISI engine used here can be operated with most of the fuel injected during the intake stroke and with an additional short injection at the time of spark, as illustrated in the top portion of Figure II.4.4. The late injection enriches the regions surrounding the spark plug, as illustrated with infrared (IR) fuel–vapor imaging [2] in the lower row of Figure II.4.5. Thanks to the enriched region, the early flame development is very fast and repeatable from cycle to cycle. An example of this is shown in Figure II.4.6, which plots the apparent heat release rate (AHRR) against the mass fraction burned for 250 individual cycles. The fuel used here is a high cycloalkane fuel, which is one out of five Co-Optima Core fuels. In this case, only 1.6 mg of fuel is injected late, which is substantially less than the image examples in Figure II.4.5. Even so, the deflagration-based AHRR is relatively repeatable, especially considering that ϕ is only 0.50 outside the enriched regions near the spark plug. The transition to an autoignition-dominated AHRR occurs for mass fraction burned $\approx 53\%$, as marked by a rapid rise of the AHRR. The magnitude of this second AHRR peak varies from cycle to cycle, but the peak has a distinct shape for almost all 250 cycles. Only five cycles display no, or only weak, end-gas autoignition. Indicated mean effective pressure variability is also very low, only 0.9%, suggesting that this technique can enable parametric fuel studies of lean autoignition limits. Such studies are currently being conducted for a range of Co-Optima fuels.

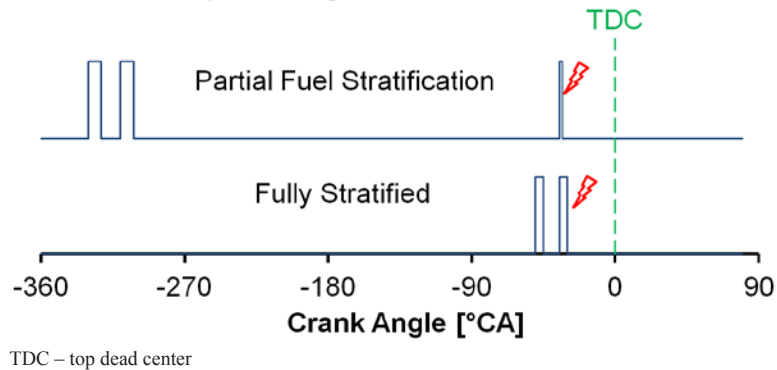


Figure II.4.4 - Conceptual comparison of fuel injection and spark timing strategies for operation with partial fuel stratification and full stratification. Figure by Magnus Sjöberg and Zongjie Hu, SNL.

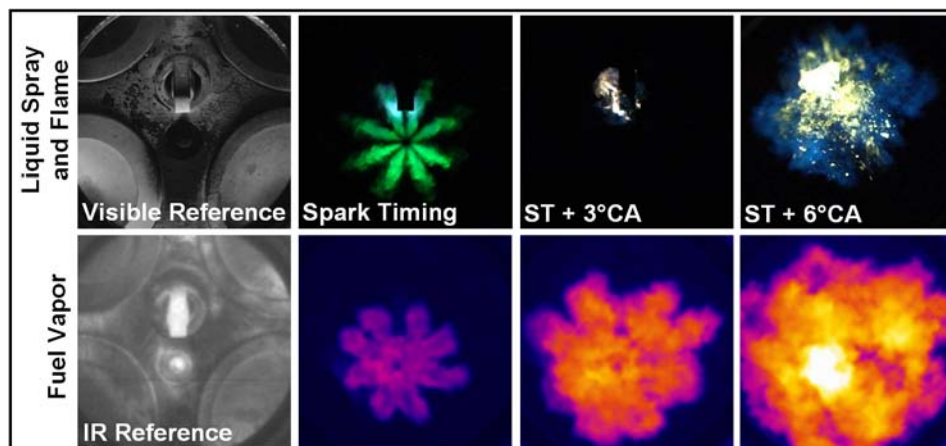
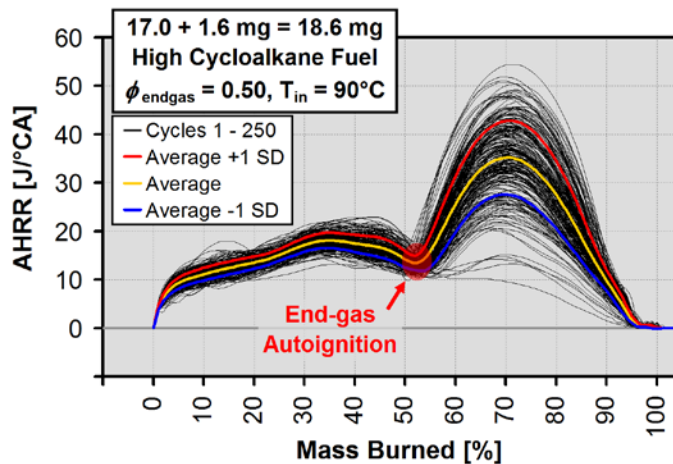


Figure II.4.5 - IR fuel–vapor imaging reveals extent of fuel stratification relative to the flame spread for operation with a late injection of 3.6 mg gasoline at the time of spark. Figure by Magnus Sjöberg, SNL.



SD – standard deviation

Figure II.4.6 - Injection of 1.6 mg of fuel at the time of spark stabilizes combustion, enabling studying autoignition of lean end-gas with $\phi = 0.50$, 1,400 rpm, $P_{in} = 100$ kPa. Figure by Magnus Sjöberg, SNL.

Conclusions

These research tasks are contributing strongly to both the Co-Optima project and to the science of fuel-combustion interactions for advanced SI engine combustion.

For the DISI engine used here, PMI is a good predictor of exhaust soot for fully warmed-up steady-state operation, both for stoichiometric well-mixed operation and for boosted stratified charge operation. However, PMI is not predictive of soot for an E30 fuel under colder transient stoichiometric operation, nor for stratified charge non-boosted operation. Specifically, for non-boosted stratified charge operation, wall wetting and pool fires become a dominating soot production pathway when E30 fuel is used.

The RIM technique works well as a diagnostics for fuel wall wetting, both with light-emitting diode- and laser-based illumination. The milky window RIM technique also allows distinguishing near-wall flames from soot flames in the bulk gases.

Lastly, it was demonstrated that partial fuel stratification is very effective for stabilizing flame development in an overall ultra-lean charge, enabling parametric fuel studies of lean autoignition limits.

References

1. Aikawa, K., T. Sakurai, and J. Jetter. "Development of a Predictive Model for Gasoline Vehicle Particulate Matter Emissions." *SAE Int. J. Fuels Lubr.* 3(2):610-622, 2010, doi: 10.4271/2010-01-2115.
2. Zeng, W., M. Sjöberg, D.L. Reuss, and Z. Hu. "High-Speed PIV, Spray, Combustion Luminosity, and Infrared Fuel-Vapor Imaging for Probing Tumble-Flow-Induced Asymmetry of Gasoline Distribution in a Spray-Guided Stratified-Charge DISI Engine." *Proc. Comb. Inst.* 36:3, pp. 3459–3466, 2017, doi: 10.1016/j.proci.2016.08.047.
3. Fioroni, G.M., E. Christensen, L. Fouts, R.L. McCormick. Private communication, April 2017.
4. Drake, M.C., T.D. Fansler, and M.E. Rosalik. "Quantitative High-Speed Imaging of Piston Fuel Films in Direct-Injection Engines using a Refractive-Index-Matching Technique", ILASS – 02, 15th Annual Conference on Liquid Atomization and Spray Systems, Madison, WI, May 2002.
5. Sjöberg, M., and W. Zeng. "Combined Effects of Fuel and Dilution Type on Efficiency Gains of Lean Well-Mixed DISI Engine Operation with Enhanced Ignition and Intake Heating for Enabling Mixed-Mode Combustion." *SAE Int. J. Engines* 9(2):750-767, 2016, doi:10.4271/2016-01-0689.

6. Manofsky Olesky L., G.A. Lavoie, D.N. Assanis, M.S. Wooldridge, and J.B. Martz. “The effects of diluent composition on the rates of HCCI and spark assisted compression ignition combustion.” *Applied Energy* 124, pp. 186–198, 2014, doi:10.1016/j.apenergy.2014.03.015.

Key Fiscal Year 2017 Publications

1. Zeng, W., M. Sjöberg, D.L. Reuss, and Z. Hu. “High-Speed PIV, Spray, Combustion Luminosity, and Infrared Fuel-Vapor Imaging for Probing Tumble-Flow-Induced Asymmetry of Gasoline Distribution in a Spray-Guided Stratified-Charge DISI Engine.” *Proc. Comb. Inst.* 36:3, pp. 3459–3466, 2017, doi: 10.1016/j.proci.2016.08.047.
2. Zeng W. and M. Sjöberg. “Utilizing boost and double injections for enhanced stratified-charge direct-injection spark-ignition engine operation with gasoline and E30 fuels.” *IJER* 18:1-2, pp. 131–142, 2017, doi: 10.1177/1468087416685512.
3. Singleton, D., J.M. Sanders, M.A. Thomas Jr., M. Sjöberg, J. Sevik, M. Pamminger, and T. Wallner. “Improved dilution tolerance using a production-intent compact nanosecond pulse ignition system.” 3rd Int. Conf. on Ignition Systems for Gasoline Engines, Berlin, Germany, November 2016.
4. Van Dam, N., S. Som, W. Zeng, M. and Sjöberg. “Parallel Multi-cycle Large-eddy Simulations of an Optical Pent-roof DISI Engine.” ASME 2017 Internal Combustion Fall Technical Conference ICEF2017, October 2017.
5. Miles, P.C. “Efficiency Merit Function for Spark Ignition Engines: Revisions and Improvements Based on FY16–17 Research and Development.” (Technical Report, Ed.) 2017.

II.5 Fuel Effects on EGR and Lean Dilution Limits on SI Combustion

Christopher P. Kolodziej, Principal Investigator

Argonne National Laboratory
9700 S. Cass Avenue
Argonne, IL 60439
E-mail: ckolodziej@anl.gov

Kevin Stork, DOE Technology Manager

U.S. Department of Energy
E-mail: Kevin.Stork@ee.doe.gov

Start Date: October 1, 2016	End Date: September 30, 2017	
Total Project Cost: \$200,000	DOE share: \$200,000	Non-DOE share: \$0

Acknowledgments

Co-Authors

Ashish Shah, Michael Pamminger, Thomas Wallner; Argonne National Laboratory

Project Introduction

Fuels with high laminar flame speed (LFS) have been observed to allow increased exhaust gas recirculation (EGR) dilution tolerance in gasoline spark ignition (SI) engines before combustion stability would deteriorate [1]. Modern SI engines benefit from higher EGR dilution tolerance by being able to achieve higher engine indicated thermal efficiency (ITE). The sources of increased ITE with increased EGR dilution include reduced throttling losses (increased volumetric efficiency), reduced combustion heat transfer losses, increased work extraction during the expansion stroke due to a higher ratio of specific heats of the working fluid, and potentially reduced combustion phasing retard to avoid knock at higher loads [2].

In Fiscal Year 2016, this project tested five fuel blends composed of a maximum of three components that varied in LFS by as much as would be expected from E10 gasoline and E85 [3]. The high LFS fuel components tested were ethanol and methanol, which, at the higher LFS fuel blend levels, allowed the engine a 4–6% increased EGR dilution limit and approximately 1–2% higher ITE. So for ethanol and methanol, the Central Fuel Hypothesis was partially justified that if one knows the LFS of a fuel blend, they could predict the relative EGR dilution tolerance and potential ITE gain in the engine. However, the EGR dilution tolerance of a 100% toluene fuel was observed to outperform its LFS compared to the ethanol and methanol blends. This introduced doubt as to whether the EGR dilution tolerance of a fuel blend could be estimated simply by the LFS of the fuel components without knowledge of other characteristics of the hydrocarbons. There was also interest from industry to test the effects of smaller variations in fuel LFS on EGR dilution tolerance, closer to what would be possible for gasoline in the near future.

In Fiscal Year 2017, the EGR dilution tolerance of 10 fuel blends (including four Co-Optima fuel candidates) were tested at approximately 30 vol% blend levels into a four-component surrogate blendstock for oxygenate blending (BOB). These fuels were tested at two engine loads with a modern single-cylinder direct injection (DI) SI gasoline engine.

Objectives

- Measure the effects of fuel blend LFS on engine EGR dilution tolerance among eight fuel components blended at a constant 30 vol%
- Test the Co-Optima Central Fuel Hypothesis regarding fuel LFS with fuel blending components from different hydrocarbon classes
- Test the LFS term in the SI merit function and improve, if required

- Investigate whether fuel blending component heat of vaporization affects EGR dilution tolerance in addition to LFS in a DI engine
- Develop a four-component surrogate BOB which matches the Research Octane Number (RON), Motor Octane Number (MON), sensitivity, aromatic level, and olefinic level of a standard E10 gasoline when mixed with 10 vol% ethanol

Approach

Various fuel blends were tested on a single-cylinder DI SI engine at two load conditions – 3.2 bar and 5.6 bar net indicated mean effective pressure (IMEP_n) – with crank angle timing of 50% mass fraction burn (CA50) held at 8 ±1 crank angle degrees after top dead center (aTDC). An EGR dilution sweep was performed with each fuel blend and engine load for its EGR tolerance limit, defined as the maximum EGR rate achievable with combustion stability parameter, coefficient of variation of IMEP_n, at 3%.

Details of various fuel blends tested are presented in Table II.5.1. A reference BOB surrogate fuel mixture was formulated using four components: iso-octane, n-heptane, toluene, and 1-hexene. The BOB surrogate was designed so that with 10 vol% ethanol it satisfied a RON of 91 and MON of 83, while containing fixed levels of 35 vol% toluene (representative aromatic) and 5 vol% 1-hexene (representative olefin). All other fuels mixtures were prepared to achieve a 10% or 30% component volume fraction at a temperature of 60°F. The LFSs of the various mixtures were calculated by an energy weighting method described by Sileghem, et al. [4] and are presented in the last row of Table II.5.1. Note that LFS was not calculated for the 30% diisobutylene mixture due to unavailability of reliable data for the LFS of diisobutylene, so its dilution tolerance is not shown in Figures II.5.2 and II.5.3.

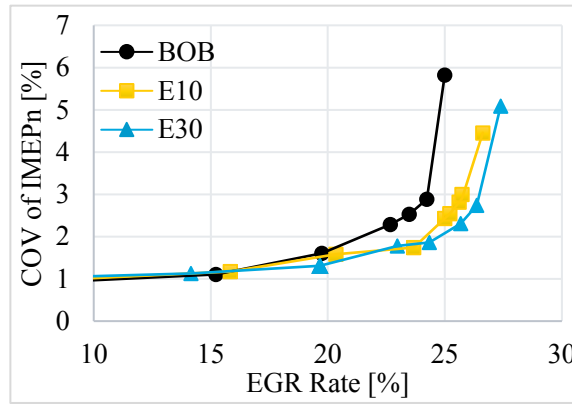
Table II.5.1 - Fuel Mixture Matrix

Fuel mix name	BOB	E10	E30	M30	IsoB30	IsoP30	DiisoB30	IsoOct30	1-Hex30	Tol30
Fuel mix #	1	2	3	4	5	6	7	8	9	10
Components	Pre-Blended Vol%									
iso-octane	31.7	28.5	22.2	22.2	22.2	22.2	22.2	52.2	22.2	22.2
n-heptane	23.9	21.5	16.7	16.7	16.7	16.7	16.7	16.7	16.7	16.7
toluene	38.9	35.0	27.2	27.2	27.2	27.2	27.2	27.2	27.2	57.2
1-hexene	5.6	5.0	3.9	3.9	3.9	3.9	3.9	3.9	33.9	3.9
ethanol		10.0	30.0							
methanol				30.0						
isobutanol					30.0					
isopropanol						30				
diisobutylene							30.0			
LFS [cm/s]	46.7	47.1	48.1	48.1	46.2	46.3	*	46.0	48.8	46.4

Results

The EGR dilution tolerance was observed to increase with the addition of a high LFS fuel component into the BOB surrogate fuel mixture. It can be seen in Figure II.5.1 that addition of ethanol, a high LFS fuel component, allows the engine to run with stable combustion with higher EGR rates compared to just the BOB alone.

Figures II.5.2 and II.5.3 show the EGR dilution limit for each fuel mixture plotted against the mixtures' estimated LFSs at 5.6 bar and 3.2 bar IMEP_n, respectively. It can be seen that the addition of high LFS components – ethanol, methanol and 1-hexene – led to a slight increase in the EGR tolerance limit of the engine. However, it was also observed that the addition of some fuel components that did not increase the estimated mixture LFS (toluene, isopropanol, and isobutanol) also led to an increase in EGR tolerance. The higher EGR dilution tolerance of toluene than expected from its estimated LFS was also observed in the



COV – coefficient of variance

Figure II.5.1 - Effect of adding high LFS ethanol component on combustion stability with EGR dilution

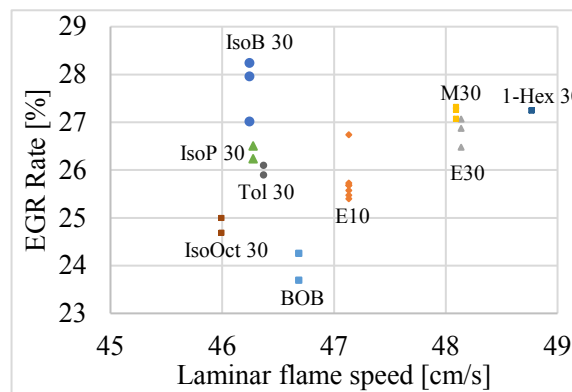


Figure II.5.2 - Variation of EGR tolerance with various fuel mixtures plotted against their LFS at 5.6 bar IMEPn

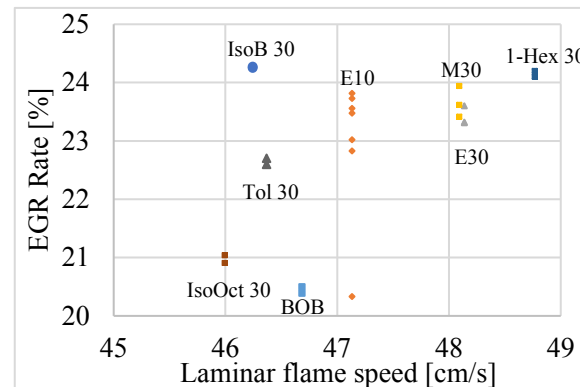


Figure II.5.3 - Variation of EGR tolerance with various fuel mixtures plotted against their LFS at 3.2 bar IMEPn

previous year. The multiple data points illustrated in Figures II.5.2 and II.5.3 of each fuel blend represent different EGR sweeps that were performed for repeatability.

Comparing the performance at 3.2 bar and 5.6 bar IMEPn, it can be seen that the addition of high LFS components led to an appreciable difference in the EGR dilution tolerance limit at 5.6 bar. However, these differences were diminished at lower loads. This can be explained by the fact that at lower load the combustion is inherently less stable and so the effect of the fuel blend LFS is not observed as much.

Figure II.5.4 compares the timing of key combustion events for five fuel mixtures at constant 25% EGR that showed a good LFS to EGR dilution limit correlation. It was observed that with the addition of higher LFS fuel

components at a constant EGR dilution level, only the time taken by the initial fuel kernel development was reduced, whereas the overall combustion duration was not affected as much. This is probably due to the range of estimated LFS tested in this study was very narrow (46–48.8 cm/s). So, the LFS effect was observed mostly in the initial flame kernel development, which is very sensitive to fuel properties and less so the remaining combustion which is also affected by other conditions in the combustion chamber (turbulence, heat loss, etc.).

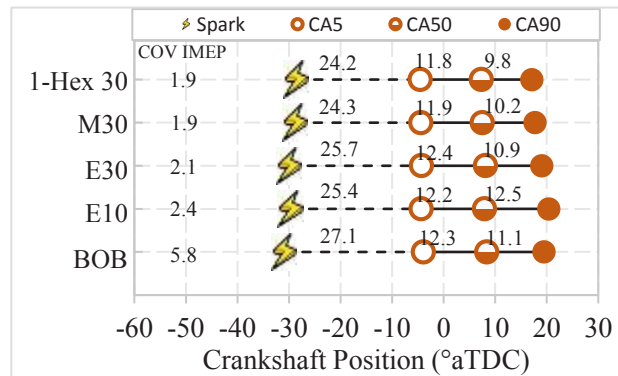


Figure II.5.4 - Comparison of timing of key combustion events for various fuel blends at constant 25% EGR

Figure II.5.5 compared the timing of key combustion events for the E30 fuel mixture at 5.6 bar and 3.2 bar IMEPn load at a constant 23% EGR. In this case, the EGR dilution tolerance of the same fuel (E30) is compared under two different engine operating conditions. The higher load operation at 5.6 bar IMEPn provided higher combustion stability than at 3.2 bar IMEPn as seen in the lower COV of IMEP (1.8% versus 2.9%). So, the EGR dilution limit of 3.2 bar IMEPn was 23% EGR, but the 5.6 bar IMEPn condition allowed for 27% EGR. It is also consistent that the more stable conditions required less spark advance and had shorter combustion duration.

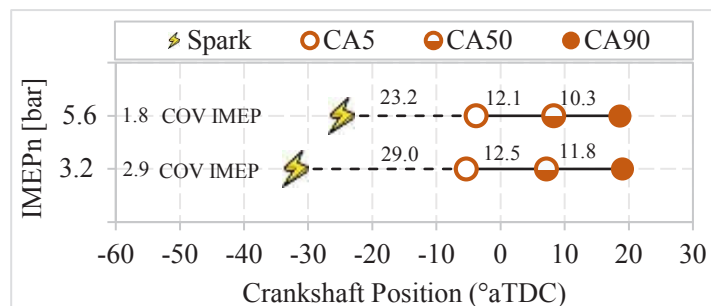


Figure II.5.5 - Comparison of timing of key combustion events with E30 fuel mixture at 5.6 bar and 3.2 bar load at 23% EGR

Conclusions

- A four-component BOB surrogate was successfully blended to meet the 91 RON and 83 MON characteristics of the E10 baseline fuel on which the Co-Optima SI merit function was created.
- The EGR dilution tolerance of the BOB surrogate and the BOB surrogate with 10 vol% ethanol was compared to 30 vol% blend levels of eight fuel components of interest to Co-Optima.
- Blends of the surrogate BOB and 0 vol%, 10 vol%, and 30 vol% ethanol, and 30 vol% methanol and 1-hexene, had EGR dilution tolerance levels consistent with their estimated LFS.
- Blends of 30 vol% of toluene, isopropanol, and isobutanol showed higher EGR dilution tolerance than was expected based on the method used to estimate their LFS.
- At 30 vol% blend levels and 5.6 bar IMEPn, it is possible to observe some trend of increased EGR dilution tolerance with higher estimated fuel blend LFS for ethanol, methanol, and 1-hexene.

- At 3.2 bar IMEP_n, the overall reduction in combustion stability and importance of other factors make it challenging to observe increased EGR dilution tolerance solely based on fuel LFS.
- Further investigation is required of toluene, isopropanol, and isobutanol to understand their increased EGR dilution tolerance over that expected based on estimated fuel blend LFS.

References

1. Ozdor, N., M. Dulger, and E. Sher. "Cyclic Variability in Spark Ignition Engines A Literature Survey." SAE Technical Paper 940987, 1994, doi:10.4271/940987.
2. Caton, J. "A Comparison of Lean Operation and Exhaust Gas Recirculation: Thermodynamic Reasons for the Increases of Efficiency." SAE Technical Paper 2013-01-0266, 2013, doi:10.4271/2013-01-0266.
3. Kolodziej, C., M. Pamminger, J. Sevik, T. Wallner, et al. "Effects of Fuel Laminar Flame Speed Compared to Engine Tumble Ratio, Ignition Energy, and Injection Strategy on Lean and EGR Dilute Spark Ignition Combustion." SAE Int. J. Fuels Lubr. 10(1):2017, doi:10.4271/2017-01-0671.
4. Sileghem, L., J. Vancoillie, J. Demuynck, J. Galle, and S. Verhelst. "Alternative Fuels for Spark-Ignition Engines: Mixing Rules for the Laminar Burning Velocity of Gasoline-Alcohol Blends." Energy Fuels 26, 4721-4727:2012.

Key Fiscal Year 2017 Publications

1. Kolodziej, C., Pamminger, M., Sevik, J., Wallner, T. et al., "Effects of Fuel Laminar Flame Speed Compared to Engine Tumble Ratio, Ignition Energy, and Injection Strategy on Lean and EGR Dilute Spark Ignition Combustion," SAE Int. J. Fuels Lubr. 10(1):2017, doi:10.4271/2017-01-0671.

II.6 Fuel Pressure Sensitivity and High-Load EGR Dilution Effects in SI Combustion

James Szybist, Principal Investigator

Oak Ridge National Laboratory
2360 Cherahala Blvd.
Knoxville, TN 37922
E-mail: szybistjp@ornl.gov

Kevin Stork, DOE Technology Manager

U.S. Department of Energy
E-mail: Kevin.Stork@ee.doe.gov

Start Date: October 1, 2016	End Date: September 30, 2017	
Total Project Cost: \$300,000	DOE share: \$300,000	Non-DOE share: \$0

Acknowledgments

Co-Author

Derek Splitter, Oak Ridge National Laboratory

Project Introduction

An organizing principle of the Co-Optimization of Fuels and Engines (Co-Optima) initiative is the central fuel properties hypothesis (CFPH), which states that fuel properties provide an indication of the performance of the fuel, regardless of the fuel's chemical composition. However, it is not yet understood whether traditional fuel properties for spark ignition (SI) engines are sufficient at characterizing antiknock performance under boosted operating conditions and with exhaust gas recirculation (EGR). This is because both the Research Octane Number (RON) and Motor Octane Number (MON) tests are conducted under naturally aspirated conditions and without EGR. Boosted engines have a different trajectory in the pressure–temperature (PT) domain, which causes differences in the kinetics that lead to autoignition and knock. Additionally, EGR has been shown to be effective at attenuating knock in some studies but less effective in other studies.

In Fiscal Year 2017, this project tested the CFPH to determine whether the central organizing principle of Co-Optima is valid for the go/no-go Co-Optima milestone. In addition, kinetics-based analysis was performed to provide fundamental insight into understanding when and why EGR is effective at mitigating knock, and when it is not.

Objectives

- Test the CFPH with regards to highly boosted SI combustion, including EGR dilute combustion, and use these findings for the Co-Optima go/no-go milestone
- Develop a fundamental, kinetics-based understanding of why EGR is effective at mitigating knock under some engine operating conditions, but less effective during other conditions

Approach

This project combines engine experiments with kinetic simulations and detailed combustion analysis to develop a detailed understanding of autoignition processes resulting in knock under varying in-cylinder conditions. The experimental portion of the project was conducted using a single-cylinder research engine facility with direct injection fueling and operating at stoichiometric SI engine conditions. Spark timing sweeps were conducted at a constant fueling rate at 2,000 rpm for eight boosted operating conditions, consisting of differences in backpressure, intake temperature, intake pressure, and EGR. Seven fuels were investigated that varied in key fuel properties of interest, such as RON, MON, octane sensitivity, and heat of vaporization. Included in the fuel matrix were three bioblendstocks candidates identified in the Co-Optima initiative as potential fuel candidates at an early stage in the initiative: ethyl acetate, methyl butyrate (MB), and anisole.

Analysis centered around determining the knock-limited combustion phasing for each fuel at each of the operating conditions investigated, as well as a determination of the in-cylinder temperature. The latter required custom combustion analysis techniques to determine the trapped residual content on a cycle-by-cycle basis based on sensor feedback of intake pressure, exhaust pressure, and intake and exhaust cam position for each cycle. Chemical kinetic modeling was done by Lawrence Livermore National Laboratory as part of a collaboration within the Co-Optima initiative. Kinetic calculations of constant-volume ignition delay were performed using a comprehensive detailed kinetic mechanism that included the Co-Optima bioblendstock candidates. Surrogate formulations were based on matching RON, MON, molar hydrogen-to-carbon ratio, hydrocarbon classes, and distillation properties.

Results

Central Fuel Property Hypothesis

The common measurements of knock resistance provide us with three fuel property candidates for the CFPH: RON, anti-knock index (AKI), or octane index (OI). These are relevant because RON is the anti-knock fuel property by which fuel is sold in Europe, and AKI is the anti-knock fuel property by which fuel is sold in the United States. OI, by contrast, is a relatively new fuel property pioneered by Kalghatgi and is defined as $OI = RON - K \cdot S$, where K is a parameter used to describe the engine operating condition and can be calculated through a multi-variable linear regression [1]. An example of the knock-limited combustion phasing midpoint (CA50) as a function of OI is shown in Figure II.6.1, which shows reasonable correlation despite the unconventional chemistry of several of the Co-Optima bioblendstock candidates. The correlation coefficients (R^2) between the knock-limited combustion phasing and the three anti-knock fuel properties (RON, AKI, and OI) are shown in Table II.6.1. For all engine operating conditions it can be seen that OI provides the best agreement. In contrast, AKI, the anti-knock fuel property by which fuel is sold in the United States, does not correlate with the actual performance in the engine under the boosted operating conditions investigated. Co-Optima bioblendstock candidates with unconventional chemistry performed in accordance with their fuel property predictions as well as the petroleum-based fuels. This information validated the CFPH, enabling the go/no-go milestone for Co-Optima to be a go.

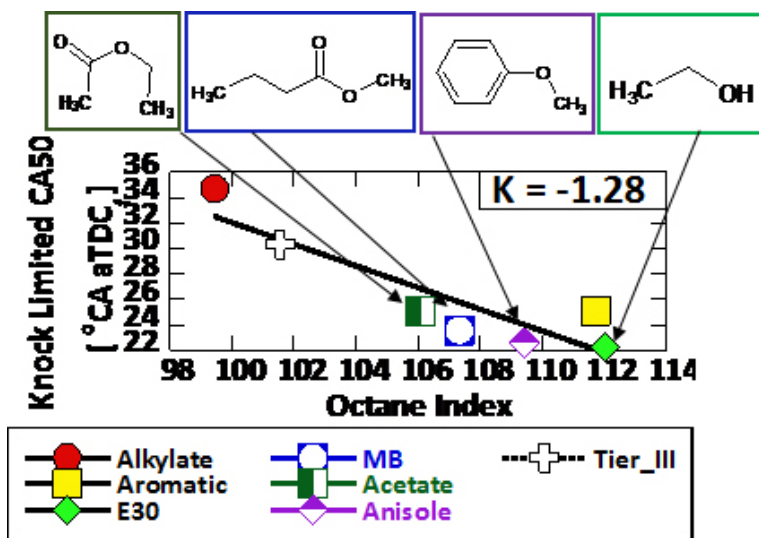


Figure II.6.1 - Knock-limited combustion phasing as a function of octane index for a single engine operating condition

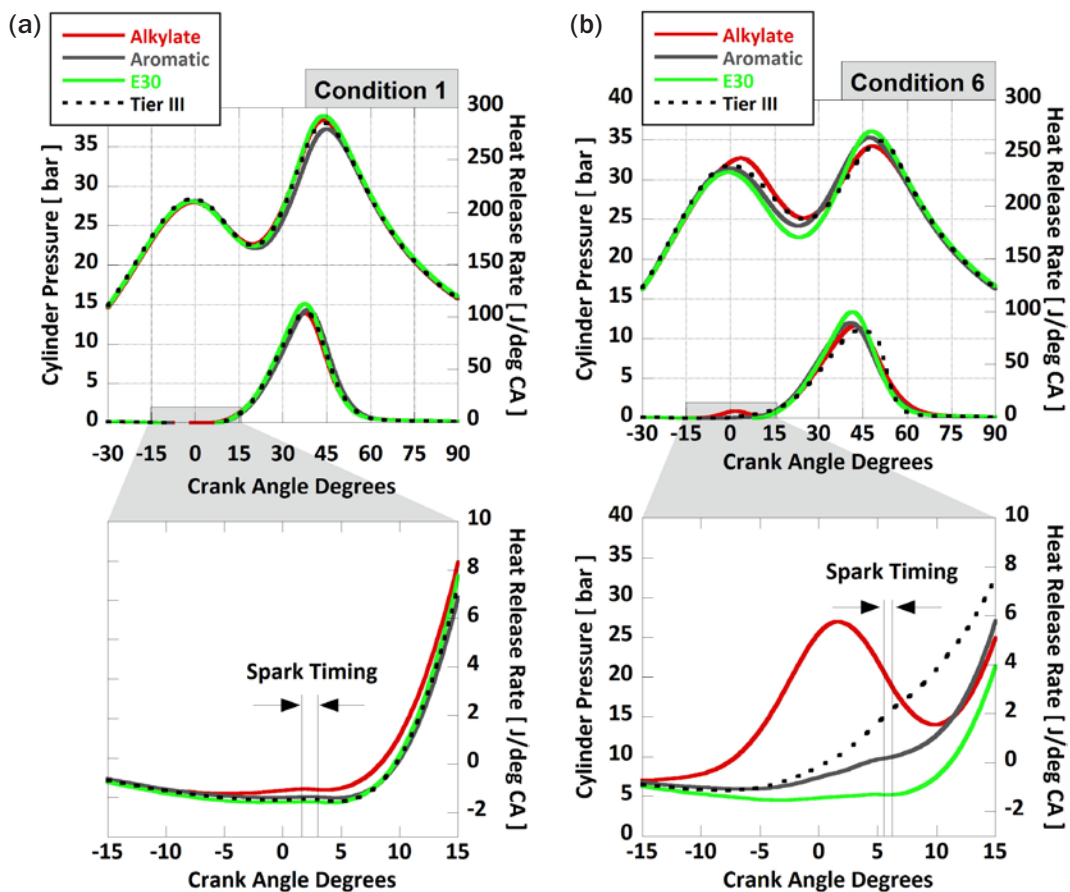
It was found, however, that there were deviations from the OI predictions for all fuels, making the OI prediction good only to a CA50 combustion phasing of ± 3 crank angle degrees. This reveals that even the OI metric, which takes engine operating conditions into account, is still a rudimentary tool to describe the complex autoignition chemistry that leads to knock in SI engines. This is revealed in Figure II.6.2 where the cylinder pressure and heat release rate is shown for two engine operating conditions for select fuels. For operating Condition 1, no heat release is observed for any of the fuels prior to the spark. However, for

Condition 6, three of the four fuels show exhibit some level of pre-spark heat release, with one fuel exhibiting classic low-temperature heat release and negative temperature coefficient behavior. These pre-spark heat release reactions are not described sufficiently by anti-knock metrics (RON, MON, AKI, or OI) to establish a better correlation of knock.

Table II.6.1 - K value and R² between knock-limited CA50 phasing and each of the three different anti-knock metrics: OI, RON, and AKI. Shading represents conditional formatting where green represents a high R² value and red represents a low R² value.

Engine Operating Condition	K ^a	R ² for OI	R ² for RON	R ² for AKI
1	-1.25	0.868	0.09	0.001
2	-1.12	0.881	0.142	0.0001
3	-0.13	0.871	0.838	0.363
4	-0.54	0.604	0.335	0.088
5	-1.28	0.768	0.211	0.002
6	-0.28	0.87	0.735	0.304
7	-0.21	0.753	0.681	0.336
8	-0.32	0.801	0.645	0.251

^aK, which is dependent on the engine operating conditions, is a weighting factor between RON and MON and is determined empirically through a multi-variable linear regression analysis.



CA – crank angle; E30 – 30% ethanol, 70% gasoline

Figure II.6.2 - Cylinder pressure and heat release rate for engine operating Conditions 1 and 6 for select fuels

Reduced Effectiveness of EGR to Mitigate Knock under Boosted Conditions

Externally cooled EGR is an efficiency-increasing technology being deployed in some SI engines to reduce pumping at light loads, and prior research shows EGR may enable further efficiency gains by mitigating knock at higher loads [2]. However, the reported effectiveness of EGR to mitigate knock varies widely, especially in comparing boosted and naturally-aspirated (NA) engines [3,4]. This portion of the project utilizes the same dataset discussed above to investigate the CFPH, but focuses instead on analyzing the results to understand the effect of EGR under boosted conditions.

As the intake pressure changes for a given engine, so does the path of the unburned fuel and air mixture in the PT domain. Figure II.6.3 shows a notional model of PT trajectories as the intake pressure increases. The PT trajectories take into account the effect that the trapped residual fraction has on the temperature and pressure at intake valve closing. Note that the solid line represents the compression process for a compression ratio of 9.2:1, whereas the dashed line represents the compression process for a compression ratio of 14:1. As the intake pressure increases, the PT trajectories move to a cooler temperature for a given in-cylinder pressure. This has a major impact on the dominant autoignition reactions that the fuel–air mixture encounters, ultimately leading to knock.

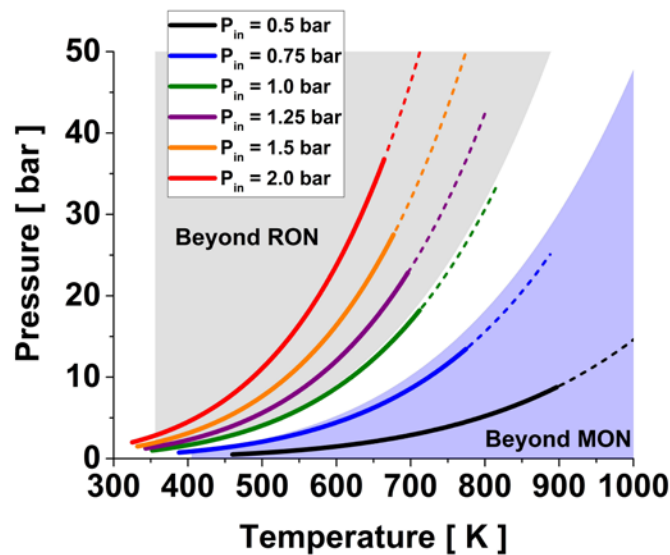


Figure II.6.3 - Notional PT trajectories for changing intake manifold pressure. Solid lines 9.2:1 compression ratio, dashed lines represent continuation of trajectory for compression ratio of 14:1.

Figure II.6.4 shows constant volume ignition delay for one of the fuels, as calculated from the chemical kinetic mechanisms. Because of the shape of the ignition delay contours, three distinct zones of autoignition can be identified. In Zone 1, the ignition delay contours are nearly vertical above a pressure threshold of about 25 bar. This means that in this zone, fuel and air mixtures have very little sensitivity to pressure, but are highly sensitive to temperature. Zone 2, though, exhibits nearly horizontal lines meaning that there is low sensitivity to temperature but high sensitivity to pressure. When kinetic simulations were performed with EGR, it was found that there was little effect in Zone 1, but that Zone 2 required a higher pressure for the same ignition delay. Thus, the kinetics in Zone 1 are not significantly attenuated by EGR, but those in Zone 2 are.

Figure II.6.5 combines the notional model of PT trajectories from Figure II.6.3 with the autoignition kinetics of Figure II.6.4. The autoignition kinetics include a single ignition delay contour, of 8 ms, but for three different EGR levels: 0%, 10%, and 20%. The changing effectiveness to attenuate knock is visualized in Figure II.6.5 for the different EGR levels. For modest intake pressures representing NA or lightly boosted engines ($P_{in} = 0.75$ to 1.25 bar), the ignition delay contours show significant separation with EGR, indicating knock propensity differences. However, for boosted engines using higher intake pressures (1.5 – 2.0 bar), the ignition delay contours show less separation, indicating very little difference in knock propensity. Thus, under boosted conditions, EGR loses effectiveness at mitigating knock.

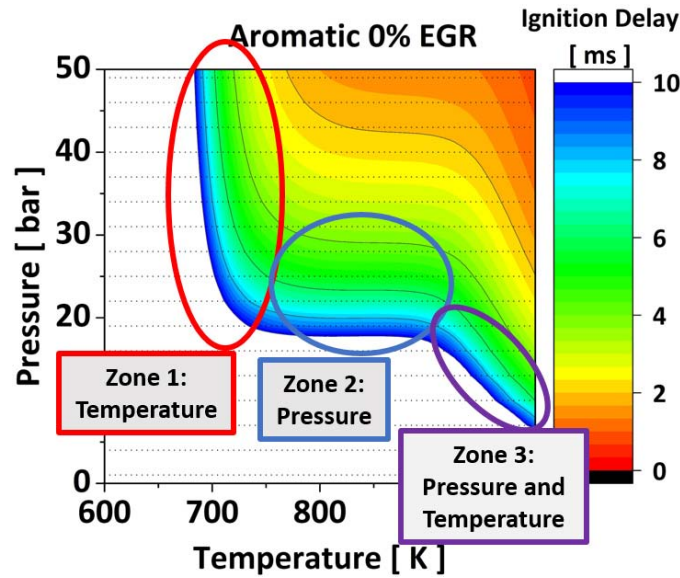


Figure II.6.4 - Ignition delay contour in the PT space for the aromatic fuel without EGR highlighting the different ignition zones

This phenomenon was investigated across fuels with variations in composition and fuel properties, including an octane sensitivity range from 1.2 to 10.7, and ethanol concentration from 0% to 30%. Experimental and computational results confirmed that the same trend was present with all fuels; EGR is effective at mitigating knock at NA or lightly boosted conditions, but loses effectiveness at higher intake pressure.

This research confirms that EGR is effective at knock mitigation for NA engines. As a result, its use at full-load can enable higher efficiency through higher compression ratio and/or advanced combustion phasing. However, there is a diminishing effectiveness at higher intake pressures that will likely prevent the same strategy from being used for boosted engines.

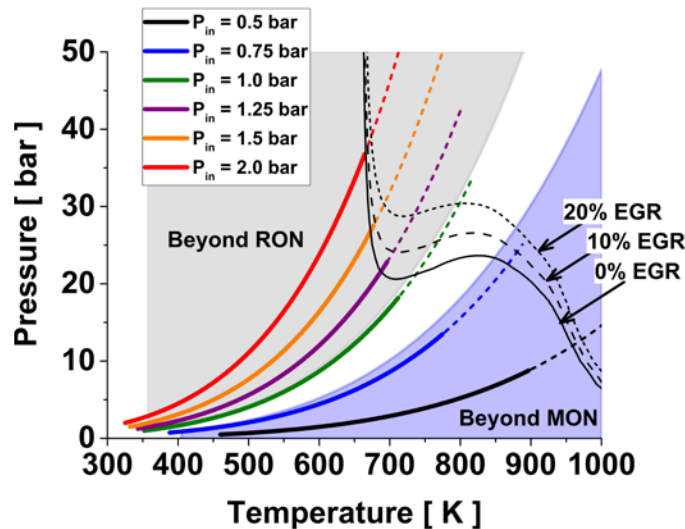


Figure II.6.5 - PT path of the unburned fuel-air mixture during compression for different intake manifold pressure (P_{in}). Also shown are lines of constant ignition delay (8 ms) for 0%, 10%, and 20% EGR.

Conclusions

- Experimental data were collected that support the use of the CFPH, which is a guiding principle for the Co-Optima initiative. The findings were used to contribute to the go/no-go milestone for the initiative.
- While RON and AKI are insufficient as fuel property indicators of knock propensity, OI was shown to correlate well with knock propensity. Further, the fuel candidates identified by Co-Optima with unconventional chemistry adhered to OI as well as fuels with conventional chemistry.
- Despite reasonable agreement with OI, the fuels exhibited differing levels of pre-spark heat release, highlighting the complex chemistry that occurs leading to knock.
- EGR use at full-load can enable higher efficiency through higher compression ratio and/or advanced combustion phasing for NA or lightly boosted engines. However, there is a diminishing effectiveness at higher intake pressures that will likely prevent the same strategy from being used for more aggressively boosted engines.

References

1. Kalghatgi, G.T. "Fuel Anti-Knock Quality - Part I. Engine Studies." SAE Technical Paper 2001-01-3584, 2001.
2. Alger T., B. Mangold, C. Roberts, and J. Gingrich . "The Interaction of Fuel Anti-Knock Index and Cooled EGR on Engine Performance and Efficiency." *SAE Int. J. Engines*. 2012; 5(3), DOI:10.4271/2012-01-1149.
3. Hoepke B., S. Jannsen, E. Kasseris, W.K. Cheng. "EGR Effects on Boosted SI Engine Operation and Knock Integral Correlation." *SAE Int. J. Engines*. 2012; 5(2), DOI:10.4271/2012-01-0707.
4. Splitter, D.A. and J.P. Szybist. "Experimental Investigation of Spark-Ignited Combustion with High-Octane Biofuels and EGR. 2. Fuel and EGR Effects on Knock-Limited Load and Speed." *Energy & Fuels*. 2014 February; 28(2), DOI:10.1021/ef401575e.

Key Fiscal Year 2017 Publications

1. Szybist, J.P., S.W. Wagnon, D.A. Splitter, W.J. Pitz, and M. Mehl. "The Reduced Effectiveness of EGR to Mitigate Knock at High Loads in Boosted SI Engines." SAE Technical Paper, 2017-24-0061, 2017.
2. Szybist, J., and D. Splitter. "Pressure and Temperature Effects on Fuels with Varying Octane Sensitivity at High Load in SI Engines." *Combustion and Flame*, 2017, 177, pp. 49–66.
3. Splitter, D., B. Kaul, J. Szybist, and G. Jatana. "Engine Operating Conditions and Fuel Properties on Pre-Spark Heat Release and SPI Promotion in SI Engines." *SAE Int. J. Engines*, 2017, 10(3), doi:10.4271/2017-01-0688.
4. Wissink, M., D. Splitter, A. Dempsey, S. Curran, B. Kaul, and J. Szybist. "An Assessment of Thermodynamic Merits for Current and Potential Future engine Operating Strategies." *Int. J. Eng. Res.*, 2017, 18(1-2), pp. 155–169, doi:10.1177/1468087416686698.
5. Szybist, J. and D. Splitter. "Understanding Chemistry-Specific Fuel Differences at a Constant RON in a Boosted SI Engine." Submitted to *Fuel* for publication consideration, August 2017.

II.7 Fuel Effects on Emissions and Aftertreatment

Matt Ratcliff, Principal Investigator

National Renewable Energy Laboratory
15013 Denver West Parkway
Golden, CO 80401
E-mail: matthew.ratcliff@nrel.gov

Kevin Stork, DOE Technology Manager

U.S. Department of Energy
E-mail: Kevin.Stork@ee.doe.gov

Start Date: October 1, 2016 End Date: September 30, 2017
Total Project Cost: \$200,000 DOE share: \$200,000 Non-DOE share: \$0

Acknowledgments

Co-Authors

Jon Burton, Bob McCormick, Earl Christensen, Lisa Fouts; National Renewable Energy Laboratory

Project Introduction

The project goals are to understand and predict the effects of blending renewable oxygenates into gasoline on particulate matter (PM) emissions. The potential of oxygenate-free gasoline to form PM has been successfully modeled [1,2] with the equation:

$$PMI = \sum_{i=1}^n \left[\frac{(DBE_i + 1)}{VP(443K)_i} \times Wt_i \right]$$

Where PMI is the particulate matter index and double bond equivalent (DBE) represents the tendency for individual fuel components to form soot; it is the sum of rings and unsaturated bonds in the fuel molecule: $DBE = (2C + 2 - H)/2$. The vapor pressure at 443 K, or VP(443K), represents the tendency for individual fuel components to evaporate. Fuel components with low VP(443K) increase PMI because their vaporization is relatively slow and they may therefore not fully evaporate and mix with air during intake and compression cycle time scales. Locally heterogeneous and/or fuel-rich combustion increases PM emissions.

Ethanol is the most ubiquitous oxygenate fuel compound and there are conflicting results in the literature about its effects on PM emissions. The conventional wisdom is that blending ethanol (which has effectively no intrinsic potential to form PM) into gasoline dilutes those hydrocarbons with high potential to form PM — high DBE and/or low VP(443K) — thereby decreasing the blend's PMI. In many studies where the fuels were splash-blended, i.e., ethanol was simply added to the gasoline, the PM emissions do indeed decrease [3,4,5]. However, other studies show increased PM under some operating conditions. For example, He and coworkers observed increased PM for an E20 blend at high load and suggested that ethanol's high heat of vaporization (HOV) slowed fuel evaporation from piston and cylinder surfaces [6]. Similar observations have been made in other studies where blending ethanol into gasoline results in higher PM emissions [7,8,9]. Thus, one objective of this project is to better understand these seemingly contradictory findings by clarifying the interactions between a fuel's HOV, the presence of low vapor pressure aromatic hydrocarbons, and engine operating conditions. A second objective of this study is to improve the PMI model to accurately account for any fuel property interactions brought about by blending ethanol into gasoline.

Objectives

The research objectives for Fiscal Year 2017 were to:

- Quantify the PM emissions from a full-factorial designed experiment fuel matrix having the variables of aromatic vapor pressure, aromatic concentration, and ethanol concentration.

- Analyze the PM emission and fuel property data to identify and characterize the fuel property interactions that affect PM.

Approach

A full factorial designed experiment fuel matrix (Figure II.7.1) was conceived to test the hypothesis that increasing fuel HOV (via increasing ethanol content) while maintaining constant aromatic content can cause PM emissions to increase. The base gasoline chosen for these experiments was the low-aromatic, high-octane Fuels for Advanced Combustion Engines (FACE) Gasoline B, into which selected boiling point aromatics and ethanol were blended. The aromatics were selected based on their VP(443K) values, which are shown along with boiling points (BPs) and structures in Table II.7.1.

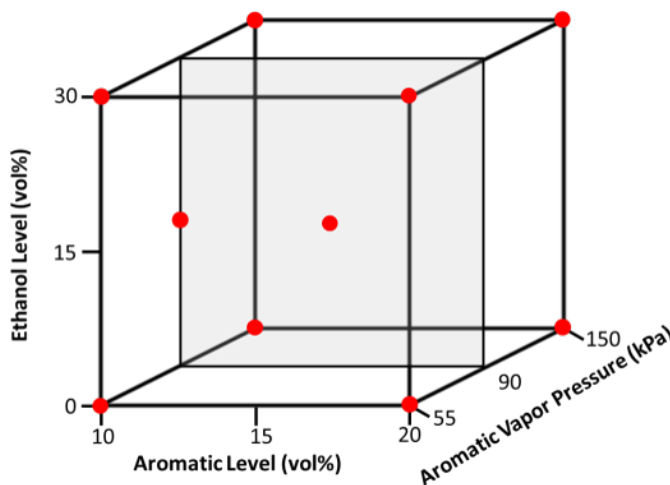


Figure II.7.1 - Full factorial experimental design fuel matrix. Tested fuels are indicated by red dots; aromatic hydrocarbon vapor pressures are at 443 K.

Table II.7.1 - Properties of Aromatics Blended into FACE B

Component	BP (°C)	Vapor Pressure @ 443K (kPa)	Structure
Cumene	153	152	<chem>Cc1ccccc1C(C)C</chem>
p-Cymene	177	84.5	<chem>Cc1ccc(C)cc1C</chem>
4-t-Butyl Toluene	191	58	<chem>Cc1ccc(C(C)(C)C)cc1C</chem>

PMI and HOV values for the fuels were computed based on their detailed hydrocarbon analysis, a gas chromatography method described in previous publications [10,11]. In addition, the fuels were characterized by the advanced distillation curve (ADC) method [12] that determines the composition of each distillate fraction by detailed hydrocarbon analysis. ADC analysis provided new insights into the azeotrope interactions between ethanol and hydrocarbons, particularly for the aromatics intentionally blended for this study.

PM emissions were measured from National Renewable Energy Laboratory’s single-cylinder gasoline direct injection engine using (1) an AVL Micro-Soot Sensor and (2) a TSI Fast Mobility Particle Sizer with sample dilution and conditioning provided by a Dekati FPS-4000 and Thermodenuder. Six engine operating conditions were investigated (see Table II.7.2), including two baseline conditions (A = 2,500 rpm, 13 bar net mean

effective pressure [NMEP], and $D = 1,500$ rpm, 10 bar NMEP) using single injections. The start of injection (SOI) for single (or in some cases the first) injections was 280° before top dead center (BTDC). Although occurring relatively early in the intake stroke, this SOI was previously found to avoid or significantly reduce spray impingement on the piston [4]. Multiple linear regression analyses of the PM emissions and fuel property data were performed to characterize and model fuel property effects on PM emissions.

Table II.7.2 - Engine Operating Conditions for PM Measurements; Intake Air Temperature Fixed at 35°C

Test Condition	Speed – Load (rpm–bar NMEP)	Target λ (or CO %)	SOI ($^\circ$ BTDC)	Spark Timing ($^\circ$ BTDC)	CA50 ($^\circ$ ATDC)	Objective
A	2500 - 13	1.0 - 1.01	280	6.5	22 ± 2	Base condition, high load with late combustion phasing. Links to previous data set
B	2500 - 13	1.0 - 1.01	Split Injection 50:50 @ 280 and 220	≈ 9	22 ± 2	Effect on PM by minimizing fuel impingement. Compare with A
C	2500 - 13	1.0 - 1.01	Split Injection 80:20 @ 280 and 80. Fix 2 nd injection pulse width = 0.68 ms	< 8	22 ± 2	Effect on PM from stratified charge combustion. Compare with A
D	1500 - 10	1.0 - 1.01	280	15	7.5 ± 1.5	Base condition at MBT combustion phasing. Compare with A, E and F
E	1500 - 10	0.92 (3.0% CO)	280	≤ 15	7.5 ± 1.5	Fuel-rich combustion emulating acceleration. Compare with D
F	1500 - 10	1.0 - 1.01	Split Injection 80:20 @ 280 and 80. Fix 2 nd injection pulse width = 0.57 ms	15	7.5 ± 1.5	Effect on PM from stratified charge combustion. Compare with D and C

ATDC – after top dead center; CA50 – crank angle for 50% mass of fuel burned; MBT – maximum brake torque

λ – actual air-to-fuel ratio/stoichiometric air-to-fuel ratio

Results

Inspection of PM results from fuels blended with the most volatile aromatic cumene (isopropylbenzene) reveals no clear effect from blending 30 vol% ethanol (see Figure II.7.2) across the range of engine operating conditions studied. The data do show a statistically significant reduction in PM from using the 50:50 split injection (Condition B) relative to the single injection case (Condition A). The PM reduction is attributed to reduced fuel spray contact with the piston and/or the cylinder liner that result from the shorter spray duration, and likely shorter spray penetration length. The reductions in PM at the lower speed and load Condition D may be explained by the longer time available for evaporation, as well as the lesser amounts of fuel injected (shorter injection duration), relative to Condition A. As expected, fuel-rich operation (Condition E) produced additional PM. The PM results from the 10 vol% cumene fuel set provide similar observations, but the overall lower PM levels and larger error bars make the condition differences less distinct. Note that results from Conditions C and F include some confounding effects that have not been fully resolved and therefore are not discussed in this report.

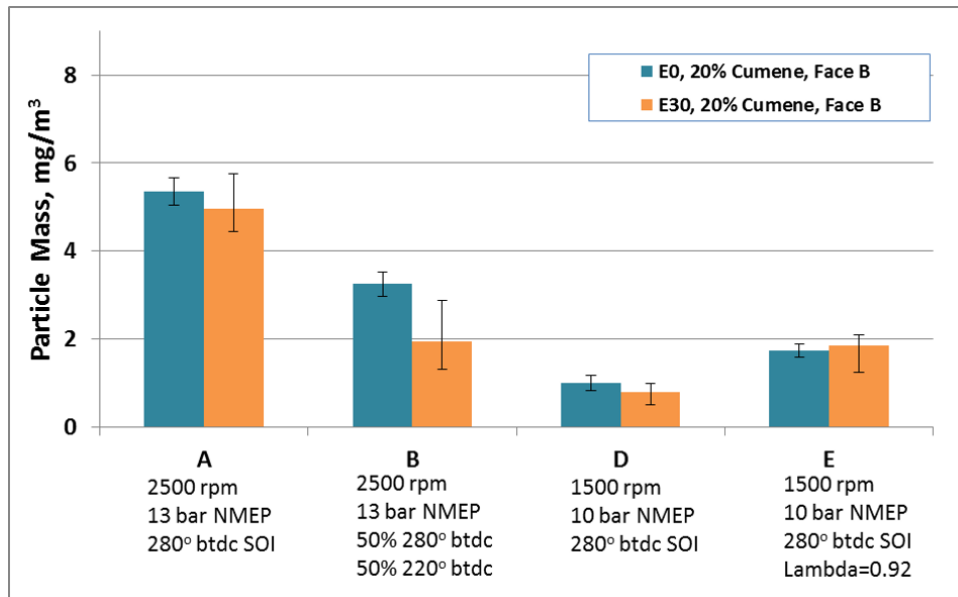


Figure II.7.2 - PM results from cumene at 20 vol%; error bars are 95% confidence intervals

Figures II.7.3 and II.7.4 show PM results from the least volatile aromatic 4-t-butyl toluene at 10 vol% and 20 vol%, respectively. At both aromatic levels the PM emissions increased more than 30% at Condition A when blended with 30 vol% ethanol. Splitting the injection 50:50 (Condition B) and reducing the speed and load (Condition D) even at fuel-rich operation (Condition E) eliminated this E30 effect on PM within experimental error. Thus, for certain engine operating conditions there appears to be a threshold of aromatic vapor pressure below which ethanol blending can lead to increased PM emissions.

Using the 50:50 split injection strategy with the 4-t-butyl toluene blends again provided significant reductions in PM, most clearly at the 20 vol% aromatic level. However, the decreases in PM at Condition D, relative to Conditions A and B, were less than those observed for the cumene blended fuels. This suggests that slower evaporation of 4-t-butyl toluene (lower vapor pressure/higher boiling point) led to locally fuel-rich combustion. This hypothesis is supported by the two to three times higher PM emissions from 4-t-butyl toluene compared to cumene blends at the globally fuel-rich Condition E.

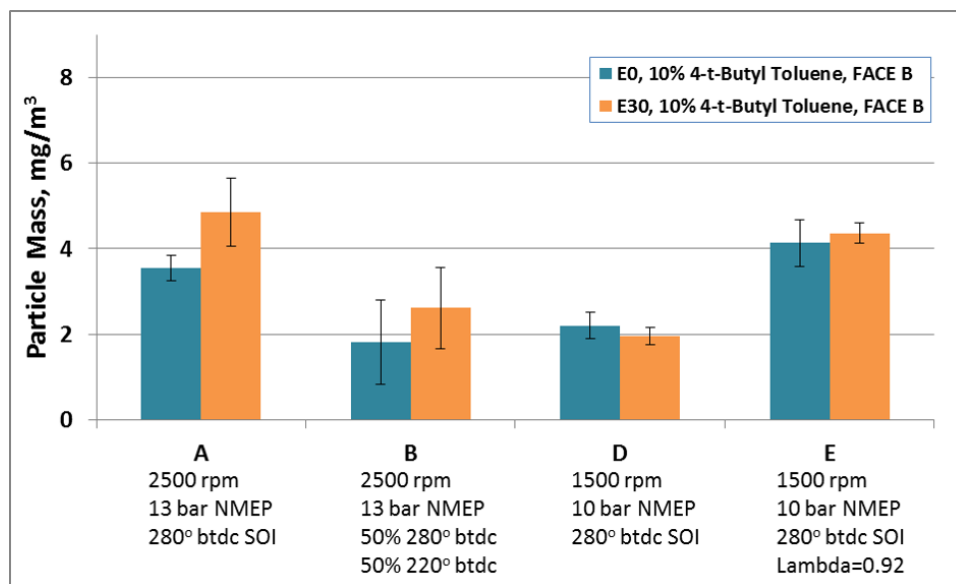


Figure II.7.3 - PM results from 4-t-butyltoluene at 10 vol%; error bars are 95% confidence intervals

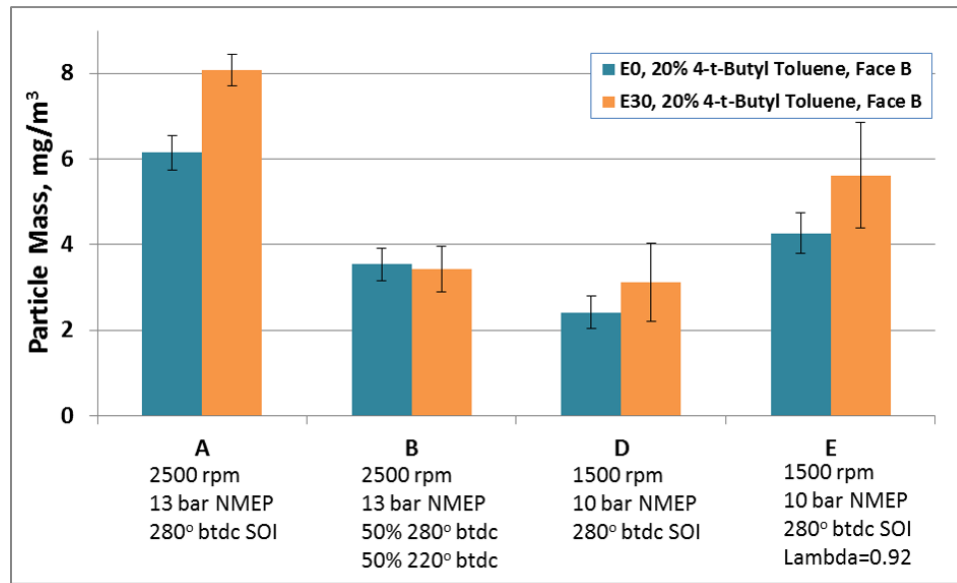


Figure II.7.4 - PM results from 4-t-butyltoluene at 20 vol%; error bars are 95% confidence intervals

PM emissions correlated poorly with the computed PMIs for these fuels typically giving linear regression $R^2 < 0.65$. This indicates that the existing PMI model does not adequately capture all relevant fuel properties affecting PM within this dataset. To better understand the results, multiple linear regression analyses were performed on the entire data set. Analysis with ethanol and aromatic concentrations expressed on a mole percent basis proved meaningful. Aromatic and ethanol molar concentrations, as well as aromatic vapor pressure were found to be statistically significant (p -values < 0.05) coefficients in the model for Condition A. Regression analysis results are summarized in Table II.7.3 and the model used to predict PM has the form:

$$x_1 + x_2 * \{EtOH\% \} + x_3 * \{Aro\% \} + x_4 * \{Aro VP@443K \}$$

Table II.7.3 - Results of Linear Regression Analysis for Condition A using mole% Concentrations of Ethanol and Aromatics in the Blends

	Condition A: 2,500 rpm
Adjusted r^2	0.838
Ethanol mole% coefficient	0.044
Ethanol mole% p-value	0.007
Aromatic mole% coefficient	0.350
Aromatic mole% p-value	0.001
Aromatic vapor pressure coefficient	-0.031
Aromatic vapor pressure p-value	0.001

ADC quantified ethanol's effects on the composition of the evaporating fluid across the distillation temperature range [13]. The ADC characterization revealed that ethanol suppressed the evaporation of aromatics in the fuel while ethanol remained in the liquid phase. The aromatics were then free to evaporate at the end of the distillation process, with the net effect that the aromatic concentrations increase in the liquid and vapor phases at the end of distillation, as shown in Figure II.7.5. Thus, there appears to be a previously unappreciated physicochemical factor arising from ethanol blending, which is independent of evaporative cooling effects from ethanol's high HOV. Both of these effects may potentially increase PM emissions.

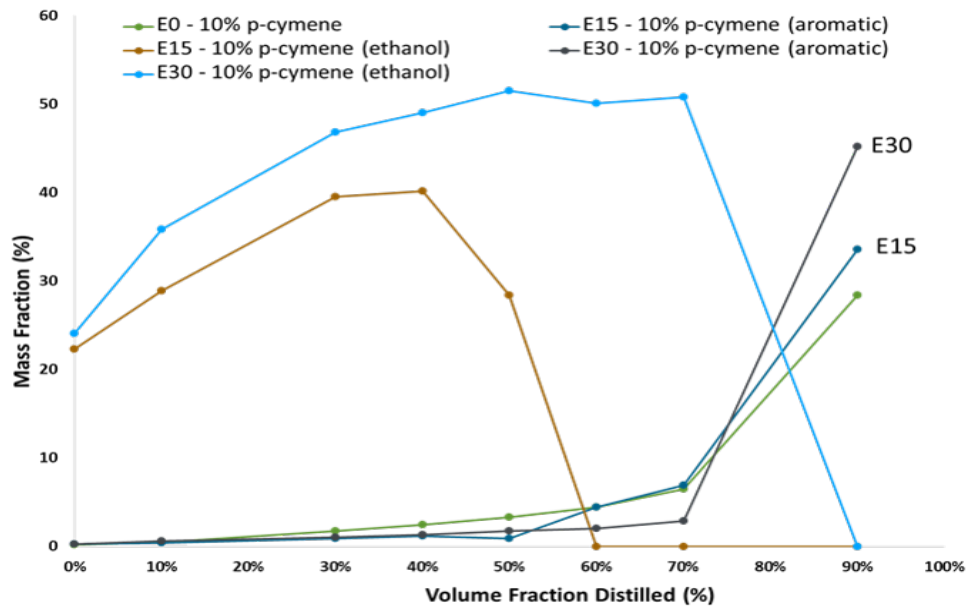


Figure II.7.5 - ADC results for p-cymene fuel blends with and without ethanol, showing ethanol suppression of p-cymene evaporation while ethanol remains in the liquid phase

A single droplet evaporation model was developed by Burke et al. [13] based on the ADC results from this study's fuel matrix. The droplet model was then incorporated into a zero-dimensional model of the engine used for the PM emissions. Relevant engine geometry, temperatures, pressures, and engine speed were included in the zero-dimensional model. Figure II.7.6 shows the modeled vapor phase concentrations of ethanol, paraffins, iso-paraffins, and aromatics in FACE B gasoline (no other aromatics added) at the surface of a fuel droplet evaporating near the end of the compression stroke. The data show that under conditions of ramping temperature increases (from compressive heating) the presence of ethanol in the fuel both increases

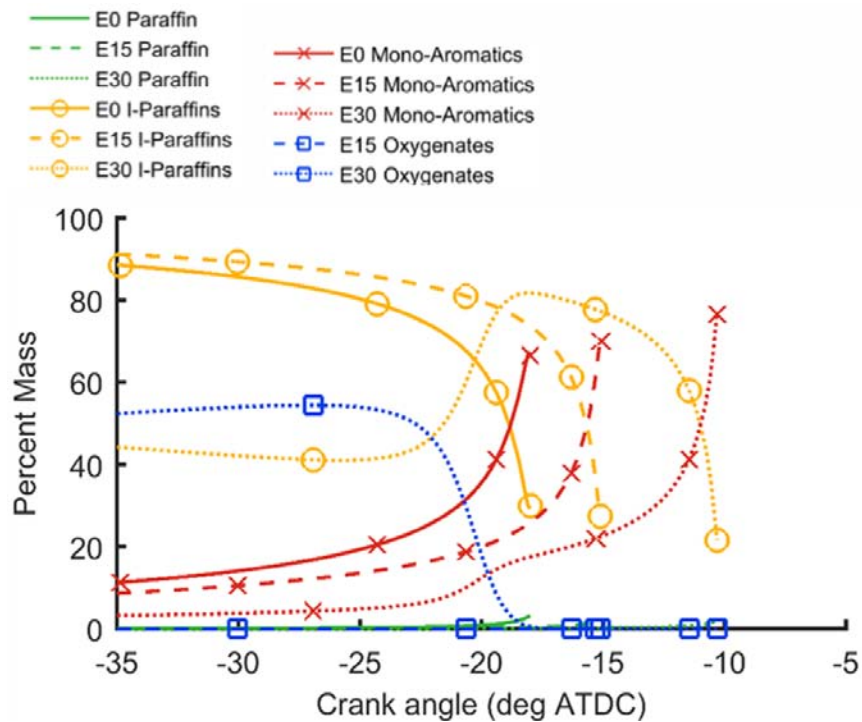


Figure II.7.6 - Modeled vapor phase concentrations of ethanol, paraffins, and aromatics from the surface of a droplet evaporating near the end of compression

aromatic concentration in the vapor phase at the end of evaporation and delays the aromatic evaporation. These observations raise the possibility of both locally fuel-rich combustion and aromatic-rich vapor when blending ethanol into gasoline, which may result in higher PM emissions.

Conclusions

Measurements of PM emissions were completed for a gasoline fuel matrix designed to test the hypothesis that high HOV fuel components, such as ethanol, can interact with co-blended low volatility aromatic hydrocarbons to increase PM beyond that predicted by the fuels' PMI. Key observations and conclusions include:

- Ethanol blending at 30 vol% can increase PM emissions relative to ethanol-free blends when:
 - Ethanol is co-blended with low volatility/high boiling aromatics, and
 - Match blending is used such that aromatics are not volumetrically diluted by ethanol, and
 - The engine operates at high speed and load, which reduces the time for evaporation and mixing, and increases the mass of fuel injected.
- Linear regressions of the dataset showed that ethanol and aromatic molar concentrations, as well as aromatic vapor pressure are statistically significant factors for predicting PM at Condition A.
- Ethanol blending both delays the evaporation of aromatics and increases the concentration of aromatics near the end of evaporation. It is not yet clear to what extent ethanol's ability to inhibit the evaporation of aromatics is the result of HOV charge cooling and consequent removal of available heat, or the result of non-ideal vapor-liquid equilibrium effects, or a combination of these effects.

References

1. Aikawa, K., T. Sakurai, and J.J. Jetter. "Development of a predictive model for gasoline vehicle particulate matter emissions." *SAE Int. J. Fuels Lubr.* 3(2):610–622. 2010. doi:10.4271/2010-01-2115.
2. Aikawa, K., and J.J. Jetter. "Impact of gasoline composition on particulate matter emissions from a direct-injection engine: Applicability of particulate matter index." *Int. J. Eng. Res.* 15(3):298–306. 2013. doi: 10.1177/1468087413481216.
3. Maricq, M.M., J.J. Szente, and K. Jahr. "The impact of ethanol fuel blends on PM emissions from a light-duty GDI vehicle." *Aerosol Sci. Technol.* 46 (5): 576–583. 2012. Burke, S.C., M.A. Ratcliff, R.L. McCormick, R. Rhoads, and B. Windom. "Distillation-based droplet modeling of non-ideal oxygenated gasoline blends: Investigating the role of droplet evaporation on PM emissions." SAE 2017-01-0581. SAE World Congress, April 2017.
4. He, X., J.C. Ireland, B.T. Zigler, M.S. Ratcliff, K.E. Knoll, T.L. Alleman, and J.T. Tester. "The impacts of mid-level biofuel content in gasoline on SIDI engine-out and tailpipe particulate matter emissions." SAE Techn. Pap. 2010. doi: 10.4271/2010-01-2125.
5. Fatouraie, M., M.S. Wooldridge, B.R. Petersen, and S.T. Wooldridge. "Effects of ethanol on in-cylinder and exhaust gas particulate emissions of a gasoline direct injection spark ignition engine." *Energy Fuels* 29: 3399–3412. 2015.
6. He, X., M.A. Ratcliff, and B.T. Zigler, B.T. "Effects of gasoline direct injection engine operating parameters on particle number emissions." *Energy Fuels* 26:2014–2027. 2012.
7. Butler, A.D., R.A. Sobotowski, G.J. Hoffman, and P. Machiele. "Influence of fuel PM index and ethanol content on particulate emissions from light-duty gasoline vehicles." SAE Technical Paper 2015-01-1072. 2015.

8. Storch, M., M. Koegl, M. Altenhoff, S. Will, and L. Zigan. "Investigation of soot formation of spark-ignited ethanol-blended gasoline sprays with single- and multi-component base fuels." *Applied Energy* **181**:278–287. 2016.
9. Coordinating Research Council. "Evaluation and Investigation of Fuel Effects on Gaseous and Particulate Emissions on SIDI In-Use Vehicles." CRC Report No. E-94-2. March 2017. https://creao.org/reports/recentstudies2017/E-94-2/CRC_2017-3-21_03-20955_E94-2FinalReport%20Rev1b.pdf
10. Ratcliff, M.A., J. Burton, P. Sindler, E. Christensen, G.M. Chupka, L. Fouts, and R.L. McCormick. "Knock resistance and fine particle emissions for several biomass-derived oxygenates in a direct-injection spark-ignition engine." *SAE Int. J. Fuels Lubr.* **9**(1):59–70. 2016. doi:10.4271/2016-01-0705.
11. Chupka, G.M., E. Christensen, L. Fouts, T.L. Alleman, M. Ratcliff, and R.L. McCormick. "Heat of vaporization measurements for ethanol blends up to 50 volume percent in several hydrocarbon blendstocks and implications for knock in SI Engines." *SAE Int. J. Fuels Lubr.* 2015. doi:10.4271/2015-01-0763.
12. Smith, B.L. and T.J. Bruno. "Improvements in the measurement of distillation curves. 3. Application to gasoline and gasoline + methanol mixtures." *Ind. Eng. Chem. Res.* **46**, 297–309. 2007.
13. Burke, S.C., M.A. Ratcliff, R.L. McCormick, R. Rhoads, and B. Windom. "Distillation-based droplet modeling of non-ideal oxygenated gasoline blends: Investigating the role of droplet evaporation on PM emissions." SAE 2017-01-0581. SAE World Congress, April 2017.

Key Fiscal Year 2017 Publications

1. Burke, S.C., M.A. Ratcliff, R.L. McCormick, R. Rhoads, and B. Windom. "Distillation-based droplet modeling of non-ideal oxygenated gasoline blends: Investigating the role of droplet evaporation on PM emissions." SAE 2017-01-0581. SAE World Congress, April 2017.
2. Burke, S., R. Rhoads, R. McCormick, M. Ratcliff, and B. Windom. "Measured and predicted vapor liquid equilibrium of ethanol-gasoline fuels with insight on the influence of azeotrope interactions on aromatic species enrichment and particulate matter formation in spark ignition engines." Submitted for SAE World Congress, April 2018.

II.8 Fuel Impacts on Emissions Control Performance and Durability

Todd J. Toops, Principal Investigator

Oak Ridge National Laboratory
2360 Cherahala Boulevard
Knoxville, TN 37932
E-mail: toopstj@ornl.gov

Kevin Stork, DOE Technology Manager

U.S. Department of Energy
E-mail: Kevin.Stork@ee.doe.gov

Start Date: October 1, 2016	End Date: September 30, 2018	
Total Project Cost: \$875,000	DOE share: \$875,000	Non-DOE share: \$0

Acknowledgments

Co-Authors

Josh A. Pihl, Sreshtha Sinha Majumdar, D. William Brookshear; Oak Ridge National Laboratory

Project Introduction

The overall objective of the Co-Optimization of Fuels and Engines Initiative (Co-Optima) is to cooperatively develop emerging high performance fuels and advanced engines to bring these technologies to the market sooner to realize a reduction in petroleum consumption. This project aims to investigate the compatibility of Co-Optima fuel candidates with emissions control systems and to identify opportunities for alternative emissions control strategies based on novel fuel chemistry. Specifically, this project is investigating the following questions.

- Is the catalytic reactivity of Co-Optima candidate fuel components sufficient to allow continued use of current emissions control technologies for both stoichiometric (light-duty) and lean operation (medium-duty/heavy-duty)?
- Do the Co-Optima candidate fuel components create opportunities for alternative low-cost lean exhaust emissions control strategies, such as alcohol selective catalytic reduction of NO over a silver-based catalyst (medium-duty/heavy-duty)?
- Does the process for creating and refining the candidate Co-Optima fuel components introduce trace level impurities into fuel blends that could poison emissions control catalysts (light-duty and medium-duty/heavy-duty)?

Objectives

- Develop mathematical terms that capture the impacts of changes in fuel composition on emissions control system performance and durability based on measurable fuel properties for inclusion in the Co-Optima merit functions
- Measure the specific fuel properties required to evaluate the emissions control merit function terms for Co-Optima blendstock candidates
- Identify and evaluate potential alternative emissions control strategies that exploit the unique chemistry of Co-Optima blendstock candidates

Approach

This research brings together targeted flow reactor studies and engine-based experiments to evaluate the compatibility of Co-Optima fuel candidates with emissions control systems and identify opportunities for

alternative emissions control strategies that make use of novel fuel chemistry. The synthetic exhaust gas flow reactor systems are designed to offer maximum flexibility to mimic exhaust conditions expected in application and further allow the exploration of the boundary conditions associated with the candidate emissions control systems. Great care has been taken to ensure the results from the flow reactors will correlate well with engine-based studies. The engine-based experiments rely on conventional commercial engines as well as simple genset-based engines for long-term aging efforts. Additionally, a comprehensive suite of materials characterization tools are employed as necessary to understand the impact of fuels and their trace constituents on the material properties of the emissions control system.

Results

Fiscal Year 2017 Accomplishments

- Developed an emissions control merit function term to quantify potential impacts of fuel composition changes on cold-start emissions of regulated pollutants (NO_x , non-methane organic gases, and CO) from light-duty spark ignition engines
- Successfully measured catalytic light-off temperatures of Co-Optima blendstock candidates and conventional petroleum-derived fuel components (30 organic compounds in total) over a hydrothermally-aged commercial three-way catalysts (TWC) to enable evaluation of the emissions control term in the light-duty merit function
- Identified trends in catalytic reactivity based on organic compound chemical structure, including effects on conversion of NO_x and CO

Modern light-duty vehicles with spark ignition engines operate at a nominally stoichiometric air–fuel ratio and utilize highly effective TWCs for removal of deleterious pollutants such as NO_x , non-methane organic gases, and CO to comply with the stringent emissions regulations. For efficient exhaust aftertreatment, the TWC should be at its optimum operating temperature. Below this temperature (cold-start), the aforementioned regulated pollutants are likely to slip out of the exhaust into the environment. To comply with the emissions regulations, the engine and emissions control system must be calibrated such that the cold-start period is minimized, and these harmful emissions are controlled at the earliest. Typically, during the cold-start period, the TWC is rapidly brought up to temperature by injecting additional fuel and delaying spark timing [1,2]. As the engine is not operating at its highest efficiency during the cold-start period to meet the emission standards, a fuel penalty is associated with such strategies. The magnitude of the fuel penalty incurred depends on the duration of the cold-start period, which in turn ties back to the temperature at which the pollutant species light-off on the TWC [1,2]. An expression was derived relating vehicle efficiency to catalytic light-off temperature, thus providing a means for quantification of fuel composition effects on cold-start emissions in terms of measurable fuel properties (Equation 1):

$$\text{merit} = 0.008^\circ\text{C}^{-1} (T_{C,90,\text{conv.}} - T_{C,90,\text{COB}}) \quad (1)$$

where $T_{C,90,\text{conv.}}$ and $T_{C,90,\text{COB}}$ are the temperatures at which 90% of the conventional fuel and the Co-Optima blend fuel are converted on the TWC, respectively. The constant term is estimated from the fractional increase in fuel consumption rate during cold start and the catalyst heating rate based on Federal Test Procedure cycle data of several vehicles [3].

In order to evaluate the emission control merit function, the catalytic light-off temperatures of 30 organic compounds (alkanes, alkenes, alcohols, ketones, esters, aromatic ethers, aromatic hydrocarbons), including Co-Optima fuel blendstocks and conventional petroleum-derived fuel components, were measured on a commercial TWC. The catalyst was a dual-zone TWC from a model year 2009 Chevrolet Malibu car. The catalyst was hydrothermally aged as per industry guidelines delineated in the U.S. DRIVE Low-temperature Oxidation Catalyst Test Protocol for 50 h under neutral/rich/lean cycles at 800°C [4]. The gas compositions for hydrothermal aging are detailed in Table II.8.1.

Table II.8.1 - Gas Composition for Hydrothermal Aging and De-Greening the Catalyst

Step	Mode	Duration (s)	Gas Composition (Balance N ₂)				
			[O ₂] %	[CO ₂] %	[H ₂ O] %	[CO] %	[H ₂] %
Hydrothermal aging	Neutral	40	-	10	10	-	-
	Rich	10	-	10	10	3	1
	Lean	10	5	10	10	-	-

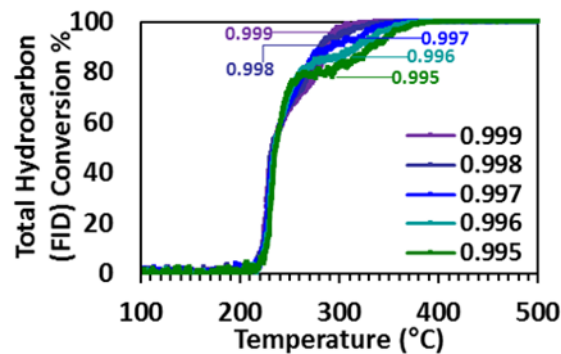
The fuel light-off measurements were carried out under synthetic engine exhaust conditions on an automated flow reactor system. A vapor delivery module was used to vaporize the liquid fuel components. The gas composition is shown in Table II.8.2. Each light-off run with the specific fuel component was repeated three times to make sure that the light-off behavior was reproducible.

Table II.8.2 - Synthetic Engine Exhaust Gas Composition

Step	Temperature	Gas Composition (Balance N ₂)						
		[O ₂] %	[CO ₂] %	[H ₂ O] %	[CO] ppm	[H ₂] ppm	[NO] ppm	[HC] ppm C ₁
Pretreatment	600°C	-	13%	13%	-	-	-	-
Gaseous HC Light-down	500–100°C	0.72%	13%	13%	5000	1670	1000	3000
Liquid HC Light-off	100–500°C	Varied to adjust λ	13%	13%	5000	1670	1000	3000

HC – hydrocarbons

A lambda (λ) sweep conducted on a baseline E10 surrogate fuel (230 ppm iso-octane, 138 ppm toluene, 100 ppm ethanol) by varying the O₂ concentration to adjust the λ showed that the highest total hydrocarbon conversion was achieved at $\lambda = 0.999$ (Figure II.8.1).



FID – flame ionization detector

Figure II.8.1 - Total hydrocarbon conversion as a function of temperature for an E10 surrogate fuel over a hydrothermally aged commercial TWC at lambdas ranging from 0.995 to 0.999

For all the fuels components investigated in this study, λ was kept constant at 0.999. Selected oxygenated and non-oxygenated hydrocarbon light-off curves representative of different functional groups (alcohols, ketones, esters, aromatic ethers, aromatic hydrocarbons, alkanes, and alkenes) shown in Figure II.8.2 revealed interesting trends associated with the type of hydrocarbon and its light-off behavior.

Considering the E10 surrogate as the baseline fuel, hydrocarbons that light off earlier than the E10 surrogate fuel are promising fuel blend candidates in terms of reactivity on existing emissions control technology (TWC) and are likely to meet the current emissions regulations with minimal modification to the existing exhaust aftertreatment architectures. A few key findings from Figure II.8.2 and Figure II.8.3 are highlighted in the following.

- Among the oxygenated fuels, the alcohols, linear ketones, and esters light-off earlier than the E10 surrogate fuel, but the aromatic ethers light-off after the E10 surrogate fuel and behave more like the non-oxygenated aromatic fuels.
- Non-oxygenated aromatic hydrocarbons light-off after the E10 surrogate fuel. Higher degrees of methyl substitution in the ring lead to higher light-off temperatures.
- Light-off behaviors of alkanes are structure sensitive. In the case of linear alkanes, increasing the number of carbon atoms in the chain lowers the light-off temperature. Furthermore, for the same number of carbon atoms, a straight chain alkane lights off earlier than a branched alkane. Cycloalkanes, on the other hand, are not significantly affected by the number of carbon atoms and demonstrate comparable light-off behavior.
- Alkene light-offs are also structure sensitive. However, the trends observed in alkenes are opposite to those observed in alkanes. In the case of linear alkenes, increasing the number of carbon atoms results in higher light-off temperatures. For the same number of carbon atoms, a straight-chain alkene lights off after a branched alkene.

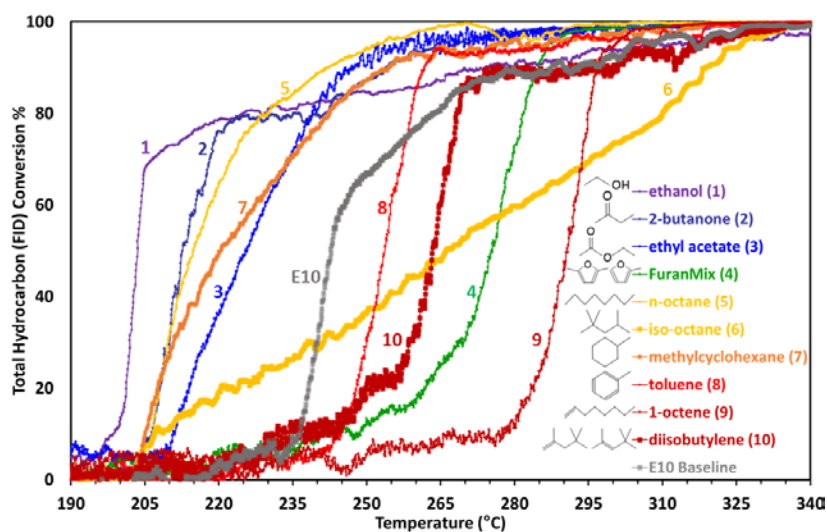
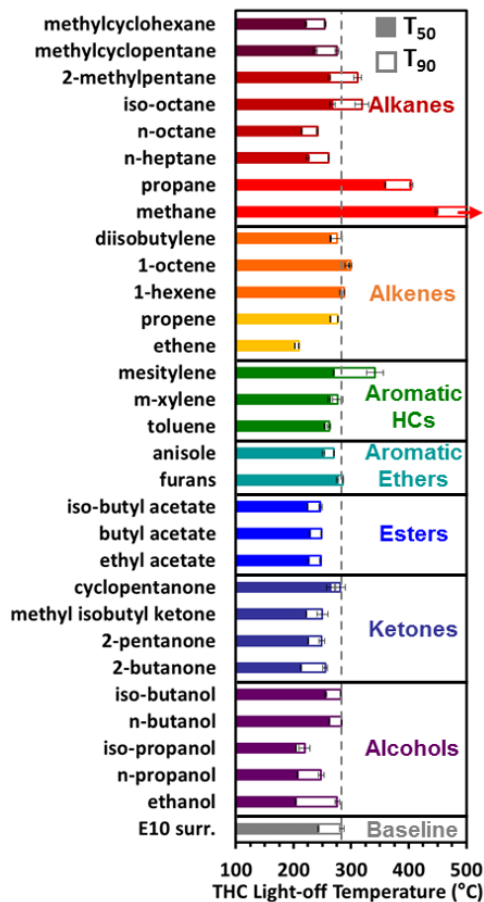


Figure II.8.2 - Comparison of total hydrocarbon conversion light-off curves over a hydrothermally aged commercial TWC for selected fuel components representative of alcohols (ethanol), linear ketones (2-butanone), esters (ethyl acetate), aromatic ethers (FuranMix: 2-methylfuran, 2,5-dimethylfuran), alkanes (n-octane, iso-octane, methylcyclohexane), aromatic hydrocarbons (toluene), and alkenes (1-octene, diisobutylene)

The effects of fuel light-off on other regulated pollutants such as CO and NO_x were also investigated. From the T₅₀s and T₉₀s for CO shown in Figure II.8.4, it can be observed that all the fuels under consideration fall under two main categories: (1) no significant impact on CO light-off and (2) inhibition of CO light-off. Alcohols with two or three carbons, esters, linear and branched ketones, and alkanes fall into the former category, while cycloketones, aromatic ethers, aromatic hydrocarbons and alkenes fall into the latter category. The CO inhibition is likely due to the formation of strongly adsorbing intermediates on the surface of the catalyst competing for the CO active sites. The NO_x T₉₀ trends across the fuels, however, follow the T₉₀ trends for the hydrocarbon light-off. As the experiments are conducted at nearly stoichiometric conditions, high NO_x conversions can only be achieved when the hydrocarbons are completely reacted.

Real world fuels are multi-component blends of hydrocarbons. Preliminary analysis involving a simple linear combination of the hydrocarbon conversions of ethanol, toluene and iso-octane to predict the light-off behavior of the E10 surrogate fuel blend exposed differences between the predicted light-off profile of the E10 surrogate fuel and its measured one. In order to improve the accuracy of the predicted light-off behavior of multi-component blends, complex chemical interactions with the catalyst surface along with any thermal effects need to be accounted for. Therefore, future work will entail additional experiments to capture these effects to accurately predict the light-off behavior of blends from their individual components.



T₉₀ – temperature at which a catalyst achieves 90% conversion of a particular species

T₅₀ – temperature at which a catalyst achieves 50% conversion of a particular species

Figure II.8.3 - Comparison of T₅₀ and T₉₀ total hydrocarbon light-off temperatures over the hydrothermally aged commercial TWC for all of the fuel components investigated. Error bars represent 95% confidence intervals calculated from three replicate runs.

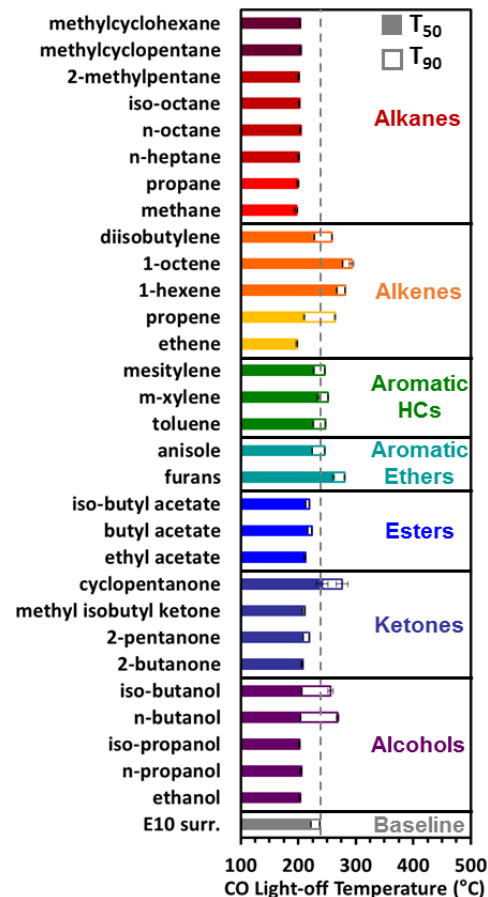


Figure II.8.4 - Comparison of T₅₀ and T₉₀ CO light-off temperatures over the hydrothermally aged commercial TWC for all of the fuel components investigated. Error bars represent 95% confidence intervals calculated from three replicate runs.

Conclusions

- A merit function explicitly capturing the effect of fuel composition changes on cold-start emissions from light-duty vehicles with spark ignition engines has been developed.
- Light-off temperatures of 30 organic compounds, including Co-Optima blendstock candidates and conventional petroleum derived fuel components, have been measured on a commercial three-way catalyst.
 - Reactivity of hydrocarbons on the TWC is strongly affected by functional groups.
 - Oxygenated hydrocarbons, with the exception of cycloketone and aromatic ethers, light-off earlier than the baseline E10 surrogate fuel.
 - Non-oxygenated hydrocarbon light-off on the TWC is sensitive to chemical structure (number of carbon atoms, branching vs. linear, number of alkyl groups substituted in the aromatic ring).
 - Regulated pollutants such as NO_x and CO are also impacted by changes in fuel composition.
- Ongoing work is focused on measuring and predicting the light-off temperatures of fuel blends.

References

1. Anderson, J., E. Rask, H. Lohse-Busch, and S. Miers. "A Comparison of Cold-Start Behavior and its Impact on Fuel Economy for Advanced Technology Vehicles." *SAE Int. J. Fuels Lubr.* 7(2), 2014. doi:10.4271/2014-01-1375.
2. Kessels, J.T.B.A., D.L. Foster and W.A.J. Bleuanus. "Fuel Penalty Comparison for (Electrically) Heated Catalyst Technology." *Oil & Gas Science and Technology – Rev. IFP*, Vol. 65, No. 1, pp. 47–54, 2010.
3. Pihl, Josh, John Thomas, Sreshtha Sinha Majumdar, Shean Huff, Brian West, and Todd Toops. "Development of a Cold Start Fuel Penalty Metric for Evaluating the Impact of Fuel Composition Changes on SI Engine Emissions Control." SAE Technical Paper Series, submitted 2017.
4. U.S. DRIVE ACEC Tech Team Low Temperature Aftertreatment Working Group. "Aftertreatment Protocols for Catalyst Characterization and Performance Evaluation: Low Temperature Oxidation Catalyst Test Protocol." 2016. www.cleers.org/acec-lowt/

Key Fiscal Year 2017 Publications

1. Pihl, Josh, John Thomas, Sreshtha Sinha Majumdar, Shean Huff, Brian West, and Todd Toops. "Development of a Cold Start Fuel Penalty Metric for Evaluating the Impact of Fuel Composition Changes on SI Engine Emissions Control." SAE Technical Paper Series, submitted 2017.

II.9 Fuel Impact on GDI PM Formation and Gaseous Emissions During Cold-Start

Melanie Moses-DeBusk, Principal Investigator

Oak Ridge National Laboratory
1 Bethel Valley Rd.
Oak Ridge, TN 37831-6472
E-mail: mosesmj@ornl.gov

Kevin Stork, DOE Technology Manager

U.S. Department of Energy
E-mail: Kevin.Stork@ee.doe.gov

Start Date: October 1, 2016	End Date: September 30, 2017	
Total Project Cost: \$188,000	DOE share: \$188,000	Non-DOE share: \$0

Acknowledgments

Co-Authors

John Storey, Samuel Lewis, Sr., R. Maggie Connatser, Shean Huff, Eric Nafziger;
Oak Ridge National Laboratory

Project Introduction

To enable new and emerging Co-Optima fuels, it is critical to evaluate their impact on emissions and compatibility with vehicle technologies. This effort investigates the effects of fuel chemistry on emissions and the functionality of the emissions control systems to identify potential challenges as well as opportunities created by new fuel compositions. The overall objective of Co-Optima is to cooperatively develop emerging high performance fuels and advanced engines to bring these technologies to the market sooner to realize a reduction in petroleum consumption.

The key focus of this project was particulate matter (PM) and gaseous hydrocarbon (HC) emissions from spark-ignited gasoline direct injection (GDI) engines. The emissions from GDI engines can be affected by oxygenated HC in the fuel; the aromatic nature of the fuel, including that of any bio-fuel added as well as the base blendstock fuel; and the specifics of the combustion and emissions control strategies. The project activity focus is to assess the impacts of candidate Co-Optima high performance fuel blendstock on the generation and composition of PM emissions from GDI engines. In Fiscal Year 2017, fuel blend choices focused on determining how well the PM Index (PMI) [1] term can accurately capture the trend of different bio-blendstock functional groups on PM production. The Co-Optima team has developed a merit function for evaluation of the impact of fuel composition on spark-ignited engine performance. The PM control term within the merit function is based on the fuel penalty associated with particulate filter backpressure, and is “turned on” at a PM threshold at which a particulate filter aftertreatment strategy would be required to meet emissions regulations. This PM threshold is represented in the control term by the PMI of the fuel, so it is important to establish the accuracy of the PMI calculation in predicting PM emissions for a wide range of fuel chemistries that were not evaluated in earlier work on the PMI. Studies this fiscal year focused specifically on cold-start PM emissions, which are the major contributors to overall PM production in spark-ignited GDI engines.

Objectives

- Demonstrate effectiveness of the PMI to predict trends in PM production for oxygenated fuel blends during cold-start operation in a GDI engine
- Quantify how changes in the oxygenate functionality of high performance fuel blendstocks impact PM production using cold-start PM emissions as the criteria

Approach

The experimental approach was designed to study the impact of different chemistry on PM production and characteristics. GDI engines generate the most exhaust PM under fuel-rich conditions, typical of start-up and acceleration. A cold-start has been shown repeatedly to produce an order of magnitude more PM than the same fuel-rich startup when the engine is already warmed up (hot-start). Since cold-start is responsible for the majority of PM mass emissions generated during the regulated Federal Test Procedure (FTP) test cycle, PM production from a series of fuels during an initial 90-s cold-start transient was used to study the fuel impact. A forced-cooled 2.0-L GDI engine on a mobile cart (known as the Oak Ridge National Laboratory start-cart) enabled multiple cold-start transient measurements per day, allowing for calculations of statistical confidence levels in the data.

The base fuel into which high performance oxygenated fuel components are blended is known as a blendstock for oxygenate blending (BOB). The BOB used in our fuel series was the same BOB used in the Co-Optima E30 base fuel, which has been used for combustion and fuel properties studies at other laboratories participating in the Co-Optima initiative. Three high performance fuel components were selected for this study from a list of promising high-performance fuel components identified by the Co-Optima team during the first quarter of Fiscal Year 2017. The three high performance fuel components (3-pentanone, methyl isobutyrate, methoxybenzene) were all oxygenated hydrocarbons with the same Research Octane Number values. The high performance fuel components were blended into the BOB at 20 vol%, and since it is anticipated that future fuels for spark-ignited engines will also contain ethanol (EtOH) at 10 vol% (E10), EtOH was also splash-blended into the fuel blend. These three fuel blends were also compared to 30 vol% ethanol (E30) and E10 fuel blends along with the BOB-only fuel for a total comparison of six fuels. All five oxygenated fuel blends were made by splash-blending with the same batch of BOB. PM samples were collected on triplicate filters with PM from six cold-starts on each. The filters were for mass and chemical composition analysis. Online instruments provided real-time analysis of particle size distributions and dry-soot mass measurements.

Results

- Demonstrated ~50% drop in PM mass during cold-start by blending 30 vol% of non-aromatic, oxygenated high performance fuel components regardless of the oxygen-containing functional group (alcohol, ketone, ester or ether)
- Demonstrated that the fuel PMI predicted trends for PM mass production during GDI cold-start for oxygenated fuel blends
- Established that the linearity and magnitude of the PMI predicted trend were dependent on how the PM mass was measured, with strong linear correlation to soot carbon or elemental carbon; inclusion of organic carbon (part of total PM mass that is regulated) resulted in poorer correlation to PMI

A GDI engine PM and gaseous HC emission sampling campaign was successfully completed this fiscal year on a series of six Co-Optima related fuel blends. Since most of the PM produced by a GDI engine is generated during cold-start, Oak Ridge National Laboratory's forced-cooled start-cart was used to study emissions during the first 90 s of an engine cold-start transient. The three oxygenated Co-Optima bio-fuel candidates (including EtOH) were chosen with different oxygenate functional groups in an effort to isolate any impact of the oxygenate functional group. Table II.9.1 summarizes the composition of each of the six fuels (ether = methoxybenzene; ketone = 3-pentanone; ester = methyl isobutyrate; alcohol/E30 = ethanol).

Table II.9.1 - Fuel Blend Naming and Splash-Blending Volumetric Composition

Fuel Blend Name	vol% BOB	vol% EtOH	vol% Bio-oxygenate
BOB	100%	—	—
E10	90%	10%	—
E30	70%	10%	20% Ethanol
Ester	70%	10%	20% Methyl Isobutyrate
Ketone	70%	10%	20% 3-Pentanone
Ether	70%	10%	20% Methoxybenzene

PM mass measurements were made by three methods: (1) gravimetric mass measurement on a Teflon™ membrane filter (Teflo) similar to Environmental Protection Agency regulatory procedures, (2) PM elemental and organic carbon from collection on a quartz fiber filter and subsequent analysis with the thermo-optical NIOSH method, thermal-optical measurement from PM collection on a quartz fiber filter measured contribution from elemental carbon and organic carbon (EC/OC) following the NIOSH method, and (3) real-time photoacoustic measurements of soot carbon aerosol by a microsoot sensor (MSS). The gravimetric (Teflo) and thermal-optical measurements (EC/OC), which include the PM mass associated with semi-volatile HCs that are adsorbed on PM soot particles, are reported as the average of triplicate filters that each contained PM from six cold-starts. The real-time MSS measurements are reported as averages of 18 cold-starts for each fuel blend. Figure II.9.1 compares the quantitative mass measurements from each method and shows the strong agreement between the gravimetric and thermal-optical measurements (Teflo and EC/OC) and lower corresponding soot carbon mass measurement by the photoacoustic method (MSS). The non-aromatic 30% oxygenate fuel blends averaged between ca. 16 to 21 mg PM emitted by the engine during each 90 s cold-start transient with the lowest coming from E30. These emissions represent a 50% reduction in PM compared to E10 for all methods. Although the E10 fuel blend used in this study was not certification fuel, MSS measurements on the Oak Ridge National Laboratory start-cart using an E10 certification fuel indicated similar mass values. The ether high performance fuel component, (methoxybenzene, also known as anisole), generated more PM per cold-start by all measurement methods than the BOB and E10 even though it contained 30 vol% oxygenated fuel. Methoxybenzene contains a simple ether attached to a benzene ring. The soot-forming tendencies of the aromatic benzene ring prevailed over the benefits typically seen of oxygenated fuel blends for reducing PM production. The increased PM mass associated with this bio-fuel blend was accurately predicted by its PMI value, supporting the assignment of the increased PM mass to the aromatic chemistry rather than the ether chemistry of the oxygenated component.

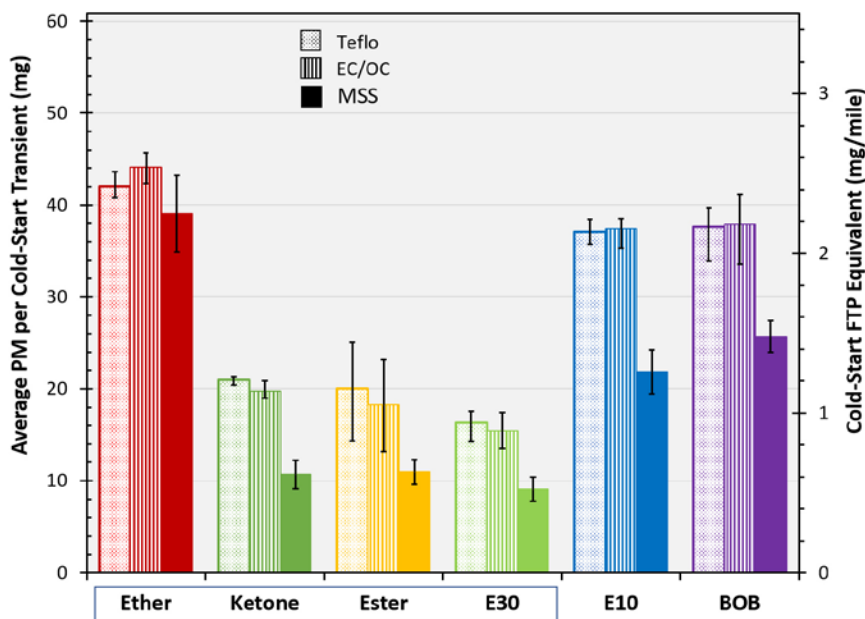


Figure II.9.1 - Six fuels, including the BOB and five bio-fuel blends, were tested for PM mass emissions on a GDI engine during a 90-s cold-start transient. The average mass measurements can be viewed in terms of mass per 90-s cold-start transient (left axis) or in terms of a cold-start FTP equivalent mass per mile (right axis). The gravimetric (Teflo; dot pattern) and thermal-optical (EC/OC; vertical line pattern) mass measurements have min/max error bars and the photoacoustic (MSS; solid pattern) has standard deviation error bars. The box around the fuel names (see Table II.9.1) indicates the 30 vol% oxygenated fuel blends.

PM mass correlations with fuel PMI are shown in Figure II.9.2. The difference between the Teflo and MSS mass data can be attributed to semi-volatile HCs of the PM that cannot be detected by the MSS' photoacoustic measurement method. The trend shown by the MSS measurements shows a more linear correlation with PMI

than the total PM mass. When the EC/OC (thermal-optical) measurement, which matches closely with the gravimetric total PM mass, is split into its elemental carbon and organic carbon fractions and plotted against PMI, the deviation from the linear correlation to PMI can be attributed to its organic carbon fraction. The organic carbon fraction measured by the thermal-optical measurement is typically attributed to semi-volatile HCs, which are not captured by the photoacoustic measurement method of the MSS. The good correlations allow prediction of cold-start PM mass trends for the six fuels based on PMI, regardless of chemical composition.

The right Y-axis in both Figures II.9.1 and II.9.2 shows how the fuels tested in this study correlate to mass per mile in regard to an FTP equivalent. The current U.S. Environmental Protection Agency PM emissions regulation for GDI vehicles is 3 mg/mi. However, the California Air Resources Board is pushing to move that to 1 mg/mi phase-in starting with Model Year 2025 as indicated by the blue dash arrow in Figure II.9.2. While the cold-start transient is one of the largest PM emission contributors during the FTP cycle used in emission regulations, more PM will be generated throughout the remainder of the test cycle. The results shown in Figure II.9.2 reinforces the need to account for all of the PM mass as regulatory limits get lower and lower. On-line measurements, such as the MSS and smoke meters, used in engine development typically do not measure the OC portion of the PM, and can thus lead to false conclusions about PM emission levels.

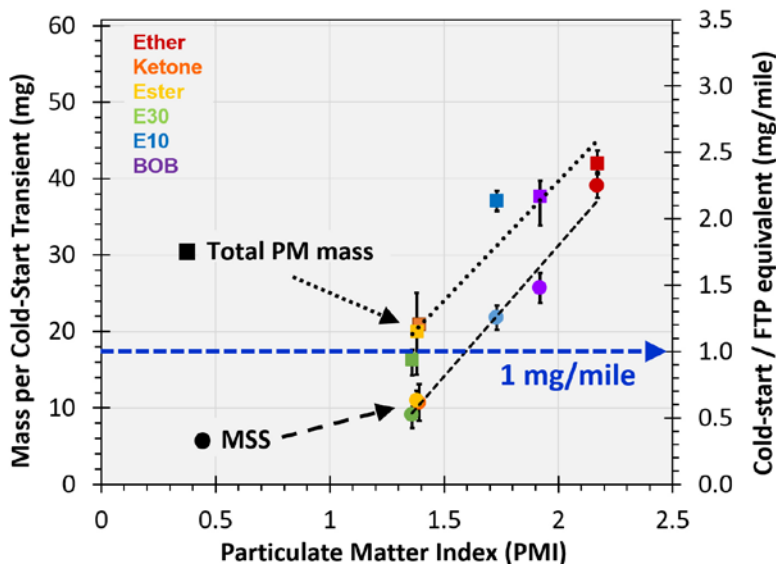


Figure II.9.2 - Six fuels, including the BOB and five bio-fuel blends, were tested for PM mass emissions on a GDI engine. All five fuels were at or above the California Air Resources Board's 1 mg/mi gravimetric mass target (blue dashed line) for the FTP combined cold- and hot-start cycle during the 90-s cold-start transient. The difference in the graph's two-plot series, Total PM and Dry-Soot, indicates the amount of semi-volatile PM mass that was counted in a gravimetric mass measurement (Total PM, squares), but not measured by an online Micro Soot Sensor (circles). The six fuels are BOB (purple), E10 (blue), E30 (green), ester (yellow), ketone (orange), and ether (red).

Conclusions

The GDI cold-start PM emission study demonstrated that splash-blending of 30 vol% oxygenated high performance fuel components reduced PM mass emission by ca. 50% regardless of the oxygenate functional group chemistry unless the oxygenated component also had aromatic properties. The study also demonstrated that the trend in PM mass measurements for a set of fuels can be predicted by the fuels' PMI values even for oxygenated fuels. However, the study suggested that as the fraction of semi-volatile HCs in PM increases, the ability of the PMI to predict GDI PM mass trends is diminished.

References

1. Aikawa, K., T. Sakurai, and J. Jetter. *SAE Int. J. Fuels Lubr.* 3(2):610–622, 2010, doi:10.4271/2010-01-2115.

Key Fiscal Year 2017 Publications

1. Moses-DeBusk, M., J. Storey, S. Lewis, S. Huff, J. Thomas, and E. Nafziger. “Fuel and Lubricant Impacts on GDI Cold-Start Particulate.” Oral presentation at 2017 CLEERS Workshop, October 3–5, 2017, Ann Arbor, MI.
2. Toops, Todd J., Lyle Pickett, Chris Powell, Bob McCormick, Matt Ratcliff, John Storey, Melanie DeBusk, Josh Pihl, William Brookshear, and Sreshtha Majumdar. “Co-Optimization of Fuels and Engines (Co-Optima): Emissions, Emission Control, and Sprays.” DOE Annual Merit Review, June 2017, available at https://energy.gov/sites/prod/files/2017/06/f34/ft057_toops_2017_o.pdf
3. Storey, J.M., M. Moses-DeBusk, S. Lewis, E. Nafziger, and S. Huff. “Biofuel Effects on PM Mass, Composition, and Size during GDI Cold Start Events.” 2017 AEC MOU Meeting, Dearborn, MI. August 2017.
4. Storey, J.M., M. Moses-DeBusk, S. Lewis, S. Huff, E. Nafziger, V. Prikhodko, and J. Parks. “Exhaust Particle Emissions from Gasoline Engines: Characterization and Approaches to Filtration.” 2017 Advanced Filtration Technologies Conference, American Filtration and Separations Society, Louisville, KY. April 2017.

II.10 Fuel Contribution to PM from Kinetically-Controlled Combustion

John M.E. Storey, Principal Investigator

Oak Ridge National Laboratory
1 Bethel Valley Rd., MS 6472
Oak Ridge, TN 37831-6472
E-mail: storeyjm@ornl.gov

Samual A. Lewis, Principal Investigator

Oak Ridge National Laboratory
1 Bethel Valley Rd., MS 6472
Oak Ridge, TN 37831-6472
E-mail: lewissar@ornl.gov

Kevin Stork, DOE Technology Manager

U.S. Department of Energy
E-mail: Kevin.Stork@ee.doe.gov

Start Date: October 1, 2016	End Date: September 30, 2017	
Total Project Cost: \$150,000	DOE share: \$150,000	Non-DOE share: \$0

Acknowledgments

Co-Authors

Melanie M. DeBusk, Raynella M. Connatser; Oak Ridge National Laboratory

Project Introduction

To enable new and emerging Co-Optima fuels to displace petroleum, it is critical to evaluate their impact on emissions and compatibility with vehicle technologies. This effort investigates the effects of fuel chemistry on emissions and the functionality of the emissions control systems to identify potential challenges as well as opportunities created by new fuel compositions.

The key focus of this project is particulate matter (PM) and gaseous hydrocarbon (HC) emissions from Co-Optima spark-ignited/advanced compression ignition (SI/ACI) engines, which are broadly characterized as having kinetically-controlled combustion processes. The project activity focus is to assess the impacts of base fuel and Co-Optima blend stocks on the generation and composition of gaseous and PM emissions from ACI engines, and the potential strategies and barriers for the mitigation of the emissions with emissions controls. Although ACI engines can have high thermal efficiency, they typically suffer from poor combustion efficiency, leading to excess HC emissions. The research is focused on improving methods for collecting and quantifying the exhaust components that contribute to the measured PM mass.

The engine that will be used is a 1.9-L light-duty diesel modified with the addition of port fuel injection for low reactivity fuels. The engine can operate in both reactivity controlled compression ignition with two fuels and in partially premixed compression ignition with one fuel. The different properties and functional groups of the Co-Optima fuel blends may impact the formation of the semi-volatile HC phase that contributes greatly to PM mass from ACI engines, so the direct effects of these compounds on PM will be identified. Because the biofuel components are primarily oxygenated, new analytical methods were developed this year to identify PM-associated HC species that are not amenable to standard analysis by gas chromatography–mass spectroscopy.

Objectives

To enable new and emerging Co-Optima fuels to displace petroleum, it is critical to evaluate their impact on emissions and compatibility with vehicle technologies. This effort investigates the effects of fuel chemistry

on emissions and the functionality of the emissions control systems to identify potential challenges as well as opportunities created by new fuel compositions.

Approach

This project utilizes the core capabilities of the Analytical Chemistry Laboratory and the multi-cylinder engine combustion laboratory at ORNL National Transportation Research Center to identify the constituents of PM produced by SI/ACI combustion. Mixing controlled combustion processes, like diesel combustion, produce PM that is largely soot carbon with between 10–30% HC compounds associated with the soot. In contrast, PM from SI/ACI combustion is largely organic with almost no soot carbon [1]. Because of this, SI/ACI PM can no longer be measured with on-line measurements such as a smoke meter or microsoot sensor. The PM mass from these combustion modes arises from condensation of low volatility organic compounds on the sampling filter media.

The use of biofuels in Co-Optima requires analytical methods to identify oxygenated combustion products. Highly oxygenated HC species are not amenable to traditional extraction methods used to determine the soluble organic fraction. Furthermore, these products are typically very polar, and thus will decompose and/or stick to the gas chromatograph column, resulting in no detection. In this study, ORNL developed a method for the extraction and analysis of oxygenated compounds from PM using polar solvents and capillary electrophoresis–mass spectroscopy for detection. These methods can be applied to PM collected from SI/ACI combustion, and thus provide insight into the combustion byproducts of Co-Optima fuels.

Results

PM was collected from a cooler used in an exhaust gas recirculation system. Approximately 20 mg of soot was extracted with a mixture of methanol and ammonium hydroxide (NH_4OH). The extraction method results in the formation of ions of oxygenated species. Capillary electrophoresis–mass spectroscopy is ideally suited to analyze these complex ionic species. Only 20 nL of the sample is required for injection, so the excess solvent load is minimized. Capillary electrophoresis has high separation efficiency, and the ion trap mass spectroscopy has high sensitivity.

Figure II.10.1 illustrates a map of the oxygenated species from the soot. The colored bars are individual compounds where the color of the bars represent the signal intensity of a given compound. The Y-axis

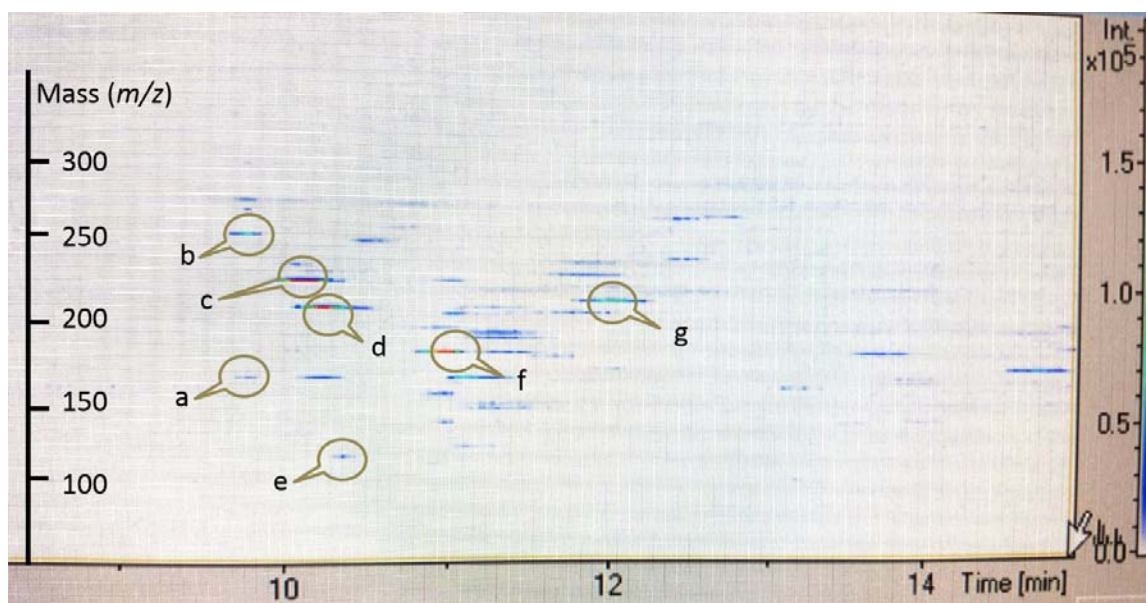


Figure II.10.1 - Three-dimensional chromatogram of ionic species extracted from soot. Each color band represents a compound and the amount of the compound is represented by the color with red being the highest concentration. The circled compounds are identified in Table II.10.1.

represents the mass and the X-axis is retention time. Table II.10.1 identifies several of the compounds which are carboxylic acids with various substituted groups.

Table II.10.1 - Polar Species Identified in Collected Soot

Identifier	Compound Name	Retention Time (min)	Mass
a	decanoic acid	8.9	171
b	benzene tetracarboxylic acid	9.8	253
c	tetradecenoic acid	10.1	225
d	hydroxy-formyl-benzene dicarboxylic acid	10.2	209
e	maleic acid	10.4	115
f	hydroxy-benzene dicarboxylic acid	11.0	189
g	naphthalene dicarboxylic acid	12.1	215

Conclusions

ORNL has been developing methods for extracting, analyzing and identifying polar species in engine PM. As biofuels and other oxygenated compounds are incorporated into Co-Optima investigations of SI/ACI combustion, these methods will be critical for identifying combustion products and partial oxidation products of the new fuels. In addition, identifying the combustion products can provide feedback to combustion simulations to assist in improving the combustion efficiency of the SI/ACI processes.

References

1. Storey, J.M., S. Curran, S. Lewis, T.L. Barone, A.B. Dempsey, M. Moses-DeBusk, R.M. Hanson, V.Y. Prikhodko, and W.F. Northrop. "Evolution and current understanding of physicochemical characterization of particulate matter from reactivity controlled compression ignition combustion on a multi-cylinder light-duty engine." *International Journal of Engine Research*, 2016. doi:10.1177/1468087416661637

II.11 Ignition Kinetic Experiments and Simulations to Support Advanced Engine Combustion Development

Brad Zigler, Principal Investigator

National Renewable Energy Laboratory
15013 Denver West Parkway
Golden, CO 80401
E-mail: brad.zigler@nrel.gov

Kevin Stork, DOE Technology Manager

U.S. Department of Energy
E-mail: Kevin.Stork@ee.doe.gov

Start Date: October 1, 2016	End Date: September 30, 2017	
Total Project Cost: \$550,000	DOE share: \$550,000	Non-DOE share: \$0

Acknowledgments

Co-Authors

Jon Luecke, Drew Cameron, Riley Abel, Greg Bogin Jr., Matt Ratcliff; National Renewable Energy Laboratory

Project Introduction

Co-development of new, high performance fuel chemistries and high efficiency internal combustion engines requires fast, accurate numerical simulation of critical processes to evaluate the interaction between fuel ignition behavior and advanced combustion strategies. These numerical simulations rely on accurate computational fluid dynamics (CFD) linked with chemical kinetic mechanisms to predict ignition and combustion performance. Since fuel composition is complex, chemical mechanisms are based on surrogate compounds frequently found in representative blends. Simulation efficiency also typically requires the use of significantly reduced versions of kinetic mechanisms.

Development of these reduced, yet accurate, chemical kinetic mechanisms is enabled by experimental input data and validation through a range of devices, including shock tubes, rapid compression machines, flow reactors, and constant volume combustion chambers (CVCCs). Experimental measurements are especially important to highlight and validate ignition performance when combining kinetic mechanisms for different chemical classes to represent a fuel blend. Novel fuel blending components can affect ignition performance in non-linear and varying antagonistic or complimentary degrees over temperature, pressure, and equivalence ratio space. Fuel kinetic mechanism development and validation therefore benefits from experimental mapping of ignition delay (ID) performance of fuel blends over engine-relevant parametric space. These experimental parametric maps of ID may also be used in simplified engine simulations to provide rapid screening predictions of engine performance with complex fuel blends for which kinetic mechanisms have not yet been developed. Since they utilize the same experimental research tasks and are tightly integrated, this project report combines reporting for both the development of ID data for kinetic mechanism development (\$250,000) and the integration of those data in spark ignition engine autoignition studies (\$300,000).

Objectives

- Develop experimental and simulation tools to characterize fuel ignition behavior in support of advanced combustion engine development for both spark ignition and compression ignition
- Support the development of research fuels, surrogates, and blends, and related reduced kinetic mechanisms to further enable co-development of advanced combustion engines and high performance fuels
- Link bench-scale CVCC-based fuel ignition measurements to single-cylinder research engine studies to enable rapid predictive feedback of engine performance for complex fuel blends

- Develop an understanding of fuel chemical and physical properties that enable furtherance of the DOE Co-Optima program research and development program for co-optimization of high performance fuels and high efficiency engines

Approach

National Renewable Energy Laboratory's (NREL's) ignition kinetics research is historically built on continual development and modification of the ignition quality tester (IQT) as a flexible research platform, both for experiments and as a simulation platform for evaluating kinetic mechanisms against experimental data [1,2,3,4,5]. The IQT is a CVCC apparatus with a spray injection system designed for direct measurement of the ID of liquid fuels under engine-relevant temperatures and pressures. In Fiscal Year 2017, NREL spent significant effort to transition most of its bench-scale ignition kinetics research to a newer (internally funded) CVCC platform, the Advanced Fuel Ignition Delay Analyzer (AFIDA) [6]. NREL's AFIDA is a more flexible CVCC research platform than the IQT, covering a broader range of pressures (up to 5 MPa) and temperatures (up to 1,000 K) with a high pressure fuel injection system that significantly reduces the spray physics effects timescales to enable greater focus on the chemical kinetics portion of ID. NREL also initiated development of a CFD model for the AFIDA to utilize with experimental data as part of the kinetic mechanism development feedback loop. NREL also commissioned a third CVCC platform in Fiscal Year 2017, the Fuel Ignition Tester to provide complementary standard derived cetane number measurements [7].

Fiscal Year 2017 research on gasoline-range fuels leveraged NREL's prior development of novel techniques to conduct ID studies over temperature sweeps at various fixed pressures, which are now used by other IQT users. The focus on gasoline-range fuels supported SI engine development, as well as other advanced strategies such as gasoline compression ignition. Inherently longer ID times typical of gasoline-range fuels allowed better mixing, reduced spray physics to affect only a small portion of the overall ID (focusing more on chemical kinetics dominated ID), and enabled studies at higher pressures relevant to engine operation. As a result, NREL's modified IQT and AFIDA produced engine-relevant ignition kinetic data for gasoline-range compounds and blends filling data voids and overlapping some conditions covered by rapid compression machines and shock tubes. Fiscal Year 2017 research focused on primary reference fuels (PRFs), toluene reference fuels (TRFs), and toluene standardization fuels (TSFs), all blended with various renewable fuel compounds, including Co-Optima Thrust 1 candidates [8]. NREL also developed a modified Livengood–Wu zero-dimensional (0D) knock integral model [9] with parametric experimental ID data to compare autoignition kinetics-based knock limit versus load and temperature to experimental engine data collected in Fiscal Year 2016. This comparison will help reveal the extent to which octane index captures the true temperature and pressure response of ignition delay for a broad range of functional groups.

NREL's approach includes strong collaboration, including a faculty joint appointment from Colorado School of Mines (Prof. Greg Bogin), a faculty sabbatical collaborative appointment from the University of Michigan (Prof. André Boehman), a graduate student intern from the University of Colorado Boulder (Drew Cameron), and an undergraduate student intern from Metropolitan State University of Denver (Riley Abel) tied to this research. NREL is sharing ID data with other researchers and has been active in applying these techniques to fuel samples shared from other DOE laboratory and industry partners, including a Coordinating Research Council Advanced Vehicles, Fuels, and Lubricants (AVFL) project known as AVFL-30 [10]. Experimental data and CVCC simulations with kinetic mechanisms under development are also shared in close collaboration with Lawrence Livermore National Laboratory. These collaborations are critical to integrating IQT- and AFIDA-based data as part the development feedback loop for kinetic mechanisms, correlating temperature and pressure parametric ID sweeps to engine studies, and developing the potential for simple CVCC techniques to provide faster screening and ignition performance insight for biofuel candidate blends.

Results

Advanced Fuel Ignition Delay Analyzer

NREL spent much of Fiscal Year 2017 characterizing, adapting, modeling, and utilizing the recently acquired AFIDA for a wide range of fuel ignition studies. Currently the only research type AFIDA outside of Europe, NREL's AFIDA, like other similar CVCCs, was originally designed for standardized measurement of ignition

reactivity with diesel-range fuels but with greater pressure and temperature capability and control than the IQT. The AFIDA uses a fuel pump adapted from high-performance liquid chromatography which holds fuel at very high pressure (120 MPa), avoiding experimental limitations in the IQT tied to low boiling point fractions of gasoline blends boiling before injection. Using a modern piezo-electric diesel fuel injector, the AFIDA's fuel injection system is capable of varying dynamically to hold a constant equivalence ratio across a temperature sweep and also significantly increases mixing and reduces the portion of ID tied to spray physics, greatly increasing focus on chemical kinetics ID. The AFIDA is equipped with a 16-place autosampling carousel with fuel sample heating and cooling capability. NREL extensively characterized the AFIDA for air charge filling over its wide range of pressures and temperatures, as well as calculating fuel mass injection control. Extensive consideration was given to defining the appropriate ID over a range of fuels and test conditions highlighting separation of low-temperature heat release. Working in close collaboration with NREL's Co-Optima Toolkit and Simulation development effort (Ray Grout and Mohammad Rahimi), temperature gradients, spray properties, and other factors have been measured to support development of a CFD simulation model for the AFIDA. This effort will continue in Fiscal Year 2018 to help link AFIDA experimental measurements with simulations evaluating reduced kinetic mechanisms, contributing, along with other measurements, to the kinetic mechanism development feedback loop.

Ignition Kinetics Studies

The AFIDA was used in initial experiments in Fiscal Year 2016 with a full boiling-range research gasoline surrogate blend, Coordinating Research Council Fuels for Advanced Combustion Engines (FACE) B, demonstrating that the AFIDA solves fuel boiling issues at higher temperatures that limit experiments in the IQT. Research continued in Fiscal Year 2017 to use the AFIDA to study ID for a range of gasoline surrogates, mapping ID for a set of 11 gasoline-range surrogate blends with various bio-derived compounds, between ~670–1,000 K and 0.5–3 MPa. The surrogate blends were previously studied in single-cylinder research engine experiments for knock-limited performance under the Co-Optima project. While the AFIDA is a flexible research platform, this study was the first known use of an AFIDA for gasoline-range fuels and required developing unique controls and test methodologies for adapting the AFIDA to gasoline- instead of diesel-range fuels. As shown in Figure II.11.1, the resulting three-dimensional surface maps of ID for two different surrogate blends provide more information on ignition resistance than Research Octane Number (RON) and Motor Octane Number alone [11]. As referenced later, these ID data may be used in simple engine simulations with a knock integral model to predict engine performance providing guidance for more focused research single-cylinder engine (SCE) experiments.

While NREL's bench-scale ignition kinetics studies are transitioning to the AFIDA, the IQT is still utilized for some research. NREL completed a series of ignition kinetics studies building on Fiscal Year 2016 research, blending ethanol into various PRF blends. These fundamental studies provide critical experimental feedback

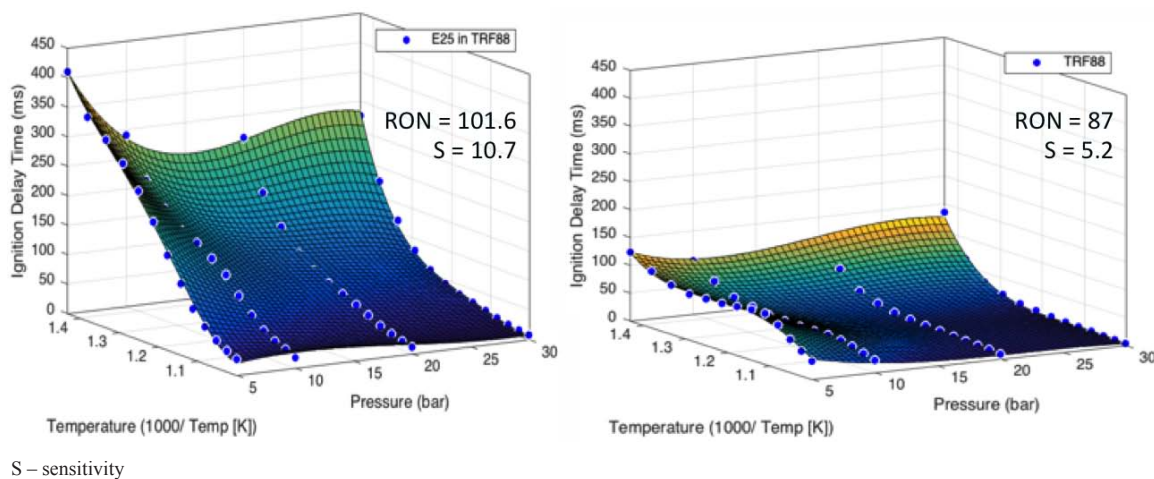


Figure II.11.1 – Three-dimensional surface maps of ID for two gasoline surrogate blends, a 25% ethanol blend into TRF88 on the left and neat TRF88 on the right [11]

of ethanol blending effects for mechanism development. While prior research had revealed non-linear blending ID behavior for ethanol blends of 10, 20, and 50 volume percent into iso-octane (Figure II.11.2), similar experiments with ethanol blended into PRF95 (5 vol% n-heptane, 95 vol% iso-octane) show much more linear behavior (Figure II.11.3) [12].

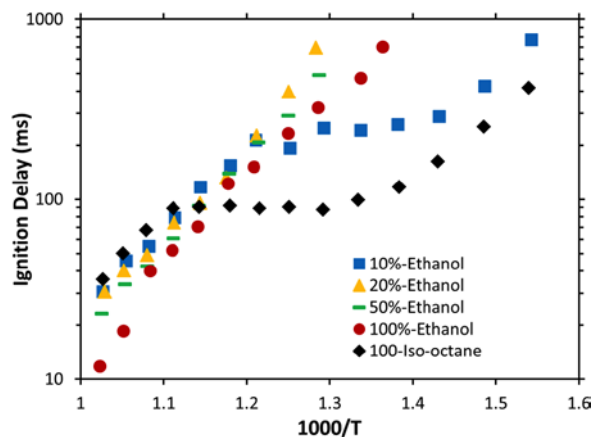


Figure II.11.2 - Constant mass injection temperature sweeps at 1.0 MPa are shown with data plotted every 25 K. A 10% ethanol blend increases ID compared to iso-octane, but it maintains negative temperature coefficient region behavior. A 20% blend exhibits much higher ID, more than a 50% blend or even neat ethanol. [11]

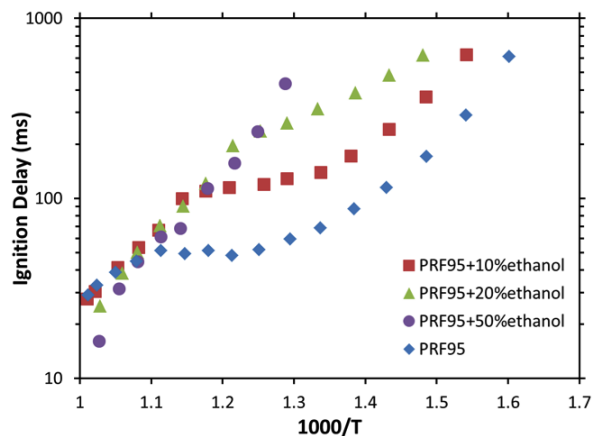


Figure II.11.3 - Constant mass injection temperature sweeps at 1.0 MPa are shown with data plotted every 25 K. Ethanol blending effects into PRF95 are much more linear than with neat iso-octane (illustrated in Figure II.11.2).

Engine Autoignition Studies

This study involved linking gasoline direct injection SCE data for gasoline-range surrogate blends in a 0D engine simulation incorporating a knock integral model integrating bench-scale CVCC ignition delay data. This was a necessary first stage to allow bench-scale IQT/AFIDA experimental data to provide initial screening regarding fuel blend knock resistance and guide more expensive engine experiments. In the process, the 0D simulations were found to be equally beneficial in guiding what temperature and pressure space were necessary to focus with CVCC ID studies.

This study incorporated experimental data from two sources. First, cylinder pressure, intake temperature, and crank angle data from NREL's gasoline direct injection SCE were collected under knock-limited steady-state conditions for gasoline surrogate blends (from Fiscal Year 2016). Engine data included iso-octane (as a reference), a TSF blend, and TRF blends with ethanol, p-cresol, and anisole. A 25 vol% ethanol blend in FACE B was also studied. Next, fuel blends were experimentally studied in NREL's IQT at various fixed pressures (~0.5–3 MPa) with temperature sweeps (~670–1,000 K) near globally stoichiometric conditions. A 0D simulation model was developed in Python to import SCE crank angle-resolved cylinder pressure and intake pressure data, and calculate cylinder temperature prior to spark ignition. The engine simulation was a two-zone

model calculating both unburned and burned fractions to match the experimental cylinder pressure after spark ignition. The unburned fraction temperature and cylinder pressure were simultaneously fed to a modified Livengood–Wu knock integral calculation [9] with a Douaud and Eyzat [13] correlation to calculate end-gas autoignition (knock) using interpolations from the IQT pressure and temperature space ignition delay data. IQT ID data from iso-octane, TSF, and TRF blends with ethanol and anisole were utilized in this initial stage 0D simulation. This initial 0D knock integral model was a critical path in NREL work, and it will undergo continual development to integrate NREL’s bench-scale CVCC ignition kinetics research and SCE experiments under Co-Optima (in collaboration with the Toolkit and Simulation team).

Conclusions

- CVCC ignition kinetics experiments quantify fuel component, surrogate blend, and full boiling range gasoline ignition performance over engine-relevant parametric space.
- Unique IQT and AFIDA data complement data from other devices such as shock tubes and rapid compression machines, and provide additional perspective than RON or Motor Octane Number values alone.
- Extensive characterization and experimental methodology development with the AFIDA have demonstrated significantly expanded capability beyond IQT-based studies for high-quality ignition kinetics experiments and simulations.
- Continued numerical simulation development with unique IQT and AFIDA data enable these experiments to be part of the feedback development loop for development of accurate, reduced kinetic mechanisms.
- IQT and AFIDA data may also be utilized in 0D knock integral simulations to link with SCE experiments, providing additional feedback with complex fuel blends for which kinetic mechanisms do not yet exist.

References

1. Bogin Jr., G.E., E. Osecky, J.Y. Chen, M.A. Ratcliff, J. Luecke, B.T. Zigler, and A.M. Dean. “Experiments and Computational Fluid Dynamics Modeling Analysis of Large n-Alkane Ignition Kinetics in the Ignition Quality Tester.” *Energy Fuels*, 28 4781–4794, 2014. DOI: 10.1021/ef500769j.
2. Bogin Jr., G.E., E. Osecky, M. A. Ratcliff, J. Luecke, X. He, B.T. Zigler, and A.M. Dean. “Ignition Quality Tester (IQT) Investigation of the Negative Temperature Coefficient Region of Alkane Autoignition.” *Energy Fuels*, 27 1632–1642, 2013. DOI: 10.1021/ef301738b.
3. Bogin Jr., G.E., A. DeFilippo, J.Y. Chen, G. Chin, J. Luecke, M.A. Ratcliff, B.T. Zigler, and A.M. Dean. “Experimental Investigation of n-Heptane Autoignition in the Ignition Quality Tester (IQT).” *Energy Fuels*, 25 5562–5572, 2011. DOI: 10.1021/ef201079g.
4. Bogin, G., A.M. Dean, M.A. Ratcliff, J. Luecke, and B.T. Zigler. “Expanding the Experimental Capabilities of the Ignition Quality Tester for Autoigniting Fuels.” *SAE International Journal of Fuels and Lubricants*, Vol. 3, Issue 1, 353–367, 2010.
5. Osecky, E.M., G.E. Bogin, Jr., S.M. Villano, M.A. Ratcliff, J. Luecke, B.T. Zigler, and A.M. Dean. “Investigation of Iso-octane Ignition and Validation of a Multizone Modeling Method in an Ignition Quality Tester.” *Energy & Fuels* 2016 30 (11), 9761–9771, DOI: 10.1021/acs.energyfuels.6b01406.
6. Seidenspinner, P., M. Härtl, T. Wilharm, and G. Wachtmeister. “Cetane Number Determination by Advanced Fuel Ignition Delay Analysis in a New Constant Volume Combustion Chamber.” SAE Technical Paper 2015-01-0798, 2015, <https://doi.org/10.4271/2015-01-0798>.
7. ASTM International. “Standard Test Method for Determination of Derived Cetane Number (DCN) of Diesel Fuel Oils—Fixed Range Injection Period, Constant Volume Combustion Chamber Method.” ASTM D7170-16, 2016, www.astm.org, DOI: 10.1520/D7170-16.

8. Foong, T.M., K.J. Morganti, M.J. Brear, G. da Silva, Y. Yang, F.L. Dryer. "The Octane Numbers of Ethanol Blended with Gasoline and its Surrogates." *Fuel*, 115 727–739, 2014. <http://dx.doi.org/10.1016/j.fuel.2013.07.105>.
9. Livengood, J.C., and P.C. Wu. "Correlation of autoignition phenomena in internal combustion engines and rapid compression machines." Symposium (International) on Combustion. Vol. 5. No. 1. Elsevier, 1955.
10. Coordinating Research Council. "Coordinating Research Council 2017 Annual Report." September 2017.
11. Cameron, Drew, M. "Autoignition Studies Of Gasoline Surrogate Fuels in the Advanced Fuel Ignition Delay Analyzer." M.S. thesis, University of Colorado Boulder, 2017.
12. Bogin Jr., Gregory E., Jon Luecke, Matthew A. Ratcliff, Eric Osecky, and Bradley T. Zigler. "Effects of Iso-octane/ Ethanol Blend Ratios on the Observance of Negative Temperature Coefficient Behavior within the Ignition Quality Tester." *Fuel*, Volume 186, December 15, 2016, Pages 82–90, ISSN 0016-2361, <http://dx.doi.org/10.1016/j.fuel.2016.08.021>.
13. Douaud, A., and P. Eyzat. "Four-Octane-Number Method for Predicting the Anti-Knock Behavior of Fuels and Engines." SAE Technical Paper 780080, 1978, <https://doi.org/10.4271/780080>.

Key Fiscal Year 2017 Publications

1. Bogin Jr., Gregory E., Jon Luecke, Matthew A. Ratcliff, Eric Osecky, and Bradley T. Zigler. "Effects of Iso-octane/ Ethanol Blend Ratios on the Observance of Negative Temperature Coefficient Behavior within the Ignition Quality Tester." *Fuel*, Volume 186, December 15, 2016, Pages 82–90, ISSN 0016-2361, <http://dx.doi.org/10.1016/j.fuel.2016.08.021>.
2. Cameron, Dew M. "Autoignition Studies Of Gasoline Surrogate Fuels in the Advanced Fuel Ignition Delay Analyzer." M.S. thesis, University of Colorado Boulder, 2017.
3. Barraza-Botet, Cesar L., Jon Luecke, Bradley T. Zigler, and Margaret S. Wooldridge. "The Impact of Physicochemical Property Interactions of iso-Octane/Ethanol Blends on Ignition Timescales." Submitted to *Fuel*.

II.12 Fuel Effects on Low Speed Pre-Ignition

Derek Splitter, Principal Investigator

Oak Ridge National Laboratory
2360 Cherahala Blvd.
Knoxville, TN 37922
E-mail: splitterda@ornl.gov

Kevin Stork, DOE Technology Manager

U.S. Department of Energy
E-mail: Kevin.Stork@ee.doe.gov

Start Date: October 1, 2016	End Date: September 30, 2017	
Total Project Cost: \$150,000	DOE share: \$150,000	Non-DOE share: \$0

Acknowledgments

Co-Authors

Gurnesh Jatana, Brian Kaul, Jim Szybist; Oak Ridge National Laboratory

Project Introduction

Downsized and turbocharged spark-ignited engines are being increasingly used by engine manufacturers to improve vehicle efficiency while reducing CO₂ emissions [1,2]. While greatly effective at improving fuel economy, the increased specific outputs of these engines makes them more prone to damaging phenomena such as pre-ignition. Although pre-ignition is not a novel process or unique to downsized boosted engines [3], the high-load low-speed operating conditions of these engines results in a particularly intense pre-ignition process which is typically referred to as low-speed pre-ignition (LSPI). LSPI events often consist of very strong knock event(s) that can cause significant damage to engine hardware, including catastrophic engine failure.

LSPI typically occurs during very high load operation at engine speeds around 2,000 rpm or below, wherein, the flame initiates before the spark is fired and leads to flame propagation at a significantly advanced combustion phasing. The increased pressure rise due to the advanced combustion phasing often causes violent end-gas knock or even super-knock for events that transition to developing detonation [4], all of which can result in catastrophic engine damage. The fundamental causes of LSPI still remain poorly understood and there is a lack of firm consensus on the underlying mechanisms that promote LSPI, but recent findings by Splitter et al. [5] highlight that fundamental fuel properties are important to LSPI event occurrence. Although there has been significant recent work to understand LSPI processes a gap still exists in the understanding of the impact of fuel properties, both physical and chemical, on LSPI behavior. This project aims to provide more clarity on the relationship between fuel properties and LSPI with fuel properties such as distillation and flame speed being specifically studied.

Objectives

- Quantify the relationship between fuel properties and LSPI frequency with respect to fuel distillation and molecular properties
- Determine if specific fuel properties affect LSPI intensity

Approach

The engine used in this study is based on a 1.6-L Ford EcoBoost engine equipped with the production center-mounted direct injection fueling system. The engine was converted to a single-cylinder engine by disabling Cylinders 2, 3, and 4, where Cylinder 1 is closest to the crank snout and Cylinder 4 is closest to the flywheel. The combustion chamber geometry and camshaft profiles on Cylinder 1 were unchanged from the stock

configuration. The engine was operated using standalone laboratory fueling and air handling systems. The engine was controlled through a custom DRIVEN-based engine controller, with automatic engine controls developed at Oak Ridge National Laboratory with calibration based on manual engine mapping. The controller used a mass airflow-based control feedback enabled tabular-based engine map for fully automatic control of fuel, air, spark timing, and camshaft phasing. All measurements presented in this study were acquired in automated operation using time varying load square wave segments at 2,000 rpm. Each segment consisted of 5 min of operation at low-load (5 bar gross indicated mean effective pressure), followed by 25 min of high-load (21 bar gross indicated mean effective pressure) operation. The first 5 min of each 25 min high-load segment were thermally transient in boundary conditions and were discarded from the analysis such that only the last 20 min of data (20,000 cycles) of each high-load segment were used for the study of LSPI behavior. Finally, nine such consecutive low-high-low load square wave segments were run for each fuel mixture to ensure sufficient LSPI event count for consistent statistical analysis. Fresh engine oil (commercially available 5W-20 Mobil 1™) was used for each fuel mixture.

The fuels used were based on premium grade Tier II E0 certification fuel, acquired from Haltermann products; product code HFO437 was used as the baseline and blendstock for this study (hereby referred to as EEE). The baseline fuel was neat EEE, which was also used as a blendstock for blending with three secondary fuel components: ethylbenzene, 2-methyl-1-butanol, and cyclopentanone. For this study, each secondary fuel was mixed with EEE to form a 25% by mass mixture. The three mixtures will be hereafter referred to as EB25, 2MB25, and CP25 for 25% by mass mixtures of ethylbenzene, 2-methyl-1-butanol, and cyclopentanone, respectively, where Table II.12.1 highlights fuel properties of EEE and the respective blends. These respective molecules were selected because they have different molecular structures but similar Research Octane Number (RON) and neat boiling points (RON ± 2 , boiling point $\pm 5^\circ\text{C}$).

A cycle was identified as LSPI if the peak recorded cylinder pressure and 5% of mass fraction burned (CA05) were both more than 3 standard deviations greater than the median maximum cylinder pressure of all the cycles. The approach is similar to that described in detail by Mansfield et al. [6]. Each individual LSPI cycle was characterized using three parameters: LSPI event start location, LSPI dwell duration, and LSPI intensity.

Results

- Confirmed that LSPI number count is highly correlated with fuel increased distillation
- Illustrated that increased fuel distillation is insufficient to describe LSPI phenomena and magnitude, even with near identical fuel distillation and octane number
- Revealed that additional fuel properties are required for LSPI propensity quantification; data supports the hypothesis of increased fuel flame speed also could promote increased LSPI propensity

The fuels tested in this project are reported in Table II.12.1, which highlights that the RON and distillation of the fuels was very similar in blended form. The blended fuels were 25% by mass of the blended molecule and 75% by mass EEE, with a control fuel of neat EEE. The fuel names CP25, 2MB25, and EB25 represent the 25% by mass blends for cyclopentanone, 2-methyl-1-butanol, and ethylbenzene, and will be used throughout the remainder of this report.

As shown in Figure II.12.1, compared to the baseline EEE, all three blended fuels nominally doubled the LSPI event count (solid bars). Although the three blended fuels increased the total LSPI number count, the ratio of LSPI cluster to single events was consistent between the fuels, with approximately 75% of all LSPI events occurring in clusters for all four fuels. However, although the cluster-to-single event LSPI event trends were similar, the blended fuels all exhibited clusters that generally were shorter in cluster event length (i.e., more clusters but generally shorter cluster duration). A possible reason of this behavior is that the ignition source in the blended fuels accumulated more quickly and there was less time for chemical or physical changes to the accumulated liquid in the top ring zone, thus the clusters occurred more frequently but were shorter in duration.

Table II.12.1 - Tested Fuels

Fuel Name	EEE	CP25	2MB25	EB25
Blended molecule	-	Cyclopentanone	2-methyl-1-butanol	ethylbenzene
Blended (%mass)	100%	25%, bal. EEE	25%, bal. EEE	25%, bal. EEE
RON (ASTM D2699)	96.3	101.3	97.2	101.0
MON (ASTM D2700)	88.8	89.8	88.2	90.2
S (RON - MON)	7.5	11.5	9	10.8
IBP (°F) (ASTM D86)	87	87	89	90
T5 (°F) (ASTM D86)	114	111	119	118
T10 (°F) (ASTM D86)	127	131	136	138
T20 (°F) (ASTM D86)	148	162	168	170
T30 (°F) (ASTM D86)	171	195	200	204
T40 (°F) (ASTM D86)	200	221	221	230
T50 (°F) (ASTM D86)	220	232	230	242
T60 (°F) (ASTM D86)	231	240	236	251
T70 (°F) (ASTM D86)	241	248	244	261
T80 (°F) (ASTM D86)	257	258	255	274
T90 (°F) (ASTM D86)	315	275	275	298
T95 (°F) (ASTM D86)	340	278	332	321
FBP (°F) (ASTM D86)	411	279	394	388

IBP – initial boiling point; FBP – final boiling point; MON – Motor Octane Number

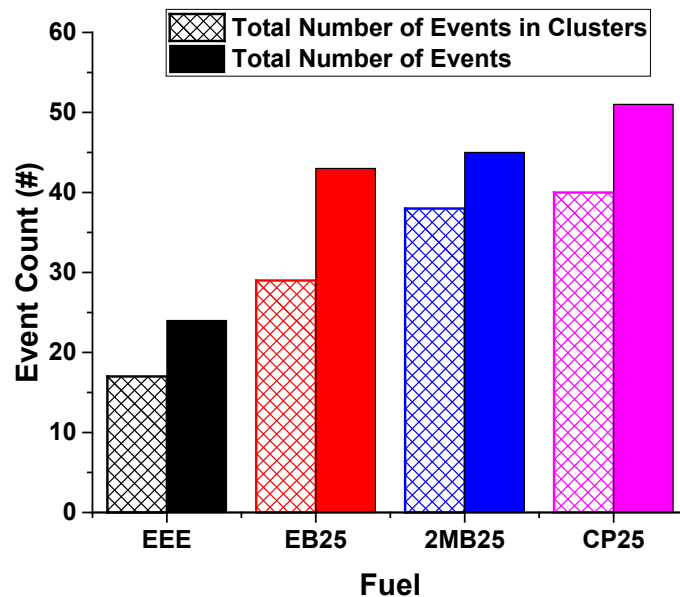


Figure II.12.1 - LSPI count for the four tested fuel combinations. (solid) LSPI event count, (crosshatch) LSPI cluster count (Figure Credit: Derek Splitter).

Interestingly, like the increase in LSPI cluster count, all three secondary fuels were observed to advance the start of pre-ignition as compared to the baseline EEE gasoline, as shown in Figure II.12.2. While, the effect of EB25 and 2MB25 on the start of LSPI events was minor, CP25 was observed to advance the mean LSPI phasing by more than 5 degrees crank angle (°CA) compared to EEE, equivalent to an entire data quartile (i.e., 25% faster). Additionally, the CP25 also exhibited the largest spread in the observed LSPI start locations, with a number of LSPI cycles starting to burn as early as 15°CA before top dead center firing. The unique results of

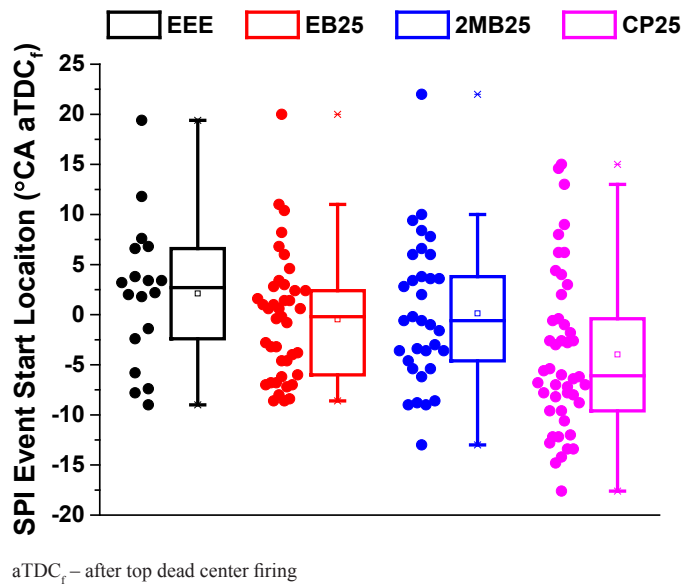


Figure II.12.2 - The effect of different fuels on LSPI event start location (Figure Credit: Derek Splitter)

the CP25 suggest that there could be unique chemical and or physical behaviors present with ketones at LSPI prone conditions.

Figure II.12.3 shows the measured dwell times for the four fuel configurations, where dwell was defined as the duration in crank angles between the start of the LSPI event until to point of maximum cylinder pressure (i.e., the duration between LSPI event start and knock event). 2MB25 was observed to have the shortest mean dwell time (~11°CA), and therefore the fastest transition from start of pre-ignition to peak-cylinder pressure. Additionally, most LSPI cycles observed with 2MB25 had similar dwell times as indicated by the relatively short interquartile range (IQR) of 5°CA. EB25, on the other hand, exhibited the slowest transition from start of pre-ignition to peak-cylinder pressure, as the mean dwell time of ~20°CA for the EB25 LSPI cycles was the longest among the four fuel mixtures studied here. Furthermore, as also shown in Figure II.12.3, the spread of the observed dwell times for all EB25 LSPI cycles was also the largest, with the measured IQR of EB25 LSPI cycles being around twice the next highest IQR (observed for EEE). Many of the long dwell LSPI cycles with EB25 were observed to have a slow enough burn rate that they never transitioned into mega-knock, as highlighted by Figure II.12.4. The LSPI dwell behavior of CP25 was observed to be similar to that of the baseline EEE fuel with both fuels having similar mean dwell times. However, CP25 did exhibit a slightly

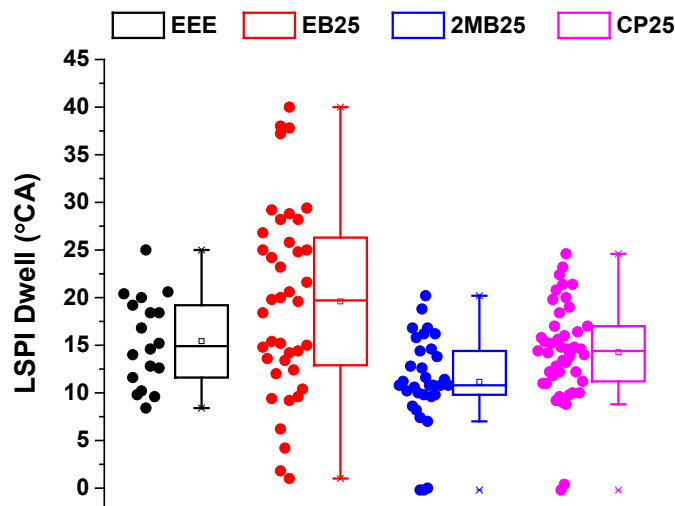
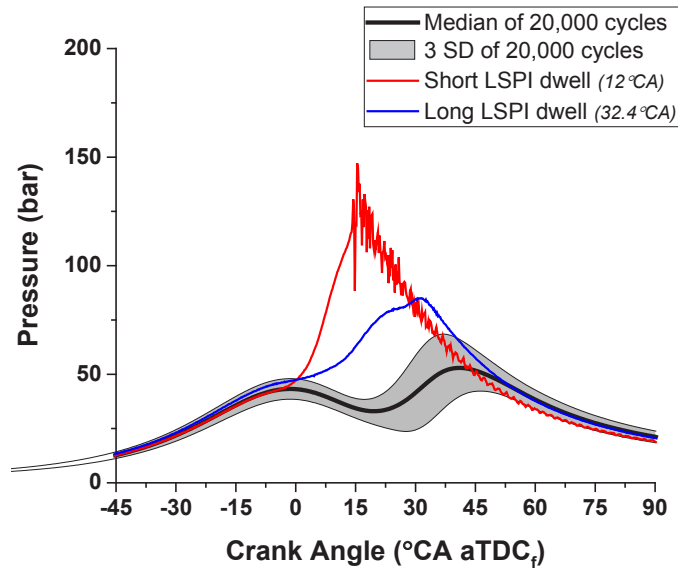


Figure II.12.3 - Impact of various fuels on LSPI dwell (Figure Credit: Derek Splitter)

shorted IQR of dwell times as compared to EEE, indicating more bias of CP25 towards slightly shorter dwell times. Lastly, it should be noted that the zero dwell times observed for the three secondary fuel mixtures were a measurement artifact created by the mega-knock events either saturating or resetting the transducer charge amplifier. The reason for these trends is thought to stem from fuel flame speed differences. It is well known that aromatics have reduced flame speed (i.e., EB25 fuel has the lowest flame speed), while alcohols often have increased flame speed (i.e., 2MB25 flame speed is increased). The fundamentals governing these processes are an area of the work under continuing investigation.



SD – standard deviation

Figure II.12.4 - Example of LSPI dwell times for EB25 exhibiting short and long dwell effects knocking behavior (Figure Credit: Derek Splitter)

The LSPI dwell time effects on knocking, where short LSPI dwell tends to exhibit increased knocking are reinforced by the trends in Figure II.12.5 where the mean LSPI intensity (ΔP , defined as the absolute pressure difference between the mean pressure of LSPI-free cycles and maximum pressure of the LSPI event) was observed to generally follow the mean measured dwell time for each fuel mixture. The 2MB25 mixture, which was observed to have the shortest dwell, also exhibits the strongest mean LSPI intensity with a number of LSPI events reaching cylinder pressures in excess of 500 bar. The CP25 mixture also produced fairly strong LSPI

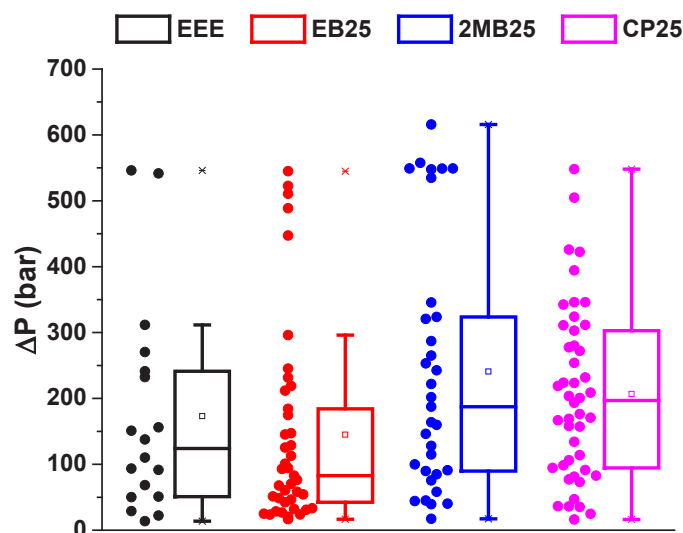


Figure II.12.5 - LSPI intensity observed with various fuels (Figure Credit: Derek Splitter)

cycles with the overall distribution being shifted towards slightly stronger LSPI events as compared to the baseline EEE fuel. While some strong LSPI cycles were observed with EB25, a large number of EB25 LSPI cycles were very mild in nature ($\Delta P < 100$ bar) resulting in a smaller mean LSPI intensity than the baseline EEE fuel. These very mild LSPI cycles were also observed to have the longest dwell durations. This suggests that although the number of LSPI events between the blended fuels was all very similar, the effect of the LSPI events varied greatly, where 2MB25 and CP25 had LSPI events much worse than EB25 or EEE, fuels with suspected reduced flame speeds.

Conclusions

- Confirmed that LSPI number count is highly correlated with fuel increased distillation
- Illustrated that increased fuel distillation is insufficient to describe LSPI phenomena and magnitude, even with near identical fuel distillation and octane number
- Revealed that additional fuel properties are required for LSPI propensity quantification; data supports hypothesis of increased fuel flame speed also could promote increased LSPI propensity

References

1. Pawlowski, Alexander, and Derek Splitter. "SI engine trends: a historical analysis with future projections." No. 2015-01-0972. SAE Technical Paper, 2015.
2. Splitter, Derek, Alexander Pawlowski, and Robert Wagner. "A historical analysis of the co-evolution of gasoline octane number and spark-ignition engines." *Frontiers in Mechanical Engineering* 1 (2016): 16.
3. Chapman, Elana M., and Vincent S. Costanzo. "A Literature Review of Abnormal Ignition by Fuel and Lubricant Derivatives." *SAE International Journal of Engines* 9, no. 2015-01-1869 (2015): 107–142.
4. Wang, Zhi, Yunliang Qi, Xin He, Jianxin Wang, Shijing Shuai, and Chung K. Law. "Analysis of pre-ignition to super-knock: hotspot-induced deflagration to detonation." *Fuel* 144 (2015): 222–227.
5. Splitter, Derek, Brian Kaul, James Szybist, and Gurneesh Jatana. "Engine Operating Conditions and Fuel Properties on Pre-Spark Heat Release and SPI Promotion in SI Engines." *SAE International Journal of Engines* 10, no. 2017-01-0688 (2017).
6. Mansfield, Andrew B., Elana Chapman, and Kenneth Briscoe. "Impact of Fuel Octane Rating and Aromatic Content on Stochastic Pre-Ignition." No. 2016-01-0721. SAE Technical Paper, 2016.

Key Fiscal Year 2017 Publications

1. Splitter, Derek, Brian Kaul, James Szybist, and Gurneesh Jatana. "Engine Operating Conditions and Fuel Properties on Pre-Spark Heat Release and SPI Promotion in SI Engines." *SAE International Journal of Engines* 10, no. 2017-01-0688 (2017).
2. Wissink, M., D. Splitter, A. Dempsey, S. Curran, B. Kaul, and J. Szybist. "An Assessment of Thermodynamic Merits for Current and Potential Future engine Operating Strategies." *Int. J. Eng. Res.*, 2017, 18(1-2), pp. 155–169, doi:10.1177/1468087416686698.

II.13 Fuel Effects on Combustion Stability and Noise for GCI

Stephen Ciatti, Principal Investigator

Argonne National Laboratory
9700 S. Cass Ave.
Bldg. 362
Argonne, IL 60439
E-mail: sciatti@anl.gov

Kevin Stork, DOE Technology Manager

U.S. Department of Energy
E-mail: Kevin.Stork@ee.doe.gov

Start Date: October 1, 2016	End Date: September 30, 2017	
Total Project Cost: \$150,000	DOE share: \$150,000	Non-DOE share: \$0

Project Introduction

In the current study, we explored the characteristic of gasoline compression ignition (GCI) combustion for three gasoline fuels with different chemical composition but similar Research Octane Number (RON). The fuels under test were all 98 RON fuels that were part of the Co-Optima Core matrix of fuels explored for spark ignition engine efficiency improvement. These fuels consisted of an alkylate blend, an aromatic blend, and an E30 (30% ethanol, 70% gasoline) blend that were fabricated to have as close to equal physical and chemical properties as possible. The current study was designed to explore the suitability of these fuels to be used in a compression ignition engine under low temperature combustion conditions. The purpose would be to discover any potential synergies between suitable fuels for advanced spark ignition engines and potential future engine combustion systems that may achieve even higher efficiency moving forward.

Different conditions of exhaust gas recirculation (EGR) and lambda were chosen to study their effects on the combustion and emission of the fuels. Multiple injection strategy was used with the combustion phasing being controlled by the start of injection (SOI) of last injection. Moreover, combustion luminosity was obtained by endoscope imaging through a small optical access into the engine combustion chamber. The results from this diagnostic provided additional insights on the in-cylinder soot formation process. The overall objective of this work is to examine the aspect of GCI operation under various conditions of fuel composition, ambient composition, and fuel stratification level, therefore provide a better understanding of the combustion and emission characteristics of GCI accordingly.

Objectives

- Quantify the differences in combustion characteristics for the three 98 RON fuels by testing them in a GCI engine, varying boost, EGR, and intake temperature
- Utilize endoscopic combustion imaging to more accurately define the boundary conditions in-cylinder to describe the combustion differences between these fuels, especially as it pertains to engine-out smoke and optical soot luminosity
- Generate a pathway for the engine to potentially “adapt” to differences in fuel properties by characterizing the impact of the input variables upon ignition timing and combustion phasing

Approach

For the purposes of this work, the engine speed was kept constant at 1,000 rpm. EGR was varied from 0% to maximum achievable level while maintaining stable combustion. The combustion phasing (CA50) was fixed constant during the EGR sweep by adjusting the SOI of second injection (namely, SOI2), or intake boost pressure. Both SOI2 and boost were demonstrated to control CA50 effectively during the experiment. It was suggested to keep CA50 constant, so that the effect of SOI or boost on the autoignition and earlier combustion

stage can be studied. Matching CA50 approach also indicates a combustion process with a reasonably similar thermodynamic conditions.

Because the global fuel–air mixture was the same, the effect of fuel stratification or other factors (i.e., boost) can be investigated more independently on the ignition and combustion. Also, different global lambda of 1.6 (richest), 1.8 (baseline condition), and 2.0 (leanest) were selected. SOI of first injection (namely, SOI1) was fixed at -50° after top dead center (aTDC). For simplicity, the reported SOI timings of both injections were obtained from the input in the electronic control unit command, rather than the measured injector current.

To obtain in-cylinder visualization of the combustion event, an AVL VisioScope system was used via an optical access sleeve machined into the cylinder head at Cylinder #4. The endoscope system allowed to record images by 0.5 crank angle degrees (CAD) interval from -5° to 30° aTDC covering most of heat release rate (HRR) profile. Note that the entire visualized combustion event was based on a collection of images from different cycles. This was due to the limitation of the camera's frame rate. However, because good combustion stability was maintained, high repeatability was acquired for all cycles. Soot luminosity was measured by the images for each fuel and compared to one another for the purpose of assessing the soot production of the combustion event along with an estimate as to the oxidation of generated soot. These measurements were able to assess differences in each fuel under the same operating conditions.

Results

The testing approach of using SOI2 to control CA50 at a given EGR level was demonstrated in Figure II.13.3 for baseline λ of 1.8. First, as EGR increased at fixed intake pressure, the oxygen concentration in the intake decreased. Therefore, the amount of fuel was reduced in order to keep the same air/fuel ratio (A/F). Mass fuel flow rate decreased almost linearly with the increment of EGR for both three fuels. E30 required higher fueling rate due to having the lowest $(A/F)_{\text{stoic}}$ ratio compared to other fuels as listed Table II.13.1. In fact, the inverses of fueling rate $(1/F)$ for three fuels at any given EGR have the same ratio with the $(A/F)_{\text{stoic}}$ ratio: E30:aromatic:alkylate as 12.83:15.07:14.43. SOI2 was adjusted to keep CA50 constant at $\sim 5^\circ$ aTDC. In general, higher EGR retarded the combustion, hence SOI2 was advanced. Here, combustion mixing time (CMT) is defined as the crank angle (CA) difference between CA50 and end of injection (EOI) of second injection. CMT increased as EGR increased. CMT of fuels did not change significantly within 10% EGR. For E30 and alkylate, the CMT varied within ± 1 CAD with EGR increased up to 15%. As EGR increased above 15%, CMT of fuels increased exponentially. At 25% EGR, E30 had longest CMT of 5.8 CAD, while it was 3 and 3.4 CAD for aromatic and alkylate, respectively. E30 appeared to be the least reactive fuel, hence required most advanced timing of second injection to keep the same combustion phasing, as shown in Figure II.13.1.

The second significant result from this study pertains to the tradeoff between intake temperature and intake boost pressure to achieve identical ignition timing. CA50 was kept constant by adjusting the injection timing while the intake boost pressure and intake temperature were also adjusted. This provided an excellent view into the amount of influence that a small amount of boost can make to reduce the required intake temperature needed to maintain combustion phasing. Both the alkylate and the aromatic fuels performed in a similar manner, as seen in Figure II.13.2, while the E30 fuel required more boost to achieve the same intake temperature reduction as the other two fuels. However, the important observation is that boost can be used with any of these high octane fuels to enhance the reactivity significantly without heating the intake air. This may have an important implication to developing this combustion technology for practical use, since many compression ignition engines have multiple boosting systems.

The third important result from this work identifies the difference between forming a significant amount of soot in-cylinder and having a significant amount of soot leave the exhaust port. As seen in Figure II.13.3, the smoke that was measured in the exhaust for the E30 fuel was ultra-low, regardless of EGR conditions or lambda. The engine-out smoke for the alkylate fuel was also quite low, until the lambda was decreased. The smoke level for the aromatic fuel was quite high regardless of operating condition. However, the in-cylinder imaging shows that the soot formation, as defined by the soot luminosity from the combustion images, was the highest for the E30 fuel. In Figure II.13.4, the soot luminosity vs. crank angle position is shown. The E30 produces the highest level of luminosity but the graph also shows that this luminosity falls away to almost zero much more rapidly

Table II.13.1 - Fuel Properties

	Aromatic	Alkylate	E30
RON	98.1	98	97.4
MON	87.8	96.6	86.6
AKI	93.0	97.3	92.0
S (RON - MON)	10.3	1.4	10.8
Specific Gravity (15 °C)	0.76	0.70	0.75
Paraffins (%)	8.16	3.02	12.89
Isoparaffins (%)	37.99	95.80	27.61
Aromatics (%)	39.77	0.75	13.77
Naphthenes (%)	7.95	0.02	6.98
Olefins (%)	4.54	0.08	5.60
Oxygenates (%)	0.00	0.00	30.37
Unidentified (%)	1.59	0.34	2.79
10% BP (°C)	29	92	59
50% BP (°C)	110	96	78
90% BP (°C)	168	113	164

AKI – anti-knock index; BP – boiling point; MON – Motor Octane Number

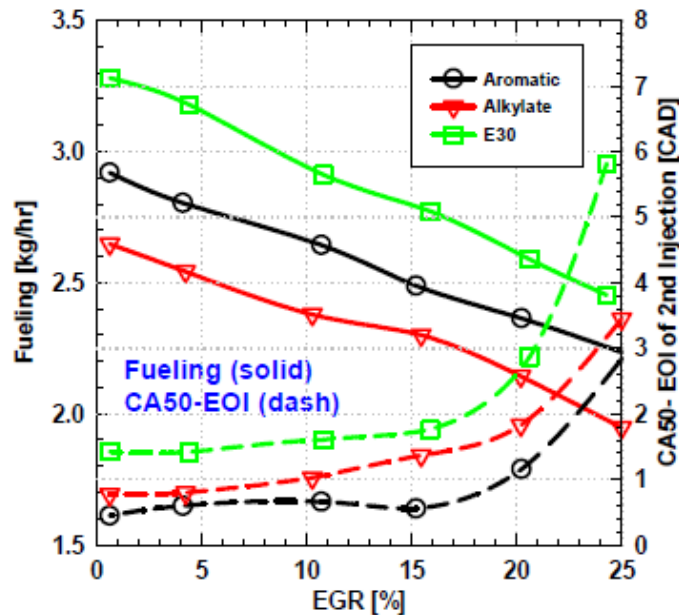


Figure II.13.1 - Fueling rate and CMT as a function of EGR for each fuel

than for the other two fuels. In Figure II.13.5, the HRRs are shown for all three fuels. The E30 has the longest ignition delay time, with subsequently the largest spike of energy.

A reasonable hypothesis is that the ethanol is preferentially evaporating during the early part of the fuel injection process, leading to a locally cool region around the fuel and delaying the autoignition of the petroleum-based hydrocarbons. However, once all the ethanol has evaporated, the oxygen contained by the ethanol in proximity provides the opportunity for very rapid oxidation of the soot created by the petroleum-based components. This hypothesis would explain the rapid rise of soot luminosity along with the very rapid combustion rate for the E30 fuel. One final item of note – when the EGR levels were around 25% for all three

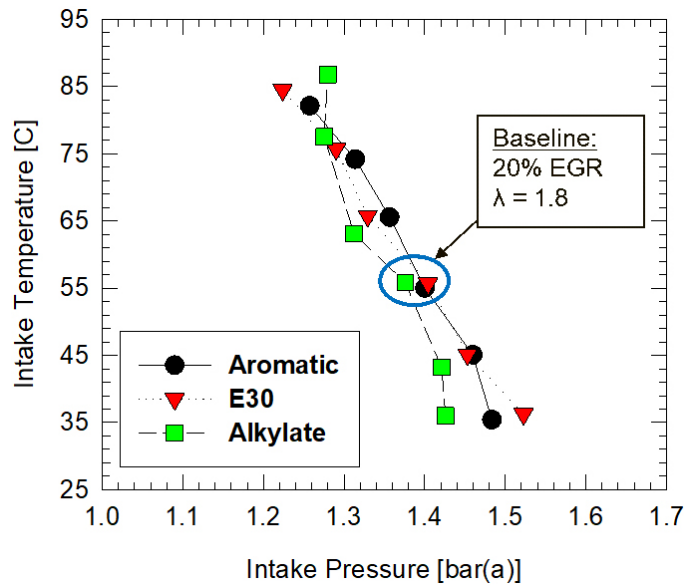


Figure II.13.2 - Tradeoff between intake air temperature and intake boost for constant combustion phasing (CA50)

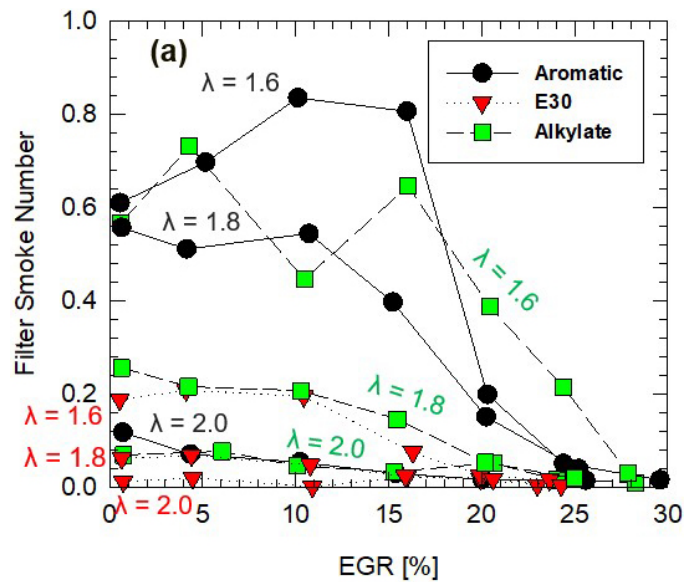


Figure II.13.3 - Engine out smoke (Filter Smoke Number) as a function of EGR for the three 98 RON fuels

fuels, the engine-out smoke dropped to almost zero. This is likely due to the combustion temperatures falling below the required pyrolysis temperature needed to form soot in the first place. Other combustion approaches have utilized this characteristic to create low smoke combustion systems. However, the current work demonstrates that higher levels of EGR are not the only method to achieve this result.

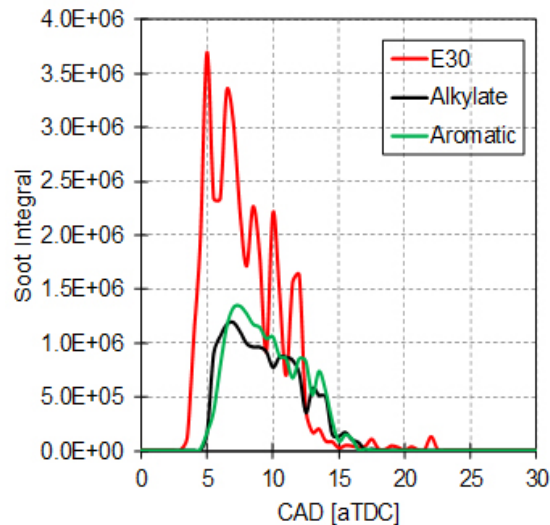


Figure II.13.4 - Soot luminosity for three 98 RON fuels as a function of engine crank angle

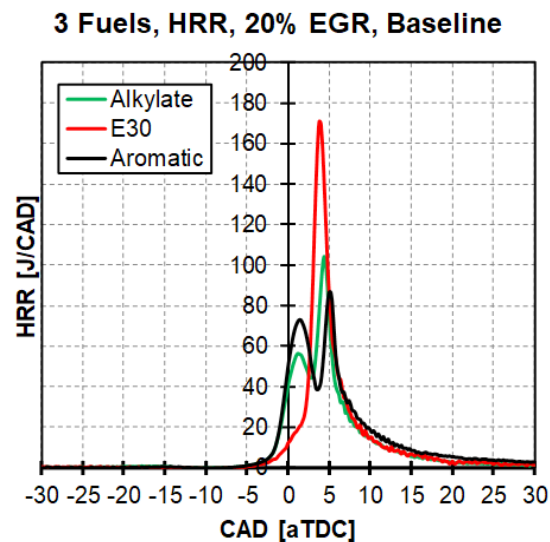


Figure II.13.5 - Heat release profiles for each 98 RON fuel

Conclusions

- All three 98 RON fuels were able to operate in a compression ignition engine with coefficient of variations of indicated mean effective pressure below 3% under all tested conditions.
- These fuels behaved differently under autoignition conditions, in particular with respect to the intake pressure–temperature tradeoff, unlike when used in spark ignition operation.
- Forming soot during the combustion event, as measured by in-cylinder soot luminosity, is not necessarily an indicator of high engine-out soot.

Key Fiscal Year 2017 Publications

1. Cung, K.D., S.A. Ciatti, S. Tanov, and O. Andersson. “Low Temperature Combustion of High-Octane Fuels in a Gasoline Compression Ignition (GCI) Engine.” *Frontiers in Mechanical Engineering – Journal of Engines and Automobile Engineering*. Journal article (in review).

II.14 Autoignition Fundamentals of Fuels for Multi-Mode Boosted SI and LTGC Engines

John E. Dec, Principal Investigator

Sandia National Laboratories
MS 9053, P.O. Box 969
Livermore, CA 94550
E-mail: jedec@sandia.gov

Kevin Stork, DOE Technology Manager

U.S. Department of Energy
E-mail: Kevin.Stork@ee.doe.gov

Start Date: October 1, 2016	End Date: September 30, 2017	
Total Project Cost: \$175,000	DOE share: \$175,000	Non-DOE share: \$0

Project Introduction

Engines using low-temperature gasoline combustion (LTGC), including homogeneous charge compression ignition (HCCI), have a strong potential to reduce fuel consumption and CO₂ emissions by 30% or more over current spark ignition engines due to their high thermal efficiencies and very low NO_x and particulate emissions. Because the LTGC combustion process is largely kinetically controlled, the fuel properties are closely coupled to the engine performance and co-optimization of LTGC engines and their fuels has a strong potential to improve performance. Toward this larger goal, it is critical to understand fuel autoignition characteristics under LTGC-like conditions, including the temperature, pressures, and high dilution levels (either lean or dilute with exhaust gas recirculation/residuals) typical of these engines. When operated in a well-mixed HCCI mode, the Sandia LTGC research engine, with its precise controls, provides an excellent platform for determining these required fuel autoignition characteristics. LTGC operating conditions are also similar to those proposed for other advanced compression ignition (ACI) concepts and for the low-temperature combustion in multi-mode LTGC/spark ignition (SI) engines for light-duty applications. They also have relevance to fuel performance in SI engines [1].

Accordingly, fundamental fuel autoignition studies have been conducted for well-premixed LTGC over a wide range of operating conditions to evaluate the Central Fuels Hypothesis and to determine whether the standard gasoline autoignition metrics (Research Octane Number [RON] and Motor Octane Number [MON]) are adequate for LTGC/ACI engines, or if additional autoignition metrics/specifications will be required. For this reason, parameters such as the ϕ -sensitivity (explained below) and intermediate temperature heat release (ITHR) that have been shown to be related to LTGC engine performance were acquired in addition to determining the fuels' autoignition propensity under multiple operating conditions. Current efforts are focused on evaluating the LTGC performance of the Co-Optima core-fuels, which have been selected to determine the effect of fuel composition on high-RON, high-sensitivity ($S = \text{RON} - \text{MON}$) fuels that are known to perform well in boosted SI engines. Understanding the performance of these Co-Optima core fuels under LTGC conditions is important because multi-mode operation, where the engine operates in LTGC mode at low-to-intermediate loads and switches to boosted SI for high loads, is thought likely to be one of the first commercial applications of LTGC/HCCI technology. It is also important to understand the potential of these fuels for full-time LTGC for future medium- and heavy-duty applications. Besides determining the performance of these fuels for LTGC operation, the results of these studies provide a database for validating chemical-kinetic models being developed for these fuels.

Objectives

Overall Objectives

- Provide fundamental understanding of the autoignition behavior of fuels at conditions relevant to LTGC operation and to other methods of ACI, in order to support the co-development of LTGC engines and fuels that optimize their performance, including:

- The performance of high-RON, high-sensitivity fuels for LTGC operation as part of a multi-mode strategy that switches to boosted SI at high loads for light-duty applications
- Determining the fuel properties required for co-optimization of full-time LTGC for medium- and heavy-duty applications
- Provide data for chemical–kinetic model development and validation

Fiscal Year 2017 Objectives

- Acquire LTGC performance data for the high-RON, high-sensitivity E30 fuel from the Co-Optima fuels matrix over the suite of LTGC operating conditions for fuel evaluation that was established last year
- Compare the performance of E30 to that of the high-aromatic Co-Optima fuel and regular E10 over a range of operating conditions
- Determine the validity and usefulness of the octane index (OI) as a means of correlating the autoignition behavior of these fuels and other fuels for LTGC engine operation
- Investigate the effect of fuel vaporization cooling on the difference in autoignition behavior between the E30 and high-aromatic Co-Optima fuels, compared to differences in autoignition chemistry
- Obtain data and compare the ϕ -sensitivity and ITHR of the Co-Optima E30 and high-aromatic fuels and regular E10
- Support the development of a merit function for ACI fuels

Approach

The performance of these fuels was evaluated in the Sandia LTGC Engine Laboratory using the all-metal single-cylinder LTGC research engine (displacement = 0.98 L) fitted with a 14:1 compression ratio piston that provides an open combustion chamber. This facility allows operation over a wide range of conditions and it has been designed to provide precise control of virtually all operating parameters for well-characterized experiments.

To determine the autoignition characteristics of these fuels, the engine was operated in a well-premixed HCCI mode across a wide range of intake temperatures ($T_{in,s}$) at an intake pressure (P_{in}) = 1.0 bar, and at selected conditions, for $P_{in,s}$ from 1.0 bar to 2.4 bar absolute. Additionally, some data were acquired using early direct injection (DI) fueling to investigate the effects of differences in the heat of vaporization (HOV) between fuels. Data were also acquired to measure key parameters relevant to LTGC operation, including the sensitivity of autoignition to variations in the local fuel/air equivalence ratio within the cylinder (ϕ -sensitivity), the amount of ITHR, and the high-load limits attainable over the intake boost range (1.0–2.4 bar). This results in a fairly large engine operation test matrix for each fuel.

Results

The Co-Optima fuels test matrix was designed to determine whether the gasoline SI autoignition metrics, RON and MON, are adequate for predicting autoignition in LTGC engines and knock in boosted SI engines for fuels with widely varying composition. The E30 fuel tested this year and the high-aromatic fuel tested previously have quite different compositions but nearly identical octane numbers, RON \approx 98 and S \approx 10.5. The E30 fuel was first evaluated at naturally aspirated conditions ($P_{in} = 1$ bar) for well-premixed operation in the LTGC engine at an equivalence ratio (ϕ) of 0.4. At these conditions, intake heating was required to achieve autoignition and the intake temperature (T_{in}) was swept over a wide range to shift combustion phasing (i.e., the 50% burn point [CA50]) from being highly retarded to overly advanced. These data are presented in Figure II.14.1 along with similar data for the high-aromatic fuel, regular E10, and several other fuels investigated previously. As can be seen, E30 requires the lowest T_{in} of any of the fuels tested, indicating that it is the most easily autoignited fuel at these conditions. In contrast, the high-aromatic fuel, with essentially the same RON and S as E30, is one of the most difficult fuels to autoignite as evident from it requiring the highest T_{in} for a

given CA50, along with the Tier 2 certification gasoline (CF-E0). Thus, these data indicate that RON and S are not sufficient to determine the autoignition quality of these fuels for LTGC at this operating condition.

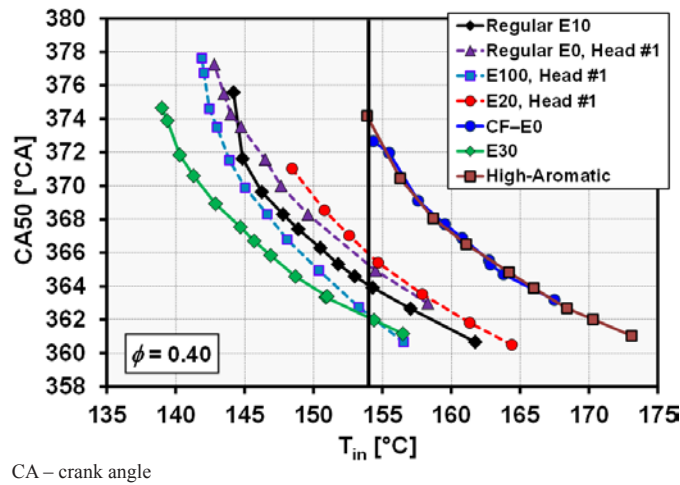


Figure II.14.1 - Combustion phasing (CA50) as a function of intake temperature (T_{in}) for various fuels for fully premixed LTGC operation at $P_{in} = 1.0$ bar, $\phi = 0.4$, 1,200 rpm

The OI is often considered to be an appropriate method for correlating the autoignition quality of fuels under LTGC conditions [2]. Determining the OI requires having CA50 data at the same T_{in} for several fuels that have different RONs and MONs. Their CA50s are then correlated with the $OI = RON - K \cdot S$, where the S is defined above and K is adjusted empirically to obtain the best linear fit between CA50 and the OI for the data at a particular operating condition. For the conditions in Figure II.14.1, all the fuels will autoignite with $T_{in} = 154^\circ\text{C}$ as indicated in Figure II.14.1 by the black line at this T_{in} . Figure II.14.2 shows the CA50s at $T_{in} = 154^\circ\text{C}$ for each of the fuels in Figure II.14.1 plotted as a function of OI with $K = 1.691$, which gave the best fit to these data. As can be seen, even with K adjusted for the best fit, the OI gives a poor correlation for these data, resulting in an $R^2 = 0.536$ as noted on the plot. This shows that even when RON and S are adapted using the OI, they are not adequate to predict LTGC autoignition for the fuels used here, which span a significant range of autoignition reactivity.

To better understand the discrepancy in LTGC autoignition reactivities of the E30 and high-aromatic fuels despite them having the same RON and MON, a study was conducted into the role that differences in the HOV might play. The 30% ethanol content of E30 increases its HOV compared to the high-aromatic fuel which contains no ethanol. The effect of the differences in HOV on the autoignition is not accounted for in the data in Figure II.14.1 because the fuels were vaporized and fully premixed with the intake air prior to being inducted into the engine, similar to the MON test. In contrast, the RON test specifies the intake air temperature prior

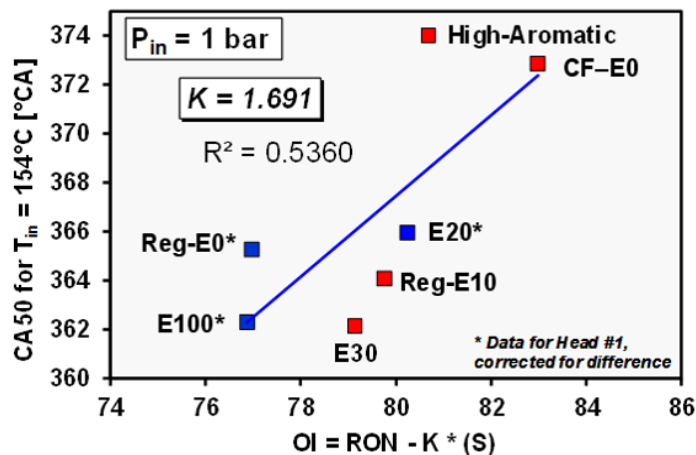


Figure II.14.2 - CA50 for $T_{in} = 154^\circ\text{C}$ as a function of $OI = RON - K \cdot S$. Based on the $T_{in} = 154^\circ\text{C}$ data in Figure II.14.1.

to introducing the fuel, so the cooling caused by fuel vaporization reduces the autoignition reactivity of the charge, increasing the RON rating of the fuel. This effect will be larger for E30 than for the high-aromatic fuel because of E30's higher HOV. To determine the extent to which this difference in HOV affects the comparison of these two fuels for LTGC operation, the CA50 vs. T_{in} sweeps in Figure II.14.1 were repeated using early DI fueling (start of injection at 60°CA after top dead center intake). As shown in Figure II.14.3, T_{in} must be increased above the premixed value for both fuels to compensate for the vaporization cooling, but the increase is greater for E30 due to its higher HOV. Accounting for this difference in HOV by using early DI fueling reduces the difference in the T_{in} s required for a given CA50 for these two fuels, compared to the difference for premixed fueling. However, the remaining difference in T_{in} between these two fuels is still significant, showing that in addition to HOV effects the chemical reactivity of autoignition is different under LTGC conditions even though the fuels have nearly identical RON and MON.

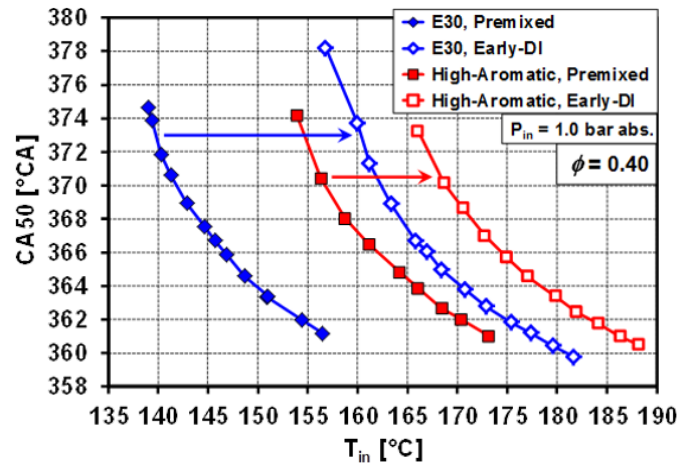


Figure II.14.3 - CA50 as a function of T_{in} for early-DI fueling compared to premixed prevaporized fueling for the Co-Optima E30 and high-aromatic fuels. The larger HOV of E30 is evident in the greater difference in T_{in} between premixed and early-DI fueling compared to the high-aromatic fuel. $P_{in} = 1.0$ bar, $\phi = 0.4$, 1,200 rpm.

Changes in the autoignition reactivity with intake pressure boost is another important factor for both LTGC and advanced SI engines. Figure II.14.4 shows the effect of increased P_{in} (simulated turbo/supercharging) on the autoignition reactivity of the two RON 98 Co-Optima fuels, E30 and high-aromatic, and the same regular E10 gasoline (RON 92, $S = 7$) shown in Figure II.14.1. In this figure, the autoignition reactivity metric is the bottom dead center temperature (T_{BDC}) required to obtain autoignition with a 10% burn point timing (CA10) $\approx 368.7^\circ\text{CA}$ or 371.5°CA (as noted on the plot). The reactivity of all fuels increases with increased P_{in} as evident from the lower required T_{BDC} s. For regular E10, a sharp increase in reactivity occurs as P_{in} is increased from 130 kPa to 160 kPa. Examination of the heat release rates (HRRs) shows that this is due to the onset of low-temperature reactions as the increased pressure shifts the fuel into the negative temperature coefficient region. However, this behavior is not seen for the two higher octane fuels, which have a reduced propensity for low-temperature reactions due to their higher ethanol or higher aromatic content compared to regular E10. The reactivity of the E30 and high-aromatic fuels still increases with boost, but this increase occurs more progressively and T_{BDC} doesn't reach the 105–110°C range until $P_{in} = 200$ kPa or 220 kPa for the E30 and high-aromatic fuels, respectively. These results demonstrate why these high-RON, high-S fuels are beneficial for allowing higher boost without knock in SI engines and why they require less exhaust gas recirculation to control autoignition in boosted LTGC engines. Although Figure II.14.4 shows that the trends in T_{BDC} with boost are very similar for the E30 and high-aromatic fuels, E30 remains consistently more reactive (lower T_{BDC}) across the range of P_{in} s presented. Finally, it should be noted that by converting these data to T_{BDC} , the results are the same for either premixed prevaporized or early-DI fueling because the vaporization cooling is essentially complete by bottom dead center (BDC).

The ϕ -sensitivity is another important fuel characteristic for LTGC and other ACI engine concepts. For ϕ -sensitive fuels, richer regions autoignite faster than leaner ones so partially stratifying the fuel distribution with a late fuel injection that does not mix completely can be used as a means of combustion-timing

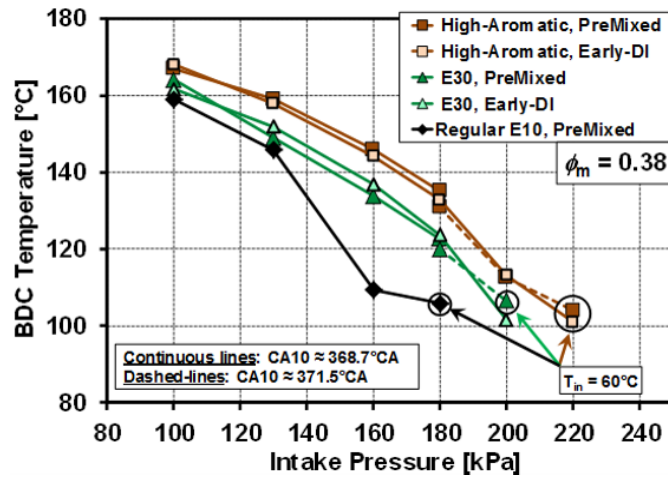


Figure II.14.4 - T_{BDC} required for a CA10 of 368.7°CA (solid lines) or 371.5°CA (dashed lines) as a function of P_{in} for the Co-Optima E30 and high-aromatic fuels and regular E10. The E30 and high-aromatic fuels are shown for both premixed prevaporized and early DI fueling. $\phi_m = 0.38$, 1,200 rpm.

control [3]. Partial fuel stratification (PFS) can also be used to reduce the HRR to allow higher loads and/or more advanced combustion phasing (for higher efficiency) without knock [4,5]. Most gasolines are ϕ -sensitive at higher intake boost pressures, but it is often desirable to have some ϕ -sensitivity at lower P_{in} s (down to naturally aspirated conditions) where these engines will operate much of the time. To avoid the extensive laboratory time required for direct measurements of ϕ -sensitivity, a fast test has been developed that provides a good indication of ϕ -sensitivity for the lower P_{in} s that are of primary interest, i.e., $P_{in} = 1.0$ – 2.0 bar. For these tests, the LTGC engine was first operated with fully premixed fueling over a range of equivalence ratios and for each data point, CA50 was advanced until the Ringing Intensity (RI) = 5 MW/m², which gives the most advanced CA50 without knock [6,7]. Then, the charge mixture was partially stratified using a PFS technique in which 90% of the fuel was premixed and 10% is directly injected at 310°CA (50° before top dead center compression). This produces a distribution of equivalence ratios in the cylinder, and if the fuel is ϕ -sensitive, the various equivalence ratios autoignite sequentially from richest to leanest reducing the HRR, which allows CA50 to be further advanced before reaching the RI = 5 MW/m² limit [4,5,8]. The more ϕ -sensitive the fuel, the greater the reduction in HRR with PFS, and the greater the CA50 advancement (Δ CA50) compared to premixed fueling.

Table II.14.1 shows this Δ CA50 (ϕ -sensitivity metric) for regular E10, the E30, and high-aromatic Co-Optima fuels for intake pressures of 1.0 bar, 1.3 bar, 1.6 bar, and 2.0 bar. These data are for an overall $\phi = 0.36$, which is approximately the middle of the ϕ -range tested. As the table shows, all the fuels have a similar strong ϕ -sensitivity at $P_{in} = 2.0$ bar, but as P_{in} is reduced to 1.6 bar, the Δ CA50s for the E30 and high-aromatic fuels decrease substantially and there is no measureable effect of ϕ -sensitivity at $P_{in} = 1.3$ bar or lower P_{in} s for these two fuels. In contrast, the Δ CA50 for regular E10 is still large at $P_{in} = 1.6$ bar and significant at $P_{in} = 1.3$ bar. The data in Table II.14.1 indicate that regular E10 is not ϕ -sensitive at $P_{in} = 1.0$ bar; however, with greater stratification it still exhibits enough ϕ -sensitivity to provide CA50 control [3]. Taken together, these results show that the E30 and high-aromatic fuels have nearly identical ϕ -sensitivities and changes in ϕ -sensitivity with P_{in} , but they are much less ϕ -sensitive than regular E10 at lower P_{in} s, which would limit the ability to use PFS to control and improve LTGC operation when using the E30 and high-aromatic fuels.

Table II.14.1 - ϕ -Sensitivities As Indicated by the Δ CA50 Between Premixed and PFS Fueling

P_{in} [bar]	Δ CA50 [°CA] for RI = 5 MW/m ²		
	Regular E10	High-Aromatic	E30
2.0	3.4	2.8	3.0
1.6	4.2	0.65	0.62
1.3	0.85	0	0
1.0	0	0	0

Conclusions

- The data show that the standard gasoline autoignition metrics RON and sensitivity ($S = \text{RON} - \text{MON}$) are not adequate to determine autoignition in LTGC engines.
 - Showed that the Co-Optima E30 was the most easily autoignited fuel tested for naturally aspirated LTGC, while the Co-Optima high-aromatic fuel was the most difficult fuel to autoignite, even though these two fuels have nearly identical $\text{RON} \approx 98$ and sensitivity ≈ 10.5
 - Showed that the OI ($\text{OI} = \text{RON} - K \cdot S$) gives only a poor correlation for LTGC autoignition at naturally aspirated conditions with an $R^2 = 0.5360$ based on a fit to the Co-Optima E30 and high-aromatic fuels, regular E10, and four other fuels
 - Compared LTGC autoignition for early-DI fueling and premixed prevaporized fueling to show that the difference in HOV between the E30 and high-aromatic fuels accounts for only part of the difference in their autoignition reactivities; there is also a significant difference in the chemical reactivity of these two fuels despite their nearly identical RON and S
 - Showed that E30 remains more reactive than the high-aromatic fuel for all P_{in} s tested from 1.0–2.0 bar absolute
- Despite the shortcoming of RON and S as metrics for LTGC autoignition timing, they do correlate with the general trend of regular E10 ($\text{RON} = 92$, $S = 7.3$) being much more reactive than the E30 and high-aromatic fuels ($\text{RON} \approx 98$, $S \approx 10.5$) for P_{in} s in the range of 1.6–2.0 bar due to the onset of low-temperature heat release at these P_{in} s for regular E10.
- The E30 and high-aromatic fuels have nearly identical ϕ -sensitivities for $P_{in} \leq 2.0$ bar, and they are much less ϕ -sensitive than regular E10 at lower P_{in} s ($1.0 \leq P_{in} \leq 1.6$ bar), which would limit the application of PFS to control and improve LTGC operation with these two fuels, compared to regular E10.
 - The E30 and high-aromatic fuels also have similar ITHR and changes in ITHR with P_{in} .
- The well-characterized measurements acquired for these studies provide a database for the validation and development of chemical–kinetic models for these fuels.

References

1. Yang, Y., J.E. Dec, M. Sjöberg, and C. Ji. “Understanding Fuel Anti-Knock Performances in Modern SI Engines Using Fundamental HCCI Experiments.” *Combustion and Flame*, 162, pp. 4006–4013, 2015.
2. Risberg, P., G. Kalghatgi, and H.-E. Ångström. “Autoignition Quality of Gasoline-Like Fuels in HCCI Engines.” SAE Technical Paper 2003-01-3215, 2003, doi:10.4271/2003-01-3215.
3. Dec, J.E. “Low-Temperature Gasoline Combustion (LTGC) Engine Research.” U.S. DOE, Office of Vehicle Technologies 2017 Annual Merit Review Presentation for Project ACS004, Washington D.C., June 2017.
4. Dec, J.E., Y. Yang, and N. Dronniou. “Boosted HCCI – Controlling Pressure-Rise Rates for Performance Improvements using Partial Fuel Stratification with Conventional Gasoline.” *SAE Int. J. Engines*, 4(1): 1169–1189 (2011), doi:10.4271/2011-01-0897.
5. Dernote, J., J.E. Dec, and C. Ji. “Efficiency Improvement of Boosted Low-Temperature Gasoline Combustion Engines (LTGC) using a Double Direct-Injection Strategy.” SAE Technical Paper 2017-01-0728 (2017) doi:10.4271/2017-01-0728.
6. Eng, J.A. “Characterization of Pressure Waves in HCCI Combustion.” SAE Technical Paper 2002-01-2859 (2002), doi:10.4271/2002-01-2859.

7. Dernette, J., J.E. Dec, and C. Ji. “Energy Distribution Analysis in Boosted HCCI-like / LTGC Engines – Understanding the Trade-offs to Maximize the Thermal Efficiency.” *SAE Int. J. Engines* 8(3): 956-980, (2015) doi:10.4271/2015-01-0824.
8. Dec, J.E., Y. Yang, and N. Dronniou. “Improving Efficiency and using E10 for Higher Loads in Boosted HCCI Engines.” SAE Technical Paper 2012-01-1107, *SAE Int. J. Engines* 5(3):1009–1032, 2012, doi:10.4271/2012-01-1107.

Fiscal Year 2017 Publications and Presentations

1. Dec, J.E., et al. “Exploratory Advanced Compression Ignition Combustion Tasks.” Team Report for the DOE Annual Merit Review, Office of Vehicle Technologies, June 2017.
2. Dec, J.E., C. Ji, and G. Gentz. “Additional Evaluation of Co-Optima Fuels.” GM/Sandia Working Group Meeting, April 2017.
3. Dec, J.E., C. Ji, J. Dernette, and G. Gentz. “Boosted-SI” Fuel Compatibility with LTGC and the Use of RON & MON as Autoignition Metrics.” Co-Optima Stakeholder Meeting, August 22, 2017.
4. Dec, J.E., C. Ji, J. Dernette, and G. Gentz. “Boosted-SI” Fuel Compatibility with LTGC and the Use of RON & MON as Autoignition Metrics.” GM/Sandia Working Group Meeting, August 31, 2017.
5. International Patent Filed: Dec, J.E, and R. Renzi, November 2016.

II.15 Accelerate Development of ACI/LTC

Scott Curran, Principal Investigator

Oak Ridge National Laboratory
2360 Cherahala Blvd.
Knoxville, TN 37932
E-mail: curransj@ornl.gov

Kevin Stork, DOE Technology Manager

U.S. Department of Energy
E-mail: Kevin.Stork@ee.doe.gov

Start Date: October 1, 2015	End Date: September 30, 2017	
Total Project Cost: \$350,000	DOE share: \$350,000	Non-DOE share: \$0

Acknowledgments

Co-Authors

Martin Wissink, Robert Wagner, James Szybist; Oak Ridge National Laboratory

Project Introduction

Advanced compression ignition (ACI) modes including low temperature combustion (LTC) modes have shown promise in reducing engine out NO_x and soot emissions relative to conventional diesel combustion while demonstrating high brake thermal efficiency. Despite these advantages, there remain challenges with ACI development, including control authority over combustion phasing, duration, and stability; limited speed/load range; high combustion noise; and high unburned hydrocarbons and CO emissions. There are a variety of approaches to achieving LTC and they address these challenges in different ways. The fuel properties best suited to each approach can depend on the performance criteria. With single-fuel strategies, controlling the level of in-cylinder equivalence ratio and temperature stratification through direct injector timing can allow the combustion mode to traverse a spectrum from kinetically controlled homogeneous charge compression ignition (HCCI) to mixing-limited combustion. Dual-fuel approaches such as reactivity controlled compression ignition (RCCI) provide additional control authority by allowing a gradient of fuel composition to be used in addition to equivalence ratio and temperature stratification.

This project focuses on investigating the potential for direct substitution of biofuels for petroleum in advanced combustion technologies. Co-evolution of these emerging technologies and biofuels represents an opportunity to reduce petroleum consumption in future engines and vehicles in a mutually beneficial way. The Co-Optimization of Fuels and Engines (Co-Optima) initiative is a collaborative effort sponsored by the U.S. Department of Energy that involves nine national laboratories as well as industry. Co-Optima takes an integrated approach to improving efficiency and reducing emissions in vehicles by simultaneously researching engines, fuels, and marketplace strategies. A major part of achieving those goals is improving the understanding the effects of fuel properties on both conventional and advanced engine concepts. This project includes collaborative research efforts between Oak Ridge National Laboratory (ORNL) and Sandia National Laboratories (SNL) to quantify the impact of chemical and physical fuel properties on efficiency and load coverage for stratified ACI combustion modes with a focus on RCCI and gasoline compression ignition.

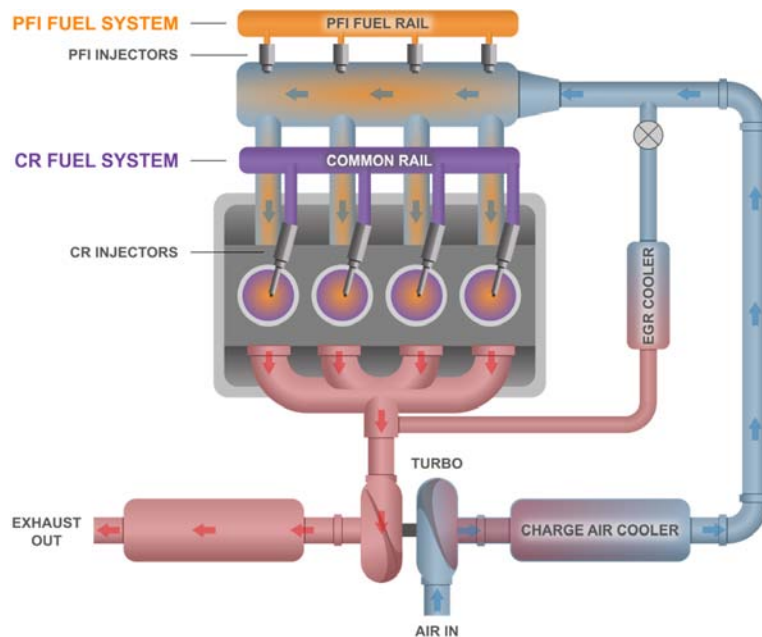
Objectives

- The overall objective of Co-Optima is to cooperatively develop emerging biofuels and advanced engine to bring these technologies to the market sooner to realize a reduction in petroleum consumption.
 - Quantify the potential of the co-evolution of fuels and a subset of the ACI combustion strategies for both single- and dual-fuel ACI

- Quantify the impact of chemical and physical fuel properties on efficiency and load coverage for stratified ACI combustion modes (dual- and single-fuel)
- Assess fuel effects on efficiency and emissions for ACI combustion modes in support of the ACI merit function

Approach

Metal engine experiments in support of the DOE Co-Optima goals focusing on ACI approaches were performed in a light-duty multi-cylinder engine laboratory. The research platform is a four-cylinder General Motors 1.9-L direct-injection (DI) turbocharged diesel engine modified to include a port fuel injection (PFI) system using conventional gasoline injectors and a DI fuel system capable of running diesel-range and gasoline-range fuels. A schematic of the dual-fuel capable ACI engine is shown in Figure II.15.1. A flexible microprocessor-based control system allowed for control over both fueling systems and complete authority over engine operating parameters allowing operation of both single-fuel and dual-fuel advanced combustion modes.



CR – common rail; EGR – exhaust gas recirculation

Figure II.15.1 - Diagram of the multi-cylinder 1.9-L ACI engine

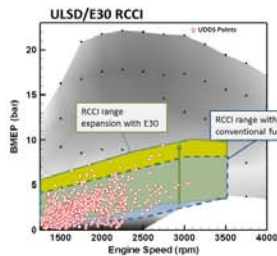
In addition to the multi-cylinder metal ACI engine experiments, ORNL collaborated with a team from SNL to gain deeper insight into fuel specific effects around ACI modes. This collaboration is focused on matching metal engine experiments to the optical work at SNL initially with matched primary reference fuel mixtures relevant to boosted spark ignition research. This collaboration, illustrated in Figure II.15.2, is focused on isolating the physical and chemical fuel effects on ACI combustion development. Additional collaborations with Lawrence Livermore National Laboratory on chemical kinetics were conducted for additional fundamental insights into fuel property impacts on ACI performance.

Results

While different combinations of high- and low-reactivity fuels have been previously demonstrated to enable RCCI, there is a lack of fundamental understanding of which properties, chemical or physical, are most important or desirable for extending operation to both lower and higher loads and reducing emissions of unreacted fuel and CO. This is partly due to the fact that important variables such as temperature, equivalence ratio, and reactivity change simultaneously in both a local and a global sense with changes in the injection of the high-reactivity fuel. In order to better understand these effects, primary reference fuels iso-octane and n-heptane, which have similar physical properties but much different autoignition properties, were selected

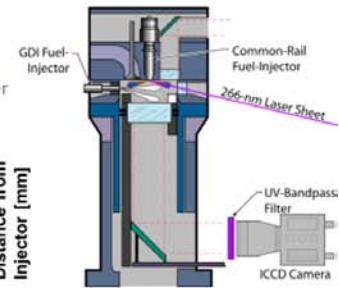
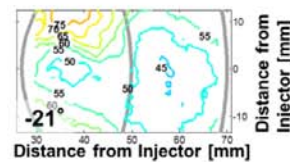
ORNL Metal Engine

- Multi-cylinder light-duty diesel engine (PFI + DI)



SNL Optical Engine

- Single-cylinder heavy-duty diesel engine (GDI + DI)
- Image combustion & in-cylinder mixing (PRF)



ULSD – ultra-low sulfur diesel; E30 – 30% ethanol, 70% gasoline blend; PRF – primary reference fuel; BMEP – brake mean effective pressure
 UV – ultraviolet; ICCD – intensified charge-couple device; GDI – gasoline direct injected

Figure II.15.2 - Collaboration between metal engine and optical engine experiments

to create both external and in-cylinder fuel blends that allow for the effects of reactivity stratification to be isolated and quantified. A combination of multi-cylinder metal experiments (ORNL) linked with optical engine experiments (SNL) for deeper insight in both fuel property effects and leading to fuel economy improvement potential. The goal of this collaboration is further the understanding of the role of both the physical and chemical properties of fuels on RCCI control and load limit. This collaboration requires the best possible matching of conditions to link results so considerable effort has gone into identifying the best possible match of in-cylinder conditions between the two labs. The focus of the coordinated experiments was to evaluate fuel combinations that have similar physical characteristics but differing chemical characteristics (i.e., reactivity). Experimental conditions were selected to best match results across the different engine platforms. The collaboration included an extended on-site visit from an ORNL researcher to SNL for the start of the optical engine experiments.

Fiscal Year 2017 tasks use fuels with different autoignition properties but similar physical properties. The experiments were organized into two sets of sweeps, both of which were performed at the same boundary conditions. For all experiments, the DI fuel rail pressure, engine speed, global equivalence ratio, intake temperature, and fueling rate were fixed, and fueling was specified on an energy basis. Intake pressure and air rate were set to achieve the desired equivalence ratio, and BMEP varied with efficiency. No EGR was used, and combustion phasing was allowed to vary as the injection strategy was changed as shown in Figure II.15.3.

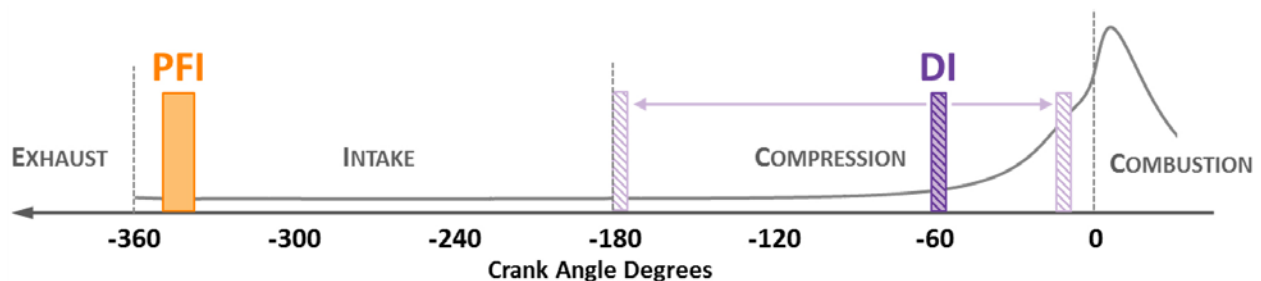
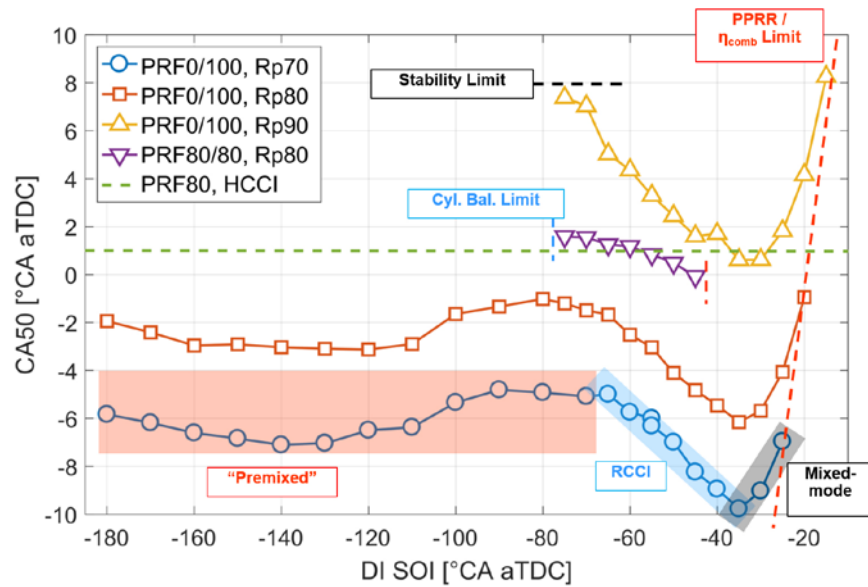


Figure II.15.3 - RCCI injection strategy used in the present study: single PFI during early intake stroke and single DI with timing swept from bottom dead center to near-top dead center of compression stroke

The main focus of the metal engines experiments at ORNL, as shown in Figure II.15.4, are to identify areas of interest in metal engine experiments and explore further in optical experiments. Specifically of interest are the transition points between combustion modes. Ultimately it is hoped to better understand the effect of reactivity gradients and fuel properties on control authority within “RCCI range” (i.e., slope of CA50 [crank angle at 50% mass fraction burned] to start of injection [SOI]/premixed ratio). The metal engine experiments also were used to understand brake engine performance and emissions.

For sweeps of high-reactivity fuel SOI timing with matched premix ratio, equivalence ratio stratification, and global PRF, the addition of reactivity stratification resulted in three times greater combustion phasing control



aTDC – after top dead center; °CA – degrees crank angle; PPRR – peak pressure rise rate

Figure II.15.4 - Mode transitions into RCCI with various combinations of PRF blends as a function of SOI timing

authority. For sweeps of premix ratio with matched equivalence ratio stratification and matched SOI timing within the range of favorable control authority for RCCI, the addition of reactivity stratification and global PRF control resulted 4–15 times greater combustion phasing control authority, depending on global PRF.

By adjusting both SOI and premix ratio, the possibility of reactivity stratification offered by a dual-fuel approach enables independent control of combustion phasing and duration across a much larger space than can be achieved with a single fuel under these nonboosted operating conditions. Experiments with diesel fuel also offered a glimpse at the potential to take advantage of the physical properties of the direct-injected fuel to influence the RCCI combustion process.

We are collaborating with Lawrence Livermore National Laboratory on chemical kinetics for additional fundamental insights into ACI performance. A single-zone temperature model was used to present experimental results of partially stratified single- and dual-fuel compression ignition combustion modes in the pressure vs. temperature space. Constant-volume ignition delay calculations were performed for compositions relevant to the experimental cases and plotted in the same space. This visualization method provides qualitative understanding of the differences between reactivity and equivalence ratio stratification, as well as semi-quantitative evaluation of ignition delay and temperature and pressure sensitivity histories for different parts of the charge. This approach also highlights the limitations of a single-zone approach and suggests future directions for experimental and computational investigations relevant to both compression and spark ignition modes.

Additional investigations were performed to understand the unexpected combustion phasing advance at early injection timings, which has not been observed in large-bore engines at similar conditions. In this work, computational fluid dynamics simulations were performed to investigate whether spray-wall interactions could be responsible for this result. Comparison of the spray penetration, fuel film mass, and in-cylinder visualization of the spray from the computational fluid dynamics results to the experimentally measured combustion phasing and emissions provided compelling evidence of strong fuel impingement at injection timings earlier than $-90^{\circ}\text{CA aTDC}$, and transition from partial to full impingement between -65°CA and $-90^{\circ}\text{CA aTDC}$. Based on this evidence, explanations for the combustion phasing advance at early injection timings are proposed along with potential verification experiments.

Conclusions

- Dual-fuel ACI transition points as a function of DI timing were clearly identified, helping to better understand ACI behavior.
- A methodology for isolating chemical and physical properties was established to help identify the relative importance of chemical and physical properties for each fuel.
- A methodology for linking optical and metal engine experiments to better understand fuel effects on ACI combustion performance was established.

Key Fiscal Year 2017 Publications

1. Roberts, G., C. Rousselle, M. Musculus, M. Wissink, S. Curran, E. and Eagle. "RCCI Combustion Regime Transitions in a Single-Cylinder Optical Engine and a Multi-Cylinder Metal Engine." *SAE Int. J. Engines* 10(5):2017.
2. Wissink, M., S. Curran, G. Roberts, C. Rousselle, and M. Musculus. "Isolating the effects of reactivity stratification in reactivity-controlled compression ignition with iso-octane and n-heptane on a light-duty multi-cylinder engine." *Int. J. Engine Research*. 10.1177/1468087417732898.
3. Wissink, M., S. Curran, S. Wagon, and W. Pitz. "Recent Progress on Understanding the Effects of Reactivity Stratification." AEC program review.
4. Curran, S., et al. "Update on ORNL Single- and Dual-Fuel Advanced Combustion." AEC program review, Southfield, MI, August 2017.
5. Wissink, M., S. Curran, et al. "Spray-wall interactions in a small-bore, multi-cylinder engine operating with reactivity-controlled compression ignition." ICEF 2017-3607, Proceedings of the ASME 2017 Internal Combustion Engine Fall Technical Conference, ICEF2017.

II.16 Co-Optima Project E2.2.2: Accelerate Development of ACI/LTC, Fuel Effects on RCCI Combustion

Mark PB Musculus, Principal Investigator

Sandia National Laboratories
PO Box 969, MS 9053
Livermore, CA 94551-0969
E-mail: mpmuscu@sandia.gov

Kevin Stork, DOE Technology Manager

U.S. Department of Energy
E-mail: Kevin.Stork@ee.doe.gov

Start Date: October 1, 2016	End Date: September 30, 2017	
Total Project Cost: \$175,000	DOE share: \$175,000	Non-DOE share: \$0

Project Introduction

Many advanced combustion approaches have demonstrated potential for achieving diesel-like thermal efficiency but with much lower pollutant emissions of particulate matter and NO_x . Reactivity controlled compression ignition (RCCI) is one advanced combustion concept, which makes use of in-cylinder blending of two fuels with differing reactivity for improved control of the combustion phasing and rate [1]. Previous research and development at Oak Ridge National Laboratory (ORNL) has demonstrated successful implementation of RCCI on a light-duty multi-cylinder engine over a wide range of operating conditions [2]. Several challenges were encountered when extending the research to practical applications, including limits to the operating range, both for high and low loads.

Co-optimizing the engine and fuel aspects of the RCCI approach might allow these operating limits to be extended. The in-cylinder mechanisms by which fuel properties interact with engine operating condition variables is not well understood, however, in part because RCCI is a new combustion concept that is still being developed and limited data have been acquired to date, especially using in-cylinder optical and imaging diagnostics. The objective of this work is to use in-cylinder diagnostics in a heavy-duty, single-cylinder optical engine at Sandia National Laboratories (SNL) to understand the interplay between fuel properties and engine hardware and operating conditions for RCCI in general, and in particular for the light-duty, multi-cylinder all-metal RCCI engine experiments at ORNL.

Objectives

Overall Objectives

- Measure in-cylinder mixing and kinetics to optimize dual-fuel heat release for noise, efficiency, and load range
- Understand mixing–ignition interaction for different fuel reactivity combinations
- Support metal-engine RCCI E.2.2.1 task work at ORNL

Fiscal Year 2017 Objectives

- Identify and demonstrate problematic low-load operating conditions from multi-cylinder all-metal engine experiments at ORNL
- Scope in-cylinder behavior using chemiluminescence imaging to guide application follow-on quantitative laser diagnostics
- Use fuel-tracer/combustion-intermediate fluorescence to quantify coupling of fuel properties with physical processes

Approach

This project uses an optically accessible, heavy-duty, direct-injection diesel engine (Figure II.16.1). To achieve dual-fueling for RCCI, a Bosch gasoline direct injector (GDI) operating with iso-octane at a fuel pressure of 100 bar was added in place of one of the five cylinder wall windows (see Figure II.16.1). For diesel-type fuels, the engine retains a centrally located light-duty common-rail (CR) injector operating with n-heptane at a rail pressure of 800 bar. A large window in the piston crown provides primary imaging access to the piston bowl, and other windows at the cylinder wall provide cross-optical access for laser diagnostics or imaging.

The optical engine experiment shown in Figure II.16.1 uses two cameras for simultaneous imaging of in-cylinder infrared (IR) and visible natural luminosity (NL) emissions. The beamsplitter transmits IR emission to an IR camera that records one image per cycle at an exposure of 130 μ s. The camera is equipped with a bandpass filter centered at 3.3 μ m with a passband of 430 nm, which was chosen to isolate emission from hot fuel vapors. After ignition, the camera also records emission from other combustion-generated sources. The visible NL emission is reflected off the beamsplitter and is directed to a high-speed complementary metal oxide semiconductor camera with an exposure of 130 μ s and a rate of 7,200 frames per second (1 image per crank angle degree).

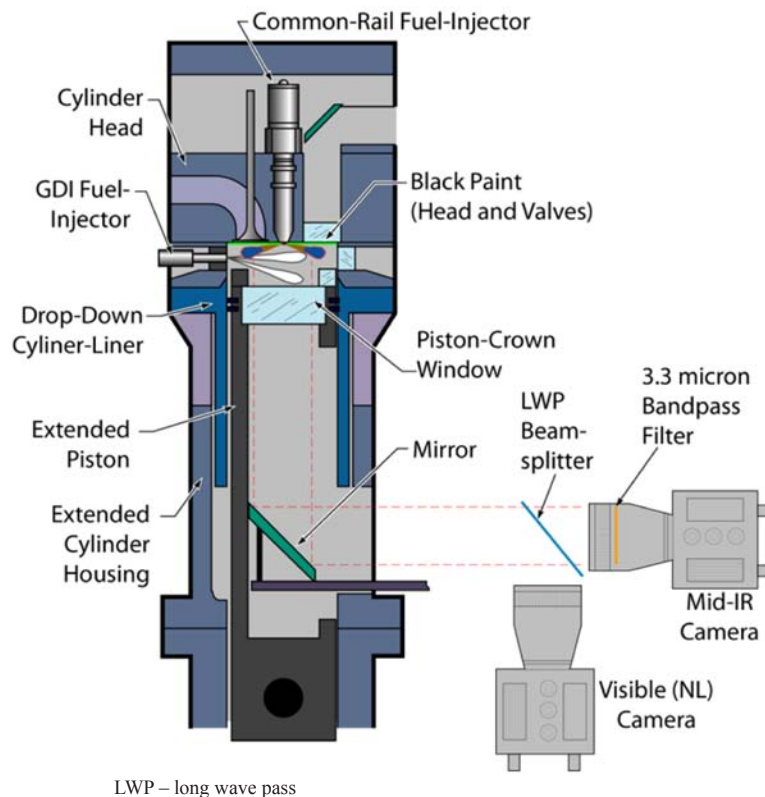


Figure II.16.1 - Schematic diagram of the heavy-duty, single-cylinder optical diesel engine and optical setup with IR emission and visible natural combustion luminosity cameras

Results

Figure II.16.2 shows the combustion phasing, represented by the crank angle timing at 50% mass-fraction burned (CA50), for a timing sweep of the CR injection in the SNL heavy-duty, single-cylinder optical engine and the ORNL light-duty, multi-cylinder, all-metal engine. Here, the high-reactivity n-heptane fuel is injected through the CR injector from a start of solenoid energizing (SSE) of 260 crank angle degrees (CAD) to 340 CAD, where 360 CAD is top dead center of the compression stroke. The low-reactivity iso-octane fuel is injected using the GDI at 60 CAD for the SNL engine, and is port injected for the ORNL engine. The nominal load is 5.6 bar gross indicated mean effective pressure. 80% of the fuel energy is delivered by the GDI injection of iso-octane, with the balance delivered by the CR injection of n-heptane, and with a global equivalence ratio of 0.35 for both fuels together.

As the CR SSE timing in Figure II.16.2 is retarded, CA50 begins to advance, yielding a range of “control authority” for which the CR SSE timing can be adjusted to control combustion phasing. In both engines, this range of control authority extends over about 30 degrees crank angle ($^{\circ}\text{CA}$) of CR SSE timing, yielding a variation of CA50 by 5–7 $^{\circ}\text{CA}$. At the earliest timings, this control authority is lost near 290 CAD, where further advancement of the CR SSE timing has little effect on CA50. At the very latest CR SSE timings, the effect on CA50 reverses, with CA50 retarding along with the CR SSE. The transition of control authority over CA50 for early injections occurs over a relatively broad range of CR SSE timings, roughly 20–30 $^{\circ}\text{CA}$, as opposed to the late injection control authority limit that occurs over roughly 5–10 $^{\circ}\text{CA}$. Despite the differences between the two experimental setups (e.g., engine speed, compression ratio, gross indicated mean effective pressure), the CA50 data for the two engines are similar. CA50 timings are within 3 $^{\circ}\text{CA}$ or less, and the CR SSE timing of the CA50 minimum is within 5 $^{\circ}\text{CA}$. This comparison provides some confidence that the in-cylinder imaging observations of combustion behavior in the single-cylinder optical engine are at least generally representative of combustion in the multi-cylinder metal engine.

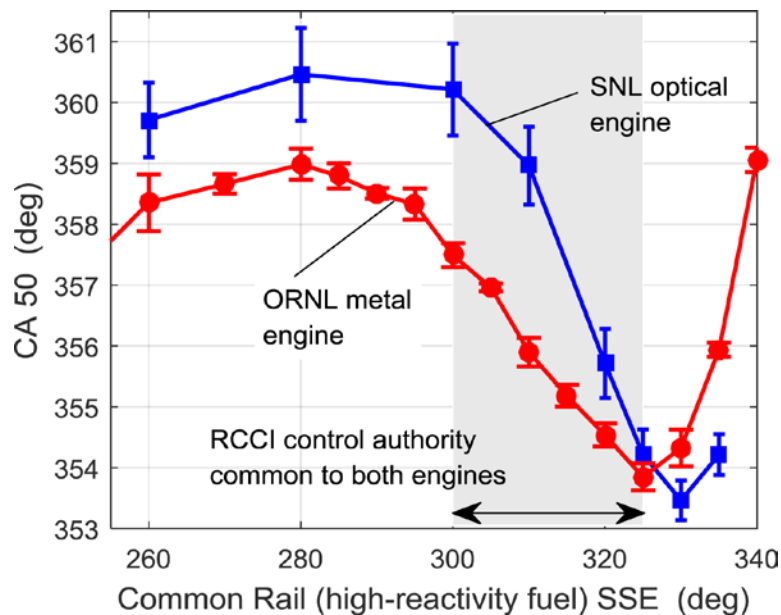


Figure II.16.2 - Combustion phasing for both the single-cylinder optical engine (with standard deviation over 36 fired cycles), and the multi-cylinder metal engine (with standard deviation over four cylinders during steady-state)

Insight into the in-cylinder mechanisms responsible for the early injection (near 300 CAD CR SSE) and late injection (near 325 CAD CR SSE) limits of the range of RCCI control authority may be gained through examination of the optical diagnostic images. Considering first the early injection control authority limit, Figures II.16.3 and II.16.4 show a series of IR and NL images near the start of the high-temperature heat release at 300 and 310 CAD CR SSE, respectively. The CR injector is in the center of the images, and the piston bowl wall forms the circular boundary within the image frames. Throughout the series of images in both Figure II.16.3 and Figure II.16.4, IR emission intensity continues to increase throughout the bowl, while the NL intensity first appears where the jets impinge on the bowl wall, and then progresses primarily along the bowl wall. There is also no notable image saturation, indicative of the absence of fuel-rich regions that lead to soot formation. The IR images for 310 CAD CR SSE (Figure II.16.4) show a greater development of high-temperature heat release [HTHR] reactions that extend into the interior of the cylinder bowl than for the 300 CAD CR SSE (Figure II.16.3). With less time for premixing, it is expected that locally richer mixtures exist. In comparing the IR image at 350 CAD in Figure II.16.4, for instance, a slightly brighter region exists in the four o'clock position near the bowl rim, and this region emits with greater intensity than the corresponding image from SSE = 300 CAD in Figure II.16.3. This slight amount of increased stratification, and subsequent slightly richer local mixtures, is likely an important contributing factor to the change in CA50 control authority.

For the late injection control authority limit, Figure II.16.5 and Figure II.16.6 show a series of IR and NL images near the start of the HTHR at 320 and 330 CAD CR SSE, respectively. The bright white saturation of the 330 CAD CR SSE NL images in Figure II.16.6 are characteristic of soot incandescence, which indicates mixtures fuel-rich enough that mixing-limited combustion is locally occurring. Increased soot luminosity is also correlated with a change in the apparent heat release rate, with the peak apparent heat release rate preceding CA50 for 330 CAD CR SSE (not shown). This peak becomes more pronounced and quickly leads to operational limits, specifically as SSE is retarded from 330 CAD to 325 CAD. The turning point in control authority over CA50 (near 330 CAD CR SSE) corresponds to a condition where soot luminosity is both prevalent and persistent (along the entire bowl wall) throughout the entire HTHR period. In the IR images, greater control authority is associated with a higher degree of fuel-vapor dispersion as identified by the loss of clearly defined boundaries between jet structures in Figure II.16.5 compared to Figure II.16.6. Within the range of CA50 control authority, reactivity gradients are apparent in the sequential autoignition that begins along the bowl rim and progresses inward (NL images of chemiluminescence in Figure II.16.4 and Figure II.16.5).

Future research will use additional laser and optical diagnostics to measure in-cylinder fuel concentration distributions to help to quantify the effects of those mixture distributions on ignition and combustion.

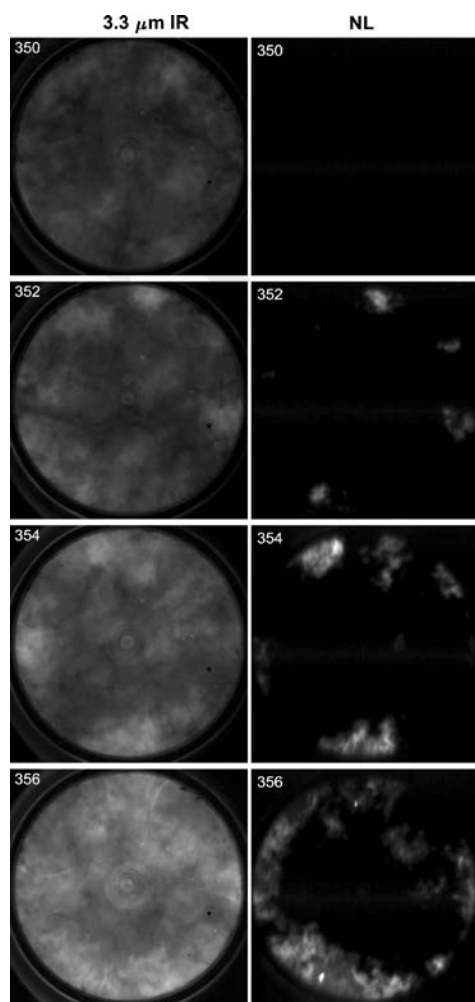


Figure II.16.3 - Simultaneous IR and visible NL images during HTHR period for 300 CAD CR SSE near the early injection control authority limit. Each pair of images corresponds to different combustion cycles, not successive images in time. The imaging crank angle is indicated in the top-left of each image.

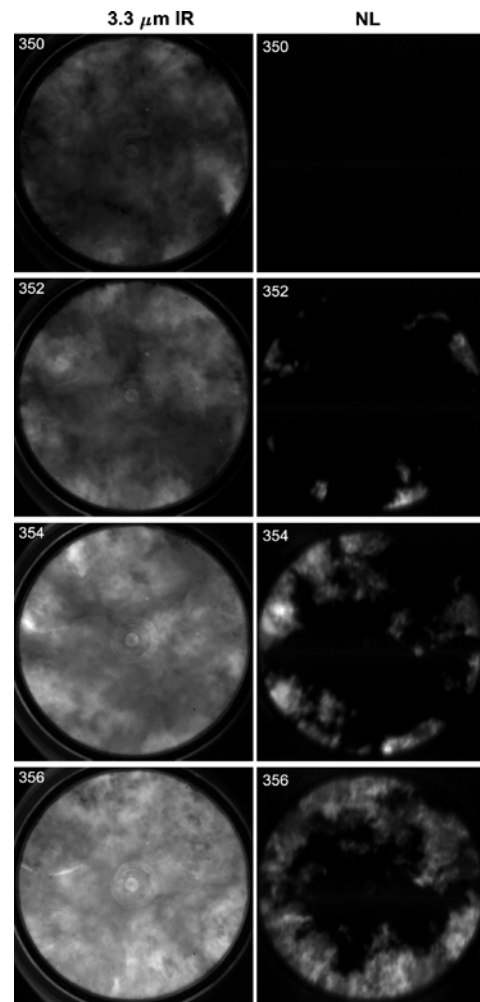


Figure II.16.4 - Simultaneous IR and visible NL images, during HTHR period for 310 CAD CR SSE, slightly retarded from the early injection control authority limit. Each pair of images corresponds to different combustion cycles, not successive images in time. The imaging crank angle is indicated in the top-left of each image.

Additionally, fuel properties including volatility and/or reactivity will be varied to better understand the interplay between fuel properties and operating conditions. Together with the all-metal engine experiments at ORNL, these data will help to provide insight into how the load limits of RCCI might be overcome through the co-optimization of fuels and engines.

Conclusions

- SNL developed a method to match operating conditions of the SNL heavy-duty, single-cylinder optical engine with those of the ORNL light-duty, multi-cylinder, all-metal engine by using the (1) same in-cylinder charge-gas density and temperature at the start of common rail injection at the midpoint of the RCCI range of control authority, (2) same premixed iso-octane fraction (80%) with n-heptane common rail injection, and (3) same global equivalence ratio (0.35).
- With operating conditions matched, even with different engine displacement (heavy-duty vs. light-duty), compression ratios, and piston geometry, the combustion characteristics are similar, with three characteristic regimes of combustion phasing control authority (pre-mixed, RCCI, and mixing-controlled) and similar heat-release shapes.

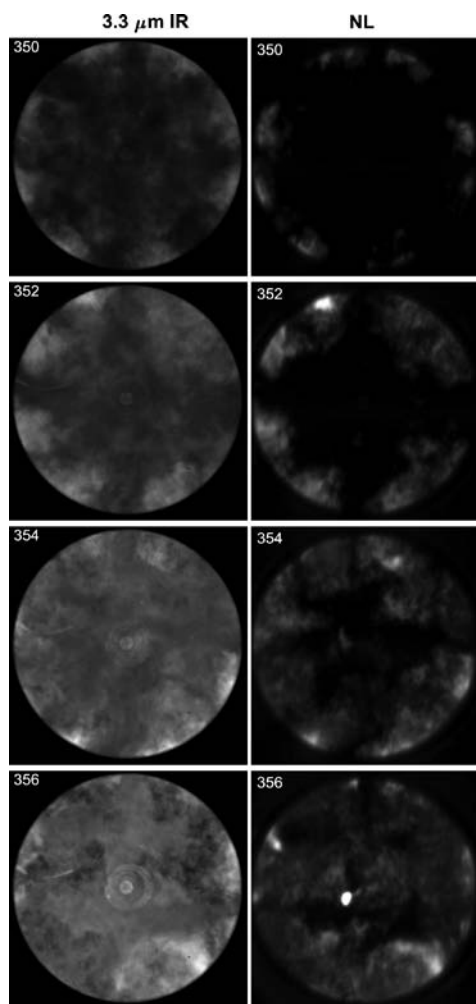


Figure II.16.5 - Simultaneous IR and visible NL images during HTHR period for 320 CAD CR SSE slightly advanced from the late injection control authority limit. Each pair of images corresponds to different combustion cycles, not successive images in time. The imaging crank angle is indicated in the top-left of each image.

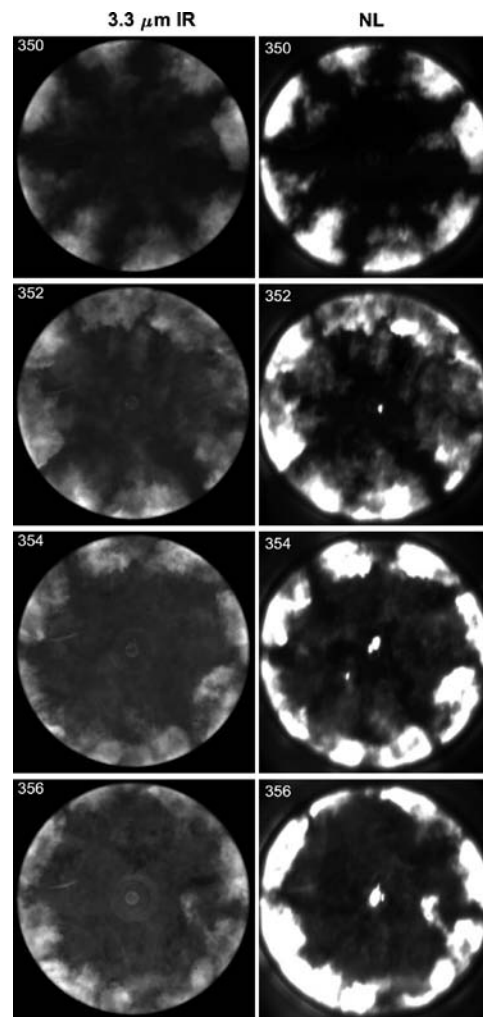


Figure II.16.6 - Simultaneous IR and visible NL images during HTHR period for 330 CAD CR SSE near the late injection control authority limit. Each pair of images corresponds to different combustion cycles, not successive images in time. The imaging crank angle is indicated in the top-left of each image.

- At the early injection limit of RCCI combustion phasing control authority, the IR images show low-temperature heat release extending farther into the interior of the cylinder as the CR SSE is retarded. With less time for premixing, stratification increases and subsequent slightly richer local mixtures may well be an important contributing factor to the change in early injection CA50 control authority limit.
- At the late injection control authority limit, loss of control authority is associated with more defined jet structures and less dispersion of the vapor fuel, which also leads to richer mixtures with increase soot formation and subsequent mixing-controlled combustion.

References

1. Reitz, R.D. and G Duraisamy. "Review of high efficiency and clean reactivity controlled compression ignition (RCCI) combustion in internal combustion engines." *Progress in Energy and Combustion Science* 46:12-71, 2015.
2. Curran, S.J., Z. Gao, V.Y. Prikhodko, A.B. Dempsey, J.M. Storey, J.E. Parks, and R.M. Wagner. "High efficiency clean combustion in light-duty multi-cylinder diesel engines." *Advanced Combustion Engines 2015 Annual Report*, DOE Vehicle Technologies Office, 2015.

Key Fiscal Year 2017 Publications

1. Wissink, M.L., S.J. Curran, G. Roberts, M.P.B. Musculus, C. Mounaïm-Rousselle. "Isolating the effects of reactivity stratification in reactivity-controlled compression ignition with iso-octane and n-heptane on a light-duty multi-cylinder engine." Accepted to *Int. J. Engine Research*, 2017.
2. Roberts, G., C. Mounaïm-Rousselle, M.P.B. Musculus, M. Wissink, S. Curran, and W.E. Eagle. "RCCI combustion regime transitions in a single-cylinder optical engine and a multi-cylinder metal engine." *SAE Int. J. Engines* 10(5), 2017.
3. Ciatti, S., S. Curran, J. Dec, A. Ickes, P. Miles, C. Mueller, and M. Musculus. "Exploratory advanced compression ignition combustion tasks." FY 2017 Vehicle Technologies Office Annual Merit Review Presentation, 2017.

II.17 Improved Mixing-Controlled Combustion Technologies and Fuels for High-Efficiency Compression Ignition Engines

Charles J. Mueller, Principal Investigator

Sandia National Laboratories
7011 East Ave., MS 9053
Livermore, CA 94550-9517
E-mail: cjmuell@sandia.gov

Kevin Stork, DOE Technology Manager

U.S. Department of Energy
E-mail: Kevin.Stork@ee.doe.gov

Start Date: October 1, 2016	End Date: September 30, 2017	
Total Project Cost: \$788,000	DOE share: \$788,000	Non-DOE share: \$0

Acknowledgments

Co-Authors

Ryan K. Gehmlich, Christopher W. Nilsen, and Yefu Wang; Sandia National Laboratories

Project Introduction

This project is focused on developing advanced combustion strategies for mixing-controlled compression ignition (CI) engines that are synergistic with renewable and/or unconventional fuels in a manner that enhances domestic energy security, economic competitiveness, and environmental quality. Specifically, the project aims to provide:

- New technologies (e.g., ducted fuel injection [DFI]) to increase the performance per unit cost, mass, and volume of future high-efficiency engine/fuel systems.
- High-quality experimental data for computational fluid dynamics model development to facilitate accurate, rapid, and cost-effective computational optimization for new technologies.
- A fundamental understanding of fuel composition and property effects by formulating and studying the performance of chemically and physically well-characterized reference fuels made from blending stocks as well as pure compounds.

Objectives

The specific objectives of research in Fiscal Year 2017 were to:

- Determine the extent to which DFI lowers soot mass in a diesel spray flame.
- Quantify the effects on DFI performance of rounding the duct inlet and tapering its outlet.
- Evaluate the impact on DFI performance of shortening the duct length from 16 mm to 8 mm and the distance from the fuel injector orifice exit to the duct inlet from 5.9 mm to 1.4 mm.
- Conduct a simplified modeling study to identify the likely source(s) of hydrocarbon (HC) emissions from mixing-controlled CI combustion.
- Measure the extent to which the four diesel surrogate fuels created in Coordinating Research Council (CRC) Project AVFL-18a match the sooting propensity of their target fuel.

Approach

The first three objectives above were accomplished by conducting DFI experiments with different ambient conditions as well as different duct inlet and outlet profiles, lengths, and standoff distances in Sandia's constant volume combustion vessel (CVCV). The diffused back illumination diagnostic was employed to quantify the mass of soot in the spray flames of these experiments. The fourth objective was achieved by analyzing prior HC emissions and liftoff length data from the optical engine of this project to gauge its consistency with a simple conceptual model developed through a collaboration with Prof. A.S. (Ed) Cheng of San Francisco State University. The fifth objective was satisfied by collaborating with both CRC and Prof. L.D. Pfefferle and Dr. McEnally of Yale University to make yield sooting index measurements of the target and surrogate fuels, and by correlating the results with the molecular-structural attributes of each of the constituent compounds in the surrogate fuels.

Results

Showed that DFI Can Attenuate Soot Levels in Mixing-Controlled CI Spray Flames by 50% to 100%

Previous DFI proof-of-concept experiments showed that DFI can dramatically reduce or eliminate soot incandescence [1], but soot incandescence is not a quantitative measure of soot mass. Figure II.17.1 presents results from diffused back illumination imaging experiments that were processed to yield quantitative soot mass. The experiments were conducted on a single, mixing-controlled CI flame in the Sandia CVCV over a range of engine-relevant conditions. The left column of images is for the free spray (i.e., no duct), where distributed red, orange, and yellow signal regions indicate the presence of appreciable amounts of soot. The right column of images is for DFI employing a steel duct with an inside diameter (D) of 2 mm, a length (L)

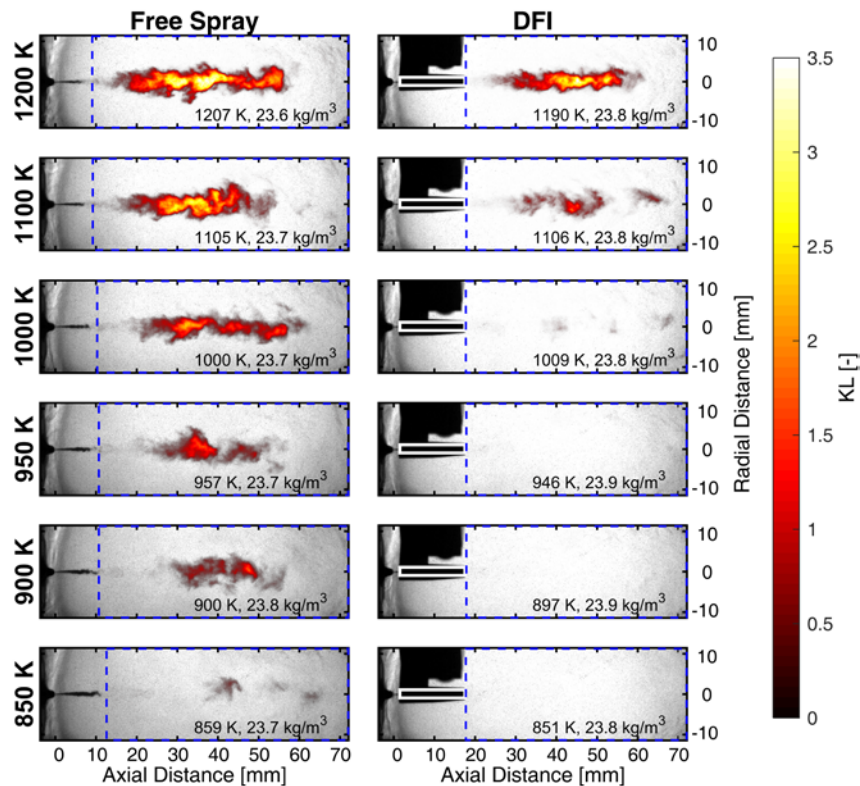


Figure II.17.1 - Quantitative images of soot optical thickness (KL) from diffused back illumination movies of free-spray combustion (left column) vs. DFI combustion (right column). False color is used to indicate higher KL values and thus higher soot concentrations. Each row of images corresponds to a different nominal ambient temperature in the combustion vessel. The actual ambient temperature and density values are indicated in the lower right region of each image frame. Each displayed image was acquired at 3.000 ms after the start of fuel injection. The duct configuration is D2L16G1.4 δ , as described in the text. The white rectangle on each DFI image indicates the location of the inner diameter of the duct.

of 16 mm, a standoff distance (G) of 1.4 mm between the injector orifice exit and the duct inlet plane, and a rounded-inlet/tapered-outlet (δ) duct configuration, i.e., D2L16G1.4 δ . DFI soot levels are below the detection limit of the diagnostic for the three lowest ambient temperatures, and obviously lower than those for the free spray at the three higher temperatures. When converted to soot mass, the data show ~50% lower soot levels for DFI even at the highest ambient temperature condition [2].

Demonstrated that Rounding the Duct Inlet and Tapering its Outlet Can Lead to Improved DFI Performance

Figure II.17.2 shows results from DFI experiments with ducts featuring four different combinations of inlet rounding and outlet tapering. The left side of the figure shows that changing from the unrounded, untapered α configuration to the rounded inlet β configuration lowers average soot mass by ~70% at 1,000 K, while the right side of the figure indicates that the δ configuration, which includes both a rounded duct inlet and a tapered outlet, completely eliminates soot at the same conditions. Despite the obvious soot benefit, it is evident that the average flame liftoff length (H_{avg}), ignition delay, and total pressure rise (ΔP) in the CVCV are not strongly affected by changing the duct inlet and outlet shapes [2].

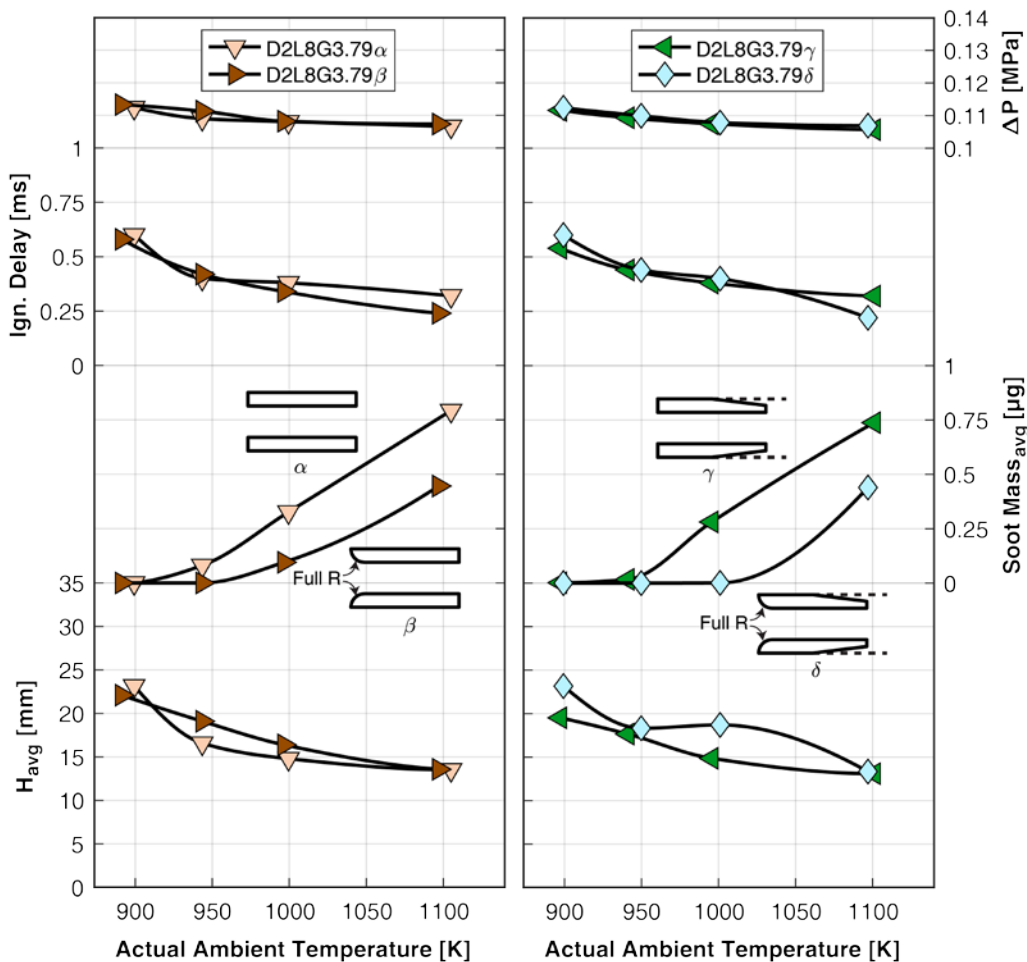


Figure II.17.2 - Comparison of duct inlet and outlet shape effects on DFI performance. The duct shape that corresponds to each Greek letter is shown for reference. All data are for D2L8G3.79 ducts at a nominal ambient density of 22.8 kg/m³.

Found that the Duct Assembly Can be Shortened by More Than Half Without Loss of Soot Attenuation Efficacy

Figure II.17.3a shows that the soot attenuation potential of a 2-mm diameter duct is not significantly affected by shortening its length from 16 mm to 8 mm. This shortening of L consistently shortens H_{avg} and the ignition

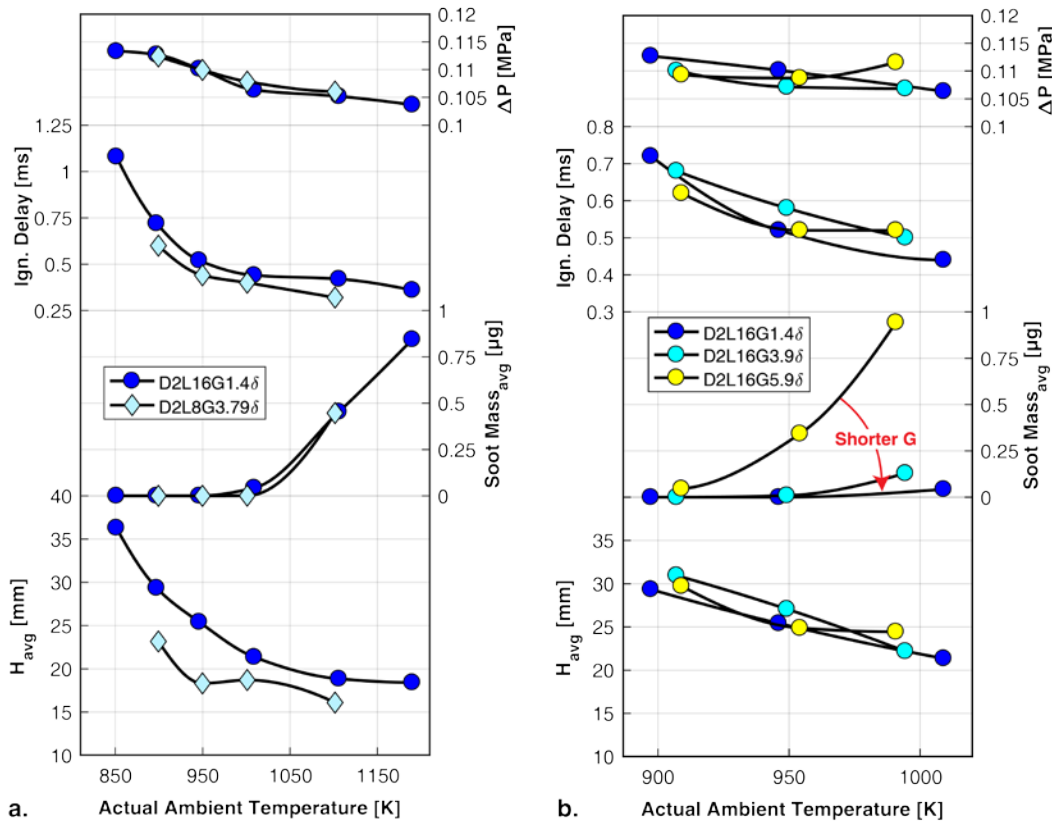


Figure II.17.3 - (a) Shortening duct length from 16 mm to 8 mm does not have a detrimental effect on soot mass for a duct with 2-mm diameter and δ configuration. (b) Decreasing the standoff distance from 5.9 mm to 1.4 mm lowers the soot mass.

delay, but it does not appear to have a large effect on the average soot mass or ΔP . Figure II.17.3b shows that shortening G from 5.9 mm to 1.4 mm lowers soot mass without significantly affecting H_{avg} , ignition delay, or ΔP . Hence, the total length of the duct assembly can be shortened from ~ 22 mm to ~ 9.4 mm, a 57% reduction, without degrading DFI performance [2].

Discovered that the Primary Mixing-Controlled CI Combustion Source of HC Emissions is Likely Fuel in Overlean Regions at the Radial Periphery of the Fuel Spray during the Quasi-Steady Mixing-Controlled Burn

As shown by the symbols in Figure II.17.4, experiments conducted with a set of reference diesel fuels in the optically accessible CI engine of this project have revealed a strong correlation between the HC emissions index (EIHC) and the flame liftoff length (H) at the end of the premixed burn (EOPMB), with increased EIHC associated with longer H-values. The correlation is largely independent of fuel properties and charge gas oxygen mole fraction, but varies with fuel injection pressure. Measurements were made for low cetane (CN:L) and medium/high cetane (CN:M/H) fuels at injection pressures of 80 MPa and 180 MPa. A transient, one-dimensional jet model was used to investigate three separate mechanisms that could explain the observed impact of H at EOPMB on HC emissions. Each mechanism relies on the formation of mixtures that are too lean to support combustion, or “overlean.” First, overlean regions can be formed after the start of fuel injection but before the end of the premixed burn. Second, during the quasi-steady mixing-controlled burn phase, longer H-values could increase the mass of fuel in overlean regions near the radial edge of the spray cone. Third, after the end of injection, a region of increased entrainment and mixing upstream of H could cause late injected fuel to become overlean. As shown by the solid lines in Figure II.17.4, the model revealed a correlation between H at EOPMB and overlean regions from the quasi-steady mixing-controlled burn (i.e., the second mechanism) that closely matched experimentally observed trends. HC emissions associated with overlean regions produced either before the end of the premixed burn or after the end of injection did not correspond as well to the experimental observations [3].

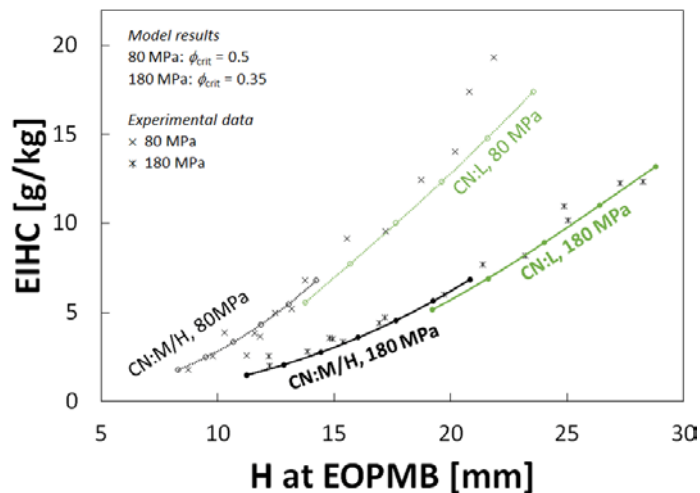


Figure II.17.4 - Lines show predicted HC emissions indices from overlean fuel during the mixing-controlled burn, for 21% oxygen and ϕ_{crit} values of 0.35 and 0.5 for the 180-MPa and 80-MPa injection pressures, respectively. Experimental data points are plotted for comparison.

Proved that the Methodology Previously Developed with Support from this Project Produces Diesel Surrogate Fuels that Closely Approximate the Sooting Tendency of the Target Fuel in Fundamental Burner Experiments

The principal investigator co-led CRC Projects AVFL-18 and AVFL-18a, which created a set of four diesel surrogate fuels that closely emulate the compositional, ignition quality, volatility, and density characteristics of their target fuel [4]. During the current reporting period, the target and surrogate fuel yield sooting indexes were measured in a laminar co-flow flame and shown to agree within an average absolute difference of 13.8% [5]. This good agreement is promising, and it indicates that the previously developed methodology produces surrogates that reasonably emulate even properties of the target fuel that were not explicitly selected for matching.

Conclusions

- The 50% to 100% lower soot levels of DFI indicate that it is a promising technology for future high-efficiency, mixing-controlled CI engines. DFI could enhance efficiency by reducing the backpressure, mass, volume, and regeneration frequency of the aftertreatment system, as well as its cost.
- A simple way to improve DFI performance is to round the inlet and taper the outlet of the duct.
- The overall length of the DFI assembly can be shortened by more than half while maintaining or improving performance. This facilitates DFI implementation in engines by making it easier to avoid interferences between the ducts and the moving valves and pistons of the engine.
- If the primary source of HC emissions from mixing-controlled CI combustion is fuel in overlean regions at the radial periphery of the spray, then DFI could improve combustion efficiency because it is expected to make these leanest mixtures more fuel-rich and hence more readily combustible.
- Optical engine testing of the CRC diesel surrogate fuels is required to determine the extent to which their combustion and emissions formation characteristics emulate that of the target fuel under mixing-controlled CI combustion conditions, and to provide data to assess computational fluid dynamics simulations of fuel effects under such conditions.

References

1. Mueller, C.J., C.W. Nilsen, D.J. Ruth, R.K. Gehmlich, L.M. Pickett, and S.A. Skeen. "Ducted fuel injection: A new approach for lowering soot emissions from direct-injection engines." *Applied Energy* 204:206–220, 2017. doi: 10.1016/j.apenergy.2017.07.001.

2. Gehmlich, R.K., C.J. Mueller, D.J. Ruth, C.W. Nilsen, S.A. Skeen, and J. Manin. "Using ducted fuel injection to attenuate or prevent soot formation in mixing-controlled combustion." Manuscript in preparation, 2017.
3. Cheng, A.S., and C. J. Mueller. "Conceptual investigation of the origins of hydrocarbon emissions from mixing-controlled, compression-ignition combustion." *SAE Int. J. Engines* 10(3):1228–1237, 2017. doi: 10.4271/2017-01-0724.
4. Mueller, C.J., W.J. Cannella, J.T. Bays, T.J. Bruno, K. DeFabio, H.D. Dettman, R.M. Gieleciak, M.L. Huber, C.-B. Kweon, S.S. McConnell, W.J. Pitz, and M.A. Ratcliff. "Diesel surrogate fuels for engine testing and chemical-kinetic modeling: Compositions and properties." *Energy & Fuels* 30 (2):1445–1461, 2016. doi: 10.1021/acs.energyfuels.5b02879.
5. Das, D.D., C.S. McEnally, T.A. Kwan, J.B. Zimmerman, W.J. Cannella, C.J. Mueller, and L.D. Pfefferle. "Sooting tendencies of diesel fuels, jet fuels, and their surrogates in diffusion flames." *Fuel* 197:445-458, 2017. doi: 10.1016/j.fuel.2017.01.099.

Key Fiscal Year 2017 Publications

1. Mueller, C.J., Nilsen, C.W., Ruth, D.J., Gehmlich, R.K., Pickett, L.M., and Skeen, S.A. "Ducted Fuel Injection: A New Approach for Lowering Soot Emissions from Direct-Injection Engines." *Applied Energy* 204:206-220, 2017, doi:10.1016/j.apenergy.2017.07.001.
2. Mueller, C.J., "Improved Mixing-Controlled Combustion Technologies and Fuels for High-Efficiency Compression Ignition Engines." U.S. Dept. of Energy Report DOE/EE-1655: *Vehicle Technologies Office FY 2016 Annual Progress Report, Fuel & Lubricant Technologies*, pp. 100–106, September 2017.
3. Mueller, C.J. "Ducted Fuel Injection." U.S. Patent Application #15,363,966; filed November 29, 2016.
4. Mueller, C.J. "Ducted Fuel Injection with Ignition Assist." U.S. Patent Application #15,364,002; filed November 29, 2016.
5. Mueller, C.J. "Ducted Fuel Injection." U.S. Patent Application #15,666,321; filed August 1, 2017.
6. Cheng, A.S. and C.J. Mueller. "Conceptual Investigation of the Origins of Hydrocarbon Emissions from Mixing-Controlled, Compression-Ignition Combustion." *SAE Int. J. Engines* 10(3):1228–1237, 2017, doi:10.4271/2017-01-0724.
7. Das, D.D., W.J. Cannella, C.S. McEnally, C.J. Mueller, and L.D. Pfefferle. "Two-Dimensional Soot Volume Fraction Measurements in Flames Doped with Large Hydrocarbons." *Proc. Combust. Inst.* 36(1):871–879, 2017, doi:10.1016/j.proci.2016.06.047.
8. Das, D.D., C.S. McEnally, T.A. Kwan, J.B. Zimmerman, W.J. Cannella, C.J. Mueller, and L.D. Pfefferle. "Sooting Tendencies of Diesel Fuels, Jet Fuels, and Their Surrogates in Diffusion Flames." *Fuel* 197:445–458, 2017, doi:10.1016/j.fuel.2017.01.099.
9. Dumitrescu, C.E., A.S. Cheng, E. Kurtz, and C.J. Mueller. "A Comparison of Methyl Decanoate and Tripropylene Glycol Monomethyl Ether for Soot-Free Combustion in an Optical Direct-Injection Diesel Engine." *J. Energy Res. Technol.* 139(4):042210, 2017, doi:10.1115/1.4036330.
10. Gehmlich, R.K., C.J. Mueller, D.J. Ruth, C.W. Nilsen, S.A. Skeen, and J. Manin. "Using Ducted Fuel Injection to Attenuate or Prevent Soot Formation in Mixing-Controlled Combustion." Manuscript in preparation, 2017.

II.18 Characterization of Biomass-Based Fuels and Fuel Blends for Low-Emissions, Advanced Compression Ignition Engines

Professor Ajay K. Agrawal, Principal Investigator

University of Alabama
359 H.M. Comer Hall
Tuscaloosa, AL 35487
E-mail: aagrawal@eng.ua.edu

Professor Joshua Bittle, Principal Investigator

University of Alabama
359 H.M. Comer Hall
Tuscaloosa, AL 35487
E-mail: jrbittle@eng.ua.edu

Michael Weismiller, DOE Technology Manager

U.S. Department of Energy
E-mail: Michael.Weismiller@ee.doe.gov

Start Date: May 1, 2017	End Date: January 31, 2020	
Total Project Cost: \$630,493	DOE share: \$567,301	Non-DOE share: \$63,192

Acknowledgments

NETL Project Manager

Ralph Nine, National Energy Technology Laboratory

Project Introduction

The ultimate goal of this project is to accelerate deployment of co-optimized fuels and engines that will reduce fuel consumption and criterion pollutants and greenhouse gas emissions. Specifically, we will acquire combustion measurements in a constant pressure flow rig (CFR) with optical access and develop models to predict combustion characteristics based on known fuel and ambient conditions. We are targeting prediction of properties relevant to lean lifted flame combustion, a mixing-controlled low temperature combustion strategy to reduce soot production in advanced compression ignition engines. Unlike other low temperature combustion strategies that rely upon chemical kinetics, the combustion or heat release rate in lean lifted flame combustion can be controlled by the fuel injection timing.

Objectives

- Experimentally investigate fuel–air mixing and subsequent ignition and combustion processes and properties in different fuel injection regimes, with particular focus on supercritical fuel injection when the surface tension is no longer present, and the mixing of the dense supercritical fluid with the ambient air depends mainly upon the influence of turbulence and real-gas effects on thermodynamics and transport properties.
- Identify synergistic opportunities offered by biofuels and their blends with conventional fuels. We seek to analyze the relationship between fuel physical and chemical properties and combustion properties to co-optimize fuels and advanced compression ignition engines.
- Perform experiments in a flexible, modular, and optically accessible flow rig (available at University of Alabama) with a continuous supply of preheated compressed air to attain the desired pressure and temperature within the chamber volume. The ability to rapidly rinse the test chamber permits acquisition of statistically significant experimental sample sizes and will allow us to collect extensive data sets for a range of test conditions and biofuel blends.

- Utilize a suite of time-resolved (TR) optical diagnostics techniques: TR-rainbow schlieren deflectometry (RSD) technique to examine fuel–air mixing and turbulent flame speed, TR-OH* chemiluminescence to quantify turbulent flame structure, and TR two-color pyrometry to characterize the soot production.
- Develop a neural network to model functional relationships between fuels' physical and chemical properties and ignition and combustion characteristics. The models will be validated against secondary sets of data not used for the initial development.

Approach

The project will systematically investigate fuel–air mixing and subsequent ignition and combustion processes in trans- and super-critical regimes at diesel conditions. Selected experiments will also be conducted at subcritical conditions for baseline comparisons. Proposed experiments are being conducted in a CFR with a continuous supply of preheated compressed air to attain the desired pressure and temperature within the chamber volume. In this CFR, the time between tests is greatly reduced (~ 0.2 Hz) by upstream control of the ambient conditions to create bulk air (or inert gas) flow rates that are minimal compared to the fuel jet velocity. High-fidelity data will be acquired simultaneously by three different optical diagnostics techniques at high temporal and spatial resolutions. These techniques will focus on different regions of the jet and flame and provide not only the time-averaged measurements, but also help delineate the instantaneous flow and chemical features. Phenomena such as autoignition, flame stabilization, and soot formation can be observed simultaneously in real-time, which will improve our understanding and provide benchmark data for computational fluid dynamics code development.

The fuel property prediction model will be developed as a neural network. A neural network is made up of input nodes (test conditions) and output nodes (combustion properties). Between these input/output node layers are any number of hidden layers where each node represents some weighted and biased transfer function that considers all possible input effects. The remaining hidden layers build on this layering affect to account for all possible first and secondary input to output interactions. The gains and biases in the hidden layers are determined by training the network with known data. After validating against other known data not used for training, the network can function as fuel based combustion property predictor.

Results

- Met key milestones and the project budget is on track
- Designed, developed, and independently tested a two-color pyrometry system
- Independently tested the OH* chemiluminescence system
- Integrated the RSD system with the CFR
- Developed plans to integrate OH* chemiluminescence and two-color pyrometry systems with CFR
- Performed baseline experiments to demonstrate successful operation of the CFR at diesel condition demonstrating fuel–air mixing, ignition, and combustion
- Obtained quantitative RSD data for a baseline experiment using *n*-heptane fuel

Two-Color Pyrometry System

We have developed a preliminary two-color soot pyrometry setup shown in Figure II.18.1. Emissions from the flame are captured by a 2-in decollimating lens which is coupled with a convex lens to deliver a 1-in collimated image into the main pyrometer optics. The collimated light is split by a 50/50 beam-splitter and then the split signal is bandpass filtered (filters are illustrated as yellow in Figure II.18.1) separately at 550 nm and 650 nm. A knife-edge prism mirror is used to project the separately filtered signals onto the camera. Additionally, a number of mirrors are utilized to ensure that the optical path length of the two signals is the same, which is necessary to maintain proper image focus. The setup allows a single camera to capture separated signals filtered at different wavelengths. In order to develop and debug the optical set up separately from the spray chamber, a simple methane flame was imaged using a Bunsen burner.

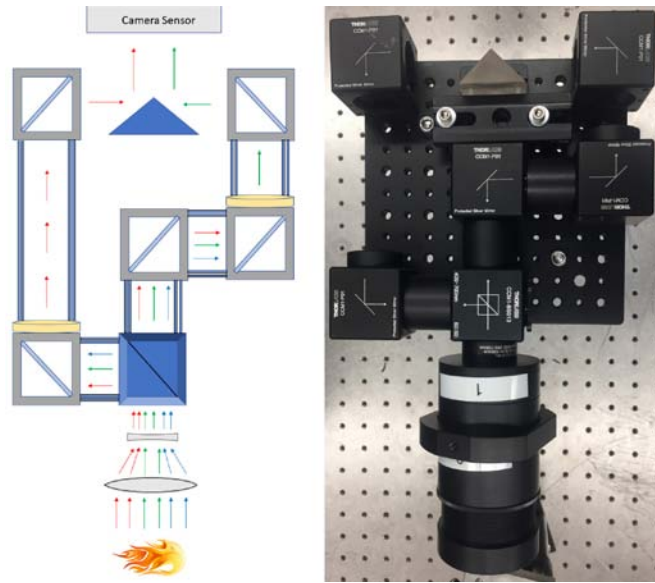


Figure II.18.1 - Two-color soot pyrometer schematic (left) and optical hardware (right) (Source: University of Alabama)

A steady Bunsen burner methane flame was utilized to develop the image processing codes and to ultimately calculate temperature throughout the flame. The left frame of Figure II.18.2 shows the double image of the field of view without the bandpass filter and the burner tip visible at the bottom of the image. This frame demonstrates the focus and double imaging enabled by the beam splitter and single camera setup. The second frame shows images of the flame at the two wavelengths. Clearly, the light emission at 650 nm is more intense. This follows from the yellow/orange color of the flame considering that 550 nm is in the green spectrum and 650 nm is in the red spectrum.

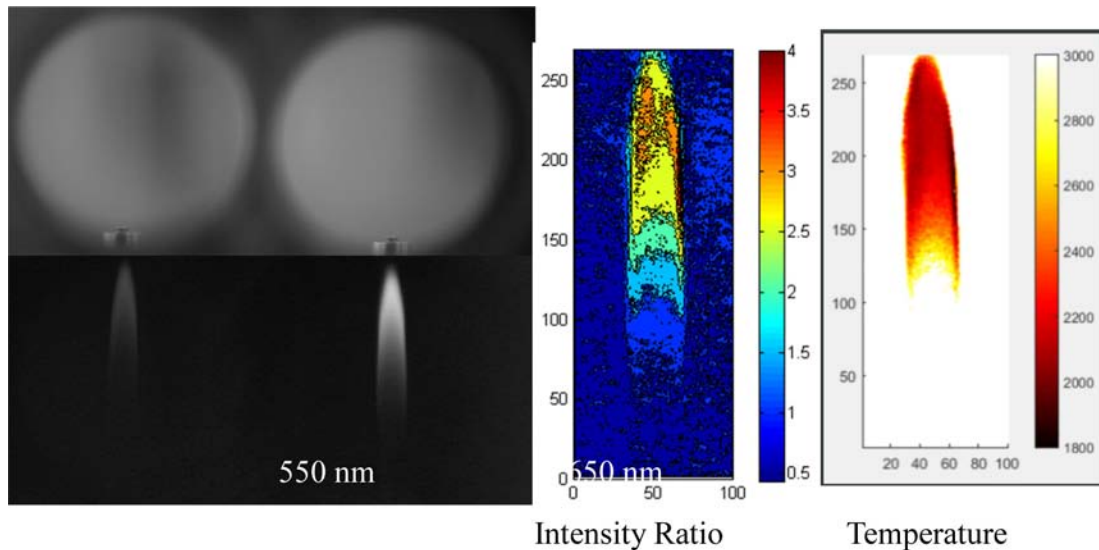


Figure II.18.2 - Two-color soot pyrometry image processing. (Left) double image of burner showing tip in focus, no filters. (Middle) double image of flames at two wavelengths. (Right) Pixel-by-pixel intensity ratio on the left and calculated temperature on the right.

The right frame of Figure II.18.2 shows the pixel-by-pixel ratio of intensity at the two wavelengths (left side) and calculated temperature assuming black-body radiation (right side). In Figure II.18.2, the calculated temperature ranges from 1,800°C to 2,800°C. The adiabatic flame temperature for a stoichiometric methane reaction at ambient conditions is approximately 1,950°C. Although the analysis provides qualitative trends, the assumption of black-body radiation clearly introduces large errors in temperature calculation.

The new CFR shown in Figure II.18.3 has been installed and integrated with the air supply and exhaust systems. The system has been tested with airflow at the maximum pressure attainable with the air compressor (34 bar) and with a heater set point of 1,100 K. To demonstrate the successful chamber operation, we include the images in Figure II.18.4 show a single frame from high-speed videos acquired by simple visual imaging. The ambient air is at 33 bar and 825 K. The fuel is *n*-heptane injected for 2 ms at 1,000 bar injection pressure. The injector is located towards the top of the image and the thermocouple used to characterize the near injector temperature is visible protruding from the left side below the injector on the left image. The image on the left was recorded at 10 kHz with an exposure time of 99 μ s, while the image on the right was recorded at 20 kHz with an exposure time of 49 μ s. These two images represent two separate injections illustrating fuel–air mixing in the near field and combustion downstream resulting from autoignition. The fuel is no longer being injected at the time of these images.

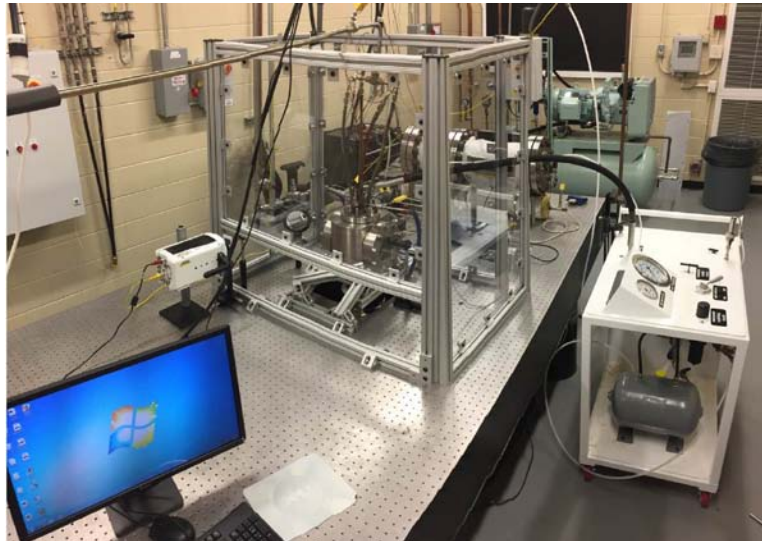


Figure II.18.3 - New CFR with air exhaust, injector cooling, and instrumentation installed (Source: University of Alabama)

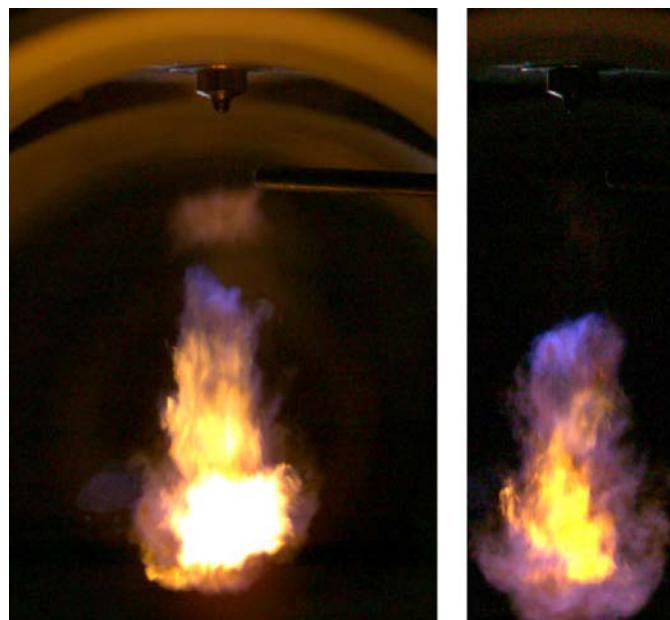


Figure II.18.4 - First reacting sprays captured in new CFR, one (left) with longer exposure time and another (right) with less exposure time (Source: University of Alabama)

Figure II.18.5 illustrates the RSD analysis steps. (a) The raw schlieren images are converted from red–green–blue format as saved by the camera to hue–saturation–value format. (b) The hue at each pixel is converted to ray deflection angle at the pixel location based on a calibration of the rainbow filter. (c) A single image provides the instantaneous ray deflection angle value at each pixel location. We perform a number of injection experiments and an ensemble average of 50 images is taken at each injection time. Thus, average deflection angle is obtained at each time step after start of injection by ensemble averaging instantaneous deflection angle at each pixel in the frame over all injections (50 in this case). (d) The average deflection angle is used to estimate the center plane fuel volume fraction in the spray through the Abel inversion process, which converts deflection angle to local fuel mass fraction. This process requires assumptions of axisymmetry and binary mixing between the fuel and air. Thus, quantitative results are valid only in the vapor region upstream of the combustion zone.

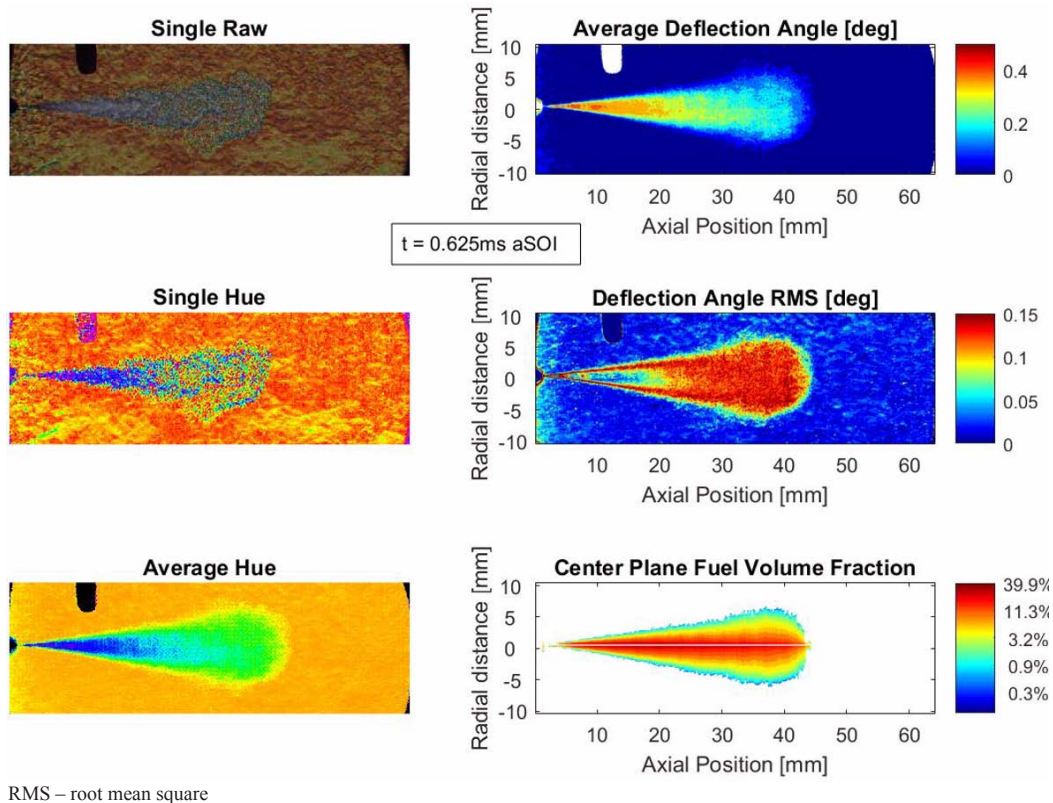


Figure II.18.5 - Image processing steps for RSD images at 0.625 ms after start of injection (aSOI) for *n*-heptane injected at 1,000 bar for 4 ms into ambient air at 30 bar and 825 K. A total of 50 injections were captured in this case.

We have also computed another feature, the deflection angle. Its fluctuations are quantified by RMS deflection angle; this is a useful way to visualize the highly turbulent regions of the jet. Specifically notice the edges of the spray near the injector representing a shear layer between the fuel jet and the ambient air. Downstream as the fuel and air become well mixed the entire spray becomes highly variable.

Figure II.18.6 shows the results at 1.3 ms aSOI at which time the reaction is underway downstream. The first thing to note is the high deflections in the reaction zone resulting from temperature induced density gradients. This is as opposed to the mixing induced density gradients near the injector. Another interesting feature is the reduction in deflection angle between the near injector spray and the downstream reaction zone. We believe this is caused by initial reactions causing slight temperature rise (reducing density to near that of the ambient in this case) prior to subsequent primary ignition. In other words there is a transition region between the dense spray near the injector and the low density reaction zone downstream in which the density gradient is approximately zero through the spray. In the future data processing codes we will have to ensure the reacting regions of the spray are not included in the fuel volume fraction calculations.

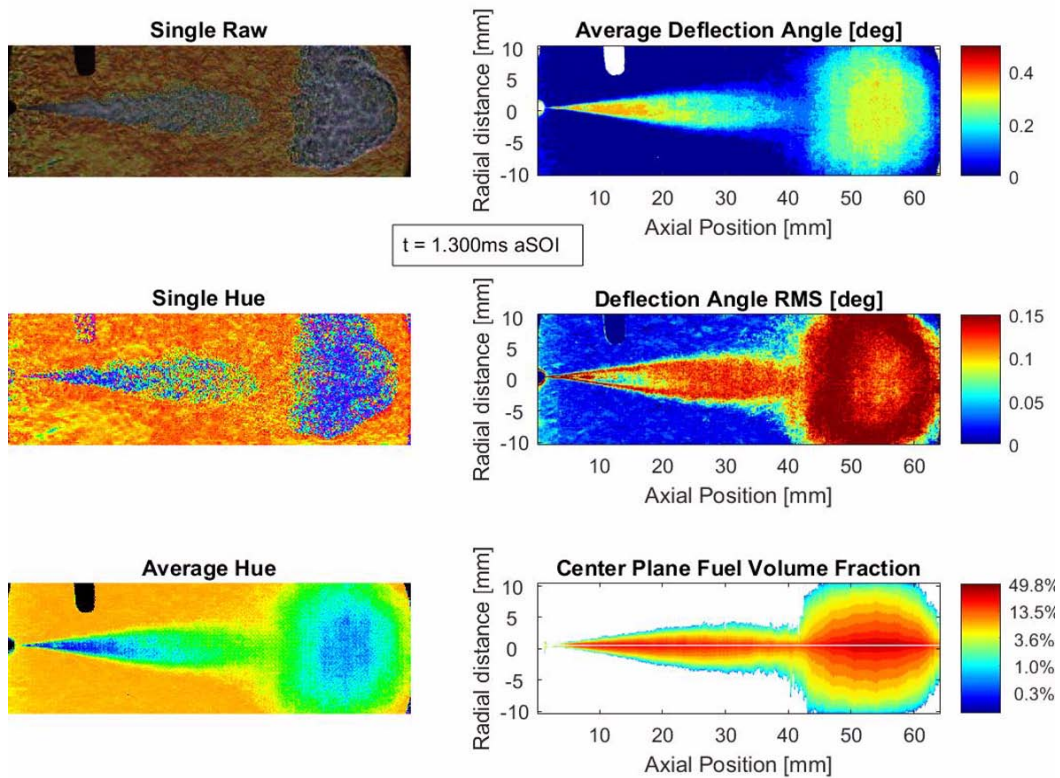


Figure II.18.6 - RSD images during combustion at 1.3 ms aSOI for *n*-heptane injected at 1,000 bar for 4 ms into ambient air at 30 bar and 825 K. A total of 50 injections were captured in this case.

Conclusions

- CFR has been operated successfully for a range of chamber pressures and temperatures
- RSD techniques have been applied to acquire quantitative fuel–air mixing data throughout the field of view at high spatial and temporal resolutions

Key Fiscal Year 2017 Publications

1. Wanstall, Christopher, Ajay K. Agrawal, and Joshua Bittle. “Quantifying liquid core of a fuel spray by rainbow schlieren deflectometry.” *Applied Optics*, vol. 56, No. 30, pp 8385–8393, October 20, 2017.

II.19 Fuel Property Database

J. Timothy Bays, Principal Investigator

Pacific Northwest National Laboratory
902 Battelle Blvd., MS K2-14
Richland, WA 99352
E-mail: tim.bays@pnnl.gov

Kevin Stork, DOE Technology Manager

U.S. Department of Energy
E-mail: Kevin.Stork@ee.doe.gov

Start Date: October 1, 2016	End Date: September 30, 2017	
Total Project Cost: \$150,000	DOE share: \$150,000	Non-DOE share: \$0

Acknowledgments

Co-Authors

Alejandro Heredia-Langner, John R. Cort, Kristin H. Jarman, Karl O. Albrecht, Daniel J. Gaspar, Gregory W. Coffey, Margaret C. Jones, Ahmet K. Bingol, John C. Linehan, Evgueni Polikarpov, Leah Stevenson; Pacific Northwest National Laboratory

PNNL Reference Number: PNNL-27078

Project Introduction

This project is focused on developing a fuel blending model that results in a set of fuel properties in the finished fuel by combining sets of chemical structures obtained from several fuel blendstocks. Understanding fuel properties and developing a blending model support the incorporation of renewable and unconventional hydrocarbon fuels into the domestic fuel supply, enhancing domestic energy security, economic competitiveness, and improving environmental quality. Specifically, this project seeks to:

- Facilitate the successful co-optimization of fuels and advanced combustion engines, enabling the introduction of future fuel feedstocks and reducing the United States' dependence on foreign oil.
- Advance an understanding of the role of the chemical structures and substructures within a fuel on fuel properties (important to current and future engine combustion strategies).
- Develop a fuel blending model based upon analytical approaches that correlate molecular structures within fuel components to fuel properties and performance, generating a predictive tool for integration into a fuel properties database.

Objectives

Fiscal Year 2017 research objectives were to:

- Conduct nuclear magnetic resonance (NMR) spectroscopic measurements needed to correlate Co-Optima fuel mixtures' chemical substructures, i.e., types of chemical bonds, with fuel properties.
- Measure the phase change behavior of four diesel surrogate fuels created in Coordinating Research Council (CRC) Project AVFL-18a at high pressures simulating those of vehicle fuel injection systems, and attempt to mitigate fuel solidification using additives provided by CRC.
- Develop a fuel blending model that results in a set of fuel properties in the finished fuel by combining sets of chemical structures obtained from each fuel blendstock.

Approach

The first portion of this project used NMR spectroscopy to identify and quantify the chemical functional groups in 27 complex fuel mixtures, leveraging bio-derived compositions produced from projects funded by the Bioenergy Technologies Office or other sources, and correlated specific functional groups to fuel performance properties. This information was then used to develop a predictive blending model by specifying the functional group population distributions needed to achieve a set of desired fuel properties, according to inferences made from the analyzed data.

The second portion of this project assessed the propensity of fuels to change from a liquid phase to a solid phase under pressures representative of fuel injection systems. This was particularly important when trying to avoid unexpected fuel solidification in diesel fuel surrogates, where a high n-alkane concentration increases susceptibility to wax crystal formation. Four diesel fuel surrogates created under the auspices of the CRC Project AVFL-18a were used to probe these changes and additives provided by CRC were used to attempt to lower the final melting point temperatures obtained at each pressure. A high-pressure apparatus custom-built at Pacific Northwest National Laboratory (PNNL) was used to monitor the solid–liquid phase equilibria of each sample or sample-additive combination. These experiments will also be extended to understanding the temperature–pressure effects associated with a single-chemical fuel blendstock having concentrations up to 20% in candidate Co-Optima fuels.

Results

Developed Predictive Models for Derived Cetane Number (DCN), T10, T50, and T90, and Started a Reid Vapor Pressure Model by Quantitatively Assessing the Pairwise Interrelationships Among 27 Functional Groups for Each of the Predicted Properties

To assess functional groups, the ^{13}C NMR spectrum of each fuel sample was broken into 27 readily understandable functional group regions. These groups were integrated and the results normalized in order to represent the functional groups as a percentage of the total ^{13}C contributions in each spectrum. Models were built to test the hypothesis that fuel properties result from combinations of one or more functional groups. These models relate the integrated areas of functional groups to fuel blendstock performance properties. In choosing to relate these two sets of information, it is necessary to use a modeling approach that reflects the constrained system of the fuel sample. The system is constrained because changing the relative abundance of any one functional group changes the relative abundance of all of the other functional groups, so the variables representing each of the functional groups are not independent. Since the sample set of 27 fuels is small, to avoid overfitting the data, PNNL has identified the simplest models that work well, generally gravitating to models having between five and nine terms. Figure II.19.1 shows models for DCN using an ignition quality tester (ASTM D6890) and the temperature at which 10% of the fuel volume was recovered during a distillation (T10) from simulated distillation measurements (ASTM D2887). Similar models have been developed for T50 and T90, where all four values are important inputs to a useful blending model. Data for Reid vapor pressure has also been taken, but modeling is not yet complete.

Developed an Initial Chemical Structure-Based Fuel Blending Model Based upon the Predictive Fuel Property Models for DCN, T10, T50, and T90

When developing a blending model, particularly in a constrained system, it is important to understand the interrelationships between the functional groups and the properties incorporated into the model. Figure II.19.2 shows two examples of how pairwise relationships can be used to assess functional groups predictive of DCN with the caption explaining these relationships. In a blending model, sets of interactions within a property prediction model may be optimized, along with values for individual components to meet a specified fuel property value. This process can be performed iteratively, stepping through models for each property, or by simultaneously optimizing model outputs for all of the properties, in order to meet the targets specified by the blending model.

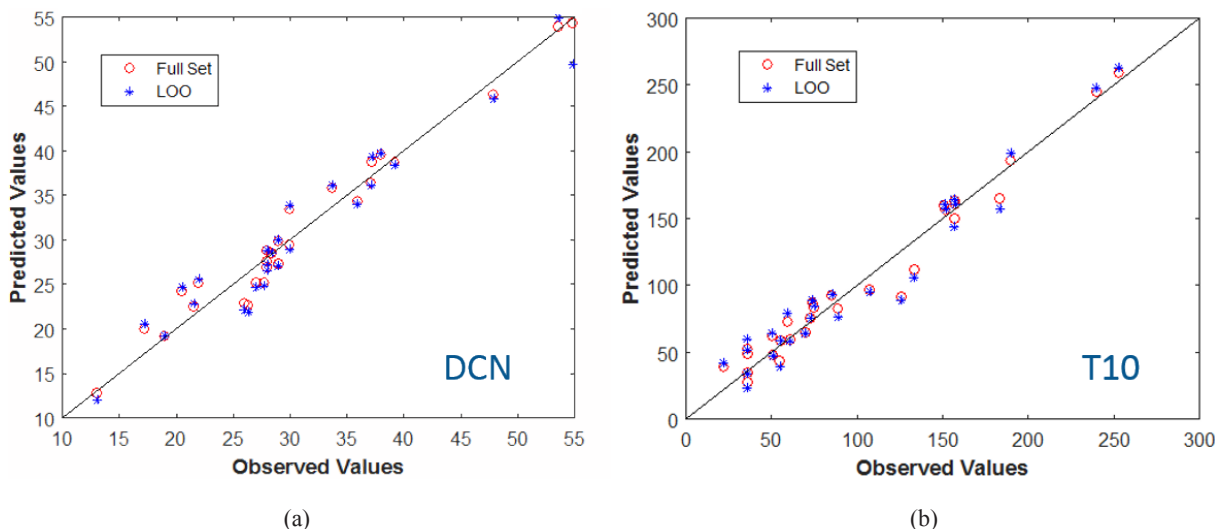


Figure II.19.1 - Representative models for DCN and T10. Observed values are compared to predicted using the full data set (Full Set, red circles), and leave-one-out predictions (LOO, blue asterisks), where one data point is removed from the model and the predictions re-run without that point. Close agreement between these values suggests that the models are not overly dependent upon any one data point. (a) Model for DCN data from ASTM D6890, where the model contains seven terms, including the intercept, five predictors, and one two-factor interaction, yielding an $R^2 = 0.9625$, $adj-R^2 = 0.9512$. (b) Model for simulated distillation T10 data from ASTM D2887, where the model contains seven terms, and uses only four regions as predictors, $R^2 = 0.9642$, $adj-R^2 = 0.9544$.

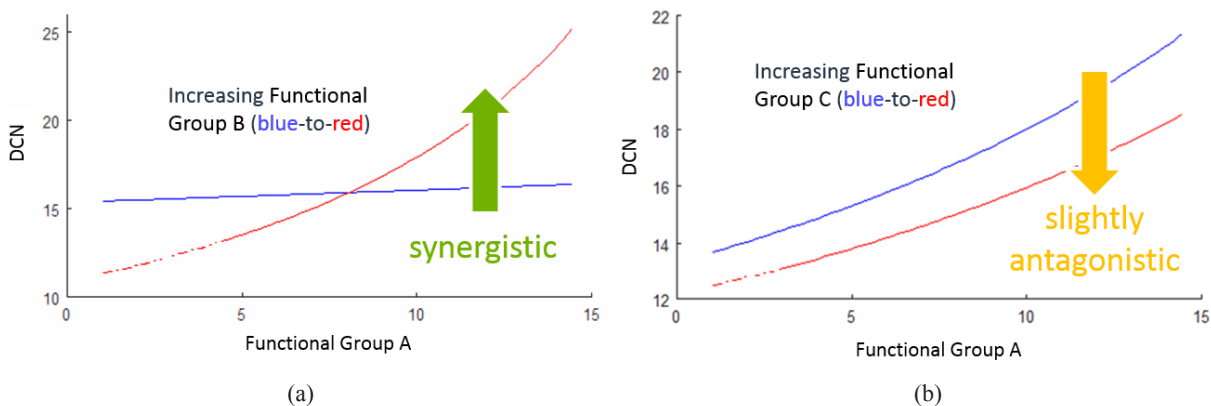


Figure II.19.2 - Blending model development. The charts above show the pairwise interactions between two sets of functional groups on the value of DCN. In both charts, the population of Functional Group A is increased from left-to-right along the X-axis. A second functional group (Functional Group B for Chart a and Functional Group C for Chart b) is held at the lowest measured value (blue line) or the highest measured value (red line). For Chart a when Functional Group B is held at the lowest measured value (blue line), the effect of increasing Functional Group A on the DCN value is nearly negligible. However, when Functional Group B is held at the highest measured value (red line), DCN increases with increasing Functional Group A, suggesting that Functional Groups A and B interact synergistically in the prediction of DCN. For Chart b when Functional Group C is held at the lowest measured value (blue line), DCN values increase with the amount of Functional Group A present in the sample. Similarly, when Functional Group C is held at the highest measured value (red line), DCN values also increase with the amount of Functional Group A. In Chart b the red and blue lines are similarly curved, but offset, suggesting that both functional groups influence predicted DCN values; however, the curvature of the red line is slightly less than that of the blue line indicating that when Functional Group C is at a maximum value, the influence of Functional Group A on predicting DCN is diminished, suggesting a slightly antagonistic interaction in the prediction of DCN with this pair of functional groups. Thus from Chart a, a blending model would benefit from using Functional Groups A and B together to predict DCN, and not benefit from comparing the Functional Groups A and C. In this figure, the functional groups are more explicitly described by the following:
 Functional Group A represents “C in open chains. CH_2 benzylic and CH_2 not adjacent to CH in an alkyl group;”
 Functional Group B represents “CH in allylic and benzylic groups and in joining tetralin ring;” and Functional Group C represents “CH, CH_2 beta from a secondary carbon and in cyclopentyl and cyclohexyl rings.”

Measured the Liquid–Solid Equilibrium Pressures and Temperatures for Four Diesel Fuel Surrogates Developed in Conjunction with the CRC from Atmospheric Pressure to 350 MPa

In collaboration with the CRC within Project AVFL-18a, the unexpected solidification of dodecane in the fuel line serving a constant volume combustion chamber forced the project team to consider the possibility that the recently developed surrogate diesel fuels may solidify under the high pressures experienced in a diesel common rail fuel injector system [1,2]. This concern arose from the high concentrations of n-alkanes used as palette compounds to match specified properties of the target diesel fuel, [2] and led to the experiments conducted at PNNL to elucidate the extent of this behavior. Methods used at PNNL to identify temperatures and pressures representing the solid–liquid equilibria line for each surrogate fuel were undertaken and previously reported with the most recent results presented in Figure II.19.3 and shown in contrast to a gas-to-liquids derived diesel (GTL-Diesel) provided by CRC [3,4].

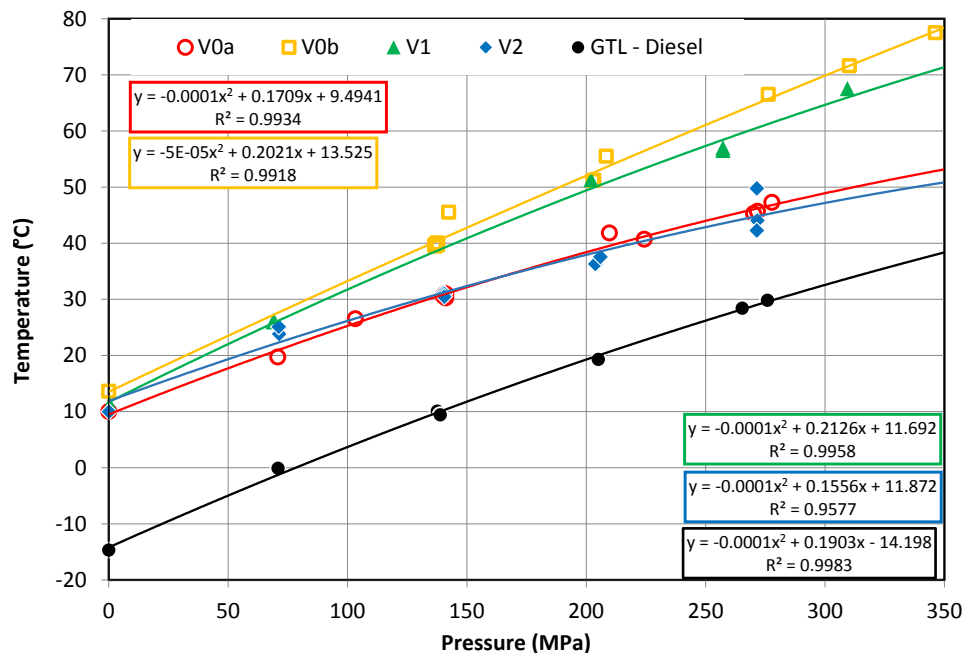


Figure II.19.3 - Comparison of the solid–liquid equilibria for four diesel fuel surrogates, V0a, V0b, V1, and V2, and GTL-Diesel. Data points for each material are shown in various colors. Compositions for each surrogate were previously reported [1,2]. Trendlines and the second order polynomial fits are presented in boxes outlined in colors corresponding to each surrogate. Each material can be expected to remain a liquid at temperatures above its respective trendline at a given pressure. Below its respective trendline, a pure material will solidify, and a multicomponent material will have at least one component freeze out.

Assessed the Influence of Eight Cold Flow Improvers at Concentrations from 500 ppm to 10,000 ppm on the Liquid–Solid Equilibrium Values for One of the Diesel Surrogate Fuels

Because the liquid–solid equilibria for the diesel fuel surrogates were in some cases well above room temperature at pressures representative of modern diesel fuel injection systems, efforts were made to forestall solidification to avoid the need to heat fuel systems in order to test the diesel fuel surrogates. Cold flow improvers were provided through the AVFL-18a team and were added to surrogate V0b, since phase behavior data indicated that V0b represented a limiting case among the four surrogates. Treat rates tested for each of the cold flow improvers ranged from the manufacturer’s recommended treatment rate, which spanned from 500 ppm to a little over 3,000 ppm, to a maximum tested treat rate of 10,000 ppm (1% v/v). Tested concentrations of cold flow improvers were adjusted to identify trends in final melting point versus additive concentration. The inset of Figure II.19.4 shows the results obtained from the introduction of eight cold flow improvers at 5,000 ppm treatment rate to diesel fuel surrogate V0b. The larger graph shows the full pressure range tested, while the inset graph emphasizes the pressure–temperature range where most of the testing occurred. As shown in Figure II.19.4, introduction of the cold flow improver did not result in lowering the liquid–solid equilibrium temperature to a degree that recommended use in one of the diesel fuel surrogates. Data points that were below

the liquid–solid equilibrium line for V0b were carefully validated by observing the photographs taken to record the final melting point of the observed crystallites. Changing the concentration to either a lower or higher value resulted in a final melting point closer to that of V0b without a cold flow improver. No reliable trends based on changing cold flow concentrations have been identified. Observations of the crystallites formed suggested that with the cold flow improvers, the crystallites were dramatically reduced in size, from relatively large discrete crystals to small crystals below the resolution of the microscope camera. These small crystallites often resembled a fog, making the melting point determination difficult. These observations were in keeping with the function of a cold flow improver, and were therefore not unexpected. A detailed description of how cold flow improvers limit crystal size can be found in CRC Report Number 671 [5].

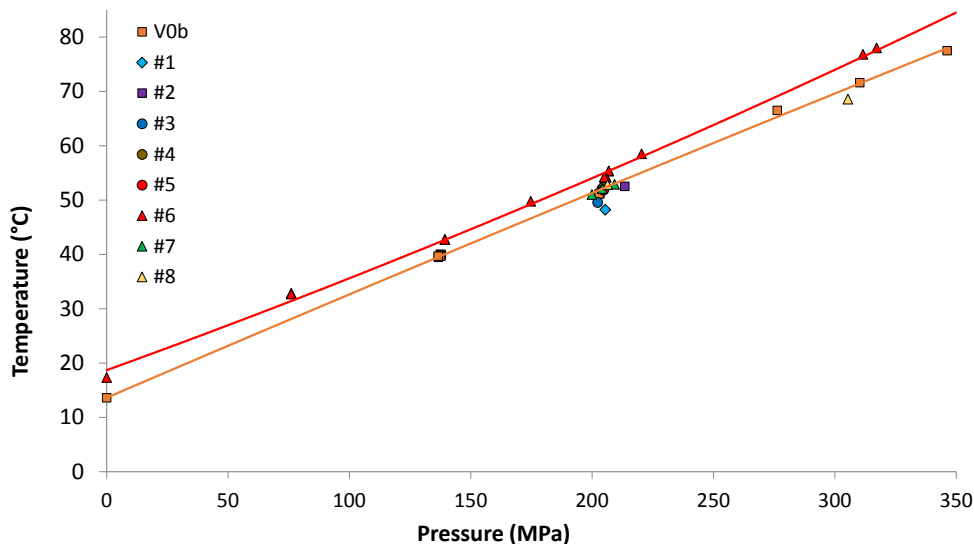


Figure II.19.4 - Comparison of the solid–liquid equilibria for diesel fuel surrogate V0b with eight cold flow improvers. The larger graph documents cold flow improver performance across a broad range of pressures, while the inset graph focuses on the area around 205 MPa, where most testing occurred. Shown here are the results derived from treat rates of 5,000 ppm for each cold flow improver in surrogate V0b.

Conclusions

- Between four and five functional groups (carbon types) can be used for high-quality fuel property predictions of four important fuel properties (T10, T50, T90, and DCN) in a data set derived from 27 complex fuel mixtures. Initial models for predicting Reid vapor pressure were promising.
- A blending model integrating these fuel properties can be used to ascertain which fuel blends to combine and the appropriate ratio of blends needed to attain a set of fuel properties. These models take into account important pairwise influences between carbon types or functional groups and will become more robust in time as additional fuel sets and properties are incorporated.
- Liquid–solid equilibria were recorded for four diesel surrogates and suggest that in some fuel injection systems the surrogate diesel fuel will require substantial heating to avoid pressure-induced fuel solidification. Additional data will further increase the understanding of these phase changes.
- Eight cold flow improvers provided by CRC were tested using diesel fuel surrogate V0b and not found to lower the final melting point. Additional work will need to be undertaken to identify a means of lowering the final melting point.

References

1. Mueller, C.J., W.J. Cannella, T.J. Bruno, B. Bunting, H.D. Dettman, J.A. Franz, M.L. Huber, M. Natarajan, W.J. Pitz, M.A. Ratcliff, and K. Wright. "Methodology for Formulating Diesel Surrogate Fuels with Accurate Compositional, Ignition-Quality, and Volatility Characteristics." *Energy & Fuels* 26 (6):3284–3303. 2012. doi: 10.1021/ef300303e.
2. Mueller, Charles, William Cannella, J. Timothy Bays, Thomas Bruno, Kathy DeFabio, Heather Dettman, Rafal Gieleciak, Marcia Huber, Chol-Bum Kweon, Steven McConnell, William Pitz, and Matthew Ratcliff. "Diesel Surrogate Fuels for Engine Testing and Chemical-Kinetic Modeling: Compositions and Properties." *Energy & Fuels* 30 (2):1445–1461. 2016. doi: 10.1021/acs.energyfuels.5b02879.
3. Stork, Kevin. "Fuel and Lubricant Technologies, 2015 Annual Report." <https://energy.gov/eere/vehicles/downloads/vehicle-technologies-office-fuel-and-lubricant-technologies-2015-annual>: U.S. Department of Energy, Energy Efficiency & Renewable Energy, Vehicle Technologies Office. 2016.
4. Stork, Kevin. "Fuel and Lubricant Technologies, 2016 Annual Report." <https://energy.gov/eere/vehicles/downloads/fuel-and-lubricant-technologies-2016-annual-progress-report>: U.S. Department of Energy, Energy Efficiency & Renewable Energy, Vehicle Technologies Office. 2017.
5. Chandler, John, David Daniels, Tony Frank, Roger Gault, Garry Gunter, Dennis Hess, Shailesh Lopes, Ken Mitchell, Manuch Nikanjam, Sheryl Rubin-Pitel, and Andre Swarts. "Diesel Fuel Low Temperature Operability Guide." Alpharetta, GA: Coordinating Research Council. 2016.

Key Fiscal Year 2017 Publications

1. Bays J.T., A. Heredia-Langner, J.R. Cort, G.W. Coffey, M.C. Jones, K.H. Jarman, A.K. Bingol, J.C. Linehan, K.O. Albrecht, D.J. Gaspar, E. Polikarpov, and L.E. Stevenson. "Fuel Property Blending Model." PNNL-26976, Pacific Northwest National Laboratory, Richland, WA. 2017. (Unpublished)

II.20 Fuel Property Blending Model

William J. Pitz, Principal Investigator

Lawrence Livermore National Laboratory
P. O. Box 808, L-372
Livermore, CA 94551
E-mail: pitz1@llnl.gov

Kevin Stork, DOE Technology Manager

U.S. Department of Energy
E-mail: Kevin.Stork@ee.doe.gov

Start Date: October 1, 2016	End Date: September 30, 2018	
Total Project Cost: \$225,000	DOE share: \$225,000	Non-DOE share: \$0

Acknowledgments

Co-Authors

Marco Mehl, Scott W. Wagnon, Kuiwen Zhang, Goutham Kukkadapu, Charles K. Westbrook;
Lawrence Livermore National Laboratory

This work was performed under the auspices of the U.S. Department of Energy by Lawrence Livermore National Laboratory under Contract DE-AC52-07NA27344.

Project Introduction

The combustion of transportation fuels in internal combustion engines are generally characterized by important properties such as Research Octane Number (RON), Motor Octane Number (MON), cetane number, and flame speed. However, predicting these properties for fuels is challenging because of complex chemical–kinetic interactions of fuel components that cause non-linear behavior. To address this issue, the Lawrence Livermore National Laboratory (LLNL) kinetic modeling team is developing chemical kinetic models that can predict RON, MON, flame speed, and other fuel properties, and can model the complex behavior of these mixtures under conditions in advanced spark ignition (ASI) and advanced compression ignition (ACI) engines. These accurate and validated chemical kinetic models are critical for developing insight into how fuel properties impact engine performance. To use these chemical kinetic models in multidimensional simulation codes, the models are reduced in size and employed to simulate combustion in ASI and ACI engines. These insights and combustion simulations will guide efforts to discover promising high-performance fuels (HPFs) and base fuel blends that provide the desired engine combustion properties under ASI and ACI engine conditions.

Objectives

LLNL is developing chemical models and associated correlations to predict the blending behavior of HPFs when mixed with conventional fuels like gasoline and diesel fuels.

Approach

Chemical kinetic models for HPFs of interest for blending with gasoline and diesel fuels are developed. Next, these chemical kinetic models are combined with kinetic models for conventional fuels to represent next-generation ground transportation fuels. Correlations are developed between engine combustion properties (such as RON, MON, octane sensitivity [OS], and cetane number) and key quantities computed from the chemical kinetic model (such as ignition delay and slope of the ignition delay curve in the low temperature chemistry region). Using the detailed chemical model and these correlations, key engine combustion properties can be predicted. Also, the detailed chemical kinetic model can be used to interpret the results in terms of the importance of different chemical paths identified by the simulations.

Results

Key accomplishments for Fiscal Year 2017:

- Octane blending behavior predicted for Co-Optima HPFs in gasoline within ± 3 octane units
- Developed new correlations to predict octane ratings using a new chemical kinetic model for gasoline with Co-Optima HPFs

In Fiscal Year 2017, the blending of HPFs in a surrogate gasoline was simulated using a newly developed chemical kinetic surrogate model for gasoline with 21 HPFs for Co-Optima that is discussed in the LLNL project entitled “Kinetic Model Development.” Because HPFs increase RON and OS (RON - MON) when blended in a base gasoline, they are attractive for use in high-efficiency, boosted, spark ignition engines. Figure II.20.1 shows that the simulated behavior for RON and OS compares well with the measured behavior for eight Tier 3 HPFs that were downselected by Co-Optima. The computed and simulated RON and OS are within ± 3 octane units.

In Fiscal Year 2017, new correlations were developed to predict octane ratings from ignition delay times (IDTs) computed with an updated chemical kinetic model for gasoline (Figure II.20.2). To get a more accurate prediction of RON, a correlation was developed for RON instead of one for anti-knock index ((RON + MON)/2) as was done previously. Additionally, experimental targets of more fuel mixtures with known RON and OS were included in the generation of the correlation including gasoline primary reference fuels (PRFs: iso-octane and n-heptane), octane-sensitive fuels, and highly octane-sensitive fuels with ethanol. For the correlations, RON was correlated with the logarithm of IDT at 775 K, while OS was correlated with the minimum slope in the negative temperature coefficient (NTC) region of the IDT curve, which occurs from 725–925 K (Figure II.20.2). The IDTs were computed for a pressure of 25 atm and for stoichiometric mixtures. These conditions correlate well with the MON and RON test.

Another important fuel property for ASI engines is flame speed. After spark ignition in an engine, high flame speeds consume the unburned gas in the combustion chamber before it can auto-ignite and cause engine knock. Engine knock can damage the engine and its occurrence limits the operating range of high-efficiency, boosted spark ignition engines. Figure II.20.3 shows the ability of the updated chemical kinetic model for gasoline surrogates to compute the flame speeds for a high-octane gasoline with moderate OS over a wide pressure and temperature range relevant to the ASI engines.

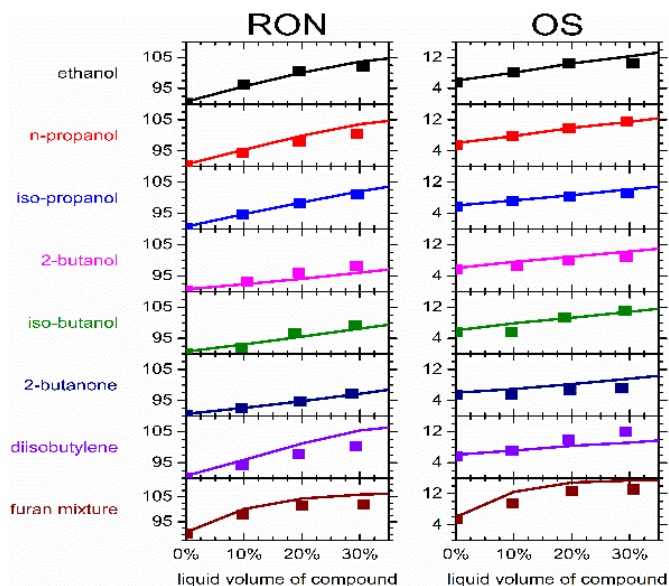


Figure II.20.1 - The predictions of octane blending of Co-Optima Tier 3 HPFs in a four-component base gasoline using the Co-Optima chemical kinetic model (curves) compared experimentally measured RON and OS (symbols) for the same four-component base gasoline (HPFs). The measurements are from McCormick et al. [1]. (Source: LLNL)

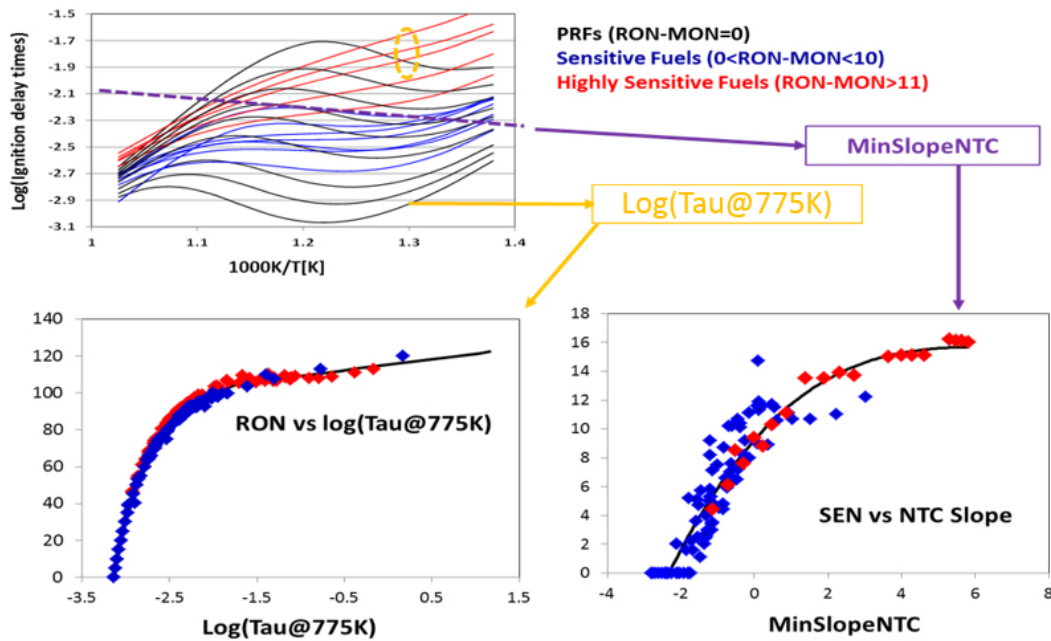


Figure II.20.2 - RON is correlated to the IDT (τ) computed by the kinetic model for stoichiometric fuel/air mixtures at 775 K and 25 atm (lower left plot). Octane sensitivity (SEN) is correlated to the computed minimum slope in the NTC region (lower right plot). The minimum slope in the NTC is defined as shown in the upper plot. (Source: LLNL)

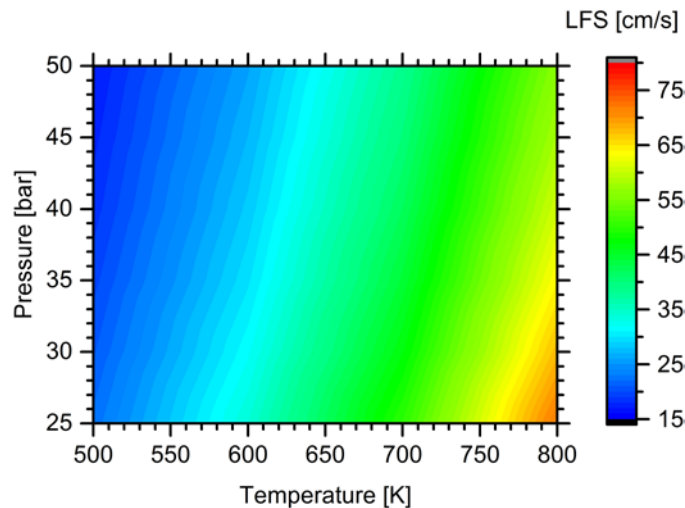


Figure II.20.3 - Laminar flame speeds (LFS) computed by the LLNL chemical kinetic model for gasoline for a high-octane and moderate-octane sensitivity over a wide pressure and temperature range relevant to ASI engines (Source: LLNL)

Phi sensitivity is a fuel property that extends the range of operation for partially-stratified compression-ignition engines by controlling excessive heat release rates [2]. Phi refers to the fuel/air equivalence ratio in the engine. Excessive heat release rates can damage this type of ACI engine, cause noise, and limit the operating range of the engine. IDTs computed by a chemical kinetic model for gasoline can be used to compute phi sensitivity and identify fuel mixtures that are phi-sensitive. The Co-Optima toolkit team used the chemical kinetic model for gasoline surrogates to compute the sensitivity for a gasoline surrogate blended with 1-hexene, ethanol, and pentanol and identified the best component to increase phi sensitivity. These results are reported in the project entitled “Virtual Fuel Blend Optimization for Advanced Compression Ignition Engines.”

Conclusions

- The octane blending behavior of eight Co-Optima HPFs was predicted using an updated LLNL gasoline surrogate model and the predictions compared well with measurements for RON and OS.
- A new correlation was developed to relate ignition delays computed by the chemical kinetic model with RON and OS, two important properties that enable high-efficiency, downsized, boosted, spark ignition engine operation.
- The chemically kinetic model for gasoline with HPFs can also be used to predict flame speeds at pressures and temperatures encountered in ASI engines.
- The chemical kinetic model can predict phi sensitivity, an important fuel property that identifies a fuel's ability to reduce excessive heat release rates under partially stratified ACI engine operation.

References

1. McCormick, Robert L., Gina Fioroni, Lisa Fouts, Earl Christensen, Janet Yanowitz, Evgueni Polikarpov, Karl Albrecht, Daniel J. Gaspar, John Gladden, and Anthe George. "Selection Criteria and Screening of Potential Biomass-Derived Streams as Fuel Blendstocks for Advanced Spark-Ignition Engines." *SAE Int. J. Fuels Lubr.* 10 (2). 2017. doi: 10.4271/2017-01-0868.
2. Yang, Yi, John Dec, Nicolas Dronniou, and Blake Simmons. "Characteristics of Isopentanol as a Fuel for HCCI Engines." *SAE Int. J. Fuels Lubr.* 3 (2):725–741. 2010. doi: doi:10.4271/2010-01-2164.

Key Fiscal Year 2017 Publications

1. Westbrook, C.K., M. Mehl, W.J. Pitz, and M. Sjöberg. "Chemical Kinetics of Octane Sensitivity in a Spark-Ignition Engine." *Combustion and Flame* 175 (2017) 2–15. <https://doi.org/10.1016/j.combustflame.2016.05.022>.
2. Zhou, C.-W., J.M. Simmie, W.J. Pitz, and H.J. Curran. "Towards the Development of a Fundamentally-Based Chemical Model for Cyclopentanone: High Pressure Limit Rate Constants for H-Atom Abstraction and Fuel Radical Decomposition." *Journal of Physical Chemistry A* 120 (36) (2016) 7037–7044. doi: 10.1021/acs.jpca.6b03994.
3. Szybist, James P., Scott W. Wagnon, Derek Splitter, William J. Pitz, and Marco Mehl. "The Reduced Effectiveness of EGR to Mitigate Knock at High Loads in Boosted SI Engines." 13th International Conference on Engines & Vehicles (SAE 2017-24-0061), 2017. <http://papers.sae.org/2017-24-0061/>
4. Kolodziej, Christopher P., Michael Pamminger, James Sevik, Thomas Wallner, Scott W. Wagnon, and William J. Pitz. "Effects of Fuel Laminar Flame Speed Compared to Engine Tumble Ratio, Ignition Energy, and Injection Strategy on Lean and EGR Dilute Spark Ignition Combustion." *SAE Int. J. Fuels Lubr.* 10 (1):82–94. 2017. doi: 10.4271/2017-01-0671.

II.21 Kinetic Mechanism Development

William J. Pitz, Principal Investigator

Lawrence Livermore National Laboratory
P. O. Box 808, L-372
Livermore, CA 94551
E-mail: pitz1@llnl.gov

Kevin Stork, DOE Technology Manager

U.S. Department of Energy
E-mail: Kevin.Stork@ee.doe.gov

Start Date: October 1, 2016	End Date: September 30, 2018	
Total Project Cost: \$1,500,000	DOE share: \$1,500,000	Non-DOE share: \$0

Acknowledgments

Co-Authors

Marco Mehl, Scott W. Wagnon, Kuiwen Zhang, Goutham Kukkadapu, Charles K. Westbrook;
Lawrence Livermore National Laboratory

This work was performed under the auspices of the U.S. Department of Energy by Lawrence Livermore National Laboratory under Contract DE-AC52-07NA27344.

Project Introduction

Predictive chemical kinetic models are needed to represent downselected bio-derived blendstocks and their mixtures with conventional fuels like gasoline and diesel for Co-Optima. These kinetic models can be used in computational fluid dynamics simulations of advanced spark ignition (ASI) and advanced compression ignition (ACI) engines so that the behavior of these fuel blends can be predicted in these engines. Enabled by kinetic models, computational fluid dynamics simulations can be used to optimize fuel formulations for ASI and ACI engines so that the engine efficiency, fossil fuel displacement, and minimum harmful emissions goals can be achieved.

Objectives

- Develop chemical kinetic models for high-performance fuels (HPF) and base fuels (e.g., gasoline and diesel) to predict their behavior at ASI and ACI engine conditions for Co-Optima
- Use chemical kinetic models to simulate combustion properties at ASI and ACI engine conditions

Approach

To develop chemical kinetic models for blends of bio-derived fuels and conventional transportation fuels, chemical kinetic models for each HPF of interest are developed, as needed. These fuel component models are developed by identifying the reaction paths for the HPF and assembling the associated rate constant, thermodynamic, and transport data. Next, these models for HPFs are combined with chemical kinetic models for conventional fuels to represent blends of HPFs and conventional transportation fuels. The models are validated by comparison of computed results to fundamental experimental data from rapid compression machines (RCMs), shock tubes, and laboratory-scale flames. Then the mechanisms are used in multidimensional engine simulation codes to assess fuel property effects in ASI and ACI engines. These simulation results can guide and inform efforts to optimize fuel and engine design for the best performance and engine efficiency, and to reduce harmful emissions.

Results

Key accomplishments for Fiscal Year 2017.

- Developed and validated chemical kinetic model for gasoline surrogate fuels with Co-Optima HPFs
- Developed new kinetic models for the Co-Optima HPFs methyl-acetate and ethyl-acetate
- Improved chemical kinetic models for methyl butanoate, di-iso-butylene, and anisole
- Validated the chemical kinetic models for 18 other Co-Optima HPFs in the combined mechanism to ensure they performed as well as reported in their respective literature publications
- Improved and validated gasoline surrogate component models upon which the HPFs and gasoline surrogate mechanisms rely (1-hexene, toluene, xylenes, trimethylbenzenes, phenol, and benzene)

In Fiscal Year 2017, the capabilities and predictivity of the Lawrence Livermore National Laboratory (LLNL) chemical kinetic models for gasoline surrogates (GSs) and Co-Optima HPFs were significantly improved. Table II.21.1 lists the GSs and the HPFs that can now be simulated with the combined chemical kinetic model. This new capability allows the representation of gasolines for a wide range of compositions and allows the treatment of many HPFs considered by Co-Optima. HPFs are fuel components or mixtures that can be blended into gasoline to increase Research Octane Number and octane sensitivity so that downsized, boosted, high-efficiency spark ignition engines can be enabled. With these kinetic model improvements, the blending properties of many HPFs with gasoline can be predicted as required by the Co-Optima Fiscal Year 2018 task entitled “Fuel Property Blend Model.” Also, the kinetic model can reliably be used to support simulations of Co-Optima engine experiments.

Table II.21.1 - Fuel Palette for the GS with HPF Chemical Kinetic Model

Fuel Class	Fuel	Fuel Palette
alcohols	methanol	GS & HPF
	ethanol	GS & HPF
	propanol (2 isomers)	HPF
	butanol (4 isomers)	HPF
	pentanol (3 isomers)	HPF
alkenes	1-hexene	GS
	2-hexene	GS
	3-hexene	GS
	di-iso-butylene (2 isomers)	GS & HPF
aromatics	toluene	GS
	ethylbenzene	GS
	xylene (2 isomers)	GS
	trimethylbenzene (2 isomers)	GS
cycloalkanes	cyclopentane	GS
esters	methyl acetate	HPF
	ethyl acetate	HPF
	methyl butanoate	HPF
furans	2-methyl furan	HPF
	2,5-dimethyl furan	HPF
iso-alkanes	iso-pentane	GS
	2-methylhexane	GS
	iso-octane	GS
ketones	acetone	HPF
	butanone	HPF
n-alkanes	butane	GS
	pentane	GS
	hexane	GS
	heptane	GS
other	anisole	HPF

To expand the number of HPFs that can be simulated, new chemical kinetic mechanisms were developed for HPFs. New mechanisms for methyl acetate and ethyl acetate were developed in collaboration with King Abdullah University of Science and Technology and National University of Ireland, Galway (NUIG). A comparison of ignition delay times (IDTs) calculated and measured for methyl acetate in an NUIG shock tube is shown in Figure II.21.1. The agreement between the experimental data and simulations is reasonable. Additionally, several kinetic models for HPFs were improved including anisole, di-iso-butylene, and methyl butanoate. Also, many kinetic models of HPFs from the literature were added to the gasoline surrogate mechanism and this greatly expanded the number of HPFs that could be simulated. These HPFs include propanols, butanols, pentanols, furans, acetone, and butanone for a total of 11 additional HPFs. These HPF kinetic models were added to the gasoline surrogate mechanism and tested to ensure that their performance in the combined mechanism was the same as that reported in the literature. The combined mechanism can now reliably simulate 21 Co-Optima HPFs in a GS mechanism. This combined mechanism can also be used by the Co-Optima project to simulate the behavior of gasoline base fuels with HPFs. The blending behavior of eight of these HPFs was tested and compared to experimental data for Research Octane Number and Motor Octane Number with good agreement. This accomplishment is reported in the Fiscal Year 2017 task entitled “Fuel Property Blending Model.”

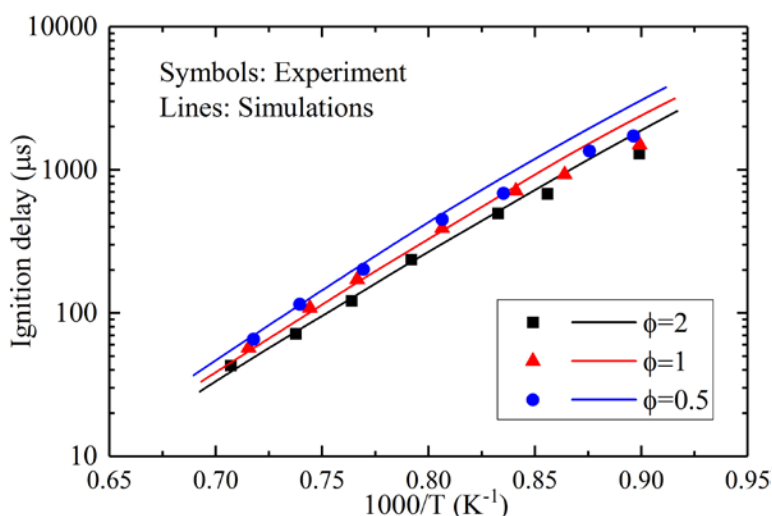


Figure II.21.1 - Experimentally measured (symbols) and simulated (lines) ignition delay times of methyl acetate in a shock tube at NUIG (LLNL)

To expand the range of gasoline fuels that can be accurately represented by the LLNL GS kinetic models, models for GSs and their blends were improved. GS component mechanisms for n-heptane, n-hexane, hexenes, ethyl-benzene, and tri-methyl-benzenes were improved so that their predictions are validated and more reliable. To demonstrate some of these improvements, the agreement of the n-heptane model with IDTs from Ciezki et al. [1] is shown in Figure II.21.2. The agreement is quite good and is improved over a wide range of pressure and two equivalence ratios. Additionally, the predicted blending behavior of n-heptane and toluene was tested for three different blends, two equivalence ratios, and two pressures in a shock tube and an RCM. The good agreement of the predicted blending behavior for one case is shown in Figure II.21.3. These improvements in GSs have enabled the representation of the Co-Optima core fuels (E30, high-olefin, high-aromatic, alkylate and high-cycloalkane core fuels) so that their combustion behavior in ASI and ACI engines can be simulated accurately. This capability allowed the simulation of exhaust gas recirculation effects on a downsized, boosted spark-ignition engine using Co-Optima core fuels and provided a chemical kinetic explanation of the loss of effectiveness of exhaust gas recirculation under these conditions compared to naturally aspirated or lightly boosted engine operating conditions [2].

The flame speeds of gasoline blends are important for spark ignition engine operation because high flame speeds help to prevent auto-ignition that leads to engine knock and to prevent combustion instabilities during engine operation with dilute mixtures [3]. Therefore, it is essential that chemical kinetic models for GSs

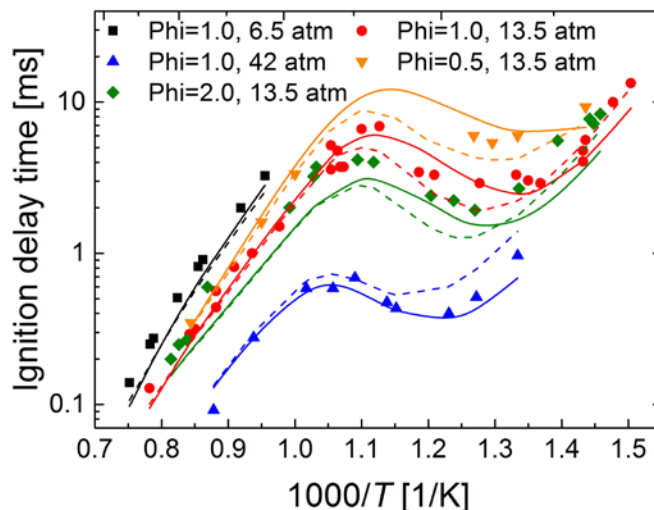


Figure II.21.2 - Simulated (curves) and experimentally measured (symbols) IDTs of n-heptane in a shock tube over a range of pressures and fuel/air equivalence ratios (Φ). The predictions by the improved LLNL model are represented by the solid curves and those by the previous model are the dashed curves. Experimental data sets are from Ciezki et al. [1]. (LLNL)

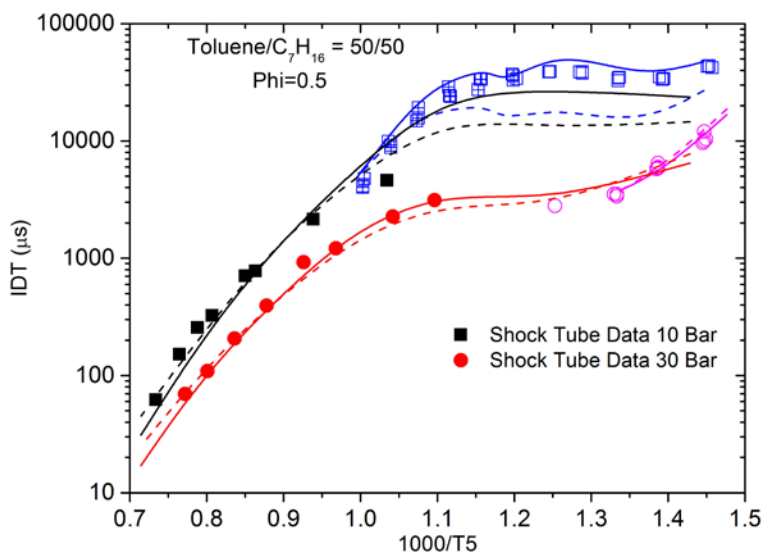


Figure II.21.3 - Simulated and measured IDTs for a toluene/n-heptane 50:50 molar blend at a fuel/air equivalence ratio (Φ) of 0.5. The IDTs were measured in a shock tube and an RCM at NUIG. (LLNL)

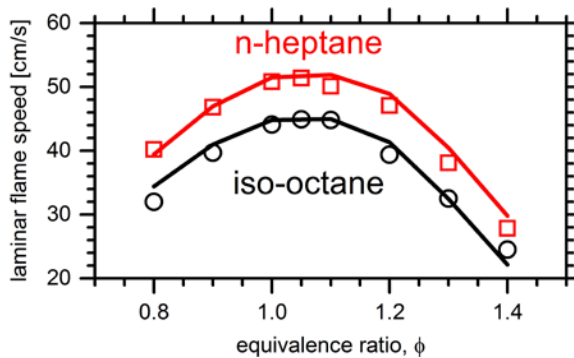


Figure II.21.4 - Simulated (curves) and experimentally measured (symbols) laminar flame speeds for n-heptane and iso-octane. The measurements are from Ji et al. [4,5]. (LLNL)

and HPFs accurately predict flame speeds. During Fiscal Year 2017, many of the HPFs and GSs in the GS mechanism with HPFs were validated to ensure that laminar flame speeds are well-predicted. For example, Figure II.21.4 shows a comparison of predicted and measured laminar flame speed for n-heptane and iso-octane with good agreement.

Conclusions

- A chemical kinetic surrogate mechanism for gasoline with 21 Co-Optima HPFs has been assembled and validated. This mechanism enables the reliable simulation of blends of many HPFs for a range of gasoline base fuels under ASI and ACI engine conditions.
- The combined mechanism gasoline surrogate with HPFs can be used to predict fuel properties to support the “Fuel Property Blending Model” Co-Optima task. Because the mechanism was validated for ignition delay over a wide range of pressures, temperatures, and equivalence ratios, it can also be used to predict auto-ignition related to engine knock under downsized, boosted spark-ignition conditions.
- New kinetic models for the Co-Optima HPFs methyl-acetate and ethyl-acetate were developed.
- The laminar flame speeds of many of the HPFs and GS compounds in the GS mechanism with HPFs were validated by comparison to experimental data from the literature.

References

1. Ciezki, H.K., and G. Adomeit. “Shock-Tube Investigation of Self-Ignition of n-Heptane-Air Mixtures Under Engine Relevant Conditions.” *Combustion and Flame* 93:421–433. 1993.
2. Szybist, James P., Scott W. Wagnon, Derek Splitter, William J. Pitz, and Marco Mehl. “The Reduced Effectiveness of EGR to Mitigate Knock at High Loads in Boosted SI Engines.” 13th International Conference on Engines & Vehicles (SAE 2017-24-0061). 2017. doi: <http://papers.sae.org/2017-24-0061/>.
3. Kolodziej, Christopher P., Michael Pamminer, James Sevik, Thomas Wallner, Scott W. Wagnon, and William J. Pitz. “Effects of Fuel Laminar Flame Speed Compared to Engine Tumble Ratio, Ignition Energy, and Injection Strategy on Lean and EGR Dilute Spark Ignition Combustion.” *SAE Int. J. Fuels Lubr.* 10 (1):82–94. 2017. doi: 10.4271/2017-01-0671.
4. Ji, Chunsheng, Enoch Dames, Yang L. Wang, Hai Wang, and Fokion N. Egolfopoulos. “Propagation and extinction of premixed C5–C12 n-alkane flames.” *Combustion and Flame* 157 (2):277–287. 2010. doi: <https://doi.org/10.1016/j.combustflame.2009.06.011>.
5. Ji, Chunsheng, S. Mani Sarathy, Peter S. Veloo, Charles K. Westbrook, and Fokion N. Egolfopoulos. “Effects of fuel branching on the propagation of octane isomers flames.” *Combustion and Flame* 159 (4):1426–1436. 2012. doi: <http://dx.doi.org/10.1016/j.combustflame.2011.12.004>.

Key Fiscal Year 2017 Publications

1. Westbrook, C.K., M. Mehl, W.J. Pitz, and M. Sjöberg. “Chemical Kinetics of Octane Sensitivity in a Spark-Ignition Engine.” *Combustion and Flame* 175 (2017) 2–15. <https://doi.org/10.1016/j.combustflame.2016.05.022>
2. Zhou, C.-W., J.M. Simmie, W.J. Pitz, and H.J. Curran. “Towards the Development of a Fundamentally-Based Chemical Model for Cyclopentanone: High Pressure Limit Rate Constants for H-Atom Abstraction and Fuel Radical Decomposition.” *Journal of Physical Chemistry A* 120 (36) (2016) 7037–7044. doi: 10.1021/acs.jpca.6b03994
3. Szybist, James P., Scott W. Wagnon, Derek Splitter, William J. Pitz, and Marco Mehl. “The Reduced Effectiveness of EGR to Mitigate Knock at High Loads in Boosted SI Engines.” 13th International Conference on Engines & Vehicles (SAE 2017-24-0061). 2017. <http://papers.sae.org/2017-24-0061/>

4. Kolodziej, Christopher P., Michael Pamminger, James Sevik, Thomas Wallner, Scott W. Wagon, and William J. Pitz. "Effects of Fuel Laminar Flame Speed Compared to Engine Tumble Ratio, Ignition Energy, and Injection Strategy on Lean and EGR Dilute Spark Ignition Combustion." *SAE Int. J. Fuels Lubr.* 10 (1):82-94. 2017. doi: 10.4271/2017-01-0671.

II.22 Kinetic Mechanism Development and Validation

S. Scott Goldsborough, Principal Investigator

Argonne National Laboratory
9700 S. Cass Avenue
Argonne, IL 60439
E-mail: scott.goldsborough@anl.gov

Kevin Stork, DOE Technology Manager

U.S. Department of Energy
E-mail: Kevin.Stork@ee.doe.gov

Start Date: October 1, 2016	End Date: September 29, 2017	
Total Project Cost: \$250,000	DOE share: \$250,000	Non-DOE share: \$0

Acknowledgments

Co-Authors

Jeffrey Santner, Dongil Kang, Toby Rockstroh; Argonne National Laboratory

Project Introduction

Fuel performance in modern spark ignition (SI) and advanced compression ignition (ACI) engines depends on many fuel properties. Although autoignition chemistry is a primary driver, heat of vaporization and flame speed, as well as chemical kinetic sensitivities to thermal and compositional stratification are also important. Furthermore, the development and propagation/amplification of pressure waves after localized autoignition events leading to excessive noise, or structural damage can also be dependent on the fuel. The capability to model and thus predict fuel performance based on fundamental measurements could significantly reduce the costs and time associated with co-optimizing fuels and engines.

The efforts of this project are primarily focused on acquiring experimental autoignition data that will (1) support the development, validation, and improvement of robust chemical kinetic mechanisms for real and surrogate fuels and (2) provide insight into the chemical effects of fuel performance in boosted SI and ACI engines.

Objectives

- Acquire autoignition data for a variety of conventional and future fuels using Argonne National Laboratory's (ANL's) rapid compression machine (RCM) facilities at conditions relevant to boosted SI, mixed-mode, and ACI engines necessary for the development and validation of chemical kinetic models, and the prediction of fuel-engine interactions
- Investigate fuel-dependent chemical kinetic processes which influence fuel performance

Approach

The work pursued for this project seeks to address challenges associated with measuring the autoignition properties of potential future fuels and fuel blends, interpreting their performance in combustion engines (in terms of knock and combustion phasing), and properly modeling their behavior in zero- and multi-dimensional simulation frameworks. The approach used in this project is based on ANL's RCM, where this device is able to access experimental conditions that are directly relevant to modern, SI and ACI engines, e.g., $T = 650\text{--}1,100\text{ K}$, $P = 10\text{--}100\text{ bar}$, $O_2 = 10\text{--}21\%$, $\phi = 0.2\text{--}2.0+$. ANL's RCM typically uses 10–20 mL of fuel to conduct tests covering a wide range of conditions with the autoignition chemistry studied over the low-, negative temperature coefficient-, and intermediate-temperature regimes. Smaller volumes can be used to explore focused operating regimes.

RCMs have been used for nearly 100 years to investigate autoignition phenomena at engine-relevant conditions and they have continually become more sophisticated [1,2]. They are capable of creating and maintaining well-controlled, elevated temperature and pressure environments where the chemically active period preceding autoignition can be decoupled from physical interactions that occur in an engine, e.g., spray breakup, turbulent fuel/air mixing, and thermal/compositional stratification. Furthermore, the operating conditions, e.g., T , P , ϕ and O_2 , can be independently varied unlike in internal combustion engines, which provides necessary insight. The ability to utilize wide ranges of fuel and oxygen concentrations within RCMs, from ultra-lean to over-rich, and spanning dilute to undiluted regimes, offers specific advantages relative to other laboratory apparatuses such as shock tubes and flow reactors, where complications can arise under such conditions. ANL's twin-piston RCM is utilized in this project where ignition times are measured and heat release rates are quantified.

Results

Key accomplishments for Fiscal Year 2017 include:

- Acquiring autoignition data over a range of thermodynamic conditions for five, compositionally diverse, high Research Octane Number (RON) Co-Optima core fuels
- Computationally investigating chemical kinetics associated with engine knock for a range of primary reference fuels (PRFs) from PRF70 to PRF100.

Experiments were conducted to characterize the autoignition behavior of five full boiling range fuels that were blended for the Co-Optima program. These fuels have high RON and four of them have Motor Octane Numbers (MON) near 87. The fuels include RON98-Alkylate, RON98-E30, RON98-A30, RON98-O30 and RON98-N30. The first one is a predominantly alkylate-containing (e.g., iso-octane) mixture, while the remaining four are blended with 30% vol/vol of ethanol, aromatics, olefins and naphthenes, respectively. The composition of the other portions of the fuels were adjusted to meet the octane number specifications. Except for the RON98-Alkylate, the base fuel for each is unique and compositionally diverse, which provided an opportunity to quantify the influence of blending behavior, fuel composition, and fuel specification on the autoignition behavior. While these fuels all had similar specifications, it was not expected that their autoignition behavior would be identical. On the other hand, this affected both anti-knock performance in boosted SI operation, as well as combustion control and noise mitigation across a variety of engine speed-load points under ACI operation, as observed in engine experiments conducted across the Co-Optima project.

RCM tests were conducted over a wide range of thermodynamic conditions covering $T = 750\text{--}1,000\text{ K}$ and $P = 5\text{--}60\text{ bar}$, with a focus on diluted stoichiometric fuel loadings. These conditions are well beyond the test protocols of RON and MON, but are relevant to modern and future engines. Representative results

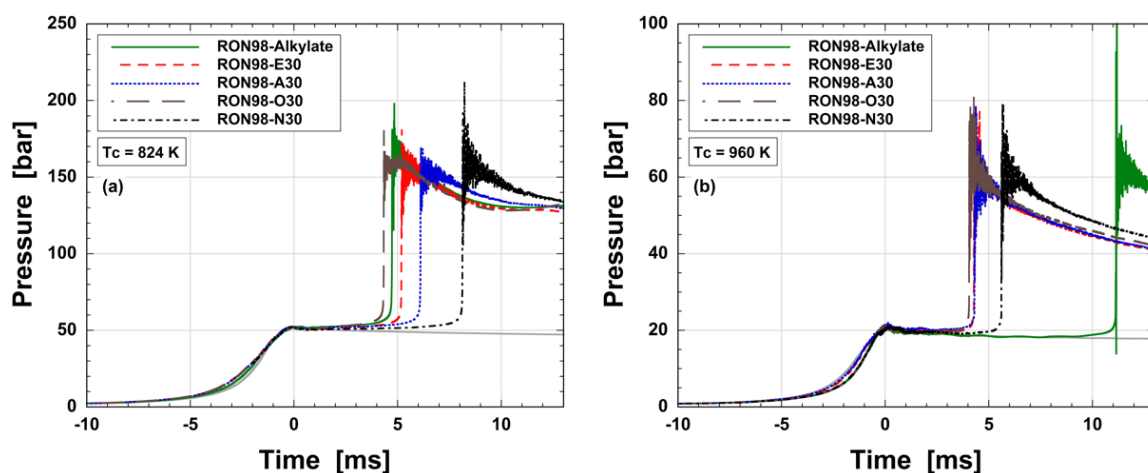


Figure II.22.1 - Experimentally measured pressure–time histories for Co-Optima core fuels indicating reactivity trends for the fuels in different combustion regimes, (a) high pressure, lower temperature, and (b) moderate pressure, intermediate temperature

are presented in Figure II.22.1 with pressure–time histories depicted at (a) $T = 820$ K, $P = 50$ bar, and (b) $T = 950$ K, $P = 20$ bar. Here, ignition delay times are on the order of $t = 3$ – 10 ms. It is immediately clear that the fuels, though rated similarly, do not react identically. In addition, the reactivity trends are observed to change with alterations in temperature and pressure. Most significant is RON98-Alkylate, which becomes much less reactive compared to other fuels at the higher temperature. Furthermore, there are differences in the rates of pressure rise at ignition for the five fuels, such that some lead to severe ringing in the pressure signal as resonant gas waves are excited due to chemical heat release. The most extreme is observed for the RON98-Alkylate at $T = 950$ K.

In addition to the experimental activities, efforts were made in Fiscal Year 2017 to computationally investigate the chemical kinetics associated with engine knock with the intent to derive techniques using the RCM platform to experimentally quantify critical processes for a range of potential fuels. While knock is a highly complex chemico-gas dynamic phenomenon in which many thermo-physical interactions are important, such as charge mixing and flame propagation, chemical kinetics of the end gas are the primary driver [3]. Knock onset has been studied extensively and is tightly coupled to chemical induction times [4]. This is the fundamental fuel property that is typically measured in RCM and shock tube tests. However, knock intensity is much less well-understood, but is tightly coupled to the rates of heat release at the onset of autoignition. Knock intensity, often parameterized by the maximum amplitude of pressure oscillation after knock onset, is perhaps a more important constraint on engine operation than knock onset [5].

Simulations were conducted for a variety of PRFs, from PRF70 to PRF100, to computationally quantify changes in the explosive characteristics of the fuels as the anti-knock performance is improved, i.e., as the iso-octane fraction and associated octane rating are increased. A wide range of relevant thermodynamic conditions were covered, including $T = 750$ – $1,100$ K and $P = 10$ – 80 bar. A reduced order physical model was employed so that detailed chemical models could be utilized; both the newly updated Lawrence Livermore National Laboratory [6] and recent Andrae [7] models were considered. A single-zone, spherically symmetric hot spot was assumed where the velocity of the outermost boundary was prescribed using the local sound speed. Both induction times (τ) and excitation times (τ_e) were monitored as proxies for knock onset and knock intensity in order to understand influences of temperature, pressure, and fuel reactivity. These are illustrated in Figure II.22.2 where isopleths of τ and ε are plotted for the Andrae model with ε being the non-dimensional excitation parameter based on the hot spot size (r_{hot}), and local sound speed (a_s) as normalization dimensions ($\varepsilon = (r_{\text{hot}}/a_s)/\tau_e$).

Sensitivity analyses were also performed along the RON and MON test protocols where A-factor perturbations were used to identify reactions and reaction classes that control the explosive behavior of the fuels, and how these change with increasing anti-knock performance. It was found that knock onset is dominated

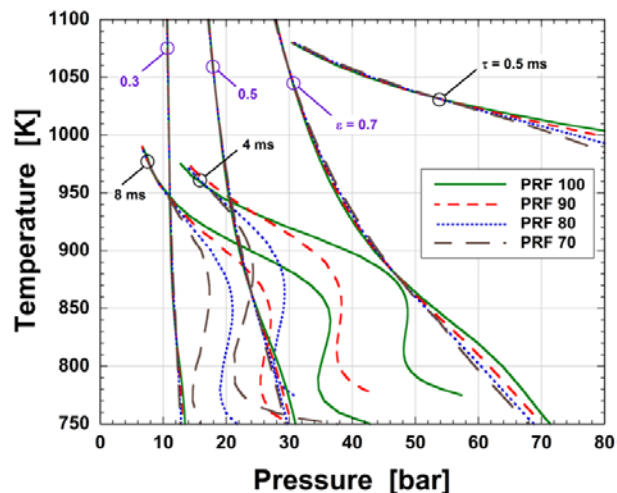


Figure II.22.2 - Computationally derived isopleths of ignition delay times (τ) and normalized heat release rates (ε) for PRF70 – PRF100 covering a wide range of thermodynamic conditions relevant to boosted SI and ACI combustion schemes

by H-abstractions, O₂-additions, and some isomerization reactions with n-heptane oxidation important. Conversely, knock intensity seems to be dominated by hydrogen chemistry, while β -scission reactions of iso-octyl radicals, along with CO oxidation are very important.

The findings of this work have implications towards understanding the effectiveness of various fuel components and blends which can increase the anti-knock resistance of fuels, as well as for controlling combustion in ACI fueling strategies. Moreover, the measurements provide insight and valuable targets for the development of robust chemical kinetic models of compositionally diverse fuels.

Work in Fiscal Year 2018 will continue coordination with Lawrence Livermore National Laboratory to generate necessary experimental datasets and identify model sub-mechanisms that can be improved through targeted tests. Measurements will be undertaken with other gasoline blends and future fuel candidates.

Conclusions

- ANL's RCM has been used to acquire autoignition data needed to better understand fuel behavior across a range of conditions beyond the test protocols of RON and MON and to provide critical validation targets for chemical kinetic modeling of compositionally diverse fuels.
- Preliminary insight into the chemical kinetics controlling knock onset and knock intensity has been derived via computational modeling of a range of PRFs, providing a basis for more complex fuels.

References

1. Goldsborough, S.S., S. Hochgreb, G. Vanhove, M.S. Wooldridge, H.J. Curran, and C.-J. Sung. *Prog. Energy Combust. Sci.* 63, 1–78, 2017.
2. Goldsborough, S.S., D. Longman, M.S. Wooldridge, R.S. Tranter and S. Pratt, “1st International RCM Workshop Meeting Report.” August 28–29, 2012.
3. Wang, Z., H. Lui, and R.D. Reitz. *Prog. Energy Combust. Sci.* 61, 78–112, 2017.
4. Bradley, D., and G.T. Kalghatgi. *Combust. Flame*, 156, 2307–2318, 2009.
5. Kalghatgi, G.T., I. Algunaibet, and K. Morganti. SAE Paper 2017-01-0689, 2017.
6. Mehl, M., S. Wagnon, K. Tsang, G. Kukkadapu, W.J. Pitz, C.K. Westbrook, Y. Tsang, H.J. Curran, N. Atef, M.A. Rachidi, M.S. Sarathy, and A. Ahmed. 10th US National Combustion Meeting (2017), paper 1A17.
7. Andrae, J.C.G. *Fuel* 87, 2013–2022, 2008.

Key Fiscal Year 2017 Publications

1. Goldsborough, S.S., J. Santner, D. Kang, M. McNenly. “Chemical kinetics of engine knock, revisited.” 10th International Conference on Chemical Kinetics, Chicago, IL. 2017.
2. “Insights into engine knock: comparison of knock metrics across ranges of temperature and pressure in the CFR engine,” (18PFL-0477) SAE World Congress, 2018.
3. Goldsborough, S.S., J. Santner, M. Doverman, A. Fridlyand, C. Kolodziej. “On the relation between RCM measurements and knock-limited engine design / operation.” AEC Winter Review Meeting, Livermore, CA, 2017.
4. Rockstroh, T., D. Kang, S. Ciatti, W. Cannella, S.S. Goldsborough. “Unravelling ϕ sensitivity: a fundamental RCM and GCI engine study.” AEC Winter Review Meeting, Livermore, CA, 2017.
5. Goldsborough, S.S., T. Rockstroh, D. Kang, S. Ciatti, W. Cannella. “Progress towards mapping fuel properties (combustion behavior) from RCMs to IC engines.” AEC Summer Review Meeting, Detroit, MI, 2017.

II.23 Small Volume Fuel Autoignition Reactor

Gina Fioroni, Principal Investigator

National Renewable Energy Laboratory
15301 Denver West Parkway
Golden, CO 80401
E-mail: gina.chupka@nrel.gov

Kevin Stork, DOE Technology Manager

U.S. Department of Energy
E-mail: Kevin.Stork@ee.doe.gov

Start Date: October 1, 2015	End Date: September 30, 2017	
Total Project Cost: \$300,000	DOE share: \$300,000	Non-DOE share: \$0

Acknowledgments

Co-Authors

Lisa Fouts, Tao Dong, Mark Nimlos, Mohammad Rahimi, Ray Grout, Spencer Lunderman, Robert McCormick; National Renewable Energy Laboratory

Project Introduction

The purpose of this project is to develop a new experimental capability for providing early-stage feedback to biofuel production research and development by identifying promising fuel candidates based on autoignition chemistry. The concept is to use a small-scale tubular flow reactor, operating at atmospheric pressure, coupled to either a molecular beam mass spectrometer (MBMS) or a set of gas chromatographs (GCs) to conduct oxidation reactions using a small volume of reactant under very dilute conditions (an approximately isothermal, plug-flow reactor). One application (using MBMS analysis) is empirical prediction of engineering autoignition metrics such as Research Octane Number (RON) and octane sensitivity (S). A second, more fundamental application, is to reveal intermediates in autoignition and potentially fine particle formation mechanisms.

Objectives

- Validate an experimental and data analysis method for predicting RON and S for unknown fuel blendstocks
- Demonstrate that the flow reactor can be simulated as an isothermal plug flow reactor and provides results consistent with well-established kinetic mechanisms (heptane and isooctane)
- Investigate the autoignition chemistry of the model biofuel, anisole

Approach

The small volume reactor consists of a 13 mm straight quartz tube that is 75 cm in length and is uniformly heated inside a ceramic tube furnace to temperatures between 473 K and 1,200 K. Fuel (via a syringe pump), helium, and oxygen are all introduced at the inlet of the reactor and are allowed to mix at the point of the needle where the fuel is introduced at a flow rate of 10 $\mu\text{L}/\text{min}$. Helium is used as a dilution gas to keep the reactor under dilute and safe operating conditions (well below the lower explosive limit). The flow of oxygen can be adjusted to look at the effect of various air to fuel ratios as desired.

Analysis of products was done by two different methods: The first was with an MBMS. The MBMS operates at a reduced pressure and effluent from the reactor is directly sampled into the mass spectrometer inlet. This allows for rapid and real time analysis of the autoignition products. For this reason, the MBMS was used to collect a large set of data on molecules and mixtures with a known RON and S to build a predictive model

for unknown bioblendstocks and mixtures. The drawback to this method is that several reaction products can have a similar mass, making the identification and quantitation of molecules difficult and convoluted. A second analysis method utilized an in-line GC system equipped with dual columns and detectors; one flame ionization detector for quantitation and a second mass spectrometer detector for identification. Additionally, we were able to collect gas canister samples for analysis of permanent gases and small hydrocarbon molecules on a separated GC equipped with a flame ionization and a thermal conductivity detector.

Results

Empirical Prediction of RON and S

For RON and S prediction, the goal was to develop an experimental method for providing early-stage feedback to biofuel production research and development by identifying promising fuel candidates (and eliminating unpromising ones) based on autoignition chemistry. Using the small volume reactor coupled to the MBMS, observables such as the temperature for low-temperature oxidation initiation, temperature for high-temperature oxidation initiation, and concentrations of intermediate and final product species versus temperature were correlated with the practical autoignition RON and S metrics. A set of bioblendstock candidates with known RON and S along with Primary Reference Fuels and Toluene Primary Reference Fuels that map RON and Motor Octane Number autoignition space were oxidized in the reactor. A total of 46 “fuels” were examined at four temperatures under stoichiometric conditions, with observation of over 100 peaks in the MBMS mass spectrum. This required less than 0.5 mL of each fuel material. These data were analyzed in different ways. First, a principal component analysis (PCA) regression was performed in an attempt to relate RON and S to the observable species as a function of temperature. This PCA model was tested using leave-one-out cross validation, where one of the 46 fuels was removed from the dataset, the PCA model was fit to the remaining data, and the model was then used to predict the RON and S of the fuel that was left out. This was then repeated for each fuel in turn. The results of this analysis approach are shown in Figure II.23.1 where the R^2 of 0.81 for prediction of RON strongly suggests that this approach could be made to work with further development. For S this approach was much less successful. Because the physical meaning of S is that it is the fuel’s autoignition temperature sensitivity [1], an analysis approach that integrates over temperature or more explicitly takes into account rates of change with temperature might prove more successful. Further, analysis of autoignition products across a larger temperature range may reveal additional species to supplement the low temperature oxidation space.

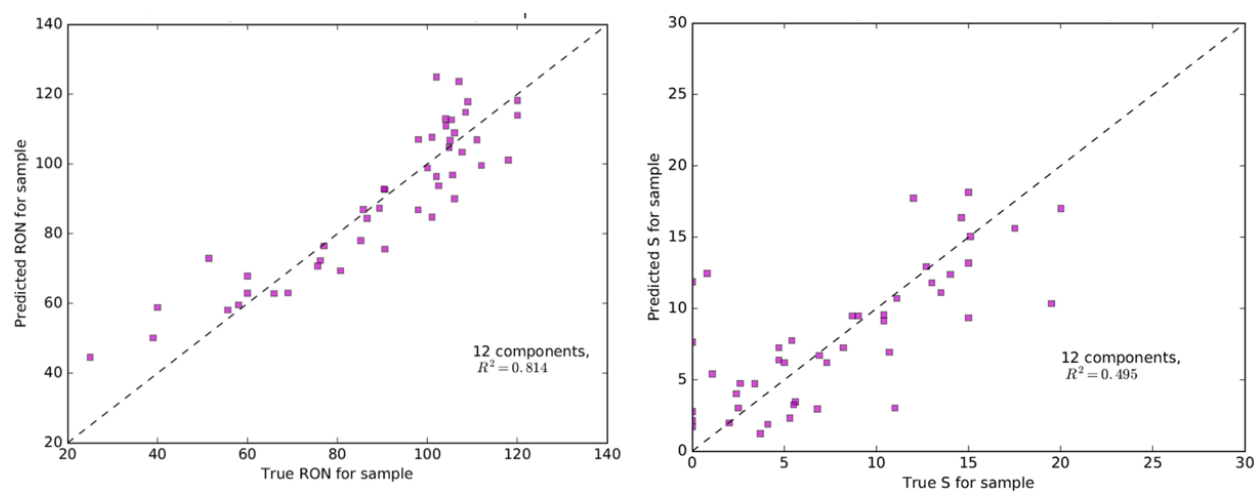


Figure II.23.1 - PCA model validation via leave-one out cross validation for prediction of RON and S

The second analysis approach that we used was a Gaussian process regression and classification to predict the RON and S values and to compare the Gaussian process results to linear models. To reduce the dimension of the data, it was integrated over temperature for each atomic mass unit number in the experimental data (because the MBMS provides a mass spectrum of the entire sample, species at any atomic mass may be from more than one parent compound). The results of leave-one-out cross validation are shown in Figure II.23.2 and indicate significantly improved predictive power for RON relative to PCA. The Gaussian process regression

can also be used as a classifier, for example to classify those compounds with RON over 90 and S over 8. The Gaussian process classification of RON > 90 and S > 8 performed well with over 95% correct classification for RON and over 87% correct classification for S in the experimental data shown in Figure II.23.3. These classification processes could be used as a first sorting tool for new emerging fuels.

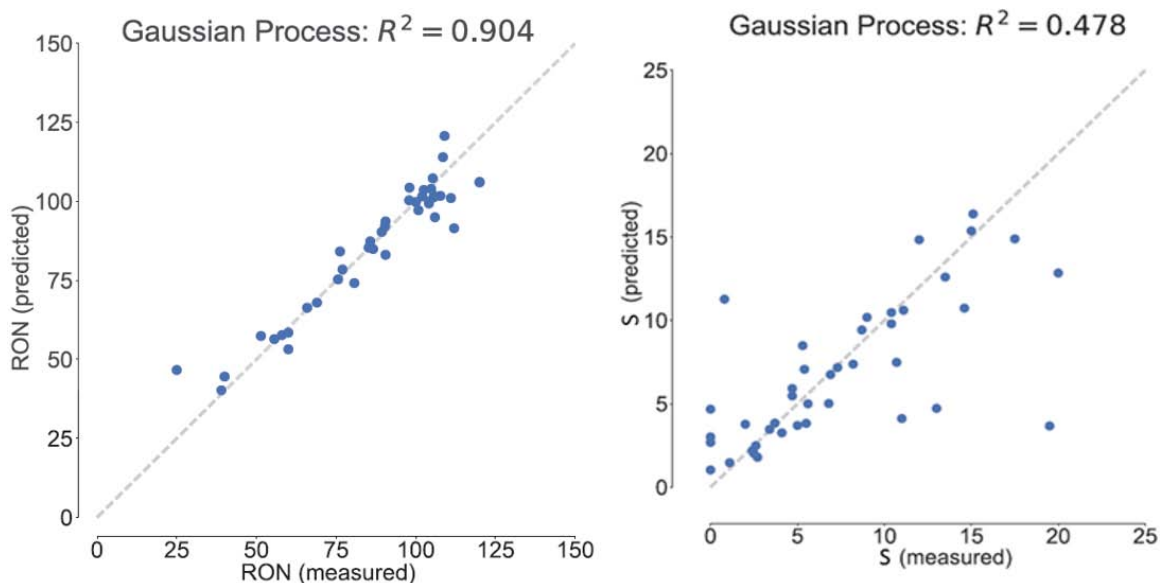


Figure II.23.2 - Gaussian process regression model validation via leave-one out cross validation for prediction of RON and S

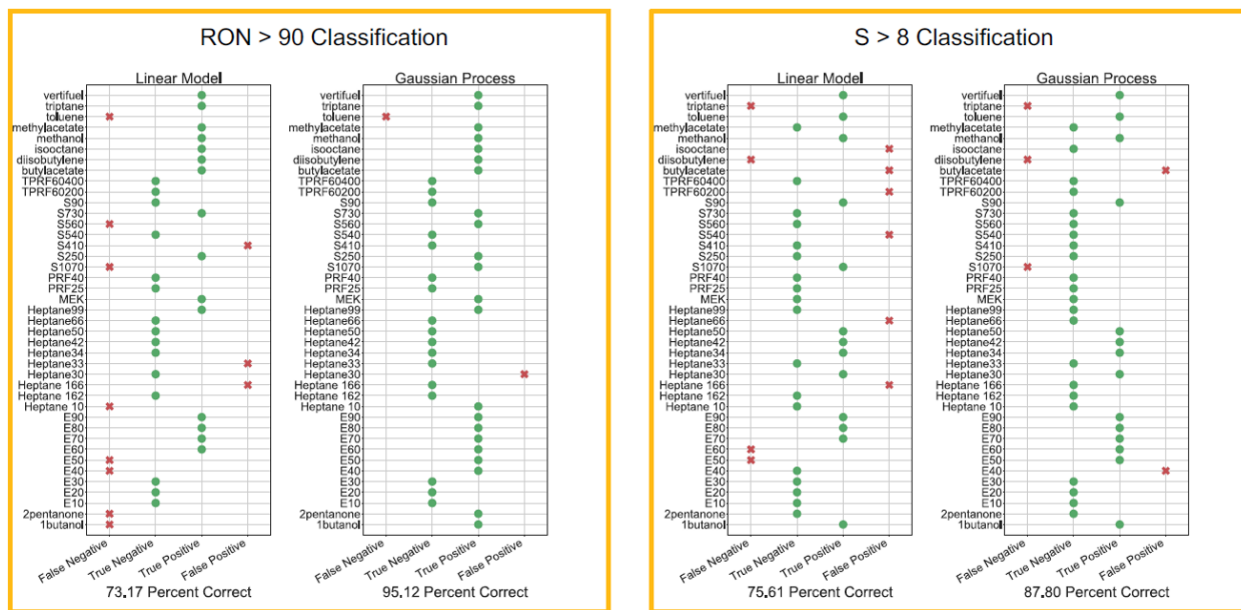


Figure II.23.3 - RON and S classification results for linear model and Gaussian process

Study of Autoignition Reaction Mechanisms

To validate the reactor for autoignition kinetic work, we choose to run and model isooctane as its reaction kinetics are well known [2]. Isooctane was run from 800 K up to 1,100 K at stoichiometric air to fuel conditions and the reaction products were measured using the GC–mass spectrometer system. Lawrence Livermore National Laboratory (LLNL) [3] modeled the reactor conditions using a one-dimensional (1D) plug flow model. Figure II.23.4 shows the reactor results for isooctane compared to the mechanism from LLNL. These results indicate that a 1D simulation closely approximates the reaction products measured in the reactor and

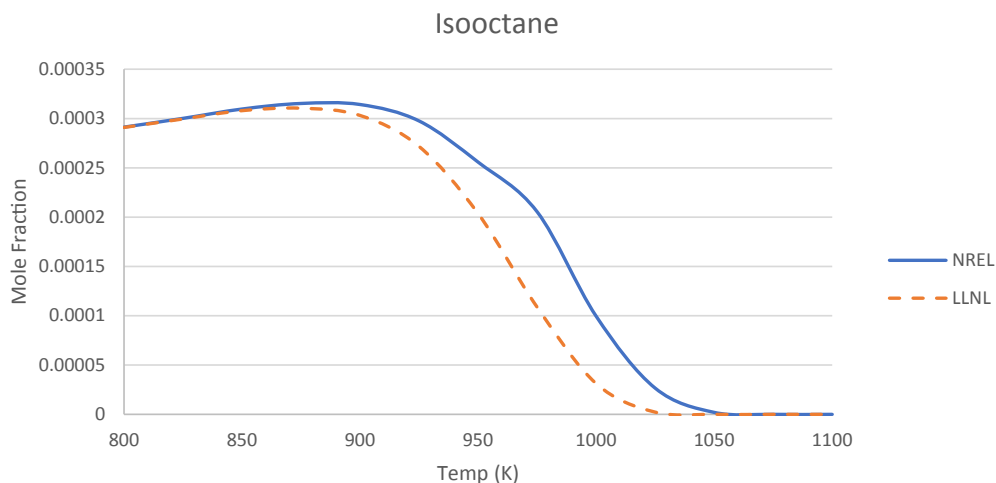


Figure II.23.4 - Comparison of isooctane in National Renewable Energy Laboratory (NREL) flow reactor to LLNL 1D plug flow model

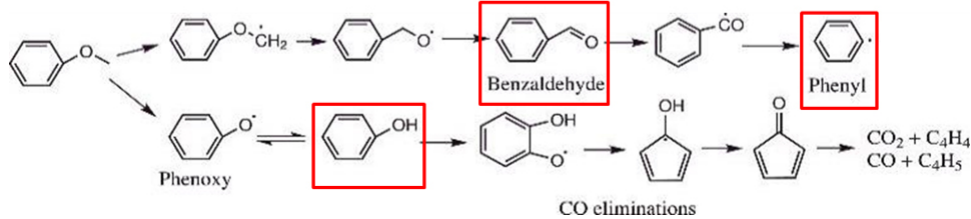
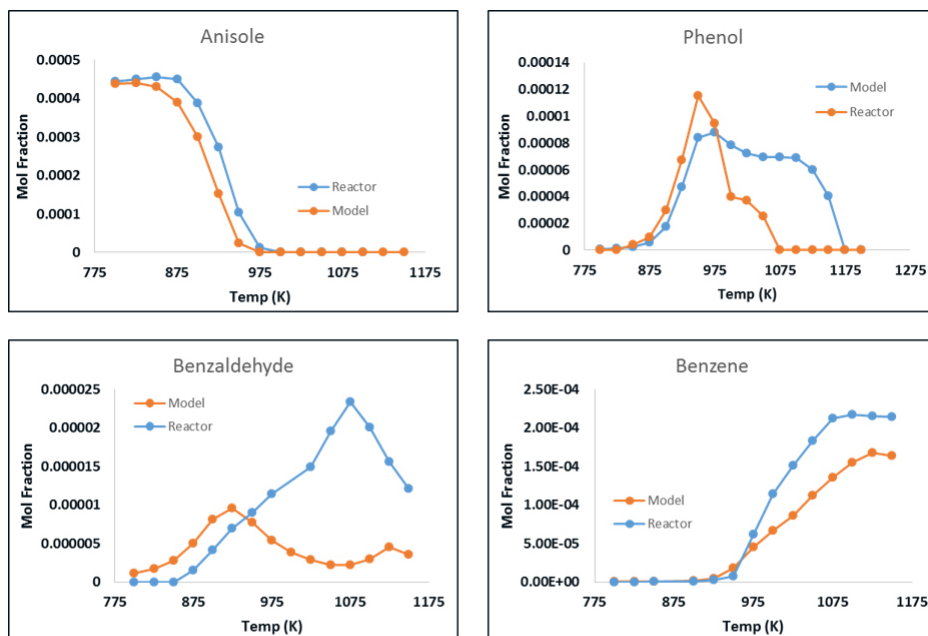


Figure II.23.5 - Comparison of reactor results and simulations for (a) anisole conversion, (b) phenol formation, (c) benzaldehyde formation, and (d) benzene formation. A skeletal reaction mechanism from Boot et al., [5] is also shown.

that our reactor can be considered a plug flow reactor. Poor temperature control (lower temperature) in the final zone of the reactor may account for the higher outlet isooctane concentrations observed experimentally.

A detailed study of the oxidation of the model biofuel anisole was also conducted from 800 K up to 1,200 K at stoichiometric air to fuel conditions and compared to the recent kinetic model published by LLNL [4]. The experimental results (Figure II.23.5) compared well for the conversion of anisole, but differed for some of

the key intermediates indicating that some key reaction rates may not be accurately estimated. These key intermediates could also be investigated in the reactor to help inform the model. Additionally, the experiments revealed the formation of naphthalene and anthracene, which are critical particulate matter precursors, demonstrating that the reactor could be used to prove particulate matter formation mechanisms as well.

Conclusions

A small volume flow reactor was developed and utilized for empirical RON and S prediction as well as for autoignition mechanistic studies with the following conclusions:

- Analysis of autoignition results for 46 pure compounds and gasoline surrogates demonstrated the ability to predict RON, or to classify compounds as having a RON or S above a threshold value, using less than 0.5 mL of reactant.
- Oxidation experiments conducted with isooctane, a compound with well-known autoignition kinetics, showed reasonable agreement with kinetic simulations of the reactor as a 1D plug flow reactor.
- Experiments examining the autoignition of the model biofuel anisole produced reaction products in good agreement with a recently published model, but the concentrations of certain intermediates were different suggesting that rates of certain key reactions are not yet accurately estimated.

In Fiscal Year 2018 research utilizing this reactor will focus on autoignition mechanistic studies.

References

1. Mittal, et al. "The Underlying Physics and Chemistry behind Fuel Sensitivity." *SAE Technical Paper No.* 2010-01-0617 (2010).
2. Mehl, et al. "A comprehensive detailed kinetic mechanism for the simulation of transportation fuels." LLNL-CONF-725343, February 28, 2017.
3. Wagnon, S. private communication to the principal investigator, August 15, 2017.
4. Wagnon, et al. "The Development and Validation of a Chemical Kinetic Model for Anisole, a Compound to Represent Biomass Pyrolysis Fuels." LLNL-CONF-725097, February 23, 2017.
5. Boot, et al. "Impact of fuel molecular structure on auto-ignition behavior – Design rules for future high performance gasolines." *Prog. Energy and Combust. Sci.* 60 (2017): 1–25.

Key Fiscal Year 2017 Publications

1. Fioroni, et al. "Small-Volume Fuel Autoignition Tester Development." Fuel and Lubricant Technologies 2016 Annual Report, <https://energy.gov/eere/vehicles/downloads/fuel-and-lubricant-technologies-2016-annual-progress-report>, accessed November 16, 2017.

II.24 Virtual Fuel Blend Optimization for Advanced Compression Ignition Engines

Matthew McNenly, Principal Investigator

Lawrence Livermore National Laboratory
7000 East Avenue
Livermore, CA 94550
E-mail: mcnenly1@llnl.gov

Kevin Stork, DOE Technology Manager

U.S. Department of Energy
E-mail: Kevin.Stork@ee.doe.gov

Start Date: October 1, 2016 End Date: September 30, 2018
Total Project Cost: \$475,000 DOE share: \$475,000 Non-DOE share: \$0

Acknowledgments

Co-Author

Russell A. Whitesides, Lawrence Livermore National Laboratory

Project Introduction

The Co-Optimization Hypothesis is one of the major hypotheses around which the Co-Optima program is organized. It states that there exists engine architectures and strategies that yield higher thermodynamic efficiencies than the current designs, and that new fuels are needed to maximize efficiency and operability across a wide range of speeds and loads. The purpose of this project is to determine, through simulation, if fuel blend candidates can be found that expand the operating range of an advanced compression ignition engine. Specifically, fuel blends that are predicted to have high octane sensitivity and phi-sensitivity are sought to optimize the performance of a partially stratified charge compression ignition (PSCCI) engine. This operating mode is selected to explore the Co-Optimization Hypothesis because engine researchers [1] have provided clear guidelines for the ideal ignition behavior of a fuel.

The ideal fuel for PSCCI should have high octane sensitivity (i.e., Research Octane Number [RON] minus Motor Octane Number [MON]). A fuel with higher octane sensitivity tends to have auto-ignition delay times less affected by pressure changes. In-cylinder pressure tends to change with engine load, so the operating range of the engine can be reduced if the auto-ignition delay changes widely. If the ignition occurs too early, it damages the engine. If the fuel-air mixture fails to ignite, the engine loses power and increases emissions. Since PSCCI does not use an ignition source like the spark plug in a gasoline engine, fuels whose auto-ignition does not undergo large changes with pressure can be used to maintain engine control over a wider range of operating loads. An ideal PSCCI fuel should also have high phi-sensitivity. Here phi refers to the symbol commonly used to represent the equivalence ratio, which is the actual fuel-air ratio normalized by the stoichiometric fuel-air ratio. A high phi-sensitivity indicates a fuel's reactivity changes significantly for relatively small changes in the fuel-air ratio, or the equivalence ratio. Fuels that have higher phi-sensitivity offer greater combustion phasing control via fuel injection timing. Later injections have a more stratified (less well-mixed) charge, which leads to the fuel rich regions igniting earlier. Phi-sensitivity therefore increases the controllability of the engine and allows it to run efficiently over a wider range of speeds and loads, while also increasing the ability to transition between different operating points.

Objectives

- Develop a phi-sensitivity metric that can be computed from a detailed fuel chemistry model that quantifies desirable ignition behavior for PSCCI engines
- Create an optimization framework that allows the performance of a large number of fuel blends to be evaluated using the new phi-sensitivity metric on the computing resources of national laboratories

- Search for any fuel blends that deliver high phi-sensitivity and octane sensitivity while maintaining a RON greater than 95
- Coordinate with Co-Optima Advanced Engine Team to test the most promising fuel blends found during the optimization process in a partially-stratified compression engine

Approach

The project takes advantage of the latest gasoline surrogate mechanism developed for the Co-Optima program at Lawrence Livermore National Laboratory [2]. This fuel model contains over 2,800 reacting species to resolve the ignition phenomenon of more than a dozen hydrocarbon blendstocks commonly found in gasoline. It also contains 16 oxygenates or bio-derived blendstocks identified in [3] as promising candidates for use in advanced spark-ignited engines. This model is used to estimate the octane number and phi-sensitivity of each candidate blend by solving over 300 constant volume ignition delay times using the high-performance combustion solver, Zero-RK, developed at Lawrence Livermore National Laboratory [4].

The RON and octane sensitivity are estimated with an updated version to the correlations described in Mehl et al. [2]. The performance of this combination of mechanism and ignition delay time correlations are found to predict the oxygenate blending performance to within three octane numbers typically. Future work will update the octane correlations with a machine learning approach developed by Whitesides [5] for this application, which is found to reproduce the RON and MON in blends to within one octane number over the training and cross-validation data sets. For this project, a new phi-sensitivity metric is created, which is detailed here in the Results section.

The RON, octane sensitivity, and phi-sensitivity are combined into a single metric that can be optimized using the standard packages found in the Python SciPy library [6]. The search conducted here is limited to fuel blends with a RON greater than 95. This constraint is handled with a penalty function that smoothly increases for blends less than 95. The penalty increases rapidly with lower RON, such that a RON of 94.9 would eliminate any possible gains in the metric function from octane or phi-sensitivity. The octane sensitivity is normalized by the model value of ethanol, which is considered an exemplar of a blendstock with an octane sensitivity sufficiently large to be beneficial for PSCCI engine performance. Similarly, the phi-sensitivity is normalized by the model value for iso-octane, which is considered an exemplar for beneficial phi-sensitivity for PSCCI control. This combined metric is then optimized using the SciPy implementation of the Nelder-Mead algorithm.

Results

There are four key accomplishments from Fiscal Year 2017.

- Developed a phi-sensitivity metric to estimate the suitability of fuel for PSCCI engines that can be computed from the latest detailed fuel chemistry model for gasoline surrogate
- Created an optimization framework that allows the performance of a large number of fuel blends to be evaluated on DOE computing resources to explore the tradeoff between phi-sensitivity and octane sensitivity
- Searched over 150,000 fuel blends using nine hydrocarbon and 10 bio-derived blendstocks for combinations that delivered high phi-sensitivity and octane sensitivity while maintaining a RON greater than 95
- Found that blends involving 1-pentanol were able to push the traditional tradeoff between the desirable PSCCI properties to achieve nearly 90% the levels identified for the blendstock exemplars with good octane sensitivity (ethanol) and phi-sensitivity (iso-octane)

A new phi-sensitivity metric, called “big-phi,” was created in this project based on guidance from Dec and Vuilleumier from the Co-Optima Advanced Engine Team. It is represented by the capital Greek letter phi (Φ) in the defining equations given in Figure II.24.1. The phi-sensitivity metric attempts to capture both the extent

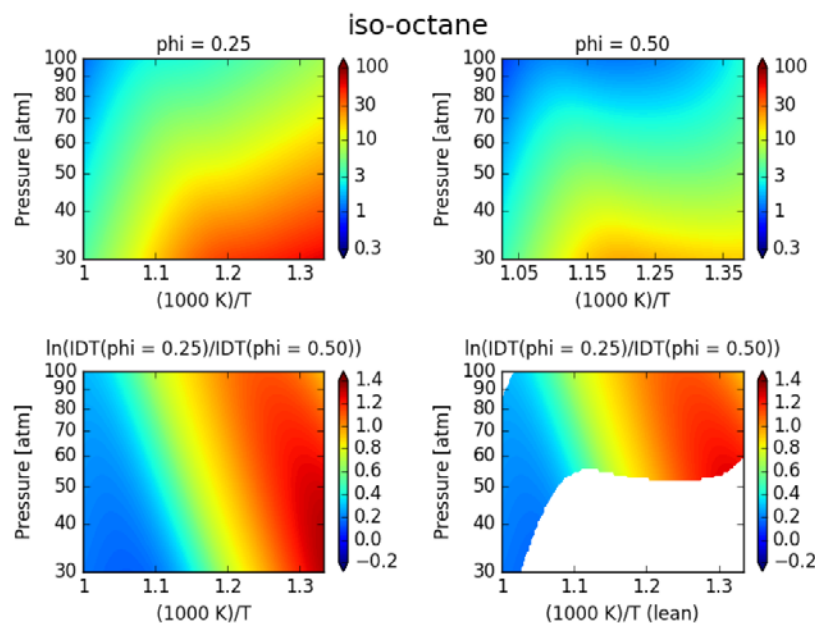
of the operating range (in terms of pressure and temperature), as well as the magnitude of the ignition delay change caused by a richer mixture. The magnitude of the ignition delay sensitivity is represented by S_ϕ , which is the logarithm of the ignition delay time t_l of a leaner mixture ($\phi = 0.25$) over the delay time t_r richer mixture ($\phi = 0.5$). The ignition delay time of the richer mixture must be within a certain range to be usable for practical engine applications, which is taken to be between 1–5 ms for this study. Outside of this range, the sensitivity S_ϕ is set to zero. To account for the change in charge temperature due to the increase in evaporative cooling in the richer mixture, t_r is computed at a temperature that is 25°C lower than the same condition for the leaner mixture t_l . The phi-sensitivity metric is defined as the integral of S_ϕ over the range of pressures (30–100 bar) and temperatures (750–1,000 K) considered meaningful for engine operation. The integrand variables are transformed to the natural logarithm of pressure η and the inverse of temperature ξ to improve the numerical approximation of big-phi with fewer ignition delay calculations. The term A is a normalization constant equal to the integration area in the transformed coordinates.

$$\Phi = \frac{1}{A} \int_{\eta_0}^{\eta_1} \int_{\xi_0}^{\xi_1} \ln S_\phi(\eta, \xi) d\xi d\eta$$

$$S_\phi(p, T) = \begin{cases} \frac{\tau_\ell}{\tau_r}, & \text{if } \tau_{min} \leq \tau_r \leq \tau_{max} \\ 1 & \text{otherwise.} \end{cases}$$

Figure II.24.1 - Mathematical definition of the phi-sensitivity metric “big-phi,” which is developed to estimate the ability of a fuel blend to improve the controllability of a PSCCI engine

An example showing the steps involved in the phi-sensitivity metric calculation is illustrated in Figure II.24.2 for iso-octane. The upper left image shows the constant volume ignition delay time t_l for the leaner mixture ($\phi = 0.25$). The upper right mixture is the ignition delay time t_r for the richer mixture ($\phi = 0.5$) at the same pressures as the leaner mixture, but with the temperature reduced by 25°C to account for the additional evaporative cooling. The lower left figure is the natural log of the ratio of ignition delay times, S_ϕ , without any limits on t_r . And the lower right figure, is the same ratio, but the regions that are too reactive ($t_r < 1$ ms) and too slow ($t_r > 5$ ms) are shown in white. It is the non-white region in the lower right figure that is integrated to obtain the phi-sensitivity metric, big-phi, defined in Figure II.24.1. The simulated RON, MON, octane sensitivity S , and big-phi are computed in Table II.24.1 for several blendstocks tested in this investigation.



IDT – ignition delay time

Figure II.24.2 - Example calculation of the constant volume ignition delay times used to construct the phi-sensitivity metric for iso-octane

Table II.24.1 - Comparison of the Model-Based Estimates for Octane Numbers and Phi-Sensitivity of Several Blendstocks in the Gasoline Chemistry Model

Blendstock	RON	MON	S (RON-MON)	Φ
1-hexene	82.4	74.9	7.5	0.58
Iso-octane	100.5	99.9	0.6	0.43
1-pentanol	87.1	75.3	11.8	0.35
1-butanol	101.5	86.2	15.3	0.13
n-heptane	-0.9	1.3	-2.2	0.08
Toluene	116.1	102.3	13.8	0.00
Ethanol	109.7	95.5	14.2	0.00

There is no guarantee that a fuel exists that has both high octane and phi-sensitivity. In fact, the conventional wisdom in the engine and fuels community suggests that one must trade-off one for the other. This is true for single components, where the fuel radical decomposition due to reactions with molecular oxygen tends to correlate phi-sensitivity with pressure-sensitivity. Recall that high octane sensitivity is associated with low pressure sensitivity. While it is unlikely that a single molecule will be able to deliver both desirable properties for a PSCCI engine, it is unknown if a mixture could be constructed to attain both. This project attempts to find a fuel blend that does achieve both properties to provide evidence in support of the Co-Optimization Hypothesis.

More specifically, the project is searching for fuel blends that have a model octane sensitivity as large as ethanol, and a phi-sensitivity as large as iso-octane. Both blendstocks are exemplars for their “good” property, but provide essentially zero benefit in terms of the other property (see Table II.24.1). Further, the fuel blend candidates must also maintain a RON greater than 95 to be considered in the optimization. Since there are two optimization objectives, octane and phi-sensitivity, the search is considered a multi-objective optimization problem. However, to simplify the initial implementation of the fuel optimization framework, both objectives are combined into a single metric with random weights uniformly distributed between zero and one for each target property. The optimization search is then repeated multiple times with different random weightings that balance the relative importance of octane sensitivity versus phi-sensitivity.

The results after analyzing over 150,000 fuel blends are shown in Figure II.24.3. The three-component toluene reference fuel (TRF), comprised of toluene, iso-octane, and n-heptane, is used as a base palette for the search.

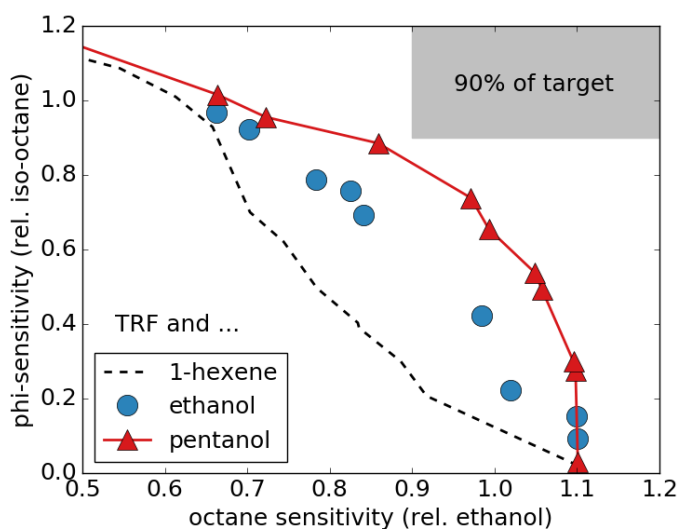


Figure II.24.3 - Trade-off between high octane sensitivity and phi-sensitivity for three four-component gasoline blends with a model-based RON estimate greater than 95. The blends containing 1-pentanol perform the best with some combination reaching nearly 90% of the target performance, specifically, an octane sensitivity better than ethanol and a phi-sensitivity better than iso-octane.

Then a fourth component is added to search to see how close to the target region (high octane and phi-sensitivity, shown in gray) can a fuel reach. Despite having the highest phi-sensitivity of any individual component, the TRF with 1-hexene shows the typical tradeoff between the two desirable properties. Replacing 1-hexene with ethanol offers blend combinations that reach 80% of the target region. The best component shown here is 1-pentanol that achieves nearly 90% of the target region. This result shows that from the simulation perspective, it appears possible to design a fuel to optimize the operation of a PSCCI engine.

The next step for this project is to optimize a fuel blend to maximize octane and phi-sensitivity over the range of pressure and temperatures specific to one of the advanced compression ignition engines operating under the Co-Optima program. This will enable the simulation approach to be validated. If proven to be true, this project along with its partners in the Advanced Engines team will provide significant evidence in support of the Co-Optimization Hypothesis.

Conclusions

This project developed a simulation-based approach to demonstrate the potential for high performance fuel blends to enable advanced compression ignition operation. If successfully validated in future engine experiments, it will provide direct evidence supporting the Co-Optimization Hypothesis, one of the major organizing ideas of the Co-Optima program. There are four key accomplishments from Fiscal Year 2017.

- Developed a phi-sensitivity metric to estimate the suitability of fuel for PSCCI engines that can be computed from the latest detailed fuel chemistry model for gasoline surrogate
- Created an optimization framework that allows the performance of a large number of fuel blends to be evaluated on DOE computing resources to explore the tradeoff between phi-sensitivity and octane sensitivity
- Searched over 150,000 fuel blends using nine hydrocarbon and 10 bio-derived blendstocks for combinations that delivered high phi-sensitivity and octane sensitivity while maintaining a RON greater than 95
- Found that blends involving 1-pentanol were able to push the traditional tradeoff between the desirable PSCCI properties to achieve nearly 90% of the levels identified for the blendstock exemplars with good octane sensitivity (ethanol) and phi-sensitivity (iso-octane)

References

1. Dec, John, Jeremy Dernotte, and Chunsheng Ji. "Increasing the Load Range, Load-to-Boost Ratio, and Efficiency of Low-Temperature Gasoline Combustion (LTGC) Engines." *SAE World Congress*, paper SAE-2017-01-0731, Detroit, MI, April 4–6, 2017. <https://doi.org/10.4271/2017-01-0731>.
2. Mehl, Marco, Scott Wagnon, Kuiwen Zhang, Goutham Kukkadapu, William Pitz, Charles Westbrook, Yingjia Zhang, et al. "A Comprehensive Detailed Kinetic Mechanism for the Simulation of Transportation Fuels." *10th US National Combustion Meeting*, paper 1A17, College Park, MD, April 23–26, 2017.
3. McCormick, Robert, Gina Fioroni, Lisa Fouts, Earl Christensen, Janet Yanowitz, Evgueni Polikarpov, Karl Albrecht, Daniel Gaspar, John Gladden, and Anthe George. "Selection Criteria and Screening of Potential Biomass-Derived Streams as Fuel Blendstocks for Advanced Spark-Ignition Engines." *SAE International Journal of Fuels and Lubricants*. 10 (2): 442–460. 2017. <https://doi.org/10.4271/2017-01-0868>.
4. McNewly, Matthew, Russell Whitesides, and Daniel Flowers. "Faster Solvers for Large Kinetic Mechanisms Using Adaptive Preconditioners." *Proceeding of the Combustion Institute*. 35: 581–587. 2015. <https://doi.org/10.1016/j.proci.2014.05.113>.
5. Whitesides, Russell. "Accurate Prediction of Research and Motor Octane Number of Gasoline Surrogates by Regression of Ignition Delay Times and Fuel Properties." *Proceeding of the Combustion Institute*. 37. 2018. (Submitted November 30, 2017).

6. Jones, Eric, Travis Oliphant, Pearu Peterson, *et al.* “SciPy: Open Source Scientific Tools for Python.” Accessed December 1, 2017. <http://www.scipy.org/>.

Key Fiscal Year 2017 Publications

1. Whitesides, Russell, and Matthew McNenly. “Meta-models for Ignition Delay Times with Applications to Surrogate Fuel Mixture Generation.” *10th US National Combustion Meeting*, paper 2A18, College Park, MD, April 23–26, 2017.
2. Whitesides, Russell. “Accurate Prediction of Research and Motor Octane Number of Gasoline Surrogates by Regression of Ignition Delay Times and Fuel Properties.” *Proceeding of the Combustion Institute*. 37. 2018. (Submitted November 30, 2017).

II.25 Dynamic Species Reduction for Multi-Cycle CFD Simulations

George A. Lavoie, Principal Investigator

University of Michigan
 Department of Mechanical Engineering
 1231 Beal Avenue
 Ann Arbor, MI 48109-2133
 E-mail: glavoie@umich.edu

Kevin Stork, DOE Technology Manager

U.S. Department of Energy
 E-mail: Kevin.Stork@ee.doe.gov

Start Date: April 17, 2017	End Date: June 30, 2020	
Total Project Cost: \$480,000	DOE share: \$432,000	Non-DOE share: \$48,000

Acknowledgments

Co-Authors

Robert Middleton, Alan Phlipot; University of Michigan Department of Mechanical Engineering

Project Introduction

Alternative fuels and advanced combustion strategies to improve engine efficiency are key components to achieving the DOE's goals of increasing energy independence and reducing greenhouse gas emissions. To that end the DOE Co-Optima project links the efforts of several national laboratories and universities working in these areas to accelerate the introduction of affordable, scalable, and sustainable high performance fuels for use in high efficiency, low emission engines. The current work supports that effort by providing significantly improved computational tools for modeling the virtual Cooperative Fuels Research (CFR) and advanced compression ignition (ACI) engines relevant to the Co-Optima project. The objective is to develop improved computational fluid dynamics (CFD) tools to radically reduce the computational expense of the gas exchange portions of the engine cycle while also significantly improving the performance of post combustion kinetics calculations during expansion. By addressing both of these problems, we strive to reduce the computational expense of a full engine cycle (720 degrees crank angle [$^{\circ}$ CA]) simulation by 80% relative to a simulation with detailed chemistry during gas exchange with the existing multi-zone model configuration. Providing such a set of tools to the DOE will enable the Co-Optima team to efficiently perform multi-cycle simulations capturing prior cycle compositional and thermal effects, improving overall model accuracy and providing insight into prior cycle influences in advanced combustion engines.

Objectives

- Develop a computationally efficient model for composition during the open portion of the engine cycle to dynamically reduce the number of species fluxed and reduce computational expense by 90% during gas exchange relative to a multi-zone simulation while maintaining accuracy
- Develop an improved multi-zone chemistry binning procedure to reduce computational expense during the expansion stroke post combustion by 50% relative to the existing zoning algorithm
- Demonstrate an overall 80% reduction in computational cost for a full (720 $^{\circ}$ CA) engine cycle simulation
- Evaluate the impact of varying fuel properties and residual composition on subsequent cycle ignition behavior in CFR and ACI engines using gasoline–biofuel blends

Approach

The project is primarily computational model based and focuses on improving model performance relative to existing baseline configurations and representative cases. Experimental studies by the national laboratories

will inform the baseline cases and fuel models to ensure that the performance benefits demonstrated by the project are relevant to conditions of interest to the DOE. All three-dimensional CFD simulations and model development in this project will occur using Convergent Science's CONVERGE software, an industry standard currently in use for other DOE projects. Convergent Science has offered support in the form of solver licenses and technical support to implement the models developed in this project as user defined functions in the CONVERGE framework. Sub-models for composition during gas exchange and combustion during expansion will be implemented and developed based on initial proof of concept simulations previously conducted in the CFD package KIVA. Validation will be conducted with comparisons to baseline simulations with the current state-of-the-art model configuration. Simulation work will leverage the high performance computing cluster Flux at the University of Michigan. As part of the overall Co-Optima project, Argonne National Laboratory (ANL) is providing support to define the operating conditions of interest to the DOE as well as providing computational meshes and chemical kinetic mechanisms.

Results

- A chemical kinetic mechanism for primary reference fuel blends currently in use at ANL for virtual CFR simulations has been provided by ANL.
- Initial simulation conditions based on the virtual CFR results presented by ANL at American Society of Mechanical Engineers Internal Combustion Engine Fall Technical Conference (Paper no. 2017-3599) have been provided to the University of Michigan. Operating conditions and results for a boosted spark ignition engine configuration have also been supplied.
- A CONVERGE mesh of the ANL virtual CFR engine has been provided by ANL. An additional mesh for the ACI engine will be provided in the following quarters as ANL and the overall Co-Optima team finalize the configuration of the ACI work for Fiscal Year 2018.

Previous work conducted using the CFD software KIVA has shown the potential for the improved models being developed during this project. Exploratory three-dimensional, full-cycle Reynolds-averaged Navier–Stokes simulations have been carried out with the dynamic species reduction method at University of Michigan with KIVA-3V modeling a homogeneous charge compression ignition engine using negative valve overlap valve events with the fully coupled multi-zone approach. A 312-species, four-component gasoline mechanism and surrogate [1] were used with a ~100,000 cell mesh (at bottom dead center). Here we have focused on reducing the cost of the gas exchange calculations, applying the approach at 80° after top dead center main combustion, reducing the number of species fluxed, and deactivating chemistry calculations while the valves are open. Reduction from 312 to approximately 40 species during the open portion of the cycle decreases the cost of the flow calculations by 83% while the valves are open. Applying our dynamic species reduction method while simultaneously deactivating chemistry during the open portions of the cycle reduces the overall expense of the full cycle calculation by 65% relative to a configuration where chemistry is active at all times and all species are fluxed. Despite the reduced compositional fidelity, the dynamic species reduction approach matched the combustion behavior predicted with all 312 species and chemistry active; however, significant differences were noted relative to the 312 species active simulations when an excessive number of species were removed from the domain. The pressure predictions are shown in Figure II.25.1. Finally, we observed significantly longer run times with positive valve overlap type valve events, indicating that relative performance improvements may be even greater with conventional valve events. Computational expenses for each portion of the cycle are shown in Figure II.25.2, where the reduction in overall computational cost with the dynamic species reduction approach is most significant during the open portions of the cycle.

Conclusions

Only one quarter of work has been conducted in Fiscal Year 2017 and there are few conclusions to report yet. The effort was primarily spent in gathering information from ANL.

Previous proof of concept simulation work has shown the potential to achieve the project goals in another modeling framework.

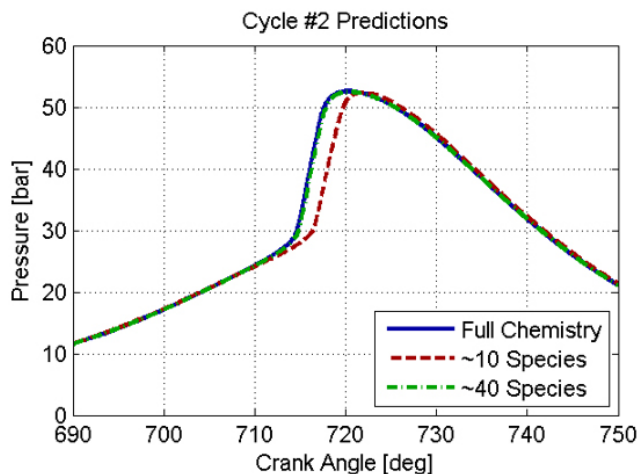
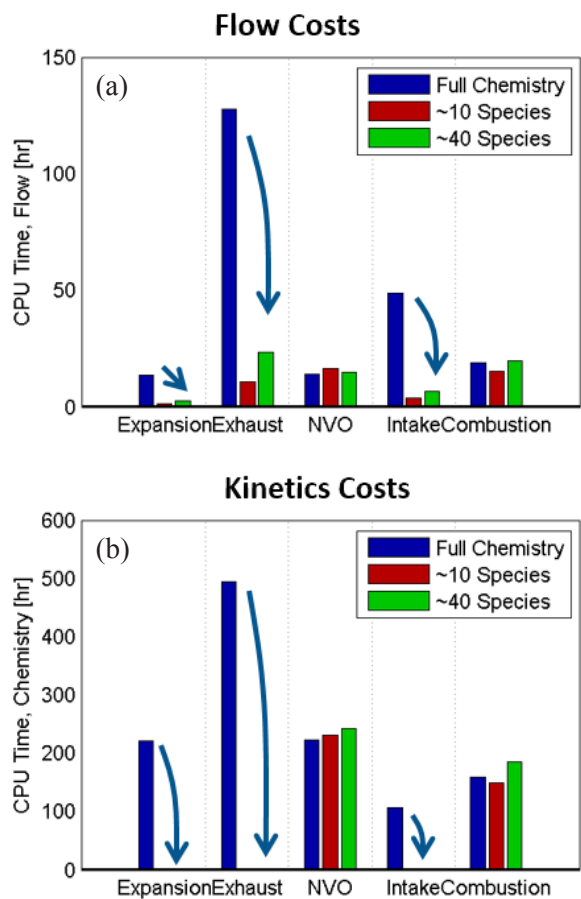


Figure II.25.1 - Predicted second cycle cylinder pressure showing good agreement between the baseline simulations and those conducted with species reduced to ~40 during gas exchange; but less agreement with further reduction to 10 species. (Proof of concept results with KIVA.)



NVO – negative valve overlap; CPU – central processing unit

Figure II.25.2 - Reduction in computational flow (a) and kinetics costs (b) using dynamic species reduction during an exploratory homogeneous charge compression ignition simulation. (Proof of concept results with KIVA.)

References

1. Mehl, M., W.J. Pitz, C.K. Westbrook and H.J. Curran. *Proc. Combust. Inst.* 33 (2011).

II.26 Micro-liter Fuel Characterization and Property Prediction

Ingmar Schoegl, Principal Investigator

Louisiana State University
3261 Patrick F Taylor Hall
Baton Rouge, LA 70803
E-mail: ischoegl@lsu.edu

Michael Weismiller, DOE Technology Manager

U.S. Department of Energy
E-mail: Michael.Weismiller@ee.doe.gov

Start Date: March 1, 2017 End Date: February 28, 2020
Total Project Cost: \$1,574,444 DOE share: \$1,359,544 Non-DOE share: \$214,900

Acknowledgments

Co-Principal Investigators

Shyam Menon, Manas Gartia, Eric Petersen, Tianfeng Lu; Louisiana State University

Project Introduction

The DOE Co-Optima initiative seeks to accelerate the introduction of affordable, scalable, and sustainable high performance fuels for use in high-efficiency, low emission engines. Co-optimized fuels and engines offer the opportunity to build on long-term research in both fuels and engines, where advances over the last ten years have identified combustion engine strategies that, especially if optimized to run on new fuels, would offer higher gas mileage and produce less engine-out pollutants than current engines.

The project “Microliter Fuel Characterization and Property Prediction” addresses DOE’s stated interest in enabling small volume (<20 μL), high throughput (>100 tests per device per month) measurements of transportation fuels and blends that are relevant to co-optimized fuels and engines. In this context, the ability to quantify the performance of a fuel in terms of autoignition metrics (e.g., octane number and sensitivity), combustion properties (e.g., flame speed) and physical properties (e.g., volatility and viscosity) is of significant interest. Predictions of fuel performance in a combustion engine require a link to be made between small volume measurements and combustion behavior of a fuel blend at engine relevant conditions.

Objectives

- Quantify combustion metrics of transportation fuels (e.g., octane number, flame speed)
- Construct an experimental prototype that can operate at elevated pressures
- Develop prediction models linking small volume measurements to engine relevant conditions
- Demonstrate small volume/high throughput testing capabilities in blind tests

Approach

The approach for micro-liter fuel characterization relies on cyclical combustion events within a heated micro-tube. This combustion mode is known as FREI (Flames with Repetitive Extinction and Ignition) and relies on self-excited instabilities that are sensitive to fuel properties. A total sample volume of 20 μL is stored on a disposable microfluidic chip, dispensed via a microelectromechanical system droplet generator, and mixed with air to create desired stoichiometry and mass flow rate. Within the micro-tube, a temperature profile (300–1,400 K) is established by external heating, whereas the desired operating pressure (25–50 bar) is regulated by a pressure controller downstream of the micro-tube. The time required to capture individual data points lies in the order of 10–20 s, which allows for high throughput testing. FREI characteristics are evaluated

for sweeps of mass flow rates and pressure. Image analysis provides information on ignition, extinction and flame propagation, which have been shown to be sensitive to fuel octane numbers.

The overall approach aligns with Sub-Topic 5 of the original funding opportunity announcement, i.e., “Small Volume, High Throughput Fuel Testing.” The main objective is to demonstrate the feasibility of micro-liter fuel characterization as a method with smaller sample volumes and higher throughput than conventional approaches (Schoegl/Louisiana State University [LSU]). A broadened scope includes engine-relevant physical fuel metrics (Menon/LSU) and thus encompasses Sub-Topic 1 (“Fuel characterization and fuel property prediction”). Small-volume testing requires microfluidic fuel delivery and sensing (Gartia/LSU). It further needs to be validated against data from established experimental methods (Petersen/Texas A&M University [TAMU]), whereas numerical analyses require reduced kinetic models (Lu/University of Connecticut [UConn]).

Results

With a project start date of March 1, 2017, this Fiscal Year 2017 report covers the first seven months of the project. After the amended contract was transmitted by DOE on April 11, the main contract was executed by LSU’s Office of Sponsored Programs on April 17. Subsequently, subcontracts to both UConn (Tianfeng Lu) and TAMU (Eric Petersen) were established, i.e., all sub-contracts necessary for the project were in place by the end of second quarter.

Key Accomplishments for Fiscal Year 2017

- Identified point of contacts and potential collaborators at DOE laboratories to meet Milestone M1.1 (second quarter, 2017: points of contact at DOE laboratories established). This initial kick-off milestone ensures that the project team is aware of ongoing Co-Optima work and key contacts at DOE. A list of test fuel candidates of interest to Co-Optima was obtained and shared with co-principal investigators.
- Redesigned microtube experiment for pressurized experiments (LSU): prior to the project, micro-combustion experiments were conducted at atmospheric pressure. A revised prototype suitable for intermediate pressure experiments was manufactured and tested in August 2017. After pressure tests up to 10 bar, micro-combustion experiments were conducted up to a pressure of 7.86 bar (100 psig), i.e., Milestone M1.2 (third quarter, 2017: micro-combustion at elevated pressure) was met on time.
- Developed basis for improved temperature measurements via multi-wavelength thin filament pyrometry (TFP). Initial experimental results point towards significant improvements over the prior approach, i.e., measurements via translating thermocouples (uncertainty worse than +/-50 K, which is insufficient to meet project goals; the approach is also not compatible with tests within sealed environments as needed for the project). Preliminary TFP data indicate that measurements with uncertainties better than +/-20 K are feasible for a measurement approach that is suited for sealed or pressurized environments.

Ongoing Work during Fiscal Year 2017

- Initiated droplet generation tests (LSU): a piezo-electric system for nano-liter fuel delivery was procured and delivered. By September 2017, initial droplet generation tests with deionized water as a calibration standard were complete and a transition to fuel droplet generation at 1 bar was under way, i.e., upcoming Milestone M1.3 (fourth quarter, 2017: nano-liter fuel delivery baseline established) is on schedule.
- Initiated large-scale experiments (TAMU): held meeting at TAMU (Petersen/Schoegl) to discuss project and define first round of tests; a literature review for existing data on Co-Optima fuel candidates (ignition delay, flame speeds) was compiled. Validation measurements involving methanol and ethanol to demonstrate capabilities of facilities are ongoing. A first summary report detailing validation tests was received by the principal investigator.
- Initiated work on chemistry reduction (UConn): after a meeting during the Annual Merit Review (Lu/Schoegl), the Fiscal Year 2017 version of UConn’s skeletal mechanism (toluene + primary reference fuel TPDFR + ethanol; 165 species) was shared with all project partners. Preliminary validation tests show excellent agreement with pre-Co-Optima work at Lawrence Livermore National Laboratory (LLNL). An

assessment with respect to LLNL’s current Co-Optima mechanism is ongoing. A first summary report was received by the principal investigator.

Relevance of Results/Major Findings

Tests at Elevated Pressures

One major objective of the project is to introduce the ability to conduct micro-combustion tests at elevated pressure levels, thus moving towards engine-relevant conditions. Figure II.26.1 illustrates an example for preliminary results at intermediate pressure (Milestone M1.2). Observations confirm expected combustion behavior with a widened extent of FREI due to reduced quenching. As anticipated, results indicate that tests at increased pressures will require reduced tube diameters. Using experiments, the cutoff for viable 1 mm inner diameter tube tests was quantified as ~5 bar for standard fuel/air mixtures.

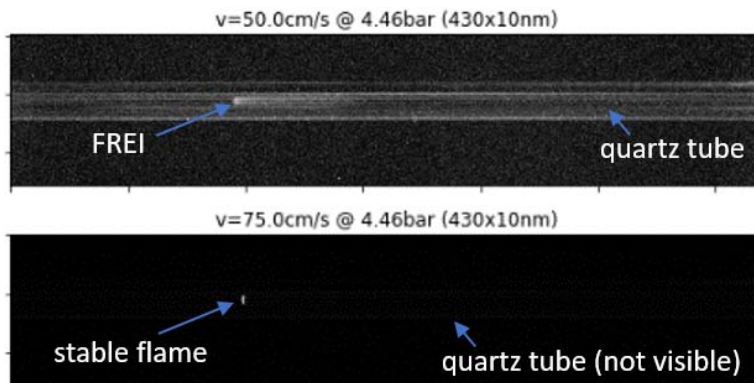


Figure II.26.1 - Micro-combustion at elevated pressure: unsteady FREI and stable flames at 4.46 bar (I. Schoegl/LSU)

Thin Filament Pyrometry

The technological premise of the project is to characterize fuels based on temperature levels that describe ignition, extinction and flame propagation within a heated quartz tube. Thus, the overall success hinges on the ability to conduct accurate temperature measurements. Prior approaches involve translating thermocouples that are, however, not sufficiently accurate and are also not compatible with pressurized environments. TFP enables temperature measurements based on radiation emitted from a thin SiC filament, which is easily captured by a machine vision camera. Based on established TFP techniques [1], a theory for an improved multi-wavelength TFP was developed and implemented. Figure II.26.2 illustrates initial results obtained for four-wavelength

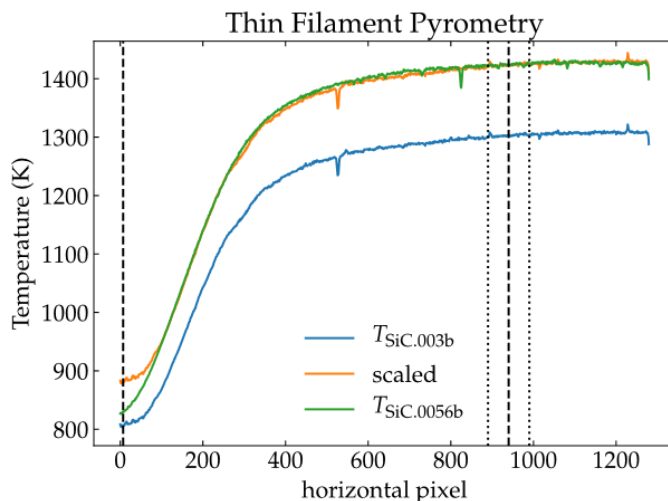


Figure II.26.2 - Preliminary results for four-wavelength TFP: 5.6 mil (142 μm) SiC filament yields calibration-free temperature measurements within 20 K of reference measurements, while 3 mil (76 μm) filament requires calibration (I. Schoegl/LSU)

TFP. While preliminary data indicate that the thickness of the filament needs to be resolved by multiple sensor pixels, results nevertheless illustrate that temperature measurements within 20 K of a reference measurement are feasible. Current limitations of calibration-free measurements are expected to be relaxed by the inclusion of additional wavelengths.

Reduced Chemistry Models

Figure II.26.3 illustrates the status of reduction work at the end of Fiscal Year 2017 based on flame speed simulations, where a skeletal mechanism with 165 species and 839 reactions was used. The mechanism is optimized for PRF60-100, T PFF with Research Octane Number from 65 to 93 and sensitivity from 1.1 to 12 with any additional percentage of ethanol, and shows excellent agreement with a detailed LLNL mechanism.

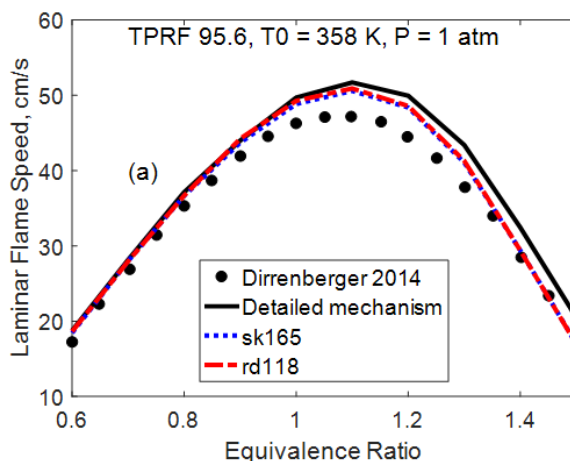


Figure II.26.3 - Flame speeds of TPRF95.6-air mixture (T. Lu/UConn)

Conclusions

The following conclusions are derived from the first seven months of the project “Microliter Fuel Characterization and Property Prediction.”

- Initial tests with a newly designed experimental prototype confirm expected combustion characteristics at elevated pressure; reductions of tube inner diameters are anticipated above ~5 bar.
- Tests with TFP, an alternative temperature measurement approach, were successful and indicate that calibration-free measurements within a pressurized environment are feasible.
- Preliminary validation tests for a reduced skeletal mechanism suitable for numerical work show excellent agreement with pre-Co-Optima mechanisms developed at LLNL.

The above two findings indicate that there are no major technological hurdles to conducting micro-combustion tests at elevated temperatures. Thus, the project is on track to attain the technical goal for Budget Period 1, i.e., “Develop experimental devices and numerical tools for small volume testing.” Further, all activities towards meeting Fiscal Year 2018 goals have been initiated.

References

1. Ma, B., G. Wang, G. Magnotti and M. Long. “Intensity-ratio and color-ratio thin-filament pyrometry: Uncertainties and accuracy.” *Combust. Flame* 161(4):908–916, 2014.

II.27 The Development of Yield-Based Sooting Tendency Measurements and Modeling to Enable Advanced Combustion Fuels

Lisa Pfefferle, Principal Investigator

Yale University
9 Hillhouse Avenue
New Haven, CT 06508-1873
E-mail: lisa.pfefferle@yale.edu

Michael Weismiller, DOE Technology Manager

U.S. Department of Energy
E-mail: Michael.Weismiller@ee.doe.gov

Start Date: May 1, 2017	End Date: April 30, 2018	
Total Project Cost: \$1,452,787	DOE share: \$1,307,505	Non-DOE share: \$145,282

Acknowledgments

Co-Authors

Charles McEnally, Yuan Xuan; Yale University

Project Introduction

Fuels derived from biomass offer many potential benefits, including reduced emissions of particulate matter (PM). PM emissions from combustion devices such as diesel engines are the second biggest source of global climate change after carbon dioxide [1]. Furthermore, PM emissions from combustion devices contribute to ambient particulate concentrations that cause about 3 million deaths worldwide each year [2]. As a consequence, PM emissions are regulated and engine manufacturers currently have to install particulate filters and other hardware to reduce emissions.

Biomass-derived fuels generally contain oxygenated hydrocarbons, which have been shown in many cases to have lower tendencies to form particulates in flames [3]; thus these fuels offer engine companies a lower cost path to meeting PM emissions standards. However, the chemical composition of biomass fuels can vary over a wide range and it is not possible to test all of them in actual engines. Therefore laboratory-scale data are necessary to choose optimal fuels and achieve the full value opportunity presented by biomass fuels for reduced emissions at lower cost.

Objectives

- Develop a database of quantitative sooting tendencies that includes all of the categories of hydrocarbons important to petroleum-derived and biomass-derived fuels
- Develop PM merit functions that can predict PM emissions from advanced combustion engines using data on sooting tendency and any other relevant fuel properties
- Identify and validate detailed chemical kinetic mechanisms that enable accurate computational fluid dynamics simulations of PM emissions from engines

Approach

In this project a fundamental fuel property called Yield Sooting Index (YSI) has been defined that characterizes the tendency of fuels to form particulates in laboratory-scale flames. It is measured by adding a small concentration of the test fuel to a methane–air flame and measuring the resulting change in the flame’s soot concentration. If the fuel has a greater tendency to form soot, then it will form more soot when added to the flame and a larger soot concentration will be measured. Since the test fuel is only a small portion of the flame’s overall fuel, the temperatures and residence times in the flame are not changed, and all of the test fuels are

forming soot in a uniform combustion environment. Some of the particular benefits of YSI are that it requires very small volumes of sample (100 μL), it allows high throughput so large numbers of fuels can be tested, and the results can be used to test the accuracy of computational simulations of soot formation.

Results

The first objective of this project is to develop a database of measured sooting tendencies (YSIs) that will improve the ability of the Co-Optima program to select optimal fuels. During Fiscal Year (FY) 2017, several tasks were accomplished towards this end.

First, the two existing incompatible databases of YSI measurements were combined together to produce a unified database. This database was then posted to the Harvard Dataverse; see Publication #3. This makes the database permanently and easily available to the entire stakeholder community and the general public.

Second, discussions with personnel at the National Renewable Energy Laboratory (NREL) showed that one of the major gaps in the current YSI database is oxygenated aromatics, so YSIs have begun to be measured for a set of these compounds. These compounds are important because anisole (methoxybenzene) is one of the Tier 2 spark ignition Co-Optima blendstock candidates. More generally, the monolignols that make up lignin contain aromatic rings with hydroxy and methoxy side-chains, so oxygenated aromatics are a common product of biomass conversion.

As of the end of FY 2017, YSI had been measured for 14 of these compounds. Each measurement has been repeated multiple times and the standard deviations are on order of ± 2 YSI units, which is comparable with earlier YSI measurements. YSIs were also measured for several related non-oxygenated aromatics and the results were consistent with earlier measurements. All of the new YSIs were measured in the new apparatus, so these measurements demonstrate that this project has achieved its milestone for fourth quarter of FY 2017, “assemble second apparatus and initial YSI measurements.”

Figure II.27.1 shows the measured YSIs for several compounds related to toluene. The results show that oxygen strongly affects the sooting tendency, and in particular can greatly reduce it. Thus oxygenated aromatics are a possible blendstock that offer the benefits of aromatics without the associated emissions penalties. However, the effects of oxygen are complicated and in some cases, such as benzyl alcohol, actually increase the sooting tendency relative to toluene. Therefore detailed data of the type being measured in this

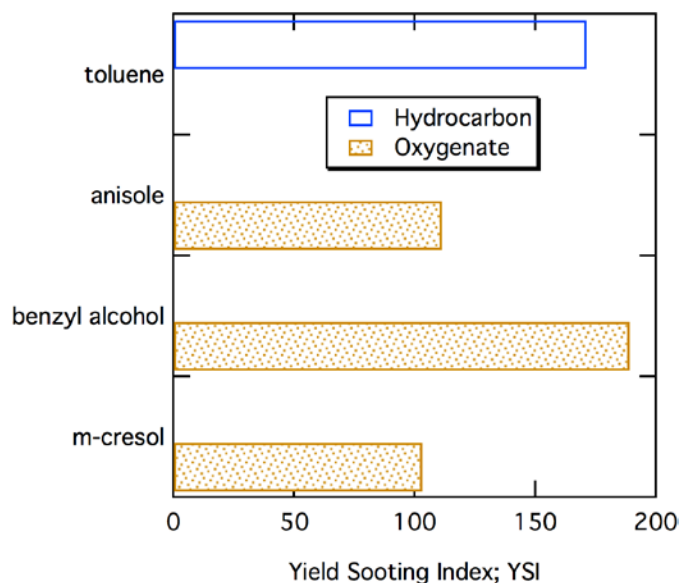


Figure II.27.1 - YSI measured for several oxygenated hydrocarbons formed by adding oxygen atoms to toluene project is necessary to choose biofuels containing these compounds wisely.

The second major objective of this project is to develop emission indices that can accurately predict the particulate emissions from real engines based on the fuel's intrinsic sooting tendency and any other relevant fuel properties. During FY 2017 several tasks were accomplished towards this end.

First, sooting tendencies were measured for the five Co-Optima test gasolines (“Core Fuels”). These are real fuels with a reproducible composition that are being used in engine experiments at Sandia National Laboratories and at Oak Ridge National Laboratory (ORNL); thus the YSI measurements for them can be used to relate YSI to engine performance and emissions.

The results are shown in Figure II.27.2. The sooting tendencies are bracketed by heptane and toluene, and increase in the order E30 (30% gasoline, 70% ethanol) < alkylate < olefin < cycloalkane < aromatic.

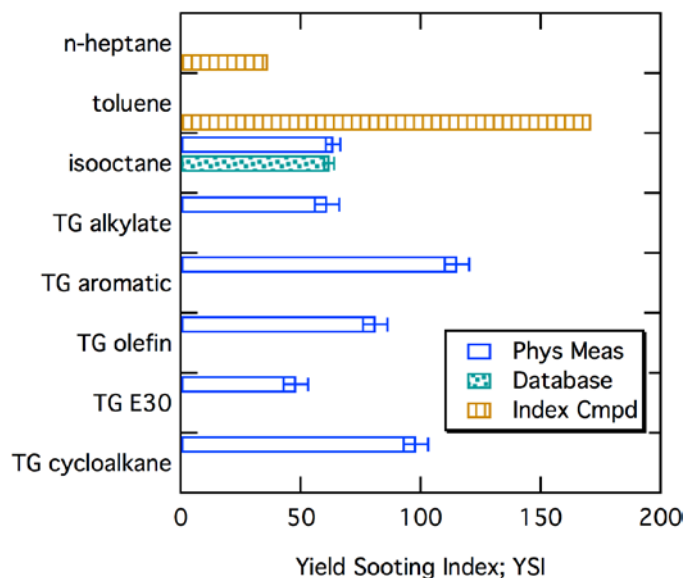


Figure II.27.2 - YSIs measured for the five Co-Optima test gasolines (TGs)

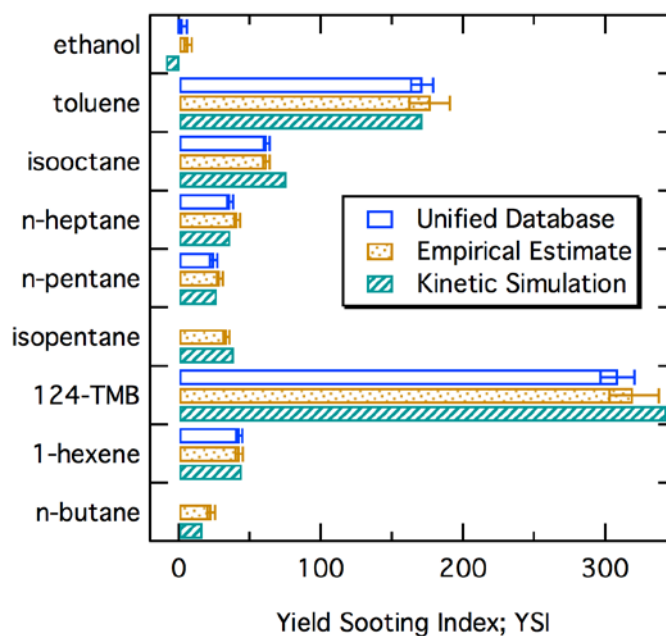
Second, YSIs were measured for surrogates to three of the test gasolines. These surrogates have been formulated at Lawrence Livermore National Laboratory (LLNL) and ORNL [4]; however, until now their performance in mimicking the sooting behavior of the test gasolines has not been tested. As originally formulated, the surrogate fuels contain n-butane (boiling point $\sim 0^\circ\text{C}$), which is not compatible with the experimental procedures used in this project. Therefore, modified surrogate fuels (MSFs) were formulated where the n-butane has been lumped into n-pentane. The kinetic simulations described below show that this modification has a negligible impact on YSI.

The YSIs of the real TG and the MSF are compared in the figure discussed in the next section. They agree fairly well; indeed, it is immediately recognizable which surrogate goes with each real fuel. This conclusion means that the surrogates can be used in computational fluid dynamics simulations to predict emissions from real engines, and that the results will only be weakly impacted by the compositional differences between the surrogates and the real fuels.

The third objective of this project is to develop efficient numerical simulation capabilities for YSIs of Co-Optima fuels, so that the ability of chemical kinetic mechanisms to reproduce soot formation under engine relevant conditions can be evaluated and improved. During FY 2017 several tasks were accomplished towards this end.

First, the YSI simulation framework was validated over a range of species. Then this framework was used to predict the YSI of the Co-Optima TG. Since these fuels are real fuels containing hundreds or even thousands of chemical compounds, surrogate fuels are necessary to perform the simulations. Surrogates have been formulated for these fuels at LLNL and ORNL as discussed in the previous section; this project examined whether kinetic simulations can reproduce the YSIs measured for these surrogates.

The YSI of the nine surrogate components were simulated using a detailed chemical model, originally developed by Pitz's research group at LLNL [5], containing 679 species and 3,495 reactions. This chemical model is then merged with an aromatic growth sub-mechanism to provide the necessary formation pathways of soot particles from gas phase soot precursors. The obtained YSI values for these compounds using kinetic simulation are then compared against those obtained using two other methodologies, physical measurement performed at Yale University and empirical estimate performed at NREL, as shown in Figure II.27.3. It is shown that, for most species considered, the simulated YSI values using detailed chemical kinetic information agree well with the measured data and with empirical estimates based on group additivity, when measurements are not available. The YSI value for ethanol is underpredicted by kinetic simulation, potentially due to missing reaction pathways or due to large chemical kinetic uncertainties. Reaction sensitivity analysis and uncertainty propagation will be performed to identify the "erroneous" reactions for ethanol, during the next period of performance.



124 TMB – 1,2,4-trimethylbenzene

Figure II.27.3 - Comparisons between YSI results for surrogate fuel components obtained using three different methodologies: physical measurement (Yale), empirical estimate (NREL), and kinetic simulation (Penn State)

Using the same chemical kinetic mechanism, the YSIs of surrogate fuels for TG alkylate, aromatic, and E30 were computed, and compared with the results obtained using the other two methodologies, as shown in Figure II.27.4. For kinetic simulation and empirical estimate, calculations are only performed on surrogate fuels, but for physical measurements, experiments are done using the actual fuels and surrogate fuel mixtures. From this comparison, it can be seen that the surrogate formulations proposed by LLNL capture quite well the sooting behavior of the actual Co-Optima core fuels, although these surrogates were originally designed to best reproduce ignition delays and laminar flame speeds. In addition, very good agreement has been found between the three methodologies, for all core fuels under investigation.

The concept of YSI was introduced to quantify the likelihood of forming soot from a given fuel, which can be seen as an inherent fuel property, independent of the specific combustion characteristics such as equivalence ratio, temperature, or pressure. However, due to the large difference between YSI measurement pressure condition (1 atm) and pressure levels in combustion devices (around 20 atm), it is necessary to examine the pressure dependence of YSI to better connect YSI to fuel sooting properties under device-relevant conditions. Although assessing pressure effects in experiments would lead to significant cost and effort (e.g., installation of a pressure vessel), it can be easily done using numerical simulations. The baseline YSI flame has been recomputed using multi-dimensional simulations and detailed chemical kinetics under a series of pressure levels from 2 atm to 10 atm. YSI values have been computed for a range of chemical compounds at 2 atm. The

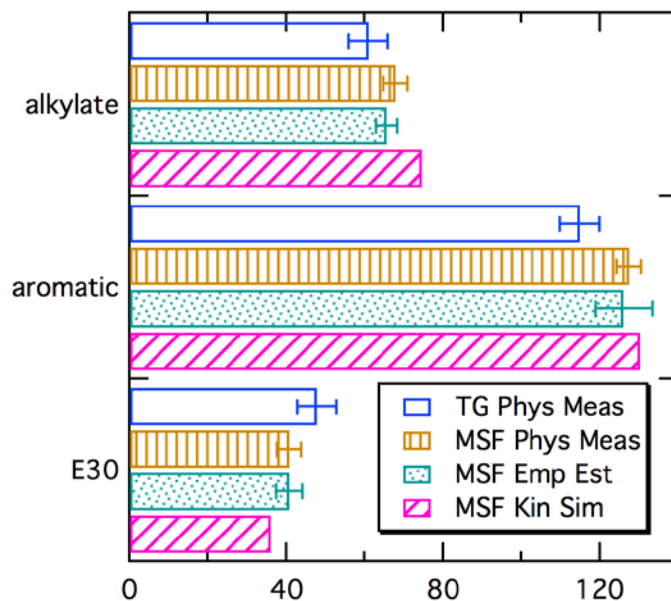


Figure II.27.4 - Comparisons between YSI results for surrogate fuels obtained using three different methodologies: physical measurement (Yale), empirical estimate (NREL), and kinetic simulation (Penn State)

results obtained are compared against their corresponding 1 atm values in Figure II.27.5, and it is shown that pressure dependence is quite weak under this pressure condition. During the next fiscal year, simulations will be performed at higher pressures (up to 20 atm) and YSI will be computed at these pressures to further quantify pressure effects of YSIs for a wider range of species.

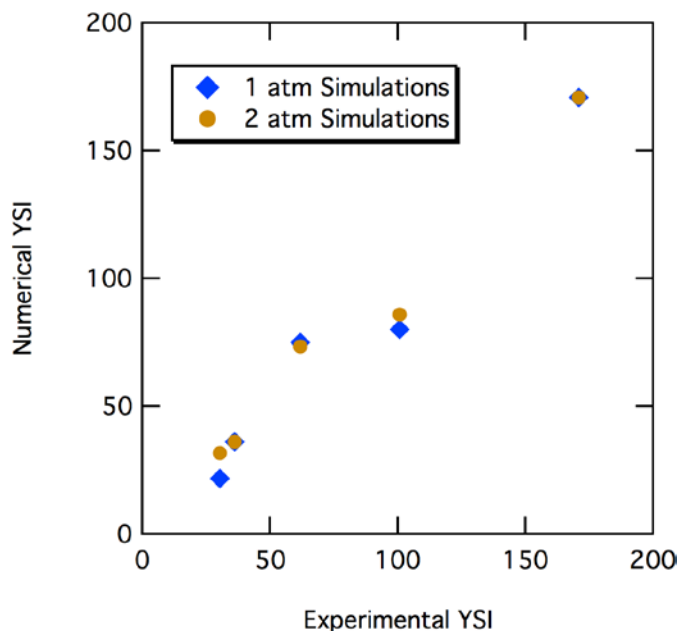


Figure II.27.5 - Predicted YSIs for a range of chemical compounds at 1 atm and 2 atm

Conclusions

- Many oxygenated aromatic hydrocarbons have much lower sooting tendencies than regular aromatics and therefore are promising low PM emissions blendstocks.
- The surrogates to the Co-optima TGs proposed at LLNL and ORNL [4]) accurately mimic the sooting behavior of the real fuels. Furthermore, the kinetic mechanisms proposed at LLNL for the surrogate fuels

(Mehl et al. [5]) are able to accurately predict this sooting behavior. These observations demonstrate that computational fluid dynamics simulations using the surrogates and kinetic mechanisms can be used to predict emissions from real engines.

- Although absolute levels of soot formation depend on pressure from 1–2 atm, this pressure dependence factors out when absolute soot concentrations are rescaled into YSI.

References

1. Bond, T.C., et al., *J. Geophys. Res. Atmos.* 118 (2013) 5380–5552.
2. Lim, S.S. et al., *Lancet* 380 (2012) 2224–2260.
3. Pepiot-Desjardins, P., H. Pitsch, R. Malhotra, S.R. Kirby, A. L. Boehman, *Combust. Flame* 154 (2008) 191–205.
4. Szybist, J., S. Wagnon, D. Splitter, W. Pitz, M. Mehl, *SAE Int. J. Engines* 10 (2017) 2305–2318.
5. Mehl M., W.J. Pitz, C.K. Westbrook, H.J. Curran, *Proc. Combust. Inst.* 33 (2011) 193–200.

Key Fiscal Year 2017 Publications

1. St. John, P.C., P. Kairys, D.D. Das, C.S. McEnally, L.D. Pfefferle, D.J. Robichaud, M.R. Nimlos, B.T. Zigler, R.L. McCormick, T.D. Foust, Y.J. Bomble, S. Kim. “A quantitative model for the prediction of sooting tendency from molecular structure.” *Energy & Fuels* 31:9983-9990 (2017).
2. Das, D.D., P. St. John, C.S. McEnally, S. Kim, L.D. Pfefferle. “Measuring and predicting sooting tendencies of oxygenates, alkanes, alkenes, cycloalkanes, and aromatics on a unified scale.” *Combustion and Flame* (In Press). <https://doi.org/10.1016/j.combustflame.2017.12.005>.
3. McEnally, C.S. D.D. Das, L.D. Pfefferle. “Yield sooting index database volume 2: sooting tendencies of a wide range of fuel compounds on a unified scale.” Harvard Dataverse, 2017, doi:10.7910/DVN/7HGFT8.szy.

III. Alternative Fueled Engines

III.1 Unconventional and Renewable Hydrocarbon Fuels

J. Timothy Bays, Principal Investigator

Pacific Northwest National Laboratory
902 Battelle Blvd., MS K2-14
Richland, WA 99352
E-mail: tim.bays@pnnl.gov

Kevin Stork, DOE Technology Manager

U.S. Department of Energy
E-mail: Kevin.Stork@ee.doe.gov

Start Date: October 1, 2016	End Date: September 30, 2017	
Total Project Cost: \$12,000	DOE share: \$12,000	Non-DOE share: \$0

Project Introduction

The objective of this project was to ensure that our chemical knowledge of future unconventional fuels is sufficient to support advanced combustion engine technology. Future diesel fuels derived from unconventional resources, e.g., upgraded pyrolysis oil, biodiesel, oil sands, or shale oil, can exhibit chemistries and molecular structures significantly different from conventional hydrocarbon resources. Because of strict fungibility requirements for pipeline transport, unconventional hydrocarbon fuels may be limited to regional areas, resulting in high concentrations of fuels with various combinations of hydrocarbon species entering the fuel market. Specifically, this project seeks to:

- Facilitate the successful introduction of future fuel feedstocks compatible with advanced combustion engines to help reduce the United States' dependence on foreign oil
- Develop analytical approaches correlating fuel component molecular structure to fuel properties and performance.

Objectives

Fiscal Year 2017 Objectives

- Support Co-Optima projects
- Contribute to Analytical Working Group meetings to foster a collaborative relationship and information exchange with groups such as CanmetENERGY and the Coordinating Research Council

Approach

Since inception, this project has sought to utilize nuclear magnetic resonance spectroscopy to identify important molecular structures and substructures present in complex fuel mixtures, and correlate the individual or aggregate contributions of those structures to properties important in the use of the fuel, such as lubricity or derived cetane number. Successful correlations have been made and led to the incorporation of this project into Co-Optima in Fiscal Year 2016.

Results

Tasks under Co-Optima subsumed the role of this project during Fiscal Year 2016. During Fiscal Year 2017, no funds were spent from this project. Residual funds will be applied to meeting Co-Optima goals and documenting results.

Conclusions

Tasks under Co-Optima during Fiscal Year 2016 and Fiscal Year 2017 have continued to show the importance of nuclear magnetic resonance in providing a molecular structure-based predictive capability for fuel properties.

III.2 Single-Fuel Reactivity Controlled Compression Ignition Combustion Enabled by Onboard Fuel Reformation

Benjamin Lawler, Principal Investigator

Stony Brook University
100 Nicolls Road
Stony Brook, NY 11794
E-mail: benjamin.lawler@stonybrook.edu

Kevin Stork, DOE Technology Manager

U.S. Department of Energy
E-mail: Kevin.Stork@ee.doe.gov

Start Date: October 1, 2015	End Date: September 30, 2018	
Total Project Cost: \$1,128,618	DOE share: \$1,014,352	Non-DOE share: \$114,266

Acknowledgments

Co-Authors

Sotirios Mamalis, Stony Brook University
Dennis Assanis, University of Delaware
Dean Modroukas, Innoveering, LLC
Marco J. Castaldi, City College of New York

Project Introduction

Reactivity controlled compression ignition (RCCI) combustion has demonstrated efficiency and emissions improvements compared to both diesel and spark-ignited (SI) combustion modes [1,2,3,4]. Specifically, RCCI has demonstrated a 20% fuel economy increase compared to SI [3], and a 5% efficiency improvement at certain engine speeds and loads over conventional diesel combustion while maintaining significantly lower engine-out soot and NO_x emissions [4]. However, RCCI is limited in its commercial viability due to the requirement of two separate fuel systems which need to be refilled by the user. To resolve this drawback of RCCI, the proposed innovation uses a single parent fuel with an onboard fuel reformer to create the necessary separation in fuel reactivity to enable RCCI combustion. In this concept, the fuel from the tank would be directed to the engine unaltered, while a branch of the fuel stream is directed to an onboard fuel reformer where the parent fuel is reformed to produce reformat: a fuel mixture of H₂, CO, and partially reacted hydrocarbon species whose properties are different from the initial parent fuel. The less reactive fuel is then port fuel injected and the higher reactivity fuel is direct injected.

This approach is innovative because fuel reformer technology and RCCI combustion could potentially have a synergistic relationship. The proposed use of an onboard fuel reformer to create the necessary fuel reactivity separation from a single fuel would help the future development and potential commercialization of “single-fuel RCCI” and the realization of the previously reported benefits of RCCI.

Objectives

The overall project objectives are to:

- Reform gasoline, diesel, and natural gas to varying levels and characterize the constituent species of their reformat mixtures as well as the autoignition tendency of the reformat mixtures in the form of an effective primary reference fuel (PRF) number.
- Evaluate the potential efficiency, emissions, operating range, and burn characteristics of RCCI using a parent fuel and its reformat mixture using computational fluid dynamics (CFD) simulations with detailed chemical kinetics as well as GT-SUITE models.

- Experimentally test each parent fuel–reformate combination in RCCI and compare reformate RCCI to published RCCI data from the literature.

The objectives during this budget year were to:

- Experimentally determine the autoignition tendency of the various reformate mixtures that were produced and characterized in the first budget period.
- Modify an existing single-cylinder diesel engine to be able to test both conventional RCCI, as well as reformate RCCI.
- Develop both system level models in GT-POWER and detailed CFD models in CONVERGE CFD and validate these models against experimental data.

Approach

The goal of this project is to determine the feasibility of RCCI combustion using a parent fuel and its reformate. Three potential parent fuels, diesel, gasoline, and natural gas, will be evaluated since these fuels are most relevant to vehicle applications. The approach to achieve the project goal is to perform a systematic and fundamental evaluation of these parent fuels in this newly conceived realization of RCCI combustion. To do this, the parent fuels will first be reformed to varying levels, and the species concentrations of the reformate mixtures, as well their autoignition properties, will be characterized. This first step will help determine which parent fuels hold the most promise to enable reformate RCCI. Once the parent fuel and reformate combinations with the largest effective octane separation have been determined, CFD and system-level models will be used in conjunction with experimental testing to evaluate the potential efficiency, emissions, burn characteristics, and operating range of single-fuel RCCI. The model simulations and the experimental results of reformate RCCI will be compared to RCCI data in the literature to put the results in the greater context of the advanced combustion community and to help evaluate the feasibility and future promise of single-fuel RCCI. Stony Brook University is responsible for all of the experimental engine testing as well as CFD and system-level modeling. The experimental testing will be conducted at the Engine Combustion Research Laboratory in the Advanced Energy Research and Technology Center at Stony Brook University. The research team has access to several high performance computing clusters available through the Institute for Advanced Computational Science. Innoveering, LLC, and City College of New York are subcontractors and they are responsible for reforming the parent fuels and characterizing the reformate mixtures.

Results

Key accomplishments of Fiscal Year 2017:

- The autoignition tendency of reformate mixtures from gasoline, diesel, and natural gas were characterized using a Cooperative Fuels Research (CFR) engine operating in homogeneous charge compression ignition (HCCI) as a diagnostic to determine an effective PRF number for each gaseous reformate fuel mixture.
- The results showed that the PRF number separation between the parent fuel and the reformate mixture was around 16 points for gasoline, 25 points for natural gas, and 113 points for diesel.
- An existing single-cylinder, diesel, research engine was modified to be able to test both conventional dual-fuel RCCI combustion, as well as RCCI using a parent fuel and its reformate.
- System level models in GT-POWER were constructed and validated against experimental data for both the CFR engine as well as the Ricardo Hydra engine that will be used for the single-fuel RCCI combustion.
- Additionally, a detailed, CFD model was constructed in CONVERGE CFD and validated against experimental data from the Ricardo Hydra engine for both conventional diesel combustion and conventional, dual-fuel RCCI combustion.

During the 2017 fiscal year, the reformate fuel mixtures produced during the previous fiscal year (2016) by reforming gasoline, diesel, and natural gas to varying degrees were tested in the CFR engine to determine

an effective PRF number for each of the parent fuels and the reformat fuel mixtures. To accomplish this objective, a large number of PRF blends were autoignited in HCCI combustion at a constant engine speed (1,200 rpm) and equivalence ratio (0.3). Meanwhile, the intake temperature and the compression ratio were varied to match the combustion phasing to a constant, predetermined value (6 crank angle degrees after top dead center). This created a PRF mapping with compression ratio and intake temperature that allows an effective PRF number to be assigned to various liquid or gaseous fuels that are autoignited under the same conditions. In this way, HCCI combustion is used as a diagnostic to determine the autoignition tendency of a particular fuel relevant to advanced combustion modes, as opposed to the research octane number test and the motor octane number test which characterize a fuel's autoignition tendency in the context of SI combustion to determine the fuel's propensity to knock. The results of this PRF mapping are shown in Figure III.2.1. Gasoline (87 anti-knock index EEE certification gasoline) is also shown in Figure III.2.1 to demonstrate the methodology for determining an effective PRF number. The average PRF number from interpolating the PRF blends at a compression ratio of 14 and 15, or extrapolating at a compression ratio of 16 is 87, which agrees well with its anti-knock index (average of the Research Octane Number and Motor Octane Number) of 87.

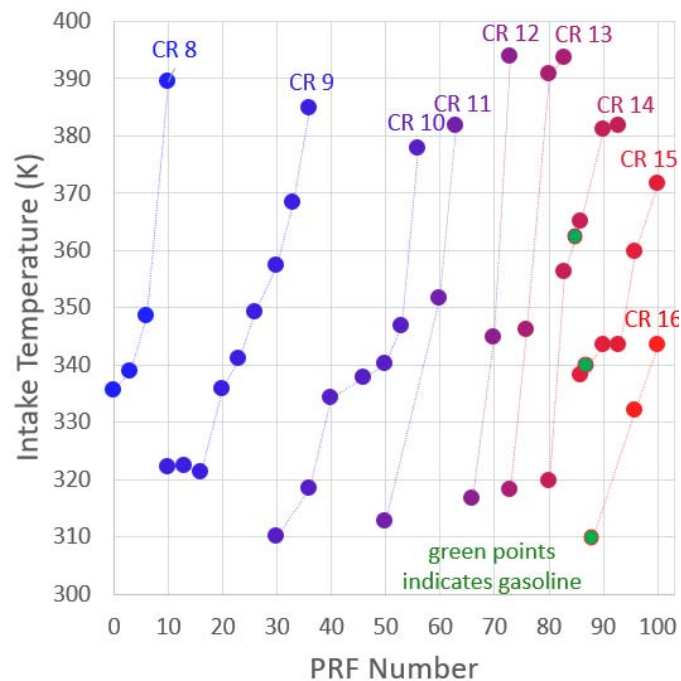


Figure III.2.1 - PRF mapping that allows the determination of an effective PRF number of any liquid or gaseous fuel within this range of compression ratio (CR) and intake temperature

Next, the reformat mixtures were autoignited in HCCI at the same conditions to determine their effective PRF numbers. Figure III.2.2 shows the PRF blends that were used to extrapolate to find the effective PRF number of the reformat mixtures. Table III.2.1 shows the determined effective PRF number of the reformat mixtures and the parent fuels. From Table III.2.1, it can be seen that the effective PRF separation between gasoline and its reformat mixtures is around 16 points on the PRF scale. The average PRF separation between natural gas and its reformat mixtures is around 25 points on the PRF scale. Finally, the average PRF separation between diesel and its reformat mixtures is around 113 points on the PRF scale. From these results, it was concluded that if the parent fuel is either gasoline or natural gas, there will not be enough reactivity separation from their reformat mixtures to successfully achieve single-fuel RCCI in the cylinder. This result is specific to the particular type of reforming technique that was used in the work (catalytic partial oxidation reaction) and it is possible that the results would change if the reforming technique is different. Contrary to gasoline and natural gas, diesel as a parent fuel exhibits a tremendous amount of reactivity separation between the parent fuel and the reformat mixture, which suggests that diesel would be an excellent candidate for single-fuel RCCI combustion. The reactivity separation between diesel and its reformat mixture is approximately 113 PRF number points, which is significantly more than conventional diesel–gasoline RCCI, which has approximately

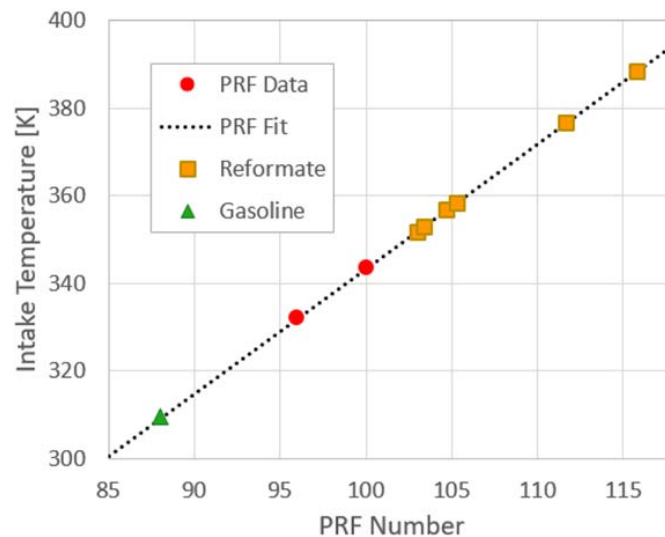


Figure III.2.2 - Determination of the effective PRF number for each of the reformat fuel mixtures

87 PRF point separation. In this variant of single-fuel RCCI, the parent diesel fuel (high reactivity fuel) would be direct injected into the cylinder, while the gaseous reformat mixture (low reactivity fuel) would be introduced in the intake port.

Table III.2.1 - Effective PRF Number for the Three Parent Fuels and Their Reformat Mixtures

	Effective PRF Number	Parent Fuel	Octane Separation with Parent Fuel
Natural Gas	130	-	-
Gasoline	87	-	-
Diesel	0	-	-
Reformat 1	103.0	Gasoline	16.0
Reformat 2	103.4	Gasoline	16.4
Reformat 3	104.7	Natural Gas	-25.3
Reformat 4	105.3	Natural Gas	-24.7
Reformat 5	111.6	Diesel	111.6
Reformat 6	115.8	Diesel	115.8

In order to test single-fuel RCCI experimentally, an existing single-cylinder, diesel, research engine was modified to be able to test conventional dual-fuel (gasoline–diesel) RCCI combustion, as well as single-fuel RCCI combustion with a parent fuel and its gaseous reformat mixture. During this 2017 fiscal year, these modifications were made to this single-cylinder research engine. Then, initial and preliminary experimental data was collected during this fiscal year. In addition to the experimental efforts to evaluate, demonstrate, and better understand single-fuel RCCI, system models and a CFD model will also be used to characterize the efficiency and combustion characteristics of single-fuel RCCI. During this fiscal year, these system-level models and CFD models were constructed in GT-POWER and CONVERGE CFD, respectively. Figures III.2.3 and III.2.4 show the system-level model of the Ricardo Hydra and CFD models that were constructed in this fiscal year.

These models were then validated against the experimental data and are being used to explore single-fuel RCCI combustion including the efficiency, energy flows, and combustion characteristics. The CFD model has been used to provide some preliminary results of single-fuel RCCI using the gaseous fuel compositions determined from the characterization of the reformat mixture with diesel as the parent fuel. The pressure and heat release rate results are shown in Figure III.2.5. The results show successful RCCI combustion with a peak gross thermal efficiency of 51.2%. The common RCCI start of injection (SOI) timing trend is present, where advancing injection timing causes combustion phasing to retard.

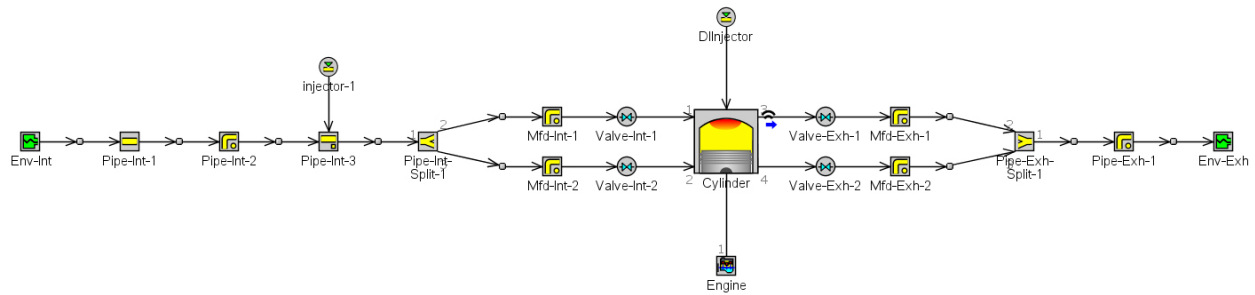


Figure III.2.3 - GT-POWER model of the diesel Ricardo Hydra engine used for dual-fuel RCCI and single-fuel RCCI

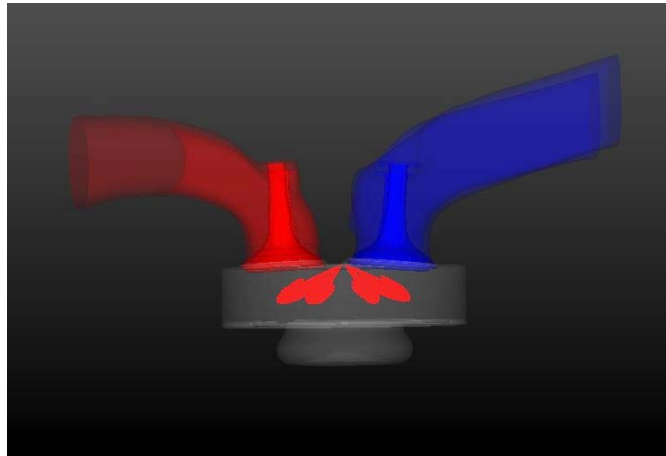
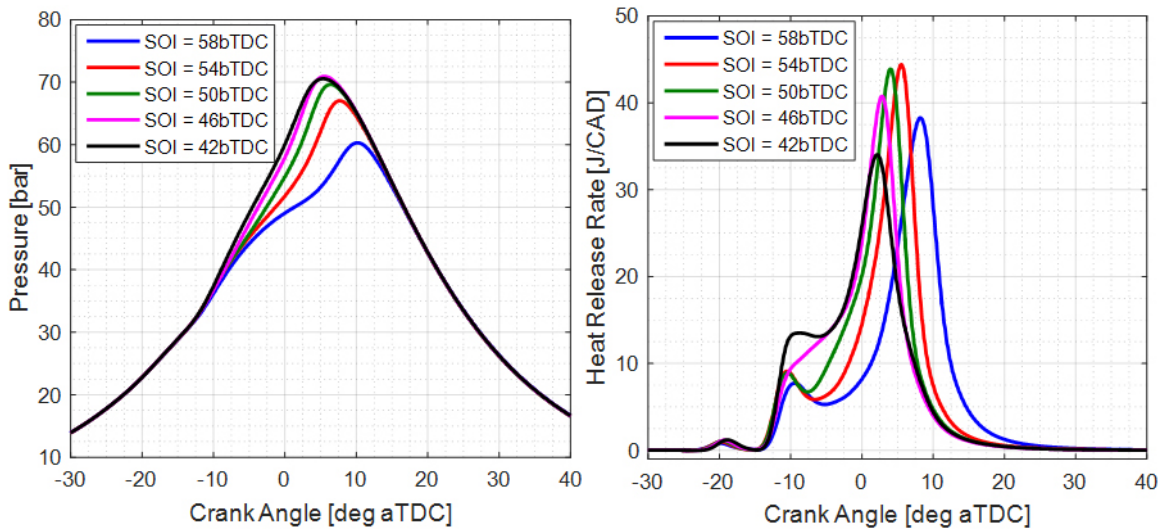


Figure III.2.4 - CONVERGE CFD model of the diesel Ricardo Hydra engine



aTDC – after top dead center; bTDC – before top dead center; CAD – crank angle degrees

Figure III.2.5 - CFD results of pressure and heat release rates of single-fuel RCCI using diesel as the parent fuel

Conclusions

In summary, the following accomplishments were made during the 2017 fiscal year.

- First, the reformate fuel mixtures produced by reforming gasoline, diesel, and natural gas were characterized by autoigniting the gaseous fuel mixtures in a CFR engine in HCCI combustion to determine an effective PRF number.

- Through these efforts, the PRF number separations were determined to be around 16 points for gasoline, 25 points for natural gas, and 113 points for diesel.
- Next, modifications were made to an existing single-cylinder, diesel, research engine to be able to test both conventional dual-fuel RCCI combustion, as well as RCCI using a parent fuel and its reformat.
- Then, system level models and a CFD model were constructed and validated against experimental data for both the CFR engine as well as the Ricardo Hydra engine.
- Finally, the CFD model was used to provide the first preliminary results of single-fuel RCCI with diesel as the parent fuel, showing successful RCCI combustion with controllable pressure rise rates, high efficiency, and low NO_x emissions.

References

1. Reitz, Rolf, and Ganesh Duraisamy., “Review of high efficiency and clean reactivity controlled compression ignition (RCCI) combustion in internal combustion engines.” *In Progress in Energy and Combustion Science*, Volume 46, 2015, Pages 12–71, ISSN 0360-1285, <https://doi.org/10.1016/j.pecs.2014.05.003>.
2. Kokjohn, Sage, Reed Hanson, Derek Splitter, and Rolf Reitz. “Fuel Reactivity Controlled Compression Ignition (RCCI): A Pathway to Controlled High-Efficiency Clean Combustion.” *International Journal of Engine Research*, Special Issue, Vol. 12, pp. 209–226, 2011.
3. Curran, Scott, Zhiming Gao, and Robert Wagner. “Reactivity Controlled Compression Ignition Drive Cycle Emissions and Fuel Economy Estimations Using Vehicle Systems Simulations with E30 and ULSD.” *SAE Int. J. Engines*, 2014.
4. Curran, Scott, Reed Hanson, Robert Wagner, and Rolf Reitz. “Efficiency and Emissions Mapping of RCCI in a Light-Duty Diesel Engine.” SAE Technical Paper 2013-01-0289, 2013.

Key Fiscal Year 2017 Publications

1. Yang, Ruinan, Hariharan, Deivanayagam, Mamalis, Sotirios, Lawler, Benjaimin, “Efficiency and Emissions Characteristics of an HCCI Engine Fueled by Primary Reference Fuels,” Submitted for review to the 2018 SAE World Congress.

III.3 High-Efficiency Cost-Optimized Spark-Ignited Natural Gas (HECO-SING) Engines – 2017

Alex Freitag, Principal Investigator

Robert Bosch LLC
38000 Hills Tech Dr.
Farmington Hills, MI, 48331
E-mail: steve.white@us.bosch.com

Kevin Stork, DOE Technology Manager

U.S. Department of Energy
Phone: (202) 586-8306
E-mail: Kevin.Stork@ee.doe.gov

Start Date: January 1, 2016	End Date: September 30, 2018	
Total Project Cost: \$2,292,934	DOE share: \$1,139,920	Non-DOE share: \$1,153,014

Acknowledgments

Co-Author

Steve White, Robert Bosch LLC

NETL Project Manager

Nicholas D'Amico, National Energy Technology Laboratory

Project Introduction

The abundance of relatively low cost natural gas in the North American market, along with energy independence, makes natural gas attractive as an alternate fuel. Natural gas also has an advantage over diesel engines in low NO_x emissions production. Natural gas does however have some technical challenges in its lower efficiency due spark ignited homogeneous combustion in comparison to diesel or gasoline, which is also a partial factor in its vehicle storage capacity limitations and thus driving range.

In order to address these challenges, the HECO-SING (High-Efficiency Cost-Optimized, Spark-Ignited Natural Gas) project was undertaken. The goal was to increase engine efficiency (fuel economy), while still meeting future emissions, in a cost-effective manner. In order to achieve these goals, high dilution combustion will be used with focus on advanced ignition systems, optimized aftertreatment selection, and creative engine controls are applied.

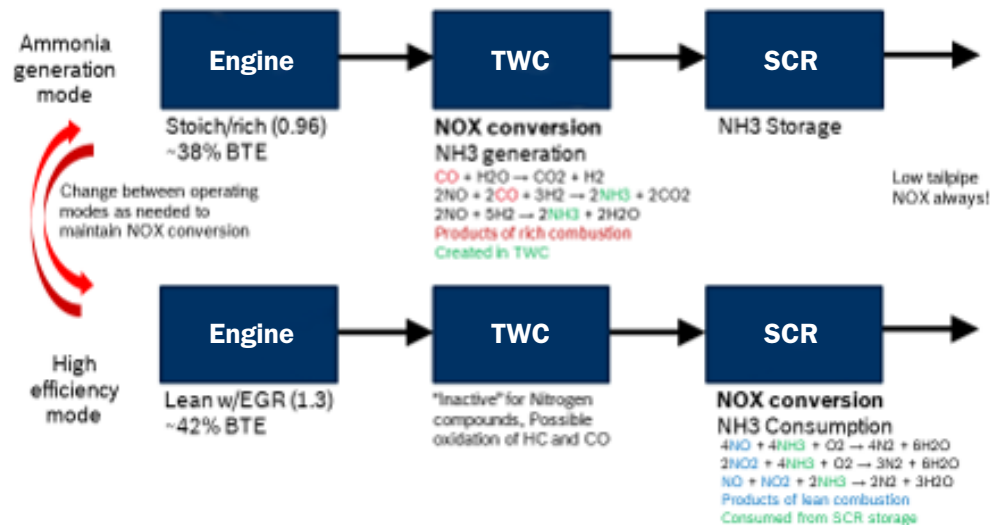
Objectives

- Develop and demonstrate a HECO-SING heavy-duty engine capable of approaching current near-diesel efficiency while achieving current Environmental Protection Agency emission regulations
- Increase engine efficiency through optimized dilution with both exhaust gas recirculation (EGR) and excess air
- Develop key enablers
 - Advanced ignition system for robust combustion with high dilution
 - Lean capable exhaust aftertreatment
 - Advanced engine and aftertreatment controls (passive selective catalytic reduction [SCR])
- Meet targets

- 2017 on-highway emissions
- Peak brake thermal efficiency >42%

Approach

In order to maintain the low cost objective for this project, a passive SCR approach was undertaken to reduce costs of the more expensive active SCR aftertreatment method. To achieve the passive SCR technique, a control strategy switching between a rich operating mode to generate NH_3 (ammonia) in the exhaust system through the three-way catalyst (TWC) rather than a complex and costly Diesel Exhaust Fluid (urea) dosing, and lean operation to increase engine operating efficiency (lower fuel consumption), was pursued. Optimum balancing of operation in the different operating modes to achieve increased efficiency while maintaining low emissions is the objective. See Figure III.3.1 for an illustration of the operating mode functions.



BTE – brake thermal efficiency; HC – hydrocarbon

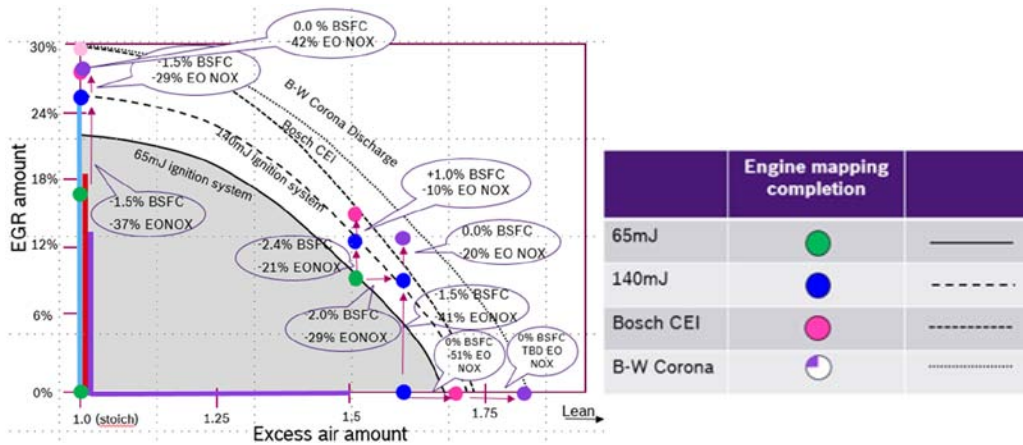
Figure III.3.1 - Passive SCR concept. Ammonia generation mode is created by running stoichiometric or nominally 5–6% rich, generating ammonia across the TWC, which is stored in the SCR. In high efficiency mode, lean operation is performed and the NO_x created in this mode is broken down by the stored ammonia.

To achieve the highest efficiency, utilizing advanced ignition systems which could extend the dilution limit boundary was investigated. Figure III.3.2 shows the comparison of different ignition systems capabilities. The ammonia generation mechanism to decompose the NO_x created while operating in the lean mode will be developed through exhaust gas simulation. EGR is utilized to minimize NO_x while assisting in combustion stability to further expand the combustion dilution operating range. The balance of all parameters and operating conditions for best overall operations to meet project goals is paramount.

In order to focus on the key areas of advanced ignition systems and aftertreatment selection and sizing, the University of Michigan (UM) and the Pacific Northwest National Laboratory (PNNL) joined with Bosch in the project. UM's concentration was in the area of researching and selective advanced ignition systems that may benefit operation in high dilute conditions, and to develop methods to quantify performance differences between the systems. PNNL's role was to select and characterize exhaust catalysts, and develop simulation models based on said characterizations, in order to allow Bosch to perform catalyst sizing and control strategies.

Results

The focus during this period was on developing the optical measurement capability for in-cylinder measurements to provide quantification of differences between the advanced ignition systems. Figures III.3.3 and III.3.4 illustrate the optical probe placement in the cylinder head, while Figure III.3.5 illustrates additional modifications required on the piston crown to provide the view of the combustion. Due to the modification made, concerns to the impact on the combustion process required verification of no resulting impact (Figure III.3.6).



BSFC – brake specific fuel consumption; TBD – to be determined; EO – engine out; CEI – controlled electronic ignition; B-W – BorgWarner

Figure III.3.2 - High dilution concepts results



Figure III.3.3 - Camera arrangement for optical in-cylinder measurement. Two optical probes were positioned toward the spark plug for viewing of ignition point and flame propagation. Cylinder #6 (rear cylinder) was used for instrumentation access. Top view. (Figure source: Bosch)

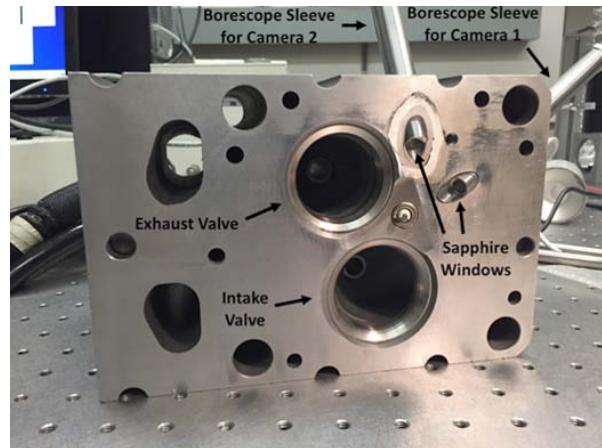


Figure III.3.4 - Two optical probes are positioned toward spark plug for viewing of ignition point and flame propagation. The cylinder #6 (rear cylinder) is used for instrumentation access. Combustion pressure probe is positioned between the two optical probes. Combustion chamber view. (Figure source: Bosch)

To provide usable image data that could later be quantified between systems, UM developed a multi-step processing technique illustrated in Figure III.3.7. As an example to demonstrate combustion differences between operating conditions to validate the effectiveness of the image processing, a sequence of the combustion progress between low dilute and high dilute conditions is demonstrated in Figure III.3.8.

In addition to the significant imaging work performed, quantifying the performance benefits was performed by running the steady state engine map data points through a Bosch developed medium-duty/heavy-duty drive cycle simulation process. Two drive cycles were selected over the range of potential cycles that were expected to match more closely in the operating range to areas of the map that the HECO-SING concept demonstrated as the best results. Each advanced ignition system was run through these two simulation cycles and results were compared to the baseline and summarized in Table III.3.1.

Once the aftertreatment system modelling has been completed and a catalyst sizing determined, the simulation process will be rerun. The system assessment process is summarized in Figure III.3.9.

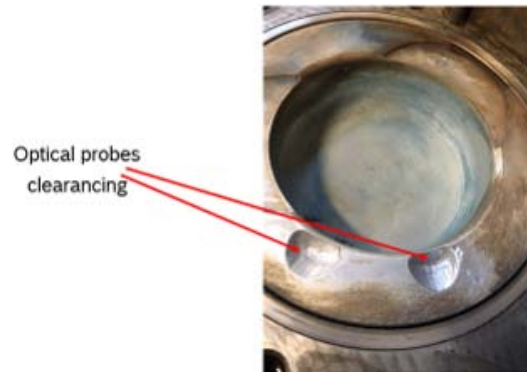


Figure III.3.5 - Clearancing of piston crown is required for optical probe protrusion into the combustion chamber and for obtaining field of view for ignition and combustion. Concerns were that modification may have affected the instrumented cylinder's effective compression ratio. As a means to quantify any impact, the combustion properties before and after the modification were compared. Results of the comparison are shown in Figure III.3.6. (Figure source: Bosch)

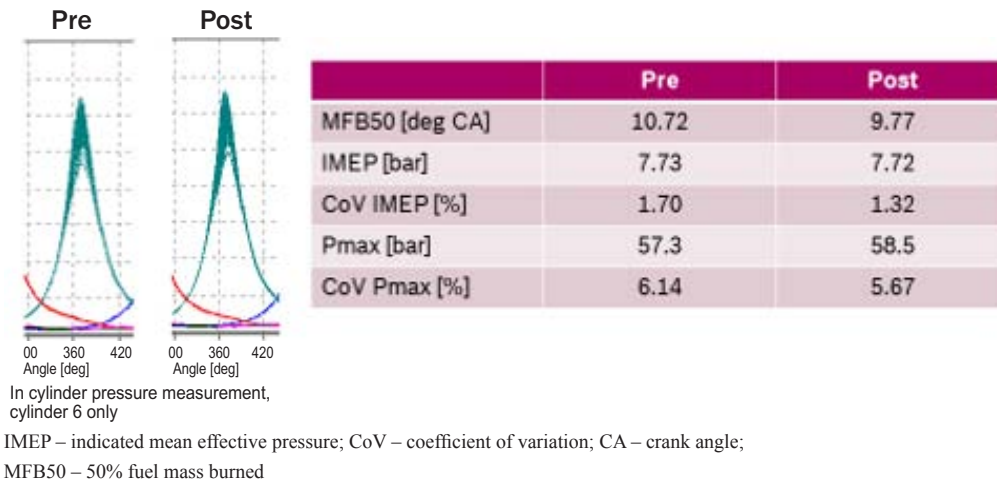


Figure III.3.6 - Verification of combustion. Comparison of combustion parameters prior to and after combustion chamber modifications indicates post modification performance equivalent to normal cycle-to-cycle variation of the pre-modification results.

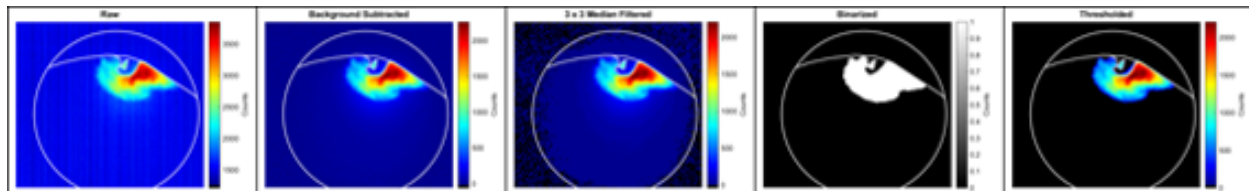


Figure III.3.7 - Image processing progression: → Raw → Background Subtracted → Median Filtered → Binarized → Threshold

Due to the results to date, while directionally indicating that each successive advanced ignition system can push the boundary limit of dilution operation further out, the results were significantly less than anticipated. This made it appropriate to rescope the project, and reduce the effort and magnitude of the project accordingly, and was approved by the DOE project management team (Figure III.3.10).

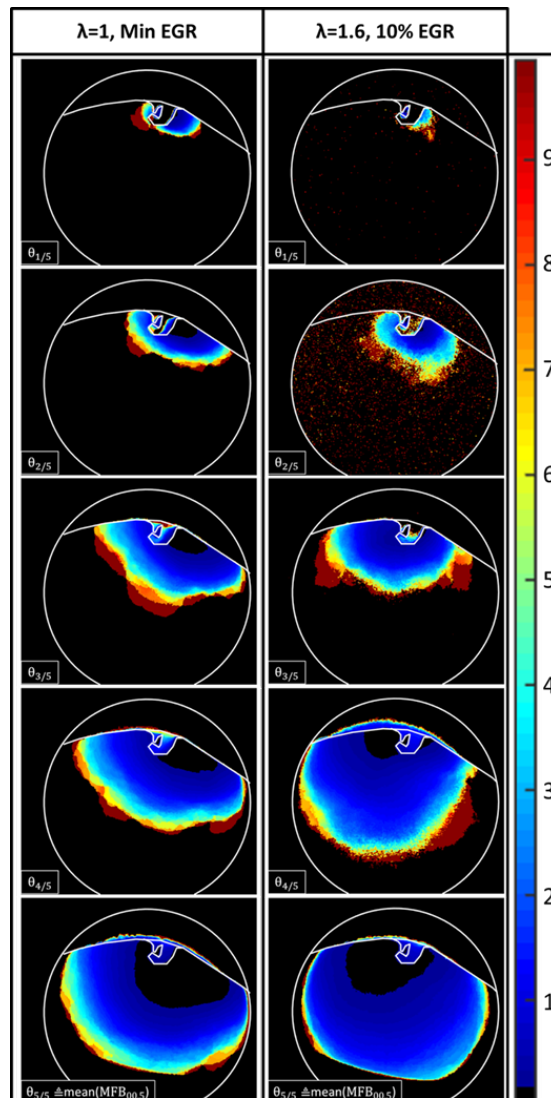


Figure III.3.8 - CoV images for five crank angles for two operating conditions. Left: 1,000 rpm, 6.8 bar IMEP, $\lambda = 1.0$, minimum (3%) EGR, $CoV_{IMEP} = 0.32\%$. Right: 1,000 rpm, 6.8 bar IMEP, $\lambda = 1.6$, 10% EGR, $CoV_{IMEP} = 1.60\%$.

Table III.3.1 - Drive Cycle Simulation Results

	Diesel*	Stoich EGR	Lean (NOx non-compliant)	Lean EGR passive SCR 65mJ ign	Lean EGR passive SCR 140mJ ign	Lean EGR passive SCR Bosch CEI	Lean EGR passive SCR B-W corona ign
UDDS Regional	5.8 MPG	5.28 MPG DGE	5.99 MPG DGE	5.34 MPG DGE	5.37 MPG DGE	5.35 MPG DGE	
vs Stoich		-	11.9%	1.2%	1.8%	1.4%	
vs Diesel	-	-9.0%	3.1%	-7.9%	-7.4%	-7.8%	
M-D Refuse Vocational	2.8 MPG	2.64 MPG DGE	2.93 MPG DGE	2.66 MPG DGE	2.71 MPG DGE	2.69 MPG DGE	
vs Stoich		-	9.9%	1.1%	2.5%	2.1%	
vs Diesel	-	-5.7%	4.6%	-5.0%	-3.2%	-3.9%	

*www.afdc.energy.gov/data/

UDDS – Urban Dynamometer Driving Schedule; DGE – diesel gallon equivalent; M-D – medium-duty

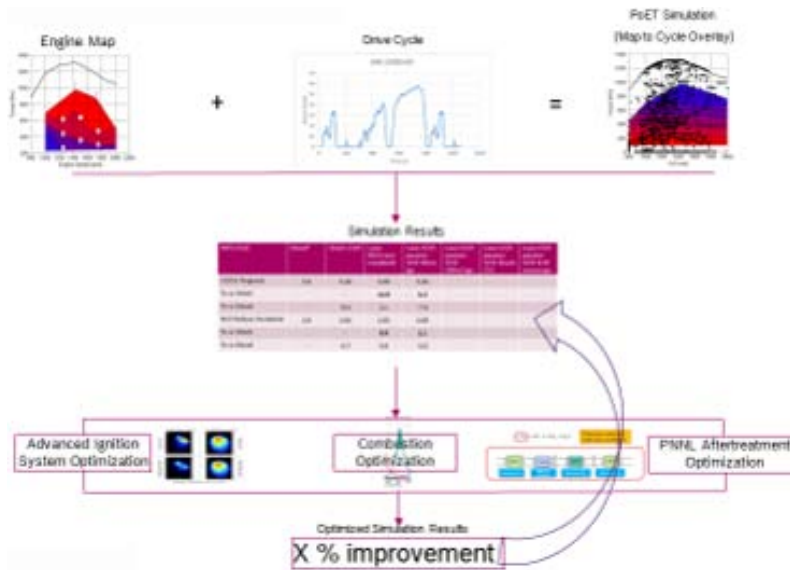
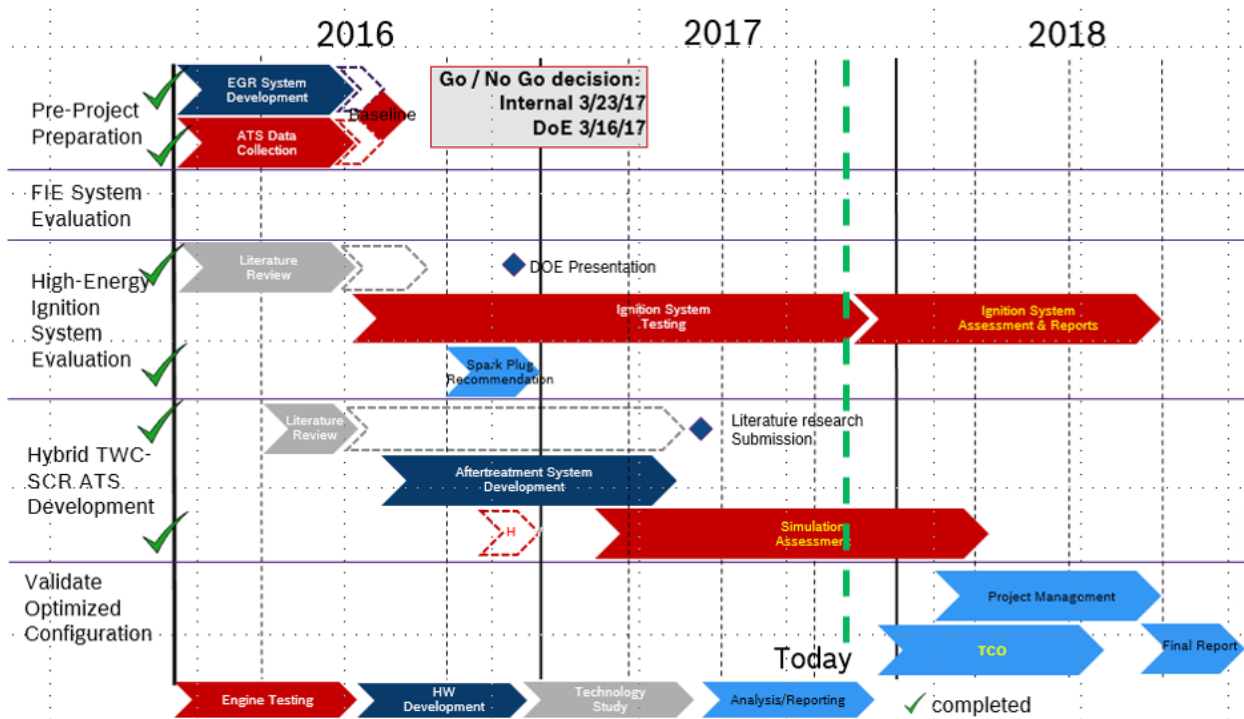


Figure III.3.9 - Process used to assess each system’s projected results over various drive cycles. Assessment of each system will be performed by a combination of simulation and actual test results. Engine map test data will be uploaded into a Bosch developed CV drive cycle program (PoET) to determine fuel efficiency and emissions projections. A scatter plot of drive data points over an engine map provides an indication of magnitude of time the vehicle operates in the improved region of the engine map on the selected drive cycle. Various drive cycles will be assessed to find applications where the HECO-SING might provide the best business case.



ATS - aftertreatment system

Figure III.3.10 - Current (rescoped) milestone

Conclusions

Use of advanced ignition systems have verified that the dilution limit of both combined enleanment and high EGR rate can be extended. Significant reduction in engine out NO_x can be achieved. However only minimal improvements in efficiency (BSFC) were obtained. It is speculated that at this high levels of EGR, that the air path is actually limiting gains in efficiency, due to the high levels of boost needed to provide the “push” for the high EGR flow rates. A complete engineering redesign would be required to both provide the higher EGR flow rates, but without the wastegate size limiting the boost needed, which is out of scope for this project.

Key Fiscal Year 2017 Publications

1. “Infrared Borescopic Analysis of Natural-Gas Ignition and Combustion Variability.” SAE paper.
2. “Infrared Borescopic Evaluation of High-Energy and Long-Duration Ignition Systems for Lean/Dilute Combustion in Heavy-Duty Natural-Gas Engines.” SAE paper.
3. Q1 DOE Quarterly Report. April 28, 2017.
4. Q2 DOE Quarterly Report. July 27, 2017.
5. Q3 DOE Quarterly Report. October 30, 2017.
6. DOE Annual Merit Review report and presentation. June 8, 2017.
7. University of Michigan provided a poster presentation on their efforts to date at the NSERC CREATE Combustion Summer School in Toronto during the week of May 21, 2017.
8. University of Michigan provided a poster presentation on their efforts to date at the Princeton-Combustion Institute Summer School on Combustion at the University of Princeton during the week if June 25, 2017.
9. University of Michigan provided an oral presentation on their efforts as a subset of their Optical Diagnostics for Engines talk at the Gordon Research Conference in Vermont on August 8, 2017.

III.4 Innovative Dual-Fuel Aftermarket Emissions Solution

Richard K. Whitaker, Principal Investigator

NG1 Technologies
9233 Park Meadows Drive
Lone Tree, CO 80124
E-mail: rwhitaker@ng1techflo.com

Michael Ippoliti, Principal Investigator

CALSTART
48 S. Chester Ave.
Pasadena, CA 91106
E-mail: mippoliti@calstart.org

Michael Weismiller, DOE Technology Manager

U.S. Department of Energy
E-mail: Michael.Weismiller@ee.doe.gov

Start Date: October 1, 2016	End Date: March 30, 2019	
Total Project Cost: \$1,278,911	DOE share: \$990,871	Non-DOE share: \$288,040

Project Introduction

The intent of this project is to develop an advanced emission control system for Class 7 and 8 heavy-duty dual-fuel vehicles that eliminates or mitigates the negative effects of currently used diesel particulate filter and selective catalytic reduction emissions treatment systems. The project will combine multiple technologies, two exhaust system technologies plus hydrogen injection, working together to increase engine efficiency and reduce most emissions directly within the cylinder.

Objectives

- Successfully test the 2012 Mack MP7 United Parcel Service (UPS) stock truck's original equipment manufacturer (OEM) exhaust aftertreatment. The test will consist of a chassis dynamometer test followed by fuel cycle testing on a vehicle test track. Both fuel and emissions were captured during the baseline stock test event (Task 1 and Task 1.1).
- Continue operating multiple vehicles equipped with the TechFlo exhaust combined with the BoostBox hydrogen catalyst for the testing of fuel and emissions (Task 1.3). The data generated from the stock equipment and aftermarket components were collected using vehicle analytics along with manual documented processes used in a comparative analysis (Milestone 1.1.1 and 1.3.1), in seeking vehicle performance improvements in fuel economy and emissions reductions.
- Perform SAE J1264 fuel test.
- Confirm a project start date for the vehicle testing at Mesilla Valley Transportation. The test date is scheduled for October 23, 2017 (Task 1 and Task 1.1).
- Complete three-dimensional computer-aided drawing modeling by the Vaztec project team for final design intent along with constructed diesel fuel injection and delivery system. The product development of a test fixture and verified test equipment in initiating serial production parts.
- Compile the data for formal reporting of all fuel and emissions performance improvements into a statistical report (Milestones 1.1.1 and 1.3.1).

Approach

The NG1 project team traveled to Pennsylvania State University to perform chassis dynamometer and track testing of a 2012 Mack MP7 UPS stock-equipped project truck donated by UPS. Institutional validated baseline stock data were generated using vehicle analytics, chassis dynamometer, and fuel cycle testing on a vehicle test track. Both fuel and emissions data were captured during the baseline stock test event (Task 1 and Task 1.1).

The NG1 project team traveled to Mesilla Valley Transportation to review the testing facilities and schedule an event that included a chassis dynamometer and an over the road test track for the 2014 Mack LNG Cummins UPS project truck (Task 1 and Task 1.1).

Multiple stock-exhaust-equipped vehicles were tested (Task 1 and Task 1.1) using the same city route and over the road method of traveling the same distance to and from a predetermined location every day for 12 mo. The NG1 project team performed initial tests during September 2016 and October 2016 prior to joining the BoostBox H2 project team. The TechFlo exhaust and the BoostBox H2 hydrogen catalyst components were combined starting on November 5, 2016, and continued through September 30, 2017. The data generated from the aftermarket exhaust testing were collected using vehicle analytics along with manual documented processes with the OEM. Aftermarket exhaust data was collected to be used in a comparative analysis (Milestones 1.1.1 and 1.3.1), in seeking vehicle performance improvements in fuel economy and emissions reductions. An additional goal is for VazTec to develop the engine system architecture for torque, horsepower, emissions, and fuel efficiency in meeting vehicle performance targets (Task 2.3 and Milestone 2.3.1).

The TechFlo exhaust system was tested using SAE J1264 on April 29, 2017, by Shay Express in Jonesboro, Arkansas. The stock muffler was used in generating a baseline for comparative analysis against the performance of the NG1 TechFlo system to determine the effects on fuel consumption rate. The test event was conducted in Memphis, Tennessee, using a repeatable route. The testing used a 2007 Freightliner Columbia equipped with a 12.7-L Detroit Diesel 60 series engine with Eaton 10-speed transmission. The test was conducted over a two-month period starting on April 29, 2017, and ending on June 30, 2017. The fuel test was divided into separate categories, Phase I and Phase II, to seek consistency and repeatability in the test results. The test results from week of June 3, 2017–June 9, 2017, were redacted as the test vehicle experienced mechanical failure leading to inconclusive results. The test that was vacated in June was administered at the completion of the Phase II stock test cycle beginning the week of August 5, 2017–August 11, 2017. The test activities included the use of one 2007 Freightliner Columbia heavy-duty truck with the same driver being used for the duration of the test event. The following test sequence and methods were followed. The stock exhaust was tested for one month and the NG1 TechFlo exhaust was tested for one month with two weeks on for the stock equipment and two weeks off using the NG1 TechFlo exhaust, reversing the method of testing for the second month. The reserved method of testing was employed to demonstrate consistency in the results regardless of the sequence of events. The test unit was driven approximately 301 mi/d on representative pick-up and delivery routes in Memphis, Tennessee.

The project team was fortunate to have a partner in Memphis, Tennessee that allowed us to collect data for over the past year on the performance of the NG1 TechFlo exhaust and Boost Box H2 system. While these vehicles are not directly part of the grant testing with the UPS system, we gained an incredible amount of information from this deployment. The data collected was based on the actual payment system from one of the largest transportation fleets in the world. The data we compiled were provided weekly from a third party to the fleet owner and was the basis of how the fleet owner was paid; that is, absolutely accurate and verifiable data in the form of fuel sheets generated each day for billing purposes. This information allowed us to complete grant Task 1, Task 1.1, and Milestone 1.1.1. Additionally, with the purchase of a five-gas analyzer on April 1, 2016, we started collecting emissions data on this same fleet towards the completion of Task 1.3 and Milestone 1.3.1.

Results

The NG1 Technologies project team traveled to Pennsylvania State University's Larson Transportation Institute on July 13–14, 2017, to participate in the UPS stock emissions testing. The test vehicle was a 2012 Mack MP7 UPS stock equipped with manual transmission. The two-day testing event was comprised of vehicle set-up and chassis dynamometer testing to measure fuel consumption and emissions (Task 1 and Task 1.1).

NG1 Technologies traveled to Larson Transportation Institute on July 27–28, 2017, to participate in the UPS stock fuel testing. The test vehicle was a 2012 Mack MP7 UPS stock equipped with manual transmission. The two-day testing event comprised of vehicle set-up and chassis dynamometer testing measuring fuel consumption and emissions along with cycle testing on the vehicle test track (Task 1 and Task 1.1).

The NG1 Technologies project team traveled to Larson Transportation Institute on October 4–6, 2017, to participate in the UPS stock fuel testing. The test vehicle was a 2014 Mack LNG Cummins UPS stock equipped with manual transmission. The two-day testing event comprised of vehicle set-up and cycle testing on the vehicle test track for measuring fuel consumption and emissions (Task 1 and Task 1.1). We observed consistency in the fuel economy data from the SAE J1264 test performed when compared to the previous reporting period using both the NG1 TechFlo exhaust (Milestone 1.1.1) and the combined use of the TechFlo and BoostBox (Milestone 1.3.1) when compared to stock. We observed an increase in fuel economy using the TechFlo exhaust on Class 8 vehicles performing city and over the road routes (Milestone 1.1.1). The combining of the NG1 TechFlo exhaust and BoostBox hydrogen catalyst technologies provided a greater than 10% improvement in fuel economy (Milestone 1.3.1) when compared to the individual component data and overall OEM stock-equipped vehicle. In establishing consistency and repeatability in data results, additional vehicle testing will be required for validation and verification purposes. The city route and over the road methods used for vehicle testing did not encounter any obstacles that would elevate risk during the period of stock and aftermarket exhaust comparative testing. The city route and over the road vehicle testing will continue into October 2017 with vehicle performance improvements presented in the next Quarterly Project Summary Report.

NG1 Technologies traveled to Mesilla Valley Transportation on August 1–3, 2017, to participate in a facility evaluation and contract discussions for scheduling a second round of stock-equipped chassis dynamometer and vehicle test track testing of the 2014 Mack LNG Cummins UPS project truck (Task 1 and Task 1.1).

Chassis dynamometer vehicle testing of the 2014 Mack LNG Cummins UPS project truck took place on September 27, 2017. Testing consisted of chassis dynamometer and vehicle test track testing measuring fuel economy and emissions on a stock-equipped Class 8 heavy-duty truck. The test track fuel testing was completed on October 6, 2017 (Task 1 and Task 1.1).

Chassis dynamometer and vehicle test track testing for the 2014 Mack LNG Cummins UPS project truck began October 23, 2017, and will continue for approximately six weeks. The six weeks of testing will be comprised of vehicle set up, chassis dynamometer, and 5,000+ miles of over the road track testing measuring fuel consumption and emissions along with using cycle testing on vehicle test tracks (Task 1 and Task 1.1).

NG1 Technologies and BoostBox H2 project teams have compiled a statistical data report of all fuel and emissions performance improvements experienced from September 1, 2016–September 30, 2017. The data were derived from operating five Class 8 heavy-duty trucks equipped with the TechFlo exhaust combined with the BoostBox hydrogen catalyst for the testing of fuel economy and emissions (Task 1.3) using a city route and over the road methods of traveling the same distance to and from a predetermined location every day for the past 12 months. Fuel and emissions data continues to be collected and imported in the statistical report. The project team will continue collection activities of baseline data and fuel consumption (Task 1 and Task 1.1) along with the collection of emissions data (Task 1.3) and continue to analyze the data (Milestones 1.1.1 and 1.3.1). The project team will continue to monitor fuel savings on multiple Class 8 heavy-duty trucks equipped with the BoostBox H2 and NG1 systems which have been running for a year without any mechanical failures. We have collected almost 10,000 data points across multiple vehicles which were compiled into Excel format for statistical analysis and charting. Initial data shows that the TechFlo improves fuel efficiency over a stock vehicle and the combination of the TechFlo and BoostBox H2 further improves fuel efficiency over a stock vehicle. This appears to be consistent with the full year of data.

The NG1 project team successfully completed an SAE J1264 fuel test. The testing was completed on August 7, 2017. The fuel economy test consisted of a single Class 8 vehicle equipped with the TechFlo exhaust (Task 1.3). The testing duration was a two-month period, June–August 2017. The fuel test was performed over repeatable city routes as a method of measuring vehicle performance. The data generated from the stock exhaust and aftermarket exhaust components were collected using vehicle analytics along with manually

documented processes used in a comparative analysis (Milestone 1.1.1 and 1.3.1) in seeking vehicle performance improvements in fuel economy and emissions reductions. The SAE test resulted in a 16.3% fuel economy improvement with the use of the aftermarket emissions equipment.

Vaztec performed three-dimensional computer-aided modeling, completing the final design intent along with constructing the diesel fuel injection and delivery system. Vaztec also developed a test fixture and verified test equipment for the initial serial production of parts (Task 2.5) and identified natural gas system requirements including storage, delivery, and injection (Task 2.6).

The NG1 team successfully completed Phase 1A of the fuel and emissions testing at Pennsylvania State University's Larson Transportation Institute. The test consisted of performing both chassis dynamometer and test track activities with the use of a 2012 Mack MP7 stock-equipped unit donated by UPS (Task 1 and Task 1.1).

Conclusions

The project team has proven the technology on a fleet in one of the harshest applications possible. The Memphis area is home to a large fleet and some of the worst roads in the country. The NG1 system was installed on two vehicles, one that was primarily line haul (250+ miles point-to-point) and one that was pickup and delivery (typically less than 20 miles between points). We installed shock monitors on our boxes to see just what our systems were experiencing, and very unexpectedly, we regularly were seeing system shocks over 20 g (20 times the force of gravity). The largest shock was at 37 g. Even in these conditions, our system survived the application and functioned for the full first year of testing. A master technician in the Memphis area stated that unlike most common failures of Class 8 trucks (turbos, alternators, etc.) cracked front springs, axle damage, and other violent impact issues from driving in the Memphis area were the most common causes for repair. We have been pleasantly pleased with the durability of our system under these conditions.

The project has thus far proven consistency in fuel economy data collected over the past 12 months while using the NG1 TechFlo (Milestone 1.1.1) and the use of the combined NG1 TechFlow and BoostBox H2 technologies (Milestone 1.3.1). We observed an average of 10% improvement in fuel economy using the TechFlo exhaust on Class 8 vehicles performing city routes (Milestone 1.1.1) and a 10% improvement in fuel economy using the combined NG1 TechFlo and BoostBox (Milestone 1.3.1), when compared to the OEM stock solution.

III.5 Utilizing Alternative Fuel Ignition Properties to Improve SI and CI Engine Efficiency

Margaret Wooldridge, Principal Investigator

University of Michigan
 Department of Mechanical Engineering
 2350 Hayward Street
 Ann Arbor, MI 48109
 E-mail: mswool@umich.edu

Kevin Stork, DOE Technology Manager

U.S. Department of Energy
 E-mail: Kevin.Stork@ee.doe.gov

Start Date: September 1, 2015 End Date: September 30, 2017
 Total Project Cost: \$1,114,024 DOE share: \$874,024 Non-DOE share: \$240,000

Acknowledgments

Co-Authors

André Boehman, George Lavoie, Robert Middleton; University of Michigan
 Mohammad Fatouraie, Bosch, LLC

Project Introduction

Downsized boosted spark ignition (SI) engines offer considerable thermal efficiency benefits compared with naturally aspirated gasoline SI engines [1,2], and ethanol offers even further fuel economy benefits [3]. However, turbocharging SI engines increases the risk of knock (normal pre-ignition) and super-knock (more infrequent, more intense, and particularly damaging ignition) in these engines. Ethanol is well known to have knock-suppressing properties compared with gasoline, including high heat of vaporization (which is not fully captured in current octane rating methods). What is currently missing is an engineering-based recommendation for the optimal blend ratio of ethanol to gasoline and strategies which leverage the intrinsic properties of ethanol to improve engine fuel economy, and a comprehensive means of mitigating (rather than simply avoiding) spark knock. In addition, ad hoc levels of 10% and 85% ethanol have not leveraged the valuable characteristics of ethanol. Achieving the DOE goal of 45% peak thermal efficiency for light-duty engines will require additional boosting and higher compression ratios, as well as strategies to mitigate knock at these high compression ratios, including stratification and the use of exhaust gas residuals (EGR). The objective of this work is to develop fuel injection and spark strategies which leverage the thermophysical properties of ethanol and other fuel supplements and EGR to maximize engine efficiencies.

Objectives

- Demonstrate the combination of fuel selection, fuel injection strategy, and mixture preparation that enables meeting the DOE targets for brake thermal efficiency of greater than 40% for SI engines and greater than 50% for compression ignition (CI) engines
- Develop ignition and fuel spray correlations that can be used to guide injection and spark timing strategies and can be used in the engine simulations
- Evaluate the impact of knock and flame limits of alternate fuels and combustion strategies on engine efficiency
- Develop spray and spark timing strategies for different fuel compositions and EGR blends that quantify sensitivity to extending knock limits and enabling higher engine efficiencies

- Demonstrate spray and spark timing strategies from single-cylinder engine studies on multi-cylinder engine; to assess impact of multiple injection pulses on the knock mitigation and the particulate matter emissions for different fuel blends with production and production-intent hardware

Approach

A combination of experimental and modeling methods was used in the project to identify strategies to achieve 45% thermal efficiency. Single- and multi-cylinder engine facilities were used to quantify the effects of fuel blends and fuel strategies, and modeling efforts were used to interpret and extrapolate the experimentally observed trends. Two single-cylinder engine platforms were used to study fuel blends using production engine hardware and using experimental hardware. The experimental engine hardware (based on a Hydra engine) was used to study the effects of EGR to mitigate knock and comparison with syngas (H₂ and CO) addition to offset stability issues that occur with high dilution. The production single-cylinder engine hardware (a Ford Fox engine where two of the three cylinders were deactivated) was used to study the effects of varying levels of ethanol in ethanol–gasoline blends at a range of intake air pressures. The lessons learned from the fuel composition and fueling strategies were applied to multi-cylinder engine studies. In-kind support by Bosch was directed toward the single-cylinder and multi-cylinder engine studies.

Results

The work in the past year has predominantly focused on completing the multi-cylinder gasoline turbocharged direct injection engine studies and the single-cylinder Hydra engine studies. The multi-cylinder engine work focused on quantifying the effects of multiple fuel injection strategies on engine performance in terms of thermal efficiency, particulate emissions, and regulated engine-out emissions. A large matrix of experimental conditions were considered and evaluated. Table III.5.1 shows an example of the range of operating parameters tested.

Table III.5.1 - Conditions Tested to Explore the Effects of Multiple Fuel Injection Events and Fuel Blends on Engine Performance

Fuel Blend Tested [Ethanol %]	E0	E30	E85				
Intake pressure [mbar]	800	900	1000	1200			
Number of Injections	1	2	3	4			
Corresponding fuel split	NA	1:1	1:1:1	1:1:1:1			
Start of Injection (SOI1) [dbTDC]	300	280	260	240	220	200	180
Pause/dwell time [CAD]	21	31.5	42	52.5	63		

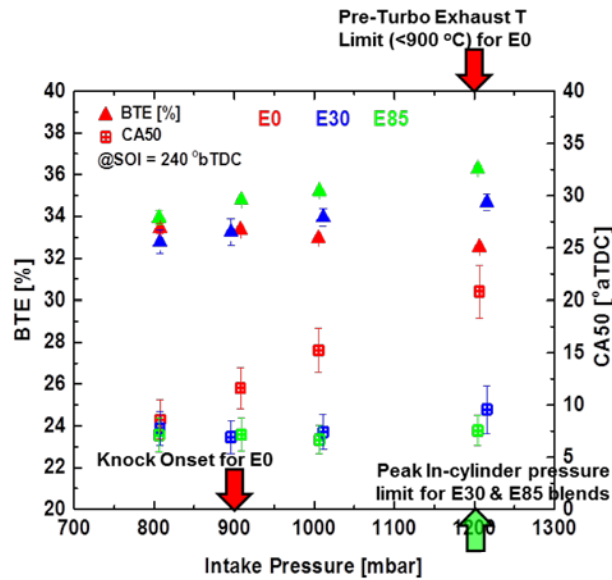
E0 – 0% ethanol, 100% gasoline blend; E30 – 30% ethanol, 70% gasoline blend; E85 – 85% ethanol, 15% gasoline blend

NA – not applicable; dbTDC – degrees before top dead center; CAD – crank angle degrees

For comparison, the production engine calibration settings were for five fuel injection events with 70% of the fuel mass injected during intake and progressively reducing fuel mass in each injection. The pause time was kept constant between each injection for this study.

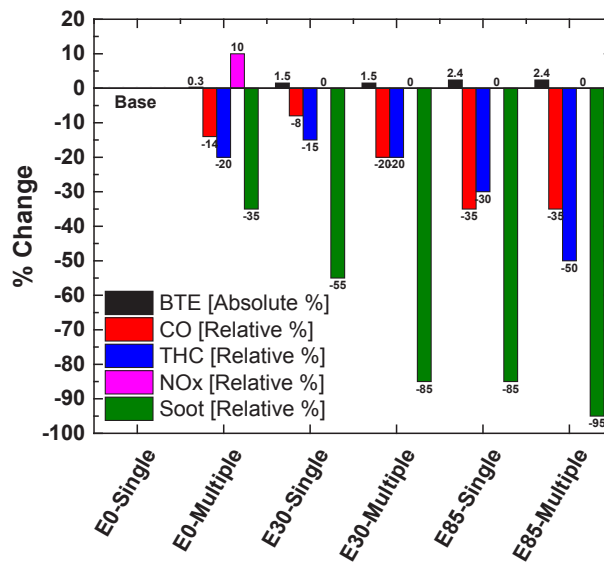
Typical results for the brake thermal efficiency (BTE) are presented in Figure III.5.1. All three fuel blends behave similarly with respect to changes in the SOI for non-knocking conditions. The BTE decreased and engine stability increased with later injection timing. Boosting the air intake pressure required retarded spark timing for E0 above 800 mbar due to knock, and an absolute BTE improvement of 3% was observed for E85 compared with E0. The ethanol blends were never knock-limited. Instead component protection limited realizing additional thermal efficiency benefits for the higher ethanol blends, as noted in Figure III.5.1. Figure III.5.2 summarizes the studies of multiple fuel injection strategies on the engine efficiency and emissions.

The work with the Hydra over the past year continued to explore the impact of EGR and air dilution with simulated reformat (as syngas) for extension of knock limits and increase of engine thermal efficiency. Figure III.5.3 shows the extent of thermal efficiency improvements reached with the port fuel injection injector



CA50 – crank angle at 50% mass fraction burned; °aTDC – degrees after top dead center

Figure III.5.1 - Sensitivity of BTE to multiple fuel injection events for different ethanol and gasoline (E0) blends



THC – total hydrocarbons

Figure III.5.2 - Summary of the benefits of ethanol blends on direct injection engine performance

alone. This work will expand to consider multi-shot direct injection in addition to port fuel injection fueling as well as EGR and syngas addition.

The work with the Hydra also expanded this year to consider various alternative fuels, to complete the ongoing studies with ethanol, and to consider particle size distribution and number emissions when using various alternative fuels. Figure III.5.4 shows particle size distribution comparisons for intake pressure of 1.4 bar condition with gasoline and 20% blends with ethanol, iso-butanol, and dimethyl furan (E20/IB20/DMF20), for comparison. The total particle number varied in the order: gasoline >> IB20 ≈ DMF20 > E20 under knock limited conditions.

Constant volume ignition delay and variable pressure reactor simulations to estimate knock limited load were conducted for the same conditions previously reported using an additional kinetic mechanism for gasoline. Predictions using the surrogate mechanism of Cai and Pitsch [4] showed a reduction in knock-limited load

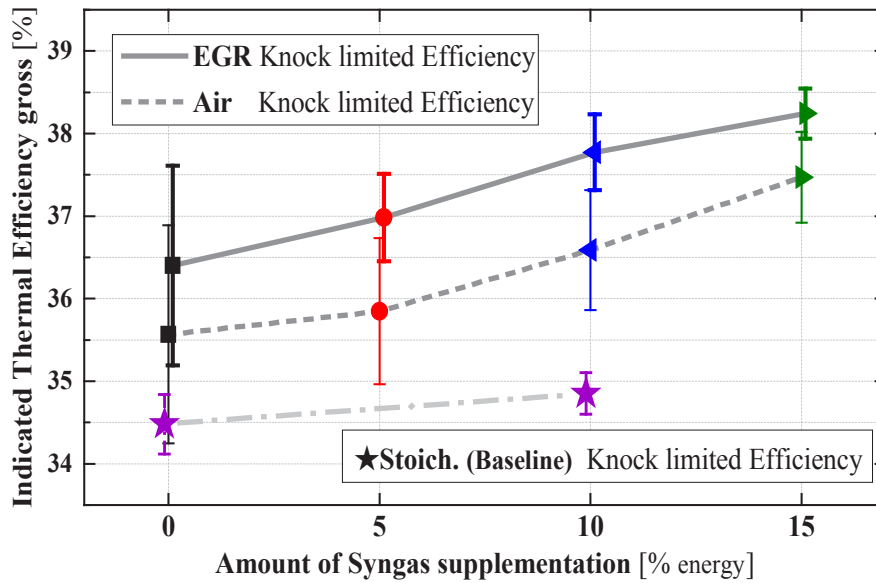


Figure III.5.3 - Indicated thermal efficiency for air and EGR dilution versus syngas supplementation

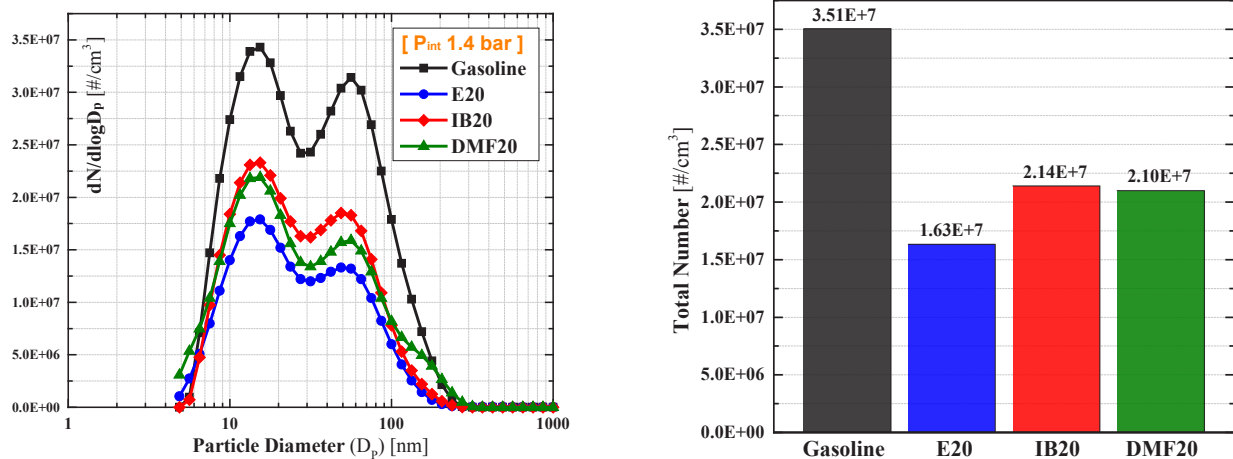


Figure III.5.4 - Particle size distributions and total number emission for gasoline, and 20% blends of ethanol, isobutanol and dimethyl furan

relative to previous results using the surrogate mechanism of Mehl et al. [5]. These results highlight the sensitivity of knock predictions to the choice of kinetic mechanism and fuel surrogate.

Conclusions

- With the Hydra single-cylinder engine, experiments with syngas supplementation under EGR dilution and air dilution demonstrated that syngas addition efficiently mitigates engine knock under both boosted and diluted conditions. In addition, supplementing syngas is more beneficial under EGR dilution than under air dilution, from the perspective of not only knock mitigation but also thermal efficiency and emissions of oxides of nitrogen.
- Both the Fox single-cylinder and the gasoline turbocharged direct injection multi-cylinder engine experiments with ethanol yielded a major improvement in terms of expanding the range of maximum brake torque operation of the engine. However, there were diminishing returns to increasing the ethanol content beyond a threshold value in the blend if knock does not constrain engine operation.

- Modeling studies of gasoline–ethanol fuel blends provided insight into the impact of fuel effects on engine efficiency. GT-POWER simulations showed half the gross thermal efficiency gain from ethanol over gasoline that was noted experimentally was due to the heat of vaporization accounting, while the other half was due to charge cooling and decreased burned gas temperatures. Variable pressure reactor simulations qualitatively replicated the experimental increase in knock-limited load for increasing ethanol fuels, while the quantitative knock limited load is sensitive to the choice of kinetic model.
- Multiple injection strategies lowered CO and THC emissions and improved thermal efficiency for increased stratified conditions. Further, multiple injection strategies which varied fuel mass further improved gas emissions and particulate emissions with similar thermal efficiency to other fuel injection strategies.

References

1. Richard, S., G. Font, F. Le Berr, O. Grasset, and M. Fremovici. “On the use of system simulation to explore the potential of innovative combustion systems: methodology and application to highly downsized SI engines running with ethanol-gasoline blends.” SAE Technical Paper No. 2011-01-04, 2011.
2. Lavoie, G., E. Ortiz-Soto, A. Babajimopoulos, J.B. Martz, and D.N. Assanis. “Thermodynamic sweet spot of high-efficiency, dilute, boosted gasoline engines.” *Int. J. Engine Res.*: 1–19, 2012.
3. Lewis, A.M., E. Ortiz-Soto, G. Lavoie, and D.N. Assanis. “Scaling and dimensional methods to incorporate knock and flammability limits in models of high efficiency gasoline and ethanol engines.” *Int. J. Eng. Res.* 16: 181–196, 2015.
4. Cai, L., and H. Pitsch. “Optimized chemical mechanism for combustion of gasoline surrogate fuels.” *Combust. Flame* 162 (5): 1623–1637, 2015.
5. Mehl, M., J.Y. Chen, W.J. Pitz, S.M. Sarathy, and C.K. Westbrook. “An approach for formulating surrogates for gasoline with application toward a reduced surrogate mechanism for CFD engine modeling.” *Energy and Fuels* 25 (11): 5215–5223, 2011.

Key Fiscal Year 2017 Publications

1. Han, Taehoon, George Lavoie, Margaret Wooldridge, André Boehman. “Effect of Syngas (H₂/CO) on SI Engine Knock under Boosted EGR and Lean Conditions.” Presented at the 2017 SAE World Congress, Detroit, MI, SAE Technical Paper No. 2017-01-0670, 2017.
2. Singh, R., M. Fatouraie, T. Burch, G.A. Lavoie, and M.S. Wooldridge. “Effects of Fuel Injection Events of Ethanol and Gasoline Blends on Boosted Direct-Injection Engine Performance.” Presented at the SAE 2017 Fuels and Lubricants Meeting, Beijing, China, SAE Technical Paper 2017-01-2238, 2017.
3. Middleton, R. “Voronoi Partitions for Assessing Fuel Consumption of Advanced Technology Engines: An Approximation of Full Vehicle Simulation on a Drive Cycle.” Submitted for the 2018 SAE World Congress, Detroit, MI, 2018.

IV. Emission Control R&D

IV.1 Joint Development and Coordination of Emission Control Data and Models: Cross-Cut Lean Exhaust Emissions Reduction Simulations (CLEERS) Analysis and Coordination

Josh Pihl, Principal Investigator

Oak Ridge National Laboratory
2360 Cherahala Blvd.
Knoxville, TN 37932
E-mail: pihlja@ornl.gov

Ken Howden, DOE Technology Manager

U.S. Department of Energy
E-mail: Ken.Howden@ee.doe.gov

Start Date: October 1, 2015	End Date: September 30, 2018	
Total Project Cost: \$1,900,000	DOE share: \$1,900,000	Non-DOE share: \$0

Acknowledgments

Co-Authors

Vitaly Prikhodko, Sreshtha Sinha Majumdar, Todd Toops, Charles Finney, Jae-Soon Choi, Zhiming Gao;
Oak Ridge National Laboratory

Project Introduction

Catalytic emissions control devices will play a critical role in deployment of advanced high efficiency engine systems by enabling compliance with increasingly stringent emissions regulations. High efficiency diesel and lean gasoline engines, for example, will require NO_x reduction catalysts with very high conversion efficiencies to meet the Environmental Protection Agency Tier 3 NO_x emissions standard. Low temperature combustion strategies, on the other hand, significantly reduce engine-out NO_x , but they generate a challenging combination of high hydrocarbon and carbon monoxide concentrations at low exhaust temperatures that will likely demand novel approaches to emissions control. Design of progressively more complex engine and aftertreatment systems will increasingly rely on advanced simulation tools to ensure that next generation vehicles maximize efficiency while still meeting emissions standards. These simulation tools will, in turn, require accurate, robust, and computationally efficient component models for emissions control devices. Recognizing this need, the DOE Advanced Engine Cross-Cut Team initiated the CLEERS activity to support the development of improved computational tools and data for simulating realistic full-system performance of high efficiency engines and associated emissions control systems. DOE provides funding to Oak Ridge National Laboratory (ORNL) to perform two complementary roles that support this goal: (1) coordination of CLEERS activities that provide a consistent framework for sharing information and supporting pre-competitive collaborative interactions among the emissions control community and (2) focused measurement, analysis, and modeling activities aimed at developing the strategies, data sets, and device parameters needed for better models of catalytic emissions control devices through collaborations with other national labs and partners in academia and industry.

Objectives

Support industry in the development of accurate simulation tools for the design of catalytic emissions control systems that will enable advanced high efficiency combustion engines to meet emissions regulations while maximizing fuel efficiency through the following activities.

- Coordinate the CLEERS activity for the DOE Advanced Engine Cross-Cut Team

- Support precompetitive collaborative interactions and provide a consistent framework for sharing information among the emissions control research and development community
- Identify emissions control research and development needs and priorities
- Collaborate with Pacific Northwest National Laboratory to develop mechanistic insights, modeling strategies, benchmark data sets, and representative device parameters for catalytic emissions control devices
- Utilize the CLEERS framework to share the resulting insights, strategies, data sets, and parameters with the emissions control community

Approach

In its administrative role, ORNL coordinates the CLEERS Planning Committee, the CLEERS Focus Group teleconferences, CLEERS public workshops, the biannual CLEERS industry priorities survey, and the CLEERS website (www.cleers.org). ORNL acts as a communication hub and scheduling coordinator among these groups and as the spokesperson and documentation source for CLEERS information and reports. The latter includes preparation and presentation of status reports to the Advanced Engine Cross-Cut Team, responses to requests and inquiries about CLEERS from the public, and summary reports from the biannual industry surveys.

Measurement, analysis, and modeling activities are conducted in close collaboration with Pacific Northwest National Laboratory and include identification of reaction mechanisms occurring over catalytic devices under relevant operating conditions, development of modeling strategies that represent key catalyst processes in a computationally efficient manner, generation of benchmark data sets for model calibration and validation, and measurement of critical device parameters needed for model development. The results of these activities are disseminated through the CLEERS information sharing apparatuses and through publications and presentations. Research directions are guided by the DOE Advanced Engine Cross-Cut Team, which collectively oversees CLEERS, and by regular CLEERS industry participant priority surveys. ORNL's CLEERS research activities have historically focused on approaches to NO_x reduction in lean exhaust such as lean NO_x traps and urea selective catalytic reduction (SCR), but have recently shifted to include low temperature aftertreatment technologies such as passive adsorbers for NO_x and hydrocarbons.

Results

Summary of Fiscal Year 2017 accomplishments:

- Organized the 2017 DOE Crosscut Workshop on Lean Emissions Reduction Simulation (CLEERS Workshop) in Ann Arbor, Michigan, on October 3–5, 2017
- Conducted the 2017 CLEERS Industry Priorities Survey
- Developed and launched a completely new CLEERS website (www.cleers.org)
- Facilitated CLEERS Focus Group teleconferences, which continue to have strong domestic and international participation (typically over 40 participants, a majority of which are from industry)
- Provided regular update reports to DOE Advanced Combustion Engine Cross-Cut Team
- Supported the Advanced Combustion and Emissions Control Low Temperature Aftertreatment Team in developing evaluation protocols for low temperature catalysts
- Measured the equilibrium NO storage capacity and release temperature of a commercially relevant passive NO_x adsorber material as a function of temperature, NO concentration, and water concentration; began developing strategies for modeling the NO adsorption/desorption process on passive NO_x adsorbers.

ORNL’s CLEERS coordination work during Fiscal Year 2017 continued to focus on activities that have been identified as high priorities by industrial participants in CLEERS, including the CLEERS Workshop, teleconferences, website, and priorities survey.

The 2017 (20th) CLEERS Workshop was held October 3–5, 2017, in Ann Arbor, Michigan. The workshop was open to participants from any organization or institution, and workshop registrations reached full capacity. The workshop program included four invited speakers, 35 contributed talks, 23 posters, and five industry panelists that discussed “Emerging Modeling Needs for Low Temperature Emissions Control.” The presentations covered a wide range of emissions control topics, including passive NO_x adsorbers, hydrocarbon traps, oxidation catalysts, particulate filters, urea and ammonia SCR, SCR-coated filters, passive SCR, lean NO_x traps, and three-way catalysts. Additional details can be found on the CLEERS website (www.cleers.org) under the 2017 Workshop heading.

ORNL continued hosting CLEERS Focus Group technical teleconferences in Fiscal Year 2017. The presentations covered a wide range of research results in emissions control experimentation, modeling, and simulation by members of the CLEERS Focus Group as well as outside experts, including Rasto Brezny (Manufacturers of Emission Controls Association), John Farrell (National Renewable Energy Laboratory), Hee Je Seong (Argonne National Laboratory), Boopathi Mahadevan (Michigan Technological University), and Balaji Sukumar (Johnson Matthey). Teleconference attendance was consistently between 40–60 participants, with well over half of those participating from industry.

The CLEERS Website (www.cleers.org) was completely redesigned in 2017. The user interface was overhauled to make the site easier to navigate, and the website content was updated to include a calendar of events. Further updates will be coming in 2018.

The latest installment of the biennial CLEERS Industry Priorities Survey was conducted in 2017. Based on feedback from the CLEERS Advisory Committee, the survey questionnaire was updated to include medium-duty diesel as a separate application area in the survey, in addition to heavy-duty diesel, light-duty diesel, and gasoline applications that were addressed previously. As in past surveys, industry participation was high; of 18 organizations that received the survey questionnaire, 15 provided responses. Figures IV.1.1–IV.1.3 highlight some of the key conclusions from the survey. Figure IV.1.1 shows that the core CLEERS activities (annual

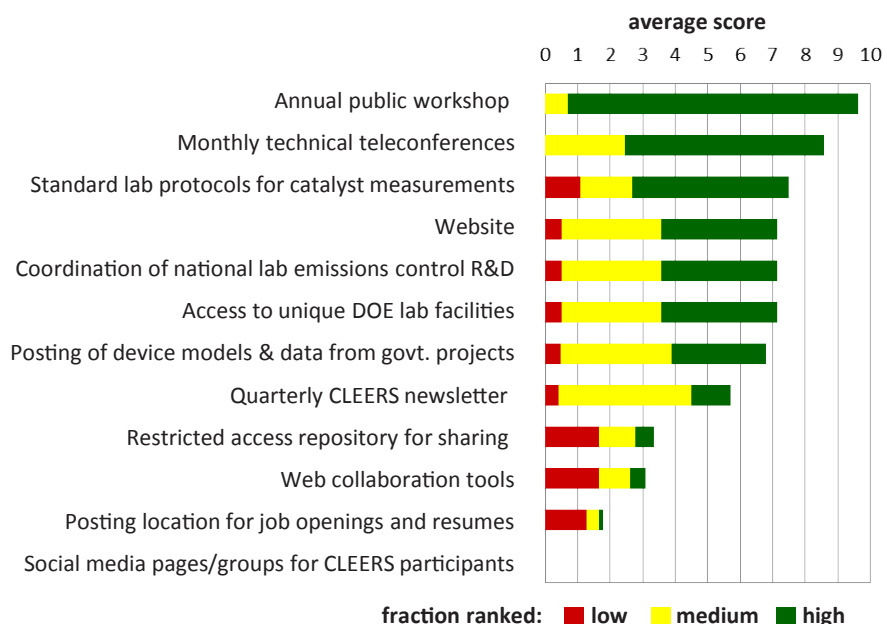
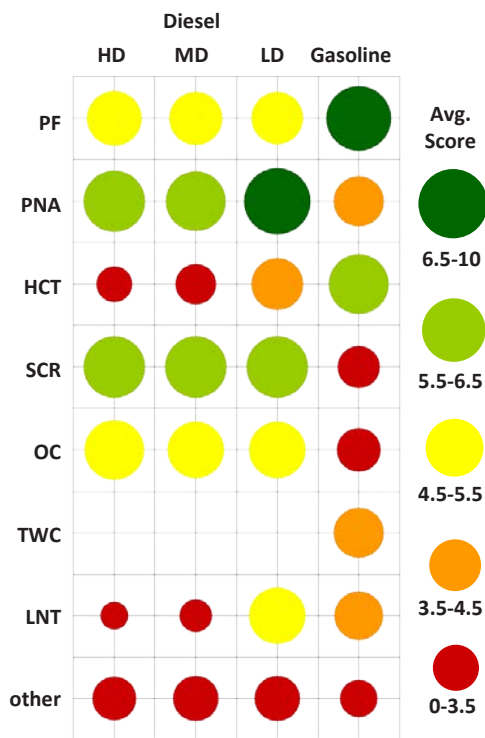


Figure IV.1.1 - Average priority scores for CLEERS organizational activities from the 2017 CLEERS Industry Priorities Survey. Responses were scored as 10 for high priority, 5 for medium priority, and 0 for low priority. The lengths of the colored segments are proportional to the fraction of respondents giving a particular priority rating.

workshop, teleconferences, experimental protocols, and website) are still considered to be high priorities by industry participants.

Within the survey questionnaire, the technical topics were categorized by emissions control technology, making it possible to average the priority scores for all topics under each emissions control technology to identify the highest priority technologies for each application (Figure IV.1.2). For all three diesel application areas, passive NO_x adsorbers and urea SCR were the highest priority technologies, while gasoline particulate filters and hydrocarbon traps were the highest priorities for gasoline applications.



HD – heavy-duty; MD – medium duty; LD – light-duty
 PF – particulate filter; PNA – passive NO_x adsorber; HCT – hydrocarbon trap; OC – oxidation catalyst; TWC – three-way catalyst; LNT – lean NO_x trap

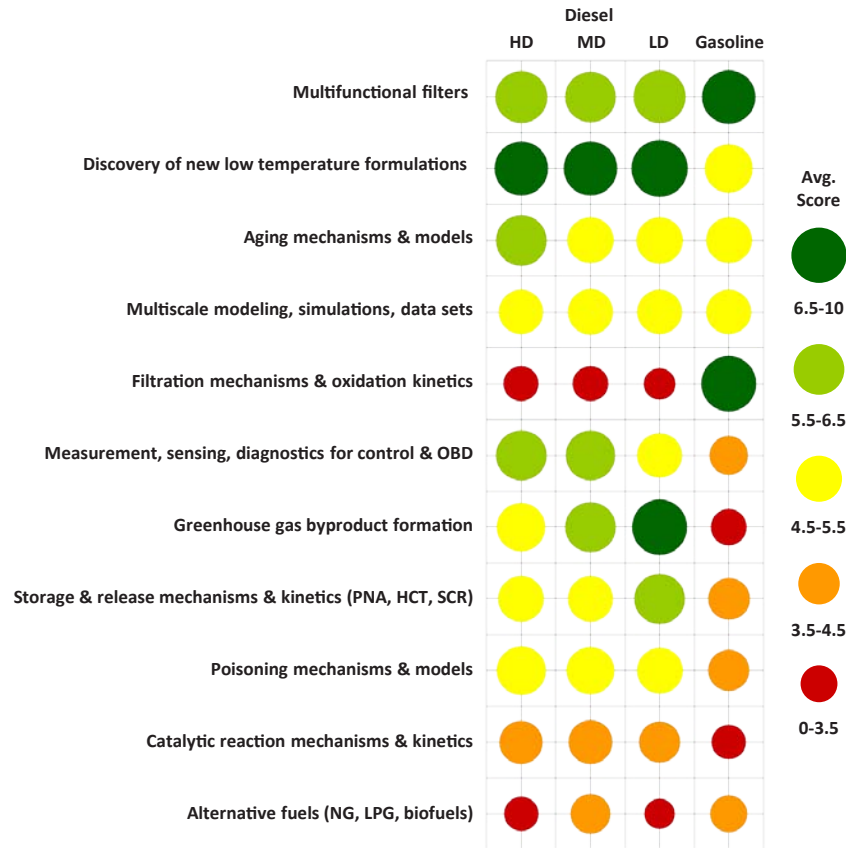
Figure IV.1.2 - Average priority scores across technologies (vertical axis) and market sectors (horizontal axis) from the 2017 CLEERS Industry Priorities Survey. Responses were scored as 10 for high priority, 5 for medium priority, and 0 for low priority. The circle diameter is proportional to the average priority score for a given technology and market sector.

Each of the technology sections within the survey questionnaire included similar topics, allowing for identification of high priority cross-cutting research areas. Figure IV.1.3 shows that multifunctional filters and discovery of new low temperature formulations both received relatively high priorities across all applications. These findings, along with other survey results, will be used in guiding future emissions control research at ORNL and elsewhere.

As in prior years, ORNL has worked closely over the past year with Pacific Northwest National Laboratory and the industry members of the Advanced Combustion and Emissions Control Tech Team Low Temperature Aftertreatment Working Group to support the development of new low temperature catalyst laboratory evaluation protocols. The protocols for oxidation catalysts and three-way catalysts are both available for download from the CLEERS website. A third protocol for low temperature trap materials has been completed and is under review.

ORNL’s CLEERS analysis activities include a combination of experiments and modeling aimed at understanding and controlling processes critical to the design and operation of emissions control systems for high efficiency engines, with a particular emphasis on modeling adsorption and desorption processes in catalytic devices. During Fiscal Year 2017, the focus of these efforts was shifted from copper-exchanged

zeolite urea SCR materials to low temperature traps. A member of Manufacturers of Emission Controls Association provided a commercially relevant catalyst that can be applied as both a passive NO_x adsorber and a hydrocarbon trap. ORNL developed and implemented experimental protocols to measure NO adsorption



OBD – on-board diagnostics ; NG – natural gas; LPG – liquefied petroleum gas

Figure IV.1.3 - Average priority scores across research areas (vertical axis) and market sectors (horizontal axis) from the 2017 CLEERS Industry Priorities Survey. Responses were scored as 10 for high priority, 5 for medium priority, and 0 for low priority. The circle diameter is proportional to the average priority score for a given research area and market sector.

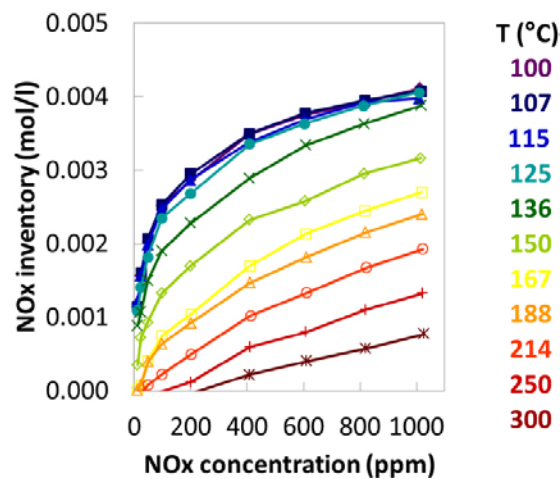


Figure IV.1.4 - NO storage capacity as a function of inlet NO concentration (X-axis) and temperature (data series) for a commercially relevant passive NO_x adsorber material

isotherms (Figure IV.1.4) on this material. Such isotherms can be used to extract the energetics of NO adsorption on the catalyst, as was done in prior years of this project with adsorption of ammonia on urea SCR catalysts.

The experiments also included a temperature-programmed desorption step to measure the stability of the NO stored on the catalyst surface. The NO adsorption/temperature-programmed desorption experiments were conducted in the presence and absence of both oxygen and water to understand how the exhaust environment impacts NO storage on passive NO_x adsorbers. Interestingly, contrary to the inhibition of adsorption phenomena by water typically observed on other emissions control catalysts, inclusion of water in the gas stream actually increased both the NO storage capacity and the stability of the stored NO, resulting in larger temperature-programmed desorption peaks that occurred at higher temperatures in Figure IV.1.5. This observation is consistent with recently reported results from other research groups [1], and has been attributed to changes in the electronic state of the NO storage site caused by water adsorption, resulting in a stronger interaction with an adsorbed NO molecule. Ongoing work at ORNL is focused on quantifying the effects of water and other exhaust species, particularly CO, on NO adsorption and desorption. The goal of this work is to guide the development of accurate models for passive NO_x adsorbers that can be used in simulation tools for the design of emissions control system architectures and control strategies with better low temperature performance.

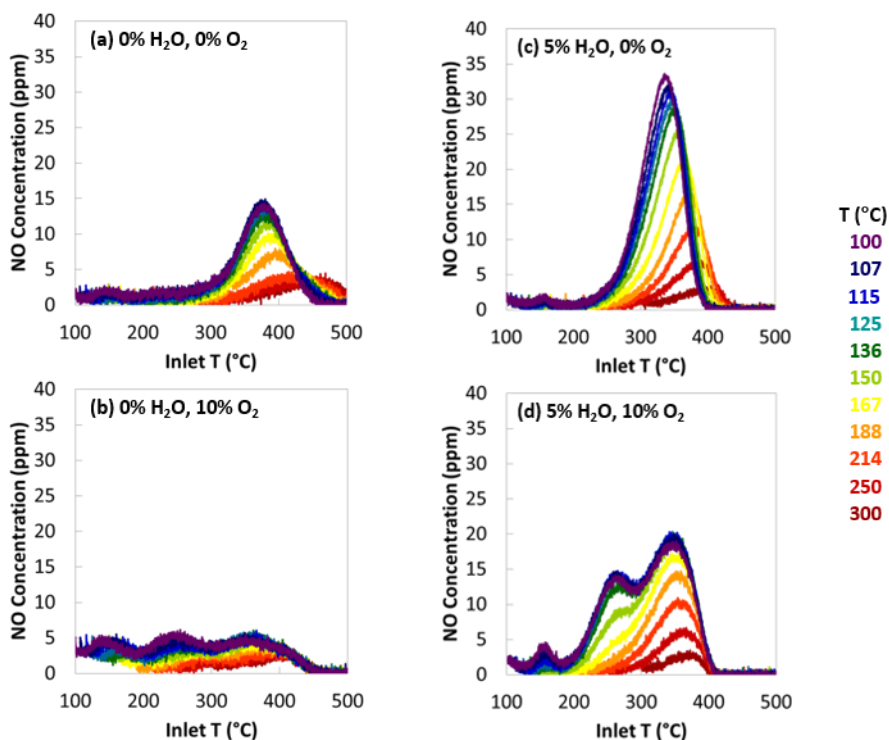


Figure IV.1.5 - NO temperature programmed desorption profiles obtained with a commercially relevant passive NO_x adsorber material after exposure to 1,000 ppm NO in the presence of (a) 0% H₂O, 0% O₂; (b) 0% H₂O, 10% O₂; (c) 5% H₂O, 0% O₂; and (d) 5% H₂O, 10% O₂

Conclusions

- CLEERS continues to be a valuable resource for the aftertreatment development community, based on the high level of participation in the CLEERS Workshop and Focus Group teleconferences, as well as priority scores from the 2017 CLEERS Industry Priorities Survey.
- Passive NO_x adsorbers and urea SCR catalysts are the highest priority technologies for diesel applications, while gasoline particulate filters and hydrocarbon traps are the highest priority technologies for gasoline applications according to the 2017 Industry Priorities Survey. Survey respondents also ranked

multifunctional filters and novel low temperature formulations as high priority research areas cutting across multiple technologies.

- NO storage and release on passive NO_x adsorbers depends strongly on the exhaust gas composition. Water increases the NO storage capacity as well as the stability of the stored NO, likely due to changes in the electronic structure of the NO storage site caused by water co-adsorption. Such effects will need to be captured in models in order to accurately simulate the performance of passive NO_x adsorbers.

References

1. Liu, Donna, et al. "An in-situ infrared and XAS study on NO adsorption on Pd/zeolite under complex gas feed." Presentation to the 2017 CLEERS Workshop, Ann Arbor, MI, 2017. https://cleers.org/wp-content/uploads/formidable/3/2017CLEERS_DonnaLiu.pdf.

Key Fiscal Year 2017 Publications

1. Choi, Jae-Soon, et al. "Reduction of the stored NO_x with CO/H₂ and hydrocarbons: a spatial resolution analysis." In *NO_x trap catalysts and technologies: fundamentals and industrial applications*. Cambridge: Royal Society of Chemistry, in press.

IV.2 CLEERS Aftertreatment Modeling and Analysis

Yong Wang, Principal Investigator

Pacific Northwest National Laboratory
P.O. Box 999, MS K2-12
Richland, WA 99354
E-mail: yong.wang@pnnl.gov

Ken Howden, DOE Technology Manager

U.S. Department of Energy
E-mail: Ken.Howden@ee.doe.gov

Start Date: October 1, 2016	End Date: September 30, 2017	
Total Project Cost: \$770,000	DOE share: \$770,000	Non-DOE share: \$0

Acknowledgments

Co-Authors

Feng Gao, Jamie Holladay, Ken Rappe, Chaitanya Sampara, Mark Stewart, Janos Szanyi, Diana Tran, Yilin Wang; Pacific Northwest National Laboratory

Project Introduction

Cross-Cut Lean Exhaust Emissions Reduction Simulations (CLEERS) is a research and development focus project of the Diesel Cross-Cut Team. The overall objective is to promote the development of improved computational tools for simulating realistic full-system performance of lean-burn engines and the associated emissions control systems. Four fundamental research projects are supported at Pacific Northwest National Laboratory (PNNL) through CLEERS: selective catalytic reduction (SCR), passive NO_x adsorber (PNA), particulate/filter, and Low-Temperature Aftertreatment (LTAT). Resources are shared among these efforts in order to actively respond to current industrial needs.

Objectives

- Promote the development of improved computational tools for simulating realistic full system performance of lean-burn engines and the associated emissions control systems
- Provide the practical and scientific understanding and analytical base required to enable the development of efficient, commercially viable emissions control solutions for ultra-high efficiency vehicles
- Lead and contribute to the CLEERS activities, e.g., lead technical discussions, invite distinguished speakers, and maintain an open dialogue on modeling issues, and closely work with the Advanced Combustion and Emission Control (ACEC) LTAT team to actively respond to current industrial needs

Approach

This program builds off PNNL's strong base in fundamental sciences by effectively leveraging capabilities from Institute for Integrated Catalysis and Environmental Molecular Sciences Laboratory. Integrated Catalysis is the largest non-industrial catalysis organization in the United States and Environmental Molecular Sciences Laboratory is a DOE scientific user facility located at PNNL. We closely collaborate with academic research groups from Purdue University, Notre Dame University, University of Houston, and Washington State University who are funded by National Science Foundation in the emission control area. We orient our program strongly towards addressing fundamental issues of broad impact to applications and commercialization by closely working with original equipment manufacturers, Tier 1 suppliers, as well as our partners and sponsors (Oak Ridge National Laboratory, DOE Advanced Engine Cross-Cut Team).

Results

Key accomplishments for Fiscal Year (FY) 2017 include the following.

- Identified that the low temperature activity of the Cu/SSZ-13 catalyst is limited by the oxidation of Cu(I) which involves the two isolated Cu(I) ions to form a transient intermediate. This provides insight in further improving the low temperature SCR activity of Cu/SSZ-13 by maximizing the Cu loading without negatively impacting NH_3 selectivity and catalyst stability. It also provides more accurate assumptions of active site requirement in SCR simulations under CLEERS.
- Quantified, for the first time, Cu species in Cu/SSZ-13 as a function of hydrothermal aging temperature using electron paramagnetic resonance. The insight gained is essential to further improving the hydrothermal stability of Cu/SSZ-13 catalysts by minimizing the dealumination and CuOH site detachment in catalyst design.
- Finalized the low temperature storage catalyst test protocol, and nearly complete the three-way catalyst test protocol.
- Confirmed NO_x storage and release properties of Pd-loaded zeolites (chabazite [CHA], ZSM-5 [MFI], Beta), and identified that the NO_x uptake involves surface reaction between Pd species and NO .
- Characterized catalyst location in three distinct coating regimes along the axial length of a commercial SCR filter using X-ray computed tomography, which is essential to understand the properties such as permeability, filtration behavior, and chemical activity of the SCR filters.

The PNNL team has identified in FY 2017 that standard SCR over low Cu loaded Cu/SSZ-13 displays complex temperature and Cu loading dependence. At low temperatures ($<250^\circ\text{C}$), SCR rates depend linearly on square of Cu loading, while at high temperatures ($>350^\circ\text{C}$), SCR rates depend linearly on Cu loading. With the aid of density functional theory calculations, we demonstrated that the low-temperature oxidation half-cycle of the SCR reaction cannot be achieved on isolated Cu ions; O_2 activation requires participation of a pair of mobile $[\text{Cu}^{\text{I}}(\text{NH}_3)_2]^+$ sites with the formation of a $[\text{Cu}^{\text{I}}(\text{NH}_3)_2]^+-\text{O}_2-[\text{Cu}^{\text{I}}(\text{NH}_3)_2]^+$ intermediate. This chemistry occurs homogeneously within the SSZ-13 pores and is the rate-limiting step at low Cu loadings. Based on which, a new low-temperature SCR mechanism proposal fully consistent with experimental SCR kinetics has been created as shown in Figure IV.2.1.

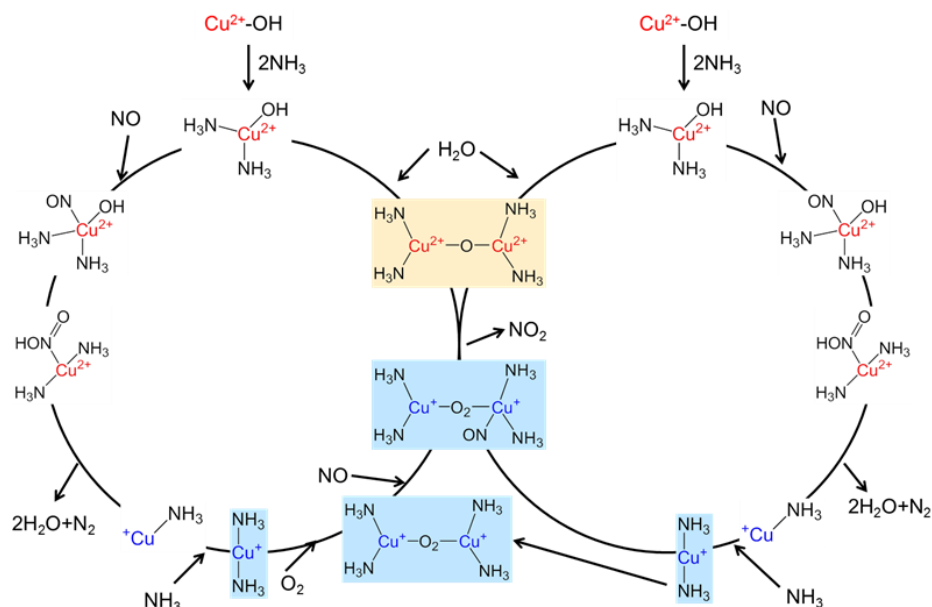


Figure IV.2.1 - Complete redox cycling of low-temperature NH_3 -SCR that involves two Cu(I) centers in the oxidation half-cycle. Key intermediates are highlighted.

At high temperatures, isolated Cu ions anchor on the SSZ-13 framework and become immobilized. In this case, the oxidation half-cycle occurs on isolated Cu(I) sites with rather high activation barriers. The importance of this study can be summarized as (1) the determination of a low-temperature SCR rate limiting step allows for the manipulation of catalysts with improved low-temperature performance and (2) identification and separation of low- and high-temperature SCR mechanisms allows for more accurate SCR kinetic simulations.

In another study, the PNNL team for the first time developed methodology in quantifying all possible Cu species in Cu/SSZ-13 catalysts at any stage of use and treatment. Using electron paramagnetic resonance as the analysis tool, the amounts of Cu^{2+} -2Z, $[\text{Cu}(\text{OH})]^+$ -Z, and CuO_x clusters can be accurately estimated. This quantification convincingly highlights the remarkable hydrothermal stability of Cu^{2+} -2Z, along with the gradual conversion of $[\text{Cu}(\text{OH})]^+$ -Z to CuO_x clusters. For an SCR catalyst with Si/Al = 12 and Cu loading of 2.1 wt%, Figure IV.2.2 presents quantification results of the three Cu moieties in catalysts following different hydrothermal treatments.

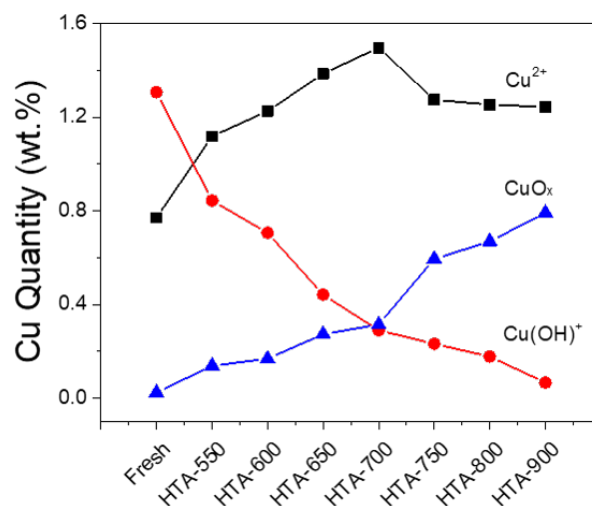
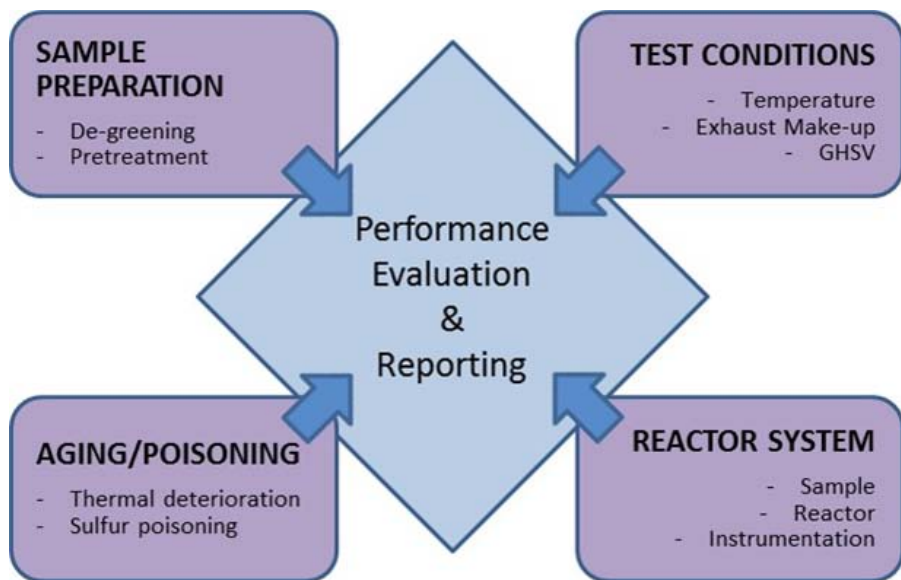


Figure IV.2.2 - Estimation of Cu^{2+} , $\text{Cu}(\text{OH})^+$, and CuO_x in fresh and hydrothermally aged (HTA) samples. SCR catalyst with Si/Al = 12 and Cu loading of 2.1 wt% was used. HTA-T represents sample aged at temperature T (in °C) for 16 h in flowing air containing 10% water vapor.

This study also identified that diffusion of CuO_x clusters larger than the primary pore openings of SSZ-13 can be regarded as a primary cause for structure destabilization of this catalyst during hydrothermal aging. This study, for the first time, suggested a number of rational design principles derived on the basis of detailed atomic-level and near-atomic-level understanding of the hydrothermal stability of Cu/SSZ-13 SCR catalysts. These principles follow from this work's elucidation of previously unexplained structure–function phenomena observed for Cu/SSZ-13, and they can guide the future development of optimum SCR catalysts.

In FY 2017, PNNL supported the activities and mission of the LTAT group of the ACEC Tech Team through (1) routine interaction via biweekly LTAT group conference calls and bimonthly ACEC Tech Team meetings, (2) low-temperature aftertreatment catalyst test protocol development, and (3) updating of the ACEC Roadmap document. The low-temperature catalyst test protocols are a pathway towards harmonized catalyst testing procedures and conditions throughout the technical community that are realistic and sufficiently capture relevant performance capability; the intent of the protocols is to accelerate the pace of catalyst discovery and innovation. This year the LTAT group completed the Low-Temperature Storage Catalyst Test Protocol (Figure IV.2.3). This protocol was reviewed and approved by the ACEC Tech Team and the Advanced Powertrain Technology Leadership Council and will be released to the CLEERS website in early FY 2018. Also in FY 2017 the LTAT group prepared and completed a Low-Temperature Three-Way Catalyst Test Protocol. This protocol was reviewed and approved by the ACEC Tech Team and is currently under review by the Advanced Powertrain Technology Leadership Council also for expected release to the CLEERS website in early FY 2018. The LTAT group is currently in discussion to determine the group's focus moving forward from the successful protocol development activities.



GHSV – gas hourly space velocity

Figure IV.2.3 - Low-temperature aftertreatment test protocol structure

In FY 2017 the PNNL team initiated studies on passive NO_x adsorber materials to be used to alleviate the so called cold start problem in exhaust control catalysis. These materials would adsorb all the NO_x from an exhaust stream at temperatures too low for the NH₃ SCR catalyst to be operational, and release all the adsorbed NO_x at temperatures near optimal operating temperatures of the SCR catalyst. To this end a series of Pd-loaded zeolite catalysts (with framework structures of Beta, MFI and CHA) were prepared and tested under varying experimental conditions and the NO_x storage and release properties of these materials were tested. Using a series of spectroscopy and microscopy tools the nature of the Pd-containing phases were monitored on the as-prepared, reduced, and oxidized PNA materials. We found that the NO_x storage and release properties of these Pd/zeolite materials strongly depend on the zeolite framework and the composition of the simulated exhaust gas stream used. All three Pd/zeolite systems showed efficient NO_x storage and release, however, the zeolite framework strongly influenced the temperature of maximum rate of NO_x release (Figure IV.2.4). The highest NO_x efficiency was observed in the absence of water in the exhaust stream, while addition of

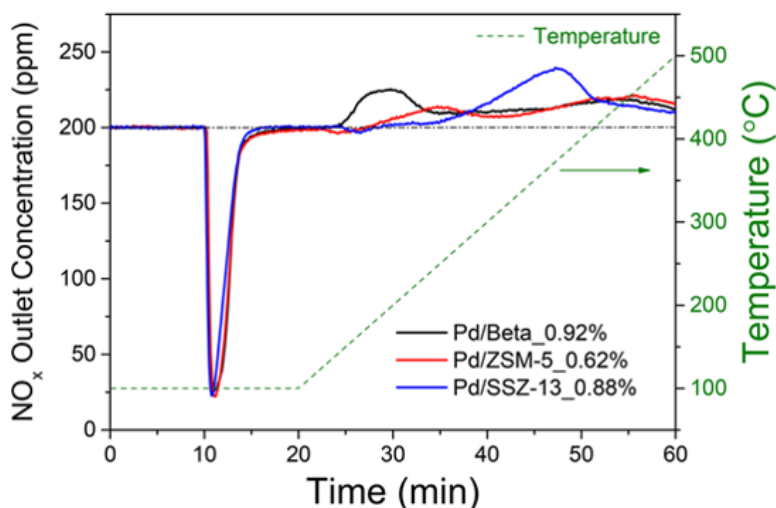


Figure IV.2.4 - NO_x adsorption at 100 °C for 10 min followed with temperature programmed desorption (10 °C/min up to 500°C). The feed gas mixture contains 200 ppm of NO_x (185 ppm of NO and 15 ppm of NO₂), 14% O₂, ~2.5% H₂O and 200 ppm of CO balanced with N₂ at a flow rate of 300 scfm.

CO greatly enhanced the performance of each storage material. Spectroscopy studies (X-ray photoelectron spectroscopy and Fourier transform infrared spectroscopy spectra of probe molecules) clearly showed the presence of Pd-containing species in different oxidation states (+1, +2, +4) and nuclearities (individual Pd²⁺ ions in cationic positions PdO_x clusters/particles). Transmission electron microscopy imaging revealed that the PdO_x species were highly mobile on/in the zeolite supports; under reducing conditions rather large metallic Pd clusters formed, while under oxidizing environments the thus formed PdO_x phase redispersed, and part of it re-entered the zeolite pores (Figure IV.2.5). These studies will provide guidance to our current and future work in understanding the roles of metal loading, zeolite structure/composition and the chemical state and nuclearity of effective active phases for PNA materials.

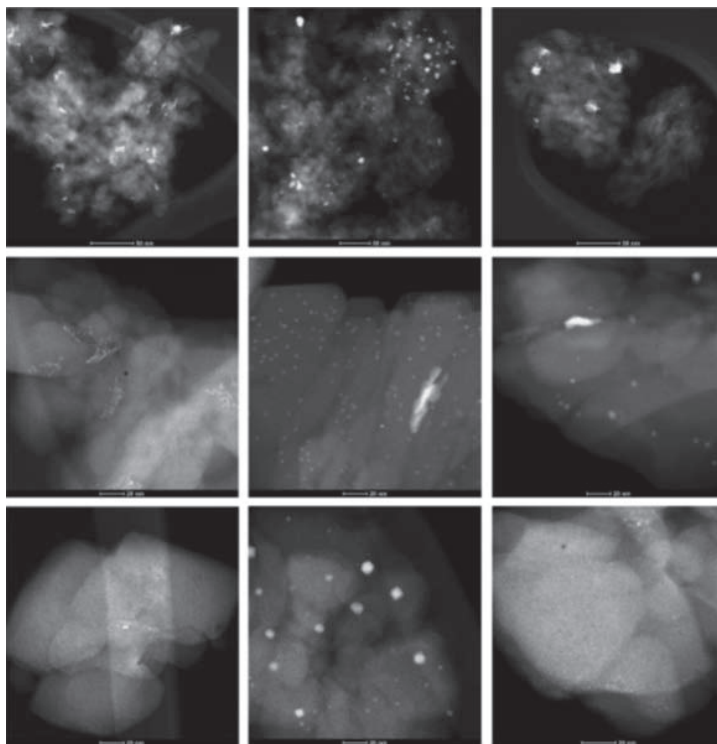


Figure IV.2.5 - Scanning transmission microscopy images of the freshly calcined (left), reduced (by 1% H₂/He at 400°C for 30 min, middle), and reoxidized (by 10% O₂/He at 500°C for 1 h, right) Pd/zeolite samples, where the upper, middle, and lower rows are images for Pd/Beta_0.92%, Pd/ZSM-5_0.62%, and Pd/SSZ-13_0.88%, respectively

In 2017, PNNL refined and extended the general one-dimensional catalyst reactor model described in last year's report. The simulation program makes efficient use of parallel computational resources in order to shorten the time required to optimize kinetic parameters. The model framework can be used for a variety of automotive catalyst applications including three-way catalyst, diesel oxidation catalyst, SCR, and PNA. Parameters for PNNL's global SCR kinetics model were also further optimized. The model includes a rational approach to catalyst aging and describes changes in the proportions of catalytic sites that take part in NO oxidation and NH₄NO₃ formation reactions. Comparisons between predicted and measured NH₃ and NO oxidation rates on a catalyst that was hydrothermally aged for 2 h at 800°C. The model was validated over six different aging conditions.

A primary goal of the CLEERS initiative is to promote more effective use of simulation tools in the inception, design, and optimization of automotive exhaust aftertreatment technologies. Many models developed in academic settings assume idealized reactor systems. Real-world aftertreatment devices often include a number of complex features, some of which can be omitted from models, depending upon specific model objectives, but others of which should be included for improved fidelity and greater insight into factors affecting device performance. PNNL examined the commercial SCR filter that was deployed on some 2015 Volkswagen diesel automobiles. Although similar technologies have been successfully deployed in Europe, this was one

of the first such deployments in the United States market. Similar concepts are being considered for other applications (e.g., three-way catalyst on particulate filter for use with advanced gasoline vehicles). Sectioning and multi-resolution X-ray scans showed unexpected patterns in catalyst distribution within the mass produced filter. Three distinct zones were observed. The upstream zone, which accounted for roughly the first 15–20% of axial length, had a relatively light coating, biased toward the upstream filter wall surface. The second zone, which accounted for roughly the next 15–20% of effective axial length, had a very heavy catalyst coating. The third zone, which accounted for the back 65–70% of effective axial length, had an intermediate catalyst coating biased toward the downstream surface of the filter wall (as shown in Figure IV.2.6). Catalyst location and morphology could impact NO_x conversion efficiency, backpressure, and filter loading behavior in multi-functional exhaust filters.

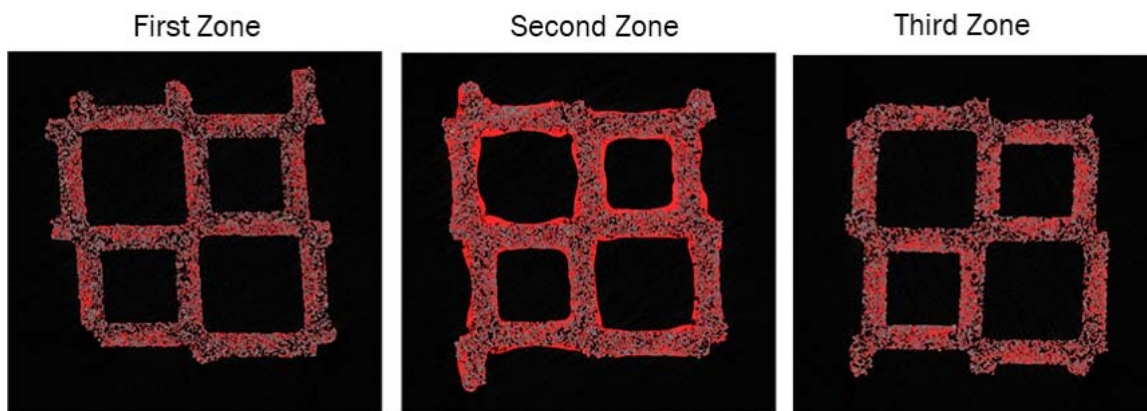


Figure IV.2.6 - Catalyst locations within small cross-sections of a commercial SCR filter (catalyst shown in red false color – note that inlet channels are larger and outlet channels are smaller in this asymmetric honeycomb filter design)

Conclusions

- Determined low-temperature SCR mechanism via kinetics, spectroscopic, and density functional theory studies for Cu/SSZ-13
- Provided atomic level understanding on the transformation of Cu active centers in Cu/SSZ-13 during hydrothermal aging
- Finalized the low-temperature storage catalyst test protocol, and nearly complete three-way catalyst test protocol
- Determined that both NO and CO are able to reduce Pd(IV) to Pd(II) or lower oxidation states and identified the origin of NO_2 formation during NO uptake in Pd-zeolites
- Characterized catalyst location in three distinct coating regimes along the axial length of a commercial SCR filter

Key Fiscal Year 2017 Publications

1. Gao, F.; D. Mei, Y. Wang, J. Szanyi, and C.H.F. Peden. “Selective Catalytic Reduction over Cu/SSZ-13: Linking Homo- and Heterogeneous Catalysis.” *J. Am. Chem. Soc.*, 2017, 139, 4935–4942.
2. Gao, F., Y. Zheng, R.K. Kukkadapu, Y. Wang, E.D. Walter, B. Schwenzler, J. Szanyi, and C.H.F. Peden. “Iron Loading Effects in Fe/SSZ-13 NH_3 SCR Catalysts: Nature of the Fe Ions and Structure–Function Relationships.” *ACS Catal.* 2016, 6, 2939–2954.
3. Kovarik, L., N.M. Washton, R. Kukkadapu, A. Devaraj, A. Wang, Y. Wang, J. Szanyi, C.H.F. Peden, and F. Gao. “Transformation of Active Sites in Fe/SSZ-13 SCR Catalysts during Hydrothermal Aging: A Spectroscopic, Microscopic, and Kinetics Study.” *ACS Catal.* 2017, 7, 2458–2470.

4. Prodinge, S., M.A. Derewinski, Y. Wang, N.M. Washton, E.D. Walter, J. Szanyi, F. Gao, Y. Wang, and C.H.F. Peden. "Sub-micron Cu/SSZ-13: Synthesis and application as selective catalytic reduction (SCR) catalysts." *Applied Catalysis B: Environmental* 201 (2017) 461–469.
5. Zelenyuk, A., J. Wilson, D. Imre, M.L. Stewart, G. Muntean, J. Storey, V. Prikhodko, S. Lewis, M. Eibl, and J. Parks. "Detailed Characterization of Particulate Matter Emitted by Lean-Burn Gasoline Direct Injection Engine." *International Journal of Engine Research*, 2016, Nov Issue, 1-13, doi: 10.1177/1468087416675708.
6. Zheng, Y., L. Kovarik, M.H. Engelhard, Y. Wang, Y. Wang, F. Gao, and J. Szanyi. "Low-Temperature Pd/Zeolite Passive NO_x Adsorbers: Structure, Performance and Adsorption Chemistry." *Journal of Physical Chemistry C*, 2017, 121(29):15793–15803. doi:10.1021/acs.jpcc.7b04312
7. Song, J., Y. Wang, E.D. Walter, N.M. Washton, D. Mei, L. Kovarik, M.H. Engelhard, S. Prodinge, Y. Wang, C.H.F. Peden, and F. Gao. "Toward Rational Design of Cu/SSZ-13 Selective Catalytic Reduction Catalysts: Implications from Atomic-Level Understanding of Hydrothermal Stability." *ACS Catal.* 2017, 7, 8214–8227.
8. Li, S., Y. Zheng, F. Gao, J. Szanyi, and W.F. Schneider. "Experimental and Computational Interrogation of Fast SCR Mechanism and Active Sites on H-form SSZ-13." *ACS Catalysis* 2017, 7(8):5087–5096. doi:10.1021/acscatal.7b01319
9. Luo, J., F. Gao, F. K. Kamasamudram, N. Currier, C.H.F. Peden, and A. Yezerets. "New insights into Cu/SSZ-13 SCR catalyst acidity. Part I: Nature of acidic sites probed by NH₃ titration." *Journal of Catalysis* 2017, 348:291–299. doi:10.1016/j.jcat.2017.02.025
10. Wang, A., Y. Guo, F. Gao, and C.H.F. Peden. "Ambient-temperature NO oxidation over amorphous CrO_x-ZrO₂ mixed oxide catalysts: Significant promoting effect of ZrO₂." *Applied Catalysis B* 2017, 202:706–714. doi:10.1016/j.apcatb.2016.02.045
11. Wang, A., B. Lin, H. Zhang, M.H. Engelhard, Y. Guo, G. Lu, C.H.F. Peden, and F. Gao. "Ambient Temperature NO Oxidation Over Cr-based Amorphous Mixed Oxide Catalysts: Effects From the Second Oxide Components." *Catalysis Science & Technology* 2017, 7(11):2362–2370. doi:10.1039/c7cy00490

IV.3 Low-Temperature Emission Control to Enable Fuel-Efficient Engine Commercialization

Todd J. Toops, Principal Investigator

Oak Ridge National Laboratory
2360 Cherahala Boulevard
Knoxville, TN 37932
E-mail: toopstj@ornl.gov

Ken Howden, DOE Technology Manager

U.S. Department of Energy
E-mail: Ken.Howden@ee.doe.gov

Start Date: October 1, 2016 End Date: September 30, 2018
Total Project Cost: \$1,200,000 DOE share: \$1,200,000 Non-DOE share: \$0

Acknowledgments

Co-Authors

Andrew J. Binder, Eleni A. Kyriakidou, Jae-Soon Choi, James E. Parks III;
Oak Ridge National Laboratory

Project Introduction

Removing the harmful pollutants in automotive exhaust has been an intense focus of the automotive industry over the last several decades. In particular, the emissions regulations for fuel-efficient diesel engines that were implemented in 2007 and 2010 have resulted in a new generation of emissions control technologies. These catalysts usually reach 90% conversion of pollutants between 200°C and 350°C, but below these temperatures, the catalysts are relatively inactive. Consequently, more than 50% of pollutant emissions occur in the first 2–3 min of the transient drive cycle required for certification and under cold-start or idling conditions. Thus, as emissions regulations become more stringent meeting the emission regulations will require increased activity during this warm-up period. To further complicate matters, the increased Corporate Average Fuel Economy standards that will be implemented over the next decade will result in the introduction of more fuel-efficient engines. Higher fuel efficiency will result in less heat lost to exhaust and lower exhaust temperatures, which further necessitates the need for increased emissions control activity at low temperatures. With this in mind the U.S. DRIVE Advanced Combustion and Emission Control (ACEC) Tech Team has set a goal of achieving 90% conversion of CO, hydrocarbons (HCs), and NO_x at 150°C. Higher Pt and Pd loadings may help to increase the catalytic efficiency, but such methods are too expensive for long-term success. Thus, this project focuses on developing new catalytic materials that are active at lower temperatures. In addition, other options to meet the emissions standards such as HC and NO_x adsorbers are being pursued; these adsorber materials can trap the pollutants at low temperature for later release and treatment at higher temperatures where catalyst are active.

Objectives

- Develop emission control technologies that achieve >90% reduction of pollutants at low temperatures (<150°C) to enable fuel-efficient engines with low exhaust temperatures to meet new U.S. Environmental Protection Agency Tier 3 emission regulations that require ~80% less NO_x and HC emissions than current standards
- Identify advancements in technologies that will enable commercialization of advanced combustion engine vehicles
- Understand fundamental surface chemistry mechanisms that either enable or limit low temperature emission control

Approach

To reach the goal of 90% conversion at 150°C a multi-functional approach will be pursued. Currently, there is a large effort being pursued in the Basic Energy Science programs that are focused on studying catalysts with very high activity regardless of the specific application. We initiate contact with these researchers to investigate their catalysts in the harsh conditions that are present in automotive exhaust, e.g., H₂O, CO₂, CO, HC, NO_x, and hydrothermal aging above 800°C. Often these catalysts show exceptional activity in single component exhaust streams, but there is significant inhibition from other exhaust species. With this in mind, we are aiming to understand the limitations of each system, but also look for synergistic opportunities when possible. This includes using traps to limit exposure of inhibiting species to active catalysts until temperatures are more amenable. Also, mixing catalytic components where the catalysts are limited by different species will be explored. Our efforts will aim to understand the processes at a fundamental level and illustrate any benefits or shortcomings of each catalyst we study, while striving to find compositions that will achieve the very challenging goal of 90% conversion of CO, NO_x, and HC at 150°C. Improving this understanding of the potential advantages and limitations of catalysts will guide the reformulation of new catalysts.

Results

Efforts this year have progressed to the study of many of our most promising materials in combination with each other to overcome drawbacks resulting from use of the individual materials alone. In our study of the mixed-oxide CuO–Co₃O₄–CeO₂ (CCC) catalyst, we had previously seen significant gains in sulfur tolerance when the catalyst was combined in physical mixture with a Pt/Al₂O₃ catalyst (Figure IV.3.1b). While the increased sulfur tolerance was evident from our micro-reactor exposure experiments, it was unclear whether the remaining post-exposure activity was resultant only from the Pt/Al₂O₃ portion of the catalytic bed (with the CCC portion being severely poisoned as in stand-alone tests) or if this physical mixture could truly allow CCC to function under conditions it was previously deactivated in. Diffuse reflectance infrared spectroscopy (DRIFTS) was utilized to study the CO binding sites over the component catalysts to determine the extent to which sulfation was able to deactivate CCC while it was the physical mixture. During these tests, the materials were exposed to a flow of 1% CO for 10 min at various temperatures to allow adsorption of CO onto the active sites of the catalysts, directly after which spectra were acquired. Figure IV.3.1a shows a comparison of the spectra for the sulfated Pt/Al₂O₃ (PtAl) and physical mixture (CCC/PtAl_{mix}) with the degreened CCC catalyst. In these spectra, low-temperature bands appearing at 2,115 cm⁻¹ can be attributed to Cu⁺–CO binding over the CCC catalyst while the bands appearing at 2,100–2,085 cm⁻¹ can be attributed to Pt–CO binding over the Pt/Al₂O₃ catalyst. The results shown for the physical mixture indicate the presence of CO binding on both components even after sulfur exposure, this is in contrast to Figure IV.3.1c which shows the complete loss of the 2,115 cm⁻¹ band after CCC is sulfated without the presence of the Pt/Al₂O₃ component. It is clear from these results that despite the normal sulfur sensitivity of CCC, the physical mixture with Pt/Al₂O₃ is able to grant some level of sulfur tolerance to the mixed oxide and allow it to remain active after sulfur exposure.

Efforts have also continued in the evaluation of potential NO and HC trapping materials as a pathway to delay these species from interacting with diesel oxidation catalyst (DOC) materials until they reach an active temperature. Utilizing a draft protocol provided by the U.S. DRIVE ACEC Tech Team for evaluation of trapping materials under more demanding simulated exhaust conditions, a series of materials including Ag and Pd ion-exchanged zeolites (BEA and ZSM-5) were tested for their adsorption and release properties. This protocol includes a 30 min storage exposure for CO, NO, as well as three families of hydrocarbons common in exhaust: short-chain (ethylene), long-chain (decane), and aromatics (toluene). This is then followed by a 20°C/min ramp to evaluate release properties. Figure IV.3.2a gives a broad overview of the storage and release efficiencies for the various catalysts. Overall, we find that decane and toluene are much more easily stored by these traps but that trapping of NO over the full 30 min test stays fairly low. With respect to the individual materials, Ag-based zeolites show higher capability for HC trapping by a small margin but are outperformed by Pd-based zeolites, and Pd/ZSM-5 in particular, for NO_x trapping efficiency. Ag-based materials also show significantly more release of decane and ethylene species in comparison to Pd-based zeolites indicating their lower activity in direct conversion of these species to CO₂ upon temperature ramp. From these results we determined that Pd/ZSM-5 showed the most promise for use in further tests. Of all the materials tested, Pd/ZSM-5 greatly outperformed the others in NO trapping efficiency, reaching 11% storage over 30 min and

66% over the first 3 min. Figures IV.3.2b and IV.3.2c show the full trapping and release profiles for total hydrocarbons (THC) and NO over Pd/ZSM-5. Results show that even after 30 min of exposure, Pd/ZSM-5 has not reached full capacity for HC storage evidenced by the remaining gap between bypass (black line) and storage (red line) measurement at the end of the storage time and onset of temperature ramp. A sharp release of both HCs and NO_x can be seen around 236°C accompanied by a large exotherm generated by conversion of HC species to CO₂ as evidence of inherent Pd/ZSM-5 oxidation activity. Unfortunately, under these conditions, improvement may still be necessary to obtain release of NO at temperatures high enough for active selective catalytic reduction downstream but the high 3-min storage high overall capacity for HCs may still be valuable for reducing inhibitors over DOC catalysts during cold-start applications.

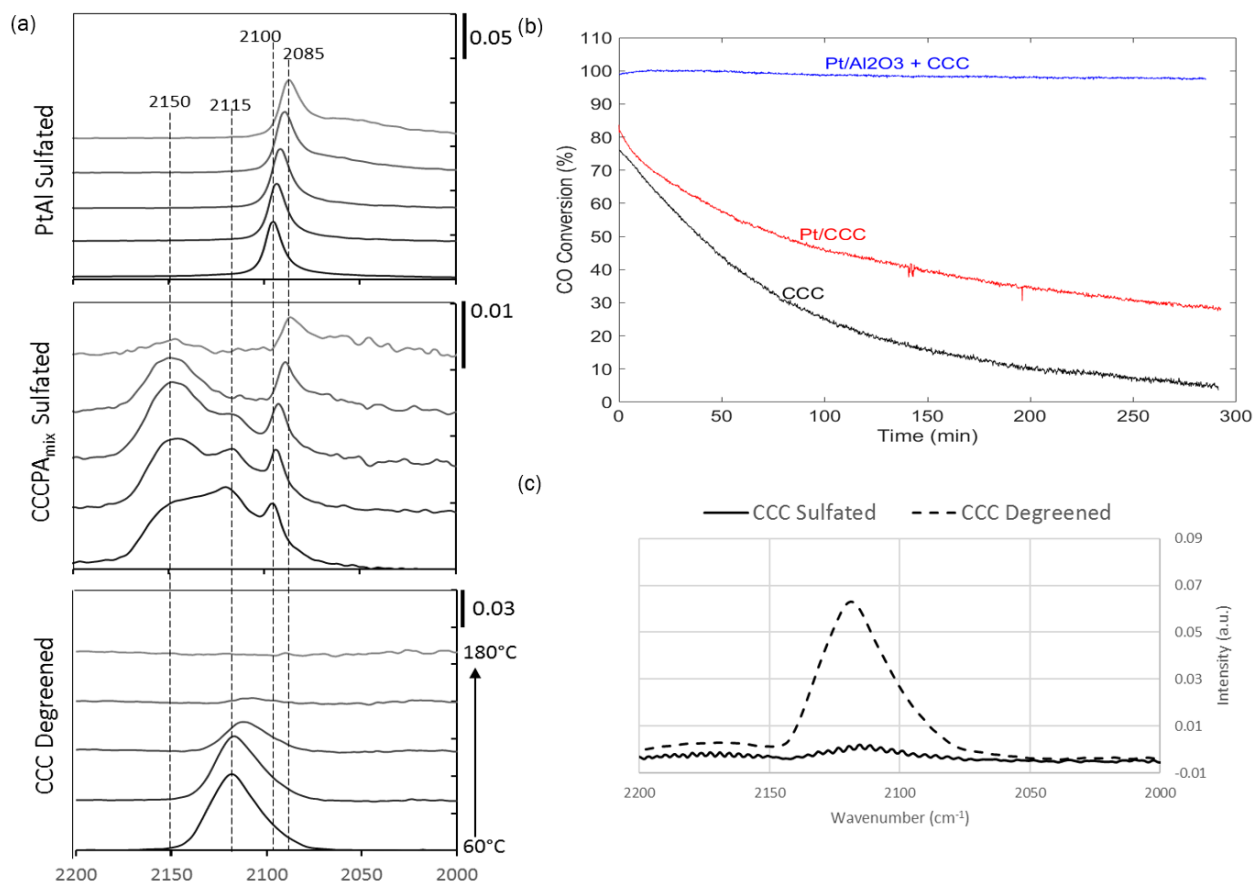


Figure IV.3.1 - (a) DRIFTS spectra of CO-binding over Pt/Al₂O₃ (sulfated) and CCC+Pt/Al₂O₃ physical mixture (sulfated) and CCC (degreened) catalysts. (b) Time-on-stream CO oxidation conversion during 5 ppm SO₂ poisoning in low temperature combustion diesel stream conditions for various catalysts. (c) DRIFTS spectra of CO-binding over degreened (dashed) and sulfated (solid) CCC catalyst.

Efforts to examine the integration of HC and NO trapping materials with traditional platinum group metal-based materials have been another focus this year. In this study, a DOC consisting of a physical mixture of high-performing Pt/ZrO₂@SiO₂ and Pd/ZrO₂@SiO₂ (precious metal deposited on a core-shell ZrO₂@SiO₂ support) was placed after a bed of Pd/ZSM-5 trapping material (Figure IV.3.3c). The trap-DOC system was then aged at 800°C for 4 h and tested using the low temperature combustion diesel protocol defined by U.S. DRIVE where the temperature was ramped at 10°C/min immediately upon exposure to the exhaust gas to best simulate a cold-start environment. The results shown in Figure IV.3.3a are evidence of the performance gains which can be made by the addition of the upstream trapping material. The DOC material baseline (Figure IV.3.3a, dashed) shows T90s = 177°C and 218°C for CO and THC, respectively. With the addition of the trapping material (Figure IV.3.3a, solid) these T90s shift to 134°C and 177°C, respectively. The trap-DOC system was then aged for 50 h at 800°C and subjected to repeated sulfation (5 h, 5 ppm SO₂, 300°C) and

desulfation (lean/rich cycling at 500°C) procedures to evaluate durability. Even after this harsh durability testing, the trap–DOC system still shows significant gains over a similarly aged DOC bed alone (Figure IV.3.3b). Analysis of the trapping material storage and release capabilities under this gas mixture before and after sulfation indicates a loss of nearly all storage for NO, ethylene, and propylene but find very limited effect on the storage of decane (Table IV.3.1) which may explain the continued, though lessened, advantage provided by the trapping material in the trap–DOC system. It is clear that integration of multiple strategies and components will be necessary to achieve the goal of >90% conversion under 150°C and continued improvement in durability is a key factor in taking these highly active materials to a practical level. Efforts in this approach will be focusing on post-aging and post-sulfation materials characterization to understand the cause of trapping and DOC deactivation in our tests.

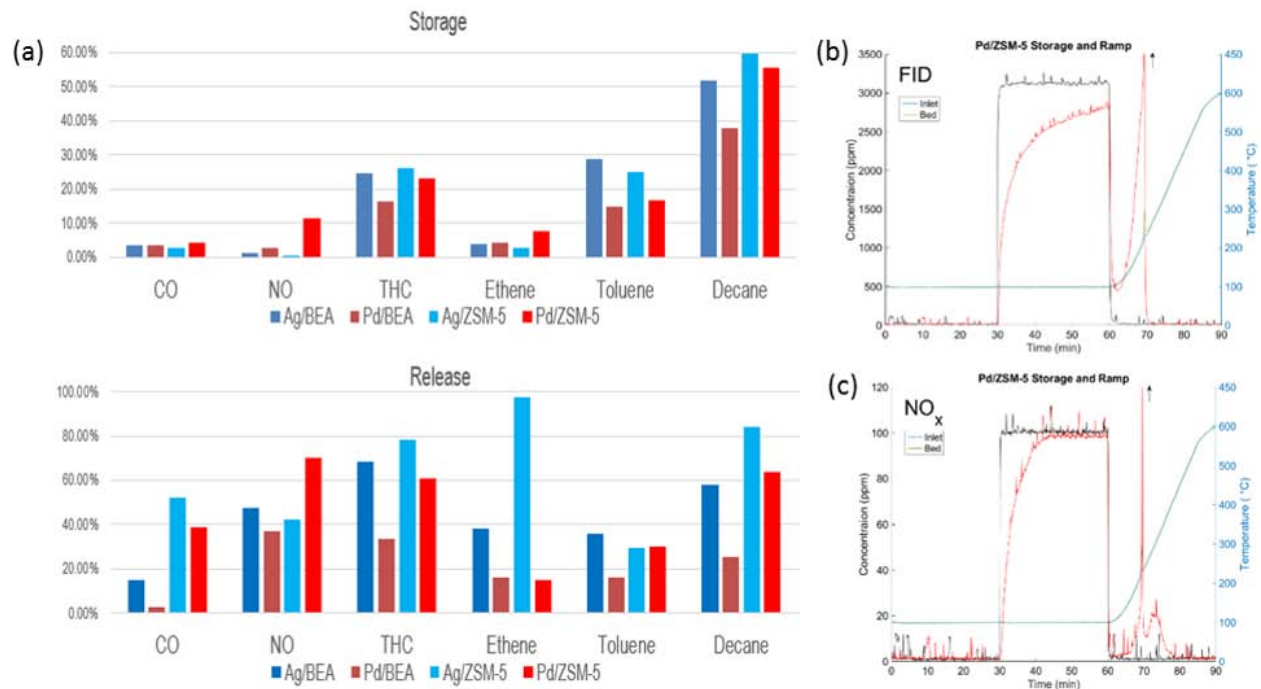


Figure IV.3.2 - (a) Overview of storage and release efficiencies for Ag and Pd-based zeolites under draft ACEC Tech Team trapping protocol. (b) THC storage and release profile (red) for Pd/ZSM-5 as determined by flame ionization detector (FID). (c) NO_x storage and release profile (red) for Pd/ZSM-5. Black lines indicate bypass baseline measurement.

Conclusions

All of the strategies being considered are focused on reducing criteria emissions at low temperatures. While the goal of >90% conversion at 150°C remains a challenge, significant advances have been achieved by integrating the knowledge gained from our varied strategies and improved understanding of the limitations of these materials has been gained. Achievements this year are summarized below.

- Analyzed potential sulfur mitigation seen in CCC+Pt/Al₂O₃ mixture; evidence indicates continued activity of CCC component even after sulfur exposure
- Evaluated HC and NO trapping materials under rigorous protocol conditions showing high potential for trapping long-chain and aromatic HCs in simulated exhaust conditions
- Demonstrated the effectiveness of integrating trapping materials with DOCs; assessed the impact of long-term aging and sulfation

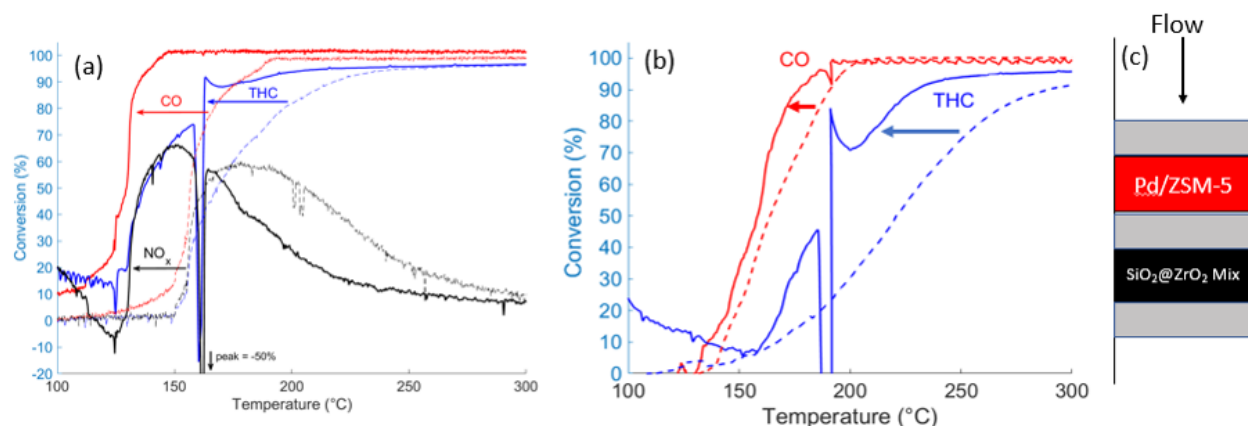


Figure IV.3.3 - Light-off comparisons of DOC (dashed) and dual-bed trap-DOC system (solid) after (a) 800°C, 4 h aging and (b) 800°C, 50 h ageing with repeated sulfations/desulfations. (c) Schematic of dual-bed trap-DOC system.

Table IV.3.1 - Storage Efficiencies of Pd/ZSM-5 Trapping Material Before and After Severe Aging

	800 °C, 4 h	800 °C, 50 h + sulfation/desulfation
NO _x	10.1%	0%
THC (C ₁)	28.2%	24.8%
C ₂ H ₄	9%	0%
C ₃ H ₆	11%	2%
C ₁₀ H ₂₂	35%	34%

Key Fiscal Year 2017 Publications

1. Wang, Chao, Andrew J. Binder, Todd J. Toops, Jochen Lauterbach, and Erdem Sasmaz. "Evaluation of Mn and Sn modified Pd-Ce based catalysts for low-temperature diesel exhaust oxidation." *Emission Control Science and Technology* 3:1 (2017) 37–46.
2. Binder, Andrew J., Todd J. Toops, and James E. Parks II. "Cu-Co-Ce Ternary Oxide as an additive to conventional PGM catalyst for automotive catalysis." submitted to *Angewandte Chemie* (September 2017).
3. Wong, Andrew P., Eleni A. Kyriakidou, Todd J. Toops, and John R. Regalbuto. "The Catalytic Behavior of Pt-Pd Bimetallic Catalysts for Use as Diesel Oxidation Catalysts." *Catalysis Today* 267 (2016) 145–156.
4. (INVITED) Toops, Todd J. "Approaches to Low-Temperature Emission Control to Enable Fuel-Efficient Engines to Meet Future Regulations," ERC-2017 Symposium: Impact of Future Regulations on Engine Technology, Madison, WI, June 15, 2017.
5. Kyriakidou, Eleni A., Todd J. Toops, Michael J. Lance, Jae-Soon Choi, and James E. Parks II. "Advanced support modifications to improve the low-temperature activity and durability of Pd-based emissions control catalysts." 25th North American Catalysis Society Meeting, Denver, CO, June 4–9, 2017.
6. Binder, Andrew J., Todd J. Toops, and James E. Parks II. "Cu-Co-Ce Ternary Oxide as an Additive to Conventional Pt/Al₂O₃ Catalyst for Lean Exhaust Catalysis." 25th North American Catalysis Society Meeting, Denver, CO, June 4–9, 2017.
7. Kyriakidou, Eleni A., Jae-Soon Choi, Todd J. Toops, and James E. Parks II. "A Comparative Study of ZSM-5 and BEA-Zeolites for Low Temperature Passive Adsorption." 25th North American Catalysis Society Meeting, Denver, CO, June 4–9, 2017.

8. Toops, Todd J., Eleni Kyriakidou, Andrew Binder, Jae-Soon Choi, James E. Parks, and Michael Lance. "Low Temperature Emission Control to Enable Fuel-Efficient Engine Commercialization." U.S. DOE Vehicle Technologies Office 2017 Annual Merit Review and Peer Evaluation Meeting, Washington D.C., June 5–9, 2017.
9. (INVITED) Toops, Todd J. "Approaches to Low-Temperature Emission Control to Enable Fuel-Efficient Engine Commercialization." Sustainable Transportation Program Seminar Series at ORNL, Oak Ridge, TN, May 12, 2017.
10. Kyriakidou, Eleni A., Jae-Soon Choi, Todd J. Toops, and James E. Parks II. "A Comparative Study of ZSM-5 and BEA-Zeolites for hydrocarbon trap applications under 'Cold-Start' Conditions." 2016 AIChE Annual Meeting, San Francisco, CA, November 14, 2016.
11. Kyriakidou, Eleni A., Todd J. Toops, Michael J. Lance, Jae-Soon Choi, and James E. Parks II. "Impact of Mixed Oxides Supports on the Durability and Low-Temperature Performance of Pd-based Diesel Oxidation Catalysts." 2016 AIChE Annual Meeting, San Francisco, CA, November 18, 2016.

IV.4 Emissions Control for Lean-Gasoline Engines

Jim Parks, Principal Investigator

Oak Ridge National Laboratory
2360 Cherahala Blvd.
Knoxville, TN 37932
E-mail: parksjeii@ornl.gov

Ken Howden, DOE Technology Manager

U.S. Department of Energy
E-mail: Ken.Howden@ee.doe.gov

Start Date: October 1, 2015	End Date: September 30, 2018	
Total Project Cost: \$1,645,000	DOE share: 1,645,000	Non-DOE share: \$0

Acknowledgments

Co-Authors

Todd Toops, Josh Pihl, Vitaly Prikhodko; Oak Ridge National Laboratory

Project Introduction

Currently, the U.S. passenger car market is dominated by gasoline engine powertrains that operate at stoichiometric air-to-fuel ratios (sufficient fuel is mixed in air such that all of the oxygen in the air is consumed during combustion). Stoichiometric combustion leads to exhaust conditions suitable for three-way catalyst (TWC) technology to reduce NO_x , CO, and hydrocarbon (HC) emissions to extremely low levels. Operating gasoline engines at lean air-to-fuel ratios (excess air) enables more efficient engine operation and reduces fuel consumption; however, the resulting oxygen in the exhaust prevents the TWC technology from reducing NO_x emissions. It is relatively straightforward to operate an engine lean over a significant portion of the load and speed operating range, so, the largest challenge preventing fuel-saving lean combustion in gasoline applications is the control of emissions, primarily NO_x . This project addresses the challenge of reducing emissions from fuel-saving lean gasoline engines in a cost-effective and fuel-efficient manner to enable their market introduction.

In this project, research has been conducted on an emission control concept known as “passive SCR” [1,2,3], where SCR stands for selective catalytic reduction. In the passive SCR approach, NH_3 is generated over the TWC under slightly rich engine operation and then stored on a downstream SCR catalyst. After returning to lean operation, the stored NH_3 reduces NO_x that is not converted over the upstream TWC. In this manner, the TWC controls NO_x during stoichiometric and rich operation of the engine, and the SCR catalyst controls NO_x during lean-engine operation. Utilizing passive SCR, the project has demonstrated NO_x emission reduction efficiencies over 99.8% on a four-cylinder lean gasoline engine. In addition, experiments have been conducted to identify catalyst material compositions that minimize fuel penalties associated with the technique and accelerated aging studies have been conducted to understand the durability of the passive SCR approach.

Objectives

- Assess and characterize catalytic emission control technologies for lean-gasoline engines
- Identify strategies for reducing the costs, improving the performance, and minimizing the fuel penalty associated with emission controls for lean-gasoline engines
- Identify a technical pathway for a lean-gasoline engine to meet U.S. Environmental Protection Agency (EPA) Tier 3 emission regulations with minimal fuel consumption and cost
- Demonstrate the fuel efficiency improvement of a low-emission lean-gasoline engine relative to the stoichiometric-gasoline engine case on an engine dynamometer platform

Approach

This project utilizes the full suite of capabilities available at Oak Ridge National Laboratory's National Transportation Research Center, including a lean-gasoline engine on an engine dynamometer, simulated exhaust flow reactors for detailed catalyst evaluations under carefully controlled operating conditions, material characterization tools for catalyst analysis, and vehicle system level modeling. The combination of catalyst studies on flow reactor and engine platforms is a key component of the project approach. Prototype catalyst formulations are first studied on flow reactors to understand catalytic function and establish operating parameters in a controlled setting; then, select catalyst combinations are studied on the engine platform to characterize performance under realistic exhaust conditions. The engine studies also enable direct measurement of fuel consumption benefits from lean-gasoline engine operation as well as measurement of fuel penalties imposed by the emission control system to function properly.

The engine platform for the project is from a model year 2008 BMW 120i vehicle sold in Europe. The four-cylinder, direct-injection, naturally aspirated engine operates in multiple modes including lean (excess air) and stoichiometric combustion. The BMW 120i employs both a TWC for stoichiometric operation and a lean NO_x trap catalyst for NO_x reduction during lean operation. Although this engine and aftertreatment combination met the relevant emissions regulations in Europe, as configured, its emissions are well above the current and pending U.S. emissions standards. Furthermore, the lean NO_x trap catalyst contains high levels of platinum group metals, which add significantly to the overall cost of the vehicle. The goal for this project is to identify emissions control technologies that can meet the U.S. EPA Tier 3 emission standards. In addition to the emissions goal, the project aims to maximize the fuel efficiency benefit from lean-gasoline engine operation and minimize system cost.

The catalysts studied in the project were either supplied or recommended by collaborating partner Umicore, a major catalyst supplier to the automotive industry. Other collaborating partners include General Motors for project guidance and the University of South Carolina for research on catalyst aging and durability.

Results

Based on bench flow reactor study results on the effectiveness of different TWC formulations for NH₃ production under rich exhaust conditions, a Pd-based TWC without oxygen storage was selected for full system studies of the passive SCR approach on the lean gasoline engine. For the study, a pseudo-transient drive cycle provided by General Motors (Figure IV.4.1) was employed to enable emissions and fuel efficiency measurements under realistic engine operation. The study, conducted on the BMW four-cylinder lean gasoline engine, demonstrated the following:

- 0.03 g/mi NO_x+HC tailpipe emissions (equivalent to the EPA Tier 3 Bin 30 level) for the pseudo-transient drive cycle
- A 6% gain in fuel economy over the stoichiometric operation baseline
- CO tailpipe emissions of 2 g/mi (or twice the EPA Tier 3 Bin 30 level)

It is important to note that the catalysts were degreened for the study but not aged to full useful life levels (150,000 mi) that are required for EPA Tier 3 emission compliance. Nonetheless, the study demonstrated effective NO_x and HC emission control with significant fuel economy gains due to the lean engine operation. However, a portion of the project is specifically focusing on measuring the impact of both thermal aging and exhaust level sulfur on the passive SCR approach. Research is continuing to improve on the demonstrated performance with a focus on minimizing the fuel penalties associated with the approach to maximize fuel economy; further control of CO emissions is also a focus of the continuing research.

Previous bench flow reactor studies showed that adding NO_x storage to the TWC can provide overall system benefits by reducing the quantity of NO_x reaching the SCR catalyst during lean operation. The effect was most beneficial at low temperatures (<400°C). An engine-based study of a TWC with a NO_x storage component was conducted and showed promising results for the potential to minimize fuel penalties associated with NH₃ generation.

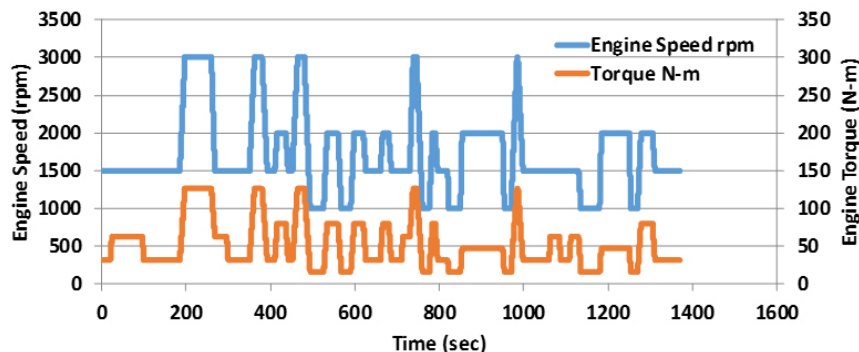


Figure IV.4.1 - Pseudo-transient drive cycle used for engine-based studies of the passive SCR system

Details from the engine-based study of the TWC with NO_x storage are shown in Figure IV.4.2. Here emissions during the lean-rich cycle required for passive SCR operation are shown. Figure IV.4.2a shows the results for the TWC with NO_x storage; note that the TWC also contains O_2 storage. For comparison, Figure IV.4.2b shows emissions data with a TWC that does not contain NO_x or O_2 storage components. Dramatic differences in the two TWC formulation results are apparent in both the lean and rich phases of the cycle. For the TWC with NO_x storage (Figure IV.4.2a), NO_x emissions downstream of the TWC (“ NO_x out”) are lower for the initial portions of the lean period when NO_x emissions are being stored by the NO_x storage component. Then, during the subsequent rich period, NH_3 emissions (“ NH_3 out”) increase dramatically as the stored NO_x is converted to NH_3 by the TWC with reductant produced by the engine during rich operation. In comparison, for the TWC without NO_x storage (Figure IV.4.2b), no sharp rise in NH_3 production is observed beyond the concentration of incoming NO_x (“ NO_x in”), and NO_x out emissions during the lean period are essentially the same as the inlet NO_x level. Based on these results, NH_3 can be produced more efficiently by the TWC with NO_x storage which can reduce fuel penalties.

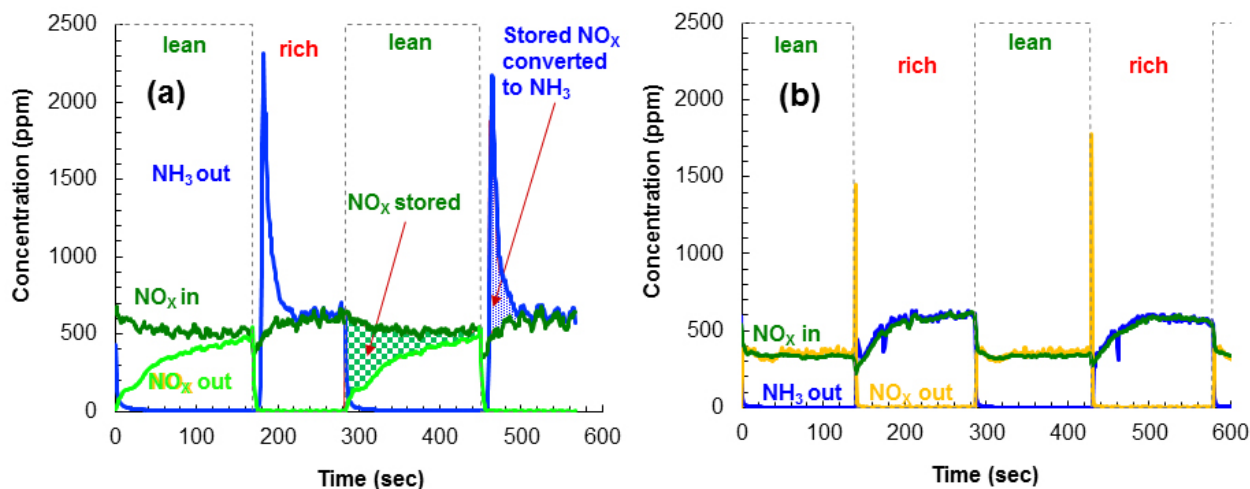


Figure IV.4.2 - NO_x and NH_3 concentration data over the passive SCR lean-rich cycle for (a) a TWC with O_2 and NO_x storage components and (b) a TWC without O_2 and NO_x storage components

As expected based on the previous bench flow reactor experiments, the benefits of NH_3 generation due to the NO_x storage component on the TWC were highly dependent on temperature. In addition, the engine-based experiments also defined the effect of equivalence ratio (λ) during rich operation on the NH_3 production. Note that as λ decreases, combustion becomes more fuel rich. Figure IV.4.3 shows NH_3 produced downstream of the TWC and the associated TWC inlet NO_x concentration as a function of λ at exhaust temperatures of 395°C (a) and 492°C (b). For the 395°C case, the concentration of NH_3 produced exceeds the inlet NO_x concentration for $\lambda \leq 0.97$. In fact, at some points NH_3 concentrations were double that of the inlet NO_x . These results show the effect of NO_x storage on increasing the net NH_3 production during rich operation. However, for the 492°C case (Figure IV.4.3b), the effect is not observed. At the higher temperature of 492°C, NO_x is not readily stored on

the TWC, and the associated benefit disappears. It is important to note that CO and HC emissions increase as λ decreases. So, while the data in Figure IV.4.3 can be used to determine the optimum NH_3 producing conditions to achieve NO_x reduction, care must be taken to avoid conditions that will increase CO and HC emissions and effect emission compliance for those emission species.

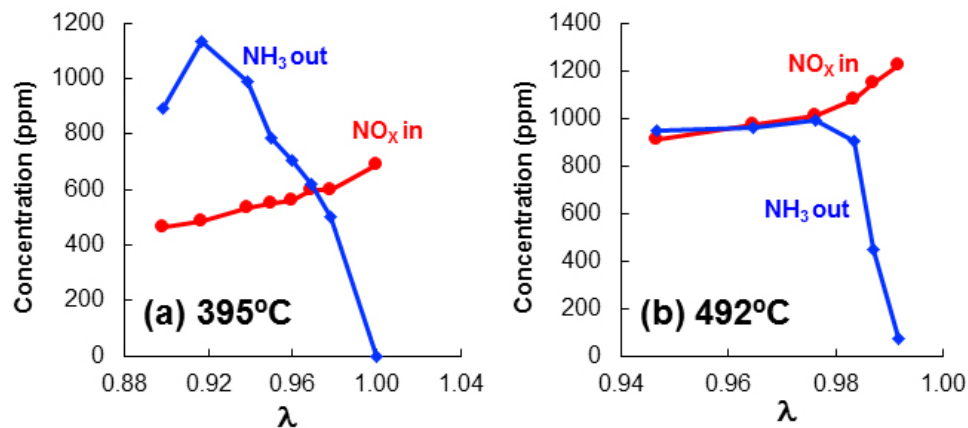


Figure IV.4.3 - Concentration of NO_x entering the TWC (" NO_x in") and NH_3 downstream of the TWC (" NH_3 out") as a function of the equivalence ratio during rich operation of a lean-rich cycle for average exhaust temperatures of (a) 395°C and (b) 492°C. Results are shown for the Pd-based TWC with a NO_x storage component.

To date, the project has demonstrated that NO_x emissions from lean-gasoline engines can effectively be controlled by a passive SCR approach that utilizes NH_3 production over a TWC to reduce NO_x over a downstream SCR catalyst. While a 6% fuel economy benefit was observed for a lean-gasoline engine employing passive SCR, more efficient NH_3 production can increase the fuel economy benefit, and adding NO_x storage to the TWC is an approach to achieve the greater NH_3 production efficiency. The project will continue to research methods to maximize the fuel economy benefit of the lean-gasoline engine while meeting EPA Tier 3 emission regulation levels.

Conclusions

- Passive SCR enacted on a lean-gasoline engine demonstrated 0.03 g/mi NO_x +HC tailpipe emissions (equivalent to the EPA Tier 3 Bin 30 level) and a 6% gain in fuel economy compared with the stoichiometric operation baseline over a pseudo-transient drive cycle.
 - More research is needed to further control CO emissions which were 2 g/mi (or twice the EPA Tier 3 Bin 30 level) and to demonstrate full useful life (150,000 mi) equivalent performance.
- A NO_x storage component added to the TWC of the passive SCR system can enable more efficient NH_3 generation as thus provides a pathway for increasing the fuel economy benefit relative to the current demonstrated level (of 6%).
 - However, the benefits of the NO_x storage component are highly temperature dependent.

References

1. Li, W., K. Perry, K. Narayanaswamy, C. Kim, et al. "Passive Ammonia SCR System for Lean-burn SIDI Engines." *SAE Int. J. Fuels Lubr.* 3(1):99–106, 2010, doi:10.4271/2010-01-0366.
2. Kim, C., K. Perry, M. Viola, W. Li, et al. "Three-Way Catalyst Design for Urealess Passive Ammonia SCR: Lean-Burn SIDI Aftertreatment System." SAE Technical Paper 2011-01-0306, 2011, doi:10.4271/2011-01-0306.
3. Guralp, O., G. Qi, W. Li, and P. Najt. "Experimental Study of NO_x Reduction by Passive Ammonia-SCR for Stoichiometric SIDI Engines." SAE Technical Paper 2011-01-0307, 2011, doi:10.4271/2011-01-0307.

Key Fiscal Year 2017 Publications

1. Prikhodko, V., J. Parks, J. Pihl, and T. Toops. "Ammonia Generation and Utilization in a Passive SCR (TWC+SCR) System on Lean Gasoline Engine." *SAE International Journal of Engines*, 9 (2), 1289–1295, 2016, DOI: 10.4271/2016-01-0934.
2. Zelenyuk, A., J. Wilson, D. Imre, M. Stewart, G. Muntean, J. Storey, V. Prikhodko, S. Lewis, M. Eibl, and J. Parks. "Detailed Characterization of Particulate Matter Emitted by a Lean-Burn Gasoline Direct Injection Engine." *International Journal of Engine Research*, November 2016, DOI: 10.1177/1468087416675708.
3. Parks, J., J. Storey, V. Prikhodko, M. Debusk, and S. Lewis. "Filter-based control of particulate matter from a lean gasoline direct injection engine." *SAE Technical Paper* 2016-01-0937, 2016, DOI: 10.4271/2016-01-0937.
4. Sappok, A., P. Ragaller, A. Herman, L. Bromberg et al. "On-Board Particulate Filter Failure Prevention and Failure Diagnostics Using Radio Frequency Sensing." *SAE Int. J. Engines* 10(4):2017, doi:10.4271/2017-01-0950.
5. Prikhodko, V., J. Parks, J. Pihl, and T. Toops. "Passive SCR for lean gasoline NOX control: engine-based strategies to minimize fuel penalty associated with catalytic NH₃ generation." *Catalysis Today*, 267, 202–209, 2016, doi: 10.1016/j.cattod.2016.01.026.
6. Brookshear, D., J. Pihl, T. Toops, B. West, and V. Prikhodko. "The selective catalytic reduction of NO_x over Ag/Al₂O₃ with isobutanol as the reductant." *Catalysis Today*, 267, 65–75, 2016, doi:10.1016/j.cattod.2016.01.034.

IV.5 Cummins-ORNL SmartCatalyst CRADA: NO_x Control and Measurement Technology for Heavy-Duty Diesel Engines

Bill Partridge, Principal Investigator

Oak Ridge National Laboratory
2360 Cherahala Blvd.
Knoxville, TN 37932
E-mail: partridgewp@ornl.gov

Ken Howden, DOE Technology Manager

U.S. Department of Energy
E-mail: Ken.Howden@ee.doe.gov

Start Date: October 1, 2015	End Date: September 30, 2018	
Total Project Cost: \$1,800,000	DOE share: \$900,000	Non-DOE share: \$900,000

Acknowledgments

Co-Authors

Josh Pihl, Oak Ridge National Laboratory
Saurabh Joshi, Neal Currier, Krishna Kamasamudram, Alex Yezerets; Cummins Inc.

Project Introduction

A combination of improved technologies for control of NO_x and particulate emissions are required to efficiently meet increasingly stringent emission regulations. This cooperative research and development agreement (CRADA) section focuses on catalyst technologies. Improved catalyst system efficiency, durability, and cost can be achieved through advanced control methodologies based on continuous catalyst state monitoring; the overarching goal of this CRADA section is to enable self-diagnosing or smart catalyst systems. These are enabled by basic and practical insights into the transient distributed nature of catalyst performance, improved catalyst models, insights suggesting control methodologies, and instrumentation for improved control. Development and application of enhanced diagnostic tools is required to realize these technology improvements.

Objectives

- Understand the fundamental chemistry of automotive catalysts
- Identify strategies for enabling self-diagnosing catalyst systems
- Address critical barriers to market penetration

Approach

The CRADA applies the historically successful approach of developing and applying minimally invasive advanced diagnostics to resolve spatial and temporal function and performance variations within operating catalysts. Diagnostics are applied to study the detailed nature and origins of catalyst performance variations; this may be spatial and temporal variations unique to each catalyst function during operating and how these vary with ageing. Measurements are used to assess and guide model development. A combination of measurements and modeling are applied to understand how catalysts function and degrade, develop device and system models, and develop advanced control strategies.

Results

In Fiscal Year 2017, the CRADA focused on assessing the transient performance of the Cummins selective catalytic reduction (SCR) model via spatiotemporally resolved intra-catalyst SpaciMS (spatially resolved

capillary inlet mass spectrometer) measurements, characterizing transient conversion inflections, conversion inflection (CI), occurring at SCR onset, and advancing SCR models and catalyst state assessment.

- Spatiotemporal performance of SCR model assessed
 - Good transient and steady-state (SS) performance in back catalyst half and effluent
 - Transient SCR-onset features at catalyst front zone not captured by model
 - Results indicate opportunity to improve robust nature of SCR model
- Transient SCR-onset CI characterized
 - Most apparent at catalyst front and becomes less apparent along catalyst length
 - Becomes more distinct with increasing temperature
 - Only occurs at SCR onset and not at SCR termination
 - More apparent for Standard than Fast SCR; Fast SCR has CI only at highest temperatures
- CIs are useful for advancing catalyst technology
 - Useful for catalyst state assessment and implementing advanced control strategies
 - Provide insights regarding catalyst mechanisms and kinetic parameters

Transient Assessment of Cummins SCR Model

The transient performance of the Cummins SCR model was assessed by comparing predicted results and experimental results over a four-step protocol. The protocol contains transient and SS regions (Figure IV.5.1); Steps 1–4 corresponding to NO cleaning, SCR, NH₃ saturation, and NO cleaning, respectively. Results from a commercial Cu/chabazite (CHA) SCR catalyst evaluated on a bench reactor at Oak Ridge National Laboratory (ORNL) were used for the analysis; reaction conditions were 300°C, 40,000 hr⁻¹ space velocity, 5% H₂O + 10% O₂ + Ar balance + 200 ppm Standard SCR (NO and NH₃). Spatiotemporal intra-catalyst measurements were made via SpaciMS in a direct sampling configuration using 200- μ m outside diameter capillaries with sampling flow of \sim 10 μ L/min.

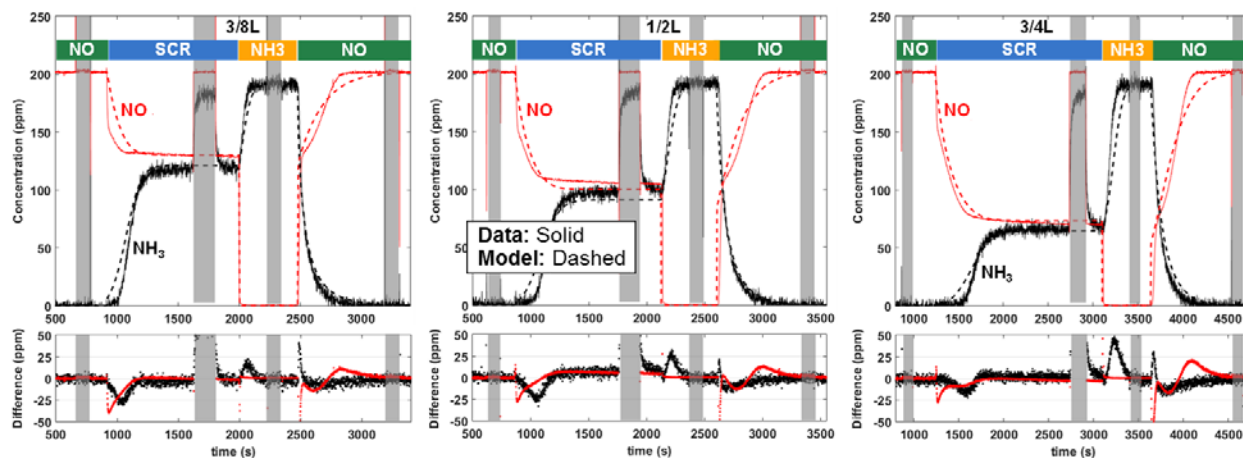


Figure IV.5.1 - Spatiotemporal comparison of model results with measurements at 3/8L, 1/2L and 3/4L, where L is the overall catalyst length. Comparison is over the four-step protocol which includes step transients and SS sections.

The grey sections are for analytical purposes and to be ignored. Top panels compare predicted and measured transient NO and NH₃ concentration distributions, and the lower panels highlight differences in the predicted and measured results.

Figure IV.5.1 shows the model comparison in the mid-catalyst regions, and how the transient and SS results match the measurements very well in this region, and by extension in the effluent. Specifically, the model captures the fast initial onset transients of Steps 3 and 4, although some differences are apparent in the slower Step 4 transient. In contrast, CIs occur at SCR onset in the catalyst front and are not captured by the model as shown in Figure IV.5.2. Conversion inflections are a transient process characterized by initial conversion growth to an intermediate value greater than exists at SS before degrading to the SS value; CI is greatest at the catalyst front where NO_x and NH_3 concentration are high, and become less distinct along the catalyst axis as conversion progresses. This demonstrates how models can produce correct effluent results without accurately reflecting the intra-catalyst detail, and how models can be most critically assessed via their ability to follow the spatiotemporal evolution of reactions throughout the catalyst. Models that accurately follow such reaction evolution are likely more robust and can be applied across a broader development space. The SpaciMS and CI measurements indicate an opportunity to improve the catalyst model that would not have been apparent with integral or effluent analysis.

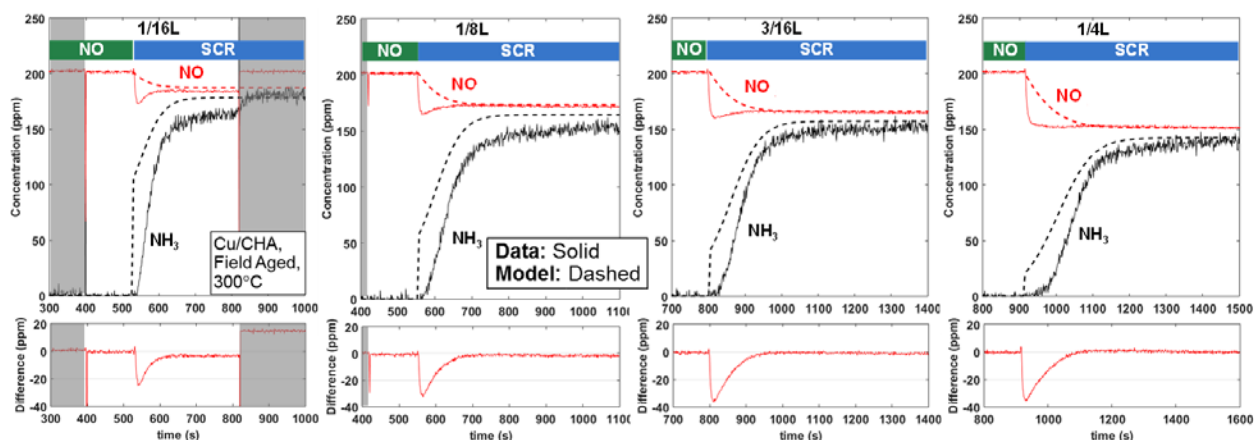


Figure IV.5.2 - Spatiotemporal comparison of model results with measurements at 1/16L, 1/8L, 3/16L and 1/4L, where L is the overall catalyst length. Comparison is over the four-step protocol which includes step transients and SS sections. The grey sections are for analytical purposes and to be ignored. Top panels compare predicted and measured transient NO and NH_3 concentration distributions, and the lower panels highlight differences in the predicted and measured results.

Characterizing SCR-Onset Transient Conversion Inflections

Spatiotemporal mapping of CI nature was investigated for a field-aged commercial Cu/CHA SCR catalyst on a bench reactor via direct-sampling SpaciMS measurements using 200- μm outside diameter capillaries with $\sim 10 \mu\text{L}/\text{min}$ sampling rate for intra-catalyst spatiotemporally resolved concentration measurement [1,2,3,4]. Figure IV.5.3, left, shows spatiotemporally distributed SCR-onset CI transients throughout the catalyst and how they are most distinct at the catalyst front; in this case CI is apparent in the front $\sim 3/8\text{L}$ and not apparent in the catalyst back or effluent [5]. Similar CI has been observed for Cu-Beta [6], and anything that causes higher NO_x and NH_3 concentrations to exist deeper into the catalyst (e.g., ageing, temperature) will cause a corresponding expansion of the CI zone [5]. Figure IV.5.3, right, shows SCR-onset transients at 400°C and 500°C, for Standard SCR and Fast SCR over a range of concentrations and ammonia-to- NO_x ratios (ANR). At 400°C, a CI transient at SCR onset is apparent for Standard SCR, but not Fast SCR, which has a fast step-like onset. At 500°C, the Standard SCR CI appears faster (higher frequency) than at 400°C, and now CI is observed under Fast SCR, albeit smaller and less distinct. Normalization shows that the onset transients do not vary with concentration or ANR (not shown). Additional measurements at 200°C and 600°C (not shown) confirm the trend of CI being increasingly apparent at higher temperatures. In general Cu/SCR CI becomes more apparent with increasing temperature, occurs only at SCR onset and not at termination, is more pronounced with Standard SCR vs. Fast SCR, and is only apparent in Fast SCR at higher temperatures.

Similar CI has been reported for Fe/SCR catalysts as due to NH_3 inhibition [7]. Such inhibition-driven CI occurs at both SCR onset and termination, and is more pronounced at lower temperatures where NH_3 capacity is greater. Thus, several aspects of Cu/SCR CI are inconsistent with those of Fe/SCR CI, which may suggest a

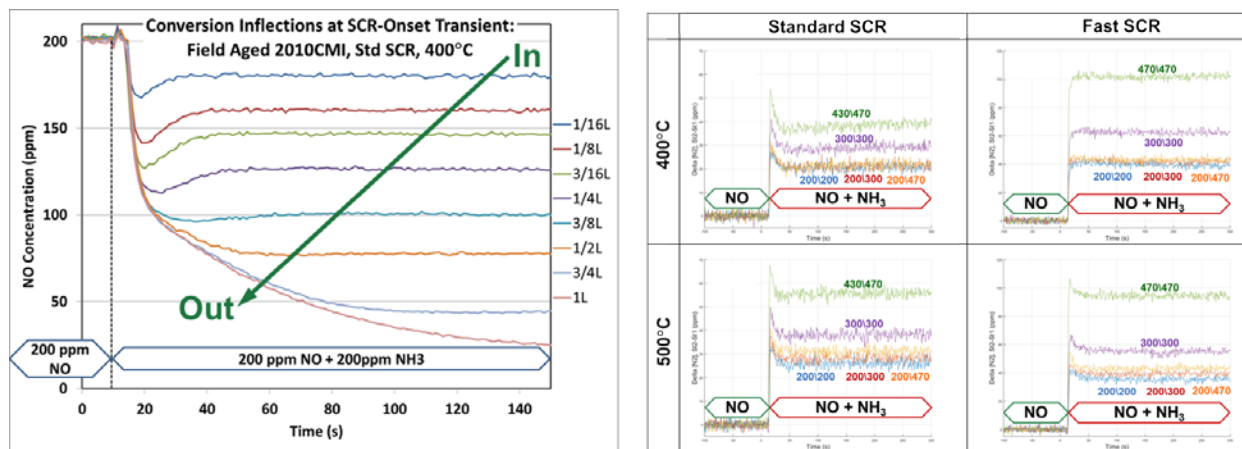


Figure IV.5.3 - (Left) Spatiotemporally resolved SCR-onset transients throughout a field-aged commercial honeycomb-monolith-supported Cu/CHA catalyst, where L is the overall catalyst length. Field-aged commercial Cu/CHA, 400 cpsi, 40,000 hr⁻¹ space velocity, 200 ppm NO + 200 ppm NH₃ + 10% O₂ + 5% H₂O + Ar balance, 400°C, 400 cpsi, 40,000 hr⁻¹ space velocity (Partridge et al. 2015). (Right) N₂ transients associated with SCR-onset for various ANR (1, 1.5, 2.4) and NO_x concentrations (200 ppm, 300 ppm, 430 ppm, and ANR~1), at 400°C and 500°C, and under Standard SCR and Fast SCR conditions. Field-aged commercial Cu/CHA, 400 cpsi, 40,000 hr⁻¹ space velocity, 10% O₂ + 5% H₂O + Ar balance, 1/8 length from catalyst inlet.

differing origin. In future work, we will use these Cu/SCR CI transients to gain mechanistic insights regarding the SCR reaction and to determine kinetic parameters for improving SCR modeling.

Advancing SCR Models and Catalyst State Assessment

Continuation of the research into early Fiscal Year 2018 has shown that CI provides insights regarding SCR mechanisms and a pathway for determining global kinetic parameters. This joint experimental- and modeling-based work has explained the nature of Cu/SCR CI via a route not related to NH₃ coverage inhibition. We will continue this research into Fiscal Year 2018 and report the results in the corresponding annual report.

Conversion inflections provide a pathway for practical catalyst state assessment for implementing advanced control strategies, e.g., actively adjusting urea dosing through the catalyst lifetime. Figure IV.5.4 shows NH₃ conversion distributions for the commercial Cu/CHA catalyst in three aged states: degreened, hydrothermal aged, and field-aged. Conversion generally flattens and uses a greater portion of the catalyst with increasing ageing. Notably, CI is observed above a common NH₃ threshold in the catalyst front regions for all aged states of the catalyst [5]; similar results are observed at a different temperature but with a different NH₃ threshold. Thus, aged state is reflected in the depth that CI extends into the catalyst with greater depth corresponding to greater ageing, a method for detecting the CI zone could be used for catalyst state assessment. While the CI features are confined to the intra-catalyst front regions as shown in Figure IV.5.3, left, they may influence the time at which conversion crosses a control threshold, e.g., the time after SCR onset to reach a 50 ppm effluent threshold may depend on the extent of intra-catalyst CI and be used to assess the same and the related aged state. This research focused on catalyst state assessment will be analyzed in the context of the new CI understanding and continue into Fiscal Year 2018.

Conclusions

A model of Cu/CHA SCR has been evaluated in terms of spatiotemporal performance throughout an operating catalyst via SpaciMS measurements. While the model has good spatial, transient, and SS performance in the back catalyst half and effluent, it misses key transient SCR-onset CI features in the front catalyst regions. The CI nature has been experimentally characterized and has many features not consistent with NH₃ coverage inhibition, i.e., it becomes more pronounced at higher temperatures and only occurs at SCR onset and not at termination. Furthermore, incorporating an inhibition term does not allow the model to accurately predict the CI nature. Further work in Fiscal Year 2018 has shown that CI details can be used to understand SCR

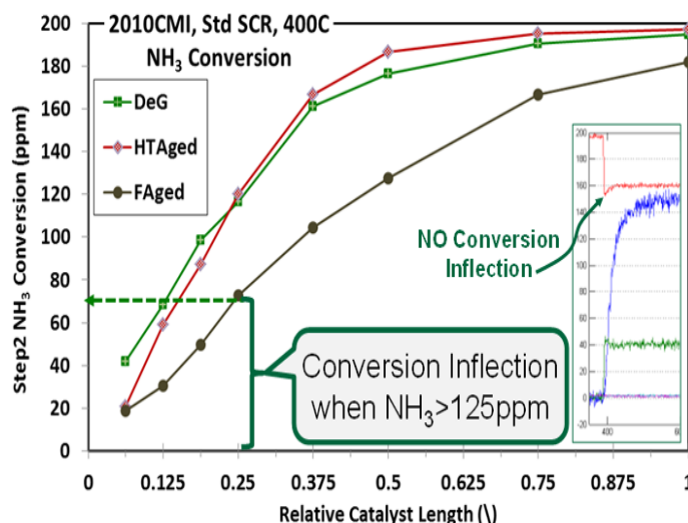


Figure IV.5.4 - Ammonia conversion distributions for a commercial Cu/CHA SCR catalyst in degreened (DeG), hydrothermally aged (HTAged), and field-aged (FAged) states. Conversion inflections occur in the front catalyst regions above a common NH_3 threshold for all aged states, extending deeper into the catalyst with increasing temperature. The threshold varies with operating temperature. In general, anything that causes high NH_3 and NO_x concentrations to exist deeper into the catalyst will correspondingly expand the CI zone [5].

mechanisms and kinetic parameters; this work will continue in Fiscal Year 2018. CIs vary with catalyst state and may provide a pathway for implementing advanced control.

References

1. Partridge, W.P. et al., SAE Paper 2000-01-2952.
2. Partridge, W.P. and J.-S. Choi, *Appl. Catal. B* 91 (2009) 144–151.
3. Morgan, K. et al., *ACS Catalysis* 6 (2016) 1356–1381.
4. Partridge, W.P. and J.-S. Choi, “ACHEM: spatially-resolved operando measurements in heterogeneous catalytic reactors.” *The Royal Society of Chemistry*, pp 1–81, 2017.
5. Partridge, W.P. et al., 2015 DOE CLEERS Workshop, <http://cleers.org/workshops/workshop2015/index.php?presentation=1>.
6. Auvray, X. et al., *Appl. Catal. B* 126 (2012) 144–152.
7. Colombo, M. et al., *Appl. Catal. B*, 111-112 (2012) 106–118.

Key Fiscal Year 2017 Publications

1. Ruggeri, Maria Pia, Tomasso Selli, Isabella Nova, Enrico Tronconi, Josh A. Pihl, Todd J. Toops, William P. Partridge. “New Mechanistic Insights in the NH_3 -SCR Reactions at Low Temperature” *Topics in Catalysis* 59:10-12 (2016) 907-912; doi.org/10.1007/s11244-016-0567-1. Archival journal publication.
2. Cunningham, Michael, Mi-Young Kim, Venkata Lakkireddy, William Partridge. “Axial NO_2 Utilization Measurements within a Partial Flow Filter during Passive Regeneration,” SAE 2017 World Congress, SAE Technical Paper 2017-01-0988. doi:10.4271/2017-01-0988. Detroit, MI, April 4–6, 2017.
3. Partridge, William. “Resolving Transient Reaction Distributions within Honeycomb-Monolith Catalysts via SpaciMS & Spaci-like Methods.” MODEGAT V, Bad Herrenalb, Germany, September 5, 2017. Invited tutorial.

4. Partridge, William. "Resolving Transient Reaction Distributions within Honeycomb-Monolith Catalysts via SpaciMS & Spaci-like Methods." Umicore AG & Co. KG, Hanau-Wolfgang, Germany, September 8, 2017. Invited.
5. Partridge, W.P., M. Salazar, J.A. Pihl, N. Currier, S. Joshi, A. Yezerets, K. Kamasamudram. "Cummins-ORNL/FEERC Emissions CRADA: NO_x Control & Measurement Technology for Heavy-Duty Diesel Engines, Self-Diagnosing SmartCatalyst Systems." 2016 DOE Vehicle Technologies Program Annual Merit Review, Washington, DC, June 9, 2016. http://energy.gov/sites/prod/files/2016/06/f32/ace032_partridge_2016_o.pdf

IV.6 Ash-Durable Catalyzed Filters for Gasoline Direct Injection (GDI) Engines

Hee Je Seong, Principal Investigator

Argonne National Laboratory
9700 South Cass Avenue
Argonne, IL 60439
E-mail: hseong@anl.gov

Ken Howden, DOE Technology Manager

U.S. Department of Energy
E-mail: Ken.Howden@ee.doe.gov

Start Date: October 1, 2015 End Date: September 30, 2017
Total Project Cost: \$1,000,000 DOE share: \$1,000,000 Non-DOE share: \$0

Acknowledgments

Co-Author

Seungmok Choi; Argonne National Laboratory

Project Introduction

GDI engines, which feature direct injection of gasoline fuel into engine cylinders typically at increased compression ratio, offer low fuel consumption and high power output. Although these benefits of GDI engines contribute to their increasing market share for passenger vehicles, their high particulate emissions will need to be significantly reduced to comply with future regulations. To achieve this goal, gasoline particulate filters (GPFs) have been developed for GDI engines, like diesel particulate filters for diesel engines. Despite the similarity in function of GPFs and diesel particulate filters, however, GPFs require high porosity filters compared to diesel particulate filters to minimize backpressure sensitivity as GDI engines present high exhaust temperatures. In addition, GPFs can act as four-way catalysts that remove NO_x , CO, and hydrocarbons as well as particulates, thanks to the three-way catalyst (TWC) inner wall coating technology. As metal additives from engine oil are produced and eventually accumulated in GPFs with increasing vehicle mileage, it is of great interest if TWC performance will be degraded with increased ash loading as seen with TWCs coated with a monolith surface equipped in conventional gasoline engines.

The deactivation of ash-loaded TWC–GPFs was characterized by studying TWC performance in a lab-flow reactor using engine exhaust. Deactivation factors on TWC coatings in GPFs were examined using various analytical tools at Argonne, identifying Pd sintering and reduction of PdO_x and CeO_2 in TWC components resulting from engine oil-derived gaseous chemicals.

Objectives

Overall Objectives

- Understand performance of TWC-coated GPFs (TWC–GPFs) with variation of filter and coating design parameters
- Determine whether TWC–GPFs are deactivated by engine oil-derived ash chemicals and find potential deactivation mechanisms
- Propose an ideal combination of filter and coating design parameters that benefits TWC performance and backpressure increase under engine oil-derived aging conditions

Fiscal Year (FY) 2017 Objectives

- Propose deactivation mechanisms of TWC–GPFs with engine oil-derived ash chemicals

- Examine interactions of ash chemicals and TWC components
- Demonstrate catalyst deteriorating factors by evaluating Pd sintering, oxygen storage capacity (OSC) in aged TWCs, Pd–OSC interaction and PdO_x/CeO₂ reducibility
- Build a lab-flow system that enables ash loading of multi-reactors and kinetic study from a lab-scale flow reactor

Approach

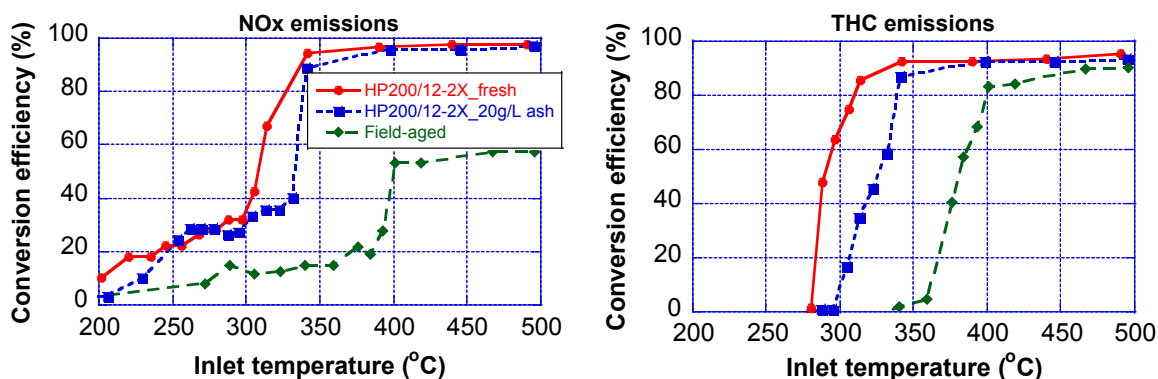
This project aims at detailing the impact of ash loading on TWC–GPF performance in variation of TWC coating level, GPF design and other parameters, ultimately proposing optimized design parameters of the TWC coating and GPF designs taking into account ash-derived chemical aging. Advanced prototype TWC–GPFs with different coating levels and filter types are prepared and their performance is examined with ash loading in terms of pressure drop, number and mass filtration efficiencies, and gaseous emissions conversion. Also, in order to find potential aging factors in TWC–GPFs, ash distributions in an aged filter are analyzed by elemental mapping of wall microstructures and by X-ray microtomography. Moreover, interactions between catalysts and ash elements (in particular phosphorus) and filter porosities are further examined. In addition, metal additive-dependent ash chemistries are explored to detail potential ash inhibiting factors by transmission electron microscopy and Advanced Photon Source (APS) facilities.

Results

FY 2017 accomplishments are listed below:

- Demonstrated/proposed deactivation mechanisms of TWCs coated in GPFs under engine oil-derived aging conditions based on extensive characterization results, distinct from surface-coated conventional TWCs on monoliths
- Built a lab-flow system and evaluated TWC performances of lab- and field-aged TWCG–PFs under identical operating conditions
- Obtained newly formulated TWC–GPFs from a participant and completed evaluation of their initial TWC performances using the lab-flow system

Gaseous emissions conversions of TWC–GPFs were noted to decrease with ash loading under a low temperature lab-aging condition, as presented in FY 2016 result. To better understand aging effects, a field-aged TWC–GPF run with 100,000 miles was also examined together with fresh and lab-aged TWC–GPF samples. Figure IV.6.1 shows that gaseous emissions conversions were delayed below 350°C with ash loading from the lab-aging condition, when the newly built lab-flow system was used, consistent with FY 2016 results from the bench-scale flow reactor. In comparison, the field-aged sample was observed to have significantly lower conversions in the examined wide temperature range. Since there was no fresh counterpart



THC – total hydrocarbons

Figure IV.6.1 - Gaseous emissions conversions of fresh and aged TWC–GPFs with temperatures at the space velocity of 40,000 h⁻¹ from the lab-flow system

of this field-aged sample available, characterization tools were employed to detail whether TWC poisoning contributed to the decreased conversions.

Scanning transmission electron microscopy–electron dispersive X-ray spectroscopy was used to examine elemental distributions of TWC and ash components for crushed TWC–GPF samples, as represented in Figure IV.6.2. Small nanoparticles of an active catalyst component, palladium (Pd), were uniformly spread on OSC materials of zirconium (Zr) and cerium (Ce) elements in the TWC for the fresh sample. In the case of the field-aged sample, however, relatively large Pd particles were found as well as small nanoparticles so that Pd distribution was not uniform, indicating Pd sintering occurred during the field-aging test, which was also observed for the lab-aged sample (data excluded). In addition, the mappings of phosphorus (P) and sulfur (S) elements derived from engine oil were almost identical to those of Zr/Ce elements, while the formers were different from that of calcium (Ca) element from engine oil. Since Ca and Zr/Ce were located on outside wall and inside wall, respectively, the result proposed that P and S were bound with Zr/Ce during the field aging.

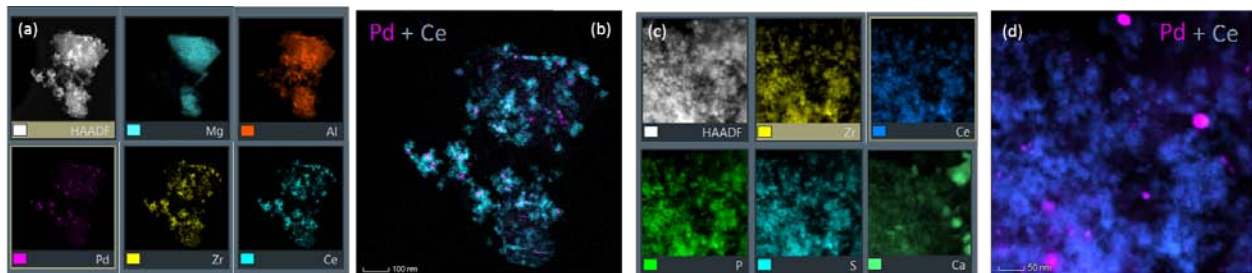
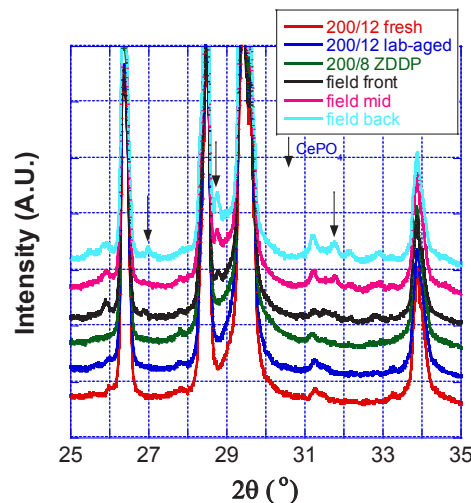


Figure IV.6.2 - Scanning transmission electron microscopy–electron dispersive X-ray spectroscopy measurements of (a) and (b) fresh TWC–GPF, and (c) and (d) field-aged TWC–GPF.

The powder X-ray diffraction (PXRD) patterns of crushed fresh and aged TWC–GPF samples indicate that there were unique CePO_4 crystalline peaks observed only for the field-aged samples (Figure IV.6.3), which tended to increase from front to back, implying that CePO_4 formation became stronger along the direction of the exhaust flow path. This result suggests that the reason why P and Ce maps show similar distributions was because of CePO_4 formation, as noted from others from conventional TWCs [1]. The contaminants present in a real (TWC. Although S compounds were not detected from the PXRD due to their low content, they were presumed to be $\text{Ce}_2(\text{SO}_4)_3$ as examined [2].



A.U. – arbitrary units

Figure IV.6.3 - PXRD patterns of TWC–GPF samples: “lab-aged” was aged with conventional engine oil, while “ZDDP” was aged with zinc dialkyldithiophosphate (ZDDP)-strengthened engine oil.

CeO_2 in the TWC is actively involved in TWC reactions to absorb and release oxygen as needed. Since the oxidation state of Ce shifts from 4+ to 3+ with aging due to increased formations of CePO_4 and $\text{Ce}_2(\text{SO}_4)_3$,

which have the Ce oxidation state of 3+, X-ray absorption near-edge structure measurements in the Advanced Photon Source were conducted using Ce L₃-edge spectra to inform oxidation states of Ce with aging. Figure IV.6.4 shows that ZDDP-strengthened oil increased the Ce³⁺ content, while conventional oil did not. Since the former contained Zn and P as major inorganic elements, the increased P content in engine oil would enhance the interaction of P and CeO₂ during aging compared to conventional oil containing less amounts of Zn and P. However, PXRD could not confirm it, probably because of low CePO₄ formation. In comparison, Ce³⁺ increased gradually from front to back, consistent with Figure IV.6.3, suggesting that CePO₄ formation increased along the direction of the exhaust flow path. Since CeO₂ lost some portion with aging due to CePO₄ and Ce₂(SO₄)₃ formations, reduction–oxidation cycles of CeO₂ during the TWC reactions were limited with aging, resulting in lower TWC performance, as understood from conventional TWCs [3].

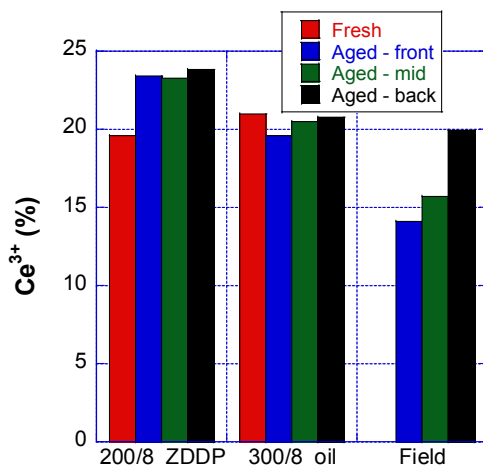
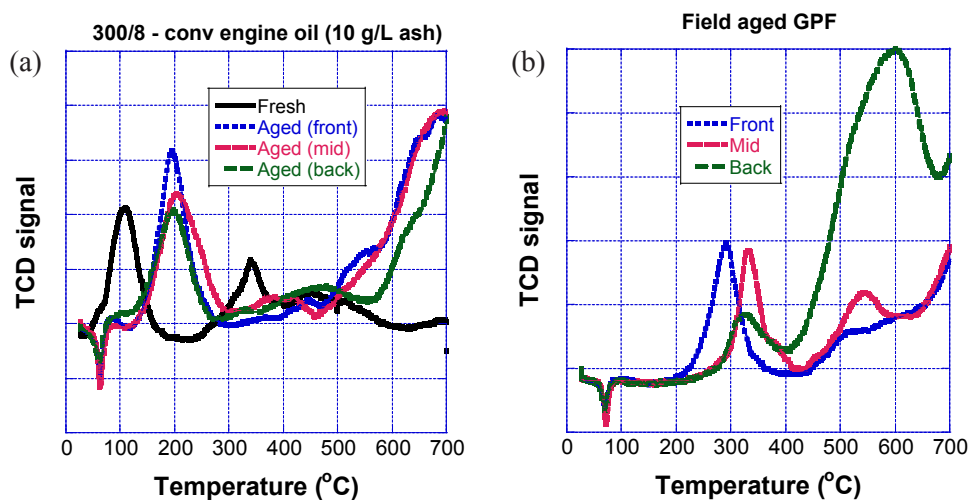


Figure IV.6.4 - Ce³⁺ percentages in a combined Ce³⁺ and Ce⁴⁺ for TWC–GPF samples using Ce L₃-edge X-ray absorption near-edge structure measurements: “ZDDP” was aged with ZDDP-strengthened engine oil, while “oil” was aged with conventional engine oil.

Since reducibility of materials provides insight into TWC components, H₂-temperature programmed reduction experiments were performed for the fresh and aged samples. Figure IV.6.5a shows that reduction peaks of the fresh samples were shifted with aging, but the aged samples were very similar regardless of sample position. The peak appearing at 100°C for the fresh sample was attributed to PdO_x reduction and H₂ spillover toward CeO₂, and the peak at 350°C indicates the reduction of surface oxygen available in OSC materials of CeO₂/ZrO₂ complexes. The peak at 200°C with aging was known to be combined reduction effects of PdO_x and CeO₂. For a better understanding, in situ Pd K-edge and Ce L₃-edge X-ray absorption near-edge structure measurements were carried out while increasing temperatures up to 300°C (data excluded). For the peak of the fresh sample at 100°C, PdO_x reduction all happened at around 50°C only and the remaining peak was due to gradual CeO₂ reduction with temperature. And, the peak at 350°C appeared to be due to further reduction of CeO₂. On the other hand, the peaks of the lab-aged samples at 200°C were found to be all related with CeO₂ reduction. In the case of Figure IV.6.5b, the patterns were similar to the lab-aged samples, although reduction upshifted to higher temperatures. As noted from the lab-aged samples, CeO₂ reduction was responsible for these peaks, and it is characterized that the reduction temperature increased along the direction of the exhaust flow path, implying that available oxygen in CeO₂ decreased as the position moved from front to back side. Since CeO₂ reduction became harder with aging, oxygen absorption/release processes would be severely limited in TWC reactions during lean–rich cycles, resulting in lower NO_x, CO, and THC conversions with aging.

One important aspect to be noted from this work is that since TWCs are coated within the GPF wall, TWC deactivation factors were gaseous chemicals including P and S from engine oil, passing through the GPF wall. Although the lab-aging was carried out at a relatively low temperature, these gaseous chemicals were poisonous enough to degrade TWC components despite detection difficulties. The results of the field-aged TWC–GPF consistently showed that TWC deterioration was more significant on back side than on front side.

Since exhaust temperatures increase along the direction of the exhaust flow path from exothermic reactions, increased temperatures seem to accelerate the deactivation process, such as increased formations of CePO_4 and $\text{Ce}_2(\text{SO}_4)_3$, and decreased oxygen absorption and release capabilities, when combined with engine oil-derived gaseous chemicals. The location of GPFs is one of crucial parameters from perspectives of fuel usage and particulate/gaseous emissions. High-temperature emissions are beneficial for increasing TWC performance and soot oxidation, while they may result in thermal aging. The current result proposes that TWC components would be more susceptible to degradation from engine oil-derived chemicals at elevated temperatures.



TCD – thermal conductivity detector

Figure IV.6.5 - H_2 -temperature programmed reduction results of lab- and field-aged TWC-GPFs

Conclusions

The following conclusions can be drawn based on the research performed in FY 2017.

- TWCs coated within the GPF wall were observed to be degraded from lab-aging and field-aging conditions.
- TWC degradation from TWC-GPFs was similar to that observed from conventional TWCs coated on monoliths: Pd sintering and PdO_x reduction, and decreased CeO_2 absorption/release capabilities from CePO_4 and $\text{Ce}_2(\text{SO}_4)_3$ formations.
- The current work proposes that TWC deactivation factors are engine oil-derived gaseous chemicals including P and S.
- Distinct from conventional TWCs, TWC degradation from the field-aged TWC-GPF was found to be more significant along the direction of the exhaust flow path, suggesting accelerated engine oil-derived chemical aging incorporation with increased temperature.

References

1. Larese, C., F. Cabello Galisteo, M. López Granados, R. Mariscal, J.L.G. Fierro, M. Furió, and R. Fernández Ruiz. "Deactivation of Real Three Way Catalysts by CePO_4 Formation." *Applied Catalysis B: Environmental* 40 (4):305–17, 2003. [https://doi.org/10.1016/S0926-3373\(02\)00161-3](https://doi.org/10.1016/S0926-3373(02)00161-3).
2. Kay, D. Alan R., W.G. Wilson, and V. Jalan. "High Temperature Thermodynamics and Applications of Rare Earth Compounds Containing Oxygen and Sulphur in Fuel Gas Desulphurization and SO_x and NO_x Removal." *Journal of Alloys and Compounds*, Proceedings of the International Conference, Rare Earths '92, 193 (1):11–16, 1993. [https://doi.org/10.1016/0925-8388\(93\)90295-X](https://doi.org/10.1016/0925-8388(93)90295-X).

3. Heo, Iljeong, Jin Woo Choung, Pyung Soon Kim, In-Sik Nam, Young Il Song, Chi Bum In, and Gwon Koo Yeo. "The Alteration of the Performance of Field-Aged Pd-Based TWCs towards CO and C₃H₆ Oxidation." *Applied Catalysis B: Environmental* 92 (1):114–25, 2009. <https://doi.org/10.1016/j.apcatb.2009.07.016>.

Key Fiscal Year 2017 Publications

1. Seong, Heeje, Seungmok Choi, Nestor J. Zaluzec, Sungsik Lee, Todd J. Toops, Michael J. Lance, Daekun Kim, and Ke Nguyen, "Deactivation of three-way catalysts coated within gasoline particulate filters by engine oil-derived chemicals." *Catalysis Science and Technology*, under review.
2. Seong, Hee Je, and Seungmok Choi, "Catalytic nanosheets to lower soot light off temperatures, method for making nanosheets to lower soot light-off temperatures," US15/643108, 2017.
3. Choi, Seungmok, Heeje Seong, Andrew Ickes, Stephen Ciatti, and Khanh Cung, "Comparison of particulate emissions from advanced and modern conventional combustion engines measured by smps, eeps, and mss." 2017 SAE World Congress & Exhibition, Detroit, MI, April 2017.

IV.7 Fuel-Neutral Studies of PM Transportation Emissions

Mark Stewart, Principal Investigator

Pacific Northwest National Laboratory
902 Battelle Boulevard
Richland, WA 99352
E-mail: mark.stewart@pnnl.gov

Ken Howden, DOE Technology Manager

U.S. Department of Energy
E-mail: Ken.Howden@ee.doe.gov

Start Date: October 1, 2015	End Date: September 30, 2018	
Total Project Cost: \$608,000	DOE share: \$608,000	Non-DOE share: \$0

Acknowledgments

Co-Authors

Jie Bao, Pacific Northwest National Laboratory
University of Wisconsin–Madison: Sandeep Viswanathan, Jonathan Molina, Yangdongfang Yang, David Rothamer, Chris Rutland, Andrea Shen, Todd Fansler, Stephen Sakai, Michael Andrie;
University of Wisconsin-Madison
Kushal Narayanaswamy, Paul Najt, Arun Solomon, Wei Li; General Motors Corporation

Project Introduction

Technologies such as spark ignition direct injection (SIDI) have led to significant gains in the fuel efficiency of engines that run on gasoline and associated fuel blends, but this increased efficiency can come at the price of higher NO_x and/or particulate matter (PM) emissions. As global fuel economy standards increase and emissions limits continue to tighten, major manufacturers are considering exhaust filtration for gasoline vehicles. Deployment of gasoline particulate filters (GPFs) on production vehicles has begun, and is anticipated to expand over the next several years in Europe and China in order to meet Euro 6 and China 6 particle number standards.

While GPF deployment for SIDI vehicles in the United States is less likely in the near-term, GPFs remain an option for gasoline PM control, and American manufacturers must continue to study and develop exhaust filter technology in order to remain globally competitive. In addition, other advanced engine technologies, such as compression ignition gasoline engines and reactivity controlled compression ignition engines, would likely also entail higher particulate emissions than traditional port fuel injected gasoline engines. Exhaust filter manufacturers now offer products designed specifically for advanced gasoline engines, including SIDI. The development of multifunctional filter technologies, such as selective catalytic reduction on filter or three-way catalyst on filter devices, add another possible dimension as vehicle manufacturers negotiate the inevitable tradeoffs between fuel efficiency, NO_x, and PM emissions, space on vehicle, and cost. Understanding the fundamental relationships between filter system characteristics and ultimate system performance will be critical as manufacturers consider various options moving forward.

Objectives

- Shorten the time required for development of filtration technologies for future engines
- Develop modeling approaches relevant to the likely key challenge for gasoline particulate filtration: high number efficiency at high exhaust temperatures and low particulate loading
- Develop new techniques for exhaust filter media characterization

Approach

General Motors Research has provided components and guidance to develop advanced research engines at the University of Wisconsin–Madison Engine Research Center (ERC). These research engines have been configured to run with a variety of fuels over a wide range of operating conditions. ERC researchers used the Exhaust Filtration Analysis (EFA) system [1], developed at the University of Wisconsin–Madison, to conduct fundamental filtration experiments in realistic exhaust streams using flat wafer samples of various filter substrates. The project team characterized a number of the porous ceramic materials used in the filtration tests through a variety of techniques, which included mercury intrusion porosimetry (MIP), capillary flow porometry (CFP), and micro X-ray computed tomography (CT), in order to understand performance differences between the various products. Existing filtration models based on porosity and pore size alone (as measured by MIP), have thus far been unable to quantitatively predict the observed trends in the behavior of the various filter products examined. Insight from fundamental experiments, filter characterization, and micro-scale modeling will ultimately be incorporated into new empirical expressions and improved device-scale models that can be used by vehicle manufacturers to optimize engine and exhaust systems in future high-efficiency vehicles.

Results

Researchers at the ERC used the EFA apparatus to collect SIDI particulate filtration data for a wide variety of different filter substrates (see Figure IV.7.1, from Viswanathan [2]). Cordierite and aluminum titanate samples from two different manufacturers were included in these studies. Figure IV.7.1 shows that the selection of filter materials covered wide ranges of porosity, pore diameter, and permeability. Porosity and median pore diameters shown were measured with MIP, while permeability values were obtained using the EFA apparatus.

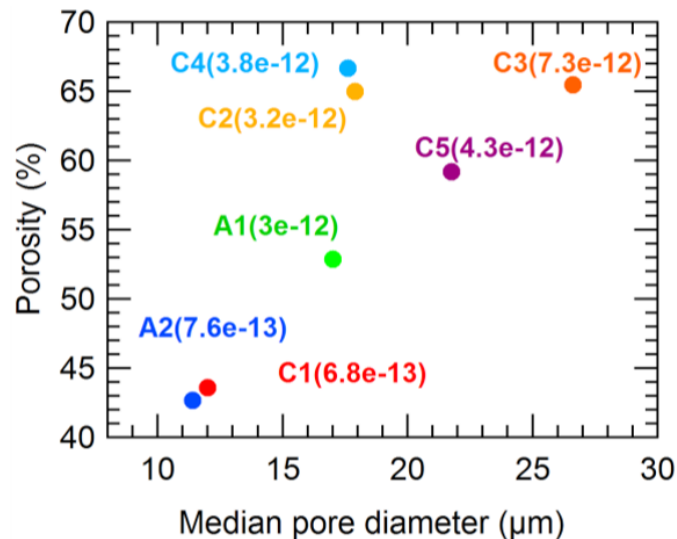


Figure IV.7.1 - Properties of filter substrates studied (measured permeabilities in m² shown in parentheses)

Fundamental filtration data obtained with the EFA apparatus included the evolution of size-resolved filtration efficiency and pressure drop over time as each of the filter samples were loaded with soot from a single-cylinder SIDI test engine. Experiments included several different engine operating modes, which generated different soot particle counts and size distributions, and were carried out at different flow velocities. Figure IV.7.2 [2] shows a summary of initial filtration behavior for removal of ultrafine 50 nm particles by the seven different filter substrates. P_{50} is penetration of 50 nm particles (ratio of particle number exiting the filter to particle number entering). Data is shown for gas velocities of 2.75 cm/s and 5.5 cm/s at the filter wall surface.

MIP is a widely used technique for characterization of pore size distributions in porous media and it has been applied to ceramic exhaust particulate filters since early in their development. Researchers at the ERC applied a less commonly used method, CFP, to the seven samples used in EFA filtration experiments. Unlike MIP,

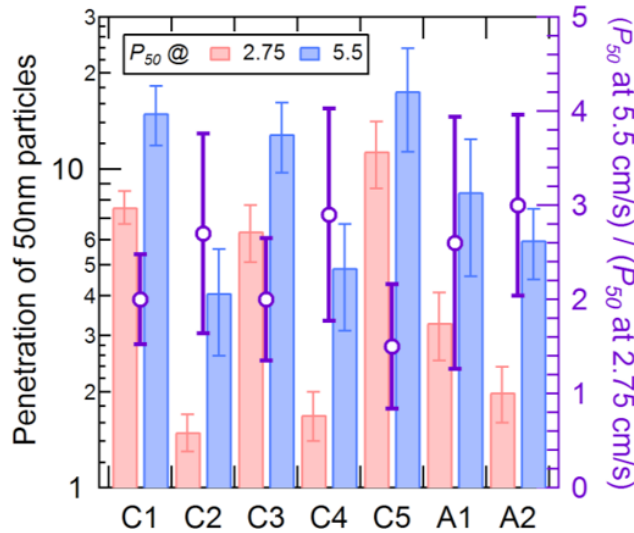


Figure IV.7.2 - Summary of initial filtration data for ultrafine particles across seven different filter substrates

which pushes a non-wetting fluid into a porous sample from all directions, CFP applies gas pressure to displace a wetting fluid and progressively increase gas flow in one direction. In the case of ceramic filter samples, this technique targets the same flow paths through the filter wall thickness which carry particle-laden exhaust during filtration, and could prove to be a valuable complement to MIP. Figure IV.7.3 [2] shows distributions of controlling throat diameters measured by CFP in six of the filter substrates. ERC students are currently testing an improved CFP apparatus, designed specifically for exhaust filter applications, which will likely lead to improved precision and repeatability in the measurements.

Pacific Northwest National Laboratory (PNNL) obtained high-resolution X-ray CT data for all seven of the filter substrates included in the ERC filtration study. These detailed, three-dimensional maps of the filter microstructures were used in a number of different ways to characterize fundamental differences between the materials. Pore network models were created using the maximal inscribed sphere method [3]. The pore network models allow detailed, quantitative examination of pore size, shape, and connectivity in the various materials. As one example, Figure IV.7.4 shows distributions of pore body diameters (the wide points in the branching networks of pores passing through the filter walls) in the seven materials examined.

PNNL also used segmented reconstructions from the X-ray CT data to conduct three-dimensional flow simulations through small sections of the seven substrates using the lattice Boltzmann (LB) method.

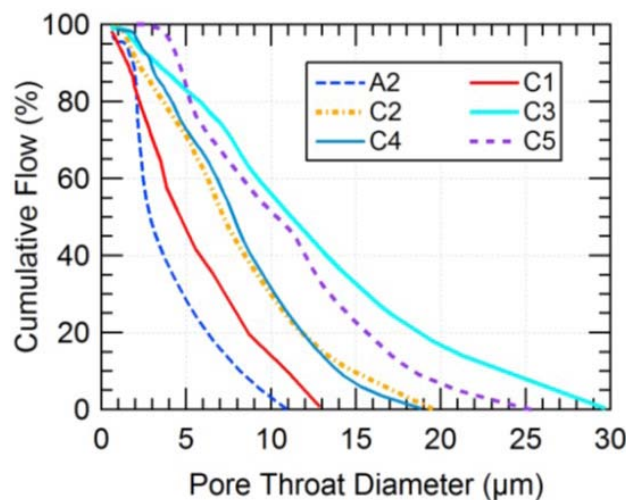


Figure IV.7.3 - Distributions of controlling pore throat diameters obtained by capillary flow porometry

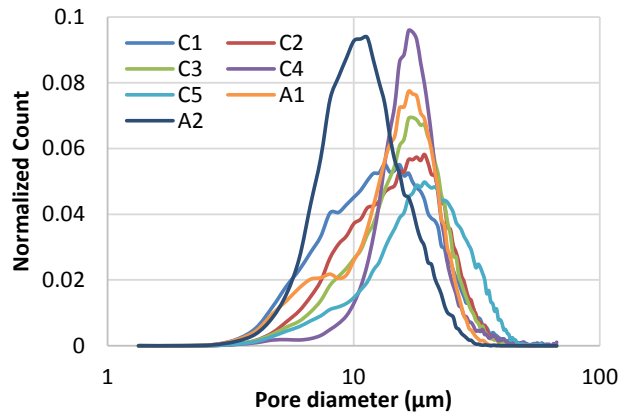


Figure IV.7.4 - Distributions of pore body sizes in pore network models generated for the seven filter substrates examined

Figure IV.7.5 shows a reconstruction of a small section of the C2 cordierite filter material and a representation of the flow field through the filter wall (flow direction from top to bottom).

The three-dimensional flow fields obtained by LB provide a rich set of information about how particle-laden exhaust moves through various materials. A current challenge is reducing these numerical datasets to simpler descriptive parameters that can be used in improved device-scale filter models. PNNL and the ERC are exploring a number of possible solutions. One example of a quantity of interest is flow tortuosity. Tortuosity is a measure of the actual path length of flowing or diffusing material as it moves through a porous medium, and is commonly used as a tunable parameter in transport models. In the case of particulate filtration, a relatively low tortuosity is associated with a well-connected pore network that results in lower local velocities within the filter wall and more exposure of flowing gas to internal surface area that can capture ultrafine particles. Distributions of streamline tortuosities from LB flow fields through the seven filter materials are shown in Figure IV.7.6.

Having assembled a large set of consistent, high-quality filtration data and developed a number of new techniques for quantitative characterization of filter media, PNNL and ERC researchers are working to synthesize these elements into improved general filtration models. Modified versions of the commonly used

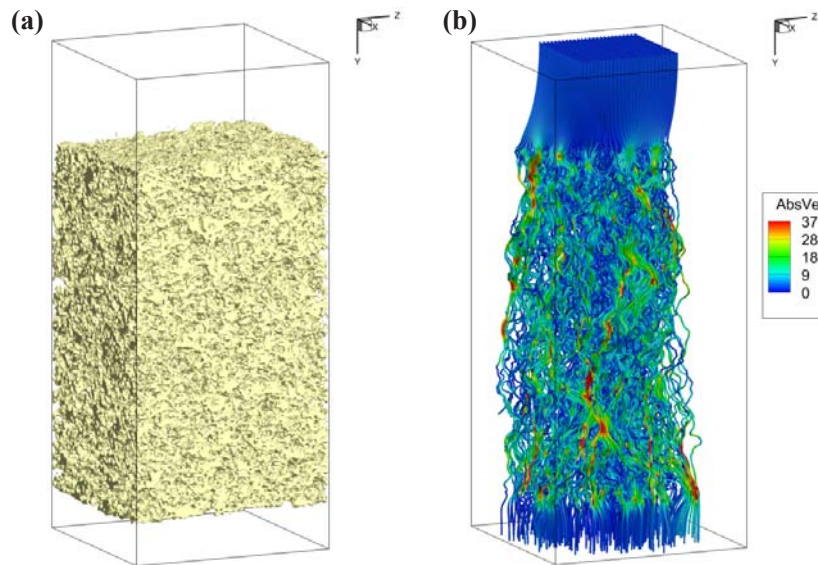


Figure IV.7.5 - Three-dimensional reconstruction of a small section of the C2 material from X-ray CT data and an associated flow field (color key indicates local gas velocities in cm/s)

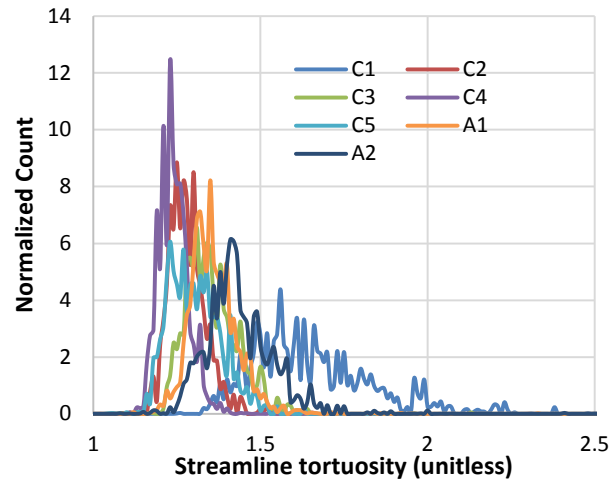


Figure IV.7.6 - Distributions of streamline tortuosities in flow fields through the various filter media studied

spherical unit collector model [4] are being evaluated, as are fundamentally different approaches, including constricted tube collector models [5].

Conclusions

- Fundamental filtration studies using real SIDI particulates showed differences in filtration behavior among a wide variety of filter materials which cannot be quantitatively explained using existing models based on porosity and median pore size obtained by mercury porosimetry.
- Capillary flow porometry is a promising method for providing information on distributions of flow-limiting throat diameters in flow paths through exhaust filter walls.
- High resolution X-ray CT data can be used to provide detailed information on the three-dimensional structure of exhaust filter media, which can be reduced to quantitative structural parameters using techniques such as pore network modeling and LB flow simulations.

References

1. Viswanathan, S., S. Sakai, and D. Rothamer. "Design & Evaluation of an Exhaust Filtration Analysis (EFA) System." SAE Technical Paper 2014-01-1558, 2014 SAE World Congress and Exhibition. Detroit, MI.
2. Viswanathan, S. "Experimental Investigation of Deep-Bed Filtration of Spark-Ignited, Direct-Injection Engine Exhaust Using Ceramic Particulate Filters." Doctoral dissertation. University of Wisconsin–Madison, 2016.
3. Dong, H. and M.J. Blunt. "Pore-Network Extraction from Micro-Computerized-Tomography Images." *Physical Review E*, 2009. 80(3): p. 036307.
4. Konstandopoulos, A.G. and J.H. Johnson. "Wall-Flow Diesel Particulate Filters — Their Pressure Drop and Collection Efficiency." SAE Tech. Pap. 890405, 1989.
5. Tien, C. and A. Payatakes. "Advances in Deep Bed Filtration." *AIChE J.*, no. 5, pp. 737–759, 1979.

Key Fiscal Year 2017 Publications

1. Viswanathan, S., D.A. Rothamer, D.E. Foster, T.D. Fansler, A. Zelenyuk, M.L. Stewart, and D.M. Bell. "Evolution of Deep-Bed Filtration of Engine Exhaust Particulates with Trapped Mass." *International Journal of Engine Research* 18 (5-6):543–559, 2017. doi: 10.1177/1468087416675094.

2. Gong, J., S. Viswanathan, D.A. Rothamer, D.E. Foster, and C.J. Rutland. “Dynamic Heterogeneous Multiscale Filtration Model: Probing Micro and Macroscopic Filtration Characteristics of Gasoline Particulate Filters.” *Environmental Science & Technology* 51 (19):11196–11204, 2017. doi: 10.1021/acs.est.7b02535.
3. Viswanathan, S., D. Rothamer, A. Zelenyuk, M.L. Stewart, and D. Bell. “Experimental Investigation of the Effect of Inlet Particle Properties on the Capture Efficiency in an Exhaust Particulate Filter.” *Journal of Aerosol Science* 113:250–264, 2017. doi: 10.1016/j.jaerosci.2017.08.002.
4. Gong, J., M.L. Stewart, A. Zelenyuk, A. Strzelec, S. Viswanathan, D. Rothamer, D. Foster and C. Rutland. “Importance of Filter’s Microstructure in Dynamic Filtration Modeling of Gasoline Particulate Filters (GPFs): Inhomogeneous Porosity and Pore Size Distribution.” *Chemical Engineering Journal* (Submitted 2017).

IV.8 Next Generation Ammonia Dosing System

Abhijeet Karkamkar, Principal Investigator

Pacific Northwest National Laboratory
902 Battelle Blvd., MS# K2-57
Richland, WA 99352
E-mail: abhi.karkamkar@pnnl.gov

Ken Howden, DOE Technology Manager

U.S. Department of Energy
E-mail: Ken.Howden@ee.doe.gov

Start Date: October 1, 2016	End Date: September 30, 2017	
Total Project Cost: \$250,000	DOE share: \$200,000	Non-DOE share: \$50,000

Acknowledgments

Co-Author

Chinmay Deshmane, Pacific Northwest National Laboratory

Project Introduction

Selective catalytic reduction (SCR) offers a number of advantages including excellent NO_x reduction efficiency over a wide range of temperatures and overall lower system cost. Currently, SCR is being used to meet the NO_x emission standards for diesel engines in Europe and North America, and also being considered for meeting the future NO_x emission standards for lean burn gasoline engine. Aqueous urea solutions (e.g., Diesel Exhaust Fluid, AdBlue) are currently used as ammonia storage compounds for mobile applications. When the aqueous urea solution is sprayed into the exhaust gas stream, urea is decomposed to release ammonia, which then reduces NO_x over the downstream SCR catalyst. Although aqueous urea solution technology has enabled automakers and engine manufacturers to meet the current NO_x emission requirements it requires a hot exhaust gas and sufficient mixing, creating challenges for low temperature NO_x emission control and aftertreatment system packaging.

For these reasons, alternative technologies have been developed as ammonia sources (e.g., solid urea, ammonium carbamate, metal ammine chloride) during the past few years [1,2,3]. These technologies promise more convenient handling and distribution of ammonia sources and help maximize the low-temperature performance of SCR catalysts and reduce the overall system volume and weight. However, none of these alternative technologies can be successfully implemented without the industry consensus.

Therefore, the United States Council for Automotive Research SCR work group, which is comprised of representatives from General Motors, Ford, and Chrysler, has decided to investigate the potential alternative ammonia carriers, define common standard vehicle interfaces, and address personal and environmental safety concerns with part suppliers and chemical companies.

Objectives

- Synthesize novel composite materials to tune thermodynamics
- Quantify the gravimetric ammonia capacity of the composites
- Optimize the molar composition of the double salts and eutectics
- Demonstrate the ability to tune the temperature of NH₃ release

Approach

Pacific Northwest National Laboratory and the United States Council for Automotive Research explored methods to improve or optimize the properties of solid state ammonia storage materials based on the information collected during the first year. This fiscal year, the project focused on ways to develop experimental protocols to synthesize and quantify novel double salts and eutectics. The novel materials were synthesized by a combination of co-precipitation and ion-exchange techniques.

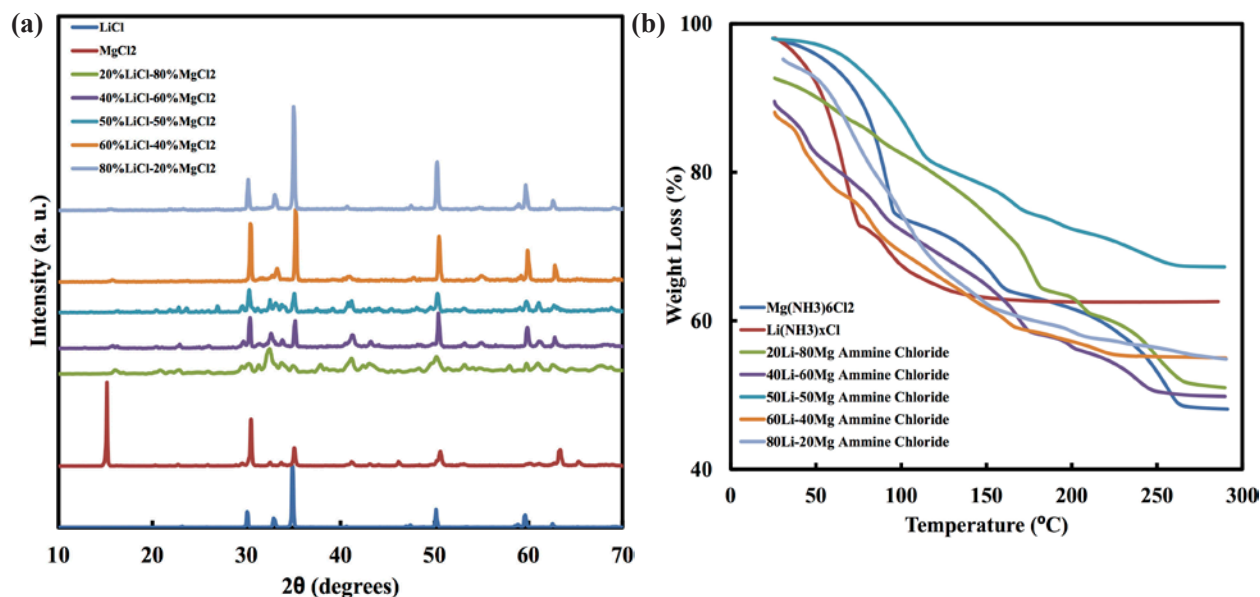
The composition of the materials was chosen based on Phase I results which suggested that the ammonia release temperature for magnesium (Mg)-based salts was greater than 140°C while the lithium (Li)-, strontium (Sr)- and calcium (Ca)-based materials had ammonia release temperature less than 40°C [3]. It is desirable to have a material that has a temperature of ammonia release that can be tuned based on the range of temperature at which the catalyst is active.

The synthesized materials were characterized using X-ray diffraction before and after ammonia capture to determine the structure and formation of a new crystallographic material. The ammonia storage and release behavior was studied using calorimetric and gravimetric studies using a simultaneous thermogravimetric analysis (TGA)–differential scanning calorimetry coupled with a mass spectrometer.

Results

- Synthesized double salts containing (1) $\text{SrCl}_2/\text{MgCl}_2$, (2) $\text{LiCl}/\text{MgCl}_2$, and (3) $\text{CoCl}_2/\text{MgCl}_2$ to stabilize novel phases
- Quantified the gravimetric capacity of the double salts and obtained comparable or higher ammonia storage capacity than the parent materials
- Demonstrated the ability to tune the temperature of NH_3 release from the double salts
- Completed recycle studies on compacted pellets

Double salts of varying molar compositions were synthesized to tune the ammonia release behavior [1,4]. The composition of lithium chloride and magnesium chloride was varied between 20 mol% to 80 mol% for each component. Figure IV.8.1a shows the powder X-ray diffraction plots of the $\text{LiCl}/\text{MgCl}_2$ double salts. At low molar loading the samples primarily show reflections associated with the major component. For example,



a.u. – arbitrary units

Figure IV.8.1 - (a) Powder X-ray diffraction plots of double salts synthesized by varying molar compositions of lithium chloride and magnesium chloride and (b) ammonia release profiles of corresponding samples obtained using a TGA instrument

the 80% LiCl 20% MgCl₂ sample shows reflections associated primarily with LiCl. However, compositions containing 40% LiCl 60% MgCl₂ shows reflections associated with a new double salts and not a physical mixture of LiCl+MgCl₂. Figure IV.8.1b shows TGA profiles for the corresponding samples. The double salts show ammonia release over a wider temperature range from 35–140°C with a nominal ammonia storage capacity ranging from 35–55 wt%.

This demonstrates the need to further explore synthetic approaches to novel materials to achieve the ability to tune ammonia storage capacity and temperature of ammonia release [1].

Additional experiments were carried out to determine other novel compositions containing transition metal chlorides as additives. These materials showed an increase in ammonia release temperature from ~100°C to 150°C as shown in Figure IV.8.2. This temperature is closer to the temperature at which the SCR catalyst is active. This example also demonstrates the ability to tune the temperature, however in contrast to the earlier example of LiCl/MgCl₂ which showed a lowering of ammonia release temperature.

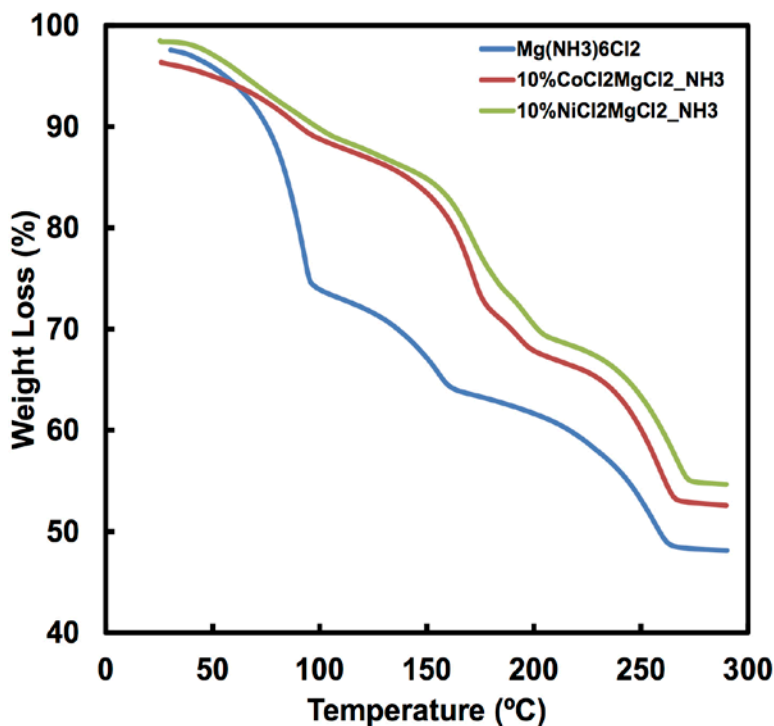


Figure IV.8.2 - TGA profile for ammonia release from MgCl₂.6NH₃ and corresponding material containing 10% CoCl₂ and NiCl₂, respectively

Conclusions

- Completed the synthesis and evaluation of several eutectic and double salts
- Characterized the NH₃ uptake capacity of the double salts to show that the capacity was in the range of 35–60 wt%
- Evaluated ammonia release behavior of double salts and demonstrated the ability to tune the temperature of ammonia release from a lower end of 35°C to a high range of 150°C for the first step
- Completed recycle studies on compacted pellets to show retention of compacted form through four cycles
- Studied effect of CO₂ on material performance

References

1. Liu, Chun Yi, and Ken-ichi Aika. "Ammonia Absorption into Alkaline Earth Metal Halide Mixtures as an Ammonia Storage Material." *Ind. Eng. Chem. Res.* 2004, 43, 7484–749.
2. Jensen, Peter Bjerre, Steen Lysgaard, Ulrich J. Quaade and Tejs Vegge. "Designing mixed metal halide ammines for ammonia storage using density functional theory and genetic algorithms." *Phys.Chem. Chem. Phys.*, 2014,16, 19732–19740.
3. Johannessen, T. "Emissions solutions for optimal DeNOx in real driving conditions." Integer Emissions Summit Asia Pacific 2016.
4. Fulks, G., G. Fisher, K. Ralmoeller, M. Wu, et al. "A Review of Solid Materials as Alternative Ammonia Sources for Lean NOx Reduction with SCR." SAE Technical Paper 2009-01-0907, 2009, doi:10.4271/2009-01-0907.

IV.9 Advanced Emission Control for High-Efficiency Engines

Yong Wang, Principal Investigator

Pacific Northwest National Laboratory
P.O. Box 999, MS K2-12
Richland, WA 99354
E-mail: yong.wang@pnnl.gov

Ken Howden, DOE Technology Manager

U.S. Department of Energy
E-mail: Ken.Howden@ee.doe.gov

Start Date: March 1, 2016	End Date: March 31, 2019	
Total Project Cost: \$2,000,000	DOE share: \$1,000,000	Non-DOE share: \$1,000,000

Acknowledgments

Co-Authors

Feng Gao, János Szanyi, Yilin Wang, Yong Wang, Alla Zelenyuk; Pacific Northwest National Laboratory

Project Introduction

This project between Cummins and Pacific Northwest National Laboratory (PNNL) focuses on a broad and very important area of critical relevance to DOE and Cummins, advanced emission control for high-efficiency engines. It specifically focuses on three areas: passive NO_x absorbers, oxidation of methane and short alkanes, and improved understanding of particulates.

The first two areas are based on PNNL's technical leadership in zeolite-based materials. The third area was completed in Year 1 to leverage the unique Single Particle Laser Ablation Time-of-Flight mass spectrometer capabilities at PNNL to help address Cummins' needs in improving the understanding of particulate properties as a function of engine operating conditions and aftertreatment systems.

Objectives

- Passive NO_x absorbers: develop next generation materials to address the cold operation, as driven by improved engine efficiency
- Oxidation of methane and short alkanes: address cold operation emissions arising from compressed natural gas vehicles
- Improved understanding of particulate matter (PM): understand the properties of exhaust PM as a function of engine operating conditions and aftertreatment

Approach

This project takes advantage of the strengths from the partners. In particular, Johnson Matthey is well known in catalyst formulation and upgrading. Cummins is well equipped in its catalysis laboratory with on-engine testing. PNNL has the state-of-the-art catalyst characterizations to provide fundamental understanding of the chemical and physical properties of the catalytic materials.

This partnership will understand fundamental relationship of particulate properties and engine operation and aftertreatment utilizing unique approaches for multidimensional real-time in situ characterization of individual exhaust particles such as the Single Particle Laser Ablation Time-of-Flight mass spectrometer. It also aims at revealing fundamental aspects of the chemistry and catalytic materials involved in passive NO_x absorbers and small alkane catalytic oxidation.

Results

Key accomplishments for Fiscal Year 2017 include:

Passive NO_x Absorber

- Finished synthesis, characterization and evaluation of the first series catalysts (Pd/ZSM-5, Pd/Beta, Pd/SSZ-13) synthesized via ion exchange; first paper published: Y. Zheng et al., *J. Phys. Chem. C*, **2017**, *121*, 15793–15803
- Finished preparation of the second series catalysts via incipient wetness impregnation; detailed characterization and evaluation are underway

Methane and Ethane Oxidation at Low Temperature

- Evaluated a large group of Pd, Pt, and PdAu catalysts supported on various supports including Al₂O₃, CeO₂, CeO₂-ZrO₂, ZSM-5, Beta and SSZ-13; promising ones have been chosen for detailed studies on deactivation mechanism and its prevention

Improved Understanding of Exhaust PM

- Comprehensively characterized chemical and physical properties of individual exhaust particles emitted during more than 80 operating conditions, including different running cycles, two aftertreatment systems, sampling at different points of the aftertreatment systems (engine out, diesel particulate filter out, selective catalytic reduction out)
- Completed data processing and identified particles with various sizes, shapes, morphologies, and compositions

A series of zeolite-supported Pd catalysts with decreasing support pore size were synthesized (Pd/ZSM-5, Pd/Beta, Pd/SSZ-13). NO_x uptake and desorption of these materials were studied using simulated exhaust containing 200 ppm NO_x (185 ppm NO + 15 ppm NO₂), 200 ppm CO, 14% H₂O, 2.5% H₂O balanced with N₂. NO_x uptake was conducted at 100°C for 10 min, followed by ramping to 500°C to release trapped NO_x. As shown in Figure IV.9.1, NO_x release temperature is dependent on the zeolite pore size, with Pd/Beta (largest pore size) being the lowest and Pd/SSZ-13 (smallest pore size) being the highest. The presence of H₂O inhibits the NO_x uptake on all three materials, while the presence of CO facilitates the NO_x storage (Table IV.9.1).

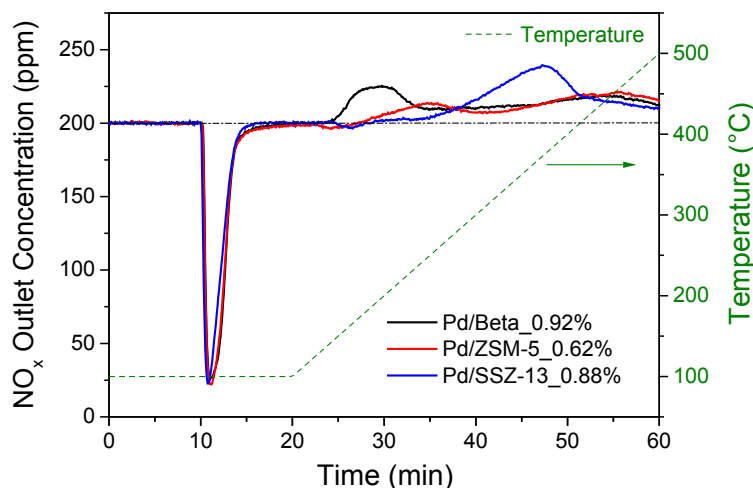


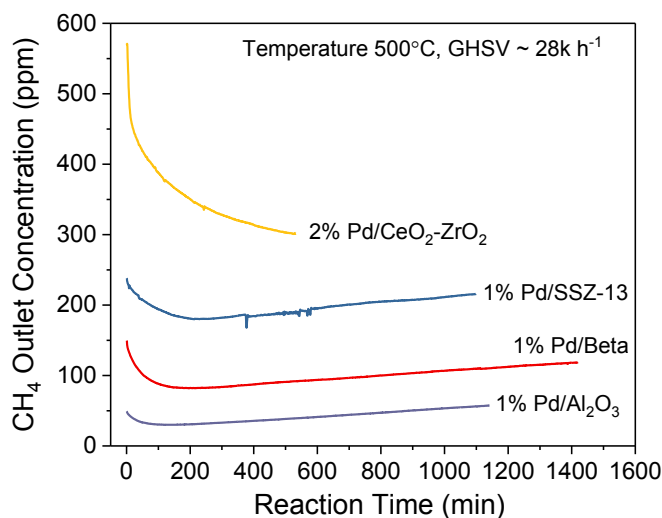
Figure IV.9.1 - NO_x adsorption and release on various zeolite supported Pd materials

Low temperature methane oxidation was first baselined using Johnson Matthey equivalent catalysts which are gamma-alumina-supported Pd catalysts. Experiments were conducted using 600 ppm CH₄, 2.5% H₂O, 6% CO₂, 10% O₂ with N₂ balance. These catalysts exhibited similar deactivation behavior as reported in the literature [1], which is due to either metal sintering or –OH inhibition [2]. Further comparison with other supported

Table IV.9.1 - NO_x/Pd Ratio during NO_x Trapping at 100 °C for 10 min

	Dry 200 ppm NO _x feed	200 ppm NO _x + 2.5% H ₂ O feed	200 ppm NO _x + 200 ppm CO + 2.5% H ₂ O feed
Pd/Beta_0.92%	1.26	0.28	0.51
Pd/ZSM-5_0.62%	0.88	0.50	0.70
Pd/SSZ-13_0.88%	1.08	0.14	0.44

Pd catalysts (Pd/Beta, Pd/SSZ-13, Pd/CeO₂-ZrO₂) suggested that Pd/Al₂O₃ gives the best performance (Figure IV.9.2). Our preliminary results suggest that bimetallic catalysts such as PdAu exhibit promising results, and thus, our future studies will focus on the Pd-based bimetallic catalysts which are expected to improve catalyst activity and stability.



GHSV – gas hourly space velocity

Figure IV.9.2 - Methane oxidation on supported Pd catalysts

Exhaust PM represents a complex mixture of particles with various sizes, shapes, morphologies, and compositions. We used a one-of-a-kind approach for multidimensional, real-time in situ characterization to study the PM properties (number concentrations, compositions, size distributions, morphologies) from the 2016 Cummins ISX diesel engine. These properties strongly depend on operating conditions and the aftertreatment systems. For example, engine out PM is dominated by fractal soot particles and contains a small fraction of ash particles. However, as shown in Figure IV.9.3, the diesel particulate filter drastically reduces particulate number concentrations, and affects particulate compositions/size distributions. High speed/high load conditions produce mostly fractal soot particles, while high speed/low load results in large fraction of larger, compact particles composed of nitrates, ash, and metals.

Conclusions

- First generation and second generation passive NO_x absorber materials were prepared via solution ion exchange and incipient wetness impregnation.
- NO_x release temperature was found to be dependent on zeolite structure: smaller pore opening, higher release temperature.
- CH₄ combustion was baselined using Johnson Matthey equivalent Pd/Al₂O₃ catalysts, and their deactivation behavior is the same as reported in literature. Proper approaches were identified to understand this deactivation behavior, including in situ and in operando diffuse reflectance infrared Fourier transform spectroscopy and scanning transmission electron microscopy.

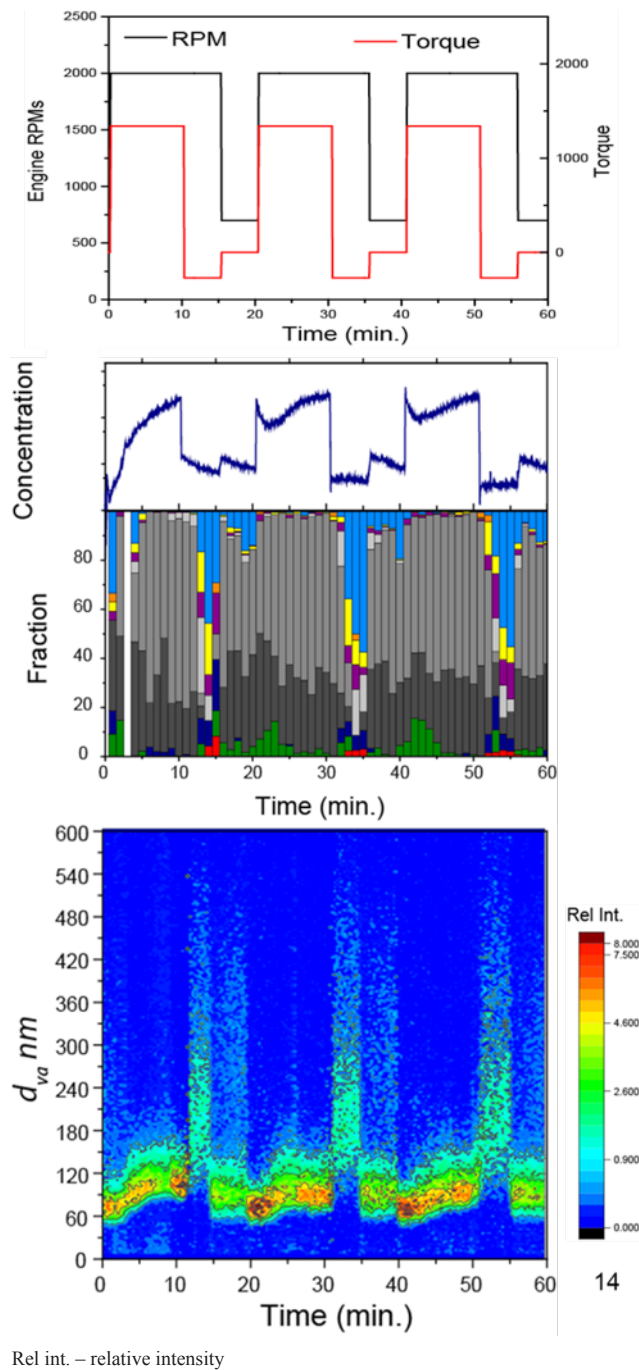


Figure IV.9.3 - PM number and concentration in the exhaust from diesel particulate filter

- Pd- and Pd-alloy-supported on other materials, especially zeolites, are also under investigation.
- A one-of-a-kind approach for multidimensional, real-time in situ characterization of individual exhaust particles provided unique insights into chemical and physical properties of emitted PM. This knowledge is critical for the development of strategies to address the tightening emission regulations and their enforcement for exhaust PM.

References

1. Ciuparu, D., M.R. Lyubovsky, E. Altman, L.D. Pfefferle, and A. Datye. "Catalytic combustion of methane over palladium-based catalysts." *Catal.Rev.-Sci. & Eng.*, 44, no. 4 (2002): 593-649.
2. Schwartz, W.R., D. Ciuparu, and L.D. Pfefferle. "Combustion of methane over palladium-based catalysts: catalytic deactivation and role of the support." *J.Phys.Chem.C*, 116(15) (2012): 8587-8593.

Key Fiscal Year 2017 Publications

1. Zhang, Y. et al. "Low-Temperature Pd/Zeolite Passive NOx Adsorbers: Structure, Performance, and Adsorption Chemistry." *J. Phys. Chem. C*, **2017**, 121, 15793–15803.
2. Szanyi, J. "Low-Temperature Pd/Zeolite Passive NOx Adsorbers: Structure, Performance and Adsorption Chemistry." Oral presentation. NAM, Denver, CO, June 4–9, 2017.
3. Gao, F. "Low-Temperature Pd/Zeolite Passive NOx Adsorbers: Structure, Performance and Adsorption Chemistry." Invited talk. ACS Fall National Meeting, Washington, DC, August 22, 2017.

IV.10 Development and Optimization of a Multi-Functional SCR–DPF Aftertreatment System for Heavy-Duty NO_x and Soot Emission Reduction

Kenneth G. Rappé, Principal Investigator

Pacific Northwest National Laboratory
P.O. Box 999
Richland, WA 99354
E-mail: ken.rappe@pnnl.gov

Ken Howden, DOE Technology Manager

U.S. Department of Energy
E-mail: Ken.Howden@ee.doe.gov

Start Date: July 1, 2016	End Date: June 30, 2020	
Total Project Cost: \$2,700,000	DOE share: \$1,350,000	Non-DOE share: \$1,350,000

Acknowledgments

Co-Authors

Bo Peng, Shari Li; Pacific Northwest National Laboratory

Project Introduction

Integrated selective catalytic reduction–diesel particulate filter (SCR–DPF), i.e., SCRf technology combines NO_x reduction and soot filtration in a single two-way device. Its development for both light-duty diesel and heavy-duty diesel (HDD) applications is motivated by emission compliance in a manner that reduces aftertreatment system volume and cost, and increases packaging flexibility. The challenges faced for successful application of SCRf technology to HDD vehicles are (1) achieving the necessary soot filtration and SCR reaction performance, (2) achieving the necessary SCR durability requirements, and (3) retaining sufficient passive soot oxidation capacity in the SCRf for it to be attractive for deployment. The first two challenges have largely been addressed and have a clear path forward [1,2,3]. The third challenge is significant in that passive soot oxidation is a significant contributor to the management of accumulated soot for HDD as it reduces the overall fuel penalty associated with the reduction of soot emissions at the tailpipe. However, the integration of current state of the art SCR catalyst technology on to a DPF results in significantly compromised passive soot management capacity of the SCRf system due to the dominating kinetics of the SCR catalyst that deplete NO₂. Thus, this work is focused on the development of an SCRf system that exhibits sufficient passive soot oxidation capacity while retaining sufficient NO_x reduction efficiency to be attractive for HDD applications. The strategy proposed is the incorporation of a selective catalytic oxidation (SCO) phase to the SCR catalyst, forming an SCO–SCR binary catalyst system, which will result in greater availability of NO₂ in the system without sacrificing the necessary NO_x reduction performance.

Objectives

- Demonstrate the successful integration of a DPF with a binary catalyst system consisting of an SCR phase and an SCO phase to enable sufficient passive soot oxidation capacity within the device
- Develop an SCR–SCO binary catalyst system that successfully enables the availability of NO₂ for achieving the necessary passive soot oxidation capacity within the integrated device while retaining high NO_x reduction efficiency and minimizing the parasitic oxidation of NH₃ (with O₂)
- Develop the fundamental understanding of the interaction of the SCR and SCO catalyst phases that will lead to an optimized binary catalyst system, identifying the necessary engineering requirements and system limitations for their integration, with a view to proper function and optimal integration

- Develop models that incorporate the SCRF catalyst system that can accelerate the optimization of the system by providing SCRF operational insight while simultaneously minimizing experimental testing
- Develop the necessary understanding to potentially lead to the design and optimization of four-way devices, which will address particulate matter, hydrocarbons, CO, and NO_x in a single unit

Approach

The program is generally arranged in four phases. Phase 1 focuses on evaluation of the feasibility of the SCO–SCR binary catalyst approach and SCO phase identification. The SCO phase builds off of a ZrO₂-base structure, with slight variations to its chemistry and behavior that potentially include phase-stabilization with yttria, addition of oxidation storage (e.g., inclusion of CeO₂), and modulation of oxidation ability (e.g., inclusion of varying amounts of Ni). Initial SCO phase performance screening will identify the classes of materials that exhibit the greatest potential for the HDD application. Phase 2 focuses on development of the SCO–SCR binary catalyst system, as well as SCRF development and optimization. This includes detailed development and investigation of the SCO–SCR binary catalyst to identify the optimum catalyst combination for scale-up and engine testing. This also includes understanding the durability requirements and limitations of the system and how that impacts the balance of the system. There exists the potential to optimize the integration of the catalyst with the DPF in manner that retains high NO_x reduction efficiency, retains necessary passive soot oxidation capacity, and exhibits acceptable back pressure on the engine when deployed. This will be accomplished by catalyst particle size optimization, advanced slurry development and filter coating techniques, and state-of-the-art DPF evaluation techniques. Phases 3 and 4 focus largely on scalability of the system from 1-in mini-core-scale to 2-L passenger-car-scale, and 2-L passenger car to HDD full-scale, respectively.

Pacific Northwest National Laboratory (PNNL) utilizes an extensive suite of standard and specialty analytical tools and test reactors to support steady-state and transient testing that are necessary provide information to address those questions that are current obstacles to system integration. At the center of this is a fully automated high-throughput screening test bench that can perform SCR screening studies as well as multi-step, multi-temperature detailed protocol testing. PNNL also has the expertise to develop laboratory and full-scale reactor models for catalyst and particular filter to simulate and help accelerate the system level optimization process. These resources are part of PNNL's Exhaust Emissions Science Lab and leverage the capabilities within the Environmental Molecular Science Laboratory, Institute for Integrated Catalysis, and Emissions Chemistry & Aerosol Research facilities.

Results

Initial efforts on the work utilized a ZSM-5-based model system for assessing the comparative impact of the variation of various chemical and physical properties of the SCRF system and SCO–SCR catalyst chemistry. This included the SCO phase impact on Cu/ZSM-5 SCR performance, the binary catalyst system SCO phase to SCR phase mass ratio, the SCRF SCO–SCR binary catalyst loading, the SCRF catalyst loading symmetry across the filter wall, and the ZrO₂ source. A fully automated, high-throughput catalyst core bench test capability was developed to support catalyst testing and study. The automation capability of the bench reactor allows itself for detailed multi-step protocol testing in consistent and repeatable fashion for assessing the various aspects of the standard and fast SCR reaction processes. The important contributing reactions governing performance include NH₃ storage, NH₃ oxidation, NO oxidation, standard SCR reaction, and fast SCR reaction. An eight-step protocol was developed for assessing each on these contributing reactions in individual fashion.

As stated in the project objectives, NO₂ availability is an area of focus for this work as passive soot oxidation is a NO₂-driven process. Thus, understanding the fate of NO₂ and its relative balance in the system is of extreme importance for understanding system performance. Five different ZrO₂-based SCO phases were combined with Cu/ZSM-5 and measured for performance. The purpose of the assessment was to understand the impact that different SCO chemistries can have on the NO₂ balance in the system. Figure IV.10.1 shows the results of this assessment. This figure demonstrates that the NO₂ in the reactor effluent (i.e., NO₂ balance in the system) is a function of both the NO_x reduction efficiency as well as the fraction of NO₂ to total NO_x in the reactor effluent,

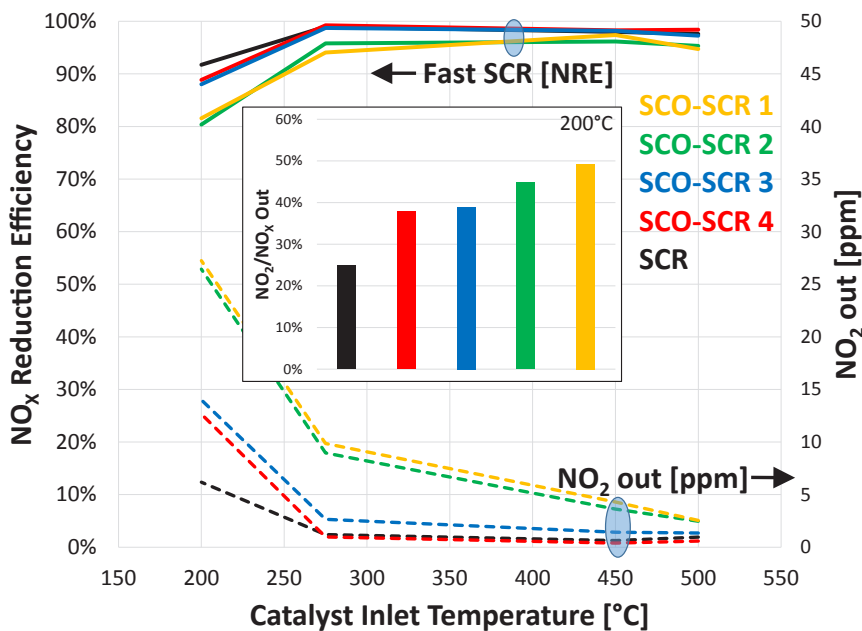


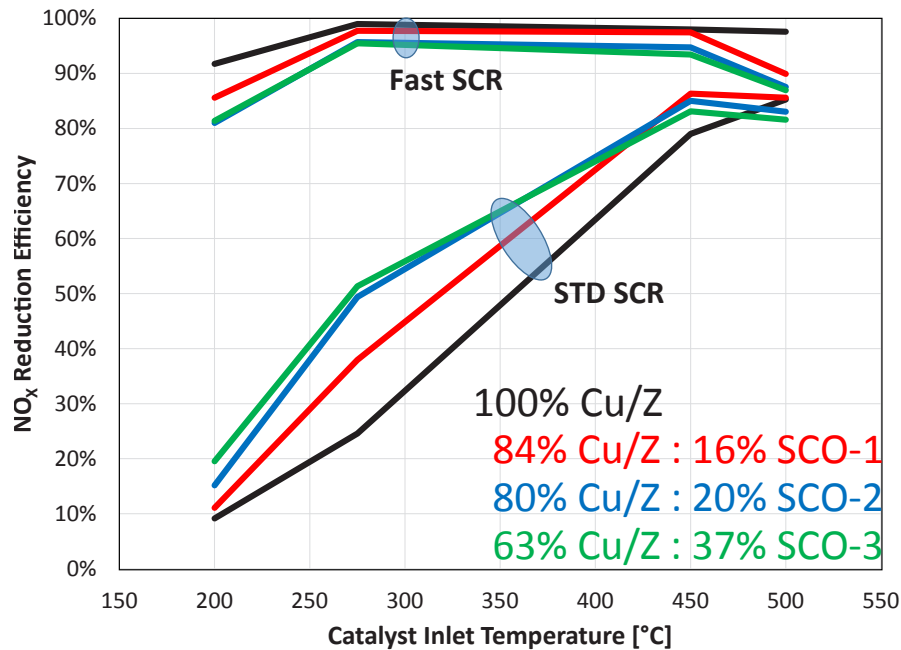
Figure IV.10.1 - Impact of different SCO phases on the NO₂ out of the SCR reaction

the latter of which is impacted by the SCO phase. These results demonstrate that the SCO phase chemistry and its impact on the SCR process and the NO_x make-up has the potential to effect NO₂ availability in the system, and thus impacting passive soot oxidation.

Further understanding the NO₂ balance in the system and the impact of the SCO phase can come from global SCR reaction performance. In pursuit of the goal of accelerating the rate of passive soot oxidation in the presence of SCR reaction, the SCO phase is employed to produce NO₂ in situ. The likely pathway of promoting this is still in question, whether it occurs via (1) NO oxidation to NO₂ which desorbs from the catalyst surface and subsequently participates in SCR reactions, or (2) NO is oxidized in the catalyst surface and continues to participate analogous to NO₂ as a surface adsorbed species. However, regardless of the pathway of participation, the effect on global SCR reaction behavior is expected to be same. If the SCO phase is in fact producing NO₂ in situ at kinetically relevant rates, then the result will be observable from the impact on both the standard and fast SCR reactions. This is demonstrated in the results that are shown in Figure IV.10.2.

Figure IV.10.2 shows that the presence of an SCO phase increases the rate SCR reduction under standard SCR reaction conditions (only NO in the inlet) and slightly decreases the rate of SCR reduction under fast SCR reaction conditions. This is the expected trend with the inclusion of increased NO oxidation to NO₂; standard SCR reaction conditions will incur a fast SCR contribution resulting in increased NO_x reduction, and fast SCR reaction conditions will incur an NO₂-only SCR contribution result in decreased NO_x reduction. This confidently demonstrates that the SCO phase is promoting NO oxidation in the system.

The goal of the program is to accelerate the rate of passive soot oxidation exhibited by the system in the presence of highly efficient NO_x reduction. Previous studies demonstrated that the presence of SCR reactions inhibits the rate of passive soot oxidation and retards the light-off of passive soot oxidation by as much as 50°C [4]. The presence of a ZrO₂ SCO phase was shown to decrease the magnitude of passive soot oxidation retard using the metrics of both CO₂ production and balance point temperature as shown in Table IV.10.1. CO₂ production is the generation of CO₂ from soot oxidation. Balance point temperature is determined as the point at which the increasing pressure drop from the temperature ramp is balanced out by the oxidation of soot decreasing the pressure drop, resulting in a slope of 0 in the pressure drop trace. As can be seen, the SCO phase shifted the CO₂ production metric by ~30°C and the balance point metric by ~25°C. This demonstrates that the SCO phase does have the ability to positively affect the passive soot oxidation activity.



STD – standard

Figure IV.10.2 - Effect of SCO phase on standard (NO only) and fast (equimolar NO, NO₂) SCR performance

Table IV.10.1 - Passive Soot Oxidation (PSO) Light-Off Metrics and Comparison to the Presence and Absence of SCO Phase

PSO metric	SCR	SCR + SCO
20-ppm CO ₂ production temperature	395°C	365°C
Balance point temperature	515°C	490°C

For the SCR application, system optimization must also consider catalyst placement within the porous filter wall for minimizing pressure drop associated with the catalyst in addition to the subsequent effect of soot. Options for catalyst placement can include loading on surface of the inlet or outlet channels, asymmetric loading within the porous filter wall towards the inlet or outlet of the filter, or symmetric loading across the porous filter wall. Previous work has identified the detrimental effect of significant catalyst loading on the inlet channel wall or within the wall close the inlet channel [4]. Figure IV.10.3 shows the comparison of three samples within different symmetries of catalyst placement across the filter wall. Results show that symmetrical catalyst placement across the filter wall leads to superior NO_x reduction performance. It is important to note that this improved performance occurs with less catalyst and at a lower pressure drop. It is expected that this is largely the result of superior catalyst dispersion within the filter and increased efficiency of gas–solid contact.

The results discussed above focus on the impact of the SCR reaction processes on the rate of passive soot oxidation exhibited in the system. However, it is also important to consider the impact of soot oxidation reactions on the SCR reaction process. Previous work suggested that the impact of soot oxidation on SCR performance was primarily attributed to the NO_x make-up, i.e., the resulting fraction of NO and NO₂ subsequent to soot oxidation. This was confidently confirmed with the current study. Figure IV.10.4 shows that the SCR NO_x reduction performance is a function of the relative contributing standard (NO only) and fast (NO and NO₂ equimolar) SCR reactions, with a more detailed explanation provided here. Under a feed gas stream containing equimolar amounts of NO and NO₂, NO_x reduction efficiency at low temperature (200°C) is fully dictated by the fast SCR feed conditions as no passive soot oxidation is occurring. However, with increasing temperature, passive soot oxidation begins to light-off and preferentially reduce NO₂ to NO. The result of this is increased contribution of the standard SCR reaction and inferior SCR reduction as compared to the fast SCR reaction. This continues to proceed until at high temperature (500°C) the passive soot oxidation reaction is

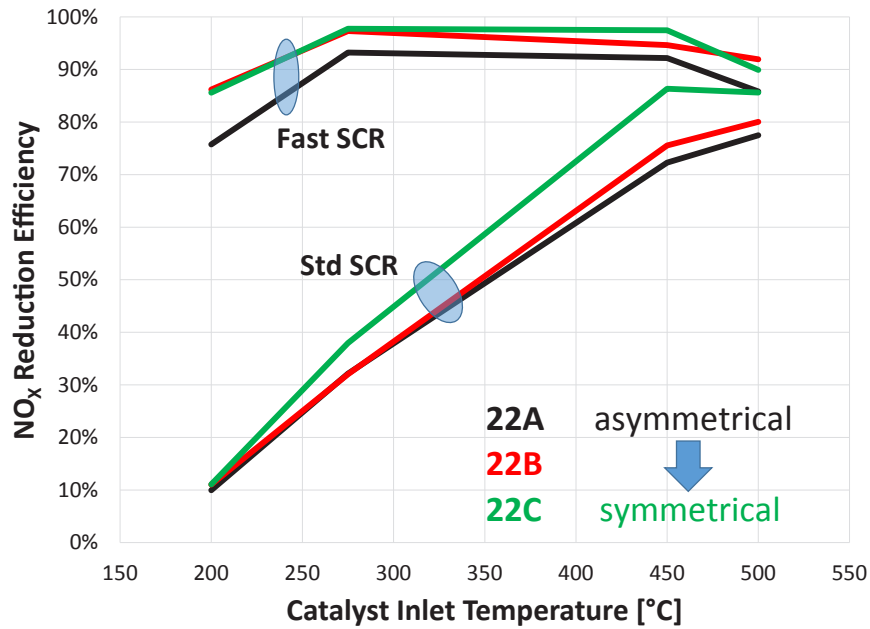


Figure IV.10.3 - Effect of catalyst washcoat symmetry on SCR NO_x reduction performance

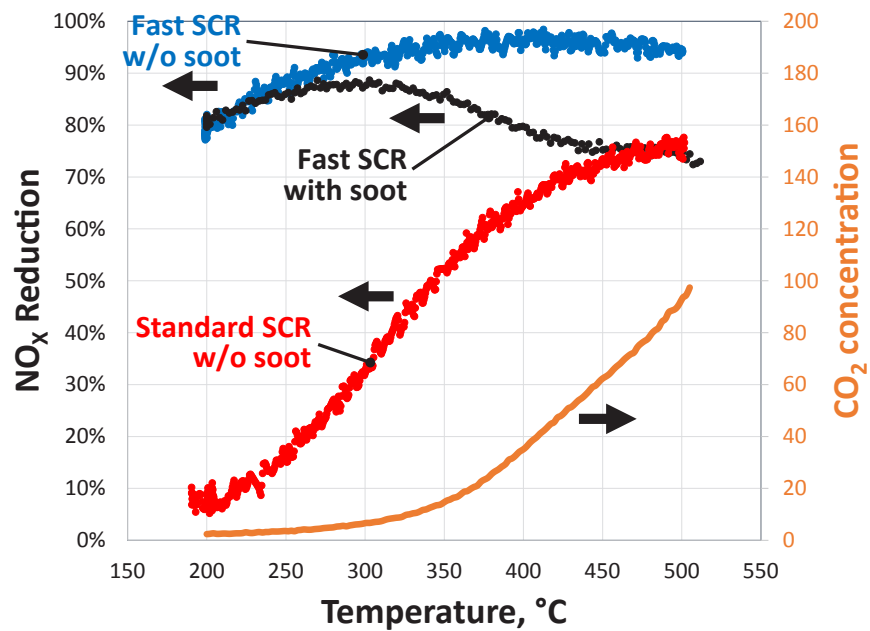


Figure IV.10.4 - Effect of passive soot oxidation on fast SCR reaction behavior

kinetically dominant and the bulk of NO₂ is reduced to NO resulting in SCR performance that is analogous to standard SCR reaction conditions (i.e., NO only).

Conclusions

- The inclusion of an SCO phase was shown to have a positive impact on the NO₂ concentration out of the SCR reactor. It was demonstrated that this effect was at least partially attributed to a comparative increase in the fraction of NO₂ in the total NO_x out of the reactor.
- Similarly, the SCO phase was shown to have a beneficial impact to the standard SCR NO_x reduction efficiency and a detrimental impact to the fast SCR NO_x reduction efficiency versus no SCO phase,

both results of which provide further corroboration of an increase on NO oxidation under SCR reaction conditions.

- The SCO phase was demonstrated to have a beneficial impact on the magnitude of passive soot oxidation exhibited in the system, decreasing the temperature of CO₂ production from soot oxidation light-off by ~30°C and decreasing the balance point temperature by ~25°C.
- Catalyst washcoat symmetry across the filter wall was demonstrated to have a beneficial impact on NO_x reduction performance. It is expected that this is the result of an indirect relationship between effective catalyst dispersion, which increases with symmetry and diffusive resistances.
- And finally, the effective of passive soot oxidation on SCR reaction performance and NO_x reduction efficiency was confidently demonstrated to be a function of the NO₂ balance in the system and kinetic relevance of the passive soot oxidation process reducing NO₂ to NO in comparison to the SCR reaction system.

References

1. Melscoet-Chauvel, I., C. Remy, T.H. Tao. “High Porosity Cordierite Filter Development for NOx/PM Reduction.” *DEVELOP ADV CERAM COMPOS* 26 (8): 11–19, 2005.
2. van Setten, B. A. A. L., M. Makkee, J. A. Moulijn. “Science and Technology of Diesel Particulate Filters.” *CATAL REV: SCI ENG* 43 (4): 489–564, 2001.
3. Beale, A.M., F. Gao, I. Lezcano-Gonzalez, C.H.F. Peden, J. Szanyi. “Recent Advances in Automotive Catalysis for NOx Emission Control by Small-pore Microporous Materials.” *CHEM SOC REV* 44: 7371–7405, 2015.
4. Rappé, Kenneth G. “Integrated SCR-DPF Aftertreatment: Insights into Pressure Drop, NOx Conversion, and Passive Soot Oxidation Behavior.” *IND ENG CHEM RES* 53 (45): 17547–17557, 2014.

IV.11 Metal Oxide-Based Nano-Array Catalysts for Low Temperature Diesel Oxidation

Pu-Xian Gao, Principal Investigator

University of Connecticut
97 North Eagleville Road
Storrs, CT 06269-3136
Email: puxian.gao@uconn.edu

Ken Howden, DOE Technology Manager

U.S. Department of Energy
E-mail: Ken.Howden@ee.doe.gov

Start Date: October 1, 2014	End Date: December 31, 2017	
Total Project Cost: \$1,830,139	DOE share: \$1,450,000	Non-DOE share: \$380,139

Acknowledgments

Co-Authors

Steven L. Suib, University of Connecticut
Todd Toops, Oak Ridge National Laboratory
Yanbing Guo, 3D Array Technology, LLC
Thomas Pauly, Umicore Autocat. USA, Inc.

Project Introduction

Clean and fuel-efficient low-temperature combustion (LTC) is preferred in the latest development of various combustion-based energy devices prompting the need of various LTC strategies including low cost, efficient, and robust catalytic emission control devices. Despite the reduced NO_x emission and increased fuel efficiency through adopting low temperature combustion modes, new challenges arise. These include, for instance, the increased hydrocarbon (HC) and CO emissions and different HC species that may be generated through these new techniques [1]. Although the research and development on efficient engine technologies, such as homogenous charge compression ignition and pre-mixed charge compression ignition [2] in the LTC regime has been in a fast-developing stage, the compatible catalytic aftertreatment technologies that operate efficiently at temperatures lower than 150°C are still lacking in industry. For example, at temperatures below 150°C , traditional diesel oxidation catalysts (DOCs) become inefficient due to the higher light-off temperature needed to activate the oxidation of CO and HCs into CO_2 and H_2O , as well as NO oxidation into NO_2 for downstream NO_x removal devices such as selective catalytic reduction structured catalysts.

In this project, we will address the above mentioned issues using our nano-array monolithic catalyst technology, i.e., in situ growth of nano-array-based catalysts on monoliths to reduce catalyst material usage, improve and demonstrate their low temperature catalytic oxidation activity and selectivity through size, shape, structure, and composition control over the nano-arrays.

Objectives

- Synthesize various metal oxide nano-arrays and porous materials (e.g., transition metal oxides, perovskites) onto monolithic cordierite substrates with high surface area, well-defined structure, and composition
- Demonstrate low cost, stable, and efficient nano-array-based monolith catalysts for low-temperature diesel oxidation
- Conduct reaction kinetics measurements upon mixed gas and simulated synthetic gas exhaust conditions, particularly on HC oxidation tests over the prepared catalysts
- Conduct transient cyclic and engine dynamometers tests over selected full-size nano-array catalysts

Approach

Low cost and green wet chemical methods are used to synthesize metal oxide nano-arrays on honeycomb substrates, followed by various porous coatings and platinum group metal (PGM) loading through sol-gel-based processes [3]. Post thermal annealing is used to improve the crystallinity and stoichiometry of nano-array-based structures. Structure, morphology, and chemical characterization are carried out using X-ray diffraction, transmission electron microscopy, scanning electron microscopy, and energy-dispersive X-ray spectroscopy. Catalyst evaluation is conducted using temperature programmed reduction, temperature programmed desorption, temperature programmed oxidation, benchtop tube reactor kinetics testing involving Fourier transform infrared and gas chromatography and mass spectrometers, and thermal and hydrothermal aging testing.

Results

By using the patent pending technology developed at the University of Connecticut, a broad spectrum of metal oxide-based nano-arrays including ZnO [4], TiO₂ [5], CeO₂, MnO₂ [6], NiO, and Co₃O₄ [7,8] have been successfully grown onto cordierite honeycomb substrates.

Pt Supported on Low-Temperature Processed TiO₂ Nano-Arrays on Cordierite Monolith

We have successfully developed a microwave synthesis of polycrystalline TiO₂ nano-arrays on a field-size cordierite honeycomb monolith with diameters up to 4.66 in and 5.66 in (Figure IV.11.1a and IV.11.1b) [9,10]. We note that utilization of microwave radiation as the heating method facilitates the growth rate, surface coverage, and uniformity of the TiO₂ nano-array as compared to conventional convection heating (hot plate). The syntheses can be accomplished in 30 min to 1–2 h for one batch compared to several hours or even days if using conventional hydrothermal synthesis as reported in literature. We employed a microwave-assisted dipcoating method to load Pt onto the TiO₂ nano-array for DOC applications. Figure IV.11.1c shows the photograph of field-size Pt/TiO₂ nano-array samples (5.66-in diameter × 3 in), which were prepared for engine dynamometer testing.

Pt/TiO₂ nano-array samples were also tested in the LTC-D simulated exhaust protocol by the Advanced Combustion and Emission Control Tech Team. The sample was hydrothermally aged at 700°C for 100 h for evaluation of hydrothermal stability. Figure IV.11.2a showed the summary for the light-off temperatures of Pt/TiO₂ nano-array in the LTC-D simulated exhaust. The samples exhibited decent oxidation activity toward CO and unsaturated HCs (propylene and ethylene) with T90 below 220°C for these gases. The Pt/TiO₂

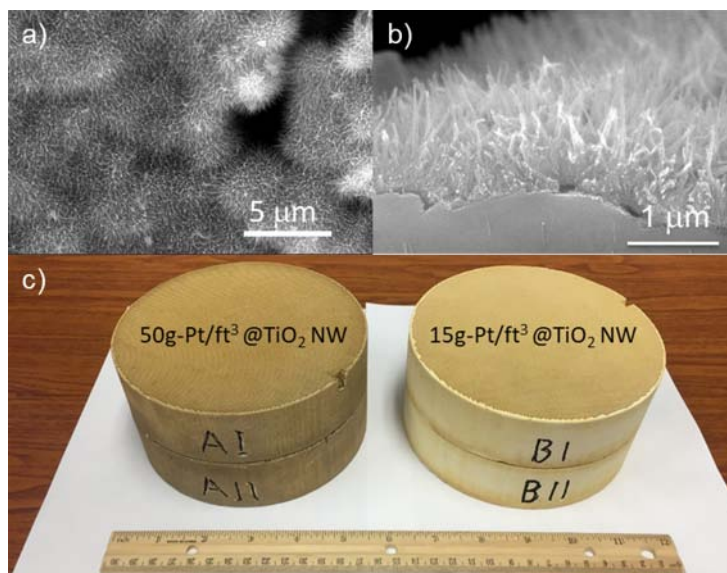
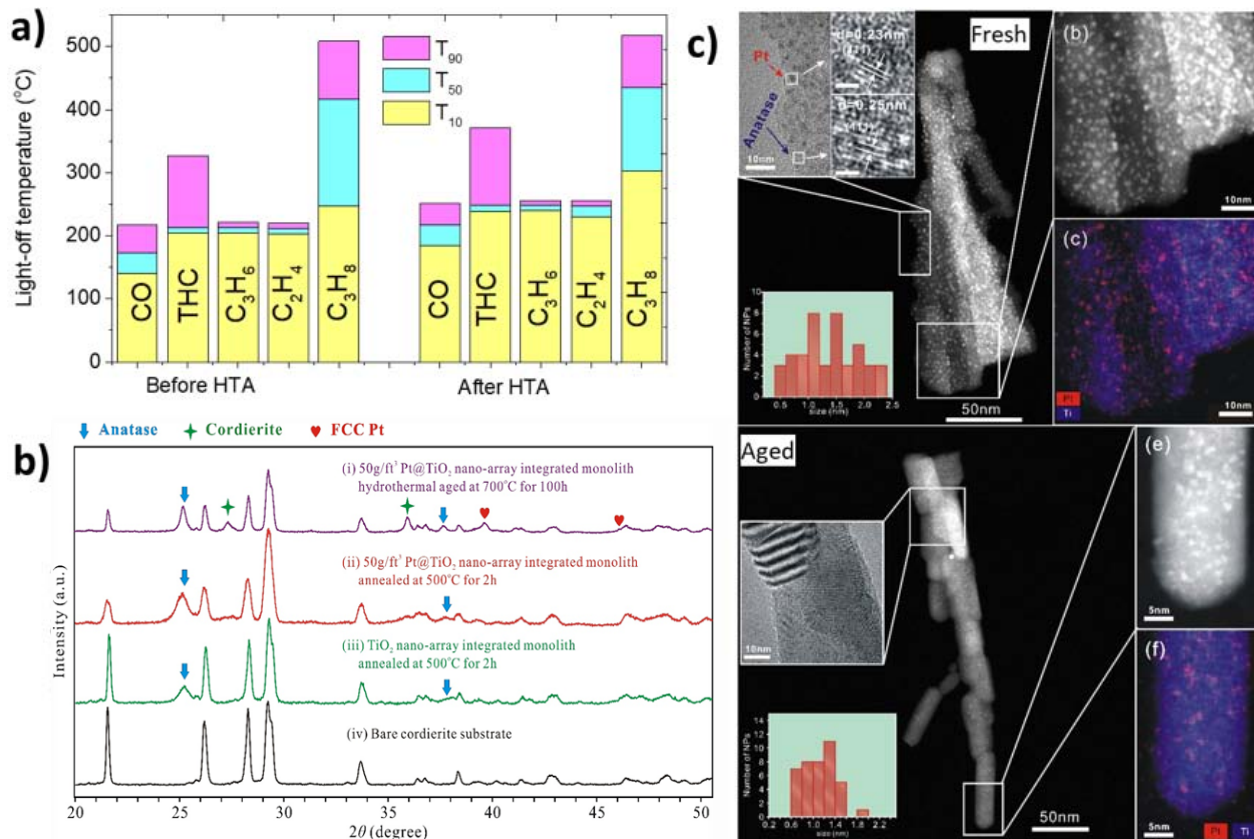


Figure IV.11.1 - (a) Top view and (b) cross-section view SEM images of low-temperature processed TiO₂ nano-array. (c) Photograph of field-size Pt/TiO₂ nano-array samples (5.66-in diameter × 3 in) for engine dynamometer testing. (Source: Gao [9], Lu et al. [10])

nano-arrays showed decent hydrothermal stability. After hydrothermal aging, T90 for CO and unsaturated HCs increase by only $\sim 35^\circ\text{C}$. After hydrothermal aging, TiO_2 is still anatase (Figure IV.11.2b) and retains nano-array morphology. The deactivation of Pt/ TiO_2 nano-arrays is likely due to the loss of active Pt sites since we observed some big Pt particles in the transmission electron microscope images (Figure IV.11.2c) and Pt peaks in the X-ray diffraction pattern (Figure IV.11.2b). However, a significant portion of small Pt nanoparticles is still observed, which explains the high DOC activity of the aged sample. It is proposed that strong metal support interaction between Pt and the TiO_2 nano-array improved the stability of Pt nanoparticles, thus the reactivity.



THC – total hydrocarbons; FCC – face centered cubic

Figure IV.11.2 - (a) DOC activity in LTC-D simulated exhaust, (b) X-ray diffraction patterns, and (c) transmission electron microscope and energy-dispersive X-ray spectroscopy scanning transmission electron microscope elemental mapping of Pt/ TiO_2 nano-array before and after hydrothermal aging (HTA) at 700°C for 100 h. (Source: Gao [9], Lu et al. [10])

Pt and Pt-Pd Supported on Hydrothermally Stable Rutile TiO_2 Nano-Arrays on Cordierite Monolith

Recently, atomically dispersed PGM catalysts have received significant interest as they have unique catalytic activity which could not compete with the nanoparticle counterpart. The catalysts also offer high selectivity and reactivity due to high metal dispersion, fewer types of active sites, low-coordination environments, quantum size effects, and enhanced electronic metal-support interactions. However, atomically dispersed catalysts are often difficult to prepare and not stable due to high surface free energy. We were able to load atomically dispersed Pt catalysts on TiO_2 nano-arrays with a volumetric Pt loading of 0.53–1.78 g/L for DOC devices employing both microwave-assisted dipcoating and developed wet-incipient impregnation [9]. Aberration-corrected high-angle annular dark-field scanning transmission electron microscopy was employed to verify the atomic dispersion of Pt on TiO_2 nano-arrays (Figure IV.11.3a). Interestingly, the Pt dispersion remains even after hydrothermal aging at 700°C for 100 h (Figure IV.11.3b). To demonstrate scalability for practical conditions, the Pt/rutile TiO_2 nano-array sample with a Pt loading of 15 g/ft³ and 2 in diameter \times 3 in were tested under highly transient feed gas conditions mimicking a heavy-duty diesel Federal Test Procedure running on a certified 2010 Cummins ISB (6.7 L) 320 hp engine. A serial DOC catalyst with a PGM loading

of 30 g/ft³ (weight ratio Pt/Pd = 6:1) was included as a reference. The Pt/TiO₂ nano-array sample and serial catalyst was aged at 650°C for 100 h in 10% steam–air flow, which represents a North American heavy-duty diesel application. Figure IV.11.3c shows the transient responses and the corresponding cumulative emission of THC and CO, respectively, of the fresh and aged Pt/TiO₂ samples. The Pt/TiO₂ samples do not show reactivity in the first 200 s due to low temperature, high exhaust flow rate, and high concentration of HC and CO. When temperature increases above 200°C, both fresh and aged samples showed good activity, especially for HCs, despite the drastic changes in the concentration and the flow rate of emission. It is interesting to note that the HC oxidation activity of the aged sample is almost as good as the fresh sample, represented by a small difference in the transient and cumulative HC emissions. The cumulative HC emissions for fresh and aged Pt/TiO₂ samples are 108 mg and 119 mg, respectively, slightly higher than that of the serial catalyst (97 mg) despite two times lower PGM usage.

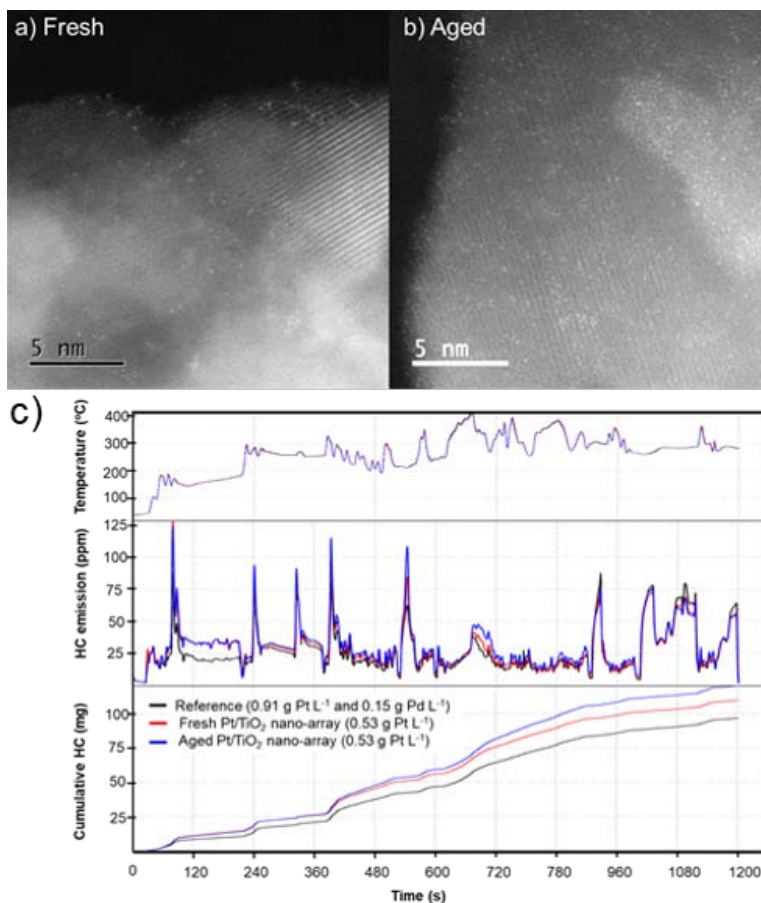


Figure IV.11.3 - Aberration-corrected high-angle annular dark-field scanning transmission electron microscopy images of Pt/rutile TiO₂ nano-arrays: (a) fresh and (b) after hydrothermal aging at 700°C for 100 h, confirming single atom dispersion of Pt (bright spots). c) Transient responses and the corresponding cumulative emission of THC and CO, respectively, of the fresh and aged Pt/TiO₂ samples. (Source: Gao [9])

Atomic layer deposition was employed for precise loading of ultrafine Pt nanoparticles (0.95±0.24 nm) on rutile TiO₂ nano-array (U-Pt/TiO₂ nano-array). The U-Pt/TiO₂ nano-array showed high catalytic activity in the conventional diesel combustion (CDC) simulated exhaust condition (Figure IV.11.4) despite ultra-low Pt loading of only 1.1 g/ft³ due to enhanced mass transport properties of the unique nano-array structure and high Pt dispersion [11]. Additionally, the light-off temperature for CO and THC could be reduced by ~60°C and 45°C, respectively, with the addition of H₂ into the simulated exhaust.

Several groups have reported that Pt-Pd bimetallic showed better CO and HC oxidation than monometallic catalysts. Additionally, replacing Pt by Pd can be an effective approach since Pd is cheaper than Pt. Therefore, we have focused on the investigation of a Pt-Pd bimetallic supported on a TiO₂ nano-array. We have tested a

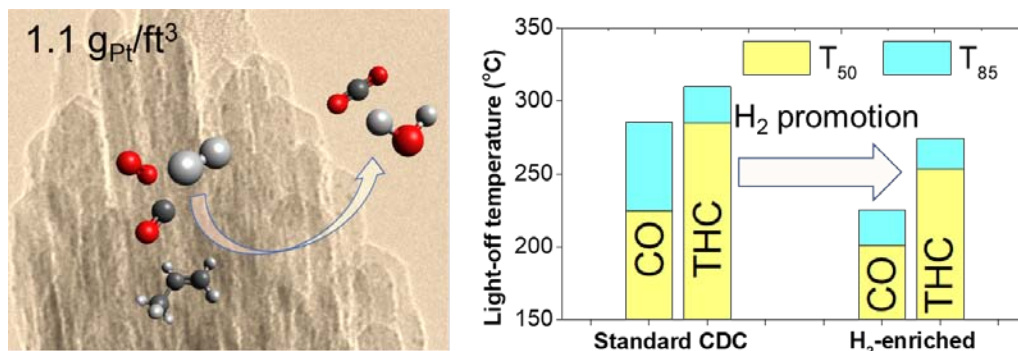


Figure IV.11.4 - DOC activity of ultra-low Pt loading on rutile TiO₂ nano-array in the CDC simulated exhaust. The addition of H₂ in the exhaust as an upstream promoter can significantly reduce the light-off temperature. (Source: Hoang et al. [11])

series of Pt-Pd bimetallics with different total PGM loading (15–70 g/ft³) and different Pt:Pd ratios (1:0, 3:2, 3:5, 0:1), and different loading methods, which showed very promising performance. Notably, the catalysts show high sulfur tolerance. Figure IV.11.5 shows the light-off curves for CO and THC of the sample with a total PGM loading of 70 g/ft³ and weight Pt/Pd ratio of 3/5 (atomic ratio Pt/Pd = 1/3). Sulfation is considered harmful for DOC catalysts since the deposition of stable sulfate species on the PGM catalysts can block access of reactants; a lot of effort has been devoted to improving sulfur tolerance of PGM catalysts. Interestingly, in our catalysts we observed the opposite trend. The oxidation activity of both CO and THC was improved after the sulfation process. Furthermore, the desulfation that involves cycling 10% O₂ and 1% H₂ for 30 min (30 s per each condition) can further improved the performance. More investigation will be conducted to understand this promotional effect.

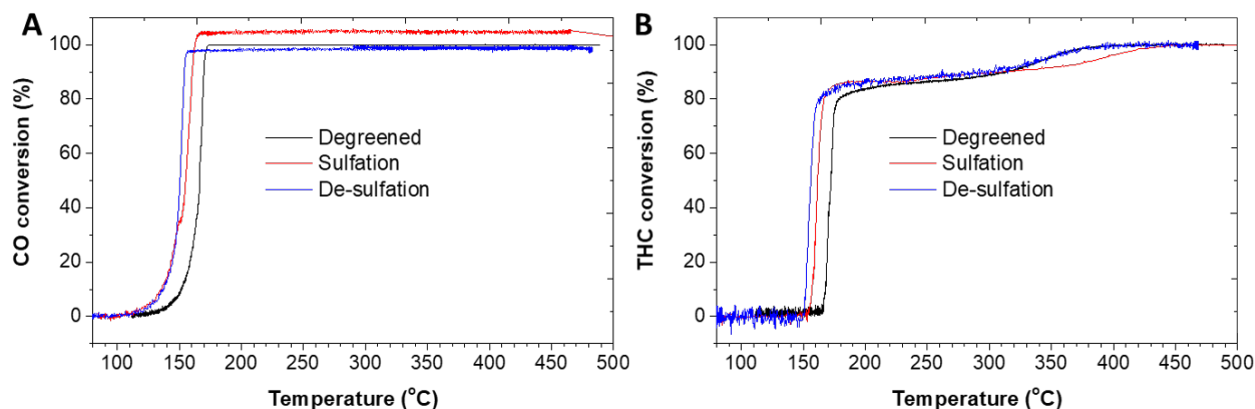


Figure IV.11.5 - Sulfur poisoning effects on CO and THC oxidation activity of Pt-Pd/TiO₂ nano-array (900 cpsi substrate, 70 g PGM/ft³, weight ratio of Pt/Pd = 3/5). (Source: Gao [9])

Conclusions

In summary, we have achieved the following accomplishments in Fiscal Year 2017.

- Demonstration of scale-up synthesis of Pt/TiO₂ nano-array for DOC activity evaluation and sulfur resistance in the simulated exhausts (CDC and LTC-D) and engine dynameters tests
- Demonstration of atomically dispersed Pt on rutile TiO₂ nano-array catalysts with remarkable hydrothermal stability for transient cyclic tests
- Demonstration of high DOC performance in the CDC simulated exhaust on ultra-low Pt loading (1.1 g/ft³) catalysts using rutile TiO₂ nano-array catalysts and added H₂ as an upstream promoter
- Demonstration of TiO₂/Pt-Pd nano-array catalysts with superb low temperature DOC activity and sulfur tolerance in U.S. DRIVE protocolled LTC-D simulated exhaust gas conditions

References

1. Zheng, M., U. Asad, G.T. Reader, Y. Tan, and M. Wang. “Energy efficiency improvement strategies for a diesel engine in low-temperature combustion.” *International Journal of Energy Research* 2009, 33 (1), 8–28.
2. Jacobs, T.J., and D.N. Assanis. “The attainment of premixed compression ignition low-temperature combustion in a compression ignition direct injection engine.” *Proceedings of the Combustion Institute* 2007, 31 (2), 2913–2920.
3. Guo, Y., Z. Ren, W. Xiao, C. Liu, H. Sharma, H. Gao, A. Mhadeshwar, and P.-X. Gao. “Robust 3-D configured metal oxide nano-array based monolithic catalysts with ultrahigh materials usage efficiency and catalytic performance tunability.” *Nano Energy* 2013a, 2 (5), 873–881.
4. Xiao, W., Y. Guo, Z. Ren, G. Wrobel, T. Lu, and P.-X. Gao. “Mechanical-Agitation-Assisted Growth of Large-Scale and Uniform ZnO Nanorod Arrays within 3D Multichannel Monolithic Substrates.” *Crystal Growth & Design* 2013, 13 (8), 3657–3664.
5. Guo, Y., G. Liu, Z. Ren, A. Piyadasa, and P.-X. Gao. “Single crystalline brookite titanium dioxide nanorod arrays rooted on ceramic monoliths: a hybrid nanocatalyst support with ultra-high surface area and thermal stability.” *CrystEngComm* 2013b, 15 (41), 8345–8352.
6. Chen, S.-Y., W. Song, H.-J. Lin, S. Wang, S. Biswas, M. Mollahosseini, C.-H. Kuo, P.-X. Gao, and S.L. Suib. “Manganese Oxide Nanoarray-Based Monolithic Catalysts: Tunable Morphology and High Efficiency for CO Oxidation.” *ACS Applied Materials & Interfaces* 2016, 8 (12), 7834–7842.
7. Ren, Z., Y. Guo, Z. Zhang, C. Liu, and P.-X. Gao. “Nonprecious catalytic honeycombs structured with three dimensional hierarchical Co_3O_4 nano-arrays for high performance nitric oxide oxidation.” *Journal of Materials Chemistry A* 2013, 1 (34), 9897–9906.
8. Ren, Z., V. Botu, S. Wang, Y. Meng, W. Song, Y. Guo, R. Ramprasad, S.L. Suib, and P.-X. Gao. “Monolithically Integrated Spinel $\text{MxCo}_3\text{-xO}_4$ (M= Co, Ni, Zn) Nano-array Catalysts: Scalable Synthesis and Cation Manipulation for Tunable Low-Temperature CH_4 and CO Oxidation.” *Angewandte Chemie* 2014, 53, 7223–7226.
9. Gao, P.-X. “Metal Oxide based Nano-array Catalysts for Low Temperature Diesel Oxidation.” DOE Vehicle Technology Program Annual Merits Review Meeting, Washington, D.C., June 5–9, 2017.
10. Lu, X., S. Hoang, W. Tang, S.C. Du, S. Wang, W. Zhong, S.L. Suib, and P.-X. Gao. “Microwave-assisted hydrothermal synthesis and manufacturing of TiO_2 nano-array integrated catalytic converters.” 2017, to be submitted.
11. Hoang, S., X. Lu, W. Tang, S. Wang, S. Du, C.-Y. Nam, Y. Ding, R.D. Vinluan III, J. Zheng, and P.-X. Gao. “Ultra-low Pt Diesel Oxidation Catalysts using Titania Nanowire Array Support.” *Catalysis Today*, 2017, <https://doi.org/10.1016/j.cattod.2017.11.019>.

Key Fiscal Year 2017 Publications

1. Hoang, S., X. Lu, W. Tang, S. Wang, S. Du, C.-Y. Nam, Y. Ding, R.D. Vinluan III, J. Zheng, and P.X. Gao, “Ultra-low Pt Diesel Oxidation Catalysts using Titania Nanowire Array Support.” 2017, *Catalysis Today*, <https://doi.org/10.1016/j.cattod.2017.11.019>.
2. Tang, W., S. Wang, W. Xiao, S. Du, X. Lu, S. Hoang, J. Ding, and P.X. Gao. “Pre-surface leached cordierite honeycombs for $\text{Mn}_x\text{Co}_{3-x}\text{O}_4$ nano-sheet array integration with enhanced hydrocarbons combustion.” 2017, *Catalysis Today*, <https://doi.org/10.1016/j.cattod.2017.10.045>.
3. Weng, J., X. Lu, and P.X. Gao. “Nano-array Integrated Structured Catalysts: A New Paradigm upon the Conventional Wash-coated Monolithic Catalysts?” 2017, *Catalysts*, 7, 253. (invited review)

4. Tang, W., Z. Ren, X. Lu, S. Wang, Y. Guo, S. Hoang, S. Du, and P.X. Gao. "Scalable integration of highly uniform $\text{Mn}_x\text{Co}_{3-x}\text{O}_4$ nano-sheet array onto ceramic monolithic substrates for low temperature propane oxidation." 2017, *ChemCatChem*, DOI:10.1002/cctc.201700795.
5. Wang, S., Y. Wu, R. Miao, Y.B. Guo, M. Zhang, A. Kinstler, Z. Ren, T. Lu, S. Suib, P.X. Gao. "Scalable Continuous Flow Synthesis of ZnO Nanorod Arrays in 3-D Ceramic Honeycomb Substrate for Low Temperature Desulfurization." 2017, *CrystEngComm*, 19, 5128–5136.
6. Tang, T., and P.X. Gao, "Nanostructured CeO_2 : preparation, characterization, and application in energy and environmental catalysis." *MRS Communications*, 2016, 6(4), 311–329.
7. Du, S., W. Tang, Y. Guo, A. Binder, E.A. Kyriakidou, T.J. Toops, S. Wang, Z. Ren, S. Hoang, and P.X. Gao. "Understanding low temperature oxidation activity of nano-array based monolithic catalysts: from performance observation to structural and chemical insights." *Emission Control Science and Technology*, 2016, 3(1), 18–36.
8. Gao, P.X. "Robust and Efficient Low Temperature Diesel Oxidation over Noble Metal Supported TiO_2 Nano-array Integrated Catalytic Converters." DOE CLEERS Workshop, Ann Arbor, MI, October 3, 2017.
9. Gao, P.X. "Multi-functional Nanostructure Integration for Emission Control and Utilization." National fall conference of America Chemical Society, Washington, DC, August 19–24, 2017.
10. Gao, P.X. "Metal Oxide based Nano-array Catalysts for Low Temperature Diesel Oxidation, DOE Vehicle Technology Program Annual Merit Review Meeting." Washington, DC, June 5–9, 2017.
11. Hoang, S., Y. Guo, W. Tang, S. Wang, A.J. Binder, E.A. Kyriakidou, T.J. Toops, J. Liu, T. Pauly, and P.X. Gao. "Exceptional Low Temperature Diesel Oxidation Activity over Single Atom Pt Supported TiO_2 Nano-Array Integrated Monolithic Catalysts." North American Meeting of the Catalysis Society, Denver, CO, June 2017.
12. Hoang, S., Y. Guo, W. Tang, S. Wang, A.J. Binder, E.A. Kyriakidou, T.J. Toops, Y. Ding, C.-Y. Nam, and P.X. Gao. "Low Temperature Propane Oxidation over Atomic Layer Deposited Pt Supported TiO_2 Nano-Array Integrated Monolithic Catalysts." North American Meeting of the Catalysis Society, Denver, CO, June 2017.
13. Wang, S., S. Du, W. Tang, and P.X. Gao. "Pt loaded Perovskite Nano-array based Monolithic Catalysts for Automotive Emission Control." North American Meeting of the Catalysis Society, Denver, CO, June 2017.
14. Tang, W., Z. Ren, X. Lu, S. Du, S. Wang and P.X. Gao. "Fabrication of spinel nanostructured $\text{Mn}_x\text{Co}_{3-x}\text{O}_4$ sheet array based monolithic catalysts for low temperature propylene and propane oxidation." North American Meeting of the Catalysis Society, Denver, CO, June 2017.
15. Tang, W., X. Lu, S. Wang, S. Du, and P.X. Gao, "In situ constructing nano-sheet array on the cordierite honeycomb and its application in catalytic combustion of hydrocarbons." North American Meeting of the Catalysis Society, Denver, CO, June 2017.
16. Hoang, S., Y. Guo, W. Tang, S. Wang, A.J. Binder, E.A. Kyriakidou, T.J. Toops, J. Liu, and P.X. Gao, "Exceptional Activity for Diesel Exhaust Combustion over Sub-nanometer Pt Supported TiO_2 Nano-Array based Monolithic Catalysts." MRS Meeting, Boston, MA, November 30, 2016.
17. Gao, P.X., and W. Tang. "Mn-Co Spinel Oxide Nano-array Based Monolith." US provisional patent filed, University of Connecticut, 2017.
18. Gao, P.X., and S. Hoang. "Low-temperature Diesel Oxidation Catalysts using TiO_2 Nano-Arrays Integrated Monolithic Substrates." US provisional patent filed, University of Connecticut, 2017.

19. Gao, P.X., X. Lu, and S. Hoang. "Microwave-assisted and low-temperature fabrication of TiO₂ nanostructured films on scalable 2D and 3D substrates." US provisional patent filed, University of Connecticut, 2017.
20. Gao, P.X., and W. Tang. "Cordierite nano-array integrated cordierite honeycomb monolith." US provisional patent filed, University of Connecticut, 2017.
21. Gao, P.X., and S. Wang. "Perovskite-Pt Nanotube Array Based Monoliths." US provisional patent filed, University of Connecticut, 2017.

V. High Efficiency Engine Technologies

V.1 Volvo SuperTruck 2: Pathway to Cost-Effective Commercialized Freight Efficiency

Pascal Amar, Principal Investigator

Volvo Group North America
 7900 National Service Rd.
 Greensboro, NC 27409
 E-mail: pascal.amar@volvo.com

Roland Gravel, DOE Technology Manager

U.S. Department of Energy
 E-mail: Roland.Gravel@ee.doe.gov

Start Date: October 1, 2016 End Date: September 30, 2021
 Total Project Cost: \$40,000,000 DOE share: \$20,000,000 Non-DOE share: \$20,000,000

Project Introduction

Volvo’s SuperTruck 2 (ST2) builds on the success of the SuperTruck project that demonstrated vehicle freight efficiency improvements in excess of the program goals. Many SuperTruck technologies with customer-acceptable payback (e.g., aerodynamics, powertrain components, tractor lightweighting) are now used in commercial trucks, thereby reducing national energy consumption.

Federal data on truck utilization shows that a majority of Class 8 long haul trucks operate at or below 65,000 lbs gross combined weight, much lower than the maximum allowed combined vehicle weight of 80,000 lbs. This implies that most trucks are under-utilized and are overdesigned, i.e., heavier and with more powerful engines than needed to meet their actual operational requirements. Volvo’s ST2 concept will therefore demonstrate a reimagined tractor-trailer designed with an integrated approach in order to maximize freight efficiency.

The project consists of three work packages organized in four sequential phases as illustrated in Figure V.1.1. Fiscal Year 2017 focused on technology evaluation and concept selection.

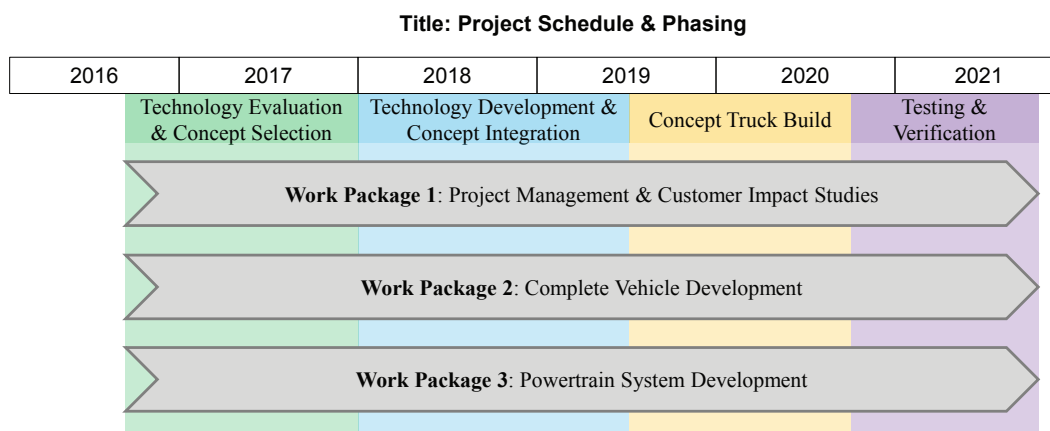


Figure V.1.1 - Project schedule and phasing (Volvo)

Objectives

- Demonstrate >100% improvement in vehicle ton-miles per gallon compared with a best in class 2009 truck, with a stretch goal of 120%

- Demonstrate 55% brake thermal efficiency (BTE) on an engine dynamometer
- Develop technologies that are commercially cost-effective in terms of a simple payback

All activities to date have been completed according to the original schedule and on budget. An overview of the main achievements during this first budget period is presented below.

Approach

Volvo’s ST2 project is currently in the first of four phases, which focuses on selecting concepts for further development. The work is divided between road tests, component tests, and analytical studies to benchmark multiple technologies and quantify complete system impact. Phase I is expected to deliver a frozen concept for the complete vehicle in the first quarter of Fiscal Year 2018.

The powertrain research in this project is guided by two goals: to demonstrate over 100% freight efficiency increase in a vehicle, and to demonstrate 55% BTE of the engine in a test cell. These goals differ not only in level of efficiency required by the powertrain solution but also in the size of the design space.

As a consequence the team is taking a two-pronged approach and will deliver one powertrain shaped as part of a total vehicle optimization toward maximum freight efficiency, and another focused on demonstrating 55% BTE. Though the dual path approach may yield two different system level approaches, significant synergies are expected in the fundamental areas of internal combustion efficiency improvement.

The Volvo SuperTruck demonstrator unveiled in September 2016 has become a test mule to evaluate technologies and aid the team in the selection of a complete vehicle concept. Figure V.1.2 illustrates how assets from SuperTruck are leveraged in the ST2 project.

Title: SuperTruck (1) evolves into SuperTruck 2





Program	Vehicle Name	Picture	Vehicle Description
SuperTruck Completed	VEV1		Mule truck used for concept selection and development of technologies for SuperTruck
	VEV2		Final SuperTruck (ST1) Demonstrator
SuperTruck 2 In Process	VEV3		ST1 rebuilt with improved technologies Mule truck used for concept selection and development of technologies for SuperTruck 2
	VEV4		Final SuperTruck 2 Demonstrator New, custom built concept truck

Figure V.1.2 - SuperTruck evolves into SuperTruck 2 (Volvo)

Results

As shown in Figure V.1.2, the Volvo ST1 demonstrator is used as a research vehicle (VEV3) for road testing and concept selection activities. A comprehensive test plan was created for the reporting period which deployed this truck on multiple on-road fuel economy tests for validation of aerodynamic simulations,

evaluation of predictive energy management concepts, as well as heating, ventilation, and air conditioning (HVAC) testing in a climate controlled chamber. During Fiscal Year 2017 this unique research vehicle accumulated close to 10,000 miles!

Using data collected by our fleet partners and through Volvo’s big data platform for customer analytics, we are evaluating the operational characteristics of long-haul fleets to ensure that the duty cycles used in our simulations are representative of real-world performance. The first delivery of this task was a 24-hr duty cycle based on customer operation which was used for testing with our research vehicle VEV3 as well as for simulation of the concept vehicle VEV4.

The overall plan for system simulation activities for the SuperTruck 2 concept selection is shown in Figure V.1.3. Studies to understand the effect of vehicle configuration on aerodynamics were completed on time. The effect of downsizing the engine was studied along with an optimization of the powertrain torque curve for the target ST2 vehicle performance requirements, and both were completed on schedule. The analysis of the power requirements of the vehicle, forecasting the tradeoffs between drivability and fuel economy, enabled the team to make an early decision on engine power and torque rating ahead of the original schedule. This helped kick-off powertrain concept selection discussions and served as input into further vehicle system level simulations. The team is now focusing on optimizing the powertrain system to ensure sufficient cooling performance while improving aerodynamics and reducing parasitic losses. Work is on track to support final concept selection by the end of 2017.

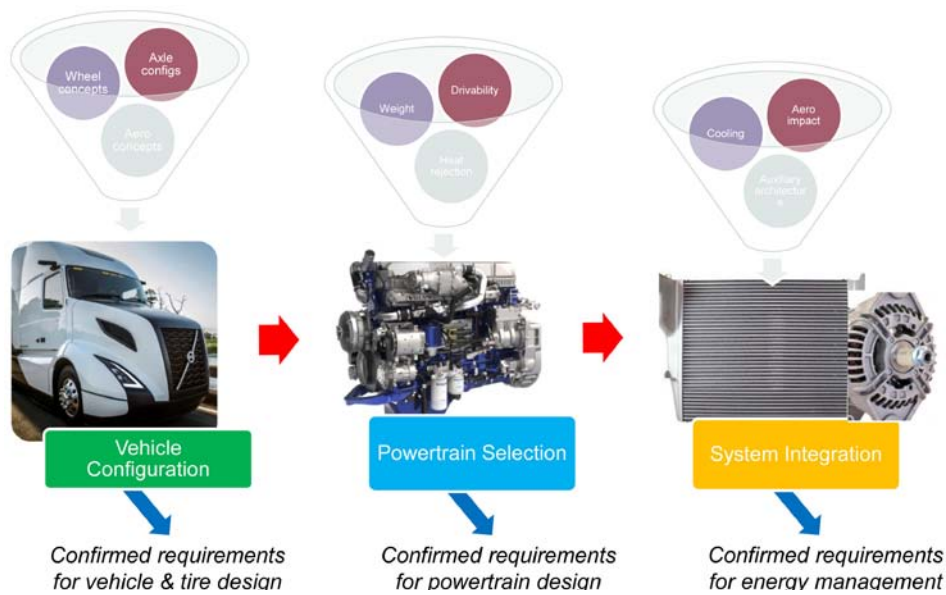


Figure V.1.3 - System simulation plan for SuperTruck 2 concept selection (Volvo)

Vehicle Configuration

A base vehicle which is representative of the vehicle configuration targeted for ST2 was defined to aid in the benchmark of concepts for the ST2 tractor, including tire evaluations at Michelin’s test track in South Carolina. We also used this truck specification to build a model in computer-aided design for virtual work on the final demonstrator. The digital mock-up was produced and shared with Metalsa who is designing a lightweight frame concept for the final demonstrator.

In preparation for the complete vehicle concept freeze at the end of 2017 we have selected a design direction for front and rear axles, suspensions, transmission, brakes and wheel end equipment, tire and fuel tank size.

Powertrain System Development

A baseline powertrain configuration was chosen for modeling activities, which consists of an 11 L Volvo engine and Volvo I-shift transmission. Advanced models for cooling systems and powertrain heat rejection

were developed during this first fiscal year in order to provide the powertrain installation team with a cooling package optimization tool.

Multiple concept and components studies have been progressing in parallel and are on track with many achievements to date. The first achievement of note is the successful installation and commissioning of a single-cylinder research engine at the University of Michigan. A newly renovated test cell with AVL test cell equipment was installed at the Walter E. Lay Automotive Laboratory, which will support the University of Michigan engine testing tasks for ST2. The engine is a Volvo six-cylinder 11 L with a Delphi F3 injection system that is operating on Cylinder #6 only. It will be used during the project to provide baseline test data for comparison with Volvo multi-cylinder engine tests, a piston and injector study for validation of Volvo models for enhancing engine performance, and then piston design and combustion studies. Experimental studies with the test engine began during summer 2017.

Another achievement is the completion of an initial evaluation of the paths to 55% BTE for a matrix of potential powertrain concepts. Oak Ridge National Laboratory (ORNL) is studying multiple exhaust aftertreatment system (EATS) architectures, component formulations, and control strategies that would enable the 55% BTE engine to achieve applicable U.S. emission levels. The key challenge is that engines operating at high BTE will have low exhaust temperatures downstream of the final expansion, requiring aftertreatment components optimized for low temperature operation or placement of aftertreatment components upstream of the final expander. Pre-expander EATS evaluations will require a synthetic exhaust flow reactor capable of operating at elevated pressures, therefore much of the work at ORNL for Fiscal Year 2017 focused on upgrading an existing flow reactor system to handle higher pressures. ORNL has procured and installed many of the hardware components required for the reactor upgrade, including gas cylinder pressure regulators and an electronically controlled backpressure regulator. Hardware installation was completed on track to begin EATS evaluations in Fiscal Year 2018. In parallel with this work Johnson Matthey is exploring aftertreatment technology options that are best suited for each of the proposed engine designs.

Combustion system optimization testing has also begun to further optimize the wave piston design which was developed as part of ST1. Work focuses on studying the impact of the wave shape, height, floor shape and interaction with injector flow rate and umbrella angle. This testing will yield an improved fundamental understanding of the wave piston combustion system, with direct applications on the ST2 engines.

Aerodynamics

Body in white architecture and key dimensions have already been decided and approved, which are aligned with the aggressive project goals while maintaining a path to future commercialization. A virtual concept model of the complete vehicle was created with these refined dimensions and computational fluid dynamics analysis is showing very promising results, with over a dozen simulation iterations to date.

Road test of the technology vehicle VEV3 with the new trailer from Wabash was performed in June 2017 in order to establish the aerodynamic baseline for aero concepts development. The results correlated very well with the computation fluid dynamics simulation results for the same vehicle configurations. We are on track with the selection of an aerodynamic concept for the complete vehicle, and ahead of schedule with the detailed aerodynamic design.

Advanced Lightweight Concepts

During this concept selection phase Metalsa has been investigating new technologies including additive friction stir as an enabler to redesign for joining, sealing, additive manufacturing and secondary processing. Additive friction stir technology could be used for near net-shape component deposition, coating, and joining of similar and dissimilar materials. Prototypes have been created to support the ongoing feasibility evaluation of these techniques.

Metalsa's Technology department is also working on a multibody dynamics model of rig test that can correlate the actual rig test and the testing from the Volvo's proving ground. The correlation of the multibody dynamics rig to actual rig test is 75% complete, and the simulations using inputs from the tractor suspension characteristics and incorporating them with the test results obtained from track testing are 50% complete.

The baseline ST2 computer-aided design models were received in March 2017 and Metalsa started selecting components to achieve weight reduction targets ahead of the original schedule.

A set of lightweight brake drums were tested on VEV3 in February 2017 to validate the weight savings (31 lbs per drum) and braking performance, which improved compared with the steel drums. We have already specified the weight target for the complete vehicle down to the detail level for front and rear suspension modules, frame assembly, axles and wheel ends, pinion gear size, and axle housing.

Concept Trailer Development

The Wabash team has defined a concept development plan which includes trailer aerodynamics and lightweight component development activities. The aerodynamic development is the key starting point because it establishes the dimensional parameters which will be used as inputs to the lightweight design.

Key achievements to date include:

- Developing a three-dimensional trailer model to be used for predictive aero simulations.
- Finalizing the baseline trailer specification and building a baseline trailer in May 2017. This trailer was the starting point for joint aerodynamic development between Volvo and Wabash.
- Establishing a method for co-optimization of the aerodynamic performance between the tractor and trailer.
- Performing a baseline aerodynamic on-road test in June 2017 using VEV3 pulling a trailer equipped with the Aerofin XL boat tail and the Ventix DRS side skirts.
- Establishing a test plan to validate lightweight panel concepts that will deliver a significant trailer weight reduction while maintaining adequate structure. Testing began at the end of the fiscal year and will continue through next fiscal year. Depending on results from this evaluation some new wall panels may be retrofitted onto the baseline trailer for further testing.

Low Rolling Resistance Tires

Michelin has assembled a project team composed of about 10 people that represent several métiers such as tire and material design, tools and methods, and process. The team is responsible for delivering the steer, drive, and trailer tires for the Volvo ST2 vehicle.

The team is currently focusing on answering key questions surrounding the impact of the vehicle concept on tire design, e.g., effect of tire diameter on choice of rolling resistance improvement technologies, fleet acceptance for increased wear to push trade-off curves in tire design, etc. A test plan was prepared to evaluate these characteristics using a truck representative of the ST2 concept at Michelin's proving grounds in the beginning of next fiscal year.

Hotel Mode

A detailed plan was defined together with Bergstrom to evaluate the hotel mode system on VEV3. The mule truck was driven to Rockford, Illinois, in April 2017 where various tests were performed in a climate chamber including ambient temperature sweeps, baseline air conditioner performance evaluation, cabin R-value, and cab pressurization testing as well as TMC no-idle testing.

Upgrades to the VEV3 HVAC systems were then performed, which included reduced power consumption of air conditioning compressors, intelligent condenser fan logic, and variable control of compressors, as well as feasibility study on potential reduction of number of compressors. Many of these tests were then repeated as an A-B comparison after upgrades were made to the vehicle's HVAC systems to improve their performance. This test campaign helped refine the requirements and sizing of the HVAC system being defined for the final ST2 demonstrator.

Complete Vehicle Energy Management

The complete vehicle energy management system which was developed in ST1 is the starting point for concept development in this project. During January and February 2017 several static and local road tests were conducted on the rapid prototyping control system to ensure that all features functioned as expected. Testing included Global Positioning System reception quality, map reading software performance, etc. Several enhancements were made to the software to ensure that it can function stand-alone. The end result was a very reliable energy management system that could be handed over to test drivers for evaluation without any intervention from engineers.

This improved energy management concept was tested on road in March 2017 near Rock Hill, South Carolina, on Interstate 77. The results showed about 4.5% improvement in the fuel economy. During the tests we learned more about the behavior of this Energy Flow Control Unit which helped us define how we can further improve it for more real-world savings. The improved version of the complete vehicle energy management system will be tested again in the next fiscal year during a dedicated performance evaluation campaign.

Conclusions

- The complete vehicle configuration has been finalized in preparation for the project concept freeze scheduled at the end of 2017.
- A base aerodynamic model has been defined, which includes body in white architecture and key dimensions.
- Detailed weight targets have been specified for each subsystem in the complete vehicle, which will yield significant payload capacity improvements.
- A concept development plan which includes trailer aerodynamics and lightweight component development activities has been defined.
- A test plan was prepared to evaluate the impact of the vehicle concept on tire design at Michelin's proving grounds during next fiscal year.
- HVAC software and calibration improvements on the ST1 mule truck resulted in approximately 20% lower energy consumption of the system, which establishes a baseline for the ST2 hotel mode concept.
- The complete vehicle energy management system which was developed in ST1 was improved as a starting point for the ST2 concept and tested on Interstate 77, yielding about 4.5% improvement in the fuel economy.

V.2 Cummins/Peterbilt SuperTruck II

Michael Ruth, Principal Investigator

Cummins Inc
PO Box 3005
Columbus, IN 47201-3005
E-mail: michael.j.ruth@cummins.com

Roland Gravel, DOE Technology Manager

U.S. Department of Energy
E-mail: Roland.Gravel@ee.doe.gov

Start Date: October 1, 2016	End Date: September 30, 2021	
Total Project Cost: \$40,000,000	DOE share: \$20,000,000	Non-DOE share: \$20,000,000

Acknowledgments

Co-Authors

Ken Damon, Peterbilt
Nicole Downing, Eaton
Stephen Miranda, Bridgestone

NETL Project Manager

Ralph Nine, National Energy Technology Laboratory

Project Introduction

The trucking industry is faced with numerous challenges to reduce petroleum consumption while meeting stringent criteria emissions regulations and providing customer value. The United States has approximately 3.5 million Class 8 vehicles on the road, consuming 4,500,000 barrels of petroleum per day. If only half of the fleet implemented half of the benefits proposed, at \$3.85/gal, the nation would see a fuel savings over \$30,000,000 annually and reduce petroleum consumption by over 500,000 barrels per day. This reduction would have a positive impact on the environment by eliminating 200,000 metric tons of CO₂ per day.

The Cummins led SuperTruck II project goals are to design, develop, and demonstrate a very high efficiency engine that is optimized around the drive cycle that will yield a very high increase in vehicle freight efficiency. The baseline for comparison will remain the 2009 vehicle where the demonstration will be done with similar vehicle specifications. The engine will maintain compliance with the current heavy-duty diesel emission regulation for line haul vehicles, while the vehicle system will remain compliant with the current greenhouse gas regulatory requirements.

Objectives

- Demonstrate a minimum of 55% brake thermal efficiency using 65 mph cruise conditions on an engine dynamometer test
- Utilize the same engine system demonstrated on dynamometer in vehicle and operating on real world drive cycles
- Achieve a minimum of 125% freight ton efficiency (FTE) over a relevant drive cycle (FTE = mpg × tons of freight)
- Track, promote, and report cost effective solutions, prioritizing solutions that have an approximate 3-yr payback period utilizing a relevant customer counsel for understanding customer acceptance and expectations

Approach

The approach for meeting the 55% brake thermal efficiency target is via careful dissection of the diesel cycle and reduction of losses via waste heat recovery (WHR). The engine will be tuned to take advantage of ideal conditions for the aftertreatment effectiveness, therefore reducing any inefficiency of the exhaust gas recirculation (EGR) and injection timing systems. The closed cycle efficiency will be optimized for high expansion ratio via rapid heat release and insulated surfaces. The open cycle will be optimized by using low pressure EGR and ideal valve events, fixed geometry turbocharger with the ultimate in tip clearance and efficiency. The mechanical efficiency of the engine system will be developed to use low viscosity oil with variable lube and cooling pumps, all while running the engine at a low enough speed to minimize spin and pumping losses. The WHR system will be a two-loop system harvesting both low quality heat from the coolant and charge cooler and high quality heat from the EGR coolers and tailpipe boiler. The WHR system will be the primary cooling system for the engine under the cruise operating conditions and only require a small radiator for sustained high load conditions.

The powertrain will integrate the WHR and an energy recovery system (motor/generator [M/G]) onto the Eaton automated transmission for compactness and efficiency reasons. During flat road and uphill operations, this system can input power to the system to reduce fuel consumption. As the vehicle operates downhill, the engine can be decoupled from the powertrain, leaving the controls to apply power from the WHR system as needed and/or to recover energy from the system through the M/G to be stored in an onboard battery.

The vehicle will achieve the high FTE with the combination of low motive resistance and light weighting. Bridgestone will be supplying tires that can meet customer requirements for longevity yet reduce rolling resistance well beyond the current commercially available tires via compound development and siping design. The vehicle structure will include a new weight saving composite design that will incorporate a kneeling suspension that will aid in the reduction of aerodynamic load. The vehicle design will incorporate aerodynamic features to improve drag in all wind conditions via moving surfaces that react to changing winds detected by the onboard Lidar system. Finally, the drive axle will incorporate an advanced control system that will ensure good low speed traction with state-of-the-art low parasitic, high speed operation.

Results

The following are the key accomplishments for Fiscal Year 2017. The accomplishments listed below are fundamental steps required to complete the objectives of the program.

The team has completed:

- Nearly 275,000 mi of data logging and reduction to understand Walmart routes from three distribution centers.
- New tread designs and compound mixing to significantly reduce the rolling resistance of the tires while maintaining tread life.
- A study to understand the benefit of using a 48 V mild hybrid system versus that of a high voltage/high power electric energy recovery system.
- The layout and data communication plan for the combined energy recovery transmission coupled system.
- Engine testing to confirm compression ratio, charge flow, and injection rates required to meet the closed cycle efficiency target for the demonstration conditions.
- The vehicle powertrain layout and build-up plan for a powertrain mule that will be the basis for system testing which will be utilized over the remainder of the program.

National Renewable Energy Laboratory engineers retrieved and analyzed data from 56 vehicle Controller Area Network bus loggers deployed at three Walmart distribution centers (Loveland, Colorado; Sanger, Texas; Grove City, Ohio). Nearly 275,000 driving miles were assessed to dissect Walmart's route types and driving patterns. The National Renewable Energy Laboratory report included program data vital to both Walmart and

the SuperTruck team on their current driving patterns (by truck and region) including mpg, time in top gear, idle time, and cruise utilization. National Renewable Energy Laboratory used their analysis to recommend two routes, comparable to the average Walmart route, in the Denton, Texas, and Columbus, Indiana, areas. Peterbilt and Cummins will use these routes for commercial assessment of the final technologies on the SuperTruck II demonstrator.

An area of primary focus for the tires has been the evaluation of different mixer technologies that are expected to yield improved rolling resistance and wear balance. Small-scale mixes were completed at the Bridgestone technical center, followed by a larger-scale mix. The team is also developing new sipe technology that will be evaluated as part of the program. It can be challenging to extract the tire with the complex, new design sipe geometries from the form tool once the cure cycle is complete. The tooling features an innovative surface treatment of the siping and a modified sipe design, which will allow for improved mold extraction from the cured tire. The first tire build occurred in June using the new tooling. No significant hurdles with tire extraction were encountered during this build. The tires were tested on a wear energy machine, the results of which will be used to help determine the sipe geometry and configuration which most improves tire wear. Nine different experimental pattern designs were tested, each representing variations of sipe shape, spacing, depth, and thickness. The results from the leading candidate showed a 39% reduction in wear energy intensity, an indicator of wear rate. This improvement in wear energy intensity will allow a reduction in tread depth in the demonstration tires, translating into a rolling resistance reduction.

The powertrain system integration team took on work to understand the benefit of electric energy recovery M/G and energy storage system (ESS) sizing. The analysis shows the diminishing return as the capacity of the M/G becomes larger than 30 kW. Additionally, the data would indicate an ESS greater than ~3 kW-hr would yield no benefit. It should be noted other cycles, with more grade and higher characteristic acceleration, will benefit more from larger M/G and more ESS capacity.

The layout and the design work has been initiated for the energy recovery system. The initial work will be a 20 kW continuous, 32 kW peak 48 V system coupled to the rear facing power take off. This arrangement will be tested at the Oak Ridge National Laboratory Vehicle Systems Integration Laboratory over various routes to ensure the hardware and software are capable and roadworthy. Additionally, the lab testing will allow Cummins to refine its models, ensuring performance predictions and demonstration will be comparable. The M/G system layout is highlighted in Figure V.2.1.

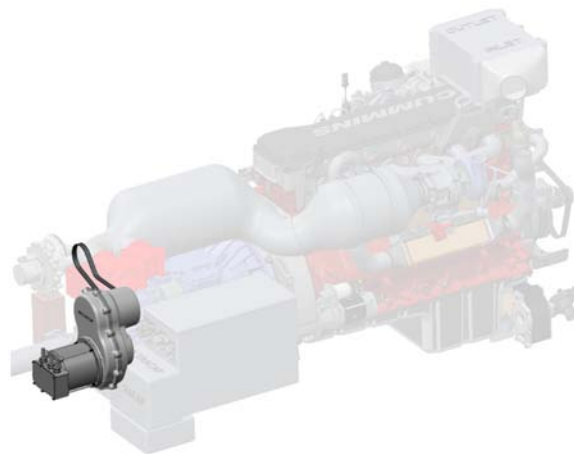


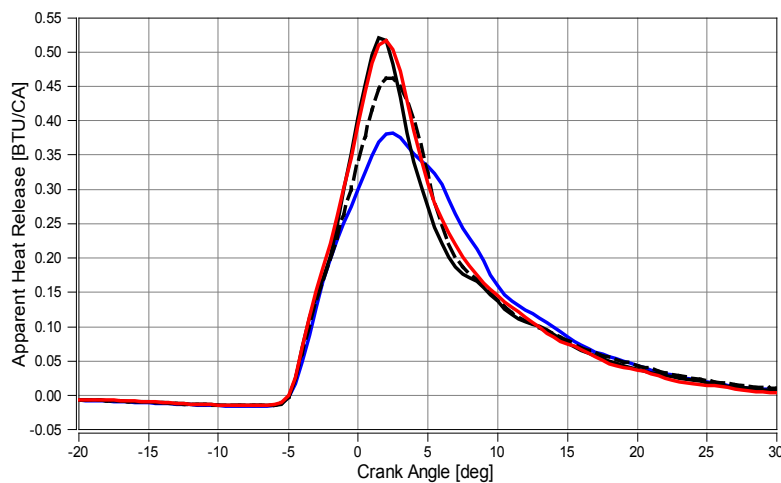
Figure V.2.1 - Powertrain layout, highlighting the location and arrangement for the M/G system coupled to the rear facing power take off

Test data from the mule development has shown several advances in closed cycle efficiency (CCE). The team continues to work on the rapid heat release rate as one of the most transferable technologies when the test platform moves from the mule to the new engine. The team has seen data close to 52% CCE, against a target of 53%. Test data from the compression ratio testing proved a loss in CCE at the highest (24:1) and lowest (17.2)

tested compression ratio. The 22.5:1 and 21:1 systems performed very similarly and are much more suitable from a cylinder pressure limit.

The combustion testing has shown a benefit to optimize the charge flow (EGR and fresh air) at 39:1 charge:fuel ratio. Testing has shown the heat rejection above 39:1 does not reduce and pumping penalty and starts to overtake any gains from increasing it. Dropping below 39:1 resulted in increased heat rejection to the coolant and exhaust with a lower CCE and brake thermal efficiency. Cummins prime path will be at or near the 39:1 charge:fuel ratio.

Finally, the combustion systems were tested at various levels of injection timing and charge:fuel ratio. Going forward, Cummins prime path will be at or near the 22:1 compression ratio. Test data for combustion systems with compression ratio greater than 21:1 responded positively to an increase in injection rate. For this testing, injection rate increase was achieved via nozzle flow increase only. Heat release data shown in Figure V.2.2 illustrates a sharper rise, higher peak, and faster decay with the increased nozzle flow injectors. This results in a more efficient burn as the cycle begins to closer approximate the Otto cycle (constant volume heat addition).



CA – crank angle

Figure V.2.2 - Heat release rate in response to increased injection rate. The lowest rate is the baseline. Increased peak rate corresponds to increased injection rate.

The partners for the Cummins led SuperTruck II team have developed a plan to execute a powertrain mule program. The mule will be used primarily to develop the powertrain that will eventually be used in the demonstrator vehicle. The mule will look substantially the same as today's current product from the outside. The underpinnings of the mule will be the same as the intended demonstration vehicle, starting with the light-weighted frame system and advanced suspension with associated controls. The powertrain will be built with the new platform engine and transmission in its current technology trim (i.e., no added technologies to be developed in the SuperTruck program). This arrangement will allow the program to track performance for added powertrain technologies. The powertrain technology additions will begin with the mild hybrid addition that will transform the vehicle to a 48 V system (with 12 V branching) and battery bank. Following the development and assessment of the mild hybrid system, the advance cooling and WHR system will be added. This change over will be in a two-stage fashion where the power turbine will be first represented by an orifice only (no power returned to the powertrain), then finally fitted with the power turbine, ensuring the system is balanced (heat addition sources) and functioning correctly. Figure V.2.3 shows the timeline intended to be followed as of this writing.

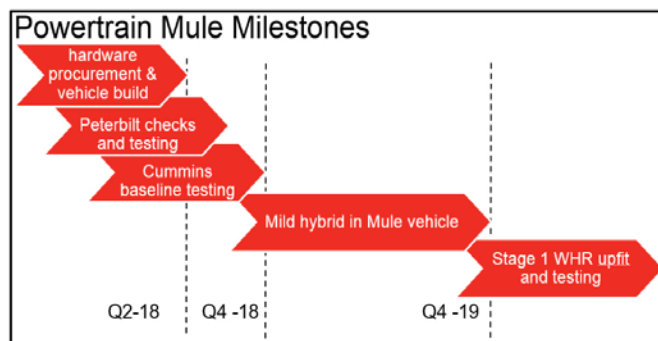


Figure V.2.3 - Powertrain mule milestones

Conclusions

The Cummins led SuperTruck II team has completed the first year of the planned five-year program. In the first year the team has concluded many goals and set direction for the remainder of the program. The following bullet list summarizes those conclusions.

- Data from nearly 275,000 miles of Walmart routes out of three distribution centers has shown the average highway Walmart route looks very similar to Denton–Vernon round trip, which also looks very similar to the overall United States highway system from a distance–grade perspective.
- Analysis shows a diminishing return as the capacity of the M/G increases above 30 kW.
- Analysis indicates an ESS greater than ~3 kW-hr would yield no benefit.
- Mild hybrid via the transmission is an effective means for energy recovery for long haul vehicles operating at/near constant speed conditions.
- Target compression ratio for future development will be centered on 22:1.
- Charge:fuel ratio for future development will be targeted at greater than 34:1 but not greater than 39:1.
- Increases in injection rate testing have defined the limit in burn rate as the increasing slope and peak has shown maximum values even as injection rate is increased, indicating other parameters in the combustion chamber must be explored in order to increase the burn rate.
- Tire effect of compound on wear and rolling resistance can have a profound impact on customer tire acceptance. Feedback from Walmart has indicated tire life, including rebuilds, must be considered in total lifecycle costing models.

Key Fiscal Year 2017 Publications

1. "DOE Quarterly Progress Report, Q1." January 30, 2017.
2. "DOE Quarterly Progress Report, Q2." April 30, 2017.
3. 2017 Annual Merit Review, June 8, 2017.
4. "DOE Quarterly Progress Report, Q3." July 30, 2017.
5. "DOE Quarterly Progress Report, Q4." October 30, 2017.

V.3 SuperTruck 2 Advanced Combustion Development at Navistar

Russell Zukouski, Principal Investigator

Navistar, Inc.
2701 Navistar Drive
Lisle, IL 60531
E-mail: russ.zukouski@navistar.com

Roland Gravel, DOE Technology Manager

U.S. Department of Energy
E-mail: Roland.Gravel@ee.doe.gov

Start Date: October 1, 2016	End Date: November 1, 2021	
Total Project Cost: \$55,595,000	DOE share: \$20,000,000	Non-DOE share: \$35,595,000

Acknowledgments

Co-Authors

James Cigler (Chief Engineer), James Park, Raj Kumar, Ryan Vojtech, Jasmeet Singh, Matthew Taylor, Jason Chen, Thomas Wallner, Buyu Wang, Michael Pamminger; Navistar, Inc.

Project Introduction

The objective of the SuperTruck 2 engine project is to research, develop, and demonstrate a heavy-duty engine that can meet 2010 federal emission standards and can achieve 55% brake thermal efficiency (BTE) demonstrated in an operational engine at a 65 mph cruise point on a dynamometer. In addition, the technologies applied to this engine should be commercially cost-effective.

Objectives

- Engine subsystem modeling
- Data analysis and technology evaluations to refine estimated performance improvements
- Gasoline compression ignition investigation

Approach

The work will include component and system level consideration of base engine architecture, air system, combustion and fuel system, advanced aftertreatment, thermal management, and waste heat recovery. It will involve analysis, development, testing, and down-selection of individual and system level engine technologies as well as integration of the final selected technologies into a prototype engine.

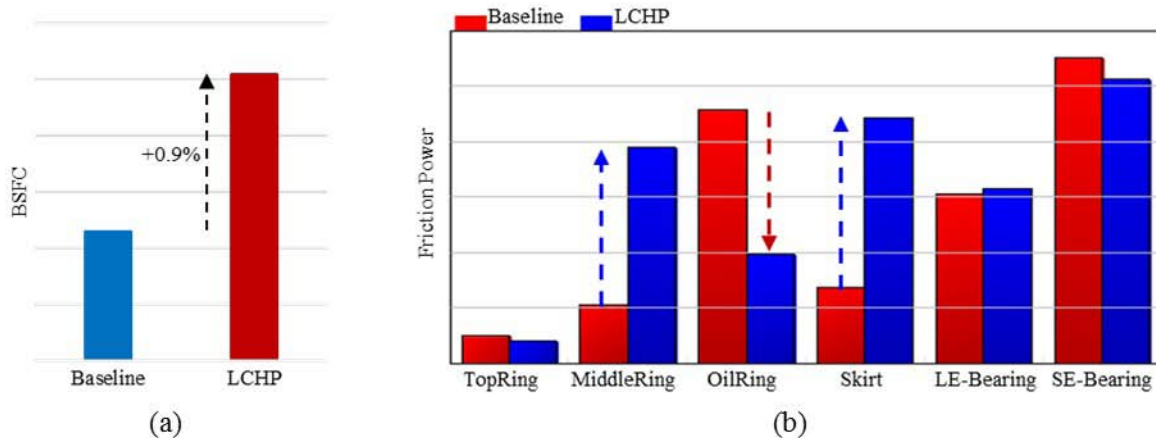
Results

Base Engine Architecture – Compression Ratio

Thermodynamically, an increased compression ratio would yield higher peak cylinder pressure and result in more cylinder cycle work, therefore better BTE. However, the dynamometer testing of a higher compression ratio than the SuperTruck 1 baseline shows no further gain in BTE. Data analysis indicates a correlation of increased friction mean effective pressure to the increase of indicated mean effective pressure with the elevated compression ratio. A detailed friction model, which was developed during SuperTruck 1, indicates that the major contribution of friction power loss is from the cranktrain, including main bearings, connecting rod large-end bearings, connecting rod small-end bearings, and piston skirts.

Low Compression Height Piston

A low compression height piston (LCHP) kit was proposed and designed by a supplier to minimize the friction loss. With the reduction of compression height, the piston skirt is approximately 25% shorter than the baseline. Other component changes include optimized piston rings, a lighter weight piston pin, and a longer but lighter connecting rod, which also features a profiled pin bore for the piston pin. This LCHP kit was installed on an engine and tested on a dynamometer. The engine was first degreened per specifications from the supplier. Unfortunately, the LCHP engine resulted in higher brake specific fuel consumption (BSFC) than the baseline at rated, Figure V.3.1a.



LE – large-end; SE – small-end

Figure V.3.1 - Results of LCHP kit evaluation. (a) BSFC comparison of baseline and LCHP engines at rated. (b) Friction power comparison of each component.

In parallel to the engine testing, the detailed friction model from SuperTruck 1, was employed to compare the friction loss between the baseline and the LCHP at the key components, Figure V.3.1b. The differences at the top ring as well as the large-end and small-end bearing of the connecting rod are relatively small; a significant friction reduction was observed at the oil ring. The increase of friction at the LCHP middle ring and piston skirt were unexpected. Further simulation study of the middle ring indicates that the friction power increase was due to the new middle ring profile. As to the friction increase at the skirt, the model shows that due to the shorter piston skirt length, the LCHP has a higher possibility of piston eccentricity and bigger piston skirt tilt angle during compression and expansion strokes. As a result, oil film thickness development became worse, thus the possibility of asperity contact and piston friction increase.

Design of Experiments Optimization for Cranktrain

Although the LCHP kit did not yield the positive results it was designed for, the experience with the detailed friction model is encouraging. Building on this experience, the friction model was used to investigate the opportunities of cranktrain friction reduction. Design of experiments was performed for the main bearing, connecting rod large-end bearing, and small-end bearing. The factors were diameter, length, and radial clearance of each component. Design of experiments optimization, without considering structure limitation and weight changes due to geometry changes, calls for reducing diameter and increasing length for both main and large-end bearings. Such changes would have significant impact on the crankshaft. Further investigation with the design team on these changes is necessary.

Air System–Turbocharger Efficiency Improvement and Exhaust Gas Recirculation (EGR) Driving Enhancement

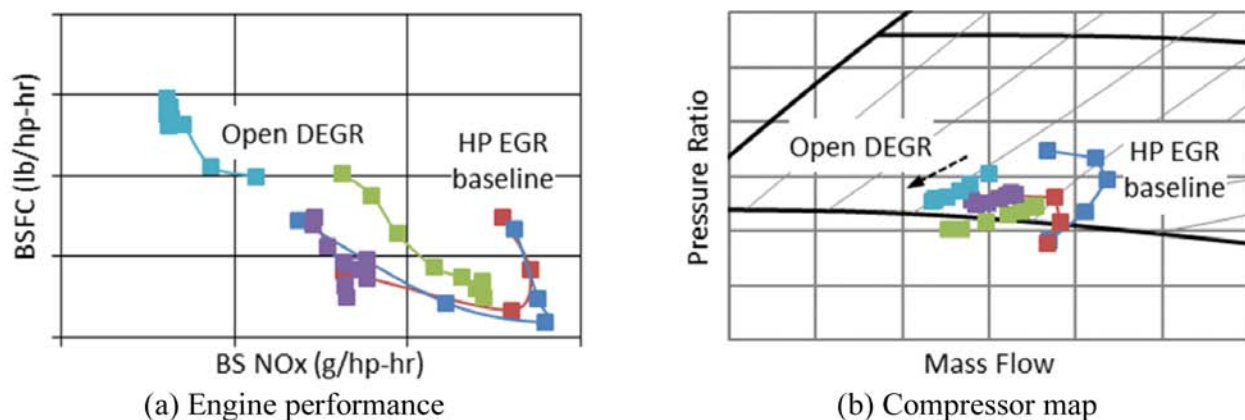
Higher turbocharger efficiency is one of the key areas for engine BTE gain. Improvements of overall turbo efficiency over the baseline are being pursued with providers. Testing was performed to evaluate the heat transfer from the turbine stage into the compressor. Analysis shows that heat transfer from the turbine back plate to the oil appears to be present but not to the compressor. Use of a stainless steel turbine housing would be beneficial in retaining heat in the exhaust. In addition, dynamic exhaust manifold pressure data were

collected and shared with the supplier. Exhaust blowdown has significantly more enthalpy than the rest of cycle. Radial turbines are generally most efficient around turbine blade tip speed ratio U/C of 0.7. A match of turbine size to minimize the U/C swing has been identified.

Besides the high efficiency turbocharger, EGR driving capability is important to meet the stringent tailpipe emissions. A GT-POWER engine model simulation shows a small percentage of EGR rate even though the boost to back engine delta pressures were positive. To improve the EGR driving capability for the SuperTruck 2 engine, the applicability of reed valves was investigated. Preliminary results show that EGR flowrate could be increased with reed valves, even though the averaged exhaust backpressure was less than the boost pressure. The corresponding NO_x emission was reduced. However, a slight BSFC penalty was observed. Further optimization and integration of a reed valve, EGR system, and turbocharger will be investigated to reduce NO_x emissions without sacrificing BSFC.

Dedicated EGR

A concept of dedicated EGR (DEGR) was investigated. An EGR valve was mounted on the exhaust manifold between Cylinders 5 and 6. This enables the EGR driving capability at any engine operating condition. If the EGR valve is fully close, Cylinder 6 becomes dedicated for EGR pumping. DEGR guarantees the availability of EGR, up to 16.6%, regardless of turbocharger configuration. The turbocharger could be optimized for low or high EGR, but in either case the peak air–fuel ratio would be compromised when removing energy from the turbine. Testing shows that DEGR would reduce NO_x at the expense of BSFC, Figure V.3.2a. This is due to the loss of mass flow, Figure V.3.2b.



HP – high pressure

Figure V.3.2 - Comparison of DEGR and HP EGR

Combustion Optimization

A typical three-dimensional combustion simulation runs from intake valve open to exhaust valve open. In contrast, a sector mesh runs from intake valve close to exhaust valve open. It allows the simulation of a sector including only one fuel spray plume. This would cut the computing time and reduce the central processing unit consumption significantly. A new bowl concept was investigated with this new technique. This new bowl was designed to increase in-cylinder air motion to accelerate the air–fuel mixing. The combustion duration was expected to be shorter with this new bowl than the baseline bowl, thus better indicated specific fuel consumption (ISFC). Unfortunately, the simulation shows that this new bowl concept performs worse than the baseline bowl.

The focus of combustion development was then turned to an advanced fuel injection strategy for rapid fuel–air mixing. This advanced fuel injection strategy was investigated via a three-dimensional simulation tool, CONVERGE 2.2. The boundary conditions were based on the 50% BTE data from the SuperTruck 1 program. Figure V.3.3 shows the comparisons of ISFC and heat release rate (HRR) of two fuel injection configurations of the new strategy with the baseline. Even though the first configuration yielded the shortest combustion duration, the best ISFC was from the second configuration. Further investigation will be continued with Bosch.

Waste Heat Recovery

Waste heat recovery plays a vital role in achieving the 55% BTE. Navistar has been working on the organic Rankine cycle (ORC) technologies for waste heat recovery. It is necessary to recover energy from all available waste heat. Based on the temperature characteristics of the heat sources, high temperature (HT) and low temperature (LT) ORC loops are proposed, Figures V.3.4a and V.3.4b. The HT loop recovers energy from high temperature heat sources, i.e., exhaust and EGR, while the LT loop is for lower temperature sources, such as engine coolant and charge air cooler (CAC).

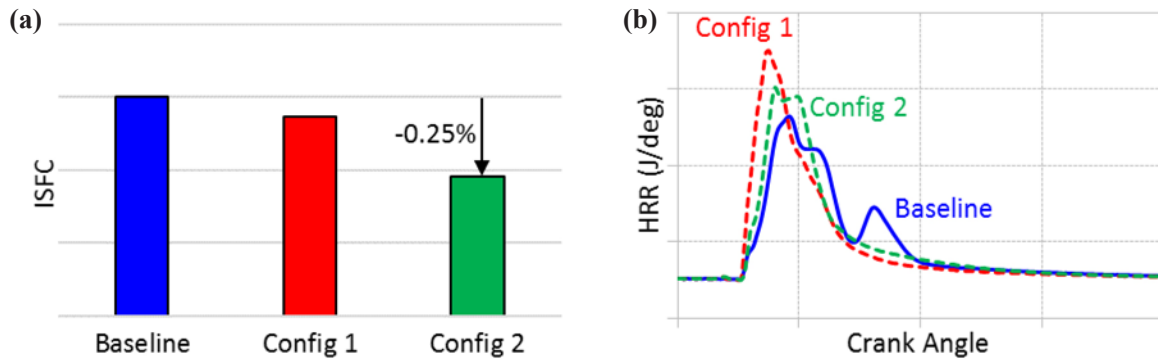


Figure V.3.3 - Advanced fuel injection strategy simulation with CONVERGE 2.2

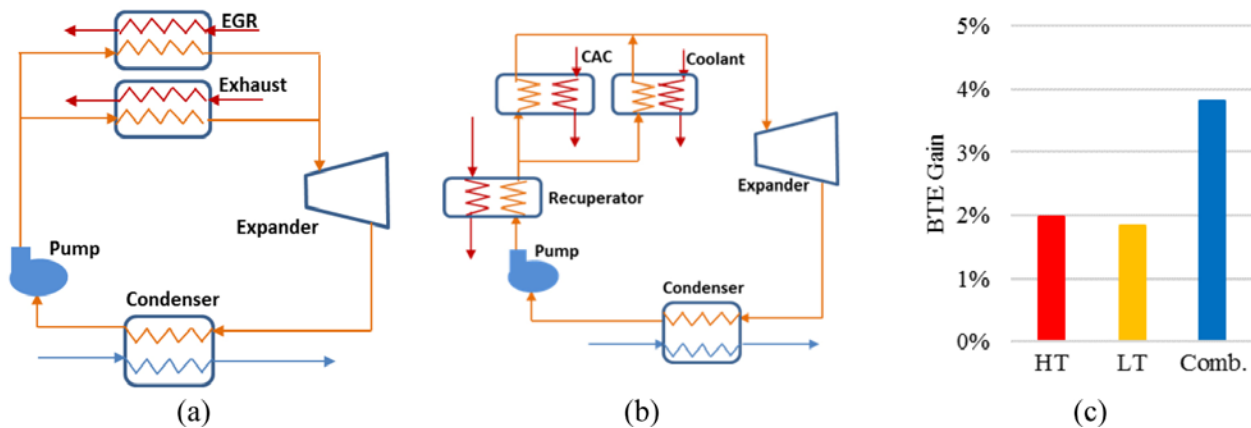


Figure V.3.4 - ORC configurations for 55% BTE: (a) HT loop ORC, (b) LT loop ORC, (c) BTE gain projection

Depending on the heat source, i.e., the operating temperatures and the available energy, it is important to select an appropriate working fluid for the ORC system. An in-house ORC model has been built to investigate the ORC system configurations and working fluid. A key constraint for all simulations is the condenser outlet pressure above the ambient in order to avoid air entrainment. Applying the 50% BTE boundary conditions from SuperTruck 1, the in-house model with a proposed working fluid projects that greater than 3.5% combined BTE gain could be achieved, Figure V.3.4c.

Engine Thermal Management

Exhaust and heat rejection through the coolant are the two major energy losses. Minimizing in-cylinder heat transfer could improve BTE. In addition, biasing energy loss from the coolant to the exhaust would benefit the aftertreatment system as well as the HT ORC system. A study was carried out to investigate the effects of oil temperature and coolant temperature on BSFC and energy distribution to the exhaust to determine the ability to bias such energy losses. Four oil temperatures (T) were evaluated, $T_1 < T_2 < T_3 < T_4$. Figure V.3.5a shows that BSFC is not sensitive to coolant temperature. However, BSFC does decrease with the increase of oil temperature initially, from T_1 to T_3 . Further increase of oil temperature to T_4 results in an increase of BSFC. This is likely due to the decrease of viscosity (deterioration of lubrication) at higher oil temperature.

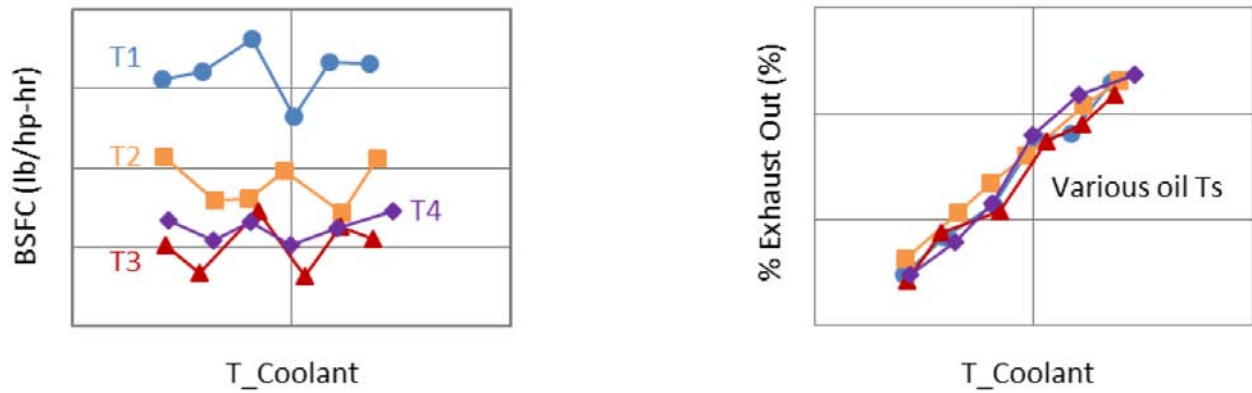


Figure V.3.5 - Effects of oil and coolant temperatures on BSFC and exhaust energy distribution

Figure V.3.5b shows more exhaust energy with the increase of coolant temperature, regardless of oil temperatures.

Gasoline Compression Ignition at Argonne National Laboratory

The current project limits fuel options to gasoline and/or diesel. Gasoline compression ignition could achieve a similar aim as dual-fuel–reactivity controlled compression ignition explored previously. Some portion of gasoline will be premixed, and additional fuel injection near top dead center may be used to trigger combustion. Combustion phasing would be controlled by premixed fuel quantity and main injection start of injection as well as intake valve closing timing, variable geometry turbine position, EGR ratio, and intake temperature. The engine and test cell hardware were updated to enable operation using gasoline. The gasoline fuel was delivered via the high-pressure common rail, diesel injection system. A lubricity improver was blended into the fuel to protect the injection system.

An aged gasoline fuel, E10 (10% ethanol, 90% gasoline), from a previous program was used to kick off the gasoline compression ignition investigation. However, the E10 testing had shown that EGR, variable geometry turbine, and intake valve closing timing were not effective enough to retard the premixed combustion event with the early pilot injection strategy. An Environmental Protection Agency Tier II Certification Gasoline, EEE, was then selected to better retard the premixed combustion event with early pilot injection due to its higher octane rating (increased Research Octane Number by 4 units compared to E10). An efficiency breakdown of these two fuels is shown in Figure V.3.6. The BTE of EEE was 1.1% lower than that of E10. However, EEE shows a 2.5% higher friction loss. This higher friction mean effective pressure is most likely not related to EEE itself. Therefore, a comparable or even higher BTE is expected for EEE operation, if the friction losses were similar for both fuels.

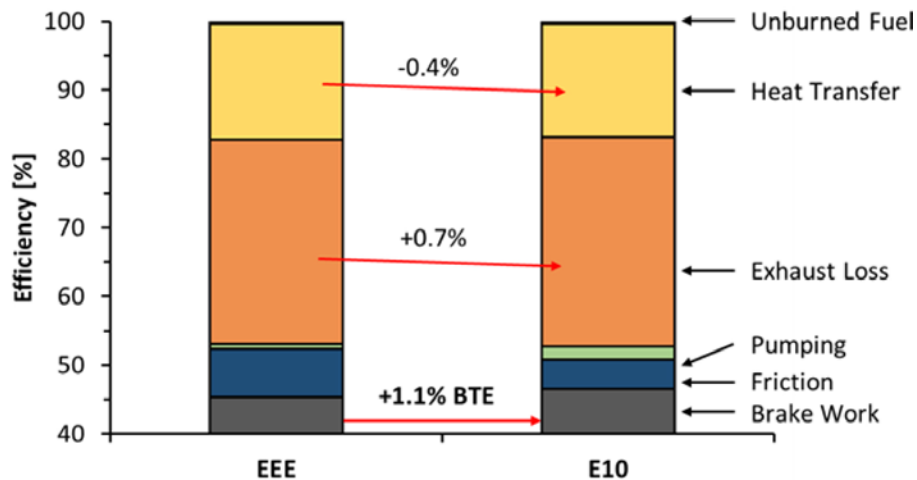


Figure V.3.6 - Efficiency breakdown and loss comparison between two gasoline fuels

Conclusions

- Modeling approach was applied to several subsystems to identify opportunities for BTE improvement. The efforts included cranktrain friction reduction, a high efficiency turbocharger, an effective EGR system, new combustion bowl concept, advanced fuel injection strategy, and ORC configurations and working fluid optimization. Based on the results, design, procurement, and evaluation will be carried out in the next budget period for turbocharger, EGR system, advanced fuel injection strategy, and ORC.
- Engine thermal management investigation was carried out in an engine test cell at Navistar. Coolant temperature control was identified as an effective means to bias waste energy to exhaust gas, which would benefit the ORC and aftertreatment performance. Depending on the grade of oil, its temperature should be controlled to an optimum for best BSFC.
- Gasoline compression ignition testing was successfully kicked off at Argonne National Laboratory. Two different gasoline fuels were tested. How to effectively retard the premixed combustion event with the early pilot injection strategy was identified as the main challenge to overcome.

Key Fiscal Year 2017 Publications

1. Kassa, M., Hall, C., Ickes, A., Wallner, T. “Modeling and Control of Fuel Distribution in a Dual-Fuel Internal Combustion Engine Leveraging Late Intake Valve Closings.” *International Journal of Engine Research* 1–13 (2016). doi:10.1177/1468087416674426.
2. Kassa, M., Hall, C., Ickes, A., and Wallner, T., “Feedforward Control of Fuel Distribution on Advanced Dual-Fuel Engines with Varying Intake Valve Closing Timings.” SAE Technical Paper 2016-01-2312, (2016). doi:10.4271/2016-01-2312.
3. Ickes, A., “Evolution of Dual-Fuel Combustion Strategies for a Heavy-Duty SuperTruck Engine.” Presented to the Advanced Engine Crosscut Team, Southfield, MI, May 11, 2017.

V.4 Improving Transportation Efficiency Through Integrated Vehicle, Engine, and Powertrain Research – SuperTruck 2

Justin Yee, Principal Investigator

Daimler Trucks North America
 4555 N Channel Ave.
 Portland, OR 97217
 E-mail: Justin.Yee@daimler.com

Roland Gravel, DOE Technology Manager

U.S. Department of Energy
 E-mail: Roland.Gravel@ee.doe.gov

Start Date: January 1, 2017 End Date: January 1, 2022
 Total Project Cost: \$40,000,000 DOE share: \$20,000,000 Non-DOE share: \$20,000,000

Acknowledgments

Co-Author

Jeff Girbach, Daimler Trucks North America

Project Introduction

The objective of the SuperTruck 2 (ST2) program is to develop and demonstrate a greater than 100% improvement in overall freight efficiency on a heavy-duty Class 8 tractor-trailer measured in ton-miles per gallon. In addition, the program will design and demonstrate an engine capable of achieving 55% brake thermal efficiency (BTE). Daimler Trucks North America (DTNA) will achieve these targets through the application of several advanced vehicle system technologies and advanced engine technologies.

The ST2 program is broken into five phases, of which we are coming towards the end of Phase 1 (Figure V.4.1). This phase has included setting up the organization of the program, brainstorming on new fuel saving technologies, using analysis to quantify the end benefits, and setting goals for the workstream teams, and then working to define the scope and direction for the design work moving forward. At the end of Phase 1, the team will be evaluating which of the main path and stretch technologies will continue on towards development for a mule truck, called “A-Sample.” The design of this truck is the main focus for Phase 2, so consolidation of effort is the key to prevent spreading resources too thin.

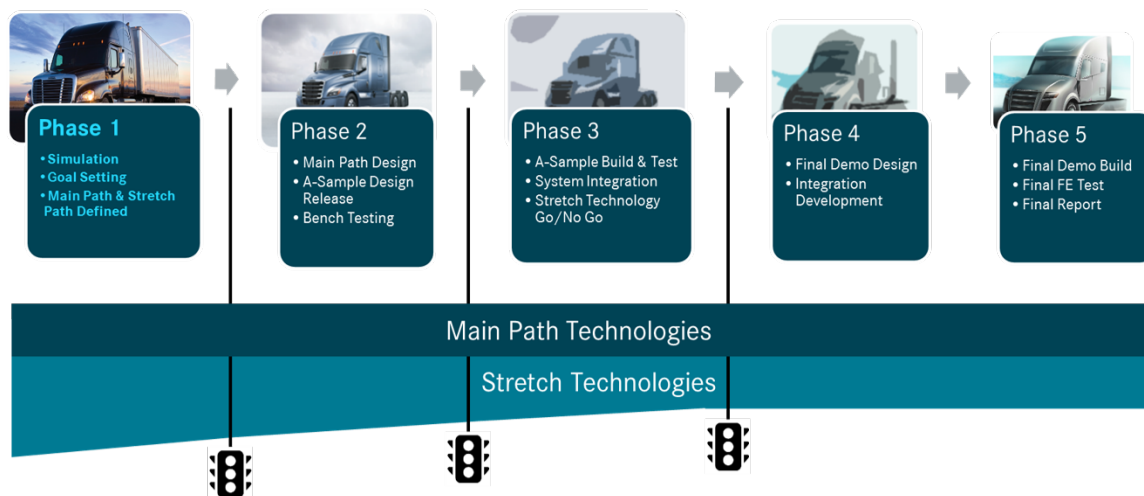


Figure V.4.1 - ST2 program phases

Objectives

There are two main objectives for the ST2 program.

- Meet or exceed the vehicle freight efficiency target for the ST2 program, specified as a 100% freight efficiency improvement over a baseline vehicle (same vehicle as used in SuperTruck 1 (ST1) – a 2009 Cascadia). DTNA has specified that they will exceed the target with a vehicle that demonstrates 115% freight efficiency improvement over a test cycle that is representative of a 24-h drive cycle (see Figure V.4.2).
- The second objective that must be met is to demonstrate in a test cell, a running technology engine that meets or exceeds a 55% BTE rating.

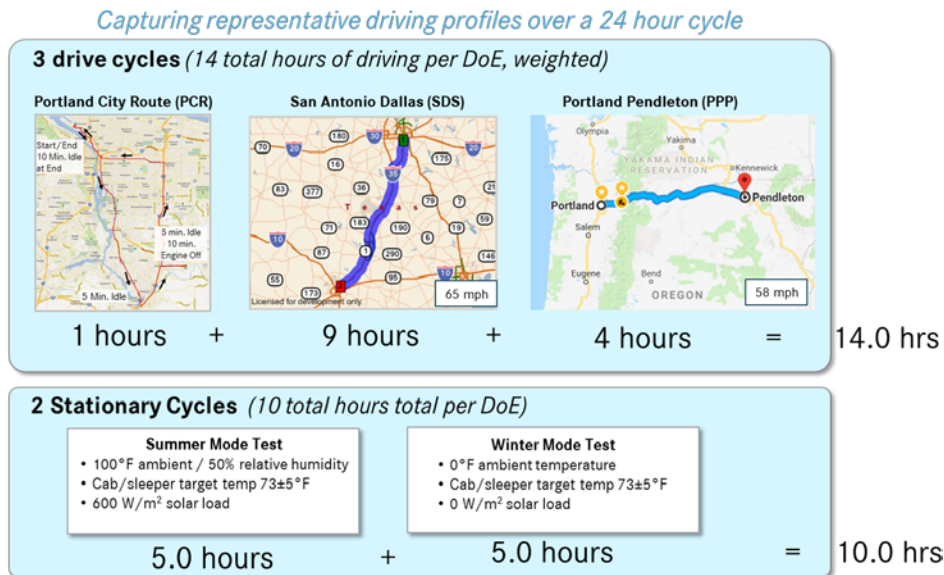


Figure V.4.2 - ST2 proposed freight efficiency test cycle

Approach

In Phase 1 of the ST2 program, simulation was the main approach used to define how the team would meet the program objectives, as well as refining the brainstorming ideas. On the engine side of the project, the best demonstrated BTE currently stands at 50% (48% core engine + 2% waste heat recovery [WHR]). A detailed combustion cycle simulation model was created to evaluate a number of fuel efficiency measures. Target improvements were developed in five main workstreams and simulated to show a pathway that reaches the 55% BTE target. Currently, simulation is being used to refine on a component level how to realize the targets. One of the methods for technology selection relies on combustion computation fluid dynamics (CFD) expertise at Oak Ridge National Laboratory to develop an iterative simulation cycle to test the various engine concepts. See Figure V.4.3.

On the vehicle portion of the program, a similar approach was used. The team was able to build on the tools and information developed in the ST1 program, mainly the fuel efficiency models. Using output of ideation sessions, a new fuel simulation was developed that led to a ST2 development roadmap. In addition, simulation of CFD was also used to investigate on a high level the potential aero reductions for the program.

One of the changes since the ST1 program was the launch of a new long haul vehicle in 2017, the New Cascadia. The ST2 program will build on the New Cascadia vehicle platform, so naturally the question arises of what freight efficiency improvement remains from the New Cascadia to the ST2 target. A fuel efficiency test was performed to compare the original SuperTruck baseline vehicle to the latest New Cascadia. Using the same weight savings, the freight efficiency difference was 71%, a testament to the ST1 program’s influence on production vehicles and DTNA’s continued efforts since 2009 to improve fuel efficiency.

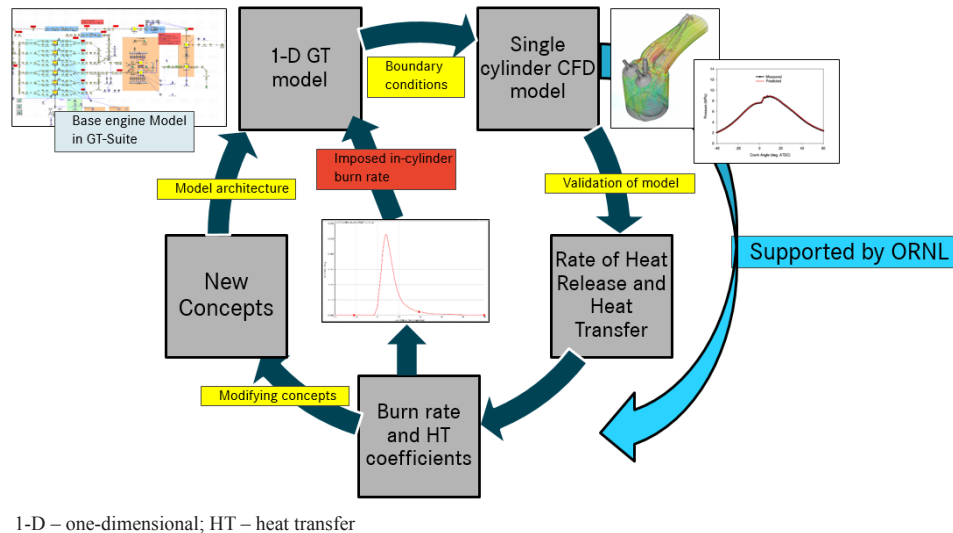


Figure V.4.3 - Detroit simulation and design process

Additional simulation in MATLAB Simulink was used to refine fuel savings concepts on a component level to solidify the basic design of systems such as 48-V implementation. While not complete, this process has helped clarify which of the many ideas have the most potential for future implementation.

Aerodynamic performance is the largest benefit of the ST2 program. Critical to defining this benefit was the beginning of vehicle integration studies. Towards the end of Phase 1, a digital mock-up was started to define the packaging space for the new truck layout. This will be important for the product designers to know their design boundaries. Their output will be used to run CFD to determine the aerodynamic output of the design. That output will then fed back to the designers for adjustments. During the process, the digital mock-up will be updated as the chassis, cooling, and engine designs solidify.

Results

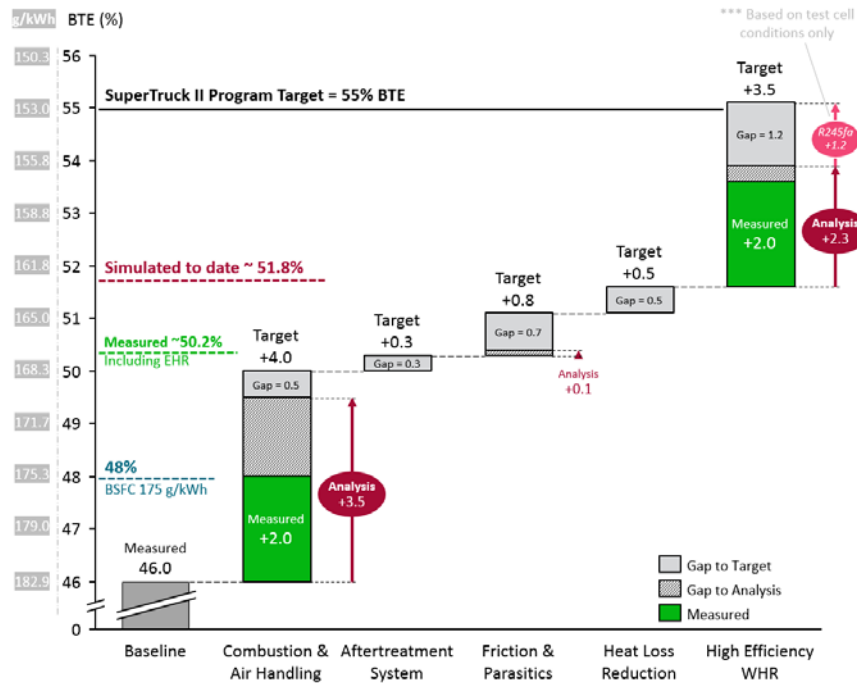
An engine roadmap was developed using the iterative method described in the Approach section. The result shows the pathway targets to reach 55% BTE in five main areas. Using a starting point efficiency of 46% BTE, the breakdown of efficiency contributions are as follows.

- Combustion & Air Handling: target = 4% BTE
- Aftertreatment System: target = 0.3% BTE
- Friction and Parasitics: target = 0.8% BTE
- Heat Loss Reduction: target = 0.5% BTE
- High Efficiency WHR: target = 3.5% BTE

At this stage in the program, we are still in the process of refining the concepts, hence there are still gaps between the target improvements and solidified designs. In Phase 2, designs will be refined and prototypes built for bench or lab testing. Physical validation give simulation feedback on their analysis accuracy and guide the development towards on-vehicle system integration. Figure V.4.4 gives a visual summary of the five workstreams, their related targets, and the gaps still remaining between the target and analysis results.

The result of baseline to New Cascadia and goal simulation has resulted in the following program targets for each workstream.

- Engine (on vehicle): target = 6% freight efficiency
- Tractor Aerodynamics: target = 17% freight efficiency

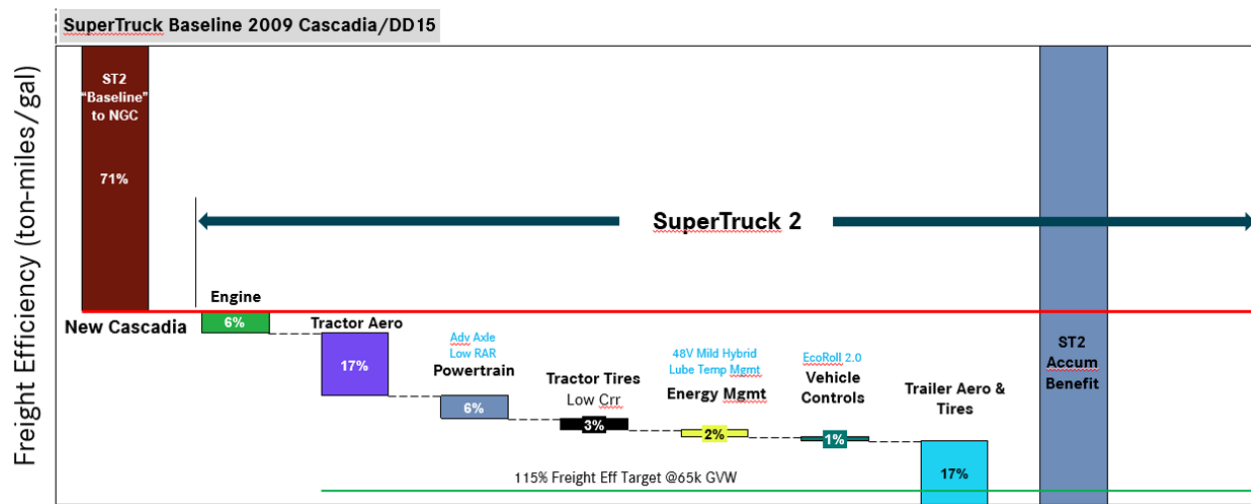


BSFC – brake specific fuel consumption; EHR – exhaust heat recovery

Figure V.4.4 - Detroit roadmap to reach the 55% BTE target

- Powertrain: target = 6% freight efficiency
- Tractor Tires: target = 3% freight efficiency
- Energy Management: target = 2% freight efficiency
- Vehicle Controls: target = 1% freight efficiency
- Trailer Aero & Tires: target = 17% freight efficiency

Figure V.4.5 shows a summary of the simulation results. One of the results of ST1 is that not all of the technologies are completely additive, so the simulation needs to slightly exceed the 115% freight efficiency target to ensure meeting the goal.



NGC – next generation Cascadia, GVW – gross vehicle weight

Figure V.4.5 - DTNA roadmap to reach the 115% freight efficiency target

Workstream teams have been created, roles and responsibilities accepted, and Tactical Implementation Plans generated to support the overall plan. Resources gaps have been identified in which professional services have been or will be hired to supplement the internal teams.

Conclusions

The ST2 program is on schedule to meet the fuel efficiency targets of 115% freight efficiency improvement over a 2009 Cascadia and the engine team is on schedule to meet their goal of a 55% BTE demonstrator engine.

- Simulation for goal setting is complete for both the engine and the vehicle program.
- Working teams for each workstream have been created and aligned with high level schedules.
- Design resources have been identified and are being put in place to support Phase 2 design work.
- Collaboration with outside suppliers is in place.
 - Oak Ridge National Laboratory
 - National Renewable Energy Laboratory
 - University of Michigan
 - Michelin Tire Corporation
- Scope definition is 75% complete in preparation for Phase 2 design work.

The ST2 program is a large bundle of projects, but two of these deserve special attention due to the level of impact they will have on the trucking industry.

The first is moving from 12 V direct current to 48 V direct current. The last time the automotive industry changed voltages was in 1955 when they moved from 6 V to 12 V. While moving to 48 V has many soft benefits, the focus of the ST2 program is to try and quantify hard benefits that justifies a customer's move to the new voltage architecture.

The second is optimization of the cooling system with split-cooling. Moving to a different radiator configuration would be a significant change to the trucking industry, but as the industry is pushed towards higher and higher levels of optimization, the cooling package must also follow. ST2 tries to answer the question of how to do this in a way that does not compromise aerodynamics and operating efficiencies so that the customer gains an overall step gain in net benefit.

ST2 is different from the first program in that it tries to tackle these difficult implementation issues up front, such that at the end of the program, there is a pathway towards future integration. Funding this research in the early stages is of large importance due to the high risk of the technologies. It allows exploration into technologies that, if implemented, have the potential to significantly reduce CO₂ on a large scale.

Key Fiscal Year 2017 Publications

1. Yee, J., Girbach, J. et al. DOE Annual Merit Review, June 2017.

V.5 Ultra-Efficient Light-Duty Powertrain with Gasoline Low Temperature Combustion

Keith Confer, Principal Investigator

Delphi
3000 University Drive
Auburn Hills, MI 48326
E-mail: keith.confer@delphi.com

Ken Howden, DOE Technology Manager

U.S. Department of Energy
E-mail: Ken.Howden@ee.doe.gov

Start Date: October 1, 2014	End Date: March 31, 2019	
Total Project Cost: \$24,112,162	DOE share: \$9,392,865	Non-DOE share: \$14,719,297

Acknowledgments

Co-Authors

Dr. Peter Olin, Mark Sellnau; Delphi

NETL Project Manager

Ralph Nine, National Energy Technology Laboratory

Project Introduction

Low temperature combustion approaches have the potential to provide significant fuel economy benefit for internal combustion engines. Gasoline direct-injection compression ignition (GDCI) is a particular approach to realizing low temperature combustion operation. GDCI is currently a moderately mature combustion technology due in large part to advances made during a previous program funded through the Department of Energy and led by Delphi (Advanced Technology Powertrain's contract DE-EE0003258).

The current project is addressing a number of technical risks and issues that must be overcome for GDCI to become a production-viable technology. These are (1) further refinement of the GDCI combustion system to achieve near-ideal air–fuel mixture preparation for high efficiency and low hydrocarbon (HC) and CO emissions, (2) demonstration of low temperature combustion transient control with high exhaust gas recirculation levels during real-world transient driving maneuvers and over a broader range of ambient conditions, and (3) development of an aftertreatment system that is effective in dealing with the low temperature challenges of a highly efficient engine.

The ultimate deliverable for this project will be a vehicle that will demonstrate a 35% fuel economy improvement over a baseline vehicle with a port fuel injection engine, while simultaneously meeting Tier 3 emissions levels.

Objectives

- Perform Gen 2 GDCI vehicle testing
- Build Gen 3 GDCI multi-cylinder engine
- Build Gen 3 GDCI exhaust aftertreatment
- Design, simulate, build, and test Gen 3 gasoline direct injection injectors
- Debug and dynamometer test Gen 3 GDCI multi-cylinder engine
- Develop improved injection strategies for high-load operation

- Build Gen 3 GDCI vehicle
- Develop and build Gen 3 electronic controls
- Begin development of Gen 3 GDCI vehicle control algorithms and software

Approach

This project will substantially expand upon the existing success of GDCI combustion. Further combustion optimization, supported by component development, will focus on improved brake thermal efficiency and reduced emissions. A key focus area is continued development of the injection process and fuel sprays to reduce engine-out HC and CO, which are especially challenging for low temperature combustion, while also improving thermal efficiency. Controls development will improve ignition timing and combustion control, with an emphasis on transient operation and cold starting. System and controls optimization work will provide robust operation over an expanded range of operating conditions, including ambient temperature and variations in gasoline composition. To meet stringent Tier 3 emission targets, a new aftertreatment system will be developed in combination with advanced controls and fast warm-up strategies to deliver an optimized solution for GDCI.

Initial work on this project leveraged the Gen 1 GDCI development vehicle from the Advanced Technologies Powertrain 1 project. That vehicle was used as an initial test bed in the development of a high performance exhaust aftertreatment system for GDCI as well as to develop calibration refinements for improved exhaust emissions and fuel efficiency.

A Gen 2 GDCI development level engine was designed and built, and used to develop refined controller hardware, including improved sensor, actuator, and control algorithms. The Gen 2 GDCI engine was retrofitted into the development vehicle and used for refinement of GDCI controls and calibration. Development of the final Gen 3 GDCI engine, Gen 3 GDCI demonstration vehicle, control systems, and aftertreatment are all based on the work done on the Gen 2 GDCI engine.

The Gen 3 GDCI engine was designed and built specifically for this project based on experience from the earlier engines. This engine, when combined with refined control systems and project specific exhaust aftertreatment, is planned to meet Tier 3 emissions levels. The culmination of the project will be realized with the Gen 3 GDCI demonstration vehicle which will demonstrate a 35% fuel economy improvement along with Tier 3 emissions levels.

Results

- The Gen 2 GDCI vehicle calibration was completed.
- The Gen 2 GDCI vehicle testing yielded 35% improvement in combined fuel economy measured relative to the baseline vehicle, but Tier 3 emissions target was not met.
- Gen 3 GDCI engine, thermal management, and aftertreatment were built for the vehicle.
- Gen 3 gasoline direct injection injectors were characterized for low smoke using both early and late injection strategies.
- Initial dynamometer testing of Gen 3 GDCI engine has been performed.
- GDCI late injection benefits in reducing HC and CO were demonstrated.
- The Gen 3 GDCI vehicle build was started, the engine was installed, and Gen 3 controllers integrated.
- Gen 3 vehicle electronic controls were developed, built, and tested on the simulator.
- Gen 3 engine control module software was developed and bench verified.

- Improved vehicle combustion feedback algorithms were developed and implemented in a real-time controller.

Gen 2 GDCI Demonstration Vehicle

Calibration of the Gen 2 GDCI vehicle was completed with a focus on the Federal Test Procedure drive cycles. The Gen 2 GDCI vehicle demonstrated 35% combined fuel economy improvement over the baseline vehicle (Environmental Protection Agency III 35%, Highway Fuel Economy Test 35%); it continues to use the aftertreatment system from the Gen 1.8 vehicle and did not meet Tier 3 emissions requirements.

Gen 3 Engine Controls

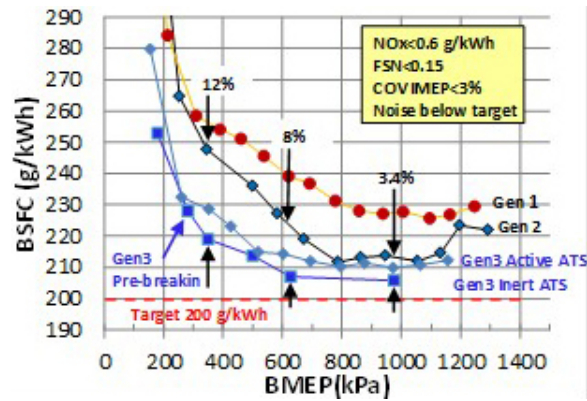
Electronic controls to support the Gen 3 GDCI engine hardware configuration were designed, built, and tested. The engine control module was upgraded to a Delphi MT92.1 version which has additional computational power, additional memory, and increased input/output ports. A new motor driver box was developed which allowed the reduction of driver boxes from three to two while supporting more input/output, faster control response, and direct dual-Controller Area Network interface. An updated version of the control software was implemented along with updated versions of the Rapid Algorithm Develop tools including the MicroAutoBox, Control Desk software, and Mathworks software. An additional controller was added to support the urea dosing system for selective catalytic reduction-based NO_x control. All system interfaces were verified on the bench and are ready for vehicle integration. Writing of control algorithms to support the new Gen 3 GDCI engine hardware content and control strategies has begun with some subsystems completed. Improved combustion analysis algorithms that utilize wavelet-based signal filters have been developed and implemented in a real-time controller that provide real-time polytropic compression and expansion coefficients. The wavelet-filtered signal is also used in the heat release calculations thereby stabilizing some of the output parameters that are used in closed loop combustion controls.

Gen 3 GDCI Engine Design and Build

The Gen 3 GDCI engines were built and initial testing completed on a dynamometer (see Figure V.5.1). Brake specific fuel consumption over the load range was improved significantly over the Gen 1 and Gen 2 GDCI engines. With an inert aftertreatment system, minimum brake specific fuel consumption (BSFC) of 205 g/kWh was achieved over the medium load range where the customer drives. Low-load BSFC was also exceptionally good (see Figure V.5.2).



Figure V.5.1 - Gen 3 GDCI powertrain

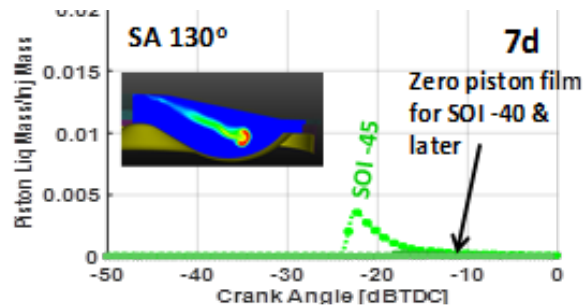


BMEP – brake mean effective pressure; FSN – Filter Smoke Number;
COV IMEP – coefficient of variation in indicated mean effective pressure

Figure V.5.2 - BSFC as a function of BMEP for Gen 1, Gen 2, and Gen 3 GDCI engines

Injection System and Strategies for Gen 3 GDCI Engines

New Gen 3 injectors were built and tested. The injectors met new design targets for spray angle and penetration, injection rate, and zero bounce for the Gen 3 “wetless” combustion system. The Gen 3 injectors are key enablers for low smoke emissions at various injection timing. Dynamometer tests were conducted to characterize the Gen 3 injection system. Smoke emissions were reduced to ultra-low levels and enabled operation at GDCI late injection. This had benefits for the combustion system including reduced HC and CO emissions, increased exhaust temperatures, and reduced sensitivity to intake air temperature. Robustness of the system was significantly improved with comparable BSFC (see Figures V.5.3, V.5.4, and V.5.5).



SOI – start of injection; dBTC – degrees before top dead center;
SA – spray angle

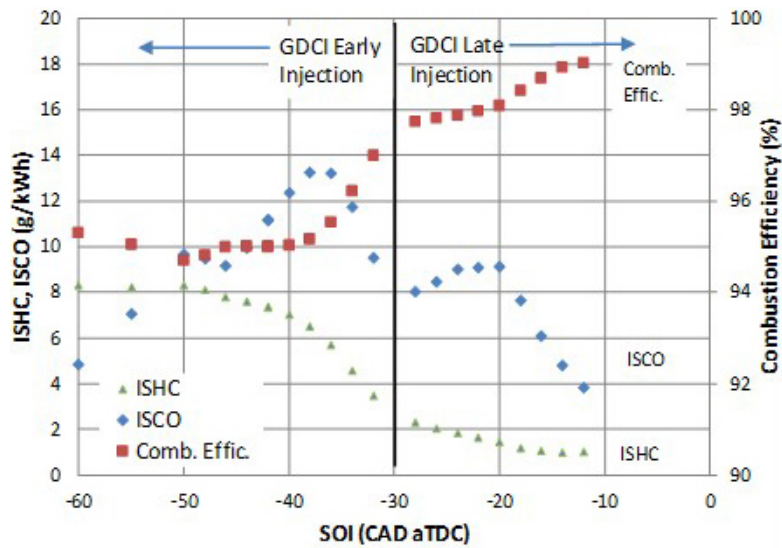
Figure V.5.3 - Gen 3 gasoline direct injection injector spray and computational fluid dynamics simulation showing wetless injection process

Cold Start Tests for Tier 3 Bin 30 Emission

Preliminary cold start tests were conducted with the Gen 3 injection system and new cold start strategies. Results showed that the first cycle burned completely and produced low HC and smoke emissions with high exhaust temperatures. The system is being developed for fast light-off of the pre-turbo catalyst.

Thermal Management System for Transient Intake Air Temperature Control

The Gen 3 GDCI engine thermal management system was developed for fast intake air temperature (IAT) control. The system modulates cold water from the low temperature radiator and hot water from the engine to achieve desired IAT on fast transients. Simulation results show that IAT was within 2–3°C of the target for the Federal Test Procedure test. A statistical analysis showed that the IAT was within 1.5°C of the target 94% of the time. Standard deviation of IAT was only 0.7°C.



ISCO – indicated specific CO; ISHC – indicated specific HC; CAD – crank angle degrees; aTDC – after top dead center

Figure V.5.4 - HC, CO emissions and combustion efficiency for GDCI early and late injection timings

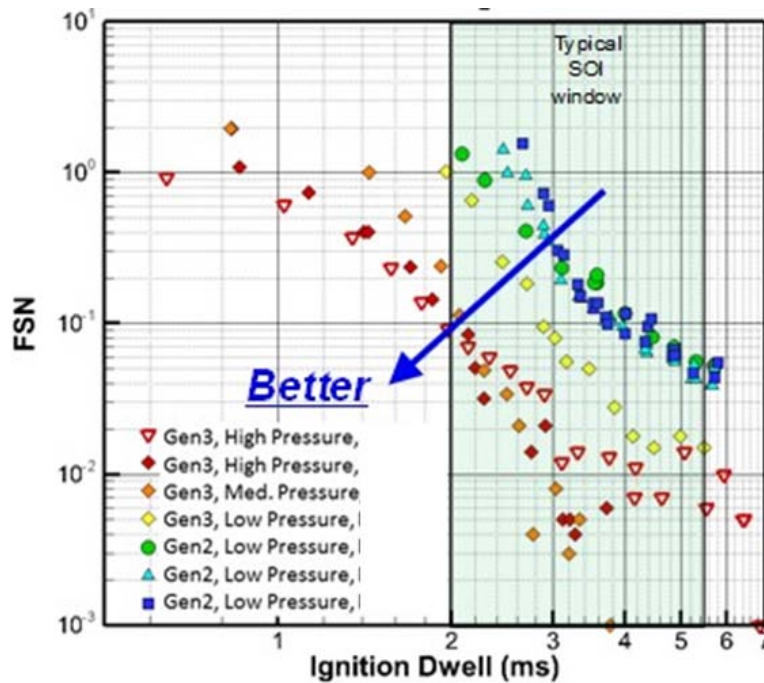


Figure V.5.5 - Smoke emissions as a function of injection dwell for Gen 3 gasoline direct-ignition injectors

Conclusions

- Gen 2 GDCI vehicle configuration capable of 35% combined fuel economy improvement over the baseline vehicle.
- Gen 2 GDCI vehicle configuration not capable of meeting Tier 3 requirements due to Gen 1.8 level aftertreatment used on the Gen 2 vehicle development platform.
- Gen 3 GDCI engines exhibit exceptional fuel economy over low-to-medium load operating conditions in initial dyno tests.

- Gen 3 GDCI engine with Gen 3 gasoline direct injection system showed smoke emissions were low and enabled use of late injection timings. GDCI late injection exhibited significantly reduced HC and CO emissions, higher exhaust temperatures, and significantly less sensitivity to intake air temperature variations. Robustness of the combustion system was improved.
- Gen 3 GDCI engine thermal management system with control algorithms improved transient control of intake air temperature in simulation. Simulated intake air temperature deviated from the target by less than 3°C over the Federal Test Procedure test. Transient vehicle tests are still needed to confirm performance of the system.

Key Fiscal Year 2017 Publications

1. Sellnau, M. “Aftertreatment for Low-Temperature Combustion and US Tier3- Bin30 Emissions.” Presented at the SAE Light Duty Emissions Control Symposium, Washington, DC, January 23, 2017.
2. Sellnau, M. “Advancement of GDCI Technology for US 2025 CAFE and Tier 3 Emissions.” Presented at the 2017 High Efficiency Internal Combustion Engine Symposium, Detroit, MI, April 3, 2017.
3. Costlow, T. “Low-Temperature Combustion Ready for Prime Time.” *SAE Automotive Engineering Magazine*, May 2017.
4. Sellnau, M. “Advancement of GDCI Technology for US 2025 CAFE and Tier 3 Emissions.” Presented at the 2017 SIA Powertrain Conference, Versailles, France, June 8, 2017.
5. Confer, K. ACE094 Merit Review DE-EE0006839, presented at the 2017 DOE Vehicle Technologies Review, Washington, DC, June 9, 2017.
6. Sellnau, M. “Advancement of Gasoline Direct Injection Compression Ignition for US 2025 CAFE and Tier 3 Emissions.” Presented at the University of Wisconsin, Madison, WI, June 14, 2017.

V.6 High Efficiency Variable Compression Ratio Engine with Variable Valve Actuation and New Supercharging Technology: VCR Technology for the 2020 to 2025 Market Space

Charles Mendler, Principal Investigator

ENVERA LLC
7 Millside Lane
Mill Valley, CA 94941
E-mail: cmendler@vcengine.com

Roland Gravel, DOE Technology Manager

U.S. Department of Energy
E-mail: Roland.Gravel@ee.doe.gov

Start Date: April 11, 2013	End Date: September 30, 2017	
Total Project Cost: \$2,784,127	DOE share: \$2,212,469	Non-DOE share: \$571,658

Acknowledgments

Subcontractors

Eaton Corporation (variable valve control and supercharging),
MAHLE Powertrain (testing),
EngSim Corporation (GT-POWER and GT-DRIVE computer modeling)

NETL Project Manager

Ralph Nine, National Energy Technology Laboratory

Project Introduction

Engine downsizing is a leading global strategy for improving vehicle fuel economy. Under normal driving conditions very little power is demanded of a vehicle's engine. The smaller the engine, the higher its efficiency at these small power levels. Accordingly, there is a global trend towards making engines smaller to increase vehicle mileage.

Turbo and supercharging may be employed so that the small engine produces the same power and torque of the larger engine being replaced. Today in Europe, about half of all new gasoline engines are turbocharged.

With an increase in boost pressure engine compression ratio (CR) must be lowered and/or spark timing retarded to prevent detonation or pre-ignition of the fuel-air mixture. This lowering of CR reduces engine efficiency at the small power levels where high efficiency is most needed. Variable compression ratio (VCR) technology solves this problem by enabling a very high CR to be used at small power levels and a low CR used only when needed at high power levels. Fuel economy benefits can be further increased with variable valve lift (VVL) and use of the Atkinson cycle at small power levels.

The potential gains in mileage are large. Dynamometer test data and GT-POWER computer modeling indicates that a boosted four-cylinder VCR engine can deliver the power and torque of a V8, while improving the mileage of a full-size pickup truck by about 40%.

Objectives

The primary objective of this project is to develop a high-efficiency VCR engine having VVL technology and an advanced high-efficiency supercharger to obtain up to a 40% improvement in fuel economy when replacing current production V8 engines with the new small displacement VCR engine.

- Target power range: 281–360 hp

- Target light and medium load efficiency: 230 g/kWh

Fiscal Year 2017 Objectives

- Dynamometer testing of the VCR prototype engine
- Develop a brake specific fuel consumption map for the VCR engine using dynamometer test data and GT-POWER modeling
- Project fuel economy values for a F150 full-size pickup truck equipped with the VCR engine

Approach

The current program includes three phases. In Phase 1, the general feasibility of attaining performance goals was assessed. Mechanical durability and functionality of the VCR mechanism was also evaluated. In Phase 2, the Envera VCR engine shown in Figure V.6.1 was designed and built. A GT-POWER model of the engine was built and first-build cam, compression ratio, and other settings developed. In Phase 3, the engine was dynamometer tested. Combustion data was then used to calibrate the GT-POWER model and further optimize engine efficiency. Fuel economy was then projected using GT-DRIVE for a full-size F-150 Ford pickup truck.

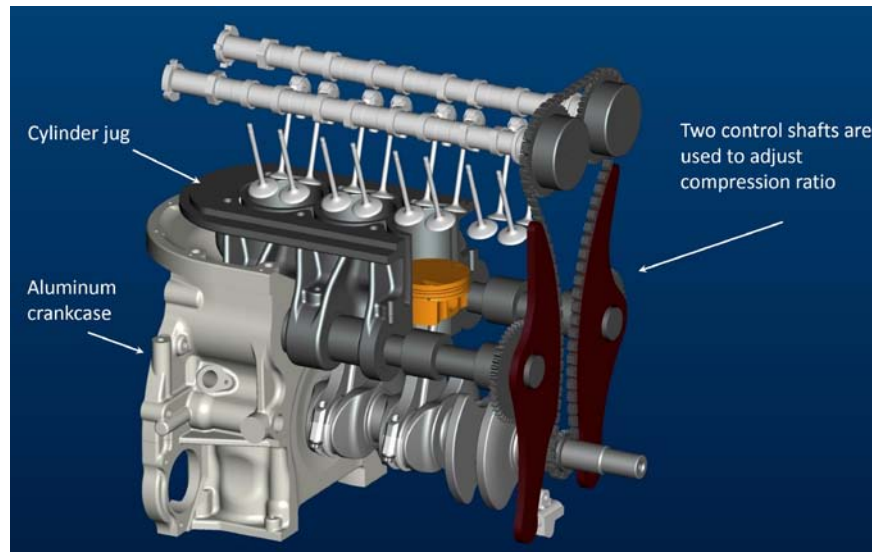


Figure V.6.1 - The Envera VCR engine

Phase 3 Vehicle Mileage Optimization

The optimization process for maximizing vehicle fuel economy included a number of steps. The first step included development of a GT-POWER model for simulating and optimizing engine efficiency. Combustion burn rate for the actual engine was not known, so assumed combustion burn rate values were used. The GT-POWER model was used to design the camshafts and develop other engine settings for initial engine dynamometer testing.

The second optimization step involved dynamometer testing of the engine and recording actual combustion burn rate data. Testing was conducted using three different cam profile options and with various exhaust gas recirculation levels. Testing was conducted at MAHLE Powertrain. Engine build and high-power testing support was provided by Hasselgren Engineering.

The third step involved updating the GT-POWER model to include actual combustion burn rate values. The GT-POWER model was then returned to further improve engine efficiency. A brake specific fuel consumption map was created. The GT-POWER modeling was performed by the EngSim Corporation.

The fourth step involved creating a GT-DRIVE model of the Ford F-150 full-size pickup truck. The initial version of the GT-DRIVE model included the stock 3.5-L V6 engine. This was done in order to calibrate and check the GT-DRIVE model against known data. GT-DRIVE modeling was conducted by EngSim Corporation.

The fifth step involved replacing the 3.5-L V6 engine in the GT-DRIVE model with the 2.4-L VCR engine and then developing a transmission shift schedule for maximizing fuel economy and meeting performance needs. The F-150 was assumed to be 200 lb lighter due to the reduced engine size, but otherwise the same. Fuel economy values were then projected. Table V.6.1 shows these “Optimization 1” fuel economy values. Optimization 1 was conducted by the EngSim Corporation.

Table V.6.1 - Fuel Economy Projections for a Ford F-150 Full-Size Pickup Truck

FUEL ECONOMY PROJECTIONS		Baseline		Optimization 1	Optimization 2
F150 PICKUP TRUCK with					GT Modeling Only
2.4L in-line 4-cylinder engine					
Variable Compression ratio		5.0L V8	3.5L V6	2.4L VCR-VVL	2.4L VCR-VVL
Variable Valve Control		6spd-a 2WD	6spd-a 2WD	6spd-a 2WD	6spd-a 2WD
Advanced Boosting		MY 2012-14	MY 2014		
Fuel economy projection method		EPA Guide	EPA Guide	Engine Testing & GT Modeling	GT Optimized CTY & HWY
Mileage Projections					
City	mpg	15	16	22.4	24.0
Highway	mpg	21	22	24.3	25.4
Combined	mpg	17	18	23.2	24.6
Percent improvement over baseline	Percent	Baseline	6	35	43

2WD – two-wheel drive; MY – model year; EPA – Environmental Protection Agency; CTY – city; HWY – highway

The sixth step involved plotting fuel consumption on brake mean effective pressure (BMEP) vs. engine speed charts for the city and highway EPA test drive cycles. These plots are shown in Figure V.6.2 and show the engine load and speed conditions where most of the fuel is consumed. On the Federal Test Procedure (FTP75) city test cycle, high engine efficiency is needed most at 3.0 bar BMEP at 1,400 rpm and at the engine idle condition. For the highway drive cycle, a high engine efficiency is needed most at 6.4 bar BMEP at 1,700 rpm.

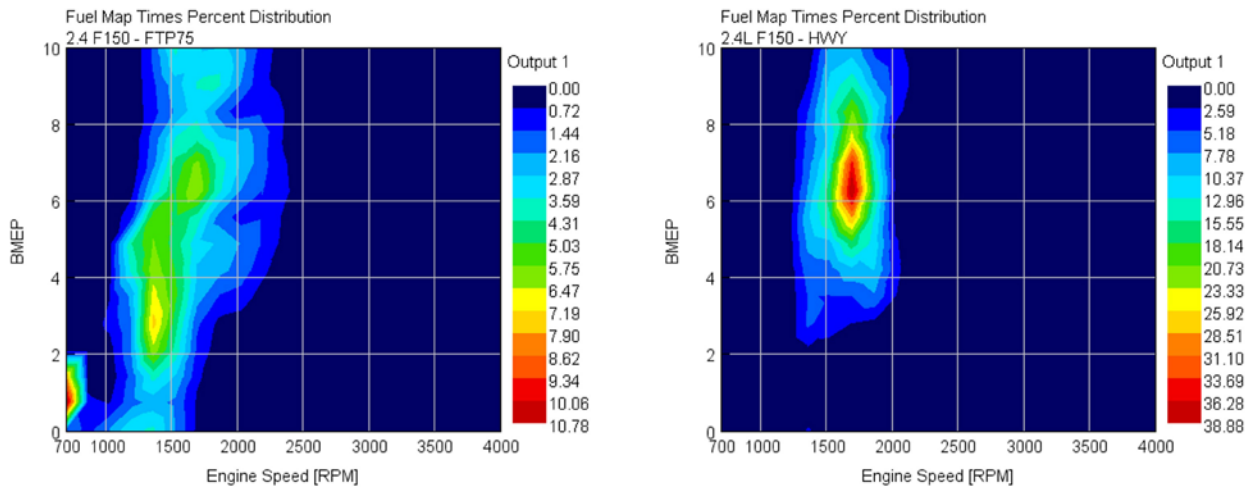


Figure V.6.2 - Fuel consumption for an F-150 pickup truck on the EPA city (FTP75) and highway test cycle

The seventh step involved optimizing VCR engine efficiency where it counts most: the city load condition of 3.0 bar BMEP at 1,400 rpm and the highway load condition of 6.4 bar BMEP at 1,700 rpm. Potential improvements in mileage were then estimated. Table V.6.1 shows these “Optimization 2” fuel economy values. Optimization 2 fuel economy values assume variable valve control on both the intake and exhaust cam shafts, in addition to the VCR. Optimization 2 was conducted primarily by Envera.

VCR Range

VCR range was evaluated for a number of different engine build configurations. High efficiency values are generally attainable with a compression ratio of 16.5. Higher CR values provide some additional benefit and a 17.6 CR value was used in the current development program.

Low compression ratio values improve turbocharger response in addition to knock (detonation) avoidance. A minimum CR value of 8.1 was used on the current program. For 2.5-L engines having a bore to stroke ratio of 0.84, a VCR travel distance of about 10 mm is desirable. An advantage of the Envera VCR mechanism is that it can provide 10 mm or more travel range. A number of other VCR mechanisms provide only about one-third of the needed travel distance.

Results

The following results were achieved in Phase 3 of the program.

- Tested the VCR engine on a dynamometer up to approximately 300 hp
- Achieved 230.4 g/kWh at 2,000 rpm and 5.36 bar BMEP
- Projected 219 g/kWh at 1,700 rpm and 6.35 bar BMEP (the highway load condition shown in Figure V.6.1)
- Achieved high efficiency values using stoichiometric combustion for attaining low tail pipe emission values using proven three-way catalytic converter technology
- Projected 35–43% fuel economy improvement for an F-150 full-size pickup truck equipped with the VCR engine

Conclusions

The current program has successfully demonstrated potential for improving full-size pickup truck fuel economy by approximately 40% by replacing existing V8 engines with four-cylinder VCR engines.

The current program also demonstrated the ability of the four-cylinder engine to provide high torque and power levels with boosting, while also providing high city and highway test cycle engine efficiency using the Atkinson cycle.

The VCR hardware is mechanically robust. The compression ratio range is about three times larger than some competing VCR mechanisms. The larger VCR range provides brake specific fuel consumption, down-sizing, and turbocharger response benefits. The VCR mechanism has a low mass production piece cost and should be considered for both engine upgrades and new development programs.

Key Fiscal Year 2017 Publications

1. DOE Annual Merit Review presentation, June 8, 2017.

V.7 Lean Miller Cycle System Development for Light-Duty Vehicles

Paul A. Battiston, Principal Investigator

General Motors LLC
800 Glenwood Ave.
Pontiac, MI 48340
E-mail: paul.a.battiston@gm.com

Ken Howden, DOE Technology Manager

U.S. Department of Energy
E-mail: Ken.Howden@ee.doe.gov

Start Date: January 26, 2015 End Date: January 31, 2020
Total Project Cost: \$20,672,201 DOE share: \$8,268,880 Non-DOE share: \$12,403,321

Acknowledgments

Co-Author

Arun Solomon, General Motors LLC

NETL Project Manager

Ralph Nine, National Energy Technology Laboratory

Project Introduction

In order to accomplish the government objective of achieving breakthrough thermal efficiencies while meeting U.S. Environmental Protection Agency emission standards, this project focuses on combining two enabling technologies in a gasoline engine: lean combustion and Miller cycle. Lean combustion requires a more complex exhaust aftertreatment system than a traditional three-way catalyst system [1]. The Miller cycle concept provides knock mitigation, increased expansion of combustion gases to extract additional work, reduced pumping losses, and increased efficiency.

The objective of the project is to research, develop, and demonstrate the new lean Miller cycle combustion concept. The lean Miller strategy will be integrated with engine downsizing, advanced thermal management, stop/start, and friction reduction to maximize efficiency to achieve a 35% improvement in fuel economy over a production baseline vehicle. A lean aftertreatment exhaust system will be developed to meet Tier 3 emissions standards. The overall system will be demonstrated in a vehicle.

Objectives

- Demonstrate a new combustion concept combining lean stratified operation with Miller cycle in a gasoline engine
- Integrate with engine downsizing, advanced thermal management, 12-V stop/start, friction reduction mechanisms, and a lean aftertreatment exhaust system
- Demonstrate a vehicle with a fuel economy improvement of more than 35% over an existing production baseline vehicle while meeting Tier 3 emissions standards

Approach

The challenges of the combustion and aftertreatment will be addressed systematically. The first step is single-cylinder engine (SCE) testing which establishes the requirements for the combustion system. This central injection, lean combustion system requires very high levels of exhaust gas recirculation (EGR) to mitigate NO_x emissions; such a highly dilute system presents a combustion challenge. Computational fluid dynamics (CFD) is being used to analyze in-cylinder flows and spray interaction and design options for optimizing

thermodynamic efficiency. This highly dilute system also presents a boost and aftertreatment challenge due to the low temperature lean exhaust and potential high cost of components. One-dimensional (1D) modeling is being used to investigate options for boost, EGR, and exhaust aftertreatment systems and provide realistic boundary conditions for the SCE testing.

These fundamentals will then be integrated into a multi-cylinder engine and aftertreatment system. The engine will be optimized and calibrated on an engine dynamometer. The final demonstration will be in a vehicle, where emissions, drivability, and performance will be confirmed. Decision gates are set up annually to assess progress and determine whether or not to continue the investigation.

Results

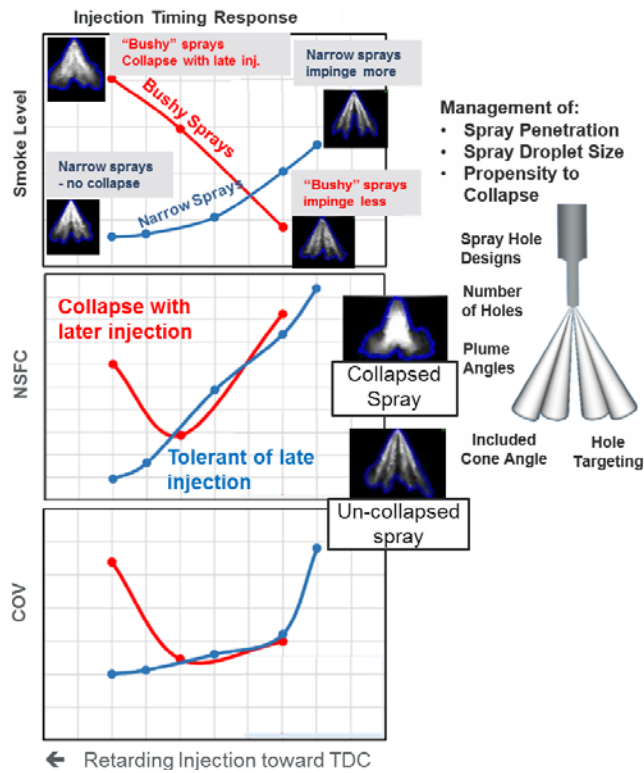
Significant progress was made in optimizing the lean Miller cycle system on the SCE to demonstrate fuel efficiency against targets and finalizing the multi-cylinder engine architecture. Key accomplishments are:

- Optimized piston, port, valvetrain strategy, and preliminary multipulse injection strategy across engine load range
- Defined combustion system design for multi-cylinder engine
- Demonstrated capability to achieve vehicle efficiency cycle targets
- Defined boost and aftertreatment systems using 1D models to address the challenges of low-temperature lean exhaust, and define SCE boundary conditions
- Finalized design and initiated procurement of the first mule multi-cylinder engine for dynamometer testing, including advanced thermal management
- Passed Go/No-Go Decision #2 in June.

CFD analysis continues to be utilized to understand the fundamental in-cylinder performance and guide SCE investigations. This includes spray, combustion, stratification, turbulent kinetic energy, burn rate, and knocking analyses. By optimizing the injection strategy, good lean stratified performance has been achieved with higher tumble. Understanding the sensitivity of spray penetration to injection timing is critical to manage combustion response. Figure V.7.1 compares the impact of two different sprays. The more “bushy” spray tends to collapse with injection retard due to the higher cylinder pressure. The collapsed spray results in rich regions at the center of the piston bowl driving poor mixing and high smoke. The “narrower spray” does not collapse under higher cylinder pressures and allows more equalization of pressure inside and outside of the overall spray cone. However, narrower sprays can result in piston impingement. An injection strategy has been developed to manage spray penetration to achieve lower smoke and fuel consumption, and improved combustion stability (coefficient of variation [COV] of indicated mean effective pressure). A key parameter that is being optimized for lean stratified operation is the spacing or dwell time between injections. Figure V.7.2 illustrates the impact of dwell time on flame turbulence and fuel–air equivalence ratio at the flame front. Closely spaced injections enable more robust flame development by improving turbulence and mixture equivalence ratio (EQR) at the right point in the combustion process and forces the flame kernel to move down and reduces piston wetting vs. single pulse. Zones of rich- and lean-EQR and burn rate are shown in Figure V.7.3 to demonstrate the impact of a closely spaced late injection event on the developing flame. The contours capture the end of the second injection event and indicate a closely spaced second injection improves EQR near the spark plug resulting in a higher burn rate contained in the bowl. Figure V.7.3 also indicates that a 0.5 ms dwell might be more effective in improving the burning rate than a 2 ms dwell. Insights gained from CFD were applied to screen 13 hardware sets on the SCE to down-select the builds with the highest potential for multi-cylinder application to achieve program targets. The prime path hardware matrix is shown in Table V.7.1.

Calibration optimization has been accomplished over a 21-point matrix spanning the speed and load range of the intended vehicle application. Environmental Protection Agency city cycle fuel consumption predictions were developed for the lean Miller cycle 2.45-L L4 engine using an SCE data and weighting method and shown in Figure V.7.4. Similar cycle estimations were predicted for the reference port fuel injection (PFI)

engine and a stoichiometric Miller cycle engine including the impact of start-stop (SS) and an eight-speed automatic transmission. The predictions indicate the hardware set has the potential to achieve program targets with the 2.45 L engine being designed for this project based on the SCE results. SCE testing continues on the hardware sets in Table V.7.1 to finalize valve timing strategy, tumble level, and compression ratio selection.



TDC – top dead center; NSFC – net specific fuel consumption

Figure V.7.1 - Sensitivity of two different spray designs to injection timing

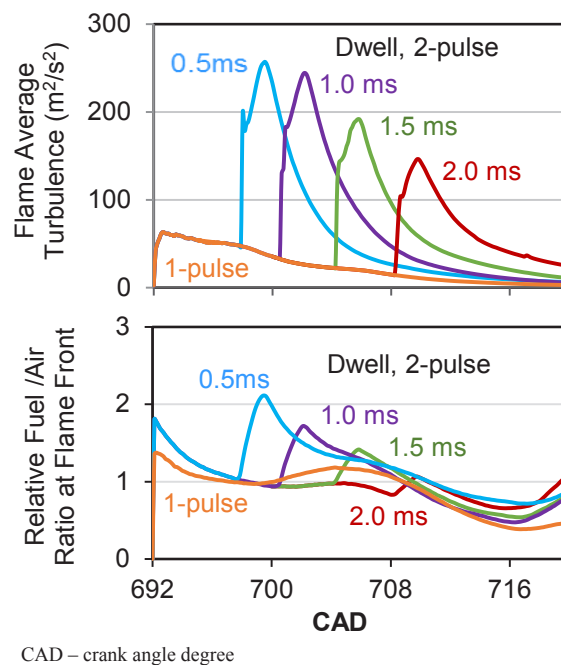


Figure V.7.2 - Sensitivity of flame turbulence and fuel/air ratio to dwell variation in a two-pulse injection strategy

Late-Pulse Injection Strategy at Stratified Part-Load

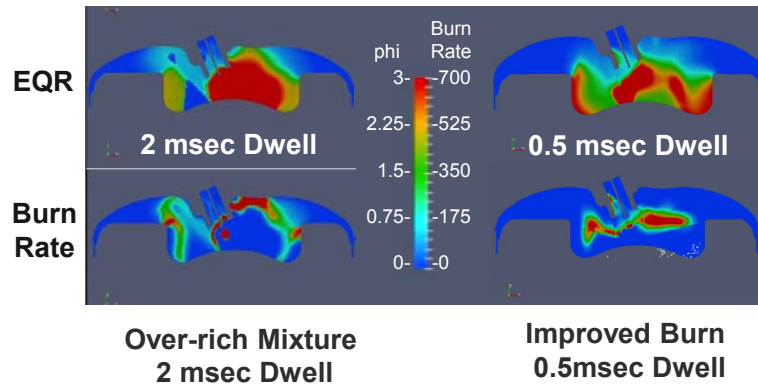


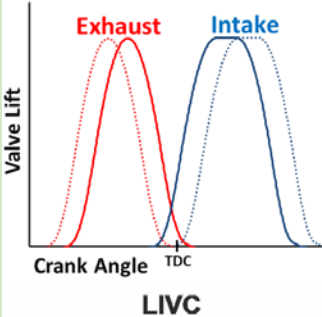
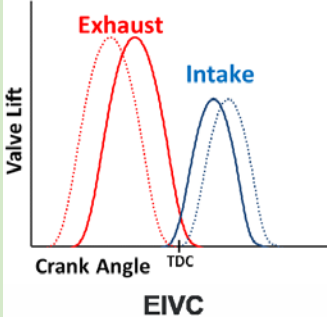
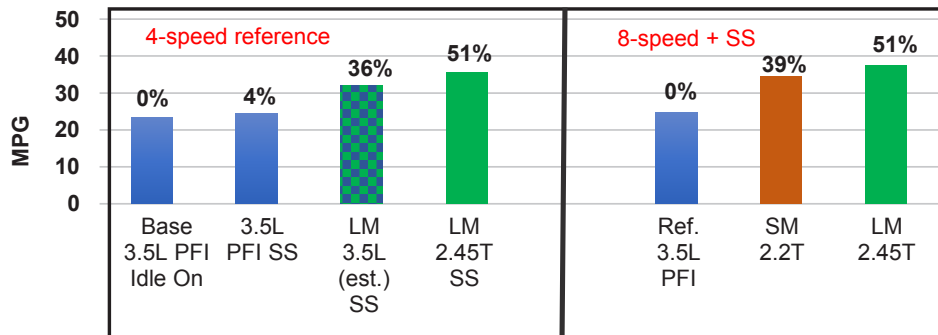


Figure V.7.3 - CFD mapping of EQR and burn rate comparing 2 ms and 0.5 ms dwell times

Table V.7.1 - Prime Path SCE Hardware Matrix

Piston	Chamber	Valve Timing Strategy	
 <p>11:1 and 12:1 compression ratio</p>	 <p>high-tumble and low tumble, open chamber</p>	 <p>LIVC</p>	 <p>EIVC</p>

LIVC – late intake valve closing; EIVC – early intake valve closing



LM – lean Miller; SM – stoichiometric Miller cycle; T – turbocharged

Figure V.7.4 - Cycle fuel economy predictions based on weighted test points

The first multi-cylinder engine variant will utilize a fixed supercharger drive. The design was released and procurement initiated. Contracts have been issued for the long-lead critical components (e.g., block, head, lower crankcase assembly, and fuel injection system) and are shown in Figure V.7.5, targeting a first engine build in first quarter 2018. This initial engine will be used for steady-state dynamometer development to first validate SCE results and demonstrate efficiency targets then continue as a mule for engine and aftertreatment steady-state control and calibration development. Learnings from the first mule engine will feed the design of

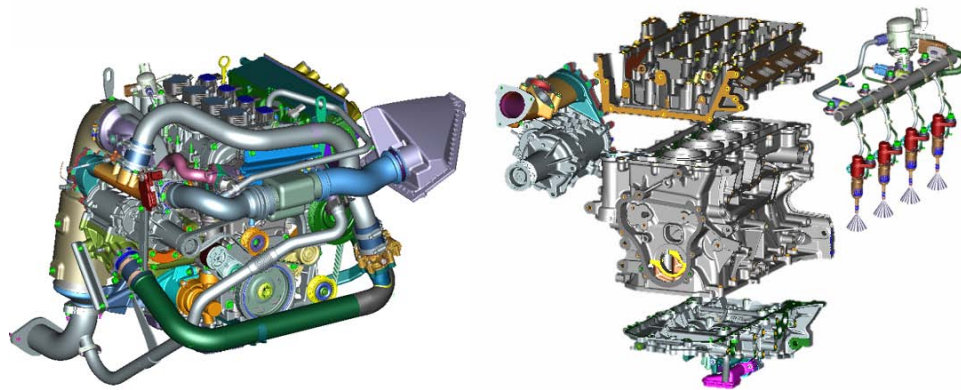


Figure V.7.5 - Critical hardware components

a second engine variant for the vehicle integration. The engine's content will support transient controls and calibration development in the final phases of the project.

Design and cost analysis for the aftertreatment and boost systems continue. Boost systems which do not depend on exhaust enthalpy and are compatible with EGR remain the prime path. A two-speed clutched supercharger has been down-selected as a potential boosting architecture for the vehicle engine. Additional investigations are underway to assess the potential for a high-power electric-compressor as an alternative.

Conclusions

The lean Miller cycle system scope of work includes analysis, SCE, multi-cylinder engine, and vehicle development. It will include full aftertreatment and controls development to meet performance targets and Tier 3 emission standards.

- Defined piston bowl, chamber, ports, valve timing strategy, and multihole injector, and injection strategy for multi-cylinder dynamometer development engine
- Demonstrated potential to achieve project cycle fuel economy target from cycle analysis using SCE steady-state results
- Initiated procurement of multi-cylinder hardware to support first dynamometer development engine

Options for lean and low-temperature aftertreatment and the boost system have been defined. 1D and three-dimensional modeling continues to be leveraged to influence combustion, boost, and aftertreatment design. The gate decision to continue controls and calibration development leading to a final transient capable package for vehicle development is planned for the second quarter of 2018.

References

1. Smith, Stuart R.. "Lean Gasoline System Development for Fuel Efficient Small Cars." DOE Final Report, Cooperative Agreement DE-EE0003379, November 25, 2013.

Key Fiscal Year 2017 Publications

1. 2017 Annual Merit Review presented on June 9, 2017.
2. One patent application and two defensive disclosures.

V.8 Improved Fuel Efficiency Through Adaptive Radio Frequency Controls and Diagnostics for Advanced Catalyst Systems

Alexander Sappok, Principal Investigator

Filter Sensing Technologies, Inc.
7 Bow Street
Malden, MA 02148
E-mail: alexander.sappok@ctscorp.com

Roland Gravel, DOE Technology Manager

U.S. Department of Energy
E-mail: Roland.Gravel@ee.doe.gov

Start Date: October 1, 2015	End Date: May 31, 2018	
Total Project Cost: \$1,378,292	DOE share: \$1,101,252	Non-DOE share: \$277,040

Acknowledgments

Co-Authors

Paul Ragaller, Leslie Bromberg; Filter Sensing Technologies, Inc.

Project Introduction

The transportation sector is responsible for 28% of U.S. energy consumption, of which over 93% is derived from petroleum sources [1]. A number of advanced combustion engines are being developed to reduce transportation sector petroleum consumption, and include lean gasoline, clean diesel, and low temperature combustion modes. Aftertreatment systems remain a barrier for these engines to achieve their full fuel-efficiency potential and market adoption (limited by efficacy and cost) [2]. This project addresses these challenges by developing a radio frequency (RF) sensor and control system, for improved monitoring and control of advanced catalyst systems to reduce engine fuel consumption while still meeting emissions requirements. Direct RF catalyst state measurements provide a path to lower costs, reduced fuel penalty and improved emissions control not possible with current technologies, and can be applied to all of the advanced combustion modes being developed by DOE and its partners.

Diesel combustion engines dominate heavy-duty applications, but high NO_x conversion (and associated lower fuel consumption) is limited by uncertainties in the selective catalytic reduction (SCR) ammonia inventory utilizing conventional gas sensors and model-based approaches. Similarly, lean gasoline engines employing passive SCR rely on the generation of ammonia over the three-way catalyst (TWC) during periods of rich operation which consumes additional fuel. Finally, low temperature combustion modes require means for storing emissions during start-up, and managing those inventories on storage traps. The RF-based approach developed in this program provides a unique, direct measurement of the catalyst storage state to enable improved controls. This approach is in contrast to conventional methods using upstream and downstream electrochemical gas sensors to indirectly infer the state of the catalyst.

Work in the second year of this program developed the production-intent sensor hardware, which was provided to industry and national laboratory project partners for bench reactor, engine dynamometer, and vehicle testing. Accurate measurements of stored ammonia levels on the SCR and oxygen inventories on the TWC were demonstrated to within 10% of the full-scale measurements, achieving the go/no-go decision criteria. RF simulations were also developed and applied to characterize the spatial sensitivity of the measurements, which is of particular interest to quantify the performance of aged catalysts. The cross-sensitivity of the RF sensing approach to other gas species and environmental noise factors was also assessed. Fleet vehicle demonstrations of RF sensing applications for SCR systems continued with several medium- and heavy-duty vehicles to evaluate the real-world performance of the sensors and quantify improvements in efficiency and emissions reduction through improved catalyst controls.

Objectives

The RF sensing technology developed in this project directly addresses barriers to the increased use of advanced combustion engines identified by DOE, namely the added cost, complexity, and durability challenges posed by existing aftertreatment systems. The project objectives have been designed to address these challenges as follows:

- Develop RF sensors and evaluate RF sensing feasibility for SCR, TWC, and hydrocarbon trap applications
- Demonstrate RF sensor accuracy to within 10% of the full-scale requirements for the measurement of stored ammonia on SCR systems
- Develop systems and implementation strategies for the most promising applications to enable low-cost and robust emission controls for dilute gasoline, clean diesel, and low temperature combustion engines
- Demonstrate and quantify improvements in fuel consumption and emissions reduction through the use of RF sensing in engine and vehicle tests with industry and national laboratory partners

Approach

The approach taken in this project is to identify, address, and overcome key technical challenges to successful RF sensor implementation early on by leveraging knowledge gained from past research and development efforts conducted by Filter Sensing Technologies (now CTS Corporation) and in collaboration with national laboratories, industry, and academia [3,4,5,6]. The previous work focused on monitoring soot and ash levels on ceramic particulate filters, not only resulted in successful development and demonstration of the RF sensing technology, but also subsequent commercialization of the sensor by CTS. Following on the success of this model, the approach and structure of this program seeks to extend the understanding gained from measuring particulate matter trapped on filters to gas species stored on catalysts.

The expected project outcomes are twofold. The first phase of this project evaluated the feasibility of RF sensing for several catalysts: (1) NH_3 storage on SCR (passive SCR and urea SCR); (2) oxygen storage on TWC; (3) NH_3 , particulate matter, and ash on combined SCR filters; and (4) hydrocarbon storage on traps. The results provide a comprehensive evaluation of the key hurdles and technology readiness for each application. The second phase is focused on SCR, the most promising near-term application. Engine and vehicle evaluations of SCR and SCR+filter for lean gasoline and diesel will position the RF sensing technology for commercial deployment following this program. The testing will be carried out with project partners including Oak Ridge National Laboratory (catalyst reactor and engine testing), Corning Incorporated (catalyst sample preparation and engine testing), New York City Department of Sanitation (fleet vehicle testing), and original equipment manufacturer partners including Cummins, Detroit Diesel, and Fiat Chrysler Automobiles. The results of the engine and vehicle tests will quantify gains in fuel efficiency and catalyst performance relative to the current state of the art, to directly address the barriers to advanced combustion engine implementation identified by DOE.

Results

A number of key milestones were achieved in 2017. The following summarizes the major project milestones and outcomes in accordance with the overall project objectives.

- Developed production-intent RF sensor hardware and software, and supplied to project partners for engine and vehicle validation on various light-duty and heavy-duty applications
- Applied RF cavity resonance models to quantify the spatial resolution of the cavity resonance measurements and validated simulation results relative to experimental measurements
- Confirmed RF sensing feasibility for direct measurement of adsorbed gas species on diesel and gasoline aftertreatment system catalysts and developed calibration functions for SCR and TWC

- Achieved the go/no-go decision criteria by demonstrating the measurement of ammonia stored on SCR catalysts to within 10% of the full-scale measurement range of 2 g/L
- Quantified the sensitivity of the RF measurements to the presence of other exhaust gas species and environmental noise factors through carefully controlled bench reactor testing
- Demonstrated RF sensor robustness through fleet vehicle evaluations with full-size SCR systems on both medium- and heavy-duty vehicles operated in New York City (urban) drive cycles

The project outcomes to date have not only confirmed the feasibility of RF sensing, which was the primary objective in the first phase of this program, but also quantified sensor accuracy to meet the decision criteria. Selected highlights of the project outcomes over the past year are presented in the following sections.

Figure V.8.1 presents the production-intent RF sensor developed during the second year of this program. The sensor consists of a control unit with integrated microcontroller and two RF antennas. The antennas are passive devices used to transmit and receive RF signals within the catalyst housing. Sensor output is over the vehicle Controller Area Network, and all RF control, signal generation, and signal processing functions are contained within the control unit. The same control unit may be used for all of the catalyst applications investigated in this program, with the only difference being the system calibrations, which are unique for different catalysts. The sensor shown in Figure V.8.1 was also distributed to project partners for subsequent testing on engine dynamometer and vehicle (on-road) applications.



Figure V.8.1 - Production-intent RF sensor including control unit and antennas (Source CTS)

Development and application of the RF cavity models and simulation tools also continued in parallel with the sensor hardware and calibration development. An example of the model output is shown in Figure V.8.2. Regions in red indicate areas of high electric field strength and correspond to spatial locations in the catalyst housing in which the RF measurements will be most sensitive to changes in catalyst storage levels. The cavity resonance modes for the first three low-order resonances A, B, and C, are shown in the figure and on the corresponding resonance curves. The low order modes show variation in the axial distribution of the resonances along the length of the catalyst, while the higher order modes provide the potential to monitor differences in radial distribution of the adsorbed gas species.

A comparison of the simulated RF resonance curves and measured RF resonance curves is also shown in Figure V.8.2. The model shows good agreement with the measured resonance behavior for the catalyst core samples evaluated on the bench reactor, particularly for the low-order resonances. Experimental validation of the simulations was one of the key focus areas of the work in this project phase. The results are useful to understand the performance of aged catalysts, which may exhibit differences in the spatial distribution of specific adsorbed gas species in an aged catalyst relative to a fresh catalyst.

Figures V.8.3 and V.8.4 present the resonance curves corresponding to the RF measurements of stored ammonia on an SCR catalyst and oxygen stored on a TWC catalyst, respectively. The measurements confirm the feasibility of applying RF sensing to directly monitor the catalyst storages state, although the specific mechanisms responsible for the observed changes in the RF signal are different for the two cases. The results further show a higher degree of sensitivity (larger change in the RF signal) for monitoring oxygen storage on a TWC relative to measurements of ammonia storage on SCR catalysts. In both cases the measurements were

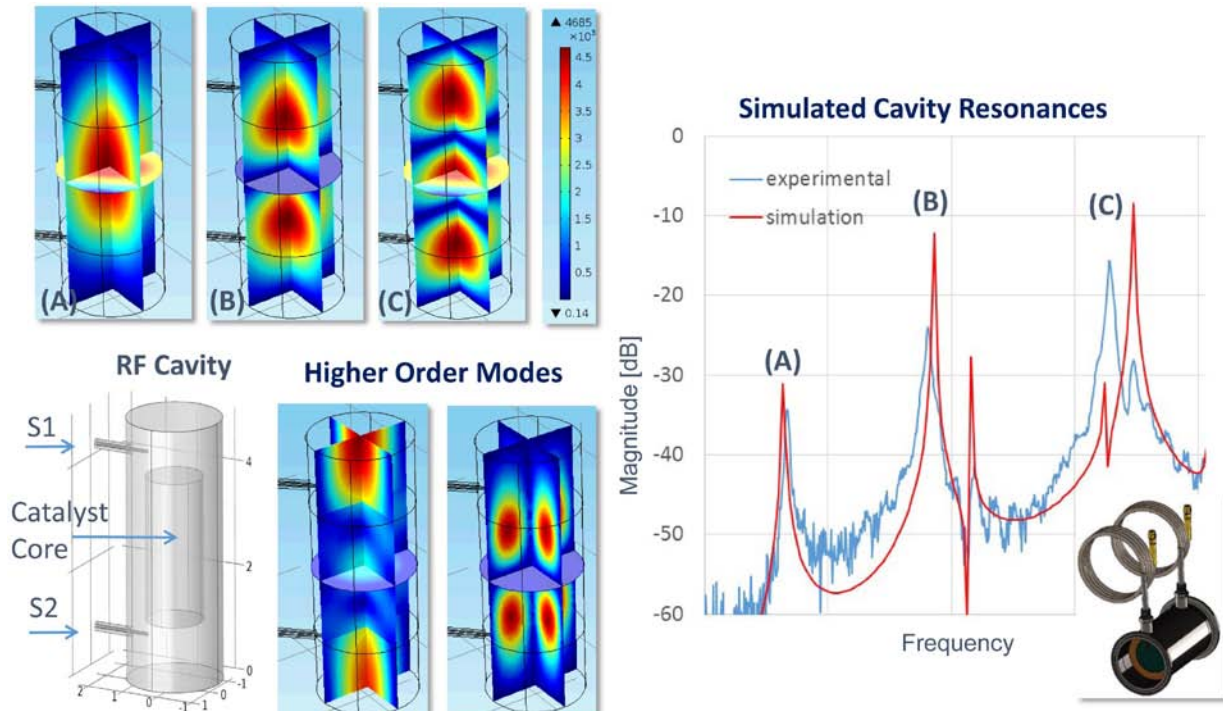
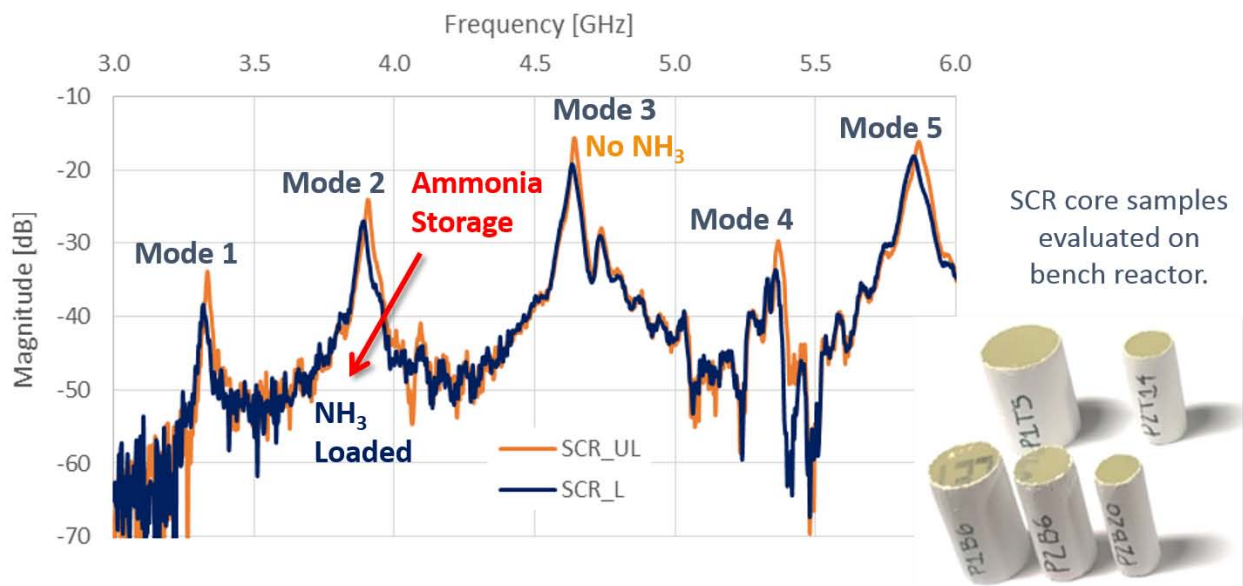


Figure V.8.2 - RF catalyst cavity simulation results and comparison with experimental measurements

carried out on commercial catalyst samples (production catalysts representative of current in-use technologies) evaluated on bench reactor systems at Oak Ridge National Laboratory and CTS.

The results shown in Figure V.8.3 indicate a reduction in the magnitude of the RF resonance modes as the catalyst is loaded with ammonia. The maximum change in the RF signal observed between the ammonia saturated and fully desorbed state is approximately -5 dB. The tests were conducted using a production Cummins ISL catalyst from a model year 2015 application. The storage of the ammonia on the copper zeolites results in increased ionic conductivity of the zeolites and increased RF signal loss, which is observed as a reduction in the signal magnitude. As shown in Figure V.8.3, the reduction in the RF signal magnitude is most pronounced at resonance.



UL – unloaded; L – loaded

Figure V.8.3 - Cavity resonance response of SCR samples in the presence and absence of stored ammonia

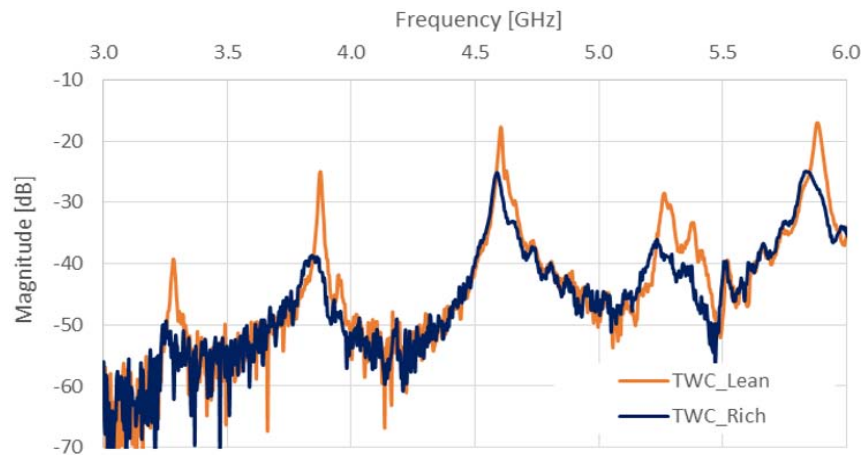


Figure V.8.4 - Cavity resonance response of TWC samples in the presence and absence of stored oxygen

Figure V.8.4 presents similar results for the case of oxygen storage on the TWC. In this case commercial TWCs from model year 2015 General Motors and Chrysler applications were utilized. Similar to the case of ammonia storage on the SCR, the presence or absence of stored oxygen on the catalyst results in a large variation in the RF signal magnitude, which is most pronounced at resonance. However, unlike the SCR case, the presence of stored oxygen results in the sharp peaks observed in the RF signal (highest magnitude resonances). On the other hand, the absence of oxygen stored on the catalyst during periods of rich operation results in a significant reduction in resonant mode amplitude. The difference in the RF resonances in the presence or absence of stored oxygen on the catalyst is attributed to a change in the conductivity of the ceria washcoat and is consistent with results reported by Moos [7].

The catalyst bench measurements corresponding to the results presented in Figures V.8.3 and V.8.4 were used to develop calibration functions for both the TWC and SCR applications. Pre- and post-catalyst Fourier transform infrared spectroscopy measurements were utilized in conjunction with commercial gas sensors and models to compute the storage levels of ammonia or oxygen on the SCR and TWC catalysts, respectively. In both cases the dielectric properties of the catalyst in its fully depleted and fully saturated states are observed to vary with temperature. Figure V.8.5a presents the RF measured ammonia storage level on the SCR catalyst relative to the estimated ammonia storage level (based on the bench reactor tests) over a range of exhaust temperature conditions. In general the storage capacity of the SCR is reduced at elevated temperatures, which is also observed in the measurements.

The results presented in Figure V.8.5 fall within the RF sensor accuracy targets (10% of full-scale measurement range) defined at the beginning of this project and meet the go/no-go decision criteria for Phase I. Given the promising results shown in the figure, work is currently underway to quantify sensor performance to monitor ammonia storage levels on the SCR catalyst on a full-size system installed on a heavy-duty engine dynamometer setup at Corning. In parallel, light-duty applications for passive SCR will also be evaluated on a lean-burn BMW engine at Oak Ridge National Laboratory in a subsequent project phase.

Figure V.8.5b also shows the RF antennas installed on a heavy-duty SCR system equipped on a Mack truck operated by the New York City Department of Sanitation fleet. Two such vehicles have been in use over the course of the past year to evaluate the robustness of the RF sensing technology for on-road applications. In addition to the Mack trucks, an additional medium-duty vehicle using a Cummins ISB diesel engine was also instrumented with the RF sensor to monitor SCR performance and is also undergoing on-road testing in New York. To date all systems are functioning as expected and no failures of the system in the field have been observed.

In parallel with the vehicle testing, additional catalyst bench reactor studies were undertaken to quantify the cross-sensitivity of the RF measurements to various system noise factors and exhaust gas species. The results are presented in Figure V.8.6 for the SCR application. The testing independently varied one exhaust parameter

while holding the others constant in order to observe the impact of each parameter on the RF signal. In general, the variation of most exhaust gas species tested showed little impact on the RF signal, with the exception being water content. Increasing water levels in the exhaust gas stream from 5% to 13% did result in a measureable change in the RF signal, although the ammonia storage state of the catalyst is also affected.

It is well known that stored water does increase the RF loss of the system and may be a parameter which could require compensation for accurate measurement of stored ammonia levels in the field. Currently, methods are being developed to utilize estimates of water levels in the exhaust (provided over Controller Area Network) to compensate the RF signal when elevated water levels are present in the system. In addition to water, the RF signal must also be compensated for temperature variations as the dielectric properties of the adsorbed gas species and catalyst do vary with temperature. Temperature correction methods have already been successfully incorporated into the sensor calibration, as shown in Figure V.8.5a, in order to meet the measurement accuracy targets. It is expected that similar correction methods may be implemented to account for the presence of high water levels in the system, if needed. Selected measurements corresponding to the tests in Figure V.8.6 were also conducted at different exhaust gas flow rates. No variation of the RF signal based on differences in flow rates was observed.

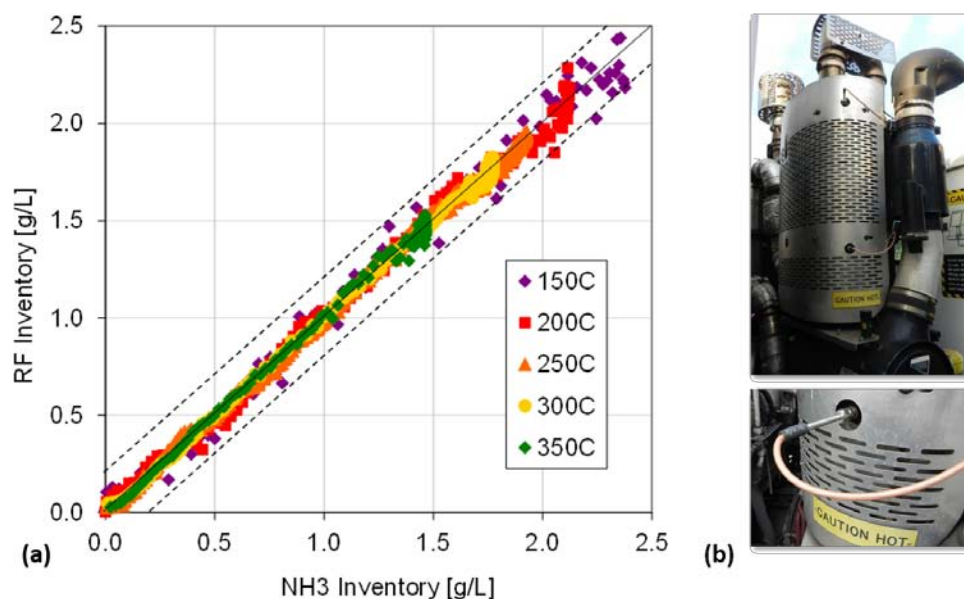


Figure V.8.5 - Calibrated RF sensor output and correlation to estimated SCR ammonia storage levels (a) and RF antennas installed on full-size SCR for vehicle testing (b) (Source Filter Sensing Technologies)

The results presented thus confirm the feasibility of RF sensing techniques to monitor the processes occurring on exhaust catalysts directly. The accomplishments in this project phase have achieved the program objectives and motivated further development and demonstration of the technology on full-size systems to be completed in the next year of this program. The planned future work includes further fleet evaluations with the production-intent sensor shown in Figure V.8.1, as well as engine dynamometer testing on a heavy-duty diesel application at Corning and light-duty testing on lean gasoline application at Oak Ridge National Laboratory.

Conclusions

Work over the course of the past year of this program has resulted in significant progress toward achieving the overall project objectives. Sensor feasibility was demonstrated in laboratory applications to meet the program performance targets and the results will be used to guide the next phase which includes sensor evaluation on full-size engine and vehicle systems. Specific accomplishments of this program phase are the following.

- Developed production-intent RF sensors which were supplied to project partners for engine and vehicle validation on various light-duty and heavy-duty applications

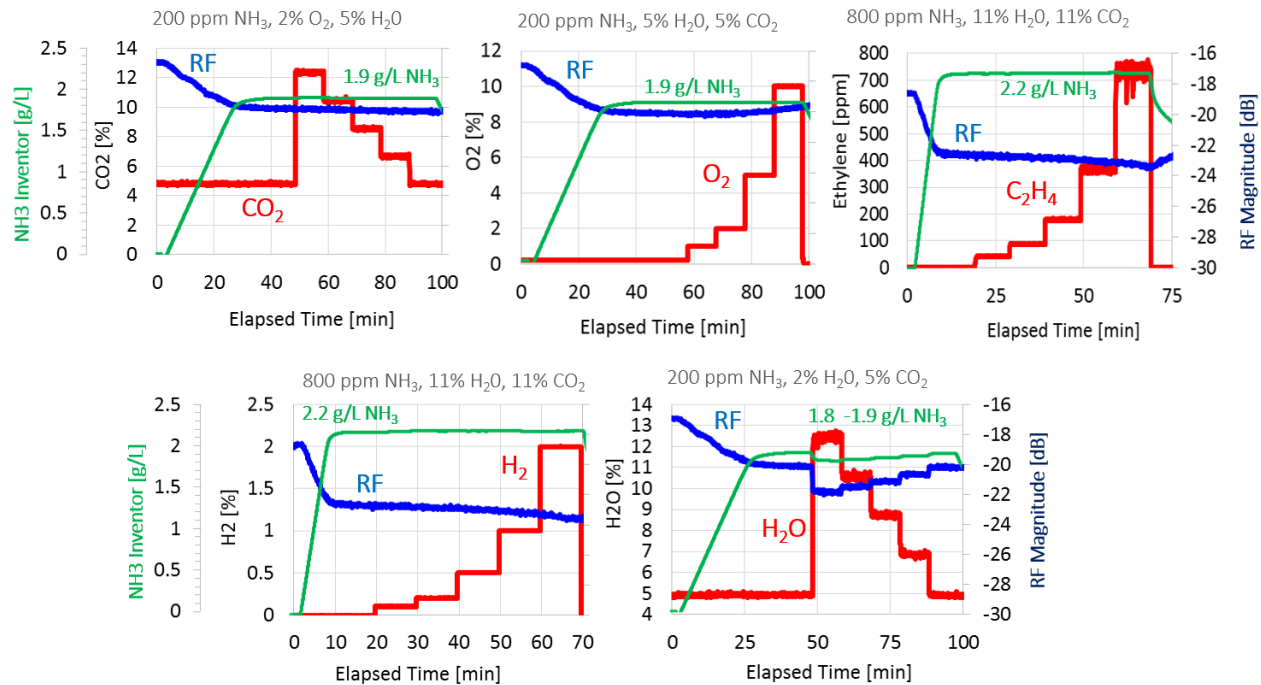


Figure V.8.6 - Analysis of RF signal response to individual exhaust gas species

- Quantified the spatial resolution of the cavity resonance measurements through application of RF simulations and validated model results relative to experimental measurements
- Directly measured adsorbed gas species on diesel and gasoline aftertreatment system catalysts and developed calibration functions for SCR and TWC systems
- Measured ammonia stored on SCR catalysts to within 10% of the full-scale measurement range of 2 g/L to achieve the program go/no-go decision criteria
- Quantified the sensitivity of the RF measurements to the presence of other exhaust gas species and environmental noise factors through catalyst bench reactor testing
- Demonstrated RF sensor robustness through fleet vehicle evaluations with full-size SCR systems on both medium- and heavy-duty vehicles operated in New York City (urban) drive cycles

The results to date demonstrate considerable potential for direct RF feedback control of the catalyst storage state to optimize the combined engine and aftertreatment system and address key barriers to the increased adoption of efficient and cost-effective advanced combustion engines.

References

1. U.S. Department of Energy, Energy Information Administration. "Annual Energy Outlook 2012." 2012.
2. U.S. Department of Energy. "Freedom Car and Vehicle Technologies Program, Multi-Year Program Plan 2011-2015." Office of Energy Efficiency and Renewable Energy, 2010.
3. Sappok, A., P. Ragaller, L. Bromberg, V. Prikhodko, J. Storey, and J. Parks. "Real-Time Engine and Aftertreatment System Control Using Fast Response Particulate Filter Sensors." SAE 2016-01-0918, 2016.
4. Ragaller, P., A. Sappok, L. Bromberg, N. Gunasekaran, J. Warkins, and R. Wilhelm. "Lifetime Particulate Filter Soot and Ash Measurements using Radio Frequency Sensors and Potential for Improved Filter Management." SAE 2016-01-0943, 2016.

5. Nanjundaswamy, H., V. Nagaraju, Y. Wu, E. Koehler, A. Sappok, P. Ragaller, and L. Bromberg. "Advanced RF Particulate Filter Sensing and Controls for Efficient Aftertreatment Management and Reduced Fuel Consumption." SAE 2015-01-0996, 2015.
6. Sappok, A. and L. Bromberg. "Radio Frequency Diesel Particulate Filter Soot and Ash Level Sensors: Enabling Adaptive Controls for Heavy-Duty Diesel Applications." *SAE Int. J. Commer. Veh.* 7(2):468–477, 2014, doi:10.4271/2014-01-2349.
7. Moos, R. "Microwave-Based Catalyst State Diagnosis - State of the Art and Future Perspectives." *SAE International Journal of Engines*, Vol. 8, No. 3, 2015.

Key Fiscal Year 2017 Publications

1. Aguilar, J., A. Sappok, P. Ragaller, L. Bromberg, et al. "Catalyst Ammonia Storage Measurements using Radio Frequency Sensing." ASME Internal Combustion Engines Fall Technical Conference, ICEF2017-3572, 2017.
2. Ragaller, P., A. Sappok, L. Bromberg, J. Pihl, V. Prikhodko, and J. Parks. "Real-Time Catalyst Monitoring and Diagnostics using Radio Frequency Sensors." Poster Presentation, CLEERS Workshop, Ann Arbor, MI, October 2017.
3. Ragaller, P., A. Sappok, L. Bromberg, J. Pihl, V. Prikhodko, and J. Parks. "Real-Time Aftertreatment System Diagnostics and Prognostics Using Radio Frequency Sensors." Technical presentation, SAE On-Board Diagnostics Symposium, Anaheim, CA, September 2017.

V.9 Integrated Boosting and Hybridization for Extreme Fuel Economy and Downsizing

Chinmaya Patil, Principal Investigator

Eaton Corporation
26201 Northwestern Highway
Southfield, MI 48076
E-mail: chinmayapatil@eaton.com

Ken Howden, DOE Technology Manager

U.S. Department of Energy
E-mail: Ken.Howden@ee.doe.gov

Start Date: October 1, 2014	End Date: December 31, 2017	
Total Project Cost: \$3,499,000	DOE share: \$1,749,500	Non-DOE share: \$1,749,500

Acknowledgments

NETL Project Manager

Jason Conley, National Energy Technology Laboratory

Project Introduction

Improvement in fuel economy in the automotive market is driven both by regulations (Environmental Protection Agency, Corporate Average Fuel Economy, EURO, etc.) as well as the increasing gas prices. Consumers demand cost-effective solutions that can reduce vehicle fuel consumption and at the same time, meet their performance (vehicle acceleration) requirements. A primary solution to reduced fuel consumption is engine downsizing and downspeeding; a smaller and slower engine will exhibit fewer friction losses and higher operating efficiency since it will be forced, for the same vehicle mass, to operate at a relative higher percentage of load.

The project will develop, build, and test a highly efficient and fully controllable technology for optimizing engine energy usage. Through energy usage and breathing optimization of a downsized and down-spiced engine, a fuel economy (FE) improvement of more than 20% will be targeted over an already turbocharged and downsized engine while maintaining or improving performance at an industry accepted cost point. Recovering both brake and exhaust energy and using it in a variable ratio boosting system (rather than a traction system) offers cost-effective, high impact hybridization independent of the drive cycle.

Objectives

The objective of this project is to develop, demonstrate, and evaluate commercialization of electrification of the air delivery and waste heat recovery (WHR) systems, to achieve a 20% FE improvement at a commercially viable cost by:

- Downsizing the engine.
- Improving the combustion efficiency.
- Optimizing the energy usage.

Approach

The project is being conducted in three budget periods.

Budget Period 1: Model-Based System Analysis and Individual Technology Risk Mitigation

The activities focused on evaluating integration of the two technologies in a model-based environment where the architecture and the component sizes were optimized. Multiple integration schemes were examined that

combined an electrically assisted variable speed (EAVS) supercharger and WHR in different ways in a model environment. The sizes of the motor, generator, and battery were optimized. The component risks were addressed, such as WHR high temperature durability, by designing and testing WHR hardware on an engine.

Budget Period 2: Design and Engine Dynamometer Testing of System and Optimize Controls

The second budget period will focus on designing and integrating the two technologies on a full engine dynamometer. The engine with the EAVS–WHR system will be calibrated on the dynamometer for emissions, performance, and FE. The supervisory-level controls to operate the two systems in a coordinated approach will be developed in preparation for powertrain-level dynamometer testing in the next budget period.

Budget Period 3: Powertrain Dynamometer Testing and Commercialization Analysis Across Multiple Vehicle Classes

The third budget period will focus on powertrain dynamometer testing, where the boosting and hybrid functions of the EAVS and WHR systems will be evaluated against the FE, emissions, performance, and cost targets. Further, the system models will be validated against dynamometer test data and the models will be used to evaluate the fuel-saving performance of the system for multiple vehicle classes. The cost estimates and commercialization feasibility of the technology will be analyzed.

The project is led by Eaton who is responsible for the development and testing of the EAVS and WHR systems, in partnership with Isuzu who is responsible for supplying the baseline engine and supporting Eaton in system calibration.

Results

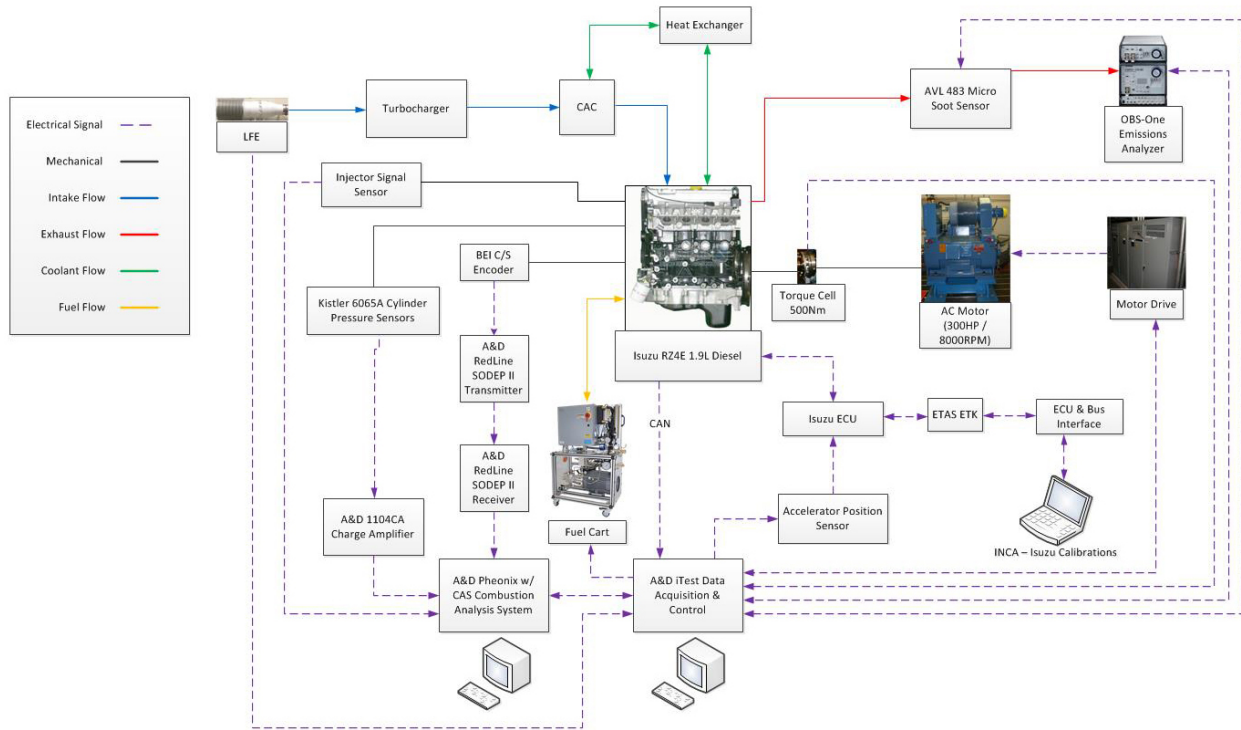
Baseline Engine Testing Completed for Benchmarked Comparison of Fuel Economy, Emissions and Performance with EAVS–Electrified WHR (eWHR) Technology

The Isuzu Spark vehicle was received at the Eaton facility in Southfield, Michigan, on January 17, 2017. The engine was subsequently removed from the vehicle and installed in the engine dynamometer test cell. The engine dynamometer mechanical integration in the test cell was completed in the planned timeframe, but an unplanned instrumentation and data acquisition gap and an accelerator position issue prevented the start of baseline engine testing in the fifth quarter of Budget Period 2. Figure V.9.1 shows the engine dynamometer test



Figure V.9.1 - Isuzu engine unmounted from the vehicle, mounted on the dynamometer (Source: Eaton)

setup. Figure V.9.2 shows the schematic of the dynamometer test setup with the key sensors for combustion and emission analysis. The baseline engine testing occupied the bulk of the sixth quarter, with focus on characterizing the baseline engine power map and obtaining repeatable engine performance for three transient drive cycles, as shown in Table V.9.1.



CAC – charge air cooler; LFE – laminar flow element; OBS – on-board sensor; ECU – engine control unit; CAS – combustion analysis system

Figure V.9.2 - Engine dynamometer test setup schematic

Table V.9.1 - Engine Dynamometer Test Plan, Including Baseline and EAVS/eWHR Technologies

Hardware	Objective	Cycle	Test Runs
Baseline RZ4E 1.9 L Isuzu engine w/turbo	Power mapping	Power map	1
	Repeatability analysis, steady state testing	Steady state torque map	10
		Performance baseline testing	US06
	FTP75		8
RZ4E + EAVS + eWHR	Power mapping	Power map	1
	Repeatability analysis/steady state testing	Steady state torque map	10
		Performance testing	US06
	FTP75		3
NEDC	3		

FTP75 – Federal Test Procedure; US06 – Supplementary Federal Test Procedure; NEDC – New European Driving Cycle

EAVS and eWHR Systems Development

The EAVS unit and ancillary components, such as the mounting brackets, pulleys, and bypass valve, have been procured, and parts are on hand. Functional testing of the EAVS has been conducted to verify the unit. The EAVS system is ready to be installed upon the completion of baseline engine testing. An image of the EAVS unit hardware is shown in Figure V.9.3.



Figure V.9.3 - EAVS unit (Source: Eaton)

The eWHR unit and the mounting manifold components have been procured, assembled, and the unit has been subjected to functional testing on a test stand. The focus of the test was to map the efficiency of the expander unit as well as the combined expander and generator unit. The eWHR unit is shown in Figure V.9.4.

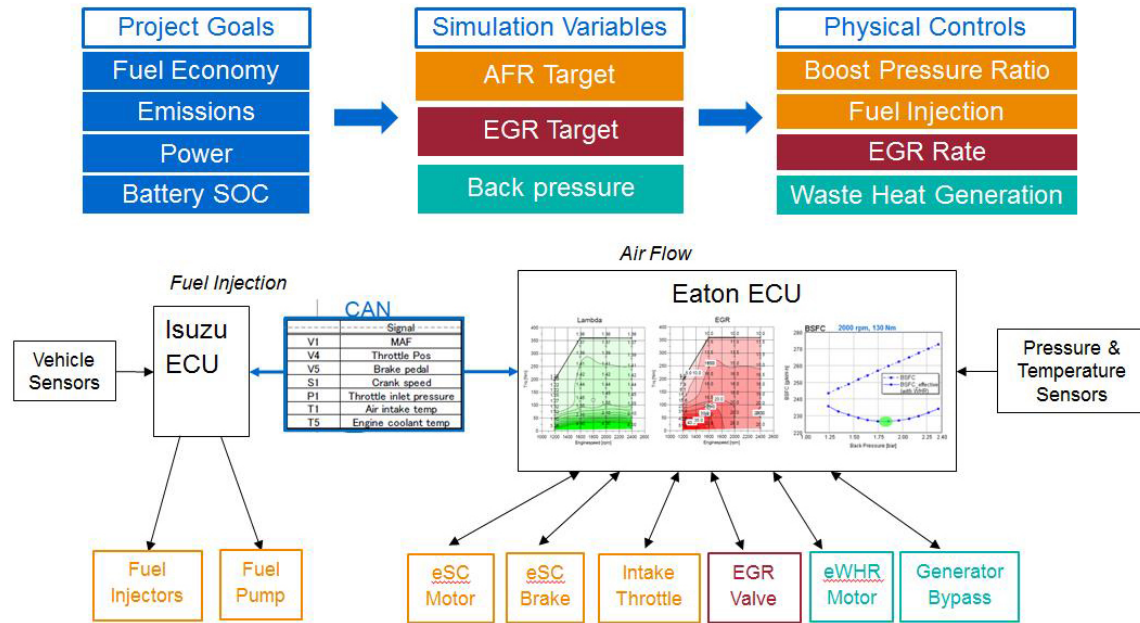


Figure V.9.4 - eWHR unit (Source: Eaton)

Controls Hardware and Software Development

System controls will be shared between Eaton and Isuzu. As shown in Figure V.9.5, Eaton will control air flow while Isuzu controls fuel flow to achieve ideal air–fuel ratio and exhaust gas recirculation (EGR) rates in order to increase fuel economy while maintaining engine output power.

The electrical hardware to interface between the Isuzu engine and the EAVS, eWHR, and EGR valve has been wired and is ready to test. Figure V.9.6 shows the assembled system.



SOC – state of charge; AFR – air–fuel ratio; ECU – engine control unit; CAN – Controller Area Network; eSC – electric supercharger

Figure V.9.5 - System control coordinated between Eaton and Isuzu ECUs



Figure V.9.6 - Control hardware (Source: Eaton)

EAVS Dynamometer Installation

Following the completion of baseline engine testing task, the variable geometry turbocharger and the EGR control valves were unmounted and the EAVS unit was installed in the air intake path. Also a diesel particulate filter and an EGR cooler were installed in the engine exhaust path and connected to the air intake through the three-way EGR valve. Figure V.9.7 shows the dynamometer test setup with the key components.

EAVS Unit Calibration via Dynamometer Testing

Steady-state calibration of the EAVS unit is currently underway. Figure V.9.8 shows the variation of engine torque produced, fuel consumed, and NO_x output at 2,000 rpm with respect to engine intake air pressure. Engine torque increases from 181 Nm to 192 Nm with boost pressure up until 170 kPa (1.7 pressure ratio), beyond which it stabilizes at 192 Nm. Steady-state fuel consumption is roughly constant at all the boost pressures. NO_x increases with increasing torque output.

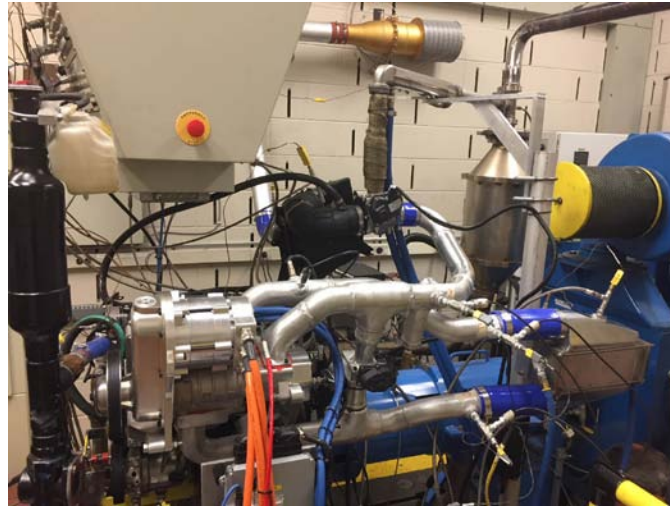


Figure V.9.7 - Dynamometer setup with EAVS and EGR valve installation (Source: Eaton)

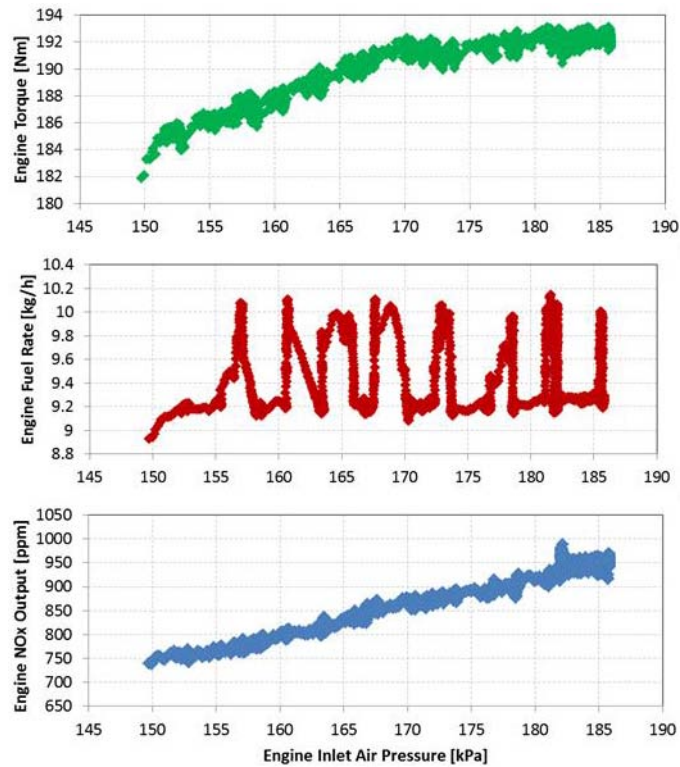


Figure V.9.8 - Engine torque, fuel, and NO_x versus boost pressure at an engine speed of 2,000 rpm

Conclusions

- Baseline engine characterization is complete.
- The EAVS and eWHR units have been designed, procured, assembled, and functionally tested.
- The EAVS unit was installed on the baseline engine following removal of the variable geometry turbocharger and the system calibration to identify the optimal boost pressures to achieve best fuel economy is currently underway.
- Next steps include installation and calibration of eWHR unit and final system evaluation for fuel economy, performance, and emissions for comparison with the baseline engine.

Key Fiscal Year 2017 Publications

1. Presentation at the 2017 DOE Vehicle Technologies Office Annual Merit Review and Peer Evaluation Meeting in Washington, DC, June 9, 2017.

V.10 Cummins 55% BTE Project

Lyle Kocher, Principal Investigator

Cummins Inc.
1900 McKinley Avenue
Columbus, IN 47201-6414
E-mail: lyle.e.kocher@cummins.com

Roland Gravel, DOE Technology Manager

U.S. Department of Energy
E-mail: Roland.Gravel@ee.doe.gov

Start Date: December 1, 2015	End Date: June 30, 2018	
Total Project Cost: \$9,000,000	DOE share: \$4,500,000	Non-DOE share: \$4,500,000

Project Introduction

The successful development of a high efficiency diesel engine system could significantly reduce petroleum usage in the United States and provide energy security for the future. The program's efforts directly address the Vehicle Technologies Office's goal of achieving 55% brake thermal efficiency (BTE) and prevailing emissions compliance. The program accelerates the development of the high efficiency enabling technologies to shorten their time to market.

The landscape of advanced heavy-duty engines includes both high temperature diffusion combustion and low temperature premixed combustion. The low temperature combustion (LTC) engines are capable of demonstrating low engine out constituent emissions and high thermal efficiencies. The high thermal efficiency is predominately due to a short combustion duration and low in-cylinder heat loss from the distributed premixed reactions. However, LTC engines suffer from controllability issues due to the lack of a direct combustion trigger and knock issues due to fuel and temperature stratification in the cylinder. These barriers currently prohibit LTC engines from entering the heavy-duty market. High temperature combustion engines are easily controllable and do not suffer from knock but emit higher levels of constituent emissions such as NO_x and particulate matter. The emissions can be treated through the application of low pressure exhaust gas recirculation and a close-coupled selective catalytic reduction on filter system. Efficiency improvements for the high temperature combustion engines can be achieved by mimicking the best traits of an LTC engine: short combustion duration and low in-cylinder heat loss. These efficiency improvements are being leveraged in this project. The efficiency of the engine system can be further improved through the addition of a waste heat recovery (WHR) system.

Objectives

- Use a diesel engine system to demonstrate in a test cell peak engine system efficiency of 55% BTE
- Develop and demonstrate an advanced, highly integrated combustion and aftertreatment system to achieve 2010 emissions compliance

Approach

The approach integrates advances in the areas of combustion, engine design, WHR, fuel injection, turbocharging, and aftertreatment to provide an optimized and integrated total engine system. Achieving 55% BTE will require virtually all engine systems to be improved with thorough effort placed on the interaction between the systems. When examining the entire system, opportunities can be created to take advantage of technologies to benefit multiple engine systems. Starting with the combustion system, a low heat rejection combustion chamber is desired to minimize the in-cylinder heat losses. The low heat rejection design will be achieved through piston material changes to low thermal conductivity materials and use of thermal barrier coatings. The low heat transfer (LHT) piston will operate with higher surface temperatures and thus have

lower in-cylinder heat losses. Additionally, the LHT piston will be able to operate with reduced piston oil cooling flow. This represents a savings of up to 40% of the lube flow and will allow a smaller, lower parasitic, lube pump to be utilized. The LHT pistons will also have higher exhaust temperatures for better turbocharger and aftertreatment performance. Similar symbiotic system level opportunities are available through the use of a close-coupled aftertreatment system and the addition of a low pressure exhaust gas recirculation loop. An integrated system designed to opportunistically take advantage of these interactions is critical to achieving the overall efficiency goals.

Results

A low heat rejection combustion system was designed to reduce in-cylinder heat transfer. The design includes application of LHT materials to combustion surfaces, reduction and/or elimination of piston oil cooling, and higher coolant operating temperature. Conjugate heat transfer analysis has been performed to maximize the benefit of an LHT combustion system while maintaining temperatures to below mechanical limitations of the selected materials. The performance of the LHT piston at different combustion timings is shown in Figure V.10.1 for cases with the piston cooling nozzle (PCN) oil flow turned on and off. In the PCN On case, oil flow is provided to the undercrown of the piston which cools the piston surface temperatures. In the PCN Off case, no oil flow is provided which leads to higher piston surface temperatures, less in-cylinder heat loss and higher thermal efficiency. Figure V.10.1 shows an increase of 0.3% BTE improvement with increased surface temperatures.

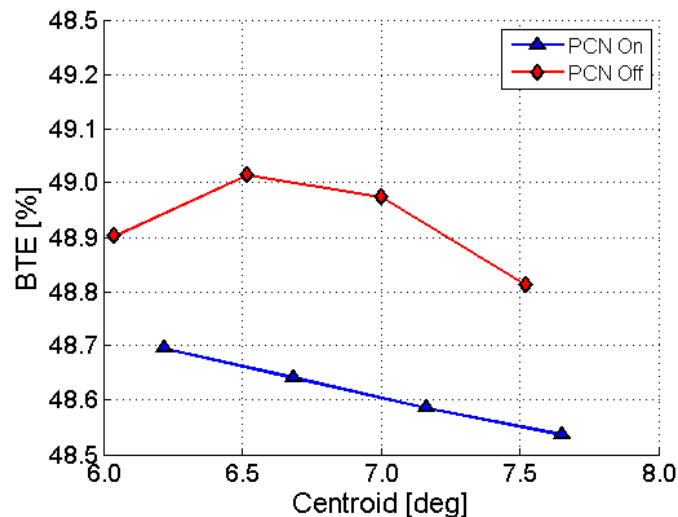


Figure V.10.1 - Effect of turning PCN flow on/off

Conventional diesel combustion is a diffusion (or mixing) controlled combustion event, meaning that the fuel is burned as soon as it has a chance to mix with entrained air to an ignitable equivalence ratio. In order to increase the rate at which the fuel is burned, the fuel needs to be introduced into the cylinder at an increased rate while ensuring that enough air can be entrained into the fuel jet for proper combustion. A new injector configuration was designed to provide a faster injection rate shape as shown in Figure V.10.2. Three different fuel injection rate shapes are shown to illustrate their impact on the combustion heat release event. Figure V.10.3 shows the measured apparent heat release rate for the injection rate shapes in Figure V.10.2. The faster opening of the Rate 3 profile and the shorter duration translates into a faster rise in heat release rate and a shorter duration of combustion. The impact on the engine efficiency is shown in Figure V.10.4 for the different rate shapes. An improvement of 0.3% closed cycle efficiency is demonstrated by optimizing the fuel injection rate shape.

An Organic Rankine Cycle WHR system has been developed to utilize available waste energy in the system. The Organic Rankine Cycle operates with a dual loop working fluid flow path composed of two separate streams of working fluid under different pressures. The higher pressure stream will recover energy from higher temperature sources and the lower pressure stream will recover energy from lower temperature sources. Both

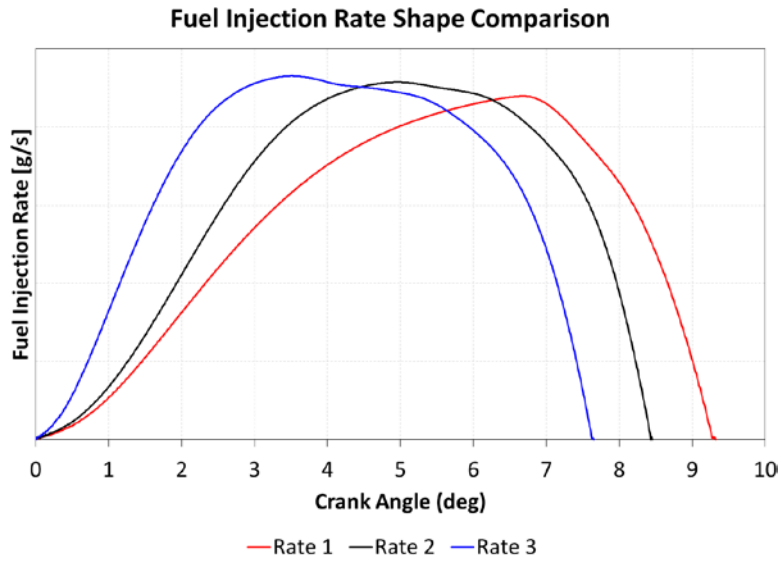


Figure V.10.2 - Fuel injection rate shape comparison

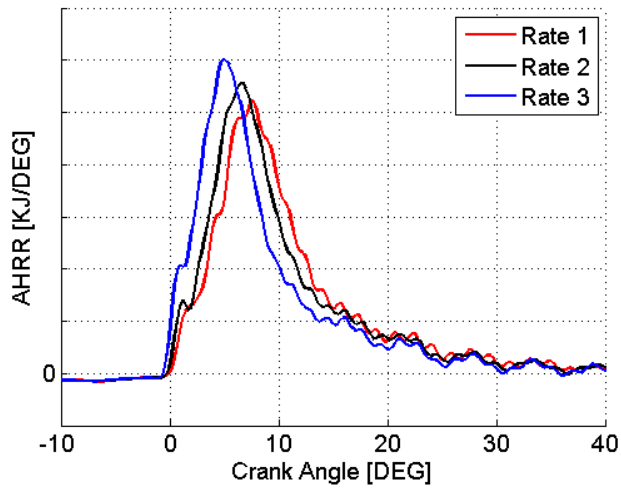


Figure V.10.3 - Apparent heat release rate (AHRR) comparison

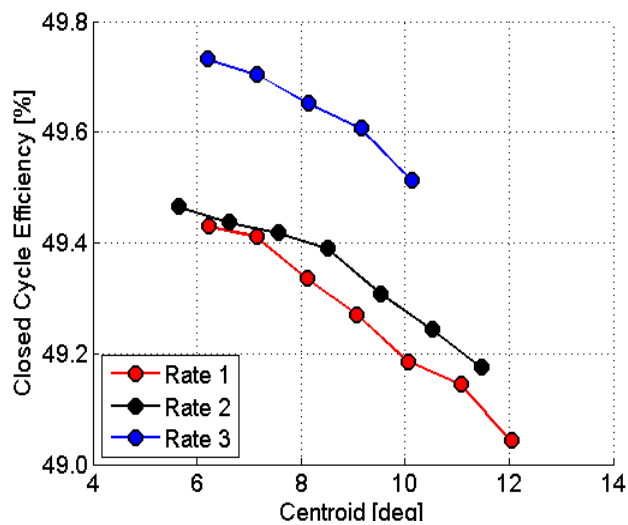


Figure V.10.4 - Closed cycle efficiency comparison

streams will pass through a common expander rotor but will approach that rotor through different sets of expander stator nozzles. To accomplish this, a new dual entry turbine expander was designed and tested in the WHR system. The complete WHR system has been integrated with the engine and is being optimized for peak performance. The WHR system has demonstrated 4.2% BTE improvement to date with more optimization work to be completed before the end of the program.

The improvements in the base engine have allowed for the demonstration of 50% BTE without WHR. The engine has been paired with a low pressure drop aftertreatment system. The system was tested over the emissions cycles and demonstrated compliance over the Ramped Model Cycle Supplemental Emissions Test and hot Federal Test Procedure cycles. Future work in the project will focus on the optimization of the engine and WHR system to achieve the overall program goal of a 55% BTE system demonstration.

Conclusions

The Cummins 55% BTE program has successfully completed the second year of the program. The program is on track to demonstrate the stated program goal of a 55% BTE system. The following progress has been demonstrated.

- Demonstrated 50% BTE in a heavy-duty truck engine without WHR
- Demonstrated emission compliance over Ramped Model Cycle Supplemental Emissions Test and hot Federal Test Procedure cycles
- Demonstrated +4.2% delta BTE from the WHR system

Key Fiscal Year 2017 Publications

1. "55BTE Program Quarterly Research Performance Progress Report." January 2017.
2. "55BTE Program Quarterly Research Performance Progress Report." April 2017.
3. DOE Vehicle Technologies Office Annual Merit Review Presentation for 55BTE Program, June 8, 2017.
4. "55BTE Program Quarterly Research Performance Progress Report." July 2017.
5. "55BTE Program Quarterly Research Performance Progress Report." October 30, 2017.

V.11 Solenoid Actuated Cylinder Deactivation Valvetrain for Dynamic Skip Fire

Hermes Fernandez, Principal Investigator

Delphi Automotive Systems, LLC
5725 Delphi Drive
Troy, MI 48098-2815
E-mail: hermes.fernandez@delphi.com

Ken Howden, DOE Technology Manager

U.S. Department of Energy
E-mail: Ken.Howden@ee.doe.gov

Start Date: January 1, 2017	End Date: July 1, 2019	
Total Project Cost: \$3,472,676	DOE share: \$1,736,338	Non-DOE share: \$1,736,338

Acknowledgments

Co-Authors

Robert Wang, Tom George; Delphi Automotive Systems, LLC

NETL Project Manager

Carl Maronde, National Energy Technology Laboratory

Project Introduction

Delphi Automotive Systems, LLC and Tula Technology, Inc. are developing an advanced combustion strategy known as Dynamic Skip Fire (DSF). The basis of this strategy is to selectively deactivate cylinders based on engine load and speed to minimize fuel consumption. Cylinder deactivation requires intake and exhaust valve as well as fuel injector deactivation to reduce engine pumping work and improve efficiency. Existing hydraulically actuated valvetrain hardware has been used on development engine and vehicle builds to prove out the fuel economy benefits of DSF. Hydraulic actuation has proven difficult to implement for production level projects due to the difficulty of adding four independent hydraulic circuits to an existing cylinder head of a four-cylinder engine.

The purpose of this project is to develop solenoid actuated valvetrain hardware which will allow DSF technology to be more easily commercialized with current overhead cam production engines. Additional benefits expected from this project include a faster and more repeatable switching response, leading to improved system reliability as well as a larger operating window for DSF to increase fuel economy.

Objectives

- The main objective of this project is to improve engine fuel efficiency by developing a production-feasible electrically actuated cylinder deactivation (e-DEAC) valvetrain which will enable internal combustion engines to operate more efficiently.
- The project is expected to enable the realization of 8% to 10% fuel economy improvement above stock operation of a non-cylinder deactivation four-cylinder engine, while maintaining production-level noise, vibration, and harshness (NVH) targets and emissions.
- This project will enable DSF technology to be more easily implemented into production engines by eliminating the complex hydraulic circuit packaging which is currently required to individually deactivate cylinders, which will allow broader market adaptations, especially on overhead cam engines.

Approach

Delphi and Tula are working together to improve engine fuel efficiency by researching, designing, developing, building, and testing a production-feasible e-DEAC valvetrain which will maximize the fuel economy benefit of Tula's DSF technology.

Tula has conducted engine and vehicle simulations to characterize cylinder deactivation and project fuel economy improvement, and define deactivation requirements. State-of-the-art software, such as GT-SUITE, MATLAB, and Simulink, were utilized for engine and vehicle performance, and NVH simulation and analysis work. Tula will also participate in engine testing and provide guidance on control strategies to minimize NVH and fuel consumption.

Delphi is responsible for all aspects of the design and development of the deactivation hardware including electrical actuators, controls, and engine management system optimization and testing. A packaging study was conducted to understand the available space for the electrical actuators, as well as their mounting and their interfaces to the deactivation mechanisms. Concepts were generated and design simulations were used to select both the deactivation mechanism and an electrical actuation concept. The build of both the selected concept and its control hardware and software is currently underway. Once the builds are completed and debugged using probe hardware, the valvetrain hardware and controls will be installed on a four-cylinder dynamometer engine. Steady-state and transient engine calibrations will then be optimized. Fuel usage and emissions at key Federal Test Procedure (FTP) steady-state speed-load points and simulated FTP operation will be documented. Data analysis will be completed and results will be reported.

Results

- Engine and vehicle simulations to characterize cylinder deactivation and to project fuel economy were completed, Milestone M1.1.
 - A Volkswagen (VW) EA888 four-cylinder 1.8 L turbocharged, gasoline direct injection engine was chosen as the target engine to allow a direct DSF system comparison of electrical vs. hydraulic cylinder deactivation.
 - GT-POWER simulations were conducted to determine deactivation engine operating windows and strategies. A model, shown in Figure V.11.1, was constructed and correlation with measured data was completed for both four-cylinder and DSF operation. Fuel consumption was mapped over the entire engine operating range and supplied to the vehicle model.
 - GT-POWER simulations were also used to estimate switching speed requirements for cylinder deactivation. With independent control of intake and exhaust valves, a 26 ms switching window is available at an engine speed of 3,000 rpm with constant cam phasing. An engine speed of 3,000 rpm represents an upper speed limit which would cover the entire range of operation on common drive cycles. The switching window is sufficient to allow DSF operation with solenoid actuation.
 - GT-SUITE vehicle simulations were used to project vehicle fuel economy for common drive cycles. A previously developed vehicle model of a 2015 VW Jetta equipped with the EA888 engine (Figure V.11.2) was used to simulate various drive cycles and project the fuel consumption benefit of DSF.
 - The fuel consumption improvements from DSF over the inline-four for the simulated drive cycles are presented in Table V.11.1. The “conservative” strategy represents the present spark timing calibration on 87 octane gasoline without the use of knock feedback control. The “aggressive” calibration represents a maximum brake torque/borderline detonation spark calibration for 93 octane gasoline. The average fuel consumption improvement for DSF over inline-four operation in Table V.11.1 for the conservative approach was 6.5%. The aggressive approach increased the average fuel consumption improvement 1.3 percentage points to 7.8%.

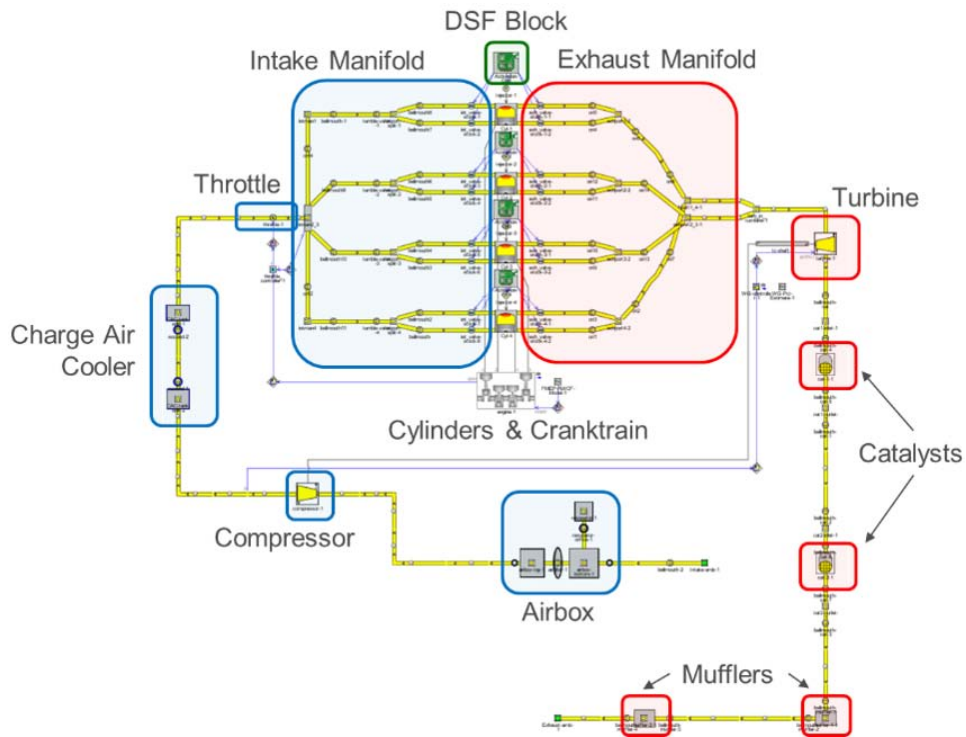
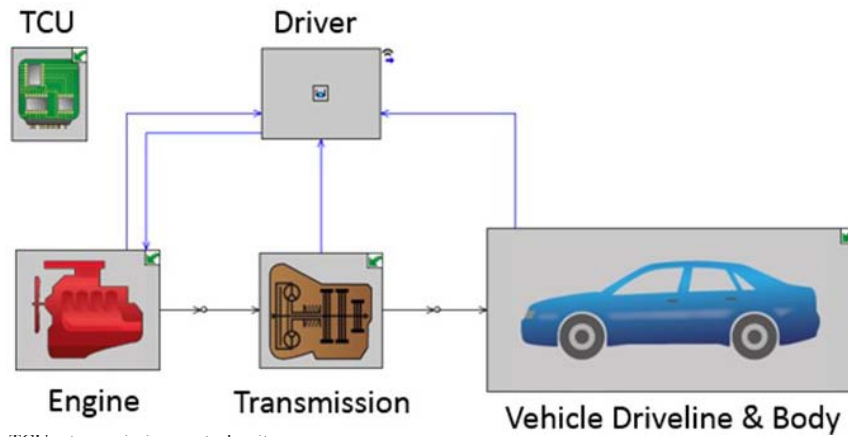


Figure V.11.1 - VW EA888 four-cylinder GT-POWER engine model



TCU – transmission control unit

Figure V.11.2 - VW Jetta GT-SUITE vehicle model

Table V.11.1 - Drive Cycle Fuel Consumption Improvement

Cycle	Conservative	Aggressive
Metro-Highway ¹	7.3%	9.0%
FTP75	8.9%	10.5%
HWFET	4.4%	6.3%
NEDC	6.3%	7.3%
WLTC	5.2%	6.5%
JC08	7.0%	8.4%
Average	6.5%	7.8%

¹Computed from FTP75 and HWFET

HWFET – Highway Fuel Economy Test; NEDC – New European Driving Cycle

WLTC – Worldwide harmonized Light vehicles Test Cycle

- The impact of parasitic losses from switching on fuel consumption improvement were estimated using simulation. For hydraulic deactivation, average fuel consumption improvement decreased by -0.11%. For solenoid deactivation, average fuel consumption improvement decreased by -0.15%. However, solenoid deactivation can be enabled earlier in cold-start drive cycles than hydraulic deactivation due to a lack of requirements on the hydraulic fluid, namely oil temperature. Enabling DSF 70 s earlier after cycle start for solenoid deactivation (30 s vs. 100 s) led to a +0.49% average fuel consumption improvement compared to hydraulic deactivation.
- The side pin concept has been selected as valve deactivation mechanism. This selected concept locates a solenoid actuator to one side of the roller finger follower where space was available in the most common cylinder head configurations. The actuator transmits motion to a lock pin via a pivoting lever. The side pin design was chosen during a concept selection process in which the Delphi team discussed and compared this concept to other concepts using functional, manufacturability, assembly size and potential cost selection criteria. For example:
 - Functionality was confirmed using NX Motion solid models to animate concepts to evaluate valve action and clearances in activated and deactivated modes.
 - Multi-physics analysis estimated full system dynamic response time.
 - Finite element strength analyses were conducted to assure that the designs did not exceed material endurance limits and to evaluate mechanism stiffness.
 - Maxwell magnetic analysis was performed to determine the necessary actuator size to meet force and stroke targets established from dynamic response analysis.
 - High-level system-level costs were estimated from the point of view of an original equipment manufacturer.
- A suitable unidirectional electromagnetic solenoid actuator was selected during an actuator concept selection process. The selected design was analyzed and developed to be manufacturable and to meet control system requirements, Milestone 2.3.
 - A three-dimensional computer-aided drawing model confirmed that the side pin mechanism and its actuators fit within the available cylinder head volume, satisfying the Budget Period 1 go/no go milestone. Figure V.11.3 shows a view of the e-DEAC components packaged in the actual cylinder head.
 - Once packaging was confirmed, a detail design and print package was completed for the probe hardware.

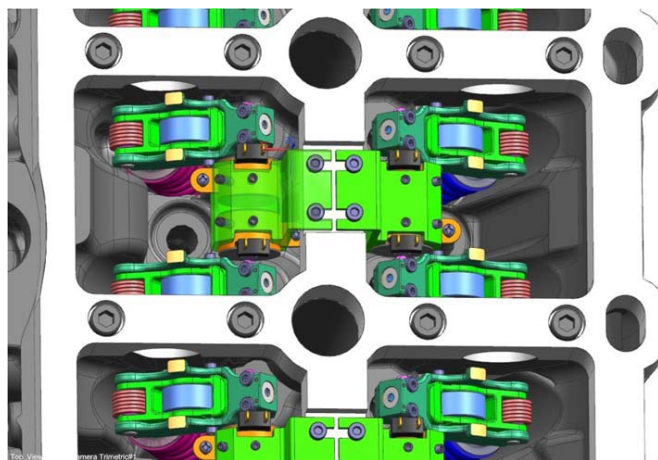


Figure V.11.3 - Full valvetrain in-cylinder head packaging

- The probe hardware has been ordered and received, and the build is now complete. A test plan for this hardware has been completed and some testing has begun.
- Force vs. displacement of the actuators has been measured and it shows very good correlation to simulation predictions, as shown in Figure V.11.4.

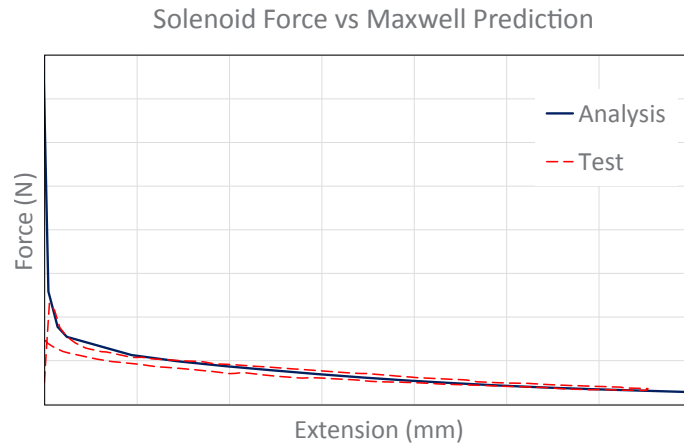


Figure V.11.4 - Probe test solenoid force vs. stroke comparison

- Optimization of the four-cylinder engine layout, a kinetostatic analysis to assure that forces and contact stresses were acceptable, selection of bearing dimensions suitable for operating speeds and loads, and a lost motion spring design to insure proper spring load in deactivated mode were also completed.
- Overall systems requirements were completed. Control functions were divided between the engine control module and the actuator control module. In conjunction, the engine control module hardware and software, as well as the engine control module-to-actuator hardware interface and interconnection requirements were completed. Figure V.11.5 shows a simple mechanization of the system.

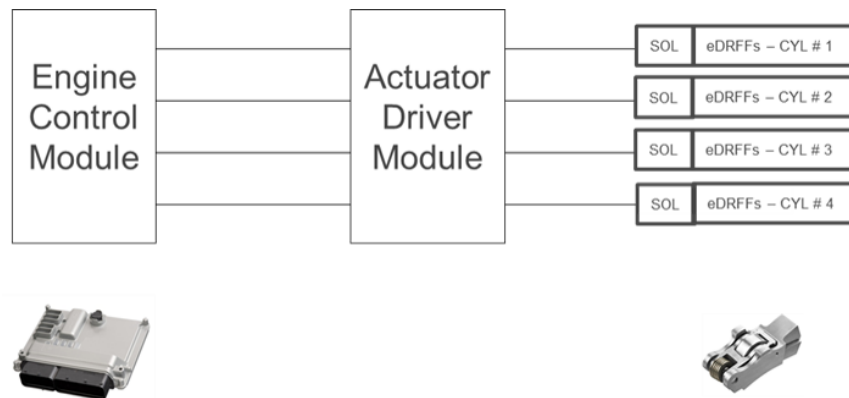


Figure V.11.5 - e-DEAC system mechanization

- The design of the actuator drive module hardware and software was selected. The “Open Loop Low-Side PWM w/Current Sense” was chosen during a concept selection process as the lowest cost approach, which could provide the peak and hold current control required by the actuator concept selection. Simulation and analysis of this selected concept is underway.

Conclusions

- Based on the packaging study, there is sufficient space to mount the selected roller finger followers and actuators. Furthermore, if required, there is room for adjustment to insure proper roller finger follower function and safe routing of the actuator electrical harness to the outside of the cylinder head.

- Simulation projects that DSF with solenoid deactivation should reduce fuel consumption at a minimum of 6.9% averaged across common drive cycles, relative to a non-cylinder deactivation four-cylinder engine.
- Preliminary testing has confirmed that the solenoid actuator design is able to meet response time requirements.

VI. Lubricant Technologies

VI.1 Surface and Lubricant Interactions

Oyelayo Ajayi, Principal Investigator

Argonne National Laboratory
9700 S. Cass Avenue
Argonne, IL 60439
E-mail: ajayi@anl.gov

Michael Weismiller, DOE Technology Manager

U.S. Department of Energy
E-mail: Michael.Weismiller@ee.doe.gov

Start Date: October 1, 2016	End Date: September 30, 2017	
Total Project Cost: \$590,000	DOE share: \$590,000	Non-DOE share: \$0

Acknowledgments

Co-Authors

Cinta Lorenzo-Martin, Nick Demas, Robert Erck, George Fenske; Argonne National Laboratory

Project Introduction

The overall objective of the project is to develop lubricant technologies that provide up to 4% gain in vehicle fuel economy. In engines, one obvious approach is the use of lower viscosity oils. This approach has been under development in the industry for over two decades leading to the introduction of lower viscosity oils into the marketplace. Further reduction of oil viscosity presents many technical hurdles, such as vulnerability of engine components to premature failure and inadequate long-term performance of the lubricant. Furthermore, new engine concepts and technologies under development by original equipment manufacturers (OEMs) will challenge the effectiveness of engine lubricants in terms of friction and wear reduction. Thus, achieving 4% fuel economy improvement (FEI) in a sustainable manner will require a better understanding of the basic lubrication mechanisms of surfaces, as well as understanding and mitigation of potential failure mechanisms.

This report relates to efforts devoted to better understanding the basic mechanisms of surface interactions with the lubricant and potential failure modes. Such understanding is necessary to develop effective lubricant technologies to meet the rather aggressive project objectives, which will require sustainable friction reduction under different lubrication regimes without compromising the reliability and durability of the components. Furthermore, understanding of the mechanisms of interaction between surfaces and lubricants will facilitate extension of new lubricant technologies to legacy vehicles as well as future vehicle technologies.

Objectives

- Develop test methodologies to enable rapid evaluation of new lubricant technologies
- Characterize the structure and composition of surface tribochemical films
- Develop mechanistic models as the basis for performance predictive modeling of lubricated surfaces
- Quantify the impact of oil aging on the tribological performance of lubricated surfaces

Introduction

Test Methodologies

This task seeks to develop accurate and reliable benchtop tests that correlate friction and wear performance to data on fuel economy, durability, and reliability from engine tests. The test methods can then be used to

evaluate technologies in a rapid, cost-effective, and repeatable manner. The goal is that the test methods be able to assess benefits that can be realized by implementing different technologies such as coatings, materials, and lubricants to screen them in the early stage of development and thus avoid expensive and time-consuming builds that will fail in full-scale tests.

Characterization of Tribochemical Films

In a previous DOE Vehicle Technologies Office-funded study on boundary lubrication mechanisms, a relationship was established between the structure of the tribochemical surface films (tribofilms) formed from additives and tribological performance [1]. This finding provides strategies for minimizing boundary friction while protecting the lubricated surfaces against wear and other failures. Using a combination of advanced techniques including focused ion beam (FIB)/high-resolution transmission electron microscopy (TEM), grazing incidence angle X-ray diffraction, micro-X-ray fluorescence, and X-ray absorption near edge structure analyses, this task will determine the structures of tribochemical surface films on in-use engine liner surfaces as well as bench-top test coupons with various advanced additive systems. The nano-mechanical properties of the surface tribochemical films will also be measured by a nano-indentation technique.

Failure Analysis

Adequate reduction in engine friction to achieve the project goal of 4% FEI will require the use of very low viscosity engine oils. As engine components operate under more severe conditions in the boundary regime with the introduction of ultra-low viscosity lubricants, they will be more susceptible to various failure modes. Accelerated wear and scuffing failures will be major issues that must be addressed to ensure reliability and durability of the engine. This task involves extensive failure analysis to determine the basic mechanisms of wear and scuffing in the engine ring and liner system. By means of a physics-of-failure approach, results of this task will be the basis of a predictive model for engine wear and scuffing to guide the development of advanced lubricant technologies.

Effect of Oil Ageing

Engine oils in vehicles are changed at regular intervals because the lubricant performance degrades with time in terms of friction reduction and surface protection. Oil aging and consequent loss of satisfactory performance occur by a combination of several mechanisms, including fuel dilution, shearing of viscosity index additives, oxidation, nitration, soot buildup, and loss of efficacy of antiwear and friction modifier additives. Oil aging changes the properties of the lubricant and often results in lowering of the FEI. This task will determine and quantify the impact of oil aging on the properties and tribological performance of engine oil. Attempts will be made to secure an adequate number of data in terms of aging time to enable the formulation of an empirical model to predict lubricant properties and performance with time.

Approach

Test Methodologies

The first step of the approach is to identify a range of conditions (temperature, speed, and load) that are relevant and critical to a fired engine at top dead center (TDC). The next step is to use actual engine components to perform tests that can simulate vehicle conditions. The last step is to replicate mechanisms and tribological features observed on engine surfaces in the lab.

Results

Test Methodologies

- Investigated test protocols based on difference contact configurations to measure friction and wear of various engine oils
- Examined the effects of starved lubrication on ring-on-liner tribological performance

Careful examination of the information obtained from tests with different configurations is needed to determine their usefulness in simulating the ring-on-liner contact and consequently their efficacy to evaluate

lubricant technologies. Two commonly used test configurations are the ball-on-flat and cylinder-on-flat under reciprocating sliding. Both of these configurations are simpler than the ring-on-liner configuration and could be useful on certain occasions. A vast majority of tribological performance tests of new additives intended for engine applications are conducted with the ball-on-flat configuration. Even though it has been shown that this configuration cannot be used to evaluate lubricants containing solid nanoparticles to reveal wear mechanisms that would be anticipated when materials with different roughness, composition, and hardness are subjected to different contact pressures, it can be useful for the evaluation of lubricants that do not contain solid particles [2].

A project baseline was established by using a conventional GF5 5W-30 oil provided by Infineum. The tribological behavior of this oil was investigated over temperatures from 22°C to 160°C. Tests were also conducted with other commercially available oils. From these tribological tests, it was observed that temperature had no significant effect on the boundary coefficient of friction, which was approximately 0.11 ± 0.01 for up to 4 h test time.

Tests were also conducted with the cylinder-on-flat configuration under the following conditions: 10-mm stroke length and 2-Hz reciprocating frequency for 1 h over a range of contact pressures between 330 MPa and 790 MPa ($P_{\max} = 1$ GPa). In terms of the ability to provide quantifiable wear, these conditions generate a line contact similar to that of the ring-on-liner test configuration. This investigation was conducted because the precise measurement of wear in realistic components with surface roughness and honing marks, as in the case of cylinder liners tested against piston rings, is difficult. These tests demonstrated that it is not possible to produce significant wear volumes using fresh oil. Wear over the width of the profilometric scans could not be quantified and any systematic appearance of wear on this scale could not be trusted. However, oils with various levels of contaminants (collected at the equivalent of 5,070 miles, 8,016 miles, and 10,411 miles) showed significant differences in wear when compared to fresh oil using the cylinder-on-flat test configuration; by contrast, the ball-on-flat test configuration showed no significant differences in either friction or wear. The boundary coefficient of friction for both configurations was approximately the same for all oils.

During this reporting period, efforts were also devoted to using an adjustable-angle reciprocating tribometer in the tilted configuration to investigate the effect of oil supply in an engine and hence replicate the starved-contact condition that the top compression ring experiences at TDC. Tests showed that the amount of oil has a significant effect on the friction and wear behavior. A sensitivity study was performed to examine the differences between oil flow rates and tribological behavior. It was found that $0.1 \mu\text{L}/\text{min}$ is at the limit of starvation and during a load increase, it produced black streaks and led to severe material wear. An increase in the flow rate to $0.2 \mu\text{L}/\text{min}$ produced black streaks and led to small and often gradual removal of material, while $0.5 \mu\text{L}/\text{min}$ produced no black streaks and led to mild polishing. The liner surfaces for representative tests are shown in Figure VI.1.1. These findings are in agreement with recent published work by Petra et al. [3].



Figure VI.1.1 - Micrographs of gray cast iron liner surfaces subjected to a scuffing load test at flow rates of (a) $0.1 \mu\text{L}/\text{min}$, (b) $0.2 \mu\text{L}/\text{min}$, and (c) $0.5 \mu\text{L}/\text{min}$

Characterization of Tribochemical Films

In-use engine liner hardware was obtained from different OEMs. The parts were from both custom engine tests and field-operated engines. No information was provided on the details of the lubricant used during the running

of the various engines. Nonetheless, the information and results of the analysis of the tribofilms from these engine liners will be extremely valuable with regard to lubricant technology development for legacy vehicles. In all the engine parts, formation of the tribofilm was observed on both the ring and the liner surfaces. The film formation on the liner was, however, non-uniform through the stroke length. In all cases, extensive tribofilms were formed in the TDC region, while no films were observed in the bottom dead center (BDC) region. At times, some limited tribofilms were formed; other times, no tribofilms were present in the mid-stroke region. These findings were somewhat expected, since TDC is under more severe contact, and the temperature is higher compared with the BDC. Hence, an extensive tribofilm formed at the TDC to protect the surface. The mid-stroke region operates primarily under the hydrodynamic regime; thus, limited formation of a tribofilm, if any, is expected. Because the BDC temperature is relatively low, formation of a tribofilm did not occur. Consequently, only the tribofilms in the TDC were analyzed.

Figure VI.1.2a shows an optical micrograph of a typical tribofilm on a honing plateau of a cast iron liner. Patchiness and non-uniformity in thickness in the tribofilm are apparent. It is also clear that the tribofilm is effective in protecting the surface even under a severe contact condition as indicated by the pronounced presence of the honing grooves. Figures VI.1.2b and VI.1.2c show the scanning electron microscopy (SEM) micrograph and the energy dispersive X-ray analysis (EDAX) spectra, respectively. The tribofilm is rich in S, P, Mg, and Ca, all of which are typical constituents of engine oil additives.

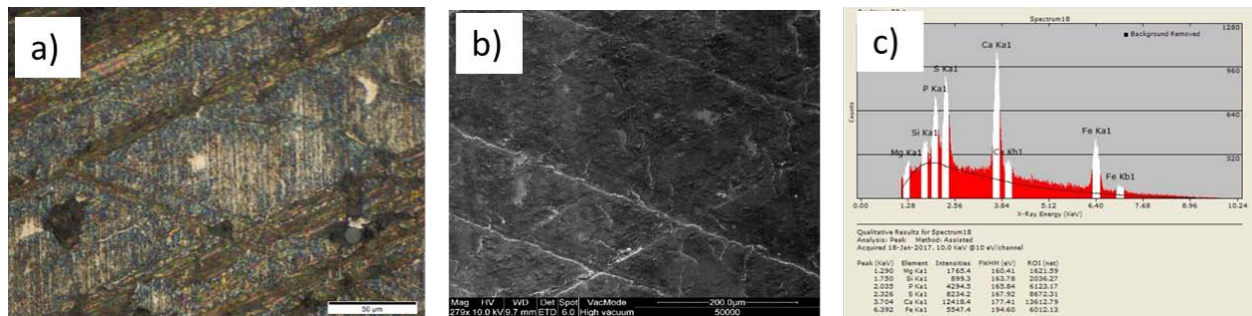


Figure VI.1.2 - Micrographs of surface of field-operated engine liner: (a) optical, (b) SEM, and (c) EDAX of tribofilm

Cross-sectional TEM analysis was conducted on several tribofilms from in-use engines. The TEM samples were prepared by the standard FIB technique. Because of the fragility of the tribofilm, special care was taken to protect the surface during sample preparation. This involves depositing a 10–50 nm gold layer on the sample, which coincidentally also acts as a marker during TEM analysis. Then, a 1 μm platinum layer was deposited in two stages. This layer was observed to be adequate in protecting the tribofilm from damage during FIB milling and thinning. The TEM analysis was conducted in a FEI Tecnai F20ST system. Several analyses were conducted, including bright field and dark field imaging, scanning transmission electron microscopy, electron energy loss spectroscopy, EDAX, and selected area electron diffraction. Figure VI.1.3a shows a TEM overview of a tribofilm from an engine. The thickness of the film is about 100–150 nm and appears to

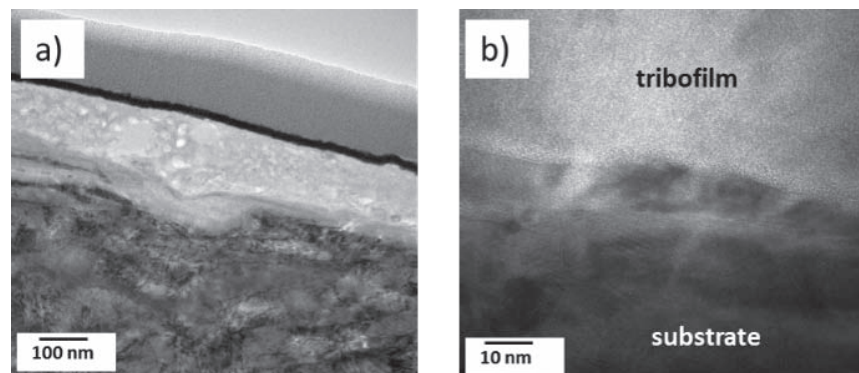


Figure VI.1.3 - TEM micrograph of tribofilm: (a) overview and (b) substrate-film interface

be non-homogeneous. The film is very well bonded to the substrate, as indicated by Figure VI.1.3b. At the nanoscale, the films consisted of nano-crystalline particles embedded in an amorphous phase. Based on our previous work, tribofilms with such a structure often exhibit relatively low friction and very good durability [1]. Hence, the film is able to protect the surface against wear and severe damage, in spite of extreme contact conditions in the TDC region.

Figure VI.1.4 shows elemental mapping on the various constituent elements in the tribofilm. The figure clearly illustrates the non-uniformity of the composition and distribution of the various elements. Again, this observation is consistent with what is known about the complex nature of tribofilms.

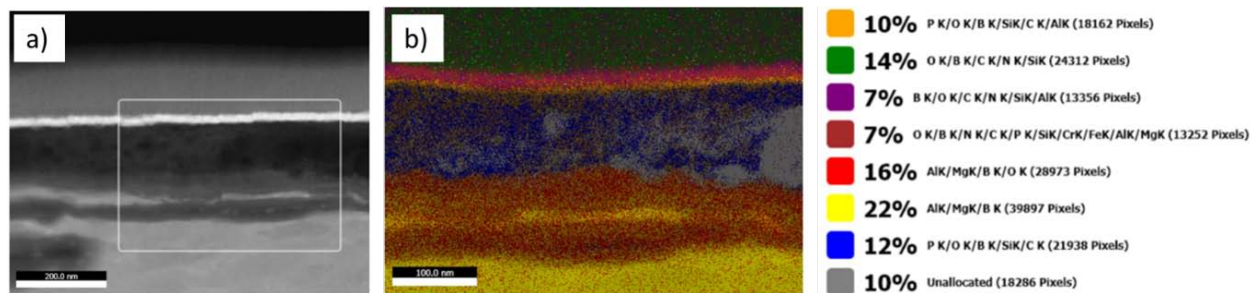


Figure VI.1.4 - Tribofilm micrographs: (a) scanning transmission electron microscopy and (b) EDAX elemental mapping

Failure Analysis

In-use samples of engine ring and liner hardware were obtained from many OEMs. These samples had different degrees of wear and surface damage, including scuffing. Some samples were from engine tests for either wear or scuffing; others were from engines that failed in the field due to a variety of reasons. Various wear and damage modes were identified at different locations on the liner surface. One prominent mode was polishing and fatigue wear. This particular wear mode involves total smoothing of the honing plateau, as shown in Figure VI.1.5a. In addition, wear by fatigue in the polished area is also evident by localized material removal in Figure VI.1.5a. This wear mode appears not to involve extensive plastic deformation either on the surface or sub-surface regions, as indicated by Figure VI.1.5b, which does not indicate much bending of the pearlite lamellae structure. Based on this observation, a linear elastic fatigue analysis is in progress in collaboration with Massachusetts Institute of Technology for the formulation of a predictive fatigue wear model.

The other prominent failure mechanism, especially in the TDC region, is scuffing. Analysis of various samples indicated that occurrence of scuffing is very well connected with the formation and removal of tribofilms. In all cases observed in the engine hardware, initiation of scuffing was preceded by the removal of the tribofilm (Figure VI.1.6a). Either independently or as a consequence, the removal of the tribofilm also coincided with severe plastic deformation of the near-surface material. Figure VI.1.6b shows the plastic strain pattern on a honing plateau of a cast iron liner surface after complete removal of the tribofilm by ethylene diamine tetraacetic acid washing. Sub-surface microstructural analysis of the scuffed area also showed a layer of about 5–10 μm of extensive plastic deformation (Figure VI.1.6c). Samples with severe scuffing clearly indicate severe plastic deformation shown by the bending near the surface of the pearlite lamellae. There is also indication of “crumbling” of the cementite phase (Fe_3C) in the pearlitic microstructure (Figure VI.1.6d). The broken cementite appears to be mechanically mixed with the ferrite to form a “metal-matrix composite” layer of about 25 μm thickness on the scuffed surface. Quantification of the near-surface strain field can be the basis for mechanistic model formulation for scuffing. If one assumes that scuffing in liner cast iron material occurs by adiabatic shear instability as was the case in steel material, it is possible to formulate a predictive scuffing model based on a critical shear strain for scuffing initiation.

Effect of Oil Ageing

Properties and tribological performance of fresh and used oils from a taxi after 5,000 miles, 8,000 miles, and 10,000 miles of operation were evaluated. Measurements showed that the viscosity of the engine was largely unchanged up to 8,000 miles. A noticeable and significant increase in viscosity was observed after

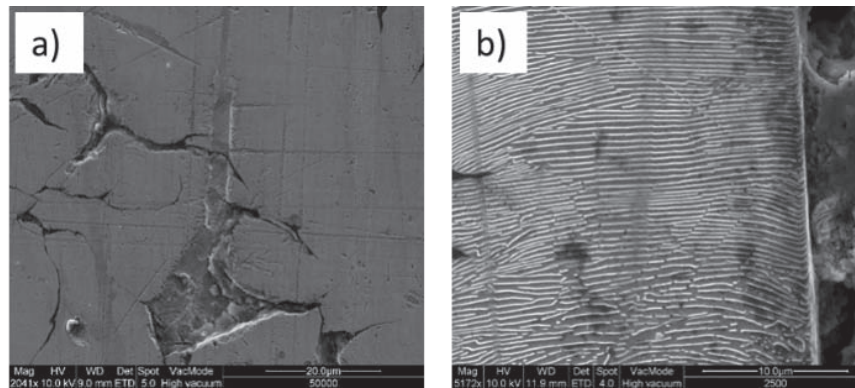


Figure VI.1.5 - SEM micrograph of (a) polishing and fatigue wear and (b) sub-surface structure

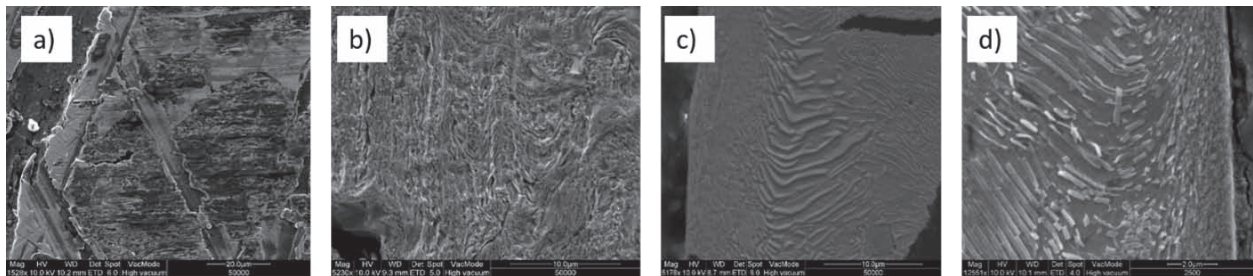


Figure VI.1.6 - SEM micrograph of (a) local tribofilm removal, (b) plastic strain pattern on the surface, (c) sub-surface plastic deformation below scuffed surface, and (d) sub-surface structure with severe scuffing damage

10,000 miles. Friction and wear tests were conducted with a reciprocating ball-on-flat contact configuration at 100°C, 2-Hz speed, 10-mm stroke length, and 1 GPa contact pressure for a duration of 1 h. The friction behavior was about the same for all the oils, whether fresh or aged. The average friction coefficient was about 0.11. Significantly more wear was observed in the tests conducted with the aged oil with the most wear occurring in tests with 8,000-mile used oil.

Conclusions

Test Methodologies

- Existing friction and wear test protocols were investigated to examine oil degradation and it was concluded that the cylinder-on-flat test protocol does not accurately assess wear and differentiate between fresh oils but can assess oils with high levels of contamination that have occurred due to oil degradation.
- The importance of oil starvation was demonstrated to better simulate the contact at TDC.

Characterization of Tribochemical Films

- Formation of the tribofilm is non-uniform along the stroke length of the engine liner. Extensive formation of the tribofilm is found in the TDC region but not the BDC region.
- The tribofilms have an amorphous and nano-crystalline phase mixture; hence, they are durable in protecting the ring and liner surfaces.

Failure Analysis

- Different wear modes were observed on the engine liner surface at different locations; fatigue, abrasive, and scuffing wear modes were present.
- Removal of the tribofilm is a necessary condition for scuffing initiation on the liner.

- Scuffing involved severe plastic deformation of near surface material; a shear instability mechanism may be a viable approach to predictive modeling.

Effect of Oil Ageing

- Oil viscosity increase was observed after 10,000 miles of engine operation; otherwise, minimal change occurred compared to fresh oil.
- Friction behaviors were similar for fresh and used (aged) oil up to 10,000 miles. Noticeably more wear was observed in tests with aged oil compared to fresh oil.

References

1. Ajayi, O.O., C. Lorenzo-Martin, R.A. Erck, N. Demas, and G.R. Fenske. "Boundary Layer Lubrication Mechanisms." FY 2011 Annual Progress Report, DOE-VTO (2011).
2. Demas, N.G., R.A. Erck, C. Lorenzo-Martin, O.O. Ajayi, and G.R. Fenske. "Experimental Evaluation of Oxide Nanoparticles as Friction and Wear Improvement Additives in Motor Oil." *Journal of Nanomaterials*, 8425782 (2017).
3. Petra, O., T. Müller, H.-J. Füber, and D. Bartel. "The Influence of Oil Supply and Cylinder Liner Temperature on Friction, Wear and Scuffing Behavior of Piston Ring Cylinder Liner Contacts – A New Model Test." *Tribology International*, 94, 306–314 (2016).

Key Fiscal Year 2017 Publications

1. Erck, R.A., N.G. Demas, and G.R. Fenske. "Enhanced Analysis of Benchtop Friction and Wear Measurements." STLE 72nd Annual Meeting, Atlanta, GA, May 21–25, 2017.
2. Demas, N.G., R.A. Erck, and G.R. Fenske. "A Novel Method for the Determination of Wear of Engine Cylinder Liner Parts." STLE 72nd Annual Meeting, Atlanta, GA, May 21–25, 2017.
3. Ajayi, O.O. and C. Lorenzo-Martin. "One More Step Closer to Better Understanding of Boundary Lubrication Mechanisms." Keynote Presentation at 21st International Conference on Wear of Materials, Long Beach, CA, March 26–30, 2017.
4. Ajayi, O.O. and C. Lorenzo-Martin. "Enhancement of Bronze Surface Properties by FSP and Second Particles Incorporation." Presented at 21st International Conference on Wear of Materials, Long Beach, CA, March 26–30, 2017.
5. Lorenzo-Martin, C., O.O. Ajayi, A. Erdemir, and R. Wei. "Tribological Performance of Quaternary CrSiCN Coatings under Dry and Lubricated Conditions." Presented at 21st International Conference on Wear of Materials, Long Beach, CA, March 26–30, 2017.
6. Ajayi, O.O., C. Lorenzo-Martin, and D. Singh. "Tribological Performance of Carbon-Ceramics Composite Materials." STLE Annual Meeting & Exhibition, Atlanta, GA, May 21–25, 2017.
7. Lorenzo-Martin, C., O.O. Ajayi, A. Erdemir, and G. Fenske. "Friction and Wear Performance of Low-Viscosity Synthetic Mixed Fluids." STLE Annual Meeting & Exhibition, Atlanta, GA, May 21–25, 2017.

VI.2 Compatibility of Lubricant Additives with Non-Ferrous Bearing Materials and Wear Mechanism in Sooted Engine Oils

Jun Qu, Principal Investigator

Oak Ridge National Laboratory
Materials Science & Technology Division
P.O. Box 2008
Oak Ridge, TN 37831-6063
E-mail: qujn@ornl.gov

Michael Weismiller, DOE Program Manager

U.S. Department of Energy
E-mail: Michael.Weismiller@ee.doe.gov

Start Date: October 1, 2016	End Date: September 30, 2017	
Total Project Cost: \$300,000	DOE share: \$300,000	Non-DOE share: \$0

Acknowledgments

Co-Authors

Chanaka Kumara, Weimin Li, Sladjian Lazarevic, Yan Zhou; Oak Ridge National Laboratory

Project Introduction

This project contains two major tasks of fundamental studies: (1) studying the compatibility of antiwear additives (AWs) and friction modifiers (FMs) with non-ferrous bearing materials and (2) investigating the wear mechanism in sooted engine oils.

Non-ferrous alloys are commonly used in connecting rod end journal bearings and bushings. However, current AWs and FMs in engine oils were designed for ferrous alloys and their compatibility with non-ferrous alloys is not well understood. This task investigates the compatibility of conventional zinc dialkyldithiophosphate (ZDDP) and Oak Ridge National Laboratory-developed ionic liquids (ILs) and organic- and Mo-based FMs with selected non-ferrous bearing materials under mixed and boundary lubrication. Fundamental understanding gained in this study will help guide future development of engine lubricants.

The soot contents in diesel and gasoline direct injection engine oils have repeatedly been reported with close correlation to the engine wear. Several wear mechanisms have been hypothesized in the literature [1], e.g., soot abrading tribofilms, soot absorbing onto AWs to deactivate their functionality, soot promoting oil degradation, soot competing with AW additives on adsorbing onto metal surfaces, soot transitioning Fe_3O_4 to more-wear-prone FeO, and soot accumulating at the contact inlet to restrict oil supply, but the actual mechanism is still being sought. In this task, a new mechanism is proposed based on carbon-catalyzed ZDDP tribocorrosion with experimental validation.

Objectives

- Investigate the wear protection functionality of conventional and new AWs (ZDDP and ILs) and friction reducing effectiveness of organic- and Mo-based FMs in lubricating non-ferrous bearing materials
- Understand the wear mechanisms in sooted engine oils by revealing the combined effects of soot and ZDDP

Approach

For the first task of studying the compatibility of AWs and FMs with non-ferrous bearing materials, a partnership was established with ExxonMobil, Lubrizol, and Cytec (recently acquired by Solvay) to obtain commercial and candidate additives. Our previous year's effort was focused on the functionality of AWs on

a steel–aluminum contact and results had been presented in the Fiscal Year (FY) 2016 annual report [2]. The compatibility of AWs and FMs on steel–bronze and steel–Teflon™ contacts was the emphasis in FY 2017. Stribeck scans were conducted to reveal the friction reducing capability and boundary lubrication tests were carried out to reveal their functionality in wear protection.

For the second task of investigating the wear mechanism in sooted engine oils, a partnership was established with Cummins and Lubrizol to learn field experience and receive carbon black (CB) particles (soot surrogate) and ZDDP for lab experiments. Boundary lubrication tests were conducted on base oils containing CB alone, ZDDP alone, and CB+ZDDP. Different ball and flat material pairs were used in an attempt to correlate the wear behavior with the alloy composition and mechanical properties.

Results

Key achievements in FY 2017 include:

- Both molybdenum dithiocarbamate (MoDTC) and organic friction modifier (OFM) worked well for the steel–bronze contact with up to 65% and 40% friction reduction in the mixed lubrication regime, respectively. For the steel–Teflon contact, the MoDTC had little effect while OFM reduced the friction moderately (10–20%) in mixed and boundary lubrication.
- ZDDP was found to substantially reduce the effectiveness of OFM on friction reducing in lubricating the steel–bronze contact. The influence of ILs on the OFM's performance depended on their ion chemistry; while three others had slightly negative impact, the phosphonium–phosphate IL exhibited an interesting synergy with the OFM providing up to 35% additional friction reduction.
- In boundary lubrication of a steel–bronze contact, ZDDP could not protect the bronze surface but made the wear performance worse. Phosphate and sulfonate ILs were incompatible with bronze. In contrast, the carboxylate IL worked well with the steel–bronze sliding with 50% friction reduction and 20% wear reduction. All the ZDDP+IL combinations performed poorly with significant wear increase.
- Blending 1 wt% CB into a poly- α -olefin (PAO) base oil significantly increased the wear volumes of both the ball and flat for an American Iron and Steel Institute (AISI) 52100 bearing steel ball sliding against an M2 tool steel flat. Adding 0.8 wt% ZDDP into the PAO+CB oil reduced the 52100 steel ball wear by >70% but surprisingly increased the M2 steel flat wear by >5 \times . The combined observations of significantly increased wear, smoother wear scar, and tribochemical reaction products with ZDDP on the worn surface indicate a rapid chemical–mechanical material removal process, hypothetically caused by CB-catalyzed tribocorrosion.
- By testing against a variety of flat materials, neither the literature-proposed hardness dependence nor the alloy composition seemed to be able to explain the wear behavior in PAO+CB+ZDDP. Instead, an interesting trend was observed. When ZDDP was introduced to the PAO+CB oil, the less wear-resistant steel was well protected, however the material removal rate of the more wear-resistant steel was much accelerated. The full mechanism behind remains to be understood.

Compatibility of AWs and FMs with Non-Ferrous Alloys

Commercial additives were provided by industrial partners, including two FMs, one MoDTC, and one OFM from ExxonMobil and a secondary ZDDP from Lubrizol. Five oil-soluble ILs, phosphonium–phosphate ($[P_{888}]$ [DEHP]), ammonium–phosphate ($[N_{888H}]$ [DEHP]), phosphonium–phosphinate ($[P_{6614}]$ [BTMPP]), phosphonium–carboxylate ($[P_{6614}]$ [C₁₇H₃₅COO]), and phosphonium–sulfonate ($[P_{6614}]$ [RO₃]), were synthesized at Oak Ridge National Laboratory as candidate AWs.

A variable load–speed journal bearing tester was used to generate Stribeck curves of a base oil (PAO 4 cSt) containing an FM at 0.8 wt% without or with an AW (ZDDP or IL) at various weight concentrations but contributing the same 800 ppm of phosphorus. Tests were carried out using an AISI 52100 steel cylinder (20-mm diameter) rotatory sliding against the inner wall of an SAE 660 bronze or Teflon sleeve bearing (25.4-mm inner diameter) with a contact length of 25.4 mm. All tests were carried out at room temperature. In

each variable load–speed journal bearing test, a 50 N normal force was applied and the sliding speed increased from 0.08 m/s to 1.2 m/s at an incremental rate of 0.005 m/s. There were 12 (or 18) continuous cycles for each setup with the first six (or nine) cycles lubricated with the neat PAO base oil to set the baseline and the second six (or nine) cycles lubricated by the oil containing an FM or an FM+AW combination (lubricant changed between Cycle 6 [or 9] and Cycle 7 [or 10] on the fly without stopping the machine). The final three Stribeck scans of PAO+MoDTC and PAO+OFM are compared in Figures VI.2.1a and VI.2.1b for steel-bronze and steel-Teflon contacts, respectively. Both FMs provided the significant friction reduction in the mixed lubrication regime for the steel-bronze contact and the MoDTC seemed to be more effective. For the steel-Teflon contact, the MoDTC had little effect while OFM slightly reduced the friction in mixed and boundary lubrication, much less effective compared with lubricating the steel-bronze contact.

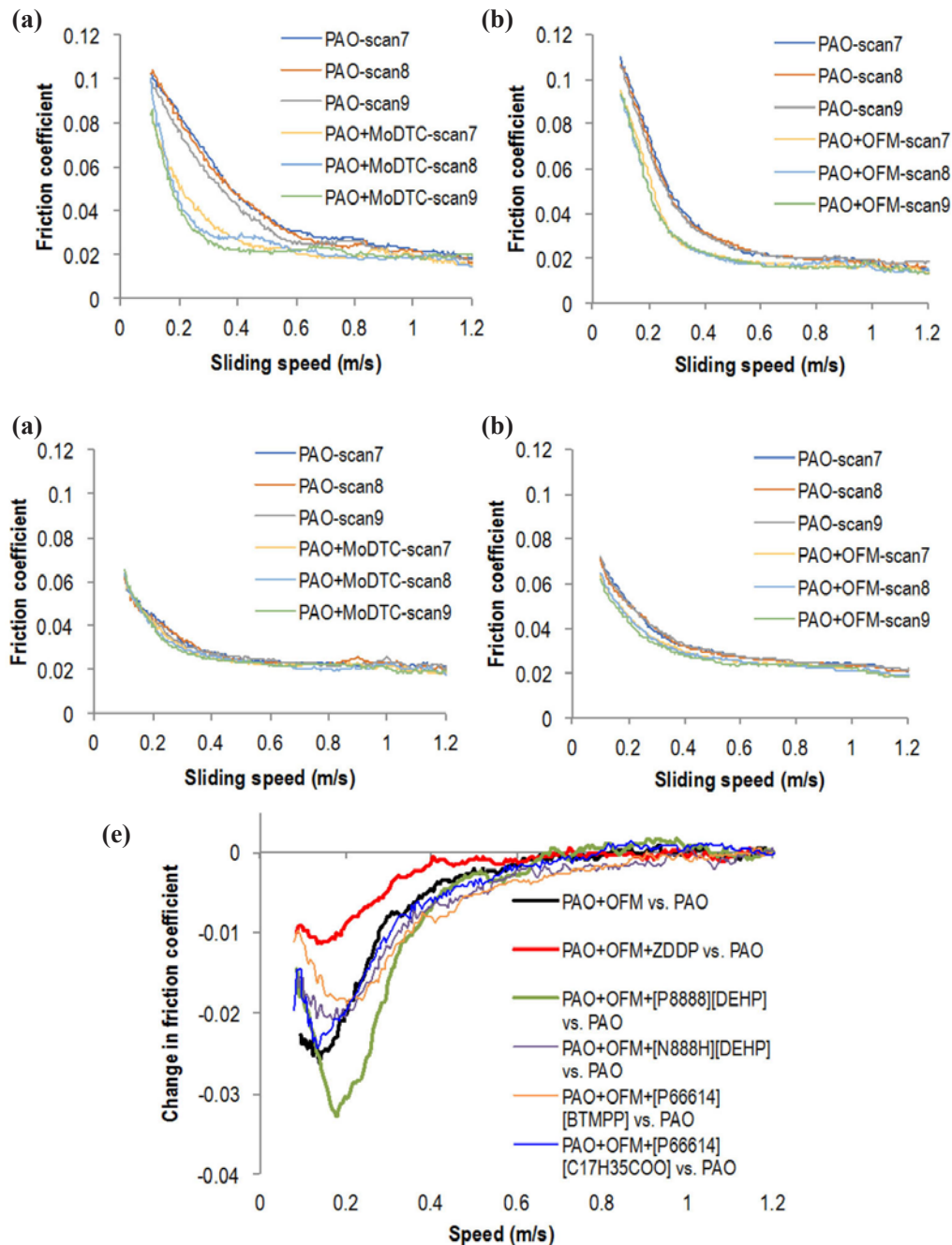


Figure VI.2.1 - Effect of MoDTC and OFM on friction for a steel–bronze and steel–Teflon contacts and impact of AWs on OFM for the steel–bronze contact

The second test matrix was to understand the impact of the secondary ZDDP and each IL of interest on the effectiveness of the OFM. The Stribeck curve of each oil containing an OFM+AW combination was compared with that of the PAO base oil and the differential is plotted in Figure VI.2.1c. Evidently, the addition of ZDDP made the OFM less effective in friction reduction and the ILs had mixed stories. Three out of four ILs also showed some conflict with the OFM in various extents but not as bad as the ZDDP. In contrast, the $[P_{8888}]$ [DEHP] exhibited an interesting synergistic effect when used together with the OFM, resulting in a further reduction in friction in the mixed lubrication regime. Since the OFM molecule is relatively stable, and chemical reactions between the OFM and ZDDP or IL is unlikely. Therefore, we hypothesize that the impact (positive or negative) of AW on OFM’s effectiveness is a result of the competition of surface adsorption between the OFM and AW molecules.

To understand the effectiveness of ZDDP and ILs on wear protection of bronze, boundary lubrication tests were conducted on a steel–bronze contact lubricated by a base oil (for SAE 0W-30 engine oil) containing a ZDDP, an IL, or a ZDDP+IL combination at the same P content of 800 ppm (GF5/6 limit). An AISI 52100 bearing steel ball (10-mm diameter) was used to rub against a SAE 660 bronze flat under a 20 N load at 100°C for 1,000 m. The friction and wear results of the bronze surface are compared in Figure VI.2.2. ZDDP slightly reduced the friction but made the bronze wear higher, which is exactly opposite to the higher friction and lower wear generally observed for steel–steel contacts. The phosphate IL, $[P_{8888}]$ [DEHP], performed similarly to ZDDP with slight friction reduction at the cost of increased wear. The sulfonate IL, $[P_{66614}][RSO_3]$, increased both friction and wear. In contrast, the carboxylate IL, $[P_{66614}][C_{17}H_{35}COO]$, reduced the friction reduction by

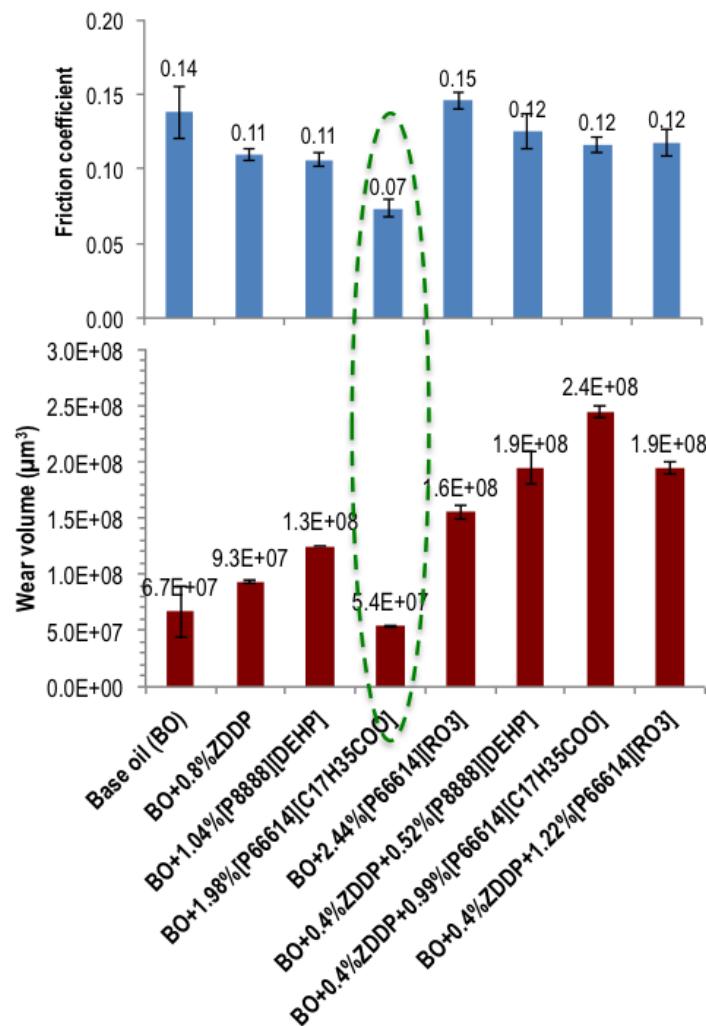


Figure VI.2.2 - Friction and wear results of a steel–bronze contact lubricated by base oils containing a ZDDP, an IL, or a ZDDP+IL combination

~50% and reduced the wear of bronze by ~20%. No correlation could be made between the friction behavior and worn surface roughness, indicating an easy-to-shear surface film by either physical adsorption or chemical reaction between the IL and the bronze surface. All ZDDP+IL combinations increased the wear of bronze and had little effect on the friction behavior. Surprisingly, the carboxylate IL, the best performer by itself, generated the highest wear when used together with ZDDP.

Wear Mechanism in Sooted Engine Oils

Boundary lubrication tests were conducted to investigate the tribological behavior of PAO 4 cSt base oils containing a carbon black (CB, R250R, as a soot surrogate), a secondary ZDDP, or both CB and ZDDP. The CB and ZDDP concentrations were 1.0 wt% and 0.8 wt%, respectively. A polyisobutylene (PIB) dispersant (1.0 wt%) was used to suspend the CB in the oil. For fair comparison, 1 wt% PIB was added to all test lubricants. Tests were carried out using an AISI 52100 steel ball (10-mm diameter) reciprocating sliding against an M2 tool steel flat at 150°C under 100 N for 1,000 m of sliding. While there was little impact for the CB and/or ZDDP on the friction behavior, their impact on wear was dramatic. The wear results are summarized in Figure VI.2.3. As expected, using the ZDDP alone effectively protected both the steel surfaces, and using the CB alone significantly increased the ball and flat wear volumes. It was noticed that the ball wear was significantly higher than the flat wear, with a ratio (52100 steel ball wear/M2 steel flat wear) around 5:1 in the neat PAO base oil, PAO+ZDDP, or PAO+CB. However, when both the ZDDP and CB were added to the base oil, the wear ratio between the ball and flat surprisingly flipped over from 5:1 to 1:4, a 20× change. Basically, adding ZDDP into the PAO+CB oil protected the 52100 steel ball with a wear reduction of >70%, but increased the M2 steel flat wear by >5×. To our best knowledge, no such an observation has been reported in the literature before. Tests were then conducted using the 52100 steel ball sliding against an A2 tool steel flat (different composition than M2 steel and less wear resistant) and similar wear behavior was observed. While the total ball and flat wear volumes were about the same when lubricated by PAO+CB and PAO+CB+ZDDP, the ball/flat wear ratio was reduced from more than 2:1 (CB alone) to less than 1:3 (CB+ZDDP).

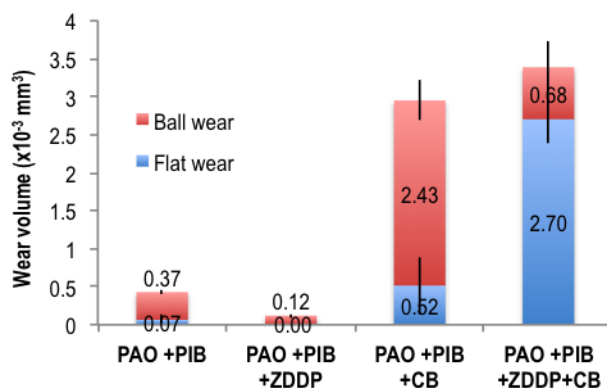


Figure VI.2.3 - While CB alone significantly increased the wear of both contact surfaces with little change in the wear ratio between the 52100 steel ball and M2 tool steel flat, CB+ZDDP together surprisingly flipped over the ball:flat wear ratio from 5:1 to 1:4

The M2 and A2 steel worn surfaces lubricated by PAO+CB and PAO+CB+ZDDP are shown in Figure VI.2.4. The wear scars generated in PAO+CB+ZDDP appeared much smoother compared with those produced in PAO+CB. In addition, the worn surfaces lubricated by the PAO+CB+ZDDP were revealed with significant amount of tribochemical reaction products with ZDDP based on surface chemical analysis (data not shown here). The combined observations of significantly increased wear, smoother wear scar, and tribochemical reaction products with ZDDP on the worn surface indicate a hypothetical chemical–mechanical polishing process (or tribocorrosion) on the M2 and A2 steel flats when both CB and ZDDP are present in the lubricant. The CB at the contact interface could act as a catalyst to trigger tribocorrosion between ZDDP and the M2 or A2 steel surface, in a similar manner to the diamond-like-carbon coating-catalyzed tribocorrosion [3]. However, why did such accelerated material removal not happen on the 52100 steel ball, whose wear rate actually was reduced instead? Results here could not be explained by the recent hardness hypothesis proposed by Spikes [4], because the 52100 bearing steel, M2 tool steel, and A2 tool steel have very similar hardness,

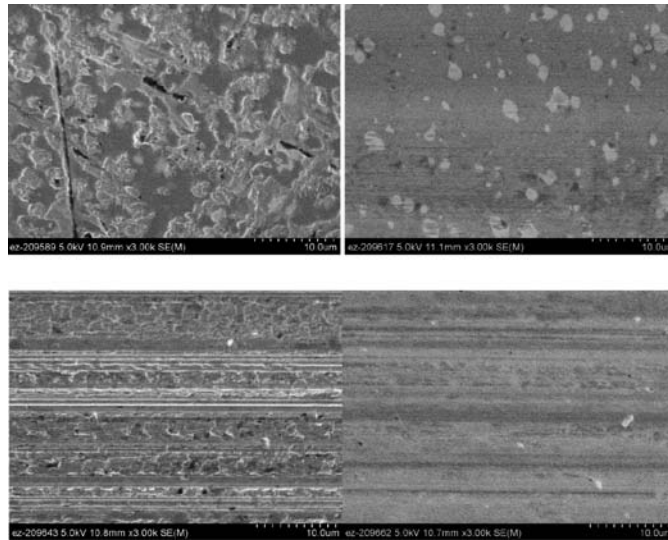


Figure VI.2.4 - The wear scars on the M2 (top) and A2 (bottom) flats lubricated by the PAO+CB+ZDDP (right) appeared much smoother compared with those lubricated by PAO+CB (left)

878, 876, and 821 HV, as measured by microindentation at 500 g-f. Two other possibilities were considered for the opposite wear behavior of the AISI 52100 steel ball and the M2 or A2 tool steel flat: (1) different contact modes due to geometries; the ball wear scar was always in contact during the test but any area on the flat wear scar was in intermediate contact and (2) different material compositions; as compared in Table VI.2.1, the element standing out is Mo, which accounts for 4.5–5.5% in the M2 steel and 0.9–1.4% in the A2 steel, but less than 0.1% in the 52100 steel. Mo seemed to be necessary for the hypothesized tribocorrosion.

Table VI.2.1 - Compositions of Ball and Flat Steels

	52100 steel	M2 tool steel	A2 tool steel
Fe	Balance	Balance	Balance
C	0.98–1.10	0.78–1.0	0.95–1.05
Mn	0.25–0.45	0.15–0.40	1.0
Si	0.15–0.30	0.20–0.45	0.5
Cr	1.30–1.60	3.75–4.5	4.75–13
Ni	0–0.25	0.30	0.3
Mo	0–0.10	4.50–5.50	0.90–1.4
V	-	1.75	-
Cu	0–0.30	0.20	0.25
W	-	5.50	-

To verify the suspected impact of the contact mode and/or material composition on the wear behavior, a variety of flat materials were tested against the 52100 steel ball with the wear results summarized in Table VI.2.2. When a 52100 steel flat (heat treated to similar hardness as the 52100 steel ball) was used, the flat wear was rather high in PAO+CB but minimal in PAO+CB+ZDDP, while the ball wear was similar in both oils. The ball/flat wear ratio increased from 1:10 to 30:1, an opposite trend compared with that for the two tool steel flats, which suggested that ball/flat wear ratio change had little to do with their different contact modes. In the test rubbing against a grey cast iron flat, the flat wear was similarly high in both PAO+CB and PAO+CB+ZDDP. The interesting observation was that the 52100 steel ball wear was one order magnitude higher when ZDDP was added to the PAO+CB oil, a totally opposite trend compared to the test rubbing against the M2 or A2 tool steel. The significant wear acceleration on the 52100 steel ball denied the necessity of Mo content for the hypothesized tribocorrosion.

Table VI.2.2 - Summary of Wear Results Tested in PAO+CB and PAO+CB+ZDDP

Ball material	Flat material	Lubricant	Wear volume (x10 ⁻³ mm ³)			
			Ball	Flat	Ball/Flat	Total
AISI 52100 steel	CL35 cast iron	PAO+CB	0.46±0.05	171±10	2.7E-03	171.5±10
		PAO+CB+ZDDP	6.05±2.55	187±26	3.2E-02	193±26
	AISI 52100 steel	PAO+CB	2.9±1.35	27.9±4.8	1.0E-01	30.8±5.0
		PAO+CB+ZDDP	3.2±0.50	NM*	3.2E+01	3.2±0.50
	A2 tool steel	PAO+CB	5.38±0.22	2.43±0.50	2.2E+00	7.81±0.54
		PAO+CB+ZDDP	1.68±0.07	5.84±0.06	2.9E-01	7.53±0.09
	M2 tool steel	PAO+CB	2.43±0.26	0.52±0.38	4.7E+00	2.95±0.46
		PAO+CB+ZDDP	0.68±0.35	2.70±0.31	2.5E-01	3.38±0.47
Silicon nitride	PAO+CB	113±46	NM*	1.1E+03	113±46	
	PAO+CB+ZDDP	14.7±6.1	NM*	1.5E+02	14.7±6.1	

NM* – not measurable, assumed $0.1 \times 10^{-3} \text{ mm}^3$ in the ball/flat wear ratio calculation

On the other hand, an interesting trend was observed among the material pairs tested so far. When ZDDP was introduced to the PAO+CB oil, the less wear-resistant steel was well protected (such as the 52100 steel balls that rubbed against the A2 steel, M2 steel, and silicon nitride flat), however the wear of the more wear-resistant steel was much accelerated (such as the 52100 steel ball that rubbed against the cast iron flat and the A2 and M2 steel flats that rubbed against the 52100 steel ball). When the ball and flat materials were the same 52100 steel, no wear acceleration occurred on either side. Such a trend did not seem applicable to non-steel materials: (1) the cast iron flat was so much softer than the CB particles, its wear rate was so high that the ZDDP could not provide meaningful protection; and (2) the silicon nitride flat was so much harder than the CB particles and was inert to ZDDP, it had no wear in either oil as expected. The full mechanism behind remains to be understood.

Conclusions

The effects of FMs, ZDDP, and ILs on the friction behavior of bronze and Teflon were investigated. Both MoDTC and OFM worked well for bronze but they did not work very well on Teflon. While ZDDP and some other ILs were found to reduce the effectiveness of OFM for bronze, the phosphonium–phosphate IL exhibited an interesting synergy with the OFM in friction reduction. The wear protection effectiveness of AWs on bronze was also studied. Phosphate (including ZDDP and ILs) and sulfonate compounds made the wear performance worse, but the carboxylate IL reduced both friction and wear for the steel–bronze sliding.

While the significantly increased wear rates by CB was expected, the selective wear protection and wear boosting by CB+ZDDP was quite surprising: CB-catalyzed tribocorrosion. Neither the literature-proposed hardness dependence nor the alloy composition seemed to be able to explain the wear behavior. Instead, an interesting trend was observed. When ZDDP was introduced to the PAO+CB oil, the less wear-resistant steel was well protected, however the material removal rate of the more wear-resistant steel was much accelerated. The full mechanism behind remains to be understood.

References

1. Olomolehin, Y., R. Kapadia, and H. Spikes, “Antagonistic Interaction of Antiwear Additives and Carbon Black.” *Tribology Letters* 37 (2009) 49.
2. Qu, J. and Y. Zhou. “Compatibility of anti-wear additives with non-ferrous engine bearing alloys.” DOE VTO FY 2016 Annual Progress Report.
3. Zhou, Y., D.N. Leonard, H.M. Meyer, H. Luo, and J. Qu. “Does the use of diamond-like carbon coating and organophosphate lubricant additive together causes excessive tribochemical material removal?” *Advanced Materials Interfaces* 2 (2015) 1500213.

4. Kontou, A., M. Southby, and H.A. Spikes, "Effect of steel hardness on soot wear." *Wear* 390-391 (2017) 236–245.

Key Fiscal Year 2017 Publications

1. Zhou, Y., J. Qu, "Ionic liquids as lubricant additives – a review." *ACS Applied Materials & Interfaces* 9 (2017) 3209–3222.
2. Zhou, Y., D.N. Leonard, W. Guo, J. Qu. "Understanding tribofilm formation mechanisms in ionic liquid lubrication." *Nature Scientific Reports* 7 (2017) 8426.
3. Guo, W., Y. Zhou, X. Sang, D.N. Leonard, J. Qu, and J.D. Poplawsky. "Atom probe tomography unveils growth mechanisms of wear-protective tribofilms formed by ZDDP, ionic liquid, and their combination." *ACS Applied Materials & Interfaces* 9 (2017) 23152–23163.
4. Zhou, Y., H. Luo, J. Qu. "Compatibility between ionic liquids-based lubricant additives and bronze and aluminum bearing alloys." *STLE 72th Annual Meeting*, Atlanta, GA, May 21–25, 2017.
5. Zhou, Y., J. Qu. "Investigation of the compatibility between anti-wear additives and non-ferrous bearing alloys." *2016 STLE Tribology Frontiers Conference*, Chicago, IL, November 13–15, 2016.

VI.3 Technology Innovation: Base Fluids, Additives, and Coatings

Lelia Cosimbescu, Principal Investigator

Pacific Northwest National Laboratory
902 Battelle Blvd., MSIN K2-44
Richland, WA 99352
E-mail: lelia.cosimbescu@pnnl.gov

Michael Weismiller, DOE Technology Manager

U.S. Department of Energy
E-mail: Michael.Weismiller@ee.doe.gov

Start Date: October 1, 2016 End Date: September 30, 2017
Total Project Cost: \$440,000 DOE share: \$440,000 Non-DOE share: \$0

Acknowledgments

Co-Authors

Abhijeet Bapat, Pacific Northwest National Laboratory
Ashlie Martini, University of California, Merced
Robert Erck, Nicholas Dema, Argonne National Laboratory

Project Introduction

This multi-lab project involving Argonne National Laboratory (ANL), Oak Ridge National Laboratory, Pacific Northwest National Laboratory (PNNL), and National Renewable Energy Laboratory was developed in response to the Fiscal Year 2017 Vehicle Technologies Office Lab Call addressing AOI 6A – Advanced Lubricants. The overall goal of the project is to improve fuel economy by up to 4% through reduction of parasitic friction losses, the use of low viscosity lubricants, advanced additives, and low-friction low-wear coatings. In addition to reducing parasitic friction losses, the lubrication system must maintain reliability and durability of traditional engine and driveline components for both new and legacy vehicles. Lubricant technologies, although often incremental, provide a relatively inexpensive and easy to implement strategy towards fuel economy.

In engines, one obvious approach to fuel economy is the use of lower viscosity oils. However, further reduction of oil viscosity presents many technical hurdles including vulnerability of engine components to premature failure and adverse effects on the long-term performance of the lubricant. Meeting the rather challenging and aggressive goal of a 4% increase in fuel economy will require innovative developments that are early technical readiness level or at the proof-of-concept stage, and likely require future development for optimization. PNNL will leverage its existing capabilities and demonstrated expertise in polymer chemistry and lubricant additives to design multifunctional viscosity index improvers (VIIs) that may provide additional benefits to viscosity profiles such as shear stability and friction and wear reduction.

Objectives

- Support DOE's mission in increasing fuel economy by increasing fuel efficiency of gasoline internal combustion engines
- Develop ionic liquid (IL)-containing polymers with a linear architecture as VIIs
- Quantify the coefficient of friction and wear of those polymers
- Design and develop low molecular weight functional polymers for increased shear stability and reduced wear and friction
- Develop a fundamental understanding of the effects of polymer polarity on the friction and wear performance of a base oil

Approach

Lubricant research was performed collaboratively at four national laboratories with industrial stakeholder input and feedback. Due to the complexity of the work proposed, the project was structured into specific focus areas, or thrusts. The work herein is focused on technology innovation, design, and synthesis – in development of advanced base fluids, additives, and materials/coatings that reduce parasitic friction losses, and specifically the design, synthesis and rheological/tribological characterization of multifunctional VIIs and base oils.

Base fluids constitute a major part of the formulation of finished lubricants, as they can themselves be designed or mixed to perform functions which are typically accomplished by additives. In addition, they are the “tuning knob” to adjust lubricants to lower viscosities, which are desirable for fuel economy benefits. Specific activities to PNNL are the development and evaluation of multifunctional base fluids (Task 1). These proposed materials possess chemical functionalities known to affect friction and wear as well as lipophilic moieties to impart oil solubility and chemical stability. Thus, they can be beneficial as additives to the existing base oils or can be used as stand-alone base fluids. The design of new and improved additives has been and will remain for a long time the major research focus in lubricants. The push for better performing, longer-lasting, more environmentally friendly additives continues to motivate new research. Additives become a particularly important component as base fluids become thinner and thinner to mitigate potential negative side effects such as pitting and wear.

Similar to the base oil strategy, the PNNL team will combine polymer moieties that are known to improve the viscosity index with various functionalities that are known to reduce friction and mechanical wear. The VIIs will be constructed with moieties such as N-containing ILs, carboxylates, and boronic esters, which are known to decrease friction and wear or form tribofilms under extreme conditions (Task 2).

The facilities and expertise associated with the team will enable holistic approaches to the development of lubrication concepts based on fundamental understanding of tribological mechanisms and the holistic design and synthesis of additives and base fluids. The material developed at PNNL will undergo tribological testing at national laboratories and university partners (ANL and University of California, Merced [UCM]). The PNNL principal investigator (Lelia Cosimbescu) has accomplished similar tasks on other DOE-funded lubricant projects and has extensive experience in molecular design and synthesis of small molecules and polymers for a variety of applications, while Abhijeet Bapat is a seasoned polymer chemist. PNNL has fully equipped synthetic and analytical laboratories to synthesize, characterize, and screen additives and lubricants. PNNL also has adequate rheological testing capabilities: Brookfield viscometer, resonance viscometer (Viscolite), and Rheometric Scientific SR-2000.

Results

Fiscal Year 2017 Key Accomplishments

- Prepared a series of low molecular weight polymers and evaluated their tribological properties
- Demonstrated their superior shear stability compared to conventional VIIs (shear loss 10× lower than benchmarks, in some cases)
- Achieved a multifunctional VII that displayed 2.5× lower wear versus standard VIIs while maintaining a high viscosity index
- Developed methodology to synthesize IL polymers
- Demonstrated the efficient synthesis of high viscosity index (VI) of IL-containing polymers via free radical polymerization

Task 1

The low molecular weight polyalkylmethacrylates (PAMAs) used in this study were originally designed to function as self-standing multifunctional base oils. However, even at low molecular weights, these compounds were too viscous to behave as self-standing base fluids when present as a neat solution and instead were diluted

in base stock solutions to function as multifunctional additives. A practical advantage of this approach is the simple, clean, and scalable synthetic pathway to obtain a product free of metals or sulfur. Homopolymers of dodecyl methacrylate, 2-ethylhexyl methacrylate, and their co-polymers with functional methacrylates (polar) were synthesized to investigate the effects of chemical composition on lubricant performance. The polymers were added to 4Yubase at a fixed concentration of 12.5% w/w and then characterized in terms of their viscosity–temperature behavior, shear stability, friction and wear. Table VI.3.1 captures composition and viscosity properties of these blends.

Table VI.3.1 - Kinematic Viscosities and VI Values for All Polymer Analogs and Benchmarks Studied

Sample	Composition	Concentration of polymer in 4Yubase	KV40 (cSt)	KV100 (cSt)	VI
4Yubase	100% 4Yubase		18.8	4.2	127
AW-1	PA ₁₂ MA-DMAEMA	12.5%	40.67	8.80	204
AW-2	PA ₁₂ MA-MEMA	12.5%	35.46	7.61	191
AW-3	PA ₁₂ MA	12.5%	40.83	9.52	228
AW-4	PEHMA	12.5%	45.06	8.98	185
AW-5	PA ₁₂ MA-EHMA-DMAEMA (low AIBN)	12.5%	55.53	12.00	219
AW-6	PA ₁₂ MA-EHMA-DMAEMA (high AIBN)	12.5%	40.06	8.5	196.8
B-1	PAMA	4.1%	55.42	12.0	274
B-2	PNNL polymer (fully formulated)	1.5%	55.5	12.0	219

KV40 – kinematic viscosity at 40°C; KV100 – kinematic viscosity at 100°C

The results in Table VI.3.1 verify that all the PAMA analogs can improve the VI of the base fluid. However, due to their low molecular weights, these compounds are added at higher concentrations (12.5% w/w) to achieve VIs equivalent to commonly used viscosity modifiers. Of the compounds explored in this work, samples AW-1, AW-3, and AW-5 have VIs above 200 and comparable to B-2.

An advantage of synthesized analogs is their potential superior shear stability, owing to their low molecular weight. In contrast, viscosity modifiers can suffer substantial shear losses in a short period of time, which makes their high VIs irrelevant. To probe for the stability of AW-1–AW-6 under shear, a CEC L45 test was performed for 20 h at 100°C against the two benchmarks, B-1 and B-2, and the data is reported in Table VI.3.2.

Table VI.3.2 - Shear Stability Data using the CEC L45 Test Method (20 h at 100 °C)

Sample	KV (cSt) before shear	KV (cSt) after shear	Viscosity Loss %
AW-1	8.906	7.640	14.1
AW-2	7.745	7.550	2.45
AW-3	10.58	8.929	15.6
AW-4	9.039	8.696	3.76
AW-5	10.88	8.854	18.6
AW-6	8.538	7.828	8.31
B-1	34.13	10.80	68.3
B-2	12.47	6.504	47.8

Overall, all candidates have far better shear stabilities than the conventional viscosity modifiers whether fully formulated or stand-alone in oil, with two candidates, AW-2 and AW-4, having an outstanding performance. After careful analysis of each analog, it was concluded that shear stability is primarily affected by molecular weight, but polarity and pendant chain length have a subtle negative effect as well.

The friction and wear properties of the different lubricant samples were evaluated at 100°C under a load of 40 N in the boundary lubrication regime (sliding time was 1 h). The coefficient of friction data for all compounds is not shown here in interest of space. However, it is worth mentioning that the results indicate that the polymers can reduce friction in boundary lubrication at least as well as traditional VIIs (i.e., Benchmarks 1 and 2). The wear, however, shows a distinct dependence on the ability of the polar co-monomer in the polymer to interact with the surface. The average (of four runs) wear volume of the polymer compounds ranges from $121\text{--}367 \times 10^3 \mu\text{m}^3$, which is lower than the average wear exhibited by benchmark B-1 ($132 \times 10^3 \mu\text{m}^3$) but higher than that of B-2 ($31 \times 10^3 \mu\text{m}^3$). These observations are expected since B-2 is a fully formulated oil additized with a zinc dialkyldithiophosphate antiwear package, while the other solutions contain base oil and polymer only, without an antiwear package. The results are shown in Figure VI.3.1.

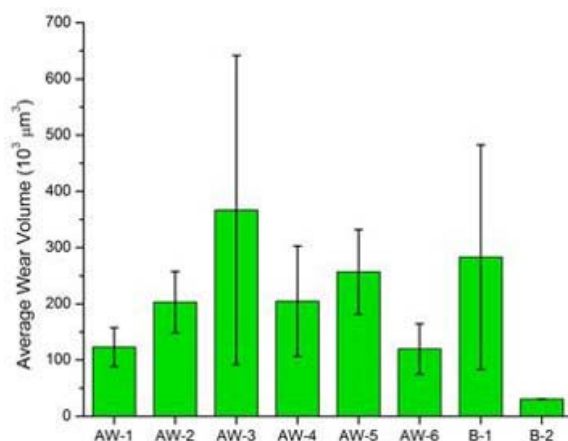


Figure VI.3.1 - Average wear volume for each sample where the error bars represent the standard deviation. Three runs were averaged (UCM).

The lowest wear among the polymer analogs is exhibited by AW-1, AW-2, AW-4, and AW-6. Of these, the first three are the most polar of the six analogs tested, which supports the hypothesis that polar polymers are more effective at reducing wear. However, AW-6, one of the more polar analogs tested, also exhibited lower wear. This may be explained by its relatively low molecular weight; the molecular weight of AW-6 is half that of the next smallest polymer. Therefore, these results indicate that low molecular weight and high polarity/propensity for surface interaction of the polymer may enable wear reduction.

Task 2

Polymers containing lipophilic and IL moieties have not been previously reported for any application. Due to their drastic difference in polarity, the copolymerization of long chain methacrylate with IL-containing monomers proved challenging. To probe the synthetic feasibility of such molecules, several IL monomers containing imidazolium or ammonium cations with selected counter-anions and capable of undergoing radical polymerization were prepared. The resulting polymers were expected to have VIs above 200 and provide friction and wear benefits. In this report, only the rheological data is presented. The polymers were dissolved in 4 cSt polyalphaolefin at a fixed concentration of 5 wt% and their viscosity–temperature behavior was evaluated, as shown in Table VI.3.3. Several synthesized compounds were not soluble in polyalphaolefin and are not reported here.

Table VI.3.3 - Kinematic Viscosities and VI Values for the IL Polymers

Sample	IL Copolymer Composition	KV40 (cSt)	KV100 (cSt)	VI
62405-58	10 mol.% styrenic imidazolium	23.27	5.59	194.3
62405-66	5 mol.% vinyl imidazolium	32.96	7.75	217.7
62405-71	5 mol.% long-chain MA imidazolium	31.9	7.39	209.7
62405-73	5 mol.% long-chain MA imidazolium	36.47	8.67	228
62405-75	10 mol.% short-chain ammonium	55.24	13.68	259
62405-77	5 mol.% long-chain ammonium	30.87	7.52	226.1
62405-79	5 mol.% long-chain ammonium	32.57	8.09	237.4
62405-81	5 mol.% vinyl imidazolium	27.61	6.85	224.2
62405-83	10 mol.% styrenic imidazolium	24.84	5.91	197.2
62405-85	10 mol.% short-chain ammonium	25.84	6.17	202.5

MA – methacrylate

Conclusions

- Low molecular weight copolymers can be easily prepared via free radical polymerization, process amenable to scale-up and commercialization.
- The loading of the polymer has to be substantially increased to achieve competitive VI values (12.5%), however the shear stability was improved by as much as 10× versus conventional VIIs.
- Surface interaction of the polymers via polar groups was observed indirectly through wear reduction; 2.5× lower wear versus standard VIIs was obtained with certain analogs.
- We developed a methodology for the preparation of IL polymers containing vinyl, styrenic, methacrylate type of monomers, and an ammonium or imidazolium cation.
- We demonstrated the efficient synthesis of high VI IL copolymers via free radical polymerization.

Key Fiscal Year 2017 Publications

1. Cosimbescu, L., B. Bhattacharya, R. Erck, S. Krueger, A. Martini, U.S. Ramasamy, J.W. Robinson, and B.J. Tarasevich. “High Efficiency Lubricant Oils and Additives Research.” Annual report 2016, PNNL-26104 (2016).
2. Cosimbescu, L., J.W. Robinson, J.T. Bays, and B.H. West. “Modified Thermoresponsive Hyperbranched Polymers for Improved Viscosity and Enhanced Lubricity of Engine Oils.” Annual report 2016, PNNL-26105 (2016).
3. Bhattacharya, P., U.S. Ramasamy, S. Krueger, J.W. Robinson, B.J. Tarasevich, A. Martini, and L. Cosimbescu. “Trends in Thermoresponsive Behavior of Lipophilic Polymers.” *Industrial & Engineering Chemistry Research*, 55(51), 12983–12990. 2016).
4. Cosimbescu, Lelia, et al. “Dual functional star polymers for lubricants.” *RSC Advances* 6.89 (2016): 86259–86268.
5. Robinson, J.W., Y. Zhou, J. Qu, J.T. Bays, and L. Cosimbescu. “Highly Branched Polyethylenes as Lubricant Viscosity and Friction Modifiers.” *Reactive and Functional Polymers* 109: 52–55, 10.1016/j.reactfunctpolym.2016.10.003 (2016).
6. Cosimbescu L., N.G. Demas, J.W. Robinson and R. Erck. “Friction and wear reducing properties of multifunctional small molecules.” Revised version submitted to *ACS Applied Materials & Interfaces*. 2017.

VI.4 High Efficiency Lubricant Oils, Additives, and Coatings

George R Fenske, Principal Investigator

Argonne National Laboratory
9700 S. Cass Ave.
Argonne, IL 60439
E-mail: gfenske@anl.gov

Michael Weismiller, DOE Technology Manager

U.S. Department of Energy
E-mail: Michael.Weismiller@ee.doe.gov

Start Date: October 1, 2016	End Date: September 30, 2019	
Total Project Cost: \$570,000	DOE share: \$520,000	Non-DOE share: \$50,000

Acknowledgments

Co-Authors

Oyelayo Ajayi, Ali Erdemir, Maria De La Cinta Lorenzo-Martin, and Osman Eryilmaz;
Argonne National Laboratory

Project Introduction

Reducing friction and wear-related losses in engines has a positive impact on improving fuel economy and durability. In particular, improving reliability of moving engine parts and driveline components under severe boundary conditions have lately become very important as vehicles are trending to greater use of low viscosity engine oils. The sections below describe three tasks to reduce parasitic friction losses while maintaining reliability.

- Develop hybrid low-viscosity base fluids as lubricants to reduce viscous shear losses
- Develop and test novel colloidal-based lubricant additives that reduce friction while ensuring reliability and durability
- Identify and develop non-ferrous coatings that incorporate catalytically active ingredients that form lubricious carbon-based boundary films from long-chain hydrocarbon molecules of lubricating oils

Objectives

Base Fluids

- Blend and quantify rheological, friction, and wear properties of binary and ternary ultra-low-viscosity hybrid base fluid from polyalphaolefin (PAO), synthetic hydrocarbon (SHC), and esters

Additives

- Synthesize colloidal friction modifier (FM), antiwear (AW), and extreme pressure (EP) functional additives with appropriate encapsulator, and quantify their friction and wear performance as blended into ultra-low-viscosity PAO base fluid

Coatings

- Develop and optimize catalytically active nanocomposite coatings (VNMe_x) to extract self-healing, durable, amorphous carbon boundary films from lubricating oils

Introduction

Base Fluids

Engine friction reduction and fuel economy improvement can be accomplished with the use of lower viscosity engine oil. The development of a synthetic, low-viscosity hybrid base fluid with optimized rheological properties can produce friction reduction in the hydrodynamic regime without compromising performance in the boundary regime.

Additives

Drop-in lubricant technology is the quickest way to achieve overall friction reduction and fuel economy improvement in legacy vehicles. The technology should be robust and flexible enough for future vehicles as well. Combining ultra-low-viscosity base fluids with advanced multifunctional tribological performance additives is a plausible approach.

Coatings

Reducing friction- and wear-related losses in engines improves both fuel economy and durability. In particular, improving the reliability of moving engine parts and driveline components under the severe boundary conditions of the low-viscosity engine oils has lately become very important. Accordingly, the aim of this task is to design and develop smart nano-composite coatings that can reduce parasitic friction losses (hence improve fuel efficiency) and reduce wear- and scuffing-related failures (hence, improve durability and reliability). During Fiscal Year 2017, this task resulted in a suite of novel catalyst coatings that can extract self-healing, highly durable, and low-friction carbon boundary films from lubricating oils. These nano-composite coating architectures incorporate metal catalysts that can convert long-chain hydrocarbon oil molecules into slick, durable, and scuff-resistant amorphous carbon boundary films.

Approach

Base Fluids

The development of hybrid base fluids was based on the principle of viscosity negative deviation in fluid mixtures to enable viscosity reduction of the composite fluid without compromising other rheological properties. Advanced hybrid/composite base fluids with improved rheological and tribological properties were based on binary and ternary mixtures of Group III–IV fluids. Various rheological properties and tribological performance attributes of the resulting hybrid fluids will be evaluated with and without model additives.

Additives

This task focused on the development of advanced lubricant additives that can deliver sustainable friction reduction for extended periods without sacrificing reliability and durability, especially in ultra-low-viscosity lubricants. The new additives were based on colloidal technology whereby physical and/or chemical mechanisms are used to engineer the surface boundary films with appropriate structure and properties. Comprehensive tribological performance and operating mechanisms of AW, FM, EP, and thermal control colloidal additives are being investigated.

Coatings

For the development of catalyst coatings, this task employed a production-scale magnetron sputtering system, and over several rounds of trials, the deposition conditions were optimized to yield truly nano-composite coatings with the right amount of catalyst metal, mechanical hardness, surface roughness, and chemical composition. Specifically, controlling and further optimizing the deposition parameters produced a series of composite coatings that consisted of Mo, V, Ni, and Cu very evenly distributed within the coating. These coatings were fully characterized by using surface and mechanical characterization tools for their surface smoothness, uniform thickness, hardness, and adhesion. Overall, most of the coatings produced were of high quality and suitable for tribological testing with the baseline oils supplied by industrial partners.

Results

Base Fluids

Several binary ultra-low-viscosity base fluids were formulated from PAO, different forms of esters, such as polyol ester (PoE) and diester, and advanced SHCs. For all the mixed fluids, comprehensive rheological performance measurements were conducted to determine kinematic, cold crank, and high-temperature high-shear viscosities, as well as traction under slide–roll contact. Friction and wear performance were also determined under unidirectional and reciprocating contact. Standard four-ball testing of lubricating capacity of the mixed fluids was also conducted. Results from the mixed-fluid tests were compared with those from single-fluid tests.

In general, the viscosity behavior shown in Figure VI.4.1 is typical for most of the mixed fluids and is consistent with the negative viscosity deviation principle. This translates to reduction in hydrodynamic frictional loss in fluid film lubrication. Such a consistent observation of the rheological properties for the mixed fluids suggests that they may be amenable to predictive modeling. Consequently, a database of measured viscosity for various binary fluids is being constructed and will eventually be used for empirical thermodynamic predictive modeling of the rheological properties of ultra-low-viscosity hybrid base fluids. Once developed and validated, such a model will be a very useful tool for base fluid technology development. The model could also have applications beyond lubricant development and formulation.

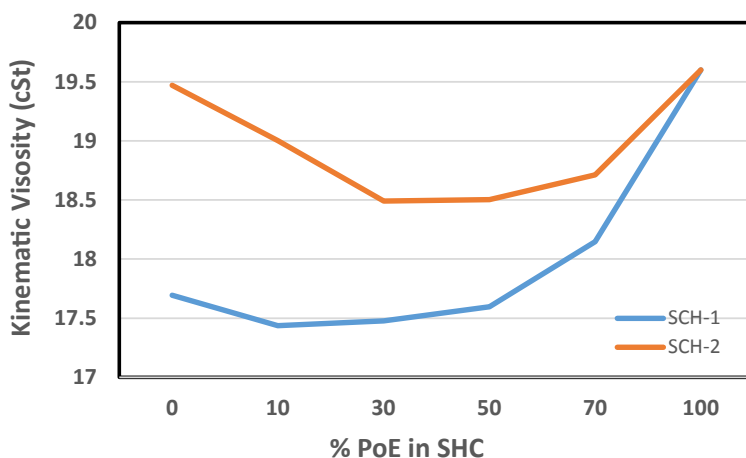


Figure VI.4.1 - Kinematic viscosity for binary ester–SHC composite fluids

In spite of the viscosity reduction in mixed fluids, friction was noticeably reduced for the vast majority of the mixed fluids. This was the case for the PAO–ester and SHC–ester mixtures. Figures VI.4.2a and VI.4.2b present the average friction coefficient during unidirectional and reciprocating sliding of a steel ball on a steel flat, respectively. The minimum friction occurred at 10–25% ester concentrations. Similar trends were observed for many other composite fluids. A much more dramatic difference occurred for wear performance. Wear was reduced by more than two orders of magnitude with some composite base fluids when compared to single-constituent fluid. Figures VI.4.2c and VI.4.2d show the wear on the flat steel surfaces from unidirectional and reciprocating sliding tests, respectively.

Under a more severe contact condition obtained in four-ball testing, all the mixed fluids reduced wear by 5–25 times compared to a single-constituent fluid, as shown in Figure VI.4.3. The superior tribological performance in terms of friction and especially wear of mixed base fluids suggests that such fluids are excellent candidates for formulation of ultra-low-viscosity engine oils. Furthermore, such fluids may require lower levels of tribological performance additives, especially zinc dialkyl dithiophosphate, whose use is being curtailed.

Additives

To assess the performance of the new colloidal additive systems in relation to state-of-the-art lubricants, friction and wear benchmarks were established with five commercially available advanced engine and gear

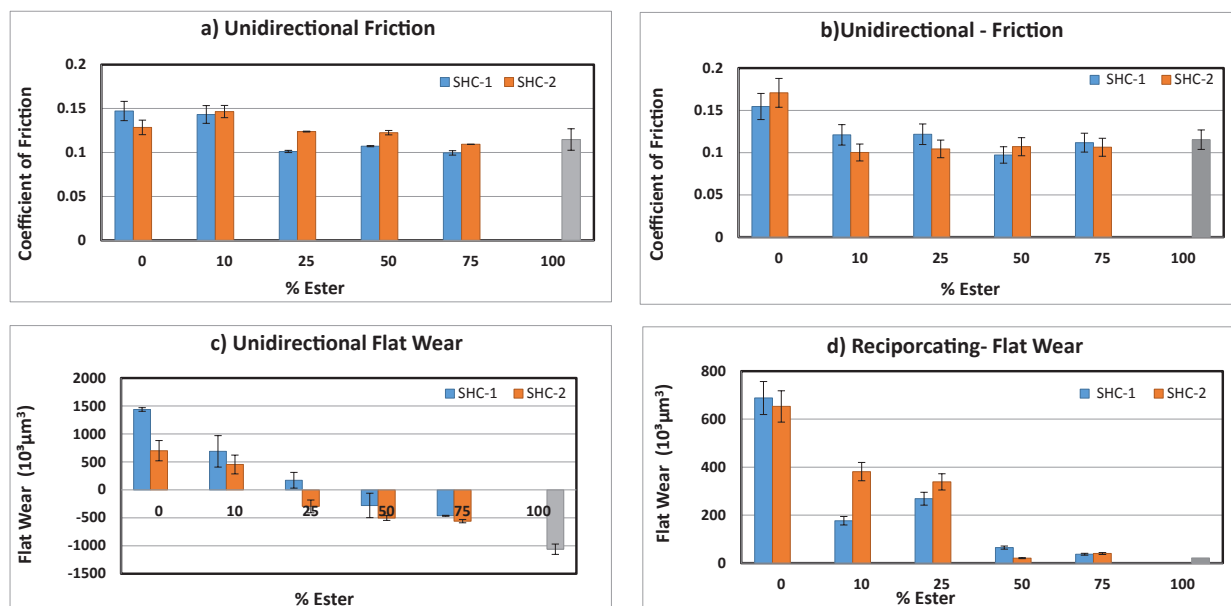


Figure VI.4.2 - Friction and wear measurement under unidirectional and reciprocating sliding

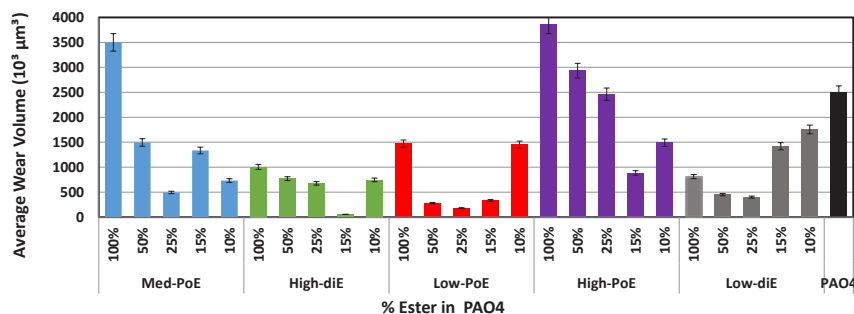


Figure VI.4.3 - Wear measurement under four-ball testing for binary ester-PAO4 composite fluids

oils under reciprocating and unidirectional sliding contact. Tests were also conducted with these oils using the standard ASTM protocol for four-ball wear testing. For these tests, FM, AW, EP, and thermal dissipator colloidal additives were formulated. The formulation process involved encapsulation of particulate systems with appropriate surfactant. The various additive systems were blended into an ultra-low-viscosity synthetic base fluid (PAO4). Kinematic, high-temperature high-shear, and cold crank viscosities indicated no noticeable change compared to the unformulated base fluid.

Several colloidal additives in ultra-low-viscosity base fluid produced friction and wear comparable to those for advanced benchmark lubricants in both unidirectional and reciprocating sliding, as well as in four-ball tests. Comparative analysis was conducted on the tribochemical films from a commercial lubricant and two colloidal additives. The nano-structure of the tribofilms formed from colloidal additives is similar to that produced from current chemical additives, as shown in Figure VI.4.4. These tribofilms consist of amorphous and nano-crystalline mixtures. They all display similar friction and wear behavior consistent with our previous observations that the nano-structure of the tribo-chemical surface film controls friction and wear under the boundary lubrication regime.

Glancing incidence X-ray diffraction and micro X-ray fluorescence analyses were also conducted on numerous tribofilms at the Advanced Photon Source to determine their structure. Results of these analyses indicated the prominence of Fe₃O₄ and ZnFe₂O₄ in surface-protected films from AW additives, although without friction reduction. Consequently, a colloidal additive system based on particles of these two oxide structures was

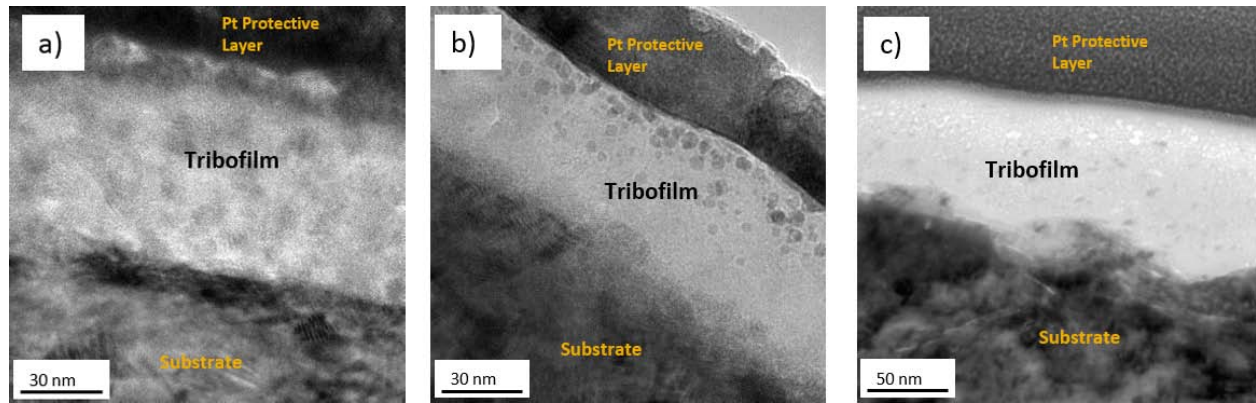


Figure VI.4.4 - Transmission electron micrographs from: (a) and (b) typical colloidal additives, and (c) typical fully formulated oil

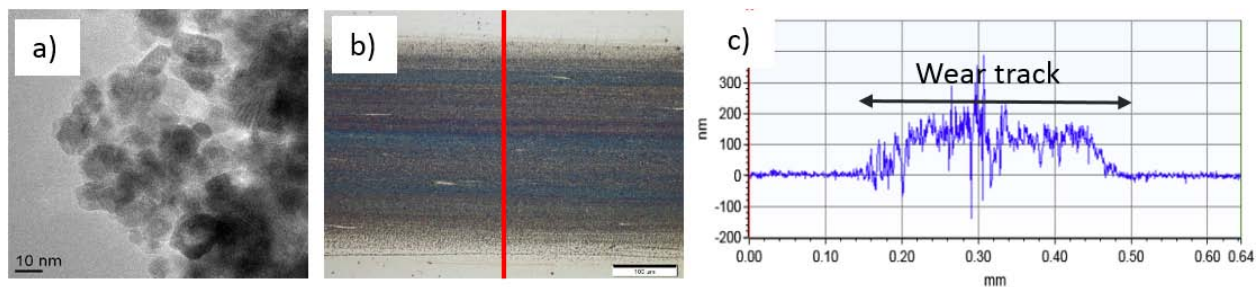


Figure VI.4.5 - (a) Transmission electron and (b) optical micrographs of ZnFe_2O_4 colloidal additives. (c) Profilometry of wear track of flat specimen tested with ZnFe_2O_4 colloidal additives.

formulated. The particles were encapsulated with oleic acid and blended with PAO4 base stock fluid. Figure VI.4.5a shows the results from transmission electron microscopy of ZnFe_2O_4 colloidal particulate components. Friction and wear tests were conducted with these new AW additives blended into ultra-low-viscosity PAO4 base stock. Under the boundary lubrication regime, the average friction coefficient was about 0.1, which is comparable to that of fully formulated lubricants under the same conditions. The impact of these new colloidal additives was much more dramatic on wear. Figure VI.4.5b shows an optical micrograph of the tribofilm formed from the ZnFe_2O_4 colloidal additive. The profilometry analysis in Figure VI.4.5c indicates the buildup of a 100–150 nm protective tribofilm on the surface.

Coatings

Analysis of the structure, chemical make-up, mechanical, and tribological properties indicates the following.

- The catalyst composite coatings has 5 wt% soft catalyst metal (such as Ni) in a hard catalyst (such as VN) matrix with very dense morphology without any columnar grains.
- The composite coatings containing 5% soft catalyst metal have hardness values ranging from 20–22 GPa, within the target of 20 GPa.
- The target adhesion value was an HF1 rating in the Rockwell C ball indentation adhesion test and the composite coatings consistently displayed adhesion values between HF1 and HF2 (more than adequate for tribological testing purposes).
- The nanocomposite coatings have friction coefficients of 0.1, even under severe boundary conditions of as high as 2.38 GPa contact pressures, and protected coated surfaces against wear. This finding confirms that these coatings may meet the durability targets of severely loaded contact interfaces of engines and driveline systems.

When tested in a used oil that was drained after 10,000 miles, the coating still protected surfaces against wear (see Figure VI.4.6) while maintaining noticeably lower friction than the uncoated test pairs. Overall, the nano-composite coatings developed during Fiscal Year 2017 reduced friction and wear losses under extreme conditions even with the use of heavily used engine oils containing all kinds of contaminants and soot. Therefore, they hold great promise for demanding engine applications in automotive and diesel engine fields.

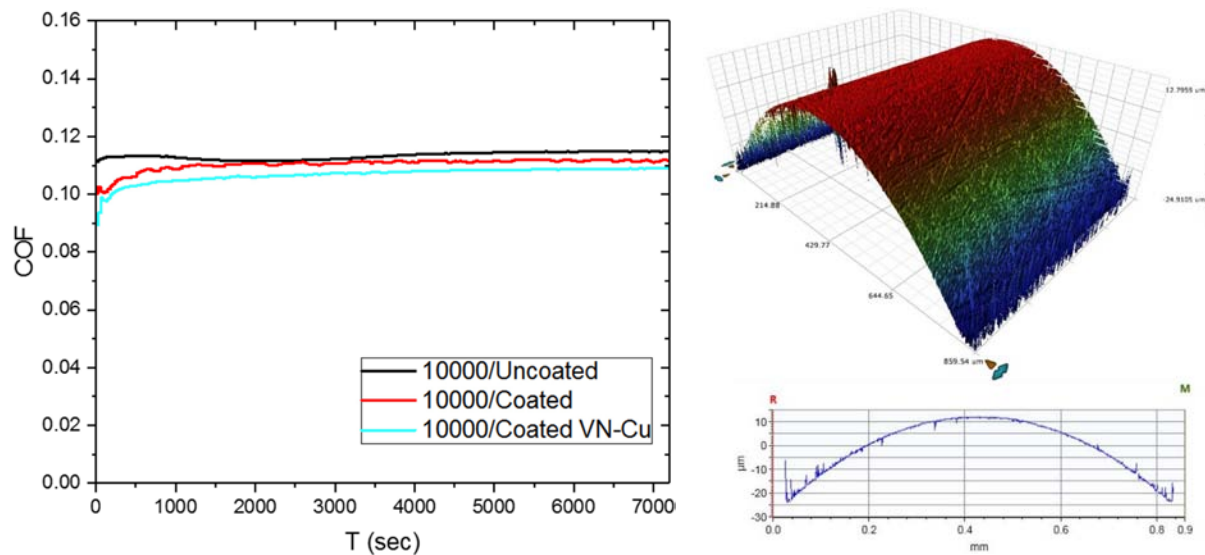


Figure VI.4.6 - (Left) Coefficient of friction (COF) and (right) wear of a VN-Cu coated steel pin against steel flat during tests in a used oil (taken after 10,000 miles). Uncoated steel has slightly higher friction, and the red friction trace is from the first generation coating. The cyan colored trace is from latest/optimized coating. Three-dimensional and line scan images confirm no wear on this coated surface despite heavily contaminated/used oil.

Conclusions

Base Fluids

- Composite fluids consisting of a binary mixture made of PAO, different esters, and advanced hydrocarbons showed a negative viscosity deviation, which may be amenable to empirical thermodynamic modeling.
- Comprehensive evaluation of tribological performance showed that mixed fluids exhibited noticeable friction reduction but very dramatic wear reduction compared to single-constituent fluids. This observation makes such fluids excellent candidates for ultra-low-viscosity lubricant formulation.

Additives

- Results during the reporting year clearly indicated the viability of colloidal based additives, especially for the ultra-low-viscosity lubricant formulation. Adequate friction and wear were achieved with different colloidal additive systems comparable to several state-of-the-art advanced lubricants.
- There is clear opportunity for further optimization and full formulation of lubricants with different functional (AW, FM) colloidal systems similar to the dispersant colloidal additives currently used in diesel engine oil.

Coatings

- Designed and developed nano-composite coatings with optimal thickness, hardness, surface roughness, and tribological properties
- Demonstrated their durability under severe boundary-lubricated sliding conditions

Key Fiscal Year 2017 Publications

1. Lorenzo-Martin, C., O.O. Ajayi, A. Erdemir, and G. Fenske. "Friction and wear performance of low-viscosity synthetic mixed fluids." STLE Annual Meeting & Exhibition, Atlanta, GA, May 21–25 2017.
2. Lorenzo-Martin, C. and O.O. Ajayi. "Determination of rheological properties of composite base fluid for lubricants." Tribology Frontiers Conference (TFC-2016), Chicago, IL, November 13–15, 2016.
3. Demas, N.G., R.A. Erck, C. Lorenzo-Martin, O.O. Ajayi, and G.R. Fenske. "Experimental evaluation of oxide nanoparticles as friction and wear improvement additives in motor oil." *Journal of Nanomaterials*, Article ID 8425782, DOI: 10.1155/2017/8425782 (2017).
4. Erdemir, A. "Hard, slick and ready to roll." *The SAE Automotive Engineering Journal*, February 13, 2017.
5. Lorenzo-Martin, C., O. Ajayi, A. Erdemir, and R. Wei. "Tribological performance of quaternary CrSiCN coatings under dry and lubricated conditions." *Wear*, 376–377: 1682–1690 (2017).
6. Erdemir, A., O.L. Eryilmaz, and G. Ramirez. "Advances in tribological coatings for more efficient and green transportation technologies." 6th World Tribology Congress, Beijing, China, September 17–22, 2017.
7. Ramirez, G., O.L. Eryilmaz, B. Narayanan, Yifeng Liao, Ganesh Kamath, Subramanian K.R.S. Sankaranarayanan, and A. Erdemir. "Investigation of the tribocatalysis mechanisms involved in the extraction of amorphous carbon boundary films from base oils." 44th International Conference on Metallurgical Coating and Thin Films, San Diego, CA, April 24–28, 2017.
8. Ramirez, G., O.L. Eryilmaz, B. Narayanan, Yifeng Liao, Ganesh Kamath, Subramanian K.R.S. Sankaranarayanan, and A. Erdemir. "In-depth studies of the in-operando formation of amorphous carbon tribofilms at lubricated interfaces." 72nd Society of Tribologists and Lubrication Engineers Annual Meeting and Exhibition (STLE), Atlanta, GA, May 21–25, 2017.
9. Erdemir, A. and O. Eryilmaz. "Extracting diamondlike carbon tribofilms from lubricating oils by catalytically active composite coatings." 6th European Conference on Tribology, Ljubljana, Slovenia. June 7–9, 2017.

VI.5 Lubricant Effects on PM Formation, Emissions Control, and Vehicle Fuel Economy

John M.E. Storey, Principal Investigator

Oak Ridge National Laboratory
1 Bethel Valley Rd., MS 6472
Oak Ridge, TN 37831-6472
E-mail: storeyjm@ornl.gov

Michael Weismiller, DOE Technology Manager

U.S. Department of Energy
E-mail: Michael.Weismiller@ee.doe.gov

Start Date: October 1, 2016 End Date: September 30, 2017
Total Project Cost: \$1,000,000 DOE share: \$1,000,000 Non-DOE share: \$0

Acknowledgments

Co-Authors

Melanie M. DeBusk, Shean Huff, Samuel A. Lewis, John Thomas, Todd Toops, Brian West;
Oak Ridge National Laboratory

Project Introduction

Approaches to improve fuel economy and reduce emissions by reducing parasitic friction losses often present unique challenges to the design and formulation of lubricants. In addition to reducing parasitic friction losses, the lubrication system must maintain reliability and durability of traditional engine and driveline components, as well as impacting the emissions and the emissions control system of the vehicle minimally. New lubrication approaches and formulations, particularly those that are backwards-compatible, can improve fuel economy across the existing fleet, so even small improvements in fuel economy can result in a big reduction in domestic fuel consumption.

As part of a multi-laboratory effort to address lubricant and additive development, Oak Ridge National Laboratory (ORNL) focused on engine and vehicle validation of new lubricant concepts. As lubricants and engines evolve to meet new fuel economy requirements, the contributions of lubricant to the particulate matter (PM) production from gasoline direct injection (GDI) engines was studied. The impact of new fuel-saving additive technologies on emissions control systems was also examined in order to understand any potential issues. Finally, a protocol was developed to link industry standard lubricant fuel savings evaluations to actual vehicle fuel economy changes.

Objectives

- By 2020, identify and validate lubricant technologies that further a 4% fuel economy goal by:
 - Reducing parasitic asperity and hydrodynamic friction losses by 25%.
 - Enabling reliable functionality of transformational technologies that improve engine thermal efficiency, including advanced Co-Optima fuels.
- By 2020, validate projected vehicle fuel economy benefits of promising lubricant concepts using experimental engine and vehicle dynamometer test data.

Approach

This project encompassed three tasks to evaluate and validate lubricant effects on emissions and fuel economy. The first task evaluated lubricant effects on PM emissions from a GDI engine during cold-start. PM emissions during cold-start can be up to ten times higher for a GDI engine [1]. In the previous year, a start-cart was constructed to enable multiple starts of an engine. The engine on the cart is a 2.0-L turbocharged GDI engine

and forced cooling was implemented to enable repeated cold-starts without a 12-h soak. Using forced-cooling, the apparatus was used to look at the impact of lube viscosity on PM production during cold-start.

The second task utilized a novel approach to aging automotive catalytic converters. It is well known that phosphorus, sulfur, and halogen elements are harmful to automotive emission catalysts. Lubricant additives, especially the most common antiwear additive, zinc dialkyldithiophosphate (ZDDP), are major sources of these elements in the exhaust. ORNL has successfully developed accelerated aging and poisoning techniques using durable engine platforms for exposing catalysts to oil additives under realistic gasoline or diesel combustion conditions. Accelerated aging and poisoning protocols allow a more detailed understanding of the mechanisms and rates of deterioration. For these experiments, lubricant equivalent to a “high-normal” consumer [2] was mixed with the fuel and the engine operated for the equivalent of 150,000 miles. Results are compared to actual field-aged catalysts.

The third task utilized vehicle experiments in ORNL’s chassis dynamometer laboratory to identify real-world improvements in fuel economy afforded by new lubricants. A lubricant is considered “fuel saving” if it results in a 2% reduction in fuel usage during an industry standard ASTM sequence test of six engine operating points. ORNL compared lubricants over city, highway, and steady-state driving cycles. For these experiments, each transient driving test is conducted five times, and the steady-state test is conducted 10 times. Fuel economy improvement is calculated based on the resultant fuel economy (mpg) of the new lubricant compared to the ASTM base lubricant.

Results

- Demonstrated lubricant contribution to PM during cold-start was greatest for low viscosity lubricants which enable higher fuel economy
- Identified 40% reduction in key catalyst sensitivity due to accelerated aging
- Demonstrated up to 5% fuel economy improvement for low viscosity lubricants

For the PM emissions research, the GDI engine operated on Environmental Protection Agency Tier III certification fuel (E10 cert). Three different lubes were studied each from the same manufacture but with different viscosities (0W-20, 10W-30, 20W-50). Since each cold-start is only 90 s long, PM from eight cold-starts were collected on a single set of filters and three sets of filters were collected for each lube. Quartz filters were used to measure the elemental carbon (EC) vs. organic carbon (OC) distribution of the carbon fraction of the PM [3]. Figure VI.5.1 shows that EC is relatively constant for the three lubricants, but the OC decreases with the highest viscosity lubricant, 20W-50. Lower viscosity lubricants are favored for fuel economy gains, but may contribute to higher PM emissions during cold-start.

Filters were also analyzed by thermal desorption/pyrolysis gas chromatography mass spectroscopy. Although not identical to the OC fraction measured by the NIOSH method and shown in Figure VI.5.1, the HC fraction resulting from the thermal desorption represents a similar, thermally labile HC fraction of the PM. The speciation of this fraction in Figure VI.5.2 thus represents the composition of the OC. Figure VI.5.2 shows that the 0W-20 has more of a lighter fraction (oil basestock components) that comes off between 29 min and 32 min compared to the 10W-30 and 20W-50. In contrast, higher desorption temperatures are required to observe the base stock components for the higher viscosity lubricants.

To understand lubricant effects on emissions controls, rapid aging of three-way catalysts (TWCs) was performed with three additives and compared to catalysts which had not been aged or were aged with no lubricant additives, as well as a TWC from a vehicle at full useful life of 117,000 miles. All of the catalysts removed the criteria pollutants, NO_x , HC, and CO, adequately, so the more sensitive water-gas shift (WGS) reaction was used to identify performance degradation. In this reaction, CO and H_2O react to form H_2 and CO_2 ; WGS activity can indicate abundance of active sites which can be lost over time due to sintering of precious metals like Pd. Figure VI.5.3 illustrates the relationship between WGS activity and temperature for the different samples. Prior to the WGS analysis all of the aged catalysts were de-sulfated in the same way. Figure VI.5.3 shows that the three catalysts exposed to engine exhaust aging with additives lost about 30% of their

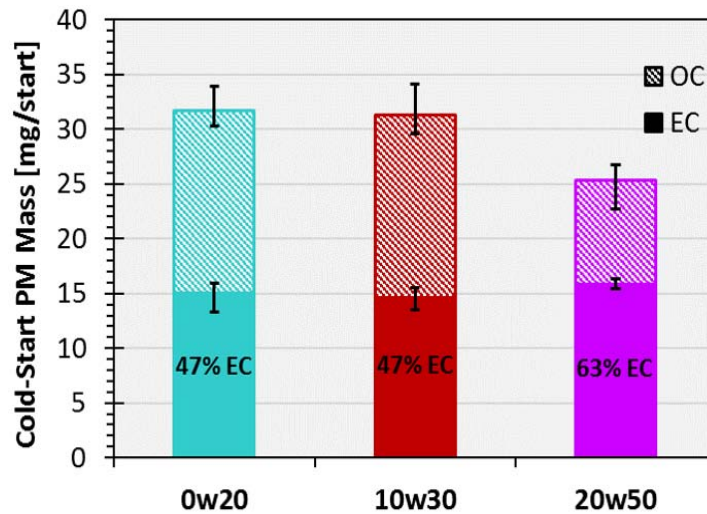
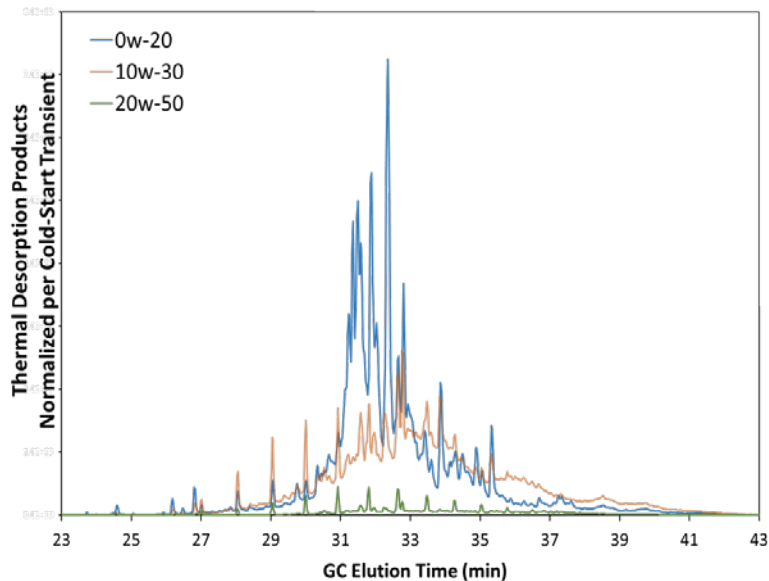


Figure VI.5.1 - Relationship between PM organic and elemental carbon (OC, EC) for the three lubricants evaluated. Points are averages of three filter samples and error bars span the max and min values for each lubricant.

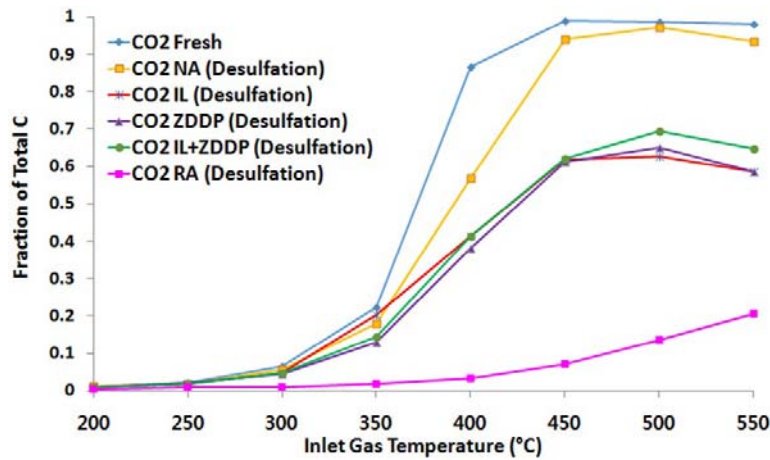


GC – gas chromatograph

Figure VI.5.2 - Chromatogram of the thermal desorption step for PM collected under cold-start conditions from a GDI engine with three different viscosity lubricants. The mass spectroscopy signal has been normalized to the mass of the PM per cold-start. The lightest weight oil, 0W-20, has the highest quantity of compounds and the heaviest oil, 20W-50, has the least amount removed by the thermal desorption step.

activity, but the catalyst that was aged on a vehicle lost about 90% of its WGS activity. Most importantly this approach illustrates that the novel lubricant additive component with ionic liquid (IL) does not deactivate TWC functionality more so than the industry standard, ZDDP. We are currently in the midst of evaluating a borated-based lubricant additive using this approach.

Fuel economy improvement for four different vehicles with 5W-30 engine oil is shown in Figure VI.5.4 for each phase of the urban driving cycle known as the Federal Test Procedure, the Highway Fuel Economy Test (HFET), and the nine steady-state cruise speeds. The most significant fuel economy improvement for any test lube is for Bag 1 of the Federal Test Procedure. This portion of the test is comprised of the first 505 s of the Federal Test Procedure. The test begins at room temperature, thus the relatively cold lubricant has higher



NA – no additive; RA – road-aged

Figure VI.5.3 - Formation of CO₂ in WGS reaction between 200°C and 550°C for TWCs aged with different lubricant additives

viscosity and thus the 5W-30 test lubricant provides the greatest fuel economy improvement as compared to the 20W-30 ASTM base lube, on the order of 3–5%.

Bag 2 of the urban cycle is on a relatively warm engine and the drive cycle for Bag 3 is identical to Bag 1 except it is run after a 10 min rest period; the engine and oil are still quite warm for the Bag 3 test. For the warm Bag 2 and Bag 3 results the average benefit drops to less than 2–3%. The HFET is a light-load test conducted on a warm engine. Fuel economy improvement on the HFET ranges from 1–2%.

The steady-state driving results range from 1–2% with the greatest improvement at the lower speeds. Similar to the HFET, the steady-state tests are conducted on a warm engine. It is interesting to note the difference between the base lubricant and the test lubricant is largest at the low speeds. The required engine power increases dramatically with increasing wheel speed. Because engine friction is a larger fraction of the total power at the slower speeds, the fuel economy difference for a lower viscosity oil is more apparent at the lower speeds.

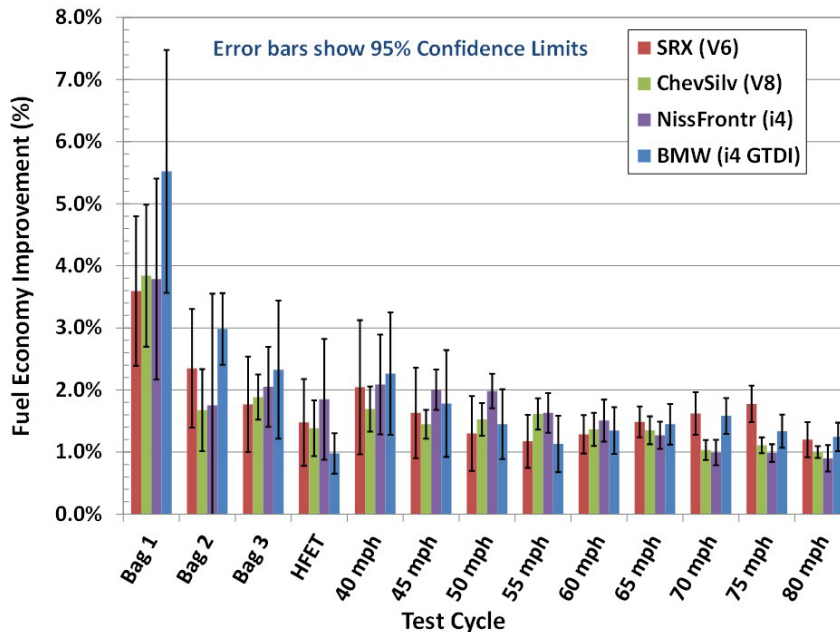


Figure VI.5.4 - Fuel economy improvement by test cycle for four vehicles with 5W-30 test lube compared to ASTM base lube

It is noteworthy that results across the various cycles for these four vehicles are fairly consistent, despite all having different engine architectures, representing a high-feature dual overhead cam V6, a pushrod V8, an inline four-cylinder, and a late model gasoline turbocharged direct-injection (GTDI) four-cylinder.

Conclusions

ORNL has been developing methods for evaluating lubricant and lubricant additive effects on emissions, emissions control devices, and real-world fuel economy. These methods are important for understanding how new materials and chemistries will perform in actual vehicle applications. PM emissions are affected by base lubricant chemistry resulting in higher PM mass emissions at cold-start. Accelerated aging technique indicates novel additives evaluated to date do not impact TWC functionality more so than the industry standard being employed. ORNL has also developed a vehicle-based method for measuring fuel economy improvement when comparing a test lubricant to the ASTM base lubricant. Statistically significant fuel economy improvements of 1–4% have been measured for various drive cycles.

References

1. Storey, J.M.E., S.A. Lewis, J.P. Szybist, J.F. Thomas, T.L. Barone, M.A. Eibl, and B. Kaul. “Novel Characterization of GDI Engine Exhaust for Gasoline and Mid-Level Gasoline-Alcohol Blends.” *SAE Int. J. Fuels Lubr.*, vol. 7, pp. 1–8, 2014.
2. West, B.H., and C.S. Sluder. “Lubricating Oil Consumption on the Standard Road Cycle.” SAE Technical Paper 2013-01-0884. doi: 10.4271/2013-01-0884.
3. NIOSH Method 5040. “Elemental Carbon (Diesel Particulate).” NIOSH Manual of Analytical Methods (NMAM), 4th Edition. 1994.

Key Fiscal Year 2017 Publications

1. DeBusk, Melanie, John Storey, Sam Lewis, Shean Huff, John Thomas, and Eric Nafziger. “Fuel and Lubricant Impacts on GDI Cold-Start Particulate Matter.” presented at 2017 CLEERS Workshop, Ann Arbor, MI, October 2017.
2. Dae-Kun Kim, D. William Brookshear, Ke Nguyen, Jun Qu, Todd J. Toops. “Impact of lubricant oil additives on the performance of Pd-based three-way catalysts.” 25th North American Catalysis Society Meeting, Denver, CO, June 4–9, 2017.
3. Storey, John, M. Moses-DeBusk, E. Nafziger, S. Lewis, S. Huff, T. Toops, J. Pihl, W. Brookshear, D. Splitter, G. Jatana, J. Thomas, B. West, and B. Zigler. “Lubricant Effects on Combustion and Emissions Control.” DOE Annual Merit Review, June 2017, available at https://energy.gov/sites/prod/files/2017/06/f34/ft049_storey_2017_o.pdf
4. Kim, D., K. Nguyen, D.W. Brookshear, T. J. Toops, and J. Qu. “Comparison of the impact of ionic liquid and ZDDP anti-wear lubricant additives on the reactivity of three-way catalysts.” SAE World Congress, April 4, 2017.
5. Storey, John, Todd Toops, Melanie DeBusk, Sam Lewis, D.W. Brookshear, Eric Nafziger, D-K Kim, and K. Nguyen. “Lubricant Effects on Emissions and Emissions Control Devices.” DOE Annual Progress Report, available at https://energy.gov/sites/prod/files/2017/10/f37/fy2016_fuels_technologies.pdf.
6. Qu, Jun, Yan Zhou, Huimin Luo, Todd Toops, D.W. Brookshear, B. Stump, M. Viola, K. Zreik, and T. Ahmed. “Development of Ionic Liquid-Additized, GF-5/6 Compatible Low-Viscosity Oils for Automotive Engine and rear Axle Lubrication for 4% Improved Fuel Economy.” DOE Annual Progress Report, available at https://energy.gov/sites/prod/files/2017/10/f37/fy2016_fuels_technologies.pdf.
7. Storey, John, Melanie DeBusk, Shean Huff, Sam Lewis, Fanfei Li, John Thomas, and Mary Eibl. “Characterization of GDI PM during start-stop operation with alcohol fuel blends.” Health Effects Institute Workshop, Chicago, IL, December 2016.

VI.6 Development of PAG (Polyalkylene Glycol)-Based Lubricant for Light- and Medium-Duty Axle Applications

Dr. Arup K. Gangopadhyay, Principal Investigator

Ford Motor Company
2101 Village Road
Dearborn, MI 48122
E-mail: agangopa@ford.com

Michael Weismiller, DOE Technology Manager

U.S. Department of Energy
E-mail: Michael.Weismiller@ee.doe.gov

Start Date: October 1, 2013	End Date: March 31, 2018	
Total Project Cost: \$700,000	DOE share: \$350,000	Non-DOE share: \$350,000

Acknowledgments

Co-Authors

Chintan Ved, Nikolaus Jost, Ford Motor Company
Dr. Ali Erdemir, Argonne National Laboratory

NETL Project Manager

Nicholas D'Amico, National Energy Technology Laboratory

Project Introduction

The intent of this project is to develop novel lubricant formulations that are expected to improve the fuel efficiency of light-, medium-, heavy-duty, and military vehicles by at least 2% over SAE 75W-140 axle lubricants (improvement based on comparative results from engine dynamometer testing, chassis dynamometer testing, or test track, e.g., SAE J1321) without adverse impacts on vehicle performance or durability.

With most gear oils, drag loss can be reduced by lowering oil viscosity. However, solely pursuing efficiency gains by means of viscosity reduction creates concern for axle component durability due to reduced oil film thickness. The PAG approach incorporates viscosity reduction along with chemistry driven friction reduction in order to improve on axle efficiency.

Objectives

- Formulate new PAG-based gear oils that will improve the fuel efficiency of light- and medium-duty applications by 2% over SAE 75W-140 grade axle oils without adverse impacts on vehicle performance or durability
- Evaluate fundamental material properties with respect to gear oil formulations
- Complete bench testing to understand intrinsic lubricant properties and their contributions to wear and efficiency characteristics in an axle
- Analyze lubricant additive-derived antiwear films using surface sensitive analytical tools
- Understand wear and efficiency performance characteristics in axles through specially designed test rigs
- Estimate vehicle fuel economy

Approach

The project begins with creating new formulations and performing laboratory bench testing to develop a fundamental understanding of friction, wear, and lubricant film forming characteristics to identify low friction mechanisms. The team is then to conduct component, dynamometer, and vehicle-level testing to assess durability and axle efficiency. The resulting test data is used to estimate PAG fuel economy benefits and is to be validated with chassis roll fuel economy dynamometer tests. Ford Motor Company is the prime contractor and provides technical direction to ensure all bench-, component-, and system-level tests are completed. Dow is instrumental in creating lubricant formulations and completing physical property testing. Argonne National Laboratory is responsible for bench-top friction testing, wear testing, and surface analytical characterization techniques.

Results

OSP Formulation Shortcomings

The previous top candidate formulations, oil soluble PAG (OSP) formulations, AW0704-A and AW0704-R, failed in shock load testing in 2016, due to poor foaming performance [1,2]. Additional system-level data were obtained to support the conclusion that stable foam generation in system-level testing was the sole deficiency of the OSP formulations AW0704-A and AW0704-R.

Formulation AW0704-A was tested in direct comparison to 75W-140 in efficiency testing in 2016 and showed significant efficiency and temperature improvement over the test profile. However, when comparing the spin-loss data for AW0704-A and 75W-140, as displayed in Figure VI.6.1, the magnitude of the variability of the power loss (hp) is considerably larger for AW0704-A than that of 75W-140 at high speed stages across all test temperatures. Although the data shows the AW0704-A power loss is less than that of 75W-140 over the majority of the data points, the amplified variability at the higher speeds of the test for AW0704-A is indicative of an unstable state, which can be attributed to foam generation during high speed spins, which correlates to the speculated root cause for failure in high speed and shock load testing.

Furthermore, the post-test gear teeth from the high speed shock load testing completed with AW0704-R were compared to that of formulation AU6615-E, which passed the test. Formulation AU6615-E will be discussed in more detail in the New Direction: OSP Top Treat section. The X-ray photoelectron spectroscopy (XPS) data shown in Figure IV.6.2 fails to present a clear indication of performance differences between AW0704-R, a failing candidate, and AU6615-E a passing candidate in the shock loading test. The inability to identify a significant difference between the effective deliveries of protective tribo-chemistries to the surfaces of the two candidate fluids further supports that foaming performance was the sole issue, thus the failure in shock load testing was not due to deficiencies in antiwear and extreme pressure chemistries.

The derivate formulation of AW0704-R, identified as AW0704-BN, was optimized for antifoam performance through ASTM D892 bench foam test screening as presented in 2016. Additional bench data, screening other performance indicators of the AW0704-BN formula, was collected and is presented in Table VI.6.1. As shown in Table VI.6.1, the changes incorporated in the AW0704-BN formulation for antifoam performance improvements did not compromise or drastically change the friction and wear performance from the preceding formulation.

However, in system level industry standard evaluations, new shortcomings of the AW0704-BN formulation arose. The results in Table VI.6.2 show the performance formulation of AW0704-BN in ASTM D5704 thermal oxidation test. The strongest aspect of the AW0704-BN performance in the thermal oxidation testing is the full retention of initial viscosity, exhibited by a 0% change in viscosity at the end of test. However, the average carbon/varnish rating shows that the formulation does compromise on performance when compared to the baseline 75W-140 by 0.5 merit points, thus being unacceptable. As seen before with formulation AW0704-A, AW0704-BN shows significant increase in pentane insolubles when compared to 75W-140. This is a consistent behavior of OSP formulations and is attributed to the base fluid formulation chemistry and is not regarded as a negative aspect of the performance.

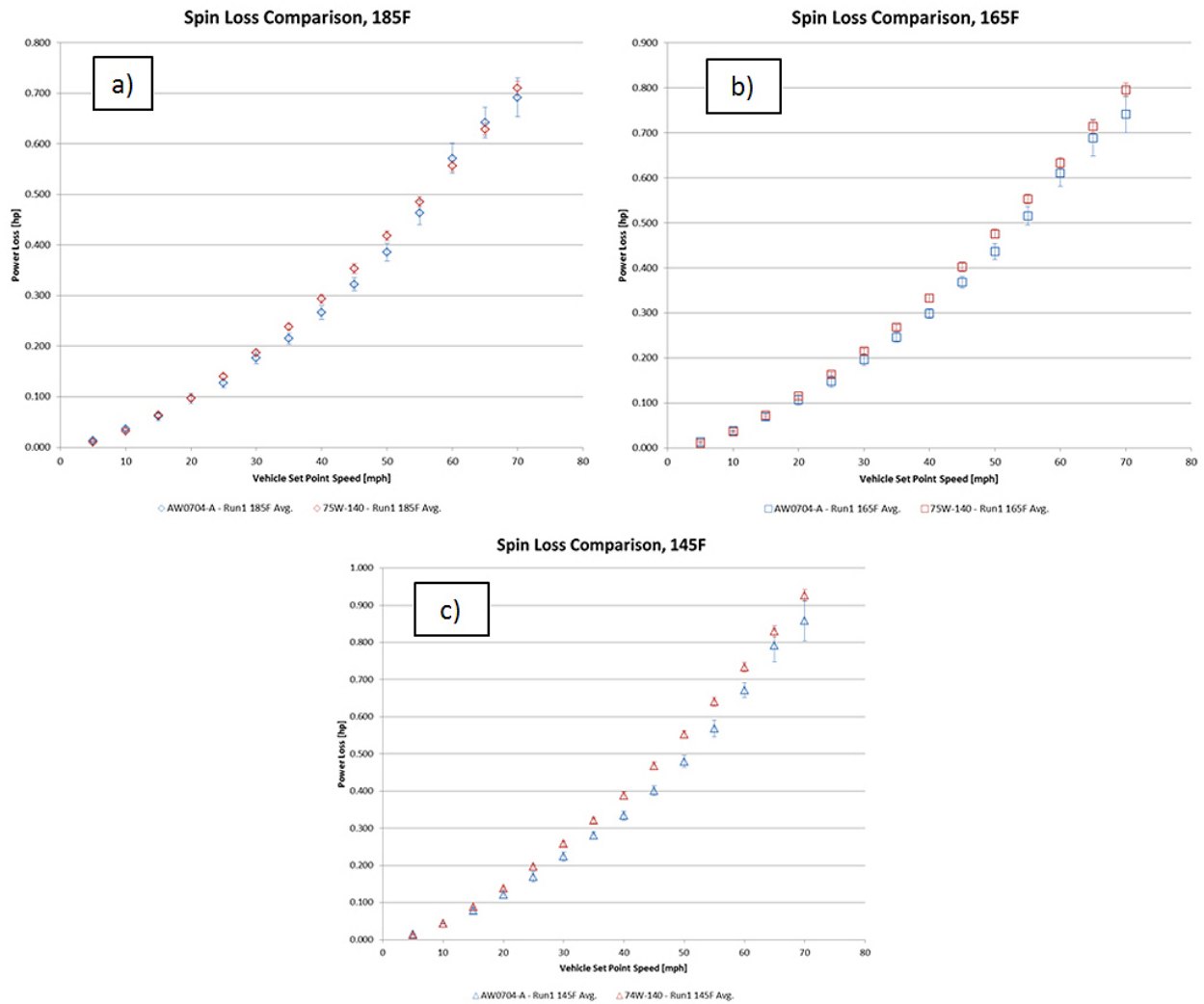


Figure VI.6.1 - Pinion drive spin loss data for AW0704-A and 75W-140. Depicted is power loss (hp) at various vehicle speeds (mph) at multiple temperatures. Graph (a) presents data at 185°F, (b) at 165°F, and (c) at 145°F. The data points represent the average of three runs and the error bars represent the standard deviation.

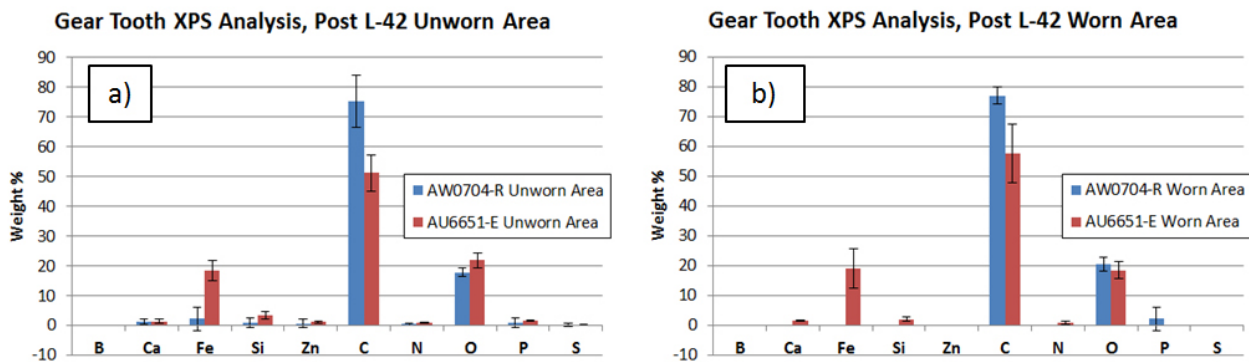


Figure VI.6.2 - Graphical display of XPS analytical data for post L-42 test gear tooth sections that completed testing in AW0704-R and AU6651-E fluids. Each bar represents three measurements and the error bars represent the standard deviation. Chart (a) depicts the unworn area and (b) depicts worn area of the gear teeth.

Table VI.6.1 - Bench Test Results for Wear, Extreme Pressure, Thermal Oxidative Stability, Rust Prevention and Copper Corrosion for 75W-140, AW0704-A, AW0704-R, and AW0704-BN Formulations

	Formulation	Wear Tests			EP Test	TOST		Rust Prevention	Copper Corrosion
		4 Ball wear (mm)	B.o.D. Disc wear (mm)	B.o.D. Ball wear (mm)	4 Ball FP (kg)	Δ TAN	Viscosity increase, %		
Baseline	750-140	0.42	0.44	0.41	420	1.5	20	Pass	2A
OSP	AW0704-A	0.36 0.42	0.32	0.31	315	1.26	3.9	Pass	1B
	AW0704-R	0.49	0.36	0.22	400	1.8	4.5	Pass	1B
	AW0704-BN	0.42	0.42	0.36	400	-	-	Pass	1B

B.o.D – ball-on-disc; TOST – Thermal Oxidative Stability Testing; EP – extreme pressure

Long-term storage stability was also found to be a significant shortcoming of the AW0704-BN. During system level testing of AW0704-BN, it was observed that precipitate formation was occurring in the samples aged approximately six months. Bench wear tests confirmed that precipitate formation resulted in compromised wear protection performance as scar results degraded from 0.42 mm for fresh fluid to 0.49 mm after a six month storage time. Testing also found that there was variation in the wear results for AW0704-BN created at different dates, comparing the 0.42 mm wear scar measured for a 2016 batch to a 0.46 mm wear scar for a 2017 batch. This batch to batch variation was deemed to be due to the variation in the raw stock additives used to create the batches. Regardless, the long-term storage data showed compromised results when compared to either fresh batch, therefore AW0704-BN was deemed to be an unsuitable candidate to continue to pursue.

New Direction: OSP Top-Treat

Formulation AW0704-BN was the solution to correct the antifoam deficiencies of the preceding OSP formulations. With the shortcomings of the AW0704-BN identified, an alternative to a full PAG option was pursued, top-treating a fully developed gear oil with OSP to utilize the PAG as a co-base fluid. The AU6615-E/F formulation is the combination of OSP base fluid into a selected commercially available gear oil. The ideal top-treat rate percent composition was determined thru initial screening in bench wear tests. The formulation is denoted AU6615-E/F because of slightly altered treat rates for the –E and –F batches, however, because of their similarities, the test data for the two are denoted to be surrogate for one another.

The OSP top-treat AU6615-E/F completed and passed system-level industry standard thermal oxidative stability testing (ASTM D5704), load carrying capacity at low speed and high torque (ASTM D6121), load carrying capacity at high speed and shock loading (ASTM D7452), and moisture corrosion resistance testing (ASTM D7038). Thermal oxidative stability test results are presented in Table VI.6.2, showing improved results to both the 75W-140 baseline and preceding OSP options. The passing post-test hardware ratings for the load carrying capacity at low speed and high torque testing are presented in Table VI.6.3. The passing post-test hardware ratings for the load carrying capacity at high speed and shock load testing are presented in Figure VI.6.3. The overall rating for ferrous components was 9.6 in the moisture corrosion testing, translating to all components being in good condition with trace amounts or no rust present.

Table VI.6.2 - Results for ASTM D5704 thermal oxidation testing. Results displayed for 75W-140, OSP options AW0704-A, AW0704-BN, and top-treat formula AU6615-E.

		Viscosity % Change	Pentane Insolubles, 5 wt.	Toluene Insolubles, % wt.	Avg. Carbon/Varnish (merits)	Avg. Sludge (merits)
Baseline	75W-140	*50	*1.5	*1.5	*7.5	*9.4
OSP	AW0704-A	2	4.69	0	9.5	9.5
	AW0704-BN	0	15.7	0.7	7	9.5
Top-Treat	AU6615-E	21	0.1	0.2	9.9	9.5

Table VI.6.3 - Ring and pinion gear inspection rating results after completion of ASTM D6121, load carrying capacity at low speed and high torques test. Results are shown for OSP AW0704-A and top-treat AU6615-E.

Gear Condition	AW0704-A		AU6615-E		Minimum Required
	Ring	Pinion	Ring	Pinion	
Wear	8	7	7	7	5.0
Rippling	10	9	10	9	8.0
Ridging	9	9	10	9.4	8.0
Pitting/Spalling	9.9	9.9	9.9	9.9	9.3
Scoring	10	10	10	10	10.0

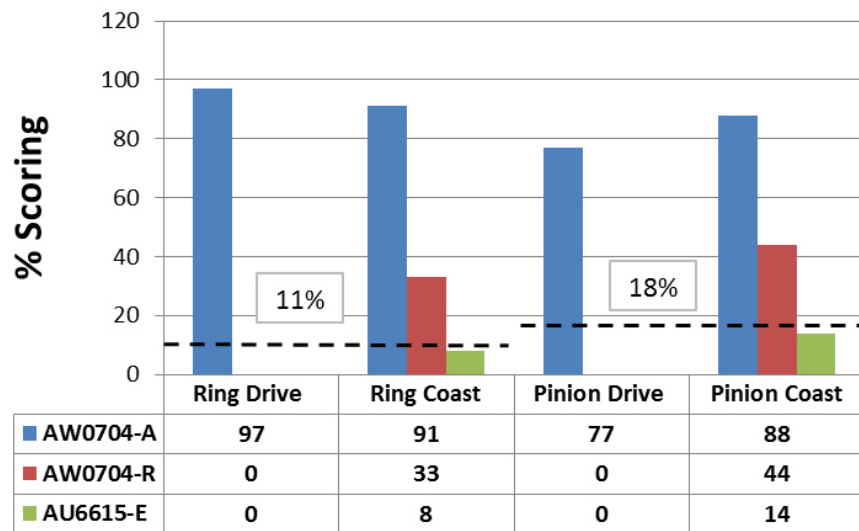


Figure VI.6.3 - High speed load carrying capacity and shock load testing post-test hardware ratings per ASTM D7452. Inspection results for AW0704-A, AW0704-R, and AU6615-E. Passing requirements are indicated by the dashed lines.

Conclusions

- The AW0704-BN successfully exhibited improved or comparable performance to 75W-140 in bench screening testing and corrected the foaming issues of its predecessors, however due to long-term stability issues does not stand as a suitable axle lubricant for production.
- The inviability of AW704-BN, the best attempt at a fully standalone PAG lubricant option, lead to the direction of OSP top-treat options being the next pathway to success.
- The OSP top-treat option AU6615-E/F successfully passed industry standard system level testing, meeting performance criteria and showing improvement to previously tested OSP formulations

References

1. Gangopadhyay, A., C. Ved, and N. Jost. “Development of PAG (Polyalkylene Glycol)-Based Lubricant for Light- and Medium-Duty Axle Applications.” DOE 2015 Annual Report Fuel and Lubricant Technologies, 76–79, 2016.
2. Gangopadhyay, A., C. Ved, and N. Jost. “Development of PAG (Polyalkylene Glycol)-Based Lubricant for Light- and Medium-Duty Axle Applications.” DOE 2016 Annual Report Fuel and Lubricant Technologies, 2017.

Key Fiscal Year 2017 Publications

1. "Optimization of a Polyalkylene Glycol Axle Lubricant Formulation." Presented at STLE Annual Meeting, Atlanta, GA, May 2017.

VI.7 Power Cylinder Friction Reduction Through Coatings, Surface Finish, and Design

Dr. Arup K. Gangopadhyay, Principal Investigator

Ford Motor Company
2101 Village Rd.
Dearborn, MI 48121
E-mail: agangopa@ford.com

Michael Weismiller, DOE Technology Manager

U.S. Department of Energy
E-mail: Michael.Weismiller@ee.doe.gov

Start Date: January 1, 2015	End Date: December 31, 2018	
Total Project Cost: \$1,070,000	DOE share: \$820,000	Non-DOE share: \$250,000

Acknowledgments

Co-Authors

Dr. Ali Erdemir, Dr. Giovanni Ramirez, Dr. Osman Eryilmaz; Argonne National Laboratory

NETL Project Manager

Adrienne Riggi, National Energy Technology Laboratory

Project Introduction

About 7–10% of the total energy input in a vehicle is lost due to mechanical friction [1] and therefore offers great opportunities for friction reduction. In an engine, about 60% of the total frictional losses occur at the interface between the cylinder and pistons and piston rings, and about 30% at the bearings [2]. The goal of this proposed study is to demonstrate friction reduction potential using advanced high porosity plasma transfer wire arc (PTWA) coatings, surface finish, and design on power cylinder system containing cylinder bore, piston rings, piston skirt, bearings and crankshaft, and advanced engine oils. Experience through years of research in this area lead us to believe that full benefit potential can be realized only by considering a systems approach.

This project developed (a) a process for depositing and honing high porosity PTWA coatings to achieve different porosity levels with improved surface finish on free-standing cylinder liners and engine blocks; (b) various techniques for characterizing coatings including porosity area percent, porosity size distribution, oxide content, etc.; (c) a method for achieving micro-polishing crankshaft journals; (d) a technique for depositing nano-composite VN-Cu and VN-Ni coatings on piston ring and piston skirts; (e) a method for laboratory friction and wear assessment for generating Stribeck curve; (f) a method for evaluating friction reduction potential of PTWA coatings, and micro-polished journals using motored cranktrain rig; and (g) a method for evaluating wear (durability) of PTWA coating and ring coatings using the radio tracer method.

Objectives

- Demonstrate deposition of PTWA coatings at various porosity levels on liners and engine blocks with improved surface finish
- Develop and demonstrate deposition of nano-composite coatings on piston rings and skirts
- Demonstrate friction benefits of micro-polished crank journals
- Demonstrate friction benefits through laboratory bench, motored cranktrain and engine, fired single-cylinder engine, and chassis roll dynamometer (vehicle) tests
- Demonstrate durability of PTWA coatings using the radio tracer method

Approach

The project goal of delivering 4% fuel economy improvement over current (2014) technologies can be achieved through a technology bundle comprising of (a) deposition of low friction coating (high porosity PTWA) on cylinder bores, (b) low friction nano-composite coatings for piston rings and skirts, (c) improved surface finish on cylinder bores and crankshaft, and (d) novel engine oil formulation (polyalkylene glycol [PAG]), an outcome of a previously DOE funded project.

Achieving the project goals necessitated partnering with key suppliers including (a) Comau for deposition of bore coatings, (b) Gehring for cylinder bore honing of PTWA coatings, (c) Paramount for mechanical roughening treatment prior to coating deposition, (d) NETZSCH for assessment of coating thermal properties, (e) Mahle, and KS for low friction piston skirt, piston ring coatings, (f) Southwest Research Institute® for single-cylinder fired engine tests, and (g) Dow chemical company for novel polyalkylene glycol engine oil.

Results

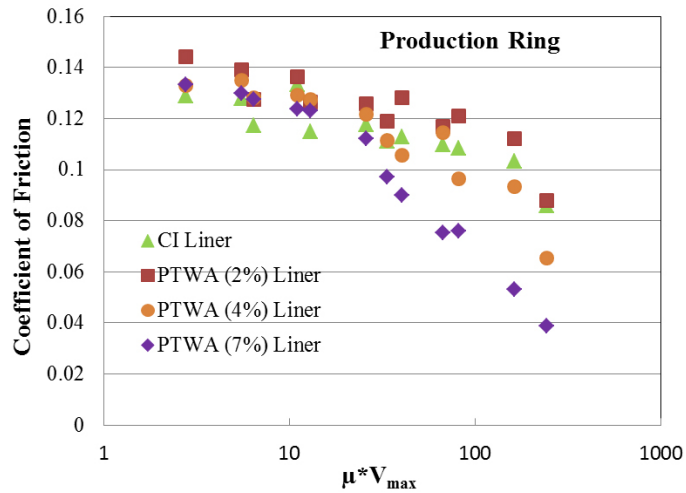
The efforts were primarily focused on preparing samples of PTWA coatings of varying porosity levels to support various friction and wear evaluations and also ensuring coatings are deposited with consistent quality, which included extensive coating characterization for porosity, oxide content, microstructure, etc. Coatings were deposited on 92.5-mm aluminum liners, and seven blocks from production in-line four cylinder engines. Liners and engine blocks were thoroughly inspected after honing for cylindricity and straightness ensuring both are within acceptable limits. Four engines were built using four such blocks for motored engine friction tests later. Attention was paid to maintain the same piston bore clearance in all bore and in all engines. This is important because piston bore clearance is probably the biggest factor influencing engine mechanical friction [3]. Attention was also paid to maintaining nominal crankshaft journal bearing clearance to avoid this being a noise factor in friction results. In parallel, nano-composite coatings were also deposited on piston rings and skirts.

Laboratory Bench Tests Friction and Wear Assessment

Sections were cut from liners for coating characterization and friction evaluation using Plint TE-77 reciprocating laboratory test rig where a section of a ring reciprocated against a liner section at various temperatures (30°C, 50°C, 80°C, 120°C), loads (50 N, 100 N, 150 N), and frequency (2, 5 Hz, 10 Hz, 20 Hz, 30 Hz) in the presence of GF-5 SAE 5W-20 engine oil. Figure VI.7.1 shows coefficient of friction as a function of engine oil viscosity and reciprocating speed. The data clearly shows low porosity PTWA coatings behave similarly to cast iron liner material but high porosity PTWA coatings showed friction benefits under a mixed lubrication regime; it appears higher porosity level helps reducing friction even more. These results were obtained with a current production ring section. Figure VI.7.2 shows coefficient of friction for one of the high porosity PTWA coatings in contact with a diamond-like carbon (DLC)-coated ring. The DLC-coated ring offered a friction benefit with cast iron liner material in both boundary and mixed lubrication regimes. However, it offered an added friction benefit in contact with the high porosity PTWA coating. Figure VI.7.3 shows a VN-Cu nano-composite coating also showed a friction benefit with high porosity PTWA coating. This coating can be applied also on the piston skirt surface for added friction benefit in an engine. Attempts were made to measure wear on the cast iron liner and PTWA sections but no measureable wear could be observed under these test conditions. These tests were designed primarily to explore friction benefits. In the past, tests were conducted using the same sample configuration but under different test conditions primarily to measure wear. It was observed PTWA coatings offered much better wear resistance than cast iron material.

Motored Friction Assessment

Figure VI.7.4 shows an image of a finished in-line four cylinder engine block with PTWA coating. Motored cranktrain tests were run to explore friction benefits with novel engine oil formulation and PTWA coated blocks. In this test, the crankshaft is rotated by an electric motor and the friction is measured by an in-line torque meter. The crankshaft is connected to pistons and rings with a connecting rod. No valvetrain is attached to the block. Therefore, the friction contributions are from bearings (mains and rods), piston rings, and piston skirt. Figure VI.7.5 shows friction benefits (6–25% depending on speed) offered by polyalkylene glycol engine oil compared to GF-5 SAE 5W-20 engine oil at 100°C. A similar friction benefit was also observed at 40°C



CI – cast iron

Figure VI.7.1 - High porosity PTWA coating shows friction benefit under mixed lubrication regime

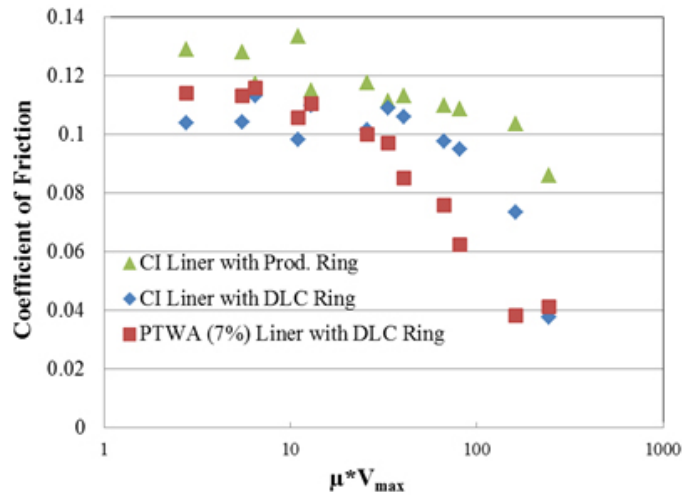


Figure VI.7.2 - DLC-coated rings show additional friction benefit with high porosity PTWA coatings under boundary and mixed lubrication regimes

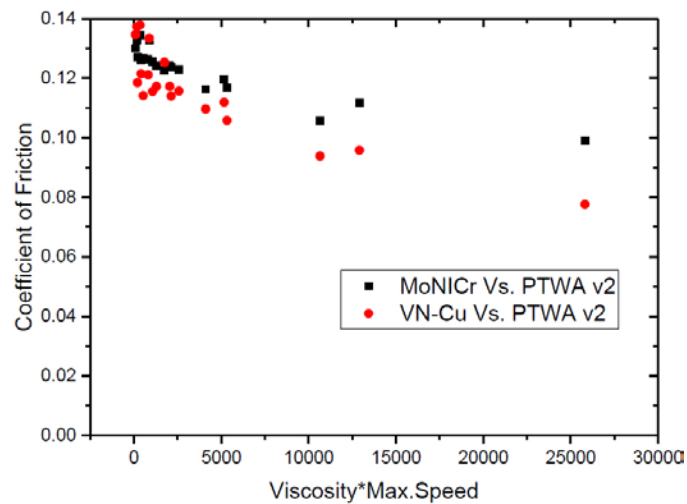


Figure VI.7.3 - Nano-composite VN-Cu coated rings show additional friction benefit with high porosity PTWA coatings under boundary and mixed lubrication regimes

and other intermediate temperatures. The polyalkylene glycol formulation used in this investigation showed significant friction benefit in motored engine tests in a prior DOE funded project.

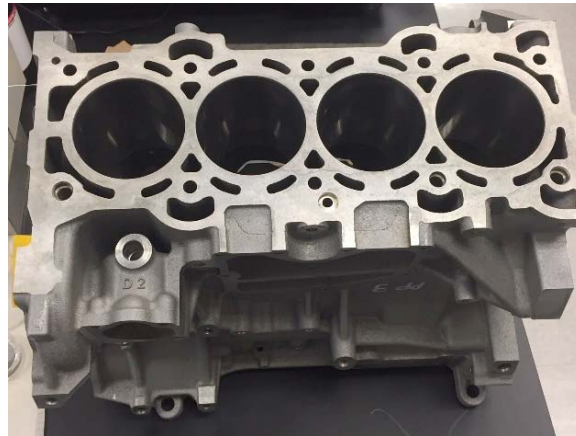
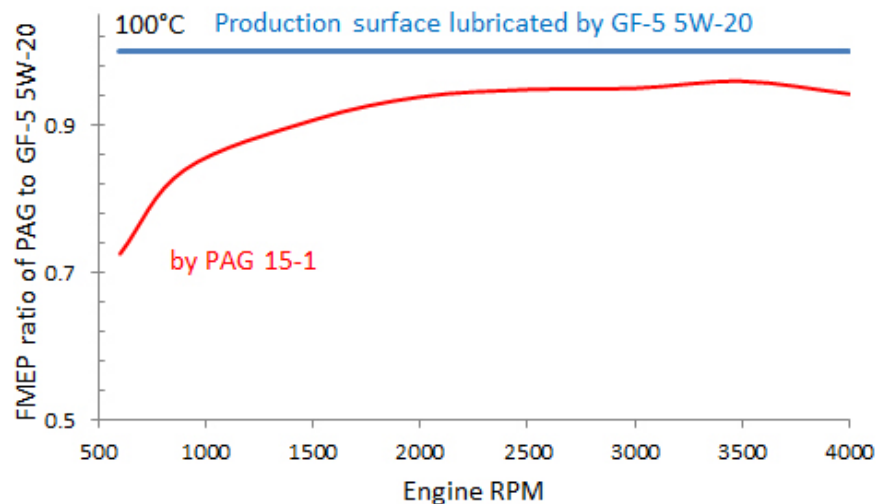


Figure VI.7.4 - PTWA coated cylinder bores in a linerless engine block (Source Ford Motor Company)



FMEP – friction mean effective pressure

Figure VI.7.5 - Polyalkylene glycol (PAG) engine oil showed significant friction benefits over GF-5 5W-20 oil

The same friction rig was used to evaluate the friction benefit of PTWA coated blocks. Figure VI.7.6 compares friction torque measured with a production engine block with cast iron liner and liner-less PTWA coated block using GF-5 SAE 5W-20 oil at 100°C. The friction benefits ranged 5–24% depending on engine speed. Similar benefits were observed at higher oil temperature (120°C) but not at less than 100°C oil temperatures.

Conclusions

- Laboratory bench tests demonstrated high porosity PTWA coatings offer friction benefits over cast liner material in the mixed lubrication regime. Piston rings with DLC or VN-Cu nano-composite coating offer additional friction benefits in the boundary and mixed lubrication regimes.
- Motored tests demonstrated a high porosity PTWA coating offers 5–24% friction benefit over a cast iron liner engine block at higher oil temperatures.
- Polyalkylene glycol engine oil offered 6–25% friction benefit over GF-5 SAE 5W-20 oil.

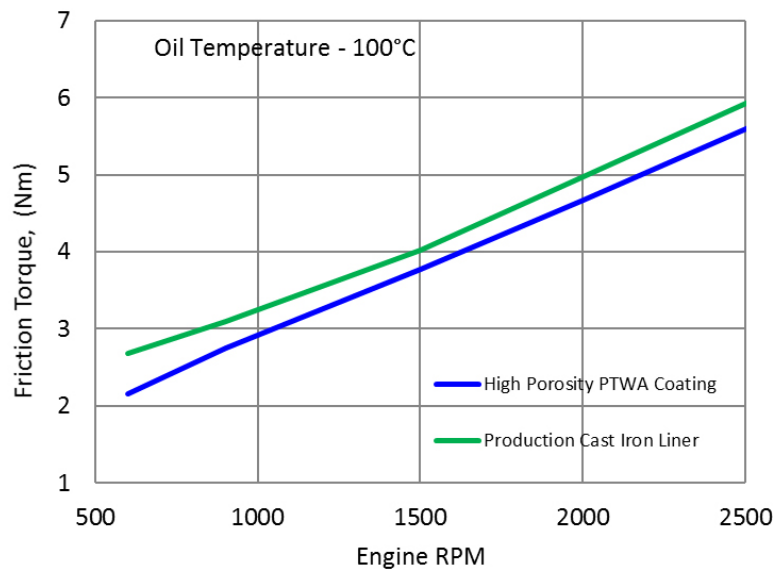


Figure VI.7.6 - Linerless engine block with PTWA coating shows friction benefits compared to cast iron liner engine block

References

1. Pinkus, O. and D.F. Wilcock. "Strategy for energy conservation through tribology." New York, ASME, 1977.
2. Kiovsky, T.E., N.C. Yates, and J.R. Bales. "Fuel efficient lubricants and the effect of base oils." *Lubrication Engineering*, 50(4), p, 307, 1994.
3. Deuss, T., H. Ehnis, M. Bassett, and A. Bisordi. "Friction power measurements of a fired diesel engine." *MTZ*, 72 (12), p. 8, 2011.

Key Fiscal Year 2017 Publications

1. "Development and characterization of a high surface porosity thermally sprayed coating." Presented at the STLE Annual meeting, Atlanta, GA, May 21–25, 2017.

VI.8 Hybrid Ionic-Nano-Additives for Engine Lubrication to Improve Fuel Efficiency

Bin Zhao, Principal Investigator

University of Tennessee Knoxville
1420 Circle Drive
Knoxville, TN 37996-1600
E-mail: bzhao@utk.edu

Michael Weismiller, DOE Technology Manager

U.S. Department of Energy
E-mail: Michael.Weismiller@ee.doe.gov

Start Date: January 1, 2015 End Date: December 31, 2017
Total Project Cost: \$1,135,274 DOE share: \$898,013 Non-DOE share: \$237,261

Acknowledgments

Co-Authors

Sheng Dai, Roger A.E. Wright, and Bryan T. Seymour; University of Tennessee Knoxville
Jun Qu, Huimin Luo, Beth Armstrong, Chanaka Kumara; Oak Ridge National Laboratory
Ashlie Martini, Hongyu Gao; University of California, Merced

Project Introduction

Energy efficiency is of great importance to the automobile industry and has drawn enormous attention in recent years. For internal combustion engines, a significant portion, 10–15%, of the fuel energy is consumed to overcome the friction. Although one can use lower viscosity lubricating oils to reduce the parasitic friction and improve the fuel efficiency, the wear protection is a great challenge. Nanoparticles (NPs) have been envisioned as potentially effective lubricant additives for friction and wear reduction. However, a major issue with the use of NPs is their dispersibility and stability in lubricating base oils. The lubrication mechanisms of NPs and the effects of various parameters are yet to be elucidated. Although efforts have been made in the past years, achieving the full potential and practical use of NPs as additives for lubricants is still a great challenge.

This project is aimed at developing hybrid organic–inorganic NPs for use as friction reducers and antiwear agents in engine lubricants. The University of Tennessee, Knoxville group synthesized polymer brush-grafted metal oxide NPs (hairy metal oxide NPs), while the Oak Ridge National Laboratory (ORNL) researchers made ionic liquid (IL)- and organic ligand-modified metal NPs. These hybrid NPs can be dispersed in the poly(alphaolefin) (PAO) base oil and have been shown to significantly reduce the friction and wear compared with PAO. The lubrication mechanisms of hybrid NPs were investigated by both experimental and computer simulation studies.

Objectives

- Synthesize poly(alkyl methacrylate) brush-grafted silica NPs with various alkyl groups and determine the effects of alkyl pendant length on dispersibility and lubrication performance of hairy NPs in PAO
- Synthesize IL- and organic ligand-modified metal NPs and demonstrate friction reduction by >20% and wear reduction by >80% relative to neat PAO
- Elucidate the interrelated effects of initial surface roughness and NP size on friction and wear behavior

Approach

The approach adopted by the project team is to make organic–inorganic/metallic hybrid NPs by functionalizing NPs with oil-soluble polymers, ILs, and organic ligands. These hybrid NPs are expected to be dispersible and stable in PAO and exhibit excellent lubrication properties. The work includes (1) synthesis of metal

oxide and metal NPs surface functionalized with various polymer brushes, ILs, and organic ligands; (2) study of the effect of polymer brush's chemical composition on the dispersity and stability of hairy NPs in PAO; (3) investigation of lubrication properties of hybrid NPs; and (4) understanding of the lubrication mechanisms of hybrid NPs and the roles of core NP and organic components by experimental and modeling studies. The University of Tennessee, Knoxville group is responsible for the synthesis of polymer brush-grafted NPs, and the tribological tests are performed at ORNL. The ORNL researchers focus on the synthesis and tribological properties of IL- and organic ligand-modified metal NPs. The computer modeling study is performed at University of California, Merced.

Results

- Synthesized a series of poly(alkyl methacrylate) brush-grafted silica NPs and revealed the effects of alkyl pendant length on the NPs' dispersibility and tribological properties
- Attained significant reductions in friction (up to 38%) and wear volume (up to 90%) using 1 wt% clear, homogeneous dispersions of hairy NPs in PAO relative to neat PAO
- Synthesized oil soluble IL-functionalized silver NPs and achieved >20% friction reduction and >90% wear reduction compared with PAO
- Synthesized oil soluble organic-modified palladium NPs and achieved >40% of friction reduction and >95% wear reduction compared with PAO
- Determined the role of the organic layer on Ag and Pd NPs in friction and wear reduction
- Elucidated the interrelated effects of initial surface roughness and NP size on friction and wear behavior using a finite element modeling approach

Polymer Brush-Grafted Nanoparticles

Surface-initiated reversible addition-fragmentation chain transfer polymerization was used to grow polymer brushes from trithiocarbonate chain transfer agent-functionalized, 23 nm silica NPs. A series of hairy silica NPs with different alkyl pendant groups in the brushes were synthesized; the degrees of polymerization (DPs) were targeted at ~30 in order to investigate the effects of polymer composition on the dispersibility and lubrication properties of hairy NPs. The hybrid NPs were purified by ultracentrifugation and characterized by thermogravimetric analysis (TGA); the molecular weights of the free polymers were determined by size exclusion chromatography. The grafting density of each NP brush sample was calculated by using the NP size, TGA data, and the DP. The characterization data for these hairy NPs are summarized in Table VI.8.1. The dispersibility and stability of the obtained hairy NPs were studied, and it was found that the hairy NPs with sufficiently long alkyl pendant groups (containing >8 carbon atoms, such as 12, 13, 16, and 18) were readily dispersible in PAO, forming clear, homogeneous dispersions, and exhibited superior stability at low and high temperatures by both visual inspection and dynamic light scattering study (Figure VI.8.1A shows the photos of PC13-NP-9.7k dispersions in PAO). Differently, poly(*n*-hexyl methacrylate) brush-grafted NPs (PC6-NP-7.0k in Table VI.8.1) cannot be dispersed in PAO at ambient conditions or at 80°C (Figure VI.8.1B), whereas poly(2-ethylhexyl methacrylate) hairy NPs (PC8-NP-7.8k) can be dispersed in PAO at 80°C (Figure VI.8.1C), but not at room temperature, with a reversible clear-to-cloudy transition observed at 54°C upon cooling.

Table VI.8.1 - Characterization Data for Poly(alkyl methacrylate) Brush-Grafted, 23 nm Silica NPs and the Corresponding Free Polymers

Hairy NPs	$M_{n,SEC}$ (kDa)	PDI	DP	Grafting Density (chains/nm ²)
PC6-NP-7.0k	7.0	1.25	32	0.72
PC8-NP-7.8k	7.8	1.23	38	0.57
PC12-NP-9.5k	9.5	1.24	29	0.52
PC13-NP-9.7k	9.7	1.20	32	0.62
PC16-NP-8.3k	8.3	1.14	27	0.28

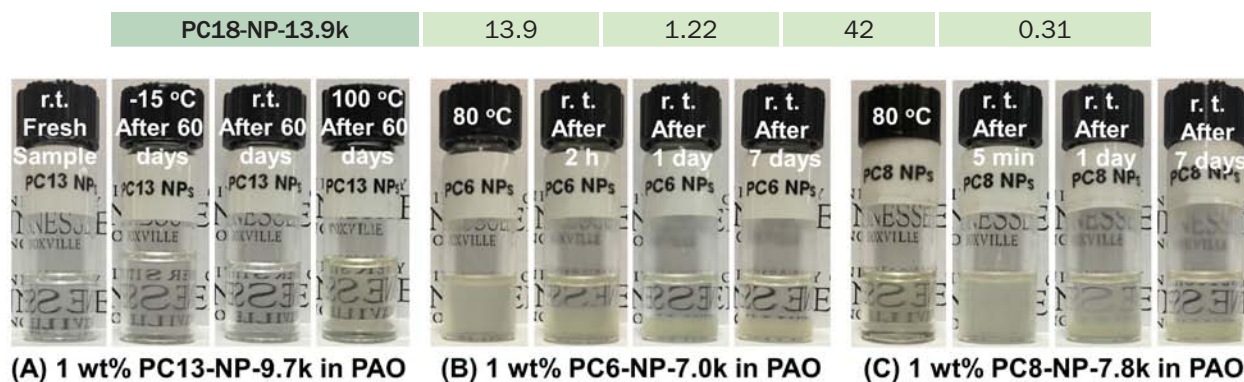


Figure VI.8.1 - Optical photos of (A) a 1.0 wt% freshly prepared dispersion and three 1.0 wt% dispersions of PC13-NP-9.7k in PAO after storage for 60 d at -15°C, room temperature (r.t.), and 100°C. (B) 1.0 wt% dispersion of PC6-NP-7.0k in PAO at 80°C and sitting at r.t. for 2 h, 24 h, and 7 d after removal from a 80°C oil bath. (C) 1.0 wt% dispersion of PC8-NP-7.8k in PAO at 80°C and sitting at r.t. for 5 min, 1 d, and 7 d after removal from a 80°C oil bath.

The tribological properties of hairy NPs were evaluated at a concentration of 1.0 wt% using a Plint TE-77 tribo-tester in a ball-on-flat (52100 steel ball against CL35 cast iron flat) reciprocating configuration at 100°C with a normal load of 100 N. For all hairy silica NPs that can be readily dispersed in PAO at r.t., i.e., PC12-NP-9.5k, PC13-NP-9.7k, PC16-NP-8.3k, and PC18-NP-13.9k, the coefficient of friction (COF) exhibited much lower values relative to PAO throughout the sliding process (Figure VI.8.2) and were similar to each other. The COF values ended at 0.08–0.10 at 1,000 m, with PC16-NP-8.3k exhibiting the largest friction reduction (38%) compared to the base oil. PC8-NP-7.8k in PAO in the homogeneous state after heating to 80°C performed similarly. In fact, the COF traces of all hairy NPs shown in Figure VI.8.2 were all below that of PAO containing 1.0 wt% zinc dialkyldithiophosphate (ZDDP), indicating better friction behavior for these hairy NPs than the widely used ZDDP. Note that adding 1.0 wt% free polymer PC13-20.8k resulted in little improvement in the friction compared with PAO, suggesting that the main function of polymer brushes is to provide colloidal stability for the core silica NPs in PAO. The similar lubrication performances of these hairy NP samples with different alkyl pendant groups highlighted the importance of the core silica NPs in the effectiveness of hairy NPs as additives. Material wear volumes were measured by optical surface profilometry for the wear scars. The wear volumes of the iron flats for clear, homogeneous PAO dispersions of hairy NPs were found to be similar and ranged from $11.7 \times 10^7 \mu\text{m}^3$ to $23 \times 10^7 \mu\text{m}^3$, which were significantly smaller, by 80–90%, than that for neat PAO ($113.0 \times 10^7 \mu\text{m}^3$). The poor colloidal stability at r.t. and NP settling in PAO dispersions of PC6- and PC8-grafted NPs greatly hindered their lubrication performance. The formation of a load-bearing tribofilm at the rubbing interface was confirmed using scanning electron microscopy coupled with energy dispersive X-ray spectroscopy, which showed the improved Si content in wear scars.

Oil-Soluble IL and Organic Ligand-Modified Metal NPs

Mercaptoundecanoic acid (MUA)-functionalized Ag NPs were synthesized and then modified to IL-NPs that were soluble in organic solvents. Oleyamine was selected for making IL Ag NPs due to its long hydrocarbon chain and the terminal amine group. Oleyamine-modified AgNPs [$\text{Ag-SC}_{10}\text{H}_{20}\text{COO}^-$] [$\text{CH}_3(\text{CH}_2)_7\text{CH}=\text{CH}(\text{CH}_2)_7\text{CH}_2\text{NH}_3^+$] showed a solubility in the PAO base oil up to 0.50 wt%. Figure VI.8.3A shows the COF traces of the neat PAO and the PAO oil with oleyamine–Ag NP–MUA as a function of the sliding distance. Oleyamine–Ag NP–MUA reduced the friction up to 23% and wear volume by ~90% (Figure VI.8.3A inset) compared to the neat base oil. Since the presence of triboactive elements, such as silver, sulfur, or nitrogen, was found to be minimal on the worn surface based on energy dispersive X-ray spectroscopy elemental analysis, the friction and wear reduction may be attributed to the physical adsorption of IL–Ag NPs to the contact surface.

Figure VI.8.3B and Table VI.8.2 summarize the friction and wear results for neat PAO base oil, organic-modified metal NPs, and the dodecanethiol (C12)-added PAO oil. Excellent friction and wear reduction was observed upon addition of Ag and Pd NPs. Particularly, the Pd NPs reduced the friction by >40% and wear by >95%. Surface characterization revealed a protective tribofilm on the worn surface. Since these NPs are hybrid

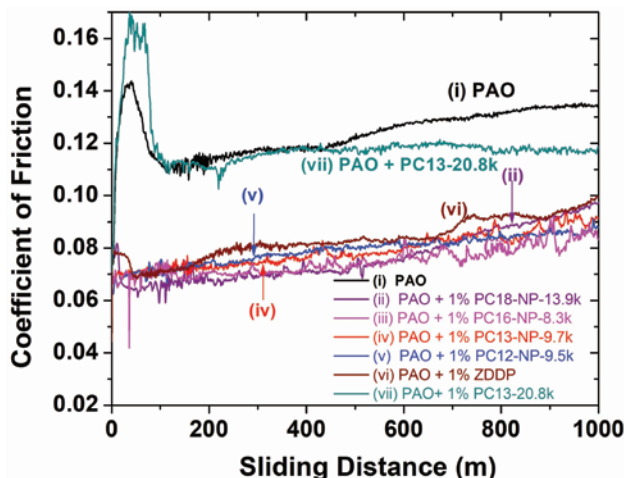


Figure VI.8.2 - Friction curves for PAO SpectraSyn™ 4 (i), PAO additized with 1.0 wt% PC18-NP-13.9k (ii), PC16-NP-8.3k (iii), PC13-NP-9.7k (iv), PC12-NP-9.5k (v), ZDDP (vi), and PC13-20.8k free polymer (vii). The tribological tests were performed using a Plint TE-77 tribo-tester at 100°C under a point contact load of 100 N for a sliding distance of 1,000 m.

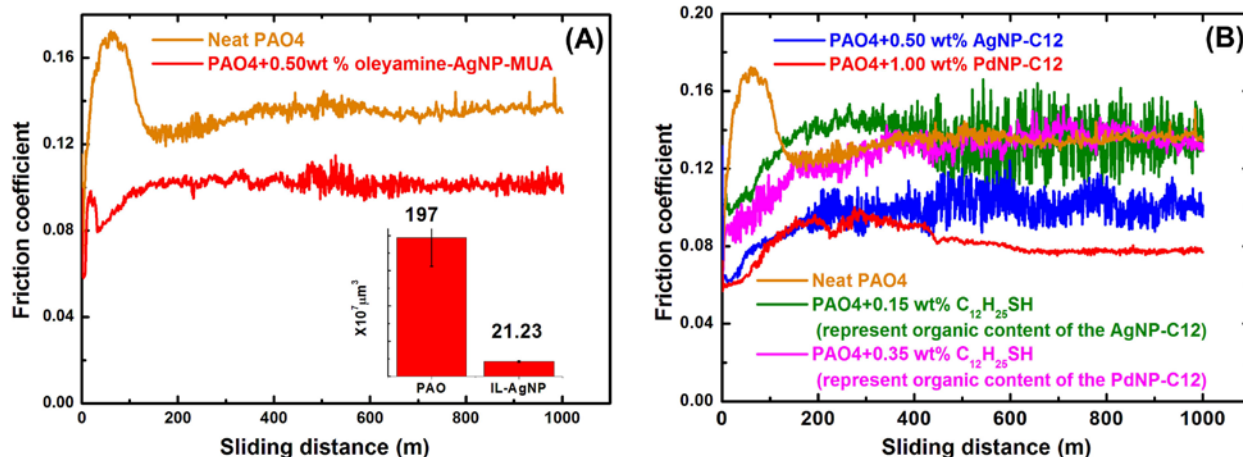


Figure VI.8.3 - (A) Friction coefficient traces of the neat PAO base oil and PAO + 0.50 wt% oleyamine-Ag NP-MUA. (Inset) Wear rates corresponding to the tribotests. (B) Friction coefficient traces showed that organic-modified Ag and Pd NPs effectively reduced friction but the organic ligand alone had little impact.

organic-metallic materials, the observed friction and wear reduction may be due to the individual or composite effect of metallic core and organic ligand. It is essential to understand the roles of the metallic core and the organic ligand of hybrid NPs in the lubrication mechanism. TGA was used to determine the organic and metallic contents of the NPs. For example, AgNP-C12 (3–6 nm) consists of 70 wt% metallic silver and 30 wt% of organic ligand ($-\text{SC}_{12}\text{H}_{25}$). Thus, 0.50 wt% of AgNP-C12 in PAO represents 0.35 wt% of metallic Ag and 0.15 wt% of dodecanethiol. It is unlikely to dissolve metallic silver or silver salt in PAO base oil. Therefore, tribotests were conducted with PAO+0.15 wt% of dodecanethiol (Figure VI.8.3B green curve) to examine the role of the ligand on friction and wear behavior. While the friction trace of the dodecanethiol coincides with that of neat PAO, the wear volume was reduced by ~87% with dodecanethiol. Focused ion beam-aided cross-sectional scanning transmission electron microscopy analysis of the worn surface showed a 100–200 nm tribofilm and elemental mapping detected sulfur. The organic ligand ($\text{C}_{12}\text{H}_{25}\text{SH}$), when used alone, effectively reduced wear, but had little impact on friction. When used to modify the NPs, the organic ligand also is a facilitator to suspend and disperse the NPs. Referring to the 65 wt% of the metallic content for PdNP-C12, 0.35 wt% dodecanethiol was used in the PAO to examine the role of organic ligand in the PdNP-C12 system, and similar results were observed (Figure VI.8.3B pink curve).

Table VI.8.2 - Wear Volumes for Flats and Balls after Tribological Tests with PAO Additized with Organic-Modified Ag and Pd NPs

Lubricant	Wear Volume ($\times 10^7 \mu\text{m}$)		
	Flat	Ball	Total
PAO 4 cSt Base Oil	196.0 \pm 40.5	0.75 \pm 0.06	196.8 \pm 40.5
PAO+0.5% AgNP-C12	10.68 \pm 1.33	0.70 \pm 0.24	11.30 \pm 1.44
PAO+0.15% SC12	24.05 \pm 1.35	0.11 \pm 0.11	24.16 \pm 1.35
PAO+1.0% PdNP-C12	5.04 \pm 1.25	0.05 \pm 0.01	5.09 \pm 1.25
PAO+0.35% SC12	14.95 \pm 0.25	0.31 \pm 1.21	15.26 \pm 1.27

Computer Simulation Study

Measurements of friction and wear of lubricants with functionalized NPs of different size revealed that the NP size could affect wear protection. Atomistic simulations suggested that this effect may be due to the effect of relative NP size on the ability of the particles to fill in valleys on the surface as the first steps towards formation of a protective tribofilm. However, the small size scale of that simulation approach limited its ability to match the corresponding experiments. Therefore, a novel modeling approach was developed, based on finite element methods. In the initial model, shown in Figure VI.8.4A, the materials were chosen to be steel for the rough surfaces and silver for the NPs, consistent with the experiments performed by Dr. Qu at ORNL. Load and shear were applied and the system was analyzed in terms of stresses within the bodies and deformation (Figure VI.8.4B). Since it has been hypothesized that the NP size effects are likely to be most important in wear protection, the model was extended to capture wear as a function of the ratio of the equivalent plastic strain to the elongation at fracture of each element in the model. The results have shown that there is indeed an effect of relative particle size and roughness on wear, but also that the direction and magnitude of this effect are determined by the overall pressure on the interface.

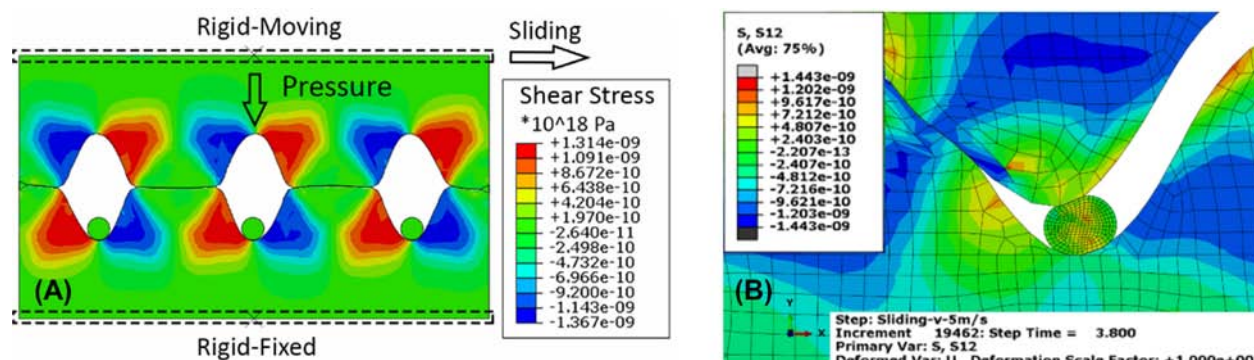


Figure VI.8.4 - Finite element model of a rough surface sliding with a nanoparticle-additized lubricant. (a) Representative model geometry and (b) close up view of the deformation of interacting asperities and a nanoparticle.

Conclusions

A variety of organic–inorganic/metallic hybrid NPs, including poly(alkyl methacrylate) brush-grafted, 23 nm silica NPs with differing alkyl pendant groups and IL/organic ligand-modified silver and palladium NPs were synthesized. The hairy NPs with a sufficiently long alkyl pendant group can be readily dispersed in PAO at room temperature, forming homogeneous and clear dispersions that are stable at high and low temperatures. The 1.0 wt% clear, homogeneous dispersions of hairy NPs in PAO exhibited significant reductions in both friction (up to ~38%) and wear (up to ~90%) compared with neat PAO. The IL-modified silver NPs were found to reduce friction by >20% and wear by >90%. The PdNP-C12 was an excellent additive, exhibiting a reduction of >40% in friction and >95% in wear. The roles of the core metallic NPs and the organic ligand were elucidated; the organic ligand, when used alone, effectively reduced wear but had little impact on friction. A finite element modeling approach was employed in the simulation study, which revealed the interrelated

effects of initial surface roughness and NP size on friction and wear behavior. These results demonstrate that oil-soluble hybrid NPs are promising lubricant additives for friction reduction and wear protection.

Key Fiscal Year 2017 Publications

1. Seymour, B.T., R.A.E. Wright, A.C. Parrott, H.Y. Gao, A. Martini, J. Qu, S. Dai, B. Zhao. “Poly(alkyl methacrylate) Brush-Grafted Silica Nanoparticles as Oil Lubricant Additives: Effects of Alkyl Pendant Groups on Oil Dispersibility, Stability, and Lubrication Property.” *ACS Appl. Mater. Interfaces* **2017**, *9*, 25038–25048.
2. Kumara, C., H. Luo, D.N. Leonard, H.M. Meyer, J. Qu. “Organic-Modified Silver Nanoparticles as Lubricant Additives.” *ACS Appl. Mater. Interfaces* **2017**, *9*, 37227–37237.
3. Peña-Parás, L., H. Gao, D. Maldonado-Cortés, A. Vellore, P. García-Pineda, O.E. Montemayor, K.L. Nava, and A. Martini. “Effects of Substrate Surface Roughness and Nano/Micro Particle Additive Size on Friction and Wear in Lubricated Sliding.” *Tribology International* **2017**, *119*, 88–98.

VI.9 Integrated Friction Reduction Technology to Improve Fuel Economy Without Sacrificing Durability

Stephen Hsu, Principal Investigator

George Washington University
2121 I St., NW, Suite 601
Washington, DC 20052

Michael Weismiller, DOE Technology Manager

U.S. Department of Energy
E-mail: Michael.Weismiller@ee.doe.gov

Start Date: October 1, 2014	End Date: September 30, 2018	
Total Project Cost: \$2,000,000	DOE share: \$1,000,000	Non-DOE share: \$1,000,000

Acknowledgments

Co-Authors

Gefei Wu, Valvoline
Tim Cushing, General Motors

Project Introduction

The combustion of fuels to transport people and goods is the major source of oil use in the United States, resulting in yearly oil imports about 10 MM barrels of oil per day in 2016. Improving the fuel economy of cars and trucks will reduce the United States' dependence on foreign oil. The new Corporate Average Fuel Economy standard has raised the fuel economy of cars and light trucks from 27.5 mpg in 2012 to 54.5 mpg by 2025. This project supports the energy independence goal.

In a worldwide effort to improve fuel economy, Japanese automakers have introduced a new class of ultra-low viscosity lubricants to reduce drag, hence improve fuel economy. This new class has three viscosity grades: 0W-16 (defined by 2.3 mPa.sec viscosity at 150°C), 0W-12, and 0W-8. The technical concern for the low viscosity oils is that the resultant thin oil film thickness may cause wear. This project aims to (1) develop a prototype 0W-20 low viscosity oil and demonstrate that it can improve fuel economy by 2%, is backward compatible, and is suitable for use by current cars and light trucks; (2) develop a prototype 0W-16 ultra-low viscosity oil and demonstrate that it can improve fuel economy by 2% against current commercial oils; and (3) develop engine durability test protocols to evaluate engine durability using the 0W-16 oil.

Objectives

- Develop 0W-20 and 0W-16 low viscosity lubricants that will improve fuel economy by 2%
- Conduct current industry standard engine tests to verify their fuel efficiency
- Use the ultra-low viscosity lubricant and measure engine durability in an engine
- Develop and measure the effects of surface textures, coatings, and other material technology that could enhance engine durability

Approach

- We formed an integrated research team including an engine manufacturer, oil company, and additive companies to jointly tackle technical challenges. The team includes General Motors (GM), Valvoline, Afton, Vanderbilt, and a group of additive component suppliers who are willing to collaborate with the team on this project, including Evonik, Chemtura, Croda, BASF, ExxonMobil, Emery, Hatco, etc. Non-disclosure agreements were signed with the additive suppliers to facilitate sampling of new additives and data exchanges.

- Valvoline and GM are the principal industrial partners. Valvoline provides formulation guidance and oil testing, and GM provides engine test development and testing on durability.
- George Washington University conducts basic and applied research in additive evaluation, additive interactions, microencapsulation of additives, and surface material technology research on coatings and surface textures.

The team was formed in 2014 for the project. Over 120 additive components and base oils have been received from industrial partners and collaborators. Several generations of formulations were developed and tested. The 0W-20 was first tested in ASTM engine dynamometer test Sequence IVE and achieved 2.4% fuel economy improvement against the current commercial lubricant, meeting one of the key objectives of the project. In preparation for the engine durability testing, a modern engine platform was chosen to reflect the rapidly changing engine technologies. This change, while necessary, caused a one year no-cost extension delay to allow for surface material technology to be fabricated on the new engine parts.

Results

For Fiscal Year 2017, the key objectives are to (1) complete engine testing of the low viscosity lubricants developed by the project team, (2) develop an engine durability test plan with GM, and (3) develop a processing technique to fabricate the textures on engine components for testing in Fiscal Year 2018.

Key Accomplishments

- The 0W-20 low viscosity lubricant developed based on new chemistry successfully demonstrated 2.4% fuel economy improvement over current commercial lubricants in an industrial standard engine tests (ASTM engine dynamometer Sequence VIE test). This is backward compatible with the legacy fleet.
- The new ultra-low viscosity lubricant developed, 0W-16, successfully passed the standard engine test, Sequence VIE with a 2.1% fuel economy improvement. This oil is for future vehicle models.
- A new 2018 platform engine has been selected for engine durability test development. This engine has been disassembled and parts have been received for surface texturing. A low cost soft mask technology has been developed to fabricate surface textures on engine parts.

DOE Technical Targets and Objective

We attained the 2015 technical target of 2% fuel economy increase for cars and light trucks (the legacy fleet) via advanced lubricants without sacrificing engine durability.

0W-20 and 0W-16 Advanced Low Viscosity Lubricants Development and Testing

To develop an advanced formulation for the low viscosity lubricants, the key factors are the use of new friction modifiers (FMs) and new viscosity modifiers (VMs). Conventional and state of the art VMs and FMs were solicited from industrial companies and collaborators, and a large number of FMs and VMs were received under non-disclosure agreements for formulation development. For FM screening, several types of bench test equipment were used: the Mini-Traction Machine for friction measurement, the Plint ring-on-liner reciprocating rig, the four-ball wear tester, the pin-on-disk machine, and the high frequency reciprocating rig. Figure VI.9.1 shows a typical example of the results of FM screening test results. The data are plotted using the Stribeck curve convention of friction values starting from a boundary lubrication regime at low speeds, entering into a mixed lubrication regime, and ending up at the hydrodynamic lubrication low friction values.

As can be seen, the baseline formulation without FM shows high friction values. When FM A is added, the boundary friction is lowered. FM B is much more effective; it lowers the boundary friction and the mixed lubrication friction. FM C shows dramatic friction reduction under boundary and mixed lubrication regimes. FM C, however, is an experimental additive not yet commercialized and while its effect on friction is excellent, it may interfere with other additives. Before FM C can be used, a range of compatibility tests have to be conducted. This is an iterative process.

After much iteration, the final formulations for 0W-20 and 0W-16 were developed. Two prototype lubricants were blended and sent for engine testing. At the time of testing, the GF-6 specifications were not finalized and Sequence IVE was undergoing precision testing. The test procedure was modified for 0W-16 since Sequence IVF was still under development, so the two formulations were tested in Sequence IVE.

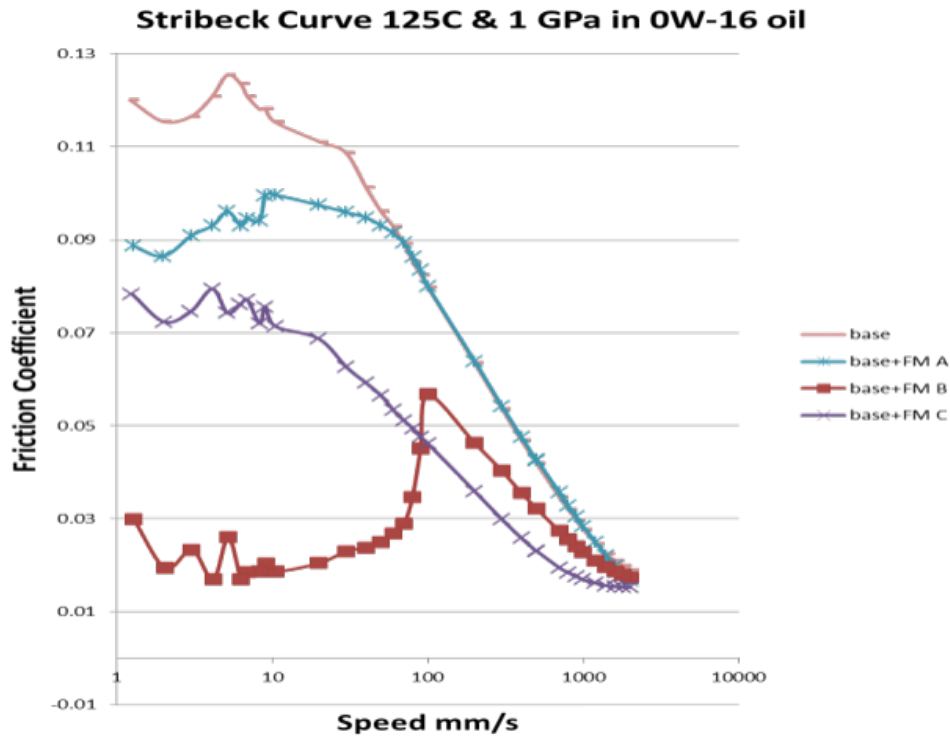


Figure VI.9.1 - Comparison of friction modifiers using the Mini-Traction Machine at 50% slide-to-roll ratio

To ensure the test results were precise, four engine tests were conducted using the same test stand and engine. Table VI.9.1 tabulated the engine test results.

Table VI.9.1 - Sequence IV Engine Dynamometer Test Results

	Candidate 0W-16 GF-6?	Candidate 0W-20 GF-6A	Baseline 5W-30 GF-5	Candidate 0W-20 GF-6	Baseline 5W-30 GF-5		
Viscosity@100	6.9	8.7	10.7	8.7	10.7	0W-20 Fuel economy Improvement Over Baseline (5W-30)	0W-16 fuel economy Improvement Over Baseline (5W-30)
Viscosity@40	28.2	36	62	36	62		
HTHS@150 °C	2.27	2.64	3.13	2.64	3.13		
Viscosity Index	220	232	163	232	163		
FEI-1 (new oil)	2.06%	1.84%	1.19%	2.13%	1.01%	0.89%	0.96%
FEI-2 (aged)	1.97%	2.37%	0.72%	2.28%	0.92%	1.51%	1.15%
FEI-SUM	4.03%	4.21%	1.91%	4.41%	1.93%	2.39%	2.11%

HTHS – high temperature high shear; FEI – fuel economy improvement

The Sequence VIE engine dynamometer test uses an internal test stand reference oil (20W-30) for comparison against the candidate oil being tested. The test stand reference oil is run prior to the candidate oil test. The percent improvement number shown in Table VI.9.1 reflects the fuel economy improvement of the candidate

oil over the test stand reference oil. Since the DOE program mandates the baseline technology to be current commercial lubricants (dominant viscosity grade of 5W-30), a current commercial 5W-30 oil was obtained and run in the series to serve as the baseline technology for comparison. The candidate oil was tested against the internal test stand reference oil then compared with the commercial baseline oil results.

As can be seen in Table VI.9.1, the baseline 5W-30 oil has the FEI-SUM of 1.91% and 1.93% over the test stand reference oil. The precision of the repeat tests is excellent. The 0W-20 formulation was also repeated to make sure the precision is within test limits. The FEI-SUM of the 0W-20 are 4.21% and 4.41% over the reference oil, not as tight as the 5W-30 baseline technology oil repeat. The results are averaged to yield the net average fuel economy improvement of the 0W-20 formulation over the baseline case to be 2.39%. The 0W-16 has a net 2.11% fuel economy improvement over the baseline case. Both formulations have demonstrated that they have exceeded the 2% fuel economy improvement goal set in the solicitation, meeting the DOE fuel efficiency goal.

Engine Durability Test Development and Evaluation of Materials Technology

Measuring engine durability using an engine dynamometer test protocol is not an easy task. The engine chosen must have the critical attributes of the majority of the engine population at that time. In 2014, at the beginning of this project, the consensus of the project team was to pick the engine used to measure fuel economy in the ASTM Sequence VI for durability testing, relating both fuel economy and engine durability under ultra-low viscosity lubricants. The engine was a 2009 V-6 engine. During the ensuing years from 2014 onward, many fuel efficient engine technologies have been incorporated into production engines. The project calls for 0W-16B category oil for the use of “future vehicle models,” so using a 2009 engine for testing may not be appropriate. The project team then decided to switch to a more modern engine for durability testing. To maintain the link to fuel economy, the new engine fuel economy will also be tested.

The new engine chosen for the project is a fifth generation 5.3 L V-8 engine. It delivers a combination of advanced technologies, including direct fuel injection, active fuel management (cylinder deactivation), and dual-equal camshaft phasing (variable valve timing) that support an advanced combustion system. The fuel economy technologies incorporated in this engine include: (1) direct injection technology, which allows the mixture to be leaner, so less fuel is required; (2) active fuel management technology, including cylinder deactivation (four out of eight) under cruising conditions; (3) variable valve timing, in which the dual-equal cam phasing system adjusts camshaft timing at the same rate for both intake and exhaust valves; and (4) advanced materials and surface treatments that were incorporated on the engine parts already.

A vehicle chassis dynamometer test will be used following an oil flush and fill. For each oil, daily testing will include using the cold start Federal Test Procedure (city drive cycle) followed by a double highway driving cycle for one day. Then the test will be repeated for five days to constitute a test sequence for that oil. The cold start Federal Test Procedure and highway drive cycle is the test sequence typical for Corporate Average Fuel Economy determination. Testing in this manner can show statistically significant improvements in efficiency from engine oil formulations at $\pm 0.5\%$ fuel economy improvement.

Preliminary Engine Durability Test Protocols and Test Plan

Two new L83 engines will be used for testing. One will be disassembled for the parts to be textured and another engine will serve as the baseline. To evaluate the friction reduction resulting from the textured components a motored engine friction evaluation may be performed. The motored friction test apparatus consists of an alternating current dynamometer coupled with a precision in-line torque meter. Following the motored friction evaluation, the engine with textured components will be installed in a vehicle and baseline Federal Test Procedure/highway fuel efficiency tests will be conducted. The vehicle will then be subjected to a corporate standard durability test. After the durability test is complete additional fuel efficiency tests may be performed. Textured components and their associated non-textured surfaces will be measured for surface morphology changes and wear depths. Measurements will be made using a phase-shifting interference microscope. The test procedure may be changed or modified if the test results warranted any changes.

Engine Surface Texture Fabrication and Evaluation

Surface textures, properly designed, can reduce interfacial friction by generating hydrodynamic pressure to transit to elasto-hydrodynamic or from boundary lubrication into hydrodynamic lubrication mode under steady state operating conditions. Many engine components today have incorporated a simple low cost micro-textural feature along the direction of sliding in the form of parallel grooves, which function to create additional lubricant reservoirs to prevent seizure due to lubricant starvation, wear debris trapping to reduce abrasion, and enhanced lubricant flow. But this comes at a cost of increased contact pressure due to reduced contact area. This kind of texture is often referred to as the passive texture. The effect on friction reduction is minimal. Active surface texture seeks to generate lift force to reduce the normal force acting on the interface. This can be achieved by putting discrete surface dimples with controlled size, shape, and depth at strategic locations of the load-bearing areas of the engine component surfaces. Under sliding conditions, the textures generate hydrodynamic fluid pressure and hydrostatic pressure due to the compression on the trapped lubricant inside the textural features (dimples, grooves, ellipses, etc.). This is referred to as the active textures, which has been proven effective in laboratory and rig tests. The drawback of this approach is the complicated fabrication processes and the high costs associated with every part that is textured. To overcome this barrier, a low cost convenient fabrication technique has been developed to texture the following engine components: piston ring, main shaft bearings, cam-roller lifters, piston pins. For evaluation the motored engine testing approach is used, followed by vehicle chassis engine dynamometer tests.

Fabrication Barriers

To fabricate complex discrete dimples on curved, irregular engine surfaces with advanced materials is a difficult challenge. Literature revealed that two categories of fabrication techniques are feasible: laser ablation texturing and microlithography-electrochemical etching. Laser texturing is limited in terms size and shape.

For microlithography fabrication techniques, the textural fabrication process has two steps: a texture pattern is made on silicon surface using micro-lithography by depositing photoresist on the surface followed by ultraviolet irradiation to develop the mask. The mask is designed for use on flat surface, not suitable for curved or rough surfaces. To be able to fabricate on curved surfaces, a soft mask made from polymeric film was directly fabricated using dry etch as shown in Figure VI.9.2. This avoids the use of a second ultraviolet irradiation to develop the texture pattern on the engine parts. The soft mask is then peeled off from the silicon wafer and wrapped around an engine component surface ready for electrochemical etching to create the texture on the surface.

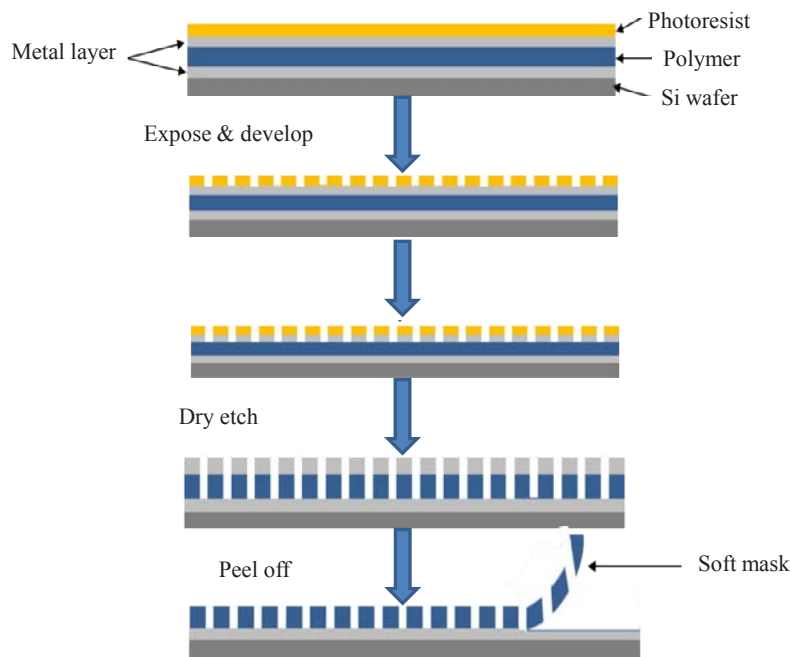


Figure VI.9.2 - Schematic diagram of the direct soft mask fabrication process with only one ultraviolet irradiation

Challenges Posed by Highly Concave Bearing Surfaces

With direct-etched soft mask technology, the cost of surface texture fabrication on flat or convex surfaces was reduced by an order of magnitude. While the creation of the master textural pattern for a specific part remains labor intensive, but duplicating the mask is quick and low cost, very similar to the cost curve for the microelectromechanical systems industry where cost per device plunges as volume goes up. This technology will make fabricating complex surface textures on engine parts practical.

For highly concave surfaces such as the bearing half shown in Figure VI.9.3, the thin soft mask has to be laid down to the inside bearing surface perfectly conformal to the surface without air bubbles. This creates microscale alignment and surface conformal contact adhesion challenges. Initial attempts failed since the engine bearing surfaces, some with coatings on them, are relatively rough and uneven as compared to silicon wafer. To overcome this obstacle, a special jig was designed and constructed to provide a stable structure where alignment and uniform contact pressure can be applied. The jig is shown in Figure VI.9.3.

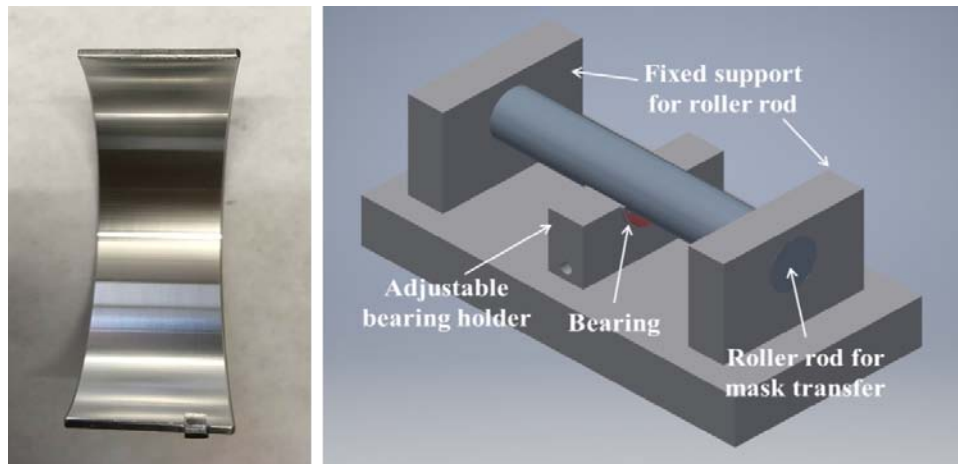


Figure VI.9.3 - Conformal contact press jig for putting on soft mask on highly concave bearing surface
(Source George Washington University)

Once the fabrication process development is completed, the texture designs began. The design is based on worn surface engine parts where we can detect the location, damage, and estimate the lubrication mechanism. Based on this information and the materials composition information supplied by GM (proprietary information), we designed various surface textural patterns on 52100 test specimens and then conducted bench testing to confirm the effectiveness of the texture design.

The engine components are currently being textured and when completed, they will be sent to GM where the parts will be reassembled into an engine and tested in motored friction test followed by fuel economy testing in an engine chassis dynamometer test.

Conclusions

The following conclusions can be made.

- Two new low viscosity, fuel-efficient lubricants, 0W-20 and 0W-16, have been developed using state-of-the-art additive components supplied by additive partners.
- These new lubricants were tested in the latest ASTM GF-6 test procedure available and multiple engine tests were conducted to demonstrate that they both exceeded 2% fuel economy improvement.
- The 0W-16 low viscosity formulation will be used in the upcoming engine chassis dynamometer testing using a modern engine equipped with many fuel efficient technologies.

- One engine has been disassembled for surface texturing at George Washington University. A novel low-cost surface texture fabrication process has been developed that will enable potential commercialization of surface texture technology. After the parts have been textured, they will be reassembled for quantitative fuel efficiency measurements at GM.

VI.10 A Novel Lubricant Formulation Scheme for 2% Fuel Efficiency Improvement

Qian J. Wang, Principal Investigator

Northwestern University
2145 Sheridan Road
Evanston, IL 60208
E-mail: qwang@northwestern.edu

Michael Weismiller, DOE Technology Manager

U.S. Department of Energy
E-mail: Michael.Weismiller@ee.doe.gov

Start Date: January 18, 2014 End Date: December 31, 2017
Total Project Cost: \$1,000,000 DOE share: \$1,000,000 Non-DOE share: \$0

Acknowledgments

Co-Authors

Yip-Wah Chung, Tobin J. Marks, Tracy L. Lohr, Michael Desanker, Jie Lu, Xingliang He;
Northwestern University
Ali Erdemir, Aaron Greco; Argonne National Laboratory

NETL Project Manager

Carl P. Maronde, National Energy Technology Laboratory

Project Introduction

Achieving more than 2% fuel efficiency improvement of light and medium vehicles requires significant friction reduction in the powertrain and drivetrain systems; if by reducing boundary friction alone, this requires at least a 30% friction reduction [1]. Better friction modifiers (FMs) are needed as a component to achieve this boundary lubrication goal. The frictional loss due to high viscous shear at high speeds cannot be simply tackled by using oil of low viscosity because this will raise the friction at low speeds. We need a chemically and mechanically stable viscosity modifier (VM) that makes the lubricant less viscous only at high shear rates. Many lubricants undergo some shear thinning in the contact interface, resulting in lower friction than expected from Newtonian flow assumptions [2,3,4,5]. A key problem to solve is to have a modified lubricant that only responds to high shear rate via molecular deformation, not scission. More friction reduction mechanisms should also be included, such as using nanoparticles; hexagonal boron nitride (h-BN or α -BN) and boron oxide (B_2O_3) are two of well-known solid lubricants, which can be excellent material choices for the nanoparticles.

Objectives

This project aims to develop novel lubricant formulations for improving vehicle fuel efficiency by at least 2% without adversely impacting vehicle performance or durability.

- Reduce friction due to asperity rubbing in the boundary lubrication regime (start-up and low-speed operations) by using new heterocyclic FMs
- Understand the boundary lubrication improvements caused by the new FMs via molecular dynamics (MD) simulations
- Temporarily reduce the lubricant viscosity (temporary shear thinning) in hydrodynamic lubrication regimes (medium- to high-speed cruise operations)
- Synthesize, test, and validate a new type of di-block copolymer VM for hydrodynamic lubrication
- Develop a surface treatment method of boron-based nanoparticles for extra tribological benefits

- Confirm at least 25–30% friction reduction through the whole lubrication regime
- Demonstrate the desirable fuel efficiency enhancement by conducting industrial scale tests

Approach

The fuel efficiency goal has to be accomplished by reducing friction in the entire operation regime. The S-and-P-free heterocyclic FMs and the shear thinning VMs should be able to significantly lower frictions in boundary (low-speed) and hydrodynamic (high-speed) lubrication regimes, respectively, and the nanoparticles-based additives will facilitate reducing extra friction and wear. The research tasks include synthesizing “designer” additives, characterizing their properties at conditions comparable to those in real-world applications, modeling the frictional and viscosity behaviors for design optimization, and testing their friction reduction capability. The present research is being conducted collaboratively by an Northwestern University–Argonne National Laboratory team, supported by collaborative industries. All additives were synthesized or prepared at the Northwestern University’s chemistry laboratory, tested at the tribology laboratories at Northwestern University and Argonne National Laboratory.

Results

Adsorption/Desorption Studies of the Heterocyclic FMs by MD Simulations

The thermally stable alkyl-cyclen additives have been repeatedly proven to be the best FMs (up to 70% boundary lubrication improvement from 25°C to 200°C). A series of high-temperature tribological tests were conducted for this specific type of heterocyclic FMs: variable-temperature sliding, linear speed ramping, reciprocating sliding, and rolling–sliding operations. In addition, ultra-thin lubricant film measurements at 125°C demonstrated a more than six times enhancement of boundary lubrication film for the alkyl-cyclen FMs, while no enhancement of the boundary lubrication film was found for the correspondent commercial FMs. Detailed results of these tests can be found in our previous quarterly and annual reports. Only MD simulations of FM molecules are discussed here to address the boundary lubrication mechanisms.

Figure VI.10.1a plots variations of the interaction energy versus simulation time for alkyl-cyclen molecules and the corresponding alkylamine FM molecules. Higher interaction energy means stronger adsorption of FM molecules to the surface. The adsorbed C12Cyc and C18Cyc molecules always have higher interaction energy than do the adsorbed C12amine and C18amine molecules no matter how the temperature varies. C6Cyc molecules have short side chains and may suffer from ineffective chain cohesion and steric repulsion due to internal rotations of the methyl terminal groups. The decreased interaction energy at high temperatures for C6Cyc molecules could lead to their desorption from the surface. A similar reduction of interaction energy with temperature is found for all adsorbed alkylamine molecules (Figure VI.10.1a), indicating their desorption as well. Desorption of the alkylamine molecules should be caused by rupture of the hydrogen bonds at elevated temperatures.

The surface coverage analysis by counting the molecules staying on the surface, as shown in Figure VI.10.1b, further demonstrates adsorption and desorption of the alkyl-cyclen or alkylamine molecules at variable temperatures. The surface coverages of the adsorbed C12Cyc and C18Cyc molecules do not decrease with temperature, meaning that desorption of these two heterocyclic molecules does not occur in this temperature range. When temperature increases from 120°C to 200°C, a clear desorption of the C6Cyc molecules is shown by reduction of the surface coverage percentage from ~90% to ~40%. The adsorbed layers of all alkylamine FM molecules deteriorate as temperature increases (Figure VI.10.1b). Fewer and fewer alkylamine molecules are able to remain bound to the surface at higher temperatures, and less than one half of the surface coverage remains at 200°C.

Figure VI.10.2 compares the mean square displacements (MSD) of different adsorbed FM molecules at 120°C. The MSD magnitude indicates atomic diffusivity of the adsorbed molecules. The average travel distances by the C12amine and C18amine molecules on the hydrated silica surface could be about one order of magnitude higher than those by the well adsorbed C12Cyc and C18Cyc molecules. The significantly lower MSD values of these two heterocyclic FM molecules imply that they are well adsorbed and do not move freely even at the high temperature. For the adsorbed C6Cyc molecules, their MSD increases greatly as the simulation time

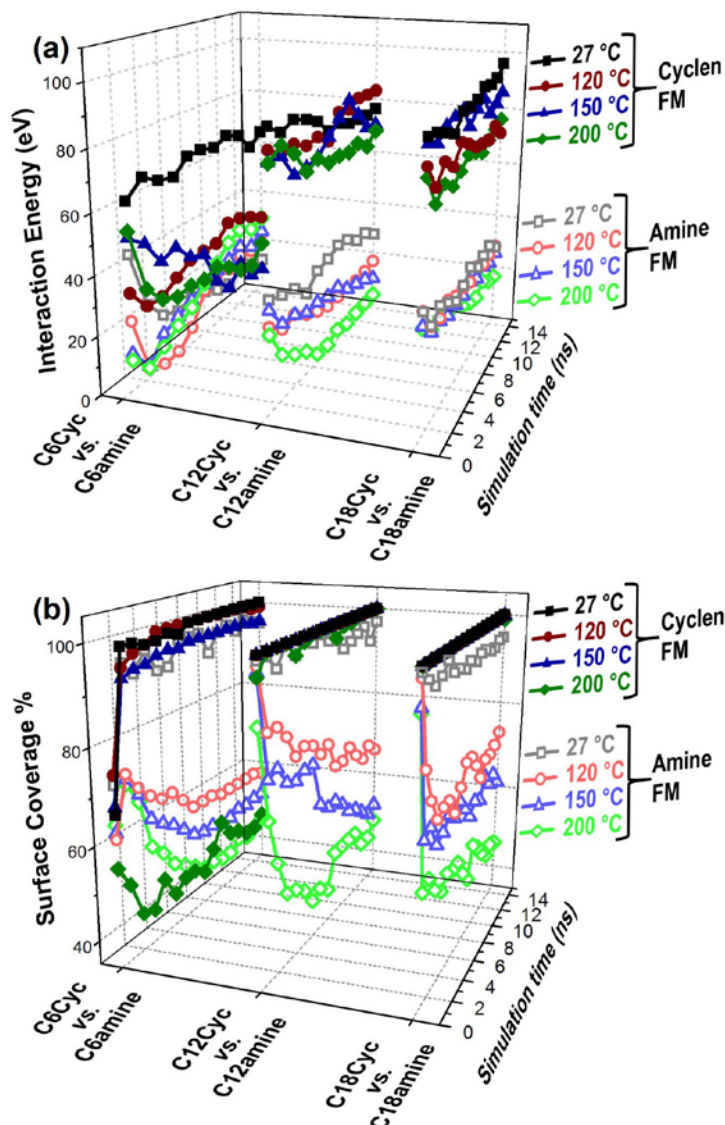


Figure VI.10.1 - MD simulation results: interaction energy (a) and surface coverage (b) of alkyl-cyclen (dark solid-dot curves) and alkylamine (light open-dot curves) FM molecules at different temperatures

increase due to desorption during the later stage. These modeling results demonstrate that the high-temperature adsorption stability of the heterocyclic C12Cyc and C18Cyc molecules is much higher than that of the conventional alkylamine-based FM molecules.

Synthesis and Test of the Diblock Copolymer for Hydrodynamic Lubrication

Atom transfer radical polymerization with a metallocene catalysis process was found to be the most suitable approach for synthesizing the diblock copolymer VMs. The presence of both branched block (Block I) and coiled block (Block II) in the polymer was confirmed by nuclear magnetic resonance spectroscopy. Gel permeation chromatography confirmed the formation of a single polymer, rather than two separate polymers. The newly developed diblock copolymer VMs are completely soluble in base oil. By adjusting the amount of catalyst or the duration of atom transfer radical polymerization process, molecular weight (M_n) of the branched block or the coiled block could be regulated, and the block ratio, ϕ , is defined by Equation 1 listed below:

$$\phi = \frac{M_n (\text{Coiled Block or Block II})}{M_n (\text{Branched Block or Block I})} \quad (1)$$

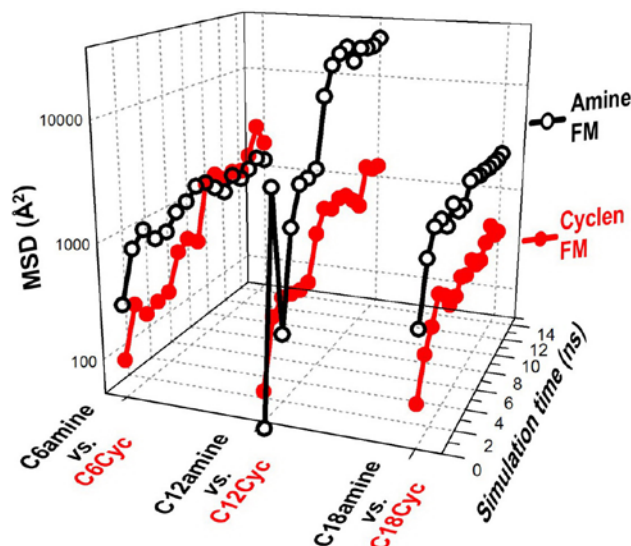


Figure VI.10.2 - MSD of the alkyl-cyclen (solid-dot curves) and alkylamine (open-dot curves) FM molecules recorded during the MD simulation at 120°C

The block ratio effect on shear thinning properties of the copolymer VMs is studied first by performing hydrodynamic lubrication tests at different slide-to-roll (S/R) ratios under 1 GPa contact pressure. Entrainment speed and temperature were maintained at 2 m/s and 125°C, respectively. Poly- α -olefin 4 cSt (PAO4) oils containing 4 wt% diblock VMs were tested. They are listed in the order of ϕ from small to large as: Diblock1 < Diblock2 < Diblock3 < Diblock4. Diblock4 with the largest ϕ fraction could decrease friction coefficient the most (Figure VI.10.3a), while the least friction reduction was found for Diblock1 with the smallest ϕ . About 50% to 60% friction is reduced in the hydrodynamic lubrication regime at 125°C by the Diblock4. An easy onset of the shear thinning process is thus proven for it.

More shear thinning experiments of the Diblock4 VM in PAO4 oils were conducted under 800 MPa contact pressure. A commercial olefin copolymer (OCP) VM was evaluated together with a fully formulated synthetic 5W30 oil and a premixed commercial VM package. Molecular weight of the commercial OCP VM is at least one order of magnitude higher than that of the newly synthesized VMs (~100s kDa vs. ~10s kDa). Because of this huge difference of the molecule sizes, concentration effects studied before (please see our previous quarterly reports) showed that 2 wt% and 8 wt% were needed, respectively, for the OCP VM and the Diblock VM in PAO4 oils for the optimum hydrodynamic lubrication results. Comparing to the commercial OCP VM, much smaller Diblock4 VM demonstrates the comparable or better shear thinning performance in Figure VI.10.3b. A premium VM formulation consisting of 65% Diblock4 and 35% OCP could bring about even greater lubrication benefits. 10 wt% of the 65Diblock/35OCP Formulation in PAO4 oil is found to perform notably better than the individual constituent VM in the same base oil at their optimal concentrations. Such a great lubrication improvement provided by the 65Diblock/35OCP Formulation outperforms the beneficial tribological performances gained from the synthetic 5W30 oil and the commercial VM packaged oil (Figure VI.10.3b).

An obvious improvement of viscosity index (VI) was demonstrated for the newly synthesized diblock VM as well in our previous report. It is noted that weight percentage of the commercial OCP used to formulate actual engine lubricants is rarely more than 3%, normally ~1% or 2%. Just 8 wt% of the much smaller Diblock VM molecules enable the base oil to have a higher VI than do 2 wt% of the much larger OCP VM molecules (~240 vs. ~189). VIs of the synthetic 5W30 oil and the commercial VM packaged oil were measured to be ~161 and ~182, respectively. The higher the VI is, the less the oil viscosity loss with temperature. The unique shear thinning process and (thermo-) thickening property are believed to originate from the structure and/or conformation changes of the new Diblock VM molecules, and the corresponding characterizations are discussed in the next section.

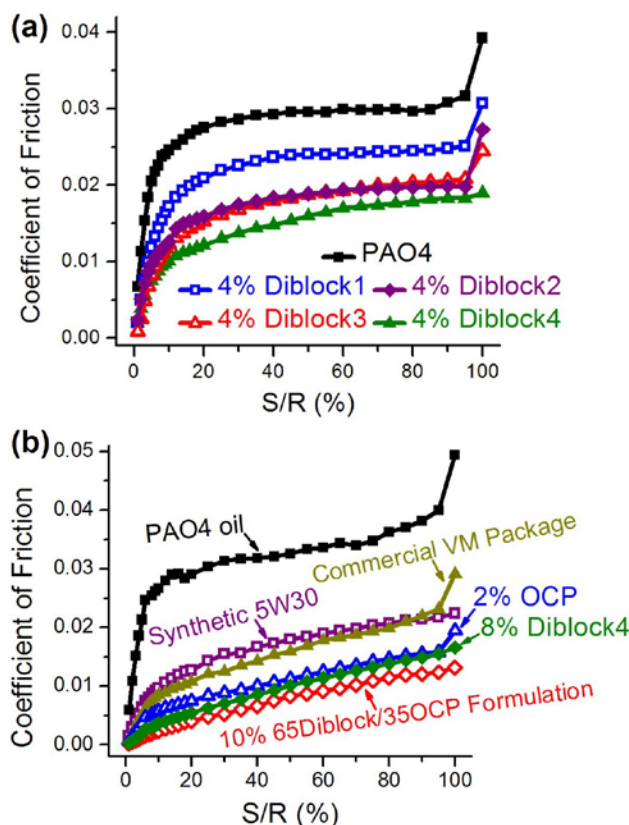


Figure VI.10.3 - (a) Variation of friction coefficients versus S/R ratio in the presence of different diblock VMs at 125°C under 1 GPa contact pressure. (b) Variation of friction coefficients versus S/R ratio in the presence of different lubricants at 125°C under 800 MPa contact pressure.

Understanding of the Viscosity Modification Behaviors

For VM molecules dispersed in a base oil, their miscibility and diffusivity are critical for the viscosity modification process. In a dilute solution system, viscosity contribution of the solute molecules is used to define intrinsic viscosity. The solution viscosity of a dilute polydisperse system can be expressed by Equation 2:

$$\frac{\eta}{\eta_s} = 1 + [\eta]c + k_h [\eta]^2 c^2 \approx 1 + [\eta]c, \text{ when } c \text{ is small} \quad (2)$$

where η (mPa·s) is the dynamic viscosity of solution, η_s (mPa·s) is the dynamic viscosity of solvent, $[\eta]$ ($\text{mL} \cdot \text{g}^{-1}$) is the intrinsic viscosity of solution, c ($\text{g} \cdot \text{mL}^{-1}$) is the solute concentration, and k_h is the Huggins coefficient. If the dynamic viscosity ratio between a VM mixture and its base oil is plotted against the VM concentration, the slope of the curve can be used to represent the intrinsic viscosity of this oil mixture. As shown in Figure VI.10.4a, the slope becomes slightly steeper after the concentration of the Block I VM in PAO4 oil exceeds $\sim 0.032 \text{ g} \cdot \text{mL}^{-1}$. No similar change on the slope is found for the Block II VM in the same oil. By linking the two blocks together, the Diblock VM in PAO4 oil induces a more abrupt increase in the slope. Different polymer conformations in the base oil could be inferred from the variable change of the intrinsic viscosity for different VM molecules. Little change of intrinsic viscosity indicates a good miscibility of the individual block molecules (e.g., Block I or Block II) with the base oil. The well miscible polymer molecules stretch themselves into a good solvent matrix, and the intrinsic viscosity mainly associates with translation motions of these molecules. However, the sudden change of the intrinsic viscosity for the Diblock VM could be due to limited miscibility of their coiled polymer molecules in a relatively poor solvent. Random walk of immiscible molecules in a poor polymer solution should have rotation and vibration degrees of freedom in addition to the translation freedom of movement. As a result, rotation and/or vibration of the sphere-like coiled Diblock molecules contribute more to the abrupt intrinsic viscosity change.

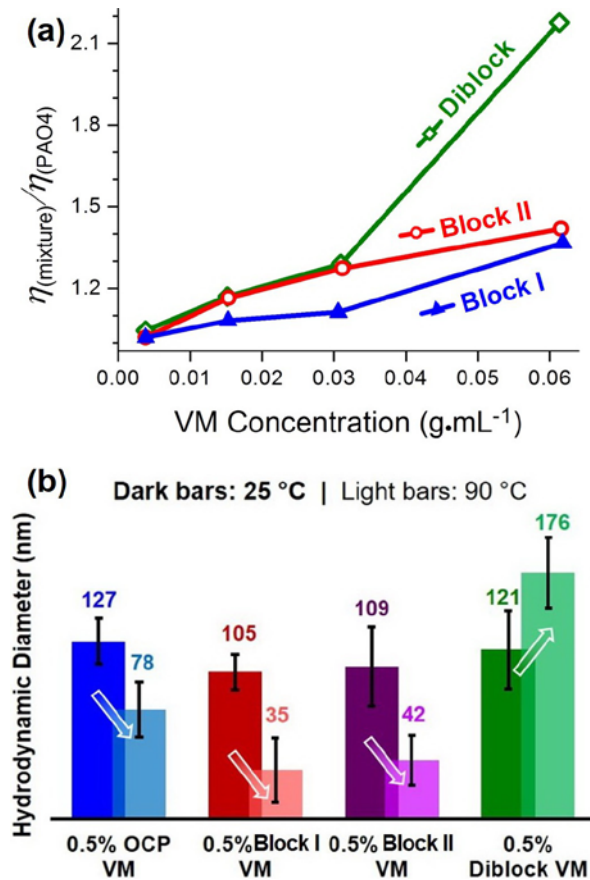


Figure VI.10.4 - (a) Variation of viscosity ratio $[\eta_{(\text{mixture})}/\eta_{(\text{PAO4})}]$ versus VM concentration at 100°C. (b) Dynamic light scattering measurements of hydrodynamic diameters for different dilute VM-PAO4 oil solutions.

Diffusivity of the VM molecules in PAO4 oil can be evaluated by conducting dynamic light scattering experiment of the corresponding dilute polymer solutions. Hydrodynamic diameters were measured to decrease as temperature increased for all VM molecules in PAO4 oil, except the Diblock VM (Figure VI.10.4b). During the dynamic light scattering experiments, hydrodynamic size of the tracer molecules moving in a continuum solvent is calculated through the Stokes–Einstein equation, Equation 3:

$$R_h = \frac{K_B T}{6\pi\eta_s D_t} \quad (3)$$

where R_h (m) is the hydrodynamic radius, K_B ($\text{J}\cdot\text{K}^{-1}$) is the Boltzmann's constant, T (K) is the absolute temperature, η_s ($\text{Pa}\cdot\text{s}$) is the dynamic viscosity of solvent, D_t ($\text{m}^2\cdot\text{s}^{-1}$) is the tracer diffusion coefficient. In a dilute solution, the hydrodynamic diameters are inversely proportional to dynamic viscosity of the base oil and diffusivity of the polymeric VM molecules. When heating the PAO4 oil from 25°C to 90°C, its dynamic viscosity decreases from ~ 29 mPa·s to ~ 4.6 mPa·s, and this viscosity loss should contribute positively to the measured hydrodynamic size. Thus in the diluted OCP, Block I, and Block II solutions, diffusivity of these molecules must be increased radically in order to achieve the reduced hydrodynamic diameters, as shown in Figure VI.10.4b. Due to the cohesive interaction originated from the alkyl-chain dispersion forces, these stretchable VM molecules can be well blended into the short olefin matrix, facilitating their diffusion processes greatly in the heated base oil. Figure VI.10.4b also shows that the hydrodynamic size of the Diblock VM-dispersed PAO4 oil is increased by ~ 1.5 times upon heating, while the solvent viscosity is decreased by ~ 6.3 times under the same condition. The positive effect of the solvent viscosity loss on the hydrodynamic size is outweighed by the reduced diffusivity of the Diblock VM molecules in PAO4 oil. Unlike the stretchable and well miscible OCP, Block I, and Block II molecules, the coiled Diblock VM molecules should act like rigid spheres in the base oil, which also have limited miscibility with the solvent. At elevated temperature, the

expanded sizes of these coiled molecules would make their diffusion processes experience more hindrance in the inadequately blended surroundings.

Hydrodynamic lubrication film formation capabilities of the OCP VM and the Diblock VM are inspected in Figure VI.10.5 before and after increasing the S/R ratio. The film thickness formed by the oil containing the Diblock VM increases after the S/R ratio changes from 0% to 10%, while that formed by the oil containing the OCP VM decreases visibly. In short, conformation changes and evolvments of different polymeric VM molecules at the molecular level dominate their performances as lubricant additives. Specifically, well-coiled block of the Diblock VM should act as a nano-bearing ball and can roll under shearing; its branched block would perform like a short tail, optimizing oil miscibility and dragging the molecule into the contacts. In the hydrodynamic lubrication tests, rolling of the coiled diblock VM molecules leads to an extra friction reduction besides a typical shear thinning process. At the molecular level, there is a proper integration of miscibility and diffusivity for the Diblock VM in PAO4 oil behind the apparent viscosity modification and shear thinning demonstrated in our experiments.

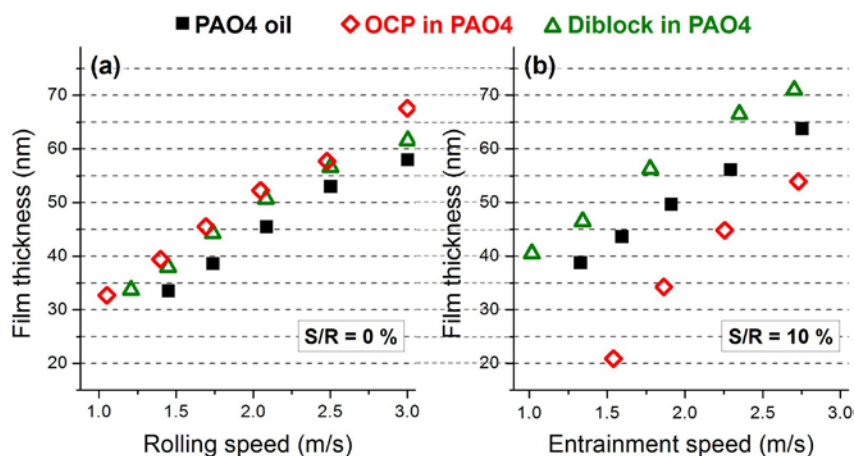


Figure VI.10.5 - Film thickness measurements at 125°C at 0% (a) and 10% (b) S/R ratio

Conclusions

- Alkyl-cyclen derivatives were developed to be the most superior heterocyclic FMs for boundary lubrication applications in terms of efficient friction reduction and great stability enhancement.
- The enhanced surface adsorption, prolonged surface residence, reduced desorption rate, and desirable boundary lubrication film reinforcement at high temperature were demonstrated to be fundamental and unique for the new alkyl-cyclen FMs.
- Novel diblock copolymer VMs were designed and synthesized successfully for hydrodynamic lubrication.
- (Thermo-) thickening and shear thinning of the diblock copolymer VMs were evaluated; block ratio and concentration effects were studied; a premium VM formulation was prepared; and its exceptional hydrodynamic lubrication performance was confirmed.
- Understanding of the viscosity modification process was established; the effects on the intrinsic viscosity, hydrodynamic size, and lubrication film formation were investigated.
- Miscibility and diffusivity were compared for different VM molecules; their hydrodynamic lubrication properties were inferred to be influenced by the corresponding conformational changes of the polymeric VM molecules.
- More than 40% friction reduction through the whole lubrication regimes was confirmed by using the new heterocyclic FMs and the new di-block copolymer VMs.

References

1. Holmberg, K., P. Andersson, and A. Erdemir. "Global energy consumption due to friction in passenger cars." *Tribol. Int.*, 47, 221–234 (2012).
2. Ehret, P., D. Dowson, and C. Taylor. "On lubricant transport conditions in elastohydrodynamic conjunctions." *Proc. R. Soc. Lond. A*, 454, 763–787 (1998).
3. Bronshteyn, L.A. and J.H. Kreiner. "Energy efficiency of industrial oils." *Tribol. Trans.*, 42, 771–776 (1999).
4. Zolper, T., Z. Li, C. Chen, M. Jungk, T. Marks, Y.-W. Chung, and Q. Wang. "Lubrication properties of polyalphaolefin and polysiloxane pubricants: Molecular structure–tribology relationships." *Tribol. Lett.*, 48, 355–365 (2012).
5. Akbarzadeh, S. and M. Khonsari. "Performance of spur gears considering surface roughness and shear thinning lubricant." *J. Tribol.*, 130, 021503 (2008).

Key Fiscal Year 2017 Publications

1. Desanker, M., X. He, J. Lu, P. Liu, D. Pickens, Z. Liu, M. Delferro, T.J. Marks, Y.-W. Chung, Q.J. Wang. "Alkyl-cyclens as effective sulphur- and phosphorus-free friction modifiers for boundary lubrication." *ACS Appl. Mater. Interfaces*, 2017, 9, 9118.
2. Desanker, M., X. He, J. Lu, Z. Liu, M. Delferro, N. Ren, F. Lockwood, A. Greco, A. Erdemir, T.J. Marks, Q.J. Wang, Y.-W. Chung. "High-performance heterocyclic friction modifiers for boundary lubrication." submitted to *Tribol. Lett.*, 2017.
3. He, X., J. Lu, M. Desanker, A. Invergo, T. Lohr, T.J. Marks, Y.-W. Chung, Q.J. Wang. "Boundary lubrication mechanisms for high-performance friction modifiers." To be submitted, 2017.
4. Three more journal papers are under preparation.

VI.11 Improved Fuel Economy through Formulation Design and Modeling

Gefei Wu, Principal Investigator

Valvoline LLC
100 Valvoline Way
Lexington, KY 40509
E-mail: gwu@Valvoline.com

Michael Weismiller, DOE Technology Manager

U.S. Department of Energy
E-mail: Michael.Weismiller@ee.doe.gov

Start Date: October 1, 2013	End Date: September 28, 2018	
Total Project Cost: \$1,195,793	DOE share: \$593,869	Non-DOE share: \$601,924

Acknowledgments

Co-Authors

Anant Kolekar, Kwame Duho, Amol Savant, Fran Lockwood; Valvoline LLC

Project Introduction

Improving automotive fuel efficiency can help reserve energy resources and reduce greenhouse gas emissions [1]. Automotive vehicles rely on lubricant films to provide wear protection to their moving components. Lubricant film thickness is, in general, determined by oil viscosity metrics: the higher the viscosity, the thicker the film. However, thicker oil films induce higher traction, which decreases the fuel efficiency. The general trend for fuel efficient lubricants is to have a lower viscosity. Nevertheless, this strategy introduces the possibility of reduced component durability, and a state-of-the-art balance in automotive lubricant formulations is needed in order to have both wear protection and fuel efficiency. Automotive lubricants consist of base oils and additives like antiwear agents, antioxidants, viscosity index improvers, corrosion inhibitors, and friction modifiers. With advanced technology of lubricant additives, low viscosity lubricants have been developed by utilizing special antiwear agents and friction modifiers, novel base oils, and viscosity modifiers.

In Budget Period 1, formulation, modeling, and benchtop testing were finished and milestones have been met on time. In Budget Period 2, dynamometer fuel efficiency (FE) verification tests and SAE J1321 were performed; most milestones were reached. The J1321 test results passed the go/no-go criteria of an overall FE improvement of >2%.

Objectives

The objective of this project is to develop novel lubricant formulations that are expected to improve the FE of medium-duty, commercial, and military vehicles by at least 2% (improvement based on comparative results from engine dynamometer testing, chassis dynamometer testing or test track, e.g., SAE J1321) without adverse impacts on the vehicle performance or durability. This will be accomplished through formulation design and modeling and testing of engine, transmission, and axle lubricants.

Target level performance:

- Engine oil: fuel economy improvement by ~2%
- Axle oil: fuel economy improvement by ~0.5%
- Whole system: fuel economy improvement by >2% using SAE J1321
- Durability penalty: none, no detriment seen in component life at 2,000 h teardown

Approach

Valvoline has the ability to formulate automotive lubricants from individual ingredients and conduct bench top, engine dynamometer, and field tests. As an independent automotive lubricant marketer, Valvoline has opportunities working with every lubricant additive supplier and can thus combine the best additives to provide the best performance lubricants. Valvoline has been doing fuel economy improvement studies in heavy-duty oils since 2010 [2,3,4,5,6,7,8,9]. In recent years, Valvoline adopted the design of experiments method in lubricant formulation and modeling work to predict the lubricant performance, which has been proven more effective in bringing new technology and products to the market. The proposed tasks will combine oil formulation, experimental design, and new additive/base oil combinations to control friction, wear, and traction; employ mathematical modeling and prediction as well as original equipment manufacturing cooperation; and utilize bench, dynamometer, track, and fleet testing to reach the target.

The engine dynamometer test was performed at National Renewable Laboratory located in Golden, Colorado. The SAE J1321 track test was conducted at Transportation Research Center located in East Liberty, Ohio. Cummins Inc., has been supportive in engine oil property requirements and engine testing procedure.

Results

The SAE J1321 test is a vehicle level fuel consumption test which quantify the fuel economy benefits in a real world operating conditions. Valvoline conducted this test at Transportation Research Center in East Liberty, Ohio. The test was performed using an industry standardized procedure: SAE J1321-2012 “Joint TMC/SAE Fuel Consumption Test Procedure – Type II” [10]. The vehicles used for this test were Class 6 medium-duty trucks which have Cummins ISB 6.7-L 240 hp engines, Meritor axles, and Allison automatic transmissions; accordingly, three kinds of oils were tested. One truck was designated as the control vehicle for all tests while the other three trucks served as the test vehicles throughout the program. The FE improvement was calculated for each test result relative to the fuel consumed of the control truck in each segment and the baseline segment of each test truck. All testing was conducted on the Transportation Research Center’s 7.5-mi test track and each segment consisted of seven laps of the track, or a distance of 52.5 mi. After each test segment, the tested oils were drained and then double flushed with new baseline or candidate oils before filling in new baseline or candidate oils for testing.

There were five Valvoline candidate lubricants (two engine oils, two axle oils, and one transmission fluid) that had been tested along with three baselines. See Table VI.11.1 for more details. The test program was designed by a statistician (see Table VI.11.2) and results (see Table VI.11.3) were analyzed by the same statistician as well using the JMP software.

Table VI.11.1 - Valvoline Candidate Oils and Baselines for J1321 Test

Oil code	Engine oil			Axle oil			Transmission fluid	
	EO base	EO 1	EO 2	GO base	GO 1	GO 2	TO base	TO 1
Oil maker	Valvoline	Valvoline	Valvoline	Cognis	Valvoline	Valvoline	Shell	Valvoline
Oil brand	Premium Blue CJ-4	PC-11 candidate	PC-11 candidate	FE	J2360 candidate	J2360 candidate	Spirax S6 A295	TES 295 candidate
Viscosity grade	15W-40	5W-30	5W-20	75W-90	75W-90	75W-80	TES 295	TES 295
Viscosity 100 °C (cSt)	15.6	9.6	9.1	15.3	15.6	9.1	7.3	7
Viscosity 40 °C (cSt)	118.7	53.5	48.2	104.4	91.5	48.2	36	35.2
Test use	baseline	candidate	candidate	baseline	candidate	candidate	baseline	candidate

Table VI.11.2 - J1321 Test Segment Design

Segment	Control Truck			Truck 1			Truck 2			Truck 3		
	Engine	Axle	Trans	Engine	Axle	Trans	Engine	Axle	Trans	Engine	Axle	Trans
TS 0	Base	Base	Base	Base	Base	Base	Base	Base	Base	Base	Base	Base
TS 1	Base	Base	Base	Base	GO 1	TO 1	EO 2	Base	Base	EO 1	GO 2	Base
TS 2	Base	Base	Base	EO 1	GO 2	TO 1	EO 2	GO 1	Base	Base	Base	Base
TS 3	Base	Base	Base	Base	GO 1	Base	EO 1	Base	TO 1	EO 2	GO 2	TO 1
TS 4	Base	Base	Base	EO 2	Base	TO 1	Base	GO 2	TO 1	EO 1	GO 1	Base
TS 5	Base	Base	Base	EO 2	GO 2	Base	EO 1	GO 1	TO 1	Base	Base	TO 1
TS 6	Base	Base	Base	EO 1	Base	Base	Base	GO 2	Base	EO 2	GO 1	TO 1

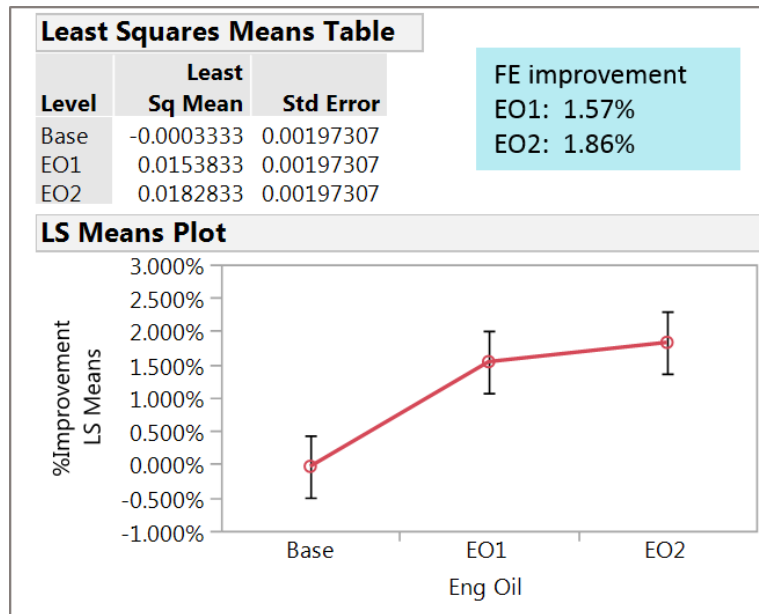
Table VI.11.3 - J1321 Test Results

	Eng Oil	Gear oil	Trans Oil	Truck	Segment	% Improvement
1	Base	GO 1	TO 1	T1	L1	0.21%
2	EO 1	GO 2	TO 1	T1	L2	2.05%
3	Base	GO 1	Base	T1	L3	-0.16%
4	EO 2	Base	TO 1	T1	L4	1.73%
5	EO 2	GO 2	Base	T1	L5	1.21%
6	EO 1	Base	Base	T1	L6	0.83%
7	EO 2	Base	Base	T2	L1	1.29%
8	EO 2	GO 1	Base	T2	L2	2.08%
9	EO 1	Base	TO 1	T2	L3	1.28%
10	Base	GO 2	TO 1	T2	L4	0.47%
11	EO 1	GO 1	TO 1	T2	L5	0.86%
12	Base	GO 2	Base	T2	L6	0.06%
13	EO 1	GO 2	Base	T3	L1	2.31%
14	Base	Base	Base	T3	L2	0.03%
15	EO 2	GO 2	TO 1	T3	L3	2.58%
16	EO 1	GO 1	Base	T3	L4	1.90%
17	Base	Base	TO 1	T3	L5	-0.81%
18	EO 2	GO 1	TO 1	T3	L6	2.08%

The statistical analysis on the testing results showed that all candidate oils are significantly different from each other in addition to being different from the baselines. Figure VI.11.1 serves as an example of statistical analysis on engine oils. The FE improvements of each Valvoline candidate are summarized in Table VI.11.4.

Table VI.11.4 - FE Improvement of Each Valvoline Candidate

Valvoline Candidate	Code	FE Improvement (%)
Engine Oil	EO 1	1.57%
Engine Oil	EO 2	1.86%
Axle Oil	GO 1	0.44%
Axle Oil	GO 2	0.72%
Transmission Fluid	TO 1	0.20%



LS – least squares

Figure VI.11.1 - Statistical analysis of FE improvement on engine oils

The statistical model can also predict the performance in FE improvement when all three kinds of oils are applied together, where greater than 2% is the key criteria of this project. Table VI.11.5 shows the data of FE improvement for different combinations of the three kinds of lubricants. It can be observed that all four combinations of Valvoline’s five candidate oils have 95% confidence intervals (CI) that included 2% FE improvement.

Table VI.11.5 - Estimated Percent Improvements for Various Oil Combinations

Engine Oil	Transmission Oil	Gear Oil	Predicted % Improvement (Lower 95% CI*, Upper 95% CI*)
EO1	Base	Base	1.06% (0.59%, 1.53%)
	T01	G01	1.68% (1.21%, 2.15%)
		G02	1.97% (1.50%, 2.44%)
EO2	Base	Base	1.35% (0.88%, 1.82%)
	T01	G01	1.97% (1.50%, 2.44%)
		G02	2.26% (1.79%, 2.73%)

Conclusions

The target of performance level of this project is overall FE >2% when a combination of Valvoline’s engine oil, axle oil and transmission fluid are applied to a medium duty Class-6 truck, which was measured by the SAE J1321 vehicle level fuel consumption test. The statistical analysis of test results showed that all four combinations of Valvoline’s five candidate oils have this potential at the 95% confidence.

References

1. Environmental Protection Agency. “Overview of Greenhouse Gases.” 2017. <http://www3.epa.gov/climatechange/ghgemissions/gases/co2.html>.
2. Kersey, V.L., A.E. Sworsiki, T.L. Caudill, J.F. Frederick, T. Bidwell, and F.E. Lockwood. “Method of Testing and Proving Fuel Efficiency Improvements.” U.S. Patent Application: 20120109579 A1, 2012.

3. Kolekar, A., A. Olver, A. Sworski, F. Lockwood. “The efficiency of a hypoid axle.” The 38th Leeds-Lyon Symposium on Tribology, 2011.
4. Kolekar, A., A. Olver, A. Sworski, and F. Lockwood. “The efficiency of a hypoid axle- a thermally coupled lubrication model.” *Tribology International*, 2013, Vol:59, Pages:203–209.
5. Kolekar, A., A. Olver, A. Sworski, and F. Lockwood. “Windage and Churning Effects in Dipped Lubrication.” *Journal of Tribology*, 2014.
6. Kolekar, A., A. Olver, A. Sworski, and F. Lockwood. “Modelling & Experimental Verification of Final Drives.” 69th STLE Annual Meeting & Exhibition, 2014.
7. Kolekar, A., A. Olver, A. Sworski, and F. Lockwood. “Lubrication system and method for reducing dip lubrication power loss.” U.S. Patent Application No. 13/965,557, WO2014028577A1 Grant No. US9360103 B2. 2014.
8. Kolekar, A., A. Olver, A. Sworski, F. Lockwood, G Wu, and X. Cheng. “Gear and Engine Oils with Reduced Surface Tension.” U.S. Patent Application: 20150148272, 2015.
9. Kolekar, A., A. Olver, A. Sworski, F. Lockwood, G Wu, and X. Cheng. “Silicon Modified Lubricant.” U.S. Patent Application: 20160257906, 2016.
10. SAE International. “J1321- 022012: JOINT TMC/SAE FUEL CONSUMPTION TEST PROCEDURE – TYPE II.” SAE International Operator Manual and Service Manual: Freightliner M16 - 2014.

Key Fiscal Year 2017 Publications

1. Wu, G., F. Lockwood, A. Kolekar, K. Duho, X. Cheng, A. Savant, and J. Burton. “Improve Fuel Economy through Formulation Design and Modeling.” DOE FY 2016 Annual Progress Report/Fuel & Lubricant Technologies, V6.

VII. System-Level Efficiency Improvement

VII.1 DOE's Effort to Improve Heavy Vehicle Fuel Efficiency Through Improved Aerodynamics

Kambiz Salari, Principal Investigator

Lawrence Livermore National Laboratory
7000 East Ave. L-090
Livermore, CA 94551
E-mail: salari1@llnl.gov

Roland Gravel, DOE Technology Manager

U.S. Department of Energy
E-mail: Roland.Gravel@ee.doe.gov

Start Date: October 1, 2017	End Date: September 30, 2018	
Total Project Cost: \$840,000	DOE share: \$840,000	Non-DOE share: \$0

Acknowledgments

Co-Principal Investigator

Jason Ortega, Lawrence Livermore National Laboratory

Project Introduction

There are roughly 2.2 million combination trucks on the road today, each traveling an average of 65,000 miles per year and consuming 12,800 gallons of fuel per year for a total of 36 billion gallons of fuel per year. These trucks consume roughly 11–12% of the total United States petroleum usage. At highway speeds, a Class 8 tractor-trailer uses over 50% of the usable energy produced by the vehicle engine to overcome aerodynamic drag. To improve the fuel economy of these vehicles, Lawrence Livermore National Laboratory (LLNL) has been conducting research in aerodynamics through use of add-on devices and a new tractor-trailer shape design. LLNL has demonstrated new drag reduction techniques and concepts for tractor-trailers and tanker-trailers. A new body shape design is proposed for the next generation of highly aerodynamic heavy vehicles with geometry, flow, and thermal integration that radically reduces aerodynamic drag and improves fuel efficiency. This project relies extensively on computational simulations and wind tunnel testing for the development of the new integrated aerodynamic body design. For the selected aero devices and concepts, additional track and on-the-road tests are performed. An important part of this effort is to join with industry in getting aerodynamic add-on devices on the road and to provide guidance to industry in design of the next generation of highly integrated heavy vehicles.

In collaboration with National Renewable Energy Laboratory, fuel-saving benefits of platooning heavy vehicles are investigated through use of scaled wind tunnel testing. The results of wind tunnel tests will be validated by National Renewable Energy Laboratory, who has established a process for conducting accurate and objective track evaluations of platooning heavy vehicles.

Objectives

- Provide guidance to industry to improve the fuel economy of a Class 8 tractor-trailer through the use of aerodynamics
- Develop innovative aerodynamic concepts for heavy vehicles that are operationally and economically feasible
- Demonstrate the potential of new drag reduction concepts and integrated shapes

- Design the next generation of integrated, highly aerodynamic tractor-trailers and tanker-trailers
- Establish a database of experimental, computational, and conceptual design information
- In collaboration with National Renewable Energy Laboratory, investigate the potential fuel savings of platooning heavy trucks
- In collaboration with the industry, promote the new LLNL proposed shape for the next generation of heavy vehicles
- On behalf of DOE, expand and coordinate industry participation to achieve significant on-the-road fuel economy improvement

Approach

In Fiscal Year 2017, we investigated the aerodynamic benefits of heavy vehicle platoons by means of a 1/50th scale wind tunnel test. Several platooning studies have been conducted in recent years by a variety of research groups (see the review articles of Tsugawa et al. [1] and North American Council for Freight Efficiency [2]). The North American Council for Freight Efficiency has compiled the data from a number of these studies (two-vehicle platoons with spacing ranging from 10 ft to 75 ft) and showed that a spacing of 40 ft to 50 ft produces an average fuel savings of 4% for the lead vehicle and 10% for the trailing vehicle. While even greater aerodynamic benefits can potentially be achieved from smaller spacing, these benefits are obscured by increased operation of the engine cooling fan in the trailing vehicle, which must run more than normal due to reduced cooling airflow at smaller spacing. For example, at spacing ranging from 20 ft to 50 ft, track tests of a two-vehicle platoon indicated that the fuel savings for the trailing vehicle decreased from 8.4–9.7% to 2.8–9.7% due to increased engine fan-on time [3].

A better understanding of this balance between aerodynamics and cooling airflow supply can be obtained by investigating heavy vehicle platoons within a more controlled environment, such as a wind tunnel. A previous heavy vehicle study utilized this type of experimental approach for a 1:15 scale two-vehicle platoon operating at close spacing with no crosswind [4,5]. In this study, we conducted a wind tunnel study on 1:50 scale two- and three-vehicle platoons in a crosswind.

Results

Experimental Setup: Wind Tunnel Facility

The Army Aeroflightdynamics Directorate 7 ft × 10 ft wind tunnel located at National Aeronautics and Space Administration Ames Research Center is utilized to investigate the aerodynamic benefits of heavy vehicle platoons (Figure VII.1.1). The wind tunnel test-section measures 7 ft × 10 ft × 15 ft. This closed-circuit wind tunnel has a contraction ratio of 14:1, a maximum wind speed of 355 ft/s, and a freestream turbulence intensity of 0.25%. The test section turntable can accommodate a 360° yaw angle, and an air exchange system allows up to 29% exchange with the outside air for temperature control. For a typical run, the wind tunnel is at a

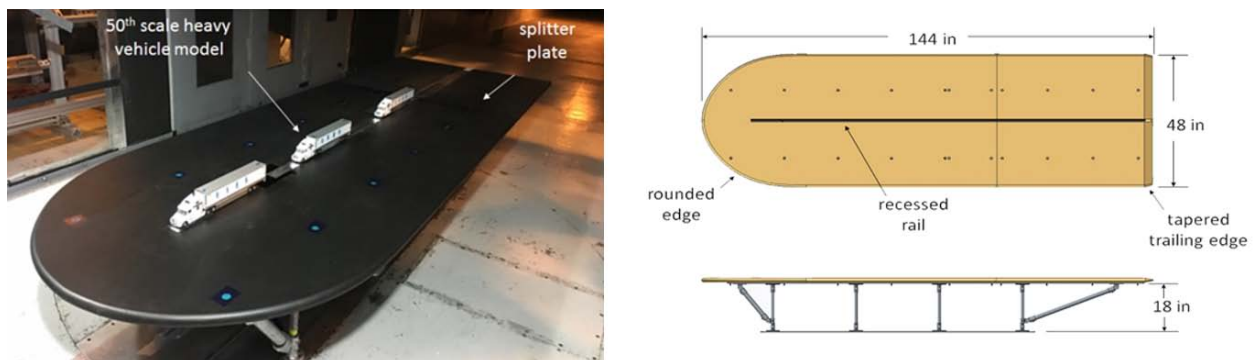


Figure VII.1.1 - Splitter plate dimensions and three-vehicle platoon in the Army 7 ft × 10 ft wind tunnel located at National Aeronautics and Space Administration Ames

dynamic pressure of 80 psf or a freestream wind speed of 270 ft/s. To improve the accuracy of measuring the dynamic pressure on top of the splitter plate, a pitot probe is added to the test section ceiling outside of the wall boundary layer and is aligned with the center of the turntable. Both the static reference pressure and dynamic pressure are provided by this probe.

Experimental Setup: Splitter Plate Design

To minimize the wind tunnel ground effect, i.e., interactions with a thick boundary layer, on the 1:50 scale heavy vehicle models, a new plywood splitter plate is designed. The plate is 48 in \times 144 in \times 1.5 in and is positioned 18 in above the wind tunnel turntable (Figure VII.1.1). The splitter plate is sufficiently long to accommodate a 320-ft full-scale vehicle separation distance. The front and side edges of the splitter plate are curved to maintain an attached flow and to provide an undisturbed center section at all yaw angles. The splitter plate trailing edge is tapered to minimize its wake and to reduce its aerodynamic drag. The shape of the splitter plate is fine-tuned by conducting a series of computational fluid dynamics simulations. Eight cylindrical pillars and four supporting connections (Kee Klamp, PN# 62-5) are used to secure the splitter plate to the test section floor. A pre-test wind tunnel investigation confirmed attached flow around the front and side edges.

Experimental Setup: Vehicle Model Description

The heavy vehicle models shown in Figure VII.1.1 are detailed die-cast representations of a Freightliner Century tractor and a 53-ft straight-frame trailer (Sword #SW2068), with the cross-sectional area of 0.0459 ft². Several modifications are made to the models in preparation for the wind tunnel test. Both the driver- and passenger-side rearview mirrors are removed along with the compressed air lines in the tractor-trailer gap. Additionally, the removable roof fairing is firmly attached to the cab using aluminum tape, while the doors, engine hood, and moveable wheels are glued in place. The tractor and trailer are rigidly connected to one another with a solid aluminum block, which sets the tractor-trailer gap to be 42 in at full-scale. All vehicles are equipped with trailer skirts (27 ft \times 3.56 ft at full-scale) and, on selected bases, with four-sided boattails ($\sim 14^\circ$ deflection angle and 48 in long at full-scale) fabricated from sheet metal (Figure VII.1.2).

Experimental Setup: Model Instrumentation

To measure the aerodynamic drag, the scale models are mounted onto the splitter plate by means of a low-friction linear bearing (Thomson MicroGuide) located within each model trailer (Figure VII.1.2). At the aft end of the bearing is a load cell (Loadstar REB7-001M-S*C01, 2.2 lbf maximum load with an accuracy of ± 0.011 lbf) that measures the body-axis force on the model. A rubber cushion coated with a lubricant is placed at the contact point between model and load cell to minimize any stiction at that interface. Two vertical struts, which extend downward from the linear bearing, attach the entire model to a recessed rail at the centerline of the splitter plate. By simply loosening the connection points between the model assembly and the rail, the model can readily be repositioned at any axial location on the splitter plate.

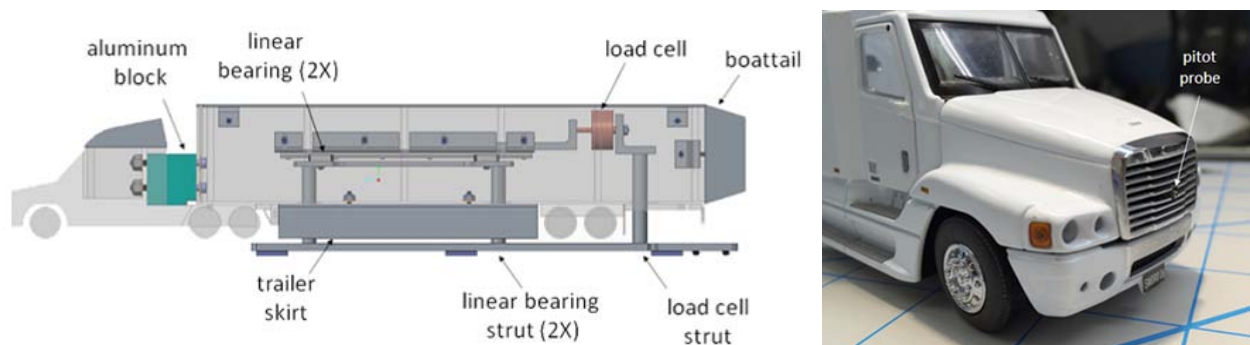


Figure VII.1.2 - Model instrumentation for body-axis force measurements and engine cooling air supply

Experimental Setup: Particle Image Velocimetry

Velocity field measurements are made in the wakes of the heavy vehicle models using a stereoscopic three-dimensional particle image velocimetry technique [6]. The flow within the wind tunnel is seeded with smoke

from a theatrical smoke generator (MDG MAX 5000 HO APS), and a horizontal plane located at the mid-trailer height is illuminated with two 0.08-in-thick laser light sheets (Quanta Ray Pro 290, 1 J/pulse output) that span the entire test section width (Figure VII.1.3). Two cameras (LaVision Image Pro MX) positioned outside of the test section record the motion of smoke within the horizontal plane, and subsequent image processing of the 2 in × 20 in field of view produces a three-dimensional velocity vector field of 38,200 vectors. Figure VII.1.3 presents a sample of a high-resolution vector field of a single vehicle wake.

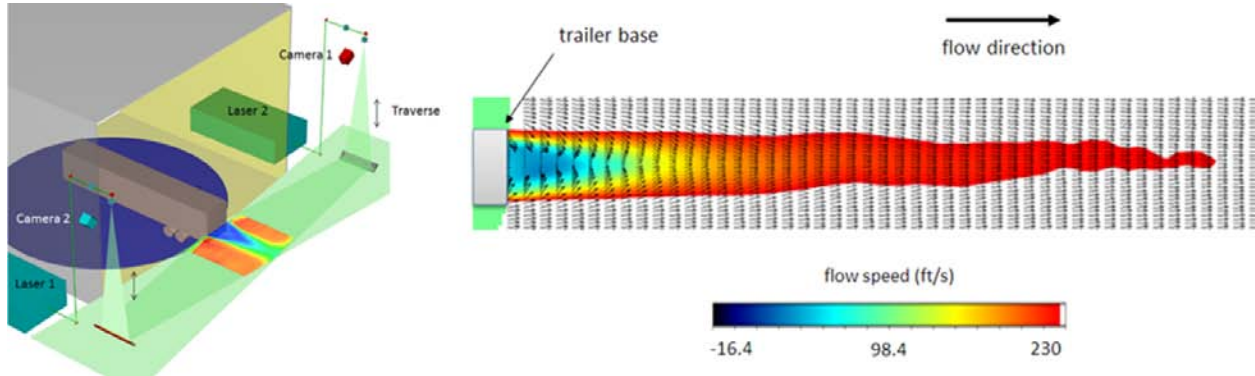


Figure VII.1.3 - Particle image velocimetry setup in the wind tunnel test section and a sample trailer wake flow field

Experimental Setup: Infrared Thermography

Thermography measurements are made with an infrared camera (FLIR SC6100 INSB 3-5 μm) mounted outside of the test section ceiling looking through an opening with a large field of view of the splitter plate and the platoon. The slight temperature differences that arise from varying heat transfer rates to the surfaces are detected by the camera and thereby qualitatively highlight the size and shape of each vehicle flow field. Figure VII.1.4 shows areas of flow separation for the two-vehicle platoon at 0° and 9° yaw, respectively. At 0° yaw, the extent of the lead vehicle wake completely covers the trailing vehicle. At 9° yaw, significant flow separation exists on the leeward side of the lead vehicle extending into the gap between the two vehicles and the leeward side of the trailing vehicle.

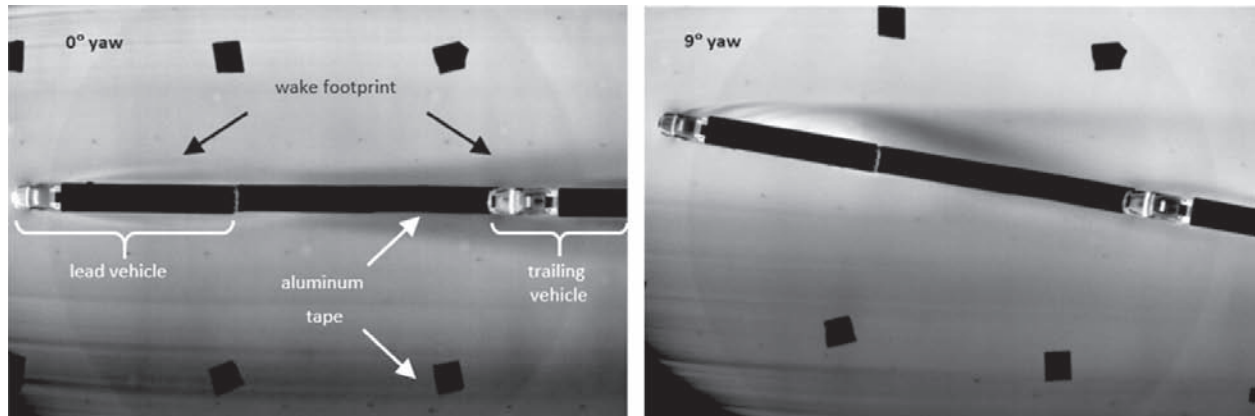


Figure VII.1.4 - Thermal images (top view) of a two-vehicle platoon with an 81-ft full-scale spacing at 0° and 9° yaw

Conclusions

The following platoon configurations are studied:

1. Two aligned vehicles: separation distances of 5 ft to 320 ft; vehicles with and without trailer boattails
2. Three aligned vehicles: 30 ft, 40 ft, and 50 ft separation distances between first and second vehicles; 5 ft to 220 ft separation distances between the second and third vehicles; vehicles without trailer boattails

- Two misaligned vehicles: separation distances of 30 ft, 50 ft, and 160 ft; misaligned percentage (0% to 50%) based upon the trailer width; vehicles with and without trailer boattails

The change in the wind-averaged drag coefficient (CD_{wa}) with vehicle spacing (Figure VII.1.5) for a two-vehicle platoon with and without a trailer boattail follows a qualitatively similar trend to that observed previously [7]. For spacing less than one vehicle length (~ 70 ft), CD_{wa} decreases rather sharply and is previously termed to be the “strong interaction” regime [7]. At larger vehicle spacing (referred to as the “weak interaction” regime), CD_{wa} changes more slowly with increasing spacing. Quite remarkably, the drag reduction benefit for the trailing vehicles is evident for spacing up to 320 ft. Furthermore, the installation of the trailer boattails yields an offset in CD_{wa} of approximately 0.1 for most spacing. The corresponding percent benefits in CD_{wa} for the individual vehicles and for the entire platoon relative to isolated vehicles with no boattail are shown in Figure VII.1.5. In the 30 ft to 50 ft regime where several fuel economy tests have previously been conducted, Figure VII.1.6 shows that the percent benefit for the platoon ranges from 21% to 23% and 10% to 13% for vehicles with and without trailer boattails, respectively.

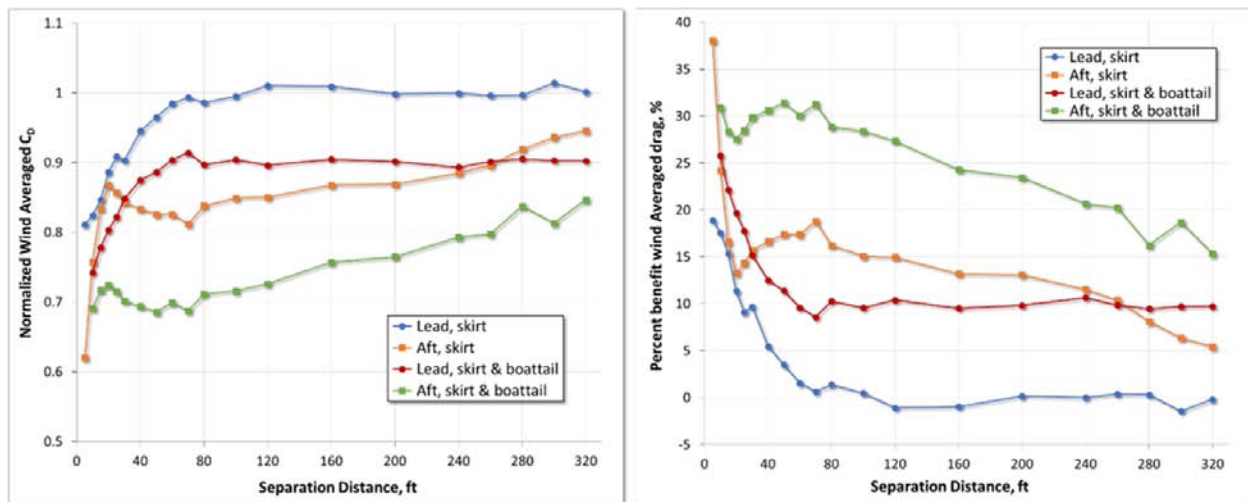


Figure VII.1.5 - Wind-averaged drag and pressure coefficient vs. vehicle spacing for a two-vehicle platoon with and without trailer boattails

The engine cooling air supply, as measured with the wind-averaged pressure coefficient (CP_{wa}) at the radiator grill, varies with vehicle spacing and becomes quite small and even negative in value when the trailing vehicle is positioned at spacing less than approximately 15 ft (Figure VII.1.6b). This observation is consistent with track test measurements in which spacing in the range of 20 ft to 50 ft required the engine cooling fan to operate due to insufficient cooling air flow (North American Council for Freight Efficiency 2016). For larger spacing, CP_{wa} for the trailing vehicles does not increase to 1, but rather remains approximately 0.7 up to 320 ft. It is interesting to note that for spacing less than 50 ft, CP_{wa} changes more quickly with vehicle spacing than the percent benefit in CD_{wa} for the entire platoon, which will be a crucial factor when determining an optimum two-vehicle spacing that provides the maximum aerodynamic benefit while still maintaining sufficient cooling air flow.

The percent benefits in the wind-averaged drag coefficients for the three-vehicle platoons are shown for 40 ft separation distance between the first and the second vehicle in Figure VII.1.7a. For these configurations, the distance between the first and second vehicles is maintained at either 30 ft, 40 ft, or 50 ft, respectively, while the distance between the second and third vehicles varies from 5 ft to 220 ft. The inclusion of the third vehicle does not significantly change the benefit provided to the lead vehicle over that of a two-vehicle platoon except at the closest spacing (Figure VII.1.7b). As the spacing between the second and third vehicle increases, the first and second vehicles exhibit percent benefits comparable to those of the two-vehicle platoon. Additionally, for all spacing up to 220 ft, the percent benefit of the third vehicle is insensitive to the relative positions of the first two vehicles (Figure VII.1.7b). The CP_{wa} at the engine radiator grills for the three-vehicle platoons

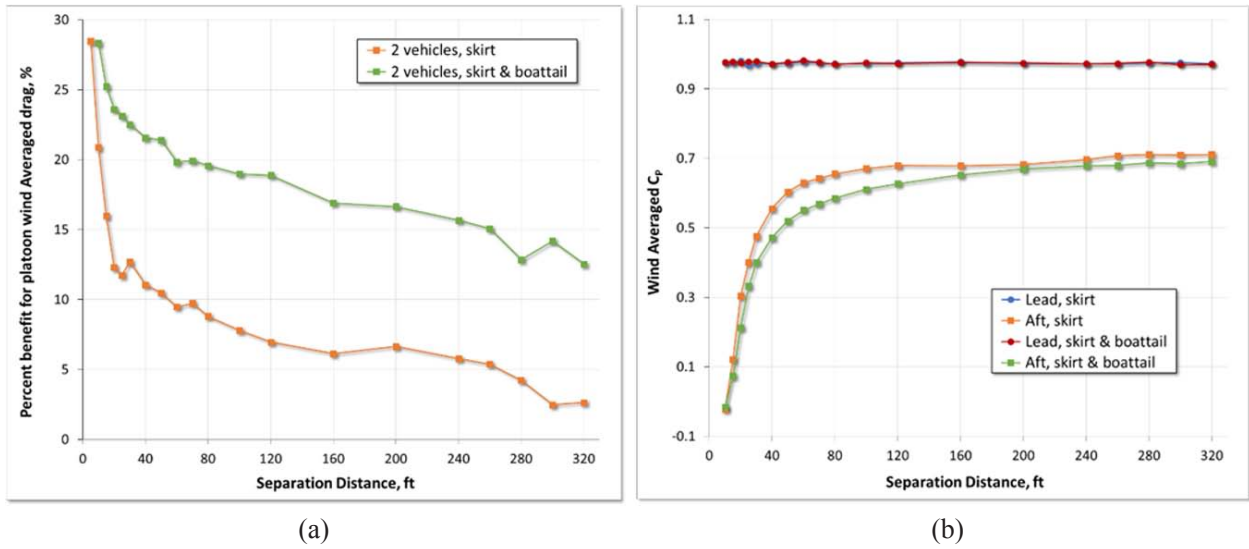


Figure VII.1.6 - (a) Percent benefit in CD_{wa} for the entire two-vehicle platoon. (b) CP_{wa} as a function of spacing for a two-vehicle platoon with and without trailer boattails.

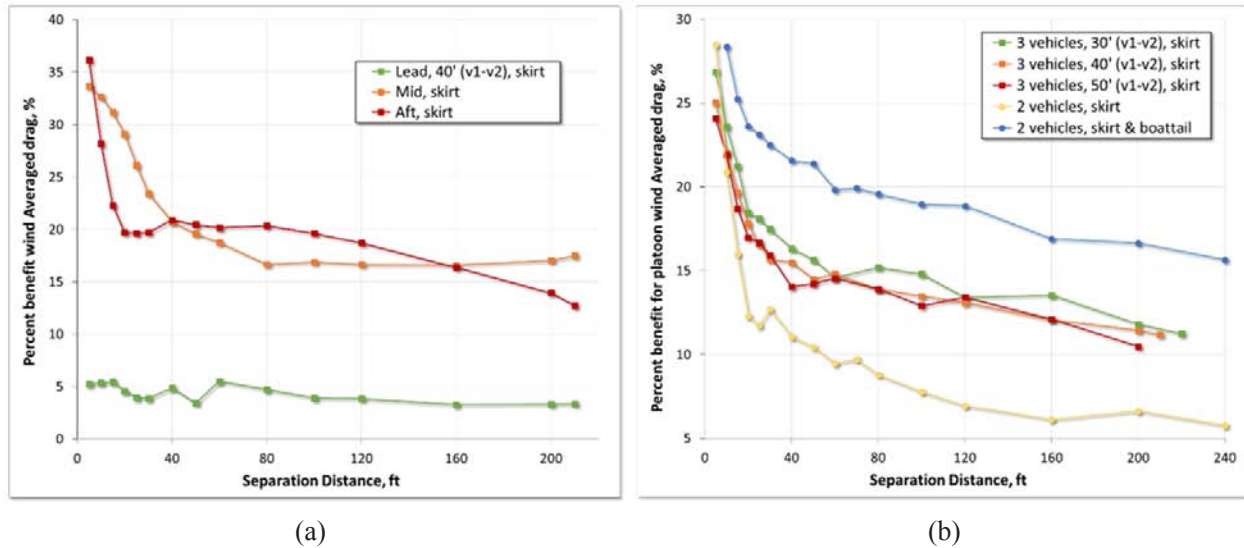


Figure VII.1.7 - (a) CD_{wa} for a 40-ft separation distance between the first and the second vehicle as a function of vehicle spacing for a three-vehicle platoon. (b) CD_{wa} for the entire three-vehicle platoon as a function of vehicle spacing.

are shown in Figure VII.1.8. The CP_{wa} values for the first and second vehicles closely follow the behavior of the corresponding two-vehicle platoons, while the value for the third vehicle asymptotically approaches a value that is slightly less than that of the two-vehicle platoon at large spacing (Figure VII.1.8a). As would be expected, this indicates that the third vehicle is immersed in a flow field that has a larger velocity deficit.

The percent benefit in CD_{wa} of the entire platoon is shown in Figure VII.1.7b as a function of spacing for all platoon configurations considered thus far. Clearly, increasing the number of vehicles in the platoon increases the overall aerodynamic benefit, an observation similar to that in Browand et al. [7]. However, a much larger benefit is achieved by simply adding boattails to the two-vehicle platoon. Additionally, the overall aerodynamic benefit of the three-vehicle platoon is not sensitive to the spacing changes of 30 ft to 50 ft between the first and second vehicle.

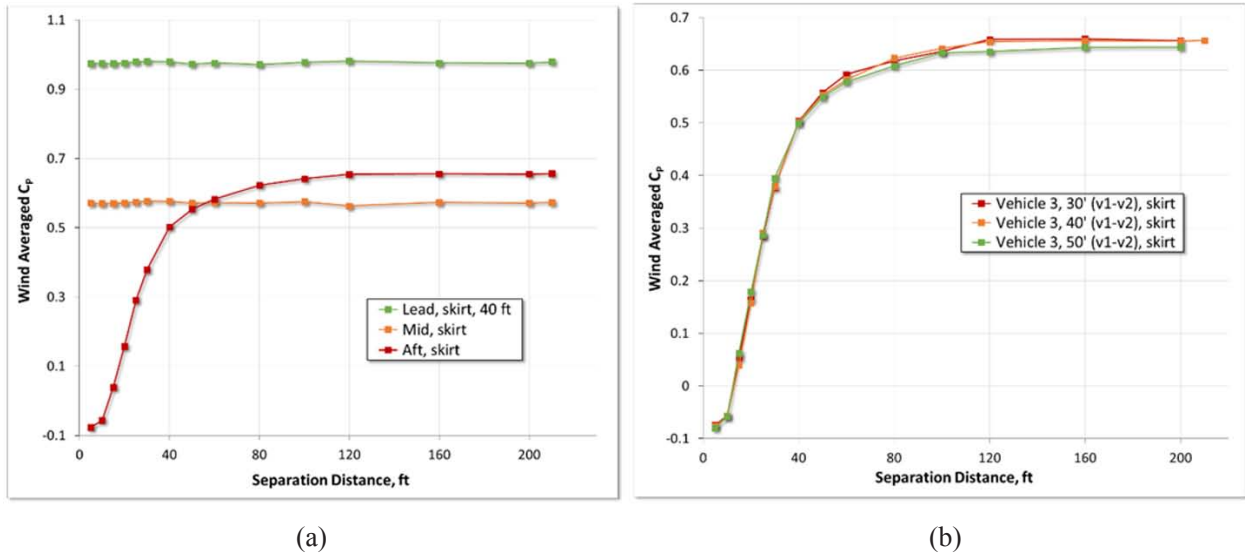


Figure VII.1.8 - (a) CD_{wa} for a 40-ft separation distance between the first and the second vehicle as a function of vehicle spacing for a three-vehicle platoon. (b) CD_{wa} for the third vehicle with multiple separation distances between the first and second vehicles.

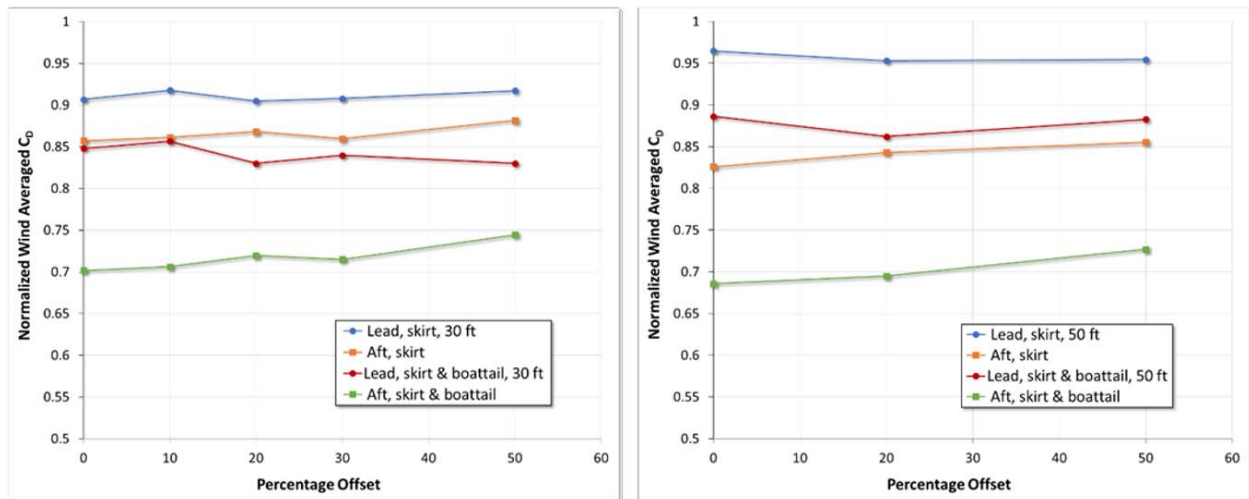


Figure VII.1.9 - CD_{wa} for a two-vehicle platoon (30-ft and 50-ft spacing) as a function of lateral misalignment

Lastly, CD_{wa} is shown in Figure VII.1.9 for two laterally misaligned vehicles at spacing of 30 ft and 50 ft with misalignments up to 50% of the trailer width. For all the spacing, the misalignment has a negligible impact on the aerodynamic drag, which is consistent with the observations from the infrared camera that the wake from the first vehicle at the location of the second vehicle is much larger than these relatively small misalignments.

References

1. Tsugawa, S., S. Jeschke, and S.E. Shladovers. "A Review of Truck Platooning Projects for Energy Savings." *IEEE Transactions on Intelligent Vehicles*, 1(1):68–77, 2016.
2. North American Council for Freight Efficiency. "Trucking Efficiency Confidence Report: Two-Truck Platooning." http://www.truckingefficiency.org/sites/truckingefficiency.org/files/reports/RMICWR_Trucking_ExecSummary_platooning_B4.pdf, 2016.

3. Lammert, M.P., A. Duran, J. Diez, K. Burton, et al. "Effect of Platooning on Fuel Consumption of Class 8 Vehicles over a Range of Speeds, Following Distances, and Mass." *SAE Int. J. Commer. Veh.*, 7(2):626–639, 2014.
4. Hammache, M., and F. Browand. "On the Aerodynamics of Tractor-Trailers." McCallen, R.C., Browand, F., and Ross, J. (Eds.). *The Aerodynamics of Heavy Vehicles: Trucks, Buses, and Trains*. Springer, Heidelberg, 2004.
5. Browand, F., and M. Hammache. "The Limits of Drag Behavior for Two Bluff Bodies in Tandem." SAE Paper 2004-01-1145, 2004.
6. Arroyo, M.P., and C.A. Greated. "Stereoscopic Particle Image Velocimetry." *Measurement Science and Technology*, 2(12):1181–1186, 1991.
7. Browand, F., M. Zabat, and P. Tokumaru. "Aerodynamic Benefits from Close-Following." Ioannou, P.A. (Ed.). *Automated Highway Systems*. Plenum Press, New York, 1997.

Key Fiscal Year 2017 Publications

1. "Wind Tunnel Investigation of the Aerodynamic Benefits of Truck Platooning." Accepted paper 2018 SAE World Congress, Detroit, MI, April 2018.

VII.2 Advanced Bus and Truck Radial Materials for Fuel Efficiency

Lucas Dos Santos Freire, Sr., Principal Investigator

PPG Industries, Inc.
440 College Park Dr.
Monroeville, PA
E-mail: dossantosfreire@ppg.com

Roland Gravel, DOE Technology Manager

U.S. Department of Energy
E-mail: Roland.Gravel@ee.doe.gov

Start Date: October 1, 2014 End Date: March 31, 2018
Total Project Cost: \$1,253,269 DOE share: \$939,950 Non-DOE share: \$313,319

Project Introduction

Precipitated silica is an amorphous particle produced commercially by the acid neutralization of a sodium silicate solution. Highly dispersible silicas (HDSs) are used as the main reinforcing filler in passenger treads. In conventional HDS/in situ silane rubber formulations, HDS and coupling agents such as 3,3'-bis(triethoxysilylpropyl)tetrasulfide are co-reacted during the rubber mixing process to create a strong interaction between the HDS and the rubber polymers to deliver improved tire performance. In recent years, to overcome the volatile organic compounds and other issues associated with the HDS/in situ silane process, Agilon[®] Performance Silicas came into the market. In the Agilon[®] process, silane coupling agents, as well as other compatibilizers, are pre-reacted onto the silica surface so that tire manufacturers do not need to control this reaction during compounding. For passenger tires, which are synthetic rubber-based, Agilon[®] products can reduce rubber mixing times by 36%, increase batch sizes by 18–27%, eliminate volatile organic compounds, and further improve the “magic triangle” of treadwear, traction, and rolling resistance (RR).

When tires are predominantly comprised of natural rubber (NR), as in the case of truck and bus radial (TBR) tires, silicas no longer provide the same benefits as in passenger tires [1,2,3,4]. NR is necessary to provide the chip and tear resistance essential for TBR applications, but NR contains proteins, organic matter, and metal ion contaminants. These contaminants are believed to interfere with the in situ coupling reaction required to effectively disperse silica in non-polar rubber yielding poor filler dispersion, tire performance, and processing properties. Agilon[®] silicas have the ability to overcome the contaminants problem since the silane coupling reaction is already completed during the silica synthesis. Bridgestone Americas Tire Operations (BATO) has evaluated existing Agilon[®] materials but not in actual TBR formulas. They identified that further improvements need to be made before Agilon[®] would be truly impactful to the tire industry. The state of the art in TBR compounds are carbon black (CB)-reinforced NR-butadiene rubber (BR) blends. The Agilon[®] tested preferentially dispersed into synthetic rubbers and this non-uniform dispersion creates performance issues for NR-synthetic rubber blends. It was hypothesized that if the Agilon[®] process could be used to control silica surface energy and morphology to produce a silica which more uniformly disperses across blends of natural and synthetic rubbers, not only will TBR tires experience a potential 20–30% reduction in rolling resistance yielding a 4–6% increase in fuel efficiency, but also silica could provide benefits in a greater range of rubber blends. In this project, several silica prototypes with different morphology and surface energy were made and compounded in the lab in a model TBR formulation. Selected prototypes were scaled-up and tires were built to evaluate on-tire performance.

Objectives

PPG Industries, Inc. and BATO propose to develop a novel surface-modified silica technology and demonstrate 4–6% improved fuel efficiency of TBR tires built from the technology. The proposed fuel efficiency increase will be achieved while maintaining or improving tear strength and tread wear (within 10% from the CB control).

- First, treated silicas which provide the optimum surface energy for TBR model formulations will be developed.
- Second, silica prototype–TBR formulation combinations will be optimized to achieve project targets in the lab.
- Finally, two tire builds will be performed to demonstrate the compounds performance in the field.

Approach

To achieve the goal of this project, a systematic and thorough investigation of the properties that enable uniform dispersion of silica in both NR and synthetic rubber was performed. The surface energy of prototype silica samples treated with a proprietary PPG process and different functional groups were determined in the first stage of the project. Treatments were found which reduce the silica surface energy, thus reducing the interfacial tension with NR and synthetic rubbers. The reduction in surface energy was dependent on the specific treatment agents used. Silica samples with the lowest surface energy obtained were compounded in NR–butadiene rubber- and NR–solution styrene–BR-based compounds. Knowledge gained in this stage was used to drive the development of new silica surface treatments and rubber formulations to control the phase distribution and enhance the dispersion of fillers throughout the TBR tread compound.

Selected silicas from the first stage of the project were scaled-up and rubber optimization work was performed in the lab. Once the optimum rubber compound containing the developed silica prototype was developed, BATO performed a tire build and testing. Tire results were evaluated and further optimization based on actual tire data was performed to optimize the silica-rubber combination and perform a final tire build. The goal is to achieve the final targets for the project in this final tire build.

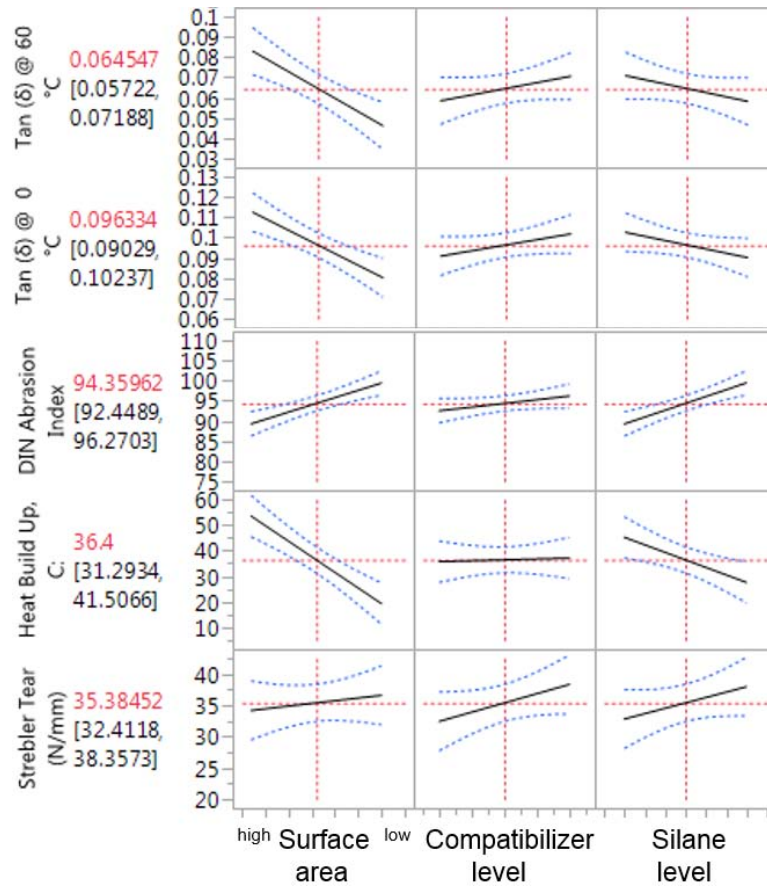
Results

Based on surface energy and rubber compounding studies, two different compatibilizer chemistries were selected to perform the treatment for the silica prototypes. Results of this work were presented earlier. The first optimization activities using these chemistries involved performing design of experiment studies around silica synthesis parameters to determine the optimum silica characteristics. We performed two design of experiments looking at different silane levels and compatibilizer levels, together with silica surface area variations. Fifteen silica samples for each chemistry were prepared and compound testing was performed at the PPG rubber lab. A model formulation provided by BATO was used. Details from one of the design of experiment studies are summarized in Figure VII.2.1. The figure shows a few of the trends obtained. As it can be seen in the figure, correlations between several compound performance parameters with silica surface area, silane and compatibilizer loading were established.

Based on these responses, the optimum silica parameters which would provide the best balance of performance according to the project targets were selected. The silica prototypes were scaled-up and compound work was performed to optimize the tread compounds to be used in the tire build. A large number of rubber mixing studies designed to obtain the optimum compound were performed by PPG and by BATO at their respective labs. These studies included:

- Cure optimization studies
- Evaluation of mixing conditions (mixing time, mixing temp., etc.)
- Tear improvement studies
- Silica loading studies
- Evaluation of additional modified silica prototypes
- Studies on variations of addition sequence of different additives
- Evaluation of process aids, polymer blends, etc.

- Final cure optimization studies, since the compounds had been largely optimized and changed since the original cure studies.



DIN – Deutsches Institut für Normung

Figure VII.2.1 - Response effects obtained on design of experiment study

These studies led to the final compound recipe for the first tire build. It can be highlighted that, upon starting the development work with a NR/BR 80/20 polymer blend, we discovered that tear resistance is mainly affected by the polymer system, and since the control compound is 100% NR, the prototype compounds need to have 100% NR to achieve the tear target. Twenty percent BR has been added previously with the expectation that it would help to achieve good dispersion and abrasion resistance, but we found that we didn't lose much of these properties by switching to 100% NR. The silica loading was increased to 37 phr, from the 30 phr used initially. This was performed to obtain higher stiffness and to have a true one to one replacement by weight of the 30 phr CB replaced from the control. Because the treated silica contains approximately 80% silica, with the remaining 20% being the chemical treatments and moisture, 37 phr of treated silica would consist of approximately 30 phr silica filler and 7 phr of treatments and moisture. Finally, curatives were adjusted so that an acceptable scorch safety and a final modulus with little reversion were obtained. The effect of crosslink density (higher with higher curatives loading) was investigated. We observed that, as expected, compound modulus increased with crosslink density. We also observed that at a modulus comparable to the CB control, tear and abrasion resistance were comparable to the CB control, while we achieved the rolling resistance indicator target (<40% of the control). The curatives loading that provided this optimum balance was selected for the final tread compound formulation. We also observed that it was essential to mix treated silica-NR at low temperature. This is, it should be mixed like CB-NR compounds are traditionally mixed, and not like untreated silica compounds are traditionally mixed.

Finally, the two silica prototypes (BXR-990 and BXR-991) for the tire build were produced at the PPG Silicas Pilot Plant, in Monroeville, Pennsylvania, and packed in 25-lb low-melt bags. The only difference between the

two prototypes was in the type of chemical treatment. The tire build was performed at BATO’s Warren County tire plant in November 2016. The control compound formulation had 100% NR and 46 phr of CB. In the silica formulations, 37 phr of silica and 15 phr of CB were used as filler. Also, the cure package loading was slightly increased to accommodate for absorption of curatives in the silica surface, and to obtain compounds with comparable stiffness. Rubber mixing at the plant proceeded as expected. The silica-based compounds processing was comparable to the processing of the CB control. All three formulations were mixed using similar mixing procedures, and they showed very comparable energy consumption. The silica compounds had slightly higher viscosity, but the higher viscosity was not significant and processing was still acceptable.

Lab and tire compound data is shown in Table VII.2.1. The Table shows normalized data for the CB control and the two silica prototypes. The data shows, once again, that the viscosity of the silica prototype is slightly higher than the CB control, as observed at the plant. Tensile properties are similar for all samples. The silica samples have slightly higher stiffness than the CB control, but within the 10% target. Tear strength of the silica compounds is similar to the CB control (within 10%), except for one of the prototypes at high temperature. The lab rolling resistance indicator ($\tan \delta$ at 60°C), is 47% and 40% lower than the CB control. The wear indicator showed in the lab a slight deficiency (10% and 7%) for the silica prototypes, but still within the target (no more than 10% deficiency).

Table VII.2.1 - Lab and Tire Data from First Tire Build

	Parameter	CB control	BXR-990	BXR-991
Viscosity		100	112	113
Rheometer	MH-ML	100	124	127
	T50	100	82	82
	T90	100	96	91
Hardness	Index	100	108	109
Tensile test at 25°C	Mod300	100	102	90
	Elongation	100	101	105
	Tensile	100	102	103
	Tensile x elongation	100	102	108
Tear, 25 °C	Load	100	95	108
Tear, 100°C	Load	100	81	96
Temp. Sweep	E' @ 30	100	104	119
Temp. Sweep	Tan δ @ 60°C	100	53	60
Tire RRC	Index	100	84	86
Lab wear	Index	100	90	93
Tire Wear	Index	100	67	75

MH – maximum torque; ML – minimum torque; RRC – rolling resistance coefficient
 T50 – time to 50% maximum torque; T90 – time to 90% maximum torque

Tires with the prototype tread compounds were built using an Ecopia R197 295/75R22.5 carcass. The two novel silica prototypes and the all-NR–CB control formulation were used to tread 12 test tires for each tread compound. The tires were used for rolling resistance test, indoor wear test, section and footprint analysis, and several endurance and high speed tests to evaluate the integrity of the treads.

Regarding actual tire data, Table VII.2.1 shows that the prototype silicas achieved 16% and 14% reduction in rolling resistance compared to the CB control. While rolling resistance is slightly higher than the target (20% reduction), the improvement versus the control are significant. Even if a 20% reduction in rolling resistance were not achieved, according to the literature, it is probable that we might already achieve about 5% fuel efficiency improvement with the 16% improvement in rolling resistance already obtained [5,6]. Unfortunately, the 10% reduction in lab wear observed worsened in the actual tires. Optimization work performed after this tire build focused mainly on improving wear resistance.

In follow-up studies, a design of studies experiment showed that adjusting the silica surface area and filler loading adjustment could provide improved tear strength and wear resistance without other performance detriments. Additional compound studies were performed to further determine the optimum filler and sulfur loadings, determine the level of other curatives, and the mixing procedure. Based on this work, a new silica prototype (BXR-1006) was developed. Also, the tire tread compound was adjusted to accommodate this new prototype with the formulation to be used in the tire build. These results are summarized in Table VII.2.2. The first column shows the CB control that was used in the first tire build and that will be used in the final tire build. The second column shows the silica compound that was used in the initial tire build, containing BXR-990 silica prototype. Finally, the last column shows the new prototype with the new, optimized formulation for this prototype. The three compound recipes shown in the table are slightly different, but the main differences apart from the filler are adjustments in filler loadings and curatives. It can be seen that the new compound based on BXR-1006 significantly improves tear resistance and abrasion compared to the silica compound from the first tire build. The abrasion resistance and hot tear strength are now equivalent to the CB control. This improvement was obtained while maintaining the improved rolling resistance indicator ($\tan \delta$ at 60°C) and other properties. The results were corroborated at PPG and BATO rubber labs. The new prototype will be scaled-up and used in the final tire build. Even though it is unknown if now the tire wear will be equivalent to the carbon black control, the significant improvement over the first tire build silica compound indicates that wear resistance should be much closer to the control.

Table VII.2.2 - Lab Compound Data of Improved Prototype

	Parameter	CB control	BXR-990	BXR-1006
Cure	ML	100	106	118
	MH	100	120	123
	MH-ML	100	123	124
	T50	100	141	134
RPA	Viscosity	100	110	120
Hardness	Shore A	100	104	99
Wear	Index	100	76	100
Tensile properties @ 25 °C	Mod100	100	135	113
	Mod300	100	108	90
	Strain @ break	100	99	111
	Tensile strength	100	108	115
Tear - Die B @ 25 °C	Load	100	106	111
Tear - Aged @ 100 °C	Load	100	80	103
Strain Sweep @ 60 °C	E'	100	106	114
	Tan δ	100	64	65

RPA – rubber process analyzer

Conclusions

In summary, the systematic study of chemical treatments, silica morphology, and surface energy allowed the development of a treated silica which provided a significant improvement in rolling resistance compared to a CB control in a NR-based TBR compound. Even though lab abrasion indicators estimated a 7–10% deficiency in wear, once the tires were build and tested, the deficiency increased to 25–33% on the tire. Through further optimization of the silica prototype, compound filler loading and cure adjustments, we were able to obtain a compound which showed significant improvements in mechanical properties in the lab, while maintaining other properties. Testing of the new silica prototype (BXR-1006) was completed in the lab and it was concluded that significant improvements in tear strength and abrasion compared to the prototypes used during initial development were obtained. This is critical because these were the deficiencies observed during the first tire build and these new results indicate that the final on-tire performance goals for the project might be achieved in the final tire build.

References

1. Okel, Tim, et al. "Agilon Performance Silicas in Natural Rubber Truck Tire Tread Compounds" 180th Technical Meeting of the American Chemical Society Rubber Division, paper #70, October 2011.
2. Okel, Tim, and Justin Martin. "Bringing Innovation to the Surface: Functionalized Silicas for Improved Natural Rubber Truck Tire Vulcanizates" 184th Technical Meeting of the American Chemical Society Rubber Division, paper #33, October 2013.
3. Okel, Tim, and Justin Martin. "Innovating the silica surface for Improved NR truck tire vulcanisates." Presentation at Tire Technology International, Cologne, Germany, February 2014.
4. Okel, Tim, and Justin Martin. "Functionalized silicas for improved NR truck tire vulcanizates." *Rubber World* 249(2), 19–24, 2014.
5. Michelin. "The Tyre. Rolling resistance and fuel savings." 2003. Accessed November 17, 2017. <https://openlab-cb.michelin.com/docs/DOC-3212>
6. Bridgestone. "Tires & Truck fuel economy. A new Perspective." 2008. Accessed November 17, 2017. <https://blog.truckenterprises.com/2012/01/04/bridgestone-tires-truck-fuel-economy-a-new-perspective/>

VII.3 Improved Tire Efficiency Through Elastomeric Polymers Enhanced with Carbon-Based Nanostructured Materials

Georgios Polyzos, Principal Investigator

Oak Ridge National Laboratory
1 Bethel Valley Road
Oak Ridge, TN 37831-6054
E-mail: polyzosg@ornl.gov

Roland Gravel, DOE Technology Manager

U.S. Department of Energy
E-mail: Roland.Gravel@ee.doe.gov

Start Date: January 7, 2016 End Date: December 31, 2018
Total Project Cost: \$1,131,000 DOE share: \$905,000 Non-DOE share: \$226,000

Acknowledgments

Co-Authors

Jaehyeung Park, Jaswinder Sharma, Tim J. LaClair; Oak Ridge National Laboratory

Project Introduction

In the United States, road vehicles account for more than 80% of motorized transportation and are considered to be the driving force for the steep growth in oil demand [1]. Several studies have indicated the importance of the tire rolling resistance for significant reductions in fuel consumption. The rolling resistance can be responsible for up to 25% of the energy required to drive at highway speeds [2] and a 10% reduction in tire rolling resistance yields fuel savings 1–2% [1,3]. The above-referred results are in excellent agreement with the research conducted for the California Energy Commission, which concluded that approximately 1.5% to 4.5% fuel consumption could be saved by using low resistance tires [4]. In response to a Vehicle Technologies Office funding opportunity announcement, we proposed to develop innovative nanocomposite materials that will reduce the fuel consumption by reducing the tire rolling resistance. The targeted fuel consumption reduction will be at least 4% compared to the state of the art, while maintaining traction and wear resistance.

In materials science of elastomers, the influence of manufactured nanomaterial filler particles is of utmost significance for the performance of innovative rubber products, i.e., passenger and commercial tires with ultralow rolling resistance but high traction. Advances in both performance areas are imperative for the development of improved tire efficiency to meet DOE's fuel consumption reduction target of 4%, all while maintaining or improving wear characteristics of the tire. Recent research efforts focus mainly on the development of composite tires based on carbon black and silica. The project goal is to replace existing fillers (such as carbon black and silica) with higher performance materials (viz., graphene, and silica nanofibers). The proposed approach capitalizes on the recent advances in nanomaterial and graphene synthesis and functionalization by our group and suggests a promising avenue for the amalgamation of cutting-edge nanotechnologies that can be utilized toward DOE's technical targets. The project will enable the fabrication and testing of scalable structures, which are anticipated to demonstrate unprecedented improvements in the rolling and wear resistance of tires used in the automotive industry. The successful implementation of the project will deliver scalable composite materials and will provide processing conditions that can be utilized in advanced tire manufacturing for breakthrough fuel savings.

Objectives

The objective of the project is to reduce the hysteretic losses of elastomers that are used for manufacturing vehicle tires. Composite elastomers based on graphene and silica nanofibers will be developed. The filler material should not compromise the wear and tear resistance of the tire. The specific objectives of the project are:

- Reduce the rolling resistance of the tire
- Replace existing fillers (such as carbon black and silica) with higher performance materials
- Tailor the viscoelastic properties of the composite elastomer
- Design of new materials with tailored and complementary properties that will provide parallel improvements
- Improve tire efficiency and meet DOE's fuel consumption reduction target of 4%
- Scale up the synthesized filler material
- Test the properties of the composite elastomers using industrial techniques
- Enable fabrication techniques that can be scaled in a manufacturing environment

Approach

Graphene nanoplatelets (GnPs) and silica nanofibers (SnFs) were synthesized using techniques that can be scaled. The GnPs were exfoliated and functionalized with organic groups in order to be compatible with the SnFs and the styrene-butadiene-rubber (SBR) elastomer. Composite elastomers were fabricated at several filler weight contents. The mixing procedure was tailored in order to achieve good dispersion of the fillers in the elastomer. We collaborated with a major tire manufacturer. Our partner provided the unfilled elastomer and the formulations and mixing protocols that are used for the fabrication of commercial tires. The properties that are necessary to improve the performance of the tire were discussed with our partner. The properties of the composite elastomers were found to depend on the dispersion of the filler material. The chemical functionality of the fillers and the mixing procedures were optimized to achieve good dispersion of the fillers in the SBR. Filler material and composite elastomers were shipped to the facilities of our partner for further testing and evaluation.

Results

Key accomplishments for Fiscal Year 2017:

- GnPs were successfully functionalized and showed good dispersion in the polymer elastomer when mixed in solution.
- Electrospun SnFs were synthesized with diameters smaller than 100 nm. The average diameter was 60 nm. The surface area was 670 m²/g. This value is approximately four times higher than the surface area of the silica nanoparticles that are currently being used in tire manufacturing (~160 m²/g).
- The combination of SnF and functionalized GnP fillers synergistically improved the mechanical performance of the elastomer.
- The weight content of the filler material was optimized.
- Elastomers filled with GnPs and SnFs were synthesized.
- It is feasible to achieve 4% reduction in the fuel efficiency and at the same time to enhance the mechanical performance of the tire. The target tand value is 0.3. The non-crosslinked composites were found to exhibit tand value of 0.13 and at the same time to improve up to 20% the mechanical properties of the elastomer.
- Spacer material was introduced between the GnPs to increase the surface area of the functionalized graphene powder. The surface area of the functionalized powder is 265 m²/g.
- Safety data sheets were generated for all synthesized material. The safety data sheets were approved by our industrial partner's safety personnel. The synthesized materials were shipped to our partner for further testing.

GnPs were functionalized using several organic groups. The group functionalities and the synthesis conditions were optimized in order to achieve good dispersion of the GnPs in the SBR elastomer. A scalable method for the synthesis of SnFs was developed. The diameter of the fibers is smaller than 100 nm. The properties of the fibers were evaluated using scanning electron microscopy (SEM) atomic force microscopy techniques. The SBR that is used in tire manufacturing was provided by our collaborator. Composite elastomers based on SBR, GnPs, and SnFs were synthesized at several weight contents of the filler material. To achieve 4% fuel saving without compromising the tire performance, the SnF and GnP contents were defined. By tuning the functionality and dispersion of the fillers we were able to reduce the hysteretic losses and at the same time to enhance the mechanical properties (modulus) of the tire elastomer. The filler materials are described in the following sections.

Functionalized GnPs

Organically modified GnPs were synthesized in a solution. The mixture was refluxed while stirring and then filtrated with a porous membrane with an average pore size of 0.2 μm . The filtrated powder was rinsed with ethanol for three times to remove the non-reacted organic groups that were physically absorbed on the graphene surface. The powder was dried in an oven at 80°C for 24 h. Schematic images of the modified GnPs are shown in Figure VII.3.1. The d-spacing between the graphene platelets increased from 8.4 \AA to 13.5 \AA due to the intercalated organic groups. The intercalated groups were found to promote the exfoliation of the GnPs in the SBR.

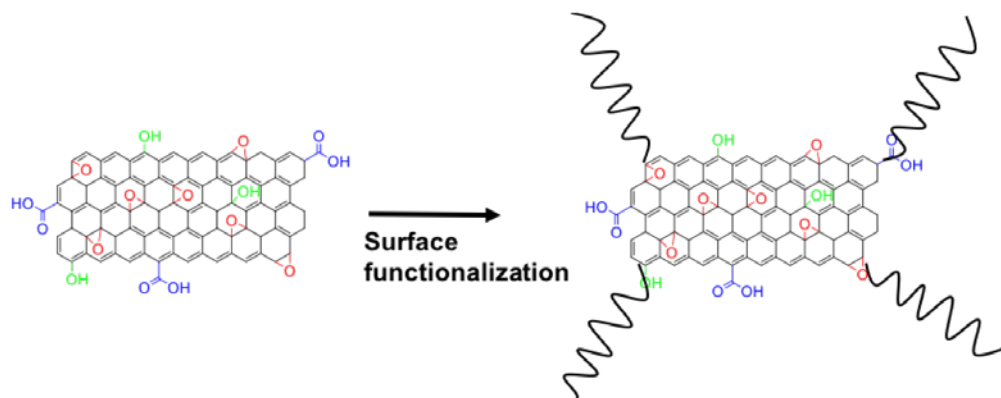


Figure VII.3.1 - Schematic images of organically modified GnPs

Synthesis of SnFs

A scalable method for the synthesis of silica nanofibers SnFs was developed. The nanofibers were fabricated using an electrospinning technique with sol-gel precursors. A schematic representation of the synthesis method is shown in Figure VII.3.2. We collaborated with a company to scale up our synthesis procedures. The company has applied our methods to produce scalable SnFs. The diameter of the fibers is smaller than 100 nm according to the SEM images shown in Figure VII.3.3. The average size is approximately 60 nm. Nitrogen adsorption and desorption measurements were performed to calculate the surface area of the SnFs. The measured surface area is 670 m^2/g . This value is approximately four times higher than the surface area of the silica nanoparticles that are currently being used in the tire manufacturing ($\sim 160 \text{ m}^2/\text{g}$).

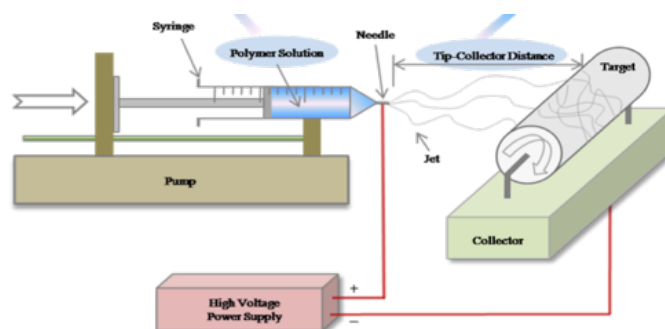


Figure VII.3.2 - Experimental setup for the synthesis of SnFs.

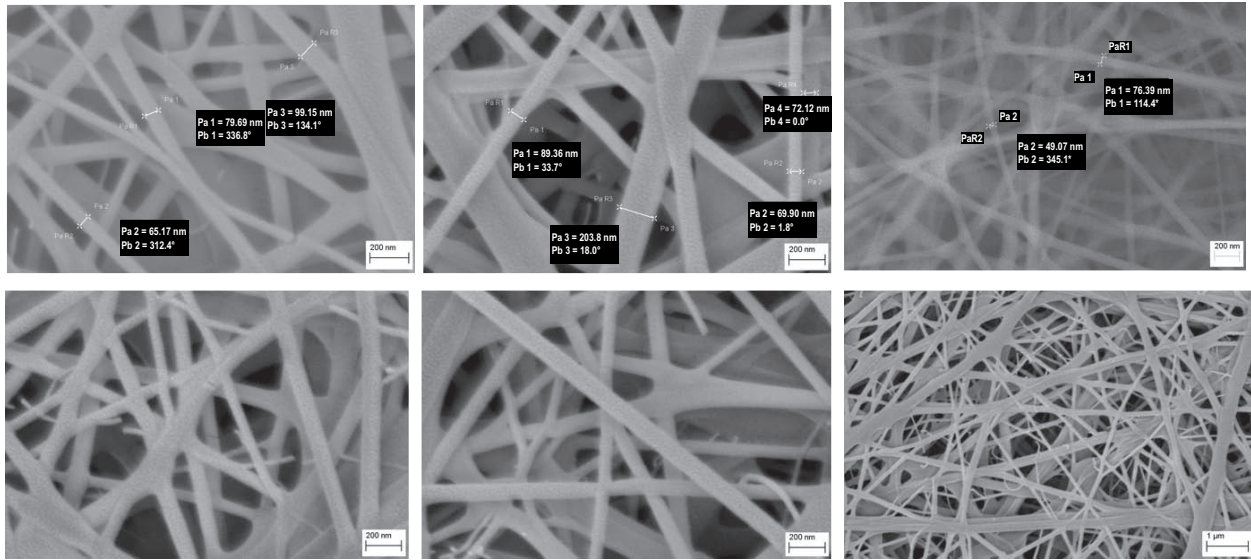


Figure VII.3.3 - SEM images of synthesized silica fibers using the experimental setup in Figure VII.3.2. The diameter of the fibers is smaller than 100 nm.

Mechanical properties of the SBR composites

The mechanical properties of the SBR composites were measured using dynamic mechanical analysis techniques. The tand value for the commercial tire elastomer is 0.46 at 23°C. In order to achieve the 4% fuel reduction, the tand value must decrease to 0.3. Dynamic mechanical analysis measurements were performed to calculate the hysteretic losses (tand values). The dynamic mechanical analysis results of the composites are shown in Figure VII.3.4. The tand of the developed non-crosslinked composite is approximately 0.13, which is adequate to achieve the targeted 4% fuel reduction. The crosslinking density of the composite elastomer must be optimized to further enhance the storage modulus values.

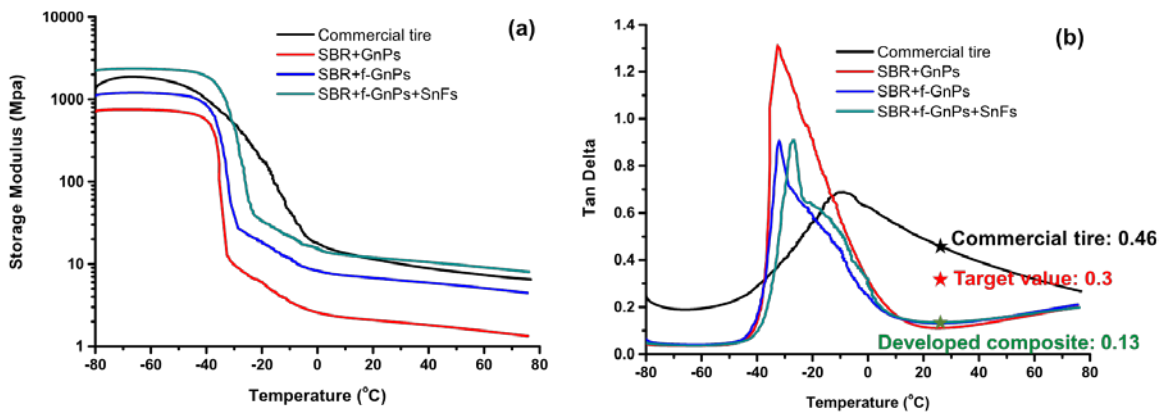


Figure VII.3.4 - (a) Modulus values of the synthesized composites at a broad temperature range. (b) Tand values of the synthesized composites at a broad temperature range. The respective values of a commercial elastomer that was provided by our industrial partner are also included.

The dispersion of the fillers in the elastomer matrix was evaluated using transmission electron microscopy and SEM techniques. The transmission electron microscopy images of the unfilled SBR, SBR filled with GnPs, and SBR filled with functionalized GnPs, are shown in Figure VII.3.5. The agglomerated structures are more pronounced when the GnPs are not functionalized (Figure VII.3.5b). The introduced organic groups on the surface of the graphene promoted the dispersion of the fillers in the elastomer (Figure VII.3.5c).

SEM images of the composites filled with SnFs and GnPs composites are shown in Figure VII.3.6. When the GnPs are not functionalized, the GnP fillers aggregate (Figure VII.3.6b). The functionalized GnPs and SnFs are compatible with the SBR matrix and result in a better dispersion of the fillers (Figure VII.3.6c).

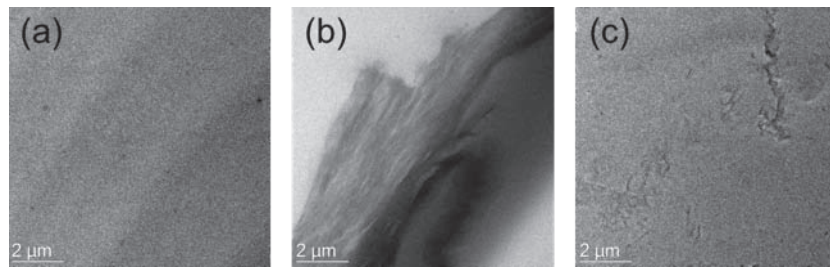


Figure VII.3.5 - Transmission electron microscopy images of the (a) unfilled SBR, (b) SBR filled with GnP, and (c) SBR filled with functionalized GnP



Figure VII.3.6 - SEM images of the (a) unfilled SBR, (b) SBR filled with GnP, and (c) SBR filled with functionalized GnP and SnF

Conclusions

The combination of GnP and SnF can reduce the rolling resistance of the tire and achieve the consumption reduction target of 4%. The synergistic improvements due to the complimentary properties of the new filler material depend on the following synthesis procedures.

- Utilize high surface area GnP and SnF fillers
- Functionalize the GnP surface to increase the interaction with the elastomer
- Optimize the mixing procedure
- Optimize the dispersion of the fillers in the elastomer
- Optimize the crosslinking density of the composite elastomer

References

1. Carpenter Jr., J.A., J. Gibbs, A.A. Pesaran, L.D. Marlina, K. Kelly, "Road transportation vehicles." MRS Bulletin 33, 439–444, 2008.
2. Lindemuth, B.E. "An overview of tire technology." Chapter 1 in "The pneumatic tire" U.S. Department of Transportation, National Highway Traffic Safety Administration, February 2006.
3. Markel, T., A. Brooker, V. Johnson, K. Kelly, M. O'Keefe, S. Sprik, K. Wipke, "ADVISOR: a systems analysis tool for advanced vehicle modeling." J. Power Sources 110, 255–266, 2002.
4. California Energy Commission, Fuel-Efficient Tires and CEC Proceeding Documents Page, www.energy.ca.gov/transportation/tire_efficiency/documents/index.html (accessed January 2008).

Key Fiscal Year 2017 Publications

1. A patent application is being prepared.

VII.4 Advanced Non-Tread Materials for Fuel-Efficient Tires

Lucas Dos Santos Freire, Principal Investigator

PPG Industries, Inc.
440 College Park Dr.
Monroeville, PA 15146
E-mail: dossantosfreire@ppg.com

Roland Gravel, DOE Technology Manager

U.S. Department of Energy
E-mail: Roland.Gravel@ee.doe.gov

Start Date: October 1, 2016	End Date: September 30, 2017	
Total Project Cost: \$1,143,464	DOE share: \$914,771	Non-DOE share: \$228,693

Acknowledgments

Co-Author

Tim Okel, PPG Industries, Inc.

Project Introduction

Precipitated silica is an amorphous particle produced commercially by the acid neutralization of a sodium silicate solution. It is primarily used as a reinforcing filler for synthetic rubber tires. Amorphous silica is known to provide a variety of benefits in tire rubber compounds, including the capability to significantly reduce rolling resistance when compared to carbon black (CB). Much emphasis has been placed on incorporating fuel-efficient silicas into tire tread compounds since the tread is often the single largest contributor to fuel consumption. However, although approximately 50% of the fuel-efficiency impact of a tire is ascribed to the tread, the remaining 50% is attributed to the energy dissipation of non-tread components. Of the non-tread tire components, roughly 20% of the energy losses are attributed to the sidewall, in many cases making it the next largest contributor to fuel-efficiency after the tread. For this reason, the sidewall is an excellent candidate to evaluate new reinforcing materials for non-tread compounds.

Agilon® silicas are a new generation of pretreated silicas which can overcome the problem of mixing silicas with natural rubber (NR), the main rubber in non-tread compounds. These silicas have been shown to provide dramatic improvements in rolling resistance compared to CB in NR-based compounds. The work in this area has been published and presented in industry magazines, conferences, and the 2017 DOE Annual Merit Review and has been well-received [1,2,3,4]. In this work, we will develop sidewall compounds containing non-treated and treated silica fillers. While the main objective is to improve rolling resistance, performance parameters relevant to non-tread components have to be taken into account. Ozone resistance, additives migration, and conductivity, are some of the parameters that are taken into account in this project.

Objectives

The objective of the project is to develop a new silica filler that can increase tire fuel efficiency by 2% while maximizing key performance properties in non-tread tire components compared to current CB-filled sidewall compounds. To achieve these goals, the developed compounds will be required to maintain or improve resistance to degradative forces while reducing compound hysteresis by approximately 25%.

The project will develop two key outcomes:

- Predictive model that maps reinforcing filler characteristics to trends in sidewall performance
- Model sidewall compound that exhibits at least a 25% reduction in energy loss compared to CB, with no more than a 5% loss of resistance to degradative forces (targeting better performance)

Approach

The first step of this project was to understand the tradeoffs in performance of different commercially available materials in model sidewall compounds and identify trends toward improved fuel-efficiency indicators and resistance to degradative forces. This was performed by systematically selecting representative commercial silica and CBs to provide a significant range in filler morphology and surface chemistries, and then evaluating their performance in a model sidewall formulation. Akron Rubber Development Laboratory facilities were used to perform certain sidewall specific tests, such as ozone resistance and antioxidants migration.

Later, similar systematic studies varying the silica morphology and surface chemistry will be performed. First, a series of silica fillers with a wide range of known silica reactants will be prepared and evaluated. Then, selected chemistries will be used to synthesize silica prototypes with different morphologies. Finally, the model sidewall compound will be optimized together with the optimum filler developed during the project to achieve the final project goal of developing a compound with 25% reduction in energy losses while maintaining other compound properties similar to the CB control.

Results

A total of ten commercial reinforcing fillers were compounded as part of the initial work on this project. These included three CBs (N330, CB1, and CB2), four non-functionalized precipitated silicas (i.e., Hi-Sil[®] silicas, designated NFPS1, NFPS2, NFPS3, and NFPS4), and three functionalized precipitated silicas (i.e., Agilon performance silicas, designated FPS1, FPS2, and FPS3). These commercial fillers were selected to represent a filler widely used in sidewall compounds (i.e., N330 CB) and a wide range in filler morphology and surface chemistries. These fillers were compounded in a model sidewall formulation using a 1.25-L internal mixer with two wing tangential rotors. The model formulation involved a 50/50 blend of NR and butadiene rubber. The total filler loading was 50 phr. The three CBs were each evaluated at this 50 phr loading. The silica-based fillers were evaluated at a 50/50 blend with N330 CB. The 50/50 blends involving the functionalized precipitated silicas were further adjusted to get on an equal SiO₂ basis with the non-functionalized precipitated silicas. The compounds were evaluated for several performance parameters including:

- Energy loss as measured by $\tan \delta$, loss modulus, and heat build-up.
- Resistance to degradative forces as measured by fatigue to failure, crack growth, abrasion, tear strength, and ozone resistance.
- Impact on the extraction, migration, and diffusion characteristics of a widely used anti-degradant protection package.
- Additional important criteria including measurements of processing, extrusion, curing, filler dispersion, and electrical resistivity.

The data generated indicates how the commercial fillers compare to each other. Selected test results are presented here. These tests were selected based on their relevance to the project targets. The ability of current commercial fillers to deliver the minimum 25% energy loss reduction (as measured by $\tan \delta$ at 60°C) in a model sidewall formulation as compared to the N330 CB reference is shown in Figure VII.4.1. The figure demonstrates the difficulties CB-based fillers have in meeting the improved rolling resistance goal and also that the silica technology available in the Hi-Sil silica platform (NFPS series) in general further enhances the ability to meet this goal. In addition, the surface functionalization available in the Agilon Performance Silica Platform (FPS series) even further increases the ability to meet the rolling resistance goal.

It is desired to achieve this energy loss and fuel-efficiency improvement without sacrificing degradative forces. Figures VII.4.2 and VII.4.3 show some of the parameters measured and being addressed in this project. It can be seen in the figures that some of the silica fillers have the potential to match or improve the fatigue and aging properties of the sidewall compound compared to the N330 CB control.

The effect of the filler selection on migration of the antioxidant (6-PPD) and wax in the model compound was also studied. Different tests were used to measure this. One of tests performed was heat and light discoloration

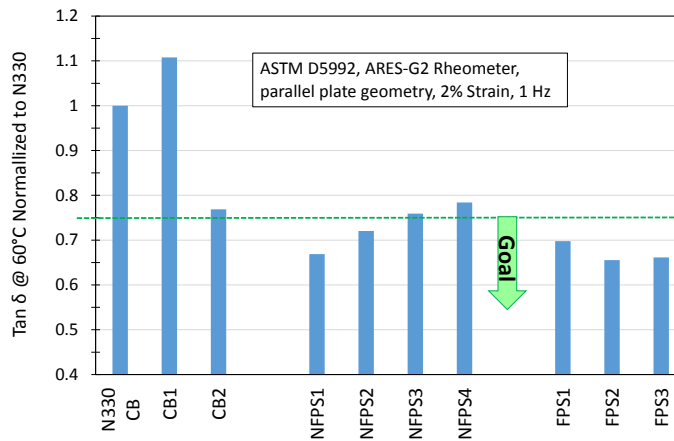


Figure VII.4.1 - Filler vs. $\tan \delta$ at 60°C, normalized to N330

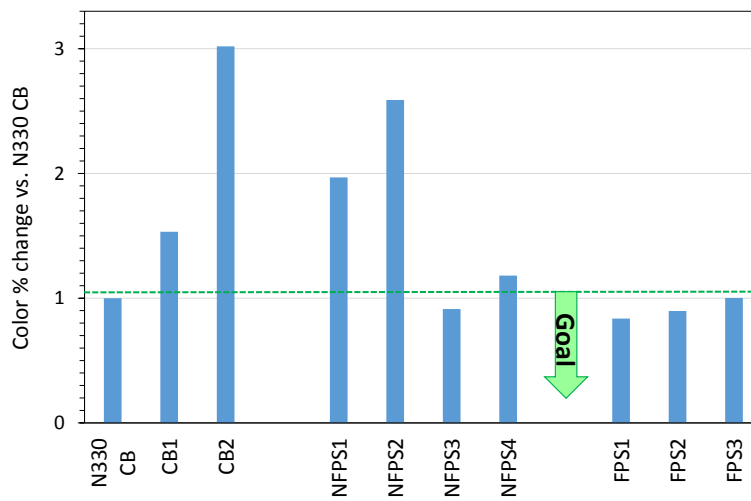


Figure VII.4.2 - Flex fatigue of different fillers

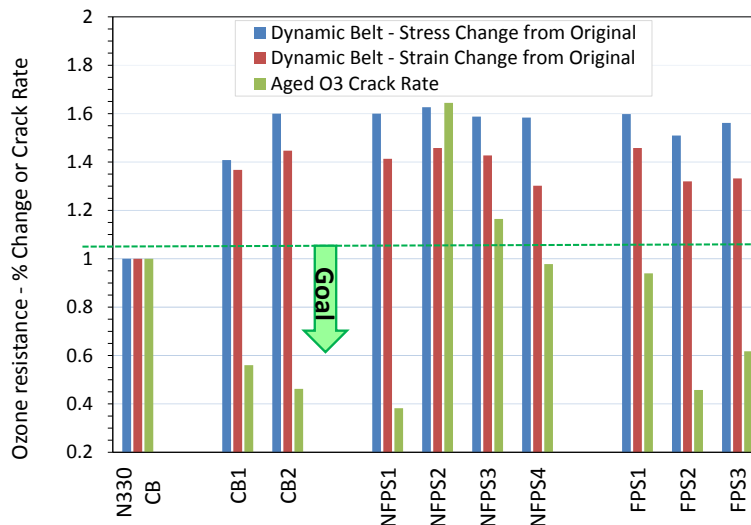


Figure VII.4.3 - Ozone resistance by bent loop and crack growth

of the sidewall compounds according to ASTM D1148-13. In this experiment, an uncured laminate containing two layers, one with 6-PPD and antiozonant wax and the second with a thin white veneer, was fabricated. The color change produced in the white veneer in a QUV oven was measured after 6 h, 24 h, 48 h, and 96 h. The change in color between 6 h and 96 h is related to degradation of the material. Color change relative to the N330 CB control is shown in Figure VII.4.4. It can be seen that all functional silicas and one non-treated silica provide adequate protection to color change. Reduction in color change is attributed to migration of antioxidants from the model sidewall compound to the white veneer.

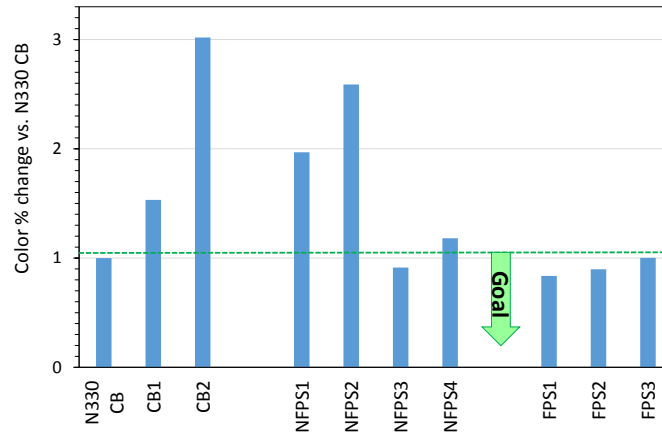


Figure VII.4.4 - Discoloration test

Finally, the diffusion constants for 6-PPD and wax were determined. An example of the data for the laminate-based on N330 is shown in Figure VII.4.5. A two-layer laminate comprised of a 0.25-inch thick layer with 6-PPD and wax next to a 0.25-inch layer without 6-PPD and wax was fabricated. The 6-PPD concentration was measured after curing at 160°C for 19 min and subsequently after aging 36 d at 50°C. The diffusion coefficients were measured for 6-PPD using the measured concentration gradient after curing. Diffusion coefficients were not measured after aging because diffusion was affected by aging. It appears that consumption as well as migration occurred during aging. Results showed that diffusion constants were in the order CB > NFPS > FPS. This is probably because interaction of the silicas with 6-PPD prevented migration. Since 6-PPD is not supposed to bloom to the surface, this might be a desirable property. Wax showed a very fast diffusion for all compounds and basically the wax concentration was homogeneous in both layers right after curing.

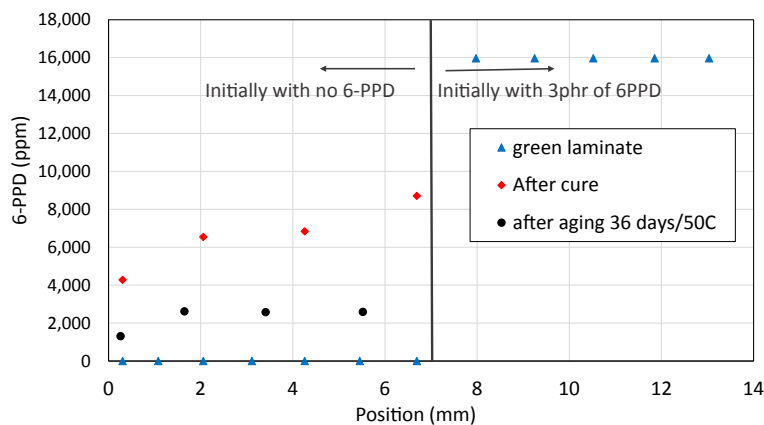


Figure VII.4.5 - 6-PPD concentration profile after cure and aging

Conclusions

A range of commercial reinforcing fillers were evaluated in a model sidewall formulation. Changes in filler morphology and/or surface chemistry can address the minimum 25% energy loss reduction goal. The silica

technology available in the Hi-Sil Silica Technology Platform in general and the surface functionalization available in the Agilon Performance Silica Technology Platform further enhance the ability to meet this goal. While studies showed promise in meeting the energy loss goals, other key performance properties required further investigation and optimization. The data generated so far provided a clear indication of where and to what extent current commercial CB- and silica-based fillers fall short in meeting these other performance goals. The data generated showed that the silica technology available in the Hi-Sil silica platform and the surface functionalization available in the Agilon Performance Silica Technology Platform show promise in producing an improved overall performance balance. The Agilon process will be used to react selected chemistries onto the silica surface and to synthesize treated silicas with chemistries that might improve overall performance in sidewall compounds. Later, silica prototypes with different morphologies will be prepared and systematically studied.

References

1. Okel, Tim, et al. "Agilon Performance Silicas in Natural Rubber Truck Tire Tread Compounds." 180th Technical Meeting of the American Chemical Society Rubber Division, October 2011, paper #70.
2. Okel, Tim, and Justin Martin. "Bringing Innovation to the Surface: Functionalized Silicas for Improved Natural Rubber Truck Tire Vulcanizates." 184th Technical Meeting of the American Chemical Society Rubber Division, October 2013, paper #33.
3. Okel, Tim, and Justin Martin. "Innovating the silica surface for Improved NR truck tire vulcanisates." Presentation at Tire Technology International, Cologne, Germany, February 2014.
4. Okel, Tim, and Justin Martin. "Functionalized silicas for improved NR truck tire vulcanizates." *Rubber World* 249(2), 19–24. 2014.

VII.5 Heavy-Duty Powertrain Optimization

Dean Deter, Principal Investigator

Oak Ridge National Laboratory
1 Bethel Valley Rd
Oak Ridge, TN 37830
E-mail: deterdd@ornl.gov

Roland Gravel, DOE Technology Manager

U.S. Department of Energy
E-mail: Roland.Gravel@ee.doe.gov

Start Date: October 1, 2016	End Date: September 30, 2018	
Total Project Cost: \$700,000	DOE share: \$700,000	Non-DOE share: \$0

Acknowledgments

Co-Authors

Adian Cook, David E. Smith; Oak Ridge National Laboratory

Project Introduction

In the United States, heavy-duty (HD) vehicles account for 22% of the nation's petroleum consumption. These vehicles also generate substantial nitrogen oxide (NO_x) and particulate matter emissions in cities and highways leading to significant environmental and health issues. This project will improve real-world efficiency of HD vehicle powertrain systems in support of DOE's overall goal of energy security and petroleum consumption reduction by approaching powertrain optimization from a variety of important aspects.

Currently in medium-duty and HD trucks, engines and transmissions are often developed separately of each other, having their own controller and set of controls. This is mostly due to the nature of different original equipment manufacturers (OEMs) developing each piece of the hardware, as well as the multiple options the fleet owners have for powertrains and final drives when ordering trucks. While these OEMs have done well in integrating their engines and transmissions together from a drivability standpoint, Oak Ridge National Laboratory (ORNL) believes there is still some opportunity to achieve further efficiency and reduce fuel consumption by utilizing a single supervisory controller to coordinate the two units.

Objectives

This project will investigate optimization opportunities throughout the entire powertrain across multiple vehicle architectures in the HD vehicle sector. The objective of this project is to utilize modeling, simulation, and advanced hardware-in-the-loop experimental methodologies to development optimized HD powertrain and vehicle systems. The results of this project will lead to increased efficiency of HD vehicles and support the 21st Century Truck Partnership.

ORNL, with the support of Cummins Inc, and Eaton Transmission, will conduct such a study first on an HD powertrain consisting of an ISX 450 15-L engine with an Eaton UltraShift Plus automated manual transmission and then on a medium-duty powertrain made of an ISB 6.7-L with an Eaton dual clutch transmission; both will be coordinated using an ORNL supervisory controller. With access to some of the control parameters in the engine and transmission controllers, ORNL will study approaches to mitigate emissions and fuel consumption during regular operation through improved engine and transmission coordination and shift optimization, considering engine operating conditions (efficiency table, emissions characteristics, etc.), and vehicle conditions (final drive, vehicle road load, etc.). The study will also look into possible optimization of cold start conditions, selective catalytic reduction thermal conditions, and diesel particulate filter regeneration events.

Approach

ORNL will characterize a representative powertrain to create a baseline vehicle model. A conventional powertrain composed of a Cummins 15-L ISX450 engine and an Eaton automated manual 10-speed UltraShift Plus transmission will be tested in ORNL's Vehicle Systems Integration (VSI) lab on several standard drive cycles. This powertrain does not feature any integration optimization and will represent our baseline.

ORNL will develop a supervisory controller to interface and further coordinate the engine and transmission controllers without drastic changes to these production controllers. It is expected that some changes will require OEM support as they might be embedded inside the controller code and calibration. Cummins and Eaton have agreed to provide limited engineering support. ORNL will develop controls strategies to identify optimum powertrain operating conditions and minimize emissions and fuel consumption by ensuring that the transmission allows the engine to operate in its best region for those criteria without affecting vehicle operation. Strategies are expected to be based on cost functions that factor in steady-state fuel economy, emissions, and transient behavior during shifts. The new control strategies will optimize shift strategies and component operations through better awareness of system-level conditions. Control strategies will first be tested in simulation using an Autonomie model populated with experimental data collected during powertrain and component testing.

ORNL will characterize state-of-the-art 2017 model year powertrain hardware marketed as SmartAdvantage by Cummins and Eaton, where the controllers have been co-optimized to improve fuel economy. This powertrain will consist of new hardware, including an X-15 Cummins engine and an Eaton "SmartAdvantage" transmission. ORNL will perform powertrain-in-the-loop testing of the state-of-the-art powertrain with the ORNL supervisory controller to debug, optimize, and validate the new coordination of the engine and transmission controllers. The SmartAdvantage powertrain and ORNL supervisory controller will be installed in the VSI lab and tested over various steady-state and transient duty cycles identical to the benchmark study. This will allow researchers to quantify the benefits of an integrated powertrain control over existing state-of-the-art systems.

Results

Powertrain Selection

To quantify the benefit of powertrain integration and optimization, one needs to establish a baseline of the current technology. ORNL currently owns a Cummins 15-L 450 hp model year 2012 ISX15 engine and a Eaton UltraShift Plus 10-speed automated manual transmission (AMT) model number: FO-16E310C-LAS.

These two components were designed to be mechanically assembled into a powertrain but their controls were not optimized to maximize fuel efficiency as a system. This powertrain is representative of most powertrains on the road for Class 8 truck long-haul applications. Therefore, it was chosen as the baseline for unintegrated powertrains. The powertrain was installed in ORNL VSI laboratory to be tested in a hardware-in-the-loop set-up (Figure VII.5.1). The powertrain is physically present in the test cell coupled to a dynamometer and the rest of the vehicle is emulated on a real-time platform to interact with the dynamometer and the engine and transmission such that they behave as if they were installed in a vehicle.

Vehicle Selection

A Kenworth T700 was selected as the emulated vehicle because the ISX engine and Eaton AMT is one of the powertrains available for purchase in that truck. Also, ORNL has access to this vehicle's road load coefficients from which it can populate a representative vehicle model. Finally, ORNL has past data collected in the VSI laboratory for that combination of vehicle and powertrain. The vehicle parameters are listed in Table VII.5.1.



Figure VII.5.1 - ISX450 engine with UltraShift Plus AMT under test in the powertrain test cell at ORNL's VSI Laboratory

Table VII.5.1 - Vehicle Parameters

Parameter	
Axle ratio	3.36:1
Tire radius	0.5 m
Axle efficiency	95.5%
Rolling coefficient	0.00584
Discharge coefficient	0.7149
Frontal area	9.6 m ²
Vehicle mass	50,000 lb, 65,000 lb, and 80,000 lb

Three different vehicle masses will be used during this project to evaluate the effect of mass on the powertrain optimization. The National Academy of Sciences has published an estimate of the mass distribution for five-axle Class 8 tractor-trailers [1] shown in Figure VII.5.2.

Assuming an unladen weight of about 35,000 lbs and a maximum gross vehicle weight of 80,000 lb, it makes sense to select equidistant weight along that distribution. So, the study will emulate total vehicle weights of 50,000 lb, 65,000 lb, and 80,000 lb. The empty vehicle test case is not considered.

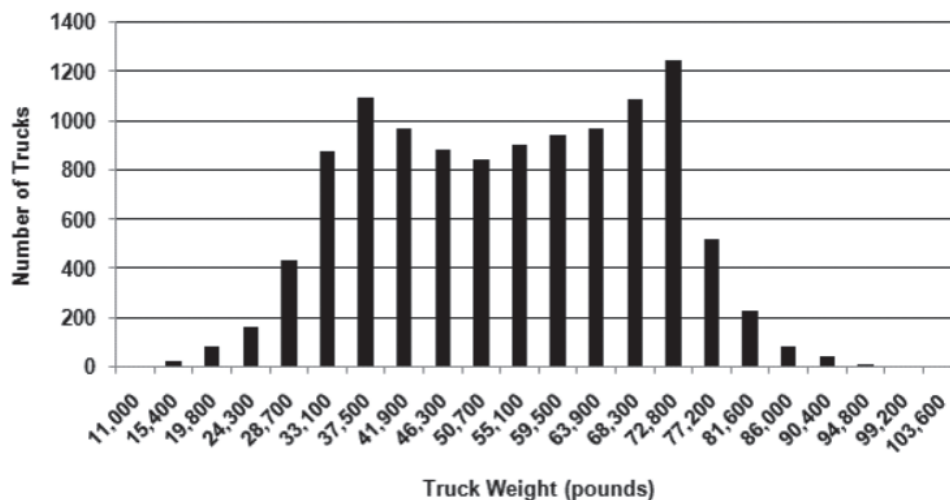


Figure VII.5.2 - Distribution of Class 8 Trucks by On-Road Vehicle Weight (Source: National Academy of Sciences 2008)

Drive Cycle Selection

Powertrain performance needs to be characterized over realistic yet manageable drive cycles. They have to be representative of real-world conditions without being too long so that they can be tested in a reasonable amount of time knowing that each combination of vehicle weight, powertrain integration, and cycle will be repeated three times to assess their repeatability. To provide some consistency, the study will implement the three tests described by the Environmental Protection Agency in the latest greenhouse gas rulemaking Phase 2 and defined in the Greenhouse Gas Emission Model 3.0:

- California Air Resources Board (ARB) transient cycle
- 55 mph cruise cycle with grade
- 65 mph cruise cycle with grade

In addition to these cycles, another cycle was extracted from the ORNL Heavy Truck Duty Cycle (HTDC) database. This cycle was recorded on a Class 8 truck driving around Lexington, Kentucky. This cycle represents real-world driving conditions, including grade, and is elevation neutral; it starts and ends at the same altitude. It also has the merit of being short for a real cycle, about 35 min. Each cruise cycle causes the engine to operate in different regions as demonstrated by the plots in Figure VII.5.3.

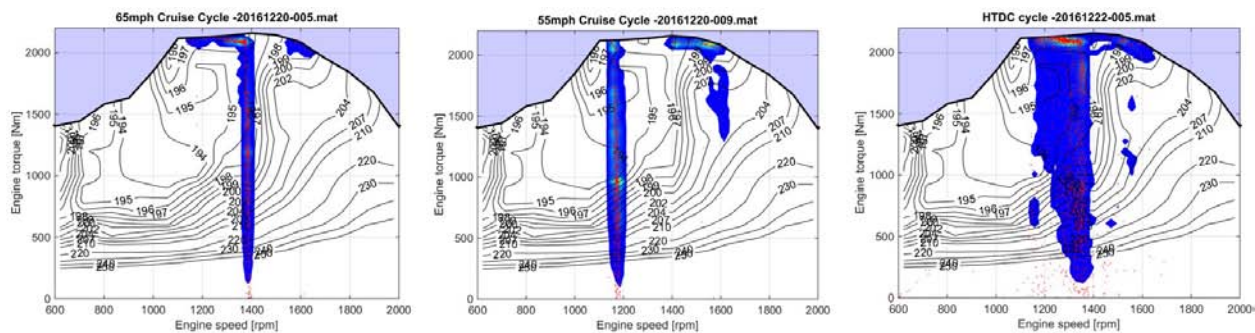


Figure VII.5.3 - Engine operating area for the three high speed tests considered in this study: 65 mph cruise, 55 mph cruise, and HTDC

Experimentation

All four cycles and weight combination were performed in the VSI lab powertrain test cell while maintaining $25^{\circ}\text{C} \pm 5^{\circ}\text{C}$. The following tailpipe emission species were measured: CO_2 , CO, total hydrocarbons, CH_4 , NO_x and NO. Fuel consumption was characterized using two Coriolis fuel flow meters, one on the fuel supply line and one on the return line. Fuel consumption was also calculated using a carbon balance method based on tailpipe emissions and airflow. Tests were performed with a fully warm engine (characterized by an oil temperature exceeding 100°C). After initial warm up, a drive cycle was performed once to condition the powertrain with the same cycle as the test cycle before conducting three repeats of the same cycle. If the coefficient of variation is more than 0.5%, two more repeats are run, otherwise the test is complete and results from that drive cycle are calculated as the average of the three repeats. During this study, results were very repeatable and we never had to perform more than three repeats. Figure VII.5.4 shows the freight efficiency of the baseline powertrain T700 Kenworth truck.

The results make sense. The ARB transient gets the worse fuel economy because of its stop-and-go characteristics, even though it is low speed cycle. The 55 mph cruise cycle gets the best fuel economy because of lower speed and lower aerodynamic drag losses. The 65 mph cruise cycle and HTDC cycle get comparable results due to the similarities in cruise speed around 65 mph. As expected, fuel economy is better for the lightly loaded truck but freight efficiency is better for the fully loaded truck.



Figure VII.5.4 - Fuel consumption for different cycles and vehicle weight

Vehicle Modelling

A model of a Class 8 truck was built with Autonomie. It is parameterized to represent the Kenworth T700 previously emulated in the VSI laboratory powertrain in the loop environment using the same vehicle parameters. Currently, the baseline model is finished as are the baseline controls. The model has been validated against the powertrain testing to make sure it is a valid platform for controls optimization and development. Validation results are found in Table VII.5.2.

Table VII.5.2 - Error Between Experimental and Simulation

Cycle	50,000 lb	65,000 lb	80,000 lb
ARB	-2.5%	-2.0%	-1.4%
55 mph w/Grade	0.8%	0.7%	0.4%
65 mph w/Grade	1.0%	0.9%	0.7%
HTDC	0.5%	0.5%	0.6%

ORNL is now working on changing the controls of the baseline model to be housed in a single supervisory block that will then be compiled onto a Raptor prototyping controller in the coming months as seen in Figure VII.5.5. This will allow ORNL to start working on communication and control pathways for the hardware in the test cell.

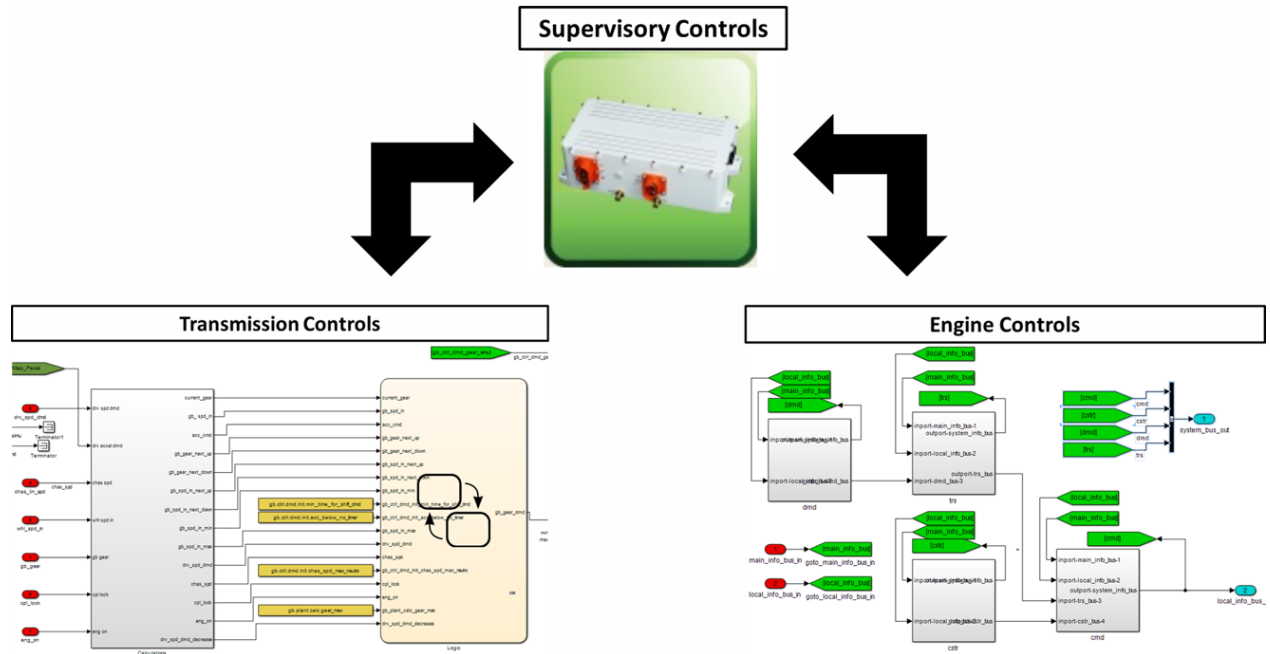


Figure VII.5.5 - ORNL is beginning to work on modelling the new single supervisory controller using the offline validated model

Conclusions

Ultimately the project is currently positioned to start making strides into the current state of the art powertrain systems. With a model that is well validated, it allows ORNL to begin looking at areas for improvement and start validation on optimization and calibration algorithms for the coming supervisory controller. In the coming months, the ORNL team will begin developing controls to take advantage of the coming advanced controller hardware.

References

1. National Academy of Sciences. “Technologies and Approaches to Reducing the Fuel Consumption of Medium and Heavy-Duty Vehicles” prepublication copy, March 2010, p. 5–45. Original source: Federal Highway Administration, Vehicle Travel Information System, 2008.

VIII. Index of Principal Investigators

A

Agrawal, Ajay	172, 296
Ajayi, Oyelayo	498
Amar, Pascal	436

B

Battiston, Paul A.	468
Bays, J. Timothy	302, 346
Bittle, Joshua.....	296
Busch, Stephen.....	29

C

Carrington, David B.....	128
Ciatti, Stephen.....	82, 267
Confer, Keith.....	458
Cosimbescu, Lelia.....	513
Curran, Scott	93, 279

D

Dec, John E.	50, 272
Deter, Dean	591
Dos Santos Freire, Lucas	575, 586

E

Edwards, K. Dean	136
Ekoto, Isaac W.	58

F

Fenske, George R.	518
Fernandez, Hermes	492
Fioroni, Gina.....	322
Freitag, Alex.....	354

G

Gangopadhyay, Dr. Arup K.....	530, 536
Gao, Pu-Xian.....	428
Genzale, Caroline L.	193
Goldsborough, S. Scott	77, 318

H

Haworth, Daniel C.	145
Hsu, Stephen	547

I

Ippoliti, Michael.....	361
------------------------	-----

K

Karkamkar, Abhijeet	413
Kim, Seung Hyun.....	179
Kocher, Lyle.....	488
Kokjohn, Sage.....	166
Kolodziej, Chistopher P.	205, 222

L

Lavoie, George A.	333
Lawler, Benjamin.....	348
Lee, Chia-Fon	151
Lee, Seong-Young.....	157
Lewis, Samuel A.	252

M

McNenly, Matthew	122, 327
Mendler, Charles.....	464
Moses-DeBusk, Melanie.....	247
Mueller, Charles J.	290
Musculus, Mark PB	36, 284

O

Oefelein, Joseph C.	141
--------------------------	-----

P

Parks, Jim.....	390
Partridge, Bill.....	395
Patil, Chinmaya.....	481
Pfefferle, Lisa.....	340
Pickett, Lyle M.....	43
Pihl, Josh.....	370
Pitz, William J.....	111, 308, 312
Polyzos, Georgios.....	581
Powell, Christopher F.....	72

Q

Qu, Jun.....	505
--------------	-----

R

Rappé, Kenneth G.....	422
Ratcliff, Matt.....	233
Ruth, Michael.....	442
Ryan, Emily.....	186

S

Salari, Kambiz.....	567
Sappok, Alexander.....	473
Scarcelli, Ricardo.....	86
Schoegl, Ingmar.....	336
Seong, Hee Je.....	401
Sjöberg, Magnus.....	198, 215
Sluder, Scott.....	210
Som, Sibendu.....	65
Splitter, Derek.....	261
Stewart, Mark.....	407
Storey, John M.E.....	252, 525
Szybist, James.....	98, 227

T

Toops, Todd J. 104, 241, 384

W

Wang, Qian J. 554

Wang, Yong 377, 417

Whitesides, Russell 117

Whittaker, Richard K. 361

Wooldridge, Margaret 365

Wu, Gefei 562

Y

Yee, Justin 453

Z

Zhao, Bin 541

Zigler, Brad 255

Zukouski, Russell 447

IX. Project Listings by Organizations

Argonne National Laboratory

I.6	Advancements in Fuel Spray and Combustion Modeling with High Performance Computing Resources	65
I.7	Fuel Injection and Spray Research Using X-Ray Diagnostics	72
I.8	RCM Studies to Enable Gasoline-Relevant Low Temperature Combustion.....	77
I.9	Advances in High Efficiency Gasoline Compression Ignition	82
I.10	Advanced Ignition Systems for Gasoline Direct Injection (GDI) Engines	86
II.2	Studies of Research Octane Number (RON) and Heat of Vaporization (HoV).....	205
II.5	Fuel Effects on EGR and Lean Dilution Limits on SI Combustion	222
II.13	Fuel Effects On Combustion Stability and Noise for GCI	267
II.22	Kinetic Mechanism Development and Validation	318
IV.6	Ash-Durable Catalyzed Filters for Gasoline Direct Injection (GDI) Engines.....	401
VI.1	Surface and Lubricant Interactions	498
VI.4	High Efficiency Lubricant Oils, Additives, and Coatings	518

Boston University

I.26	Development and Multiscale Validation of Euler-Lagrange-Based Computational Methods for Modeling Cavitation Within Fuel Injectors	186
------	---	-----

CALSTART

III.4	Innovative Dual-Fuel Aftermarket Emissions Solution.....	361
-------	--	-----

Cummins Inc.

V.2	Cummins/Peterbilt SuperTruck II.....	442
V.10	Cummins 55% BTE Project.....	488

Daimler Trucks North America

V.4	Improving Transportation Efficiency Through Integrated Vehicle, Engine, and Powertrain Research – SuperTruck 2	453
-----	--	-----

Delphi

V.5	Ultra-Efficient Light-Duty Powertrain with Gasoline Low Temperature Combustion	458
-----	--	-----

Delphi Automotive Systems, LLC

V.11	Solenoid Actuated Cylinder Deactivation Valve Train for Dynamic Skip Fire	492
------	---	-----

Eaton Corporation

V.9 Integrated Boosting and Hybridization for Extreme Fuel Economy and Downsizing481

Envera LLC

V.6 High Efficiency Variable Compression Ratio Engine with Variable Valve Actuation and New Supercharging Technology: VCR Technology for the 2020 to 2025 Market Space.....464

Filter Sensing Technologies, Inc.

V.8 Improved Fuel Efficiency Through Adaptive Radio Frequency Controls and Diagnostics for Advanced Catalyst Systems.....473

Ford Motor Company

VI.6 Development of PAG (Polyalkylene Glycol)-Based Lubricant for Light- and Medium-Duty Axle Applications530

VI.7 Power Cylinder Friction Reduction Through Coatings, Surface Finish, and Design536

General Motors LLC

V.7 Lean Miller Cycle System Development for Light-Duty Vehicles.....468

George Washington University

VI.9 Integrated Friction Reduction Technology to Improve Fuel Economy Without Sacrificing Durability547

Georgia Institute of Technology

I.27 Turbulent Spray Atomization Model for Diesel Engine Simulations193

Lawrence Livermore National Laboratory

I.14 Chemical Kinetic Models for Advanced Engine Combustion.....111

I.15 Model Development and Analysis of Clean and Efficient Engine Combustion.....117

I.16 Improved Solvers for Advanced Combustion Engine Simulation.....122

II.20 Fuel Property Blending Model308

II.21 Kinetic Mechanism Development312

II.24 Virtual Fuel Blend Optimization for Advanced Compression Ignition Engines327

VII.1 DOE’s Effort to Improve Heavy Vehicle Fuel Efficiency Through Improved Aerodynamics567

Los Alamos National Laboratory

I.17 2017 KIVA-hpFE Development: A Robust and Accurate Engine Modeling Software128

Louisiana State University

II.26 Micro-liter Fuel Characterization and Property Prediction336

Michigan Technological University

I.22	Spray-Wall Interaction at High-Pressure and High-Temperature Conditions	157
------	---	-----

National Renewable Energy Laboratory

II.7	Fuel Effects on Emissions and Aftertreatment	233
II.11	Ignition Kinetic Experiments and Simulations to Support Advanced Engine Combustion Development.....	255
II.23	Small Volume Fuel Autoignition Tester.....	322

Navistar, Inc

V.3	SuperTruck 2 Advanced Combustion Development at Navistar	447
-----	--	-----

NG1 Technologies

III.4	Innovative Dual-Fuel Aftermarket Emissions Solution.....	361
-------	--	-----

Northwestern University

VI.10	A Novel Lubricant Formulation Scheme for 2% Fuel Efficiency Improvement.....	554
-------	--	-----

Oak Ridge National Laboratory

I.11	High Efficiency Clean Combustion in Light-Duty Multi-Cylinder Engines.....	93
I.12	Stretch Efficiency for Combustion Engines: Exploiting New Combustion Regimes	98
I.13	Neutron Imaging of Advanced Transportation Technologies	104
I.18	Accelerating Predictive Simulation of Internal Combustion Engines with High Performance Computing	136
II.3	Improving Vehicle Fuel Economy Through Increasing Fuel Octane Ratings	210
II.6	Fuel Pressure Sensitivity and High-Load EGR Dilution Effects in SI Combustion.....	227
II.8	Fuel Impacts on Emissions Control Performance and Durability	241
II.9	Fuel Impact on GDI PM Formation and Gaseous Emissions During Cold-Start.....	247
II.10	Fuel Contribution to PM from Kinetically-Controlled Combustion	252
II.12	Fuel Effects on Low Speed Pre-Ignition.....	261
II.15	Accelerate Development of ACI/LTC.....	279
IV.1	Joint Development and Coordination of Emission Control Data and Models: Cross-Cut Lean Exhaust Emissions Reduction Simulations (CLEERS) Analysis and Coordination	370
IV.3	Low-Temperature Emissions Control to Enable Fuel-Efficient Engine Commercialization.....	384
IV.4	Emissions Control for Lean-Gasoline Engines.....	390
IV.5	Cummins-ORNL SmartCatalyst CRADA: NO _x Control and Measurement Technology for Heavy-Duty Diesel Engines	395

Oak Ridge National Laboratory (Continued)

VI.2 Compatability of Lubricant Additives with Non-Ferrous Bearing Materials and Wear Mechanism in Sooted Engine Oils505

VI.5 Lubricant Effects on PM Formaiton, Emissions Control, and Vehicle Fuel Economy525

VII.3 Improved Tire Efficiency Through Elastomeric Polymers Enhanced with Carbon-Based Nanostructured Materials.....581

VII.5 Heavy-Duty Powertrain Optimization591

The Ohio State University

I.25 Development of a Physics-Based Combustion Model for Engine Knock Prediction 179

Pacific Norhwest Natiional Laboratory

II.19 Fuel Property Database302

III.1 Unconventional and Renewable Hydrocarbon Fuels.....346

IV.2 CLEERS Aftertreatment Modeling and Analysis377

IV.7 Fuel-Neutral Studies of PM Transportation Emissions407

IV.8 Next Generation Ammonia Dosing System.....413

IV.9 Advanced Emission Control for High-Efficiency Engines.....417

IV.10 Development and Optimization of a Multi-Functional SCR-DPF Aftertreatment System for Heavy-Duty NO_x and Soot Emission Reduction422

VI.3 Technology Innovation: Base Fluids, Additives, and Coatings513

The Pennsylvania State University

I.20 Development and Validation of Predictive Models for In-Cylinder Radiation and Wall Heat Transfer 145

PPG Industries, Inc.

VII.2 Advanced Bus and Truck Radial Materials for Fuel Efficiency575

VII.4 Advanced Non-Tread Materials for Fuel-Efficient Tires.....586

Robert Bosch, LLC

III.3 High-Efficiency Cost-Optimized Spark-Ignited Natural Gas (HECO-SING) Engines – 2017...354

Sandia National Laboratories

I.1 Light-Duty Diesel Combustion.....29

I.2 Heavy-Duty Low-Temperature and Diesel Combustion & Heavy-Duty Combustion Modeling36

I.3 Spray Combustion Cross-Cut Engine Research43

Sandia National Laboratories (Continued)

I.4	Low-Temperature Gasoline Combustion (LTGC) Engine Research	50
I.5	Gasoline Combustion Fundamentals	58
I.19	Large Eddy Simulation Applied to Advanced Engine Combustion Research	141
II.1	Alternative Fuels DISI Engine Research: Autoignition Metrics	198
II.4	Advanced Light-Duty SI Engine Fuels Research: Multiple Optical Diagnostics of Well-Mixed and Stratified Operation	215
II.14	Autoignition Fundamentals of Fuels for Multi-Mode Boosted SI and LTGC Engines	272
II.16	Co-Optima Project E2.2.2: Accelerate Development of ACI/LTC, Fuel Effects on RCCI Combustion	284
II.17	Improved Mixing-Controlled Combustion Technologies and Fuels for High-Efficiency Compression Ignition Engines	290

Stony Brook University

III.2	Single-Fuel Reactivity Controlled Compression Ignition Combustion Enabled by Onboard Fuel Reformation	348
-------	---	-----

University of Alabama

I.24	Development and Validation of Physics-Based Submodels of High Pressure Supercritical Fuel Injection at Diesel Conditions	172
II.18	Characterization of Biomass-Based Fuels and Fuel Blends for Low-Emissions, Advanced Compression Ignition Engines	296

University of Connecticut

IV.11	Metal Oxide-Based Nano-Array Catalysts for Low Temperature Diesel Oxidation	428
-------	---	-----

University of Illinois at Urban-Champaign

I.21	Model Development for Multi-Component Fuel Vaporization and Flash Boiling	151
------	---	-----

University of Michigan

II.25	Dynamic Species Reduction for Multi-Cycle CFD Simulations	333
III.5	Utilizing Alternative Fuel Ignition Properties to Improve SI and CI Engine Efficiency	365

University of Tennessee, Knoxville

VI.8	Hybrid Ionic-Nano-Additives for Engine Lubrication to Improve Fuel Efficiency	541
------	---	-----

University of Wisconsin

I.23	Development and Validation of a Lagrangian Soot Model Considering Detailed Gas Phase Kinetics and Surface Chemistry	166
------	---	-----

Valvoline LLC

VI.11 Improved Fuel Economy Through Formulation Design and Modeling562

Volvo Group Trucks North America

V.1 Volvo SuperTruck 2: Pathway to Cost-Effective Commercialized Freight Efficiency.....436

Yale University

II.27 The Development of Yield-Based Sooting Tendency Measurements and Modeling to Enable
Advanced Combustion Fuels340

(This page intentionally left blank)

U.S. DEPARTMENT OF
ENERGY

Office of
**ENERGY EFFICIENCY &
RENEWABLE ENERGY**

For more information, visit:
energy.gov/eere/vehicles/vehicle-technologies-office

DOE/EE-1708 • May 2018